

The Effect of Swirl on Array of Turbulent Impinging Jets

Sudipta Debnath*, Md Habib Ullah Khan, Zahir U. Ahmed, Md. Mahmudul Alam

Department of Mechanical Engineering, Khulna University of Engineering & Technology, Khulna-9203, BANGLADESH

ABSTRACT

Impinging jets are widely used for their effective heat and mass transfer for several decades. Arrays of jet impingement have also been studied before due to its practical relevance to electronics cooling. A number of jet variations and jet-to-jet orientations have previously been studied, mainly to further improve the magnitude and uniformity of heat transfer. In recent years, swirling jets has also gained interest in heat transfer application due to their inherent mixing and spreading characteristics, which is believed to be an improvement on overall heat and mass transfer. As such, this paper numerically investigates an array of circular jets with and without swirl that impinges vertically onto a flat surface located at a fixed vertical distance $H = 2D$ and at Reynolds number equals to 11,600, where D is the nozzle diameter. As the entire was symmetric, only quarter of the model was constructed for numerical analysis to save computational cost. In this case, numerical calculations were done via commercial software package ANSYS Fluent using SST $k-\omega$ turbulence model. Inlet conditions were taken from experimental data. The jet flows were in downward direction and gravity was not considered. This paper also compares numerical predictions with previously published literature for non-swirling and swirling jets.

Keywords: Swirl jet, Impingement, Turbulence, Heat transfer, CFD.

1. Introduction

Jet impingement is one of the most effective media for removing heat from heated surfaces with high heat flux. The high heat removal rate of jet impingement had gained a prior position of research topic among the researchers for several decades. Impinging jets are widely used in various engineering and industrial applications, such as cooling of turbine blades and micro electric components, quenching and annealing of non-ferrous sheet metals, tempering of glass, freezing of tissues in cryosurgery [1].

Jet is a stream of fluid that is projected into a surrounding medium, usually from some kind of a nozzle, aperture or orifice. Jets can travel long distances without dissipating. Swirl means to move with an eddying or whirling motion.

In majority of the previous research, orthogonal jet impingements onto flat surfaces or plates from which heat transfer occurs are primarily focused. The jet flows emanating from a nozzle may either be non-swirling or swirling, with their own pros and cons. Jets can also be categorized into circular jet, slot jet, inclined jet etc depending on the orifice opening or geometric arrangements. Their effects on fluid flow and heat transfer behavior are also different. For example, heat transfer by convection from a hot gas jet to a plane surface was observed to increase as twice as the initial value with the change of axis-symmetric angle of the jet from 15° - 90° [2]. Again, for the same flow rate the circular jet yielded 8% higher heat transfer than the slot jet [3]. In comparison to non-swirling jet, swirling jets were examined by many researchers. Research out comes suggest that swirling jets are beneficial over non swirling jets. It had been found that swirling jet has higher Nusselt number and better uniformity in heat-transfer which is the prior criteria in many cooling

operations to reduce fracture and to improve grain growth for higher strength [4].

In order to experiment that whether increasing the number of jets increases the heat transfer or not jet arrays were studied by several researchers during the past decades. Jet interference in impingement arrays is the main striking difference compared to a single jet. It is reported that in case of array impinging jet the nozzles spacing of from 4-6 diameters results best heat transfer results [5]. Results of many investigations on circular non-swirling jets are in a good agreement that single jet yields better heat transfer than that of array impinging jets [6]. The central jet has the shortest core and the highest kinetic energy due to higher number of neighboring jets and the reverse is true for peripheral jets [7]. For larger jet-to-jet distance regardless of jet-to-plate distances the cross flow doesn't disturb the fluid motion of the neighboring jets. It had also been reported that the jet-to-jet distance is the major factor whereas jet-to-plate is the minor [8]. The above results are valid only for non-swirling jets. As such, it would be interesting to examine swirling flows in arrays, as single swirling jets were found to have rather different behaviors.

In this paper, an array of circular air jets is studied to determine the effect of swirl on heat transfer during cooling by an array of swirl jets. The effect of swirl jets that impinged vertically onto a flat surface located at a fixed vertical distance $H/D = 2$ and at Reynolds number equals to 11,600 were studied. The widely used $k-\omega$ model does not properly represent the flow features and highly over predicts the rate of heat transfer and yields physically unrealistic behavior [9]. SST $k-\omega$ turbulence model is a combination of the k -epsilon in the free stream and the k -omega models near the walls. It does not use wall functions and tends to be most accurate

* Corresponding author. Tel.: +88-01759999904
E-mail addresses: ssudipta69@gmail.com

when solving the flow near the wall. Hence this model had been used to calculate the results in this analysis.

2. Numerical Methodology

An array of 25 circular nozzles were considered for developing the swirling and non-swirling impinging jets. The nozzles are arranged in inline and staggered arrangements. All of them were axi-symmetric, equally spaced in 3 circles around a central nozzle in which the diameter of first circle is $5D$, the second circle $9D$ and the third circle $13D$. The diameter of each nozzle is 40 mm, the distance between the centers of two corresponding nozzle is 80 ($2D$) mm while the distance between them is 40 (D) mm. As the entire two models were symmetric, only quarters of the models were constructed for numerical analysis to save computational cost. Jet-to-plate distance was $H=2D$ and the radial extent of circular plate is considered $16D$.

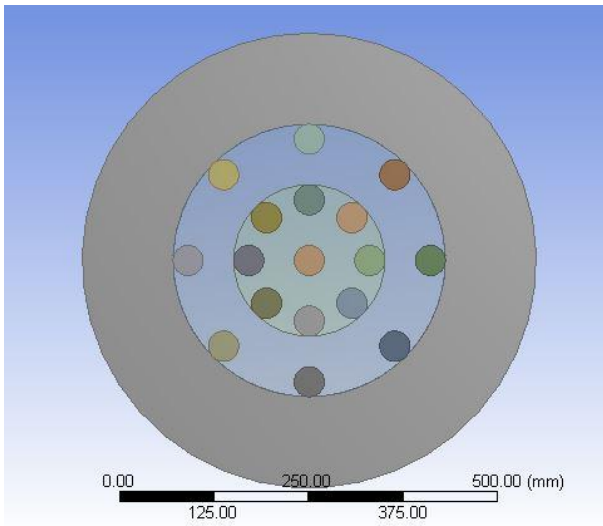


Fig.1 Top view of the array of nozzles

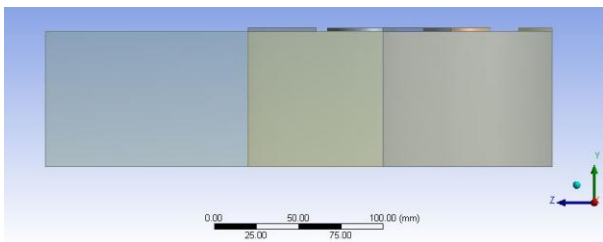


Fig.2 Front view of the array of nozzles

For numerical simulation, SST $k-\omega$ viscous model is used for solving the problem. Air was taken as fluid with the following properties: Density- 1.225 kg/m^3 , Specific Heat- 1006.43 J/kg-K , Thermal Conductivity- 0.0242 W/m-K and Viscosity- $1.78e-05 \text{ kg/m-s}$. Inlet conditions of the swirling impinging jets were taken from Ahmed et al. [11] in which swirling jet was produced with an aerodynamic swirl generator. The profile of the data was set as the inlet boundary

conditions in all nozzles. The fluid inlet temperature is set to ambient (300K). Outlet boundary was set as pressure outlet with backflow turbulent intensity 5% and backflow turbulent viscosity ratio 10 similar to the numerical simulation of Ahmed et al. [12]. Symmetry boundary condition was applied in two side surfaces for non-swirling jets and periodic boundary conditions for swirling jets. In this regard, corresponding surfaces were match controlled during meshing in order to impose periodic boundary. The pressure velocity coupling was solved using the coupled solver with Green-Gauss Cell special discretization for gradients, PRESTO for pressure and second order upwind was used for momentum, turbulent kinetic energy, specific dissipation rate and energy. All the residuals were set to 10^{-05} for accuracy except energy to 10^{-06} . Mesh consisting of 898k nodes was used to predict the final result. Inflation was applied with 15 layers and growth rate of 1.2 near the plate region and the mesh was generated from fine mesh near the axis to coarser mesh in the radially outward direction.

3. Data Validation

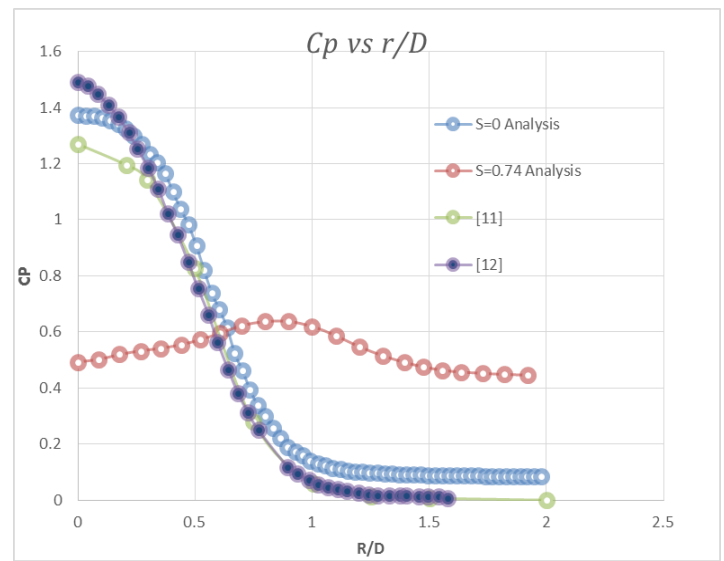


Fig.3 Data validation of C_p vs R/D chart

Fig. 3 presents a comparison of the effect of swirl on the radial distributions of (impingement surface) static pressure for $S=0$ and 0.74 and $H=2D$ at $Re=11600$ between the current simulation data and experimental data derived from the literature. The current numerical data is found to be in good agreement with the literature except for swirl number 0.74 C_p decreases (with radial distance) from a maximum at the stagnation point and shows a Gaussian-like distribution, with maximum C_p at the center line similar to non-swirling flows. The radial position of the maximum C_p moves outward due to the higher centrifugal effects as swirl number increases. The reduction is largely attributed to the axial deceleration of the swirl flow.

4. Results and Discussion

Fig. 4 shows the C_p variation for non-swirl and swirl inline jets at impinging plane along the radial line in horizontal direction where $r/D=0$ indicates the origin and $r/D=16$ indicates the end of the fluid body. It is observed from the figure that for non-swirl, reductions of C_p occur particularly around the impingement regions between the jets and gradually decreases in between $6D$ to $16D$.

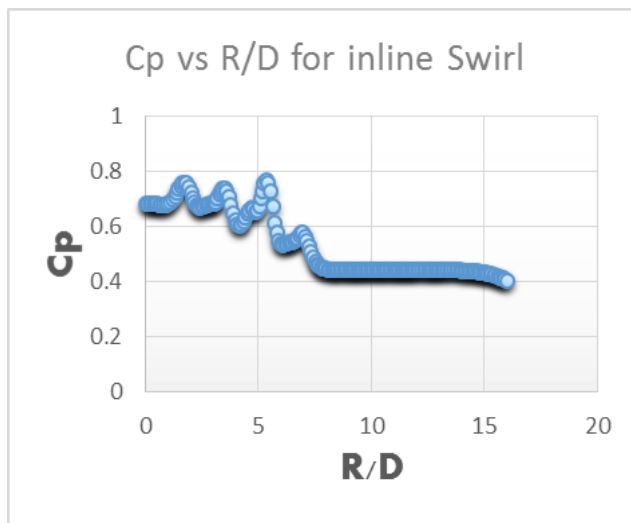
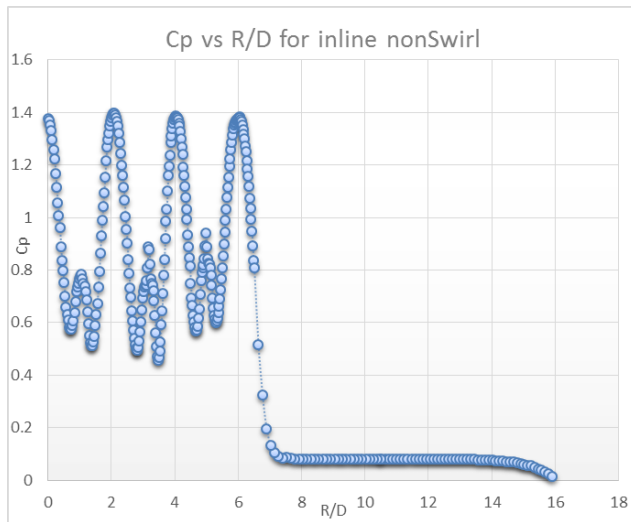


Fig.4 C_p for $S=0$ and $S=0.74$ at inline arrangement of nozzles

For swirl it is observed that gradual increasing and reduction of C_p happened in between impinging region ($r/D < 8$). The radial position of the maximum C_p moves outward due to the higher centrifugal effects as swirl number increases. The results show that pressure is found to be the maximum in the stagnation regions where the flow strikes the plate and then it reduces fast both radially and circumferentially. For swirl flow the pressure is relatively more uniformly distributed over the impingement plate than non-swirl flow.

Fig. 5 represents the velocity streamline of array impinging jet for non-swirl and swirl flow for both inline and staggered arrangements of jets. The origin $(0,0)$ corresponds to the center and the flow is distributed radially between 0 to $16D$.

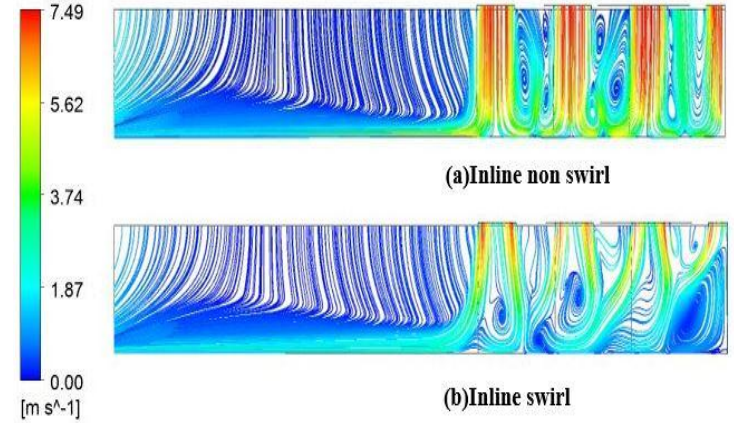


Fig.5 Velocity streamlines for $S=0$ and 0.74 at inline arrangement of nozzles

It is seen that a recirculation region appears between two jets for both non-swirling and swirling flows. For non-swirling jets, the jets create a fountain, with an upward movement of the flow, whereas in swirling jets such upward fountain is not evident. Rather, the flow passes between recirculating zones, which occurs between the first two jets from the center and between the jets near the wall. It is also clear from the above streamlines that for non-swirl flow the jet strikes the heated plate whereas swirl jets deviates from well before the impingement surface resulting a moderate recirculation around the stagnation zone. It is clear that from $4.5 D$ to $16 D$ both the streamline of swirl flow and non-swirl flow are closely attached to the heated plate. Depending on the distance or proximity of the neighboring jet the flow field may vary with significant changes which may affect the heat transfer distribution over the impingement surface. The results for velocity streamlines ensure that the strength of recirculation for swirl flow is greater than that of non-swirl flow and the distance between the neighboring jets plays a great role in this recirculation effect.

Fig. 6 shows contour map of convective heat transfer coefficient (h) over the range $S=0$ and $S=0.74$ in near-field ($H=2D$) impingement for the case of inline arrangement.

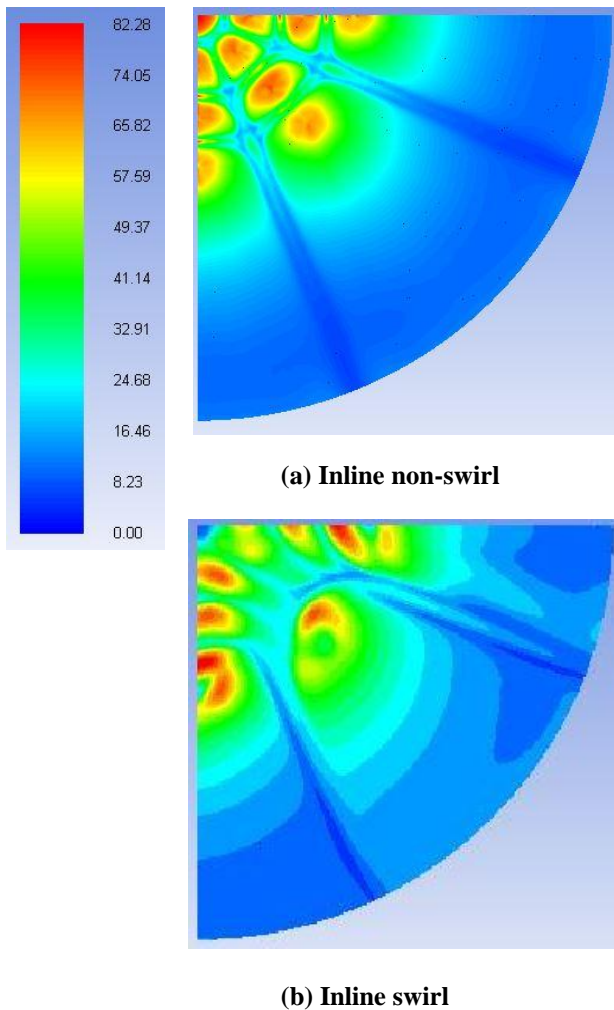


Fig.6 Convective heat transfer coefficient for $S=0$ and 0.74 at inline arrangement of nozzles

For $S=0$, a higher convective heat transfer coefficient (h) band appears outside the jet center with a lower h zone occurring immediately at the jet center. Outside the periphery of this higher h zone, another (outer) low h zone occurs, before heat transfer peaks up again at even further radial distances. For the swirling jets, a strikingly difference heat transfer behavior is predicted. In this regard, maximum heat transfer occurs between the neighboring nozzles, not below the nozzle as in the case of non-swirling jet arrays. Additionally, the lowest heat transfer occurs under the central jet, which perhaps due to the recirculation seen in the velocity streamline. The occurrence of relatively two maxima in convective heat transfer coefficient (inner and outer) have been attributed to the rapid change of radial velocity in the streamline deflection region and to destruction of the thermal boundary layer by the large-scale eddies which strikes the surface. The minima in h around the jet center may also be attributed to the weak penetration of shear layer induced turbulence, which is particularly true at $H = 2D$ due to this relatively small impingement distance.

5. Conclusion

This paper describes the behaviors of an array of incompressible turbulent impinging air jets for both non-swirl and swirl flows. The governing equations are solved using a commercial software package Ansys Fluent v16.2, by using a turbulence model SST $k-\omega$. The study is performed for two conditions: non-swirling ($S = 0$) and highly swirling ($S = 0.74$) for a nozzle-to-plate distance of $2D$ at $Re=11,600$. Velocity streamline, pressure distribution, heat transfer distribution are investigated for both of these arrangements separately. The results for velocity streamlines ensure that the strength of recirculation for swirl flow is greater than that of non-swirl flow. The distance between the neighboring jets plays a great role in this recirculation effect. The pressure distribution indicated a more uniform distribution for swirl impinging arrays than its non-swirling counterpart. This distribution also plays a great role for achieving a better result in the goal of impingement cooling. Convective heat transfer coefficient distribution showed the larger heat transfer zones in the stagnation zone for non-swirling jets and between the neighboring jets for swirling jets.

NOMENCLATURE

- C_p : Coefficient of pressure
- P : Pressure, Pa
- S : Swirl Number
- h : Convective heat transfer coefficient
- R : Radial distance, m
- T : Temperature, K
- D : Diameter of nozzle, m
- H : Distance between nozzle tip and plate, m
- Re : Reynolds Number

REFERENCES

- [1] Behnia, M., Parneix, S., and Durbin, P., Accurate modeling of impinging jet heat transfer, Center for Turbulence research, Annual Research Briefs, pp. 149-164, 1997
- [2] Womac, D. J., Ramadhyani, S., and Incropera, F. P., Correlating equations for impingement cooling of small heat sources with single circular jets, Journal of Heat Transfer, vol. 115(1), pp. 106-155, 1993
- [3] Fitzgerald, J. A., and Garimella, S. V., Flow field effects on heat transfer in confined jet impingement, Oceanographic Literature Review, V. 1(45), pp. 199, 1998
- [4] Cooper, D., Jackson, D.C., Launder, B.E., Liao, g.x. Impinging jet studies for turbulence model assessment. Part I: Flow-field experiments, Int. J. Heat Mass Transfer, Vol. 36, pp. 2675-2684, 1993

- [5] Brevet, P., Dejeu, C., Dorignac, E., Jolly, M., and Vullierme, J., J., Heat transfer to a row of impinging jets in consideration of optimization, *International Journal of Heat and Mass Transfer*, vol. 45(20), pp. 4191-4200, 2002
- [6] Viskanta, R., Heat transfer to impinging isothermal gas and flame jets, *Experimental Thermal and Fluid Science*, vol. 6(2), pp. 111-134, 1993
- [7] Geers, L. F., Tummers, M. J., and Hanjalic', K., Experimental investigation of impinging jet arrays, *Experiments in Fluids*, vol. 36(6), pp. 946-958, 2004
- [8] Wienand, J., Riedelsheimer, A., and Weigand, B., Numerical study of a turbulent impinging jet for different jet-to-plate distances using two-equation turbulence models, *European Journal of MechanicsB/Fluids*, vol. 61, pp. 210-217, 2017
- [9] Behnia, M., Parneix, S., and Durbin, P. A., Prediction of heat transfer in an axisymmetric turbulent jet impinging on a flat plate, *International Journal of Heat and Mass Transfer*, vol. 41(2), pp. 1845-1855, 1998
- [10] Geers, L. F., Multiple impinging jet arrays: an experimental study on flow and heat transfer, PhD Thesis, Technical University, Delft , The Netherlands, 2004
- [11] Ahmed, Z. U., Al-Abdeli, Y. M., and Guzzomi, F. G., Impingement pressure characteristics of swirling and non-swirling turbulent jets, vol. 68, *Experimental Thermal and Fluid Science*, pp.722–732, 2015
- [12] Ahmed, Z. U., Al-Abdeli Y. M., and Matthews, M. T., The effect of inflow conditions on the development of non-swirling versus swirling impinging turbulent jets, vol. 118, *Computers & Fluids*, pp. 255-273, 2015

Design, Construction and Performance Test of a Box Type Solar Cooker

Al Aman, Syed Istiaq Mahmud, Md. Nawsher Ali Moral, Jamshedul Islam, Shahinur Rahman

Department of Mechanical Engineering, Khulna University of Engineering & Technology, Khulna-9203, BANGLADESH

ABSTRACT

Solar energy is that produced by the sun's light. It is one of the largest renewable resources which is used for various domestic and industrial purposes like cooking, dehydration, drying, heating power generation etc. and available almost everywhere. The paper provides information about the collection of solar energy by a box type solar cooker. Solar cooker retains heat from the sun and focus it in a container that holds the food and traps the gathered heat. Capturing and thermal conversion are accomplished by the greenhouse effect, thermal conversion is accomplished with a material that absorbs solar energy and thereby increases its own internal energy. A cover system consisting of one or several layers of materials such as glass, which transmit the solar radiation but do not transmit thermal radiation the reflected light is either absorbed by other materials within the space or because it doesn't change wavelength, passes back out through the glass. The maximum temperature inside the cooking pot was found to be 114° C with no load condition at a radiation level of 223-313 W/m².

Keywords: Solar Cooker, Solar Energy, Thermal Conversion, Greenhouse Effect.

1. Introduction

In modern civilization, energy is a fundamental requirement for an industrial society. Considerable effort is therefore being devoted to find new sources of energy to power different machines efficiently. Demand on energy is growing because of vigorous development of industry day by day. Solar radiation is an energy resource many times larger than man's energy needs. Human beings have been able to make use of these resources only on a limited scale mainly for drying crops and producing salt from brines. The direct utilization of solar energy involves its conversion directly to thermal energy. Solar radiation of all wavelengths is converted to thermal energy by using a black surface to absorb the radiant energy using a flat plate collector. A solar oven is one of the direct thermal technologies and basically it consists of collector systems. The collector systems consist of a concentrator and a receiver. The concentrator reflects and focuses sun light on the receiver using aluminum foil, glasses or mirrors as reflector. The receiver is a black body which absorbs the solar radiation and converts it to heat. Using renewable energy is the most promising solution for meeting the growing energy demand of the 21st century. Renewable energy is energy which comes from natural resources such as sunlight, wind, rain, tides and geothermal heat. In 2008, about 19% of global final energy consumption came from renewable energy [1]. Energy resources are diminishing chronologically, but solar energy is an ideal source in many ways. Its use does not diminish a given reservoir as in the case of fossil fuels. For this reasons many organizations and governments have given emphasis on the use of solar energy in efficient ways.

.In developing countries like Bangladesh energy consumption for heating and cooking is a great part of the total energy consumption. In rural areas of Bangladesh cooking is mainly made by wood. In the urban areas of Bangladesh this purpose is served by

using gaseous or liquid fuels. But, in most of the areas mainly woods are used for heating food which is a major cause of deforestation [2]. The most of the energy requirement for cooking are met by noncommercial fuels such as firewood, agricultural waste and animal dung cake in rural areas. For cooking purpose 85% of population of developing countries like Bangladesh use domestic fuel such as wood, cow dung etc. [3]. Among various type of solar oven the box type solar oven is a good solution for use of solar energy for heating purpose as its low cost, easy construction and better output.

2. Literature Review

Earth receives 174 petawatts (PW) of incoming solar radiation (insolation) at the upper atmosphere. Approximately 30% is reflected back to space while the rest is absorbed by clouds, oceans and land masses. The spectrum of solar light at the Earth's surface is mostly spread across the visible and near-infrared ranges with a small part in the near-ultraviolet [5]. The sun's energy is created in the interior region of the sun as a result of continuous fusion reaction. The relative coolness of the outer surface of the sun is an indication that the energy created in the interior is dissipated by radiation from the outer surface of the sun. The intensity of solar radiation reaching earth's atmosphere has been determined more by a series of high-altitude measurements made by using balloons, aircraft and spacecraft from 1967 to 1970. The resulting energy is known as the solar constant and its value is 1353 W/m², when the earth is at its mean distance from the sun. As the earth moves around the sun in a slightly elliptical orbit, the distance between them varies from 98.3% of the mean distance when the earth is closest to the sun to 101.7% of the mean distance when the earth sun distance is maximum [6]. Earth's land surface, oceans and atmosphere absorb solar radiation, and this rises their temperature. Warm air containing evaporated water from the oceans rises,

causing atmospheric circulation or convection. When the air reaches a high altitude, where the temperature is low, water vapor condenses into clouds, which rain into the earth's surface, completing the water cycle. The latent heat of water condensation amplifies convection, producing atmospheric phenomena such as wind, cyclones and anti-cyclones. Sunlight absorbed by the ocean and land masses keep the surface at an average temperature of 14°C. By photosynthesis green plants convert solar energy into chemical energy, which produces food, wood and the biomass from which fossil fuels are derived [7]. Solar energy is the most abundant energy resource and it is available for use in its direct (solar radiation) and indirect (wind, biomass, hydro, ocean etc.) forms. Even if only 0.1% of this energy reaching the earth could be converted at an efficiency of 10%, it would be four times larger than total world's electricity generating capacity of about 5000 GW [8]. Not all energy expressed by the solar constant reaches the surface of the earth because of strong absorption by carbon-di-oxide, ozone and water vapor in the atmosphere. The solar radiation incident on the earth's surface is also depends on the atmospheric content of dust and other pollutants. The box type solar cooker has the Achilles heel of slow heating rate, low temperature delivery and low cooking efficiency. One of the drawbacks of the cooker is attributed to partial shading of water vapors on the inner surface of the glazing, which dampens the intensity of radiation. This kind of cooker depends on the greenhouse effect in which the transparent glazing permits the passing of shorter wavelength solar radiation but is opaque to radiation coming from relatively low temperature heated objects [22].

The solar constant (G_{sc}) is the energy from the sun, per unit time, received on a unit area of surface perpendicular to the direction of propagation, at mean earth-sun distance, outside of the atmosphere. The availability of very high altitude aircraft, balloons and spacecraft has permitted direct measurement of solar radiation most or the earth's entire atmosphere. The measurements were made with a variety of instruments in nine separate experimental programs. The resulted in a value of solar constant G_{sc} of 1353 W/m² with an estimated error of $\pm 1.5\%$ [10]. The solar energy is produced in the interior of sun's sphere by fusion reaction at temperature of many millions of degree. The temperature at the outer surface of the sun is approximately 5762 K. The amount of solar energy intercepted by the planet earth is 5000 times greater than the sum of all other inputs (terrestrial located 150, nuclear geothermal and gravitational energies and lunar gravitational energy) of this amount 30% is reflected to space and 47% is converted to low temperature heat and radiated back into space and 23% power the evaporation cycle of biosphere. Less than 0.5% is represented in the kinetic energy of the wind and waves and in photosynthesis storage in plants. 99% of sun's energy is contained within the wavelengths 0.28 to 4.96 μ m. Since solar energy is concentrated at short wavelengths as

opposed to much longer wavelengths for most "earth bound" thermal radiations a particular material may exhibit entirely different absorbance and transmittance properties for the two types of radiation. The classic of this behavior is "greenhouse effect". Ordinary glasses transmit radiation very rapidly of wavelength below 2 μ m. Practically all the low temperature radiation emitted by the objects in the green house is of such a long wavelength character that remains trapped in the green house. Countries like USA, France, Canada and other developed countries are using solar energy in many fields such as industrial sector, building heating and cooling, agricultural drying, power production etc. [11].The total solar energy absorbed by Earth's atmosphere, oceans and land masses is approximately 3,850,000 exajoules (EJ) per year. In 2002, this was more energy in one hour than the world used in one year. The amount of solar energy reaching the surface of the planet is so vast that in one year it is about twice as much as will ever be obtained from all of the earth's non-renewable resources of coal, oil, natural gas, and mined uranium combined [7].

3. Methodology

3.1 Design of the Proposed Solar Oven

In the proposed box type solar oven more solar radiation can be trapped. The oven can work for a longer period of the day. The construction of this oven is however, slightly harder than usual box type but it can be considered reasonable in respect to its improved performance. The isometric and top view of proposed solar oven is shown in Fig.1 and 2.

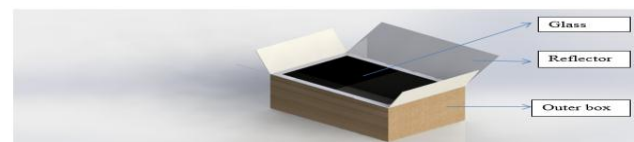


Fig.1 Isometric View of Box Type Solar Oven



Fig.2 Top View of Box Type Solar Oven

In solar oven was made up of glass, glass frame, M.S. sheet as collector and outer wood box. The outer box was made of 1 inch thick wood. The dimension of outer box made of wood and collector box of mild steel are shown in Fig.3 and 4.

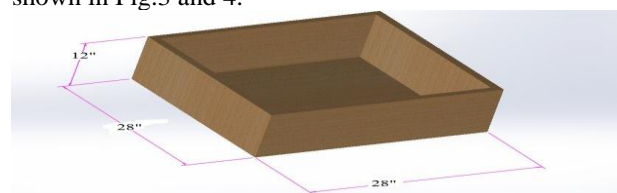


Fig.3 Outer Box made of wood

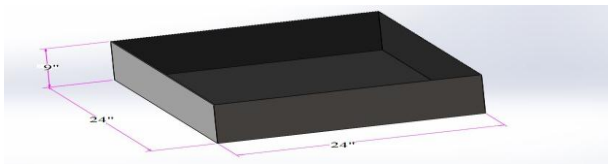


Fig.4 Collector box of M.S. Sheet

The oven consists of collector of M.S. sheet of 2 mm thickness. The M.S. sheet was encased in a box made of wood. The clearance between the M.S. sheet and the encasing were filled with cotton to provide thermal insulation. The clearance between the outer box and the M.S. sheet collector which filled with cotton is 2 inch. The Glass frame gives support to the glass is made by wood of 1 inch thickness and 3 inch breadth. The dimensions of the frame contains the glass is shown in Fig.5

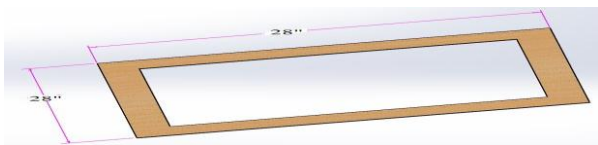


Fig.5 Glass Frame

The solar oven consist a glass of 5 mm thickness. The dimension of glass in inch is shown in Fig.6.



Fig.6 Single Glass

The dimension of reflector (mirror) frame made of wood is shown in Fig.7

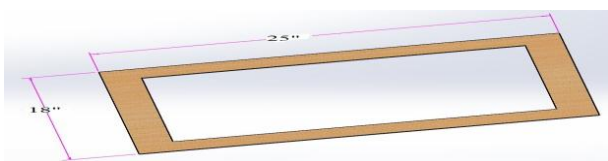


Fig.7 Wood frame for reflector (mirror)

The dimension of reflector (mirror) is shown in Fig.8



Fig.8 Reflector (mirror)

The pot has diameter of 18.5 cm and height of 8 cm.



Fig.9 Dimension of Pot

3.2 Construction of the solar oven

At first outer box of the oven was made by wood according to the proposed design and specification. After that an inner box was made by M.S sheet kept inside the outer box made by wood and the space between the two boxes is filled with cotton insulation. The inner surface of the mild steel was painted black. Then the upside of this box was covered by a transparent glass with frame. Four mirrors as reflector were attached with the box by eight hinged joints.



Fig.10 Construction of the box type solar oven

A hole was made in one side of the box to enter thermocouple wire. One end of the thermocouple wire is connected to the digital temperature indicator box which displays the temperature and other end is immersed at the pot.



Fig.11 Top view of the constructed oven

3.3 Material Selection for the Proposed Solar cooker

However common factors, on which selection of materials for box type solar cooker generally depends on are thermal, optical and radiation properties, availability of material, cost of material, durability, portability, ease of maintenance and adaptability to local skill

3.3.1 Material for Collector

The factors on which the choice of collector materials depends are high thermal conductivity, good corrosion resistance, adequate tensile and compressive strength, cost of material, ease of fabrication, and resistance to stagnation temperature conditions. A list of materials generally employed as collector is given in Table 1.

Table 1 Properties of metals used for collector

Material	Density (kg/m ³)	Thermal Conductivity (W/m°C)	Specific heat (kJ/kg°C)
Copper	8954	386	0.383
Aluminum	2707	204	0.996
Mild steel sheet	7833	54	0.465

So copper and aluminum are the best suited as collector material. But high cost associated with them led to choose the third option mild steel sheet also known as M.S. sheet as collector material.

3.3.2 Material for Outer Box

Partex board, woods etc. are suitable as the material of outer box. Among this two, partex board is rigid and lightweight. It can cut easily and glued easily for the entire construction. On the other hand, wood is comparatively durable but heavy weighted. Wood is easily available to us and its cost is lower than partex board. Therefore, wood is selected in this purpose.

3.3.3 Material for Reflecting Surface

For reflecting systems, materials of high quality and good specular reflectance properties are required. Due consideration must be given to the effect of accumulation of dust and contamination, stability, reflective coating, environmental effect, cleaning problem and cost. Good candidates reflecting materials are mirror and Aluminum foil. Most fresh Aluminum surfaces have reflectivity of 80-85% while reflectivity of mirror surface (ρ) can achieved more than 95%.

3.3.4 Material for Insulation

As the main function of thermal insulating materials is to reduce heat losses from the collector walls and floor, the desired characteristics of an insulating material are low thermal conductivity, stability at high temperature, self-supporting feature without tendency to settle, no contribution in corrosion, ease of application. Thermal conductivity of glass wool is lower than cotton wool. But cotton wool has lower cost, available at local market and use of cotton wool is also easier than glass wool.

3.3.5 Cover Material

The most critical factors for the cover materials are strength, durability, non-degradability and solar energy transmittance. Window glass is mostly performed for solar ovens of a box type as cover materials have high transmittance (τ) for solar radiation, glass does not degrade in sunlight, it protected from thermal strains and impacts is more, durable than most plastic glazing, glass has less percentage of expansion in length. So, less allowance is required. The glass is more available in both rural and urban areas than other cover material.

3.3.6 Material for Pot

As the pots should have high absorption capability of heat, aluminum pots can be used which are also light in weight, commonly found in this country and most importantly can be made darkened to its external surface. Paint required for the interior of the collector and exterior of pots should nontoxic and fumeless in both hot and cold condition. It also should have moisture resistance property. Black paint, which has the property to increase the absorption capability of the material on which it is coated. Therefore, above description of wide range of material helps to find out the appropriate material for several components of the proposed box type solar oven and can be summarized as shown in Table 2.

Table 2 Selection of material for solar cooker

Component	Selected material
Outer box	Wood
Insulation	Cotton
Collector	M.S. sheet
Reflector	Mirror
Cover material	Plain glass
Cooking pots	Aluminum pots
Coating material	Black paint

4. Experimental Results Analysis

4.1. Experimental Setup

The entire constructed oven set in such a way that no turning is required towards the sun. The cooker was placed under open sky directing to the sun. By manual arrangement it was ensured that reflector of the cooker is perfectly directed to the sun.



Fig.12 Experimental Setup

To evaluate the performance of the solar cooker the following equipment's are used:

4.1.1 Solarimeter

It is used to measure the solar intensity in W/m^2 . It has a sensor that is placed in the atmosphere and the display shows the instant solar intensity.



Fig.13 Solarimeter

4.1.2 Thermocouple wire and Digital Temperature indicator

One end of the thermocouple wire is connected to the digital temperature indicator box which displays the temperature and other end is immersed at the pot. This thermocouple was T type (copper/constantan) thermocouple which overall range is $-200^{\circ}C$ to $400^{\circ}C$ and typical accuracy is $1^{\circ}C$. For the best accuracy, this thermocouple often used for food monitoring and environmental applications.



Fig.14 Digital Temperature Indicator

4.2 Experimental Procedure

To evaluate the performance and characteristics of the constructed box type solar cooker the following type of procedure were performed:

According to the measurement different amount of foods were taken into the pot and positioned at the right direction toward the sun. Temperature inside the pot was recorded by digital temperature indicator after every five minute interval. At the same time solar intensity and solar energy were also recorded from the solarimeter. Pizzas, sandwich, Burger, vegetable roll, chicken cutlet etc. were used as a food for this purpose. Different amount of food were used at different day. A fixed amount of food was heated up for a fixed time interval and the quality after heating up was compared. The time required for heating up to a fixed temperature of a fixed amount of food was thus determined.

4.3 Overall Thermal Efficiency

Overall thermal efficiency was calculated by following equation (EI-Sebaili and Ibrahim):

$$\eta_u = \frac{m_f C_f \Delta T_f}{I_{av} A_c \Delta t} \quad (1)$$

Where η_u = overall thermal efficiency (%), m_f = mass of cooking food (kg), C_f = specific heat of cooking food (j/kgK), ΔT_f = difference between the maximum and ambient air temperature, I_{av} = average solar intensity (W/m²) during the time interval, A_c = the aperture area (m²) of the cooker, Δt = time required to achieve the maximum temperature of the cooking fluid (s).

4.4 Cooking Power

The cooking power of the different solar cookers was calculated using equation given by Kundapur and Sudhir

(2009) as follows:

$$P = \frac{T_{w_2} - T_{w_1}}{t} m_w C_{p_w} \quad (2)$$

Where, P = cooking power (w), T_{w_2} = final food temperature (°C), T_{w_1} = initial water temperature (°C), m_w = mass of food (kg) C_{p_w} = food heat capacity, t = time(s).

4.4 Result

The performance of the box type solar oven was found to be depend on climate parameters like ambient temperature, solar radiation etc. design parameters like properties of black paint used inside the collector and outside the pot, properties of absorber plate material, insulation properties and on the operational parameter like amount and type of food kept for heating, number of pot used etc. The variation of the temperature inside the pot for a sunny day it is shown in Fig.15. It was seen that the temperature inside the pot increased with the time of the day and maximum temperature reached at about 12:30 PM when the solar intensity was 313 W/m².

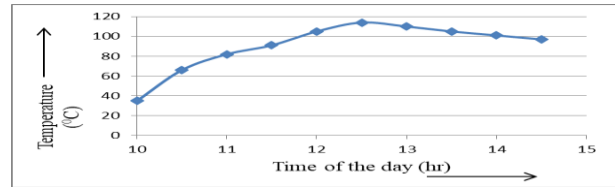


Fig.15 Variation of temperature inside the pot with time of the day (Without load)

The variation of temperature with time of heating element inside the pot are shown in following figures:

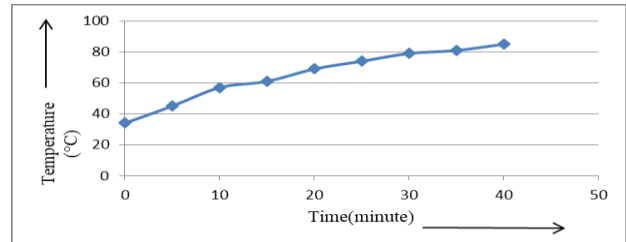


Fig.16 Temperature Vs. time curve for 85 gm. chicken cutlet (12/04/16; 12:10PM-1:00PM)

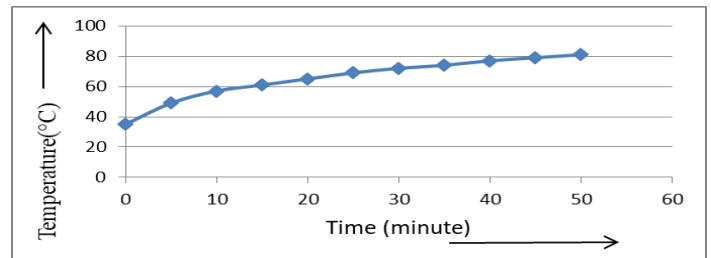


Fig.17 Temperature Vs. time curve for 475 gm. pizza (11/04/16; 11:00AM-11:45AM)

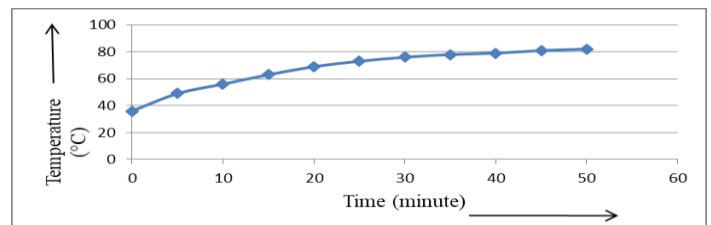


Fig.18 Temperature Vs. time curve for 75 gm. vegetable roll (13/04/16; 1:30PM-2:20PM)

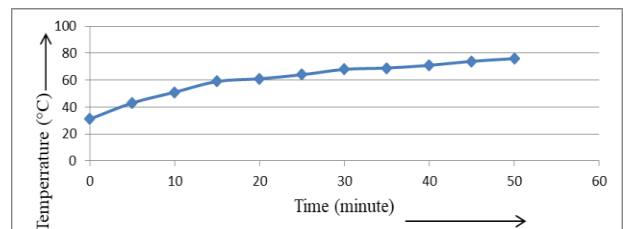


Fig.19 Temperature Vs. time curve for 81 gm. sandwich (14/04/16; 10:30AM-11:20AM)

Temperature was maximum when radiation intensity of the sun was maximum. In fig.15 to 19 Temperatures Vs. time curve for different load at different days are shown.

From these Figures it is clear that the temperature inside the pot increases as the time increases. In fig.15 maximum temperature inside the pot was found 114°C without any load at an available radiation level of 223-313 W/m². In fig.16 maximum temperature inside the pot was found 87°C within 45 minutes at a radiation level of 223-304 W/m². In fig.17 maximum temperature inside the pot was found 81°C within 50 minutes at a radiation level of 267-313 W/m². It is also clear from this that as radiation level decreases, the time required for heating increases.

5. CONCLUSION

The box type solar cooker represents a potential alternative way of heating upon the conventional ways. After the construction of the proposed cooker, the experimental results have shown many effective utilities. After construction of the experimental setup, the data were analyzed. As efficiency of heating of the constructed cooker is found to be remarkable, this type of solar cooker system can be used in remote and rural areas where national grid line is unreachable or highly expensive, In terms of life time limit, it is more worth than most other energy sources. The main problem for box type solar cooker is its capital cost, which make it economically uncompetitive with a majority of other energy sources. Its cost will be further reduced if its commercial fabrication is possible in our country.

RECOMMENDATIONS

Besides a lot of promises the constructed oven has some drawbacks. In Bangladesh it is very difficult to use solar cookers during the days when the sky is cloudy. So recommendations for further study for both performance and construction improvements are more reflectors can be used to increase the boosting of solar radiation and thus the temperature of the enclosure will be increased. An attempt can be taken to modify the solar cooker to accept a small amount of electrical energy in addition to solar energy so that heating becomes possible in cloudy days. For this purpose, auxiliary energy can be supplied by either built-in electrical heating element under the absorber plate.

ACKNOWLEDGEMENT

The experiment setup was made in KUET workshop and all the experiment were performed in Energy Park (infront of Heat Engine Lab) of Mechanical Engineering Department, KUET under the direct supervision of Prof. Dr. Md. Nawsher Ali Moral, Dean, Faculty of Engineering, North Western University, Khulna, Bangladesh.

REFERENCES

- [1] "Renewable 2010 global status report", <http://www.ren21.net/portals>
- [2] http://en.wikipedia.org/wiki/Renewable_energy_policy_of_Bangladesh

- [3] Baker Jhon ED, "Solar Nest-A Very Low Cost Solar Oven", 22 Caddy Avenue, west Leederville, Western Australia.
- [4] "Natural Forcing of the Climate System", Intergovernmental panel on Climate Change, http://www.grida.no/climate/ipcc_tar/wg1/041.htm#121.(Retrieved 2007-09-29).
- [5] Ozisic M. Necati, "HEAT TRANSFER, A basic approach", International Edition, McGraw-Hill Book Company, Printed in Singapore (1985).
- [6] Wikipedia, the free encyclopedia, http://en.wikipedia.org/wiki/Solar_energy
- [7] World Energy Resources, 2013 Survey: Summary, World Energy Council.
- [8] http://en.wikipedia.org/wiki/Solar_power_by_country
- [9] Duffie Jhon A. and Beckham William A., "Solar Engineering of Thermal Process", Second Edition, John Wiley & Sons, New York (1991).
- [10] Duffie Jhon A. and Beckman William A., "Solar Engineering of Thermal Processes", A Wiley-Interscience Publication, Jhon Wiley Sons, Newyork, USA (1980).
- [11] http://rredc.nrel.gov/solar/old_data/
- [12] Nasima Akter, "Alternative Energy Situation in Bangladesh A Country Review", Paper presented at the Regional Training Orientation Course on Alternative Energy Technologies, organized by APPROTEC ASIA Philippine Social Development Center, Philippines at July 1997.
- [13] Helali, Maksud & Hossain M.A., "Solar Radiation Maps of Bangladesh", Paper presented at 31st Annual convention of the Institute of Engineers of Bangladesh, held at Khulna (1987).
- [14] Garg H.P. and Prakash J., "Solar Energy Fundamentals and Applications", 1st Edition, Tata McGraw Hill Book Company, India (2000).
- [15] Ali chaouki; Rabhi kamel; Attyaoui slimen; Jallouli Ibrahim & Ben bacha habib, "Theoretical Study And Design of a Hybrid Solar Oven."
- [16] Ghai M.L.;Pandhar B.S. and Dass Harikishan, "Manufacture of reflector type direct solar oven", Journal of Scientific and Industrial Research,12A,212-216 (1953).
- [17] Lof G.O.G. and Fester D.A, "Design and Performance of folding Umbrella type Solar Oven", Proceedings of UN conference on New Sources of Energy, Rome, Paper S/100,5,347-352 (1961).
- [18] Duffie J.A.;Lof G.O.G and Beck B,"Laboratories and field studies of plastic reflector solar ovens", Proceeding of UN conference on New sources of energy, Rome, Paper S/87,5,339-346 (1961),.
- [19] Tabor H, "A solar oven for developing countries", Solar Energy, 10,153-157 (1966).
- [20] Lampinen, Ari, "Reducion of Tropical Deforestation by Massive Use of Solar Ovens," Technology of life, Finland, 18.10.1994.
- [21] Sedighi M, Zakariapour M, A review of direct and indirect solar cookers. *Sustain Energ* 2: 44–51 (2014).

ICMIEE18107

Design, Simulation, and Economic Analysis of an Optimal Mini-grid Solar-Fuel Cell Hybrid Power Generation System for a Remote Island of Bangladesh

Sk. Suzauddin Yusuf^{1*}, Md. Mahmudul Alam², Md. Hasan Ali³, Nirendra Nath Mustafi⁴
^{1,2} Department of Mechanical Engineering,

Bangladesh Army University of Science and Technology, Saidpur Cantonment-5311, Saidpur, BANGLADESH

³Department of Industrial and Production Engineering,

Bangladesh Army University of Science and Technology, Saidpur Cantonment-5311, Saidpur, BANGLADESH

⁴Department of Mechanical Engineering,

Rajshahi University of Engineering and Technology, Rajshahi-6204, BANGLADESH

ABSTRACT

It is the international trend to promote renewable energy, as part of energy security as well as greenhouse gas emission reduction. Wind and solar energies can be used to supplement the conventional energy sources predominantly in remote coastal localities of Bangladesh. Feasibility study of renewable resources of Kutubdia, an off-grid remote island, is presented in this paper. Purpose of this study is to design, simulation, and economic analysis of a stand-alone optimal mini-grid Solar-Fuel cell hybrid power generation system in a remote island of Bangladesh to satisfy the energy demands in a sustainable way by HOMER ENERGY software. Three Fuel cell are added to ensure uninterrupted power supply due to the intermittent nature of renewable resources. Optimum size of different components, electrical load with a certain random variability, fraction of renewable energy, excess electricity, performance of its different components, environmental impacts, cost of energy(COE), net present cost(NPC), annualized cost are analyzed in this paper.

Keywords: Hybrid energy system; Mini-grid; Renewable energy; Fuel Cell; Environmental impact; HOMER optimizer.

1. Introduction

Bangladesh, for the first time in history, has fulfilled the eligibility criteria set by the United Nations to be recognized as a developing country, crossing over from the list of least developed countries (LDCs) [1]. Electricity demand of Bangladesh is increasing day by day. At present, 83% of the total population has come under the electricity coverage and per capita generation has increased to 433 kWh. The government has already set a target to become a middle income country by 2021 and develop country by 2041. In the fiscal year 2016-2017, the highest peak generation was 9,479 MW with total generation capacity was 13,555 MW. Bangladesh Power Development Board prepared generation expansion plan to achieve generation capacity 24,000 MW by 2021 with the aim to provide quality and reliable electricity to the all people across the country for desired economic growth and social development [2]. Since Bangladesh is facing to the depletion of domestic gas supply, various issues such as sustainable development harmonizing with economic optimization, improvement of power quality, and the discipline of operation and maintenance for power plants need to be addressed holistically. Furthermore, energy subsidy is also a tough challenge, because there's always a concern that drastic increase of fuel and electricity prices may trigger another negative effect on the national economy. Integrating intermittent renewable energy resources, such as PV and Wind generation, to achieve CO₂ emission reduction is a priority task for most countries worldwide. However, such renewable resources have high initial cost, low utilization rate and intermittent generation [3].

The objective of "Renewable energy policy 2008" of Bangladesh is to achieve 10% of total energy demand

from the renewable sources by 2020 [4]. Wind and solar energies are the most attractive renewable energy resources that can be used to complement the increasing demand of conventional energy sources particularly in Bangladesh [5,6]. Bangladesh has 4,01,678km power distribution line with 9.27% distribution system loss [2]. But only about 40% of rural households have access to grid electricity [7]. Many remote localities along with the coastal areas are not connected to grid electricity. Hybrid renewable energy systems are becoming popular as stand-alone power systems for providing electricity in remote areas due to advances in renewable energy technologies and subsequent rise in prices of petroleum products [8]. A stand-alone optimal mini-grid hybrid power generation system is designed by using HOMER ENERGY software in which fixed capacity fuel cell generators are added along with a feasible renewable energy technology to meet the electricity demand in a reliable and sustainable manner. Environment pollution is considerably reduced as compared to any conventional system, due to reduction of fossil fuel consumption.

2. Site of Proposed Project

Kutubdia Island is famous for the Light-House and all other mysterious creation and divine beauty. It is surrounded by the Bay of Bengal. Administration of Kutubdia Thana was established in 1917 and was turned into an Upazila in 1983. It consists of 6 union parishads, 9 mouzas and 29 villages[9]. It is an upazila of Cox's Bazar district in the division of Chittagong, Bangladesh. It is located in between 21°43' and 21°56' north latitudes and in between 91°50' and 91°54' east longitudes [10]. Adult literacy rate is about 35% with per capita income is 4884.49 BDT. Total area of Kutubdia is 215.8 km² in

which agricultural land is 8903.22 hectares. Kutubdia is off grid area or remote area and distance from main land is 91 km [11].

3. Mini-Grid & HOMER software

A mini grid, also sometimes referred to as a "micro grid or isolated grid", can be defined as a set of electricity generators and possibly energy storage systems interconnected to a distribution network that supplies electricity to a localized group of customers. They involve small-scale electricity generation (10 kW to 10MW) which serves a limited number of consumers via a distribution grid that can operate in isolation from national electricity transmission networks. Mini-grids have a unique feature as they can operate autonomously without being connected to a centralized grid. Hybrid mini-grid systems often incorporate a 75-99% renewable supply. Conversely as the cost of fossil fuel increases, mini-grid systems are becoming more economically attractive as the cost of renewable energy resources decrease [12]. The HOMER (Hybrid Optimization of Multiple Energy Resources) micro grid software navigates the complexities of building cost effective and reliable micro grids that combine traditionally generated and renewable power, storage, and load management. HOMER is the global standard in microgrid software, based on decades of listening to the needs of users around the world with experience in designing and deploying microgrids and distributed power systems that can include a combination of renewable power sources, storage, and fossil-based generation (either through a local generator or a power grid). It is the world's leading micro grid modelling software. It was developed by the National Renewable Energy Lab (NREL), a division of the U.S. Department of Energy [13].

4. Electrical demand in Kutubdia

Based on data obtained from Ref. [11], the electrical load data of Kutubdia is imported in the software with 10% day to day and 20% time step random variability. The electrical load in a year with random is presented in Fig.1. Annual average electricity demand of this island is 15,108.21 kWh/day. The yearly average load is 629.51 kW and load factor is 0.54. Minimum load 29.39 kW is found in month of May and peak load 1,167.5 kW in the month of August.

5. Feasibility of Renewable Resources in Kutubdia

Solar and wind are the available renewable energy in this island. The potentials and feasibility of these sources are described below;

5.1 Wind energy

The monthly average wind speed data in this island, fluctuated from 2.70 m/s to 4.87 m/s at 50 meter above the surface of earth, is imported in this software from NASA Surface meteorology and solar energy database. Maximum wind speed 4.87 m/s is found in June. Studies have found that average wind speeds in a

particular location need to exceed at least 6–8 m/s for a small wind turbine to be economically viable [14]. It is not feasible to operate a wind turbine proficiently and parsimoniously, as the average wind speed in Kutubdia over a year is only 3.55m/s, which is quite low.

5.2 Solar energy

Solar Global Horizontal Irradiance (GHI) data is taken from National Renewable Energy Lab database. Fig.3 shows the solar radiation data used in the simulations in which the left vertical axis represents the daily radiation data while the right one represents the clearness index. The solar GHI in Kutubdia is between 3.828 kWh/m²/day and 5.979 kWh/m²/day. The annual average solar radiation is 4.81 kWh/m²/day. Solar GHI is high (above the average) from February to May (summer season), with a peak in the month of April, while solar irradiance is low in July, August, and September due to rainy season.

6. Proposed hybrid system

The proposed hybrid system consists of fuel cells, PV panels, Converters, and Batteries. This power generation system is designed for 25 years' lifetime. The life span of PV panels, batteries, converter and fuel cells are considered as 20,10, 15, and 8 years' respectively. The optimum size of all the components is determined by HOMER optimizer. Fig.4 shows the schematic diagram of proposed hybrid system. In this system, three 250 kW fuel cell generator are connected to the DC bus as it produces DC output. Battery bank and PV panels are also connected to the DC bus. Converter is placed between the two buses. Load is connected to the system through AC bus. The sizes of each component are shown in Table 1.

7. Simulation results and analysis

Result of simulation is divided into electrical analyses, environmental impact, and economic analyses which are described in the following articles. Dispatch strategy of this simulation was cycle charging.

7.1 Electrical analysis

Electrical analysis includes the simulation results and analysis of fuel cell generators and PV panel output, competitive electric production, renewable energy fraction, and performance of battery and converter. Table 4 represents energy production by different components, consumption, and excess electricity.

7.1.1. Fuel cell's output

In this proposed system, three 250 kW dc fuel cell generator are used. Average consumption of natural gas by these fuel cell is 2,351 m³/day. Initial capital cost of each generator is \$750,000 and operation and maintenance cost is \$5/hour. Mean electrical efficiency is 48.2%. The expected life time is 50,000 hours and specific fuel consumption is 0.210 m³/kWh. Capacity factors of these generators are 63.9%, 70.7% and 52.0% respectively. HOMER calculates the mean electrical

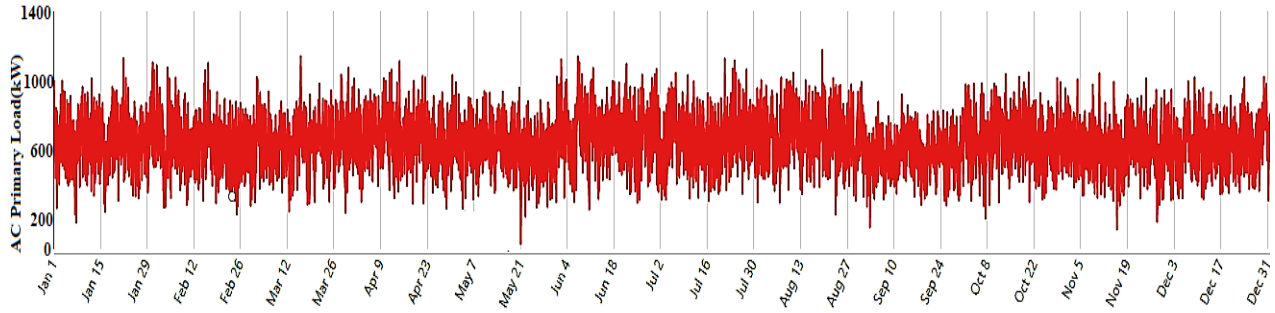


Fig.1Electrical load of Kutubdia in a year with random variability [11].



Fig.2 Monthly average wind speed data (NASA Surface meteorology and solar energy database).

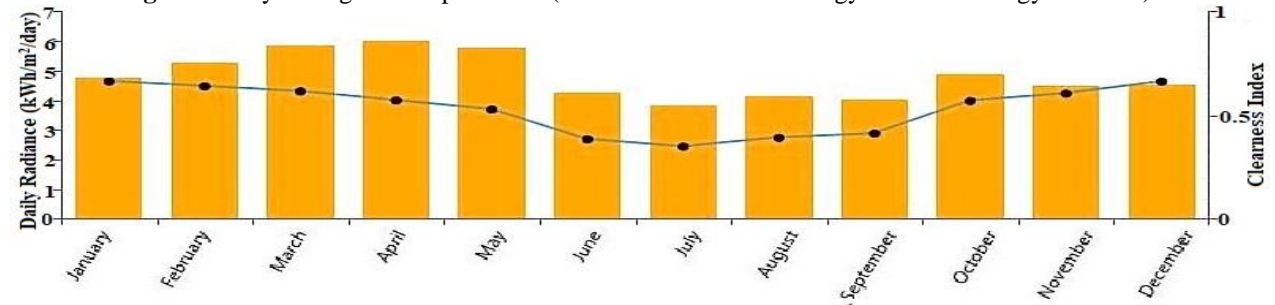


Fig.3 Monthly average solar global horizontal irradiance (National Renewable Energy Lab database).

efficiency (η_{gen}) of the generator over the year, defined as the electrical energy out divided by fuel energy in, which is shown in the following equation;

$$\eta_{gen} = \frac{3.6 \cdot E_{gen}}{m_{fuel} \cdot LHV_{fuel}} \quad (1)$$

where E_{gen} is the generator's total annual electrical production (kWh/yr), m_{fuel} is the generator's total annual fuel consumption(kg/yr) and LHV_{fuel} is the lower heating value of the fuel (MJ/kg). The factor of 3.6 arises because 1 kWh = 3.6 MJ.

7.1.2 PV output

Flat plate PV panel is considered in this proposed system to harness solar energy. Efficiency at standard test conditions is 13% and nominal operating cell temperature is 47°. By using Homer optimizer, the size of flat plate PV panel is found 1,419 kW. PV panels produce 2,161,610 kWh/yr and 5,922 kWh/day, and its capacity factor is 17.4%. Maximum and mean output is 1,407 kW and 247 kW respectively. HOMER uses the following equation to calculate the output (P_{PV}) of the PV array.

$$P_{PV} = Y_{PV} f_{PV} \left(\frac{\bar{G}_T}{\bar{G}_{T,STC}} \right) [1 + \alpha_P (T_C - T_{C,STC})] \quad (2)$$

Table 1 System architecture.

Device	Size
Flat plate PV	1,419 kW
Fuel Cell	750 kW
Lead Acid Battery	3,584 kWh
Converter	1,633 kW

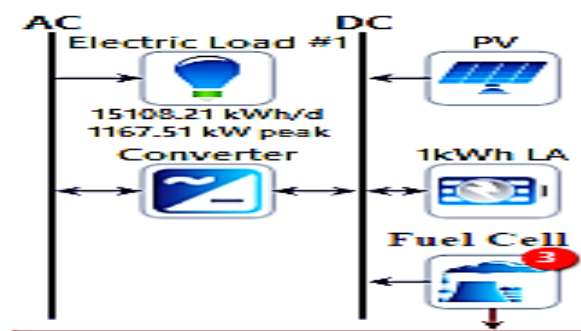


Fig.4 Diagram of power generation system.

Here, Y_{PV} is the rated capacity of the PV array under standard test conditions (kW), f_{PV} is the PV derating factor(%), \bar{G}_T is the solar radiation incident on the PV array in the current time step(kW/m²), $\bar{G}_{T,STC}$ is the incident radiation at standard test conditions (1 kW/m²),

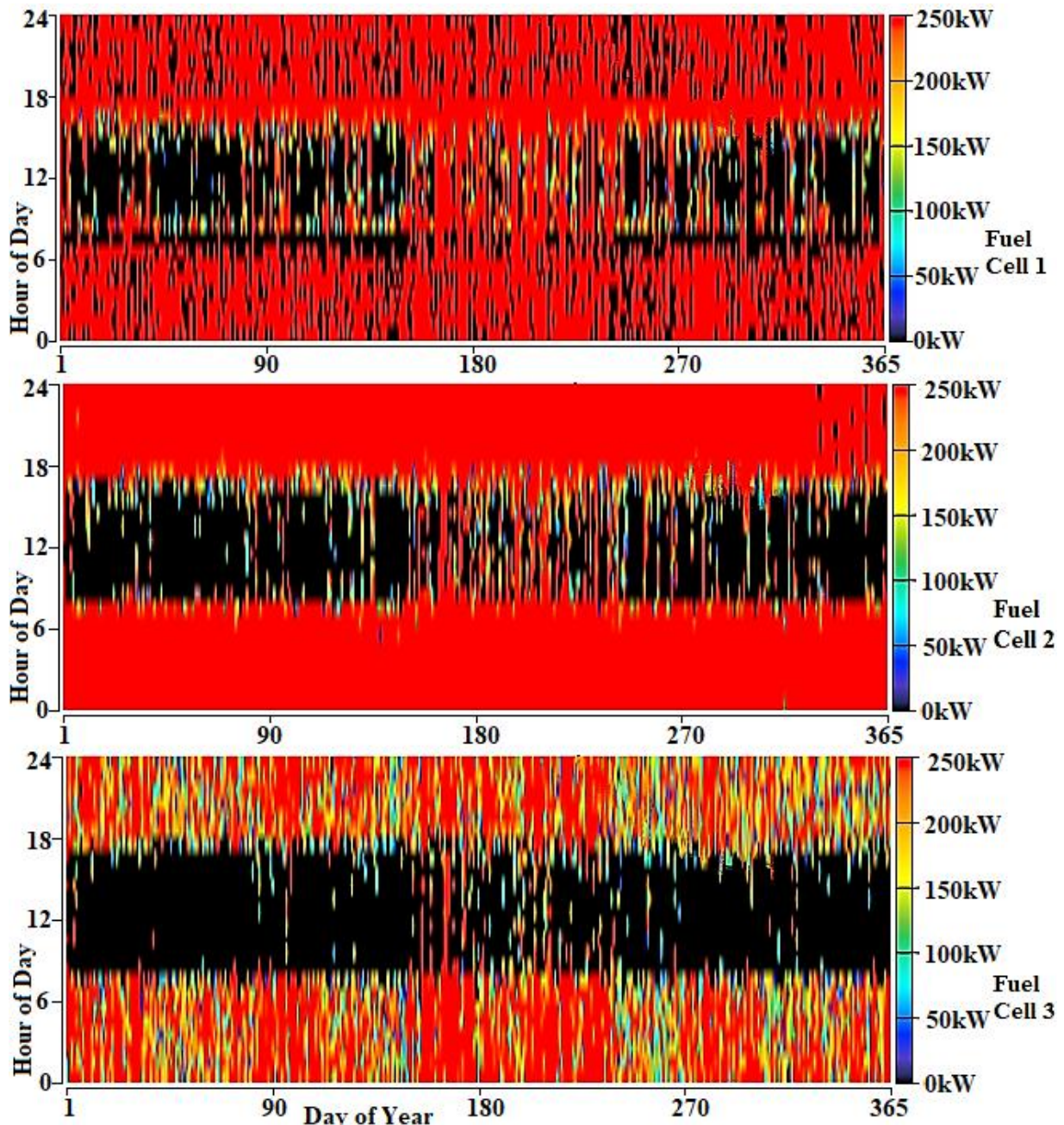


Fig.5 Fuel Cells power output in a year.

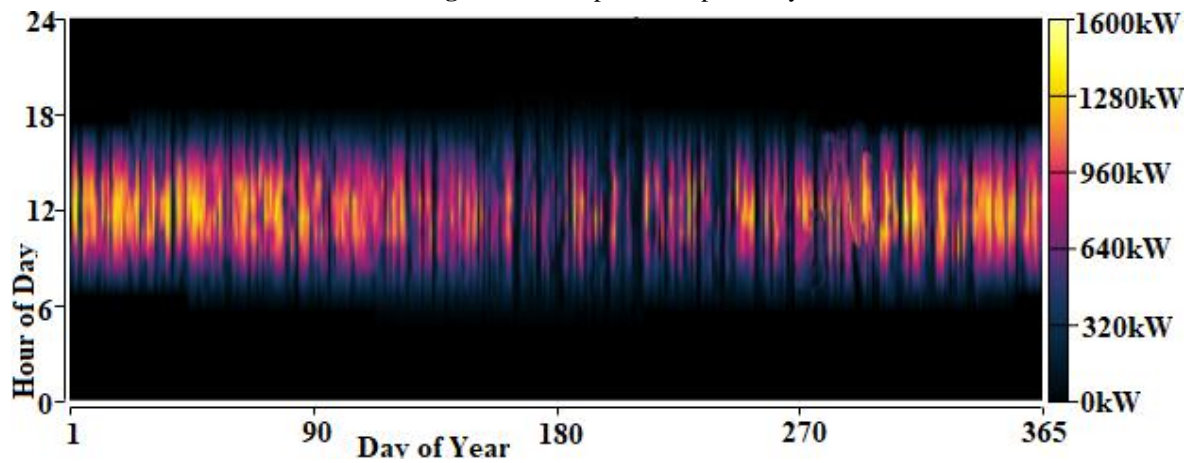


Fig. 6 Power output in a year by PV panels.

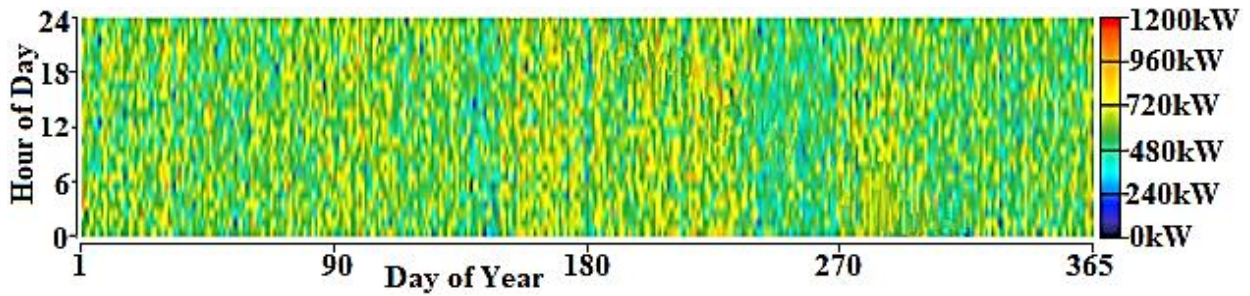


Fig.7 Converter output in a year.

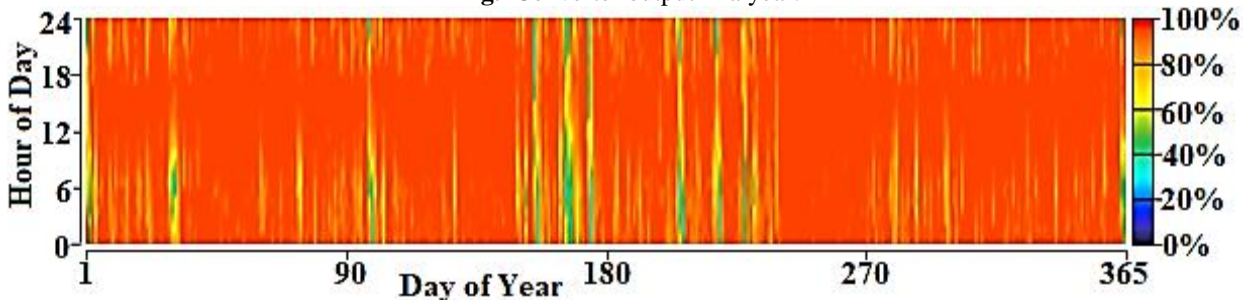


Fig.8 State of charge of battery in a year.

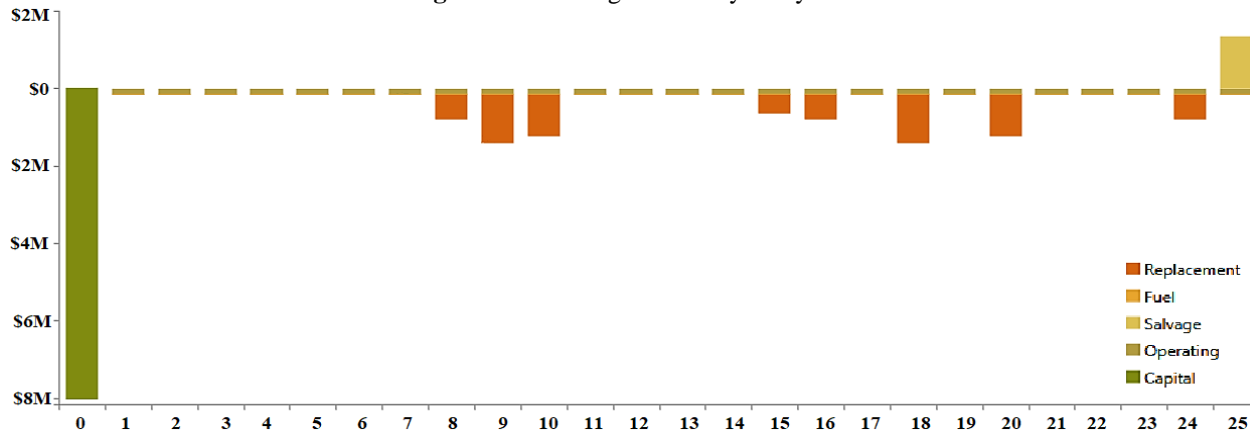


Fig.9 Cash flow in 25 years by cost type.

α_p is the temperature coefficient of power (%/°C), T_c is the PV cell temperature in the current time step (°C), $T_{c,STC}$ is the PV cell temperature under standard test conditions (25 °C).

7.1.3. Comparative electrical production

Total energy produced by this system is 6,247,228 kWh/year while average demand is 5,512,129 kWh/year. Energy generated by PV panels is 2,161,610 kWh/year. So, renewable energy fraction is 34.8%.

Table 2 Comparative production and consumption.

Components	Energy/year (kWh/yr)	Percentage(%)
Fuel Cell 1 output	1,399,213	22.4
Fuel Cell 2 output	1,548,280	24.8
Fuel Cell 3 output	1,138,124	18.2
PV output	2,161,610	34.6
Total Production	6,247,228	100
Average demand	5,512,129	-
Excess energy	403,433	6.46

Table 3 Annualized Costs by components

Component	Capital (\$/yr)	Replacement (\$/yr)	O&M (\$/yr)	Fuel (\$/yr)	Salvage (\$/yr)	Total (\$/yr)
Generic 1kWh Lead Acid	40,726.64	86,714.05	35,840.00	0.00	22,594.03	140,686.67
Generic 250kW Fuel Cell 1	28,408.65	49,970.76	29,005.00	11,165.72	2,613.59	115,936.55
Generic 250kW Fuel Cell 2	28,408.65	75,778.63	32,240.00	12,355.28	20,383.38	128,399.18
Generic 250kW Fuel Cell 3	28,408.65	50,039.11	28,290.00	9,082.23	4,491.70	111,328.30
Generic flat plate PV	161,290.85	0.00	14,193.81	0.00	0.00	175,484.66
System Converter	18,556.00	19,750.19	0.00	0.00	6,862.91	31,443.28
System	305,799.45	282,252.74	139,568.81	32,603.23	56,945.60	703,278.64

7.1.4. Performance of battery and converter

Batteries are used to store excess electricity and utilized this energy during shortage. Annual throughput of 3,584 kWh Lead Acid batteries is 186,052 kWh/yr and expected life time is 10 years. Minimum state of charge is set to 40% and bus voltage is 12 V. A converter is used in this proposed project to convert dc power to ac as all loads are ac type. Size of converter is 1,633 kW with capacity factor 38.5%. Maximum and mean output is found 1,168 kW and 629 kW respectively.

7.2. Environmental impact

This hybrid system reduces notable amount of emissions due to use of significant fraction of renewable energy technology. It decreases the consumption of fossil fuel. So, it is a more environment friendly power generating system. The emission of different gases is determined by simulation which shown in Table 4.

Table 4 Emission of pollutants.

Pollutant	Emissions (kg/yr)
Carbon dioxide	1,664,869
Carbon monoxide	172
Unburned hydrocarbons	0
Particulate matter	0
Sulfur dioxide	0
Nitrogen oxides	17.2

7.3. Economic analysis

Project life time is expected as 25 years. Cash flow in 25 years by cost type is presented in fig.9 and annualized costs by components are shown in Table 3. Different types of costs like replacement cost, fuel cost, salvage cost, operating cost, and capital cost are shown in fig.9. Price of natural gas in Bangladesh is 0.04\$/m³ and inflation rate is 6.04%. Fuel cost of fuel cell generators is 32,603.23\$/yr. From this simulation, the operating and net present cost is 397,479.20\$/yr and 18,566,840.00\$

respectively and cost of electricity is found 0.1276\$/kWh. This indicates a feasible system. HOMER finds the optimal system by determining the lowest possible initial capital costs, operating costs, net present costs, and cost of per unit electricity.

8. Conclusion

To meet ever increasing per capita electricity demand of Bangladesh, integration of renewable energy technology is essential. This proposed hybrid power generation system can be a perfect long term solution to meet the energy demand in many remote localities like Kutubdia island. Cost of electricity found from this simulation is \$0.1276/kWh which is acceptable. Both cost of electricity and environmental pollutions are lower than the proposed project in [8], as natural gas is used instead of diesel and fraction of renewable energy is increased.

REFERENCES

- [1] Dhaka Tribune. Available online: <https://www.dhakatribune.com/bangladesh/2018/03/18/developing-bangladesh-new-identity-2/>.
- [2] Bangladesh Power Development Board (BPDB). Annual Report 2016–2017, BPDB, Dhaka. Available online: http://www.bpdb.gov.bd/bpdb_new/index.php/site/annual_reports/e445-c332-c830-6930-2bf2-2651-a538-fa23-852b-02bb.
- [3] Power & Energy Sector Master Plan (PSMP 2016) Final Report. Available online: http://open_jicareport.jica.go.jp/pdf/12269742.pdf.
- [4] Renewable Energy Policy of Bangladesh, Power Division, Ministry of Power Energy and Mineral Resources, Government of the People's Republic of Bangladesh. 18 December 2008. Available online: http://www.iea.org/media/pams/bangladesh/Bangladesh_RenewableEnergyPolicy_2008.pdf.
- [5] Sk. Suzaiddin Yusuf, Md. Shariful Islam, Robiul Islam Rubel, Md. Abu Shaid Sujon, Rafiqul Alam Beg, Construction, and Performance Test of a Portable Solar Photovoltaic Water Pumping System for Irrigation and Household Water Supply, *International Conference on Mechanical, Industrial and Materials Engineering 2017 (ICMIME2017)*, Paper ID: ET-83 (2017).
- [6] Sanjoy Kumar Nandi, Mohammad Nasirul Hoque, Himangshu Ranjan Ghosh, Swapan Kumar Roy, Potential of Wind and Solar Electricity Generation in Bangladesh, *International Scholarly Research Network ISRN Renewable Energy*, Volume 2012, Article ID 401761 (2012).
- [7] World Bank. Lighting Up Rural Communities in Bangladesh. January 2015. Available online: <http://www.worldbank.org/en/news/feature/2014/01/15/lighting-up-rural-communities-in-bangladesh>.
- [8] Sk. Suzaiddin Yusuf, Nirendra Nath Mustafi, Design and simulation of an Optimal Mini-Grid Solar-Diesel Hybrid Power Generation system in a remote Bangladesh. *International Journal of Smart Grids, ijSmartGrid*, [S.l.], v. 2, n. 1, March, p. 27-33, mar. 2018. ISSN 2602-439X (2018).
- [9] Offroad Bangladesh. Available online: <http://offroadbangladesh.com/places/kutubdia-island/2/>.
- [10] Kutubdia Upazila, BANGLAPEDIA. Available online: http://en.banglapedia.org/index.php?title=Kutubdia_Upazila.
- [11] Md. Tanjil Sarker, Md. Anisur Rahman, Prf. Dr. Zahid Hasan Mahmud, Electricity Demand Load Forecasting for a Remote Area of Bangladesh, *International Journal of Scientific & Engineering Research*, Volume 8, Issue 1, January-2017 265-277 (2017).
- [12] Mini Grids. Available online: https://energypedia.info/wiki/Mini_Grids.
- [13] HOMER ENERGY. Available online: <https://www.homerenergy.com/>.
- [14] Wind turbine system. Available online: <http://www.level.org.nz/energy/renewable-electricitygeneration/wind-turbine-systems/>.

Boundary Layer Flow of Micropolar Fluid over a Stretching Conical Surface with Magnetic Effect

M. Ali*¹, M. A. Alim², R. Nasrin³, Md. Delowar Hossain⁴

^{1,4} Department of Mathematics, Chittagong University of Engineering & Technology, Chittagong-4349, BANGLADESH

^{2,3} Department of Mathematics, Bangladesh University of Engineering & Technology, Dhaka-1000, BANGLADESH

ABSTRACT

Similarity solution of unsteady forced convection magnetohydrodynamic boundary layer flow and heat transfer over a porous stretching cone are analyzed. The governing partial differential equations are transformed into ordinary differential equations by using local similarity transformations. The transformed equations are solved numerically subject to the boundary conditions by using Nachtsheim-Swigert iteration technique along with the 4th order Runge-Kutta integration scheme. The numerical results are checked against previously published work for special cases of the problem in order to access the accuracy of the numerical method and found to be in good agreement. The results indicates that the fluid velocity decreases for increasing values of magnetic parameter, porosity parameter and unsteadiness parameter but the reverse results arises for pressure gradient parameter, material parameter and stretching ratio parameter. The heat transfer rate decreases for increasing values of stretching ratio parameter, material parameter, pressure gradient parameter but increases for magnetic parameter, unsteadiness parameter, porosity parameter, Prandtl number and wall temperature parameter. The numerical results are presented graphically and also in tabular form.

Keywords: MHD, microrotation, pressure gradient, stretching.

1. Introduction

The micropolar fluids are fluids which contain microstructure that can undergo rotation. Physically, it represent fluids consisting of randomly oriented particles suspended in a viscous medium. The presence of this type of fluid can affect the hydrodynamic of the flows so that it can be distinctly non-Newtonian. The boundary layer flow of micropolar fluid driven by a continuous stretching surface are important in a number of industrial engineering processes such as colloidal suspensions, the aerodynamic extrusion of plastic sheets, annealing and thinning of copper wires, cooling of metallic plate in a bath, animal blood, body fluids, fluid flowing in brain and so forth. The theory of micropolar fluids was originally formulated by Eringen [1] by taking the local effects arising from the microstructure and the intrinsic motion of the fluid into the account. After that, Adekeye et al. [2] identified that a strong flow circulation arises at particular value of Grashof number and heat transfer rate is significant at certain interval of inclination. Hussein et al.[3] shown that the solid volume fraction has a significant influence on stream function and heat transfer, depending on the value of Hartmann and Rayleigh numbers. Ahmed et al.[4] observed that the skin friction coefficient decreases as the Reynolds number and the suction/injection parameter increases, while the local Nusselt number increases as the Reynolds number and the suction/injection parameter increases. Reddy [5] obtained that the momentum boundary layer thickness is elevated whereas thermal boundary layer thickness is decelerates with the higher values of nanoparticle volume fraction, Norfarahanim [6] discussed Marangoni boundary layer flow in micropolar fluid with

suction/injection, Siva Reddy [7] analyzed the heat and mass transfer on the MHD flow of micropolar fluid in the presence of viscous dissipation and chemical reaction, Mostafa et al.[8] studied the MHD flow and heat transfer of a micropolar fluid over a stretching surface with heat generation and slip velocity, Ali et al. [9] studied the similarity solution of MHD free convection heat and mass transfer flow over a porous medium in a rotating system with hall current and heat generation, Ishak et al. [10] discussed magnetohydrodynamic (MHD) flow of a micropolar fluid towards a stagnation point on a vertical surface and found that the micropolar fluid delays the boundary layer separation, Das [11] studied the influence of thermophoresis and chemical reaction on MHD micropolar fluid flow with variable fluid properties and found that in presence of different physical effects can be modified the flow, heat and mass transfer, Bhattacharyya et al. [12] examined the effects of thermal radiation on micropolar fluid flow and heat transfer over a porous shrinking sheet, Redha et al. [13] analyzed the thermal radiation effect on heat and mass transfer in steady laminar boundary layer flow of an incompressible viscous micropolar fluid over a vertical flat plate, in presence of magnetic field, Mohanty et al. [14] studied the effect of micropolar fluid over a stretching sheet through porous media on heat and mass transfer. Recently, Reddy [15] investigated the influence of Soret and Dufour effects on MHD heat and mass transfer flow of a micropolar fluid with thermophoresis particle deposition. Siva Gopal [16] analyzed the effect of Soret and Dufour on unsteady convective heat and mass transfer flow of a micropolar fluid through porous medium past a permeable

* Corresponding author. Mobile: +88-01713109929

E-mail addresses: ali.mehidi93@gmail.com

stretching sheet. The aim of the present work is to investigate the unsteady flow and heat transfer of an electrically conducting micropolar fluid over a stretching cone with uniform transverse magnetic field. The flow is subjected to a transverse magnetic field of strength B_0 which is assumed to be applied in the positive y -direction and normal to the flow direction.

2. Geometry of the present problem

Let us consider the two dimensional unsteady forced convection laminar flow over a stretching cone. The flow is supposed to be electrically conducting. The coordinate system is considered in such a way that x -axis coincides with the surface of the cone, and y -axis is perpendicular to it. A transverse magnetic field of strength B_0 is applied orthogonal to the surface of the cone as depicted in Fig. A. Suppose that β is the half angle of the cone, r is the radius of the cone. The temperature near the surface is considered as $T_w = T_\infty + \frac{ax^s}{1-ct}$, where a is constant, s is the wall temperature parameter, T_∞ is the free stream temperature. We assume that the velocity of a point on a cone is proportional to its distance from the leading edge.

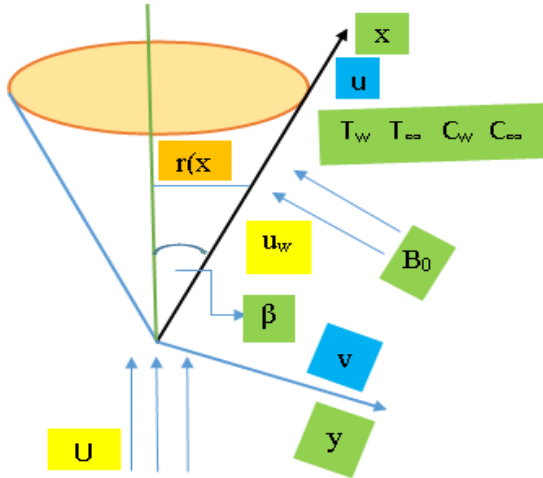


Figure A: Physical model and coordinate system

3. Governing equations and similarity solution

Under the above assumptions and usual boundary layer approximation, the dimensional governing equations of continuity, momentum, microrotation, and energy are:

Equation of continuity:

$$\frac{\partial(ru)}{\partial x} + \frac{\partial(rv)}{\partial y} = 0 \quad (1)$$

Momentum equation:

$$\frac{\partial u}{\partial t} + u \frac{\partial u}{\partial x} + v \frac{\partial u}{\partial y} = U \frac{dU}{dx} + \frac{dU}{dt} + \left(\frac{\nu + \chi}{\rho} \right) \frac{\partial^2 u}{\partial y^2} + \frac{\chi}{\rho} \frac{\partial N}{\partial y} - \left(\frac{\sigma B_0^2}{\rho} + \frac{\nu}{k} \right) (u - U) \quad (2)$$

Angular momentum equation:

$$\frac{\partial N}{\partial t} + u \frac{\partial N}{\partial x} + v \frac{\partial N}{\partial y} = - \frac{\chi}{\rho j} \left(2N + \frac{\partial u}{\partial y} \right) + \frac{\gamma}{\rho j} \frac{\partial^2 N}{\partial y^2} \quad (3)$$

Energy equation:

$$\frac{\partial T}{\partial t} + u \frac{\partial T}{\partial x} + v \frac{\partial T}{\partial y} = \frac{\kappa}{\rho c_p} \frac{\partial^2 T}{\partial y^2} \quad (4)$$

When microrotation parameter $R = 0$, we obtain $N = 0$ which represents no-spin condition i.e. the microelements in a concentrated particle flow-close to the wall are not able to rotate. Again, the constant R is varies in the range of $0 \leq R \leq 1$. According to Guram and Smith [17], for strong concentration $R = 0$ and this indicates $N = 0$, it describes the microelements nearby the wall surface are unable to rotate. While $N = 0.5$ denoted for weak concentration which signified the disappearance of the anti-symmetric part of the stress tensor. By following the recent work we assuming that $\gamma = \left(\mu + \frac{\chi}{2} \right) j = \mu \left(1 + \frac{K}{2} \right) j$, $K = \frac{\chi}{\mu}$ is the micropolar parameter or material parameter. The Newtonian kinematic viscosity is now supplemented by the Eringen micropolar vortex viscosity, χ . In the present work, we assume that the micro-inertia per unit mass j is constant.

The boundary conditions of the above equations are as follows:

$$u = \frac{ax^m}{1-ct}, v = 0, N = -R \frac{\partial u}{\partial y}, T = T_w \text{ at } y = 0$$

$$u \rightarrow U = \frac{bx^m}{1-ct}, N \rightarrow 0, T \rightarrow T_\infty \text{ as } y \rightarrow \infty$$

The governing partial differential equations are transformed into ordinary differential equations by applying local similarity transformation such as:

$$\eta = y \sqrt{\frac{u}{2\nu x(1-ct)}}, N = u \sqrt{\frac{u}{2\nu x(1-ct)}} H(\eta)$$

$$\psi = \sqrt{\frac{2\nu ux}{(1-ct)}} (1+n) f(\eta),$$

$$ur = \frac{\partial \psi}{\partial y}, vr = -\frac{\partial \psi}{\partial x}, \theta(\eta) = \frac{T - T_\infty}{T_w - T_\infty}$$

Using this dimensionless quantities, the governing equations together with the boundary conditions are reduced to a set of ordinary differential equations so that the numerical solutions can be calculated easily.

$$(1+K)f''' + \left(\frac{1+m}{2}\right)ff'' + m(1-f'^2) + KH'$$

$$+ M(1-f') + 2A\left(1-f' - \frac{1}{2}\eta f''\right) = 0 \quad (6) \square$$

$$\left(1 + \frac{K}{2}\right)H'' + \left(\frac{1+m}{2}\right)fH' + \frac{1-m}{2}f'H$$

$$- \frac{2K\zeta}{Re}(2H + f'') - A\left(H + \frac{1}{2}\eta H'\right) = 0 \quad (7) \square$$

$$\theta'' + Pr(1+n)f\theta' - \frac{2Prsf\theta}{1+m}$$

$$- \frac{2A}{1+m}\left(\theta + \frac{1}{2}\eta\theta'\right) = 0 \quad (8)$$

The transform boundary conditions are:

$$f(0) = 0, f'(0) = 1, H(0) = -\frac{1}{2}f''(0), \theta = 1 \text{ at } \eta = 0$$

$$f'(\infty) \rightarrow \lambda, H(\infty) \rightarrow 0, \theta \rightarrow 0 \text{ as } \eta \rightarrow \infty$$

Where η_∞ is the value of η at which boundary conditions are achieved, the prime denotes differentiation with respect to η and also

$$K = \frac{\kappa}{\rho\nu}, K^* = \frac{2\nu x}{ku}, A = \frac{c}{ax^{m-1}}, \lambda = \frac{b}{a},$$

$$Pr = \frac{\nu}{\alpha}, M = \frac{\sigma B_0^2 x}{\rho u}, Re = \frac{ux}{\nu}, \zeta = \frac{x^2}{j}$$

are the material parameter, porosity parameter, unsteadiness parameter, stretching ratio, Prandtl

number, magnetic parameter, Reynolds number, microinertia density constant respectively.

4. Results and discussion

The Numerical calculation of linear velocity, angular velocity, and temperature for different values of dimensionless parameters are carried out. For the purpose of our simulation we have chosen $M = 0.3$, $m = 0.2$, $K = 0.4$, $K^* = 0.4$, $\lambda = 0.1$, $A = 0.22$, $Re = 100$, and $Pr = 1.0$ throughout the calculation while the parameters are varied over range as shown in the figures. Fig.1 clearly shows that the effect of magnetic field is more prominent at the point of peak value, because the presence of M in an electrically conducting fluid produces a resistive force against the flow which is known as drag force and it is prominent at the peak point. As a result linear velocity profiles decreases. Similar result arises for porosity parameter that are displayed in Fig.6. The fluid of linear velocity increases for increasing values of pressure gradient, stretching ratio and material parameter which have depicted in Fig.2, Fig.3 and Fig.4. From Fig. 5 it is observed that the linear velocity decreases up to certain values of η and then increases. The angular velocity decreases for increasing values of magnetic parameter, porosity and unsteady parameter which have depicted in Fig.7, Fig.11 and Fig.12. From Fig.9 and Fig.10 it is observed that the angular velocity increases for increasing values of stretching ratio and material parameter. From Fig. 8 it is observed that the microrotation decreases up to certain values of η and then increases. The temperature decreases for increasing values of magnetic parameter, material parameter, unsteady parameter, porosity parameter, Prandtl number and wall temperature parameter which have depicted in Fig. 13 and Fig.16 – Fig.20 but the reverse result arises only for pressure gradient parameter and stretching ratio parameter that have displayed in Fig. 14 and Fig. 15. Further the heat transfer rate has compared with Mohammadi et al.[18] for various values of m with $M = K = K^* = A = \lambda = 0$. The results have shown in Table 1 and it is observed that the present results and those of [18] are almost similar.

Table 1: Comparison of local skin friction $f''(0)$ for different values of m Mohammadi et al.[18]

	Mohammadi <i>et al.</i>	Present results
m	$f''(0)$	$f''(0)$
0.0	0.469589	0.46964
1/11	-	0.65500
1/3	0.927601	0.92768
1.0	1.232587	1.232587

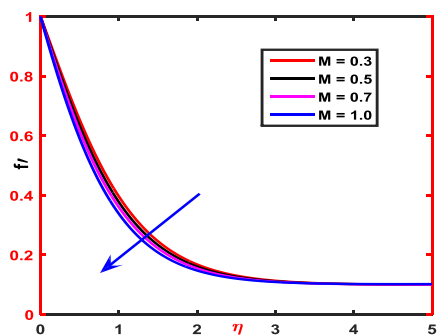


Fig.1. Velocity profiles for magnetic parameter

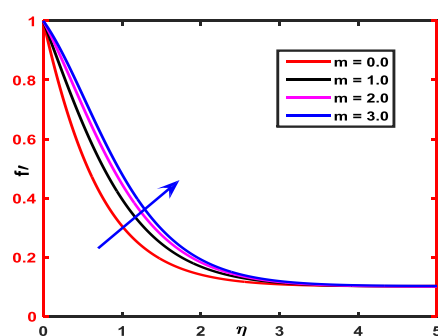


Fig.2. Velocity profiles for pressure gradient

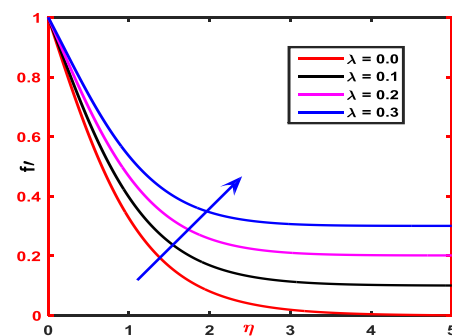


Fig.3. Velocity profiles for stretching ratio

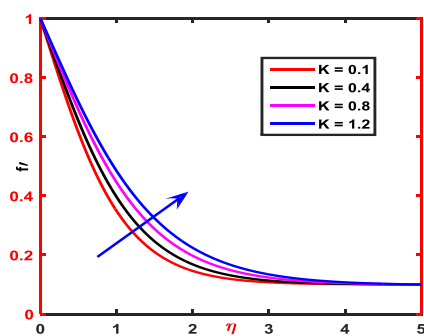


Fig.4. Velocity profiles for material parameter

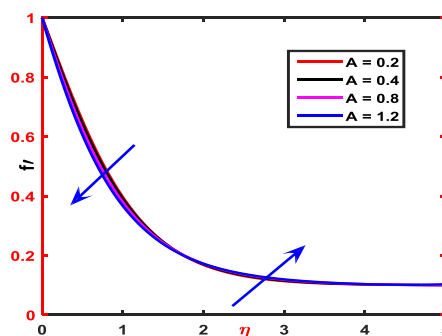


Fig.5. Velocity profiles for unsteady parameter

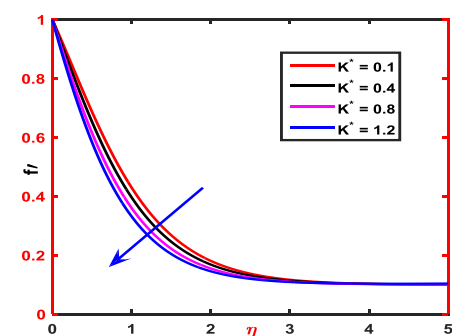


Fig.6. Velocity profiles for porosity parameter

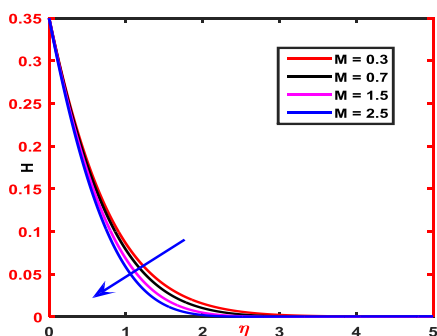


Fig.7. Angular velocity for magnetic parameter

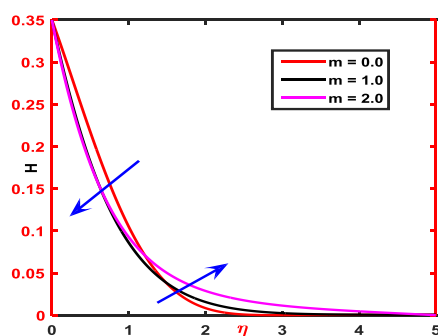


Fig.8. Angular velocity for pressure gradient parameter

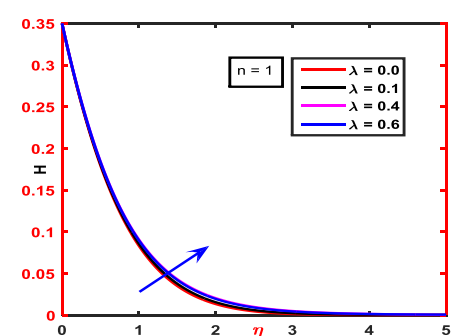


Fig.9. Angular velocity for stretching ratio parameter

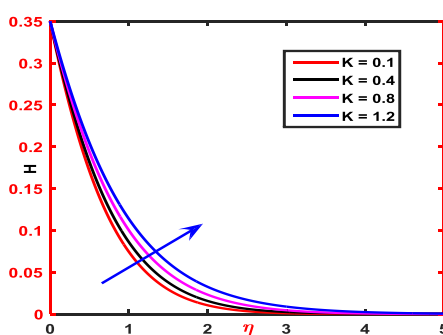


Fig.10. Angular velocity for material parameter

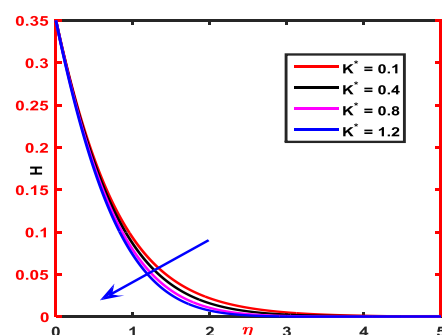


Fig.11. Angular velocity for porosity parameter

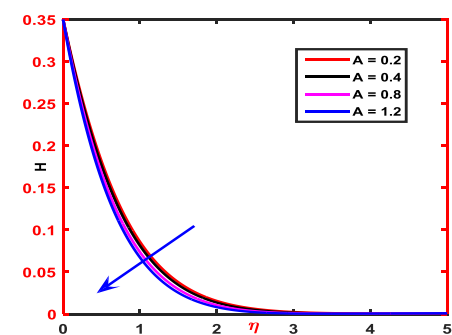


Fig.12. Angular velocity for unsteady parameter

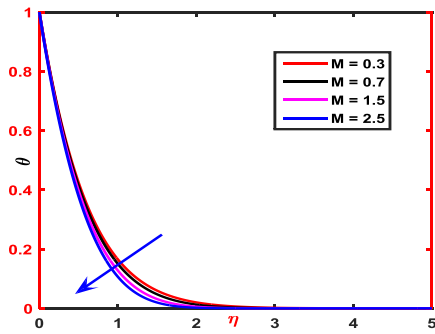


Fig.13. Temperature profiles for magnetic parameter

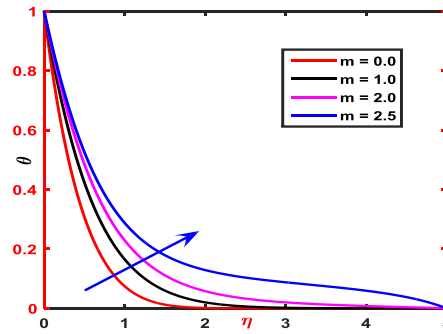


Fig.14. Temperature profiles for pressure gradient parameter

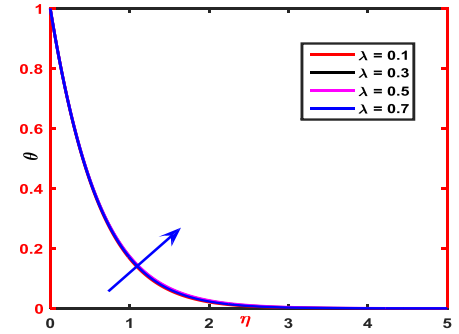


Fig.15. Temperature profiles for stretching ratio parameter

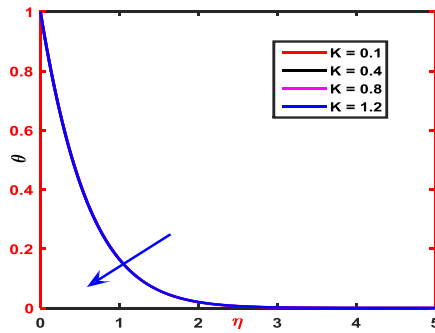


Fig.16. Temperature profiles for material parameter

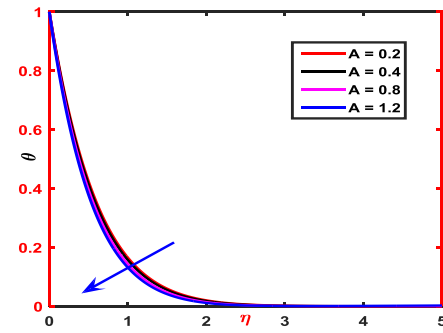


Fig.17. Temperature profiles for unsteady parameter

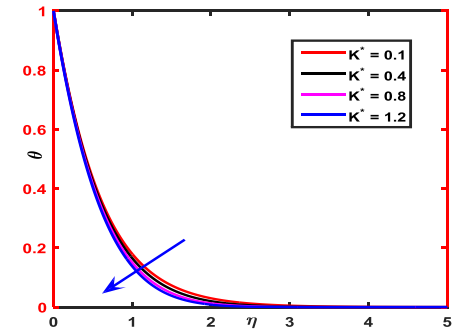


Fig.18. Temperature profiles for porosity parameter

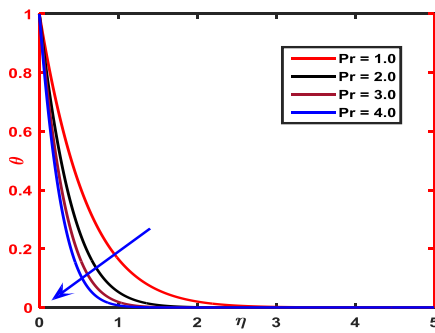


Fig.19. Temperature profiles for Prandtl number

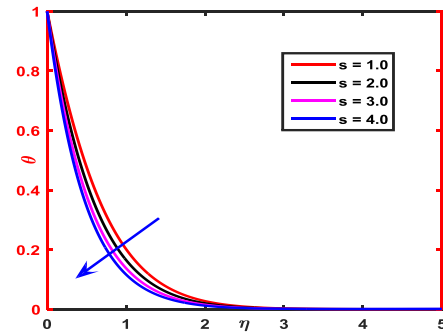


Fig.20. Temperature profiles for wall temperature parameter

5. Conclusions

The conclusions of the present problem are as follows:

- The fluid velocity within the boundary layer are decreases with the increasing values of magnetic parameter and porosity parameter but the reverse trend arises in case of pressure gradient, stretching ratio and material parameter. The fluid velocity decreases up to a certain values of eta and then increases for increasing values of unsteady parameter.
- The angular velocity are decreases for increasing values of magnetic parameter, porosity parameter and unsteady parameter but increases for the increasing values of stretching ratio and material parameter. The

angular velocity decreases up to a certain values of eta and then increases for pressure gradient parameter.

- The heat transfer rate increases for increasing values of magnetic parameter, wall temperature parameter, material parameter, Prandtl number, porosity parameter and unsteady parameter but the rate decreases only for stretching ratio and pressure gradient parameter.

NOMENCLATURE

MHD magnetohydrodynamic

c_p specific heat at constant pressure, $\text{Jkg}^{-1}\text{K}^{-1}$

κ thermal conductivity, $\text{w m}^{-1}\text{K}^{-1}$

β semi vertical angle, degree

g	acceleration due to gravity, ms^{-2}
σ	electrical conductivity, sm^{-1}
K^*	permeability of the porous medium
K	material parameter
μ	coefficient of viscosity, $\text{kg m}^{-1}\text{s}^{-1}$
ν	kinematics viscosity, m^2s^{-1}
ρ	fluid density, kg m^{-3}
B_0	magnetic field intensity, Am^{-1}
u	velocity component along x axis, ms^{-1}
v	velocity component along y axis, ms^{-1}
a	stream velocity constant
b	free stream velocity constant
c	unsteady constant
A	unsteady parameter
η	similarity variable
f	dimensionless stream function
H	microrotation
m	pressure gradient
T	fluid temperature, k^{-1}
T_w	plate temperature, k^{-1}
T_∞	free stream temperature
ψ	stream function

REFERENCES

- [1] A. C. Eringen, Theory of micropolar fluids, *J. Math. Mech.*, vol. 16, pp. 1–16, (1966).
- [2] T. Adekeye, I. Adegun, P. Okekunle, A. K. Hussein, Oyedepo S., Adetiba E. and Fayomi O., Numerical analysis of the effects of selected geometrical parameters and fluid properties on MHD natural convection flow in an inclined elliptic porous enclosure with localized heating, *Heat Transfer-Asian Research*, Vol. 46, pp. 261-293 (2017).
- [3] S. Ahmed, A. K. Hussein, H. Mohammed, and S. Sivasankaran, Boundary layer flow and heat transfer due to permeable stretching tube in the presence of heat source/sink utilizing nanofluids, *Applied Mathematics and Computation*, Vol. 238, pp. 149-162 (2014).
- [4] S. Ahmed, A. K. Hussein, H. Mohammed, I. Adegun, X. Zhang, L. Kolsi, A. Hasanpour, and S. Sivasankaran, Viscous dissipation and radiation effects on MHD natural convection in a square enclosure filled with a porous medium, *Nuclear Engineering and Design*, Vol. 266, pp. 34-42 (2014).
- [5] S. Reddy and A. J. Chamkha, Heat and mass transfer characteristics of MHD three-dimensional flow over a stretching sheet filled with water-based alumina nanofluid, *In. J. Numer. Methods Heat and Fluid Flow*, January 2018.
- [6] N. M. Ariffin, Norihan M. Arifin, and N. Bachok, Marangoni boundary layer flow in micropolar fluid with suction/injection, *AIP Conference Proceedings*, Vol. 1795, (2017).
- [7] S. R. Sheri and M. Shamshuddin, Heat and mass transfer on the MHD flow of micropolar fluid in the presence of viscous dissipation and chemical reaction, *Procedia Engineering*, Vol. 127, pp. 885 – 892, (2015).
- [8] A. A. Mostafa Mahmoud, S. Waheed, MHD flow and heat transfer of a micropolar fluid over a stretching surface with heat generation and slip velocity, *Journal of the Egyptian Mathematical Society*, Vol. 20, pp. 20–27, (2012).
- [9] M. Ali, M. A. Alam and M. A. Alim, MHD free convection heat and mass transfer flow through a porous medium in a rotating system with hall current and heat generation, *IEEE Xplore Digital Library*, pp. 404 – 408, (2014).
- [10] A. Ishak, R. Nazar, and I. Pop, Magnetohydrodynamic (MHD) flow of a micropolar fluid towards a stagnation point on a vertical surface, *Comput. Math. Appl.*, vol. 56, pp. 3188-3194, (2008).
- [11] K. Das, Influence of thermophoresis and chemical reaction on MHD micropolar fluid flow with variable fluid properties, *Int. J. Heat Mass Transfer*, vol. 55, pp. 7166–7174, (2012).
- [12] Bhattacharyya, S. Mukhopadhyay, G. C. Layek and I. Pop, Effects of thermal radiation on micropolar fluid flow and heat transfer over a porous shrinking sheet, *Int. J. Heat Mass Transfer*, vol. 55, pp. 2945–2952, (2012).
- [13] A. Redha, M. N. Bouaziz and S. Hanini, Numerical study of micropolar fluid flow heat and mass transfer over vertical plate: effects of thermal radiation, *Sci. Tech.*, Vol. 41, pp.15-22, (2015).
- [14] B. Mohanty, S. R. Mishra, and H. B. Pattanayak, Numerical investigation on heat and mass transfer effect of micropolar fluid over a stretching sheet through porous media, *Alexandria Eng. J.*, vol. 54, pp. 223–232, (2015).
- [15] R. Sudarsan, and A. J. Chamkha, Soret and Dufour effects on MHD heat and mass transfer flow of a micropolar fluid with thermophoresis particle deposition, *J. Naval Arch. Marine Eng.*, vol. 13, pp. 39-50, (2016).
- [16] S. Gopal, and P. Siva, Unsteady hydromagnetic heat and mass transfer flow of a micropolar fluid past a stretching sheet with Thermo-Diffusion and Diffusion-Thermo effects, *Int. J. Comput. Appl.*, Vol. 7, pp. 81-97, (2017).
- [17] G. S. Guram and A.C. Smith, Stagnation Flows of Micropolar Fluids with Strong and Weak Interactions, *Computers and Mathematics in Applications* Vol.6, pp. 213-233, (1980).
- [18] F. Mohammadi, M. M. Hosseini, A. Dehgahn, F. M. Maalek Ghaini, Numerical Solutions of Falkner-Skan Equation with Heat Transfer, *Studies in Nonlinear Science*, Vol. 3, pp. 86-93,(2012).

Effect of Nano Particle and Aspect Ratio in Natural Convection Heat Transfer in a Rectangular Enclosure: A Numerical Analysis

Md. Shariful Islam*, Mohammad Ilias Inam

Department of Mechanical Engineering, Khulna University of Engineering & Technology, Khulna-9203, BANGLADESH

ABSTRACT

This numerical study investigates the natural convection heat transfer characteristics of water-based nanofluid in a rectangular enclosure. Nanofluid contains copper as nanoparticle. The effect of volume fraction of particle (ϕ) and Aspect ratio (A) have been studied in this numerical study. A series of Direct Numerical Simulation (DNS) have been conducted into the range of $0 \leq \phi \leq 0.1$ and $0.5 \leq A \leq 2.0$ at fixed Rayleigh Number, $Ra = 5 \times 10^6$. A Commercial software ANSYS Fluent v16.1 (student version) has been used for these simulations. These numerical results demonstrate that the heat transfer rate increases almost linearly with respect to the particle volume fraction, however Nusselt number (Nu) decreases. Numerical results also demonstrate that heat transfer rate increases with respect to Aspect ratio up to $A = 1$, after that it starts to decrease. .

Key words: Convection, Aspect Ratio, Nanofluid, Volume fraction, DNS.

1. Introduction

Enhancement of heat transfer in the systems is an essential topic from an energy saving perspective. Over the past decade, nanofluids, have been reported to possess substantially higher thermal conductivity for example, copper has a thermal conductivity 700 time greater than water and 3000 greater than engine oil. This makes them very attractive as heat transfer fluids in many applications. Nanofluids would be useful as coolants in the automobile and electronics industries. However, the reported high thermal conductivity sometimes cannot be reproduced, and the potential mechanisms leading to the enhancement are still under scrutiny. Due to these reasons, nanofluids have been a controversial topic [1]. The past decade has witnessed several studies of convective heat transfer in nanofluids. Khanafer et al. [2] were the first to investigate the problem of buoyancy-driven heat transfer enhancement of nanofluids in a two-dimensional enclosure. Putra et al [3] did the same. Jou and Tzeng [4] numerically investigated the heat transfer performance of nanofluids inside two dimensional rectangular enclosures. Their results show that increasing the volume fraction causes a significant increase in the average heat transfer coefficient. But there is a contradiction in case of Nusselt number's response with volume fraction. Santra et al. [5] have conducted a similar kind of study, up to $\phi = 10\%$, using the models proposed by Maxwell-Garnett and Bruggeman. Hwang et al. [6] have carried out a theoretical investigation of the thermal characteristics of natural convection of an alumina-based nanofluid in a rectangular cavity heated from below using Jang and Choi's model [7] for predicting the effective thermal conductivity of nanofluids (and various models for predicting the effective viscosity). Oztop and Abu-Nada [8] investigated heat transfer and fluid flow due to buoyancy forces in a partially heated enclosure using nanofluids using various types of nanoparticles.

The natural convection studies corresponding to the parallelepiped enclosures can be classified into two elementary classes: i) heating from a horizontal wall (heating from below); ii) heating from a vertical wall. Calcagni et al. [9] made an experimental and numerical study of free convective heat transfer in a square enclosure characterized by a discrete heater located on the lower wall and cooling from the lateral walls. A steady laminar natural convection in 2D enclosures heated from below and cooled from above for a wide variety of thermal boundary conditions at the sidewalls has been carried numerically by Corcione [10]. A numerical investigation of natural convection of air in a vertical square cavity with localized isothermal heating from below and symmetrical cooling from the side walls was investigated by Aydin and Yang [11]. The same problem by replacing a constant flux heat source instead the localized isothermal heat source at the bottom wall has been analyzed by Sharif and Mohammad [12]. They investigated the effect of aspect ratio and inclination of the cavity on the heat transfer process. The effect of heater and cooler locations on natural convection in square cavities has been reported by Turgoklu and Yucel [13]. Natural convection in a square enclosure heated periodically from part of the bottom wall has been investigated by Lakhali et al. [14]. There are good number of papers which deal with natural convection with non-uniform temperature boundary conditions, for example, natural convection in rectangular enclosure with sinusoidal temperature on the upper wall and adiabatic boundary condition on rest walls Sarris et al. [15], natural convection in a square cavity with the different boundary conditions: uniform as well as nonuniform heating of bottom as well as side walls Roy et al. [16], and cooling by sinusoidal temperature profiles on equally divided active side wall with other sides are insulated Bilgen and Yedder [17]. Natural convection in air-filled 2D square enclosure heated with a constant source from below and cooled from above is

* Corresponding author. Tel.: +88-01738115432
E-mail addresses: sharifulmekuet@gmail.com

studied numerically by Nader et al. [18]. A numerical study to investigate the steady laminar natural convection flow in a square cavity with uniformly and non-uniformly heated bottom wall, and adiabatic top wall maintaining constant temperature of cold vertical walls has been performed by Basak et al. [19] with the help of penalty finite element method. In the same geometry, the numerical study deals with natural convection flow in a closed square cavity when the bottom wall is uniformly heated and vertical wall(s) are linearly heated whereas the top wall is well insulated has been reported by Sathiyamoorthy et al. [20].

In this paper effect of volume fraction of nanoparticle in heat transfer in a rectangular enclosure with heating from vertical wall, is observed. Effect of aspect ratio of the enclosure filled with nanofluid also investigated.

2. Physical Model

Fig. 1 shows a schematic diagram of a rectangular enclosure with heating from left vertical wall. The fluid in the enclosure is a water based nanofluid containing Cu as nanoparticles. The problem is solved in transient state. The flow is assumed to be laminar. It is assumed that the base fluid (i.e. water) and the nanoparticles are in thermal equilibrium and no slip occurs between them. The thermo-physical properties of the Cu Nano particle and base fluid are given in Table 1. The left wall is hot wall, maintained at a temperature T_h . The right wall is cold wall, maintained at temperature T_c . Temperature of left wall is higher than the right wall. Top and bottom walls are insulated. All four walls remain stationary. Here we assume that fluid velocity at all fluid–solid boundaries is equal to that of the solid boundary i.e. no slip condition and fluid temperature at all fluid–solid boundaries is equal to that of the solid boundary wall temperature i.e. no jump condition. The thermo-physical properties of the nanofluid are assumed to be constant except for the density variation, which is approximated by the Boussinesq model.

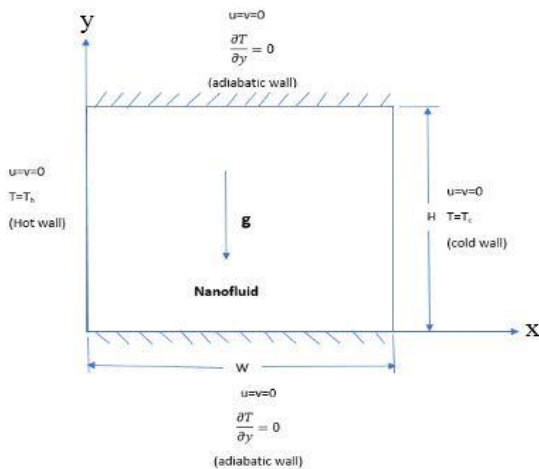


Fig.1 A typical sketch which shows the Problem with necessary condition.

3. Computational Details

The general momentum equation is also called the equation of motion or the Navier-Stoke's equation; in addition, the equation of continuity is frequently used in conjunction with the momentum equation. The equation of continuity is developed simply by applying the law of conservation of mass to a small volume element within a flowing fluid. The governing continuity, momentum and energy equations are-

$$\text{Continuity: } \frac{\partial \rho}{\partial t} + \frac{\partial}{\partial x}(\rho u) + \frac{\partial}{\partial y}(\rho v) = 0 \quad (1)$$

x momentum:

$$\frac{\partial u}{\partial t} + u \frac{\partial u}{\partial x} + v \frac{\partial u}{\partial y} = -\frac{1}{\rho} \frac{\partial p}{\partial x} + \frac{\mu}{\rho} \left(\frac{\partial^2 u}{\partial x^2} + \frac{\partial^2 u}{\partial y^2} \right) \quad (2)$$

y momentum:

$$\frac{\partial v}{\partial t} + u \frac{\partial v}{\partial x} + v \frac{\partial v}{\partial y} = -\frac{1}{\rho_{nf}} \frac{\partial p}{\partial y} + \frac{\mu_{nf}}{\rho_{nf}} \left(\frac{\partial^2 v}{\partial x^2} + \frac{\partial^2 v}{\partial y^2} \right) - \frac{1}{\rho_{nf}} (\rho \beta)_{nf} g (T - T_c) \quad (3)$$

$$\text{Energy: } \frac{\partial T}{\partial t} + u \frac{\partial T}{\partial x} + v \frac{\partial T}{\partial y} = \alpha_{nf} \left(\frac{\partial^2 T}{\partial x^2} + \frac{\partial^2 T}{\partial y^2} \right) + \frac{q''}{\rho c_p} \quad (4)$$

Here the term $-\rho g$ on the right side of the eq. (3) represents the body force exerted on the fluid element in the negative y direction [21].

The Boundary conditions are

At the time $t = 0$,

$$T = \frac{T_c + T_h}{2}$$

$$u = v = 0; \quad \text{at all } (x, y)$$

At the time $t > 0$,

$$\text{Left wall: } u = v = 0 \quad T = T_h$$

$$\text{Right wall: } u = v = 0 \quad T = T_c$$

Top and bottom walls are adiabatic.

Time step size is 0.1 sec, which is shown time dependency test and the total time for the calculation is 120 seconds.

The following dimensionless parameters are defined to show different results later:

$$X = \frac{x}{W} \quad Y = \frac{y}{H} \quad \theta = \frac{T - T_c}{T_h - T_c} \quad (5)$$

The effective properties of nanofluid are calculated as follows-

$$\rho_{nf} = (1 - \phi) \rho_f + \phi \rho_s \quad (6)$$

$$\alpha_{nf} = \frac{k_{eff}}{(\rho c_p)_{nf}} \quad (7)$$

The heat capacitance of the nanofluid is expressed as (Abu-Nada [22]; Khanafer *et al.* [2]):

$$(\rho c_p)_{nf} = (1 - \phi)(\rho c_p)_f + \phi(\rho c_p)_s \quad (8)$$

The effective thermal conductivity of the nanofluid is approximated by the Maxwell–Garnetts [23] model

$$\frac{k_{nf}}{k_f} = \frac{k_s + 2k_f - 2\phi(k_f - k_s)}{k_s + 2k_f + \phi(k_f - k_s)} \quad (9)$$

The use of eq. (9) is restricted to spherical nanoparticles where it does not account for other shapes of nanoparticles. The viscosity of the nanofluid can be approximated as viscosity of a base fluid if containing dilute suspension of fine spherical particles and is given by Brinkman [24]:

$$\mu_{nf} = \frac{\mu_f}{(1-\phi)^{2.5}} \quad (10)$$

Rayleigh no. and Nusselt numbers are defined as-

$$Ra = \frac{g\beta\Delta TH^3}{\nu\alpha} \quad Nu = \frac{hH}{k}$$

Physical property of the Cu-water nanofluid is determined from following Table 1.

Table 1 Thermo-physical properties of base fluid and Nano-particles [25]

Property	Water	Cu
ρ (kg/m ³)	997.1	8933
C_p (J/kgK)	4179	385
K (W/mK)	0.613	400
$\alpha \cdot 10^7$ (m ² /s)	1.47	1163.1
β (K ⁻¹)	0.00021	0.000051

4. Results and Discussion

This section includes mesh or grid independence test, time dependency test, model validation with some previously published paper and finally effect of volume fraction and aspect ratios are shown.

4.1 Grid Independence Test

The solutions for different mesh size have been studied in order to determine independence of each solution. Five structured meshes are used and temperature at midplane in y direction are plotted along x direction. Fig. 2 shows variation of temperature with x coordinate. It is clear from graph that there is slight or no change in temperature curve. Finally, 100×100 mesh is selected for square cavity. For other aspect ratios mesh number is selected with reference to this.

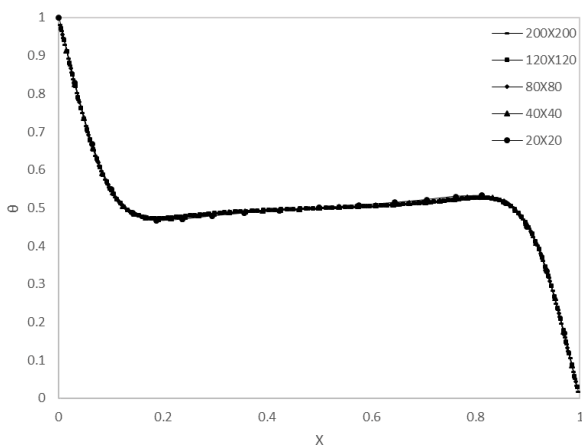


Fig.2 Variation of static temperature along x direction for different mesh (A=1, Ra=5×10⁶, φ = 0.1).

4.2 Time Dependency Test

In a similar fashion as mesh dependency test, for different residual values and time step sizes temperature is plotted against x coordinate. Finally, residual value for energy equation is selected as 10⁻⁹ & with respective others residual as 10⁻⁶. And time step size is selected as 0.1 sec.

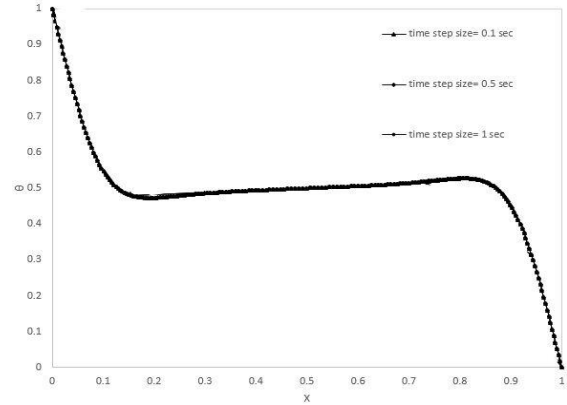


Fig.3 Variation of static temperature along x direction (midplane in y direction) for different time step size (A=1, Ra=5×10⁶, φ = 0.1)

4.3 Model Validation

The problem is solved by finite-volume based commercial software package ANSYS Fluent v16.1 (student version). It has been validated against solutions obtained in the literature as shown in Table 2. Natural convection of air inside a square cavity whose two sides are set to differential temperatures while keeping the top and bottom surfaces at adiabatic condition is a classic case for validation. Average Nusselt number for the hot wall calculated from the present model is compared with the data available in the literature and found good agreement for various Rayleigh numbers.

Table 2 Comparison of average Nusselt number for the hot wall obtained by various studies with present study for different Rayleigh numbers.

Ra	Nu						
	Present work	Vahl Davis [22]	Fusegi et al. [23]	Comini et al. [24]	Khanafer et al. [9]	Bilgen [25]	Kobra [26]
10 ⁴	2.240668	2.243	2.302		2.245	2.245	2.2448
10 ⁵	4.526406	4.519	4.646	4.503	4.522	4.521	4.5216
10 ⁶	8.862388	8.799	9.012	8.825	8.826	8.8	8.8262

4.4 Effect of Volume Fraction of Nanoparticle on Heat Transfer

Contours of static temperature are shown in fig.4. Contours are drawn for the time of 120 sec. For same time, with increasing volume fraction there is significant difference in the contours. For lower volume fraction change in temperature distribution is less than that of higher volume fraction. For high volume fraction change in temperature distribution in left upper side and right lower side is more prominent than lower volume

fraction. Similarly, in case of stream function (fig.5), maximum value of stream function increases with increase in volume fraction and contour takes a regular shape in higher volume fraction. The change is due to equivalent thermal conductivity.

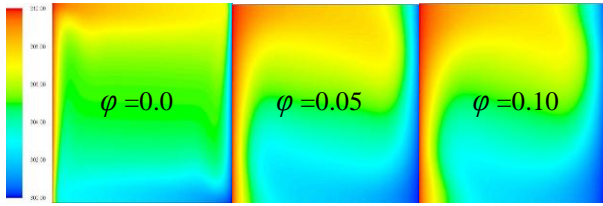


Fig.4 Contours of Static temperature with and without Nano particle ($Ra=5 \times 10^6$, time=120 sec).

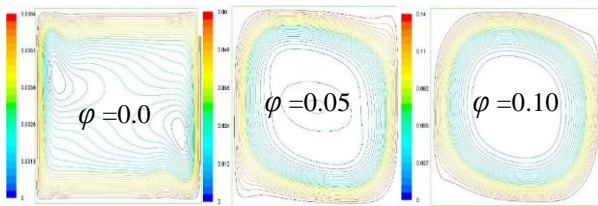


Fig.5 Contours of stream function(streamlines) with and without Nano particles ($Ra=5 \times 10^6$, time=120 sec).

Fig. 6 shows variation of local heat transfer coefficient and Nusselt number at hot wall and fig.7 shows average heat transfer coefficient and Nusselt number at hot wall for different volume fraction. Fig. 6 shows that local heat transfer coefficient increases with increase in volume fraction whereas local Nusselt number decreases with increases in volume fraction. Considering single graph in fig.6 it is seen that heat transfer coefficient first increases to a maximum value, then starts to decrease and goes to a minimum value. Fig. 7 shows that average heat transfer coefficient increases with increase in volume fraction and Nusselt number decreases with increase in volume fraction. Which justify the previous studies [2-3]. The reason behind this is, with increase in convective heat transfer coefficient thermal conductivity also increases and increase in conductive heat transfer is more prominent than convection.

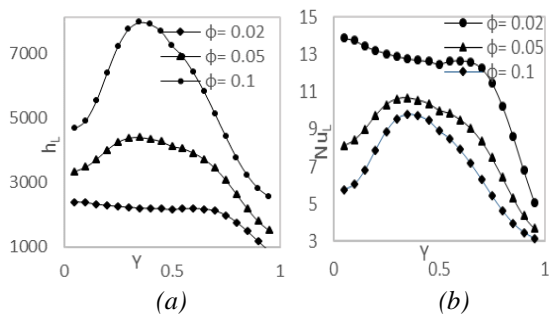


Fig.6 Variation of local (a) convective heat transfer coefficient and (b) Nusselt number along hot wall for different volume fraction ($Ra=5 \times 10^6$, time=120 sec)

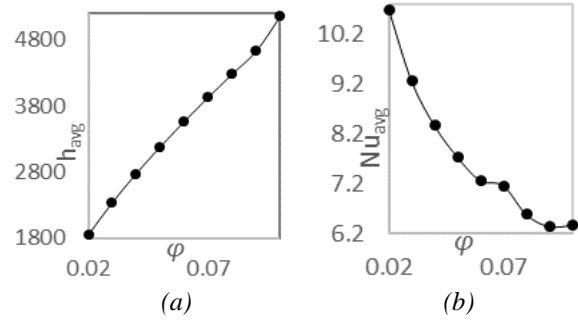


Fig.7 Variation of average (a) convective heat transfer coefficient and (b) Nusselt number with volume fraction along hot wall ($Ra=5 \times 10^6$, time=120 sec).

4.5 Effect of Aspect Ratio of Enclosure on Heat Transfer

Contours of static temperature are shown in fig. 8. Contours are drawn for the time of 120 sec. For same time, with increasing aspect ratio there is significant difference in the contours. Analyzing, contours it is prominent that temperature distribution is maximum when aspect ratio is unity. But maximum magnitude of stream function (fig. 9) increases up to aspect ratio 1.5 then start to decrease.

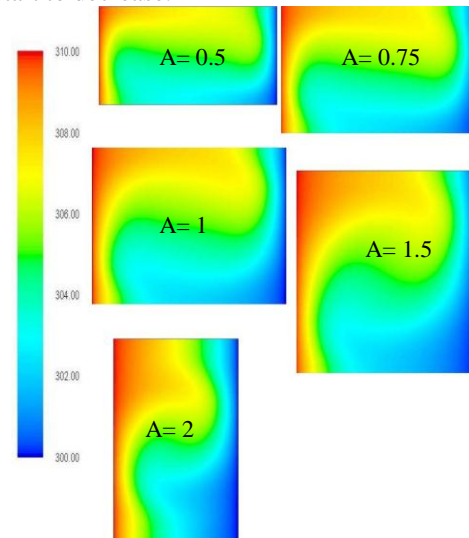


Fig. 8 Contours of Static temperature for different Aspect Ratio ($\Phi = 0.10$, $Ra=5 \times 10^6$, time=120 sec).

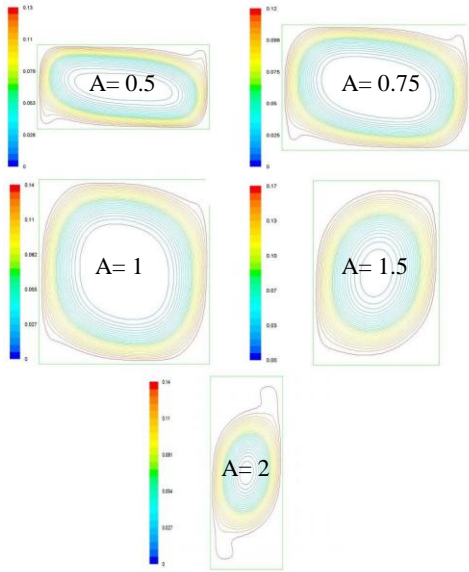


Fig. 9 Contours of Stream function (Streamlines) for different Aspect Ratio ($\Phi = 0.10$, $Ra=5 \times 10^6$, time=120 sec).

Variation of local heat transfer coefficient and Nusselt number are shown in fig. 10. Fig. 10(a) shows that local heat transfer coefficient increases with increase in aspect ratios. If aspect ratio further increased, maximum value of heat transfer coefficient also increases, but after a peak value it decreases sharply than that for other aspect ratios. Similar phenomena occur for local Nusselt number, as shown in fig.10(b). Considering figure 11, it is clear that average heat transfer coefficient as well as average Nusselt number increases with increase in aspect ratios up to one, after that, start to decrease. Which justify the previous investigations [30].

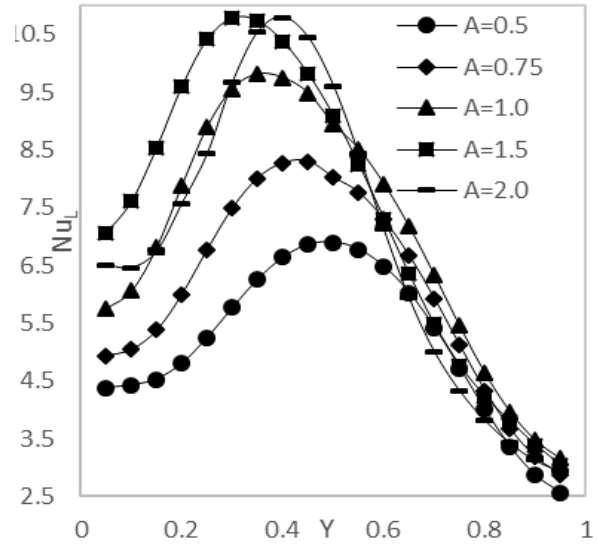
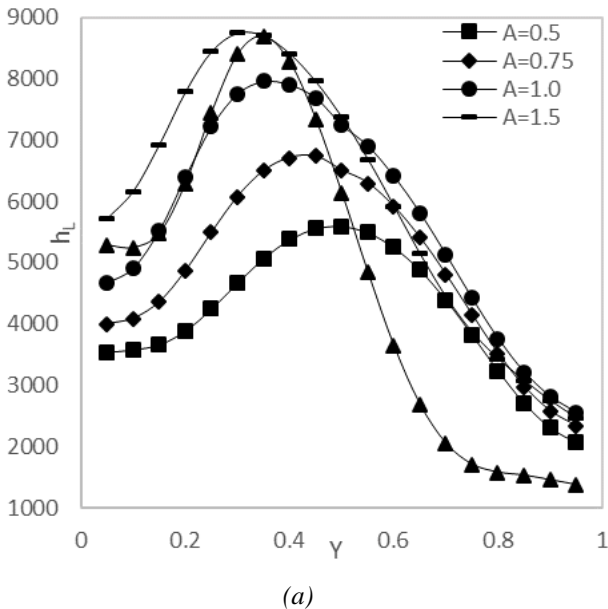


Fig. 10 Variation of local (a) convective heat transfer coefficient and (b) Nusselt number along hot wall for different aspect ratio ($\Phi = 0.10$, $Ra=5 \times 10^6$, time=120 sec).

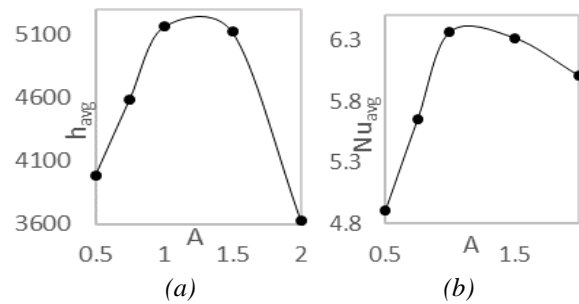


Fig.11 Variation of average (a) convective heat transfer coefficient and (b) Nusselt number with aspect ratio along hot wall ($\Phi = 0.10$, $Ra=5 \times 10^6$, time=120 sec).

5. Conclusion

A comprehensive investigation on natural convection in a rectangular enclosure filled with nanofluid is presented. The investigation is done to show the enhancement in heat transfer due to use of nanofluid instead of using pure fluids. The parameters investigated are, the solid volume fraction and aspect ratio. The results clearly show that-

- ❖ The amount of heat transfer is increased remarkably with increase in volume fraction of nanoparticles, but the Nusselt number decreases with increase in the same.

- ❖ Amount of heat transfer as well as Nusselt number increased with increase in aspect ratio up to one, beyond this value heat transfer and Nusselt number decreased. It is found that maximum heat transfer (and Nusselt number) is obtained at aspect ratio One.

REFERENCES

- [1] <http://web.mit.edu/nanoengineering/research/nanofluids.shtml>
- [2] Khanafer, K., Vafai, K., Lightstone, M., 2003. Buoyancy-driven heat transfer enhancement in a two-dimensional enclosure utilizing nanofluids 46, 3639–3653
- [3] Nandy Putra, Wilfried Roetzel, Sarit K Das. Natural convection of nano-fluids. *Int journal of Heat and Mass Transfer* 39(2003) 775-784
- [4] R.Y. Jou, S.C. Tzeng, Numerical research of nature convective heat transfer enhancement filled with nanofluids in rectangular enclosures, *Int. Commun. Heat Mass Transfer* 33 (2006) 727–736
- [5] A .K. Santra, S. Sen, N. Chakraborty, Study of heat transfer augmentation in a differentially heated square cavity using copper–water nanofluid, *Int. J. Thermal Sci.* 47 (2008) 1113–1122
- [6] K.S. Hwang, J.H. Lee, S.P. Jang, Buoyancy-driven heat transfer of water-based Al_2O_3 nanofluids in a rectangular cavity, *Int. J. Heat Mass Transfer* 50 (2007) 4003–4010
- [7] S.P. Jang, S.U.S. Choi, The role of Brownian motion in the enhanced thermal conductivity of nanofluids, *Appl. Phys. Lett.* 84 (2004) 4316–4318.
- [8] Oztop Hakan F, Abu-Nada Eiyad. Numerical study of natural convection in partially heated rectangular enclosures filled with nanofluids. *Int Journal of Heat and Fluid Flow* 29 (2008) 1326–1336
- [9] B. Calgagni, F. Marsili, M. Paroncini, Natural convective heat transfer in square enclosures heated from below, *Appl. Therm. Eng.* 25 (20 05) 2522–2531.
- [10] Corcione M. Effects of the thermal boundary conditions at the sidewalls upon natural convection in rectangular enclosures heated from bellow and cooled from above. *Int J Therm Sci* 2003;42:199–208.
- [11] Aydin O, Yang WJ. Natural convection in enclosures with localized heating from below and symmetrical cooling from sides. *Int J Numer Methods Heat Fluid Flow* 2000;10:5: 519–529.
- [12] Sharif MAR, Mohammad TR. Natural convection in cavities with constant flux heating at the bottom wall and isothermal cooling from the sidewalls. *Int J Therm Sci* 2005;44:865–78.
- [13] Turgoklu H, Yucel N. Effect of heater and cooler locations on natural convection in square cavities. *Numer Heat Transfer* 1995;A 27:351–8.
- [14] Lakhali EK, Hasnaoui M, Vasseur P, Bilgen E. Natural convection in a square enclosure heated periodically from part of the bottom wall. *Numer Heat Transfer* 1995;A 27:319–33.
- [15] Sarris IE, Lekakis I, Vlachos NS. Natural convection in a 2D enclosure with sinusoidal upper wall temperature. *Numer Heat Transfer* 2002;A 36:513–20.
- [16] Roy S, Basak T. Finite element analysis of natural convection flows in a square cavity with non-uniformly heated wall(s). *Int J Eng Sci* 2005;43:668–80.
- [17] Bilgen E, Yedder RB. Natural convection in enclosure with heating and cooling by sinusoidal temperature profiles on one side. *Int J Heat Mass Transfer* 2007;50:139–50.
- [18] Nader BC, Brahim BB, Taieb L. Influence of thermal boundary conditions on natural convection in a square enclosure partially heated from below. *Int Commun Heat Mass Transfer* 2007;34:369–79.
- [19] Basak T, Roy S, Balakrishnan AR. Effects of thermal boundary conditions on natural convection flows within a square cavity. *Int J Heat Mass Transfer* 2006;49:4525–35.
- [20] Sathiyamoorthy M, Basak T, Roy S, Pop I. Steady natural convection flows in a square cavity with linearly heated side wall(s). *Int J Heat Mass Transfer* 2007;50:766–75.
- [21] Ozisik M. Necati(1985). Heat Transfer(Int. Edition).Singapore: McGraw-Hill. ISBN 0-07-047982-8
- [22] Abu-Nada, E., 2008. Application of nanofluids for heat transfer enhancement of separated flows encountered in a backward facing step. *Int. J. Heat Fluid Flow* 29, 242–249.
- [23] J.C. Maxwell-Garnett, Colours in metal glasses and in metallic films, *Philos. Trans. Roy. Soc. A* 203 (1904) 385–420
- [24] Brinkman, H.C., 1952. The viscosity of concentrated suspensions and solutions. *J. Chem. Phys.* 20, 571–581.
- [25] Ogut E.B. Natural convection of water-based nanofluids in an inclined enclosure with a heat source. *Int Journal of Thermal Sciences* 4 8 (2009) 20 63–2073
- [26] D.V. Davis, Natural convection of air in a square cavity a bench mark numerical solution. *Int J Numer Method Fluids*, 3 (1983) 249–64.
- [27] T. Fusegi, J.M. Hyun, K. Kuwahara, and B. Farouk, A numerical study of three-dimensional natural convection in a differentially heated cubical enclosure, *Int. J. Heat Mass Transfer*, 34 (1991) 1543–1557.
- [28] G. Comini, G. Cortella, and M. Manzan, A stream function-vorticity-based finite element formulation for laminar convection, *Num Heat Transfer, Part B*, 28 (1995) 1-22.
- [29] Kobra F, Quddus N, Alim Abdul. Heat transfer enhancement of Cu-water nanofluid filled in a square cavity with a circular disk under a magnetic field. 10th *International Conference on Mechanical Engineering, ICME* 2013.
- [30] Alom parvez, Kumar Ashok, Kapoor S, Ansari S.R. Numerical investigation of natural convection in a rectangular enclosure due to partial heating and cooling at vertical walls .*Commun Nonlinear Sci Numer Simulat* 17 (2012) 2403–2414

ICMIEE18-111

Implementation of 9S Approach in a Jute Industry: A Case Study

Md. Sumon Rahman^{1*}, Md. Ariful Islam², Md. Tahiduzzaman¹, Md. Shohanur Rahman¹

¹Department of Industrial and Production Engineering, Jessore University of Science & Technology, Jessore-7408, BANGLADESH

²Business Administration Discipline, Khulna University, Khulna - 9208, BANGLADESH

ABSTRACT

Productivity improvement is one of the foremost intentions of any manufacturing industry. This productivity may fall due to various non-value-added activities. In this study, implemented “9S” is actually an extension in basic and conventional “5S” (Sort, Set in order, Shine, Standardize and Sustain) system which is a Japanese system for overall organizational adjustment and good maintenance of places in a selected jute industry (Platinum Jubilee Jute Mill) which is situated in Khulna, Bangladesh. Authors have extended this basic 5S system by incorporating Safety, Spirit, Simplicity and finally Skill. It creates a dynamic environment where improvement efforts in safety, quality, cost, delivery and creativity are heartened with the participation of all employees. The purpose of the study is to improve productivity by implementing the 9S approach in a new manner of 5S. After proper implementation of 9S in selected jute industry the productivity improved from 1477.63 tons to 1837.04 tons of jute product.

Keywords: 9S, Productivity, Jute product, Case Study.

1. Introduction

To earn the profit is the main goal of a manufacturing industry through reducing or eliminating all kinds of non-value added activities. Non-value added activities are those the customers do not pay for. The concept 9S is the extension of 5S which help an organization to reduce waste and improve productivity. 5S was established in Japan and was identified as one of the methods that used as a principle of continuous improvement, also called kaizen [1]. 5S is a workplace organization method that uses a list of five Japanese words: *seiri*, *seiton*, *seiso*, *seiketsu*, and *shitsuke*. English equivalent words are “Sort”, “Set In order”, “Shine”, “Standardize” and “Sustain”. This helps to organize a work space for efficiency and effectiveness by detecting and eliminating the items used, retaining the area and items, and sustaining with a new manner. Normally 5S is viewed as a part of a broader concept known as visual control, visual workplace or visual factory [2], [3]. The objective of this study has developed the productivity of selected jute industry to respond to the improvement process implementation 9S and the need to eliminate existing non-value added activity and wastes. In here, 9S is the extended from basic conventional 5S to advanced 9S such as Safety, Spirit, Simplicity, and Skill.

2. Literature Review:

In 2017 researchers implemented the 5S methodology in a Food and Beverage industry to save money, space, increase productivity by decreasing rejection of components.[4] To promote the service quality in health care provision In the Sri Lankan health sector 5S used as the entry point [5].It is possible to improve the quality of the work by proper implementing of the 5S

approach.[6] Researchers applied the 6S kaizen method in a laboratory to facilitate the work process, reduce waste, improve worker safety, and also improve staff performance. [7] 5S method is very important and has a positive correlation to the overall performance of production results [8]. It has proved that 5S is an effective method for improving housekeeping, health and safety standards in the workplace as well as environmental performance. The study also concluded that effort and participation from top management is a must for proper implementation of 5S [9].

3. Meaning of 9S

Basically 9S is the advanced extension of conventional 5S [10] technique. The steps of 9S process are as follows:

3.1. Sort:

Sort means, removing all unnecessary items from the working area. It helps an employee to easy access to their equipment.

3.2. Set in Order

The practice of orderly setup so the right item can be picked efficiently (without waste) at the right time and easy to access for everyone. A place for everything and everything in its place .

3.3. Shine

Clean the work area and tools as they always are ready to be used for the workers.

3.4. Standardize

It means the best practice within the workplace. It ensures that all setup and tools are in right condition by promoting visible and modest directions.

3.5. Sustain

Implementing behaviors and ways to continue the recognized standards over the long term and making the workplace organization the key to managing the process for success.

3.6. Safety

It means creating the working environment safe and free from any kind of recognizable hazard.

3.7. Spirit

It means teamwork. None can't implement 5S individually. It is very essential "S" of 9S as without spirit or teamwork, 5S or 9S couldn't be sustained or even executed.

3.8. Simplicity

For an efficient and successful manufacturing system must be simple. The Simpler system is easy to understand, easy to execute, and easy to implement for workers and management.

3.9. Skill.

Skill means the ability to do something well. Skilled workers play an important role in their occupations that are economically productive. The Proper training program helps the workers to become more skillfulness.

4. Methodology:

The focus of this study is to analyze the working area of the selected jute industry. The industry was first visited in April 2017 before 5S implementation. The first step is to identify problems by using the method of observation and note the production data on the condition of different production lines. Assessment 9S concept is applied to the production floors. Then the industry was revisited in accordance with different stages of implementation of 9s during a six months period from April 2017 to September 2017. Data was collected from the previous condition of the industry (before the implementation of 9S) and existing condition of the industry (after the implementation of 9S). Then in the value analysis of the assessment results 9S, pictures are taken before and after implementation of 9S and data are recorded, so that can be given recommendations for continuous improvement (Kizen).

5. Result and Discussion:

The selected jute mill produces two types of jute products as hessian and sacking jute cloth and bag using about 1800 loom machine. Before implementation of 9S observed three months on the production process and collected production data from April 2017 to September 2017. The monthly status among (winding section,

weaving section, finishing section) is being showed by table-1.

Table- 1: Monthly production data (Before 9S implementation)

		April	May	June	
Windin g	Sacking (ton)	50.89	45.25	46.91	Total
product ion	Hessian(ton)	16.96	15.08	14.30	
Weavin g	Sacking (ton)	188.2	161.3	158.1	
product ion	Hessian(ton)	2	6	5	
Bag Product ion	Sacking (ton)	62.74	53.78	50.71	
	Hessian(ton)	169.7	141.6	147.7	
	Sacking (ton)	8	5	9	
	Hessian(ton)	56.59	47.21	50.26	
Total		545.1	464.3	468.1	1477.
		8	3	2	63

After successful implementation of 9S, the productivity increased from previous months which present as table-2.

Table-2: Production after implementation of 9S

		July	Augu st	Septe mber	
Windin g	Sacking (ton)	61.72	85.44	110.70	Total
Produc tion	Hessian (ton)	20.18	58.48	70.23	
Weavi ng	Sacking (ton)	165.6	192.3	200.96	
Produc tion	Hessian (ton)	9	0	66.98	
Bag Product ion	Sacking (ton)	57.89	64.10	66.98	
	Hessian (ton)	150.9	168.1	187.92	
	Sacking (ton)	7	4		
	Hessian (ton)	53.32	59.38	62.641	
Total		509.7	627.8	699.43	1837.
		7	4		04

<u>Term</u>	<u>Before</u>		<u>After</u>	
1.Sort	Unnecessary parts are placed in floor		Removed unused part from workplace	
2.Set in order	Products pickup randomly		Products pickup in a systematic way	
3.Shine	Workplaces are not net & clean		Net & clean workplace	
4.Standaedized	No proper container used		Used standard container	
5. Sustain				For sustaining the '9S' technique effectively and to strictly adhere to it in the organization, operators, supervisors and floor managers audits are conducted periodically.
6. Safety	No mask used		Used mask	
7.Spirit(team-work)		Discussion between worker and management did not hold About 9S.	Group work to sustain 9S	



8. Simplicity		No working flow- chart are found	Provided a simple working flow - chart	
9. Skill	No training program was held		Training program hold periodically	

Fig.-1: 9S implementation report

After successful implementation of 9S, the results are presented showing the improvements in different parts of the selected jute industry for different S of the 9S system on different occasions are as shown in figure- 1.

The monthly improvement of productivity is as shown in figure- 2.

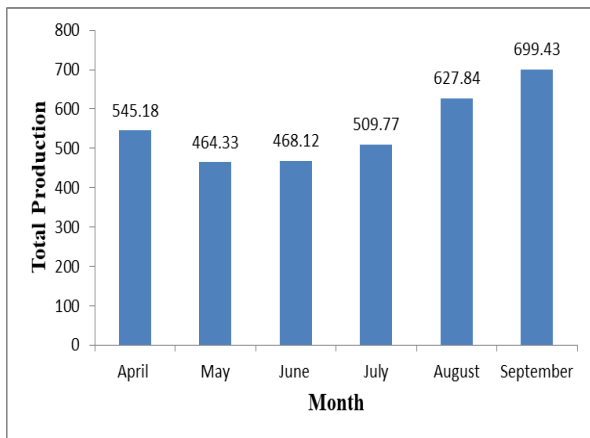


Fig. - 2: Monthly production rate.

From figure- 2, it shows that productivity is increasing from July to September. Before implementation of 9S, the total production was 1,477.63 tons which shown in table -1. On the other hand, after successfully implementation 9s concept the total production increased as 1,477.63 tons to 1,837.04 tons which shown in table -2. As a result due to the implementation of 9S concept productivity improved 359.41 tons. If this concept is sustained for day long then the productivity will be improved continuously.

6. Conclusion:

From this study, it can be seen that successful implementation of 9S plays a very important role in the

fastener or any manufacturing industries to find out and eliminate various types of non-value added activities. In this study, before implementation of the 9S method the total productivity of three months was 1,477.41 tons and after implementation of the 9S method the total productivity of three months calculated 1,837.04 tons indicating the improvement of production rate and reduces the unnecessary usages of properties. The results showed that the 9S methodology can be effectively used in this sector. From this study it can be concluded that by proper implementation of 9S concepts can help a jute industry to achieve high benefit without higher investment, it can be applied to any industry.

REFERENCE

- [1] Hirano, Hiroyuki. *JIT Factory Revolution: A Pictorial Guide to Factory Design of the Future*, 1988.
- [2] Ortiz, Chris A. and Park, Murry. *Visual Controls: Applying Visual Management to the Factory*. New York: Productivity Press, 2010.
- [3] Jump up^ Galsworth, Gwendolyn D. *Visual Workplace: Visual Thinking*. Portland, Ore: Visual-Lean Enterprise Press, 2005.
- [4] Sk. Riad Bin Ashraf et al, Implementation of 5S Methodology in a Food & Beverage Industry: A Case Study, *International Research Journal of Engineering and Technology (IRJET)* Volume: 04 Issue: 03 | Mar -2017
- [5] K.W.C.U. Kendangamuwa, S. Sridharan, D R K Herath, R.M.M.K. Ratnayake, "Factors Contributing to the Sustainability of 5S Programmes in Government Hospitals in Regional Director of Health Services Area Kurunegala,"

- [6] Y. Johana, N. M. Hardi, L. Abdullah, N. Jumadi, W.N.S.W. Mohammad, N. S. Taharuddin, "The Sustainability of QE/5S Implementation in an Administration Office of a Higher Education Institution," 2014, <https://www.researchgate.net/publication/278244980>
- [7] AD Sari¹, MR Suryoputro², and FI Rahmillah³ A study of 6S workplace improvement in Ergonomic Laboratory, Materials Science and Engineering 277 (2017) 012016
- [8] Cristina Veres (Harea)^{Pa}, POF, Liviu Marian^{PaP}, Sorina Moica^{PbP}, Karam Al-Akel^{Pa} Case study concerning 5S method impact in an automotive company, Procedia Manufacturing 22 (2018) 900–905
- [9] Rahman, M.N.A; Khamis ,N,K; Zain, R,M;, Deros, B,M; and Mahmood, W,H,W; "Implementation of 5S Practices in the Manufacturing Companies: A Case Study," American Journal of Applied Sciences 7 (8): 1182-1189, pp.1184-1186, 2010.
- [10] H. Hirano. 5S for Operators: 5 Pillars of the Visual Workplace, (SteinerBooks), 1996.

ICMIEE18-113

Numerical Investigation of Laminar Convective Heat Transfer and Friction Factor of a Pipe by Using Al₂O₃-Water Nanofluid

Md. Insiat Islam Rabby^{1,*}, Md. Safwat Amin Alvi¹, Md. Sazedur Rahman¹, A.K.M Sadrul Islam¹

¹ Department of Mechanical Engineering, Military Institute of Science & Technology, Dhaka, BANGLADESH

ABSTRACT

The Numerical study of laminar convective heat transfer of aluminum oxide (Al₂O₃) - water nanofluid for the developed region through a plain tube is presented. The second order single phase energy equation, mass and momentum equation are solved by using finite volume method with the ANSYS FLUENT 16 software. The plain pipe's diameter is 5mm and length is 750mm. Aluminum oxide (Al₂O₃) nanoparticles with different volume fraction (1% - 5%) using with water which is considered as the base fluid are analyzed for a range of Reynolds number from 100 to 1400 at constant heat flux 500 W/m² at the tube wall. The result reveals that for increasing the Reynolds number the Nusselt number and heat transfer coefficient are increased linearly and friction factor decreased linearly in the developed region for both water and Al₂O₃-H₂O nanofluid. At constant Reynolds number, by increasing the volume fraction of Al₂O₃ nanoparticles from 1% to 5% the value of Nusselt number increased rapidly from 0.27% to 15%, heat transfer coefficient increased 7.2% to 31.5% and friction factor increased very little from 0.1% to 2%.

Keywords: Convective heat transfer, friction factor, nanofluids, nanoparticles volume concentration and thermal conductivity.

1. Introduction

The most fundamental and effective topics of thermal engineering is heat transfer which influences our everyday life significantly and discusses about generation and creation, demeanor, principle, metamorphosis and permutation of thermal energy and heat between physical systems. This is the main stagnation of thermodynamics. Effective amount of heat removal or addition moving from one process stream to another is one of the major challenges in numerous industries, including power generation, transportation, manufacturing, air conditioning, cooling, heating, lubricating etc. Apart from conduction fluid also carry out energy and heat. In automobiles, refrigerators, heat exchangers, air-condition system, cooling and lubricating system etc. system's energy transfer is carried by fluid. On the other hand fluid is the main phenomena to control the behavior of heat transfer. From last few decades to improve heat transfer efficiency, heat transfer rate, thermal conductivity and to reduce pumping power, pressure loss, frictional loss between any physical systems several methods has been developed. Among these methods some are utilization of extended surface of the physical system, application of vibration to the heat transfer surface, use of micro channels, utilization of fins etc. But one important investigation is heat transfer can also be improved significantly by increasing the thermal conductivity of the working fluid. And so at present maximum researchers give more concentration on improving the thermal conductivity of working fluids because water, ethylene glycol and engine oil which are commonly used as heat transfer fluid but this fluid have relatively low thermal conductivity when compared to the thermal conductivity of solids. So by adding small amount of solid particles with the base or working fluid, the thermal conductivity of

the fluid can be increased noticeably. And by using these concept researchers has been made nanofluid which is the combination of base fluid (water, engine oil or ethylene glycol) and very small amount of solid particles at Nano scale size (1nm to100nm). Al₂O₃, CuO, TiO₂, SiC, SiO₂, Fe₂O₃, MgO etc. particles are used as nanoparticles to mix with base fluids. Different researchers carried out their investigation on nanofluids. In 1995-1996 Choi and Eastman [1] reinvestigated with their Nano scale metallic particle and carbon nanotube suspensions in Argonne National Laboratory. Choi and Eastman have tried to suspend various metal and metal oxides nanoparticles in several different fluids (Choi (1998) [2]; Choi et al.(2001)[3]; Choi et al. (2005); Choi et al. (2006); Eastman et al. (2001)[4]; Eastman et al. (1999); Eastman et al. (2004)) and their result are promising. From their investigation they also observed that many things remain vacuous about these suspensions of Nano-structured materials, Choi and Eastman have been termed these as "Nano fluid" Xuan and Li, 2003[5] examined the convective heat exchange and the stream highlights of Cu- water Nano fluids in a 10-mm inward distance across tube. The trial comes about because of their investigation, in the turbulent area showed that the friction factors of the Nano fluids, between 1 and 2 vol. % fractions are generally the same as those of water flow. Williams et al., 2008 [6] experimentally explored the turbulent stream of alumina- water and zirconia- water Nano fluids in tubes. They found that current connections for single-stage stream can enough anticipate Nano fluid stream convective heat exchange and weight drop. Rea et al., 2009[7] led an investigation on the laminar convective warmth exchange and weight drop of alumina- water and zirconia- water Nano fluids in a tube with 4.5-mm inward width. Their discoveries demonstrated that, with

* Corresponding author. Tel.: +88-01635881451
E-mail addresses: insiatislam8@gmail.com

appropriately measured Nano fluid properties, there is no deviation in convective heat exchange and weight drop of Nano fluid spill out of customary single-stage stream hypothesis. Heris et al.,2013 [8] played out an exploratory investigation to decide the pressure drop and heat exchange qualities of Al_2O_3 /water and CuO/water nanofluids in a triangular conduit under consistent heat flux where the flow was laminar. Their outcomes demonstrated that, at similar estimations of nanoparticle volume division and Reynolds number, utilizing Al_2O_3 nanoparticles is more beneficial than CuO nanoparticles. Wen and Ding, 2004[9] also investigate with laminar convective heat transfer using Al_2O_3 nanofluid. Hwang and Choi, 2009[10] also worked on it and showed that 3% volume concentration Al_2O_3 nanofluid gives 8% enhancement of heat transfer coefficient N.K Chavda and Makwana [11] carried an experiment on different pipe and pipe fittings to investigate the friction factor and loss coefficient by using CuO/water nanofluid and the result shows that friction factor increases with the increment of concentration of CuO/water nanofluid compared to water.

2. Physical Model and Boundary Conditions:

A two dimensional tube with a steady heat flux that is supplied on its surface to investigate heat transfer rate and corresponding friction factor. In order to investigate the performance of Nano fluid through a tube, a numerical study has been carried out by employing the well-known commercial computational fluid dynamics software ANSYS Fluent. A laminar flow through a two dimensional circular shape pipe with 5mm diameter and 750 mm length is presented. A constant uniform heat flux of $500 W/m^2$ is applied at the wall boundary of the tube and fluid is permitted to stream with a fitting speed and uniform temperature of 303 K at the inlet of the tube with a presumption of no slip condition on the tube wall. All the fluid dynamic and heat exchange parameters are extricated after the hydrodynamic and thermal improvement of the fluid stream and in this case the entrance length is $x/D=60$ beyond which all the measurements are taken. For calculating the heat transfer enhancement and friction factor the temperatures are taken at a line which is situated 750mm from inlet and pressures are taken at lines 725mm and 715mm from the inlet.

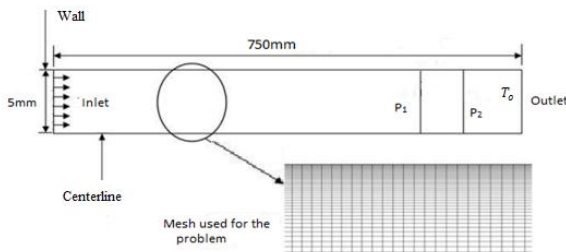


Fig.1 Physical model of the numerical problem and the corresponding mesh of the domain (Tube)

3. Numerical Method and Methodology:

We use a commercial computational fluid dynamics software ANSYS (Fluent) for this numerical analysis. All

the governing equations for mass, momentum, energy, and laminar quantities are solved using a control volume technique. At inlet laminar inlet velocity and at the outlet boundary pressure outlet is considered. Under relaxation factors 0.4 for pressure, 0.785 for momentum equation, 1 for energy equation, and 0.8 for density equation are considered for circular tube. Al_2O_3 -water nanofluids with different particle volume fractions (1, 2, 3, 4, and 5%) are tested with a wide range of Reynolds number (100-1000 for circular tube) and then results are compared with base fluid water.

3.1 Governing Equation:

The governing equation continuity, momentum and energy for forced convection under laminar flow and steady-state conditions are expressed as follows:

Continuity Equation:

In steady flow, the amount of mass within the control volume under remains constant, and thus the conversation of mass can be expressed as

$$\frac{\partial u}{\partial x} + \frac{\partial v}{\partial y} = 0 \quad (1)$$

Momentum Equation:

For laminar flow, the momentum equation can be expressed as:

$$\rho \left(u \frac{\partial u}{\partial x} + v \frac{\partial u}{\partial y} \right) = \mu \frac{\partial^2 u}{\partial y^2} \quad (2)$$

Energy Equation:

Energy can be transferred by heat, work, and mass only, the energy balance for a steady-flow control volume can be write explicitly as

$$\begin{aligned} (E_{in} - E_{out})_{by\ mass} &= -\rho c_p \left(u \frac{\partial T}{\partial x} + T \frac{\partial u}{\partial x} \right) dx \cdot dy - \rho c_p \left(v \frac{\partial T}{\partial y} + T \frac{\partial v}{\partial y} \right) dx \cdot dy \\ &= -\rho c_p \left(u \frac{\partial T}{\partial x} + T \frac{\partial T}{\partial y} \right) dx \cdot dy \end{aligned} \quad (3)$$

3.2. Thermal and fluid dynamic Properties of Nanofluids:

The Reynolds number for the flow of Nano fluid is

$$\text{expressed as: } Re = \frac{\rho_{nf} U_{av} D_h}{\mu_{nf}} \quad (4)$$

The rate of heat transfer Q_{nf} to the tube wall is assumed to be totally dissipated to Nanofluid flowing through a circular tube, raising its temperature from inlet fluid bulk temperature T_{bi} to exit fluid bulk temperature T_{bo} . Thus,

$$Q_{nf} = m_{nf} C_{p_{nf}} (T_{bo} - T_{bi}) \quad (5)$$

Where m_{nf} the mass flow rate of nanofluid is, $C_{p_{nf}}$ is the specific heat of Nano fluid at constant pressure.

The average heat transfer coefficient h_c is given by:

$$h_c = \frac{Q_{nf}}{A_w (\Delta T)} \quad (6)$$

Where A_w is the surface area of circular tube and the temperature difference between the wall and calculated as:

$$T = \frac{(T_w - T_o) - (T_w - T_i)}{\ln\left(\frac{T_w - T_o}{T_w - T_i}\right)} \quad (7)$$

So the expression of average Nusselt number is defined as follows:

$$Nu = \frac{h_c D_h}{K_{nf}} \quad (8)$$

$$\text{Pressure difference: } \Delta P = \frac{f L \rho U^2}{2 D_h} \quad (9)$$

Then, the Darcy friction factor, for laminar flow is:

$$f = \frac{64}{Re} \quad (10)$$

Dynamic Viscosity:

The dynamic viscosity For Al_2O_3 -water Nano fluid is given by Maiga et al.(2004)[12]:

$$\mu_{nf} = (1 + 7.3\phi + 123\phi^2) \quad (11)$$

Thermal Conductivity:

A wide range of experimental and theoretical studies were conducted in the literature to model thermal conductivity of nanofluids. The existing results were generally based on the definition of the effective thermal conductivity of a two-component mixture. . There are several thermal conductivity equations among them we use Pak and Cho equation for Al_2O_3 -water nanofluid. The following formulas are given by Pak and Cho (1998) [13], equation

$$K_{nf} = K_{bf}(1.0021 + 7.3349\phi) \quad (12)$$

Density:

Using classical formulas derived for a two-phase mixture density (Xuan and Roetzel, 2000) of the nanofluid as a function of the particle volume concentration and individual properties can be computed using following equation [14]:

$$\rho_{nf} = \rho_p \phi + \rho_{bf}(1 - \phi) \quad (13)$$

Specific Heat:

Using classical formulas derived for a two-phase mixture, the specific heat capacity (Pak and Cho, 1998) of the nanofluid as a function of the particle volume concentration and individual properties can be computed using following equation [13]:

$$C_{nf} = (1 - \phi)C_w + \phi C_p \quad (14)$$

4. Code Validation Test

For laminar tube flow at uniform velocity and constant heat flux water has been passed through the tube and a range of Reynolds number of 500-1400 has been considered for calculating Nusselt numbers and a range of

Reynolds number 100-1000 has been considerate for calculating friction factor. At fully developed zone the obtaining Nusselt number is compared with the constant value of Nusselt number for laminar tube flow 4.346 at constant heat flux and the Nusselt numbers obtained from Shah theoretical equation (2009) which is shown in Figure 2 that gives a good agreement with only 2% error and are constant. The friction factor obtaining at fully developed zone is compared with Darcy-Weisbaceh equation [15] which is shown in Figure 3 that give only 1.5% error. The correlation developed by Shah Equation [15] for laminar tube as follows:

$$Nu = 1.302 \left(\frac{x^*}{2}\right)^{-\left(\frac{1}{3}\right)} - 0.5, \quad x^* \leq 0.003 \quad (15)$$

$$Nu = 4.364 + 0.263 \left(\frac{x^*}{2}\right)^{-0.506} e^{-41\left(\frac{x^*}{2}\right)}, \quad x^* > 0.03 \quad (16)$$

$$\text{Where, } x^* = \frac{2(x/D)}{Re Pr}$$

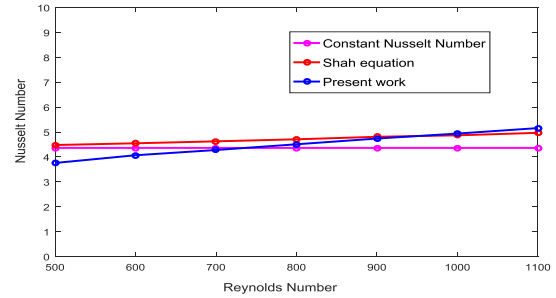


Fig. 2: Comparison of Nusselt number between Shah equation and constant Nusselt number at constant heat flux for laminar tube flow and present work for different Reynolds number of water.

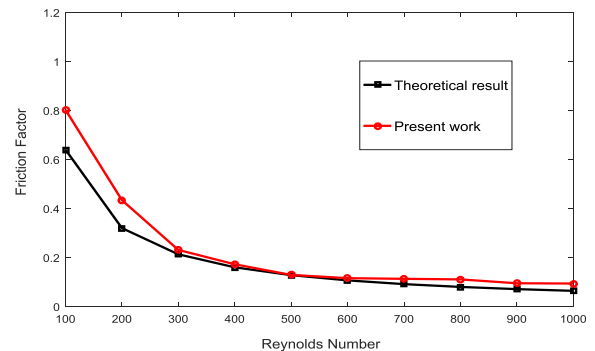


Fig.3: Comparison of friction factor between Darcy-Weisbaceh equation and present work for different Re.

5. Result and discussion:

The figure 4, show the effect of volume fraction and Reynolds number on the Nusselt number for Al_2O_3 -water, from the figure it has been obtained that the Nusselt number of the nanofluid used in the present work increases with the increase in Reynolds number and Volume fraction of the nanofluids. This is occurred because of the increment of the effective thermal

conductivity and an increase of energy exchange rate resulting from the irregular and chaotic motion of ultrafine particles of the nanofluids with the increases of the volume fraction as well as increment of convection with the increase in Reynolds number. This phenomena is explained by Hsien-Hung Ting, 2015 [16]“Actually a higher Reynolds number corresponds to higher fluid velocity and temperature gradient, which in turn results in a higher value of nusselt number”. S. Zeinali Heris, 2006 [8] worked with laminar convective heat transfer of circular tube by using Al_2O_3 -water and CuO -water nanofluids and investigated that the nusselt number is increased for both nanofluids respectively with increasing the volume fraction of the nanofluids and with the increment of Peclet number that indicates the increment of Reynolds number and this trend is observed in figure 5. Pak and Cho et el [15] also investigated that the Nusselt number for fully developed turbulent flow increased correspondingly to the increasing volume fraction as well as Reynolds number for $\gamma\text{-Al}_2\text{O}_3$ -water and TiO_2 -water nanofluids which trend is also similar to the present work.

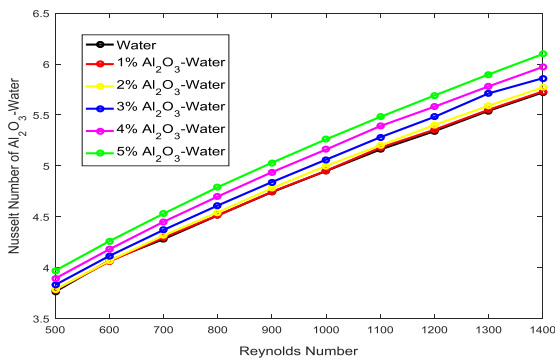


Fig. 4: Comparison of Nusselt Number of different volume fraction Al_2O_3 - H_2O for different Reynolds Number

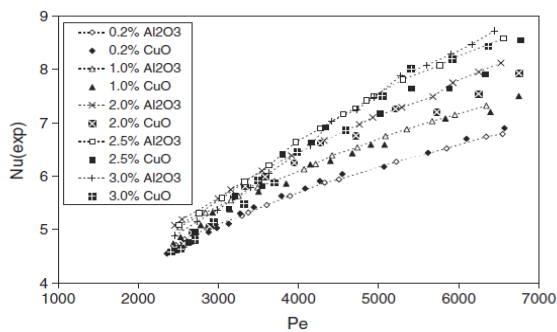


Fig. 5: Experimental Nusselt number versus Peclet number nanofluids (S. Zeinali Heris, 2006 [8])

Fig. 6 indicates the pressure drop of nanofluid with increase of Reynolds number at different volume fractions. From the fig it is observed that for different nanofluid pressure drop is increasing with increase of Reynolds number for different volume fractions and the pressure drop is becoming higher with increase of volume fraction. This increment is comparatively more than pure water. The figure 7 shows the comparison of friction

factor of different nanofluids with pure water for different Reynolds number. From figure it has been observed that the friction factor of the four nanofluids is remaining almost same. And by increasing the volume fraction of nanoparticles the friction factor increases very slightly 0.25% to 0.85% than the pure water. This similar trend is also reported by Hwang and Choi, 2009[16] (showed at figure 8) with Al_2O_3 -water under laminar tube flow and Xuan and Li, 2000 and Pak and Cho, 1998 [10] under turbulent flow. According to Li and Xuan, 2000[14] the friction factor of Cu -water nanofluid with low volume fraction of particles is almost not changed that satisfied the present result.

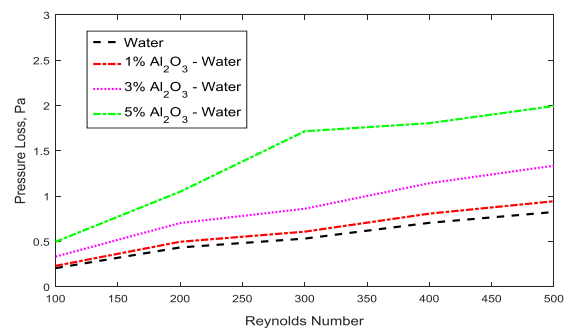


Fig. 6: Comparison of pressure loss with Reynolds number for different Volume Fraction of Al_2O_3 -water.

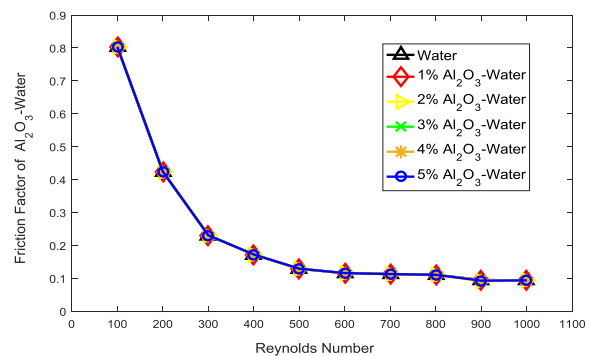


Fig. 7: Comparison of friction factor and Reynolds number of different volume fraction of Al_2O_3 -water.

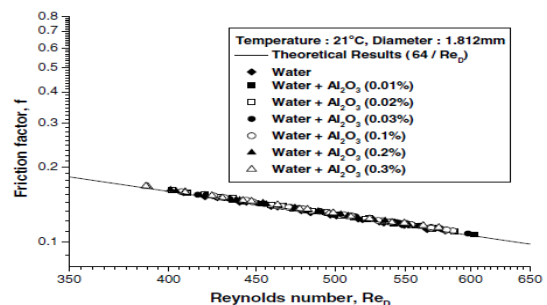


Fig. 8: The friction factor of water-based Al_2O_3 NF in fully developed laminar flow. (Hwang, 2009[10])

The figure 9 represents the effect of volume fraction of nanofluids on heat transfer co-efficient for different

Reynolds number. From the figures it is observed that the value of heat transfer coefficient increases rapidly with the increase of volume concentration and Reynolds number. This is due to the increases of the thermal conductivity and decreases of the specific heat capacity of the Nano fluid which increases the Nusselt number with higher velocity and temperature gradient and this phenomenon increases the heat transfer coefficient gradually. According to Wen and Ding, 2006[9] the numerical study of the particles migration due to viscosity gradient and a non-uniform shear rates leads to higher heat transfer coefficient of nanofluids. From the figures the increment of heat transfer coefficient compared to pure water is 7.2% to 31.5% for Al₂O₃-water with respect to 1% to 5% volume concentration for Reynolds number 500 to 1400. S. Zeinali Heris and Esfahany, 2006[8] investigated convective heat transfer of circular tube by using Al₂O₃-water nanofluid and observed that the heat transfer coefficient increases rapidly with the increases of Reynolds number with respect to increase of volume concentration that satisfied the present work. Another same investigation was carried by Lin-wen Hu , 2000[18] with Al₂O₃-water and Zirconia-water and reported that at fully developed region the heat transfer coefficient increases 27% for Al₂O₃-water and 3% for zirconia-water nanofluid that also almost similar to the present work. Sezer Ozerinc, 2010 [19] also proposed that for Al₂O₃-water nanofluid the heat transfer coefficient increases rapidly compare to pure water with the increment of Reynolds number and volume fraction.

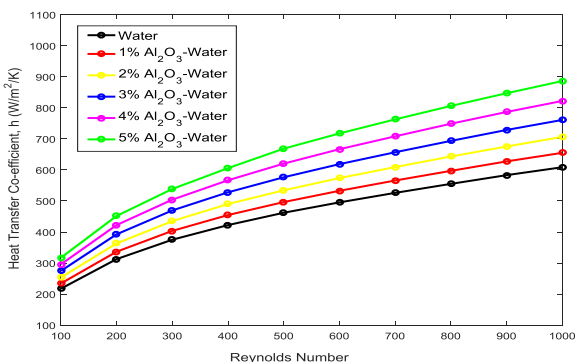


Fig. 9: Comparison of Heat Transfer Coefficient with Reynolds of different volume fraction of Al₂O₃-water.

The table 5.1 shows the performance comparison of different volume fraction of Al₂O₃-water nanofluid with base fluid. From the table it is clear that at constant heat transfer coefficient the Reynolds number, Nusselt number and velocity of nanofluid has been reduced and the thermo physical property likes thermal conductivity, density, viscosity has been increase by increasing the volume concentration compared to pure water. . And to get same heat transfer coefficient nanofluid needs lower volumetric flow rate compared to pure water. This reduction is 11.25% for 1% Al₂O₃-water and maximum 40.39% for 5% Al₂O₃-water nanofluid compared to pure water. And to get this advantage of volumetric flow rate and other fluid parameters the friction factor of Al₂O₃-water

nanofluid is increased very small amount compared to pure water.

Table 1: Comparison of the performance of different volume concentration of Al₂O₃ nanoparticles with base fluid.

Type of fluid parameters	Water	1% Al ₂ O ₃	2% Al ₂ O ₃	3% Al ₂ O ₃	4% Al ₂ O ₃	5% Al ₂ O ₃
Heat Transfer coefficient W/m ² .K	600	600	600	600	600	600
Reynolds number	960	810	675	550	463	395
Nusselt number	4.85	4.55	4.25	4.00	3.8	3.65
Velocity m/s	0.1538	0.13677	0.121995	0.10744	0.098666	0.091788
Friction factor	0.0955	0.1122768	0.11779643	0.13566956	0.19978800	0.2864115
Thermal conductivity	0.615	0.6614	0.7065	0.7516	0.7967	0.8418
Density Kg/m ³	996	1025.74	1055.48	1085.22	1114.96	1144.7
Volumetric flow rate, m ³ /s	3.015e-6	2.68e-6	2.395e-6	2.105e-6	1.934e-6	1.799e-6
Reduction in volumetric	-	11.25%	20.5%	30.46%	36.092%	40.39%

8. Conclusion

In the present work Al₂O₃-water nanofluid have been analysed through a typical circular tube to investigate the heat transfer enhancement and the friction factor. The heat transfer coefficient, Nusselt Number and Pressure drop increase with the increase in volume fraction for the nanofluid as well as with the Reynolds number compared to pure water. And to get more heat transfer coefficient and volumetric flow rate advantage use of Al₂O₃-water nanofluid is best compared to pure water.

REFERENCES

[1] J.A. Eastman, S. U. S. Choi, S. Li, L. J. Thompson, and S. Lee, "Enhanced thermal conductivity through the development of nanofluids," Fall Meeting of the Materials Research Society (MRS), Boston, USA, 1996.

[2] S.U.S. Choi, "Nanofluid technology: current status and future research," Korea- U.S. Technical Conference on Strategic Technologies, Vienna, VA, T. Nosoko, A.1998.

[3] S.U.S. Choi, Z.G. Zhang, W. Yu, F.E. Lockwood, E.A. Grulke, "Anomalous thermal Conductivity enhancement in nanotube suspensions." Appl. Phys. Lett., 79(14), 2252-2254, (2001).

[4] S.U.S. Choi, Z.G. Zhang, W. Yu, F.E. Lockwood, E.A. Grulke, "Anomalous thermal Conductivity enhancement in nanotube suspensions." Appl. Phys. Lett., 79(14), 2252-2254, (2001).

[5] Y. Xuan Q. Li, "Investigation on convective heat transfer and flow features of nanofluids," ASME J. Heat Transfer 125, 151–155 (2003).

[6] Williams, W., Buongiorno, J., and Hu, L.-W., "Experimental Investigation of Turbulent Convective Heat Transfer and Pressure Loss of Alumina/Water and Zirconia / Water Nanoparticle Colloids (Nanofluids) in Horizontal Tubes," ASME J. Heat Transfer, 130(4) p. 042412 (2008).

[7] Rea, U., McKrell, T., Hu, L.-W., and Buongiorno, J., "Laminar Convective Heat Transfer and Viscous Pressure Loss of Alumina-Water and Zirconia-Water Nanofluids," Int. J. Heat Mass Transfer, 52, pp. 2042–2048 (2012).

[8] S. Z. Heris, S.G. Etemad, M.N. Esfahany, "Experimental investigation of oxide nanofluids laminar flow convective heat transfer," Int. Commun. Heat Mass Transfer 33 (2006) 529–535.

[9] Y. Ding, H. Alias, D. Wen, R.A. Williams, "Heat transfer of aqueous suspensions of carbon nanotubes (CNT nanofluids)," Int. J. Heat Mass Transfer 49, 240–250 (2006).

[10] Kyo Sik Hwang , Seok Pil Jang , Stephen U.S. Choi, "Flow and convective heat transfer characteristics of water-based Al₂O₃nanofluid in fully developed laminar flow regime"International Journal of Heat and Mass Transfer 52, 193–199(2009).

[11] N. K. Chavda , G. V. Patel , M. R. Bhadauria , M. N. Makwana "Effect of nanofluid on friction factor of

pipe and pipe fittings: part ii effect of copper oxide nanofluid" International Journal of Research in Engineering and Technology vol 04, issue 04, apr-2015.

[12] E.B. Maiga, C.T.Nguyen, N. Galanis and G. Roy, "Heat transfer behaviors of nanofluids in a uniformly heated tube", Superlattices and Microstructures, vol.35, pp.543 –557(2004).

[13] B.C. Pak, Y. Cho, "Hydrodynamic and heat transfer study of dispersed fluid with submicron based Al₂O₃ and CuO nanofluids in a triangular duct", J. Disper. Sci. Technol. 34, 1368–1375(2013).

[14] Y. Xuan, W. Roetzel, "Conceptions for heat transfer correlation of nanofluids," Int. J. Heat Mass Transfer 43, 3701–3707(2000).

[15] R.K. Shah, "Laminar flow friction and forced convection heat transfer in ducts of arbitrary geometry," Int. J. Heat Mass Transfer vol 18, 849e862 (1975).

[16]] Kyo Sik Hwang , Seok Pil Jang , Stephen U.S. Choi, "Flow and convective heat transfer characteristics of water-based Al₂O₃nanofluid in fully developed laminar flow regime" International Journal of Heat and Mass Transfer 52, 193–199(2009).

[17] Ulzie Rea, Tom McKrell, Lin-wen Hu, Jacopo Buongiorno "Laminar convective heat transfer and viscous pressure loss of alumina–water and zirconia–water nanofluids International Journal of Heat and Mass Transfer," 52, 2042–2048(2009).

[18] Sezer özerinç, "Heat transfer enhancement with nanofluids," a thesis submitted to the graduate school of natural and applied sciences of Middle East technical university, 2010.

Nomenclature

- C_p: Specific heat at constant pressure
- D_h: Hydraulic diameter
- f :Friction factor
- h : Average heat transfer coefficient
- k :Thermal conductivity
- m :Mass flow rate _
- v : Volumetric flow rate
- Δp : Differential pressure loss
- Q : Heat transfer
- T : Temperature
- T₀ : Reference temperature, 273 K
- u : Velocity of flow at inlet

Significance of Cotton Cultivation to Keep Sustainable RMG Sector in Bangladesh

Md. NurUddin*, Nayan Chandra roy, Md. Delwar hassain, and Md. Abdur Rahim

Department of Textile Engineering, Dhaka University of Engineering & technology, DUET-1707, Bangladesh.

ABSTRACT

The root (backward linkage) of RMG sector is fiber and cotton is the major fiber crop. The textile industry of Bangladesh predominantly depends on imported cotton. Annual demand is approximately 7 million bales (480 lbs. or 218 kg per bale) where, Bangladesh produces only 0.16 million bales in a year, which is less than 3% of the total requirement in spite of being agriculture dependent country. RMG sector is being contributed more than 80% of the total export earnings. This study illustrates that how we can reduce dependency on imported cotton and save the partial imported cost. To keep sustainable RMG sector, Bangladesh should cultivate cotton as well as reduce over dependency on imported cotton. In a year, more than \$3 billion is being spent to import cotton. If we can produce 1 million of bales in 2,42,000 hectares of land then we can save about 12% of total imported cotton, along with, \$279 million can be saved.

Keywords: Backward Linkage, Cotton Cultivation, Sustainable RMG Sector, Saving imported cost.

1. Introduction

Bangladesh has a glorious history in textile production. Backward linkage means the subsectors for RMG industry includes cotton production, spinning (cotton and synthetic yarn), weaving and knitting, dyeing and printing, and accessories [13]. Cotton is one of the important cash crops in Bangladesh. It is the main raw materials of textile industry. Annual requirement of raw cotton for textile industry of Bangladesh is estimated around 7 million bales (480 lbs. per bale) [6]. Local production is only about 0.16 million bales. Less than 3% of the national requirement is fulfilled through the local production. Remaining about 97% is fulfilled by imported raw cotton from different cotton exporting country including India, Australia, USA; Africa etc. according to the United States Department of Agriculture Bangladesh's cotton import will creep up day by day. The highest domestic cotton production was 160,000 bales in recent year, though Bangladesh is an agriculture dependent country. This amount of domestic production is negligible proportion of the total requirement of the country's textile industry. Although cotton is important cash crop, systems sceneries is rather marginal. The Garments industry has been flourishing in Bangladesh; [3] Readymade garments (RMG) accounts for about more than 76% of the total export earnings [2]. But cotton production did not increase as expected due to several constrains.

2. Research Aims

The aims of this research regarding the significance of cotton fiber production to keep sustainable RMG sector in Bangladesh are as follows:

- To reduce dependency on imported cotton by increasing domestic production for keeping sustainable RMG sector.

- To cultivate unused land for increasing domestic production of cotton fiber and to create workplace by establishing ginning factories.

3. Literature Review

Cotton is growing mainly in south eastern zone, middle zone and northern part of Bangladesh [6]. It covers 32 districts of Bangladesh mainly Kushtia, Chuadanga, Jhenaidah, Meherpur, Magura, Jessore, Rangpur and Thakurgaon etc. Two types of cotton are grown in Bangladesh namely- i) Upland cotton (*Gossypium hirsutum*) & ii) Hill cotton (*Gossypium arboreum*) [5]. American cotton is cultivated in the South western region. Hill cotton is an indigenous variety and cultivated in Jhum system. Hill cotton is used for handloom cloths as well as grown for export. The total land area suitable for cotton cultivation estimated 2,42,000 hectares. cotton production is taking place in 35 districts out of 64 districts in Bangladesh. Although Bangladesh is agriculture dependent country, it can meet up only less than 3% of its cotton demand [1]. In recent year cotton is planted at 43,000 hectares [5], but production is about 160,000 bales. Genetically modified (GM) cotton can be cultivated in Bangladesh. Most importantly Bt cotton can be harvested easily. Bt stands for *Bacillus thuringiensis*. It is genetically modified cotton that has self-defense mechanisms to battle insects and pests like Bollworms which attack cotton balls in particular. This defense artillery is created by fusing genes of naturally occurring bacteria *Bacillus thuringiensis* commonly referred to as Bt. This fusion of genes creates a protein which protects the crop from external attacks by insects and pests. Colored cotton also can be cultivated. Colored cotton can be used by treating only pretreatment process [2].



Fig.1 Cotton growing area in Bangladesh (CDB) [7]

Table 2 Cotton production in Bangladesh (CDB) [7]

Year	Area harvested (hectare)	Production(bales)	Production(tones)
2005/06	49,770	77,000	14,000
2006/07	42,100	70,530	12,824
2007/08	28,707	42,380	7,705
2008/09	32,600	50,600	9,200
2009/10	31,500	66,000	12,000
2010/11	33,500	80,000	15,545
2011/12	36,000	103,000	18,727
2012/13	39,000	129,000	23,455
2013/14	42,000	144,000	26,182
2014/15	42,700	152,534	27,675
2015/16	42,800	153,280	27,869

Table 1 Growth of imported cotton (CDB) [7]

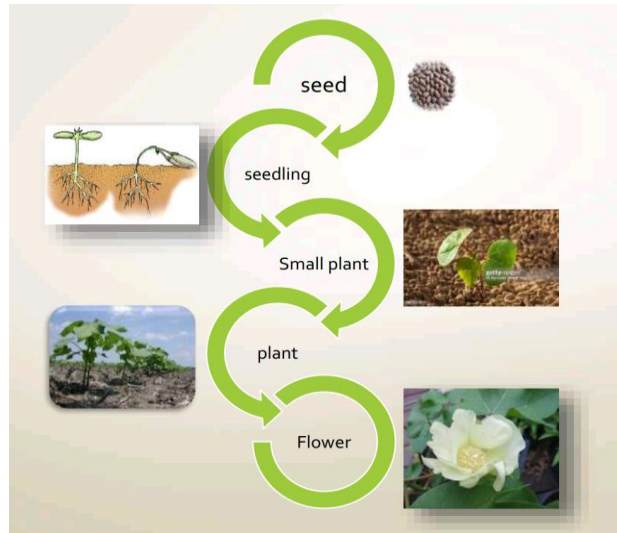
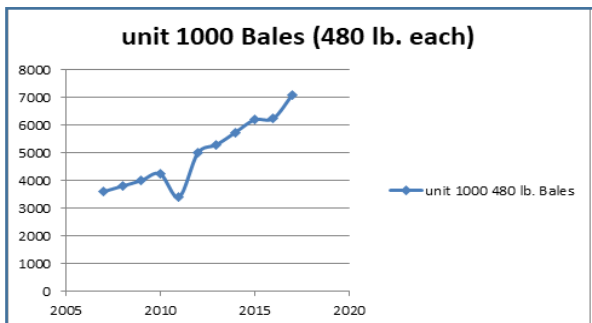


Fig.3 Life cycle of cotton [12]

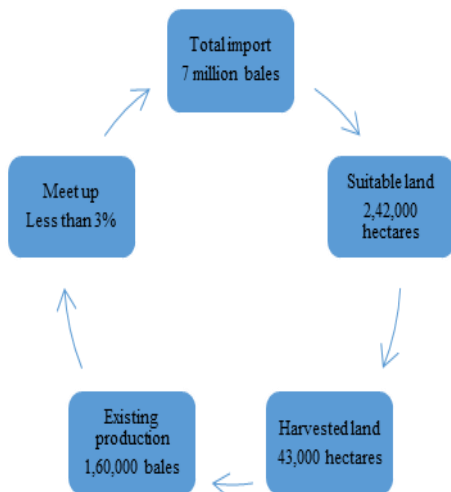


Fig. 2 Present scenery of cotton cultivation



Fig.4 Cultivation process of cotton [10]

4. Important by-products from cotton seed (Cotton oil, Oil cake)

Cotton oil is one of the important edible used in many countries of the world which is lower in cholesterol than Soyabean. Cotton oil cake is another by-product of cotton seed and it is produced during well extraction. The oil cake is generally used for livestock feeding and fish feed. Cotton oil cake has high demand in the market for multiple uses with high percentage of protein.[12]



Fig.5 By-product of cotton [3]

5. Discussion

In Bangladesh existing suitable land for cotton cultivation is approximately 2,42,000 hectares. Nowadays about 43,000 hectares of land is being cultivated, if we cultivate at remaining unused land(199000 H) then about 1 million of bales can be possible to produce in a year which may reduce about 12% bales of total import.

6. Present problems

1. High price of pesticides and fertilizers
2. Pest attack
3. Difficulties of getting loans and high bank interest
4. Lack of training facilities
5. Lack of proper knowledge
6. Lack of modern technologies and management practices of cotton cultivation
7. Hazardous chemicals are used

7. Solution of problems

1. Can be used eco-friendly pesticides
2. Modern agriculture technology can be used
3. Developing information network related to cotton research and development
4. Providing higher education and training to create qualified manpower
5. Need positive approach of government

8. Recommendations

Genetically modified (GM) cotton can be cultivated in Bangladesh. Most importantly Bt cotton can be harvested easily. Bt stands for Bacillus thuringiensis. It is genetically modified cotton that has self-defense mechanisms to battle insects and pests like Bollworms which attack cotton balls in particular. This defense artillery is created by fusing genes of naturally occurring bacteria Bacillus thuringiensis commonly referred to as Bt. This fusion of genes creates a protein which protects the crop from external attacks by

insects and pests.[2] Colored cotton also can be cultivated. Colored cotton can be used by treating only pretreatment process.

9. Advantages of Bt Cotton

- This eliminates the use of large amount of pesticides and insecticides which are harmful for the environment
- Increases yield of cotton due to effective control of bollworms
- Potential reduction in the cost of cultivation (depending on seed cost and insecticide costs).
- Reduction in environmental pollution by the use of insecticides.
- Bt cotton is ecofriendly and does not have adverse effect on parasites, predators, beneficial insecticides and organisms present in soil.

Table 3 Possible future scenery at a glance

Parameters	Possible Outcomes	Existing Sceneries
Suitable land	2,42,000 hectares	43,000 hectares
Number of bales	1 million	0.16 million
Demand meet up%	App. 12%	Less than 3%
Domestic production cost	\$150 million	\$24 million
Market price	\$429 million	\$69 million
Saved	\$279 million	\$45 million

10. Conclusion

The study tried to show the compatibility of domestic cultivation in Bangladesh to improve cotton production, which is the main backward linkage of RMG. It is clear to all that, day after day the volume of imported cotton is being increased. This over dependency on imported cotton may not be sustainable for RMG sector in Bangladesh. Any time, this importing may be interrupt due to lack of diplomatic activities or any other problems. On that situation we need domestic production to keep the sustainability of RMG sector in Bangladesh. This illustrates present and future prospects of cotton cultivation as well as by-product produced from cotton seed. If the remaining unused land could be cultivated then we can save approximately 12% of imported cotton which may save about \$279 million per year of imported cost. Beside this, workplace can be created by establishing ginning factory. Although Cotton cultivation is much pesticide consuming, nevertheless, genetically modified Cotton may cultivate which may consume less pesticides.

11. References

- [1] Journal of textile and apparel technology management, NC state university, vol-6, issue-2, fall 2009, Available: file:///C:/Users/MD%20NUR%20UDDIN/Desktop/thesis/backward%20linkage%20of%20garments.pdf
- [2] Wikipedia contributors. (2018, April 20). Bt cotton. In *Wikipedia, The Free Encyclopedia*. Retrieved 14:02, May 2, 2018, Available: from https://en.wikipedia.org/w/index.php?title=Bt_cotton&oldid=837303052
- [3] Sher-e-bangla agricultural university Homepage, Available: file:///C:/Users/MD%20NUR%20UDDIN/Downloads/SAU201401_01-12-05228_11.pdf [Accessed, 30 May, 2018]
- [4] Research gate Homepage, Available: https://www.researchgate.net/publication/275524220_Cotton_Production_in_Bangladesh_Current_Scenario_and_Prospect,
- [5] Backward Linkages In The Textile And Clothing Sector of Bangladesh Homepage, Available: file:///C:/Users/MD%20NUR%20UDDIN/Desktop/thesis/Backward%20Linkages%20in%20the%20Textile%20and%20Clothing%20Sector%20of%20Bangladesh.pdf [Accessed, 15 June, 2018]
- [6] Textile today Homepage, Available: <https://www.textiletoday.com.bd/rationalization-bangladesh-cotton-import/> [Accessed, 10 July, 2018]
- [7] Cotton development board Homepage, Available: <http://www.cdb.gov.bd/> [Accessed, 12 July, 2018]
- [8] The daily star Homepage, Available: <http://www.thedailystar.net/business/bangladesh-grow-10pc-cotton-needs-2025-1350994> [Accessed, 30 June, 2018]
- [9] Bd news24.com Homepage, Available: <https://bdnews24.com/business/2016/04/27/bangladesh-eyes-increasing-local-cotton-production> [Accessed, 15 June, 2018]
- [10] The daily observer Homepage, Available <http://www.observerbd.com/details.php?id=83647> [Accessed, 7 April, 2018]
- [11] Cotton Bangladesh Homepage, Available: <http://cottonbd.blogspot.com/> [Accessed, 5 March, 2018]
- [12] US Department of Agriculture Homepage, Available: US department of agriculture, <https://naldc.nal.usda.gov/download/ORC00000166/D>
- [13] <https://www.google.com/search?q=backword+linkage+of+RMG>

CFD Study on Aerodynamic Effects of NACA 2412 Airfoil as Rear Wing on a Sports Car

Shamudra Dey^{1,*}, Ranabir Saha²

¹ Department of Mechanical Engineering, Shahjalal University of Science & Technology, Sylhet-3114, BANGLADESH

² Department of Mechanical Engineering, Bangladesh University of Engineering & Technology, Dhaka-1000, BANGLADESH

ABSTRACT

In the present research, aerodynamic effects of NACA 2412 airfoil as rear wing on a sports car has been investigated using Computational Fluid Dynamics (CFD) approach. The sports car has been modeled in the commercial software SOLIDWORKS 2016. Two different types of simulations were run: one for the flow around a simplified high speed sports car model with a rear wing, which is actually a NACA 2412 airfoil and the other for the flow without using a rear wing. The analysis has been carried out in ANSYS 15.0 FLUENT using k-epsilon model and for the velocity condition of 60 m/s. The effect of rear wing has been visualized from the aerodynamics perspective. Graphs of drag and lift coefficients and figures of velocity streamline, pressure distribution, Turbulence Kinetic Energy for both models have been discussed and compared. The details of the aerodynamic study has been presented in the paper.

Keywords: Computational Fluid Dynamics, Rear wing, Sports car, Lift, Velocity streamline

1. Introduction

After many years of research in automobile engineering, the ideal water drop body shape, very less sharp corner, smooth upper surface finish and other methods have been adopted in designing modern vehicle bodies for better aerodynamics [1]. When a sports car is driven at a very high speed especially on the highway and race circuits, it has propensity to lift over. Such incidents can take place, because as the higher pressure air is in front of the wind shield; it accelerates, causing a sudden pressure drop. This lower pressure creates lift on the car's roof as the air passes over it. In the worst case, once the air makes its way to back window, the notch created by the window dropping down to the trunk leaves a lower pressure space that the air fails to fill properly [2]. The separated flow is resulted in lower pressure, which creates lift which then acts upon the trunk surface area. An added rear wing can diffuse the airflow passing a vehicle, which minimizes the turbulence, adds downward pressure to the back end and reduces lift acted on the rear trunk to allow a vehicle to corner faster and be more stable at high speeds [1, 3].

Several literatures have been reviewed in this research work. Most of the papers available in the literature reflected upon the subject of flow analysis over passenger cars and drag reduction. As drag reduction has close relationship to fuel consumption, most of the authors have focused on drag reduction rather than vehicle safety and comfortable. Computational analysis to reduce the drag is performed by Barbut et al. [4], Rouméas et al. [5] on road vehicle and by Guilmineau [6] on the simplified car body (Ahmed body). Islam and Mamun [7] performed numerical and experimental study to measure the aerodynamic drag, but their work was concentrated on sedan car only [8]. This research paper focuses on using NACA 2412 airfoil as rear wing on a sports car to achieve significant reduction in lift

force to ensure vehicle safety from aerodynamics perspective.

2. Problem formulation & CAD model description

Aerodynamic forces and moments from the air is experienced by the car when it moves through the air. The force that works in the direction opposite to the vehicle moving, is called drag, and the force perpendicular to the drag and normal to the ground is called lift. The drag and lift forces can be expressed in a non-dimensional form - the drag and lift coefficients, C_D and C_L , are defined respectively as:

$$C_D = \frac{\text{Drag force}}{(\rho v^2 A)/2} \quad (1)$$

$$C_L = \frac{\text{Lift force}}{(\rho v^2 A)/2} \quad (2)$$

An image has been provided (Fig.1) below to show the forces acting on a running car:

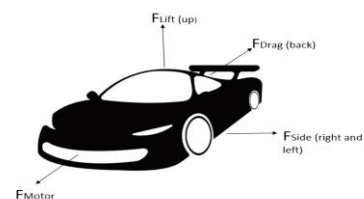


Fig. 1 Forces acting on a running sports car

The solid modelling of the present work has been done in the commercial software SOLIDWORKS 2016. The NACA 2412 airfoil with -3° angle is designed and

* Corresponding author. Tel.: +88-01879800785

E-mail addresses: shamudra.mee15@gmail.com

installed on the rear end of the sports car as rear wing. The designed car is basically a prototype which is scaled down to 1:24 (prototype to model) due to our computational limitation and desired accurate result. The solid modelling (Fig.2) of both cars (with or without rear wing) has been provided below:



Fig.2 Solid Model of sports car for both conditions

The maximum length and width of the prototype car is 140.41 mm and 87.18 mm and height (from the chassis to rooftop) is 39.13 mm. It should be noted that all the dimensions are normal & from point to point. The solid models have been imported to ANSYS Design Modeler, where a virtual wind tunnel is created around the sports car. This virtual wind tunnel is basically our computational domain. An image (Fig.3) of computational domain (sports car with rear wing) has been provided below:

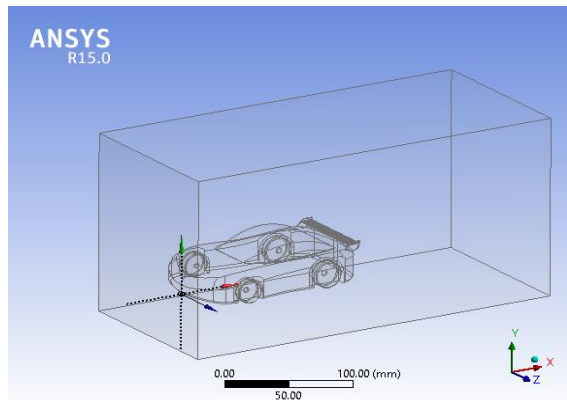


Fig.3 Computational domain

3. Mesh generation in ANSYS

The triangular shape surface mesh with lower skewness and higher orthogonal quality has been used due to its proximity to changing curves and bends. These elements easily adjust themselves to the complex bodies used in automobile and aerospace applications [2]. With technical changes in the ANSYS ICEM CFD Meshing, the generated meshing for the sports car with rear wing can be visualized in the image (Fig. 3) provided below. The image shows a partial view of the meshing for better understanding about mesh generation. The CAD

geometry of sports car without rear wing has 5, 05, 870 nodes and 27, 27, 068 elements, while the CAD geometry of the same sports car with the rear wing has 5, 59, 227 nodes and 30, 46, 978 elements.

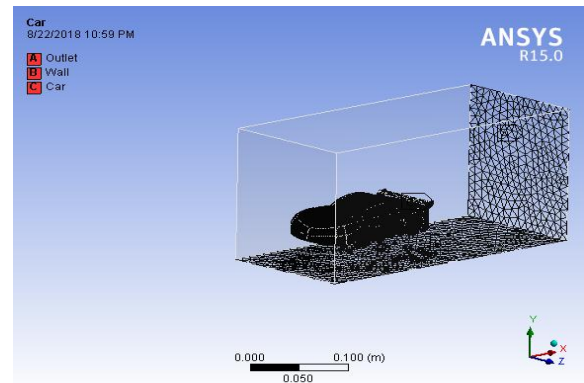


Fig.4 Mesh generation over the designed sports car with rear wing

4. Methodology of the CFD study

Aerodynamic study of air flow over a body can be executed using CFD approach or analytical method. On one hand, analytical method of solving air flow over an object can be done only for simple flows over simple geometries just like laminar flow over a flat plate. If the flow of air gets complicated as in flows over a bluff body, the flow becomes turbulent and it is impossible to solve Navier- Stokes and continuity equations analytically [2]. Favre-averaged Navier-Stokes equations are used here, where time-averaged effects of the flow turbulence are considered. Flow simulation is employed using transport equations for the turbulent kinetic energy and its dissipation rate, the well-known k-ε model [8].

4.1 Setup of Model:

Following steps have been taken for setting up the solving techniques in FLUENT solver for 3D, steady state, incompressible flow using serial processing technique:

- (1) The meshed model is imported in solver and mesh is checked.
- (2) The solver specifications such as pressure based, steady and absolute velocity formulation are set.
- (3) Double equation based realizable k-epsilon model with non-equilibrium wall function is selected with default model constants. The k-epsilon model is a general purpose turbulence model, which is very simple to implement and converges faster. The model predicts the flows in many practical cases and is particularly good for external aerodynamics.

(4) Air is selected as the fluid and the Aluminum is selected as the solid and required properties (density, viscosity etc.) have been specified.

(5) In case of boundary conditions, the required inlet velocity flow condition of 60 m/s (216 km/h) is given as the input and the outlet is kept as pressure outlet. This particular inlet velocity condition has been selected to investigate the aerodynamic performance of the car at high speed and to compare the results with several literatures [9-14].

(6) Pressure velocity coupling based solution control is adopted for present study under the custom relaxation factors.

After these steps, the solution procedure has been initialized using hybrid initialization and the numerical solution has been done for 500 iterations with the reporting interval of 1.

5. Result & Discussion:

5.1 Grid sensitivity analysis

A grid sensitivity analysis has been carried out for the sports car model without rear wing to validate the mode. The workstation used for this CFD (Computational Fluid Dynamics) study is a Lenovo laptop with core i5 fifth generation processor and 8 GB ram. In this grid sensitivity analysis, the main priority has been given to the values of Coefficient of drag (C_D), Coefficient of Lift (C_L) and optimal computation duration. By analyzing the result from the table of grid sensitivity analysis and considering the computational limitation, the medium type mesh with 5, 05, 870 nodes and 2, 27, 068 elements have been preferred for the present work. This medium type mesh has been used for all four CFD simulations in this research. The duration of numerical solution for this type of mesh is 540 minutes approximately.

Table 1 Grid sensitivity analysis

Mesh type	Nodes	Elements	C_D	C_L
Coarse	396652	2135381	0.0012906	0.0006944
Medium	505870	2727068	0.0013274	0.0007822
Fine	529297	2851543	0.0013394	0.0007863

After the grid sensitivity analysis is being carried out, CFD Analysis is done for the preset inlet parameters

and results are obtained through it. The results are achieved for two cases: one for the flow over the sports car body without rear wing and another for the flow over the same car with the rear wing made of NACA 2412 airfoil.

5.2 CFD analysis of sports car without rear wing

The below figures shows the giving of the required boundary conditions in different panels as mentioned earlier.

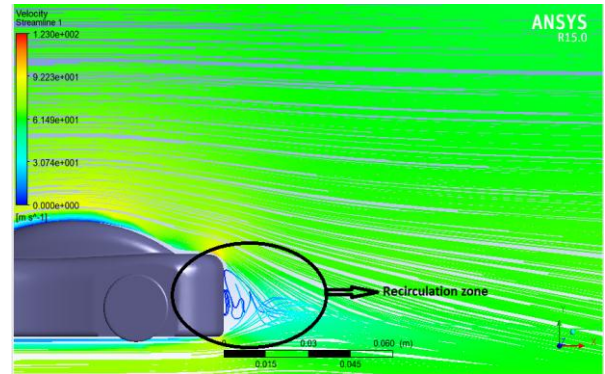


Fig.5 Velocity streamline over the sports car body without rear wing

Fig. 5 is about the velocity streamline over the car (without rear wing), which are a family of curves that are instantaneously tangent to the velocity vector of the flow. The distribution of the velocity streamline in front of the car is higher. On the rear side of the sports car, a recirculation zone can be visualized, which has occurred due to turbulent nature of the flow. Different streamlines at the same instant in a flow do not intersect, because a fluid particle cannot have two different velocities at the same point.

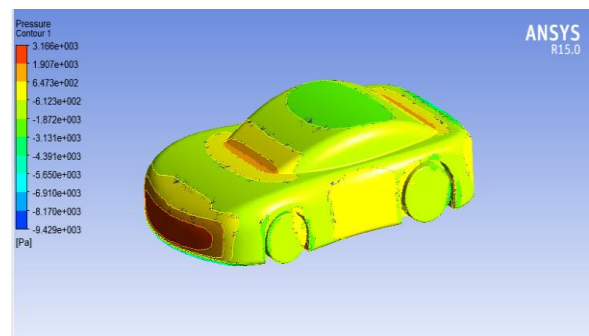


Fig.6 Pressure distribution on the body of the sports car without rear wing

Fig.6 is about the distribution of pressure on the car body. Pressure is higher in the front of the car. The

pressure is also higher at the beginning of the front windshield of the car, but just after that region, pressure distribution becomes negative. This lower pressure creates lift on the car's roof as the air passes over it. In this figure, streamline has not been shown for better visualization.

Fig.7 is about the distribution of Turbulence Kinetic Energy on the car body. The increment in the value of energy is observed in wheel region of the car.

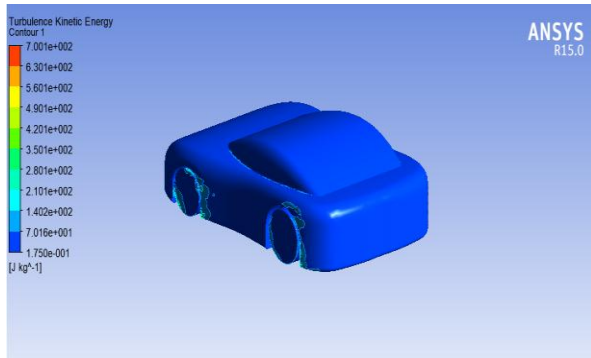


Fig.7 Turbulence Kinetic Energy distribution on the sports car without rear wing

5.2 CFD analysis of sports car with rear wing

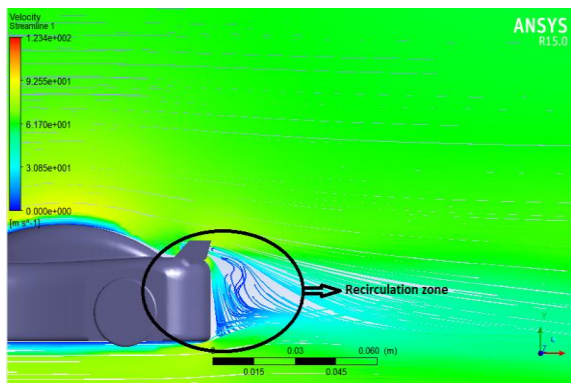


Fig.8 Velocity streamline over the sports car body with rear wing

Fig.8 is about the velocity streamline around the sports car when the rear wing is used. The velocity is higher in front of the car but, in the rear region, velocity is significantly lower as rear wing is installed. Besides, due to the effect of rear wing, the recirculation zone of air flow is almost gone.

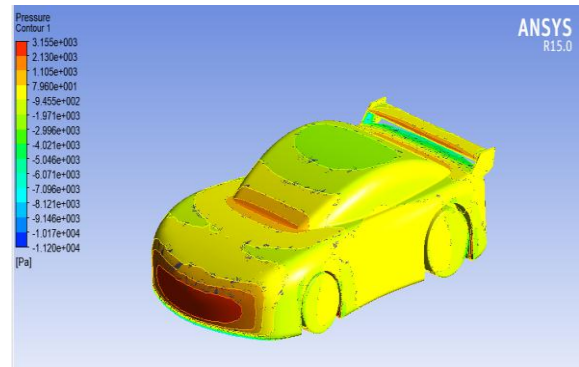


Fig.9 Pressure over the sports car body with rear wing

Fig.9 is about the pressure distribution due to the air flow over the sports car with rear wing. As the rear wing has been installed, a higher pressure region has been observed on the rear wing of the car. This higher pressure region creates down ward force which reduces lift and thus, the research objective is achieved.

The distribution of Turbulence Kinetic Energy (Fig.10) is almost same as the distribution on the sports car without rear wing. But in this case, increment of energy is visualized in few region on the rear end of the sports car.

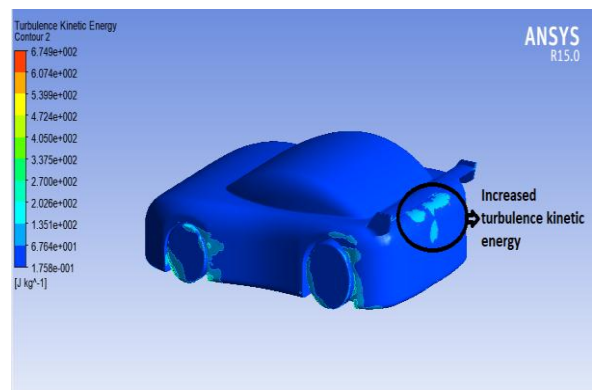


Fig.10 Turbulence Kinetic Energy distribution on the sports car with rear wing

5.4 Comparison of graphs of C_L & C_D

The graphs of C_D & C_L versus iterations have been plotted from this CFD study. A significant lift reduction has been observed in the graph of sports car with rear wing. In that numerical investigation, value of C_L is found to be negative, which ensures downward force. The obtained values are small because the solid geometry model is scaled down to a definite ratio, which has been discussed earlier. Graphs of C_L & C_D for

both conditions (with or without rear wing) have been plotted below:

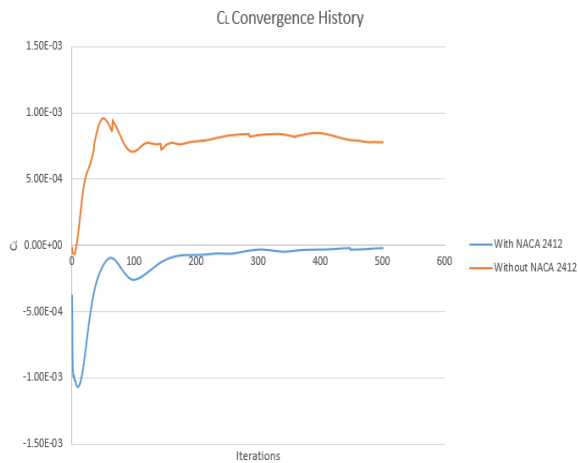


Fig.11 C_L vs. iterations for both conditions

From the graph of C_L (Fig.11), the value of C_L for the sports car solid model without rear wing and with rear wing has been found to be 0.00078223 and -0.00001688 respectively. The differences between the plotted lines in the graph can be visualized. As the lift has been reduced due to the installation of rear wing made of NACA 2412 airfoil, the downward force is achieved due to this negative C_L value.

In Fig.12, the graph of C_D has been plotted for the sports car solid model without and with rear wing. The value of C_D has been found to be 0.00132745 and 0.00152692 respectively. It is known that, drag force is created opposite of the direction that the vehicle is moving towards.

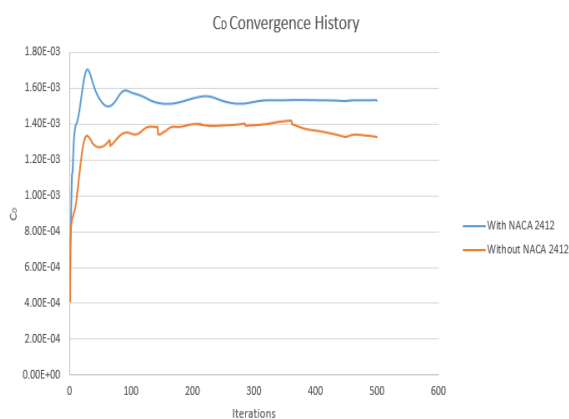


Fig.12 C_D vs. iterations for both conditions

The value of C_D has been increased when the NACA 2412 airfoil rear wing has been installed. From our hypothesis, the increment of drag force has occurred due -3° angle of the rear wing, which has created extra

drag force. Our future research will try to identify the definite cause of such behavior and come out with a better design and solution through CFD analysis.

Table 2 below summarizes the result of plotted graphs of C_L & C_D , drag force and lift force for both conditions:

Table 2 Results obtained from CFD study

Sports car	C_L	Lift force (N)	C_D	Drag force (N)
Without rear wing	0.000782	1.70455	0.00133	2.92702
With rear wing	-1.688e-05	-0.0372	0.00153	3.36685

5.5 Validation of the CFD analysis

To validate the CFD analysis, the study has been compared to several published scholarly articles. The solid geometry model of this analysis is scaled down to 1:24. In case of solid model without NACA 2412 rear wing, the pressure coefficient and viscous coefficient are found to be 0.00114069 and 0.000186748 respectively. Therefore, 85.9% of the total drag is pressure drag and rest is friction drag. This result has been compared to the popular Ahmed Body aerodynamics experiment for the validation purpose. According to the research conducted by Ahmed et al. on 1984, for a basic bluff vehicle body, up to 85% of the total drag is pressure drag and rest is friction drag. The wind tunnel speed was kept 60m/s [9]. The Mathematical model and physics setup which are used in the present analysis have followed several literatures [8][10-14]. The inlet velocity condition and specifications of the solid geometry model in those studies were different from our present research. So, in case of comparison, the main focus has been given to the flow visualization and the effect of NACA 2412 rear wing on the sports car.

6. Conclusion & future research possibilities

The results of this CFD study have been compared to the similar studies that have been done previously [9-14]. Our main research objective has been achieved as lift is reduced by creating downward force in case of the sports car model with NACA 2412 airfoil made wing. From the CFD analysis carried on two different models of sports car (with or without rear wing), the following conclusions can be drawn.

- (1) Vehicle stability is increased on high speed by the reduction of significant amount of lift force. It has been achieved by the installation of NACA 2412 airfoil as the

rear wing. Thus, safety is ensured highly and tendency to lift over at high speed has been minimized. This research also focuses to reduce accidental risks of high speed sports car. Leading sports car companies such as Bugatti, Porsche and Mercedes have been using different technologies for rear wing and trying to maximize the efficiency by eliminating the side effects at low speeds and increase the benefits on high speeds. For them, the key reason is safe driving. Also, the recirculation zone at the rear end is minimized, which ensures the cleanliness of the rear wind shield.

(2) Secondly, the feasibility of installing NACA 2412 airfoil as the rear wing of a sports car has been studied from aerodynamics perspective. Further studies can be done to find the efficient angle for the NACA 2412 airfoil made rear wing so that lift to drag ratio can be maximized, which has been a popular research topic for past few years.

NOMENCLATURE

- ρ : Density of the fluid, kgm^{-3}
- V : Velocity of the flow, m/s
- A : Projected area, m^2
- C_D : Coefficient of Drag, no units
- C_L : Coefficient of Lift, no units

REFERENCES

- [1] Xu-xia Hu, Eric T.T. Wong, A Numerical Study on Rear-spoiler of Passenger Vehicle, *World Academy of Science, Engineering and Technology, International Journal of Mechanical and Mechatronics Engineering*, Vol:5, No:9, 2011.
- [2] G.Ganesh, V.Vasudevan, Analysis of Effects of Rear Spoiler in Automobile Using Ansys, *International Journal of Scientific & Engineering Research*, Volume 6, Issue 6, June-2015 762, ISSN 2229-5518.
- [3] Ridhwan Bin Che Zakem, Aerodynamics of Aftermarket Rear Spoiler, Malaysia Pahang University (2008).
- [4] Dan Barbut, Eugen Mihai Negrus, CFD analysis for road vehicles - case study, *Incas Bulletin*, 3(2011) 15-22.
- [5] M. Rouméas, P. Gilliéron, A. Kourta, Drag Reduction by Flow Separation Control on a Car after Body, *International Journal for Numerical Methods in Fluids*, 60(2009) 1222–1240.
- [6] Emmanuel Guilmineau, Computational Study of Flow around a Simplified Car Body, *Journal of Wind Engineering and Industrial Aerodynamics*, 96(2008) 1207–1217.
- [7] Md. Munir Islam, M.Mamun, Computational Drag Analysis over a Car Body, *International Conference on Marine Technology*, Dhaka, Bangladesh, 2010.
- [8] S.M. Rakibul Hassan, Toukir Islam, Mohammad Ali, Md. Quamrul Islam, Numerical Study on Aerodynamic Drag Reduction of Racing Cars, *10th International Conference on Mechanical Engineering, ICME 2013*, Dhaka, Bangladesh.
- [9] Ahmed et al., Some Salient Features of Time-Averaged Ground Vehicle Wake, *SAE Technical Paper Series, International Congress & Exposition*, Detroit, Michigan.
- [10] Cakir, Mustafa, CFD study on aerodynamic effects of a rear wing/spoiler on a passenger vehicle (2012), *Mechanical Engineering Masters Theses. Paper 1*, Santa Clara University.
- [11] Bhamre et al., Experimental and numerical aerodynamics investigation of car, *International Journal of Engineering Development and Research*, Volume 4, Issue 2, ISSN: 2321-9939.
- [12] A. Kourta, P. Gilliéron, Impact of the Automotive Aerodynamic Control on the Economic Issues, *Journal of Applied Fluid Mechanics*, Vol. 2, No.2, pp. 69-75, 2009, ISSN 1735-3645.
- [13] A R S Azmi et al., Study on airflow characteristics of rear wing of F1 car, *IOP Conf. Ser.: Mater. Sci. Eng.*, 243 012030.
- [14] Philipp Epple et al., Aerodynamic Devices For Formula Student Race Cars, *Proceedings of the ASME 2014 International Mechanical Engineering Congress and Exposition*, Montreal, Quebec, Canada.

Recovery of Liquid Fuel through Thermal Pyrolysis of Medical Waste (Waste Syringe) in a Batch Reactor

Adnan Abedeem¹, Uday Som², Farzana Rahman³, Md. Rezaul Karim⁴ and Md. Moniruzzaman⁵ and Md. Shameem Hossain^{1*}

¹Department of Energy Science and Engineering, Khulna University of Engineering and Technology, Khulna- 9203, Bangladesh

²Department of Chemical Engineering, Jessore University of Science & Technology, Jessore-7408, Bangladesh

³Department of Physics, Jahangirnagar University, Savar, Dhaka

⁴Department of Chemical Engineering, Z. H Sikder University of Science & Technology, Shariatpur, Bangladesh

⁵Designated Reference Institute for Chemical Measurements, Bangladesh Council of Scientific & Industrial Research, Dhaka, Bangladesh

ABSTRACT

Various types of plastic materials are important items of medical waste one of which is syringe wastage covers an important fraction of plastic medical waste. These plastic syringes have a great potentiality to be used as liquid or gaseous fuel as well as source of hydrocarbon. High density Polyethylene and Polypropylene are the main components of syringes. The pyrolysis process was accomplished in a batch reactor. Gas Chromatography-Mass Spectrometry and Fourier Transform Infra-Red Spectroscopy analysis of pyrolysis liquid were carried out in this study which specified the presence of aromatic compounds, alkenes and alkanes. The chemical and physical properties of the pyrolysis liquid were much closer to commercial fuel like diesel and gasoline. The density, viscosity and calorific value of the liquid product were 758 kg/m³, 4.75 cSt and 39.561 MJ/kg. The maximum amount of liquid yields was 53 wt. % at 220°C and char yields 70.00 wt. % at 180°C respectively. The gas yield increased from 10 to 18 wt. % over the whole temperature range, while char yield decreased from 70 to 29 wt. %. It could be used as an alternative source of energy.

Keywords: Medical Waste, Plastics Syringe Wastage, Pyrolysis, Liquid Fuel, Batch Reactor

1. Introduction

Due to fossil fuel crisis in past decade, mankind has to focus on developing the alternate energy sources. The focused alternative technologies are bio-ethanol, bio-diesel, bio-fuel, waste oil recycling, pyrolysis, gasification, dimethylether, and biogas [1]. Plastic plays a significant role in improving our lifestyles in several sectors such as healthcare, packaging, construction, automotive, electronic, food industry and many more. The growth of the world population has caused the requirement of commodity plastics to further increase. According to statistic, the worldwide production of plastic has reached about 299 million tons in 2013 and has enlarged by 4% over 2012 [2]. Although medical wastes (plastic syringe) represent a comparatively small segment of the total plastic waste generated in a society, medical waste supervision is considered a vital issue worldwide [3]. The percentage of plastic medical waste ended up in landfill is still very high. Plastics may possibly take up to millions of years to degrade in nature. They degrade steadily since the molecular bonds containing hydrogen, carbon, nitrogen, chlorine and few other elements that make plastic very long-lasting. The continuous dumping of plastic in the landfill would unquestionably cause serious environmental problem [4]. Healthcare division is rising at a very speedy pace, which in turn has led to inconceivable increase in the amount of medical waste production in developing countries, especially by clinics, hospitals and other healthcare establishments.

As a developing country, Bangladesh produces a large amount of medical waste every day. A study on Khulna City Corporation (KCC) reveals that there are about 150 health care facilities in KCC and the total waste generation in Khulna city is about 520 ton/day and the amount of clinical waste generation is 2.5 ton/day [5]. Another study on Rajshahi City Corporation (RCC) suggests that the amount of medical waste collected by the RCC is 2-2.5 ton/day [6]. A further study on Jessore Municipality focused on the regular generation rate of Health Care Waste (HCW) which was 0.49 kg/patient/day, 1.59 kg/bed/day and 0.11 kg/test/day [7]. Plastics have turned out to be a key threat because of their non-biodegradability and high visibility in the waste stream. Littering also results in minor problems such as blockage of drains and animal health troubles. Their occurrence in the waste stream poses a severe problem when there is lack of well-organized end-of-life management of plastic waste [8]. Medical waste is proficient of causing diseases and disorder to people, either through straight contact or ultimately by contaminating soil, surface water, groundwater, and air [9]. Until now, there was no efficient structure for suitable medical waste management in Bangladesh to safeguard our environmental health dangers [10]. Pyrolysis is a process with comparatively little cost from which an extensive distribution of products can be gained. It is one of the most operative and hopeful procedure to acquire liquid fuel from the medical plastic waste [11]. In the procedure of pyrolysis, where heating of raw material occurs in the nonexistence of

* Corresponding author. Tel.: +88-01714506150
E-mail addresses: shameemkuet@gmail.com

oxygen, the organic compounds are decayed generating liquid and gaseous products, which can be used as alternative fuels and / or sources of chemicals. Meanwhile, the inorganic substance, free of organic matter, remains unaffected under the solid portion and can be re-used later [12]. Thermal cracking occupies the scission of extensive polymer molecules simply by exposure to elevated temperatures under inert atmospheric conditions. This type of process generates a heterogeneous hydrocarbon (HC) mixture, whose accurate composition depends mainly on process circumstances and plastic type [13]. Catalytic pyrolysis has quite a few advantages over the thermal process although catalysts are expensive and the design of the reactor has to consider the opportunity of avoiding catalyst poisoning and deactivation by the adulterants in the feedstock. To avoid these difficulties thermal pyrolysis process has been used in this experiment [14]. The purpose of the current study has been to analyze the effect of thermal cracking on the products obtained by thermal pyrolysis of Polyethylene and Polypropylene, focusing on the composition of liquid fractions, variations with the physical and chemical properties and the compound type. The percentage of various yields has also been studied. A detailed discussion is made with results obtained by different experimental procedure that may contribute to an improved understanding of the potential of the thermal pyrolysis process as a promising medical waste recycling process.

2. Materials and Methods

2.1 Collection and Preparation of Raw Materials

In this study, only the plastic portions of syringe waste have been used. Plastic-based medical wastes, used as feed material throughout the experimental investigations which were collected from Doratana Hospital that is located at Jessore Sadar in Jessore district. Syringe wastes were chopped cross-section wise varied size like $2\text{ cm} \times 1.5\text{ cm} \times 0.75\text{ cm} = 2.25\text{ cm}^3$. Fig. 1 shows the cutting tool and the size of the prepared raw materials compared with a coin.



Fig. 1 Preparation of Raw Materials

2.2 Experimental Set-up and Method

In this study a fixed-bed pyrolysis reactor was used. Fig. 2 shows the (2-D) schematic view of the experimental unit which consists of reactor body and condenser as well as other parts. The N_2 gas inlet and heat sensor unit was positioned at the below portion of the reactor. Two 10 mm diameter tube heater of a total capacity of 1 kW were fixed in equal spacing inside the reactor. The experiment was performed for plastic syringe waste. The temperature inside the chamber was recorded by thermocouple sensors and 1.5 kg raw material was taken for the experiment. Before starting the operation, air inside the reactor was removed by flowing N_2 gas for 2 minutes.

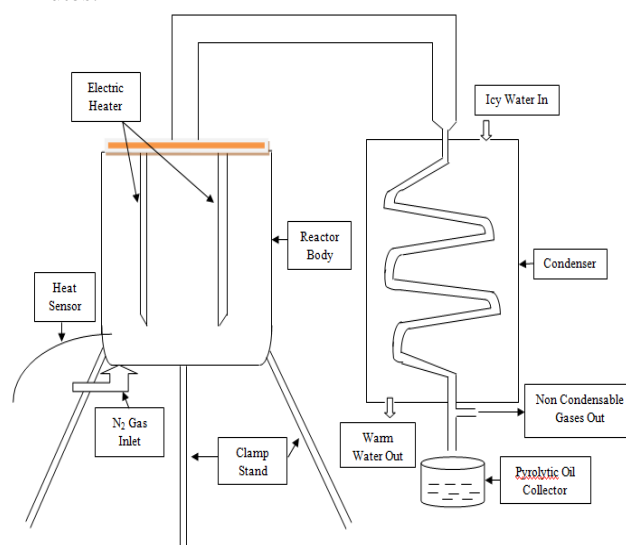


Fig. 2 Schematic diagram (2-D) of the Experimental Set-up

The reactor heater was switched ON and the temperature of the reactor was allowed to raise 250°C indicated by the temperature recorder as the melting temperatures of Polypropylene (PP) and High Density Polyethylene (HDPE) are 166.01 and 132.39°C respectively [15]. After the decomposition of plastic based materials the pyrolytic vapour created and was passed through the condenser pipes. Condensable gases were condensed and collected as liquid form in the oil collector. Non condensable gases were flown away in the atmosphere.

For GC-MS analysis, Shimadzu GCMS- TQ8040 with inbuilt database library was used in this study. The carrier gas was Helium of 99.9999% pure and 5% diphenyl 195% dimethyl polysiloxane (Rxi-5ms) of $0.25\mu\text{m}$ with dimension of 30m and 0.25mm ID was used as column. The obtained pyrolytic oil was filtered through $0.45\mu\text{m}$ membrane syringe filter and then $1\mu\text{l}$ was injected into the instrument. The following program was adopted for the GC/MS experiment.

Table 1, 2 and 3 shows the Gas chromatography condition, Oven temperature program and mass spectrometry condition respectively.

Table 1 Gas Chromatography (GC) Condition

GC Condition	
Column Oven Temperature	75 °C
Injection Temperature	250 °C
Injection Mode	Split less
Pressure	79 kPa
Total Flow	12.2 ml/min
Column Flow	1.2 ml/min
Purge Flow	5.0 ml/min

Table 2 Oven Temperature Program

Rate	Temperature (°C)	Hold time (min)
-	75.0	0.0
5.00	150.0	1.0
10.0	240.0	1.0
5.00	270.0	3.0

Table 3 Mass Spectrometry (MS) Condition

MS Condition	
Ion Source Temperature	230 °C
Interface Temperature	250 °C
Detector Gain	1.13 kV + 0.2 kV
End Time	35 min
Acq. Mode	Q3 Scan
Event Time	0.5 sec
Scan Speed	2000
m/z Range	50- 1000

For FTIR analysis, Shimadzu IRPrestige-21 ranging from 400- 4500 nm equipped with liquid sample holder having cell thickness of 0.5 mm with NaCl window was used for the FTIR analysis. The sample was injected into the cell and analyzed in the instrument.

3. Result and Discussion

Results and the discussions of the present study are described below:

3.1 Comparison of Evolved Pyrolytic Liquid Properties with other Commercial Fuels

The properties of evolved pyrolytic oil from syringe waste are very important for understanding the quality of the pyrolytic liquid. Table 4 compares some physicochemical properties of pyrolytic oil with diesel and gasoline. Density of pyrolytic oil is lower than diesel but higher than gasoline. Kinematic viscosity of the pyrolytic oil is similar with diesel but higher than gasoline. Gross calorific value of the produced oil in this study is slightly lower than Diesel and Gasoline.

Table 4 Comparison of Properties of Pyrolytic Oil with Diesel and Gasoline [16-18]

Physical Properties	Present Study (Syringe Waste)	Literature Value	
		Diesel	Gasoline
Density (kg/m ³), 30 °C	758	820 to 860	780
Kinematic Viscosity at 40 °C (centistokes)	4.75	3 to 5	1.17
Gross Calorific Value (MJ/Kg)	39.561	42 to 44	42.5

3.2 Gas Chromatography-Mass Spectrometry (GCMS) Analysis

The major products of plastic syringe waste are condensable liquids. It is difficult to identify the different and numerous components of the liquids. GC/MS analysis is a very resourceful process as it quantifies the components effectively. GC/MS analysis was carried out for pyrolytic oil obtained from this experiment. The purpose of the test was to get an idea of the nature and types of compound of such liquids, in order to determine the possible ways of treating and recycling them.

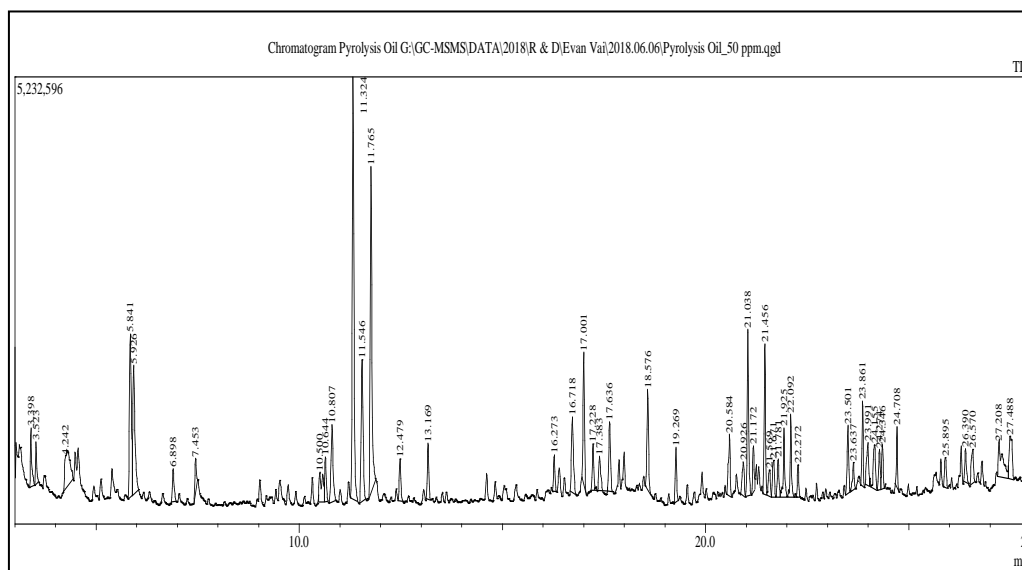
**Fig. 3** Chromatogram of pyrolysis liquid derived from syringe waste

Fig.3 demonstrates the chromatogram of pyrolytic liquid obtained from syringe waste. It is a two-dimensional plot with the ordinate axis giving concentration in terms of detector response and the abscissa represents the time. The detector gives response as a peak whose height should be ideally reliant on concentration of the particular component.

Table 5 shows the most probable compounds allocated and their area percentage compared to the total area of the chromatogram, which gives an idea of their relative concentration in the pyrolytic liquids. It can be seen that evolved pyrolysis liquids have a higher concentrations of Isodecyl methacrylate, 11-Methyl dodecanol etc.

Table 5 GC/MS characterization of pyrolysis of syringe waste

Retention Time	Area %	Compounds Name
4.242	2.84	2-Decene, 4-methyl-, (Z)-
5.842	4.86	Isodecyl methacrylate
5.925	4.33	2-Undecene, 4,5-dimethyl-, [R*,S*-(Z)]-
6.9	0.86	n-Tridecan-1-ol
7.45	0.77	(2,4,6-Trimethylcyclohexyl) methanol
10.5	1.61	Butyric acid, 2-phenyl-, dec-2-yl ester
10.642	1.06	Dodecane, 4,6-dimethyl-
10.808	2.44	9-Eicosene, (E)-
11.325	10.92	11-Methyldodecanol
11.55	4.44	11-Methyldodecanol
11.767	8.72	11-Methyldodecanol
12.483	1.01	1-Heptanol, 2,4-diethyl-
13.167	1.32	Bicyclo[2.2.1]heptane-2,5-dione, 1,7,7-trimethyl-
16.273	0.80	Decane, 1-iodo
16.718	2.27	2,4 -Di-tert-butylphenol
17.001	2.95	1-Decanol, 2-hexyl-
17.228	1.11	1-Decanol, 2-hexyl-
17.383	0.94	Eicosane
17.636	1.84	1-Decanol, 2-hexyl-
18.576	2.42	n-Nonenylsuccinic anhydride
19.269	1.16	2,5-Cyclohexadien-1-one, 2,6-bis(1,1-dimethyl-)
20.584	1.68	Eicosane
20.925	1.03	1-Cyclopentyleicosane
21.042	3.70	Hexatriacontyl trifluoroacetate
21.175	1.00	Heptacos-1-ene
21.458	3.27	1-Decanol, 2-hexyl-
21.567	0.81	Nonadecylpentafluoropropionate
21.675	1.08	1-Cyclopentyleicosane
21.925	1.66	1-Decanol, 2-hexyl-
22.092	1.77	10-Dodecen-1-ol,7,11-dimethyl-
22.272	0.74	Cyclononasiloxane, octadecamethyl-
23.501	1.65	Tetrapentacontane
23.633	0.74	Cyclohexane,1,2,3,5-tetraisopropyl-
23.858	1.63	Triacetylheptafluorobutyrate

23.991	1.31	11-Methyltricosane
24.158	1.52	Octatriacontylpentafluoropropionate
24.275	1.02	Ethyl14-methyl-hexadecanoate
24.35	1.11	Cyclohexane,1,2,3,5-tetraisopropyl-
24.708	1.02	Cyclohexane, 1,2,3,5-tetraisopropyl-
25.892	0.82	Hexacosylonyl ether
26.392	0.81	Tetrapentacontane, 1,54-dibromo-tert-Hexadecanethiol
26.567	1.19	Cyclohexane, 1,2,3,5-tetraisopropyl-
27.208	2.43	Cyclononasiloxane, octadecamethyl-
27.488	1.93	Cyclodecasiloxane, eicosamethyl-
29.330	1.52	Cyclodecasiloxane, eicosamethyl-
31.194	1.40	Tetracosamethyl-Cyclodecasiloxane
33.140	1.46	

3.3 Compositional Group Fourier Transform Infra-Red (FTIR) Spectroscopy Analysis

From the FTIR analysis it is discovered that the oil obtained from syringe wastes are mostly the hydrocarbon compounds containing both aliphatic and aromatic compounds. Effect of aromatic compounds in evolved pyrolytic oil is enrichment of cyclic group as well as octane number. The FTIR results are shown in Fig.4 and Table 6.

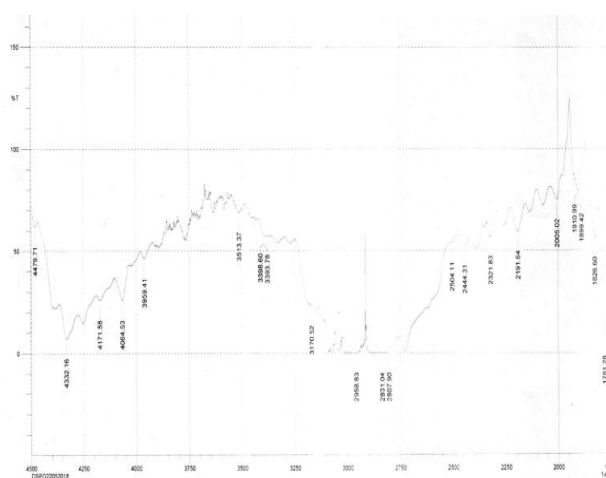


Fig. 4 FTIR Spectra of pyrolytic liquid derived from plastic syringe waste

Fig. 4 gives us an idea about FTIR spectra of pyrolytic oil produced from plastic syringe waste. The different absorbance range (cm^{-1}) represents special functional groups and respective class of compounds.

Table 6 illustrates the indicated compounds of the pyrolytic oil. Absorbance peaks between $4000\text{--}4500\text{ cm}^{-1}$ absorbance range indicates the presence of aliphatic and aromatic compounds. Similarly absorbance peaks among $3500\text{--}4000\text{ cm}^{-1}$ indicate the presence of alcohol and phenol functional groups.

Table 6 FTIR Functional Groups and Indicated Compounds of Pyrolytic Oil

Absorbance Range (cm ⁻¹)	Functional Group	Class of Compound	Present Study (Syringe Waste)
4050-4500	C-H	Aliphatic, Aromatic	4064-4479
3500-4000	O-H	Hydroxyl Group	3513-3959
3150-3400	N-H	Amines	3170-3398
2190-2510	C≡C	Alkynes	2191-2504
1800-2010	C=O	Aldehyde, Ketone	1826-2005

4. Conclusion

In this study, pyrolysis of medical wastes (waste syringe) was experimented. The density, viscosity and calorific value of derived pyrolytic oil are promising compared with diesel and gasoline. The percentage of the solid, liquid and gaseous products was also measured. From the scrutiny of the GC-MS data the liquid yield of product were containing considerable amount of cyclic and aromatic groups. The presence of Isodecyl methacrylate, 11-Methyldodecanol suggests that it can be used in various chemical and painting industries as well as oil and gas industries. FTIR results shows upper absorbance range as it specifies the presence of aliphatic and aromatic class compounds. The pyrolytic oil produced from this experiment can be proposed as a feasible unconventional resource for various kinds of chemical, oil and gas industries. This study also suggests a sustainable way of medical waste management towards a safe and healthy environment.

REFERENCES

- [1] B. K. Kumar, N. L. Deepak, P. Avinash, Performance and Emission Characteristics of Bio-Diesel using Tyre Pyrolysis Oil, *International Journal of Mechanical Engineering*, Vol. 2, pp 27-35 (2015)
- [2] S. D. A. Sharuddin, F. Abnisa, W. M. A. W. Daud, M. K. Aroua, Pyrolysis of Plastic Waste for Liquid Fuel Production as Prospective Energy Source, *IOP Conf. Series: Materials Science and Engineering*, 334 (2018)
- [3] Y.W. Cheng, F.C. Sung, Y. Yang, Y.H. Lo, Y. T. Chung, K. C. Li, Medical waste production at hospitals and associated factors, *Waste Management*, Vol. 29, pp440-444 (2009)
- [4] S. D. A. Sharuddin, F. Abnisa, W. M. A. W. Daud, M. K. Aroua, A Review on Pyrolysis of Plastic Wastes, *Energy Conversion and Management*, Vol. 115, pp 308-326 (2016)
- [5] S. Arifurrahman, A. S. M. Akid, M. Majumder, S. Khair, Scenario of Clinical Waste Management: A Case Study in Khulna City, *Global Journal of Researches in Engineering Civil and Structural Engineering*, Vol. 13, pp 01-07 (2013)
- [6] M. Z. Alam, M. S. Islam, M. R. Islam, Medical Waste Management: A Case Study on Rajshahi City Corporation, *J. Environ. Sci. & Natural Resources*, Vol. 6(1), pp 173 - 178 (2013)
- [7] M. S. Rahman, C. Moumita, K. Rikta, Medical Waste Management System: An Alarming Threat (A Case Study on Jessore Municipality, Bangladesh), *Journal of Environmental Science & Natural Resources*, Vol. 6(2), pp 181-189 (2013)
- [8] A. K. Panda, R. K. Singh, D. K. Mishra, Thermolysis of waste plastics to liquid fuel A suitable method for plastic waste management and manufacture of value added Products-A world prospective, *Renewable and Sustainable Energy Reviews*, Vol. 14, pp 233-248 (2010)
- [9] PRISM Bangladesh: Survey Report on Hospital Waste Management in Dhaka City, *Unpublished Report Dhaka: PRISM Bangladesh* (2005)
- [10] U. Som, M. S. Hossain, Medical Waste Management is Vital for Safe Town Development: An Incident Study in Jessore Town, Bangladesh, *European Journal of Sustainable Development Research*, Vol. 2(3), pp 36 (2018)
- [11] U. Som, F. Rahman, S. Hossain, Recovery of Pyrolytic Oil from Thermal Pyrolysis of Medical Waste, *Journal of Engineering Sciences*, Vol. 5(2), pp H5-H8 (2018)
- [12] D. Almeida, M. F. Marques, Thermal and Catalytic Pyrolysis of Plastic Waste, *Polimeros*, Vol. 26(1), pp 44-51 (2016)
- [13] M. S. Abbas-Abadi, A. G. McDonald, M. N. Haghghi, H. Yeganeh, Estimation of Pyrolysis Product of LDPE Degeneration using Different Process Parameters in a Stirred Reactor, *Polyolefins Journal*, Vol. 2, pp 39-47 (2015)
- [14] S. M. Al-Salem, A. Antelava, A. Constantinou, G. Manos, A. Dutta, A review on thermal and catalytic pyrolysis of plastic solid waste (PSW), *Journal of Environmental Management*, Vol. 197, pp 177-198 (2017)
- [15] J. Lin, Y. Pan, C. Liu, C. Huang, C. Hsieh, C. Chen, Z. Lin, C. Lou, Preparation and Compatibility Evaluation of Polypropylene/High Density Polyethylene Polyblends, *Materials*, Vol. 8, pp 8850-8859 (2015)
- [16] M. S. Hossain, A. Abedeen, M. R. Karim, M. Moniruzzaman, M. J. Hosen, Catalytic Pyrolysis of Waste Tyres: the influence of ZSM-catalyst/tire ratio on Product, *Iranian Journal of Energy and Environment*, Vol. 8(3), pp 189-193 (2017)
- [17] Md. Shameem Hossain and A. N. M. M. Rahman, Catalytic Pyrolysis of Tire Wastes for Liquid Fuel. *Iranica Journal of Energy and Environment* 8 (1): 88-94 (2017)
- [18] N. U. Hasan, M. M. Rahman, R. I. Rahat, Characteristics comparison of pyrolysed oils obtained from waste of plastic, tyres and biomass solid, *Proceedings of the 2017 4th International Conference on Advances in Electrical Engineering (ICAEE)*, 28-30 September, Dhaka, Bangladesh

Numerical Study of a Stand-alone Flat Plate Solar Water Heater using Rectangular Flow Channel with Fin

F. Rashid, M.R.I Sarker, S .S.Tuly, J. Ferdous, R. A. Beg

Department of Mechanical Engineering, Rajshahi University of Engineering & Technology, Rajshahi-6204,
BANGLADESH

ABSTRACT

This paper presents a study of fluid dynamics behavior and thermal performance of a flat plate solar water heater. Flat plate solar collectors have lower efficiency since large heat losses occur from the collector surface by convection and radiation. This paper presents a model of a flat plate solar water heater having rectangular flow path with fin. In this study, the performance of a flat plate solar water heater having rectangular flow channel with fin is compared with the performance of conventional solar collector. The sole purpose of this study is to enhance the thermal performance considering the effect of enhanced turbulence of the working fluid. A CFD model is developed using Discrete Ordinate radiation model to solve radiation effect and model for analyzing fluid flow inside the systems Numerical simulation model solution is carried out using finite volumes method. Results showed that the flow behavior of the solar collector was approximately rotational type. The maximum thermal efficiency was 41.75%, which was 13.43% higher than a conventional one. The numerical results also showed that presence of fin inside the flow channels over the absorber plate provided an increase in the outlet temperature than the conventional one.

Keywords: Flat plate solar water heater, thermal efficiency, Fluid dynamics behavior.

1. Introduction

The use of the renewable energy especially the solar energy is continuously increasing and gaining popularity because of the high price of conventional energy resources and serious environmental pollution problem [1, 2]. One of classical way of using solar energy is to make hot water. Usually, the system consists of two main elements, i.e., a solar collector and a storage tank. Solar energy preservation is a topic of renewable energy has been the primary interest of many researchers for the last two centuries, because it can reduce the cost of domestic water heating up to 70% [3]. Solar energy collectors (solar water or air heater) are special kind of heat exchangers that transform solar radiation energy to internal energy of the transport medium [4].

A solar water heater (SWH) is an environmentally friendly device which absorbs renewable solar energy to produce hot water [4]. The solar thermal energy can be used in solar water-heating systems, solar pool heaters, and solar space-heating systems. Flat-plate collectors are the most common solar collector for solar water-heating systems in home and solar space heating [5].

The solar hot water system produces hot water of 50°C to 70°C depending upon the solar intensity and number of solar collector panels [6, 7]. Solar water heaters are characterized by its thermal performance that depends on the transmittance, absorption and conduction of solar energy and the conductivity of the working fluid [8, 9]. The requirement of hot water per day for industrial and commercial sector is around 2, 40,000 liters. The overall installed capacity of thermal collectors is capable of producing around 25 million liters of hot water per day

at 60°- 70°C [8]. Therefore, its requirement is increasing day by day.

Flat plate collector thermal efficiency enhancement is now the interest of many researchers due to its low heat transfer characteristics

Reasons for low efficiency of flat plate collector are mentioned below:

- i. Poor convective heat transfer between the collector working fluid and the absorber tubes.
- ii. Collector plate temperature increases consequently as the thermal loss increases.

Methods to improve the efficiency are mentioned below:

- i. Factors effect on convective heat transfer
- ii. Commercial known method to improve the efficiency (area of heat exchanger, mass flow rate).
- iii. Working fluids.

Most flat plate collectors have two horizontal pipes at the top and bottom, called headers, and many smaller vertical pipes connecting them, called risers. The risers are welded (or similarly connected) to thin absorber fins. Heat-transfer fluid (water or water/antifreeze mix) is pumped from the hot water storage tank (direct system) or heat exchanger (indirect system) into the collectors' bottom header, and it travels up the risers, collecting heat from the absorber fins, and then exits the collector out of the top header [10]. Solar collectors are of double pass or single pass; it may contain fin or other extruded parts for enhancing efficiency. Fluid flow phenomenon greatly affects the heat transfer in a thermal system [11]. Hence it is required to understand the flow characters of a solar collector in order to determine the thermal performance in an efficient way. A numerical model

* Corresponding author. Tel.: +88-01709300178

E-mail addresses: icmieekuet@gmail.com

was developed to study the flow distribution in unglazed transpired plate collectors using TASC Flow-CFD code [12, 13]. CFD transient predictions were verified using indoor testing employing a solar simulator [14]. Effects of flow distribution through the absorber tubes are uniform under high mass flow rates [15].

The aim of this work is to study the effect of operating (change of mass flow rate) and design parameters (fins with rectangular channel) on the efficiency of standalone flat plate solar collectors. In this study, numerical analysis of the flat plate solar water heater is carried out with computational software named ANSYS FLUENT. The effect of adding ribs with rectangular fin with different mass flow rate was studied. Mesh independency test is carried out with different meshes of assured quality which yields the accurate prediction.. Velocity and temperature profiles of different zones of the flat plate are also observed.

2. Methodology

Geometry mainly describes the physical interpretation of the flat plate solar collector, shown in Fig. 1 and Fig. 2 with identifying the components and regions of the collector. The Fig. 1 shows the inlet and outlet sections of the collector which mainly indicates the change of temperature of the working fluid and this affects the efficiency much. The model studied in this project was built in aluminum absorber plate, which contains 2 risers, 12 rectangular flow paths; in every flow path it contains 5 rectangular fins at equal distance. These fins increase residence time as well as turbulence of the flowing fluid. These also increase roughness of the absorber plate. The inlet and outlet diameters are equal and it is 0.01905 m (0.75 inch).

Length of the collector plate is 0.9144 m (36 inch)

Width of the collector plate is 0.609 m (24 inch)

Width of the rectangular channel is 0.0254 m (1 inch)

Central distance of each successive channel is 0.0254 m (1 inch)

Length of each fin is 0.0127 m

Width of each fin is 0.00635 m

Distance of each successive fin is 0.1524 m (6 inch)

Area of the collector, $A_c = 0.786 \text{ m}^2$

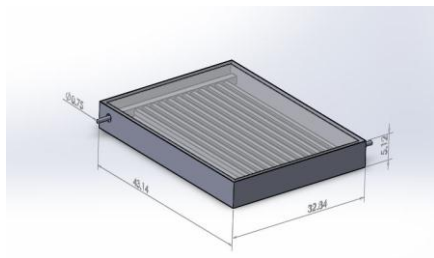


Fig. 1: Schematic of flat plate solar water heater (With rectangular flow path and fin)



Fig. 2: Fins inside the flow path

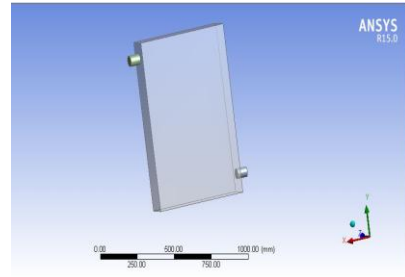


Fig. 3: Schematic of flat plate solar water heater (Without flow path and fin)

The geometry was exported to CFD software and meshing was generated with different face and edge sizing. The tetrahedrons elements in flow domain were adapted in flat plate meshing. Meshing is mainly the subdivision of the domain into a number of smaller, non-overlapping sub domains. Medium mesh size was used in this study. Two mesh models were generated separately which are shown in Fig. 3 and Fig. 4 respectively. For Orthogonal quality of mesh 1 the value is 0.787258 which has an ideal value of close to 1. Aspect ratio is a measure of the stretching of the cell. Generally, it is best to avoid aspect ratio excess of 5 in the flow.

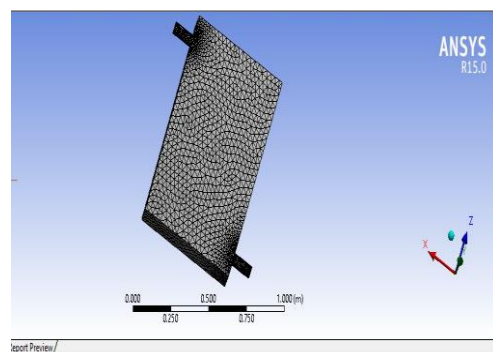


Fig. 4: Mesh model (With rectangular flow path and fin)

From the tests it is found that mesh quality is good. Numbers of nodes are 20836 and number of elements are 114690 for the mesh 1.

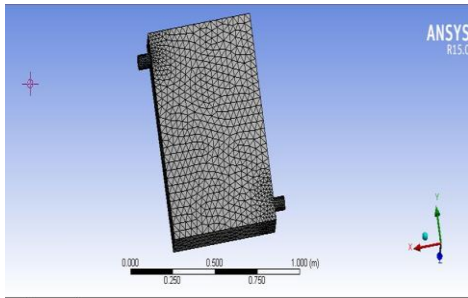


Fig. 5: Mesh model (Without rectangular flow path and fin)

For Orthogonal quality of mesh 2 the value is 0.84764 which has an ideal value of close to 1. In mesh 2 aspect ratio used is 1.90129. Numbers of nodes are 6250 and number of elements are 30215 for the mesh 2.

Modeling is the next step for CFD analysis after meshing is completed. It includes choosing various models for different criteria. Generally there are turbulence and radiation model. In turbulence flow the velocity field always fluctuates. As a result, the transported quantities such momentum, energy and species concentration fluctuate. Generally the FLUENT offers various turbulence models. The standard K- ϵ (epsilon) model was used to capture the turbulence flow in this study of a flat plate collector due to its suitability for a wide range of turbulence flows. The standard K- ϵ model for the simple scheme of turbulence used two equation models. In which the solution of two separate transport equation allows the turbulent velocity and length scales, which are to be independently determined. Standard wall function was taken as near-wall treatment. For standard K- ϵ (epsilon) turbulence model it is allowed to use standard wall function and this function works reasonably well for broad range of wall bounded flow like in flat plate solar collector in this study.

For radiation model, Discrete Ordinate radiation model was adopted in this project, which is more advantageous and used for a simpler radiation and for acceptable accuracy. For setting up the Discrete Ordinate radiation model the 3 steps are followed. These are: After choosing DO model, it provides options for Angular Discretization, Theta divisions and Phi divisions. These theta and phi divisions define the number of control angles used to discretize each octant of the angular space. The number of bands is set to be zero, indicating that only gray radiation is to be modeled. When a non-zero Number of Bands is specified, the radiation model provides options to show the wavelength intervals.

In this project, for Boundary condition (shown in Table 1) all the water inlet surfaces were defined as mass flow rate at inlet. The mass flow rate, temperature of the working fluid (water), mass fraction of all species, turbulent intensity is specified. Before FLUENT can begin solving governing equations, flow field guessed initial values, used as initial values of the solution, had to be provided. Once the initial values had been provided, the iteration was performed until a converged result is obtained.

Table 1: Boundary conditions for fluid flow

Domain	Water inlet	Water outlet	Glass plate	Absorber with fin
Type	Mass flow inlet	Pressure outlet	Wall	Wall
Flow direction	Negative Y direction	Negative Y direction	Positive Z direction	Negative X direction

At the inlet the working fluid is at ambient temperature and this is the lowest temperature of the collector. Working fluid temperature is highest at outlet section by absorbing heat from the solar radiation as passing over the absorber plate. The rectangular fins increase the surface area and residence time for the working fluid so that it can absorb more heat.

3. Results & Discussion

Fig.6 and Fig.7 show the velocity streamline of flat plate collector for model 1 and model 2 respectively. Model 1 and Model 2 represent the condition for mesh 1 and mesh 2. These contours show the fluid flow characteristic. These also show the effect of turbulence. The laminar sub layer on the lower part of the collector is responsible for lower efficiency of collector but the roughness of the collector helps to remove the layer and makes the fluid flow more turbulent.

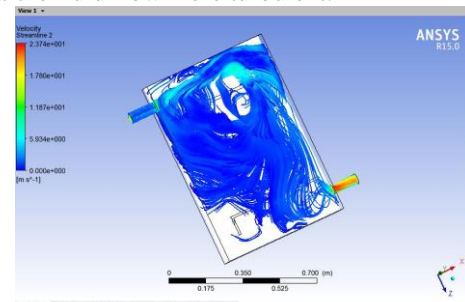


Fig. 6: Velocity streamlines (For Model 1)

The fins inside the rectangular flow passages designed in this study contribute to make the flow more turbulent (In Fig.7). Due to the hindrance to flow caused by fins, the residence time of fluid inside the collector increases. Turbulence in flow also increases. As a result outlet temperature rises and flow velocity decreases.

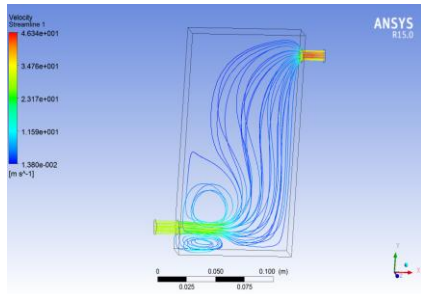


Fig. 7: Velocity streamlines (For Model 2)

Velocity was higher in flat plate collector without fin and flow channels (Fig. 7) as there was no hindrance to flow. And so there is more uniformity in flow streamlines.

Fig. 8 & Fig. 9 show the temperature contours of flat plate solar collector for model 1 and model 2. Scale beside the contours indicates the temperature of different zones. The working fluid (water) when enters to the collector with an ambient temperature then it passes over the absorber. Through glass plate heat from solar energy tracked in the collector and gradually the fluid become hot absorbing this heat. Lowest temperature is at inlet, comparatively higher at wall side of wooden box, then increases in the middle of the collector and the highest is at outlet.

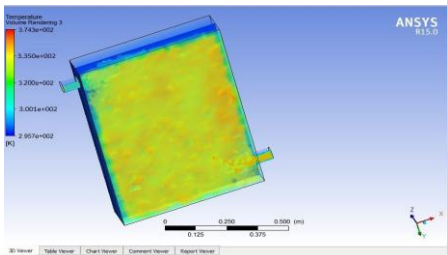


Fig. 8: Temperature contour (For Model 1)

Fig. 8 shows temperature contour of flat plate solar collector for model 1 i.e. with fin & flow channel. It shows that the temperature at inlet is 305 K and water passing through the rectangular flow channels with fin inside. Water exits at a temperature around 338 K. Here temperature rise is 33 K.

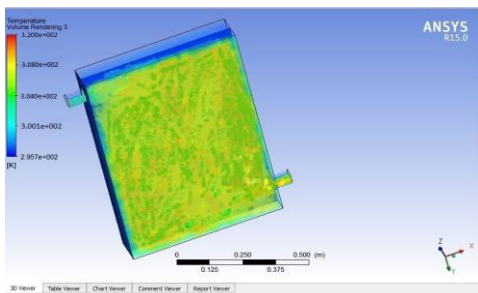


Fig. 9: Temperature contour (For Model 2)

Fig. 9 shows temperature contour of flat plate solar collector for model 2 i.e. flat plate solar collector without fin & flow channel. The scale on the side indicates the temperature distribution. It shows that the

temperature at inlet is 299 K and water passing through the rectangular flow path it exits at a temperature around 307 K. Here temperature rise is only 8 K which is much lower than the model 1 analyzed in this study. From the temperature contours, it can be said that flat plate solar collector with fin & flow channels is more efficient and satisfactory than the one which is without any fin & flow channel.

Fig. 10 shows the efficiency of experimental and numerical set up, the efficiency of designed model is higher than the conventional simple model without rectangular flow path and fin, and thus it validates the model. The numerical value of efficiency is 5% higher than experimental value.

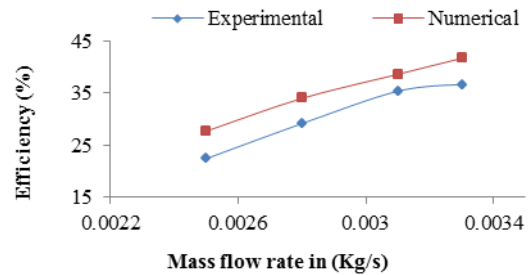


Fig. 10: Efficiency Vs. Mass flow rate curve

Fig. 11 shows the Heat transfer co-efficient for different mass flow rate, the value of heat transfer co-efficient increases with the increase in mass flow rate. Higher Mass flow rate and fin enhanced the turbulence results in enhanced the heat transfer coefficient.

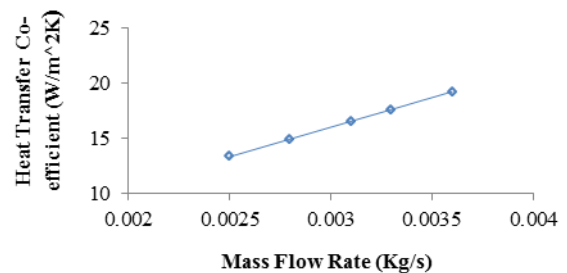


Fig. 11: Heat transfer co-efficient Vs. Mass flow rate curve

Fig. 12 shows the relationship between temperature and mass flow rate, fall in temperature with increase in mass flow rate. The difference between numerical and experimental value is within an acceptable range of variation that proof the validation of the model.

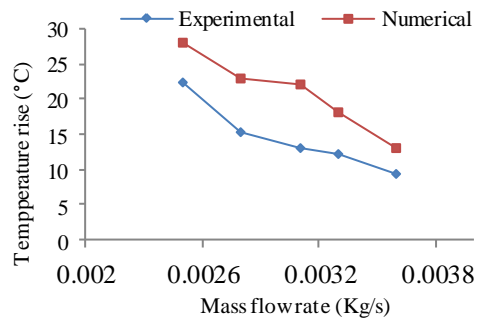


Fig. 12: Heat transfer co-efficient Vs. Mass flow rate curve

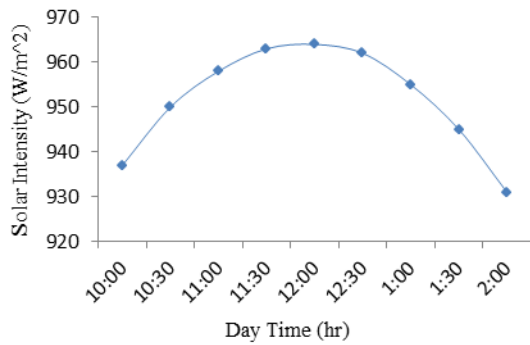


Fig. 13: Solar intensity Vs. Day time curve

Fig. 13 shows the change of solar intensity with respect to day time, the intensity increases to a highest value with day time and then decrease. The highest value of solar intensity was found at around 12.00 PM. The latitude and longitude of Rajshahi is 24.36° North & 88.62° east respectively.

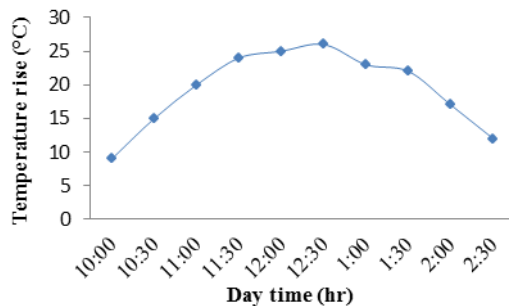


Fig. 14: Temperature rise Vs. Day time curve (clear weather)

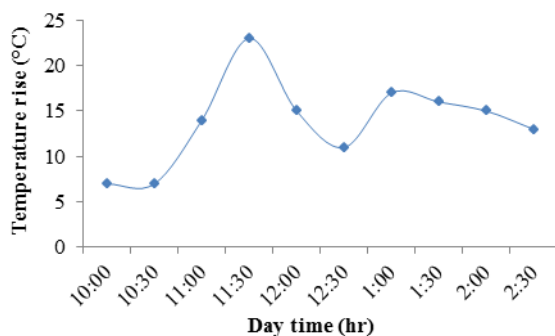


Fig. 15: Temperature rise Vs. Day time curve (cloudy weather)

Fig. 14 & Fig. 15 show the change of temperature with respect to day time in clear and cloudy weather respectively. In clear weather highest temperature obtained at 12:30 AM after then temperature decrease, on the other hand for cloudy weather the highest temperature was obtained at 11:30 AM and he minimum temperature was found at 10:30 AM and then at 12:30 PM due to cloudy weather.

4. Conclusion

A numerical model is developed to study the effect of rectangular channel with fin in a solar water heater. Considering different mass flow rate of water input, the flow behavior of working fluid was observed and the temperature and velocity at outlet were obtained. The mass flow rate was varied from 9 Kg/hr to 13 Kg/hr. The highest efficiency was obtained 41.75% (Numerically) and 36.7% (Experimentally). The highest efficiency is found at highest mass flow rate. It was also found that the temperature rise decreases with increase in mass flow rate, at the same time the heat transfer co-efficient increases with increase in mass flow rate. From CFD results, it is concluded that-

- i. The best result was obtained on clear sunny days.
- ii. Collector outlet temperature during day varies depending on solar intensity and it is directly proportional to solar intensity.
- iii. The value of heat transfer co-efficient increased with the increase in mass flow rate.
- iv. From the numerical values of efficiency it was found that solar water heater with fin inside the rectangular flow path was 28% more efficient than that of without fin & flow path. From temperature contours it is seen that solar water heater with fin & flow path gave around 25 K more temperature rise than the solar water heater without fin & flow path.
- v. Analyzing the thermal performances and flow characteristics it is seen that solar water heater with fin was more efficient than solar water heater without fin.
- vi. Analyzing the flow characteristics it is seen that increase of turbulence in the flow channel gave better performances.

5. REFERENCES

1. Dincer, I., Renewable energy and sustainable development: a crucial review. *Renewable and sustainable energy reviews*, 2000. **4**(2): p. 157-175.
2. Wüstenhagen, R., M. Wolsink, and M.J. Bürer, Social acceptance of renewable energy innovation: An introduction to the concept. *Energy policy*, 2007. **35**(5): p. 2683-2691.
3. Buckles, W. and S. Klein, Analysis of solar domestic hot water heaters. *Solar Energy*, 1980. **25**(5): p. 417-424.
4. Pangavhane, D. and R. Sawhney, Review of research and development work on solar dryers for grape drying. *Energy conversion and management*, 2002. **43**(1): p. 45-61.
5. Diakoulaki, D., et al., Cost benefit analysis for solar water heating systems. *Energy Conversion and Management*, 2001. **42**(14): p. 1727-1739.
6. Shukla, R., et al., Recent advances in the solar water heating systems: A review. *Renewable and Sustainable Energy Reviews*, 2013. **19**: p. 173-190.

7. Lunde, P.J., Solar thermal engineering: space heating and hot water systems. New York, John Wiley and Sons, Inc., 1980. 635 p., 1980.
8. Okonkwo, G. and A. Nwokoye, Experimental investigation and performance analysis of thermosyphon solar water heater. *Advances in Natural and Applied Sciences*, 2012. **6**(2): p. 128-138.
9. Huang, B., et al., Performance evaluation of solar photovoltaic/thermal systems. *Solar energy*, 2001. **70**(5): p. 443-448.
10. Alvarez, A., et al., Experimental and numerical investigation of a flat-plate solar collector. *Energy*, 2010. **35**(9): p. 3707-3716.
11. Ibrahim, A., et al., Recent advances in flat plate photovoltaic/thermal (PV/T) solar collectors. *Renewable and sustainable energy reviews*, 2011. **15**(1): p. 352-365.
12. Selmi, M., M.J. Al-Khawaja, and A. Marafia, Validation of CFD simulation for flat plate solar energy collector. *Renewable energy*, 2008. **33**(3): p. 383-387.
13. Subiantoro, A. and K.T. Ooi, Analytical models for the computation and optimization of single and double glazing flat plate solar collectors with normal and small air gap spacing. *Applied energy*, 2013. **104**: p. 392-399.
14. Gunnewiek, L., E. Brundrett, and K. Hollands, Flow distribution in unglazed transpired plate solar air heaters of large area. *Solar energy*, 1996. **58**(4-6): p. 227-237.
15. Gadi, M.B., Design and simulation of a new energy-conscious system (CFD and solar simulation). *Applied energy*, 2000. **65**(1-4): p. 251-256.

Effect of Inertia and Gravity on Three Dimensional Non-isothermal Film Stability

Kazi Rumman Islam*, Zahir. U. Ahmed

Department of Mechanical Engineering, Khulna University of Engineering & Technology, Khulna-9203, BANGLADESH

ABSTRACT

In three dimensional Newtonian film casting process inertia and gravity plays an effective role on the physical mechanism in non-isothermal condition. This paper investigates the effect of inertia and gravity on critical draw ratio of non-isothermal film casting process using both linear stability analysis. An Eigen value problem is solved from a system of linear ODE equations as nonlinear two-point boundary value problem. Neutral stability curves indicate that in non-isothermal condition gravity and inertia tends the process to be more stable than in isothermal condition. The disturbance frequency is found to be more sensitive to thermal effect. The growth rate of oscillation increases (decreases) above (below) the critical draw ratio results show that the critical draw ratio for the effect of different parameters is greater than the classical value of $Drc=20.218$ for isothermal condition.

Keywords: Non-isothermal, Film casting, draw resonance, draw ratio, Stability

1. Introduction

In the process of casting polymer melt is extruded through a slit die to form a shape of sheet and stretched by a chill roll after traveling some distance through ambient air. The polymer is then quenched and prepared for further processing or wind up. The distance between the die exit and chilled roller is relatively small. Mainly the film is cooled by the chill roller but there also occurs a solidification process between die exit and chill roll while travelling thorough the ambient air. Generally chill roller take-up velocity is greater than extrusion velocity from die exit. The ratio of take up velocity to die exit velocity is termed as draw ratio (Dr). This is an important parameter in the analysis of film casting stability. As the film is drawn uniaxially, the film thickness is reduced in response to the conservation of mass to a predetermined value at the take-up point by choosing the appropriate draw ratio. Although a larger draw ratio for a higher production rate of polymer is generally expected, this process, however, is limited by an instability known as "draw resonance". Thus, there exists a critical draw ratio above which periodic variation in film thickness occurs, as observed in practice.

Significant experimental and theoretical efforts had done from the half of last century to study various parameters on the draw resonance instability [1-3]. The mathematical model was first developed by Kase and Matsuo [4,5]. In another investigation Pearson and Matovich [6] analyzed a linear stability for a Newtonian fiber spinning process. At the same time Gelder [7] analyzed the problem neglecting gravity, inertia and surface tension effects for a Newtonian fiber spinning in isothermal condition and Gelder [7] approximate the critical draw ratio is 20.21. However Pearson and Matovich [6] showed in their analyses that for the instability of the system the critical draw ratio is approximately 20.2 for a Newtonian model. In agreement with the experimental study of Donnelly and Weinberger [8]. Using

a modified Giesekus rheological model Iyengar and Co [9] investigated the stability of polymeric film casting to infinitesimal and finite amplitude disturbances.

In general sense fiber spinning and film casting are related, there are some basic differences between them. The flow and the disturbances in fiber spinning are considered to be axisymmetric, whereas the flow in film casting is planar and disturbances are generally three dimensional [10]. For the first time draw resonance study in film casting process was performed by Yeow [11] assuming a film of small thickness and infinite width which leads to a one dimensional viscous Newtonian model. Neglecting the effects of inertia and gravity on the Newtonian film casting he investigated stability using the classical hydrodynamic linear theory and the resultant eigen-value problem was numerically solved.

Two dimensional fiber drawing in non-isothermal condition are also studied in the literature [12-17]. Alaie and Papanastasiou [18] studied the film casting of a BKZ-type fluid in an isothermal and non-isothermal steady-state analysis. It was concluded that thinning of the extruded film is enhanced by shear thinning and by air cooling often down to solidification at about the glass transition temperature upstream the chillroll. Regarding Newtonian films. Scheid et al. [19] extended Yeow's [11] model to account for non-isothermal effects. He analysis the one dimensional model in terms of Stanton (St) number between two region, one is advection dominated cooling for $St \ll 1$ and another is transfer dominated cooling for $St \gg 1$. Due to the typical geometry of large film widths compared to the thickness, surface tension effects are usually negligible. Extensional study cover the effects of inertia and gravity on the stability behavior in the one dimensional case of infinite width are available from Cao et al. [20] and Bechert et al. [21]. In isothermal condition and for two dimensional film inertia or gravity was found to have

* Kazi Rumman Islam. Tel.:+88-01682419281

E-Mail addresses: kazirummanislam13@gmail.com

profound effect on the draw resonance. Ahmed et al. [24] performed a three dimensional linear stability analysis of the film casting process in isothermal condition accounting gravity and inertia effects, they observed a stability enhancement caused by the three dimensional perturbations. Bechert et al. [25] investigated the stability nature of draw resonance under the influence of inertia, neck-in and gravity in isothermal condition. As such it appears that the effect of inertia and gravity on three dimensional non-isothermal film casting has previously not addressed adequately in the past and the current paper will investigate this effect systematically.

2. Mathematical model and Boundary conditions:

In this section, the general formulation is implemented for non-isothermal Newtonian fluid film casting as extension of Ahmed et al. [24]. Consider a non-isothermal and incompressible thin film of Newtonian fluid, is continuously drawing from an extrusion die. The film is taken up by a winder or chill roll placed at a certain distance L from the die. The problem is defined by the Fig.1. Let the density and viscosity of thin-film flow of an incompressible Newtonian fluid are ρ and μ respectively. In this study inertia and gravity are assumed to be relatively important compared to surface tension effect.

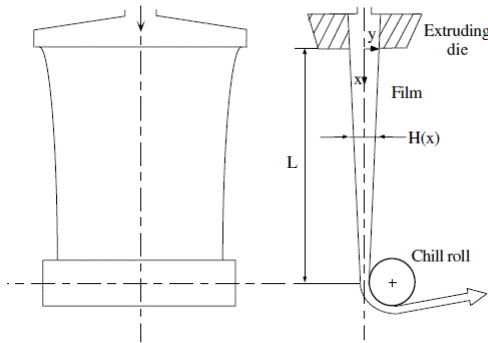


Fig.1: Schematic of the film casting process and non-dimensional coordinates and variables.

The film thickness and velocity are respectively H_0 and U_0 at the exit of Die. The film length between the Die and winder/chill roll is L. The width of the film is very large compared with its thickness and is much larger than L.

Let u , v and w denote the dimensionless velocities in the streamwise, spanwise and depthwise directions respectively and h is dimensionless film thickness. The dimensionless co-ordinates are x , y , z and time t . The aspect ratio will be denoted by $\epsilon = H_0/L$ and will be considered small. u is taken to depend only on x , y and t . Five dimensionless parameters come in the problem Reynolds number Re , Froude number Fr (or equivalently G), Peclet number Pe , Boit number Bi and the draw ratio Dr introduces as,

$$Re = \frac{\rho U_0 L}{\mu}, Fr = \frac{U_0^2}{gL}, G = \frac{Re}{Fr} = \frac{\rho g L^2}{\mu U_0}, Dr = \frac{U_L}{U_0}, Pe = \frac{\rho c_p U_0 L}{k} \text{ and } Bi = \frac{h_m L^2}{k H_0}$$

where h_m convective heat transfer co-efficient and U_L is the velocity at the chill roll. Ahmed et al. [24] derived the continuity and momentum conservation equations based on Schultz et al. [13] asymptotic analysis which is the base of our paper. This paper used the final deduced form of continuity and momentum conservation equations of Ahmed et al. [24] except further deduced the procedure.

$$\begin{aligned} \delta_t + (\delta u)_x + (\delta v)_y &= 0 \\ Re \delta(u_t + uu_x + vv_y) &= [\delta(4u_x + 2v_y)]_x \\ &\quad + [\delta(u_y + v_x)]_y + \delta G \\ Re \delta(v_t + uv_x + vv_y) &= [\delta(4v_y + 2u_x)]_y \\ &\quad + [\delta(u_y + v_x)]_x \end{aligned} \quad (1)$$

The conservation of energy equation becomes (neglecting viscous dissipation)

$$\rho c_p \left(\frac{\partial T}{\partial t} + u \frac{\partial T}{\partial x} + v \frac{\partial T}{\partial y} \right) = k \left(\frac{\partial^2 T}{\partial x^2} + \frac{\partial^2 T}{\partial y^2} + \frac{\partial^2 T}{\partial z^2} \right) \quad (2)$$

Apply kinematic condition at free surface boundary value in the energy equation and integrating with respect to z over h_1 to h_2 (let $\delta = h_2 - h_1$)

$$\rho c_p \delta \left(\frac{\partial T}{\partial t} + u \frac{\partial T}{\partial x} + v \frac{\partial T}{\partial y} \right) = \delta k \left(\frac{\partial^2 T}{\partial x^2} + \frac{\partial^2 T}{\partial y^2} \right) - 2k [h_m (T - T_s)] \quad (3)$$

Simplifying by dimensionless co-ordinates and numbers the equation becomes

$$Pe \left(\frac{\partial \theta}{\partial t} + u \frac{\partial \theta}{\partial x} + v \frac{\partial \theta}{\partial y} \right) = \frac{\partial^2 \theta}{\partial x^2} + \frac{\partial^2 \theta}{\partial y^2} - \frac{2Bi\theta}{\delta} \quad (4)$$

3.0 Steady State solution

Here we analysis the energy equation to study non-isothermal condition only. Governing equation of steady state are considered as follows

$$\begin{aligned} Re \delta_s u_s u'_s &= 4(\delta_s u''_s + \delta'_s u'_s) + \delta_s G \\ (\delta_s u'_s + \delta'_s u_s) &= 0 \\ Pe u_s \theta'_s &= \theta''_s - 2Bi\theta_s / \delta \end{aligned} \quad (5)$$

Where the subscript s indicates the steady state and a prime denotes total differentiation with respect to x . The corresponding boundary conditions are given by as follows:

$$\begin{aligned} u_s(x=0) &= 1 \quad u_s(x=1) = Dr \quad \delta_s(x=0) = 1 \quad \theta_s(x=0) = 1, \\ \theta'_s(x=1) &= 0 \end{aligned}$$

In isothermal condition including gravity and inertia fang et.al [21] experimented the flow in the range of

inertia $Re \in [0,0.2]$ and gravity $G \in [0,100]$. Based on the rheological properties of polymer fluid the ranges are chosen considering commercial film casting and fiber spinning process.

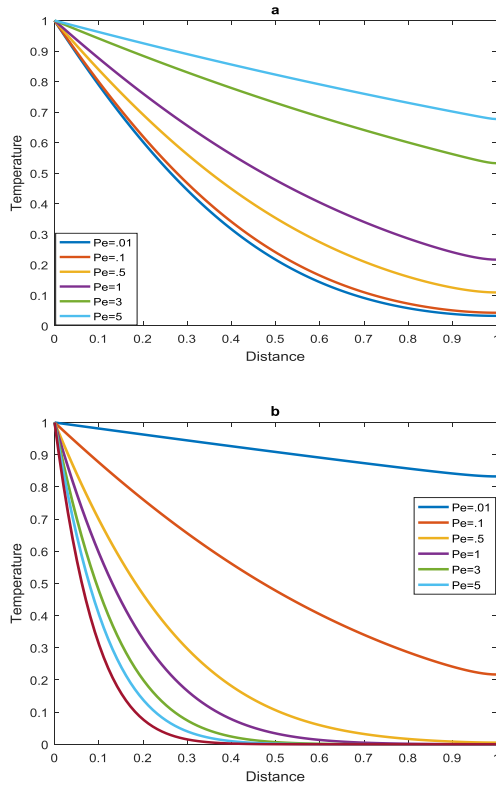


Fig.2: Influence of Peclet number (a) and Biot number (b) on the steady state temperature distributions at $G=50$, $Re = 0.01$, $DR = 20.0$, $Bi=1$ (a) and $Pe=1$ (b).

In our study we take this range for the ease of comparison with previous result to better illustrate the non-isothermal effect. Our results agreement closely with Fang et al. [10] for velocity and thickness near the die exit and take up point. Stretching velocity is higher at take up point at inertia increases. Gravitational effect is low at $G < 15$. As the high temperature liquid film travel through air gap there occurs heat transfer to ambient air. Bulk fluid are stretched by chill roller from the die exit and heat diffusion occurs travelling through air and the heat transfer occurred through surface. Fig.2 shows that (a) as the increase of Peclet number the temperature is dissipated more slowly with the distance from die exit and Fig.2 (b) as the increase of Biot number the temperature is dissipated more rapidly with the distance from the die exit. In polymer film casting Peclet number is high and Biot number is moderately low in practical cases.

4.0 Linear Stability Analysis

Solving the eigenvalue problem neutral stability curve are obtained and resulting draw ratio is called critical draw ratio. The imposed infinitesimal perturbation amplify exponentially with time above this critical value considered infinitesimal disturbances as super position

to steady state flow. Thus perturbed steady state temperature film thickness and velocities are as

$$\begin{aligned} u(x,y,t) &= u_s(x) + U(x) e^{\lambda t +iky} \\ v(x,y,t) &= V(x) e^{\lambda t +iky} \\ \delta(x,y,t) &= \delta_s(x) + \Delta(x) e^{\lambda t +iky} \\ \theta(x,y,t) &= \theta_s(x) + O(x) e^{\lambda t +iky} \end{aligned} \quad (6)$$

where δ_s and u_s indicate the steady state solutions and Δ , U , and V are complex perturbation amplitudes. k represents the real wavenumber for the disturbances along the span wise direction. In this case, k is the complex eigen-value (with λ_r being the growth or λ_i decay rate and being the disturbance frequency). Assume the flow velocity in the depth wise direction (z) is decoupled from the flow in the (x, y) plane and is dictated by the continuity equation. Upon the substitution of expressions (6) into Eqs. (1), (4) and eliminating δ_s , δ_s' , u_s'' in terms of u_s and u_s' using steady state equation the linearized Eqs. are rearranged and the disturbance frequency is recast as a first order equation to yield the perturbation variables are found to satisfy the following linearized differential equations are rearranged

$$\begin{aligned} U'' &= (Reu_s/4 + 2u_s'/u_s) U' + (Reu_s'/4 - u_s''/u_s^2 + k^2/4) U \\ &\quad + \lambda (ReU/4 + \Delta u_s') + 3iku_s'V/2u_s - 3ikV'/4 \\ V'' &= (Reu_s/4 + u_s'/u_s) V' + 4k^2V \\ &\quad + \lambda ReV - 3ikU' + (iku_s'/u_s) U \end{aligned} \quad (7)$$

$$\Delta' = (u_s'/u_s^3)U - \lambda \Delta/u_s - U'/u_s^2 - u_s'\Delta/u_s - ikV/u_s^2$$

$$O'' = Pe(\lambda O + u_s O' + \theta' U + u_s \theta' O/\delta_s) + k^2 O + 2Bi O/\delta_s - (\Delta/\delta_s)(Pe u_s \theta_s' + 2Bi \theta_s'/\delta_s)$$

the corresponding boundary conditions are

$$\begin{aligned} U = V = \Delta = O = 0 \text{ and } U' = 0 \text{ at } x=0, \\ U = V = \Delta = O = 0 \text{ at } x=1 \end{aligned}$$

Ahmed et al. [24] is solved the linear eigen-value problem as a nonlinear two-point boundary value problem. Only the disturbance frequency is considered unknown variable in this case while the critical draw ratio is determined upon using an iterative technique. $\lambda' = 0$. where a prime denotes total differentiation with respect to the problem is solved by MATLAB using the function 'bvp4c'. The collocation polynomial provides a fourth-order accurate C1-continuous solution in the interval of integration.

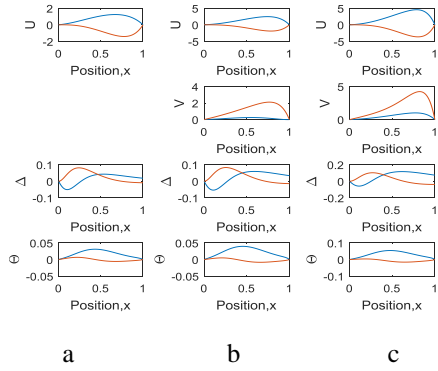


Fig.3: Solutions to the eigenvalue problem at $Dr=25$ for $G=10$, $Pe=1$, $Bi=5$ (a) $k=0$, (b) $k=2$, and (c) $k=4$, with the blue line and the red line representing the real and imaginary parts of complex-valued perturbations respectively.

The Fig.3 indicates the flow strengthening resulting from three dimensional. Overall amplitudes of U , Δ and Θ are not influenced significantly. The extreme position of U are changed with the increasing of wavenumber k , real part of V remain close to zero whereas Δ and Θ are not effectively influenced.

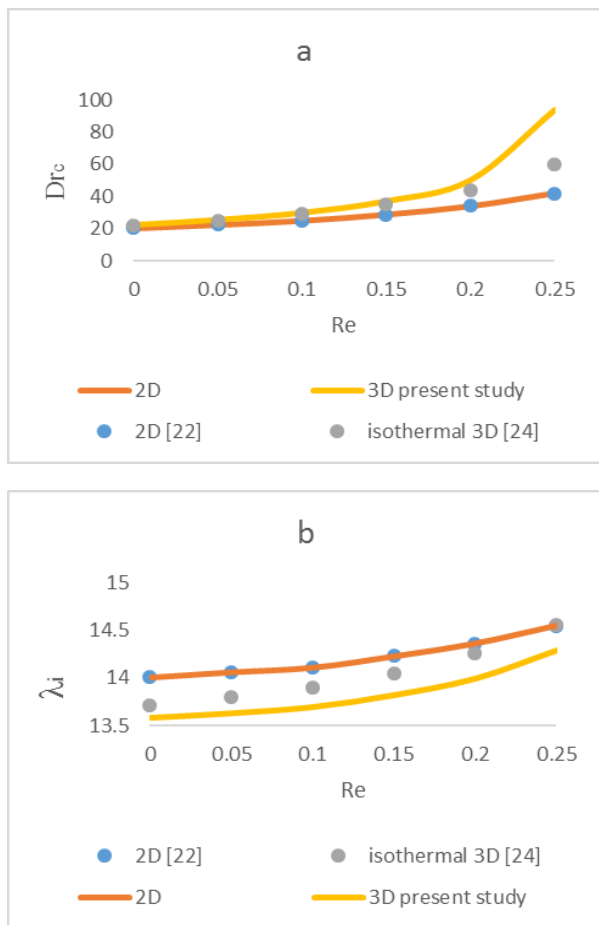


Fig.4: Comparison of (a) critical draw ratio and (b) disturbance frequency with 2D [22] and isothermal 3D [24] disturbance by taking $G=0$, $Pe=0$, $Bi=0$.

Note that the 2D results from the current formulation (by setting $k=0$) almost overlap with those obtained by Fang et al. [10] and non- isothermal 3D results from current formulation (by setting $k=1$, $Pe=0$, $Bi=0$) in the absence of inertia and gravity is predicted as 22.637 which is higher than the isothermal 3D critical value of 22.15 obtained by Ahmed et al. [24].

The comparison of neutral stability curves for 2D, isothermal 3D and non-isothermal 3D flows is depicted in Fig. 4 That gives an indication that the non-isothermal 3D film flow is more stable, at least in the absence of inertia and gravity.

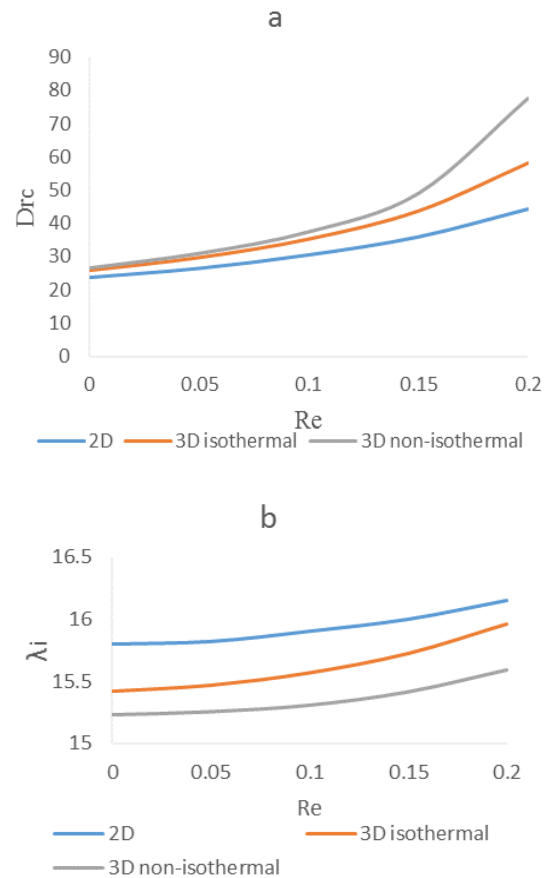


Fig.5: comparison of (a) the critical draw ratio and (b) disturbance frequency for 2D, isothermal and non-isothermal ($Pe=1$, $Bi=1$) 3D flows for $G=10$.

The enhanced stability is even more evident at higher inertia, as shown in Fig.4. In contrast, the oscillation frequency is lower for the non-isothermal 3D flow. At wide range of inertia. However, at large inertia ($Re>0.2$) the frequency for isothermal 3D flow is higher than the 2D flow but the frequency for non-isothermal 3D flow is relatively lower at large inertia. This is shown in Fig. 4. Both inertia and gravity have a significant stabilizing influence on the film casting in non-isothermal condition. This is illustrated in Fig.5, where the critical draw ratio is plotted against Re for $G=10$. The critical draw ratio increases with Re , indicating that inertia delays draw resonance. The non-isothermal effect is more infl-

ential at higher inertia say, $Re > 0.2$, as shown in Fig.5. The discrepancy between the predictions based on linear stability and reality can then be explained by the stabilizing influence of inertia and gravity in non-isothermal condition. The disturbance frequency is increased monotonically with both Re and G . Since the typical draw ratio in an industrial film casting process is about 28 to 31 for polypropylene and somewhat higher for polyethylene [13], it is assumed that for higher inertia (say, $Re > 0.20$) the film casting process is stable for all practical purposes.

Here the critical draw ratio is higher for non-isothermal 3D flow than isothermal 3D flow. On the contrary, the disturbance frequency is lower for non-isothermal 3D flow. In Fig.6 shows the increase in wavenumber with inertia indicates an almost complete stabilization of the practical processes. The disturbance frequency decrease with the increase of wavenumber.

5.0 Transient response of inertia and gravity in non-isothermal flow

Linear stability analysis is useful only in predicting the onset conditions of the instability in film casting, but fails to predict the actual spatio-temporal response once analysis is conducted here to examine the stability of the system to finite amplitude disturbances. The nonlinear response in the absence of inertia and gravity examined by Iyengar and Co [11] using a finite-element approach to discretize the full equations spatially and resulting equations are integrated in time. In the present analysis, the system of nonlinear time-dependent partial differential equations is discretized using a finite-difference method and solved as a boundary value problem.

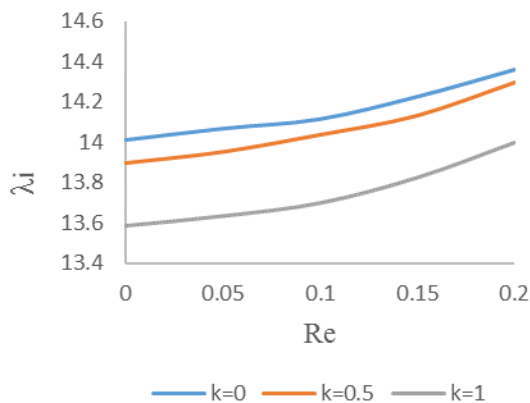


Fig.6: Influence of wavenumber on the disturbance frequency over the range $Re \in [0, 0.2]$, $k \in [0, 1]$, $Pe=1$ and $Bi=1$.

The disturbances are introduced by adding finite amplitude disturbances onto the steady-state solutions. Long time is needed (1–10 h of CPU time) per run as small time step ($\Delta t = 0.01$) needed for convergence. To obtain an accurate numerical result, an extremely small time step is used, i.e. $\Delta t = 0.001$. The nonlinear analysis is conducted for several draw ratios corresponding to

draw ratios below, near and above the critical value. The response of the film thickness at the take-up point ($x = 1$) is displayed in Fig.8 Linear stability analysis predicts the onset of a Hopf-bifurcation (over stability) at the critical draw ratio.

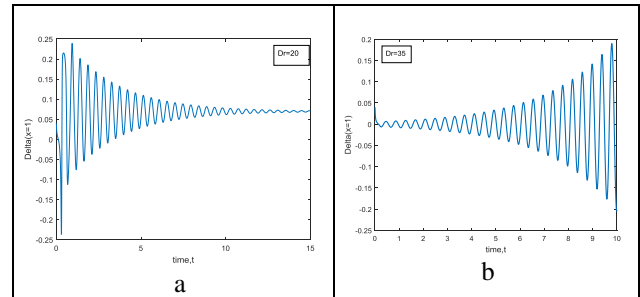


Fig.7: Transient response of film thickness at take-up point $h(x = 1, t)$ for draw ratio (a) 20 and (b) 35 for $Re=.1$, $Pe=474$ and $Bi=750$.

The Fig.7 shows that for a draw ratio of 20.0 the film thickness at the take-up point exhibits damped oscillation. The disturbance decays with time, but remains symmetric with respect to the steady state. For a draw ratio of 35.0, the disturbance is amplified and grows relatively slowly. Due to the slow growth of the amplitude, sustained oscillation will not be reached until a time large enough. It is noted that beyond the critical draw ratio the sustained disturbance consists of narrow, sharp peaks alternating with wide, flat bottoms, reflecting a dissymmetry with respect to the steady state.

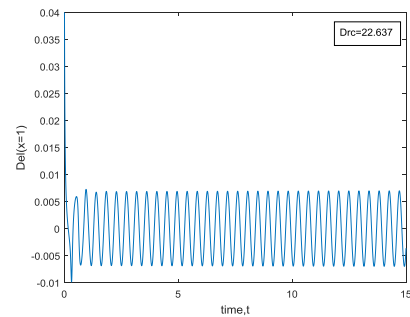


Fig.8: Transient response of film thickness for $Re=0$, $G=0$, $Pe=1$ and $Bi= 1$.

It can be seen that increasing of Biot number as well as decreasing of pecelet number improves the flow stability as Tian et al. [23] investigated the effect of cooling on the stability of film casting with three different convective heat transfer coefficients (h_m). He found the increase in h_m reduces the amplitude of the draw resonance significantly.

6.0 Conclusion

In the non-isothermal film casting process the role of inertia and gravity in draw resonance is investigated for a Newtonian film both linear and nonlinear stability analysis, which focuses on the transient response are

carried out in this study. For linear stability analysis, the eigenvalue problem is treated as a two-point boundary-value problem including the steady state which is determined simultaneously.

The steady state film thickness (velocity) is found to increase (decrease) with the increasing inertia. Gravitational effect has the opposite influence. Also Peclet number and Biot number has opposite influence. Increasing of Biot number improves the flow stability. It is concluded here that although both inertia and gravity stabilize the process, inertia is more influential than gravity on the stability. Certain combinations of the flow parameters, lead to a dramatic increase in the critical draw ratio by non-linear analysis.

NOMENCLATURE

Dr	Draw ratio
U_o	Velocity
H_o, δ	Thickness
μ	Viscosity
ρ	Density
Drc	Critical draw ratio

REFERENCES

- [1] R.E. Christensen, Extrusion Coating of Polypropylene, *SPE J.*18, p.751, (1962).
- [2] J.C. Miller, Swelling Behavior in Extrusion, *Polym. Eng. Sci.*, Vol. 3(2), pp. 134–137, (1963).
- [3] M.A. Matovich and J.R.A. Pearson, Spinning a Molten Thread line: Steady State Isothermal Viscous Flows, *Ind. Eng. Chem. Fundam.* Vol.8 (3), pp.512–520, (1969).
- [4] S. Kase, and T. Matsuo, Studies on Melt Spinning. I. Fundamental Equations on the Dynamics of Melt Spinning, *J. Polym. Sci. A*, Vol.3, pp.2541–2554, (1965).
- [5] S. Kase and T. Matsuo, Studies on Melt Spinning. II: Steady State and Transient Solutions of Fundamental Equations Compared with Experimental Results, *J. Appl. Polym. Sci.*, Vol.11, pp. 251–287, (1967).
- [6] J. R. A. Pearson and M. A. Matovich, spinning a molten Thread line: Stability, *Ind. Eng. Chem. Fundam.*, Vol. 8(4), pp. 605–609. (1969).
- [7] D. Gelder, The Stability of Fiber Drawing Processes, *Ind. Eng. Chem.*, Vol.10, pp. 534–535, (1969).
- [8] G. J. Donnelly and C. B. Weinberger, Stability of Isothermal Fiber Spinning of a Newtonian Fluid, *Ind. Eng. Chem. Fundam.*, Vol.14, pp.334–337, (1975).
- [9] V. R. Iyengar, and A. Co, Film Casting of Modified Giesekus Fluid: Stability Analysis, *Chem. Eng. Sci.*, Vol. 51(9), pp. 1417–1430, (1996).
- [10] F. Cao, R. E. Khayat, and J. E. Puskas. Effect of inertia and gravity on the draw resonance in high-speed film casting of Newtonian fluids. *International Journal of Solids and Structures*, Vol. 42, pp. 5734–5757, (2005).
- [11] Y. L. Yeow, On the Stability of Extending Films: A Model for the Film Casting Process, *J. Fluid Mech.*, Vol. 66, pp. 613–622, (1974).
- [12] B.P. Huynh and R.I. Tanner, Study of the non-isothermal glass fiber drawing process. *Rheol. Acta.* Vol. 22, pp. 482 (1983)
- [13] W. Schultz and S. Davis, One-dimensional liquid fiber, *J. Rheol.* Vol. 26, pp. 331 (1982).
- [14] W. Schultz, Slender viscoelastic slender fiber flow. *J. Rheol.* Vol. 33, pp. 1329 (1987).
- [15] S.E. Bechtel, K.D. Bolinger, J.Z. Cao and M.G. Forest, Torsional effects in high-order viscoelastic thin filament models. *SIAM J. Appl. Math.* Vol.55, pp.58 (1995).
- [16] S. E. Bechtel, M. G. Forest and Q. Wang, Non-isothermal modeling of fiber spinning. *Recent Adv. Non-Newtonian Flow Publ. by ASME*, Vol.141, pp.37 (1992).
- [17] Q. Wang and G. M. Forest, Numerical simulations of non-isothermal fiber spinning processes. *Numerical Methods for Non-Newtonian Fluid Dynamics, Publ. by ASME*, Vol.179, pp. 11–20, (1994).
- [18] S.M. Alaie and T.C. Papanastasiou, Film casting of viscoelastic liquid. *Polym. Eng. Sci.* Vol.31 (2), pp. 67–75, (1991).
- [19] S. Scheid, B. Quiligotti, R.G. Tran and H. A. Stone. On the (de) stabilization of draw resonance due to cooling. *Journal of Fluid Mechanics*, Vol.636, pp. 155–176, (2009).
- [20] M. Bechert, D. W. Schubert, and B. Scheid. Practical mapping of the draw resonance instability in film casting of Newtonian fluids, *European journal of Fluids Mechanics*, Vol.52, pp.68–75, (2015).
- [21] C. Fang, R.E. Khayat and J.E. Puskas, Effect of Inertia and Gravity on the Draw Resonance in High-Speed Film Casting of Newtonian Fluids, *Int. J. Solids Struct.*, Vol.42, pp. 5734–5757, (2005).
- [22] R. German., R. E. Khayat and J. K. Cui, Influence of Inertia and Gravity on the Stability of Filament Jet Flow, *Phys. Fluids*, Vol.18, pp. 064108, (2006).
- [23] Fucheng Tian, Xiaoliang Tang, Tingyu Xu, Junsheng Yang, and Chun X., Nonlinear stability and dynamics of non-isothermal film casting. *Journal of Rheology*, Vol.62, pp.49, (2018).
- [24] Z. U. Ahmed and R. E. Khayat. Three Dimensional Film Stability and Draw Resonance. *Journal of Fluid Engineering*, Vol.134, pp.101302, (2012).
- [25] M. Bechert, D. W. Schubert, and B. Scheid. On the stabilizing effects of neck-in, gravity, and inertia in Newtonian film casting. *Physics of Fluids (1994-present)*, 28:024109, (2016).

Study of Alternative Fuel Extracted from Solid Waste

Susmita Das Puja^{1,*}, Md. Golam kader²

¹ Department of Mechanical Engineering, Khulna University of Engineering & Technology, Khulna-9203, BANGLADESH

² Professor, Department of Mechanical Engineering, Khulna University of Engineering & Technology, Khulna-9203, BANGLADESH

ABSTRACT

Pyrolysis is the process of heating of an organic material in the absence of oxygen. A mini pyrolytic plant was made by using a pressure cooker as reactor. A external heating source had been used for heating purpose. 1 kg of plastic bottle cap and a mixture of bottle cap and tire (750g bottle cap, 250 gram tire) were processed. Around 200g liquid fuel had been extracted for both sample. Physical property of that extracted oils were checked. Density of the oil from only bottle cap sample was found 731 kg/m³ and of mixed sample was 743 kg/ m³, where density of conventional fuel such as diesel is 820 - 850 kg/m³ and gasoline is 719-780 kg/m³. kinematic viscosity of pure bottle cap sample oil at 40°C was found 1.8 cSt and mixed sample was 2.2 cSt, where diesel has a value of 2-4.5 cSt and gasoline has 1.95-3.3 cSt. Gross calorific value of pure sample was found around 40.98 MJ/Kg and of mixed sample 39.5 MJ/Kg. Flash point of pure one was near around 63°C and of mixed one was 73°C. Diesel has a calorific value of 44-46 MJ/Kg and gasoline has a value of 43.2 MJ/Kg. The physical properties of pyrolytic oil is comparable with diesel and gasoline

Keywords: Pyrolysis, pyrolytic oil, kinematic viscosity.

1. Introduction

Bangladesh is a densely populated country in Asia. Crisis of power is one of the major problems in Bangladesh. Her per capita energy consumption is much below the world average. Energy consumption mix is estimated as: indigenous biomass 60%, natural gas 27.45%, oil 11.89%, coal 0.44% and hydro 0.23%. More than 77% of the country's population lives in rural areas and meeting most of their energy needs from traditional biomass fuels[1]. Pyrolysis is the process of heating of an organic material in the absence of oxygen. Biofuel can be extracted from solid wastes such as rubber, medical waste, rice husk and others which contain lignin. Researchers have been conducted for biodegradable and non-biodegradable waste materials. Rubber and plastics are non-biodegradable. About 20.50 million bicycle/rickshaw tires become scrap every year and wait for disposal which is about 37%(wt) of total tire waste production in Bangladesh. According to a estimation of every year, about 31,000 tons bicycle/rickshaw tires, 5160 tons motorcycle tires, and 28,900 tons bus/truck tires become scrap and are disposed and this amount is increasing [2]. Bangladesh generates about 3,36,000 tons of plastic wastes per year and around 17,000tons/year is going to the landfill . Among them, 30% (2,01,600 tons) is solid waste and rest 60% is liquid 69% of that total amount is recycled. Basic purpose of that experiment is to recycle solid waste by pyrolysis and extract fuel from it. 1 kg of plastic bottle cap and a mixture of bottle cap and tire (750g bottle cap, 250 gram tire) were processed. Gross calorific value of pure sample was found around 40.98 MJ/Kg and of mixed sample 39.5 MJ/Kg. Flash point of

pure one was near around 63°C and of mixed one was 73°C. Diesel has a calorific value of 44-46 MJ/Kg and gasoline has a value of 43.2 MJ/Kg. The physical properties of pyrolytic oil is comparable with diesel and gasoline.

2.Method:

Scrap tire and cap of plastic bottle was collected from local area of Khulna. Both waste materials was cut into pieces. Those materials were gently cleaned and dried carefully. Reactor is most important part of a pyrolysis plant. Here for this experiment a pressure cooker has been used to do the job of the reactor. A 3.5 Litre pressure cooker has been used. About more than 1 kg of bottle cap was able to feed at a time. As the pressure rises, the temperature of the material inside the sealed pot (the pressure cooker) also rises above the normal boiling point temperature. The outlet pipe is designed such that the vapor produced in the reactor can easily flow through them. The condenser pipe which is made of copper is of smaller diameter so that the vapor coming through the outlet pipes can easily condense as condenser is submerged in a biker filled with icy water. The collector pipe connected at the end of the condenser can collect the pyrolytic liquid fuel. A pressure cooker has been used as reactor so that advantages of both increased pressure and temperature can be used. It is effective as in a reactor with heater, there a film of melted material formed around heating surface, which might damage the heater and reduce efficiency. The reactor (pressure cooker) was externally heated by using a external heating source in one direction.

3. Construction Parameters:

To construct the pyrolysis plant following items is being used.

- Pressure cooker
- Outlet pipe
- Condenser
- Collector
- Thermocouple
- Heater
- Temperature recorder
- Insulating material
- Necessary equipments for proper connection.

3. Design Specification

- A pressure cooker of 3.5 litter volume.
- Length of outlet pipe : 483 mm
- Diameter of condenser pipe: 13mm
- Diameter of outlet pipe: 25mm

4. Experimental Setup:

Here for pyrolysis of bottle cap a pressure cooker has been used to do the job of the reactor. The pyrolysis reactor is fed with biomass from top part. Inside the reactor the biomass is heated and undergoes chemical and physical processes being transformed into biochar. The reactor was insulated by using rope and mud. Outlet pipe has a total length of 483 mm . Actually it is a summation of two individual pipe of length 254mm . and 228mm. connected by a elbow joint. It collect the vapor from the pressure vessel and send it to the condenser. The condenser was made by copper pipe of 13mm diameter . Heat for the experiment was supplied by an external source to be exact a electric heater. The following figure shows the experimental sep up.

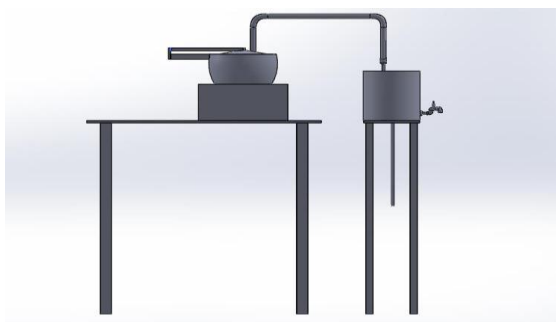


Fig 1: CAD model



Fig 2: Experimental setup.

5. Experiment Procedure:

In this experiment two different type material has been processed. One is waste bottle caps and other one is mixture of bottle caps and waste tires. The shredded waste was placed into the reactor. The total system was placed on a electric heater and heat was continuously supplied to the reactor. Around 1000g of waste was placed in the reactor. As heat is continuously supplied to the reactor the temperature inside the cylinder was increased gradually. A thermocouple is connected with the inner side of the reactor through which temperature reading was shown in the temperature recorder. The experiment was performed for different temperatures. For bottle cap, the experiment was done between the temperature range of 300°C to 350°C the flaring of white vapor began to come at 303°C through the condenser pipe. So, the volatile material began to form around this temperature. At a certain temperature the white vapor with high volatile material began to come out through the condenser. In the condenser the vapor is condensed and turned into liquid and this liquid is collected with the collector as the gravitational force works on it. There is a gateway for passing the uncondensed gas to atmosphere. It was noticed that as the temperature is increased, the time required to condense the vapor is decreased. The more increasing temperature increases more liquid oil from the material within a shorter time. In this way the heating process is carried out up to a certain time. At a point the white vapor stopped to flare. Then time is calculated through a stopwatch. The absence of white vapor indicates that pyrolysis process is completed and all the waste is converted into gas, liquid oil and char. The char was collected from the reactor and weighted. The amount of gas that passes to the environment is calculated by subtracting the weight of oil and char from the total weight of the bottle cap. Similar procedure was done for mixture of bottle cap and tires. For the mixed sample, 750g bottle cap waste and 250g tire waste were mixed together and given to the reactor. The experiment was done between the temperature range of 287°C to 327°C. white gasses started to come out at 290°C.

6. Result and Discussion:

Total two sample was tested. Each sample was tested for three times to reach on a reliable conclusion. During the extraction of fuel from waste material following data was taken. Two materials were tested at different days. The data collected during pyrolysis process is shown in the appendix and the result obtained from the data is shown in Table.

Table no:1: data table for bottle cap sample

No of Obs	Mass of feed (kg)	Room temperature	Condenser temperature initial	Condenser final temperature	Starting temperature of pyrolysis	Final temperature of pyrolysis	Time (min)
1	20	18	18	30	303	350	145
2	20	21	21	32	300	344	130
3	40	21	21	33	304	348	150

Table no.2: data of collected output from the experiment

No of observation	Mass of feed material (kg)	Uncondensed gas (gm)	Amount of ash (gm)	Mass of liquid (gm)
1	1	350	450	200
2	1	366	484	150
3	1	256	520	224

Table no.3: data table for mixture of bottle cap and tire sample:

No of Obs	Mass of feed (kg)	Room temperature	Condenser temperature initial	Condenser final temperature	Starting temperature of pyrolysis	Final temperature of pyrolysis	Time (min)
1	1	22	19	31	287	327	135
2	1	23	20	32	290	325	140
3	1	21	20	35	292	350	155

Table no.4: data of collected output from the experiment

No of observation	Mass of feed material (kg)	Uncondensed gas (gm)	Amount of ash (gm)	Mass of liquid (gm)
1	1	350	400	250
2	1	330	470	200
3	1	280	500	220

Various properties of obtained pyrolytic oils have been tested in the laboratory. The extracted oils was brown in color. Both the oils has an acidic smell. All the properties have been tested carefully. Flash point was determined by using flash point measuring instrument. Density was measured in laboratory by digital weight measuring machine and volumetric beaker. . viscosity

was measure at first by capillary tube method and then saybolt viscometer. Calorific value was measured by using oxygen bomb calorimeter . Comparison between conventional fuel and extracted fuel have been discussed below in table:

Table 6: physical properties analysis of obtained liquid product and commercial fuel:

Properties	Extracted Oil from bottle cap sample	Extracted Oil from mixed sample	Diesel	Gasoline
Density (ρ) (kg/m ³)	731.11	743.33	820 - 850	719-780
Kinematic Viscosity (cSt)	1.8	2.22	2-4.5	1.95-3.3
Gross Calorific Value (MJ/Kg)	40.983	39.511	44-46	43.2
Flash Point °C	63	73	53-80	N/A

REFERENCES

- [1] M. R. Islam, M.S.H.K. Tushar, H. Haniu, Production of Liquid Fuels and Chemicals from Pyrolysis of Bangladeshi Bicycle/rickshaw Tire Wastes, Science Direct Journal of Analytical and Applied Pyrolysis, Elsevier, 2008, Vol. 82, 96–109.
- [2] <https://en.wikipedia.org/wiki/Pyrolysis>
- [3] M. R. Islam, M. U. H. Joardder, S. M. Hasan, K. Takai, H. Haniu, Feasibility Study for Thermal Treatment of Solid Tire Wastes in Bangladesh by Using Pyrolysis Technology ,Science Direct Journal of Waste Management, Elsevier, 2011.

Integrated Approach of Ergonomics and MCDM into Truck Drivers' Seat Comfort: A Case Study in Bangladesh

Pobitra Halder^{1,2,*}, Chitrlekha Karmaker², Mustafizur Rahman²

¹Chemical and Environmental Engineering, School of Engineering, RMIT University, Melbourne, Victoria 3000, Australia

²Department of Industrial and Production Engineering, Jessore University of Science and Technology, Jessore-7408, Bangladesh

ABSTRACT

Seats are one of the most significant components for automotive vehicles. Prolonged driving a truck in Bangladesh is not so comfortable because no one design the seat properly considering anthropometric data. The improper seat design causes various health problems. Therefore, the improvement of seating posture is the urgency for reducing health issues. In this paper, a total of 120 Bangladeshi truck drivers were taken as sample for measuring anthropometric data. A comparison of health status between drivers and normal people showed that drivers suffer much than the control group. The relevant feedbacks required for the analysis were collected from the expert's opinion. The integrated approach (AHP-TOPSIS) found that among four health issues, back pain is more critical health issue associated with the existing seat dimension. Finally, the study suggested seat width as the most decisive design parameter on which designers should give much attention while designing truck drivers' seat.

Keywords: Anthropometry; Seat dimensions; Truck driver; AHP-TOPSIS; Bangladesh.

1. Introduction

Seating comfort is a very key factor for drivers and other members of the workplace who are exposed to spend most of their time sitting [1]. Comfort is such a factor that helps to improve productivity as well as the level of the user's satisfaction. In Bangladesh, the truck drivers are used to frequently work 50 or more hours a week. For driving safely and comfortably, seating comfort for drivers are essential and proper designed automotive seats can play a vital role in improving the comfort and work environment for the driver [2-4].

Ergonomics deals with the fitting of the task to the individual for their comfort, not the individual to the task. The concept of ergonomic design of equipment, furniture, vehicle etc. are now broadly used in the industrial, agricultural, and service sectors to improve working efficiency as well as safety issues [5-7]. There is a close relationship between the body dimensions of the users and seat dimensions of the vehicles. Therefore, properly designed vehicle's seats are necessary for sitting comfort which is made based on the body dimensions of the users.

A number of researchers and engineers have revealed that several factors, for instance, seat-interface pressure distribution, whole-body vibration, pressure change rate etc. affect theseating comfort of individuals [8-11]. Frechin et al. conducted a study on the effects of vibration and acceleration on an active seat [12]. The purpose of the study was to isolate the passengers and equipment in the vehicle from the negative impacts of vibration and acceleration and suggested the ways for compensating to ascertain extent. Similar research works were conducted for driving seating comfort by several researchers [13-15]. Mehta et al. reviewed the existing seat dimensions and anthropometric considerations of tractor seat design [16]. The authors recommended proper measurements for optimal seat design of the tractor

operator in India. Chimote and Gupta applied the integrated approach of ergonomics and fem into truck driver's seat comfort [17]. The objectives of the study were to conduct survey amongst the truck drivers, examine the travel time factor, and seat discomfort and recommend best alternatives of optimal drivers' seat with the aid of ergonomics and advanced design tools such as CAD and CAE. Ajayeoba and Adekoya conducted a study of measuring anthropometric data of 939 passengers (612 male and 327 female) in Nigeria for the investigation of the fitness of seats of 92 locally made commuter buses and suggested modified seat dimensions based on anthropometric data [18]. Lucas and Onawumi outlined some suggestions from the ergonomic point of view to recommend in-vehicle interface design of taxicabs in Nigeria [19]. Marquez and Garcia outlined suggestions 22 based on ergonomics to improve the design of a passenger vehicle in Venezuela [20].

From the literature, it is quite evident that the improvement of seating systems has become the subject of intense interest to many researchers for many years. There are many research opportunities for designing the truck driver's seat ergonomically in Bangladesh as the study related to truck driver's seat design is limited in the literature. Recently, our research group conducted two studies on designing truck driver's seat considering body dimensions [21,22]. In these studies, we measured the actual anthropometric measurements of the Bangladeshi truck drivers from Khulna zone and seat dimensions of three truck bands (TATA, ASHOK LEYLAND, and ISUZU) for exploring the existing mismatch and developed a model for predicting the seat dimension based on the drivers' anthropometry. Recently, the analytic hierarchy process (AHP) has been employed successfully in ergonomics in Bangladesh [23,24]. The aim of the current study is to study the existing seat

* Corresponding author. Tel.: +61469773675
E-mail addresses: pobitra.halder@gmail.com

dimensions and anthropometric measurements of the drivers for establishing a proper design guide using integrated AHP and technique for order preference by similarity to ideal solution (TOPSIS) approaches.

2. Research methodology

The study was conducted at the Central storage depot in Khalishpur, Khulna, Bangladesh. For this purpose, a set of structured written questionnaire form were circulated among the 120 truck drivers aged between 30 to 60 years and 10 doctors as the expert. The forms include details regarding their sitting posture, body part dimensions, and health-related problems due to prolonged driving. The sample size employed in this study was determined based on the Hicks recommendation considering 90% confidence level, $z = 1.64$ and 6% sampling error [25]. Four anthropometric measurements, for example, popliteal height (PH), hip breadth (HB), buttock popliteal length (BPL), and sitting shoulder height (SSH) were measured. The integrated AHP-TOPSIS techniques were implemented according to the previous study [26]. The AHP analysis was conducted to identify the most severe problem among four health issues. Finally, TOPSIS technique was applied to sort out seat dimensions on which designers should give much attention while designing truck drivers' seat. Following are the steps for this study.

Step 1: To analyze the truck seat design by TOPSIS a decision matrix having R criteria/attributes and C alternatives are needed. The decision matrix is represented as

$$DM = [X_{ij}]_{mn} \quad (1)$$

Where, X_{ij} is the performance of ith alternative with respect to jth attribute.

Step 2: The normalized decision matrix is calculated based on the average decision matrix by using equation (2).

$$ND_{ij} = \frac{x_{ij}}{\sqrt{\sum_i x_{ij}^2}}, j = 1, 2, 3 \dots n \quad (2)$$

Where, nr_{ij} are the elements of the normalized decision matrix of ith alternative with respect to jth attribute.

Step 3: To combine the TOPSIS and AHP process for evaluating the truck seat design it is necessary to determine the relative importance of different attributes with respect to the overall objective. AHP builds a hierarchy of decision items using comparisons between each pair of items expressed as a matrix and produce weighting scores which are combined with the analysis of TOPSIS.

Let, CM represents an $n \times n$ pair-wise comparison matrix

$$CM = \begin{bmatrix} 1 & K_{12} & \dots & K_{1n} \\ K_{21} & 1 & \dots & K_{2n} \\ \vdots & \vdots & \dots & \vdots \\ K_{n1} & K_{n2} & \dots & 1 \end{bmatrix} \quad (3)$$

Where, K_{ij} is the element of the pair-wise comparison matrix. The diagonal elements in the matrix CM are self-compared and those elements have equal importance, thus $K_{ij}=1$, where $i=j, i=1, 2, \dots, n$. The values on the left and right sides of the matrix diagonal represent the strength of the relative importance of the ith attribute compared with the jth attribute. Thus, $K_{ij} = 1/K_{ji}$, where $K_{ij} > 0, i \neq j$, as CM is a positive reciprocal square matrix.

Let, W_i denotes the importance degree for the ith attribute, then,

$$W_i = \frac{(\prod_{j=1}^n K_{ij})^{1/n}}{\sum_{i=1}^n (\prod_{j=1}^n K_{ij})^{1/n}}, i, j = 1, 2, 3 \dots n \quad (4)$$

Let, C denotes an n-dimensional column vector describing the sum of the weighted values for the importance degrees of the attributes, then

$$C = [C_i]_{n \times 1} = AV, i = 1, 2, 3 \dots n \quad (5)$$

Where,

$$AV^T = \begin{bmatrix} 1 & K_{12} & \dots & K_{1n} \\ K_{21} & 1 & \dots & K_{2n} \\ \vdots & \vdots & \dots & \vdots \\ K_{n1} & K_{n2} & \dots & 1 \end{bmatrix} [W_1, W_2 \dots W_n] = \begin{bmatrix} C_1 \\ C_2 \\ \vdots \\ C_n \end{bmatrix} \quad (6)$$

(6)

The consistency values for the attributes can be represented by the vector CV,

$$CV = [cv_i]_{1 \times n} \text{ Where, } cv_i = C_i/W_i, i = 1, 2, 3 \dots n \quad (7)$$

The maximum Eigen value λ_{max} can be determined as follows

$$\lambda_{max} = \frac{\sum_i cv_i}{n}, i = 1, 2, 3 \dots n \quad (8)$$

$$CI = \frac{\lambda_{max} - n}{n - 1} \quad (9)$$

If $CI = 0$, the evaluation for the pair-wise comparison matrix is implied to be perfectly consistent. Generally, a consistency ratio (CR) can be used as a guide to check the consistency by the ratio given by equation (10),

$$CR = \frac{CI}{RI} \quad (10)$$

The Saaty nine-point preference scale is adopted for constructing the pair-wise comparison matrix which deals with two distinct sets of numbers; i.e. one set {1, 3, 5, 7, 9} signifies the gradual priority in the importance of one criterion relative to the other as one moves from left to right of the set, whereas the other set {2, 4, 6, 8} contains the in-between preferences, which may or may not be used based on the preference scale. Therefore, the intermediate values are employed to interpolate the scale values if such preferences do exist.

Step 4: The weighted normalized fuzzy decision matrix was constructed by using weight of each problem and each design criteria that was obtained in AHP process following by equation (11).

$$WM = ND_{ij}W_j \quad (11)$$

Step 5: The best alternative has the shortest distance from the positive ideal solution and the farthest distance from the negative ideal solution. Here, the positive ideal solution and the negative ideal solution were found by equation (12) and (13).

$$WM^+ = \left\{ \left(\sum_i^{\max} WM_{ij} / j \in J \right), \left(\sum_i^{\min} WM_{ij} / j \in J' \right) \text{ for } i = 1, 2, \dots, m \right\} = WM_1^+, WM_2^+ \dots \dots WM_n^+ \quad (12)$$

$$WM^- = \left\{ \left(\sum_i^{\min} WM_{ij} / j \in J \right), \left(\sum_i^{\max} WM_{ij} / j \in J' \right) \text{ for } i = 1, 2, \dots, m \right\} = WM_1^-, WM_2^- \dots \dots WM_n^- \quad (13)$$

Where, $J = (j = 1, 2, \dots, n) / j$

Here, WM^+ and WM^- positive ideal solution (PIS) and negative ideal solution (NIS).

Step 6: The separation of each alternative from the ideal solution is given by

$$d^+ = \sqrt{\sum_j^n (WM_{ij} - WM_j^+)^2}, i=1, 2, 3, \dots, n \quad (14)$$

$$d^- = \sqrt{\sum_j^n (WM_{ij} - WM_j^-)^2}, i=1, 2, 3, \dots, n \quad (15)$$

Step 7: The relative closeness of a particular alternative to the ideal solution is calculated using equation (16).

$$CC_i = \frac{d_i^-}{(d_i^+ + d_i^-)}, i = 1, 2, 3, \dots, n \quad (16)$$

The higher value of closeness coefficient indicates that an alternative is closer to PIS and farther from NIS simultaneously. Here, d^+ and d^- means the summation of distance under positive ideal solutions and negative ideal solutions respectively.

3. Results and discussion

The health-related data of the truck drivers and normal people (control group) were collected from December, 2013 to November, 2014. The control group was the people selected in this study were not related to the driving. In our previous study we observed that the most frequent problems faced by drivers were back pain, foot cramp, neck pain, and muscle weakness[21]. A comparison chart between drivers and control group is developed which is portrayed in Fig. 1. More than 90% of drivers suffer from back pain and 83% suffer from foot cramps whereas the values of that for normal people are 40% and 34% respectively. Moreover, approximately 77% and 75% of the drivers suffer from neck pain and muscle weakness but the percentages for

normal people are relatively low. We hypothesized that these problems were because of the improper design of truck drivers' seat[21].

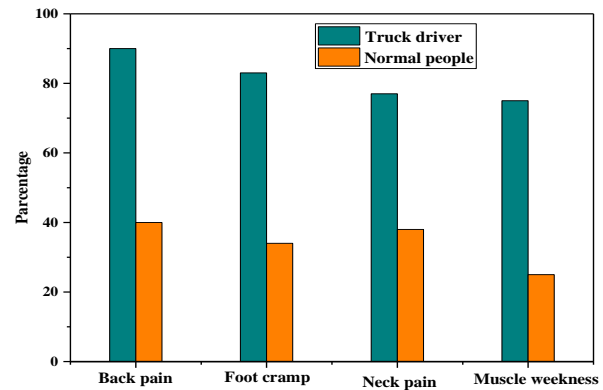


Fig.1 Comparison of health issues between truck drivers and normal people

The next step of this study is to identify the most crucial anthropometric measurement related seat dimension causing ergonomics problems. For this, firstly, the analytical hierarchy process (AHP) was applied to determine the weight of the four problems (attributes) faced by the drivers. A total of three groups consisting of 30 people were considered for making comparison matrix. They expressed their opinions using Saaty's 1-9 scale[27]. After that, an aggregated pair-wise comparison matrix was prepared using the opinion values. For all attributes, geometric means along with normalized weights were calculated with some developed formulas as described in the methodology section. With the aim of checking the validity of decision maker's judgments, a consistency ratio (CR) was calculated using random index data for respective number of attributes. The value of CR is approximately 8% which is less than Saaty's proposed CR value (0.1) indicating that the judgments specified by the decision makers are absolutely correct. The overall results for AHP analysis are presented in Table 1. Geometric mean value of different attributes varies from 3.37 to 0.30. The results revealed that among four health issues, back pain has the highest normalized weight with a value of 0.57. The second highest weight is muscle weakness with a normalized weighted value of 0.26 and neck pain has the lowest weight value of 0.05. In summary, the most severe problem among four issues suffered by the drivers is back pain.

At the final portion of the research work, TOPSIS approach was applied to sort the seat dimensions for designing truck drivers' seat. For each of the design criteria, the decision matrix was formed by taking the linguistic assessment of three decision makers. Then, linguistic variables were converted into numerical values. For example, the first decision maker expresses 'F' for showing the severity of seat height for causing back pain. Then, the linguistic variable 'F' was converted into numerical value 6. An aggregated

decision matrix was formed using average technique and weighted normalized matrixes were developed. Weighted normalized values were obtained by multiplying the weights of criteria (health issues) and corresponding normalized values of all alternatives (four concerned design parameters). Finally, positive and negative ideal solutions were calculated as presented in Table 2. The results revealed that the highest weighted normalized value (0.33) of back pain problem

is observed for backrest height whereas, in the case of muscle weakness, the highest weight is found for seat height. It can be seen from the Table 2, that the back pain has the highest PIS and NIS values followed by muscle weakness, foot cramp and then neck pain. The estimation of d^+ , d^- and closeness coefficient of four concerned design parameters using PIS and NIS values is illustrated in Table 3.

Table 1 Normalized weights of attributes for AHP analysis

Attributes	Back pain	Foot cramp	Neck pain	Muscle weakness	Geometric mean	Normalized weight
Back pain	1.00	5.00	7.00	3.67	3.37	0.57
Foot cramp	0.20	1.00	3.00	0.33	0.67	0.11
Neck pain	0.14	0.33	1.00	0.16	0.30	0.05
Muscle weakness	0.29	3.00	6.33	1.00	1.53	0.26

Consistency Ratio = 0.08 < 0.10

Table 2 Weighted normalized decision matrix, PIS and NIS for TOPSIS.

	Seat height	Seat width	Seat depth	Backrest height	PIS	NIS
Back pain	0.32	0.20	0.23	0.33	0.20	0.33
Foot cramp	0.07	0.06	0.03	0.07	0.03	0.07
Neck pain	0.03	0.02	0.02	0.03	0.02	0.03
Muscle weakness	0.17	0.11	0.11	0.16	0.11	0.17

Table 3 Computation of d^+ , d^- and closeness coefficient

	Seat height	Seat width	Seat depth	Backrest height
d^+	0.14	0.02	0.03	0.14
d^-	0.01	0.15	0.12	0.01
Closeness coefficients	0.81	0.10	0.06	0.87

It can be seen from the Table 3 that the backrest height has the highest closeness coefficient value of 0.87 and the second highest design factor is seat height having a value of 0.81. Seat depth has the lowest coefficient of value 0.06. Therefore, the most critical parameter is backrest height among the four concerned alternatives on which designers should give much attention to backrest height while designing truck drivers' seat.

4. Conclusion

Due to prolonged driving on the ergonomically unfit seat, truck drivers suffer various health-related problems. Therefore, vehicle's seats are required to be designed in such a way that the seats provide enough comfort and safety to drivers. Considering ergonomics or human factors for designing the seat or any furniture are very crucial. This research work identified the most common

physical problems of drivers' occurred due to improper seat design. The paper also found the most critical seat dimensions responsible for the physical problem. As the concept is relatively new and quite obvious so it will be a helpful guideline for Bangladeshi industrial engineers and manufacturers to design drivers' seat according to their anthropometric data.

REFERENCES

- [1] P.K. Halder, E. Sarker, Static Anthropometric Characteristics of Bangladeshi Vehicle Driver: A Case Study, *Scientifica*. 2016 (2016).
- [2] D.D.I. Daruis, B.M. Deros, M.J.M. Nor, Malaysian sitting anthropometry for seat fit parameters, *Human Factors and Ergonomics in Manufacturing & Service Industries*. 21 (2011) 443–455.
- [3] M. Kolich, Automobile seat comfort: occupant preferences vs. anthropometric accommodation, *Applied Ergonomics*. 34 (2003) 177–184.

- [4] S.J. Park, C.-B. Kim, C.J. Kim, J.W. Lee, Comfortable driving postures for Koreans, *International Journal of Industrial Ergonomics*. 26 (2000) 489–497.
- [5] R.T. Vyavahare, S.P. Kallurkar, Anthropometry of male agricultural workers of western India for the design of tools and equipments, *International Journal of Industrial Ergonomics*. 53 (2016) 80–85.
- [6] J.M. Mahoney, N.A. Kurczewski, E.W. Froede, Design method for multi-user workstations utilizing anthropometry and preference data, *Applied Ergonomics*. 46 (2015) 60–66.
- [7] G. Bolstad, B. Benum, A. Rokne, Anthropometry of Norwegian light industry and office workers, *Applied Ergonomics*. 32 (2001) 239–246.
- [8] E. Ghaderi, A. Maleki, I. Dianat, Design of combine harvester seat based on anthropometric data of Iranian operators, *International Journal of Industrial Ergonomics*. 44 (2014) 810–816.
- [9] S. Hiemstra-van Mastrigt, I. Kamp, S.A.T. van Veen, P. Vink, T. Bosch, The influence of active seating on car passengers' perceived comfort and activity levels, *Applied Ergonomics*. 47 (2015) 211–219.
- [10] B. Ozsoy, X. Ji, J. Yang, J. Gragg, B. Howard, Simulated effect of driver and vehicle interaction on vehicle interior layout, *International Journal of Industrial Ergonomics*. 49 (2015) 11–20.
- [11] H.-J. Wilke, P. Neef, B. Hinz, H. Seidel, L. Claes, Intradiscal pressure together with anthropometric data – a data set for the validation of models, *Clinical Biomechanics*. 16 (2001) S111–S126.
- [12] M.M. Frechin, S.B. Arin, ACTISEAT: active vehicle seat for acceleration compensation, in: *Proceedings of the Institution of Mechanical Engineers, Part D: Journal of Automobile Engineering*, 2004: pp. 925–933.
- [13] N. Nawayseh, M.J. Griffin, Effect of seat surface angle on forces at the seat surface during whole-body vertical vibration, *Journal of Sound and Vibration*. 284 (2005) 613–634.
- [14] J.-D. Wu, R.-J. Chen, Application of an active controller for reducing small-amplitude vertical vibration in a vehicle seat, *Journal of Sound and Vibration*. 274 (2004) 939–951.
- [15] M. Kolich, D. Wan, W.J. Pielemeier, R.C. Meier, M.L. Szott, A comparison of occupied seat vibration transmissibility from two independent facilities, *Journal of Vibration and Control*. 12 (2006) 189–196.
- [16] C.R. Mehta, L.P. Gite, S.C. Pharade, J. Majumder, M.M. Pandey, Review of anthropometric considerations for tractor seat design, *International Journal of Industrial Ergonomics*. 38 (2008) 546–554.
- [17] K. Chimote, M. Gupta, Integrated approach of ergonomics and fem into truck drivers seat comfort, in: *1st International and 16th National Conference on Machines and Mechanisms*, IIT Roorkee, India, 2013: pp. 183–188.
- [18] A.O. Ajayeoba, L.O. Adekoya, Evaluation of the ergonomic suitability of passenger seats in molue buses in Nigeria, *Journal of Mechanical Engineering*. 1 (2012) 4–11.
- [19] E.B. Lucas, Ergonomic Evaluation of In-Vehicle Interface Design of Taxicabs in Nigeria, *International Journal of Engineering Research and Applications*. 3 (2013) 566–572.
- [20] M.A. Márquez, J.M. Garcia, Ergonomics of urban public passengers transportation, in: *9th Annual Applied Ergonomics Conference*, 2006.
- [21] P. Halder, T. Mahmud, E. Sarker, C. Karmaker, S. Kundu, S. Patel, A. Setiawan, K. Shah, Ergonomic considerations for designing truck drivers' seats: The case of Bangladesh, *J Occup Health*. 60 (2018) 64–73.
- [22] T. Mahamud, S.A. Noor, P.K. Halder, S.K. Biswas, A mismatch between seat measurements and body dimensions of truck drivers in Bangladesh, in: *International Conference on Mechanical, Industrial and Energy Engineering*, KUET, Khulna, Bangladesh, 2014: pp. 1–4.
- [23] P. Halder, E. Sarker, C. Karmaker, AHP based Anthropometric Analysis of University Hall Bed Design in Bangladesh, *Journal of The Institution of Engineers (India): Series C*. (2018) 1–9.
- [24] R.K. Chakraborty, M. Asadujjaman, M. Nuruzzaman, Fuzzy and AHP approaches for designing a hospital bed: a case study in Bangladesh, *International Journal of Industrial and Systems Engineering*. 17 (2014) 315.
- [25] C. Hicks, Research methods for clinical therapists : applied project design and analysis, Churchill Livingstone/Elsevier, 2009.
- [26] N.D. Chakladar, S. Chakraborty, A combined TOPSIS-AHP-method-based approach for non-traditional machining processes selection, *Proceedings of the Institution of Mechanical Engineers, Part B: Journal of Engineering Manufacture*. 222 (2008) 1613–1623.
- [27] T.L. Saaty, The analytic hierarchy process : planning, priority setting, resource allocation, McGraw-Hill International Book Co, 1980.

Investigation of the Effect of Sample Geometry on Drying Energy Requirement of Plant-Based Food Materials

Md. Washim Akram^{1,*}, Mohammad U. H. Joardder²

¹ Department of Mechanical Engineering, Bangladesh Army University of Science & Technology, Saidpur-5310, BANGLADESH

² Department of Mechanical Engineering, Rajshahi University of Engineering & Technology, Rajshahi-6204, BANGLADESH

ABSTRACT

Drying is a simultaneous heat and mass transfer phenomena; primarily remove water to extend the shelf life of food materials. Over the course of drying, food quality deteriorates significantly along with taking huge energy. From the literature, it is found that both food properties and drying conditions affect the energy consumption criteria. However, there is a very limited number of research found that conducted investigation on the effect of sample geometry on energy requirement to dry. In this study, three typical shapes with a constant volume of selected food materials have been investigated to attain a correlation between sample geometry and energy requirements. The amount of energy requirement during drying of Brinjal, Carrot, and Radish varies significantly with the variation of sample geometry. The minimum energy was required for sliced samples of selected food materials; whereas, cylindrical shaped samples took higher energy. The minimizing amount of energy also reduces the environmental pollution and GHG (Green House Gas). It can be concluded that sample compactness remarkably affects the energy requirement.

Keywords: Plant-based food material, food drying, energy requirement, sample geometry, environment pollution

1. Introduction

Generally, the different plant-based food materials contain about 80-90% moisture. The micro-organism growth is higher due to this higher amount of moisture content. Every year 1.3 billion tonnes of fruits and vegetables are wasted due to the lack of maintaining appropriate preserving techniques [1, 2]. There are lots of food preserving techniques within which drying technique is crucial because, it prevents the growth of yeasts, mold, and bacteria [3]. But drying technology is energy intensive. Approximately 15% of industrial energy is consumed by the drying process. On the other hand, the food quality also depends on the simultaneous heat and mass transfer during drying [4, 5]. In addition to sample properties and drying conditions, sample size and shape influence quality and energy requirement. However, there is an insignificant amount of research are reported in connection with the effect of sample shape and size on the quality and energy requirement during drying.

Energy requirement during drying of the sliced agricultural product was reviewed in which it was found that the minimum amount of energy requirement during drying of sliced shaped plant-based food materials are between 4.22 and 24.99 MJ/kg water removed [6]. The effect of aspect ratio and shape on effective moisture diffusivity and drying kinetics of potatoes, green beans and peas were analyzed where the diffusion coefficient and drying constant for potatoes, beans and peas were found in descending order [7]. The quality of dried

foods and the amount of energy requirement during drying was studied where it was found that the energy consumption of the Infrared-Hot Air settings was lower that's why the thermal efficiency was higher compared to the Hot Air or Infrared-Cold Air settings [8]. Drying characteristics, energy requirement and drying efficiency during drying of potato slices was studied in which it was found that the maximum and minimum specific energy requirement for potato drying were 5.882 (MJ/kg water) and 4.645 (MJ/kg water) [9]. The energy consumption of main types of food drying like infrared drying, microwave drying, hot air convective drying, vacuum drying and convective dryer with microwave pretreatment were investigated where it was found that during pomegranate drying the maximum and minimum amount of energy was required for vacuum and microwave dryer. On the other hand, for infrared drying, the drying time increased with air velocity which results in the larger amount of energy consumption [10]. It is crucial to dry foods with low cost, minimum energy and less time [11, 12].

However, there is no comprehensive study that investigated the effect of the shape of the sample associated with the energy consumption of the plant-based food materials during drying. In this study, authors thoroughly investigated the effect of different shape on the drying energy requirements and correlate with environmental pollution.

* Corresponding author. Tel.: +88-01778384882
E-mail addresses: washimme11ruet@gmail.com

2. Materials and methods

2.1 Materials

Different types of plant-based food materials like Brinjal, Carrot, and Radish were collected from the local market in Rajshahi, Bangladesh. The initial moisture content of the fresh food materials was measured by oven drying method [13]. The initial mass of the Brinjal, Carrot and Radish samples were about 4.5 gm, 9 gm, and 8.5 gm respectively. The samples were dried in a convective dryer at $60 \pm 2^{\circ}\text{C}$ until the weight did not change between two weight intervals. Physical properties of the food material samples such as average diameter, thickness, and mass were slightly different for slice, rectangular and cylindrical shape respectively.

2.2 Sample Preparation and Drying Method

The samples were stored in a refrigerator at 4°C before using for the drying experiment. The convective dryer in which the experiment was performed was started about 30 min before drying experiments to achieve steady-state conditions before each drying run. At the start of each experiment, the materials were washed and cut into slices with 7.97 mm thick and 36.13 mm in diameter, rectangular shapes with 10 mm thick and 28.6 mm length, and cylindrical shapes with 19.18 mm height and 23.3 mm in diameter that are placed each sample on each separate tray. The slice, rectangular and cylindrical shape sample with their dimensions are shown in Fig.1. The experiment was performed at the temperature around 60°C and a constant air velocity of 0.7 m/s. During the experiment, the relative humidity of the inlet air was around 57%. Air flowed perpendicularly to drying surfaces of the samples. During the drying process, the tray was taken out at 30-min interval and weighed using a digital electronic balance. The measurement range of the balance was 0–100 gm with an accuracy of 0.01 gm. All the dimensions of the samples were measured 30-minute time interval by digital slide calipers. All weighing and measuring processes were completed within 30 seconds during the drying process. The experiments were replicated thrice, and the average of the moisture content at each value was used for constructing the drying curves.

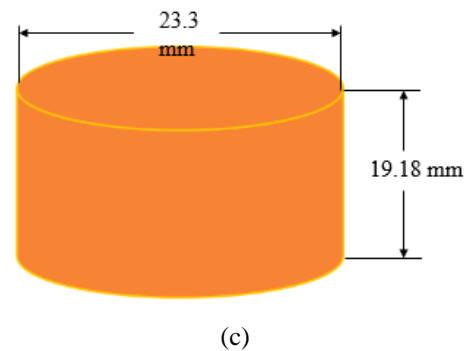
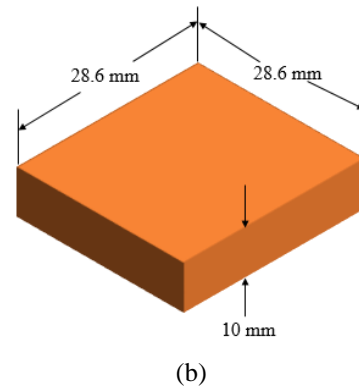
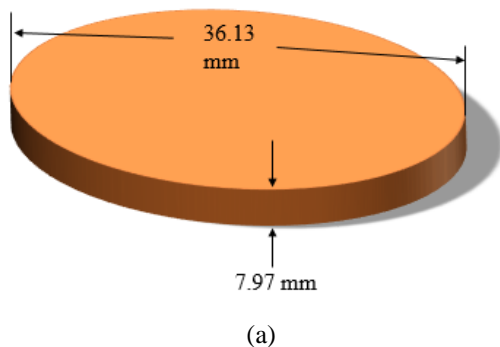


Fig.1 Types of samples used in this experiment are (a) slice; (b) rectangle; (c) cylinder

In this experiment, a simple convective dryer was used shown in Fig.2. A hygrometer was used to measure the humidity inside the drying chamber. The dryer was run by electric energy. It consists a heater and a fan. The heater converts the electric energy into heat energy and the fan transfer the atmospheric air into the drying chamber at a certain speed.

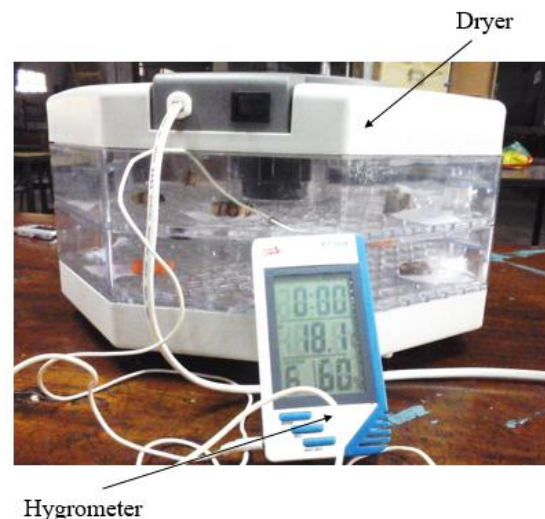


Fig.2 Convective dryer used in this experiment

2.3 Energy Calculation of Convective Drying

In convective drying, total energy consumption is the summation of energy required for drying samples and

blowing air, which is described by the equation (1) [14]:

$$E_t = \rho_a A v c_a \Delta T * D_t \quad (1)$$

Where, ρ_a is air density (kg/m³), E_t is total energy consumption (kWh), v is air velocity (m/sec), A is cross-sectional area of container in which sample is placed (m²), ΔT is a temperature difference between inlet and outlet air (°C), c_a is specific heat (kJ/kg °C), D_t is the total drying time of each sample (h) [15].

In this experiment, the air density, cross-sectional area of the dryer, air velocity, specific heat capacity, and the temperature difference between input and output remains the same. In convective drying, the condition $\rho_a A v c_a \Delta T$ can be represented by the energy consumption of the dryer E_c . So, the equation (1) can be written as

$$E_t = E_c * D_t \text{ kWh}$$

$$E_t = 3.6 E_c * D_t \text{ MJ}$$

Energy requirement for 1 kg sample

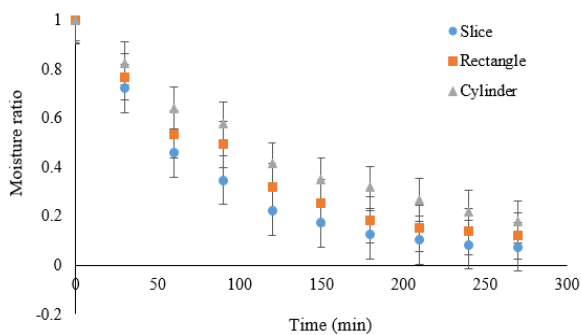
$$e_t = \frac{3.6(E_c * D_t)}{C} \text{ MJ/kg} \quad (2)$$

Where, C is the capacity of the dryer (1 kg)

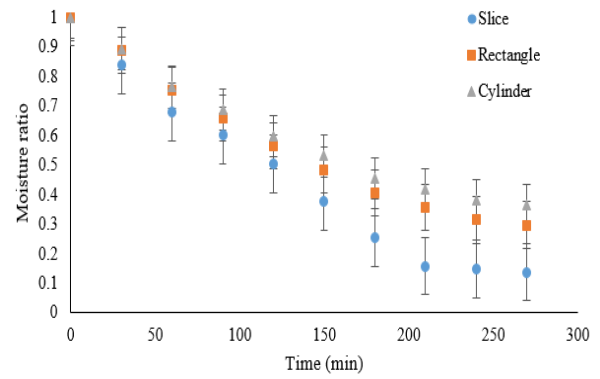
3. Results and discussion

3.1 Drying Kinetics

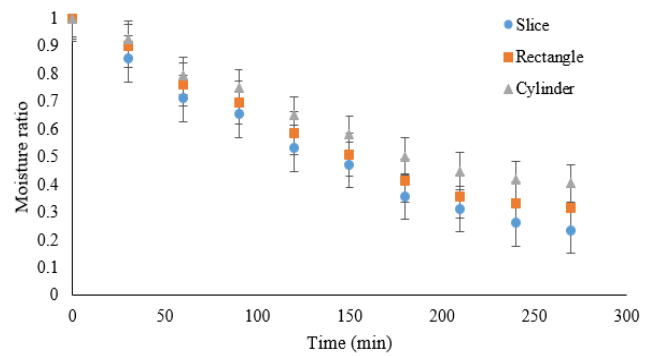
Moisture ratio variation with drying time for different plant-based food materials like Brinjal, Carrot, and Radish are shown in Fig.3. These figures also hold the pattern of minimizing moisture ratio with drying time for slice, rectangular and cylindrical shape food sample. The rate of moisture transfer is faster for slice sample instead of the rectangular and cylindrical sample because of having more surface area of the sliced sample. That's why the time required for drying is also minimized and a large amount of energy can be saved by using slice sample during drying of plant-based food material.



(a)



(b)



(c)

Fig.3 Variation of moisture ratio with drying time for (a) Brinjal; (b) Carrot; and (c) Radish

3.2 Energy Consumption

The amount of energy savings can be represented by Table 1. Energy consumed by the dryer for slice sample is 14.4 ± 0.72 , 16.2 ± 0.81 and 16.63 ± 0.83 MJ/kg of water for Brinjal, Carrot, and Radish respectively. The amount of energy required for the rectangular and cylindrical sample are also shown in the table. Table 1 clearly shows that energy requirement for slice sample is lower than the rectangular and cylindrical sample for obtaining the same amount of moisture content. For microwave and convective hybrid solar dryers, the minimum energy requirement for drying sliced crops range from 4.22 – 24.99 and 5.21 – 90.4 MJ/kg of water removed respectively [16].

According to the common heat transfer sense, with the increased surface area, the rate of heat transfer is increased. Using slice sample instead of the rectangular or cylindrical sample gives more surface area to transfer heat. It also gives the better appearance and color. The percentage of energy savings for slice sample compared to the rectangular and cylindrical sample are 35.75%, 32.67%, 33.12% and 63%, 57.11%, 57.36% for Brinjal, Carrot, and Radish respectively. Only the change of shape without changing the other drying perimeter like temperature, humidity, moisture content etc. gives the

remarkable amount of energy saving which is the key focus of this paper.

Surface area to volume ratio of the samples is another important criteria for measuring drying kinetics and amount of energy savings. The higher surface area to volume ratio (mm^{-1}) implies larger heat and mass transfer rate because of getting a larger surface area for the same volume. The surface area to volume ratio for slice sample is 0.361 mm^{-1} . On the other hand, the values are 0.339 mm^{-1} and 0.275 mm^{-1} for the rectangular and cylindrical sample. As a result, the amount of energy required for slice sample during drying is lower than rectangular and cylindrical sample because of the above-mentioned reason.

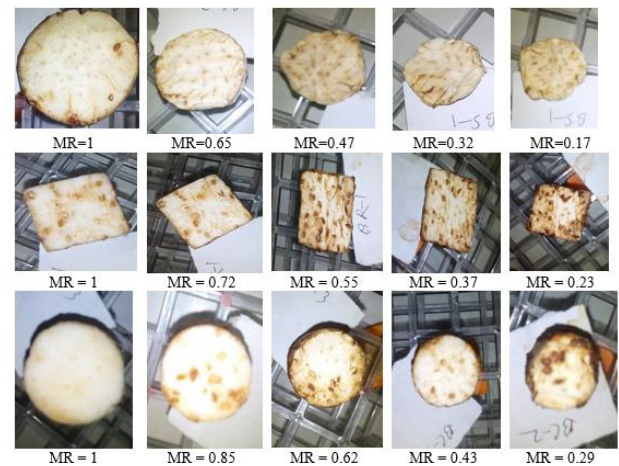
Table 1 Energy requirement during drying for different sample of porous plant-based food materials

Food materials	Energy requirement (MJ/kg of water)		
	Slice	Rectangle	Cylinder
Brinjal	14.4 ± 0.72	19.55 ± 0.98	23.47 ± 1.17
Carrot	16.2 ± 0.81	21.49 ± 1.07	25.45 ± 1.27
Radish	16.63 ± 0.83	22.14 ± 1.10	26.17 ± 1.31

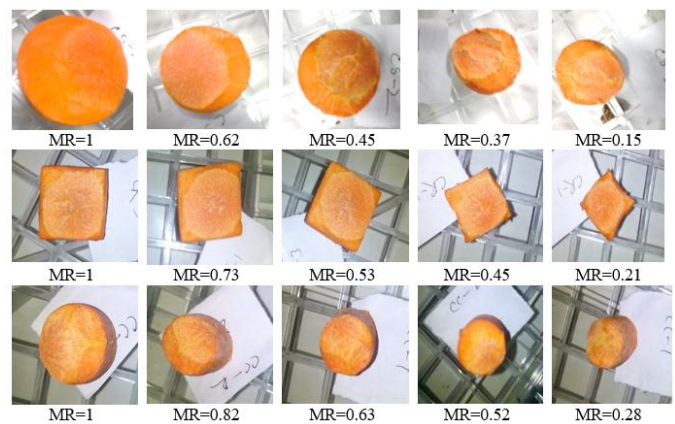
3.3 Deformation

The deformation of the Brinjal is shown in Fig.4(a). For maintaining time of drying (4 hours for each sample) and the softness of Brinjal, the deformation of the Brinjal appeared clearly compared to the Carrot and Radish. If the drying time of Carrot and Radish sample is more, than the deformation of the samples would appear clearly. The deformation of the Carrot and Radish are shown in Fig.4(b) and Fig.4(c). The appearance of the samples are given according to their moisture content and drying time. All the readings are shown here maintained one hour time interval. The deformation kinetics depends on size and shape of the sample during drying. For slice sample throughout moisture transfer the change of shape, strain, roughness is smaller than the rectangular and cylindrical sample that's why the shrinkage produced for the slice sample is comparatively lower than the other two samples used in this study.

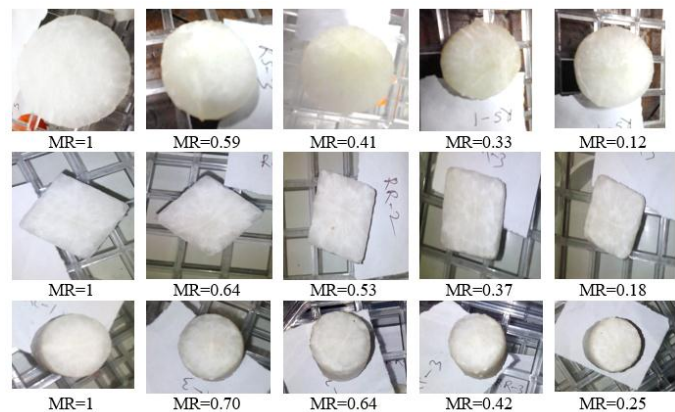
Due to higher deformation and roughness of the rectangular and cylindrical sample than the slice sample, the appearance of the rectangular and cylindrical sample are not so good. The appearance of the dried food is a crucial factor. If the dried sample appear very ugly, it is not so attractive to eat which is another phenomenon established here. For slice sample, the appearance of the plant-based food material during drying is brighter than the rectangular and cylindrical sample.



(a)



(b)



(c)

Fig.4 View at different stages of the slice, rectangular and cylindrical samples during drying of (a) Brinjal; (b) Carrot; and (c) Radish

4. Conclusion

The drying characteristics like energy consumption and drying kinetics of different plant-based food materials are studied in this experiment. Three different sample shapes are analyzed here. There are many factors on which the drying parameters depends on like temperature, humidity, drying time, sample shapes and size etc. In this study, the sample shapes are represented

more significantly with practical implementation. Only by changing the shape of the sample instead of changing another parameter can be saved a large amount of energy during drying of plant-based food material. Consequently, the amount of GHG production as like as environmental pollution during food drying is also reduced.

5. Acknowledgment

The authors are grateful to the Department of Mechanical Engineering, Bangladesh Army University of Science and Technology, Saidpur and Rajshahi University of Engineering and Technology, Rajshahi for supporting the project successfully.

REFERENCES

- [1] J. Gustafsson, C. Cederberg, U. Sonesson, and A. Emanuelsson, *The methodology of the FAO study: Global Food Losses and Food Waste-extent, causes and prevention*-FAO, 2011. SIK Institutet för livsmedel och bioteknik, 2013.
- [2] J. Gustavsson, C. Cederberg, U. Sonesson, R. Van Otterdijk, and A. Meybeck, *Global food losses and food waste*. FAO Rome, 2011.
- [3] M. A. Karim and M. N. A. Hawlader, "Mathematical modelling and experimental investigation of tropical fruits drying," *Int. J. Heat Mass Transf.*, vol. 48, no. 23–24, pp. 4914–4925, 2005.
- [4] K. J. Chua, A. S. Mujumdar, M. N. A. Hawlader, S. K. Chou, and J. C. Ho, "Convective drying of agricultural products. Effect of continuous and stepwise change in drying air temperature," *Dry. Technol.*, vol. 19, no. 8, pp. 1949–1960, 2001.
- [5] R. Jumah and A. S. Mujumdar, "Modeling intermittent drying using an adaptive neuro-fuzzy inference system," *Dry. Technol.*, vol. 23, no. 5, pp. 1075–1092, 2005.
- [6] N. R. Nwakuba, S. N. Asoegwu, and K. N. Nwaigwe, "Energy requirements for drying of sliced agricultural products: a review," *Agric. Eng. Int. CIGR J.*, vol. 18, no. 2, pp. 144–155, 2016.
- [7] W. Senadeera, B. R. Bhandari, G. Young, and B. Wijesinghe, "Influence of shapes of selected vegetable materials on drying kinetics during fluidized bed drying," *J. Food Eng.*, vol. 58, no. 3, pp. 277–283, 2003.
- [8] H. S. El-Mesery and G. Mwithiga, "Performance of a convective, infrared and combined infrared-convective heated conveyor-belt dryer," *J. Food Sci. Technol.*, vol. 52, no. 5, pp. 2721–2730, 2015.
- [9] H. Darvishi, A. R. Asl, A. Asghari, and G. Gazori, "Mathematical modeling, moisture diffusion, energy consumption and efficiency of thin layer drying of potato slices," *J. Food Process. Technol.*, vol. 4, no. 3, 2013.
- [10] A. Motevali, S. Minaei, and M. H. Khoshtagaza, "Evaluation of energy consumption in different drying methods," *Energy Convers. Manag.*, vol. 52, no. 2, pp. 1192–1199, 2011.
- [11] H. Darvishi, M. Azadbakht, A. Rezaeiasl, and A. Farhang, "Drying characteristics of sardine fish dried with microwave heating," *J. Saudi Soc. Agric. Sci.*, vol. 12, no. 2, pp. 121–127, 2013.
- [12] S. Jan Kowalski, "Mathematical modelling of shrinkage during drying," *Dry. Technol.*, vol. 14, no. 2, pp. 307–331, 1996.
- [13] N. P. Zogzas, Z. B. Maroulis, and D. Marinou-Kouris, "Densities, shrinkage and porosity of some vegetables during air drying," *Dry. Technol.*, vol. 12, no. 7, pp. 1653–1666, 1994.
- [14] M. Aghbashlo and H. Samimi-Akhijahani, "Influence of drying conditions on the effective moisture diffusivity, energy of activation and energy consumption during the thin-layer drying of berberis fruit (Berberidaceae)," *Energy Convers. Manag.*, vol. 49, no. 10, pp. 2865–2871, 2008.
- [15] O. İsmail, "Effect of drying methods on drying characteristic , energy consumption and color of nectarine," vol. 2, no. 2, pp. 801–806, 2016.
- [16] K. N. Nwaigwe, N. R. Nwakuba, S. N. Asoegwu, and K. N. Nwaigwe, "Energy requirements for drying of sliced agricultural products: A review Energy requirements for drying of sliced agricultural products: A review," no. June, 2016.

Numerical Study of Pumping Power and Volumetric Flow Rate Advantage of SiC-Water Nanofluid through a Channel

Md. Insiat Islam Rabby*, Farzad Hossain, Md. Ehsanul Hasan, Md. Abdullah Al-Amin, A.K.M Sadrul Islam
Department of Mechanical Engineering, Military Institute of Science & Technology, Dhaka, BANGLADESH

ABSTRACT

The numerical analysis of laminar heat convective heat transfer of Silicon Carbide (SiC) - water Nanofluid for the developed region through two parallel plates is presented in this present work. The second order single phase energy equation, mass and momentum equation are solved by using finite volume method with the ANSYS FLUENT 16 software. The distances between two parallel plates are 4mm and length 600mm respectively. Silicon Carbide (SiC) is used as nanoparticle and water is used as the base/working fluid for the investigation. At the time of simulation 1% to 5% volume concentration of the SiC nanoparticles are used for mixing with water to produce Nanofluid. A wide range of interval of Reynolds number from 500 to 1100 at constant heat flux 500 W/m^2 at the channel wall has been also introduced. The result reveals that for increasing the Reynolds number the Nusselt number and heat transfer coefficient are increased linearly in the developed region for both water and SiC-H₂O nanofluid. At constant Reynolds number by increasing the volume fraction of SiC-H₂O nanofluid from 1% to 5% the value of Nusselt number and heat transfer coefficient has been increased compared to pure water. And at constant heat transfer coefficient SiC-water nanofluid required 10% to 80% less pumping power and 4% to 25% less volumetric flow rate compared to pure water.

Keywords: Volume concentration, constant heat flux, pumping power, volumetric flow rate.

1. Introduction

From the last few decades the importance and research on nanotechnology is the most fundamental and effective topics of thermal engineering. At present to improve heat transfer efficiency and heat transfer rate nanoparticles are used with base fluids. Beside this the utilization of pumping power to get this enhancement is also less and this is the most advantage thing to using nanoparticles in working fluids. Basically by adding small amount of solid particles with the base or working fluid, the thermal conductivity of the fluid can be increased noticeably. And by using these concept researchers has been made nanofluid which is the combination of base fluid (water, engine oil or ethylene glycol) and very small amount of solid particles at Nano scale size (1nm to 100nm). Al₂O₃, CuO, TiO₂, SiC, SiO₂, Fe₂O₃, MgO etc. particles are used as nanoparticles to mix with base fluids. Different researchers carried out their investigation on nanofluids. In 1995-1996 Choi and Eastman [1] reinvestigated with their Nano scale metallic particle and carbon nanotube suspensions in Argonne National Laboratory. Choi and Eastman have tried to suspend various metal and metal oxides nanoparticles in several different fluids (Choi (1998) [2]; Choi et al. (2001) [3]; Choi et al. (2005); Choi et al. (2006)[4]; Eastman et al. (2001); Eastman et al. (1999); Eastman et al. (2004)) and their result are promising. From their investigation they also observed that many things remain vacuous about these suspensions of Nano-structured materials, Choi and Eastman have been termed these as "Nano fluid" Xuan and Li, 2003[5] examined the convective heat exchange and the stream highlights of Cu- water Nano fluids in a 10-mm inward distance across tube. The trial comes about because of their investigation, in the turbulent area

showed that the friction factors of the Nano fluids, between 1 and 2 vol. % fractions are generally the same as those of water flow. Williams et al., 2008 [6] experimentally explored the turbulent stream of alumina-water and zirconium-water Nano fluids in tubes. They found that current connections for single-stage stream can enough anticipate Nano fluid stream convective heat exchange and weight drop. Rea et al., 2009[7] led an investigation on the laminar convective warmth exchange and weight drop of alumina-water and zirconium-water Nano fluids in a tube with 4.5-mm inward width. Their discoveries demonstrated that, with appropriately measured Nano fluid properties, there is no deviation in convective heat exchange and weight drop of Nano fluid spill out of customary single-stage stream hypothesis. Heris et al., 2013 [8] played out an exploratory investigation to decide the pressure drop and heat exchange qualities of Al₂O₃/water and CuO/water nanofluids in a triangular conduit under consistent heat flux where the flow was laminar. Their outcomes demonstrated that, at similar estimations of nanoparticle volume division and Reynolds number, utilizing Al₂O₃ nanoparticles is more beneficial than CuO nanoparticles. Wen and Ding, 2004[9] also investigated with laminar convective heat transfer using Al₂O₃ nanofluid. Hwang and Choi, 2009[10] also worked on it and showed that 3% volume concentration of Al₂O₃ nanofluid gives 8% enhancement of heat transfer coefficient. M. Monjur and A.K.M [11] investigated on energy savings of heat exchanger and they showed that for constant heat transfer coefficient Al₂O₃-water, CuO-water and TiO₂-water required less pumping power and volumetric flow rate compare to pure water. P.A. Ingole, S.M. Shinde and P.A. Patil [12] investigated on pumping power of car radiator

* Corresponding author. Tel.: +88-01635881451
E-mail addresses: insiatislam8@gmail.com

by using Al₂O₃ -water nanofluid and they find that 2% volume concentration Al₂O₃-water need 23.81% less pumping power compared to pure water.

From the above literature review it is clear that almost all the researches are on heat transfer enhancement argumentation of nanofluid but the justification of implementing nanofluid in terms of increased pumping power due to the improvement of thermo-physical properties has not been studied elaborately. And so the present work focus on how SiC-water nanofluid influences the pumping power and volumetric flow rate of 2 dimensional single phase laminar convective channel flow.

2. Physical Model and Boundary Conditions:

A 2D Parallel plate with a steady heat flux connected on its surface can be considered as the least difficult case to investigate heat transfer rate and corresponding pumping power requirement. In order to investigate the performance of Nanofluid in a channel, a numerical study has been carried out by employing commercial computational fluid dynamics software ANSYS Fluent. Laminar flows through a channel the distance between two horizontal plates are 4mm and 600 mm length is presented. A constant uniform heat flux of 500 W/m² is applied at the wall boundary of the parallel plates and fluid is permitted to stream with a fitting speed and uniform temperature of 303 K at the inlet of the parallel plates with a presumption of no slip condition on the parallel plate's wall. All the fluid dynamic and heat exchange parameters are extricated after the hydrodynamic and thermal improvement of the fluid stream and in this case the entrance length is x/D=60 beyond which all the measurements are taken. For calculating the heat transfer enhancement and friction factor the temperatures are taken at line which is drawn 590mm distance from inlet and pressures are taken at 565mm and 555mm from the inlet.

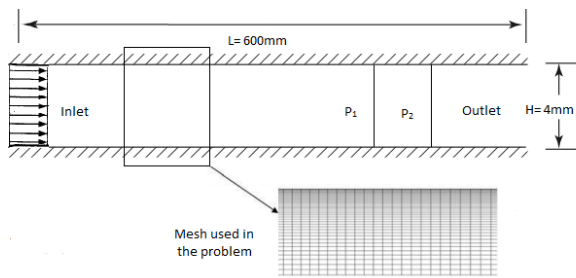


Fig.1 Physical model of the numerical problem and the corresponding mesh of the domain.

3. Numerical Method and Methodology:

A commercial computational fluid dynamics software ANSYS (Fluent) for this numerical analysis has been used. All the governing equations for mass, momentum, energy, and laminar quantities are solved using a control volume technique. At inlet laminar inlet velocity and at the outlet boundary pressure outlet is considered. Under relaxation factors 0.4 for pressure, 0.76 for momentum equation, 1 for energy equation, and 0.9 for density

equation are considered for parallel plate. SiC-water nanofluids with different particle volume fractions (1, 2, 3, 4, and 5%) are tested with a wide range of Reynolds number (400-1100 for parallel plate) and then results are compared with base fluid water.

3.1 Governing Equation:

The governing equation for continuity, momentum and energy for forced convection under laminar flow and steady-state conditions are expressed as follows. Beside this equation for Reynolds number, Nusselt number, heat transfer rate, average heat transfer coefficient, friction factor, pressure difference, pumping power and thermophysical properties equation (density, specific heat, viscosity, thermal conductivity etc) of nanofluids also expressed here.

Continuity Equation:

In steady flow, the amount of mass within the control volume under remains constant, and thus the conversation of mass can be expressed as

$$\frac{\partial u}{\partial x} + \frac{\partial v}{\partial y} = 0 \quad (1)$$

Momentum Equation:

For laminar flow, the momentum equation can be expressed as:

$$\rho \left(u \frac{\partial u}{\partial x} + v \frac{\partial u}{\partial y} \right) = \mu \frac{\partial^2 u}{\partial y^2} \quad (2)$$

Energy Equation:

Energy can be transferred by heat, work, and mass only, the energy balance for a steady-flow control volume can be write explicitly as

$$\begin{aligned} (E_{in} - E_{out}) &= -\rho c_p \left(u \frac{\partial T}{\partial x} + T \frac{\partial u}{\partial x} \right) dx \cdot dy - \rho c_p \left(v \frac{\partial T}{\partial y} + T \frac{\partial v}{\partial y} \right) dx \cdot dy \\ &= -\rho c_p \left(u \frac{\partial T}{\partial x} + T \frac{\partial T}{\partial y} \right) dx \cdot dy \end{aligned} \quad (3)$$

The Reynolds number for the flow of Nanofluid is

$$\text{expressed as: } Re = \frac{\rho_{nf} U_{av} D_h}{\mu_{nf}} \quad (4)$$

The rate of heat transfer Q_{nf} to the tube wall is assumed to be totally dissipated to Nanofluid flowing through a channel, raising its temperature from inlet fluid bulk temperature T_{bi} to exit fluid bulk temperature T_{bo} . Thus,

$$Q_{nf} = m_{nf} C_{p_{nf}} (T_{bo} - T_{bi}) \quad (5)$$

Where m_{nf} the mass flow rate of nanofluid is, $C_{p_{nf}}$ is the specific heat of Nano fluid at constant pressure.

The average heat transfer coefficient h_c is given by:

$$h_c = \frac{Q_{nf}}{A_w (\Delta T)} \quad (6)$$

Where A_w is the surface area of circular tube and the temperature difference between the wall and calculated as:

$$T = \frac{(T_w - T_o) - (T_w - T_i)}{\ln\left(\frac{T_w - T_o}{T_w - T_i}\right)} \quad (7)$$

So the expression of average Nusselt number is defined as follows:

$$Nu = \frac{h_c D_h}{K_{nf}} \quad (8)$$

$$\text{Pressure difference: } \Delta P = \frac{f L \rho U^2}{2 D_h} \quad (9)$$

Then, the Darcy friction factor, for laminar flow is:

$$f = \frac{64}{Re} \quad (10)$$

The pumping power per unit length in laminar flow is given by:

$$W = \frac{(\pi/4) D^2 U_{av} \Delta P}{L} \quad (11)$$

Thermal and fluid dynamic Properties of Nanofluid:

Dynamic Viscosity:

In 2007, Chen et al. showed a relation for finding the viscosity of nanofluids up to the volume fraction 10% Chen et al. eqⁿ [13]:

$$\mu_{nf} = \mu_{bf} [1 + 10.6\phi + (10.6\phi)^2] \quad (12)$$

Thermal Conductivity:

A wide range of experimental and theoretical studies were conducted in the literature to model thermal conductivity of nanofluids. The existing results were generally based on the definition of the effective thermal conductivity of a two-component mixture. . There are several thermal conductivity equations among them for SiC we use Maxwell mode equation [14]

$$K_{nf} = \frac{K_p + 2K_{bf} + 2(K_p - K_{bf})\phi}{K_p + 2K_{bf} - (K_p - K_{bf})\phi \times K_{bf}} \quad (13)$$

Density:

Using classical formulas derived for a two-phase mixture density (Xuan and Roetzel, 2000) of the nanofluid as a function of the particle volume concentration and individual properties can be computed using following equation [15]:

$$\rho_{nf} = \rho_p \phi + \rho_{bf} (1 - \phi) \quad (13)$$

Specific Heat:

Using classical formulas derived for a two-phase mixture, the specific heat capacity (Pak and Cho, 1998) of the nanofluid as a function of the particle volume

concentration and individual properties can be computed using following equation [16]:

$$C_{nf} = (1 - \phi)C_w + \phi C_p \quad (14)$$

4. Code Validation Test

For laminar channel flow at uniform velocity and constant heat flux water has been passed through the channel and a range of Reynolds number 400-1100 has been considered for calculating Nusselt numbers. At fully developed zone the obtaining Nusselt number is compared with the constant value of Nusselt number 8.23 (at constant heat flux for parallel plate) and with the Pahor and Turton [17] theoretical equation which is shown in Figure 2.

Pahor and Turton equation at constant heat flux as follows:

$$Nu = 8.24 \left(1 + \frac{3.79}{Pe^2} + \dots\right), \quad Pe \gg 1 \quad (15)$$

$$Nu = 8.118(1 - 0.031Pe), \quad Pe \ll 1 \quad (16)$$

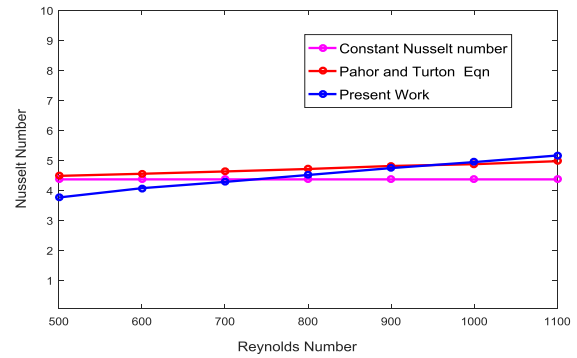


Fig. 2: Comparison of Nusselt number between Pahor and Turton equation, constant Nusselt number at constant heat flux and present work

5. Result and discussion:

The figure 3 shows the effect of volume fraction and Reynolds number on the nusselt number of SiC-water, from the figure it has been obtained that the Nusselt number of the nanofluid used in the present work increases with the increase in Reynolds number and Volume fraction of the nanofluids. This is occurred because of the increment of the effective thermal conductivity and an increase of energy exchange rate resulting from the irregular and chaotic motion of ultrafine particles of the nanofluids. S. Zeinali Heris, 2006 [8] worked with laminar convective heat transfer of circular tube by using Al_2O_3 -water and CuO-water nanofluids and investigated that the nusselt number is increased for both nanofluids respectively with increasing the volume fraction of the nanofluids and with the increment of Peclet number that indicates the increment of Reynolds number and this trend is observed in figure 4. Pak and Cho et al [16] also investigated that the Nusselt number for fully developed turbulent flow increased correspondingly to the increasing volume fraction as well as Reynolds number

for $\gamma\text{-Al}_2\text{O}_3$ -water and TiO_2 -water nanofluids which trend is also similar to the present work.

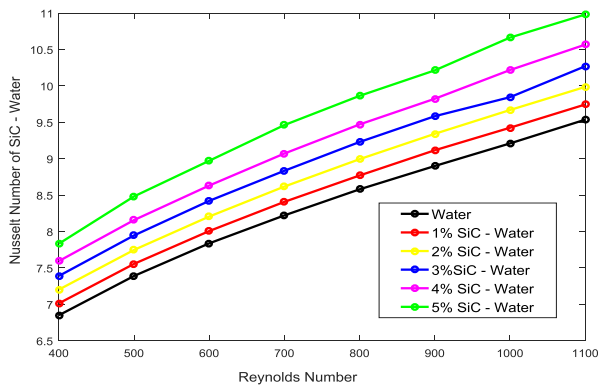


Fig. 3 Comparison of Nusselt number with Reynolds number of different volume fraction of SiC-water Nano fluid

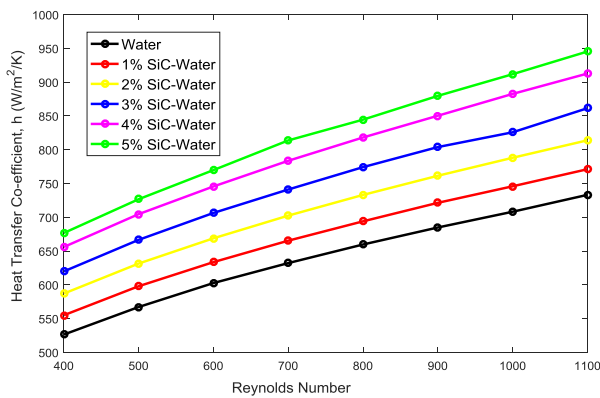


Fig. 4: Comparison of Heat transfer coefficient with Reynolds number of different volume fraction of SiC-water Nano fluid

The figure 5 represents the effect of volume fraction of nanofluids on heat transfer co-efficient for different Reynolds number. From the figures it is observed that the value of heat transfer coefficient increases rapidly with the increase of volume concentration and Reynolds number. This is due to the increases of the thermal conductivity and decreases of the specific heat capacity of the Nano fluid which increases the Nusselt number with higher velocity and temperature gradient and this phenomenon increases the heat transfer coefficient gradually. According to Wen and Ding, 2006[9] the numerical study of the particles migration due to viscosity gradient and a non-uniform shear rates leads to higher heat transfer coefficient of nanofluids. From the figures the increment of heat transfer coefficient compared to pure water is 7.2% to 31.5% for Al_2O_3 -water with respect to 1% to 5% volume concentration for Reynolds number 500 to 1400. S. Zeinali Heris and Esfahany, 2006[8] investigated convective heat transfer of circular tube by using Al_2O_3 -water nanofluid and observed that the heat transfer coefficient increases rapidly with the increases of Reynolds number with respect to increase of volume

concentration that satisfied the present work. Another same investigation was carried by Lin-wen Hu, 2000[18] with Al_2O_3 -water and Zirconia-water and reported that at fully developed region the heat transfer coefficient increases 27% for Al_2O_3 -water and 3% for zirconia-water nanofluid that also almost similar to the present work. Sezer Ozerinc, 2010 [19] also proposed that for Al_2O_3 -water nanofluid the heat transfer coefficient increases rapidly compare to pure water with the increment of Reynolds number and volume fraction. Figure 5 represent the effect of volume fraction on pumping power for different Reynolds number and the figure shows us that with the increase in Reynolds number with respect to volume concentration the required pumping power is also increasing both for water and four nanofluids. And it is also observed from the figures that the Nanofluid required more pumping power compared to pure water. At relatively lower Reynolds number the difference among the values of pumping power per unit length for different volume fraction is comparatively smaller. The figure 6 shows the variation of changing pumping power per unit length of nanofluids with different values of heat transfer coefficient and volume concentration. From graphs it is seen that by increasing the values of heat transfer coefficient, the pumping power becomes higher. The pumping power for SiC-water nanofluids is reduced 11% to 83% for $\phi = 1\%$ to 5% compared to pure water for same heat transfer rate. A similar trend is also analyzed by M. Monjurul Ehsan [11] for turbulent convective heat transfer of pipe flow by using Al_2O_3 -water, CuO-water and TiO_2 -water nanofluids.

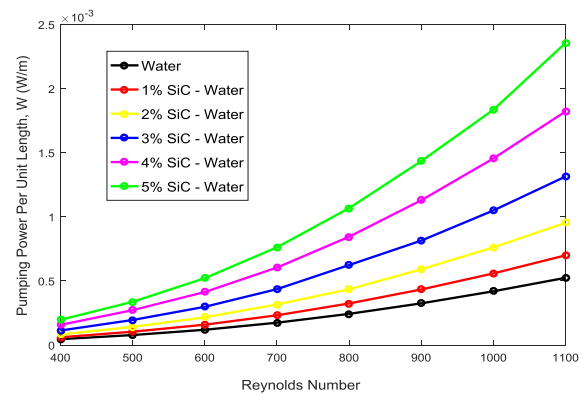


Fig. 5: Comparison of Pumping power with Reynolds number of different volume fraction of CuO-water Nano fluid

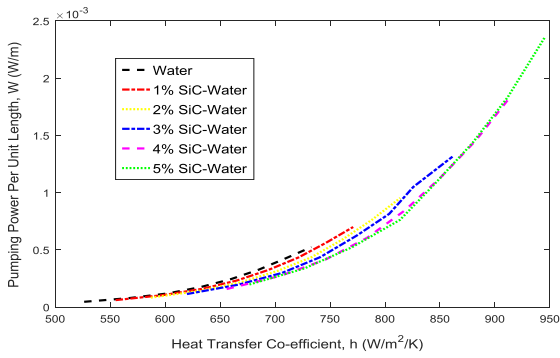


Fig. 6: Comparison of Pumping power with Reynolds number of different volume fraction of CuO-water nanofluid

The table1 shows the performance comparison pumping power advantage and reduction of volumetric flow rate of different volume fraction of SiC-water nanofluid with base fluid. From the table it is clear that at constant heat transfer coefficient the Reynolds number, velocity pumping power and volumetric flow rate of nanofluid has been reduced compared to pure water and the reduction is increased by increasing the volume concentration of the nanofluid. And so to get same heat transfer coefficient nanofluid needs lower pumping power and volumetric flow rate compared to pure water. This reduction is 11% to 83% for pumping power and 8% to 24.2% for volumetric flow rate compared to pure water.

Table 1: Comparison of the performance of different volume concentration of SiC-water nanoparticles with base fluid.

Type of fluid parameters	Water	1% SiC	2% SiC	3% SiC	5% SiC
Heat Transfer coefficient W/m ² .K	700	700	700	700	700
Reynolds number	967	810	695	585	450
Velocity m/s	0.0968 5	0.04 4323 723	0.041872 801	0.038 94605 4	0.0367 05767
Thermal conductivity	0.633	0.65 2	0.671	0.691	0.711

Pumping power per unit length W/m	0.0003 87	0.00 0341	0.000230	0.000 150	0.0000 655
Power advantage (%)	-	11.8 8%	40.56%	61.24 %	83%
volumetric flow rate, m ³ /s	4.868 E-06	4.45 E-06	4.20952E -06	3.915 9E-06	3.6900 7E-06
Reduction in volumetric flow rate	-	8.47 %	13.5%	19.6 %	24.2%

8. Conclusion

In the present work SiC-water nanofluid have been analyzed through a typical channel to investigate the heat transfer enhancement and pumping power and volumetric flow rate reduction. The heat transfer coefficient and Nusselt Number drop increase with the increase in volume fraction for the nanofluid as well as with the Reynolds number compared to pure water. And to get same heat transfer coefficient SiC-water required less pumping power and volumetric flow rate compared to pure water.

REFERENCES

- [1] J.A. Eastman, S. U. S. Choi, S. Li, L. J. Thompson, and S. Lee, "Enhanced thermal conductivity through the development of nanofluids," Fall Meeting of the Materials Research Society (MRS), Boston, USA, 1996.
- [2] S.U.S. Choi, "Nanofluid technology: current status and future research," Korea- U.S. Technical Conference on Strategic Technologies, Vienna, VA, T. Nosoko, A. 1998.
- [3] S.U.S. Choi, Z.G. Zhang, W. Yu, F.E. Lockwood, E.A. Grulke, "Anomalous thermal Conductivity enhancement in nanotube suspensions." Appl. Phys. Lett., 79(14), 2252-2254, (2001).
- [4] S.K Das, S.U.S. Choi, H.E. Patel, Heat Transfer in Nanofluids-A Review, heat transfer Eng. 27 (10) 3-19, (2006).
- [5] Y. Xuan Q. Li, "Investigation on convective heat transfer and flow features of nanofluids," ASME J. Heat Transfer 125, 151-155, (2003).
- [6] Williams, W., Buongiorno, J., and Hu, L.-W., "Experimental Investigation of Turbulent Convective Heat Transfer and Pressure Loss of Alumina/Water and Zirconia / Water Nanoparticle Colloids (Nanofluids) in Horizontal Tubes," ASME J. Heat Transfer, 130(4) p. 042412, (2008).
- [7] Rea, U., McKrell, T., Hu, L.-W., and Buongiorno, J., "Laminar Convective Heat Transfer and Viscous

- Pressure Loss of Alumina-Water and Zirconia-Water Nanofluids,” *Int. J. Heat Mass Transfer*, 52, pp. 2042–2048, (2012).
- [8] S. Z. Heris, S.G. Etemad, M.N. Esfahany, “Experimental investigation of oxide nanofluids laminar flow convective heat transfer,” *Int. Commun. Heat Mass Transfer* 33, 529–535, (2006).
- [9] Y. Ding, H. Alias, D. Wen, R.A. Williams, “Heat transfer of aqueous suspensions of carbon nanotubes (CNT nanofluids),” *Int. J. Heat Mass Transfer* 49, 240–250 (2006).
- [10] Kyo Sik Hwang, Seok Pil Jang, Stephen U.S. Choi, “Flow and convective heat transfer characteristics of water-based Al_2O_3 nanofluid in fully developed laminar flow regime” *International Journal of Heat and Mass Transfer* 52, 193–199, (2009).
- [11] M. Monjurul Ehsan, Shafi Noor, Sayedus Salehin and A.K.M. Sadrul Islam, “Application of Nanofluid in Heat Exchangers for Energy Savings”, *Thermofluid Modeling for Energy Efficiency Applications*, Edition:1st, Chapter:4, pp.73-101, 2015.
- [12] P.A. Ingole, S.M. Shinde, Dr. P.A. Patil, “Experimental Investigation of Pumping Power and Effectiveness of Car Radiator Using Al_2O_3 ,” *Nanofluid International Conference on Ideas, Impact and Innovation in Mechanical Engineering (ICIIME 2017)* ISSN: 2321-8169 Volume: 5 Issue: 6 135 – 141, 2017.
- [13] H. Chen, Y. Ding, Y. He, C. Tan, Rheological behaviour of ethylene glycol based titania nanofluids, *Chem. Phys. Lett.* 444 (4–6), 333–337, (2007).
- [14] Maxwell, J. C., *A Treatise on Electricity and Magnetism*, Clarendon Press, Oxford, 1873.
- [15] Y. Xuan, W. Roetzel, “Conceptions for heat transfer correlation of nanofluids,” *Int. J. Heat Mass Transfer* 43, 3701–3707(2000).
- [16] B.C. Pak, Y. Cho, “Hydrodynamic and heat transfer study of dispersed fluid with submicron based Al_2O_3 and CuO nanofluids in a triangular duct”, *J. Disper. Sci. Technol.* 34, 1368–1375(2013).
- [17] Hatton, A.P and Turton J.S “Heat transfer in the thermal entry length with laminar flow between parallel walls at uniform temperature”, *Int. J. Heat and Mass Transfer*, 5, 673-679, (1962).
- [18] Ulzie Rea, Tom McKrell, Lin-wen Hu, Jacopo Buongiorno “Laminar convective heat transfer and viscous pressure loss of alumina–water and zirconia–water nanofluids *International Journal of Heat and Mass Transfer*,” 52, 2042–2048, (2009).
- [19] Sezer özerinç, “Heat transfer enhancement with nanofluids,” a thesis submitted to the graduate school of natural and applied sciences of Middle East technical university, 2010.

k: Thermal conductivity
m: Mass flow rate
v: Volumetric flow rate
 Δp : Differential pressure loss
Q: Heat transfer
T: Temperature
 T_0 : Reference temperature, 273 K
u: Velocity of flow at inlet

Nomenclature

C_p : Specific heat at constant pressure
 D_h : Hydraulic diameter
f: Friction factor
h: Average heat transfer coefficient

Optimization of an Emergency Relief Supply Model using Genetic Algorithm along with a Framework for Structuring Humanitarian Logistics Distribution Network

Shekh Rasel¹, Md. Mahmudul Hasan Bhuiyan¹, Khairun Nahar^{2}*

¹Department of Industrial & Production Engineering, Rajshahi University of Engineering & Technology,
Rajshahi, Bangladesh

^{2*} Assistant Professor, Department of Industrial & Production Engineering, Rajshahi University of Engineering & Technology,
Rajshahi, Bangladesh

ABSTRACT

The work is aimed towards formulating a disaster related emergency relief supply model of humanitarian relief goods and then solving with Genetic Algorithm and a more traditional approach of Linear Programming by considering collected data of a sample relief work. The model includes surpluses and shortages goods as variables and vehicle space as constraint. The constraints on demand, available minimum inventory and maximum labor level, load capacity of the vehicle, distribution center (DC) space all of which affect a relief distribution system directly used in the model. The model determines and optimizes the amount of relief supplies to be stocked, loads to be transported in each trip, labor level required, and the amount of surpluses and shortages goods so that the total cost is minimized. We compared results obtained by Genetic Algorithm and Linear Programming techniques. It is found that the Genetic Algorithm has better performance than the traditional Linear Programming. Finally a comprehensive framework for restructuring the transportation and distribution system of humanitarian relief items is provided.

Keywords: Optimization; Emergency relief logistics; Vehicle constraint; Penalty cost; Genetic algorithm.

1. Introduction

In recent years, the number of natural disasters has increased to great extent and the severity has grown. As a result some people lose their lives. Many people are deprived of food. The objective of disaster response in the humanitarian relief chain is to rapidly provide relief (emergency food, water, medicine and supplies) to areas affected by large-scale emergencies, so as to minimize human suffering and death. Cost control is a vital aspect in this regard although mostly it is ignored thinking about the non-profit nature of the work. But as the number of relief activities carried out has increased with the number of disaster occurrences, hence comes the importance of looking at budgetary aspects and optimization of goods to be distributed among sufferers [15].

Emergency relief supply problems are a class of optimization problems in the domain of operations research (Zhang et al. 2014) [18]. Classical relief supply problems are modeled as linear programming problems for minimizing the cost of delivering integral quantities of goods from m sources to n demand points while balancing supply and demand. In emergency situations, there can be various kinds and a huge number of supplies to be delivered in a cost effective, timely and efficient manner. The relief supply work is heavily constrained by bottlenecks, such as the availability of DC and vehicle space, maximum labor level and the capacity of transportation network [1, 3]. Also the available information is often uncertain, incomplete and inconsistent.

In order to solve optimization problems various methods have been implemented previously. Initially Linear Programming method was widely used [13]; but as the name suggests it was helpful only in case of solving linear

problems. Later on with the advancement of several computational techniques many nature inspired algorithms have been developed. Genetic Algorithm is one of the older such algorithm. The proposed emergency relief supply model is solved with such Linear Programming (IPM) and Genetic Algorithm techniques [7, 10].

Chansiri Singhtau (2015) proposes a mathematical model and examines the performance of an exact algorithm for a location-storage-transportation problem in humanitarian relief. The model determines the location of distribution centers in a relief network, the amount of relief supplies to be stocked at each distribution center and the vehicles to take the supplies to meet the needs of disaster victims under capacity restriction, transportation and budgetary constraints. Branch and bound algorithm is applied for these problems. The results show that this algorithm can solve problem sizes of up to three candidate locations [14]. Min-Xia Zhang, Bei Zhang and Yu-Jun Zheng (2014) conducted a survey of recent advances in bio-inspired meta-heuristics. They proposed a typical transportation planning problem and develop a new algorithm based on the BBO meta-heuristic for the problem. They demonstrated the competitive performance of BBO algorithm (which provided better result) with Linear Programming and GA algorithms [17].

Complex transportation planning may also involve multiple criteria or objectives, such as time and cost [2]. A simple approach to handle multiple objectives is to transform them into a single objective. For example, in the study of an urgent relief distribution problem, Liu and Zhao (2007) combined the objective functions of transshipment time and cost into a single one based on weight aggregation [8].

* Corresponding author. Tel.: +88-01916800200

E-mail addresses: khairun.nahar@ipe.ruet.ac.bd, shapla05.ipe@gmail.com

The relief-distribution model by Tzeng et al. (2010) considers three objectives, including minimizing total cost, minimizing total travel time and maximizing satisfaction of fairness. The model is resolved by maintaining the third objective while transforming the first and second objectives into constraints [16].

Xie and Hu (2009) modeled an inventory routing problem in emergency logistics with fuzzy demands which are converted to deterministic demands by Yager's fuzzy number ranking method. They solve the problem using a heuristic algorithm that coordinates inventory control and route optimization for minimizing total cost. Computational result shows that the benefits can be obtained from the integration of inventory and routing [19].

Yan and Shih (2009) also integrated roadway repair and relief distribution along with storage function into a network flow model, which is a multi-objective, mixed-integer and multiple-commodity problem. They transformed it to a single-objective problem using the weighting method and developed a heuristic algorithm that first solves a sub-problem and then, repeatedly incorporates the remaining tasks, until a complete solution is obtained [20].

Jin Qin, Yong Ye, Bi-rong Cheng, Xiaobo Zhao and Linling Ni (2016) formulated an optimization model for emergency relief goods supply problem with insufficient supplies, in which the objective function was to minimize distribution and labor operation costs [12].

There have been many works on planning, routing, transportation, distribution and logistics management of humanitarian relief work system. Authors have signified one subsystem over another in most papers. An emergency relief supply network does not include only carrying goods to destination, but other aspects of purchasing, storing, transporting items to end users etc. all are part of the whole system. Thus more comprehensive work on realizing all aspects of humanitarian relief network is needed indeed.

2. Model Development

The proposed mathematical model is formulated with the help from various literatures; by creating a new objective function, adding budgetary constraints and changing the transportation cost function to make the problem match the real situation. The formulated model considers inventory cost, vehicle related cost, labor level and wage, finally penalty cost for both surpluses and shortages of relief goods. Both the penalty costs are borne by the suppliers due to incorrect amount of relief supplies to the distributors. These penalty costs incur because of the fact that the distributors can hardly delay the supplies as the demand needs to be fulfilled as quickly as possible. The sole purpose of this model is to identify the quantity of relief items to be stored, and determining the assignment of vehicles to supply the humanitarian aid items so as to minimize the total cost [4, 6, 7, 9 and 11]. Considering all these aspects the mathematical model is formulated as follows:

2.1 Notations:

IC_{nt} = Inventory cost per unit for nth item in period t (TK/unit)

IQ_{nt} = Inventory level for nth item in period t (Units)

VC_{nt} = Vehicle cost per unit for delivering nth item in period t (TK/unit)

VQ_{nt} = Vehicle loads to be delivered for nth item in period t (Kg's)

LC_{nt} = Labor cost to hire one worker for nth item in period t (TK/man-hour)

LQ_{nt} = Labor hours hired for nth item in period t (Man-hours)

$PC1_{nt}$ = Penalty cost per unit surplus for nth item in period t (TK/unit)

$PQ1_{nt}$ = Quantity of surpluses goods for nth item in period t (Units)

$PC2_{nt}$ = Penalty cost per unit shortage for nth item in period t (TK/unit)

$PQ2_{nt}$ = Quantity of shortages goods for nth item in period t (Units)

FD_{nt} = Forecasted demand for emergency supplies at demand point (Units)

IQ_{ntmin} = Minimum inventory level for nth item in period t (Units)

DCS_{nt} = Distribution center space per unit for nth item in period t (Sq meter)

DCS_{ntmax} = Maximum distribution center space available in period t (Sq meter)

VQ_{ntmax} = Maximum vehicle loads to be delivered for nth item in period t (Kg's)

VS_{nt} = Vehicle space per unit for nth item in period t (Sq meter)

W = Maximum load capacity of the vehicle (Kg)

LQ_{ntmax} = Maximum labor hours hired for nth item in period t (Man-hours)

G_{nt} = Number of goods remaining in inventory after transportation (Units)

T_{work} = Time spent for loading, unloading and distributing emergency goods (Hours)

T_{travel} = Time spent by vehicle for travelling with emergency goods (Hours)

2.2 Formulation of Objective Function

$$(1) \text{ Inventory cost: } \sum_{n=1}^N \sum_{t=1}^T IC_{nt} IQ_{nt}$$

$$(2) \text{ Vehicle cost: } \sum_{n=1}^N \sum_{t=1}^T VC_{nt} VQ_{nt}$$

$$(3) \text{ Labor cost: } \sum_{n=1}^N \sum_{t=1}^T LC_{nt} LQ_{nt}$$

$$(4) \text{ Penalty cost for surplus: } \sum_{n=1}^N \sum_{t=1}^T PC1_{nt} PQ1_{nt}$$

$$(5) \text{ Penalty cost for shortage: } \sum_{n=1}^N \sum_{t=1}^T PC2_{nt} PQ2_{nt}$$

Objective function,

Minimize,

$$Z = \sum_{n=1}^N \sum_{t=1}^T [IC_{nt}IQ_{nt} + VC_{nt}VQ_{nt} + LC_{nt}LQ_{nt} + PC1_{nt}PQ1_{nt} + PC2_{nt}PQ2_{nt}]$$

2.3 Formulation of Constraints

(1) Constraints on carrying inventory and distribution center space

The level of inventory should be typically more than forecasted demand so that there is no shortage of relief items. On the other hand, there should not be too much excess of stocks that the space of local warehouse is incapable of storing them.

$$FD_{nt} \leq IQ_{nt} \text{ for } \square n, \square t$$

$$IQ_{nt} \geq IQ_{ntmin} \text{ for } \square n, \square t$$

$$\sum_{n=1}^N \sum_{t=1}^T DCS_{nt} * IQ_{nt} \leq DCS_{tmax} \text{ for } \square n, \square t$$

(2) Constraints on load capacity and available space of vehicle

There are some restrictions on the total weight and the total volume of vehicles. The use of vehicles with relief goods for transportation actually distinguishes the proposed emergency model from the normal relief supply model. This signifies the necessity of quick response.

$$VQ_{nt} \leq VQ_{ntmax} \text{ for } \square n, \square t$$

$$\sum_{n=1}^N \sum_{t=1}^T VS_{nt} * VQ_{nt} \leq W \text{ for } \square n, \square t$$

(3) Constraints on labor level

Availability of labor for both inventory control and relief distribution is a crucial aspect in this type of activity. A maximum time for each vehicle type is imposed. Each vehicle trip is assumed to visit only one demand point at a time.

$$LQ_t \leq LQ_{tmax} \text{ for } \square t$$

$$LQ_t = T_{work} + T_{travel} \text{ for } \square t$$

(4) Constraints on surpluses and shortages goods

The amount of emergency supplies distributed to each demand point should be consistent with that of actual demands as much as possible, and both the excessive and insufficient distribution could affect the whole system.

$$\sum_{n=1}^N \sum_{t=1}^T PQ1_{nt} \leq (IQ_{ntmax} - FD_{nt}) \text{ for } \square n, \square t$$

$$\sum_{n=1}^N \sum_{t=1}^T PQ2_{nt} \leq G_{nt} \text{ for } \square n, \square t$$

(5) Non negativity constraint

$$IQ_{nt}, VQ_{nt}, LQ_t, PQ1_{nt}, PQ2_{nt} \geq 0 \text{ for } \square n, \square t$$

3. Data Description

We have used primary data (table 1 to table 6) for emergency relief goods which were collected from project integrate department under UNO office of Ishwarganj upazila, Mymensingh. There was a major flood occurred in several remote unions in the year 2017. The government used the UNO office and local food storage for providing relief goods to the victims. In our case, we have used the data of a relief work in which the humanitarian items were distributed among two demand points. Around 1000 people were served in the demand points. A truck of 4 ton of capacity was used as a transportation mode for 2 days of several trips. Penalty costs were incurred from the suppliers' side in this relief work. All the other relevant data are given as follows:

Here, Number of items, $n = 3$ (n_1 = Water bottle, n_2 = Rice sack, n_3 = Dry food packet)

Number of period, $t = 2$ (days)

Table 1: Inventory Cost
(TK/unit)

n	t	
	1	2
1	4.5	4.5
2	30	30
3	12.85	12.85

Table 2: Vehicle Cost
(TK/unit)

n	t	
	1	2
1	2	2
2	1.8	1.8
3	8	8

Table 3: Labor Cost
(TK/man-hour)

n	t	
	1	2
1	80	100
2	80	100
3	80	100

Table 4: Penalty cost for Surplus
(TK/unit)

n	t	
	1	2
1	4.5	1.3
2	30	10
3	12.86	5

Table 5: Penalty cost for shortage
(TK/unit)

n	t	
	1	2
1	6.5	4.6
2	43	35
3	19	17.5

Table 6: Data for Constraints

Item	Period	
	1	2
FD _{1t} (Units)	3000	3800
FD _{2t} (Units)	420	660
FD _{3t} (Units)	855	1100
IQ _{1tmax} (Units)	3500	4000
IQ _{2tmax} (Units)	500	700
IQ _{3tmax} (Units)	975	1200
DCS _{1t} (Sq meter)	.045	.045
DCS _{2t} (Sq meter)	.075	.075
DCS _{3t} (Sq meter)	.05	.05
DCS _{tmax} (Sq meter)	200	200
VQ _{1tmax} (Kg's)	1500	1500

VQ _{2tmax} (Kg's)	2000	2000
VQ _{3tmax} (Kg's)	500	500
VS _{1t} (Sq meter)	.0036	.0036
VS _{2t} (Sq meter)	.0058	.0058
VS _{3t} (Sq meter)	.0045	.0045
LQ _{tmax} (Man-hours)	15	10
G _{1t} (Units)	63	80
G _{2t} (Units)	20	25
G _{3t} (Units)	50	58

Also, (I) W= 4000 Kg. (II) T_{work} = 7 Hours, 5 Hours; T_{travel} = 3.5 Hours, 4 Hours.

4. Result Analysis

In this case we use Genetic algorithm (GA) because it is more robust than conventional techniques. Unlike older systems, they do not break easily even if the inputs changed slightly, or in the presence of reasonable noise. GA is much more efficient in solving single objective situation and can solve both discrete and continuous problems.

Here all the programs were run in MATLAB 2013a in core (TM) i3 1.7 GHz pc with a 4 GB of RAM. The results Obtained from Genetic Algorithm and Linear Programming are tabulated in table 7.

Table 7: Result Obtained from Genetic Algorithm & Linear Programming

Variables	Genetic Algorithm	Linear Programming
IQ ₁₁ (Units)	3500	3500
IQ ₁₂ (Units)	4000	4000
IQ ₂₁ (Units)	500	1200
IQ ₂₂ (Units)	700	1400
IQ ₃₁ (Units)	975	975
IQ ₃₂ (Units)	1200	1200
VQ ₁₁ (Kg's)	1560	914
VQ ₁₂ (Kg's)	342	1609
VQ ₂₁ ((Kg's)	800	1677
VQ ₂₂ (Kg's)	1276	1677
VQ ₃₁ (Kg's)	450	526
VQ ₃₂ ((Kg's)	303	152
LQ ₁₁ (Man-hours)	10.50	10.50
LQ ₁₂ ((Man-hours)	9	9
LQ ₂₁ (Man-hours)	10.50	10.50
LQ ₂₂ (Man-hours)	9	9
LQ ₃₁ ((Man-hours)	10.50	10.50
LQ ₃₂ (Man-hours)	9	9
PQ ₁₁ (Units)	115	0
PQ ₁₂ (Units)	0	80
PQ ₁₂₁ (Units)	67	10
PQ ₁₂₂ (Units)	8	10

PQ ₁₃₁ (Units)	56	94
PQ ₁₃₂ (Units)	0	0
PQ ₂₁₁ (Units)	0	16
PQ ₂₁₂ (Units)	10	0
PQ ₂₂₁ (Units)	6	0
PQ ₂₂₂ (Units)	11	0
PQ ₂₃₁ (Units)	26	0
PQ ₂₃₂ (Units)	0	58
Obj. Function Value, Z (Tk.)	103020	144920

Results obtained from the two solution technique as shown in table 7, it is found that Genetic Algorithm approach is found to be inferior to IPM of Linear Programming technique as cost minimization being the main objective..

I. The demand, for 1st item (water bottle) was 3000 units in 1st period and 3800 units in 2nd period; for 2nd item (rice sack) was 420 units in 1st period and 660 units in 2nd period; for 3rd item (dry food packet) was 855 units in 1st period and 1100 units in 2nd period. Between the GA and LP, the major difference of total cost is incurred due to the significant variation of required quantity of rice sack to be stored. Also according to both the solution technique, there should be 3500 units and 4000 units of water bottle, 975 units and 1200 units of dry food packet inventoried in two periods. These values equal the maximum inventory level for the two items in each period.

II. In case of vehicle loads to be transported, the result obtained from GA shows that a significant larger loads of water bottle (1560 Kg's) should be transported in the first period. Whereas result from LP specifies to transport a relatively smaller loads of water bottle (914 Kg's) in the first period. On the other hand, GA assigns 800 Kg's and 1276 Kg's of rice sack for transportation in two periods respectively. But result from LP tells to transport 1677 Kg's of rice sack in both the periods which is quite larger.

III. The required labor level of 10.50 man-hours in the first period and 9 man-hours in the second period found out to be similar for both the solution technique.

IV. The highest number of surplus goods is found out to be water bottle (115 units) and dry food packet (94 units) with GA and LP respectively. These large surplus goods will help to response quickly for emergency supplies. But this also affects the cost minimization function adversely.

V. From the solution obtained from LP, it shows us that there is no shortage of rice sack in any of the period. It means that there is enough supply of units which will fulfill the demand. Again, the total number of shortage items is found out to be less with GA (53 units) than with LP (74 units). Hence we can say that GA provides solution in which there is better continuous supply of humanitarian items.

5. Framework for Relief Goods Transportation & Distribution

Humanitarian logistics is a complex environment which needs a better management of the relief operations. One of the key issues that relief organizations can address is the

distribution network configuration which has a great impact on delivery time and costs; two major elements; whose central purpose is to rapidly provide aid to the affected population [5].

5.1 Identification of Critical Problems

- i. Humanitarian supply chains lag behind in technology implementation, best practices, and operating efficiency.
- ii. The associated large demands for relief products pose challenges to the logistics planning authorities with the level of uncertainty adding to the complexity.
- iii. There may exist irregularities in the size, the timing, and the location of relief product demand patterns.
- iv. In addition, disaster-driven supply chains are typically formed as incident-responsive ones with temporary configurations of disparate resources.
- v. Lack of communication, information and collaboration with local forces, ignoring systematic network formulation, less response planning are other key elements that affect a humanitarian relief distributing system adversely.

The cause-effect diagram in figure 1 shows the specific reasons or causes which ultimately lead to adverse effect (e.g., excessive cost incurs, missed delivery, extra time requires).

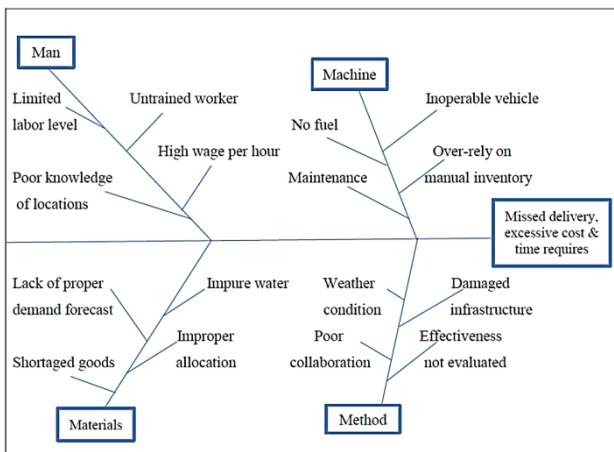


Figure 1: Cause-effect Diagram for Finding out Problems in Relief Work

5.2 Implication of a Structured Process

On the basis of reviewing of various literatures, data and result analysis, a proper structured relief distribution network is presented as shown in figure 2. This includes five different phases of operation:

Phase 1: Time varying relief demand forecast.

It should be taken into account the pre-disaster preparations including the procurement, the pre-positioning, and the storage of disaster relief items.

Phase 2: Affected area grouping.

There can be multiple area points which can be taken under a single network. The evaluation of number of disaster affected points, distances from the distribution center (DC), transportation mode available, and integration with locals.

Phase 3: Determination of distribution priority.

Depending on the damage scale of a disaster, various relief

items, be it water, food or medicines of forecasted quantities are stored in a local DC. Major affected area point should be prioritized so that the most vulnerable people get first.

Phase 4: Group based relief distribution.

The affected areas can be grouped as individual demand points. The distance of a demand point from DC; along with level of necessity are considered while prioritizing relief materials distribution.

Phase 5: Dynamic relief supply.

This phase comes into picture when urgent relief demand is not satisfied. The shortaged items need to be procured quickly because of the emergency condition. There can also be excess of items which remain in inventory.

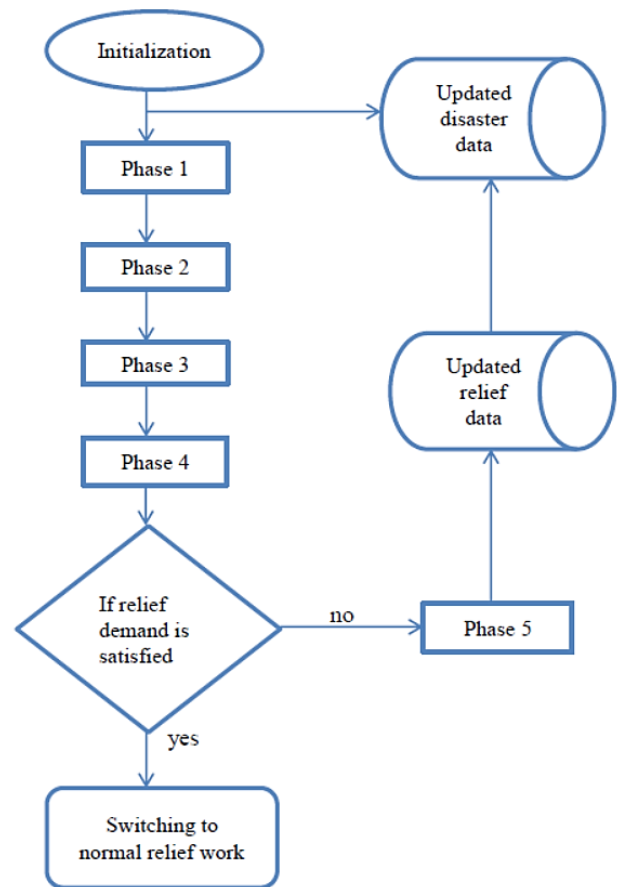


Figure 2: Relief Distribution System Design

6. Conclusions & Discussions

In this paper, we formulated an emergency relief supply model for real world situation. Then GA and Linear Programming method was implied to get optimized value. The optimized results from Genetic Algorithm and Linear Programming are Tk.103020 and Tk.144920 respectively. Since the mentioned problem is concerned about minimization of cost, the Genetic Algorithm shows better result here. Besides, the framework which is provided for

structuring such relief work in phase-wise system; including from determining the amount of humanitarian logistics required to proper distribution of these items. However the model cannot be applied in case of situation where relief goods are not inventoried before go for transportation. Penalty cost for surplus and shortage per unit items were assumed to an extent because there was no absolutely accurate data available. Where cost minimization was our main purpose, the sensitivity analysis of the vital resource restrictions such as the number of DC's, the number of vehicles, etc. is an interesting area for future research.

REFERENCES

- [1] D. Berkoune, J. Renaud, M. Rekik, A. Ruiz, "Relief Supply in Disaster Response Operations", *Socio Economic Planning Sciences*, vol. 46, pp. 23–32 (2012).
- [2] A. M. Caunhye, X. Nie, S. Pokharel, "Optimization Models in Emergency Logistics: a Literature Review" *Socio-Economic Planning Sciences*, vol. 46, issue 1, pp. 4-13 (2012).
- [3] G. Chai, C. Fang, X. Gao, Q. Zhao, "A Cost-based Study on Highway Traffic Emergency Rescue Sites Location using Heuristic Genetic Algorithm", *Journal on Computer Information System*, pp. 507–514 (2012).
- [4] S. Chen, Y. Zheng, C. Cattani, W. Wang, "Modeling of Biological Intelligence for SCM System Optimization", *Comput. Math. Methods Med.*, doi:10.1155/2012/76970 (2010).
- [5] M. Hamedi, A. Haghani, S. Yang, "Reliable Transportation of Humanitarian Supplies in Disaster Response: Model and Heuristic", *In Proceedings of the 15th Meeting of the EURO Working Group on Transportation, Procedia-Social and Behavioral Sciences*, pp. 1205–1219 (2012).
- [6] C. F. Han, "Genetic Algorithm for Solving Problems in Emergency Management", *15th International Conference on Natural Computation, Tianjin, China*, pp. 259–264 (2009).
- [7] C. Lewis, "Linear Programming: Theory and Applications", *Math. Program. Ser. B* 92 (2002), 453-480 (2008).
- [8] M. Liu, L. Zhao, "A Composite Weighted Multi-objective Optimal Approach for Emergency Logistics Distribution", *IEEE International Conference on Industrial Engineering and Engineering, Austin, TX, USA*, pp. 968–972 (2007).
- [9] A. K. Mollah, S. Sadhukhan, P. Das, M. Z. Anis, "A Cost Optimization Model and Solutions for Shelter Allocation and Relief Distribution", *International Journal of Disaster Risk Reduction*(2016).
- [10] L. Na, L. Zhi, "Emergency Relief Goods Multi-mode Transportation Based on Genetic Algorithm", *IEEE 2nd International Conference on Intelligent Computation Technology and Automation, Changsha, Hunan, China*, pp. 181–184 (2010).
- [11] P. C. Nolz, K. F. Doerner, W. J. Gutjahr, R. F. Hartl, "A Bi-objective Metaheuristic for Disaster Relief Operation Planning", *Multi-Objective Nature Inspired Computing, Springer: Berlin/Heidelberg, Germany*, pp. 167–187 (2007).
- [12] J. Qin, Y. Ye, B. Cheng, X. Zhao, L. Ni, "An Optimization Model for Emergency Logistics Problem with Insufficient Supplies", *Journal of Operational Research*, vol. 62, pp. 183–188 (2016).
- [13] R. Robere, "Interior Point Methods and Linear Programming", *European Journal of Operational Research*, 218(3):587-601(2012).
- [14] C. Singhtaun, "An Exact Algorithm for Location-storage-transportation Problems in Humanitarian Relief", *International Journal of Social, Behavioral, Educational, Economic, Business and Industrial Engineering*, vol. 9, no. 3 (2015).
- [15] H. A. Taha, "Operations Research: an Introduction: Eighth Edition", *Pearson Education, Inc* (2007).
- [16] G. H. Tzeng, H. J. Cheng, T. D. Huang, "Multi-objective Optimal Planning for Designing Relief Delivery Systems", *Transp. Res. Part E: Logist. Transp.*, vol. 43, pp. 673-686 (2010).
- [17] M. Zhang, B. Zhang, Y. Zheng, "Bio-inspired Meta-heuristic for Emergency Transportation Problem", *Zhejiang University of Technology*, 288 Liuhe Road, Hangzhou 310023, China, doi:10.3390/a7010015 (2014).
- [18] Y. J. Zheng, H. F. Ling, S. Y. Chen, "Efficient Multi-objective Tabu Search for Emergency Equipment Maintenance Scheduling in Disaster Rescue", *Optim. Lett.* vol. 7, pp. 89–100 (2012).
- [19] B. Xie, X. Hu, "A Model and Heuristic Algorithm for Inventory Routing Problem in Emergency Logistics", *In Proceedings of the 9th International Conference of Chinese Transportation Professionals, Harbin, China*, vol. 9, pp. 154-160 (2009).
- [20] Yan, S.; Shih, Y.L. 2009, "A Time-space Network Model for Work Team Scheduling after a Major Disaster", *J. Chin. Inst.*, vol. 30, pp. 63–75.

Barriers against the Development of Solar Cooker & its Solution

Tamal Chowdhury^{1,*}, Hemal Chowdhury², Piyal Chowdhury³, Abul Hasnat¹, Birol Barua¹, Rabiul Islam¹
¹Department of Electrical & Electronic Engineering, Chittagong University of Engineering & Technology
²Department of Mechanical Engineering, Chittagong University of Engineering & Technology
³Chittagong Collegiate School & College, Chittagong

ABSTRACT

Cooking with natural gas is not only unhygienic but also results in green house gas emission. So, the alternative method of cooking should need to be checked. Solar cooker provides an efficient way to cook food without any consumption of fuel. The feasibility of solar cooker in rural regions of Bangladesh has been checked. But this renewable energy market faces some barriers against its development. This paper gives an analytic view of the barriers against the development of the solar cooker energy market and tries to suggest some solution in order to overcome this barrier.

Keywords: Solar Cooker; Change agent, Bangladesh.

1. Introduction

A sustainable development is achieved when there is no depletion of natural resources and more emphasis is given on renewable energy resources. Clean cooking technology can play a vital role in achieving this goal. Solar cooker a device that makes direct use of sunlight to cook food or pasteurize drinks is such a technology. Operating principle of these devices are that they use mirrors to concentrate sunlight which is converted to heat & used for cooking [1]. Many local and international organizations have supported solar cookers in many countries. Various types of solar cookers are available, such as the box cooker, panel cooker, and the parabolic reflector cooker etc. They all have the same general principle of using solar radiation as a cooking source with different design [2]. Solar cooker can be classified mainly into two categories, direct and indirect on the basis of heat transfer mechanism to cooking pot [3]. A review of the direct and indirect type's solar cooker performance with numerical, experimental and theoretical analysis can be found in [4]. Box, panel and parabolic reflector comprise of direct type solar cooker. Direct type solar cooker mainly depends on sunlight but for indirect type solar cooker heat is transferred to cooking pot by heat transfer fluid. Table 1 shows the comparison between different types of solar cookers [5]. Most of the solar cookers have been tested in rural areas of India [6] & Burkina Faso [7, 8].

In Bangladesh, several households have started using solar cooker. Design and testing of parabolic and two axis spherical solar cooker have been carried out in [9], [10]. Several solar cookers with parabolic reflectors have already been developed and field tested by the Institute of Fuel Research and Development (IFRD) in Bangladesh. The cookers have successfully heat water quickly to its boiling point on a clear sunny day [11].

2. Potential of Solar Cooking Bangladesh

On a clear sunny day for any solar cooker the minimum direct radiation required is 4 KWh/m² and for Bangladesh, average global horizontal radiation is 4.806 KWh/m² [12]. The following figures (1-2) presents the global horizontal and direct normal radiation Patterns in Bangladesh and the no of days solar cooker can be used [13]. The figures denote that there are approximately 294 days where global horizontal radiation is above 4.0 KWh/m². It can be also found that there are approximately 145 days where direct normal radiation is above 4.0 KWh/m². Table 1 denotes that the most suitable solar cooker for Bangladesh is Box type cooker. Although higher temperature can be gained from parabolic reflector type cooker, it requires skill and training.

Table 1: Comparison between different types of solar cookers [5]

	Parabolic reflector type cooker	Panel-type cooker	Box type cooker
Solar Radiation	direct only	direct only	direct and diffused
Cooking Temperature	260-538 ⁰ C	90-150 ⁰ C	150-200 ⁰ C
Safety	involves risk; training required for use	moderately safe	safe
Insulation	poorly insulated	poorly insulated	Well insulated; temperature is unaffected by

* Corresponding author.

E-mail addresses: tamalshanto@gmail.com

			winds
Cooking Time	fastest	slowest	moderate
Possible Cooking Methods	frying, grilling and roasting	boiling, baking, simmering and steaming	boiling, baking, simmering and steaming
Cost(\$)	349	86	350

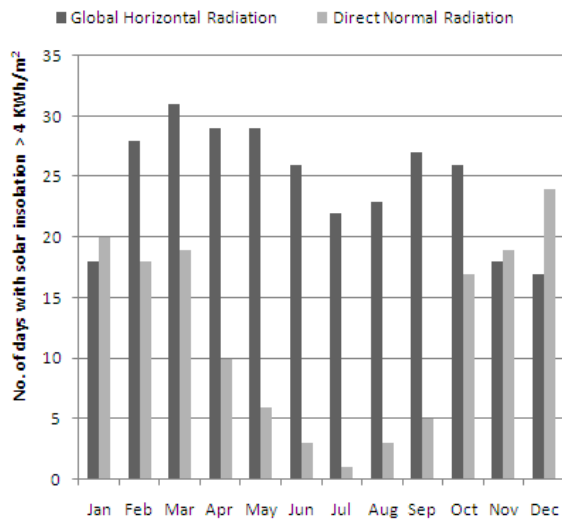


Figure 1: Number of days a solar cooker can be used [13].

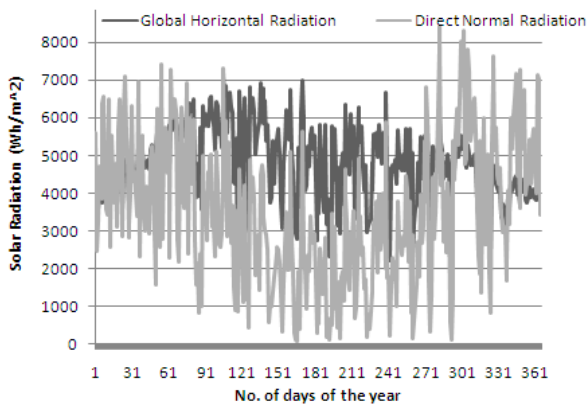


Fig 2: Global Horizontal and Direct Normal Radiation Patterns in Bangladesh [13].

3. Barriers Against the development of Solar Cooker

By reviewing several literatures various barriers have been found that slow down the growth of solar cooker energy technology. These barriers also persist in Bangladesh & they have been listed below in the table 2.

Table 2: Barrier against the development of solar cooker

<i>Barrier</i>	<i>Description</i>	<i>Reference</i>
Lack of knowledge & education	Education affects decision making. Educated people are likely to adopt clean technologies as they know the benefit of it.	[14]
Poor people's technology	Most of the solar cooker technology is developed for the people with low socio economic status. As people consider it a technology for the poor, the whole project loses overall value & attractiveness.	[15]
Alternative Fuel	People living in rural area have access to biomass. They use them as fuel to cook not knowing that results in increase of greenhouse gas.	[16]
High Complexity	Most people hardly think solar cooker can cook. So people having limited food ration do not risk wasting their food.	[17]
Disturbing cooking method	Many customers have the belief that solar cooker requires major changes in cooking behavior. They see problems such as longer	[18,19]

	cooking time, lower capacity, outdoor cooking and change of taste and texture of the food	
Lack of industry Standards	No of industry that manufactures solar cooker is limited and their products have low standards. This results in lower reputation of solar cookers and the users' perception of the concept	[20]
Low income	Many people in developing country have small income. They cannot afford to buy expensive solar cooker without government providing subsidy on those devices. Cash and credit in some communities may even be new and unknown practices.	[21]
Lack of flexibility:	Cannot be operational in cloudy days and night.	[22]
Limited Access to Sunlight	People living in cities do not have access to solar for cooking purposes. People living in Dhaka do not have adequate space in their apartment for solar cooking purposes.	[13]
Cultural Resistance	In solar cooker all the	[23]

	ingredients along with food are left on the sun until it gets cooked. A study conducted in Gujarat reports that many housewives have found this unacceptable.	
--	---	--

4. SOLUTIONS TO THE BARRIERS

It is the customers who ultimately determine the market success of a new product. Innovation needs to be adopted by customers otherwise market diffusion will not take place [21]. So to do this, proper communication is necessary. Communication can be through the mouth or having a close relationship with customers. So proper communication can help in overcoming these barriers.

The use of change agents is a great way to overcome these barriers. A change agent is a personal being who influence the customers by his communicating skill [22]. A change agent must have several characteristics [23]. These characteristics can help to eradicate the barriers that hinder the development of solar cooker. They have been given below.

- Local knowledge:

Change agents should have local knowledge. They should know about the customers' needs, attitudes, beliefs, social norms and leadership structure. It helps change agents to choose what information that is relevant to attract to the customers. This knowledge will help to improve the understandings of rural people on the solar cooker.

- Similar socioeconomic status:

The change agent needs to have same socio economic status as the customer. This is very essential for the change agent as communication is said to be far more efficient when the communicator and receiver are homophilous.

- Technical knowledge:

Technical knowledge is very important for change agent as he needs it to explain the customers about the technology properly. Since customers find solar cookers are high in complexity, technical knowledge will aid change agents so that they can properly help customers in the adoption process. To prevent cultural resistance, this knowledge will open a new path for the development of solar cooker.

- Alternate means of cooking:
In order to prevent flexibility problem, alternate means of cooking should need to be adopted. Implementation of biogas stoves can play an effective role here.

- Implementations of Laws:
The problem of limited access to sunlight can be addressed by implementing laws on urban building designs. The buildings should have adequate space on the rooftop for solar cooking purposes.

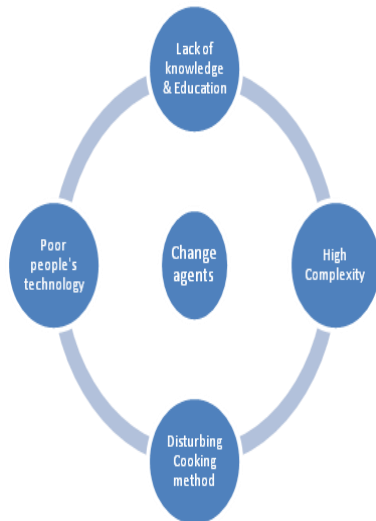


Figure 3: Functions of change agent.

In figure 3 the barriers that can be solved by efficient change agents have been listed. In order to increase solar cooker status change agent, should promote solar cooker as a highly desirable product [17]. He should give a proper demonstration on solar cooker's operation, should provide training to develop people's ability by training them. He should provide the knowledge how to work with cooker during cloudy and night time. This can be by providing a hybrid solution [17].

5. Conclusion

Bangladesh has huge solar energy resources. This paper highlights the barrier against the development of solar cooker and suggest some solutions. From the analysis can be said that government should proper subsidy to develop solar cooker energy market. Introduction of change agent by industries to solve the misunderstanding of people will play a great role to overcome the obstacles of solar cooker energy development in Bangladesh.

REFERENCES

[1] J. Goldemberg, Leapfrog energy technologies, *Energy Policy* 26 (10) (1998) 729–741

[2] R.M. Muthusivagami, R. Velraj, R. Sethumadhavan, Solar cookers with and without thermal storage—a

review, *Renew. Sustain. Energy Rev.* 14 (2) (2010) 691–701.

[3] Harmim A, Merzouk M, Boukar M, Amar M. Solar cooking development in Algerian Sahara: towards a socially suitable solar cooker. *Renew Sustain Energy Rev* 2014;37:207–8.

[4] Sedighi M, Zakariapour M. A review of direct and indirect solar cookers. *Sustain Energy* 2014;2:44–8.

[5] “Different Solar Cooker Types”. Available at: <http://www.solarcooking-oven.com/solar-cooker-types.html>

[6] P.P. Otte, Solar cooking in Mozambique—an investigation of end-user's needs for the design of solar cookers, *Energy Policy* 74 (2014) 366–375.

[7] H.M. Toonen, Adapting to an innovation: solar cooking in the urban households of Ouagadougou (Burkina Faso), *Phys. Chem. Earth Parts A/B/C* 34 (1) (2009) 65–71.

[8] T. Sesan, Navigating the limitations of energy poverty: lessons from the promotion of improved cooking technologies in Kenya, *Energy Policy* 47 (2012) 202–210.

[9] Erina Baynojir Joyee, “Design and Construction of a Parabolic Dish Type Solar Cooker”, UG Project report. Department of Mechanical Engineering, KUET, 2014

[10] Md. Rafsunjani, Erina Baynojir Joyee, A. N. M. Mizanur Rahman, “Development and Testing of a Two-axis Tracking Spherical Solar Cooker”, UG Project report. Department of Mechanical Engineering, KUET, 2014

[11] ASTAE –Asia Sustainable and Alternative Energy program, The World Bank, Bangladesh. Available at: <http://web.worldbank.org/WBSITE/EXTERNAL/COUNTRIES/EASTASIAPACIFICEXT/EXTEAPASTAE/0,contentMDK:21042042~menuPK:2900734~pagePK:64168445~piPK:64168309~theSitePK:2822888,00.html>

[12] SWERA Solar Resource Information. URL: <http://swera.unep.net/index.php?id=solar>

[13] T. H. Alam and S. A. Chowdhury, "Solar cooking and its prospects in Bangladesh," *2nd International Conference on the Developments in Renewable Energy Technology (ICDRET 2012)*, Dhaka, 2012, pp. 1-4.

[14] LEWIS, J. J. & PATTANAYAK, S. K. 2012. Who adopts improved fuels and cookstoves? A systematic review. *Environmental Health Perspectives*, 120, 637-645.

[15] OTTE, P. P. 2013. Solar cookers in developing countries-What is their key to success? *Energy Policy*, 63, 375-381.

[16] Tony L. Baptista, Kelly Curnow, Brad J. Hiranaga, Bryan D. Magnus, Denée Perry “A Market-Based Strategy for Introducing Passive Solar Ovens in Kenya”

[17] WENTZEL, M. & POURIS, A. 2007. The development impact of solar cookers: A review of solar cooking impact research in South Africa. *Energy Policy*, 35, 1909-1919

[18] VANSCHOENWINKEL, J., LIZIN, S., SWINNEN, G., AZADI, H. & VAN PASSEL, S. 2014. Solar cooking in Senegalese villages: An application of best-worst scaling. *Energy Policy*, 67, 447-458.

[19] MACCLANCY, J. 2014. Solar Cooking: Why is it Not Yet Global? *Food, Culture & Society*, 17, 301-318.

[20] WILKINS, G. 2010. Technology transfer for renewable energy, Taylor & Francis.

[21] TALKE, K. & HULTINK, E. J. 2010. Managing diffusion barriers when launching new products. *Journal of Product Innovation Management*, 27, 537-553.

[22] ROGERS, E. M. 2010. *Diffusion of innovations*, New York, Free Press

[23] AUSTIN, J., STEVENSON, H. & WEI- SKILLERN, J. 2006. Social and commercial entrepreneurship: .same, different, or both? *Entrepreneurship theory and practice*, 30, 1-22.

Biodiesel Production from Chicken Skin: a Green Energy for Bangladesh

Tamal Chowdhury^{a*}, Hemal Chowdhury^b, Pranta Barua^a, Rabiul Islam^a, Bodiuss Salam^b

^aDepartment of Electrical & Electronic Engineering, Chittagong University of Engineering & Technology, Chittagong, BANGLADESH

^bDepartment of Mechanical Engineering, Chittagong University of Engineering & Technology, Chittagong, BANGLADESH

ABSTRACT

From the slaughtering and processing of livestock, a huge amount of animal discards are produced. Much of this waste biomass is animal fat and skin and these discards can be used to produce biodiesel. In this study, chicken skin was used as raw materials for biodiesel production. Chicken skin was extracted from a local shop and subjected to transesterification. The products of transesterification were Fatty acid methyl esters (FAME) and glycerol. After separating glycerol it was observed that the yield percentage was 35%. Then FAME produced was tested for two parameters namely calorific value, Kinematic viscosity.

Keywords: Chicken skin; Transesterification; Biodiesel.

1. Introduction

Due to the rapid growth of population, consumption of fossil fuels have been increasing day by day. Energy consumption influences increasing energy demand which results in scarcity of energy resources. As a result, reserves of fossil fuels are quickly depleting. Besides excessive use of these fuels result in greenhouse gas emission. So there is a dire need of alternative fuels for transportation and power generation sector. During the past few years, biodiesel has attracted attention as an attractive alternative fuel source [1]. Biodiesel comprised of mono-alkyl esters of long chain fatty acids which can be obtained from vegetable oils, animal fats, waste oils by transesterification in the presence of catalysts [2]. But food versus fuel, high manufacturing costs play an important role in the development of biodiesel production from vegetable oils in developing countries [3]. So finding the non food feedstock is necessary for development of Biodiesel production in developing countries. Chicken skin and fats are the ultimate solution for ending food versus fuel debates. Chicken skin contains between 8 and 20% of the total weight [4]. During the butchering and organ removal process, the fat in the abdominal cavity is normally removed. But the skin, where the subcutaneous fat is located is not removed.

Bangladesh being a developing country depends much on agriculture. This sector contributes to 14.75% GDP of this country [5]. Number of poultry birds for Bangladesh was 320,633 thousand heads in 2016 and number of poultry birds of Bangladesh increased from 62,000 thousand heads in 1967 to 320,633 thousand heads in 2016 growing at an average annual rate of 3.86 % [6]. But unfortunately, no of poultry processing industries in this country is few. Chicken fat is used as feedstock for animals. But a large amount of chicken feathers, skin are considered as waste.

This paper deals with the extraction of biodiesel from chicken skin. Firstly Chicken Feathers were collected from local shops. Then from feathers, chicken skin was obtained. The skin was subjected to transesterification to obtain biodiesel.

2. Experimental Procedure

2.1 Materials: Waste chicken skin, distilled water, potassium hydroxide (catalyst), methanol (solvent) .

2.2 Apparatus:

- 4 beakers
- Electronic balance machine
- 1 magnetic stirrer
- Separating funnels
- Stove
- Glass rods

2.3 Extraction of Fat from Chicken:

Waste chicken skin was bought from a local shop. Then it was manually de-feathered in the kitchen. After de-feathering, the skin was thoroughly washed using tap water. It was then cut into small pieces. Then the skin was cooked for 15 minutes in a pan. Then the oil sample was taken into a beaker (Figure 1) and measured in an electronic balance machine. It was found that the volume of oil was 70mL. Methanolic potassium hydroxide solution was prepared in a beaker using 1.79g of KOH (Potassium Hydroxide) pellets (measured using an electronic balance) dissolved in 60 mL of methanol. After dissolving the pellets into the methanol with the help of a glass stirrer, the methanolic KOH solution was poured into the fat sample. Then it was placed inside the magnetic stirrer apparatus (Figure 2). After stirring for 45 minutes the magnetic bar of the stirrer was taken out by forceps and washed with methanol. Then the stirring sample was placed in a separating funnel for 24 hours

* Corresponding author. Tamal Chowdhury
E-mail addresses: tamalshanto@gmail.com

for separating the layer. It was seen that two layers were formed from transesterification, a red and a yellow layer (Figure 3). The red layer was waste glycerol, the yellow layer was biodiesel. After separating glycerol, biodiesel was extracted (Figure 4). Then it was heated to get rid of any residual catalysts or soaps. In this study, 5 samples were taken and then the samples were taken to test the viscosity and heating value test.

3. Results & Discussion

Table 1 shows the amount of materials involved during the course of Biodiesel.

Table 1: Amount of materials involved in the production of biodiesel

Material	Chicken Skin
Amount of raw material(g)	200
Weight of oil (g)	179
Volume of Methanol Added (mL)	26ml
Mass of KOH Pellets Added (g)	1% of total weight of oil with beaker(179g)
Volume of Biodiesel Produced (mL)	80

3.1. Calculation to find how much methanol and KOH required:

Weight of oil (with beaker) = 179mL
 Average molecular weight = 858.21g
 Now converting to mole = 0.21 mol

Considering 1:3 molar ratio, mole of CH_3OH = 0.21×3
 = 0.63 mol

Now 1mol CH_3OH = 32gm
 0.63 mol CH_3OH = 0.63×32 gm
 = 20.16gm

& volume of methanol = $20.16 / 0.79$ (density of methanol) = 25.51 mL

Amount of KOH = 1% of 179g
 = 1.79g

Biodiesel obtained from chicken skin =

= Volume of biodiesel extracted / Amount of raw material

= 35% (considering w/w %)

Here m is calculated by using the following equation

$m = \text{density} \times \text{volume}$

3.2. Thermo physical test:

Table 2: The fuel property comparing with diesel following the testing method of ASTM

Table 2: Thermo physical properties of biodiesel

Property	Diesel	Biodiesel	Experimented Biodiesel	Test Method
Density(g/cc)	0.8-0.85	0.87-0.88	0.874	ASTM D1448
Kinematic Viscosity (Cst)	2-5	2-6	5.8	ASTM D445
Net Calorific value(MJ/Kg) (Lower calorific value)	40-50	40-45	41	ASTM D6751

A typical bomb calorimeter was used to measure net calorific value. To measure viscosity, Saybolt viscometer was used. The thermo physical property result shown above states that, the experimented biodiesel fulfills all requirements of fuel property.



Fig. 1 Manual extraction of oil from pan

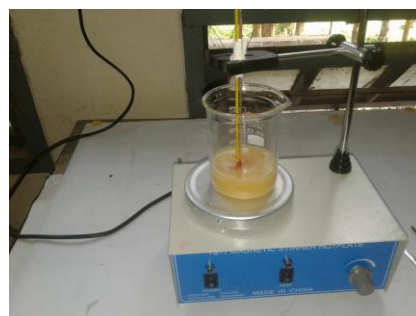


Fig. 2 Magnetic stirring



Fig. 3 Separation process in separating funnel



Fig. 4 Extracted biodiesel after separation

4. Conclusion:

This paper deals with the production of biodiesel from chicken skin. In this paper, the yield percent of biodiesel is found 35% from chicken skin (200gm) and the fuel property are checked to ensure the property of biodiesel. Above property shows that the energy content of diesel is much higher than biodiesel but the density of diesel is lower than biodiesel. The kinematic viscosity of diesel and biodiesel are close enough. By increasing yield percentage of biodiesel, biodiesel can be used as an alternative fuel to diesel.

ACKNOWLEDGEMENTS

The authors would like to thank Chittagong University of Engineering & Technology's Mechanical and Chemistry department for providing necessary equipments in order to finish the work. We would also like to thank Dr.Arafat Rana, Assistant Professor of Chittagong University of Engineering & Technology for providing then magnetic stirrer. The authors would also like to thank Azad family for helping in the biodiesel extraction process)

REFERENCES

[1] Shay E.G. 1993. Diesel Fuel from Vegetable Oil: Status and Opportunities. *Biomass Bioenergy*. 4(4):227-242.

- [2] Moser B.R., 2009. Biodiesel Production, Properties and Feedstocks, *InVitro Cell.Dev. Biol.-Plant*. 45:229-266.
- [3] Sylvester C. Izah and Elijah I. Ohimain, "The challenge of biodiesel production from oil palm feedstock in Nigeria".
- [4] Lilia L. Méndez-Lagunas^{1, *}, Samuel Siles-Alvarado², Juan Rodríguez-Ramírez¹, Laura A. Aquino-González , "Fatty Acid Profile Composition of Chicken Skin".
- [5] <http://www.moa.gov.bd>. Accessed: 4th July 2018
- [6] <https://knoema.com>. Accessed: 2nd July 2018.

Feasibility of Integrated Pico Hydro System at Choto Komoldoho, Mirsharai

Tamal Chowdhury^{a*}, Hemal Chowdhury^b, Piyal Chowdhury^c, Abul Hasnat^a, Birol Barua^a

^{a*} Department of Electrical & Electronic Engineering, Chittagong University of Engineering & Technology, Chittagong, BANGLADESH

^b Department of Mechanical Engineering, Chittagong University of Engineering & Technology, Chittagong, BANGLADESH

^c Chittagong Collegiate School & College, Chittagong, BANGLADESH

ABSTRACT

Renewable energy can be an effective option to meet up the electricity demand of people. Where grid connection is not possible, power generation from renewable energy resources can help to meet up the load of these off-grid places. This present study aims to find out the feasibility of Pico hydro scheme on the waterfall of Choto Komoldoho, Mirsharai, Chittagong, Bangladesh. The Pico hydro system was integrated with PV to form a hybrid system. The whole system was simulated by Homer software. It was found from the simulation that the cost of energy is \$ 0.270 /kWh which is 21.6 taka in BDT (1US=80 Taka).

Keywords: Pico hydro, Choto Komoldoho, Homer.

1. Introduction

In the era of fast technological development, renewable energy sources have drawn a lot of attention for generating electricity. Different renewable energy sources like wind, biomass, tidal/wave, micro-hydro and PV are used as they are inexhaustible in nature and their capability of delivering clean power. These renewable energy sources are the best alternative for power generation where grid connection is not available and where grid connection cost is high. By combining several locally available renewable sources to form a hybrid system this problem can be solved as it will ensure both the quality and reliability of electricity supply [1-5]. Hydro-power plant is a plant that converts the kinetic energy of the falling water into mechanical energy by the turbine. This turbine then drives an electric generator to produce electrical energy. People started using hydro-power to produce mechanical work for mainly agriculture purposes thousands of years ago. In 1882, the first hydro-power plant was built to produce electric energy. It was considered the first technology used to produce electricity from a renewable source [6]. Now almost 20% of worldwide needs are fulfilled by hydropower plant [7]. Hydro-power plants can be classified according to size or capacity as shown below [6] in table 1.

Table 1: Hydro system classification

Hydropower plant	Capacity
Pico Hydro	< 0.005 MW
Micro Hydro	< 0.1 MW
Mini Hydro	< 1 MW
Small Hydro	between 1-100 MW
Medium Hydro	>100 MW
Large Hydro	>500 MW

Being a developing country Bangladesh faces difficulty in ensuring reliable power to everywhere in the country. Due to the lack of availability of transmission and distribution network infrastructure and lack of adequate generation, about 45% of the population remains off-grid and grid connected places face acute load shedding [8]. For developing their sustainable energy, Bangladesh government has adopted many renewable schemes. At present natural gas contributes to 80% of total electricity generation in Bangladesh [8]. Most of the power plant in Bangladesh operates on natural gas, few on oil and coal. But due to the shortage of gas, several units of power plants have stopped working in Chittagong, the port city of Bangladesh [9]. Kaptai Hydropower plant is the only renewable energy source which is connected to the grid. It accounts for around 2.58% of total electricity generation [8]. To improve the condition Bangladesh government has adopted Renewable Energy Policy. It obligates that 5% of total electricity production will be achieved by 2015 and 10% by 2020 [8].

* Corresponding author.

E-mail addresses: tamalshanto@gmail.com

2. OBJECTIVES OF THIS RESEARCH

The objective of this research is to find out the feasibility of Pico hydro scheme at Choto Komoldoho, Chittagong, Bangladesh. First, the available head and then the available flow rate were measured to estimate the power generation capability from this site. Then Homer software was used to simulate the proposed hybrid system in order to find out per unit cost of the simulated system.

3. Data collection

Choto Komoldoho, Mirsharai, Bangladesh.

A. Survey on Choto Komoldoho waterfall

Choto Komoldoho is an unfamiliar trail. Several streams can be found on this trail. It is located between Dhaka Chittagong highways, Mirsharai. The survey was conducted in January 2018.

Distance: 1.5 hours of bus journey from Chittagong town.

Availability of Water: All seasons.

Measuring flow for Choto Komoldoho waterfall:

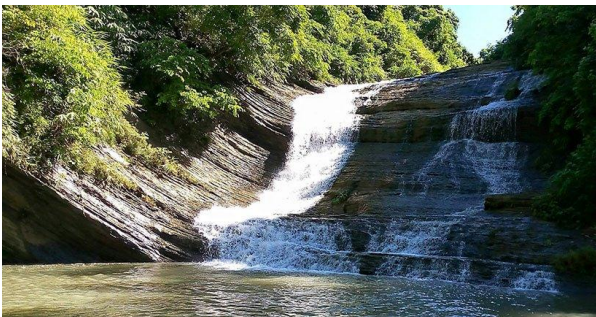


Figure 1: Choto komoldoho

To measure the flow rate bucket method was used. For this, a bucket of 10 liters (2.65gallon) was used. To measure the time taken to fill up the whole bucket, stopwatch was used.

Table 2: Flow rate measurement

No of observation	Time (s)
01	5.05
02	5.02
03	6.02
04	5.20
05	5.10
06	5.20
07	6.30
08	6.00
09	6.10
10	5.4

Average time, $t = 5.5$ s

Flow rate, $Q = 28.90$ gal/min
 $= 2.2$ lit/s

$= .0022$ m³/s

The flow rate was found after dividing the volume of the bucket by average time.

Actual Flow: $0.83 * 0.022 = .001826$ m³/s. (A correction factor 0.83 should be used as the velocity of upper and lower surface of the stream is not equal due to the wind and other natural impacts)

Head, H = 140 feet = 42.67m

Considering 8% losses of the available head the net head becomes 39.26 m.

Theoretical Power:

For 50% overall efficiency,

The Power, $P = \text{efficiency} (\%) * \text{flow rate} * \text{head} (m) * \text{Gravitational acceleration} * \text{Density of water}$
 $= 0.5 * 0.001826 * 39.26 * 9.81 * 1000 = 0.35$ KW

4. Simulation

By renewable software ‘Homer’ [10], per unit cost analysis can be evaluated of a hybrid system.

A process to design integrated Hydropower plant in ‘Homer’:

A. Components Selection:

For designing this model first ‘Add/Remove’ button ‘Hydro and primary load, PV, Hydro and Converter, Battery’ is selected (figure 2).

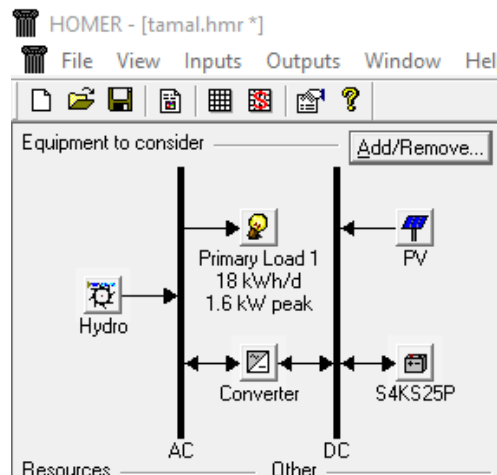


Figure 2: Optimum Model

B. Renewable Resources Input

Solar Resource Data input

Twelve months of solar radiation data for ‘Mirsharai was collected’ using ‘Homer’ Software via the internet (figure 3).

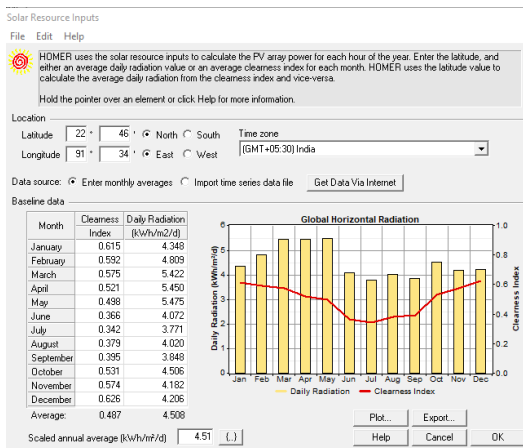


Figure 3: Daily radiation data of Mirsharai.

Hydro Resource Data Input:

The survey was conducted in January 2018. Rainy season in Bangladesh starts from the middle of June and ends to the middle of August. Based on the summer and rainy season of the country, hydro data have been inputted (figure 4).

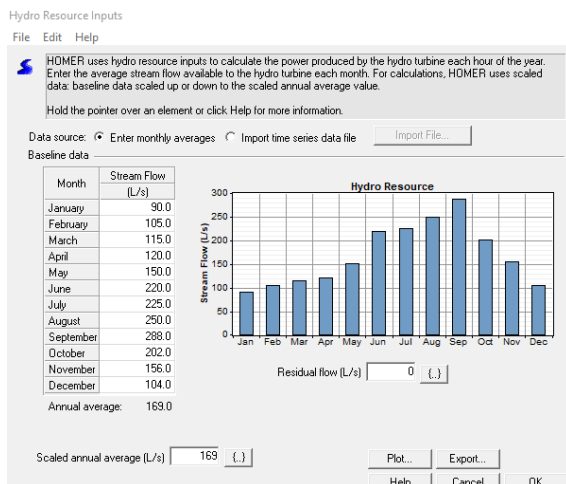


Figure 4: Hydro Resource data

C. Cost and Size Parameters Input in 'Homer

For this renewable project, the standard capital cost has been inputted in Homer.

Table 3: Capital cost of various components in Homer

Input Parameters	Values
7 KW PV	2520 \$/year
Battery Capital Cost	3150 \$/year
Converter Capital Cost	158 \$/year
0.359 KW Pico Hydro Capital Cost	1500 \$/year

For this renewable project operation and maintenance cost with replacement cost has also been inputted in Homer.

Table 4: Operation and maintenance cost with replacement cost of various components in Homer

Input Parameters	Values
Hydro Operation & Maintenance Cost	100 \$/year
Hydro System replacement Cost	400 \$/year
Solar System replacement Cost	2520 \$/year
Solar Operation & Maintenance Cost	70 \$/year
Battery Operation & Maintenance Cost	70 \$/year
Battery replacement Cost	2450 \$/year
Converter Operation & Maintenance Cost	10 \$/year
Converter replacement Cost	158 \$/year

D. Per unit Cost Simulation

To find the optimum sizes various sizes have been considered in this simulation of Homer. After simulation, it was found that the optimum size for PV is 7KW, 7 batteries, 2 KW converter is required. From simulation result, it was found that COE is \$0.270/KW which is 21.6 taka in BDT (1US=80 Taka).

Figure 5 depicts per unit cost of the proposed hybrid system.

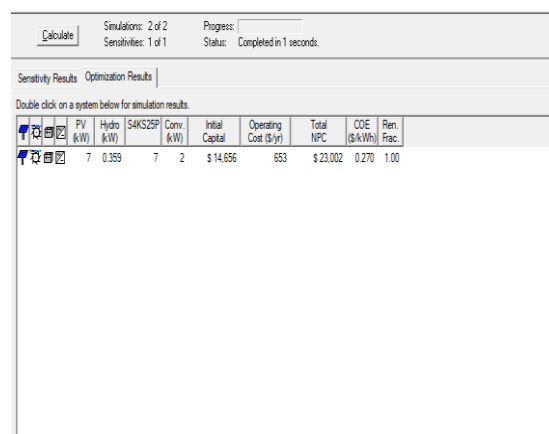


Figure 5: Per unit cost result.

5. Conclusion

In this paper, a hybrid system was designed to meet up the load for Choto Komoldoho, Mirsharai. The system comprised of PV array, Pico hydro scheme, converter and battery. It was found that the system meets the demand when the cost of energy is \$0.270/KW. It was

also found that the optimum size of PV panel was 7 KW. The government should emphasize more renewable energy projects like Pico hydro to reduce pressure on fossil fuel. Being a renewable form of energy it will reduce environmental pollution.

REFERENCES

- [1] J.K. Kaldellis, K.A. Kavadias, “Cost--benefit analysis of remote hybrid-wind-diesel power stations: Case study Aegean Sea islands”, *Energy Policy*, Vol. 35, No. 3, pp. 1525-1538, 2007.
- [2] Nayar C.V, Lawrance WB, Phillips SJ, “Solar/wind/diesel hybrid energy systems for remote areas”, *Energy Conversion Engineering Conference IECEC-89*, Vol. 4. pp. 2029-34, 1989.
- [3] O.C. Onar, M. Uzunoglu, M.S. Alam, “Dynamic modeling, design and simulation of a wind/fuel cell/ultra-capacitor-based hybrid power generation system”, *Journal of Power Sources*, Vol. 161, No. 1, pp. 707-722, 2006.
- [4] P.K. Goel, B. Singh, S.S. Murthy, N. Kishore, “Isolated Wind—Hydro Hybrid System Using Cage Generators and Battery Storage”, *IEEE Transactions on Industrial Electronics*, Vol.58, No.4, pp.1141-1153,2011.
- [5] Th.F. El-Shatter, M.N. Eskandar, M.T. El-Hagry, “Hybrid PV/fuel cell system design and simulation, *Renewable Energy*”, Vol. 27, No.3, pp. 479-485, 2002.10A1-1139
- [6] Nasr Al Khudhiri, Sharul Sham Dol, Mohammad S. Khan, *Design of Hydro-power Plant for Energy Generation for a Mid-size Farm with Insufficient Water Distribution Networks.*
- [7] Stefan BREBAN, Mehdi NASSER, Arnaud VERGNOL, Vincent COURTECUISS2, Benoît ROBYNS, Mircea M. RADULESCU, *Study of a grid-connected hybrid wind/micro-hydro power system.*
- [8] Alimul Haque Khan ,A thesis on Analysis of an Electrical Microgrid in a Remote Area Based on Distributed Energy Resources, Bangladesh University of Engineering & Technology, Dhaka.
- [9] <https://www.dhakatribune.com/bangladesh/nation/2017/12/14/severe-gas-crisis-hits-port-city-chittagong/> Accessed: 4th July 2018
- [10] Homer Energy, URL: <http://www.homerenergy.com/> Accessed: 4th July 2018

Analysis of a Solar PV System for Aeration System in Aquaculture

Tamal Chowdhury^{a*}, Hemal Chowdhury^b, Piyal Chowdhury^c, Abul Hasnat^a, Birol Barua^a, Rabiul Islam^a

^aDepartment of Electrical & Electronic Engineering, Chittagong University of Engineering & Technology, Chittagong, BANGLADESH

^bDepartment of Mechanical Engineering, Chittagong University of Engineering & Technology, Chittagong, BANGLADESH

^cChittagong Collegiate School & College, Chittagong, BANGLADESH

ABSTRACT

Artificial fish ponds harvester often face the problem of lacking the oxygen content in ponds. If there is too much oxygen, fish can even get sick. This will result in a great reduction of income for fish harvesters. Solar aeration can play a vital role in improving the water quality by removing dissolved gases. This aeration system can be applicable where electricity is not available. This paper discusses the feasibility of solar aeration system in rural places of Bangladesh. Homer software was used to simulate the aeration system for small scale ponds of a place called Godagari, Rajshahi. It was found that the optimal sizing of photovoltaic 2 kW, 2 battery of 400 Ah and inverter of 0.6 kW and Cost of energy is about 0.463 \$/kWh which is 37.04 taka in BDT (1 US=80).

Keywords: Aquaculture; Solar aeration; Homer.

1. Introduction

Aquaculture provides food security to more than 20 million people worldwide [1]. As one of the fastest growing industries in the world, it maintained an annual rate of 7% between 1970 and 2000 and 6.2% between 2000 and 2012 [1]. In developing countries, such as Bangladesh fish forms a staple diet obtaining 57% of their protein intake from fish [2]. Between the period 1985- 2013, aquaculture grew at a rate more than twice that of marine and capture fisheries, contributing about 45% of Bangladesh's total annual fish production [3]. So, this industry is a major economic driver contributing to 4.4% of the GDP in Bangladesh [4]. About 73% of rural people are involved in fish farming practice [5]. People in rural area of Bangladesh is suffering from extreme hardship and poverty. In order to reduce rural poverty rate, Bangladesh government has turned to aquaculture, a way of meeting the nutritional needs of the rural poor, a fifth of whom are suffering from chronic food insecurity and malnutrition [6]. Government's efforts have resulted in promoting small scale form of aquaculture. According to a report, about 20% of rural households have a homestead pond, covering a combined area of 265,000 hectares [7]. Farmers operating these ponds do not have any technical knowledge. Besides, these ponds are used for multipurpose process. As a result water quality becomes bad and it hampers fish productivity.

This paper is an attempt to check the feasibility of solar aeration for a place called Godagari, Rajshahi. Mathematical modeling has been done to find the no of solar modules and capacity of battery. Simulation is performed on Homer software to find the feasibility of the system. This study is developed from the reference no [8].

2. Aeration

Air contains approximately 20.95% oxygen. The pressure of oxygen in the atmosphere drives the oxygen in the water until the pressure of oxygen in the water is equal to pressure of oxygen in the atmosphere. When these pressures are equal, the water is said to be equilibrium with dissolved oxygen (DO). Several factors such as temperature, salinity affect dissolved oxygen concentration. When water contains more DO than a specific level for a given temperature and pressure, the water is called supersaturated. Water may also contain less DO than saturation. It may be happened at night as this is the period when oxygen content is low. At night dissolved oxygen declines due to respiration of plants, fishes and other pond organisms. In production ponds, DO may decrease by 5–10 mg l⁻¹ at night, and in un-aerated ponds, DO concentrations at sunrise may be less than 2 mg l⁻¹. The less percentage of dissolved oxygen can severely affect aquaculture [9].

The process of bringing water and air into close contact by exposing drops or thin sheets of water to the air or by introducing small bubbles of air and letting them rise through the water is called Aeration. Aeration is done by aerators. Aerators are generally two types; splashers and bubblers. Aerator improves water quality by mixing oxygen from atmosphere to water. As a result, dissolved oxygen content increases [10].

3. Cost for Different Types of Aeration System

There are mainly three types of aeration system such as: solar, windmill & electric aerator. The cost of a aeration system is determined by a combination of up front capital investment, annual operating costs, annual maintenance costs and projected life expectancy. Capital investment can be low as \$ 500 for a shallow pond while it can be high as \$8000 for a large

* Corresponding author. Tel.: +88-01709300178

E-mail addresses: icmieekuet@gmail.com

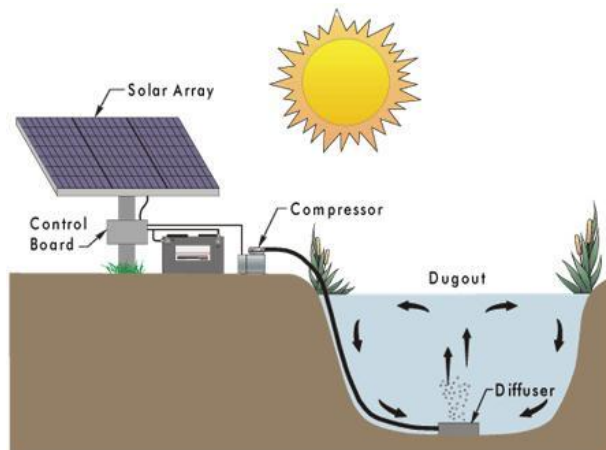
aquaculture [11]. Operation cost is determined by the number of amps needed to power an electric motor multiplied by the electricity cost in the area [11]. Table 1 shows the capital investment(CI) , average annual cost(AOC), average operation cost(AC), annual maintenance cost (AMC) and life expectancy(LE) of different aeration system [11].

Table 1: Assessment of different cost and life expectancy of different aeration systems.

Aeration systems	CI \$	AOC \$	AMC \$	LE Years	AAC \$
Electric	750	180	35	4	402.50
	1500	240	35	5	575.00
	2500	240	35	5	775.00
Solar	2995	0	50	10	349.50
	6500	0	50	10	700.00
Windmill	1500	0	75	20	150.00
	2500	0	75	20	200.00
	3500	0	75	20	250

4. Solar aeration

Solar aeration system consists of solar arrays (solar panels) that convert sunlight into Direct Current (DC) electricity. Then it can be used directly or stored in batteries for use at night or on cloudy days.



When the sun shines, charges are stored on battery. The battery powers a compressor that forces air through a diffuser at the bottom of the pond. Here in figure 1 arrows indicate that, the movement of air throughout the entire volume of water.

Solar aeration system consists of:

- 1) Solar panels (sized to supply enough power for calculated consumption)
- 2) Batteries to store excess power
- 3) Compressor
- 4) Inverter
- 5) Air diffuser
- 6) Weighted feeder hose

It is same as electric aerator except solar power acts as its power source.

5. Design procedure

The whole procedure of PV system sizing is given below

- Load Calculation
- Assess solar resource
- Select days of autonomy
- Size battery bank
- Size module array

5.1 Load calculation

Aeration is necessary when oxygen content is lower in the air. So aeration will be needed in the evening. Here the time period considered from 10 p.m. to 6 a.m. Table 2 shows load calculation for Godagari.

Table 2: Load calculation

No	Utilization	Power	Value (unit)	Working time	Energy demand (kwh)
1	Diffuseror blower	70W	1	8 hours(10 p.m.-6 a.m.)	0.560
2	Indoor lighting	20W (CFL)	2	4 hours(6 p.m.-10 p.m.)	0.160
3	outdoor lighting	20W (CFL)	4	12 hours(6 p.m.-6 a.m.)	0.960
					Total=
					1.680 kwh

So the daily load is 1.680 kwh.

5.2 PV system sizing

For solar resource we have considered a place called Godagari (24°28'N 88°19.8'E).It is an Upazila of Rajshahi district. This place's scaled annual average solar resources are 4.8 kWh/m²/d[13]. Figure 2 contains the daily radiation of Godagari.

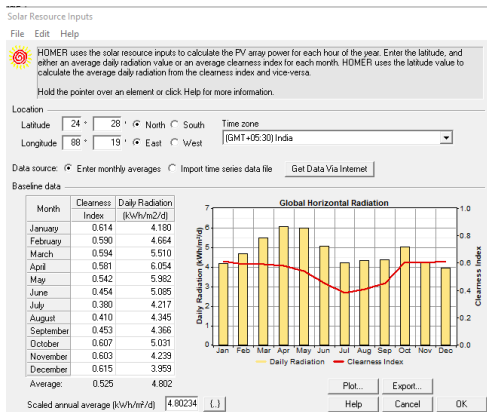


Fig. 2: Daily radiation of Godagari [9]

From the Figure 2, it can be seen that the least unfavorable month for solar radiation is December (3.95). Now calculating peak solar hour (PSH) for the worst month is 3.95h/day.

Here peak solar hours are the no of hours of 1kW/m² irradiance that would yield the same amount of energy. Now the system comprises of

- 1) PV
- 2) Cables
- 3) Charge regulator
- 4) Battery
- 5) Inverter
- 6) Load

So, the required power (for PV) is

$$P_{PV} = (\text{Load}) \div (n_{\text{bat}} * n_{\text{reg}} * n_{\text{inv}} * n_{\text{wir}})$$

$$= (1.6 \text{ kWh/day}) \div (0.61)$$

$$= 2.62 \text{ kWh/day}$$

Assumption:

- Battery efficiency, $n_{\text{bat}} = 80\%$
- Inverter efficiency, $n_{\text{inv}} = 90\%$
- Wiring efficiency, $n_{\text{wir}} = 95\%$
- Charge regulator efficiency, $n_{\text{reg}} = 90\%$

$$\text{Peak power } (P_{\text{peak}})$$

$$= P_{PV} \div (\text{PSH})$$

$$= (2.62 \text{ kWh/day}) \div (3.95 \text{ h/day})$$

$$= 0.67 \text{ kWp}$$

String length

Operating voltage $V_{DC} = 48 \text{ V}$
 Module voltage $V_m = 12 \text{ v}$ (assuming: string with four module)
 String length is $N_s = V_{DC} \div V_m$
 $= 4$

No of strings

(Assume 50wp module)
 $N_p = P_{\text{peak}} \div (N_s * P_m)$
 $= 0.67 \text{ kWp} \div (4 * 50)$
 $= 3.35 \approx 4$

So the total no of modules are

$$N = N_s * N_p = 4 * 4 = 16$$

So the required area $A = N * A_m$
 $= 16 * 0.4$ (Assuming per module area is $A_m = 0.4 \text{ m}^2$)
 $= 6.4 \text{ m}^2$

Battery Capacity (C_B):

$$C_B = (\text{DOA} * \text{load}) \div (\text{DOD})$$

Here,

- DOA is days of autonomy
- DOD is depth of discharge

Days of autonomy is the no of consecutive days without being recharged a battery bank can provide energy to the load. It would be slightly less than the maximum no of continuous cloudy days for the site.

When selecting a battery depth of discharge is the one of the key figure that should be considered. DOD is the rate how deeply the battery is discharged.

Assuming DOA is 5 days and DOD is 0.7

$$\text{Battery capacity } C_B = \frac{5 \times \left(\frac{1.6 \text{ kWh}}{\text{day}} \right)}{48 \text{ volt} \times 0.61} \div 0.7$$

$$= 392 \text{ Ah}$$

6. System Modeling

The system considered here is an exemplary model for fulfilling the energy demand for Godagari. The system consists of PV array, Battery, Inverter and electrical load. HOMER Software is used for modeling where capital cost, replacement cost and O&M cost for each component has been considered as input parameters.

6.1 PV Array

2 kW PV panels have been considered here. The capital cost of 1KW panel is considered to be \$500.00 and replacement cost is \$500.00 with operating and maintenance cost of \$10.00 per year. Life time of each panel have been considered 25 years with derating factor of 80. Figure 3 shows the PV inputs in Homer.

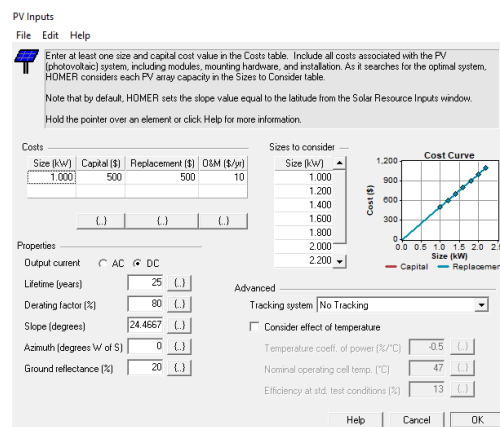


Fig. 3: PV inputs in Homer

6.2 Converter

DC to AC converter of 0.6 kW has been considered in the simulation. The capital and replacement cost for per kilowatt is considered here to be \$79 and \$79 respectively with O&M cost of \$5 per year. The lifetime is considered 15 years with 90% efficiency. Figure 4 shows the converter inputs of Homer.

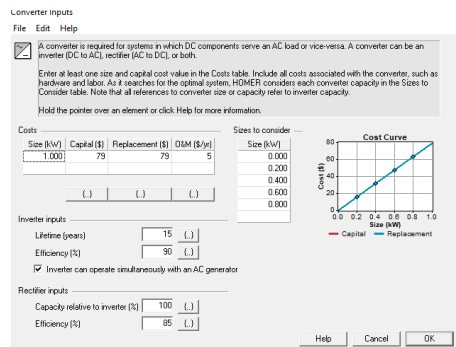


Fig.4: Converter inputs in Homer.

6.3 Energy Storage

For energy storage batteries have been considered in the simulation. The Model used is USB-US 305 with nominal capacity of 400 Ah and throughput is considered to be 673.20kWh. The capital and replacement cost is considered to be \$450 and \$350 respectively. The O&M cost is considered \$5.000 per year.

7. Result

From Figure 5, it can be seen that the optimal sizing of photovoltaic 2 kW, 2 battery of 400 Ah and inverter of 0.6 kW and COE is about 0.463 \$/kWh. Here COE is quite high. It may be due to lack of availability of components in that proposed location. Lack of availability of components result in high cost.

Sensitivity Results		Optimization Results						
Double click on a system below for simulation results.								
	PV (\$/W)	US-305 (kWh)	Comp. (kWh)	Initial Capital	Operating Cost (\$/yr)	Total NPC	COE (\$/kWh)	Ren. Frac.
	2.0	2	0.6	\$ 1,947	120	\$ 3,480	0.463	1.00

Fig. 5: Simulation result

8. Conclusion

In this paper, a design optimization of solar powered aeration system for a small-scale of fish pond by HOMER software is presented. This system meets the feasible demand of 1.60 kWh/day load by Photovoltaic 2 kW, 2 battery of 400 Ah, Inverter 0.2 kW when COE is about 0.463 \$/kWh. Solar aeration can be a useful method in improving the quality of water in

Bangladesh. Many farms which suffer loss due to bad water quality can use this method to improve not only the water quality but also improve the productivity of fish.

REFERENCE

- [1] FAO, The state of world fisheries and aquaculture, vol. 2014, 2014.
- [2] High Level Panel of Experts on World Food Security, "Sustainable fisheries and aquaculture for food security and nutrition," Fao, no. June, pp. 1–119, 2014.
- [3] FRSS, 2014. Fisheries Statistical Yearbook of Bangladesh. Vol. 30. Fisheries Resources Survey System (FRSS), Department of Fisheries, Bangladesh., 2014.
- [4] J. L. Fiedler, K. Lividini, E. Drummond, and S. H. Thilsted, "Strengthening the contribution of aquaculture to food and nutrition security: The potential of a vitamin A-rich, small fish in Bangladesh," Aquaculture, vol. 452, pp. 291–303, 2016.
- [5] Mohammad Ferdous Alam and Madan Mohan Dey. A Background Paper on Bangladesh Fisheries.
- [6] Ben Belton, Nasib Ahmed, and Khondker Murshed-e-Jahan. 2014. Aquaculture, employment, poverty, food security and well-being in Bangladesh: A comparative study. Penang, Malaysia: CGIAR Research Program on Aquatic Agricultural Systems. Program Report: AAS-2014-39.
- [7] Ben Belton et al. Review of aquaculture and fish consumption in Bangladesh Studies and Reviews 2011-53. The WorldFish Center, November 2011.
- [8] Iqib Prasetyaningsari, Agus Setiawan and Ahmad Agus Setiawan, "Design optimization of solar powered aeration system for fish pond in Sleman Regency, Yogyakarta by HOMER software."
- [9] Boyd, C.E., 1990. Water Quality in Ponds for Aquaculture, Alabama Agricultural Experiment Station, Auburn University, Alabama, pp. 482.
- [10] Boyd, C.E., Teichert-Coddington, D., 1992. Relationship between wind speed and reaeration in small aquaculture ponds. Aquac. Eng. 11, 121–131.
- [11] <https://www.outdoorwatersolutions.com/resources/aeration-costs>. Accessed: 28 october ,2018
- [12] https://www.google.com/search?q=solar+aeration+system&source=lnms&tbm=isch&sa=X&ved=0ahUKEwjGz5bt9KDbAhUIpo8KHdxOD6YQ_AUICygC&biw=1366&bih=609#imgrc=xVf229MFa9CKWM: Accessed: 4th July 2018.
- [13] The HOMER energy website, <http://www.homerenergy.com>. Accessed: 2nd July 2018

Assessment of Water Saturation Using Archie's Formula, Indonesia Equation and Simandoux Model of Shahbazpur Gas Field (SBZ 01)

Jebin Fouzia*, Shehab Uddin

Department of Petroleum and Mining Engineering, Chittagong University of Engineering & Technology, Chittagong, BANGLADESH

ABSTRACT

Reservoir quality assessment is a process for quantitatively assigning reservoir properties, recognizing geologic information and uncertainties in spatial variability. A petroleum reservoir is a heterogeneous system with large intrinsic complexity. A good reservoir is one that is commercially productive; it produces enough oil or gas to pay back its investors for the cost of drilling and leaves a profit. The improvement of reservoir performance analysis is one of the most important existing and emerging challenges to geoscientists and engineers. The aim of this study is to use an integrated technique in computing an essential parameter - water saturation of Shahbazpur gas field (SBZ 01). This study shows the assessment of water saturation using Archie's formula, Indonesia equation and Simandoux model with the help of wireline log data. Well logging plays an essential role in the determination of the production potential of a reservoir. The process involves lowering a number of instruments into a borehole with the purpose of collecting data at different depth intervals. The assessment of water saturation is undertaken to determine the reservoir's capability to both store and transmit fluid. According to wireline log data analysis, the average water saturation found from Archie's formula is 17.30 percent, by Indonesia equation 40.00 percent and by Simandoux model 52.14 percent. This analysis is very important to predict the overall performance of a reservoir as well as to enhance the production and life of the reservoir. The aforementioned analyzed results can be used for further reservoir evaluation and reservoir properties analysis.

Keywords: Water Saturation, Reservoir Quality, Archie's Formula, Indonesia Equation, Simandoux Model

1. Introduction

The quality of a reservoir is defined by its hydrocarbon storage capacity and deliverability. A reservoir rock is a subsurface rock that has effective porosity and permeability which usually contains commercially exploitable quantity of hydrocarbon or fluid. [1]

One of the key issues in reservoir quality assessment using well log data is the prediction of petrophysical properties such as porosity and water saturation. Over the life of the reservoir, many crucial decisions depend on the ability to accurately estimate the formation permeability and water saturation.

However, the prediction of such properties is complex, as the measurement sites available are limited to isolated well locations. This requires an integrated knowledge of the tool responses and understanding of the geology of the region, together with various mathematical techniques in order to derive interpretation model that relates the log data to the petro physical properties. Establishment of an accurate well log interpretation model is not an easy task due to the complexity of different factors that influence the log responses. [2]

2. Overview of Shahbazpur Gas Field

The principal objective of drilling Shahbazpur well no. 1 was to investigate hydrocarbon potentiality, specially

the gas play in the sandstone of Miocene age and to collect detail Geological information of the southern platform of Bengal fore deep which has not yet been studied due to the lack of sufficient well. [3]

Moreover, drilling of Shahbazpur well 1 would be considered to study the stratigraphy, structure, sedimentation, condition of deposition, identification of the onset of overpressure, source rock potential of the sediments and the migration and accumulation of Hydrocarbons. In this regards all available previous Geological and other related information were re-evaluated and it was observed that the best structure to be taken for immediate exploration was the Shahbazpur structure. [3]

3. Location of the Study

The Shahbazpur Gas Field lies in the Bhola District in the South part of Bangladesh. Shahbazpur gas field was discovered in 1994 with an estimated reserve of 0.465 trillion cubic feet of gas, out of which 0.35 trillion cubic feet is extractable from the first and second well. [4]

Name of the well : Shahbazpur
Classification : Exploratory
Proposed depth : 3750 m
Location : 90° 45' 13.8''
22° 27' 55.7''
Ground elevation : 3.3 m MSL
Type of trap : Anticlinal

* Corresponding author. Tel.: +88-01682761593
E-mail addresses: jebin.fouzia@yahoo.com

Primary objective : Hydrocarbon prospect in Miocene

The entire area is a deltaic flat land and composed of recent sand, silt and clay. The surface topography of the area is represented by crops field with river canals. [4]

The highest elevation is 3.3m in central part of the island and gradually decreased towards the margin of the island. The area is surrounded by the Bay of Bengal in the south, Tetulia river in the west, Shahbazpur river in the east and Ganeshpura river in the north. [4]

4. Research Methodology

Water saturation is the ratio of water volume to pore volume. Water bound to the shale is not included, so shale corrections must be performed if shale is present. We calculate water saturation from the effective porosity and the resistivity log. [5]

The Archie equation was the first empirical model built (1942) to estimate the water saturation in non-conductive matrix rocks. It usually works well with clean clastic sandstones and carbonate rocks. The Indonesia equation works well with fresh formation water. The parameter Rshale (resistivity of shale) is usually taken from the resistivity reading of a nearby pure shale, assuming that the clay cements & silt, and the shale nature, are similar to those of the shaly sand. The Simandoux model for the resistivity log follows the classical form also, but it must be linearized, so the result does not often look similar to the usual response equation. [6]

Lithology has been identified with the help of spectral and gamma ray log. After that hydrocarbon bearing zone is detected by the interpretation of other logs-resistivity, density-neutron. Shale volume has been calculated by using gamma ray log as well as true resistivity method and then the results have been compared and then reservoir thickness has been determined by using the gamma ray log data. The interpretation is also continued by comparing with resistivity and porosity logs. Reservoir area has been determined by seismic data. Then the formation water resistivity has been generated by interpretation of resistivity log. Inverse Archie's method has been used in this study.

4.1 Determination of Water Saturation

Water saturation has been determined using three method- Archie's formula, Indonesia equation as well as Simandoux model.

Archie Equation to calculate the water saturation is as follows:

$$S_w = \sqrt[n]{\{(a \times R_w) / (\Phi^m \times R_t)\}} \quad (1)$$

Simandoux model for calculating water saturation is:

$$S_w = \{(0.4R_w / \Phi_e^2)\} \times [\sqrt{\{(V_{sh}/R_{sh})^2 + (5\Phi_e^2) / (R_w \times R_t)\}} - (V_{sh}/R_{sh})] \quad (2)$$

Indonesia equation for estimation of water saturation:

By using Indonesia model water saturation in both the uninvaded zone and the flushed zone can be calculated. Water saturation for un-invaded zones,

$$S_w = (1/R_t) [\{V_{cl}^{(1-0.5V_{cl})} / (R_{cl})^{0.5}\} + \{\Phi_e^{0.5m} / (aR_w)^{0.5}\}] \quad (3)$$

Water saturation for flushed zone,

$$S_{xo} = (1/R_{xo}) [\{V_{cl}^{(1-0.5V_{cl})} / (R_{cl})^{0.5}\} + \{\Phi_e^{0.5m} / (aR_{mf})^{0.5}\}] \quad (4)$$

5. Estimation of Water Saturation

Water saturation is calculated using three different methods. The value of average water saturation estimated from Archie, Indonesia and Simandoux model are 17.3%, 40%, 52.14% respectively.

Values of derived water saturation are shown in Table 1 and details calculation of estimating water saturation using Archie's formula is shown at Appendix 1.

The maximum water saturation using Archie's formula is determined at depth of 2599 m. The maximum value is 0.215. And the minimum value is 0.126 at depth of 2592 m. Value of Archie's exponent is taken as 1.4 and the value of cementation factor is taken as 1.54. The determined water saturation from Archie's formula are shown in Fig. 1.

Table 1 Values of estimated water saturation

Depth	S_w (Archie's)	S_w (Indonesia)	S_w (Simandoux)
2588	0.195	0.39	0.49
2589	0.165	0.39	0.52
2590	0.204	0.43	0.56
2591	0.198	0.40	0.52
2592	0.126	0.37	0.54
2593	0.141	0.34	0.43
2594	0.148	0.34	0.43
2595	0.154	0.38	0.47
2596	0.165	0.40	0.52
2597	0.164	0.38	0.47
2598	0.198	0.41	0.53
2599	0.215	0.51	0.69

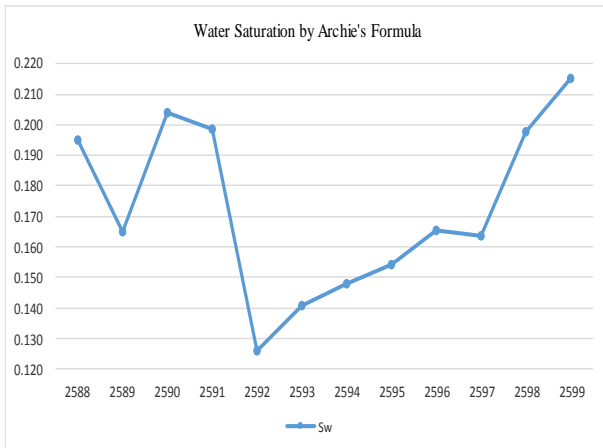


Fig.1 Water saturation (Y axis) vs. depth (X axis) using Archie's formulae

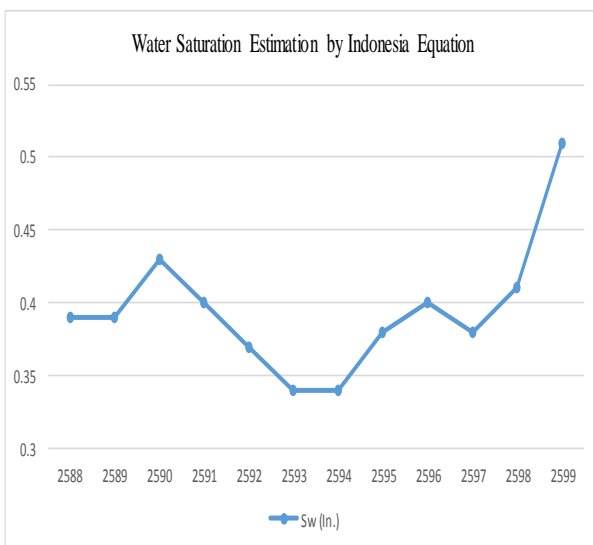


Fig. 2 Water saturation (Y axis) vs. depth (X axis) using Indonesia Equation

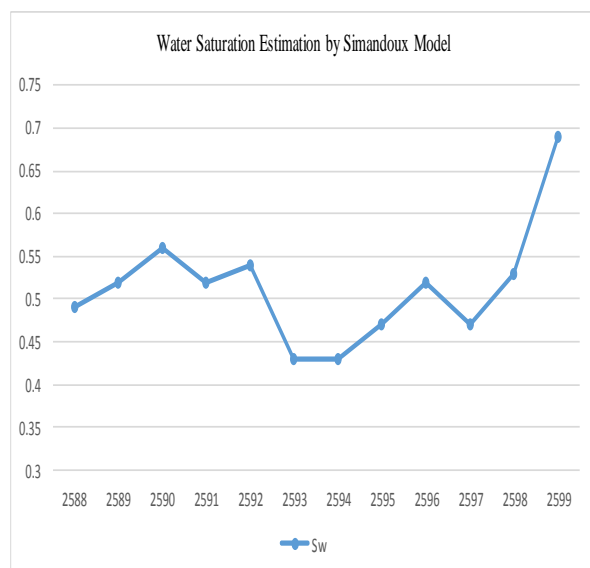


Fig.3 Water saturation (Y axis) vs. depth (X axis) using Simandoux Model

Appendix 2 shows the estimation of water saturation using Indonesia equation and Appendix 3 shows the estimation of water saturation by Simandoux model. The maximum water saturation using Indonesia equation is determined at depth of 2599 m. The maximum value is 0.51. And the minimum value is 0.34 at depth of 2593 as well as 2594 m.

The maximum water saturation using Simandoux model is determined at depth of 2599 m. The maximum value is 0.69. And the minimum value is 0.43 at depth of 2593 as well as 2594 m. Estimated water saturation by Indonesia and Simandoux model are graphically represented at Fig. 2 and Fig. 3.

6. Conclusion & Recommendation

This work has introduced the practical application of wireline log and water saturation. All calculation in this work has been done without consideration of mud composition, mud temperature plus other sophisticated parameter. After the analysis of different logs it is detected that the value of average water saturation found from Archie's formula, Indonesia equation and Simandoux model are 17.3%, 40%, 52.14% respectively.

To estimate the water saturation of any reservoir more accurately, the special or routine core analysis is required. The estimated formation water resistivity may change depending upon the values of Archie's exponent and cementation factor.

To assess the quality of the gas reservoirs of Bangladesh more accurately, special logging tools such as Nuclear Magnetic Resonance (NMR) and Formation Micro-Scanner (FMS) logs can be run.

NOMENCLATURE

- R_t : True Resistivity
- R_w : Water resistivity
- Φ : Porosity
- S_w : Water saturation
- a : Archie's exponent
- m : cementation factor
- n : Saturation exponent, it is the gradient of the line defined on the plot.
- V_{sh} : Shale volume
- Φ_e : Effective porosity
- R_{ct} : Clay zone resistivity
- R_{xo} : Flushed zone resistivity
- R_{mf} : Mud filtrate resistivity

REFERENCES

- [1] Allaby, Ailsa; Allaby, Michael, Oxford Dictionary of Earth Sciences 2 ed., Oxford University Press. p. 320. ISBN 0-19-280079-5, (1999).

- [2] "The Making of Oil: Birth of a Reservoir", Schlumberger Excellence in Educational Development, (June 2015).
- [3] Geological Technical Order Report of Shahbazpur Well No. 1, Bangladesh Petroleum Exploration Company Limited, BAPEX, Well Services Division, pp. 1-5 (April 1996).
- [4] Geologging report, Bangladesh Petroleum Exploration Company Limited, BAPEX; Well Services Division, pp. 45-49, (April 1996).
- [5] Bates, R. J., and Jackson, J. A., ed. Dictionary of Geological Terms 3 ed.,. American Geological Institute. p. 299. ISBN 0-385-18101-9, (1984).
- [6] Hilchie, Douglas W., Wireline: A history of the well logging and perforating business in the oil fields. Boulder, Colorado: Privately Published, (2014)

Appendix 1 Water saturation estimation by Archie's formula

Base, m	Log values		Calculated		Constants		Calculated				
	Rt	Rxo	Porosity	Rw	Rmf	a	m	Sw	Sxo	BVW	MHI
2588	8.0	10.0	16.87	0.10 0	0.43 6	1.4	1.54	0.19 5	0.76 0	0.033	0.25 6
2589	10.0	15.0	18.13	0.10 0	0.43 6	1.4	1.54	0.16 5	0.58 7	0.030	0.28 1
2590	8.0	12.0	15.92	0.10 0	0.43 6	1.4	1.54	0.20 4	0.72 5	0.032	0.28 1
2591	8.0	10.0	16.48	0.10 0	0.43 6	1.4	1.54	0.19 8	0.77 4	0.033	0.25 6
2592	15.0 0	18.0	19.73	0.10 0	0.43 6	1.4	1.54	0.12 6	0.50 2	0.025	0.25 1
2593	12.0 0	12.0	19.74	0.10 0	0.43 6	1.4	1.54	0.14 1	0.61 5	0.028	0.22 9
2594	10.0 0	15.0	20.89	0.10 0	0.43 6	1.4	1.54	0.14 8	0.52 6	0.031	0.28 1
2595	9.0	15.0	21.21	0.10 0	0.43 6	1.4	1.54	0.15 4	0.52 0	0.033	0.29 6
2596	8.0	13.0	20.86	0.10 0	0.43 6	1.4	1.54	0.16 5	0.56 6	0.035	0.29 2
2597	9.0	14.0	19.58	0.10 0	0.43 6	1.4	1.54	0.16 4	0.57 3	0.032	0.28 6
2598	8.0	13.0	16.56	0.10 0	0.43 6	1.4	1.54	0.19 8	0.67 6	0.033	0.29 2
2599	6.0	8.0	17.88	0.10 0	0.43 6	1.4	1.54	0.21 5	0.81 2	0.038	0.26 5
Average	9.2 5	12.92	18.65					0.17 3	0.63 6	0.032	0.27 1

Calculation:
Formation depth: 2595m

Water saturation, Sw = [(FRw/Rt)]0.5 for uninvasion zone by Archie's formula

$$Sw = [(aRw)/(\Phi m \times Rt)]0.5 = [(1.4 \times 0.1)/(0.211.54 \times 9)]0.5 = 0.154 \text{ for un-invasion zone}$$

$$Sxo = [(aRmf)/(\Phi m \times Rxo)]0.5 = [(1.4 \times 0.436)/(0.211.54 \times 15)]0.5 = 0.520 \text{ for flushed zone}$$

$$\text{Bulk Volume Water (BVW)} = \text{Water saturation} \times \text{Porosity} = 0.154 \times 0.21 = 0.033$$

$$\text{Moveable Hydrocarbon Index, MHI} = Sw/Sxo = 0.154/0.520 = 0.296$$

Appendix 2 Water saturation estimation by Indonesia equation

TVD meter	Vcl	Log values, ohm-m			Calculated			Constants		Calculated			
		Rcl	Rxo	Rt	Φe	Rw	Rmf	a	m	Sw	Sxo	MHI	BVW
2588	18.52	3	10.0	8.0	20.19	0.10	0.436	1.4	1.54	0.39	2.06	0.19	0.08
2589	18.52	3	15.0	10.0	17.04	0.10	0.436	1.4	1.54	0.39	1.92	0.20	0.07
2590	18.52	3	12.0	8.0	17.57	0.10	0.436	1.4	1.54	0.43	2.10	0.20	0.08
2591	18.52	3	10.0	8.0	19.14	0.10	0.436	1.4	1.54	0.40	2.15	0.19	0.08
2592	18.52	3	18.0	15.0	13.37	0.10	0.436	1.4	1.54	0.37	2.11	0.18	0.05
2593	18.52	3	12.0	12.0	18.61	0.10	0.436	1.4	1.54	0.34	2.01	0.17	0.06
2594	18.52	3	15.0	10.0	20.71	0.10	0.436	1.4	1.54	0.34	1.65	0.21	0.07
2595	18.52	3	15.0	9.0	19.66	0.10	0.436	1.4	1.54	0.38	1.72	0.22	0.07
2596	18.52	3	13.0	8.0	19.14	0.10	0.436	1.4	1.54	0.40	1.89	0.21	0.08
2597	18.52	3	14.0	9.0	19.66	0.10	0.436	1.4	1.54	0.38	1.78	0.21	0.07
2598	18.52	3	13.0	8.0	18.61	0.10	0.436	1.4	1.54	0.41	1.93	0.21	0.08
2599	18.52	3	8.0	6.0	16.52	0.10	0.436	1.4	1.54	0.51	2.69	0.19	0.09
Average			12.9	9.3	18.65					0.40	2.00	0.20	0.07

Calculation:
Formation depth: 2595m
Water saturation for un-invasion zones, Sw = (1/Rt)[{Vcl (1-0.5Vcl)/(Rcl) 0.5} + {Φe 0.5m/(aRw)0.5}]

$$Sw = (1/9)[\{0.167 (1-0.5 \times 0.167)/3 0.5\} + \{0.196 0.5 \times 1.54/(1.4 \times 0.10)0.5\}] = 0.38$$

Water saturation for flushed zones, Sxo = (1/Rxo)[{Vcl (1-0.5Vcl)/(Rcl) 0.5} + {Φe 0.5m/(aRmf)0.5}]

$$Sxo = (1/15)[\{0.167 (1-0.5 \times 0.167)/30.5\} + \{0.196 (0.5 \times 1.54)/(1 \times 0.436)0.5\}] = 1.72$$

Bulk Volume Water (BVW) = Water saturation × porosity = 0.38 × 0.196 = 0.07

Moveable Hydrocarbon Index, MHI = Sw/Sxo = 0.38/1.72 = 0.22

Appendix 3 Water saturation estimation by Indonesia equation

TVD meter	Resistivity, ohm-m			Calculated (%)			BVW
	<u>Rt</u>	<u>Rcl</u>	<u>Rw</u>	<u>Vsh</u>	<u>Φe</u>	<u>Sw</u>	
2588	8.0	3.0	0.10	24.65	20.19	49.45	0.100
2589	10.0	3.0	0.10	20.41	17.04	52.40	0.089
2590	8.0	3.0	0.10	29.53	17.57	56.79	0.100
2591	8.0	3.0	0.10	20.41	19.14	52.17	0.100
2592	15.0	3.0	0.10	10.68	13.37	54.54	0.073
2593	12.0	3.0	0.10	20.41	18.61	43.80	0.082
2594	10.0	3.0	0.10	13.49	20.71	43.15	0.089
2595	9.0	3.0	0.10	14.73	19.66	47.90	0.094
2596	8.0	3.0	0.10	13.49	19.14	52.20	0.100
2597	9.0	3.0	0.10	13.49	19.66	47.91	0.094
2598	8.0	3.0	0.10	27.50	18.61	53.63	0.100
2599	6.0	3.0	0.10	13.49	16.52	69.83	0.115
Average				18.52	18.35	51.98	0.095

Calculation:

Formation depth: 2595m

Water saturation, $S_w = \left\{ \frac{0.4R_w}{\Phi e^2} \right\} \times \left[\sqrt{\frac{(V_{sh}/R_{sh})^2 + (5 \Phi e^2) / (R_w \times R_t)}{(V_{sh}/R_{sh})}} \right]$

$S_w = \left\{ \frac{0.4 \times 0.10}{0.1962} \right\} \times \left[\sqrt{\frac{(0.147/3)^2 + (5 \times 0.1962) / (0.10 \times 9)}{(0.147/3)}} \right] = 0.479$

Gas saturation, $S_g = 1 - 0.479 = 0.521$

Bulk Volume Water (BVW) = Water saturation × porosity = $0.479 \times 0.196 = 0.094$

Proposition of Additive Manufacturing Technique for Artificial Bone Implantations and Its Feasibility Assessment via Cost Analysis

Nusrath Zahan¹, M.Fakhrul Islam Jony², and Khairun Nahar^{3*}

¹Department of Industrial & Production Engineering, Rajshahi University of Engineering & Technology, Rajshahi, Bangladesh

²Lira Group of Industries, Gulshan 2, Dhaka, Bangladesh

^{3*}Assistant Professor, Department of Industrial & Production Engineering, Rajshahi University of Engineering & Technology, Rajshahi, Bangladesh

ABSTRACT

Osteoarthritis (OA) of the hip is the most common joint disease in elderly people and associated with significant physical disability. Pain relief is a primary treatment of hip OA. When the patient with hip OA has failed medical treatment modalities and remains in pain, the patient should be referred for hip replacement surgery in which the damaged surfaces of the joint is removed and replaced with a set of artificial ball-and-socket implants. In this research, a proposition for Additive Manufacturing (AM) is advocated to produce the bone implant to enhance the customer satisfaction along with minimization of costs. AM is fundamentally different because it creates product by successive deposits of material instead of using removal or forming processes. Because of this difference, the cost and operational characteristics are distinct from traditional manufacturing. For this reason, additive manufacturing is placed in an end-to-end supply chain context and a stochastic optimization model is proposed to help a manufacturer decide when AM is best for them. Two business models are also proposed based on the additive manufacturing technology: manufacturing dominant model and retailer dominant model to investigate the financial viability of these models.

Keywords: Biomedical implants; Additive manufacturing; Supply chain; Cost analysis; Stochastic programming model; Business model innovation.

1. Introduction

The burden of musculoskeletal conditions is rising all over the world; Osteoarthritis (OA) is one of them which cause pain in the limb. In a healthy person, the bones joints are cushioned by cartilage, allowing for unconstrained movement of the joint. With OA, the cartilage breaks down and as the cartilage deteriorates, bone rubs on bone, resulting in pain and reduced mobility. Pain relief is a primary goal in treating of these patients. In the critical stage of OA, the medical treatment fails and patients remain in pain with limitations of physical function in daily life. This patients would be helped best with a surgery in which an artificial bone implant is replaced to match their anatomy. For this bone implantation surgery most of the patients either go to abroad or the manufacturing of the bone implants is held in other country and they are purchased with a high transportation cost. In both cases the whole process of surgery is very costly and time consuming. For this reason we need a convenient process that can be proven as a very supportive way of enhancing customer satisfaction by minimizing the cost of artificial bone implant.

In this case, Additive Manufacturing can be proposed as an effective way. AM is a collection of modern technologies which creates products by the addition of layers in the third dimension instead of subtracting or forming material, which are used in other manufacturing methods. Huang et al (2013) discussed that additive manufacturing can produce a final product in one build, there is limited exposure to hazardous conditions and there is little hazardous waste [7]. According to Tuck and Hague

(2006) and Walter et al. (2004), by being a very strong enabler of product customization, 3D printing can have remarkable impacts on downstream sections of the supply chain, such as production and distribution [9]. A study on 3d printing and its future, Koff & Gustafson (2014) said that the most inspiring use of 3D printing is in the healthcare industry, where 3D printing has the potential to save lives or dramatically improve them. It is designed to print bone joint and tissue structures using data from medical scans, such as CT or MRI [12]. Jia, F., Wang, X., Mustafee, N., Hao, L. (2015) showed the difference between two business model for the chocolate industry for both standard & customized product. 3D chocolate printing provides the technology for manufacturing chocolates layer-by-layer, thus offering customers enhanced product value and personalized consumption experience [4]. This research work discusses the additive manufacturing in perspective of Bangladesh for artificial hip bone implantation surgery. By introducing additive manufacturing this research reveals the possibilities of increasing capacity, reduction of cost and time in hip replacement surgery.

2. Mathematical Statements

In this section a stochastic cost model is developed to quantify the supply-chain level costs associated with the production of artificial hip implants using both traditional manufacturing and Additive Manufacturing (AM) technologies and investigated the economic feasibility of using these technologies to fabricate hip implants in Bangladesh. This model mainly focused on modeling

* Corresponding author. Tel.: +88-01916800200

E-mail addresses: khairun.nahar@ipe.ruet.ac.bd, shapla05.ipe@gmail.com

system-level costs such as inventory, transportation the effects of product lead time on the overall transportation costs.

2.1 Model formulation: Let's consider a scenario where a set of customers (C) need a set of products (I) in a set of time periods (T). The products (I) can be manufactured by a set of traditional manufacturing plants (P) and a set of Additive manufacturing plants (A). Both traditional and Additive manufacturing plants receive product materials from a group of suppliers (S). There are costs associated with supplier selection, product transportation, facilities opening and operating, inventory management, and production. Our approach here is to design an effective supply chain considering possible use of traditional manufacturing system or Additive manufacturing systems. We have developed a MILP model to get optimal configuration of a supply chain variant.

Sets:

a : Set of Additive manufacturing plants; c : Set of customers; i : Set of products; p : Set of traditional manufacturing plants; s : Set of suppliers; t : Set of time periods; w : Set of warehouse.

General Parameters:

- i. $demand_{it}$: demand of product
- ii. $mfg_capacity_{pit}$: TM plant capacity
- iii. $mfg_var_cost_{pit}$: TM variable cost
- iv. $mfg_oper_cost_{pit}$: TM plant operation cost
- v. $mfg_open_cost_p$: TM opening cost

Distribution Parameters:

- i. $wh_var_cost_{wit}$: warehouse variable cost
- ii. $wh_oper_cost_{wit}$: warehouse operating cost
- iii. $wh_open_cost_w$: warehouse opening cost

Supply Parameters:

- i. $supplier_capacity_{sit}$: Supplier capacity
- ii. $tsupplier_cost_{sit}$: supplier unit cost for TM plant
- iii. $amsupplier_cost_{sit}$: supplier unit cost for AM plant

Additive manufacturing Parameters:

- i. $am_mach_hours_{at}$: AM machine capacity
- ii. $am_cap_usage_{it(w)}$: hours to build 1 product
- iii. $am_oper_cost_{ait}$: AM plants operating cost
- iv. $am_mach_purchcost_{ait}$: AM machine purchase cost
- v. $am_mat_cost_{it(w)}$: AM materials cost per KG
- vi. $am_mat_usage_{it}$: AM materials usage per product
- vii. $am_open_cost_a$: AM location opening cost
- viii. $am_var_cost_{ait}$: AM variable cost

Transportation Parameters:

- i. $am_trans_cost_{acit}$: unit transportation cost from AM location to customer
- ii. $ib_trans_cost_{pwit}$: unit transportation cost from TM plant to warehouse
- iii. $ob_trans_cost_{pwit}$: unit transportation cost from warehouse to customer
- iv. $tsupply_trans_cost_{spit}$: unit transportation cost from supplier to TM plant
- v. $amsupply_trans_cost_{sait}$: unit transportation cost

from supplier to AM plant

Inventory Parameters:

- i. aii_a : AM plant's starting inventory
- ii. $inventory_hold_cost_i$: holding cost
- iii. p_{ii}_p : TM plant's starting inventory
- iv. w_{ii}_w : warehouse starting inventory
- v. M : a sufficiently large number

Integer Decision Variables:

- i. aii_{ait} : AM starting inventory
- ii. aei_{ait} : AM ending inventory
- iii. p_{ii}_{pit} : TM starting inventory
- iv. pei_{pit} : TM ending inventory
- v. w_{ii}_{wit} : warehouse starting inventory
- vi. wei_{wit} : warehouse ending inventory
- vii. fsp_{spit} : supply of materials for product i from supplier s to manufacturer p at time t
- viii. fsa_{sait} : supply of materials for product i from supplier s to AM plant a at time t
- ix. fpw_{pwit} : supply of product i from TM plant p to warehouse w at time t
- x. fwc_{wcit} : supply of product i from warehouse w to customer c at time t
- xi. fac_{acit} : supply of product i from AM plant a to customer c at time t
- xii. $am_oper_machines_{ait}$: number of AM machines operating at time t to produce i
- xiii. $am_production_{ait}$: no. of product i is produced by AM plant a at time
- xiv. $p_production (P,I,T)$: no. of product i is produced by TM plant p at time t

Binary Decision Variables:

- i. $y_{wcit} = 1$ if customer c gets supply of product i from warehouse w at time t
- ii. $z_{acit} = 1$ if customer c gets supply of product i from Additive manufacturing plant a at time t
- iii. $x_{wcit} = 1$ if warehouse w is open for product i at time t
- iv. $xa_{ait} = 1$ if Additive manufacturing plant a is open for product i at time t
- v. $xp_{pit} = 1$ if traditional manufacturing plant p is open for product i at time t
- vi. $sp_{spit} = 1$ if supplier s supplies material for product i to plant p at time t
- vii. $sa_{sait} = 1$ if supplier s supply material for product i to AM plant a at time t

The formulation is the following:

Minimize

$$\begin{aligned} & \sum_{s \in S} \sum_{p \in P} \sum_{i \in I} \sum_{t \in T} tsupply_trans_cost_{spit} * fsp_{spit} + \\ & \sum_{s \in S} \sum_{a \in A} \sum_{i \in I} \sum_{t \in T} amsupply_trans_cost_{sait} * fsa_{sait} \\ & + \sum_{p \in P} \sum_{w \in W} \sum_{i \in I} \sum_{t \in T} ib_trans_cost_{pwit} * fpw_{pwit} + \\ & \sum_{w \in W} \sum_{c \in C} \sum_{i \in I} \sum_{t \in T} ob_trans_cost_{wcit} * fwc_{wcit} + \\ & \sum_{a \in A} \sum_{c \in C} \sum_{i \in I} \sum_{t \in T} am_trans_cost_{acit} * fac_{acit} + \\ & \sum_{w \in W} \sum_{i \in I} \sum_{t \in T} wei_{wit} * inventory_hold_cost_i + \\ & \sum_{p \in P} \sum_{i \in I} \sum_{t \in T} pei_{pit} * inventory_hold_cost_i + \\ & \sum_{a \in A} \sum_{i \in I} \sum_{t \in T} aei_{ait} * inventory_hold_cost_i \\ & + \sum_{a \in A} \sum_{i \in I} \sum_{t \in T} am_var_cost_{ait} * am_production_{ait} \\ & + \sum_{p \in P} \sum_{i \in I} \sum_{t \in T} mfg_var_cost_{pit} * p_production_{pit} \\ & + \sum_{p \in P} \sum_{i \in I} \sum_{t \in T} xp_{pit} * mfg_open_cost_p + \\ & \sum_{a \in A} \sum_{i \in I} \sum_{t \in T} xa_{ait} * am_open_cost_a + \end{aligned}$$

$$\begin{aligned} & \sum_{w \in W} \sum_{i \in I} \sum_{t \in T} xw_{wit} * wh_open_cos_w + \\ & \sum_{s \in S} \sum_{p \in P} \sum_{i \in I} \sum_{t \in T} tsupplier_cost_{sit} * sps_{pit} + \\ & \sum_{s \in S} \sum_{a \in A} \sum_{i \in I} \sum_{t \in T} amsupply_cost_{sit} * sa_{sait} + \\ & \sum_{p \in P} \sum_{i \in I} \sum_{t \in T} mfg_oper_cost_{pit} * xp_{pit} + \\ & \sum_{a \in A} \sum_{i \in I} \sum_{t \in T} am_oper_cost_{ait} * xa_{ait} + \\ & \sum_{w \in W} \sum_{i \in I} \sum_{t \in T} wh_oper_cost_{wit} * xw_{wit} \dots (1) \end{aligned}$$

The objective function is to minimize total supply chain cost.

Subject to...

$$\sum_{w \in W} \sum_{i \in I} y_{wcit} + \sum_{a \in A} \sum_{i \in I} z_{acit} = 1 \dots (2)$$

Every customer is served by either warehouse or AM plant

$$xw_{wit} \geq y_{wcit}, \dots (3)$$

If a customer is assigned to a warehouse then that warehouse must be up

$$xa_{ait} \geq z_{acit}, \dots (4)$$

If a customer is assigned to a AM plant then that plant must be up

$$fwc_{wcit} = y_{wcit} * demand_{cit} \dots (5)$$

Amount of flow from warehouse w to customer c for product i at time t

$$fac_{acit} = z_{acit} * demand_{cit} \dots (6)$$

Amount of flow from Additive manufacturing plant a to customer c for product I at time t

$$wii_{wit} + \sum_{p \in P} fpw_{pwit} = wei_{wit} + \sum_{c \in C} fwc_{wcit} \dots (7)$$

Flow balance for warehouse

$$wii_{wit} = wii_w, \dots (8)$$

At time t = 1 every warehouse has a given inventory

$$wii_{wit} = wei_{wi(t-1)}, \dots (9)$$

At time t > 1 initial inventory is the ending inventory of t-1 time period

$$pii_{pit} + \sum_{s \in S} fsp_{spit} = pei_{pit} + \sum_{w \in W} fpw_{pwit} \dots (10)$$

Flow balance for traditional plant

$$pii_{wit} = pii_p, \dots (11)$$

At time t =1 every manufacturing plant has a given inventory

$$pii_{wit} = pei_{pi(t-1)}, \dots (12)$$

At time t > 1 initial inventory is equivalent to the ending inventory of t-1 time period

$$aai_{pit} + \sum_{s \in S} fsa_{sait} = aei_{ait} + \sum_{c \in C} fac_{acit} \dots (13)$$

Flow balance for Additive manufacturing

$$aai_{ait} = aii_w, \dots (14)$$

at time = 1 AM plant has a given inventory

$$aai_{ait} = aei_{ai(t-1)}, \dots (15)$$

At time t > 1 initial inventory of AM plant is equivalent to the ending inventory of t-1 time period

$$pii_{pit} + \sum_{w \in W} fpw_{pwit} - pei_{pit} \leq mfg_capacity_{pit}, \dots (16)$$

Capacity constraint for traditional factory

$$aai_{pit} + \sum_{c \in C} fac_{acit} - aei_{ait} \leq am_mach_hours_{ait} * am_oper_machines_{ait} / am_cap_usage_{it}, \dots (17)$$

Capacity constraint for Additive manufacturing plant

$$\sum_{a \in A} fsa_{sait} + \sum_{p \in P} fsa_{spit} \leq supplier_capacity_{sit}, \dots (18)$$

Capacity constraint for supplier

$$am_production_{ait} = aii_{ait} + \sum_{c \in C} fac_{acit} - aei_{ait}, \dots (19)$$

Total production at AM plant at time t

$$p_production_{pit} = pii_{ait} + \sum_{w \in W} fpw_{pwit} - pei_{ait}, \dots (20)$$

Total production at traditional plant at time t

$$p_production_{pit} \leq xp_{pit} * M, \dots (21)$$

If there is a production from a traditional plant then that traditional plant must be up

$$am_production_{pit} \leq xa_{pit} * M \dots (22)$$

If there is a production from a AM plant then that AM plant must be up

$$fsa_{sait} \leq sa_{sait} * M, \dots (23)$$

If there is a flow from a supplier to a AM plant then that

supplier-plant relation is on

$$fsp_{spit} \leq sp_{spit} * M, \dots (24)$$

If there is a flow from a supplier to a traditional plant then

that supplier-plant relation is on

$$am_oper_machines_{ait} = am_production_{ait} / am_mach_hours_{ait}, \dots (25)$$

Number of AM machines required to run at time t in AM plant.

2.2 Numerical Illustration

In this section, data gathered from the professionals and 6Axis technologies are applied to the above model and solved by using the GAMS software to find the best possible solution. The input data and result of the decision variables are given in Table 1 and Table 2. Finally the total supply chain costs of both models are presented in Table 3.

Table 1 Input Parameters

General Parameters	Unit	AM Parameters	Unit
$demand_{it}$	238	$am_mach_hours_{at}$	2400
	364	$am_cap_usage_{it(w)}$	1
	201	$am_oper_cost_{ait}$	34000 BDT
	169	$am_mach_purchase_cost_{ait}$	3500000 0 BDT
$mfg_capacity_{pit}$	1000	$am_mat_cost_{t(w)}$	37100
$mfg_var_cost_{pit}$	63615 BDT	$am_mat_usage_{it}$	1.3kg
$mfg_oper_cost_{pit}$	354000 BDT	$am_open_cost_a$	11500 BDT
$mfg_open_cost_p$	1083000 00 BDT	$am_var_cost_{ait}$	48200 BDT
Distribution Parameters		Supply Parameters	
$wh_var_cost_{wit}$	2670 BDT	Supplier capacity	12000
			10500
10000			
9000			
$wh_oper_cost_{wit}$	10000 BDT	Supplier unit cost for TM plant	19824
$wh_open_cost_w$	640000 BDT		15310
Transportation Parameters			14500
$am_trans_cost_{acit}$	0.00	$ob_trans_cost_{pwit}$	40000 BDT
$ib_trans_cost_{pwit}$	50 BDT		
$inventory_hold_cost_i$	100 BDT		

*Source: 6Axis Technologies.Unimed &Unihealth Pharmaceuticals Ltd

Table 2 Solution of Integer Decision variables

Results	Unit		
	Period 1	Period 2	Period 3
aii_{ait}	0	0	0
aei_{ait}	0	0	0
pii_{pit}	1200	1200	0
pei_{pit}	1200	0	0
wii_{wi}	500	219	1074
wei_{wit}	219	1074	727
$fspi_{spit}$	5400	5675	5400
fsa_{sait}	345	448	451
fpw_{pwit}	0	1200	0
fac_{acit}	69	92	78
	112	127	125
	57	71	73
	43	55	71
$am_oper_machines_{ait}$	1		
$am_production_{ait}$	281	345	347
$p_production$	0	2400	0

Table 3 MIP solution of total supply chain cost

TM Plant	AM Plant
283291370.00	88879156.00

From table 2 and table 3 it can be seen that both the starting and ending inventory of AM plant remains zero because this plant anticipates only by the customer demand. On the other hand TM plant maintains the production schedule by forecasting demand based on different specification of hip prosthesis. Another advantage of AM plant is that there is no need of warehouse in this plant, which also reduces the total supply chain cost. Finally the additive manufacturing technology maintains the quicker response with respect to customer demand compared to the TM plant. So, based on the above analysis it can be said that Additive manufacturing is economically feasible for the production of artificial hip implant as the total supply chain cost of AM plant is lower than that of TM plant.

3. Bio Implant Business Model

Additive manufacturing technology represents a revolutionary manufacturing approach which can engage consumers to create and produce hip bone locally and share their digitized product design and innovation globally. But robust business models are necessary for ensuring the economic sustainability of additive manufacturing of hip prosthesis which will account the profitability aspects of the supply chain constituents, viz., the manufacturer and the hospital, and the utility derived by the end user. Towards this, we present two business models 1) the manufacturer-dominant model 2) the distributor dominant model where the manufacturer of artificial bone adopts this technology, with production taking place at the manufacturer’s plants and

manufacturers sell the product to the local distributors (hospitals). The latter scenario is that of a distributor adopting this technology with the final production taking at hospital. The purpose of this section is to outline two business models for additive manufacturing of hip prosthesis and make comparison between them in terms of the earned profit.

3.1 Manufacturer-dominant business model

The manufacturer dominant model is the first supply-centric business model innovation. Here the manufacturer is responsible for the customized manufacturing of hip bone. The conventional supply chain channel is complemented by processes pertaining to the production of customized hip bone, wherein, (a) hospitals order personalized product through the distribution center, (b) the orders are communicated to the manufacturer, (c) the hip bone manufactured using process materials and additive manufacturing machine, (d) the manufacturer transports the customized product back to the distribution center, and (e) the hospitals collect the products from the distribution- center (Fig. 1).

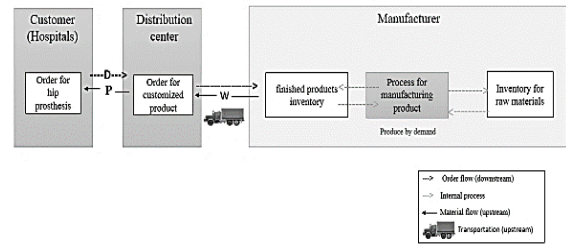


Fig. 1: Manufacturer-Dominant supply chain model

The proposed supply-chain structure also includes the customer–manufacturer channel which facilitates communication between the hospital and the manufacturer with the objective of fulfilling customer demand. In the customer–manufacturer channel the role of the distribution center is made redundant. Fig. 1 shows the customer demand for products (D) the corresponding prices are P. Finally the variables W refer to the price the distributor has to pay to the manufacturer for the products.

3.2 Distributor-dominant business model

In this supply chain model, the product is created using the additive manufacturing technology by the distributor. The hip bone is manufactured using processed materials which have to be ordered from the supplier. Compared to the previous model wherein the manufacturer has processes pertaining to production, in second model this is incorporated with distributors' processes. The variables shown in Fig. 2 are similar to those in Fig. 1 since in both scenarios customer demand exists for product (D) however, unlike the previous scenario wherein the manufacturer fulfilled the order, in this model the customer receives the product from the distributor. The price for D is P. For both models 1 and 2 there is no inventory subsequent to the process for manufacturing product since this is a make-to-order strategy. Finally, for both models presented, there exists an inventory for raw material at distribution center since it is make-to-order.

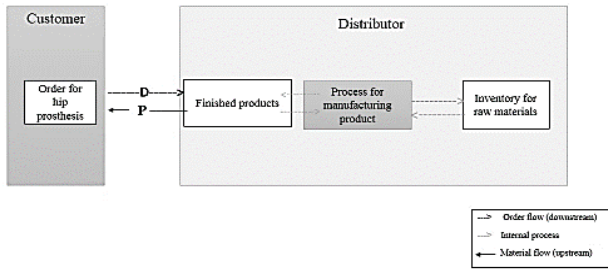


Figure 2: Distributor-Dominant supply chain model

Brief Study of business models:

The additive manufacturing technology will enable manufacturers and distributor to produce hip prosthesis based on customer preferences; this is especially true for the manufacture of product with shape-customization. In additive manufacturing technology, production does not commence until an order is received with clear customer preference information. For the purpose of comparison, we have implemented real data collected from the local market and hospitals for all the business models outlined in the previous section. These are discussed next.

Parameter definitions:

In this section we present the modeling parameters which have been used in the subsequent equations to calculate inventory and the profitability functions pertaining to the supply-chain centric business models.

(T) Operating cycle, (k) order times, (n) produce times, (Q) economic order quantity, (D) demand for hip prosthesis, (P) price of product, (W) purchase price of distributor, (C_h) inventory holding cost, (C_o) cost of transportation each time, (C_p) operating cost each time, (C_u) production cost of product, (C_s) ordering cost

Business model 1: manufacturer-dominant supply chain

Additive manufacturing of hip bone by the manufacturer decreases the inventory cost of the distributor. In the manufacturer-dominant model, the distributor only bears the inventory costs for finished products. In this part we analyze the profit of supply chain under manufacturer-dominant model. The finished products sales of the distributor will, to a certain extent, be affected by the sale of products. In this model the distributor's profit function is:

$$DP_1 = \frac{(p - w)D - c_o^d - c_h^d}{T}$$

After the introduction of customized production, the profit of double-channel supply chain under manufacturer-dominant model is:

$$MP_1 = \frac{\sum_1^k (w - c_u^m) Q^m - c_p^m - c_h^m - c_s^m}{T}$$

Business model 2: Distributor-dominant supply chain

Under the distributor-dominant supply chain, the product is manufactured by the distributor. For enabling the on-demand manufacture of customized hip bones using additive manufacturing the distributor has to set up a raw material inventory. As a result of the introduction of raw material inventory, distributor's inventory cost will be

higher compared to models 1 but distributors 'transportation cost will be eliminated compared to the previous model. Under the distributor -dominant model the distributor will produce the products and the raw materials will be purchased from supplier for producing hip bones by additive manufacturing process. The profit function is:

$$DP_2 = \frac{(p - c_u^d)D - c_h^d - c_s^d - c_p^d}{T}$$

4. Finding and Analysis

Table 4 represents the required data for the profit analysis of the manufacturer dominant model. In this model, as the manufacturer adopt AM technology, manufacturer's profits increase comparative to distributor's profit.

Table 4 Data and result for manufacturer dominant model

Distributor	Cost (BDT)	Manufacturer	Cost (BDT)
Price of product, P	93550	Holding cost, c_h^m	40
Inventory holding cost, c_h^d	20	Operating cost, c_p^m	34000
Transportation cost, c_o^d	40000	Production cost, c_u^m	53253
Purchase price of distributor, w	69300	Supply unit cost, c_s^m	16439
DP_1	1946393	MP_1	1960253

On the other hand, Table 5 shows the profit of distributor in the model 2. In this case distributor's profit increases significantly in comparison to the first model as distributor adopt additive manufacturing technology.

Table 5 Data and result for distributor dominant model

Distributor	Cost (BDT)
Price of product, P	93550
Inventory holding cost, c_h^d	40
Supply unit cost, c_s^d	16439
Operating cost, c_p^d	34000
Production cost, c_u^m	53253
DP_2	3243590

From the above analysis, it has been found that, the profit of distributor in distributor dominant model is significantly higher than that in manufacturer dominant model. So it would be economically feasible if the distributor adopts the additive manufacturing technology for the production of artificial hip implant and it is important for the manufacturer to adopt the technology first, otherwise if the distributor adopts the technology first, the manufacturer can be replaced. Finally it can be said that the one who adopts the technology first (whether it is manufacturer or distributor) gain higher profits. And if manufacturer allows distributor to adopt the technology and dominate the products market, then he will be squeezed out of market or disrupted by the additive manufacturing technology.

5. Conclusions

In conclusions it can be said that, we have developed a stochastic optimization model to quantify the supply-chain level costs associated with the production of artificial hip implants and investigated the economic feasibility. Then we have formulated the programming code using GAMS software and the MIP solution of the two models given the result that additive manufacturing would be economically beneficial for the production of artificial hip bone implants. We have also formulated two business models for the production of artificial hip implants considering supply chain constituents and analyzed their profitability functions with the aim of experimenting economic viability of the new additive manufacturing technology enabled business models in artificial bone implantation. The results show that 1) whoever between distributor and manufacturer adopts the AM technology first gain higher profits than the other; 2) Manufacturers risk being left out of market if distributors adopt this technology first successfully and assume a dominant position on the market.

REFERENCES

- [1] S. Wang, An analysis of manufacturers' supply and demand uncertainty based on the dynamic customization degree, *Int. J. Prod. Res.* 49 (10), 3023–3043 (2011).
- [2] D. S. Thomas, S. W. Gilbert, Costs and effectiveness of Additive manufacturing: A literature review and decision, (2014).
- [3] M. Ruffo, C. Tuck, R. Hague, Cost estimation for rapid manufacturing-laser sintering production for low to medium volumes. Proceedings of the Institution of Mechanical Engineers, *Part B: Journal of Engineering Manufacture*, 220, 1417-1427 (2006).
- [4] F. Jia., X. Wang, N. Mustafee, L. Hao, Investigating the feasibility of supply chain-centric business models in 3D chocolate printing: A simulation study, *Technological, Forecasting & Social Change*, (2015).
- [5] M. Ruffo, C. Tuck, R. Hague, Make or buy analysis for rapid manufacturing, *Rapid Prototyping Journal*, 13, 23-29 (2007).
- [6] C. Lindemann, U. Jahnke, M. Moi, R. Koch, Analyzing product life cycle costs for a better understanding of cost drivers in additive manufacturing, *23th Annual International Solid Freeform Fabrication Symposium—An Additive Manufacturing Conference*, Austin Texas USA 6th-8th August (2012).
- [7] S. H. Huang, P. Liu, A. Mokusdar, L. Hou, Additive manufacturing and its societal impact: A literature review, *International Journal of Advanced Manufacturing Technology*, 67, 1191-1203 (2013).
- [8] D. Y. Golhar, S. Banerjee, An Optimal Ordering Strategy for a Third-Party Managed Supply Chain,

International Journal of Production Research. Vol. 51, Issue 10, pp. 2969 – 2980(2013).

- [9] C. Tuck, R. Hough, Management and implementation of rapid manufacturing, <https://doi.org/10.1002/0470033991.ch10>, (2006).
- [10] Y. He, M. Ye, C. Wang, A method in the design and fabrication of exact-fit customized implant based on sectional medical images and rapid prototyping technology, *The International Journal of Advanced Manufacturing Technology*, 28, 504-508 (2006).
- [11] M. A. J. M. Gebler, C. Visser, A global sustainability perspective on 3D printing technologies. *Energy Policy*, 74, 158-167 (2014).
- [12] W. Koff, P. Gustafson, 3D Printing and the future of manufacturing (2014).

Appendix:

Data of monthly enlisted patient of hip (OA) from different hospitals in Bangladesh-

M H → ↓	LabAid Hospital	Pongu Hospital	Apollo Hospital	United Hospital
January	20	27	14	13
February	13	29	11	8
March	17	25	15	12
April	19	31	17	10
May	21	28	23	11
June	27	34	18	17
July	23	33	13	14
August	21	32	17	13
September	18	34	19	16
October	25	37	18	19
November	19	30	21	17
December	16	24	15	19
Total	238	364	201	169

Prosthesis Production cost-

Object weight(grams)	1360
Printing Time (Hours)	1
Electricity Tariff (£/Kwh)	0.16
Printer Power (watts)	7000
Filament Cost (£/Kg)	380.56
Printer Purchase(£)	428650
Printer lifetime(years)	25
Daily usage(hours)	8
Repairs Costs%	10
Failure Rate%	2.5
Total Cost(£)	549

Production price is calculated from

www.3dprinthq.com/cost/desktop.php

1£=97 BDT, So that the total production cost, £549=53253 BDT.

Study of Heat Transfer Enhancement in Tubular Heat Exchanger with Twisted Tape Inserts

Sadman Hassan Labib¹, Md. Riad Arefin Himel¹, Jobayer Ibn Ali¹, Anjan Goswami^{2,*}

¹ Department of Mechanical and Production Engineering, Ahsanullah University of Science and Technology (AUST), Dhaka-1208, Bangladesh.

² Assistant Professor, Department of Mechanical and Production Engineering, Ahsanullah University of Science and Technology (AUST), Dhaka-1208, Bangladesh.

ABSTRACT

In the present work an experimental investigation has been carried out to study the convective heat transfer augmentation in a double pipe counter flow heat exchanger (HE) with twisted tape insert. Also, the results are compared with a basic heat exchanger (BHE) of similar length, diameter and flow rate. The HE consists of a 140 inches long copper tube with diameter of 1inch which is centered in a PVC pipe having a diameter of 2inch. Hot fluid is allowed to flow through the inner copper tube and the cold fluid was allowed to flow through the annular passage between copper tube and the PVC pipe. Experiments were conducted at different mass flow rates of the hot fluid for both the BHE and MHEs. The effects of inserted twisted tapes and twist ratio on heat transfer rate, pressure drop and thermal performance factor characteristics have been investigated extensively. A twist ratio is defined as the ratio of twist length (y) to twisted tape width at the large end (W). The experiments were carried out by using twisted tapes with three different twist ratios (y/W) of 4.5, 6.0 and 7.5. All cases were tested under turbulent flow regime for Reynolds number between 20000 and 50000. The thermal performance indicators, i.e. heat loss from hot fluid, overall heat transfer coefficient, effectiveness, Nusselt Number etc. have been found to be enhanced for the modified HEs compared to that for the basic one. Also, the thermal performance factor tended to increase with decreasing tape twist ratio. The effectiveness of HEs is found to be increased with modifications with twisted tapes. However, after a certain limit of the mass flow rate of the hot fluid the variation in HE's effectiveness becomes less significant compared to that found up to that limiting mass flow rate.

Keywords: Basic Heat Exchanger, Modified Heat Exchanger, Twisted Tapes, Twist Ratio, Turbulent Flow.

1. Introduction

Heat exchangers are widely used device working as heating and cooling system in different industries like oil refineries, power plants and even residential areas [1-2]. Thermal performance improvement of many heat exchangers are needed for energy saving, lower operating cost moreover for better efficiency. Heat transfer augmentation methods are used in the heat exchanger systems to enhance the heat transfer rate and improve the thermal performances [1-13]. Bergles [1] categorized 13 heat transfer enhancement techniques in 'active' and 'passive' methods. External power is required for surface vibration, fluid vibration, injection, suction and electric or acoustic fields which are active methods of heat transfer enhancement. Passive techniques employ different surface geometry for heat transfer enhancement. Treated surface, rough surface, swirling flow devices, coiled tubes and surface tension devices are included in passive techniques of improving thermal performance of heat exchangers [2].

Heat transfer enhancement in heat exchanger has been subjected of many experimental and analytical investigation. Generally turbulent promotor which is called 'turbulator', one of the passive techniques widely used in heat transfer enhancement in the form of vortex flow or swirl flow devices such as rib, fin, baffle, winglet, propeller, grove roughened surfaces [3-9]. These turbulators are inserted in pipe flow to increase heat transfer surface area, to provide an interruption of

thermal boundary layer development and to cause increased heat transfer by increasing turbulence intensity or fast fluid mixing. A number of investigations have been made using various turbulators with different configurations to heat transfer enhancement in the heated tube of heat transfer, such as twisted tube [10], wire-coils [11], grooved tubes [12], compound turbulators [13].

Guo et al [14] numerically studied the contribution to thermal performance of the conventional, short-width and center cleared twisted tapes. Configuration optimization of regularly spaced short-length twisted tapes in a circular tube for turbulent heat transfer was carried out by Wang et al. [15] by using computational fluid dynamics (CFDs) modeling. Eiamsa-ard et al. [16] presented experimental study on convective heat transfer in a circular tube with short-length twisted tapes inserted under uniform heat flux. Eiamsa-ard et al. [17] performed experimental works on heat transfer and friction factor characteristics in a heat exchanger fitted with twisted tape elements. They made their analysis for both continuously placed twisted tape and twisted tape placed with various free spaced in circular tube. Jaisankar et al. [18] experimentally examined the heat transfer, friction factor and thermal performance caused by twisted tape for solar water heater. The tape width, rod-diameter effects, and phase angle effects on heat transfer and pressure drop were analyzed experimentally in a circular tube fitted with regularly spaced twisted

* Corresponding author. Tel.: +88-01913776863

E-mail addresses: anjan05me@gmail.com sadman.me.aust@gmail.com

tape elements by Saha et al [19]. But they did not compare their studies with a basic heat exchanger. In the light of above circumstances, the present study is focused to an extensive investigation of the thermal performance enhancement in double pipe heat exchanger with twisted tapes. For this, first of all, thermal performance study has been conducted in a basic double pipe heat exchanger (BHE). Then, twisted tape of copper with different twist ratios of 7.5, 6 and 4.5 have been inserted, and the thermal performance of the modified heat exchangers (MHEs) has been explored in a range of Reynolds number from 20000 to 50000. Finally, a comparative study has been conducted among the BHE and MHEs to explore the degree of the heat transfer augmentation.

2. EXPERIMENTAL SETUP

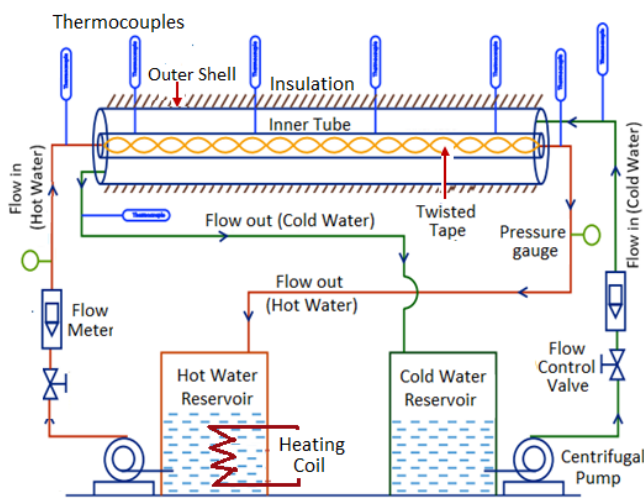


Fig. 1 Schematic of the Experimental Setup (The setup is installed at the Project Lab of Dept. of Mechanical and Production Engineering, AUST)

A detail of the experimental setup is displayed schematically in Fig. 1. This experimental setup is installed at the project lab under the Dept. of Mechanical and Production Engineering, AUST. In this setup, both hot and cold stream is water and it is supplied by two 0.5 hp power pumps. The flow rate of hot and cold both fluids are controlled by ball valve and the flow rate is measured by means of volumetric flow meter. In double pipe heat exchanger copper pipe of 1 inch external diameter is used as tube and PVC pipe of 2 inch internal diameter is used as shell. There are total eight pen type thermocouples used in the apparatus to measure the temperature of both hot and cold fluids at different points. The hot fluid is heated by a 1 kW portable water heater. Twisted tape made of copper used as turbulator to investigate the thermal performance improvement of the heat exchanger. Positioning of twisted tapes inside the copper tube and the thermocouples on the upper surface of the copper tube attached by solid seal are shown in Fig. 2. The twisted tapes with the length of 25 cm, width of 2 cm and 0.3

cm thick are shown in Fig. 3. Total number of 13 twisted tapes are inserted in copper tube. Twisted tapes having twist ratio (y/W) of 7.5, 6 and 4 are inserted to study the thermal performance of the heat exchanger for different twist ratio.

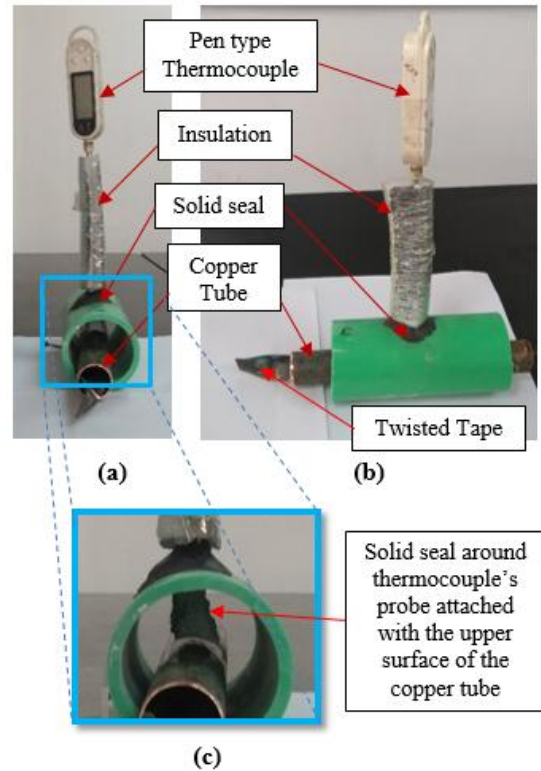


Fig. 2 Positioning of twisted tape and the thermocouple in heat exchanger: (a) & (b) truncated portion of the heat exchanger to show fittings, and (c) a magnified view to show the thermocouple probe's fitting with the outer wall of copper tube to measure the wall temperature.

Two pressure gauges are used to measure the pressure drop in both shell and tube explicitly, due to insertion of twisted tapes in the pipes which interrupts normal flow of fluid. The experiments are conducted by varying flow rate in terms of Reynolds numbers ranging from 20000 to 50000. First hot water and cold water are brought into desired temperature. Temperature of cold water is generally room temperature. The hot water temperature is about 30°C more than cold water. Heater connection is turned off before starting the procedure. Ball valves are regulated to get desired flow. Ball valve for cold water pipeline is always fixed. Two pumps are started at the same time. Data is taken from eight (8) thermocouples. Two for cold water inlet and outlet temperature, two for hot water inlet and outlet temperature and another four for wall temperature of the hot water tube. Data is also taken from two pressure gauges mounted on the hot water pipe at inlet and outlet. The setup runs for 30 minutes for every data collection session. Data is taken after 1 minute of interval. For modified heat exchanger 13 twisted tapes are inserted

inside the copper tube. Rests of the procedures are all the same for varying twisted tapes with various twist ratios.

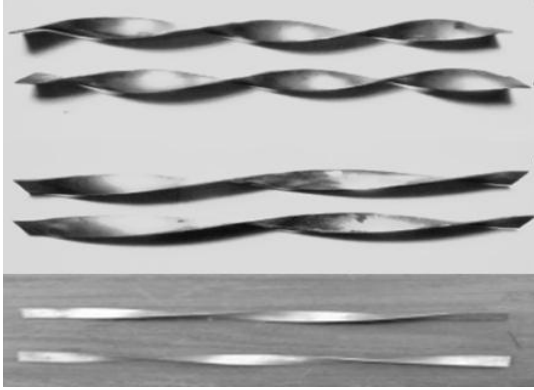


Fig.3 Twisted tapes with different twist ratios (y/W = 4.5, 6, 7.5 (from top to bottom))

3. DATA ANALYSIS

The purpose of the current work is to determine the effect of using twisted tapes in heat transfer rate of the heat exchanger. For investigation all calculations have to done for basic heat exchanger and modified heat exchanger with different twisted ratios.

The steady state of the heat transfer rate is assumed to be equal to the heat loss from the hot fluid in tube can be expressed as follows:

$$Q_H = Q_{conv.} \quad (1)$$

where,

$$Q_H = mC_{p,H} (T_o - T_i) \quad (2)$$

The convection heat transfer from tube can be written by

$$Q_{conv.} = hA (T_w - T_b) \quad (3)$$

in which the bulk temperature is found by

$$T_b = (T_o + T_i)/2 \quad (4)$$

and, the average wall temperature is calculated as:

$$T_w = \Sigma t_w / 4 \quad (5)$$

where, t_w local wall temperature maintaining equal distance along the length of the hot tube. The average wall temperature T_w is computed by using 4 points of local wall temperatures.

The average heat transfer coefficient (h) and Nusselt number (Nu) are estimated as follows:

$$h = mC_{p,H} (T_o - T_i) / A(T_w - T_b) \quad (6)$$

the heat transfer is calculated from the average Nu which can be obtained by

$$Nu = hD/k \quad (7)$$

Reynolds number (Re) is estimated by

$$Re = \frac{VD}{\nu} \quad (8)$$

where, V is the velocity of hot fluid inside the tube.

Effectiveness and overall heat transfer coefficient is obtained as follows:

$$\epsilon = \Delta T \text{ (of fluid with minimum heat rate)} / \Delta T_{max} \quad (9)$$

and, the overall heat transfer coefficient is found by

$$U = Q_H / A \Delta T_m \quad (10)$$

where, ΔT_m is logarithmic mean temperature difference (LMTD) and it expressed as

$$\Delta T_m = \frac{(T_{H out} - T_{C in}) - (T_{H in} - T_{C out})}{\ln[(T_{H out} - T_{C in}) / (T_{H in} - T_{C out})]} \quad (11)$$

All of thermo-physical properties of water are determined at the overall bulk water temperature T_b , Eq. (4).

4. RESULTS AND DISCUSSION

4.1 Validation of Experiments on Basic Heat Exchanger

In this study, the experimentally obtained Nusselt number values for the basic heat exchanger (BHE) are compared with the correlation of Dittus-Boelter as given below:

$$Nu = 0.023 Re^{0.8} Pr^{0.4} \quad (12)$$

Fig. 4 shows the variation of Nusselt number as function of Reynolds number for experimental study and that for the Dittus-Boelter correlation. For both cases, with the increase of flow velocity in terms of Reynolds number, the heat transfer in terms of Nusselt number also increases. This occurs due to the fact that the heat transfer rate enhances with higher flow velocity of the working fluid. The experimental results display a good agreement with the results obtained from Dittus-Boelter correlation.

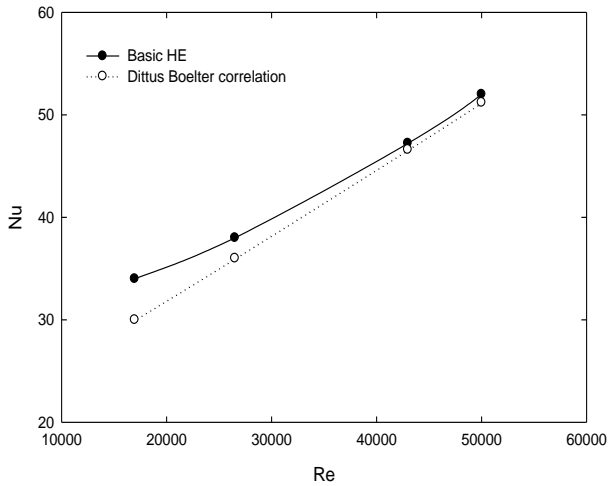


Fig.4 Variation of Nusselt number as a function of Reynolds number for Basic Heat Exchanger (BHE).

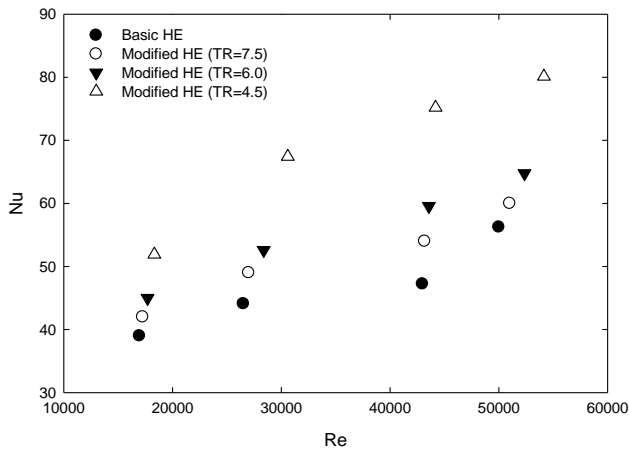


Fig.5 Variation of Nusselt number with Reynolds number for BHE and MHEs

4.2 Effect of inserting Twisted Tape and Twist ratio

Insertion of twisted tape in the copper tube causes smaller annular flow area for the hot fluid than in basic heat exchanger. With the decrease of flow area, the flow velocity increases. Twisted tape generates secondary flow inside the copper tube along with the interruption of normal fluid flow. Turbulence caused by higher flow velocity and twisted tapes, accompanying with secondary fluid flow causes increase in the heat transfer. Twisted tapes with lower twist ratio has more twist than the twisted tapes with higher twist ratio. With higher twists the tapes generate rapid secondary flow and turbulence which results higher heat transfer than other twisted tapes with high twist ratio. The variations of Nusselt number with Reynolds for modified HEs with three different twist ratio along with basic HE is shown in Fig. 5. Reynolds number is a function of velocity and velocity itself is a function of mass flow rate and Nusselt number is also proportional to the flow velocity. Both Reynolds number and Nusselt number are higher in the MHE with $TR = 4.5$, than both the BHE and the

other MHEs with $TR = 6.0, 7.5$, for different mass flow rate of hot water. Fig. 5 displays that, the insertion of twisted tape increases turbulence of the flow and thus increases the velocity of the flow which increases heat transfer in terms of Nusselt number. It also shows the linear behavior of Nusselt number variation along Reynolds number for both BHE and MHEs. The rate of heat loss from the hot fluid of the inner tube with mass flow rate of hot fluid for both the BHE and MHEs is displayed in Fig. 6. Insertion of twisted tape in copper tube causes swirl flow of hot fluid as well as turbulence. For these reasons heat loss increases with the increase of mass flow rate of hot fluid which indicates augmentation of heat transfer rate due to twisted tape insertions. The heat loss is found to be the highest in MHE with $TR = 4.5$ and the least in the BHE. Nusselt number is related to the heat transfer rate. Higher the Nusselt number means there is more convective heat transfer rate. With the increase in mass flowrate, Nusselt number increases in terms of heat transfer rate. Variation

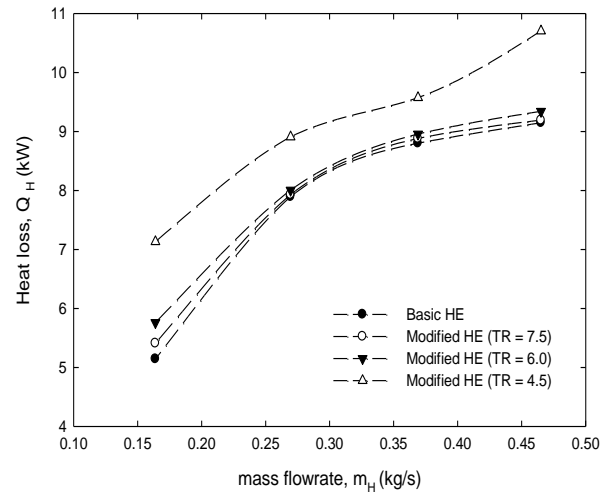


Fig. 6 Variation of heat loss from hot fluid with its mass flowrate

of Nusselt number as function of mass flowrate is shown in Fig. 7. From Fig. 7, Nusselt number is higher in the MHE with $TR = 4.5$ than the BHE and the other MHEs ($TR = 6.0, 7.5$). As the mass flow rate increases, the Nusselt number increases for all types of the heat exchangers. Fig. 8 shows the variation of Reynolds number with mass flow rate of hot fluid. Reynolds number increases for constant mass flowrates and is the highest for the MHE with lowest twist ratio than the MHEs and the BHE. Twisted tape with lowest twist ratio has denser twists than other which help the tape to generate more turbulence. This results in higher Reynolds numbers for the MHEs compared to that for BHE. The variation of overall heat transfer coefficient as function of mass flow rate of hot fluid for BHE and MHEs is displayed in the Fig.9. The overall heat transfer coefficient increases with the increase of mass flow rate of hot fluid for all types of heat exchangers. As heat transfer enhancement method (insertion of

twisted tape) applied, the overall heat transfer coefficient increases with constant mass flow rate of hot fluid. The overall heat transfer co-efficient is found to be higher in the MHEs

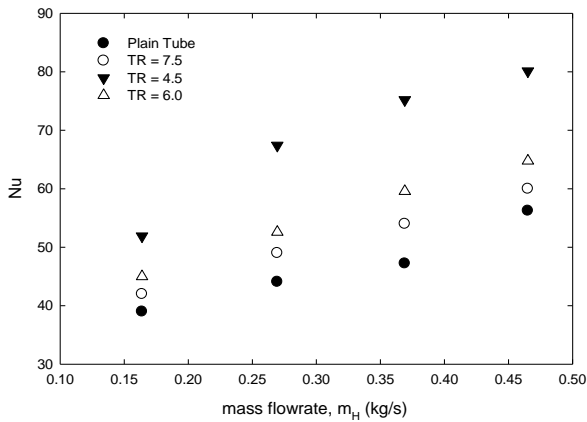


Fig. 7 Variation of Nusselt number with mass flowrate of hot fluid

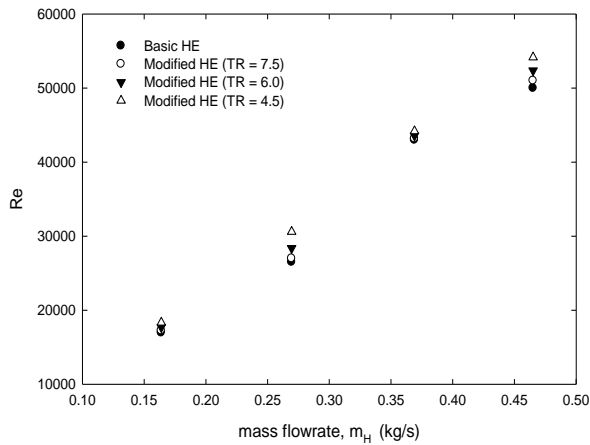


Fig. 8 Variation of Reynolds number with mass flowrate of hot fluid

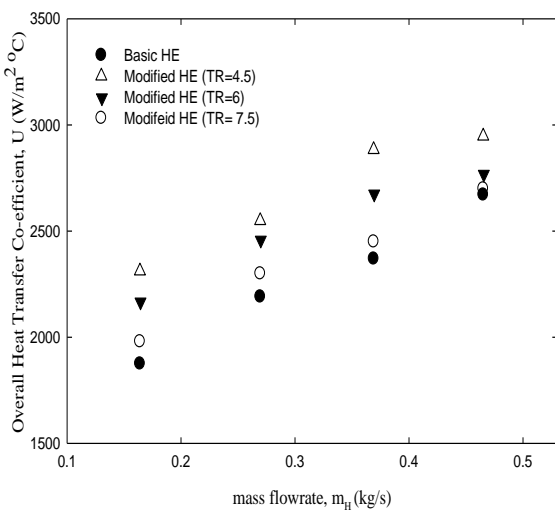


Fig. 9 Variation of Overall heat transfer coefficient with mass flowrate of hot fluid

than the BHE. The overall heat transfer co-efficient depends on the surface area. Twisted tape with low twist ratio has more twist that tends to more surface area. So the overall heat transfer coefficient is the minimum in the BHE and the maximum in the MHE with twisted tape having twist ratio of 4.5. The variation of effectiveness with mass flowrate of hot fluid for all heat exchangers is shown in Fig. 10. The comparison of effectiveness among the BHE and the MHEs displays that the effectiveness increases along with the increase in mass flow rate of hot fluid for all cases. The effectiveness of the MHE with TR = 7.5 is higher than the BHE, and the effectiveness of the MHE with TR = 6.0 is higher than both the BHE and the MHE with TR = 4.5. For the MHE with TR = 4.5, the effectiveness is found to be the maximum. In the present study, for different mass flow rate of hot fluid and for both basic and modified heat exchangers effectiveness is computed from the recorded data. The lines of effectiveness of the BHE and that of

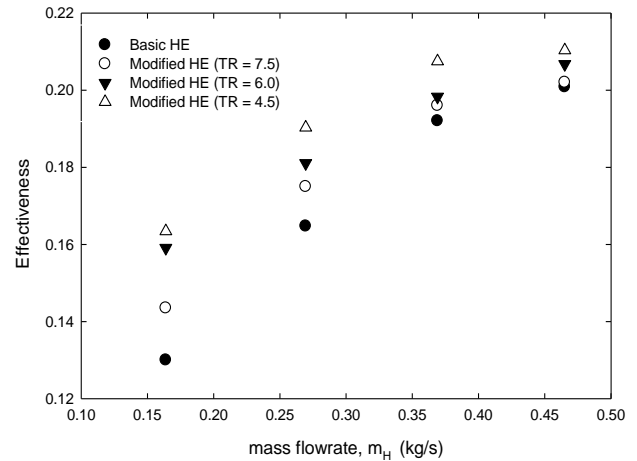


Fig. 10 Variation of Effectiveness with mass flowrate of hot fluid

the MHEs (with TR = 7.5, 6.0, 4.5) nearly follow the same trend. But it is found that as the mass flow rate increases the difference in effectiveness decreases between the heat exchangers. This means, the effectiveness achieved by applying twisted tape inserts is limited to the mass flowrate of the fluid. Hence, it can be inferred that beyond a limit of the mass flow rate, in terms of effectiveness, the achievement in MHEs becomes insignificant compared to that achieved in the BHE.

5. Conclusion

In this study, an experimental investigation on different performance indicators in a tubular heat exchanger (HE) of basic and modified with twisted tape inserts has been carried out following variable flow of hot fluid and constant flow of cold fluid in a closed circuit. According to the experiments, the major findings can be summarized as follows:

(i) Heat transfer rate was found to be enhanced in modified heat exchangers compared to that of basic heat exchanger. The rate of heat transfer enhancement was ~14.1% for HE with TR of 4.5, ~6% for HE with TR of 6.0, and ~2.5% for HE with TR of 7.5 in the modified heat exchangers (MHEs) compared to that of the basic heat exchanger (MHE).

(ii) Reynolds number increases for the MHEs as twisted tape generate turbulence in the fluid flow.

(iii) Nusselt number is found to be increased in the MHEs due to the augmentation in the heat transfer rate through the inner copper tube wall.

(iv) The effectiveness of the MHEs is limited to the mass flow rate of the fluid through the inner tube. After a limit of mass flow rate, the effectiveness becomes less significant compared to that occurs at lower mass rates.

6. NOMENCLATURE

- c_p : specific heat at constant pressure, $\text{kJ} \cdot \text{kg}^{-1} \cdot \text{K}^{-1}$
 Re : Reynolds number
 Pr : Prandtl number
 h : specific enthalpy, $\text{kJ} \cdot \text{kg}^{-1}$
 U : overall heat transfer coefficient, $\text{W}/\text{m}^2 \cdot \text{°C}$
 T : temperature, K
 t : Celsius temperature, °C
 k : Thermal conductivity, W/mK
 ν : Kinematic viscosity, m^2/s

REFERENCES

- [1] A. E. Bergles, Techniques to augment heat transfer, in Handbook of Heat Transfer Applications, 2nd edition (McGraw-Hill, New York, 1985), ch.1.
- [2] A. E. Bergles, ExHFT for fourth generation heat transfer technology, in Experimental Thermal and Fluid Science 26 (2002), pg. 335-344.
- [3] K. Yongsiri, P. Eiamsa-ard, K. Wongcharee, S. Eiamsa-ard, Augmented heat transfer in a turbulent channel flow with inclined detached-ribs, Case Stud. Therm. Eng. 3 (2014) pg. 1–10.
- [4] P. Promvonge, S. Skullong, S. Kwankaomeng, C. Thiangpong, Heat transfer in square duct fitted diagonally with angle-finned tape–Part 1: experimental study, Int. Commun. Heat Mass Transf. 39 (5) (2012), pg. 617–624.
- [5] C. Thianpong, T. Chompookham, S. Skullong, P. Promvonge, Thermal characterization of turbulent flow in a channel with isosceles triangular ribs, Int. Commun. Heat Mass Transf. 36(2009),pg.712–717.
- [6] P. Promvonge, S. Skullong, S. Kwankaomeng, C. Thiangpong, Heat transfer in square duct fitted diagonally with angle-finned tape–Part 2: numerical study, Int. Commun. Heat Mass Transf. 39 (2012), pg. 625–633.
- [7] S. Skullong, C. Thianpong, N. Jayranaiwachira, P. Promvonge, Experimental and numerical heat transfer investigation in turbulent square-duct flow through oblique horseshoe baffles, Chem. Eng. Process.: Process. Intensif. 99 (2016), pg. 58–71.
- [8] S. Eiamsa-ard, S. Rattanawong, P. Promvonge, Turbulent convection in round tube equipped with propeller type swirl generators, Int. Commun. Heat Mass Transf. 36 (2009), pg. 357–364.
- [9] P. Promvonge, C. Khanoknaiyakarn, S. Kwankaomeng, C. Thianpong, Thermal behavior in solar air heater channel fitted with combined rib and deltawinglet, Int. Commun. Heat Mass Transf. 38 (2011), pg. 749–756.
- [10] M.M.K. Bhuiya, M.S.U. Chowdhury, M. Saha, M.T. Islam, Heat transfer and friction factor characteristics in turbulent flow through a tube fitted with perforated twisted tape inserts, Int. Commun. Heat Mass Transf. 46 (2013), pg. 49–57.
- [11] P. Promvonge, Thermal performance in circular tube fitted with coiled square wires, Energy Convers. Manag. 49 (2008), pg. 980–987.
- [12] Y. Wang, Y.L. He, Y.G. Lei, J. Zhang, Heat transfer and hydrodynamics analysis of a novel dimpled tube, Exp. Therm. Fluid Sci. 34 (8) (2010), pg. 1273–1281.
- [13] P. Promvonge, Thermal enhancement in a round tube with snail entry and coiled-wire inserts, Int. Commun. Heat Mass Transf. 35 (2008), pg. 623–629.
- [14] J. Guo, A. Fan, X. Zhang, W. Liu, A numerical study on heat transfer and friction factor characteristics of laminar flow in a circular tube fitted with centercleared twisted tape, International Journal of Thermal Sciences 50 (2011), pg.1263–1270.
- [15] Y. Wang, M. Hou, X. Deng, L. Li, C. Huang, H. Huang, G. Zhang, C. Chen, W. Huang, Configuration optimization of regularly spaced short-length twisted tape in a circular tube to enhance turbulent heat transfer using CFD modeling 31(2011), pg. 1141-1149.
- [16] S. Eiamsa-ard, C. Thianpong, P. Eiamsa-ard, P. Promvonge, Convective heat transfer in a circular tube with short-length twisted tape insert, International Communications in Heat and Mass Transfer 36 (2009), pg. 365–371
- [17] S. Eiamsa-ard, C. Thianpong, P. Promvonge, Experimental investigation of heat transfer and flow friction in a circular tube fitted with regularly spaced twisted tape elements, International Communications in Heat and Mass Transfer 33 (2006), pg. 1225–1233.
- [18] S. Jaisankar, T.K. Radhakrishnan, K.N. Sheeba, Experimental studies on heat transfer and friction factor characteristics of forced circulation solar water heater system fitted with helical twisted tapes, Solar Energy 83 (2009), pg. 1943–1952
- [19] S.K. Saha, A. Dutta, S.K. Dhal, Friction and heat transfer characteristics of laminar swirl flow through a circular tube fitted with regularly spaced twisted-tape elements, International Journal of Heat and Mass Transfer 44 (2011), pg. 4211–4223.

Drive Cycle of Heavy Vehicles in Dhaka City: A Case Study

M. Fahim Asif Khan, Mirza Farhan Hasin, Md. Jubayer Hossain*, Anjan Goswami, and Mozammel Mia

Department of Mechanical and Production Engineering,
Ahsanullah University of Science and Technology (AUST), Dhaka-1208, Bangladesh

ABSTRACT

In this present work, a case study of non-legislative drive cycle for heavy vehicles in Dhaka, the capital of Bangladesh, has been presented. The methodology is as follows (i) two major routes were chosen (ii) the data was analyzed in terms of speed-time and acceleration-time profile graphically (iii) lastly, the findings were compared with international drive cycles. For measurement purpose, a GPS device, having low response time, was used for recording the time-distance values. It has been found that the average speed for heavy vehicles was 7.949 km/h which is significantly lower compared to other international drive cycles. Furthermore, it was noticed that for 89.156627% of travel time the speed was below 30 km/h, for 4.8192771% of travel time the speed was between 30 to 60 km/h and for 6.0240964% of travel time the speed was between 60-90 km/h. The research outcomes can be of direct interest to the Bangladesh Road and Transport Authority (BRTA), Dhaka Metropolitan Police (DMP, Traffic) and other transportation authorities to effectively plan Dhaka city's traffic system.

Keywords: Drive cycle; Speed-time profile; Heavy vehicle; Dhaka City.

1. Introduction

Dhaka city, the capital of Bangladesh, a country in south-east Asia, is a place of work and habitat of over 18 million people [1]. Within very small geographical area of 1528 km², the population density is 28748 per sq. km [1]. Despite this fact, the city of Dhaka is one of the fastest growing megacities in the world. Oddly, this huge populace moves from one place to another for their necessity – mostly by public and private transport systems such as car, bus, bike etc. Over population and less space, together, contribute to frequent traffic jam. As such, countless amount of valuable and workable time is wasted on the roads. Moreover, the consumptions of fuel in idle condition of vehicles and associated emission of exhaust gases such as CO₂, HC, CO, NO_x etc. are higher than the usual condition. These emissions are harmful for the environment and one of the major causes of global warming. In USA 28% of greenhouse gases are emitted by their transportation sector[2].

Traffic condition influences the economical and environmental state of a country. When the traffic condition is congested, vehicles remain idle for most of the travel time, which leads to higher consumption of fuel, an uneconomic state. Moreover, a person has to stay in road for a long period which leads to the wastage of his workable time and causes mental agony. In 2017, World Bank reported that traffic jam in Dhaka eats up 3.2 million working hours per day[3]. Moreover, when a vehicle remains idle, it emits more exhaust gases. These harmful gases disrupt the environmental balance drastically. Bangladesh Atomic Energy Commission reported that automobiles in Dhaka emit 100 kg lead, 3.5 tons SPM, 1.5 tons SO₂, 14 tons HC and 60 tons CO in every day[4].

To control the contribution of transportation to environmental and economical degradation, measuring the traffic performance has to be taken as an initial step

to eventually control such degradation. Reportedly, one of the most effective ways to understand the traffic performance is by constructing a drive cycle. Drive cycle is defined as a series of data points representing the speed of vehicle versus time sequenced profile developed for a certain road, route, specific area or city[5]. It represents the driving pattern of a road along with various parameters i.e. speed, acceleration, distance, time etc. Driving patterns influence exhaust emissions and fuel consumption[6, 7].

The necessity of constructing a drive cycle is perceived through the ages by different countries. By means of that, some well renowned drive cycles have been constructed and followed by most nations around the world. New European Driving Cycle (NEDC) and FTP-75 are highly accepted drive cycle and followed by the nations or states of Europe and America respectively. However, it is to be noted that every route is unique by itself. Therefore, the driving pattern of all the roads is unlikely to be represented by a single common drive cycle. Otherwise, underestimation or overestimation takes place due to lack of precision. In order to overcome this gap many countries have stopped following a common drive cycle and devised their own drive cycle.

Ho et al. [8] conducted a study on the Singapore Drive Cycle (SDC). In order to attain 7-11% carbon emission reduction by 2020, authors realized the shortcoming of following the NEDC and developed one drive cycle. It was a 2400 second speed versus time profile to represent the driving pattern for passenger cars in Singapore. Microscopic estimation model showed that as compared to SDC, the NEDC underestimates most of the vehicular emissions (fuel, CO₂, HC and NO_x by 5%, 5%, 22% and 47% respectively) and overestimates CO by 8%. The SDC is thus more suitable than the NEDC that is currently in use in Singapore to generate more accurate fuel consumption and emissions ratings.

* Corresponding author. Tel.: +88-01911099149
E-mail addresses: hossain.jubayer@gmail.com

Fotouhi and Montazeri-Gh [9] developed a drive cycle for the city of Tehran by using a new approach based on data clustering. Majority of the drive cycles are developed using the random approach method of combining a number of micro trips and a repetitive process is then executed to determine the most representative cycle. Instead of adopting this typical approach, they conducted a new method with less computation. It is a 1533 second speed time series, with an average speed of 33.83 km/h and a distance of 14.41 km. Kamble et al. [10] developed drive cycle for city of Pune, India. In Pune drive cycle five important parameters of time-space profile was considered in methodology. Therefore, it made the drive cycle a more accurate representation of their heterogeneous traffic behavior.

Considering the fact that, the most popular medium of transportation in Indian subcontinent is public bus; a drive cycle for heavy vehicle is needed to be constructed. In order to achieve this target, a drive cycle for intra city buses has been developed in Chennai, India by Nesamani et al. [11]. The emission rate and fuel consumption by buses of Chennai are estimated with European Drive Cycle, which does not go with their road pattern. Therefore overestimation and underestimations are originated. In order to precise the estimation; they constructed a specific drive cycle for intra city buses. Along with other parameters, they have determined the percentage of creeping mode, cruise mode and average running speed to increase the accuracy of their work. Furthermore, they have divided the data into 6 groups including three peak and non-peak periods and three different road widths and analyzed in accordance to it.

Despite serious urgency for developing a drive cycle for public bus transportation mode in Dhaka city, hardly there is any recent useful study on its drive cycle. Although a drive cycle has been constructed some years ago by Adnan et al.[12]for passenger cars, it is essentially required to be updated due to changes in routes, addition of new routes and flyovers. In this respect, the objective of this research work is to construct a recent and practical drive cycle of heavy vehicles *i.e.* public buses for two major routes of Dhaka city and to further analyze and compare the results.

2. Methodology

Among different available modes of transportation *i.e.* bus, compressed natural gas driven vehicles, private cars, motor cycles, the current study was conducted on buses only. This is due to the fact that bus is one of the mostly used modes of transportation – a mode that associates low transportation cost. Moreover it is highly convenient among students and low-earners in respect of availability and affordability. It is to be noted that with the increase of number of buses (as well as other

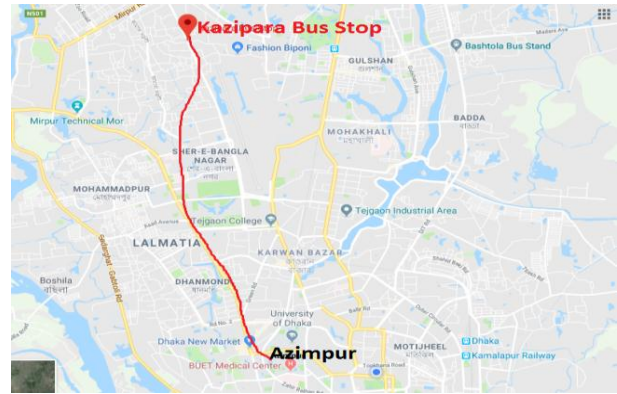


Fig.1 Route navigation of Kazipara-Azimpur-Kazipara

models of vehicles) the new routes are not increased. As such, the existing routes are used by this increased number of vehicles. This outnumbering of buses is causing congestion of traffic and uncomfortable movement. Based on this scenario, the study concentrated on tracking the driving pattern of public bus and analyzing the outcomes to reach a conclusion. To conduct the study, the methodology is divided in 4 steps.

2.1 Route selection

Two different routes were selected to cover the range of distances to be travelled as shown in Figure 1. The route selection was conducted based on strategic planning to make the center point at Kazipara so that the vehicles can move along two opposite directions from the center. In one side, the vehicles moved along Kazipara-Uttara route, and on the other side, the vehicles moved along Kazipara-Azimpur. It is to be noted that these routes are two of the busiest routes in city of Dhaka.

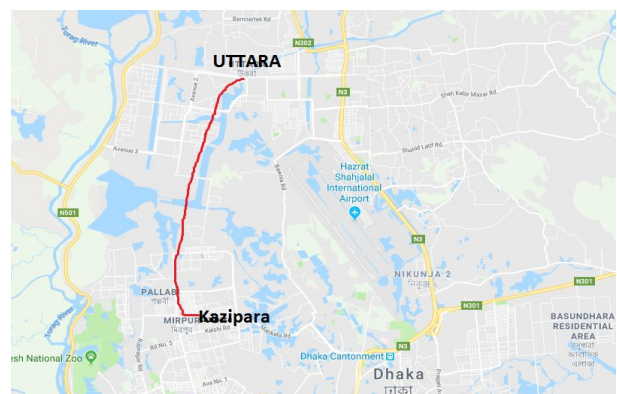


Fig.2 Route navigation of Kazipara-Uttara-Kazipara

Table 1 Characteristics of the vehicle

Vehicle name	Engine capacity	Type
Eicher Skyline	3289 cc	Passenger Bus

2.2 Data collection

The characteristics of the used buses are listed in Table 1. Two typical public buses were equipped with GPS device (Etrex-10) to record the distance with respect to time. To make the data collection robust, the data was recorded in two different time of the day. This variation in time of data collection facilitated the opportunity to accommodate the frequent changes in the vehicles speed and acceleration throughout the day. It is to be mentioned that the data was collected as an up and down method i.e. during the forward trip and backward trip of the same route.

2.3 Analysis

After collecting all the measured raw data from the GPS device, the values were graphically analyzed. From the analysis, all the necessary parameters such as velocity and acceleration had been derived and calculated. For a clear vision of the driving pattern, some graphs such as velocity versus time, acceleration versus time, and percentage versus speed range were drawn from those values.

2.4 Drive cycle generation

Lastly, the driving cycle was developed that best represent the driving pattern of the selected routes (roads) in Dhaka city. To choose the method, it is kept in consideration that the outcomes are maintaining high level of accuracy but it is easy to calculate. Hence, the average velocities for each of the two routes were calculated from the measured values of time and travelled distance. Afterward, an overall average velocity from the average velocities of both routes was calculated. Finally, between the two routes, the route that is carrying the closest value of average velocity to the overall average velocity was taken as the standard to develop the drive cycle for the city of Dhaka.

3. Results and discussion

The decisive parameters of the selected two routes (e.g. ‘Kazipara-Uttara-Kazipara’ and ‘Kazipara-Azimpur-Kazipara’) are listed in Table 2. Both of these average values are astonishingly low. The average speed of the bus along the Kazipara-Uttara-Kazipara is only 75%

Table 2 Value of the parameters of each route

Parameters	Kazipara-Uttara-Kazipara	Kazipara-Azimpur-Kazipara
Total Distance (km)	30.04	18.60
Total Time (hour)	3.43	2.69
Average Speed (km/hr)	8.77	6.91

higher than the average walking speed of a human while the other route (Kazipara-Azimpur-Kazipara) resulted in an average speed that is 40% higher than the typical human walking speed. It can also be seen that the average speed along the Kazipara-Uttara-Kazipara route is higher than the average speed of Kazipara-Azimpur-Kazipara route. By taking average of all the average velocities of the two routes, the overall average velocity came out 7.95 km/h. This statistics raises serious concern about these routes’s sustainability in terms of environment, economy and development.

For further analysis of the selected routes, the data is presented for the Kazipara-Uttara-Kazipara route as the standard route for having the average velocity of 8.77 km/h that is closest to the overall average velocity. Moreover, to be precise, the driving cycle has been formulated for a micro-trip of this route consisting of 4 standard operations such as idle mode, acceleration mode, deceleration mode and cruising mode. Figure 3 exhibits the standard speed-time profile i.e. the drive cycle for bus. The trip is 4.108 km long having travel time 1249s. The average speed of this cycle is 11.84 km/h which is a little higher than the overall average velocity 8.77 km/h. It can also be observed that the speed hardly remains constant. At several times the speed of bus was 0 km/h. It is also appreciable that at two different time segments the speed increased significantly. For the first case, approximately at 440s of the travel time, the speed of the bus started to increase gradually till it reached at maximum speed approx. 68 km/h at the travel time of 480s. After that the speed started to plummet reaching zero speed at travel time of approx. 570s. A similar rise-and-fall pattern of speed can be observed in between 1130s to 1229s. These two sudden increases of travel speed can be accredited to the congestion free road at that time. For Pune, India the average speed as reported as 19.55 km/h. Hence, the average speed of Dhaka city is approx. 40% below that of Pune, India. With respect to European drive cycle, the average speed of Dhaka city is 65% less [10]. The outcome is the combined result of two separate activities, boarding and alighting passengers at

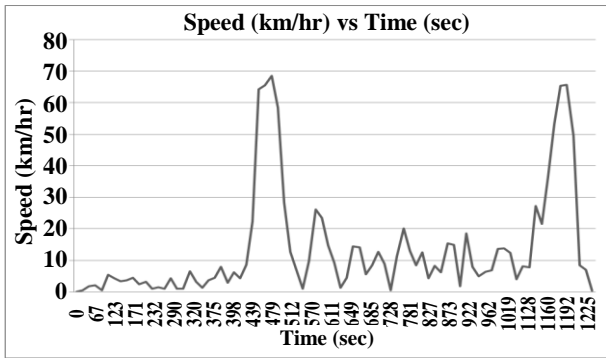


Fig.3 Speed (km/hr) versus Time (sec) Graph

numerous points, and the congested traffic that resisted the vehicle from running at a constant speed. Figure 4 shows the acceleration pattern for the elementary micro-trip *i.e.* drive cycle. A number of sharp spikes *i.e.* sudden accelerations and decelerations are observed suggesting high emission at this phase. This sudden acceleration-deceleration can be imputed to the short span of free road, sudden change of lanes of other vehicles, appearance of slow moving vehicles etc. As can be seen from Figure 3, from 0s to 300s, the acceleration-deceleration was somewhat close to zero. However, after that time period, there is a sudden acceleration followed by deceleration. Even beyond that period, the acceleration-deceleration is quite abrupt and in great magnitude. Two major decelerations can be found at approx. time period of 510s and 1210s.

Figure 5 demonstrates the percentage of time the bus was run at different speed range. Note that the speed range is taken as increment of 10 km/h. Astonishingly, for 63.86% time the bus ran below 10 km/h speed. This value of speed is quite unorthodox when it is compared to different drive cycles of the world. As it can be also seen that the percentage of time the vehicle is run is declining with the increase of speed. As such, the percentage of time that the vehicle was run in between 30-60 km/h is lowest. But, the speed spectrum (40-60 km/h) is typically considered as fuel efficient speed zone. Evidently, as the bus in Dhaka city is running with that much low speed for that amount of time, then the fuel as well as operating cost becomes higher for the bus.

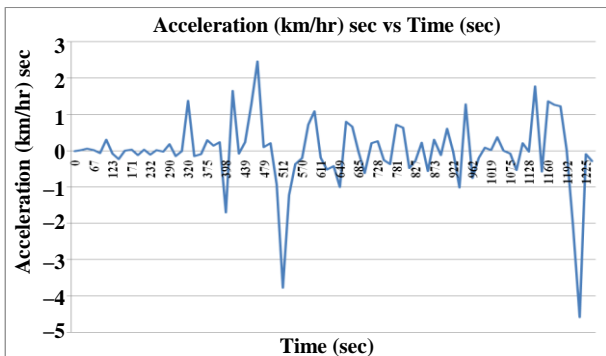


Fig.4 Acceleration (km/hr)/sec versus Time (sec)

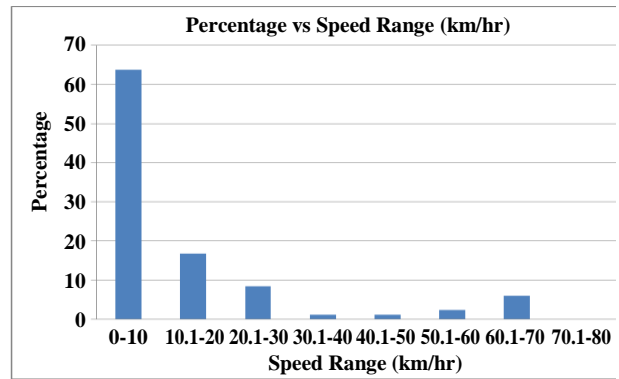


Fig.5 Percentage versus Speed Range Graph

In parallel, the increased fuel consumption is causing environmental degradation.

A broader classification of the speed distribution is shown in Figure 6. From this figure, it is blatant that, for almost 89.15% of the travel time the speed of the vehicle remained between 0-30 km/hr. And only for the rest 10.85% of the travel time the speed exceeded it.

4. Conclusion

From the current study, it has been found that the overall average speed for heavy vehicle (bus) is 7.95 km/hr. However, for the micro-trip of bus *i.e.* drive cycle, the average speed was found as 11.84 km/h. The speed remained below 30 km/hour for 89.15% of travel time and it was above 60 km/hour for about 10.85% of travel time.

This average speed is drastically low for heavy vehicles in Dhaka city, especially when compared with international drive cycles. Consequently, the comfort traveling is compromised, valuable time is wasted, environmental harm is caused, and most importantly the sustainable city development is hampered.

Hence, to cope up with sustainability index of city development, proper steps need to be taken by the administration to duly regulate the buses by following the results of drive cycle of Dhaka city. In fact, it can be further improved to make it comparable with international drive cycles.

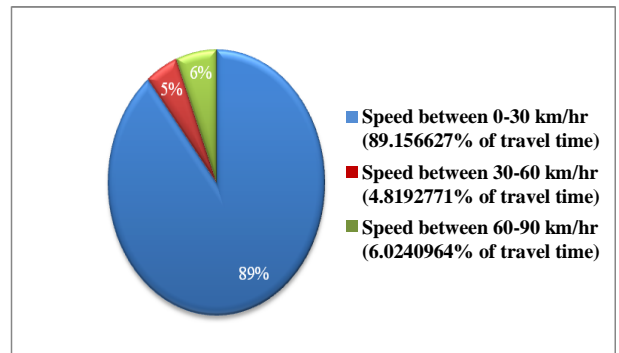


Fig.6 Speed Range Percentage

REFERENCES

- [1] S. Ahmed, K.M. Nahiduzzaman, M.M.U. Hasan, Dhaka, Bangladesh: unpacking challenges and reflecting on unjust transitions, *Cities*, 77 (2018) 142-157.
- [2] EPA, United States Environmental Protection Agency.
- [3] The Daily Star, July 19, 2017
- [4] G. Alam, Environmental pollution of Bangladesh—its effect and control, *Pulp and Paper*, 51 (2009) 13.17.
- [5] F. Ab Ghafar, Driving cycle for small and medium duty engine: case study of Ipoh, Universiti Tun Hussein Onn Malaysia, 2015.
- [6] [6] N. Arun, S. Mahesh, G. Ramadurai, S.S. Nagendra, Development of driving cycles for passenger cars and motorcycles in Chennai, India, *Sustainable cities and society*, 32 (2017) 508-512.
- [7] K. Brundell-Freij, E. Ericsson, Influence of street characteristics, driver category and car performance on urban driving patterns, *Transportation Research Part D: Transport and Environment*, 10 (2005) 213-229.
- [8] S.-H. Ho, Y.-D. Wong, V.W.-C. Chang, Developing Singapore Driving Cycle for passenger cars to estimate fuel consumption and vehicular emissions, *Atmospheric Environment*, 97 (2014) 353-362.
- [9] A. Fotouhi, M. Montazeri-Gh, Tehran driving cycle development using the k-means clustering method, *Scientia Iranica*, 20 (2013) 286-293.
- [10] S.H. Kamble, T.V. Mathew, G. Sharma, Development of real-world driving cycle: Case study of Pune, India, *Transportation Research Part D: Transport and Environment*, 14 (2009) 132-140.
- [11] K. Nesamani, K. Subramanian, Development of a driving cycle for intra-city buses in Chennai, India, *Atmospheric Environment*, 45 (2011) 5469-5476.
- [12] A. Adnan, T. Shireen, N. Quddus, A driving cycle for vehicular emission estimation in dhaka city, *International Conference on Mechanical Engineering 2011 (ICME2011)* 18-20 December 2011, Dhaka, Bangladesh, 2011.

Study on Bio-Fertilizer Extraction and Management of Municipal Solid Waste of Khulna City

Debasish Adhikary*, Md. Shahidul Islam

Department of Mechanical Engineering, Khulna University of Engineering & Technology, Khulna-9203, BANGLADESH

ABSTRACT

The increasing population of Bangladesh leads to the growth of urban areas and slums which in turn, generating a huge volume of wastes. In this study, Main focus is given on bio-fertilizer extraction from municipal solid waste as well as analyzing present waste generation and management procedure. Although major portion of solid waste is organic but unsatisfactory solid waste management system creates some common problems. At the same time, those wastes have a potential value of producing organic bio-fertilizer. The total daily household wastes generated in Khulna City areas is about 500 tons and from this total waste it is possible to produce 200 tons of compost daily. But only 1.5 tons of compost is producing per day in Rajbandh by RUSTIC and generating about 10,000 taka profits. In this context, to meet up the growing demand of bio-fertilizer, it is the best way to use renewable resources like municipal solid waste.

Keywords: Municipal solid waste, Solid waste management, Bio-fertilizer, Khulna city.

1. Introduction

Municipal solid waste comprises of all the wastes arising from human and animal activities those are normally solid and are discarded as useless or unwanted things. It may be heterogeneous mass of throw-away from the urban community as well as the more homogenous accumulation of agricultural, industrial and mineral wastes. It includes durable goods, non-durable goods, containers and packaging, food wastes, yard wastes and miscellaneous inorganic wastes from residential, commercial, institutional, and industrial sources. Least Developed Asian Countries like Bangladesh is not too much concerned and anxious about her environmental problems on Municipal Waste Management. In the major cities of Bangladesh, per capita production of waste is 0.5 kg/day but only 0.2 kg of waste per capita is carried to the final disposal site. The rest is disposed locally [1]. The total daily household solid wastes generated in Khulna City areas is about 490 to 510 tons. Around 40% of total household wastes are managed by different organizations [2]. Because of unsatisfying solid waste management system in Khulna city, some common problems are occurring such as diseases, fire hazards, odor for nuisance atmosphere, water pollution and consequently economic losses [3]. To prevent those problems, it becomes necessary to manage properly the municipal solid waste rather than dumping outside the main city. These municipal solid wastes can be used to produce bio-gas by anaerobic digestion process and generate electricity and it can also be used to produce bio-fertilizer [4].

Objectives of the Study are followed:

- (1) To study the recent potential of municipal solid waste in KCC area.
- (2) To study existing bio-fertilizer extraction process from Municipal Solid Waste (MSW).
- (3) To disclose the existing Municipal solid waste management practice.
- (4) To find out the efficient way to extract bio-fertilizer from municipal waste among a few alternatives.

2. Methodology

2.1 Research Design

This research is mainly descriptive in nature. Both primary and secondary data is used to prepare this research. The primary data is collected from various sources such as interview, talking with experts and people directly or indirectly related to waste management. Secondary information such as statistical data, reports, MSWM (Municipal Solid Waste Management), transportation related data etc. is collected from various Government offices and Non-Government Organizations (NGOs), CBOs such as:

- (1) Khulna Development Authority (KDA).
- (2) Khulna City Corporation (KCC).
- (3) Demographic information from Bangladesh Bureau of Statistics (BBS).
- (4) Journals and papers relevant to the study from NGOs and various web sites.

Information is also collected from informal talking with the personalities who are directly or indirectly related with this matter.

2.2 Survey

A survey was conducted in Rajbandh Landfill located in Botiaghata Thana in Khulna city. Questionnaires were prepared and interview of the persons related with the administration and management of the wastes was taken. Around 20 questions were asked to Md. Anisur Rahman (Conservancy Officer of KCC), Md. Abdur Sattar (Conservancy Officer RTD of KCC), Anowar (Supervisor of Conservancy Transport Support Authority), Md. Liton (Driver), Md. Amjad Hossain (Driver), Md. Abul Basahar (Driver), Moral Noor Mohammad (Executive Director, RUSTIC), Md. Sohel (Store and Delivery manager), Hozrat Ali (Senior Compost field maker), Md. Rashed (Senior Compost field maker), Nasima and Asma (Compost field worker), Sagor and Raja (Farmer), Nurul Islam (Field Supervisor in Rajbandh), Ilias (Field Co-supervisor in Rajbandh) and they answered gently.

3. Literature Review

(According to the Khulna City Corporation Ordinance, 1984) Khulna City Corporation (KCC) is responsible for collection, transportation, and treatment of solid waste in Khulna City but KCC does not collect any waste in 7 wards out of 31 wards because these wards are situated remote area and waste are locally managed there. Sometimes causes few regional affect for constructive factors but in the rest of 24 wards only 20% wastes where collect by KCC and 80% wastes are not managed properly (Conservancy Department of Khulna and RUSTIC).

Hoque [5] reported that the location of disposal (secondary) sites of KCC represent the unconsciousness about the environmental and public health hazards arising from disposing of waste in improper location.

Richard et al. [6] reported that in the rapidly growing cities of developing countries, urban solid waste management is currently been regarded as one of the most immediate and serious issues for city authorities. Due to inadequate and often inefficient solid waste management and visible environmental degradation, solid waste generated at an increasing rate has also become an important environmental issue for the residents of the major cities of Least Developed Asian Countries (LDACs) like Bangladesh.

Alamgir and Ahsan [7] said that management of this steeply increasing vast quantity of solid wastes is a very complex process indeed. Due to severe financial constraints, absence of appropriate technology, lack of people's awareness, motivation and participation, ineffective legislation and law enforcement to protect the environment and to handle the waste, the whole system is becoming a threat to city dwellers, planners and other stakeholders including these factors, resource and other constraints and limitations, KCC has not been able to manage well entirely the whole task of solid waste disposal.

Sultana T. [1] stated the existing Municipal Waste Utilization of Khulna City Corporation and determined the ecological footprint of waste generation of KCC area. She also recommended the way by which the ecological footprint of waste generation can be very effective tool for sustainable waste utilization in KCC area.

Alamgir and Ahsan [3] stated most of the wastes of landfill are waghered to our soil nutrition and to ensure our food security, intensive cultivation and applied commercial fertilizer are also degrading air soil health.

Kashem [8] stated in his research that, if the municipal waste which is generated in Khulna city is managed properly, it can be a potential resource. By using waste, biogas can be produced and the residue of biogas can be used as compost fertilizer.

4. Eco-Friendly Waste Management Approaches and Disposal Alternatives

Waste management and disposal treatment is an appropriate management technique based on prevailing socio-economic settings, technological capabilities and

waste separation into the organic, inorganic, depositional, thermal, recycling, reduce and reuse treatment [9]. In Bangladesh, the Solution for MSW management handled separately as the situation varies city by city, within different regions of the city and within different parts of the region [10]. There are lots of alternatives for managing Municipal Waste like Recycle of Wastes, Waste Reduction and Reuse, Incineration, Pyrolysis and Gasification, Open Burning, Controlled Dumps, Biological Waste Treatment as Composting, Anaerobic Digestion and Integrated Solid Waste Management. Among those Biological Waste Treatment as Composting is most suitable process for waste management in Khulna City.

4.1 Potentials of Composting in Khulna City

The factors which favor for composting are: waste generated in Khulna is suitable for composting as around 78% of it is compostable. Moisture content of 50 to 60 percent is optimum for aerobic composting. The typical moisture content of Khulna city is 55 percent, which is within the acceptable range for composting. Source separated organic waste, free from toxic and clinical wastes, which are essential for good quality compost, can easily be obtained in Khulna. House to house collection of waste and separate collection of clinical and hospital waste are being introduced in Khulna with community participation by NGOs/ CBOs and active support of KCC [11].

4.2 Possibilities of Using Composts in Agriculture in Khulna City

An enormous amount of commercial fertilizer has been spilled over to improve our agricultural production and now a day our agriculture is going to depend as an artificial fertilizer day by day. But it is a threat to our soil health, crop yield and natural habitat because use of commercial fertilizer and pesticides to land again and again causes many affect to soil nutrition's, soil water and plant resistant to pathogen. Although this report shown the solid waste management of KCC by compost production but also our farmers can produce it easily by their agricultural waste, domestic waste and other villagers' sources. So in future, the compost manure of waste management can played an important role to our agriculture in Bangladesh.

5. Existing Municipal Solid Waste Management in Khulna City

5.1 KCC Initiatives for Solid Waste Management

Khulna City Corporation (KCC), the only public sector organization responsible for collection, transportation and disposal of solid waste in Khulna City, is not providing satisfactorily level of conservancy services [12]. It collects 40 to 50 percent of the total waste and the rest is used for land reclamation. Very insignificant portion is also collected by the scavengers. This results in odor and obnoxious conditions in Khulna City according to Sabikunnahar [13]. With 50 garbage trucks, 462 cleaners, and an annual budget of Taka 175.00

lakes, according to vehicles support facilities of KCC. KCC is not well equipped to cater satisfactorily the need of conservancy services of the city dwellers of Khulna. Over the years, KCC has increased its staff size and equipment, but these are insufficient in terms of quality and quantity according to the need [14].

Table 1 Facilities of manpower, infrastructure and transport in KCC.

Facilities of manpower, infrastructure and transport in KCC.		
Manpower	Supervisory	40
	Sweepers etc	104
	Drain cleaners	358
	Drivers	37
	Spray men	31
	Fogger Operators	5
	Truck Helpers/Labors	79/54
Physical Infrastructure	Secondary collection Points	60
	Dustbins	1200
	Metal waste containers	45
Transport and Vehicles	Covered Trucks	5
	Normal Trucks	10
	Container Carries Truck	11
	Rickshaw Vans	200
	Tractors	4
	Damp Truck	8
	Paur-tetar	2
	Vacutac	4
	Night soil carrier	6

5.2 Current Situation of Wastes Generated from KCC
 Khulna City Corporation consists of 31 wards and the wastes of 24 wards out of 31 were collected by Conservancy Department Activity of City Corporation. Seven wards (No 1 to 7) are situated in the remote area and manage their wastes locally. Sometime the wastes of above seven wards cause few regional effect for constructive factors.

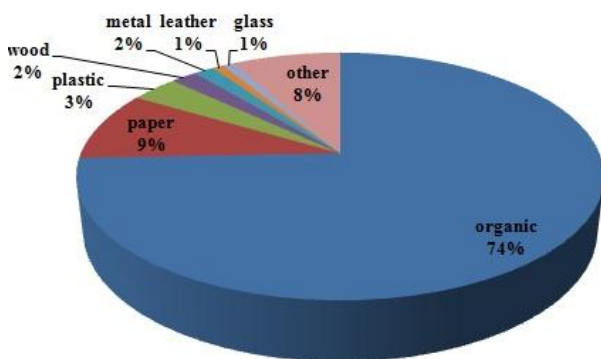


Fig.1 Distribution of different wastes in percentage generated from KCC [1], [7].

Only 40-50% wastes are collected by KCC and 60-50% wastes are not collected and managed (Conservancy Department of KCC). It has been observed that 70% to 80% of the generated waste is organic in nature and these are easily bio-degradable and the rest 30% to 20%

of the total waste generated are inorganic and non-biodegradable.

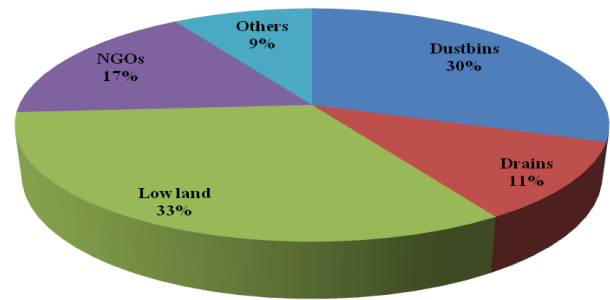


Fig.2 Current Distribution of KCC Wastes [2].

It has been estimated that at present Khulna city generates 490 to 510 metric tons of solid wastes per day with a per capita of about 0.3 to 0.5 Kg/day [15]. Conservancy Department of KCC is responsible for the collection, transportation and disposal of solid waste in Khulna city. Apart from this, a number of government and semi-government organizations are giving emphasis to manage solid wastes that is being generated in their own premises and compounds [16].

5.3 Solid waste collection system

The KCC is considered as the most important organization involved in waste collection. The collection services in urban centers concentrate only in the removal of wastes from communal bins. Wastes removal services involve manual collection from the bins and manual loading of the collection vehicles. However, recently, some NGOs, CBOs and private organization work with city authorities. But the situation remains unchanged. The strengths and drawbacks at all levels of the existing wastes management system are identified by Waste-safe [17].

Table 2 Involvement and area coverage by different NGOs.

Name of NGO/CBO	Area Coverage(Ward)
Prodipan	6,12,17,18 and 24
Prasanti	119 Health Care Center
Amadar Paribartan	30
ASODE	24(part)
Shabolambi	25 and 26(part)
Muktir Alo	11
Niharika	23
RUSTIC	30(part)
Centre of Human Development	18(part)
Unnayan	15 and 16(part)
	25(part)

The wastes generated in the home is stored and collected everyday by a primary collector who transports the waste to the nearby transfer point, normally in a rickshaw van and transport points are

placed where waste is unloaded from primary collection vehicles to be taken away by secondary transport. KCC has a collection area of 47 sq. km. with total number of conservancy staff about 462 and 1200 dustbins. There are minimum 10 to 20 dustbins in each ward. Some of the dustbins are open at the top and some are covered. KCC estimates about 510 ton of wastes are generated daily in the city area and only 300 to 320 ton are collected by its workers and the remaining are dumped irregularly. KCC has 60 secondary disposal sites and some disposal sites are placed with demountable container, from where workers collect wastes with recommended KCC vehicles to the final disposal site in a regulated timetable. It has regular 22 to 25 trips to the final disposal site daily. Rajbandh is the main dumping station of the KCC. It is at the western side of Khulna City and of about 25 acres. The waste truck of the KCC is reported to dump their wastes in many illegal places. This is due to lack of skilled manpower and knowledge and also the lack of sufficient places.

5.4 Existing recycling process in KCC

The KCC does not perform any kind of resource recovery activities. Wastes of some market value are being reclaimed or salvaged informally. The housewives separate the refuse of higher market value such as papers, bottles, fresh containers, old cloths, and shoes and sell them to street hawkers (locally called feriwallas). Then salvaging is carried out by wastes pickers (mostly the children of slum dwellers). The items include broken glass, can, card board, waste paper, rag, plastics, metals and miscellaneous wastes discarded by households. The estimated number of scavenger of Khulna city is nearly 600, who are annually earning BDT 4,500,000 by removing solid waste [18].

6. Bio-Fertilizer Extraction from Municipal Solid Waste

Composting is the process of decomposing organic matter, whether manure, crop residue or municipal wastes, by a mixed microbial population in a warm, moist aerobic environment. On the other hand, Composting is certainly one of the most natural types of recycling processes there are. It happens in the open air (in a ditch or a heap) or an enclosure (silo, etc) and consists simply of organic waste transforming in the presence of oxygen in the air. Over a total of six months (generally spring and summer), it happens in two stages: Decomposition during which any still-intact organic material is attacked by high temperature bacteria (50-70°C). Maturation during which the fresh compost transforms little by little into compost rich humus thanks to the action of low-temperature yeast (35-45°C). Materials and chemicals required for composting are Bamboo, Leader, Boding a windrow, Thermometer, Turning the pile and Mineral addition. Few things are avoided for composting like Meat and meat byproducts, Oil, Dairy products, Diseased plants, Invasive plants gone to seed, Yard waste treated with pesticides and conventional fertilizers.

6.1 Steps of Making Compost

Making good compost depends on having the proper sources of nutrients with a balance of carbon and nitrogen, keeping the pile of compost moist and making sure that there is adequate aeration. Different levels of processing are required for achieving the decomposition. The compost pile can heat up to 60-70°C due to the microbial activity. However, high temperatures will result in substantial losses of nitrogen in the form of ammonia gas. Farmers with many years experience at compost-making recommend that temperatures are kept below 55°C to avoid overheating and nutrient losses. The most commonly used materials for the compost pile are manure mixed with livestock bedding. When the bedding (which is predominantly carbon) is mixed with the raw manure (which is an excellent source of nitrogen), the balance of carbon to nitrogen (25-35:1) will be achieved which is needed to begin the composting process.

Steps of Making Compost are breaking of wastes pile, Bedding for composting, Turning/mixing, Additional materials used for composting, Rebidding and Manufacturing process. During composting of first bedding, at the initial stage the temperature rises at 50°C to 55°C within 12 to 15 days. Then new materials should be added to the composting system during turning or mixing. For favorable composting, the physical, chemical, biological and degradable changes occurred under the extra component are used to influence the composting activity like watering, soil, cow-dung, fire-ashes, light sources etc. After that the temperature regain at 50°C to 55°C and this treatment are runs under 15 to 20 days and in the last bedded treatment and within 15 to 17 days to complete all microbial activity, the temperature is come down from 15 to 18°C. Then the pile is breakdown and this raw compost is spreader-up to everywhere around the bed and it rests for 1 to 3 days for normal temperature.

6.2 Sign of the completion of composting

Sumon [19] found, the material should have a pleasant "woody" odor and a friable texture similar to a good potting soil. The material will likely feel moist and cool and have a dark brown color.

Table 3 Composition of finished compost [20].

Parameter	Result
Present Composition	
Color	Grey
Physical conditions	Non-granular
Odor	Absence of foul odor
Moisture	17.0%
pH	7.0
Organic Carbon	10.65%
Total Nitrogen(N)	0.95%
C:N	11.2:1
Phosphorus (P)	0.70%
Potassium (K)	1.25%
Sulfur (S)	0.29%

Zinc(Zn)	0.04%
Copper (Cu)	0.016%
Chromium (Cr)	18.28ppm
Cadmium(Cd)	0.18ppm
Lead (Pb)	22.57 ppm
Nickel(Ni)	24.44 ppm
Inert material	<1%

6.3 Cost and Profit Analysis of composting in Rajbandh According to KCC, daily waste generation in Khulna city is 490-510 tons. RUSTIC says that after an initial screening they collect 3.75 to 4.00 tons of waste and from that they collect 2.50 tons of compostable waste. Finally they produce 1.5 tons of bio-fertilizer.

The materials required for composting are cow dung, saw dust, water, fire ash etc. Cow dung is the most useable part which is collected from different domestic sources and its cost is 2.00Tk per kg. Every bed needs 40 kg everyday 10 beds are placed so; 400 kg cow-dung is used. Its total cost is 800.00 Tk. Useable sawdust and shred wood per bed 10 kg and for 10 bed needs 100 kg which cost is 166.70Tk, oil cost 170Tk and Others cost (tools) for every day 310.00Tk.

All management activities of composting are carried out manually by RUSTIC where waste collectors are generally women and child.

Table 4 Expenditure for workers and employees.

Employees	Man power (per day)	Per day bill (Tk)
Female workers	10	2000
Male workers	5	1250
Coordinator	1	666.67
Total	16	3916.67

6.4 Net Income (per day)

Selling price per kg= 11Tk

Material Cost per day=800Tk+166.70Tk+170Tk+310Tk
= 1446.70Tk

Labors cost per day = 3916.67Tk

Total cost per day =1446.70Tk+ 3916.67Tk
= 6640.07Tk

Cost per kg for finished product = $\frac{\text{Total cost per day}}{\text{Finished product per day}}$
= $\frac{6640.07 \text{ Tk}}{1500 \text{ kg}} = 4.42\text{Tk}$

Net income per bag= Market value of finished product per kg - Cost per kg = 11Tk – 4.42k = 6.58Tk

Net profit per day= Net profit per kg * finished product per day= 4.58Tk * 1500 kg = 9870Tk

From the results of RUSTIC, it is clear that the compost production by Solid waste management in Khulna city is profitable. Now, present profit is around 9870.00Tk

per day. But if it is possible to use half of the total waste that is 250 tons then usable and degradable waste is two third which approximately 168 tons and the finished products will be approximately 100 tons/day. In that case, per day income could be 658000.00Tk. From previous calculation to produce 100 tons of bio-fertilizer/day 27 tons of cow dung and 7 tons of sawdust will be needed which is easily gettable from nearest cow farm and village.

Finally if it is possible to use of all waste from Rajbandh landfill which is around 500 tons then the compostable waste will be two third that is approximately 334 tons and the finished products will be approximately 200 tons/day. In this case, per day income could be 1316000.00Tk.

7. Discussion

The Main goal of the project is to find out the recent potential of municipal solid waste in KCC area and disclose the existing Municipal solid waste management practice. Firstly, existing waste generation is a burden for its dumping due to lack of dumping sites of Khulna city. In addition, most of the residents of KCC throw their waste outside of the dustbin, on the road into the drainage system. Decentralizing ultimate dumping site could be a better option for transportation of waste and composting. In this situation, Municipal Solid Waste has a great significance to produce ecologically sustainable organic bio-fertilizer from the biodegradable waste by using the composting. There are also some problems like waste collection problem, transportation problem, lack of financial support, lack of public awareness, lack of worker and infrastructure and insufficient tax collection which need to be solved as well. It is almost impossible to find any viable comparative information in this field of study. Because no other organization rather than RUSTIC working on bio fertilizer production from Municipal Solid Waste in Khulna.

At the same time, composition of Municipal Solid Waste changes in every seven kilometers [12] and for this reason data from this project cannot be compared with other projects from different state or country. On the other hand, Khulna University of Engineering & Technology (KUET) has a project up and running to produce bio fertilizer from their daily waste collection of their university campus. But their average bio fertilizer production per day is only 1.67 kg [21] and it will be an informational bias to compare the whole Khulna city waste disposal and management project with the small project of KUET.

8. Conclusions

The main constraints are weak organization and limited budget allocation for wastes management. From the discussion of this report the following conclusions can be drawn.

Municipal waste contains various compositions with specific merit of each. So waste needed to be separated with its merit to compost, reuse or recycle. More than

200 tons of organic compost can be produced in Khulna city if the total generated organic waste is recycled every day. The decentralized community based composting plants can generate employment for the poor, especially the women, and offers new prospects for small entrepreneurs to take part in recycling business. Improvement in overall environment of the neighborhood is possible by checking illegal disposal of waste on roads, drains. At the same time waste is directly collected from household recently which is very much appreciated. Public awareness about waste disposal is very important and they need to be responsible enough to dump their daily waste in selective places. Awareness about using compost as a replacement of chemical fertilizer should be increased to sell more compost to farmers.

9. Acknowledgements

I would like to express my gratitude to my honorable head of the department Prof. Dr. Sobahan Mia and my project supervisor Prof. Dr. Md. Shahidul Islam, Professor, Department of Mechanical Engineering, Khulna University of Engineering & Technology. His keen guidance, moral as well as logistic support and continuous supervision made me possible to bring out this research.

REFERENCES

- [1] T. Sultana, Salequzzaman, A. Iqbal, A. Hoque, Ecological footprint of waste generation as a sustainable tool for solid waste management in the Khulna City Corporation of Bangladesh, International Conference on Complex Systems (ICCS2006), Boston, MA, USA, pp. 6-8, (2006).
- [2] Annual Report, Khulna City Corporation (KCC), Khulna, (2014).
- [3] A. Alamgir, M. Ahsan, Characterization of Municipal Solid Waste and Nutrient of Organic Component in Bangladesh, Electronic Journal of Environmental, Agricultural and Food Chemistry, no. 6(4), pp. 1945-1956, (2007).
- [4] M. Salequzzaman, A. Iqbal, M. N. Amin, Contexts and Prospects of Renewable Energy Resources in KCC Area: A Case Study of Waste to Electricity from Existing Solid Waste, PREGA Training Workshop, Khulna, (2005).
- [5] M.A. Hague, Site Suitability Analysis for Solid Waste Disposal Using GIS: A Case Study on KCC area, Khulna University, Khulna, Graduate Thesis, (2005).
- [6] H. K. Richard, T. L. Glanville, T. D. Ahn, Optimum moisture levels for biodegradation of mortality composting envelope materials, Waste Management, no. 28, pp. 1411-1416, (2008).
- [7] A. Alamgir, M. Ahsan, Municipal Solid Waste and Recovery Potential: Bangladesh Perspective, Iranian Journal of Environmental Health Science and Engineering, no. 4(2), pp. 67-76, (2006).
- [8] A. Kashem, Potential Resource Recovery from Municipal Solid Wastes of Khulna City Corporation Bangladesh, Khulna University, Khulna, Graduate Thesis, (2007).
- [9] M Zahur, Solid Waste Management of Dhaka City: Public Private Community Partnership, BRAC University Journal, vol. IV, no. 2, pp. 93-97, (2007).
- [10] T. K. Rahman, S. Dev, P. K. Roy, Compost Fertilizer from Municipal Solid Wastes and its Application in Urban Agro-forestry Nurseries: A Case Study on Khulna City, Journal of Bangladesh Institute of Planners, no. 6, pp. 191-199, (2013).
- [11] Debasish Adhikary, Md. Shahidul Islam, Feasibility Analysis of Eco-Friendly Municipal Waste Management in Khulna City, International Conference on Mechanical Industrial and Materials Engineering (ICMIME), Rajshahi, p. 66, (2015).
- [12] Feasibility Study on Municipal Solid Waste Management in Khulna City, KCC, Khulna, Bangladesh, Study Report, (2005).
- [13] Mst. Sabikunnahar, Cost-Benefit Analysis of Solid Waste Management of Khulna City Corporation, Khulna University, Khulna, Graduate Thesis, (2006).
- [14] Documentation and Publishing Wings, Statistical Yearbook of Bangladesh, Bangladesh Bureau of Statistics (BBS), Dhaka, (2012).
- [15] M. N. Mohammad, Annual Report and Brochure of Rural Unfortunates Safety Talisman Illumination Cottage (RUSTIC), RUSTIC, Khulna, Bangladesh, Annual Report and Brochure, (2003).
- [16] World Bank, Health Facility Waste Management Study in Bangladesh, World Bank, Dhaka, (2002).
- [17] Best Practices on Solid Waste Management of Nepalese Cities, First ed. Kathmandu, Nepal: Practical Action Nepal, (2008).
- [18] I. Enayetullah, A.H.M.M. Sinha, A Study on Resource Recovery from Solid Waste in Khulna City, The World Bank, Dhaka, Waste and Sanitation Program in South Asia, (2000).
- [19] N. Sumon, Solid Waste Management: A Review”, Environmental Engineering Program, Asian Institute of Technology, Pathum Thani, Thailand, A Review, (2000).
- [20] M. N. Mohammad, Activity Report on Solid Waste Management, RUSTIC, Khulna, Bangladesh, Activity Report, (2014).
- [21] Debasish Adhikary, Study on Bio-Fertilizer Extraction and Management of Municipal Solid Waste of Khulna, Khulna University of Engineering & Technology, Khulna, M.Sc. Engg. Project, (2016).

Design and Numerical Analysis of Suspension Geometry for a Formula Student Race Car

Shafi Md. Istiak*

Department of Mechanical Engineering, Rajshahi University of Engineering & Technology, Kazla-6204, BANGLADESH

Abstract

Formula Student (or Formula SAE (F-SAE)) is a worldwide university competition, organized by the Society of Automotive Engineers (SAE), which encourages university teams to design, build, and compete with a Formula-student race car. Design analysis of suspension especially for racecar is very crucial to achieve maximum performance and handling. Suspension design may vary depending on the road terrain and the vehicle purpose itself. The main objective of this project is to design and numerical analysis of a suspension system for a student formula car. We discussed the conditions, factors and FSAE rules that should be considered to design a student formula race car. According to the desired performance some packaging parameters are selected and other suspension and sprung parameters are calculated. Then according to the calculation the suspension geometry is determined with an optimized result by numerical simulation in Lotus Suspension Analysis. Further this process can be followed for designing suspension system for any kind of vehicles.

Keywords: Suspension design, Formula Student, Race car suspension, Lotus suspension analysis, Vehicle dynamics.

1. Introduction: The Formula Student event is a competition between schools that has built their own formula style race cars according to the Formula SAE rules. The overall goal of Formula student is to provide students with the opportunity and experience of taking part in all aspects of Engineering including; management, design, manufacturing, marketing and to increase the 'people skills' of the students by working as part of a large team. The way in which this is conducted is by enabling the students to design, develop and manufacture a single seated race car.

Student formula competition is not familiar in Bangladesh. Though it is one of the biggest automotive competition in the world for students, there is a few teams recently started participating in this type of competition from Bangladesh. A team from Rajshahi University of Engineering and Technology participated in Formula Student Japan 2017 as the first team from Bangladesh[1].

Design analysis of suspension especially for racecar is very crucial to achieve maximum performance and handling. Suspension design may vary depending on the road terrain and the vehicle purpose itself. In case of designing a suspension system for formula student competition lot of problems has been faced by the designers. There are many parameters that should be determined according to the required performance. A perfect guideline can help the designers to design the suspension system properly. Some steps should be followed to design a suspension system for a student formula car. The designers have to take some decisions based on experience in case of designing a formula student car. So a guideline can help new designers to take the decisions. In this paper a suspension designing process is described with numerical analysis.

2. Vehicle level targets: The main design requirements of the suspension design of a Formula Student race car may be like the followings:

- i. The ability to keep all four wheels in contact with the ground at the correct angles in order to exploit the maximum tractive force of the tyres.
- ii. Determining the suspension geometry according to packaging parameters.
- iii. To ensure the expected camber change and toe change during bump; change of camber during roll and percent of anti-dive & anti-squat.
- iv. Compliance with F-SAE rules.

3. SAE rules for Suspension System: For designing a suspension system firstly the suspension rules of SAE for student formula competition should be checked properly. The rules are the followings:

According to the rules of FSAE rule book 2017-2018,

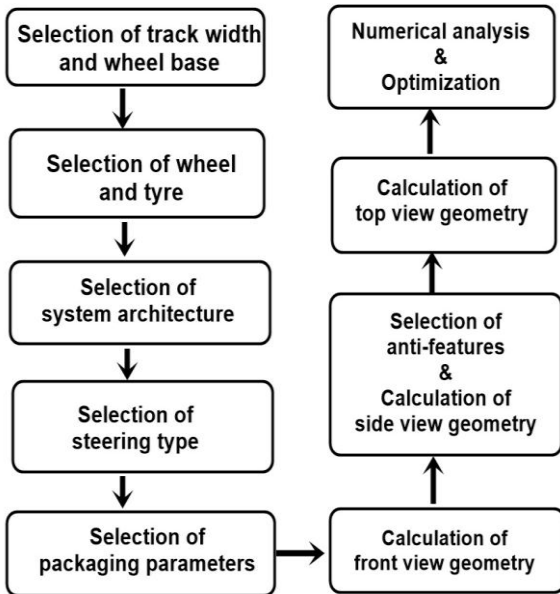
Rule T6.1.1: The car must be equipped with a fully operational suspension system with shock absorbers, front and rear, with usable wheel travel of at least 50.8 mm (2 inches), 25.4 mm (1 inch) jounce and 25.4 mm (1 inch) rebound, with driver seated. The judges reserve the right to disqualify cars which do not represent a serious attempt at an operational suspension system or which demonstrate handling inappropriate for an autocross circuit [2].

Rule T6.1.2: All suspension mounting points must be visible at Technical Inspection, either by direct view or by removing any covers. [2]

* Shafi Md. Istiak. Tel.: +88-01773088087

E-mail addresses: istiak2212@gmail.com

4.1 Work flow chart:



4.2 Deciding track width and wheel base: The wheel base and track width of both front and rear should be determined properly.

Wheel track B is determined by the empirical formula in following equation.

$$B = kL \quad (1)$$

Where L is the wheelbase and the k is the dimensionless unit. The optimum value of k is ranged from 0.90-0.96. But it depends on the required performance, conditions and factors[2].

4.3 Wheel and tyre selection: The FSAE rule 2017-2018 for wheel diameter for a student formula car are followings:

According to the rule **T6.3.1**, the wheels of the car must be 203.2 mm (8.0 inches) or more in diameter.

Generally two types of rim is used in student formula competition. They are 10 inch rim and 13 inch rim. The size of the rim is selected according to design perspective. Design of FSAE wheels is aimed at producing the lightest possible wheel with the lowest possible mass moment of inertia while maintaining a high level of lateral stiffness.

4.4 System architecture: For the front suspension the following need to be considered.

Type of suspension: There are generally following types of suspension for front.

1. Macpherson strut (Generally not used in FSAE car)
2. Double wishbone, damper to lower wishbone
3. Double wishbone, damper to upper wishbone
4. Double wishbone, pushrod/pull rod to damper
5. Double wishbone pushrod/pull rod to rocker arm
6. Double wishbone, anti-roll bar etc.

For the rear suspension there are many more possible suspension types, in practice.

A double wishbone, damper to upper or lower wishbone suspension system with its roll center little above the ground would give the best suspension geometry but due to their compact design and excellent rolling resistance, a push rod suspension or a pull rod suspension system is recommended for formula student car.

4.5 Type of steering: Steering system is strongly related with suspension system. The position of the track rod has impact on the combined performance with suspension system. The position of the tie rod ball joint should be perfect, otherwise bump steer will occur. The type of steering actuator should be determined. Such as 'Rack and pinion' or 'Recirculating ball' type steering. Rack and pinion is the most used steering system in formula student. Location of the steering actuator should be determined. It will be in front of or behind the wheel center.

4.6 Packaging Parameters Selection: There are some parameters which are called packaging parameters and they should be determined for designing the suspension geometry. The packaging parameters are tire size, rim diameter and width, wheel offset, kingpin inclination, mechanical trail, scrub radius, spindle length, the caster, the camber, tie rod position, rack location, track width, the upper and lower ball joint positions and tie rod outer position [Fig. 4.6.1 & 4.6.2]. Upright or knuckle geometry can be determined from these packaging parameters. In automotive suspension, a steering knuckle is that part which contains the wheel hub or spindle, and attaches to the suspension and steering components. It is variously called a steering knuckle, spindle, upright or hub as well.

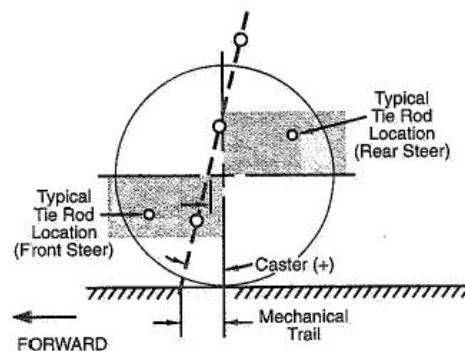


Fig.4.6.1 Packaging parameters [5]

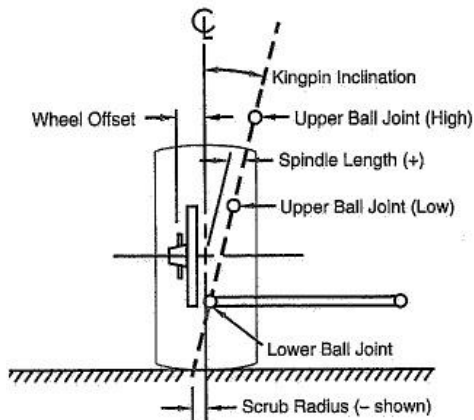


Fig.4.6.2 Packaging parameters [5]

Wheel offset: The offset of a wheel is the distance from the hub mounting surface to the center line of the wheel. The wheel offset is measured in millimeters and results in a positive, negative, or zero offset. Positive offset is when the hub mounting surface is toward the front or wheel side of the wheel. It is common to find a positive offset in newer and front wheel drive vehicles. Negative offset is when the hub mounting surface is toward the back or brake side of the wheels centerline. Zero offset is the hub mounting surface is even with the centerline of the wheel.

Kingpin inclination: In suspension systems, the kingpin is set at an angle to the vertical plane when viewed from the front or rear of the vehicle. This angle is known as the king pin inclination. The purpose of the KPI is to produce vertical displacement of the vehicle in during steering in an upward direction. The larger the KPI, the larger the effect. This lifting effect produces a self-centering torque similar to that of caster. The KPI also generates scrub radius.

Mechanical trail: Mechanical Trail (or Real Trail) refers to the length of the lever that, when combined with the contact patch, produces a self-righting effect on the steering.

Scrub radius: The scrub radius is the distance in front view between the king pin axis and the center of the contact patch of the wheel, where both would theoretically touch the road. The kingpin axis is the line between the upper and lower ball joints of the hub.

Track width: Track width is the distance between the centers of 2 tires mounted on same axle. There is front track width and rear track width in case of a 4 wheeled car.

Caster angle: The caster angle or castor angle is the angular displacement of the steering axis from the vertical axis of a steered wheel in a car measured in the longitudinal direction.

Camber: Camber angle is the angle made by the wheels of a vehicle; specifically, it is the angle between the vertical axis of the wheels used for

steering and the vertical axis of the vehicle when viewed from the front or rear. It is used in the design of steering and suspension.

Roll center: The roll center of a vehicle is the notional point at which the cornering forces in the suspension are reacted to the vehicle body.

Based on the literature survey, knowledge about the cars from the Formula Student 2003 is at KTH an over view of static set up is given below.

- Kingpin inclination angle between 0° and 8°
- Scrub radius between 0mm and 10mm
- Caster angle between 3° and 7°
- Static camber adjustable from 0° to -4°
- Camber gain 0.2-0.3 degrees/roll angle at front axle
- Camber gain 0.5-0.8 degrees/roll angle at rear axle
- Maximum roll angle about 2°
- Roll center height between 0mm and 50mm in front and slightly higher at rear
- Well controlled and predictable movement of the roll axle
- Minimize bump steer
- 50% - 65% of the roll stiffness on the rear axle.[4]

4.7 Front view geometry: For designing front view geometry; roll center height, instant center position and fvs length (Fig. 4.7.1) should be calculated. The lower wishbone length is kept larger than the upper wishbone to keep the camber rate low. Low camber rate ensure handling and stability. The roll center of a vehicle is the notional point at which the cornering forces in the suspension are reacted to the vehicle body.

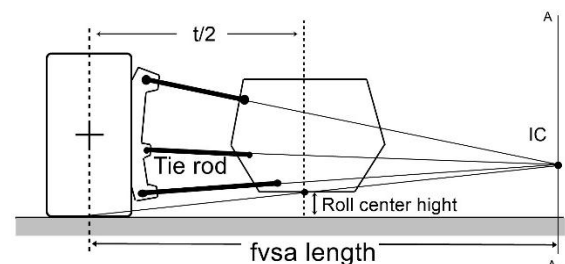


Fig.4.7.1 Front view geometry

The required parameters can be calculated from 2D drawing of the front view. The 2D design of the front view of the suspension system can be designed by the following steps:

1. Establish front view swing arm length (A-A)
2. Establish roll center location and project from ground contact point from RC to line A-A, establishing RC.
3. Project line from outer ball joint to IC.
4. Choose control arm length to get inner pivot locations.
5. Contact tie rod outer pivot to IC.
6. Establish tie rod length [5].

The fvsa length can be determined by the following equation: [5]

$$fvsa = \frac{t/2}{(1 - \text{roll camber})} \quad (2)$$

Where t=track width.

$$\text{Roll camber} = \frac{\text{Wheel camber angle}}{\text{Chassis roll angle}} \quad (3)$$

4.8 Side view geometry: The side view geometry can be designed by the process that is described in the book ‘Race Car Vehicle Dynamics’ by William F. Milliken and Douglass L. Milliken [5]. The calculation can be developed through two steps.

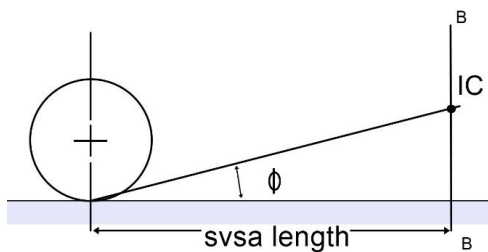


Fig.4.8.1 Side view geometry

1. Angle Φ that's establishes anti-dive. (Fig. 4.8.1)
2. Determining svsa length which gives line BB [5].

Anti-dive describes the amount the front of the vehicle Dives under braking. As the brakes are applied, weight is transferred to the front and that forces the front to dive. Anti-squat is suspension's mechanical resistance to compression due to forces from the engine. Formula Student car is a rare wheel drive car with outboard braking. So, for a rare wheel drive car with outboard braking, the equation of determining anti-dive and anti-squat for independent suspension is following: [5]

$$\text{Anti-dive} = (\% \text{front braking}) \tan \Phi_F (l/h) \quad (4)$$

The equation for determining anti-squat in rare is following: [5]

$$\text{Anti squat} = \frac{\tan \Phi_R}{h/l} \quad (5)$$

Here l is wheel base and h is the height of CG.

Selecting anti-features: Before selecting the amount of anti-dive and anti-squat we should think about its effects. Mainly the side view instant center affects the wheel path. The wheel moves through a curve which has a center located on the same location with the instant

center. Instant center affect the caster angle. For front suspension if the location of the IC in rearward and above or forward and below the wheel center then the wheel will move forward during bump. Otherwise if the IC is rearward and below or forward and above the wheel center then the wheel will move rearward during bump. In case of passenger car anti-dive is important. But for racing car though anti-dive and anti-squat has effect on grip, it can't change the performance much. But in case of drag racing anti-squat over 100% increase the grip of rare wheel which is called Pro-lift. So using anti-feature in drag racing car and passenger car is fruitful. To avoid complexity keeping 0% anti-dive is logical for FSAE car. Anti-dive will be 0% when the value of Φ will be zero. Here 0% anti-dive is used to design the suspension system. [5]

4.9 Top view geometry: There are two factors that are considered for designing the geometry of top view.

1. The maximum force on front wishbone occurs during maximum braking. The load on wishbone member reduces as the spread increases (fig. 4.9.1). So the wishbone should be spread as large as possible avoiding clash with rim.
2. If the chassis pivots are at some angle with the longitudinal center line of the car (fig.4.9.1), then there is a perpendicular component with the wishbone pivot axis of braking force which oppose the longitudinal weight transfer. For that reason some anti-dive is introduced [6].

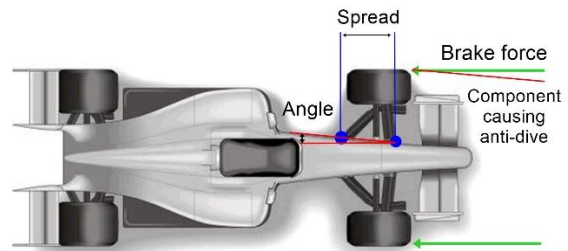


Fig. 4.9.1 Wishbones in top view

5. Data for front suspension: As we are designing and simulating a suspension system, so we have to select some parameters according to desired performance. The packaging parameters data and different vehicle data are collected from a student formula team from Rajshahi University of Engineering and Technology which participated in Formula Student Japan 2017. [1]

Table 1 Types of systems.

Systems	Types
Suspension system	Double wishbone, push rod to damper
Architecture	Rack and pinion

Table 2 Packaging parameters data.

Parameters	Value
Wheel base	1570 mm
Wheel track	1200 mm
Rim diameter	10 inch
Rolling radius	177.8 mm
Kingpin inclination	7 degree
Scrab radius	9.5 mm
Caster angle	2 degree
Roll center height	25.4 mm
Static Camber	2 degree
Roll angle	5 degree
Bump	40 mm (FSAE rule T6.1.1)
Rebound/ Jounce	40 mm (FSAE rule T6.1.1)

From the packaging parameters data, the geometry for upright or knuckle is determined.

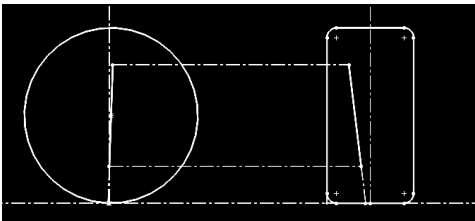


Fig. 5.1 knuckle/upright geometry

Table 3 Calculated data for fvsa of front suspension. From equation 2 and 3 and by 2D drawing of the geometry the following values are calculated.

Parameters	Value
Roll camber	0.59
Fvsa length	1670 mm
Fvsa height	71.4 mm
Roll center height	25.4 mm
Upper control arm length	293 mm
Lower Control arm length	387 mm
Tie rod length	309.5 mm

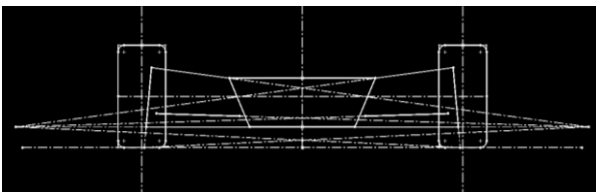


Fig. 5.2 Front view geometry 2D drawing

Table 4 Selected data for side view swing arm.

Parameters	Value
Vehicle mass	300 kg
Vehicle load on front axel	135 kg
Vehicle load on rare axel	165 kg
Percent of anti-dive	0%

Percent of front braking	60%
Height of CG	300 mm (approximately)
CG distance from front axel	900mm (approximately)
CG distance from rare axel	670 mm (approximately)
Deceleration for maximum braking	1.7 g

Table 5 Calculated data for svsa of front suspension:

Formula student car is built to run on smooth and flat road. So there will be no bump in the race track. Also we need camber change during cornering. For 100% anti-dive there will be no camber change for rolling. So there is no need to keep anti-squat. In case of formula student car 0% anti-squat is perfect.

Parameters	Value
Angle Φ_R	0 degree
Svsa height	-
Svsa length	-

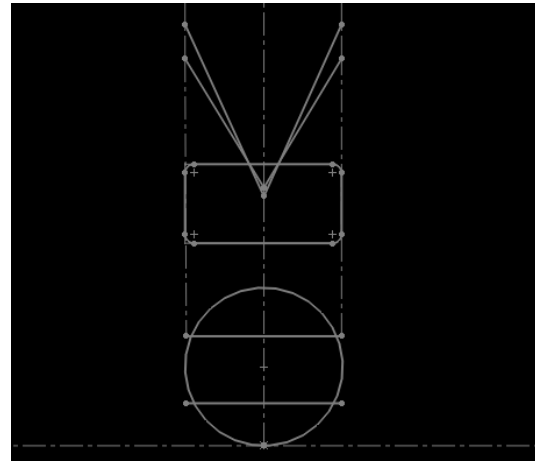


Fig. 5.3 Top and side view 2D drawing

6. Numerical analysis & optimization: From the assumed packaging parameters data and calculated data a model of suspension system is designed and simulated in 'Lotus Suspension Analysis' software. The roll angle, camber, toe and bump are plotted to analyze the performance of the system.

From the numerical analysis, the system can be optimized by changing the selected packaging parameters according to the required performance.

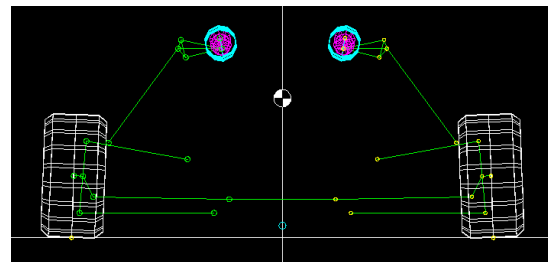


Fig. 6.1 Front view of front suspension

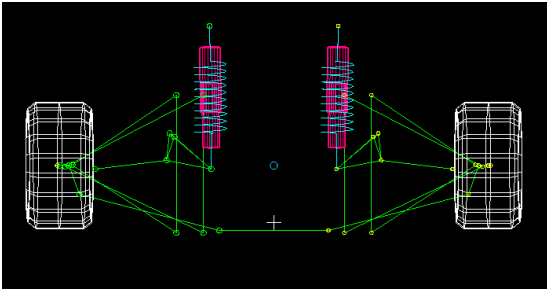


Fig. 6.2 Top view of front suspension

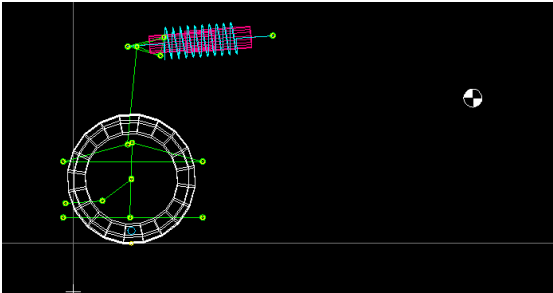


Fig. 6.3 Side view of front suspension

From roll vs camber graph (fig. 6.4) we can see that at maximum roll of 5 degree the camber is zero. So during cornering the inner tyre will be at maximum contact with the road. So the inner tyre friction will be maximum.

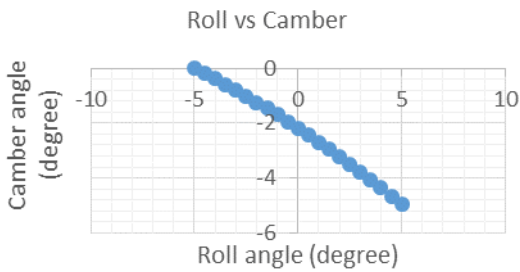


Fig. 6.4 Roll vs camber graph

From the bump vs camber graph (fig.6.5) there is some negative camber change for bump. As formula student car is an on road car, so camber change in bump will not affect the performance much.

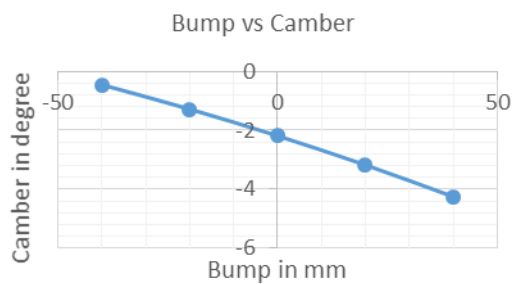


Fig. 6.5 Bump vs Camber graph

From the bump vs toe graph (fig.: 6.6) we can see that the toe angle has a little change for bump travel which will not affect much. The toe change for bump travel should be near zero.

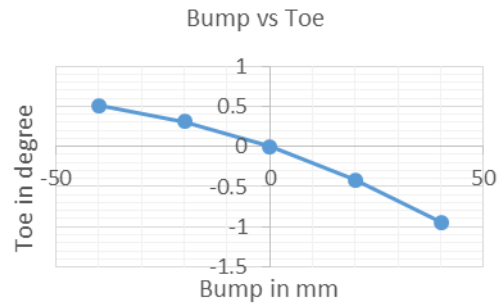


Fig. 6.6 Bump vs toe graph

Here, for the formula student car suspension system the percentage of anti-dive is proposed to keep zero. Here we can see in the bump vs % anti-dive graph (fig.:6.7) that the percentage of anti-dive is very low.

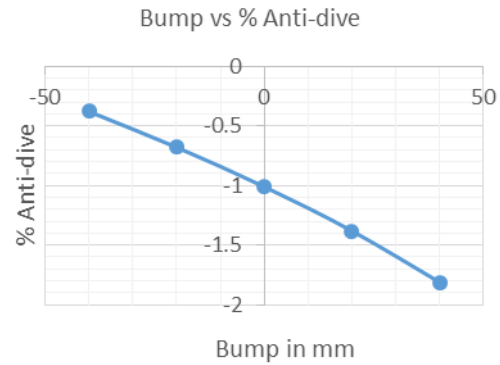


Fig. 6.7 Bump vs % anti-dive graph

7. Rear suspension: The rear suspension can be designed following the same procedure of front suspension. In case of rear suspension the anti-squat should be calculated instead of anti-dive and the track rod position should be determined instead of tie rod.

8. Discussion: For designing a suspension system of a formula student car, a process is described with the objectives to ensure the angle maximum tractive force between wheel and road; determining the suspension geometry and ensure the expected camber change and toe change during bump; camber change with rolling and percent of anti-dive & anti-squat. By numerical analysis in 'Lotus Suspension Analysis' software we showed that the all objectives are satisfied for the designed suspension system. Though there is some fluctuation from the expected result but that is not affect the expected performance. Also the system satisfy the SAE rule for formula student competition. Overall an optimize suspension system is designed for a formula student car according to required performance.

9. Conclusion: Suspension designing is depends on designer choice. A suspension should be designed

according to the required performance. The suspension system for a road car and off road car won't be same. Designer should consider different suspension factors, road condition and purpose of the vehicle for designing a suspension system. By following the above process, suspension system for any kind of vehicle can be designed.

REFERENCES

- [1] Japan, S.F. (2017, April 21). *15th registered team*. Retrieved from <http://www.jsae.or.jp/formula/en/15th/registeredteams.html>
- [2] 2015 Formula SAE rules. (2015). 1st ed. [ebook] FSAE, p.57. Available at: http://students.sae.org/cds/formulaseries/rules/2015-16_fsae_rules.pdf [Accessed 31 Mar. 20
- [3] J. W. Wirawan, Ubaidillah, R. Aditra, R. Alnursyah, R. A. Rahman, and S. I. Cahyono, "Design analysis of formula student race car suspension system," in *AIP Conference Proceedings*, 2018, vol. 1931, no. 1, p. 30051.
- [4] A. Theander, "Design of a suspension for a formula student race car," *Veh. Dyn. Aeronaut. Veh. Eng. R. Inst. Technol.*, 2004.
- [5] W. F. Milliken and D. L. Milliken, *Race car vehicle dynamics*, vol. 400. Society of Automotive Engineers Warrendale, 1995.
- [6] D. Seward, *Race car design*. Macmillan International Higher Education, 2014.

Performance Analysis of Nylon Made Vortex Tube

Tirtha Sen Gupta^a, Radif Uddin Ahmed^a, Hemal Chowdhury^{a*}, Tamal Chowdhury^{b*}, Md. Tazul Islam^a

^aDepartment of Mechanical Engineering, Chittagong University of Engineering & Technology, Chittagong, BANGLADESH

^bDepartment of Electrical & Electronic Engineering, Chittagong University of Engineering & Technology, Chittagong, BANGLADESH

ABSTRACT

A Vortex tube is a cooling machine which separates the flow of air or gas into two components: hot and cold streams. In spite of its limited use, it has several advantages over the conventional cooling system. In this study, an experimental investigation is carried out to find the performance of Nylon made vortex tube. Effects of varying cold mass fraction on the thermodynamic features of the tube were examined. A thermodynamic analysis is also performed to determine the key aspects of the tube.

Keywords: Ranquee Hilsch vortex tube (RHVT); Nylon; Refrigeration.

1. Introduction

Refrigeration is one of the research areas that are deeply associated with human lives. Refrigeration system provides cooling effect which is necessary to store food and for human comforts. Refrigeration system uses many refrigerants. The use of refrigerants can lead to the problems like ozone depletion and global warming. So it is necessary to look for a system that is eco-friendly. A vortex tube is a nonconventional eco-friendly device which was initially invented by the French physicist Georges J. Ranque in 1933. It was then developed by the German engineer Rudolf Hilsch in 1947 [1]. That is why it is called Ranquee Hilsch vortex tube (RHVT). In this device fluid like oxygen, air is used as the working medium for refrigeration process. The construction of the tube is simple as all the parts are stationary. It contains following components [2-3].

- Vortex Chamber
- Inlet nozzles
- Working tube
- Control valve (in hot end)
- Orifice (in cold end)

One of the main advantages of vortex tube is that it has no rotating part. It is circular in shape. A high - pressure gas is made to pass to the vortex tube through the tangential nozzles. As a result, velocity is increased which produces an effect called the swirl effect. Hot and cold end make up the two exits of the vortex tube. The hot exit is located in the outer radius near the far end of the nozzle and the cold exit is in the center of the tube near the nozzle. Being lower in temperature closer to the axis, the gas comes out through the cold exit. The gas coming out through the hot exit has a high temperature near the periphery of the tube. Figure 1 shows flow structure in a vortex tube [4].

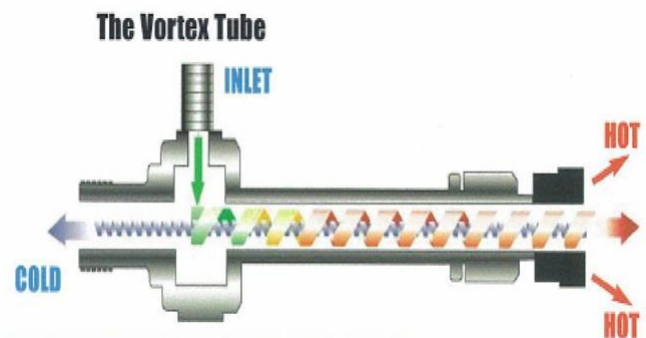


Fig. 1: Flow structure in a vortex tube

2. Literature Review

A great number of studies have been conducted to analyze the performance of the vortex tube. The effect of various parameters such as pressure gradient, viscosity, flow structure and acoustic structure on energy separation in vortex tube was reported by Xue and Arjomandi (2010)[5]. Rafiee et al. (2017) conducted numerical and experimental study about heat transfer and energy separation in a counter - flow vortex tube by using different shapes of hot outlet control valves [6]. An experimental analysis conducted by Kırmacı (2009) shows the refrigeration performance of a vortex tube which uses air and oxygen as working fluids [7]. Thakare et al. (2017) showed that the insulated condition of vortex tube gives better performance than non-insulated condition [8]. Effect of different nozzle materials on the thermal performance of the vortex tube was shown by Kırmacı et al (2017) [9]. Saidi and Yazdi (1999) carried out an exergy analysis of vortex tube to optimize vortex-tube energy separation [10]. Dinçer et al. (2010) investigated the performance of the vortex tube with a range of inlet pressure 200 kPa to 380 kPa [11]. Performance of PVC as vortex tube material was shown in [12]. In this study, an attempt is made to find out the performance of a counter-flow nylon made vortex tube. Here Oxygen gas is used as the working fluid due to its availability. No other study to

authors knowledge has been conducted before to use nylon as vortex tube material. This study attempts to find out the feasibility of nylon as vortex tube construction material.

3. Assumptions

The followings assumptions are made for analysis

- No heat transfer towards and from the surrounding. The process is adiabatic.
- Flow is assumed to be turbulent.
- The outlet and atmospheric pressure are equal.
- No friction and losses take place.
- Mass flow rate is constant

4. Design and Constructional Features

Some of the constructional features of vortex tube are shown below:

- Material : Nylon
- Cold tube length =215 mm
- Cold inner tube diameter=12 mm
- Cold outer tube diameter= 19mm
- Hot tube outer diameter=39mm
- Hot tube inner diameter=24 mm
- Hot tube length= 505 mm
- Nozzle = 2mm
- Number of nozzle used=6
- Nozzle material=Nylon
- Chamber outer diameter =93mm
- Chamber inner diameter=49mm

5. Thermodynamic analysis:

This section represents some of the basic thermodynamic concepts for analyzing the Vortex tube. Cold mass fraction is the most essential parameter while analyzing a vortex tube. It can be defined as the ratio of cold mass released to the total input mass.

$$\epsilon = \frac{m_c}{m_i} = \frac{T_i - T_h}{T_c - T_h} \quad (1)$$

Where, m_c = Cold mass released, m_i = mass input, T = Temperature, i , c , h represents inlet, cold and hot.

Hot air temperature difference is the between hot air temperature and inlet temperature while cold air temperature difference is the difference between the inlet temperature and the cold air temperature.

$$\Delta T_h = T_h - T_i \quad (2)$$

$$\Delta T_c = T_i - T_c \quad (3)$$

Considering the gas behave like an ideal gas and the expansion is isentropic, the isentropic efficiency can be written as ,

$$\eta_{is} = \frac{T_c}{T_{is}} \quad (4)$$

The exit temperature of gas for isentropic expansion can be written as:

$$T_{is} = T_i \left(\frac{P_e}{P_i} \right)^{\frac{\gamma-1}{\gamma}} \quad (5)$$

Where, P_e is outlet pressure equaling ambient pressure and P_i is inlet pressure.

Cooling effect produced by the cold air of vortex tube can be written as:

$$Q_c = m_c C_p (T_c - T_i) \quad (6)$$

Here, m_c is cold mass flow rate and C_p is constant pressure specific heat for gas.

The heating effect produced by the vortex tube is:

$$Q_h = m_h C_p (T_h - T_i) \quad (7)$$

Here, is m_h hot mass flow rate.

The Coefficient of performance (COP) of a refrigerator can be defined as the ratio of refrigerating effect produced by the RHVT and work done on the system. The COP of a RHVT can be expressed as,

$$COP = \frac{\gamma \epsilon}{\gamma - 1} \times \frac{(T_i - T_c)}{T_i \left(\ln \frac{P_i}{P_e} \right)} \quad (8)$$

6. Results and Discussion

In this analysis, the aim is to determine the effect of the cold mass fraction on various properties of vortex tube such as isentropic efficiency, COP, cold air temperature drop and hot air temperature drop while keeping the mass flow rate constant to 1 kg/s. The various data and parameters used in this study are shown in Table 1 and Table2.

Table1. Data of the vortex tube used in this study .

P (bar)	T _i (°C)	T _h (°C)	T _c (°C)	ε
2	26.9	33.4	23.5	0.66
3	26	37.5	18.3	0.60
4	21.8	40.1	10.1	0.61
5	18.1	43	4.9	0.65

Table2: Calculated parameters of the vortex tube

ΔT _c °C	ΔT _h °C	T _{is} °C	η _{is}	COP	Q _c (watt)
3.4	65	32.72	0.72	0.04	3.12
7.7	11.5	35.48	0.52	0.05	7.06
11.7	18.3	29.74	0.34	0.06	10.74
13.2	24.9	28.54	0.18	0.062	12.11

Figure 2 shows the effect of the cold mass fraction on cold temperature difference and hot temperature difference. With the decreasing of the cold mass fraction, hot temperature difference at first increases for 0.65 but gradually it decreases for 0.61 and 0.60. When cold mass fraction decreases from 0.66 to 0.65, cold air temperature difference increases from 3.4 to 13.2 K. Further decreasing of the cold mass fraction results in decreasing cold air temperature difference.

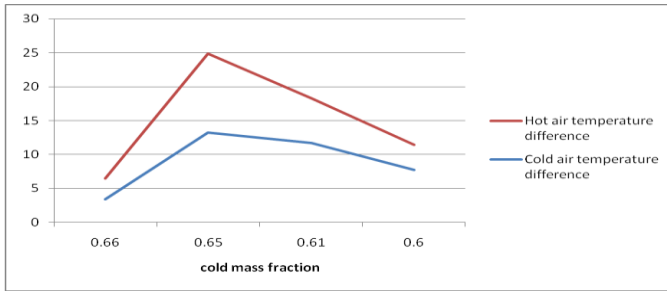


Fig. 2: Effect of cold mass fraction on hot and cold air temperature difference .

Figure3 shows the effect of the cold mass fraction on cooling effect of the vortex tube. From Figure 4, it can be seen that when ϵ is decreased from 0.66 to 0.65 the cooling effect increases from 3.12 watt to 12.11 watt. With the further decrease of ϵ , cooling effect decreases resulting in 7.06 watt.

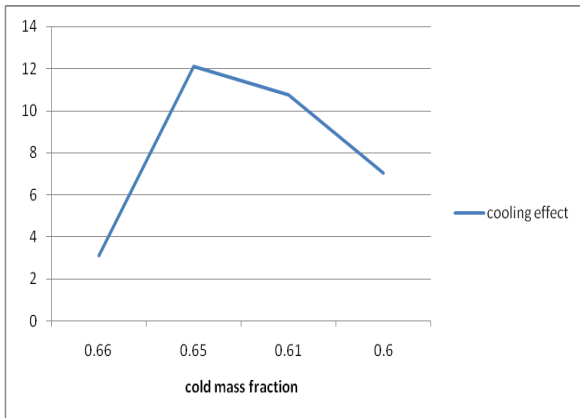


Fig. 3: Effect of cold mass fraction on cooling effect of vortex tube .

Figure 4 shows the effect of ϵ on COP. Maximum COP obtained is 0.06 and minimum COP obtained is 0.04. Here we assumed that the compression occurs in reversal isothermal process.

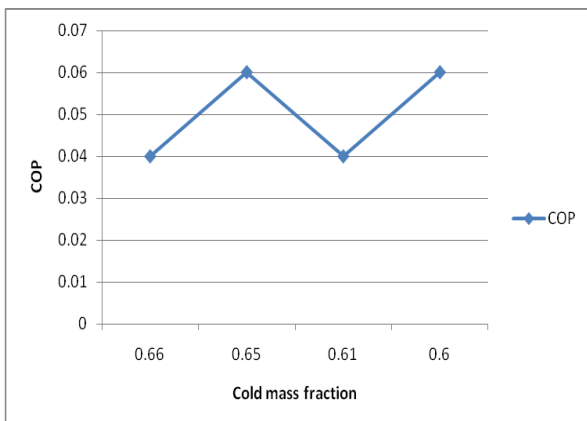


Fig.4: Effect of cold mass fraction on COP

Figure 5 shows the effect of the cold mass fraction on the isentropic efficiency of the vortex tube. When cold mass fraction ϵ decreased from 0.66 to 0.65, then the isentropic efficiency decreases from 72 % to 18% . With

the further decrease of ϵ to 0.60, isentropic efficiency increases to 52%.

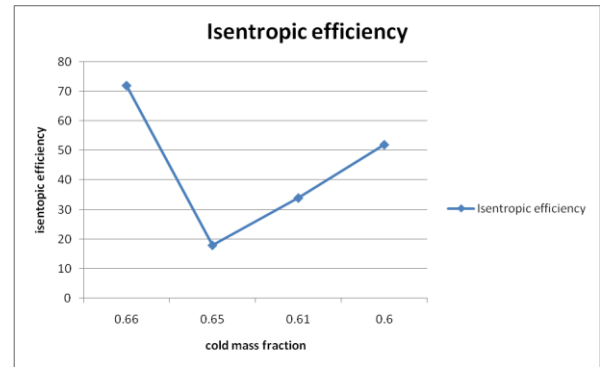


Fig. 5: Effect of the cold mass fraction on the isentropic efficiency of the vortex tube.

8. Conclusion

In this analysis, an experimental investigation has been carried out on the performance of nylon made vortex tube. Effect of the cold mass fraction on various properties of vortex tube has been presented while keeping the mass flow rate constant. Some of the major findings of the study can be summarized as below:

- Maximum COP is 0.06.
- Maximum isentropic efficiency is 72%.
- Maximum cooling effect is 12.11 watt.
- With the decreasing of the cold mass fraction, hot air temperature difference at first increases but gradually it decreases.

The study mainly focuses on finding the prospect of nylon in constructing the vortex tube and evaluating various thermodynamic prospects while keeping the mass flow rate of gas constant. The results can be varied by changing the mass flow rate and changing the assumptions as mentioned above.

REFERENCE

- [1] Hamdy, A.K.; Seif, T.A. Computational investigation of different effects on the performance of the Ranque-Hilsch vortex tube. *Energy*, 2015, 84, 207–218.
- [2] Xue, Y.; Arjomandi, M.; Kelso, R. Energy analysis within a vortex tube. *Exp Therm Fluid Sci* 2014, 52, 139-145.
- [3] Li, N.; Zeng, Z. Y.; Wang, Z.; Han, X, H.; Chen, G. M. Experimental Study of the energy separation in a vortex tube, *International Journal of Refrigeration*, 2015, 55, 93-101 .
- [4] <http://www.universalvortex.com/ProprietarySelfHeatingVortexTubes/tabid/98/Default.aspx>.(accessed: 28.10.2018)
- [5] Xue Y.; Arjomandi, K. R. A critical review of temperature separation in a vortex tube. *Experimental Thermal and Fluid Science*, 2010, 34, 1367-1388 .

- [6] Rafiee, S.E.; Sadeghiazad, M.M. Experimental and 3D CFD investigation on heat transfer and energy separation inside a counter flow vortex tube using different shapes of hot control valves, *Applied Thermal Engineering*, 2017, 110, 648-664 .
- [7] , V. Exergy analysis and performance of a counter flow Ranque–Hilsch vortex tube having various nozzle numbers at different inlet pressures of oxygen and air, *International Journal of Refrigeration*, 2009, 32, 1626-1633 .
- [8] Thakare, H.R.; Parekh, A.D., Experimental investigation & CFD analysis of RanqueHilsch vortex tube, *Energy*, 2017, 133, 284-298 .
- [9] Volkan Kirmaci, Hüseyin Kaya, Ismail Cebeci, An experimental and exergy analysis of a thermal performance of a counter flow ranque-hilsch vortex tube with different nozzle materials, *International Journal of Refrigeration* (2017)
- [10] Saidi, M.H., Allaf Yazdi, M.R., 1999. Exergy model of a vortex tube system with experimental results. *Energy* 24, 625–632.
- [11] Dincer, K.; Avci, A.; Baskaya, S.; Berber, A. Experimental investigation and exergy analysis of the performance of a counter flow Ranque–Hilsch vortex tube with regard to nozzle cross-section areas. *International Journal of Refrigeration*, 2010, 33(5), 954- 962.
- [12] M.M.Rahman, M.R.Sheikh, M.M.Hossain, M.R.Hald er. Design, construction and performance test of a Vortex tube cooling system constructed by locally available materials. Conference on Engineering ,Research, Innovation and Education (CERIE) 2011, 132-4.

Feasibility Study of Pico Hydro Power Plant in Shongrapunji Waterfall for Clean Environment

Syed Tahmid Hussan^{1,*}, Pranta Barua²

¹Department of Petroleum and Mining Engineering, ²Department of Electrical & Electronic Engineering
Chittagong University of Engineering & Technology, Chittagong-4349, BANGLADESH

ABSTRACT

Electricity from the energy of combustion of fossil fuel is increasing day by day in Bangladesh. In this case, increasing carbon compounds in environment is a great threat. Besides, in many hilly remoted regions there is no access of electricity. Another energy resources cannot meet the demand of electricity due to lack of transportation, lack of management and high cost of energy. To solve the problem, pico-hydro powerplant can be an alternative energy source for such kind of hilly remoted regions. Shongrapunji waterfall can be a resource of hydroelectricity for remoted hilly regions around Jafiong of Sylhet. The paper represents the overall important data of Pico-hydro powerplant and evaluates the feasibility of Shongrapunji water fall as a resource of pico-hydropower plant. To justify the feasibility, flow rate, water head of Shongrapunji waterfall is recorded and approximate power generation, COE are calculated using HOMER software.

Keywords: Pico-Hydro, Shongrapunji, Electricity, Environment, Waterfall

1. Introduction

The value of electricity is enormously growing worldwide for its versatile and widely used form of energy. The expanding new technologies and industries cannot be thought for a little moment without electricity. In simple sentence, accessibility of useable energy in the form of electricity has gradually assumed as an indispensable part of our everyday life. The demand for electrical energy in developing country like Bangladesh in particular generally get raised at a rate faster than the rate at which number of peoples are increased. The distance between demand and availability of electricity therefore retain a challenge in technologically developing and advanced countries. Bangladesh will need an average 34,000 MW of power by 2030 to sustain its economic and industrial improvement of over 7 percent. [1] As 2015, 92% urban population and 67% rural population have the access to the electricity for their source of light. [2] That means 33% of rural people are still away from electricity. Bangladesh has 15 MW solar energy capacity through rural households and 1.9 MW wind power in Kutubdia and Feni. Bangladesh has planned to produce 5% of total power generation by 2015 & 10% by 2020 from renewable energy sources like wind, waste & solar energy. [3][4]

The objective of this research is to show that the waterfall has enough feasibility to set up pico-hydro power plant. Jafiong is a hilly station and popular tourist destination in the Division of Sylhet, Bangladesh. It is about 60 km from Sylhet town and maximum populations are Khasi tribe [5]. Their living vicinity named 'Khasi Polli' is very near to the Shongrapunji waterfall.

For small and remote areas like Jafiong that require only a small amount of electricity in the range of 1 kW to 5 kW. Pico-Hydro-Power plant with smaller turbines of 200 to 300 watts may power a single home a head of 1

meter. [6] Total height of Shongrapunji waterfall is about 40 meters on average. It has a wide water falling surface with divided streamline at bottom side. Total power from four streamline is about 1.73kW which is enough for one house. If all streamlines are used for this purpose, then total Khasi Polli would be under electric supply only from Pico-Hydro-Power-Plant of Shongrapunji waterfall.



Fig.1 Shongrapunji waterfall

2. Methodology

The methodology for establishing a pico-hydro power plant is very necessary as it is the only stage where feasibility of pico-hydro power plant is determined. The methodology comprises of

- Power estimation
- Selection of turbine

2.1 Power estimation

For feasibility of electricity production, it is necessary to check how much power can be achieved to have a feasible output for consumers. Here is a defined formula

to calculate the output power theoretically. The formula is given below [7-9]:

$$P_{in} = H * Q * g$$

$$P_{out} = \eta * H * Q * g \dots \dots \dots (1)$$

Here,

η = overall efficiency of hydropower plant.

as a rule of thumb, it is determined 50% considering all losses. On that point overall efficiency includes turbine efficiency, electrical efficiency, mechanical efficiency etc.. [8-9][12]

H = available water head (m)

Q = water flow rate (liters/s)

From the equation (1), it is realized that available water head and water flow rate are main parameters to determine the output power.

2.2 Water flow rate measurement

To determine water flow rate, there are different methods that can be used to measure. From different methods, bucket method is the simplest method to be applied [10]. It is feasible in pico-hydro power plant in that sense, as the water flow rate is small and the location of consumers is far from waterfall. By this method, first of all it is necessary to take a bucket of known volume. Then, the bucket is kept at the water flow of waterfall and measure the time to fill up the bucket from stopwatch. Then if the volume is divided by the time to fill up, the flow rate is calculated simply. By using the method, 5-6 trials should be repeated to measure exact water flow rate, Q.

2.3 Water head measurement

There are many methods of head measurement. As the houses are far from water reservoir, the simplest and most practical method for head measurement is water-filled tube and calibrated pressure gauge [10]. Through this method, the pressure gauge reading in psi can be converted to head in meters using the following equation of pressure to head conversion [10]:

$$H = 0.704 * P \dots \dots \dots (2)$$

Where,

H = Head (meter)

P = Pressure (psi)

the mentioned equation (2) is simply a pressure head (psi) to (meter) conversion equation. As pressure gauge measures pressure as psi unit, but for calculation purpose it is needed to convert to meter unit for pressure head [11].

2.4 Selection of turbine

As a small amount of power generation is possible in Pico hydro power (<1kw). So, low head turbine is much suitable for this. There are two types of turbine based on action of flow. They are:

- 1) Impulse turbine
- 2) Reaction turbine.

For low head hydro power, reaction turbine is suitable and also cost-effective. Types of reaction turbine is given below [13-14]:

- 1) Francis turbine
- 2) Kaplan turbine
- 3) Kinetic turbine.

Besides them, many latest turbine with less power loss can be applicable for low water head. It is best suit to select type of low head turbine during practical implementation for better efficiency.

3. Theoretical calculation

For calculating flow rate, we have used bucket method for different four sites by the help of a 25 litre bucket and a stopwatch for time calculation. From Table 1- Table 4, the data of time calculation is recorded and given below.

Table 1 Time for filling up bucket (Site 01)

No. of Trials	Time(s)
01	2
02	2.09
03	2.5
04	2.4
05	2.1
06	1.9

Average Time, $t_{avg.} = 2.12s$

Flow rate, Q = 11.81 L/s

Head, H = 15m; $\eta = 50\%$

Output Power, $P = \eta * H * Q * g = 868W$

Table 2 Time for filling up bucket (Site 02)

No. of Trials	Time(s)
01	6.4
02	6.2
03	5.8
04	6.6
05	6.4

Average Time, $t_{avg.} = 6.28s$

Flow rate, Q = 3.98 L/s

Head, H = 11.8m; $\eta = 50\%$

Output Power, $P = \eta * H * Q * g = 230.12W$

Table 3 Time for filling up bucket (Site 03)

No. of Trials	Time(s)
01	3.3
02	4.2
03	3.2
04	3.4
05	4

Average Time, $t_{avg.}=3.62s$
 Flow rate, $Q=6.9L/s$
 Head, $H=10m$; $\eta=50\%$
 Output Power, $P = \eta * H * Q * 9.8 = 338W$

Table 4 Time for filling up bucket(Site 04)

No. of Trials	Time(s)
01	4.7
02	4.8
03	5.4
04	5
05	5.2

Average Time, $t_{avg.}=5s$
 Flow rate, $Q=4.98L/s$
 Head, $H=12m$; $\eta=50\%$
 Output Power, $P = \eta * H * Q * 9.8 = 292.8W$

Total power can be achieved from four sites
 $= (868 + 230.12 + 338 + 292.8)W$
 $= 1.73kW$

4. Simulation of integrated energy model

4.1 Component selection

First, we have to design our model. For this simulation modeling we have use ‘‘HOMER Micro-grid pro’’ software which is reliable and perfect for off-grid renewable energy modeling [15]. From ‘Add/Remove’ button we’ve selected ‘primary load, PV, Hydro, Converter and a Battery storage. Though the simulation is for Pico hydro power plant, for reasonable cost of energy (COE) and having a good monthly solar radiation in Jaflong, we have integrated this solar energy. At night, to get power supply from solar energy, we have also used a battery storage. As the wind speed in Jaflong is not well enough (1.9 m/s recorded from NASA), it is not designed in integrated off-grid model. Now our off grid integrated renewable model is ready.

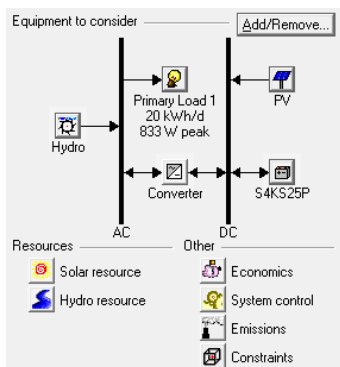


Fig. 2 Off-grid integrated model by HOMER

4.2 Solar Resource Data

We have collected the 12 months(mentioned in Table - 05)solar radiation data for ‘Jaflong’ using ‘Homer’ Software via internet.

Table 5 Monthly solar radiation data

Months	Clearance Index	Solar radiation (kWh/m ² /day)
January	0.624	4.176
February	0.589	4.604
March	0.542	4.996
April	0.490	5.097
May	0.470	5.187
June	0.379	4.261
July	0.347	3.860
August	0.384	4.071
September	0.381	3.650
October	0.571	4.688
November	0.638	4.423
December	0.648	4.100
Average	0.486	4.425

4.3 Hydro resource data input:

We have visited ‘Shongrampunji water fall-Jaflong, Sylhet’ at June, 2018. In Bangladesh, rainy season starts from the middle of June and ends to the middle of August. We’ve inputted the hydro resource in Table 6 based on the summer and rainy seasons of our country. Table 7 and Table 8 includes accordingly capital cost of different components and operation and maintenance cost of them [16-17].

Table 6 Hydro source data of Shongrampunji waterfall

Month	Flow rate (L/s)
January	300
February	350
March	250
April	250
May	300
June	500
July	650
August	650
September	500
October	450
November	380
December	300

Table 7 Capital cost and size of different components

Components	Capital Cost (\$)
1.73 kW Pico hydro power plant	1500
1kW Solar Panel	1800
Converter	200
Battery Storage	200

Table 8O & M and replacement cost of components

Components	Cost
O & M cost for solar panel	\$5/year
O & M cost for hydro power plant	\$100/year
Replacement cost of solar panel	\$5000
Replacement cost of hydro power	\$750

First of all, we have simulated the model considering capital cost and the simulation result is given below in Table 09.

Table.9Simulation result of integrated model with capital cost

Initial Capital	Operating Cost (\$/yr)	Total NPC	COE (\$/kWh)	Ren. Frac.
\$ 1,900	124	\$ 3,491	0.037	1.00
\$ 11,900	183	\$ 14,240	0.153	1.00

With capital cost, the COE is feasible if power supply is occurred only by hydro power and battery storage . As the COE when considering solar panel, it is **12.85 taka/kWh (\$0.153)** and without solar panel COE will be **3.11 taka/kWh (\$0.037)**.

If we consider the system model without capital cost, then the simulation result is given below mentioned in table 10.

Table.10Simulation of integrated model without capital cost

Initial Capital	Operating Cost (\$/yr)	Total NPC	COE (\$/kWh)	Ren. Frac.
\$ 0	124	\$ 1,591	0.017	1.00
\$ 0	183	\$ 2,340	0.025	1.00

The result says that, without capital cost except operation and maintenance cost, the COE will be **1.42 taka/kWh(without solar panel)** and **with solar panel** it will be **2.10 taka/kWh**.

5. Result and Discussion

- Water is available almost at all time. We have visited it twice at the end of rainy season and water flow rate was almost same as first visit.
- The initial capital cost is high enough if PV solar cell is considered. If capital cost of PV solar panel is managed somehow, then it can be

a good energy resource for consumers of Jaflong.

- As the output power for different sites are variable, total power output can be changed. Having big stones in water flow, the regular water flow is hampered and hence the water head is also low. If these stones are removed, then regular water flow and a better water head can be obtained that causes increase in power output.
- As the power output is small, it can be used for small electric load like battery charging, or one energy saving bulb etc. It is applicable mostly for remote areas around Shongrapunji waterfall where there is no access of electricity.

6. Conclusion

Pico-hydro power plant is an attractive and environment-friendly energy resource that can be the best future source of energy for remote hilly regions where access of electricity is impossible.

In this regard we have selected Songrapunji water fall that is the best location for small-scale pico-hydro power plant.

We have collected and evaluated data of Songrapunji Water fall mathematically and via HOMER. The result says that this site is enough feasible and can be more feasible using solar panel with energy storage which ensures power supply 24/7.

So, in future if Govt. can co-operate financially and technically, then people will get electricity who are deprived of it that is mentioned earlier.

REFERENCES

- [1] <https://thehimalayantimes.com/business/government-plans-to-sign-energy-pact-with-bangladesh/T>
- [2] <http://www.bangladeshbd.info/statistic/source-of-light-in-bangladesh-2015/>
- [3] Md. A. Akbar, "An assessment of the geothermal geothermal potential of Bangladesh", United Nations University, Geothermal Training Program, Orkustofnun, Grensasvegur 9, IS-108 Reykjavik, Iceland, Reports 2011, Number 5.
- [4] Das, Vivekananda (April 2017). "A Study on the Prospect of Geothermal Energy in Bangladesh", Global Journals Inc. (USA). 17: 33–37.
- [5] http://en.banglapedia.org/index.php?title=Khasia,_The
- [6] https://en.wikipedia.org/wiki/Pico_hydro
- [7] H. Zainuddin, M. S. Yahaya, et.al., "Design and Development of Pico-hydro Generation System for Energy Storage Using Consuming Water

- Distributed toHouses". World Academy of Science, Engineering and Technology, International Journal of Electrical and Computer Engineering, Vol:3, No:11, 2009
- [8] Vineet Kumar Singh, Neha Singh Chauhan and Deepti Kushwaha, "An Overview of Hydro Electric Power Plant", ISST Journal of Mechanical Engineering, Vol. 6 No. 1, (January - June 2015), p.p. 59-62, ISSN 0976-7371
- [9] Mehta, V. and Mehta, R. (2017). Principles of Power System. 4th ed. New Delhi-110 055: S. Chand & Company Ltd., Pages: 23-25
- [10] A. Harvey, A. Brown, P. Hettiarachchi and Inversin, "Micro hydro design manual: A guide to small-scale waterpower schemes", Intermediate Technology Publications, 1993.
- [11] <https://www.convertunits.com/from/PSI/to/meter+of+head> (Date of Access: 10/11/2018)
- [12] P. Maher and N. Smith, "Pico hydro for village power: A practical manual for schemes up to 5kW in hilly areas," 2nd ed., Intermediate Technology Publications, May 2001.
- [13] <https://www.slideshare.net/daudsangenkhan/types-of-turbine-their-application>(accessed:11/8/2018)
- [14] Mehta, V. and Mehta, R. (2017). Principles of Power System. 4th ed. New Delhi-110 055: S. Chand & Company Ltd., Page: 22
- [15] HomerEnergy, URL: <http://www.homerenergy.com/>(accessed:12/08/2018)
- [16] EnergyBangla URL:<http://energybangla.com/bds-solar-power-costliest-in-asia/>(accessed:14/08/2018)
- [17] Energypedia: URL:https://energypedia.info/wiki/Pico_Hydr_Power(Accessed:14/08/2018)

Agricultural Scenario and Solar Irrigation System of Bangladesh

M. S. Islam*, Md. Bakhtierkhalzi, Sabbir Ahmed, Pronob Das

Department of Mechanical Engineering, Rajshahi University of Engineering & Technology, Rajshahi, BANGLADESH

E-mail: sohag09me@gmail.com

ABSTRACT

Bangladesh is an agronomic country where two third of the total population directly or indirectly involves with agriculture and about 14.75% of gross domestic product (GDP) emanates from the agriculture sector. Although Bangladesh's economy is dependent on agriculture, she is not self-sufficient in food. Besides, frequent natural disasters such as flood, drought, and cyclone cause damage to crops every year. To provide food for her overpopulation, a large amount of food grains is imported every year. The total amount of cultivable land is about 85,60,964 hectares, of which 1154141 hectares land are being unirrigated every year. The typical irrigation systems of Bangladesh are primarily diesel based and electricity based pump. At present, 1.31 million diesel based pumps and 313,929 electricity based pumps are in operation for irrigation and it demolishes above 1.06 million tons of diesel and about 1400 MW electrical power individually. The power crisis in Bangladesh along with high diesel cost make the solar irrigation system as a promising alternative to power and diesel based pumping systems. The main objective of the study is to present a review of agricultural scenario, conventional pumping method, the prospect of solar pumping in Bangladesh. The study focuses on the update on advancement, barrier and remedies and socioeconomic benefit of the solar irrigation system. Since, Bangladesh is an energy starving country and most of the farmers are poor, therefore solar irrigation may be supportive for the farmer as well as in the total crop production in Bangladesh.

Keywords: Bangladesh, Agricultural scenario, pumping method, Solar irrigation, Advancement.

1. Introduction

Bangladesh is a middle income South Asian country and its economy ranks 46th in terms of nominal gross domestic product (GDP). It covers a total land area of 147,570 square kilometers [1]. Bangladesh has a population about 162.9 million [2], making it one of the densely populated countries of the world. Bangladesh is an agrarian country, where the majority of the land is being utilized for agriculture [3,4]. From the World Bank report, the farming area is just over 70% of the aggregate land. The country has about 14.76 million hectares of aggregate land, of which 56% are net irrigable [5]. The total land utilization pattern of Bangladesh. The forest area covers only 11.73% of the total land. The net cropped area is 69.4 % where more than 16% lands are not used for cultivation [6]. Around 60-70% of the population involves agriculture for their livelihood. But recently, the portions of agriculture in GDP declined steadily in recent years, which were recorded at 15.51%, 14.77%, 14.17%, and 13.75% in the years 2014-15, 2015-16, 2016-17 and 2017-18 respectively [7]. Agriculture, forest and settlement used the majority of the land area in Bangladesh. A fraction of the land area is being used to meet industrial and other miscellaneous social and administrative needs. Moreover, the existing cultivable land areas are being acquired by new industries and residences to meet the vital demand of the growing population.

Bangladesh is mystically enchanted with auspicious natural resources for the production of crops all year round. She produces rice, wheat, sugarcane, pulses, tea, jute, maize, potato, oilseeds, vegetables, various spices. Among them, rice is the overwhelming harvest in

Bangladesh, covering 75% of cropped areas, and includes 70% of the estimation of product yield [8]. According to the fiscal estimate of BBS, the volume of food grain production in FY 2015-16 stood at 386.93 lakh tons among which Aus accounted for 22.89 lakh tons, Aman 134.83 lakh tons, Boro 189.37 lakh tons, wheat 13.48 lakh tons and maize 26.36 lakh tons. In spite of producing large quantity of food grains per year, Bangladesh is not self sufficient in food and as a result, she needs to import lots of rice per year which accounts for a loss of foreign currency. The main barriers for agricultural growth includes weather and climatic variations such as too little or too much rain, cyclones and storm surges, floods and increasing salinity along the coastal areas, drought, heat waves, cold and fog and water logging, etc. Due to frequent drought and scarcity of water during dry season, a significant amount of lands remains uncultivable every year. Earlier, irrigation was done by river water. But, recently many rivers suffer from the scarcity of water, especially in dry seasons. Therefore, underground water has been becoming the main source of water for irrigation which enforces the farmers to use diesel and grid-connected water pumps.

The energy demand of the country is growing significantly due to the quick increment of population, rapid alteration in economy and industrializations. Incrementing energy demand is not only diminishing the reserve of fossil fuel e.g natural gas & coal but additionally affecting the environment. Fig.1 illustrates the power consumption pattern of the country. Inadequate amount of power generation retards the economic development as well as desertification

* Corresponding author. Tel.: +88-01670063586

E-mail addresses: sohag09me@gmail.com

problems in rural area. The energy is utilized in all sectors of the economy including domestic, agriculture, industry, and other service sectors. Domestic sectors consume about 23050 M kWh electricity which is about 50.89% of total power consumption occurs [9]. The electricity demands in agriculture sectors have been steadily increased and it consumes about 3.61% of country's energy. Besides, new pumps have been installed in every year to meet the demand of irrigation during dry season. Fig.2 shows the installation of new pumps for the last few years. The numbers are increasing and the corresponding energy require driving them increases which results in high power consumption in agricultural sectors. Actual demand of electricity was unable to meet in the last few years due to insufficiency of generation. Therefore, load shedding has increased and Bangladesh is currently facing a shortage of 250MW electricity. The situation becomes terrible during irrigation seasons, when gap between actual energy demand and supply reaches around 2000 MW along with the poor quality of power services such as frequent voltage fluctuations, unreliable and erratic supply especially in rural areas. Due to lack of proper electricity, farmers depend on diesel based pump. Bangladesh government usually provides subsidy BDT 22-26 per liter of diesel to make diesel pumping affordable to the farmers which creates an extra pressure on domestic economy. Over 1.75 million irrigation pumps are being utilized in the country of which 82% are diesel engine operated and 18% are electrically operated [10].

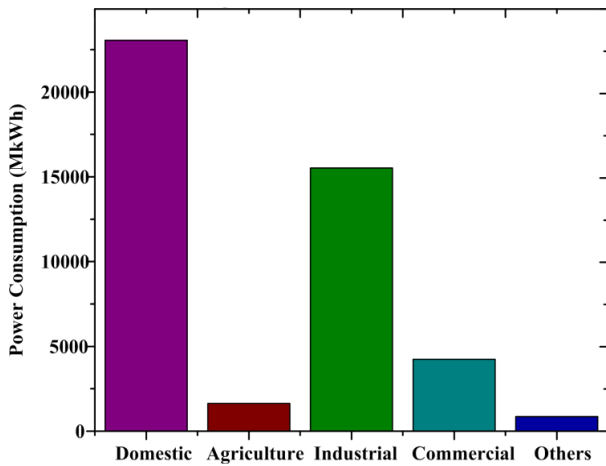


Fig.1 Power consumption pattern of Bangladesh [9]

Approximately 40% individuals of the country live in the remote zone, which is far from subsisting grid line and sometimes isolated from the main land. In some cases, the grid power won't be accessing the majority of the remote and disconnected region for the following 20-50 years. Besides, the underground water level in some regions of the country, e.g Varendra area is too deep and not practical to withdraw water by diesel pumps. In this manner, many land areas still remain non-irrigable and un-cultivable during dry seasons. Many areas of Bangladesh (Charland, hilly area, coastal

area, etc.) are out of grid connection and hence they are not cultivated properly. Less arable land and limited natural resources increase the importance of developing new agricultural technologies. Therefore, it is high time to incorporate sustainable methods to irrigate cultivable land to increase food security as well as economic development. Solar irrigation system would be a probable solution.

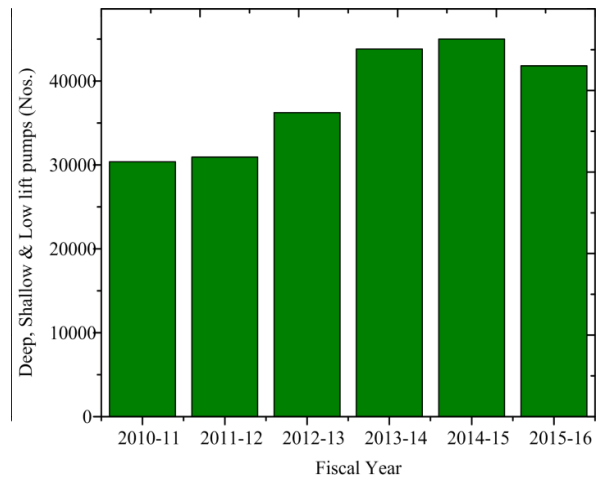


Fig.2 Pump installation scenario in recent years [6]

Solar energy is more reliable and richly available in Bangladesh with a variation of average irradiation in between 4 and 6.5 kWh/m²/day [11]. Introducing solar irrigation will not only reduce burden on energy sector but also encourage farmers to cultivate more land under irrigation which helps to improve rural economy as well as national economy. Solar photovoltaic pumping offers alternative way to the farmers of Bangladesh from the energy crisis [12-14]. Abu-Aligah [15] demonstrated that the photo voltaic pumping system is a good alternative for irrigating crops in the off grid areas. It was reported that solar based pump was much cheaper on life-cycle cost basis than diesel engine for small to medium sized wells [16]. Proper policy and financial subsidies should be provided by the GoB to popularize solar pumping within the country [17-18]. This paper represents the agricultural scenario, conventional pumping method, prospect of solar pumping, solar irrigation system and focuses on update on advancement, barrier and remedies and socioeconomic benefit of the solar irrigation system in Bangladesh.

2. Agricultural Scenario of Bangladesh

Agriculture is the huge employment sectors in Bangladesh since it utilizes 47% of the total work force and involves 16% of the nation's GDP [19]. The majority of the populations earn their living from agriculture. There are three types of aggregate land in Bangladesh including one crop land, two crop land, and three crop land. In the year of 2016-17, the one crop land is 2354821.74 ha, two crop land is 3847274.49 ha and three crop land is 1715430.38 ha [10]. Rice is the staple food of Bangladesh, which contributes about 70%

of total calorie supply and about the half of the aggregate protein. Bangladesh is the fourth most rice producer in the world in which about 75% of agricultural land is planted to rice [20]. Bangladesh is also a large exporter of jute. There are other agricultural crops, i.e., wheat, potato, pulses, vegetables, spices, tea,

16, wheat imports are forecast at 3.8 million tons where the actual amount was 4.72 millions ton. The consumption of wheat follow the increasing trends in recent year which is expected to cross 6.72 million tons in 2017. Bangladesh sources wheat from India, Russia, Ukraine, Canada, Australia, and the United States.

Table 1 Production rate of major agricultural crops in Bangladesh [16]

Year	Rice Production '000' tons	Jute Production '000' Bales	Sugarcane Production '000' tons	Tea Production '000' lbs.	Pulses Production '000' tons	Oilseeds Production '000' tons	Tobacco Production '000' tons
2008-09	31317	-	5233	130073	196	661	40
2009-10	31975	924	4491	132277	218	786	54
2010-11	33542	1523	4671	133380	232	730	79
2011-12	33889	1452	4603	133379	240	787	85
2012-13	33833	7611	4469	139994	265	804	181
2013-14	34357	7436	4508	145728	352	844	85
2014-15	34710	7501	4434	145727	378	934	94
2015-16	34710	7554	4208	142198	378	934	88

which are partly produced and the rest are imported to meet the domestic demand. The most cultivable region of Bangladesh is includes Borguna, Barisal, Chittagong, Comilla, Noakhali, Mymensingh, Narsingdi, Bagerhat, Jessore, Naogaon, Rajshahi, Rangpur, Sylhet region. In the above area, all types of crops are grown up in huge quantity. Table 1 demonstrates the production of major agricultural crop from 2008-09 to 2015-16 [21]. In 2016, the production of rice was 34.7 million tons and the production of jute was around 7.55 million bales. The production of food is increasing per year due to incorporation of new techniques but it is inadequate to feed the over population. Moreover, various natural calamities such as floods and drought damage our crop and causes food shortage. As a result, in spite of producing high amount of food grains, Bangladesh is not self-sufficient in food. Every year it often requires to imports huge amount rice from the neighbor countries to satisfy its rice demand and to confront nourishment emergencies because of the dry season, surge and numerous other catastrophic events. Bangladesh turns out to be a net rice importing country due to the huge domestic consumption. To keep pace with the population increase, demand for import also needs to increase to mitigate food crisis. The increasing volatility of international grain markets over the past few decades results a consumption of huge foreign currency. Fig.4 shows the rice and wheat import scenario for the last few years and their corresponding cost. Imports of rice grains are low compared to wheat mainly due to the adequate domestic supply of rice. In 2016, Bangladesh imports about 0.07 million tons of rice and 5.5 million tons of wheat which cost about 119 and 915 million USD respectively. The country's rice consumption needs are estimated at around 34.8 million tons in FY 2014-15 slightly up from an estimated 34.6 million tons in FY 2013-14 [22]. Bangladesh imports rice from India, Srilanka, Vietnam, Cambodia and Myanmar. In 2015-

3. Conventional Pumping Method

In Bangladesh, surface water, ground and rainwater are the main sources of irrigation. About 795,000 million m³ surface water discharges through the two main rivers i.e Ganges and Brahmaputra [23]. In the dry season, Bangladesh extremely experiences shortest of water particularly for irrigation and consequently the farmers to a great extent rely upon groundwater at the dry season. The DTW, STW, and low lifting pump LLP are ordinarily utilized for substantial and medium scale water lifting in Bangladesh. Table 2 shows the various type of tube wells utilized for irrigation in Bangladesh. In the year of 2015-16, a total of 1,627,166 irrigation pumps were operated to irrigate 5,313,729 ha lands. Among them 313,909 were operated by electrical motor to irrigate 2,248,697 ha. and 1,313,257 were operated by diesel engines to irrigate 3,065,032 ha land [24]. Besides in the fiscal year 2015-16 29,718 ha lands were irrigated by Manual & Artesian well method, 18,336 ha lands were irrigated by traditional method and 1,28,564 ha lands was irrigated by gravity flow. About 17.55 millions farmers get the benefits irrigation and this number is increasing steadily. About 42.3% areas are irrigated by electricity and the rest by diesel based pumps. Diesel pump consumes about 18.1% of country's total annual petroleum consumption. The government owned organization BADC and BMDA operates only 2.11% of total pump, where rest 1592908 pumps are operated by other organizations and private entrepreneurs. Fig.3 show the area irrigated under different crops. In 2014-15, about 18.17 million acres land are irrigated by different pumping methods in Bangladesh. Rice including aman and boro covers about 13.54 million acres of crop land. Farmers in areas without electricity grid coverage are compelled to use diesel-powered irrigation pump. Every year, diesel pumps consume 1 million tons of diesel worth \$900 million [25].

Table 2 No of different types of tube wells used for irrigation in Bangladesh [24]

Fiscal year	DTW		STW		LLP		Total
	Operated by electricity	Operated by diesel	Operated by electricity	Operated by diesel	Operated by electricity	Operated by diesel	
2012-13	32,412	2910	253,473	1,270,136	10,856	159,713	1,729,500
2013-14	33,179	2855	273,755	1,290,036	10,417	160,624	1,770,866
2014-15	33,714	2852	276,347	1,273,364	10,496	156,679	1,753,452
2015-16	34,647	2332	269,847	1,147,161	9415	163,764	1,627,166

The consumption of diesel fuel to irrigate these land emit excessive CO₂ emission which is a threat to the environment. The high price of diesel puts extra pressure to the farmers and result in excessive production cost which is a main barrier for sustainable agriculture.

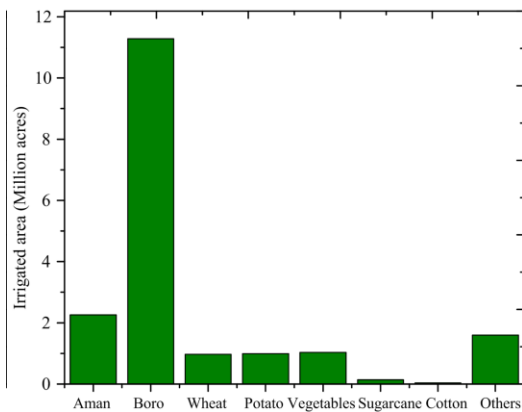


Fig.3 Irrigated area for different crops in Bangladesh [6]

4. Solar irrigation system

Solar powered irrigation pumps are a low cost and reliable irrigation alternative as Bangladesh is not enriched in power generation.

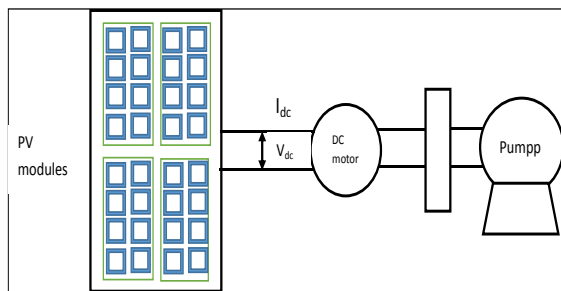


Fig.4 Typical block diagram of a direct coupled DC solar irrigation system

A solar pump can supply water for virtually three crops irrigations along the year. A solar irrigation system consists of a PV array, a DC motor or an AC motor pump set and a powerful converter with a controller. Fig.4 shows a typical block diagram of a direct coupled DC solar irrigation system.

In Bangladesh, the solar irrigation system has paramount advancement in the last 10 years. At the beginning, centrifugal pumps were mainly utilized in solar irrigation system having the hydraulic efficiency of 25-30%. Later higher capacity multistage submersible pumps were introduced, which can withdraw water from a few meters to few hundred meters with distribution capacity up to 500 m³/h. Multistage solar irrigation system consists of a PV array, a DC-DC converter, a DC-AC inverter and a motor pump set. In a solar irrigation system, the pump utilizes the produced electricity in solar panel. The management of AC or DC current is controlled by the electric motor where the speed and output power are adjusted by the controller. The system is feasible to be used as the alternative of conventional diesel based pumping system. The main cost of the solar pump is the Panel cost (45%) followed by the installation cost (18%), motor cost (16%), pump cost (10%), and pipes and fittings cost (4%) [20].

5. Solar Energy Resources in Bangladesh

Bangladesh is a semitropical region lying in northeastern part of South Asia gets plentiful sunlight year round due to its geographical locations [26]. Bangladesh receives 70% of sunlight During dry season. It receives an average solar radiation of 4 to 6.5 kWh/m²/day and the yearly solar radiation is as high as 1700 kWh/m²[27].

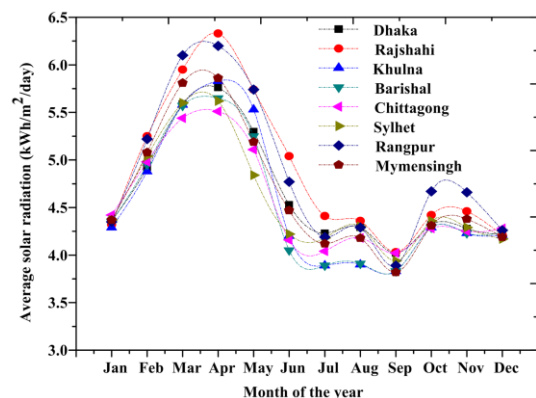


Fig.5 Incident solar radiation on different locations in Bangladesh throughout the year [27]

Fig.5 shows the solar irradiation on the eight divisions of Bangladesh round the year. Greatest measures of

radiation accessible in the month between March-May and least during November to January. Bangladesh has the normal bright sunshine hour in the dry season of around 7.6 hours and in monsoon season of around 4.7 hours per day. The maximum sunshine hours got is in Rangpur with readings going from 3.6 to 8.9 hours and in Chittagong 3.7 to 8.7 hours. Ideal locations for a solar power plant should have flat lands with minimum cloud cover, high solar radiation availability and exhibit high average sunlight hours throughout a year. The lowest cloud average is in Rajshahi and Khulna with readings ranging from 0.6 to 6 okta and 0.4 to 6.4 okta respectively. Rajshahi receives the most solar radiation with the ranging from 4.03 to 6.33 kW/hour/m².

7. Advancement of solar irrigation in Bangladesh

Because of the fast growth of population in Bangladesh, a remarkable percent of residents will live without power. Besides, the future capacity shortage threatens the grid expansion rate to connect rural areas, which directly affects the irrigation system in rural areas. In order to solve this problem, Bangladesh government has prepared a renewable energy policy in 2008 effective from 2009, where an objective was set to create 2000 MW electrical power by 2020 from renewable energy source assets.

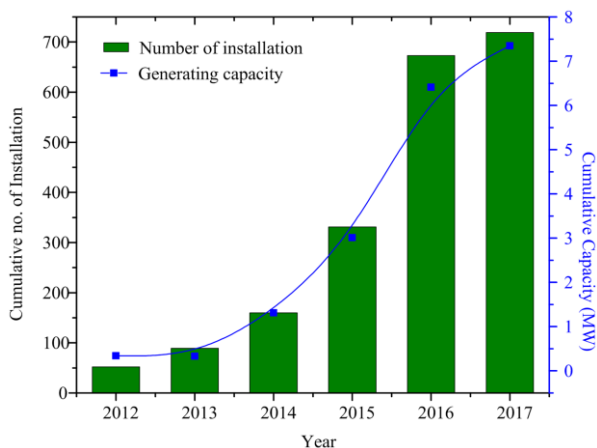


Fig.6 Cumulative increasing number of solar irrigation for last 6 years.

At present, about 719 solar irrigation pump with a capacity of 7.5 MW are being operated with the support of IDCOL in the different locations of Bangladesh [28]. IDCOL financing solar irrigation projects by receiving fund from World Bank, Asian Development Bank, Kreditanstalt fur Wiederaufbau (KfW), Japan international Corporation Agency (JICA), Global Partnership on Output-Based Aid (GPOBA) and Bangladesh Climate Change Resilience Fund (BCCRF). IDCOL has an mission to install 1550 solar irrigation pumps by 2018. IDCOL gives up to 50% subsidy and arranging 35% soft loan with the assistance of donor agencies. Under this programme, owners or individual investors of the irrigation system required to contribute just around 15% of project cost. The soft loan may have a maximum tenure of 8 years with 9

months grace period and an interest rate of 6% per annum.

7. Socioeconomic benefit

Environment friendly and cost effective solar irrigation system getting popular among the farmers of Bangladesh since it creates a scope for sustainable agriculture practices over diesel based irrigation system. Besides, the farmers will be able to enhance their product yield through irrigation round the year by solar irrigation which not only brings various socioeconomic benefit to the society but also reduces the dependency on conventional energy system. It also reduces government's subsidy for agriculture as well as import of diesel fuel. In remote areas, solar irrigation system witnesses rapid adoption since the irrigation cost has dropped almost half compared to diesel based irrigation system. They are more reliable, operated without pollution and noise, easier to install and lower maintenance cost compared to conventional pumping methods. It also motivates the farmers to shift their attention from expensive, CO₂ emitting diesel powered water pump as it provides reliable water supply throughout the year with benefits to good harvest and household income. Solar pumps require fewer amount of land and water in operation with minimum wastage since additional drainage system is not required to irrigate the land. It will also decreased the burden of government's ability to produce electricity and the cost of energy production. Solar irrigation has a high potential value as it brought sustainable benefits to agronomy.

8. Barrier and Remedies

Though solar energy is abundant in nature and environment friendly, installation of solar pump requires extensive infrastructure and equipment. Since most of the farmers in Bangladesh are poor they can't afford to install a solar irrigation system due to high initial investment. This is the main barriers for rapid expansion of solar pumps. Besides, the raw materials required for the photovoltaic cells, reflectors and other auxiliaries are imported, these increases the cost of solar system. Due to the imposition of import duty on solar panels and other accessories, the initiatives taken by different organizations to promote solar irrigation in agricultural sector faces serious hindrance. As a result, this system failed to become economically feasible and the investors show less interest even after government provides 50% of the initial cost. Maintenance and repairing is an important concern since there is a lack of skilled technicians and experts. Artificial solar based irrigation system is mainly used for boro paddy cultivation in dry season. The solar panels are able and continue to generate electricity throughout the year. But this energy is used only in dry season and remains unused during the rest of the year since there are no such facilities to supply this unused electricity to the grid or other consumers. This situation makes solar irrigation system less effective both technically and

financially. In order to irrigate crop land, solar irrigation extensively uses ground water. Since, ground water has limited reserve, excessive use causes underground the aquifer to fill up by saline water from the sea. This adverse effect is alarming signal for the agriculture in many areas of Bangladesh. Besides, solar irrigation creates unemployment to the community whose income depends on diesel based pumping system and hampers their livelihood security. Social awareness's are required to promote solar irrigation in Bangladesh through publicity in print and social media. The government can provide more subsidy and exempted tax from solar accessories to make it feasible for the farmers.

9. Conclusion

This paper reviews the socioeconomic status of Bangladesh in terms of its current scenarios of agriculture, rice production, methods of irrigation, energy and environmental conditions, solar irrigation and its advancement to prospect. All that discussion delivers a clear forecasting that, solar irrigation could be one of the vital options to create sustainable development in agriculture. Because the main advantages of solar irrigation pumps over hand pumps or diesel based pumps are their practically zero maintenance, long useful life, zero requirements of fuel, zero contamination, and easy to install. The review helps to draw the attention to the investor to invest in this field and helps in further research. Keeping in view the high installation costs of solar water pumps especially for large irrigation and water supplies, more incentives are required to be provided by governments to make the technology further attractive alternative to diesel and electrical water pumping.

References

- [1] "Health Bulletin 2016". Directorate General of Health Services (DGHS). p. 13. Retrieved 11 September 2017.
- [2] "World Population Prospects: The 2017 Revision". ESA.UN.org (custom data acquired via website). United Nations Department of Economic and Social Affairs, Population Division. Retrieved 10 September 2017.
- [3] Islam MR, Islam MR, Beg MRA. Renewable energy resources and technologies practice in Bangladesh. *Renew Sustain Energy Rev* 2008;12:299–343.
- [4] AMMM Ahmed, Roy . K. Utilization and conservation of water resources in Bangladesh. *J Dev Sus Agr* 2007;2(1):35–44.
- [5] Ministry of power, energy and mineral resources, government of the people's republic of Bangladesh. www.powerdivision.portal.gov.bd .(accessed 23 october 2015)
- [6] Statistical Year Book Bangladesh, BBS 2016, Statistics of agriculture. Page no. 123.
- [7] Gross domestic product (GDP) of Bangladesh. Bangladesh Bureau of Statistics 2017-2018. <http://www.bbs.gov.bd/site/page/dc2bc6ce-7080-48b3-9a04-73cec782d0df>.
- [8] The principal food crops grown in Bangladesh. <http://bankofinfo.com>.
- [9] Bangladesh Power Development Board. Power consumption pattern. Annual Report 2016-2017 (Accessed 26 August 2017)
- [10] Bangladesh Agricultural Development Corporation. Organization wise summary of irrigation equipment used area irrigated and benefited farmers. www.badc.gov.bd. [Accessed 13 December 2015]
- [11] Islam MR, Guo YG, Zhu JG. A multilevel medium-voltage inverter for step-up transformerless grid connection of photovoltaic power plants. *IEEE J Photovolt* 2014;4(3):881–9.
- [12] Khan, S.I., Sarkar, M.M.R. and Islam, M.Q., 2013. Design and analysis of a low cost solar water pump for irrigation in Bangladesh. *Journal of Mechanical Engineering*, 43(2), pp.98-102.
- [13] Khan, M.T.A.I., Sarkar, S., Hossain, S., Ahmed, A.U. and Pathik, B.B., 2014, February. The feasibility study of solar irrigation: Economical comparison between diesel and photovoltaic water pumping systems for different crops. In *Electrical Information and Communication Technology (EICT), 2013 International Conference on* (pp. 1-5). IEEE.
- [14] Hasnat, M.A., Hasan, M.N. and Hoque, N., 2014, December. A brief study of the prospect of hybrid solar irrigation system in Bangladesh. In *International conference on mechanical, industrial and energy engineering* (pp. 25-26).
- [15] Abu-Aligah, M.: Design of photovoltaic water pumping system and compare it with diesel powered pump. *Jordan J Mech Ind Eng*5(3), 273–280 (2011).
- [16] Anon (Anonymous): Feasibility assessment for the replacement of diesel pumps with solar pumps. Final Report. September 2006, Namibia Renewable Energy Programme (NAMREP), Ministry of Mines and Energy, Namibia. p. 76 (2006).
- [17] Hoque, N., Roy, A., Beg, M., Rafiqul, A. and Das, B.K., 2016. Techno-economic evaluation of solar irrigation plants installed in Bangladesh.
- [18] Chowdhury, S.A., Aziz, S., Groh, S., Kirchoff, H. and Leal Filho, W., 2015. Off-grid rural area electrification through solar-diesel hybrid minigrids in Bangladesh: resource-efficient design principles in practice. *Journal of cleaner production*, 95, pp.194-202.
- [19] "The World Factbook". Central Intelligence Agency. Retrieved 24 February 2016.
- [20] Hossain, M. A., et al. "Feasibility of solar pump for sustainable irrigation in Bangladesh." *International Journal of Energy and Environmental Engineering* 6.2 (2015): 147-155.

- [21] Production rate of major agricultural crops, Statistical Year Book of Bangladesh-2016. Bangladesh Bureau of Statistics (BBS). Page No-137
- [22] Grain and Feed Annual of Bangladesh (2015). Global Agricultural Information Network, USDA foreign agricultural service. GAIN Report Number: BG5003, Page No: 3-5.
- [23] AMMM Ahmed, Roy . K. utilization and conservation of water resources in Bangladesh. J Dev Sus Agr 2007;2(1):35-44.
- [24] Bangladesh Agricultural Development Corporation. Organization wise summary of irrigation equipment used area irrigated and benefited farmers, 2015-16. www.badc.gov.bd. [Accessed 23 December 2017]
- [25] Solar-Powered Pumps Reduce Irrigation Costs in Bangladesh
<http://www.worldbank.org/en/results/2015/09/08/>
- [26] Shakir-ul haque Khan, Towfiq-ur-Rahman, Shahadat Hossain. A brief study of the prospect of solar energy in generation of electricity in Bangladesh
- [27] Abdul Mannan Akanda, A.K.M Enamul Hoque, Md. Alauddin. Shimul Borua Hybridization of hydropower, wind energy, solar PV cell in Chittagong Bangladesh.
- [28] Renewable Energy/Energy Efficiency Status Report (Installed). Sustainable & Renewable Energy Development Authority (SREDA). (Accessed on 27 March 2017)

An Automatic Solar Tracking System Using Programmable Logic Controller

M. E. Hoque, F. Rashid*, S. Shahriar, M. K. Islam

Department of Mechanical Engineering, Rajshahi University of Engineering & Technology, Rajshahi-6204,
BANGLADESH

ABSTRACT

Recent research shows that about 36% more energy can be obtained by tracking the motion of sun by using solar panel as compared to solar panel at fixed position. In this paper, the tracking process is governed and controlled by programmable logic controller (PLC) where two stepper motors are used to guide the motion of the solar panel in azimuth and elevation angle. The azimuth and solar altitude angles of sun were calculated at 24.3636°N, 88.6241°E (Rajshahi, Bangladesh). It is observed that automatic solar tracking is providing better performance than fixed solar panel and maximum surplus energy was obtained about 36%. The experimental results are obtained for the voltage-current characteristics and power generation at the output of solar panel both for tracking and without tracking. An automatic solar tracking system can easily be employed in industry and suitable for mass energy production.

Keywords: Tracking system, programmable logic controller, solar panel, azimuth angle, elevation angle.

1. Introduction

Human is the biggest driver of energy demand. Population and economic growth will drive higher but the world will use energy more efficiently and toward lower- carbon fuels. Most of the countries rely heavily on coal, oil, and natural gas for its energy. Fossil fuels are non-renewable, that is, they draw on finite resources that will eventually dwindle, becoming too expensive or too environmentally damaging to retrieve. Finding sufficient supplies of clean energy for the future is one of society's most daunting challenges. Alternative renewable energy sources such as sun energy can be substituted for exceeding human energy needs[1]. In contrast, the many types of renewable energy resources- such as wind and solar energy-are constantly replenished and will never run out. Most renewable energy comes either directly or indirectly from the sun. Sunlight, or solar energy, can be used directly for heating and lighting homes and other buildings, for generating electricity, and for hot water heating, solar cooling, and a variety of commercial and industrial uses [2]. Renewable energy is simple enough; the electricity we need every day, created by sources that are naturally replenished. There is no definition of what renewable energy is and debate rages about which sources can produce renewable energy. The sun is regarded as the source of energy for its constant duration and hygienic state, and its remarkable efficiency of not polluting the environment, as other kinds of energy, like coal and the derivations of oil that cause the pollution of atmosphere and environment[3].

Solar energy is intermittent and changeable. Daily and seasonal changes in solar energy are possible. Furthermore, the radiation amount of solar energy is determined by atmospheric conditions. Because of all these characteristics, certain solar energy applications require the storage of energy. When compared to other conventional sources of energy, solar energy has a low density. However, it is possible to convert solar energy

into mechanical or electrical (as in the PV in example) energy with adequate efficiency [4].

Solar energy conversion is widely used to generate heat and produce electricity. A comparative study on the world energy consumption released by International Energy Agency (IEA) shows that in 2050, solar array installations will supply around 45% of energy demand in the world [5]. Solar cells are systems which are composed of semiconductor materials and which convert solar energy directly into direct current electrical energy. The amount of electrical energy which will be obtained from PV systems is directly proportional to the intensity of the sun light which falls on the panel. A solar collector or photovoltaic module receives the maximum solar-radiation when the sun's rays strike it at right angles. Tilting it from being perpendicular to the sun will result in less solar energy collection by the collector or the module. Therefore, the optimal tilt angle for a solar energy system depends on both the site latitude and the application for which it is to be used [6]. However, the change observed in sun light does not occur linearly, for this reason it is desired that the solar panels be fixed in way that they face the sun or that they have a system which tracks the sun. Sun-tracking systems are designed in a way to track the sun on a single axis (according to the azimuth angle) or in a way to track the sun on both axes (according to the azimuth and solar altitude angles) [7]. As the sun position changes throughout the day, the solar system must be adjusted so that it is always aimed precisely at the sun and, as a result, produces the maximum possible power [8]. Various studies were conducted on sun-tracking systems by using a number of different methods. The solar tracking system can be controlled by Programmable Logic Controller (PLC). The calculated required positions of the tracking surface are determined in the PLC. The PLC controls the actuator, which, in turn, moves the tracking surface into the calculated positions [9].

* Corresponding author. Tel.: +88-01

E-mail addresses: frrashed10@gmail.com

PLC is used as a device for controlling the output for the motor. If the sun is not visible during a short period due to cloudy weather, the PLC is set with a program which will engage the motor rotation to halt which only will be reactivated due to a sensor which will detect availability of the sun to continue its next cycle. In this experiment PLC-100 trainer is used. It has the following specification [10]:

- AC power supply (100V-240VAC,50/60Hz)
- PLC main unit (Fatek FBs 24MC)
- Digital input(14points)
- Digital output (10 points)
- Support 16high speed counter
- Support 0.1 ms high speed counter
- Execution speed (Average): 0.33 micro seconds/sequential instruction
- Four communication port (USB, RS-232, RS-485, Ethernet, Expansible up to 5 ports)
- One 4-digit thumb wheel switch
- One stepped motor
- One encoder
- One 24dc motor
- One micro switch
- One buzzer
- One 4*4 keypad
- One 24-dc expansion power
- Provide I/O module expansion port& DIO extension port
- traffic light control module
- tank filling device module

2. Methodology

The factor in which design criteria depends are dimension of the panel, capacity of the panel, weight of the panel, selection of structural material, selection of stepped motor and space available.

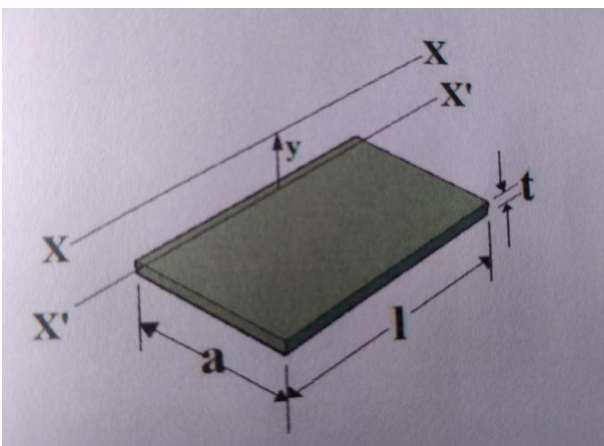


Fig. 1: PV panel

Length, $l=0.1651\text{m}$

Width, $a=0.1397\text{m}$

Thickness, $t=0.0089\text{m}$

Programmable Logic Controller (PLC) is a special computer device used in industrial control systems. Due

to its robust construction, exceptional functional features like sequential control, counters and timers, ease of programming, reliable controlling capabilities and ease of hardware usage – this PLC is used as more than a special-purpose digital computer in industries as well as in other control-system areas [11], The main purpose of this project is two. One is control the solar panel and other is to obtain the maximum output from the solar panel by tracking with PLC. It has 14 digital input and 10 digital outputs. At first a ladder diagram was downloaded to PLC which is based on timer. The timer setup in such a way that the panel will turn 15° per hour. In this experiment, two stepper motor is used each having 5 wires.

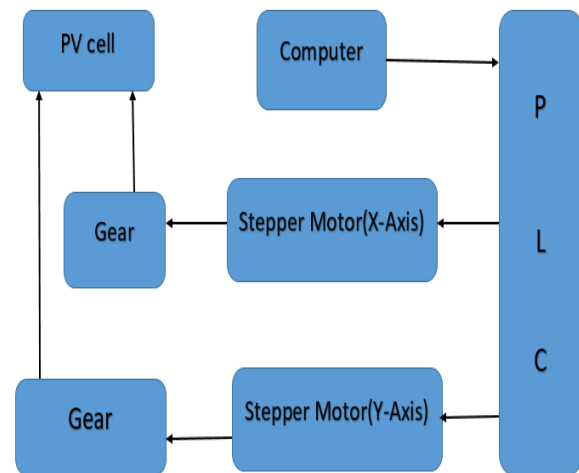


Fig.2: Schematic arrangement of the project

The polarity of the motor is White>Ash>Violate>Green>Blue and another motor is Gray>Black>Red>Orange>yellow. The wires are connected to the output port of the PLC. After checking all the connection with PC, PLC and stepper motors, the program is initialized and makes it online to the PLC. Then run the program and turn on the input switch. Then the solar panel will start moving according to program and getting required tracking values from multi-meter.

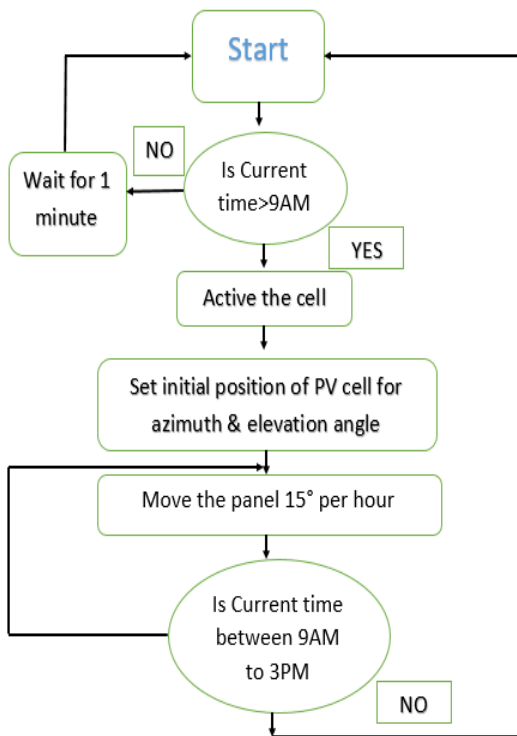


Fig. 3: Flow chart of working process

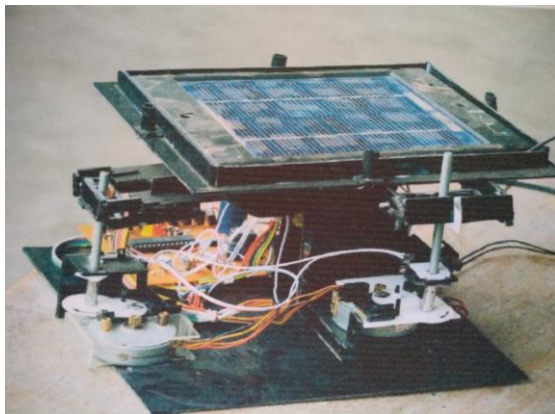


Fig. 4: Designed solar tracker

Designed solar tracker consists of two stepper motor, rack, pinion, light sensor and flexible stand. Flexible stand holds the solar panel. Stepper motor from the two side of the panel rotate the pinion so that the panel can turn in a desired angle with the help of the rack.

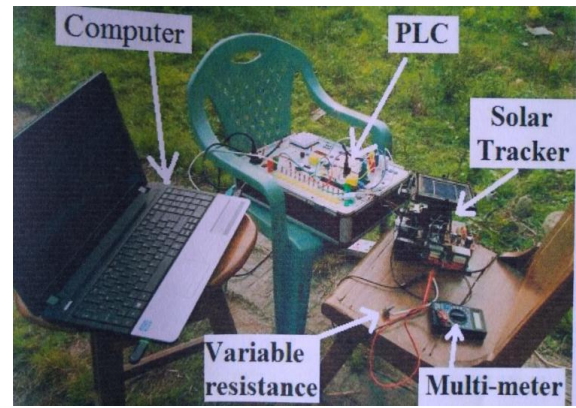
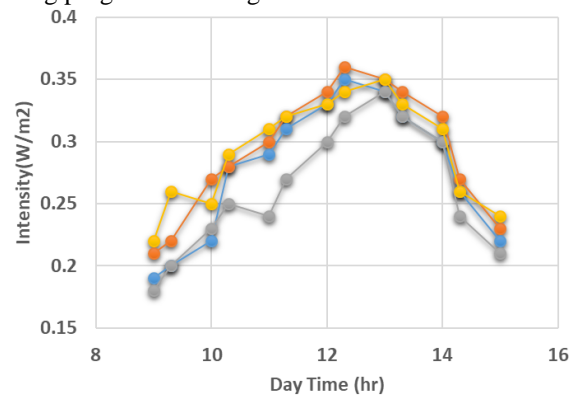


Fig. 5: Experimental setup

Experimental setup consists of a computer, PLC, solar tracker and a multimeter. When direction of sunlight changes the sensor mounted will identify a change in the intensity of light. The sensor output and corresponding program logic will then force the solar panel to adjust accordingly in the direction of high intensity of sunlight by using stepper motor, pinion and rack. PLC is controlled and programmed by using a computer.

3. Results & Discussion

Figure 6 shows the tracking results with and without using programmable logic controller.



- current without tracking (08-12-13)
- Current with tracking (08-12-13)
- Current without tracking (09-12-13)
- Current with tracking (09-12-13)

Fig.6: Intensity Vs Day Time Curve

Figure 6 shows the relation between daytime and intensity. At the beginning of the day the intensity of light is low. As hour advances the intensity of light increases and becomes maximum in the afternoon period after that intensity decreased. Figure 6 also represents that with tracking system using programmable logic controller, the intensity is greater compared to without tracking system.

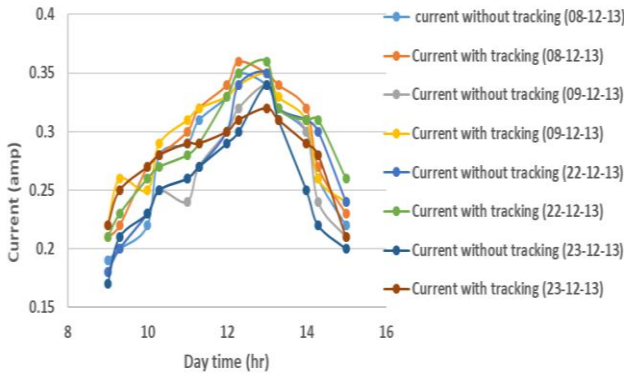


Fig.7: Current vs Day Time Curve

Figure 7 shows the day time vs current relation. As the day advances the amount of current that are produced is increasing. Tracking solar panel produced more current as compared to non-tracking panel. Since tracking panel changes its direction with respect to high intensity of sunlight.

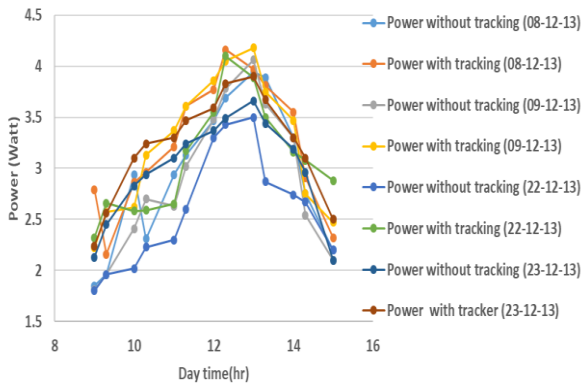


Fig.8: Power vs Day Time Curve

Figure 8 shows the relation between day time and power. It is seen that the power produced is maximum in the afternoon and after that it decreased gradually. Tracking panel produces more power than the panel without tracker.

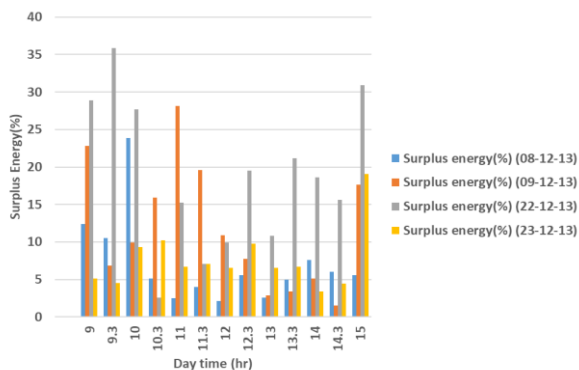


Fig.9: Surplus energy vs Day time

Figure 9 shows the relation between surplus energy and day time for various days.

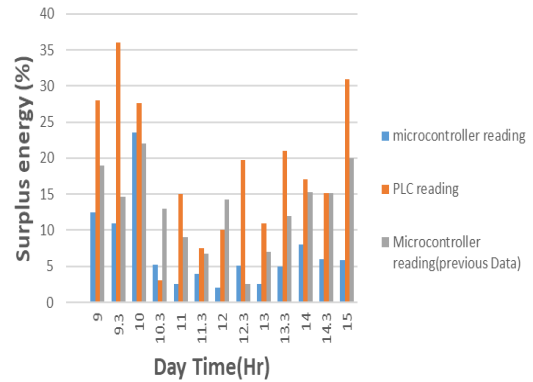


Fig.10: Comparison curve of surplus energy

Figure 10 shows the comparison of surplus energy based on micro controller reading, PLC reading and micro controller reading (previous data). From the graph it is seen that higher surplus energy from reading and lower value gets from micro controller reading (previous data), from the experimental results of variation of intensity with day time characteristic it is seen that solar irradiation increases with day. Time up to 12.30PM and then decreases and also there are some fluctuations of intensity due to flow of some cloudy sky and abnormal atmosphere. Therefore, during the central part of the day, the output fall of the solar cell will be at or near its maximum because the sun light is arriving at a regardless of the orientation of the solar cell, mainly because the sunlight has to travel obliquely through the atmosphere at these times, arriving at a low angle. This decreases the intensity of the sun. Also since the sun travels through an angle of 15° per hour, it becomes close to perpendicular to the collector for a period of approximately 2 hours. Beyond this time the intensity of the sunlight decreases due to the increase in air mass. The angle between incident sunlight and the normal to the collector increases. These two factors cause the energy collected by the collector to decrease relatively rapid during the hours before 10AM and after 1.30PM. As a result, there are some fluctuations on PV cell characteristics

4. Conclusion

An automatic solar tracking system has been developed to study the effect of tracking system in capturing solar power. In this experiment a panel tracker has been developed to increase the amount of power generated by the solar panel as the sun traverses across the sky. A PLC was used to control the movement of the solar panel. Without the tracking system the amount of solar intensity capturing is lower than the solar intensity with using PLC tracking system. From this paper it is seen that without tracking system the maximum amount of power developed is 3.5 W/hr, on the other hand with tracking system the maximum power developed is 4.5 W/hr. In case of surplus energy, without tracking system the amount of surplus energy is lower than the surplus energy with tracking system.

REFERENCES

- [1] H. Mousazadeh, A. Keyhani, A. Javadi, H. Mobli, K. Abrinia, and A. Sharifi, "A review of principle and sun-tracking methods for maximizing solar systems output," *Renew. Sustain. Energy Rev.*, vol. 13, no. 8, pp. 1800–1818, 2009.
- [2] "Importance of Renewable Energy and Types of Renewable Energy Resources." [Online]. Available: <https://www.renewableenergyworld.com/index/tech.html>. [Accessed: 17-Sep-2018].
- [3] S. Abdallah and O. O. Badran, "Sun tracking system for productivity enhancement of solar still," *Desalination*, vol. 220, no. 1–3, pp. 669–676, 2008.
- [4] C. Sungur, "Sun-tracking system with PLC control for photo-voltaic panels," *Int. J. Green Energy*, vol. 4, no. 6, pp. 635–643, 2007.
- [5] S. Mekhilef, R. Saidur, and A. Safari, "A review on solar energy use in industries," *Renew. Sustain. Energy Rev.*, vol. 15, no. 4, pp. 1777–1790, May 2011.
- [6] A. Al-Mohamad, "Efficiency improvements of photo-voltaic panels using a Sun-tracking system," *Appl. Energy*, vol. 79, no. 3, pp. 345–354, 2004.
- [7] C. Sungur, "Multi-axes sun-tracking system with PLC control for photovoltaic panels in Turkey," *Renew. Energy*, vol. 34, no. 4, pp. 1119–1125, 2009.
- [8] S. Abdallah and S. Nijmeh, "Two axes sun tracking system with PLC control," *Energy Convers. Manag.*, vol. 45, no. 11–12, pp. 1931–1939, 2004.
- [9] S. Abdallah, "The effect of using sun tracking systems on the voltage-current characteristics and power generation of flat plate photovoltaics," *Energy Convers. Manag.*, vol. 45, no. 11–12, pp. 1671–1679, 2004.
- [10] "FBs-24MA Δ - \odot C / Products / FATEK AUTOMATION CORP." [Online]. Available: <http://www.fatek.com/en/prod.php?act=view&no=4>. [Accessed: 17-Sep-2018].
- [11] "PLC Working Principle with Industrial Applications." [Online]. Available: <https://www.edgefx.in/industrial-applications-of-programmable-logic-controller/>. [Accessed: 17-Sep-2018].

Development of Water Transport Network in the Northern Region of Dhaka City

Abu Sumaiya^{1, *}, Nazmul Alam Nahid², Md. Mashiur Rahaman³, Khandaker Rasel Hasan⁴,
ABM Mahbubar Rashid⁵

^{1, 2, 3} Department of Naval Architecture and Marine Engineering, Bangladesh University of Engineering and Technology, Dhaka-1000, Bangladesh

⁴ Department of Port and Shipping Management, Bangabandhu Sheikh Mujibur Rahman Maritime University, Dhaka, Bangladesh

⁵ Metacenter Ltd., Dhaka-1000, Bangladesh

ABSTRACT

All the megacities in the world suffer from traffic jam at certain hours of the day. But in Dhaka, traffic jam is the most severe and regular affliction in the daily life. People here have to kill hours simply sitting in the jam and that brings sufferings not only to themselves but also to the productivity. Northern region of the Dhaka city is one of the most important areas of Bangladesh with highly promising projects of the Government of the People's Republic of Bangladesh at Bashundhara Residential Area, Purbachal New Town etc. Therefore, with the existence of rivers and canals in and around that region, there is a possibility to develop a waterways network. At present, road transport is the only mode of transportation for accessing with other parts of the Dhaka City. The proposed waterways network will ensure the safety of the natural environment and bring a source of entertainment in the city life. Many cities around the world like London, Paris, New York, Shanghai, Venice etc. have already implemented successful waterways network inside the city.

Keywords: Water transport network, vacuum infusion process, modular concept, turning circle.

1. Introduction

Despite the construction of several flyovers, allowing people to park their vehicles in designated streets and bus stops and stern actions against wrong side driving, traffic congestion in Dhaka continues to aggravate, causing serious sufferings to city commuters. Traffic jam has turned daily trips into nightmares. Furthermore, it makes the existing public transport very inefficient and most importantly adds unbearable and unsafe level of both noise and hazardous air pollution.

This exasperating level of traffic congestion is already handicapping the economic growth and development. According to a World Bank report, in the last 10 years, the average traffic speed in Dhaka has dropped from 21 kmph to 7 kmph, and by 2035, the speed might drop to 4 kmph, slower than the walking speed. Another study, commissioned by Brac Institute of Government and Development, says traffic congestion in Dhaka eats up around 5 million working hours every day and costs the country USD 11.4 billion every year [1]. Many government and public transport agencies have drafted policies, undertook projects and implemented programs to solve the problem but yet, there is no improvement. An urban transport plan was commissioned with the US consulting group Louis Berger and Bangladesh

Consultant Ltd. A comprehensive transport plan was devised for Greater Dhaka City and its adjoining areas

(Tongi, Gazipur, Savar, Narayanganj, Keraniganj, Narshingdi and Manikganj) covering around 4000 km². The plan looked at 15 key policy issues including safety, pedestrian preferences, management, mass transit systems etc. Almost 70 different policy recommendations were produced under these 15 issue areas. Ten comprehensive transportation strategies were then evaluated, using a base case of no BRT (Bus Rapid Transit) or metro service and a number of alternatives were explored. The adopted plan included roads, a three-line Mass Rapid Transit (MRT) and three-line BRT. It included provisions for 54 new roads in and around the city, three part elevated expressways and a circular waterway program [2].

But still, the citizens of Dhaka are suffering because our traffic system as well as the steps planned to reduce the traffic jam are failing us. It is high time we thought of alternative ways. In and around Dhaka City there are some rivers and canals those can be used for its internal passenger transport linking some of the busiest locations of Dhaka.

2. Locations and Particulars

The selected routes connect some of the busiest and most important areas of Dhaka City like- Sadarghat, Gabtoli, Ashulia, Uttara, Purbachal New Town, Gulshan etc.

In Table 1, detailed locations, proposed landing stations,

important areas adjacent to the routes, total distance by waterways, rivers or canals being used etc. are mentioned. In Fig.1, the whole concept is shown as a complete network in a map. Also in Fig. 1, the red lines indicate the routes whereas the black circles show all the proposed landing stations.

PRESENT CONDITIONS OF THE RIVERS AND CANALS

Rampura Khal and some parts of the above mentioned rivers remain almost unused throughout the year. Balu and Shitalakshya rivers are presently being used for transporting local cargoes. There are housings on the both sides of these waterways. Their surroundings continue to be shrunked and polluted due to creep of construction and dumpage of massive quantities of garbage from the neighborhoods.

While visiting the respected areas it was found that in some areas extremely polluted water full of odor. The authors also noted the alarming rate of illegal encroachment and sewerage pipelines discharging sewerage.

PRESENT SCENARIO OF PUBLIC TRANSPORT

Presently the main public transport in all of the routes are buses (both local and counter bus service). In 2010, Bangladesh Inland Water Transport Corporation launched two water buses in Sadarghat- Ashulia route to ease nagging traffic congestion of the capital city. Another circular water route stretching from Ashulia to Kanchpur Bridge (via Tongi) was introduced in the second phase. But the project could not be popular for various reasons [3].

Table 1 Detailed locations and particulars of the waterways network.

No	Proposed routes	Proposed Landing Stations	Adjacent important spots	Total distance by waterway	River/ Canal used
1	Sadarghat→Gabtoli→Ashulia→Tongi	Sadarghat, Gabtoli, Ashulia, Tongi	Chandrima Model Town, Amin Bazar, Dia Bari, Tamanna World Family Park, Eastern Housing, Birulia Launch Terminal, Uttara (Sector 10, 11, 16, 18), Several universities.	37 km	Buriganga river, Turag river
2	Rampura→Purbachal	Rampura Khal, Purbachal New Town (Sector 10,18)	Banasree, Kayet Para, Kapotakkha Green City, Beraid Boat Ghat, Jalshiri Abason, Bashundhara Residential Area	17.5 km	Rampura Khal, Turag river, Balu river
3	Rampura→Chanpara→Kanchpur Bridge	Rampura Khal (near bus stand), Chanpara, Kanchpur Bridge	Banasree, Khilgaon (Trimohoni bazar), Demra	15.5 km	Rampura Khal, Balu river, Shitalakshya river
4	Kanchpur Bridge→Chanpara→Beraid Boat Ghat (Gulshan)→Bashundhara Residential Area	Kanchpur Bridge, Chanpara, Beraid Boat Ghat, Bashundhara	Demra, Kayet Para, Kapotakkha Green City, Gulshan	19 km	Shitalakshya river, Balu river
5	Kanchan Bridge→Kanchpur Bridge	Kanchan Bridge (Purbachal Sector 4,5,6), Kanchpur Bridge	Welcare Green City, Rupganj, Murapara	18.5 km	Shitalakshya river
6	Uttara (Abdullahpur)→Purbachal New Town→Beraid Boat Ghat (Gulshan)→Chanpara→Kanchpur Bridge	Uttara (Abdullahpur), Purbachal (Sector 1), Beraid Boat Ghat, Chanpara, Kanchpur Bridge	Tongi (opposite to Abdullahpur), Kapotakkha Green City, Jalshiri Abason, Gulshan, Kayet Para, Demra	33.5 km	Turag river, Balu river, Shitalakshya river

PHYSICAL CONSTRAINTS ASSOCIATED WITH DEVELOPMENT OF WATER TRANSPORT NETWORK

Some physical constraints such as bridges, dams, bends, and rapid change of direction were noted by physical survey. Bridges constructed across the routes at some spots are presenting obstacles for required air draft for the water buses. But the most important factor here is the polluted water and surroundings that must be taken care of with priority.

PROPOSALS TO CHECK THE CONSTRAINTS

Bridges in some areas have to be reconstructed providing necessary air draft. This criterion has to be

maintained for new bridges those are being planned to be constructed. Dredging in some spots of the routes is a must to maintain the required draft for shallow water boat, especially in winter. Severely polluted water is a major problem for the passengers to travel through waterways. Therefore, water purification plants have to be developed in highly polluted regions of the proposed routes for waterway network. Also social awareness has to be increased among the locals living in the adjacent areas of the water routes by proper initiatives.



Fig.1 Proposed waterways network (red line) and landing stations (black dots).

PRIORITIES TO BE CONSIDERED BEFORE DESIGNING WATER BUSES FOR THIS NETWORK

The main objective of the present study is to design a waterway and to set priorities to design a water bus that will lead to a saving of time and money along with lessening affliction related to the traffic jam. Therefore, an optimum shallow water draft boat with moderate speed and size is necessary for the proposed waterways network. Special attention should be taken so that the operation of the boat will not be a reason for pollution

of the rivers and canals. Again, as there are residential buildings beside the water routes, the boat should not be a source of noise [4].

For the construction purpose, environment friendly Fiberglass Reinforced Plastic (FRP) and Vacuum Infusion Process (VIP) can be prioritized. Fig.2 shows a schematic diagram of VIP method. The Vacuum Infusion Process utilizes vacuum to infuse resin into the laminate. The first step is to load the fabric fibers and core materials into the mold. Also ribs, inserts and any other components can be added, and this is done without

resin. Next the dry material is seal closed using a vacuum bag or a counter mold. High vacuum pump (25 in Hg or more) is used to remove all of the air in the cavity and

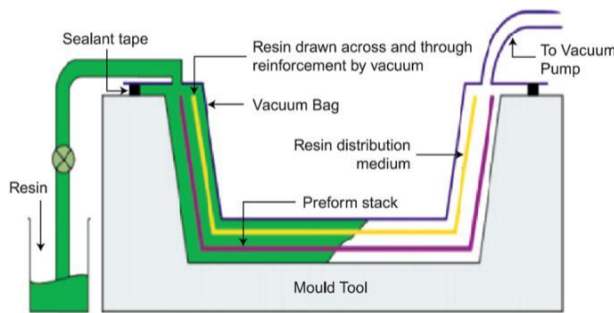


Fig.2 Vacuum Infusion Process.

consolidate the fiber and core materials. Still under vacuum, resin is infused into the mold cavity to wet out the fabric fibers and core [5][6].

In the construction sector, “modular concept” has become a buzz-word for boat building industries. Hull parts are constructed as units (as modules) that can be delivered to anywhere and can easily be assembled. It ensures that resources can be applied at multiple work places in fabrication yards or even at different yards [7]. This concept is already being used in some design firms in Bangladesh i.e. Metacenter Design and Marine for their design and construction purpose. In Fig.3, boat parts constructed following modular concept are shown.

As pollution control is one of our prime concerns, implementation of eco-friendly power source (solar or electric) is proposed to avoid fossil fuels. Also the turning circle (the smallest circle in which the boat can turn without reversing) will be such that the water bus will not face any difficulty in the narrower zones.

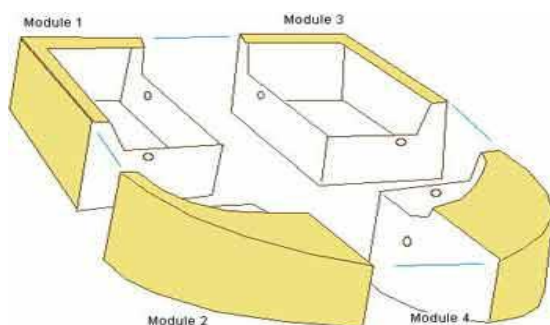


Fig.3 Modular concept.

Capacity of the boat will be such that the project will lead to a profit within a specified time. All measures of safety of passengers must be present in the water bus. A mentionable percentage of young generation uses bicycles for their daily movement. So a space has to be allocated in each water bus with a facility of carrying bicycles also. For that reason and for the ease of the

passengers, the landing stations and the deck of the water bus have to be of same height. Aesthetics of the water buses is important also so that those can add not only ease but also beauty and versatility to the city area [8].

REQUIRED OPERATIONAL SPEED

The speed of the water buses has to ensure faster and safer movement than that of road. As there is no jam condition in waterways, 15 kmph speed level (taking almost double of the average road speed, which is 7 kmph) for travelling is proposed, then the speed stands

$$= \frac{15 \times 1000}{60 \times 60}$$

$$= 4.17 \text{ m/s}$$

$$= \frac{4.17}{0.5144}$$

$$= 8.11 \text{ knot}$$

Therefore, the speed can be fixed at 8 knot.

4. Landing Stations

Landing stations must be in such areas where passengers, after leaving the water bus will have an easy access to rickshaws, cars, bus stations etc. Already there exist several landing stations (Beraid boat ghat, Ashulia landing station etc.). A landing station has to be economic, light, with the same height as the deck of water bus, easily maintainable and movable. Usage of HDPE (high density poly ethylene) is proposed as the main material for construction of landing stations as it will fulfill most of the criteria.

5. Conclusion

Northern region of the Dhaka city is one of the most important areas of Bangladesh with highly promising projects. There is existence of rivers and canals in that region which is almost unused at present. Therefore, there is a possibility to develop a waterways network for passengers and cargos transport. In present study, waterways transport network is proposed with landing stations for handling passengers and cargos. If the proposed waterways network can be implemented practically, it can not only be a reliable and effective alternative of the road transport but also be a suitable usage of the unused or less used rivers, canals etc.

REFERENCES

- [1] www.thedailystar.net/opinion/society/traffic-jam-the-ugly-side-dhakas-development-1575355.
- [2] en.wikipedia.org/wiki/Transport_in_Bangladesh.
- [3] www.daily-sun.com/arcprint/details/237479/Dhaka.

- [4] Md. Mashiur Rahaman, Mir Tareque Ali and LaboniAfroz, Study on the development of water transport network for passengers in the Gulshan-Banani_HatirJheel Lake of the capital city of Bangladesh, *Journal of Shipping and Ocean Engineering* 5 (2015) 195-202.
- [5] www.vacmobiles.com/resin_infusion.html
- [6] www.compositeworld.com
- [7] Cdr (rtd) Kamal Kanagat, Cdr (rtd) RK Chakervarti and Lt. Cdr (rtd) AnandKannan, Modular ship construction-a paradigm shift.
- [8] Md. Mashiur Rahaman, Molla Hafizur Rahman, Mohammad AbulHashem, M. Rafiqul Islam, Design study of boat for Gulshan-Banani-Hatirheel Lake in the capital city of Bangladesh, *10th International Conference on Marine Technology, MARTEC 2016, Procedia Engineering* 194 (2017) 211-217.

ICMIEE18-185

Prediction of Resistance, Sinkage and Trim of a Bulk Carrier by Computational Fluid Dynamics Method

Md. Rakibul Hasan, Md. Abdur Rahim, Md. Sharier Islam, Md. Mashiur Rahaman*

Department of Naval Architecture & Marine Engineering, Bangladesh University of Engineering & Technology
DHAKA-1000, BANGLADESH

ABSTRACT

Prediction of resistance, sinkage and trim has always been a challenging task for the naval architects at the design stage to achieve optimum power requirement and fuel consumption for desired speed. Previously, experimental methods laid the foundation of ship design. Later, towing-tank experiments become more practical but long dated, expensive, limited on the availability of physical tanks. Flow characteristics differ significantly from full scale due to insufficient Reynolds similarity at model test. Now-a-days, the applications of computational fluid dynamics (CFD) are advancing rapidly in marine hydrodynamics fields. CFD solves Reynolds similarity problem by offering both model and full scale results with a great details of flow fields. In this paper, a commercial CFD code STARCCM+ is used to simulate and compute the calm water resistance, sinkage and trim of a bulk carrier. The simulation results were compared with experimental data which mark a wealthy harmony between two results.

Keywords: resistance, CFD, marine hydrodynamic, STARCCM+, bulk carrier,.

1. Introduction

Bulk carriers play an important role in international maritime transport and trade. A bulk carrier, bulk freighter, or colloquially, bulker is a merchant ship specially design to transport unpackaged bulk cargo such as grain, coal, ore and cement in its cargo holds. Bulk carriers are ranked as the second most common type of ship in the world, accounting for over 20 percent of the global merchant fleet. The statistics illustrated in Fig.1 represents the world's merchant fleet between January 1, 2008 and January 2017 [1] with a breakdown by type. Of the around 52,000 merchant ships trading internationally, some 11,000 ships were bulk carriers.

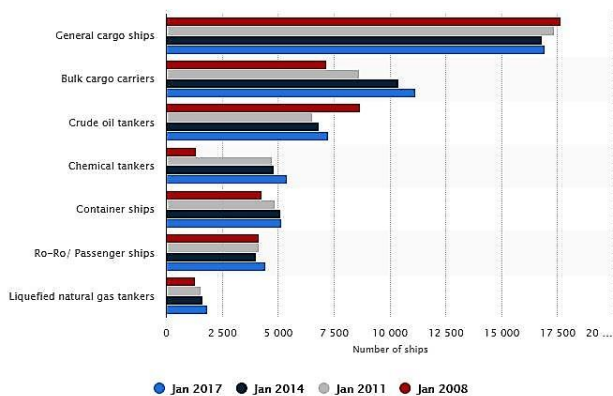


Fig.1 Number of merchant ships by type (2008-2017).

Resistance is one of the important factor related to ship. And prediction of resistance is must in order to obtain an economically profited design that will fulfill the mandatory regulations imposed by IMO [2] having an appropriate speed because if the speed gap is too large, the owner can refuse the ship. Empirical methods are the simplest and fastest among of three different ways of resistance prediction but can be applied only at the earliest design stage when principal particulars and hull coefficients have lack of accuracy. Towing tank experiment (2nd method) is not too much acceptable method when compared to the third method, numerical solutions which is also known as Computational Fluid Dynamics (CFD) described by Lars Larsson and Hoyte C. Raven (2010) [3]. According to Versteeg & Malalasekera (2007, p.1) [4], "Computational Fluid Dynamics or CFD is the analysis of systems involving fluid flow, heat transfer and associated phenomena such as chemical reactions by means of computer-based simulation". Application of CFD is rapidly increasing in ship hydrodynamics. Main advantage of CFD analysis is its flexibility and ability to fulfill both Froude and Reynold similarities where towing tank method is unable to fulfill Reynold similarity. In this paper, CFD technique is used to predict the resistance, sinkage and trim of Japan Bulk Carrier (JBC) without Energy Saving Device (ESD). The JBC hull was selected as one of the test cases in the framework of the Tokyo 2015 Workshop on Numerical Ship Hydrodynamics (T2015) [5]. It is a Cape size bulk carrier designed by National Maritime Research Institute (NMRI), Yokohoma University, Ship Building Research Centre of Japan (SRC). The hull design and measurements were conducted

with the support of ClassNK as part of the ClassNK joint R&D for Industry Program. Also, LDV measurement data in the wind tunnel are available from Technical University of Hamburg-Harburg. The simulations are performed through a finite volume based commercial code STARCCM+. Finally, the numerical results are compared with the experimental values and a good agreement is found.

2. Physical Phenomena

Three governing equations on which Computational Fluid Dynamics is based on are Continuity equation, Navier-Stokes equation, and Energy equation. The Bernoulli equation is derived from the momentum equation for inviscid flows, where viscous effects are negligible. Star-CCM+ uses the Volume of Fluid model exclusively for free surface flows. In this model, the various fluid phases are assumed to be immiscible and all phases share velocity and pressure fields. This VOF model is a segregated flow model, with the pressure and velocity fields coupled using an implementation of the SIMPLE algorithm originally proposed by S. Carretto [6]. STAR-CCM+ offers a wide variety of turbulence modelling options, including Spalart-Allmaras, $k - \epsilon$, $k - \omega$, Reynolds Stress Transport. In this thesis, the turbulent viscosity is calculated using the realizable $k - \epsilon$ turbulence model. The $k - \epsilon$ model is a two equations model using the turbulent kinetic energy k and the turbulent dissipation rate ϵ .

The interaction between the fluid and the ship is very important for the flow and the resistance on the hull. The two primary degrees of freedom (DOF) for ships in calm water are heave and pitch. The pitch and heave of the ship is dependent on the speed of the ship. At a certain speed the ship obtains a pitch and a heave through equilibrium of static and hydrodynamic forces acting on the ship. The equilibrium pitch and heave are called the dynamic pitch and heave. The fluid-body interaction is modelling using a dynamic fluid-body interaction (DFBI) model in STAR-CCM+. The DFBI model calculates the forces on the ship at certain intervals and translates and rotates a number of times the ship until the ship reaches an equilibrium.

It is important to model the boundary layer flow as it is used to calculate the frictional resistance on the ship. For the case studying in this paper, the Froude number are relatively low. The low Froude number causes the majority of the total resistance to be frictional resistance. A non-dimensional distance from a cell to the nearest wall is called the y^+ value. The y^+ value for the cells near the wall is called the wall y^+ value, and it is an indication of how well the boundary layer is discretized. The volume mesh consists of hexahedrons in a structured grid. The mesh is generated using the trimmer-mesh function in STAR-CCM+. Boundary layer mesh is used on the hull surface in order to make a good estimation of the shear stresses on the hull.

3. Geometry

Bulk carriers have an important role in international maritime transport. In this paper, we carried out a numerical study on a model of bulk carrier vessel. JAPAN Bulk Carrier (JBC) is a Cape size bulk carrier and the present numerical simulations are carried out for the JBC model. In Fig.2, the geometry of bulk carrier model is shown and the characteristics of the ship and that of the model are listed in Table 1.

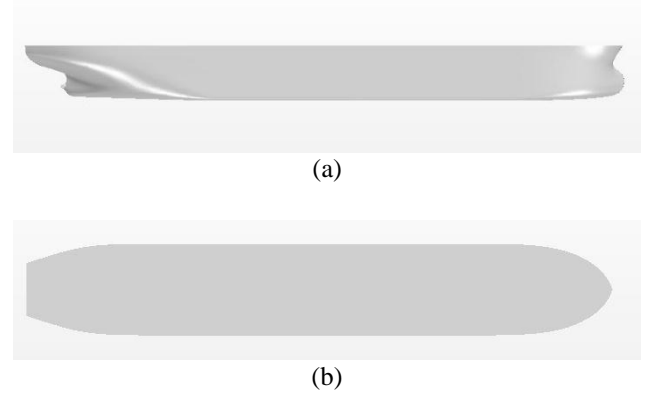


Fig.2 Geometry of JBC hull. (a) Side view, (b) Top view.

Table 1 Ship and model principal particulars.

Main Particulars		Full Scale	Model Scale
Scale of model (λ)		40	
Length between perpendiculars	L_{PP} (m)	280.00	7.00
Length of waterline	L_{WL} (m)	285.00	7.125
Maximum beam of waterline	B_{WL} (m)	45.00	1.125
Depth	D (m)	25.00	0.625
Draft (mid)	T_M (m)	16.50	0.4125
Displacement volume of hull	∇ (m ³)	178369.9	2.7872
Wetted surface area of hull	S_0 (m ²)	19556.1	12.201
Block coefficient	C_B	0.858	0.858
Midship section coefficient	C_M	0.9981	0.9981
Moment of inertia	K_{xx}/B	0.4	0.4
Moment of inertia	K_{yy}/L_{PP} K_{zz}/L_{PP}	0.25	0.25

Conditions for resistance tests are calm water condition, without rudder, without propeller, without ESD, FR_{z0} , $Re = 7.46 \times 10^6$, $Fr = 0.142$, $U = 1.179 \text{ ms}^{-1}$, $\rho = 998.2 \text{ kgm}^{-3}$, $\nu = 1.107 \times 10^{-6} \text{ m}^2/\text{s}$ and $g = 9.80 \text{ ms}^{-2}$ which are developed by the workshop organizing committee (NMRI, 2015).

The JBC hull is placed within a virtual towing tank as shown in Fig.3.

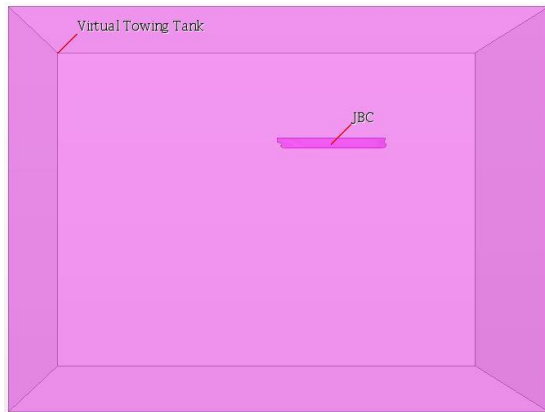
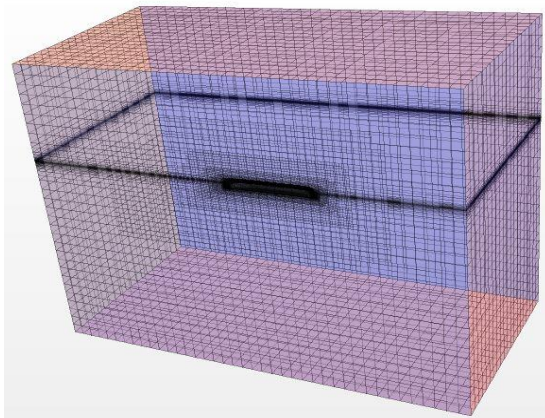


Fig.3 Computational Domain

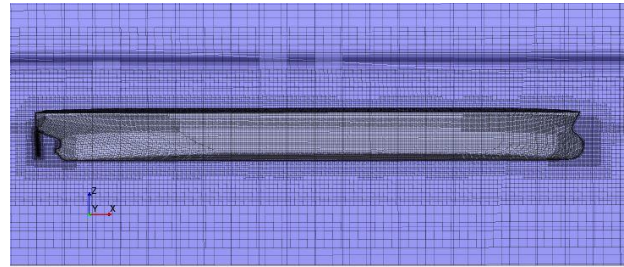
The coordinate origin is at aft perpendicular and still water surface. The still water surface is at 0.4125 m above the keel. Due to symmetry conditions, only half of the body is modeled.

4. Mesh Generation

Resistance analysis are generally performed using a trimmed volume mesh within prism layers on the wetted surface of the hull. Using trimmed cells means that the mesh is aligned with the undisturbed free surface. The background domain [7] extends to $-1.5Lpp < x < 5.0Lpp$, $-1.5Lpp < y < 1.5Lpp$, $-1.0Lpp < z < 0.5Lpp$, and the hull domain has a much smaller region with a range of $-0.15Lpp < x < 1.2Lpp$, $-0.13Lpp < y < 0.13Lpp$, $-0.2Lpp < z < 0.2Lpp$. Finite volume method requires grid cells in order to discretize the partial differential equations and approximate algebraic equations. The simulation was run for three volume mesh. All snapshots and monitor plots shown in this paper are for the case of Mesh 1. Details grid distributions are shown in Fig.4 (a & b) for Mesh 1.



(a) Grid distributions within the computational domain.



(b) Grid distributions around the hull.

Fig.4 Grid distributions for Mesh 1 (a & b).

5. Boundary Conditions

Before creating the volume mesh, it is mandatory to set the appropriate boundary types. The boundaries of the hull are defined as wall with no slip conditions. Following boundary conditions (Fig.5) are applied to the faces of the domain and the hull surface: -

<u>Boundary Name</u>	<u>Boundary Type</u>
Tank.Bottom	Velocity Inlet
Tank.Inlet	Velocity Inlet
Tank.Outlet	Pressure Outlet
Tank.Side	Symmetry Plane
Tank.Symmetry	Symmetry Plane
Tank.Top	Velocity Inlet

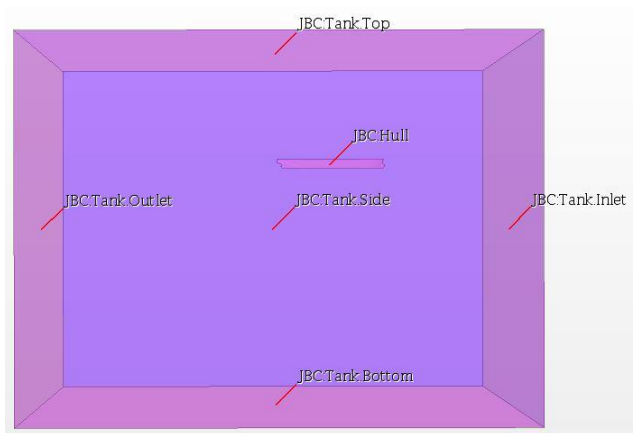


Fig.5 Computational domain with boundary conditions.

Two Eulerian phases (air and water) are created. The properties of water are liquid state, constant density and turbulent flow whereas air is in gaseous state.

6. Results and Discussion

In these simulations, the ship is allowed to move with two degrees of freedom to account for sinkage (Z Motion) and trim (Y Rotation). One of the most important factor is the setting of initial center of mass [3.507, 0.0, 0.313] m,m,m. A large deviation can be produced for inappropriate value of center of mass. The simulations have been carried out

for around 2700 time steps with a time step of 0.04s, total physical time was 108+ seconds. Release time of one second was set which released the hull one second after the start of the simulation. It took more than three days (five cores computer) to complete the simulations. Fig.6 shows a close-up water surface around ship hull on the symmetry plane at the end of the simulation respectively. As the hull moves through the water, it produces a Kelvin wake pattern (Fig.7).

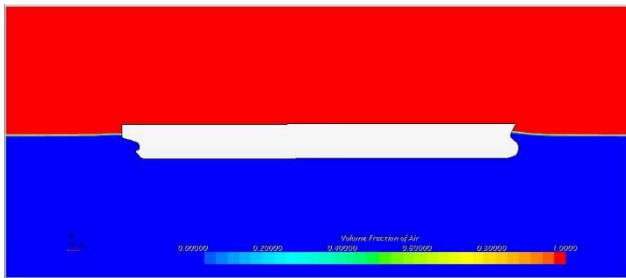


Fig.6 Free surface at the time, 108 s.

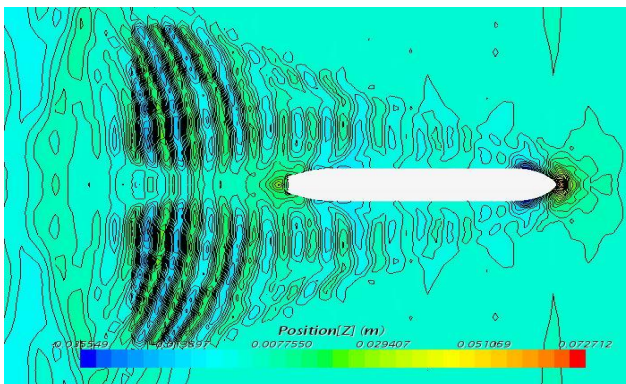


Fig.7 Kelvin wave pattern for speed of 1.179 ms^{-1} and a time step of 0.04s.

Forces obtained from the simulations have to be multiplied by 2 because only half of the geometry was modeled due to symmetry. The residuals up to 27000 iterations are shown in Fig.8.

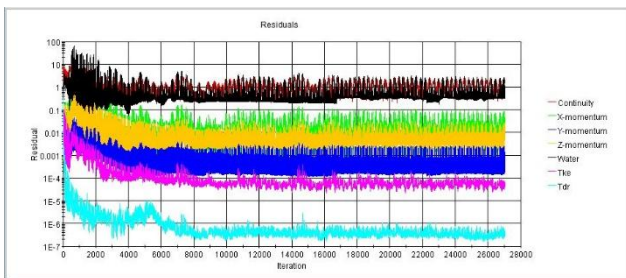


Fig.8 Convergence of residuals for high mesh resolution and a time step of 0.04s (Mesh 1).

A plot of total drag over time is shown in Fig.9 and shear and pressure drag is represented in Fig.10. From Figs. 8 - 10 it is indicated that the strong oscillations start converging almost 30 second later, which is level out after approximately 80-85s.

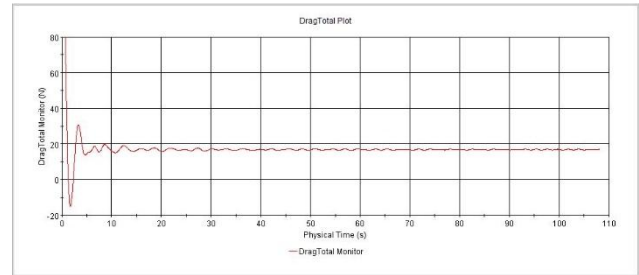


Fig.9 Convergence of the total drag.

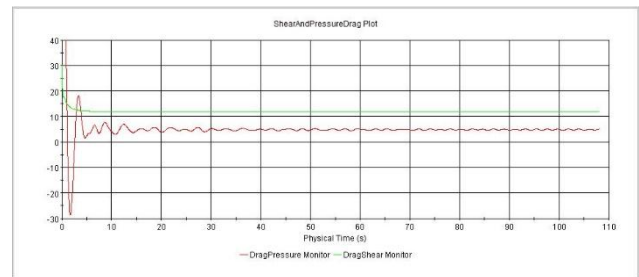


Fig.10 Convergence of the shear and pressure drag.

All Corresponding forces are obtained by averaging the numerical results from physical time 20s to 108s and the comparison with the experimental data are tabulated in Table 2. The calculated average number of oscillation of drag due to wave is 18.595. Since experimental values are not available for other parameters without total resistance, sinkage and trim, only simulation results for them are listed. It is expected that, the deviation decreases with increasing mesh refinement. As can be observed from the results, mesh 1 with the highest resolution predicts total resistance with highest accuracy. It is also the same for the prediction of sinkage.

Table 2 Comparison of CFD results and experimental results [resistance coefficient ($\times 10^3$)].

Mesh No	Parameter	EFD	CFD	Deviation*
M 1	C_T	4.289	4.3787	-2.09%
	C_F		3.078	
	C_P		1.198	
M 2	C_T	4.289	4.511	-5.18%
	C_F		2.805	
	C_P		1.121	
M 3	C_T	4.289	4.181	2.52%
	C_F		2.807	
	C_P		1.138	

But the trim results that are tabulated in Table 3 show relatively large deviation for Mesh 1 & 3. This exception may be due to the increase in grid spacing in z-axis. However, to better capture the trim, a good mesh refinement in z-axis may be required.

Table 3 Comparison of CFD results and experimental results [Sinkage (%L_{pp}), Trim (degree)].

Mesh No	Parameter	EFD	CFD	Deviation*
1	Sinkage	-0.086	-0.093	2.52%
	Trim	-0.18	-0.147	18.33%
2	Sinkage	-0.086	-0.0846	-5.18%
	Trim	-0.18	-0.183	-1.67%
3	Sinkage	-0.086	-0.096	11.63%
	Trim	-0.18	-0.165	8.33%

Note: a positive (+) sinkage value is defined upwards and a positive (+) trim value is defined bow up.

*Comparison error, $E\%D = (D-S)/D \times 100$; where D is the EFD value and S is the simulation (CFD) value.

7. Conclusion

In present study, a commercial computational fluid dynamics method named STAR-CCM+ is used to predict the resistance, sinkage and trim for a bulk carrier model in calm water for $F_r = 0.142$. The numerical results are compared with the available experimental results. In general, the agreement with the experimental references throughout the investigated cases have been good. In case of high-resolution mesh, the deviation between numerical and experimental result for resistance and sinkage is less than 5 % but for trim the deviation is more than 10%. The possible reason may be due to the increase in grid spacing in z-axis. Also, there may be an issue with the VOF method which does not guarantee the conservation of energy near the free surface interface, with the minimum mesh resolution requirements then ensuring an accurate enough approximation to yield acceptable results. However, with the VOF method implemented in Star-CCM+, where both phases are solved for on a co-located grid, this criticism, which was of the original implementation of Hirt and Nichols^[8] where the air phase was omitted from the solution, would appear to be less valid. Another possibility of occurring the deviation is that a minimum resolution is required to capture all the relevant spectral components making up the free surface wave system.

REFERENCES

- [1] www.statista.com/statistics/264024/number-of-merchant-ships-worldwide-by-type
- [2] B. Barrass and D.R. Derrett. *Ship Stability for Masters and Mates (6th ed.)*.
- [3] Lars Larsson and Hoyte C. Raven. (2010). *Ship Resistance and Flow*. Jersey City, New Jersey: The Society of Naval Architects and Marine Engineers.
- [4] Versteeg, H. K., & Malalasekera, W. (2007). *An Introduction to Computational Fluid Dynamics (2nd ed.)*.
- [5] NMRI. (2015). *Tokyo 2015 A Workshop on CFD in Ship Hydrodynamics*. Retrieved from <http://www.t2015.nmri.go.jp/>
- [6] Caretto, L., Gosman, A., Patankar, S., and Spalding, D. (1973). *Two calculation procedures for steady, three-dimensional flows with recirculation*.
- [7] Stern, F., Wilson, R., and Shao, J. (2006). *Quantitative V&V of CFD simulations and certification of CFD codes*, International Journal for Numerical Methods in Fluids 50(11), 1335–1355.
- [8] Hirt, C. W. and Nichols, B. D. (1981). *Volume of fluid (VOF) method for the dynamics of free boundaries*. Journal of computational physics, 39(1):201–225.

ICMIEE18-187

Heat Storage System: A Modern Way to Reuse and Recycle Energy to Reduce Thermal Pollution

*Md. Fahel Bin Noor**, Ahsan Habib, Bijoy Mallick

Department of Mechanical Engineering, Chittagong University of Engineering & Technology, Chittagong-4349,
BANGLADESH

ABSTRACT

Waste heat is a large amount of thermal energy, which is unused and emitted to the environment by some mechanical processes or, emitted from machines and machinery parts. Waste heat is always generated while producing mechanical output by using the temperature difference. Firstly, the paper deals with the study of waste heat produced in different types of power plants and industries. Secondly, designing the way to restore and reuse the waste heat produced as a by-product in the industries by implementing thermal storage system for lower temperatures, which is environment-friendly as well as efficient enough to restore and recycle a large amount of heat. The ways of enhancing the efficiency of heat storage, without disturbing the operational process of the furnace are prescribed thoroughly. The paper further deals with the feasibility of waste heat in the industries and shows its quality is good enough for different uses in the industries. Calculates the efficiency of the prescribed heat storage model, as well as the calculation of the net energy stored in the heat storage system, is also shown in the paper.

Keywords: Waste heat, Thermal storage, Heat loss, HTF, Water.

1. Introduction

In this era of industrialization, lots of importance is given to reducing the waste heat produced in different industries and power plants. There are also several technologies which are applicable to reuse the waste heat, produced in an industry because of different mechanical or thermal processes. Several processes can be done to store the heat emitted by these operations. One of them is the thermal heat storage system.

Thermal storages of small heat storing capacity can help nullify the variations on the load side introduced by minor disruptions of weather. e.g. by the appearance of clouds [1]. A large amount of energy is wasted in the industry as hot flue gas, emitted from machinery and heated products. To improve the energy efficiency of an industry, reusing of those waste heats is thought of as a very attractive way nowadays which can also help to reduce the production cost by saving fuel cost. This reduction of waste heat emission from industry can also contribute to making the whole process more nature-friendly as heat is a crucial factor for the greenhouse effect [2].

A large quantity of hot exhaust gases is produced from boilers, hot ovens, machinery outputs and furnaces of different types of plants. Though the energy lost in waste flue gases cannot be fully recovered and used. However, much of the heat could be improved and recycled by adopting the necessary procedures as prescribed in this study.

If a recovery process is designed for storing waste heat, then this heat can be reused when heat is needed for another unit like space and surface heating, water preheating for increasing boiler efficiency, combustion air preheating etc.

This paper deals with a brief discussion of short-term sensible thermal storage at low temperatures. We have considered here storage systems for different purposes like space heating and water pre-heating in industries and

different types of power plants, systems in which the application temperature generally varies from 25°C to 95°C. Storage temperatures between 25°C and 95°C shall hence be considered in this paper.

2. Renewable waste heat sources for storing

In developing countries, there should be always some special application of renewable energy technologies for better production as well as to make the production cost-efficient. For the feasibility of waste heat recovery, the temperature of waste heat is a very important factor. It is must that waste heat temperature has to be greater than the temperature of the heat sink. Waste heat quality depends on the temperature difference between the source and the sink. Larger the difference better the quality of stored heat. The temperature difference between the source and sink effects on:

- i. Heat transfer rate per unit area of the surface of the heat exchanger.
- ii. The efficiency of the heat storage system

The higher the temperature of the waste heat, a heat storage system becomes more cost-effective and efficient. In the study of renewable waste heat, it is significant that there must be some use for the recycled exhaust gas heat or stored heat. Some examples of use would be preheating of air before combustion, space and surface heating, or boiler feed water pre-heating etc. [3].

The waste heat from exhaust gases range varies in different processes of production. Usually, the flue gases from industries and power plants like glass melting furnace, steel electric arc furnace, steam boiler exhaust, annealing furnace cooling, hydrogen plants etc. are some examples of plants and processes with higher temperature flue gases. This variation in temperature gives us the opportunity to classify the thermal storage system. Hence, waste heat qualities are classified

dividing temperature ranges of the waste heat into three types:

- i) Low
- ii) Medium and
- iii) High.

Various ranges and sources of different waste heat are as follow: [4]

Table 1 Classification of waste heat sources [4]

Temp. Range	Example Sources	Temp (°C)
High (>650°C)	Nickel refining furnace	1370-1650
	Steel electric arc furnace	1370-1650
	Zink refining furnace	760-1100
	Copper furnace	900-1090
	Hydrogen plants	650-980
	Open hearth furnace	650-700
	Glass melting furnace	1000-1500
	Fume incinerators	650-1450
	Steel heating	925-1050
Medium (230-650°C)	Steam boiler exhaust	230-480
	Gas turbine exhaust	370-540
	Dying and baking oven	230-600
	Catalytic crackers	425-650
	Annealing Furnace Cooling System	425-650
Low (<230°C)	Cool water Furnace doors	32-55 32-88
	Welding machines	32-232
	Hot process liquids	

3. Choosing a heat storage system

Thermal energy storage (TES) is the technology of storing thermal waste heat as thermal by heating or cooling a storage medium fluid so that, the stored thermal energy can be reused later for any other thermal operations.

There are three kinds of TES systems possible and those are as follow: [5]

- i. Sensible TES system which is done on the basis of storing thermal energy with the help of heating or cooling a solid or liquid type storage medium (e.g. rocks, water, molten salts), with water-based storage being the cheapest option.
- ii. Latent heat storage system which uses phase change materials or PCMs.
- iii. Thermo-chemical storage (TCS) system which uses chemical reactions to store heat and release thermal energy later.

The following data in Table 2 Represents that, sensible heat storage technology is more cost-saving process than any other storage systems for lower temperature operations: [5]

Table 2 Different heat storage types [5]

Type of Storage	Capacity kWh/t	Efficiency (%)	storage period	cost(€/kwh)
Sensible (hot water)	10-50	50-90	d/m	0.1-10
PCM	50-150	75-90	h/m	10-50
Chemical reactions	120-250	75-100	h/d	8-100

For choosing proper TES material for storing thermal energy efficiently, we have to think about its higher specific heat (C_p) and lower thermal conductivity ($>0.3w/m-k$). Also, the material should have a higher boiling point than waste heat temperature, suitable heat transfer fluid (HTF) should be chosen for better heat transfer. Water has the highest specific heat ($4200J/kg-k$). Hence, its heat capacity is large enough to be used as a storage medium, compared to other substances. So, it can store more thermal energy per unit of its weight. It is also non-toxic and available free of charge or at low cost in most of the countries [6].

But sensible heat storage using water as a storage medium is suitable only for those waste heat temperature below $100^\circ C$. For low temperature ($30-95^\circ C$) waste heat, water is selected as thermal storage because of its higher specific heat. Though there are different types of heat recovery systems, this paper only deals with the low-temperature renewable waste heat recovery system and water is used as a heat transfer fluid.

4. Design of the proposed heat storage system

Fig.1 Shows the designed thermal heat storage system for lower temperatures.

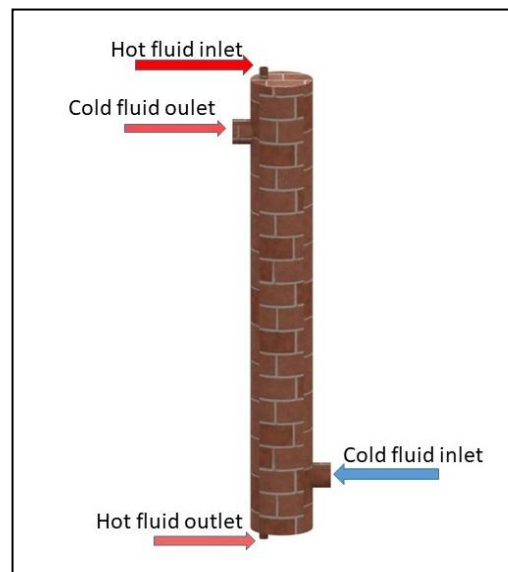


Fig.1 Heat storage model

In the prescribed design, for increasing contact surface area between hot and cold fluid we have used the helical tube. And due to lower heat capacity and higher value of thermal conductivity, we have used copper as the material of our helical tube which helped us to enhance heat transfer rate from hot to the cold fluid as well as increase the efficiency of our storage system. Also, the thickness of the spiral tube has been taken very small (0.5mm) for lowering thermal resistance of the pipe wall. The HTF was passed slowly through the helical copper tube so that, the quality of heat is not decreased. For making the storage thermally insulated, good insulating materials like fiberglass, brick wall etc. can be used. Brick is used in shell wall for better insulating performance in the above-mentioned thermal storage system. Fig.2 Shows the designed helical copper tube used in the thermal heat storage.

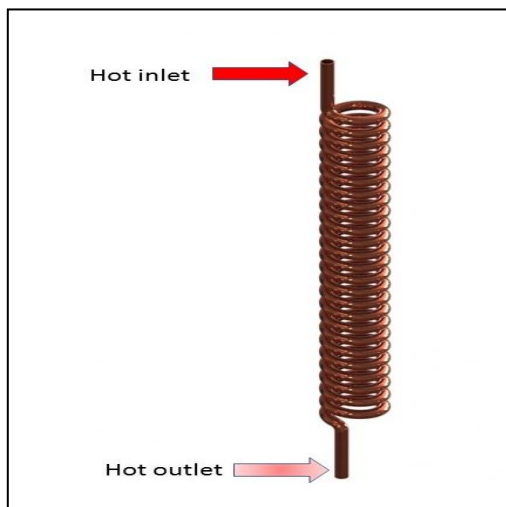


Fig.3
Syste
heat
exan
the
syste
proc
exch
syste

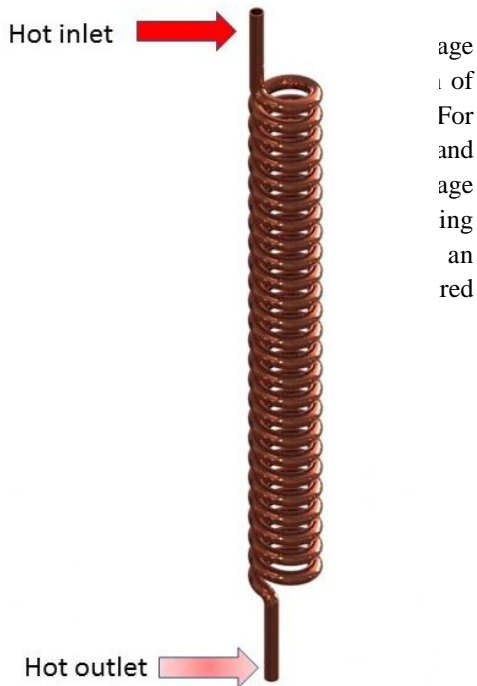


Fig.3 t



5. Mesh generation and simulation analysis

We have performed a simulation of prescribed waste heat storage system via ANSYS (version 16.0) simulation software for analyzing the performance of our proposed design. Some assumptions and conditions were considered for this renewable waste heat storage design and simulation: [3]

- The flow in the sensible heat storage mechanism is in steady flow condition.
- Shell and helical tube type heat storage was used.
- The mass flow rate of each fluid (both hot fluid and cold fluid) is kept constant without any variation with time.
- Constant velocity of the fluids is considered, which is flowing through the storage system. So, kinetic and potential energy also considered being constant.
- The outer shell surface of the storage system is thermally insulated and no heat transfer will occur between the storage wall and surroundings.

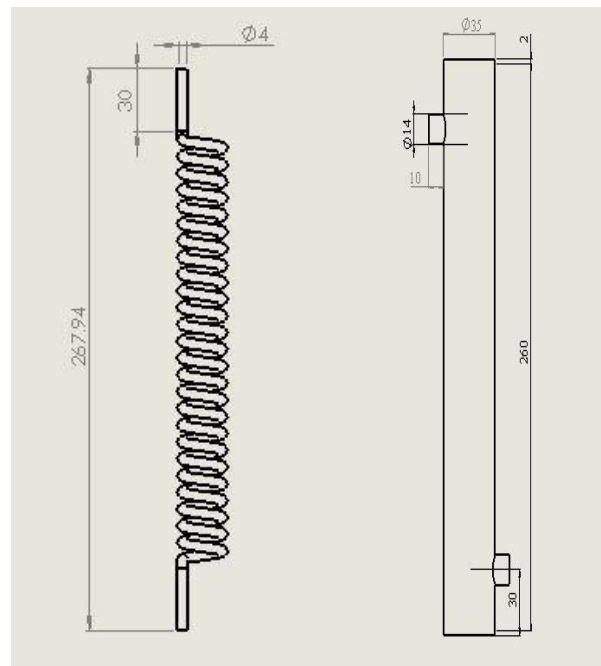


Fig. 4 Drawing view of spiral tube and shell

Fig.4 shows the drawing and necessary dimensions of the model that has been used in the modeling and simulation processes. Computational domain and value of different elements were taken as follow:

Coil Diameter = 20mm, Tube outer diameter = 5mm, Tube inner diameter = 4 mm, Tube thickness = 0.5mm, Coil length = 267.94mm;

Shell length = 260 mm, Shell diameter = 35 mm, Shell inlet diameter = 14mm, Shell outlet diameter = 14mm.

Here, the discretization of the fluid volume was done by following the principle of finite element analysis method. The mesh for the simulation process was generated using the mesh tools of ANSYS design modeler. Here, for meshing, coil body element size was

5×10^{-4} m and fluid domain element size was 5×10^{-4} m. The shell element size was 2×10^{-3} m and total element number was 6085921. The number of nodes was 1405023. Boundary Conditions for the simulation was as follow:

Cold inlet: Velocity inlet = 0.007ms^{-1} ,
 Hot inlet: Velocity inlet = 0.05ms^{-1} ,
 Cold outlet: Pressure outlet = 0 pa,
 Hot outlet: Pressure outlet = 0 pa,
 Cold fluid pressure drop in shell = 0.195pa,
 Hot fluid pressure drop in tube = 264.1pa;

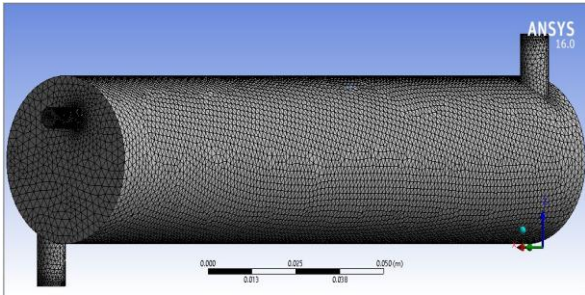


Fig. 5 Meshing of the heat storage system

Fig.5 represents the generated mesh of the heat storage system.

The result of the simulation is given below in fig.6 along with the output result of the simulation process:

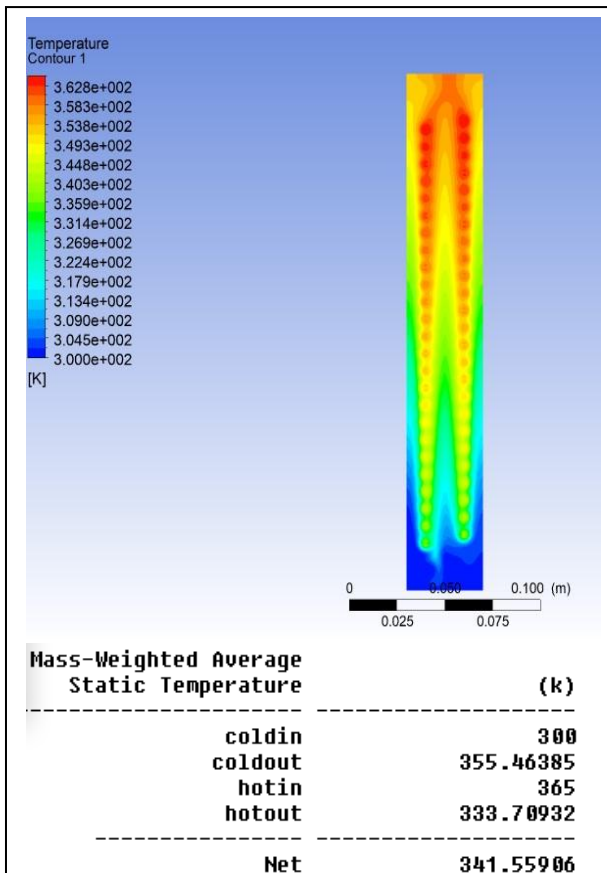


Fig.6 Simulation analysis of waste heat storage

Thus, from fig.6, the results of simulation provide us with a clear idea that, while using water as thermal storage for lower temperature. For 92°C (365k) of the hot fluid inlet, we got 60.709°C (333.709k) in the hot fluid outlet of the helical coil. We also used water as a heat transfer fluid (HTF). Again, the cold water will intake transferred heat, so the inlet temperature of the cold fluid in the storage tank is 27°C (300k) and outlet 82.46°C (355.46K). The rise in temperature of the cold-water outlet is caused due to waste heat.

The accuracy of the simulation depends on the number of elements and nodes. With the increase in the number of elements as well as nodes in the finite element analysis we can find the results more accurately. So, we used a higher number of nodes and elements to find accurate results.

So, the simulation shows that the waste heat can be used to store up as thermal energy with this process by transferring the heat to a storage medium (cold fluid).

6. Energy stored and efficiency calculation

The amount of stored heat in the prescribed heat storage and the efficiency of the storage is as follow:

5.1 Stored heat

The net amount of energy that can be stored in the prescribed sensible heat storage depends on the temperature change of the storage material and can be expressed in the form as follow: [7]

$$E = m \int_{T_1}^{T_2} C_p dT \quad (1)$$

Here, m is the mass of storage medium fluid and C_p signifies the specific heat of HTF (water), at a constant pressure. T_1 and T_2 denote the minimum and maximum temperature levels between which the storage operates. $(T_2 - T_1)$ represents the temperature difference of the sensible waste heat thermal storage system. So, Equation (1) can be re-written as follow:

$$E = m \cdot C_p \cdot (T_2 - T_1) \quad (2)$$

Here, for per unit of volume of storage (v), and density of water (ρ), we can write-

$$E = \rho \cdot v \cdot C_p \cdot (T_2 - T_1) \quad (3)$$

$$E = 1000 \times 1 \times 4200 \times (82.46 - 27)$$

$$E = 232.932 \times 10^6 \text{ J}$$

So, the net amount of energy that can be stored per unit volume of the prescribed heat storage is sufficient enough. It can be supplied and used for different purposes like space heating and water pre-heating in industries or, power plants and thus increase producibility without any loss of the extra amount of fuel.

5.2 Efficiency calculation

The efficiency of a heat storage system is defined as the ratio of the thermal energy extracted from the storage to the thermal energy stored in it. [7]

In this paper, we have used a thermal storage system, where hot fluid from our concerned industry, charging into our storage at 360K temperature through inlet point and leaving the system at 331.92842K temperature through outlet point. And our storage medium fluid water, charging at 300K temperature into storage system through inlet point and leaving at 326.81486K through outlet point by gaining thermal energy. Now efficiency can be written as:

$$\eta = \frac{\text{Thermal energy extracted from the storage}}{\text{Thermal energy stored in the storage}} \quad (4)$$

Equation (5) represents the efficiency of the thermal storage which can be further written as follow:

$$\eta = \frac{mC(T_{co}-T_{ci})}{mC(T_{hi}-T_{ho})} \quad (5)$$

Where,

\dot{m} = Mass flow rate.

C = Heat capacity of the thermal storage medium.

T_{ci} = Inlet temperature of cold water.

T_{co} = Outlet temperature of cold water.

T_{hi} = Inlet temperature of hot water.

T_{ho} = Outlet temperature of the hot fluid.

V_c = Cold fluid velocity.

V_h = Hot fluid velocity.

ρ = Density of storage medium.

Now, from Equation (5), the value of efficiency have been obtained for the prescribed heat storage model as follow:

$$\eta = \frac{1000 \times 0.007 \times 1 \times (355.46 - 300)}{1000 \times 0.049 \times 1 \times (365 - 333.709)}$$

$$\eta = 25.32\%$$

So, we can see the waste heat was used to store the thermal energy to the cold fluid and a large amount of heat was stored by this process. We can also get a clear idea about the efficiency of the prescribed storage system from the above-simulated data.

Another simulation was done by changing the hot inlet temperature from 365k to 360k. The cold inlet was kept 300k like the previous simulation. It was found that the hot outlet and cold outlet temperature changes along with the change of hot inlet temperature. For 360k hot inlet, the hot outlet temperature was found 331.92k and the cold outlet temperature was found 326.81k. When the efficiency reduces to only 13.64%. So the higher the difference of the temperature the higher the efficiency of the storage system.

Further improvement of efficiency is possible by choosing proper fluid velocity through the storage and varying heat transfer conditions.

7. Analysis of a blast furnace and reduction of thermal pollution

As a case study in a steel re-rolling mill (BSRM, Chittagong), a blast furnace was observed. The furnace is also named dual fuel furnace because two different types of fuels are used to run this blast furnace. They are natural gas and oil. The oils can be of two types. They are HFO oil and LDO oil. Even after completing all the desired works of this furnace, the flue gas (waste gas) still contains a high amount of heat which can be used as another source of thermal energy if it can be recycled as mentioned in this paper. To utilize this large amount of heat, the chemical components of flue gas should be observed and are given below: Main chemical components of flue (waste) gas for a blast furnace[8] are: water vapor, nitrogen (typical contents about 75-80%), carbon dioxide (typical contents 7-15%), carbon monoxide (CO) and hydrogen (H₂) due to incomplete combustion (typical contents 50-150 ppm), oxygen (O₂) due to excess of air (typical contents 2-8%), nitrogen oxides NO_x (NO+ NO₂) due to N₂ and O₂ combination at high temperatures (typical contents <100ppm.), sulfur dioxide (typical contents <200ppm.), unburned hydrocarbons and ashes. Typical sulfur content in HFO and LDO is accordingly (0.1-4.5%) (maximum) [9-10] and 1.2-1.8% (maximum).

This sulfur content is important because [11], to avoid the possibilities of corrosion due to the condensation of sulfur oxide gases, the temperature of the flue gas is to be kept above the dew point temperature of the sulfuric acid. It is observed that for about 5% sulfur content in flue waste gas, the sulfuric acid dew point temperature is about 150°C. So, at an average 150°C, the flue gas should be released in the environment to avoid the harm of corrosion and pollution on furnace operation. The observed furnace in a steel re-rolling mill (BSRM, Chittagong), releases waste heat at chimney exists in an amount of average of (200°C to 300°C) which is one type of medium temperature waste heat sources. So, it can be said that if the amount of waste heat in the chimney exit can be reduced by storing and can be kept at an average of 150°C, it will be adequate to avoid corrosion of sulfur content and the operations of the entire furnace process will not be harmed. The rest 150°C or more than it can be recovered and recycled by implementing heat storage systems as prescribed in this paper, for any type of process where such amount of heat is required. For example: boiling of water, surface heating, refrigeration process, room pre-heating etc.

8. Conclusion

Waste heat recovery is a significant concept that is another source of renewable energy as well as a way to make industries and power plants more efficient. In this paper, we have discussed various possible waste heat

sources and types of heat storage system depending upon waste heat temperature, also showed a low cost and efficient heat storage system with better HTF like water. A simulation analysis of the prescribed storage system is shown properly along with the detailed mesh generation data. Hence, with the help of simulated data, the net energy stored per unit volume was measured. Then, the efficiency of the storage system is calculated. The net stored energy per unit volume of the storage medium is 232.932×10^6 J and efficiency is about 25%. The efficiency indicates that a good quality and quantity of stored heat can be used further in different industrial processes and productions. The application of stored heat is also shown in this paper along with the thermal pollution reduction possibilities in an industry. Finally, we can say that, in a country like Bangladesh, which is yet to be developed, waste heat can be another alternative source of energy which can provide the required energy to different fields and thus can reduce the wastage of energy by eliminating the wastage of thermal energy.

NOMENCLATURE

- c_p : specific heat at constant pressure, $\text{kJ} \cdot \text{kg}^{-1} \cdot \text{K}^{-1}$
 ρ : density of fluid, $\text{kg} \cdot \text{m}^{-3}$
 E : energy stored, kJ
 p : pressure, kPa
 T : temperature, K
 V : volume, m^3

REFERENCES

- [1] A. Abhat. Short term thermal energy storage. *Revue de Physique Appliquee*, 1980, 15 (3), pp.477-501.
[2] <https://beeindia.gov.in/> (accessed 28/09/2017)
[3] Chowdhury, Tamal & Salam, Bodius & Chowdhury, Hemal & Barua, Pranta. (2018). "Waste Heat Thermal Storage ,A Way to Renewable Energy".
[4] waste heat recovery-Bureau of Energy Efficiency, <https://www.beeindia.gov.in/sites/default/files/2Ch8.pdf>
[5] S. Khare n, M.Dell'Amico, C.Knight,S.McGarry "Selection of materials for high temperatures sensible storages" *Solar Energy Materials & Solar Cells* 115 (2013) 114–122
[6] http://Wikipedia.org/wiki/Hot_water_storage_tank
[7] O. Ercan Ataer, (2006), "STORAGE OF THERMAL ENERGY", in *Energy Storage Systems*, [Ed. Yalcin Abdullah Gogus], in *Encyclopedia of Life Support Systems (EOLSS)*, Developed under the Auspices of the UNESCO, Eolss Publishers, Oxford ,UK,

- [<http://www.eolss.net>]
[8] www.eurotron.co.kr/ (accessed 28/09/2017)
[9] www.marquard-bahls.com/ (accessed 29/9/2017)
[10] www.eecpowerindia.com/ (accessed 29/09/2017)
[11] <https://mrpl.co.in/> (accessed28/9/2017)

Feasibility Study of Hybrid Renewable Energy System for Electrification of Kutubdia

Tamal Chowdhury^{a*}, Hemal Chowdhury^b, Piyal Chowdhury^c, Monirul Islam Miskat^d

^aDepartment of Electrical & Electronic Engineering, Chittagong University of Engineering & Technology, Chittagong, BANGLADESH

^bDepartment of Mechanical Engineering, Chittagong University of Engineering & Technology, Chittagong, BANGLADESH

^cChittagong Collegiate School & College, Chittagong, BANGLADESH

ABSTRACT

Bangladesh has been experiencing several problems over the past few decades. Day by day, the no of population is increasing significantly. Sufficient amount of power generation in a sustainable way is an important issue for this rapidly increasing population and economic development. As a result, the country has been struggling. Hybrid system can play a vital role in the electrification of rural development. In this study, a renewable hybrid system has been proposed for Kutubdia island. The simulation was designed by Homer software and planned to apply in Kutubdia city to meet the electricity demand. The optimum system consists of PV array, diesel generator, biogas generator, wind turbine for power generation and battery for surplus energy storage. Economical analysis was also carried out and it was found that COE is \$0.221/kW which is 17.68 taka in BDT (1 US=80 taka).

Keywords: Hybrid System, Homer software, Kutubdia.

1. Introduction

Approximately 80% of the people of Bangladesh live in rural area and 40% of people have access to electricity [1]. The biggest portion of her energy demand is met up by fossil fuels such as natural gas, coal etc. As the population is increasing, the demand for electricity is increasing continuously. As a result, fossil fuels consumption is also increasing. According to the World Bank, fossil fuel energy consumption (% of total) in Bangladesh was reported at 73.77% in 2014. Various dangerous gases emit from the combustion of fossil fuels. These gases are harmful for the environment. The only solution for this problem is to utilize renewable energy as they are environment -friendly. It is estimated that about 44% of the world population does not have access to grid electricity because of the higher cost grid connection, dispersed population [1]. Due to generation capacity shortage, it is quite difficult to provide power the places that are connected to the grid. Furthermore, for various places like islands grid connection becomes difficult and costly. So efficient use of local resources is the most useful solution in this case. It will help the government to reach its vision which is to provide most of the power from renewable energy sources. Hybrid system can play an effective role in this regard. For several off grid places Monpura island[2] Adorsho Char [3], Sandwip[4], Saint Martin's Island [5] and Nijhum Dip [6] feasibility of hybrid system have been checked. But for an Island like Kutubdia, it is yet to be conducted.

2. Overview

Kutubdia lies between 21°49'N to 91°51.5'E. It is in the Cox's Bazar district which is in the division of Chittagong, Bangladesh. It is generally an island [7]. It covers an area of 215.79 sq. km. About 125279

population live on the island. Approximately 9 secondary schools, 32 primary schools, 7 madrasah and 1 college can also be found here. Moreover, it has 8 bazaars and 190 religious institutes. No of cows and buffalos in Kutubdia are approximately 13236. Number of electrification in villages of Kutubdia is none according to [8].

Here figure 1 shows the satellite image of Kutubdia.

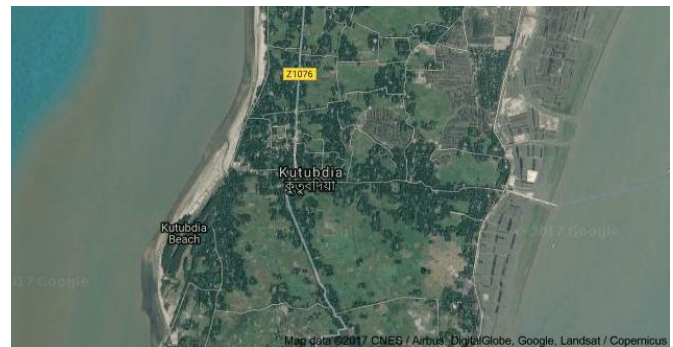


Fig. 1: Satellite Image of Kutubdia Island.

The government has set up a wind battery hybrid power plant in Kutubdia. But it does not provide power all the time. People only get power only 3 hours a day and 3 to 4 hours during night time. Only 50% of people get benefitted for that project [9]. So this study is an attempt to check the feasibility of solar wind biomass integrated hybrid system in Kutubdia.

3. Load Profile

In this simulation the load is supplied by the Hybrid system and basic loads like-bulbs, fans and pumps are considered. The load has been divided into two divisions-residential load and non-residential Load.

* Corresponding author. Tel.: +88-01709300178

E-mail addresses: icmieekuet@gmail.com

Table 1: Load description for residential load

Type	Load Description
Household	1 CFL(20 watts) 1 Fan (40 watts)

Table 2: Load Description for different Non-residential Load

Type	Load description
Religious Institutions	3 CFL(20 watts) 2 Fan (40 watts)
College & Secondary School	4 CFL(20 watts) 4 Fan (40 watts)
Primary School	2 CFL(20 watts) 2 Fan (40 watts)
Bazaars(considering 10 shop in a bazaar)	1 CFL(20 watts) 1 Fan (40 watts)
Madrasah	3CFL(20 watts) 2 Fan (40 watts)

During summer, irrigation pumps are used for agricultural purposes. Here in this simulation, a 2 KW irrigation pump is considered. Here summer load is considered from January - October and winter load is from November – February. Figure (2-4) shows winter, summer & annual load of Kutubdia.

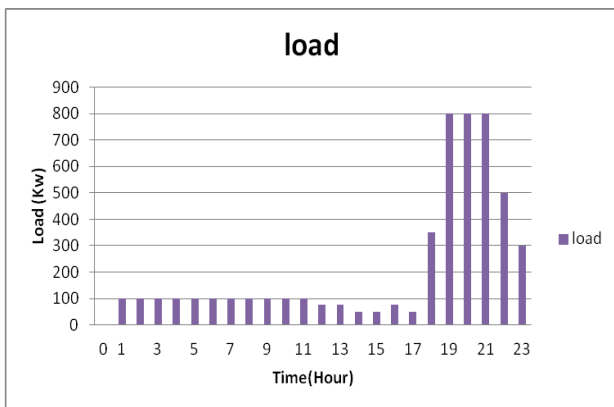


Fig. 2: Winter load (November to February)

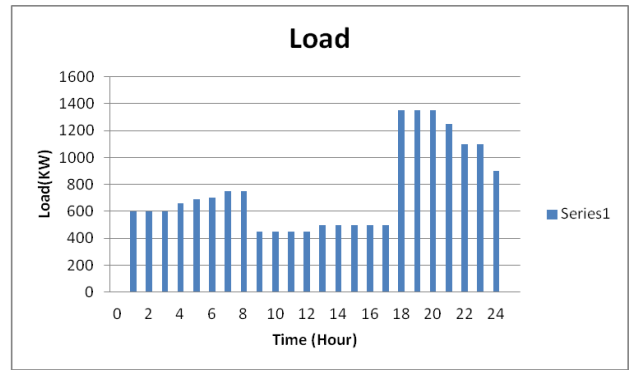


Fig. 3: Summer Load (January to October)

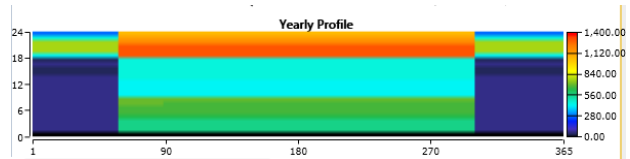


Fig. 4: Yearly load profile.

4. Renewable Resources

In this simulation different renewable energy sources have been used.

Wind Resources

Figure 5 shows the average wind speed data of different months of Kutubdia [10].

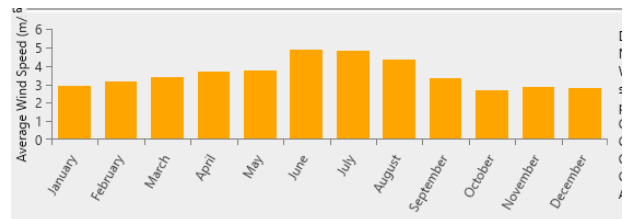


Fig. 5: Average Wind Speed

Solar Resources

Figure 6 shows the average solar radiation data and clearness index data of different months of Kutubdia [10].

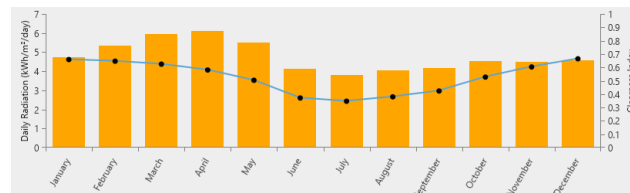


Fig. 6: Daily Solar Radiation and Clearness Index

Biomass Resources

Kutubdia has 13236 no cows and buffaloes [8]. In South Asian perspective, each cattle gives 8-10 Kg fresh manure per day [11]. So, the total manure production of

Kutubdia is 120 tons. By considering a 20% collection rate, it is found that 24 tons of manure are produced daily.

Figure 7 shows the monthly manure production of Kutubdia.



Fig. 7: Monthly manure production of Kutubdia

5. Hybrid System Modeling

Homer software [12] is used for simulating the following system.

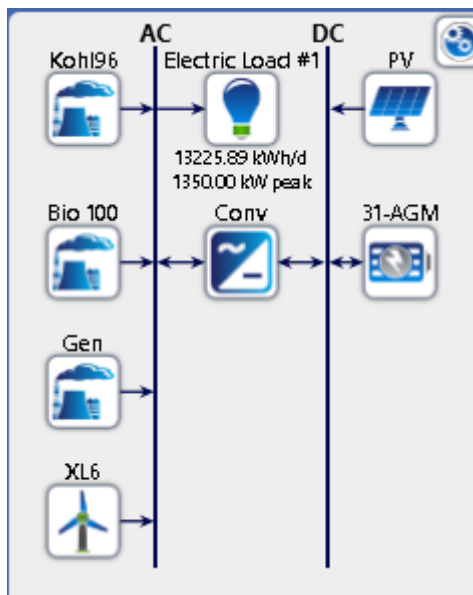


Fig. 8: System model

Diesel Generator

For the simulation purpose the, diesel generator considered here Kohler 96kW. The capital & replacement cost of the generator considered here is \$35000.00 and \$30000 respectively. The operation and maintenance cost is considered \$2.00 per hour for the generator. The lifetime is considered 15000 hours in this simulation for the diesel generator.

PV Array

The capacity of PV panels has been considered 3KW in this simulation. The capital and replacement cost is of each panel is considered \$5000.00 \$4000.00 respectively with operating and maintenance cost of \$10.00 per year. The life time of PV panel is assumed to be 25 years.

Energy Storage

For the purpose of storing the generated energy batteries are required. The battery used here is Trojan 31-AGM . The nominal voltage of battery considered here is 12V and its throughput is 673.20kWh. The capital and replacement cost of battery considered here to be is \$450 and \$350 respectively. The O&M cost is considered \$11.000 per year.

Converter

A converter is required for the purpose of conversion of DC into AC power. The capacity of the converter is considered 100kW in the simulation. With O&M cost of \$100 per year, the capital and replacement cost of the converter is assumed to be \$6500 and \$100 respectively. The life time of the converter is assumed as 10 years. The efficiency of the converter considered here is 96.30%.

Wind Turbine

For simulation purpose, the model considered here is Bergey Excel 6. The capacity of the turbine is considered as 6 kW. The hub height of the turbine is 30 m. The capital and replacement cost of battery considered here to be is \$20000.00 and \$12000.00. The O&M cost is considered \$40.00 per year. The lifetime of the turbine considered to be is 20 years.

Biogas Generator

For simulation purpose, the rating of the Biogas Generator considered here is 100kW. The capital and replacement cost of biogas generator considered here is \$40000.00 and \$ 30000.00. Biomass Resources will be used as fuel and \$0.1 per hour is considered the O&M cost of the biogas generator. The lifetime is considered 15000 hours in this simulation for the biogas generator.

Generator

For the generation of electricity generator is required. The rating of the generator considered here is 1500kW. Diesel is to be used as fuel and the capital & replacement cost considered here is \$500. The operation and maintenance cost is considered \$0.03 per hour for the generator.

6. Result Analysis

Architecture										Cost			System
PV (kW)	XL6 (kW)	Koh196 (kW)	Bio (kW)	Gen (kW)	31-AGM (kW)	Conv (kW)	Dispatch	CC	NFC	Operating cost	Initial capital	Ren. frac.	
(\$)	(\$)	(\$)	(\$)	(\$)	(\$)	(\$)		(\$)	(\$)	(\$)	(\$)	(%)	
96.0	500	1,500						CC	\$0,221	\$13,884	\$995,127	\$950,000	58
1	96.0	500	1,500					CC	\$0,222	\$13,884	\$995,142	\$970,000	58
		500	1,500					CC	\$0,276	\$17,999	\$1,2794	\$950,000	48
		500	1,500					CC	\$0,279	\$17,940	\$1,2794	\$970,000	48
	96.0		1,500					CC	\$0,466	\$30,194	\$2,1664	\$750,000	0.0
	1	96.0		1,500				CC	\$0,468	\$30,194	\$2,1994	\$770,000	0.0
			1,500					CC	\$0,495	\$30,994	\$2,3394	\$770,000	0.0
		1		1,500				CC	\$0,495	\$30,994	\$2,3394	\$770,000	0.0
	96.0	500	1,500	1			9,999,999	LF	\$11,94	\$74594	\$11,294	\$60194	58
	3.23	96.0	500	1,500	1		9,999,999	LF	\$11,94	\$74594	\$11,294	\$60194	58
	1	96.0	500	1,500	1		9,999,999	LF	\$11,94	\$74594	\$11,294	\$60194	58
	3.23	1	96.0	500	1,500	1	9,999,999	LF	\$11,94	\$74594	\$11,294	\$60194	58

Fig. 9: Comparison between different simulated systems

Different size for PV systems, wind turbines and generators have been considered in this simulation. From this Homer software has calculated the optimum system which is shown in figure 9. The result is explained below.

Cost Analysis

From simulation the cost of electricity is found \$0.221 which is 17.68 taka in BDT. The Capital cost found in this simulation is \$950,000 & the Net Present Cost of this hybrid system is \$13,800,000. As Kutubdia is an off-grid place, it has not been blessed with modern technological equipments. So an extra cost is needed to transport these equipments. Hence the cost of energy is high.

Emission Analysis

Emission analyses have also been done in this study. It can be seen from table 3 that the emission of greenhouse gases is quite low as the system is 100% renewable. The environmental analysis represented that the hybrid system emits zero SO₂ and negligible CO₂ and CO emission.

Table 3: Emissions Due to Hybrid Power Plant

Quantity	Value(kg/yr)
Carbon dioxide	600.26
Carbon mono oxide	16.5
Unburned Hydrocarbon	0.72(g/fuel)
Particulate matter	0.1(g/fuel)
Sulphur dioxide	0
Nitrogen dioxide	15.5

7. Conclusion

Day by day people need for energy is increasing. It is quite difficult to meet up this demand. Proper utilization of renewable sources can help in meeting up this demand. As the grid connection is very expensive, the hybrid system proposed here will be effective for meeting up the electricity demand of rural Kutubdia. At present, the government has set up wind power plant at Kutubdia. Beside this people also rely on the diesel generator for electricity. The use of diesel generator results in the emission of harmful gases. The hybrid system proposed here reduces the emission of greenhouse gases. Besides the proposed system can provide electricity for the proposed place. So it can be stated that this proposed hybrid plant is feasible for providing power to Kutubdia Island.

REFERENCES

- [1] R. Sen, S. Bhattacharyya, "Off – grid Electricity generation with renewable energy technologies in India: An application of Homer", *Renewable Energy*, pp 388-398, Vol 62, February 2014.
- [2] Mohammed Shahriar Arefin, Md. Kaiser Raihan and Hamed Hasan Alvee, "A STUDY ON FEASIBILITY OF RENEWABLE HYBRID POWER GENERATION PLANT IN MANPURA ISLAND",
- [3] Sayedus Salehin, A.K.M. Sadrul Islam, Rawhatul Hoque, Mushfiqur Rahman, Aynul Hoque, Emrul Manna, "Optimized model of a solar PV-biogas-diesel hybrid energy system for Adorsho Char Island, Bangladesh", 2014 3rd International Conference on the Developments in Renewable Energy Technology (ICDRET), IEEE Xplore, Dhaka, Bangladesh, pp. 1-6,
- [4] Nishat Anjum Khan, Amit Kumar Sikder, Shammya Shananda Saha, "Optimal planning of off-grid solar-wind-tidal hybrid energy system for sandwip island of Bangladesh", 2nd International Conference on Green Energy and Technology, IEEE Xplore, Dhaka, Bangladesh, pp. 41-44,
- [5] Key statistics of Bangladesh Power Development board, http://www.bpdb.gov.bd/bpdb/index.php?option=com_content&view=article&id=5&Itemid=6/
- [6] 7.5 MW off Grid Wind-Solar Hybrid System with HFO/Diesel Based Engine Driven Generator in Hatiya Island, Noakhali, http://www.bpdb.gov.bd/bpdb/index.php?option=com_content&view=article&id=26/
- [7] Md Wajed Ali Kutubi (2012), "Kutubdia upazila", in Sirajul Islam and Ahmed A. Jamal, *Banglapedia: National Encyclopedia of Bangladesh* (Second ed.), Asiatic society of Bangladesh.
- [8] <http://203.112.218.65:8008/WebTestApplication/userfiles/Image/District%20Statistics/Cox%60s%20Bazar.pdf>.
- [9] Kalam Azad, Muhammad Alam, "Wind Power for Electricity Generation in Bangladesh". Available at, <https://www.researchgate.net/publication/252069104>
- [10] NASA surface meteorology and solar energy website, <https://eosweb.larc.nasa.gov/cgi-bin/sse/grid.cgi/>
- [11] MA Gofran, *Biogas Projukti*, Chapter 3, ISBN 984-32-1781-5
- [12] The HOMER energy website, <http://www.homerenergy.com>

Production of Syngas using Entrained Flow Gasification of Pine Bark Biomass Aiming to Reduce Greenhouse Gas Emission from Power Generation

M. Shahabuddin*, Sankar Bhattacharya

Department of chemical engineering, Monash University, Wellington Rd, Clayton, 3800 VIC, Australia

ABSTRACT

In this study, CO₂ gasification characteristics of pine bark biomass have been explored using state of the art entrained flow gasifier. The effect of temperature, CO₂ concentration (gasification reagent), and particle size on carbon conversion and syngas yield have been analysed. The results show that increasing temperature and CO₂ concentration in the feed increases the carbon conversion, though the effect of CO₂ concentration is minimal. The influence of particle size on carbon conversion was also dominant. A full carbon conversion was achieved at a temperature of 1400 and 1200 °C with 20 % CO₂ using particle size 250-300 and 90-106 μm respectively. Higher conversions between 1-14%-point from smaller particle size under different operating conditions were determined. The analyses on syngas yield show that increasing temperature increases the generation of CO but decreases H₂ and CH₄. A higher gas yield and heating value from larger particle size were determined.

Keywords: Entrained flow, CO₂ gasification, Pine bark biomass, syngas, heating value

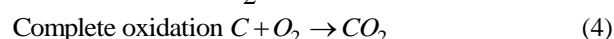
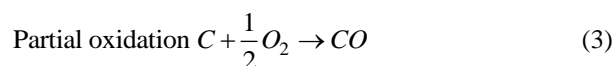
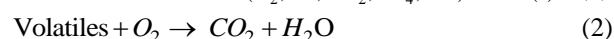
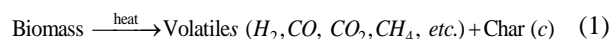
1. Introduction

Gasification is the process of converting carbonaceous solid fuels (i.e., biomass, coal, petcoke, etc.) into gaseous fuels (syngas) and chemicals. The key advantages of gasification over conventional combustion are the higher efficiency and lower emission. Furthermore, the integration of CO₂ capture and syngas cleaning system with gasification plants makes it more favourable for power generation. The by-product of gasification plant: CO₂ is potentially used for enhanced oil and methane recovery, while other pollutants such as H₂S and NH₃ are respectively be used for the production of sulfuric acid and fertiliser.

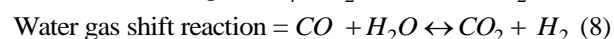
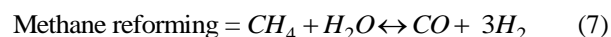
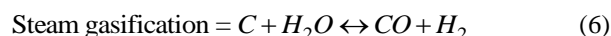
Currently, 81% of global energy and 66.7% of electricity is generated from fossil fuels such as coal, natural gas and petroleum oil [1]. These fossil fuels emit 99.4% of the world CO₂. The concern over depletion of fossil fuel reserve and greenhouse gas emissions are the driving forces to use alternative renewable sources like biomass for power generation, which has the potential to replace fossil fuel based power generation [2]. Biomass-the fourth largest source of global energy, supplies about 10% of world energy followed by three major sources of fossil fuels [3]. Currently, the syngas is predominantly generated from conventional fuel sources, for example, coal and natural gas. However, the advantages of biomass gasification over other conventional solid fuels are its renewability, availability, abundance, and higher gasification reactivity [4].

Most of the commercial gasifiers are operated in two-stages consisting of combustion and gasification. In the combustion zone, volatiles and fixed-carbon present in the biomass are oxidised (Eq.1-4) resulting in the generation of CO₂ and H₂O with a ratio of roughly 4:1.

Hence, gasification reactions in reductor zone are mainly governed by the CO₂, which is a rate-limiting process. Thus, understanding of CO₂ gasification phenomena is more important than H₂O gasification. The gases (CO₂ and H₂O) generated in the combustor zone are then transferred to the reductor zone for gasification of raw biomass/char, resulting in the generation of CO and H₂ in addition to a minor amount of CH₄ and C₂H₆ [4].



In the reductor zone, a rapid devolatilisation of biomass particles produces volatiles and solid char. This char is then gasified in the subsequent stage with the presence of CO₂ and H₂O. The key reactions those are involved in the gasification process include Boudouard reaction, steam gasification, methane reforming and water gas shift reactions as shown in Eq. 5-8.



The gasification characteristics such as char conversion, gas yield and pollutant emission depend on the reaction rate of the aforementioned reactions. The reaction rate of these reactions are further influenced by the operating conditions, reactor configurations, and fuel properties. Kirtania and Bhattacharya [5] studied the effect of

* Corresponding author. Mob.: +61470605227
E-mail addresses: md.ahmmad@monash.edu

particle size, and temperature using the CO₂ concentrations of 5, 10 and 20% in an entrained flow gasifier for spruce and coconut shell biomass char. Three gasification temperatures of 800, 900 and 1000 °C and two particle size of 150-250 and 500-600 µm were chosen for the study. The residence times for spruce char were nine and 4.5 s, while the residence times for coconut shell char were determined to be seven and 2.5 s for lower and smaller particle size respectively. The result showed that a maximum conversion of 8 % and 50% for coconut shell and spruce chars were achieved using lower particle size under extreme operating conditions of 1000°C and 20% CO₂. The effect of CO₂ concentration was found to be dominant only for spruce char and at the highest temperature of 1000°C. It was stated that lowering the particle size did not favour the conversion for coconut shell char, though almost a double carbon conversion from lower particle size was determined in the case of spruce char. Thus, it was concluded that the conversion is independent to the particle size for the car with lower reactivity, hence increasing the temperature should be a better choice.

Sripada, et al. [6] investigated the gasification characteristics of pine bark biomass under entrained flow conditions with a residence time between 7-8 s. The results showed that operating conditions such as temperature and CO₂ concentration has a significant effect on carbon conversion and gas yield. Increasing temperature and CO₂ concentration lead to increase the carbon conversion. A maximum of 98% conversion was achieved at a temperature of 1200 °C with 40% CO₂ using particle size: 90-106 µm. The gas yield results showed that increasing CO₂ feed rate decreases the yield of syngas. In addition, increasing the temperature leads to an increase in the production of CO but decreases H₂. Moreover, the highest lower heating value (LHV) of the product gases was determined to be of 4.18 MJ/m³ under the operating conditions of 1200°C and 10% CO₂.

From the literature, it is known that increasing temperature and CO₂ concentration increases the carbon conversion for all biomass including pine bark. However, based on the authors' knowledge, the effect of particle size on carbon conversion and syngas yield for pine bark biomass is not studied in the literature. Furthermore, most of the studies in the literature were carried out at low temperatures of up to 1000°C. However, the practical entrained flow gasifier is operated at high temperatures of above 1000°C. Hence, in this study, high-temperature CO₂ gasification study is carried out for pine bark biomass using different particle size. The result of this study will provide a better understanding, especially the effect of particle size on gasification characteristics of pine bark biomass under CO₂ atmosphere. Moreover, the result will be applicable in the case of designing a gasification-based power plant using the substantial domestic reserve of pine bark biomass in Australia.

2. Materials and method

The CO₂ gasification study for pine bark biomass was carried using an electrically heated entrained flow gasifier, while a number of analytical instruments were used for the characterisation of raw pine bark sample. The following sections present the key steps those were followed to complete the experiments.

2.1 Sample preparation

Pine bark biomass studied in this study was first grounded into the desired particle sizes of 250-300 µm and 90-106 µm. The reason for selecting these size ranges are to make the study analogous to the industrial application. The grounded particles were then sieved by sieve shakers with the help of Taylor sieve shaker machine. Before conducting the experiment, the samples were oven dried overnight to ensure the particles free from moisture.

2.2 Sample characterisation

The proximate analysis was carried out using a TGA with the model number Netzsch STA 449 F3 following the standard: AS1038.1. The ultimate analysis was conducted by TruSpec CHNS analyser using ISO 29541 standard. The details of the operating conditions of TGA can be found in ref. Tanner and Bhattacharya [7]. The proximate and ultimate analyses results of pine bark biomass are shown in Table 1.

Table 1. Proximate and ultimate data for pine bark biomass

Particle size (µm)	Proximate analysis (dry basis)				
	Moisture	Volatile	Fixed carbon	Ash	
90-106	2.7	69.92	22.11	5.27	
250-300	2.77	71.79	22.41	3.03	
90-106	Ultimate analysis (dry basis)				
	C	H	N	S	O
	53.93	5.51	0.14	0.01	34.38

2.3 Experimental setup and operating procedures of the reactor

The entrained flow reactor used in this study is located in the chemical engineering department of Monash University, Australia. The major components of the reactor are shown in Fig. 1. This reactor imitates the reductor zone of the Mitsubishi heavy industry (MHI) commercial gasifier. The total length and internal diameter of the reactor tube are 3.80 and 0.090 m respectively. The reactor tube is made of alumina capable of sustain under high temperatures. The reactor is heated with eight independent electrical heating elements. During experiments, the sample is fed from the top of the reactor via a screw feeder with a feed rate of about one g/min. A precision balance installed in the feeder box gives a sample feed profile over time. Furthermore, the reactant gas: CO₂ is injected from the top of the reactor, which is pre-heated with a

temperature of 500°C. Different CO₂ concentrations of 10, 20 and 40% by vol. were used balancing with pure N₂. A total flow rate of 16 L/min is maintained throughout the experiment. A national instrumentation LabVIEW software is dedicated to controlling the gas and sample feed rates. The solid char/ash is collected via a series of impingers from the downstream of the reactor. The product gases (i.e., H₂, CO, CH₄) were measured using an online micro-GC. The details of the experimental setup and operating procedures can be found elsewhere [8].

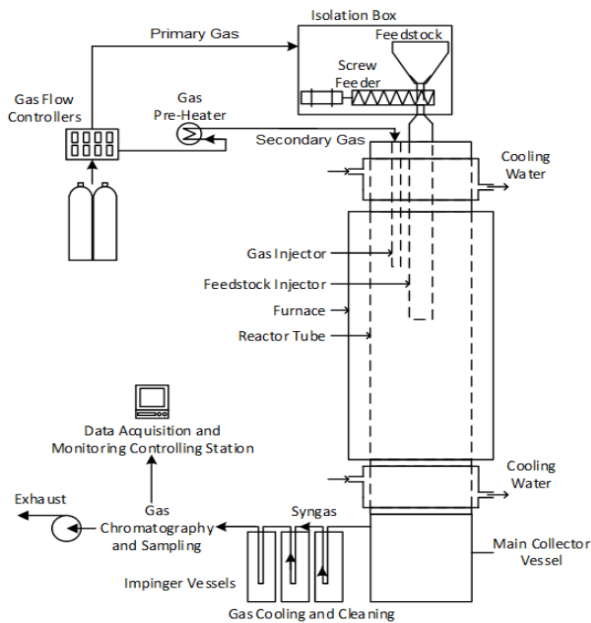


Fig. 1 Schematic diagram of the experimental setup [6]

3. Results and discussion

The carbon conversion was calculated by ash tracer method, which is verified by the gas-phase carbon conversion. The following equation (Eq. 9) was used to calculate carbon conversion by ash tracer method.

$$X (\%) = \left(1 - \frac{w_{c,out}}{w_{c,in}} \right) \times 100 \quad (9)$$

Where, X is the carbon conversion, $w_{c,in}$ and $w_{c,out}$ are the weight of the carbon input and output respectively. The carbon content in the feed pine bark and post-gasified char/ash were determined by ultimate analysis.

The discrepancy between gas-phase and solid-phase carbon conversion was found to be 5-10% under different operating conditions. The sources of error in solid phase carbon conversion are incomplete char recovery from collection vessels and an error from precision balance. Whereas, the gas-phase carbon conversion might be influenced by fluctuating CO₂ feed rate and a measurement error from the Micro-GC. The quality and quantity of syngas during gasification depend on several factors including temperature, system pressure, reactant concentrations, residence time, reactor configurations and particle size. The reactor used in this

study was an entrained flow reactor operated under atmospheric pressure. Based on the operating conditions the residence time for particle size 90-106 μm was calculated to be 7-8 s, which is 2.5-3.5 s for the large particle size of 250-300 μm [6, 9]. Considering the facilities available, this study predominantly tested the effects of temperature, CO₂ concentration, and particle size on syngas gas yield.

The effect of temperature, CO₂ partial pressure and particle size on carbon conversion is shown in Fig. 2. It is observed that increasing temperature and CO₂ concentration increase the carbon conversion. However, the influence of temperature is dominant as compared to that of CO₂ partial pressure. Considering equilibrium concentration, the feed of CO₂ was excess under all operating conditions. Thus, the effect of CO₂ concentration on carbon conversion was not significant. The carbon conversion using particle size 250-300 μm at 1000°C with 10% CO₂ is found to be 75%, which is increased by 2.57 %-point with 20% CO₂. However, under the same CO₂ concentration, increasing the temperature from 1000°C to 1200°C leads to increase the carbon conversion by 10%-point. The key equations those involved in gasification reaction were Boudouard and steam gasification. However, the influence of steam gasification was significantly low as compared to that of Boudouard reaction because of the low moisture content in the biomass. The reaction rate of these reactions increases with increasing temperature and CO₂ concentration. Hence, a higher conversion with increasing temperature and CO₂ was observed.

Besides, the effect of particle size on carbon conversion is significant as decreasing the particle size increases the carbon conversion. It can be seen that, decreasing the particle size from 250-300 to 90-106 μm (factor of ~2.8) increases the carbon conversion by 11, 9.43, and 8.64%-point under different CO₂ concentrations (10-40% vol.) and at a temperature of 1000°C. It is clear that 1200°C was not sufficient under any CO₂ concentrations to achieve 100% carbon conversion using the larger particle size of 250-300 μm. A temperature of 1400°C and 20% CO₂ concentration were required to reach full carbon conversion for large particle size, whereas 100% carbon conversion was achieved at a temperature of 1200°C and 20% CO₂ using smaller particle size. The diffusion limitation from large particle size prevented the reactant gas from diffusing through the micro-pores of the particle, hence a slower conversion. Furthermore, the lower residence time from larger particles led to the incomplete carbon conversion.

The production of gases during gasification is the result of devolatilisation and consumption of carbon left in the char. The devolatilisation is the first stage of gasification, resulting in the formation of H₂, CO, CO₂, CH₄ and some other minor species. In single stage gasification, both homogeneous and heterogeneous

reactions take place simultaneously under the presence of these gases and char.

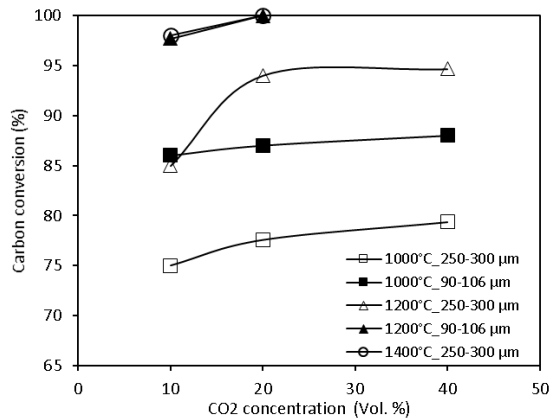


Fig. 2 The effect of CO₂ partial pressure and particle size on carbon conversion at various temperatures

The major gas components those produced during gasification is presented in Fig. 3 under various operating conditions. A significant variation in the yield of H₂ and CO were observed under different temperature, CO₂ concentrations, and particle size. However, the variation in the production of CH₄ was negligible, especially at higher CO₂ concentration. In addition, the yield of CH₄ was significantly low, particularly at 1200°C. Presumably, at a temperature above 1000°C, available CH₄ is being consumed by the Steam methane reforming reaction, which consequently decreases the yield of CH₄ [10].

The production of CO was increased with increasing temperature due to the higher carbon conversion owing to the Boudouard reaction being dominant. On the other hand, the yield of H₂ was decreased with increasing temperature and CO₂ concentration because of the water gas shift (WGS) reaction, which was favoured in the reverse direction [11].

The effect of particle size on the yield of gas species was also significant. It is observed that larger particle size results in higher syngas yield under all temperature and CO₂ concentration. The larger particles are appeared to be significantly unreacted, which resulted in the WGS reaction to be dominant as compared to those of smaller size particle. Hence, larger particle size yields more H₂ and CH₄ as compared to that of smaller particle size. However, the higher CO yield from larger particle size is not clear. It was expected that the contribution of Boudouard reaction on overall reaction would be much more significant using lower particle size consuming more carbon to produce more CO. Further analysis is therefore required to figure out the reason behind this unexpected trend.

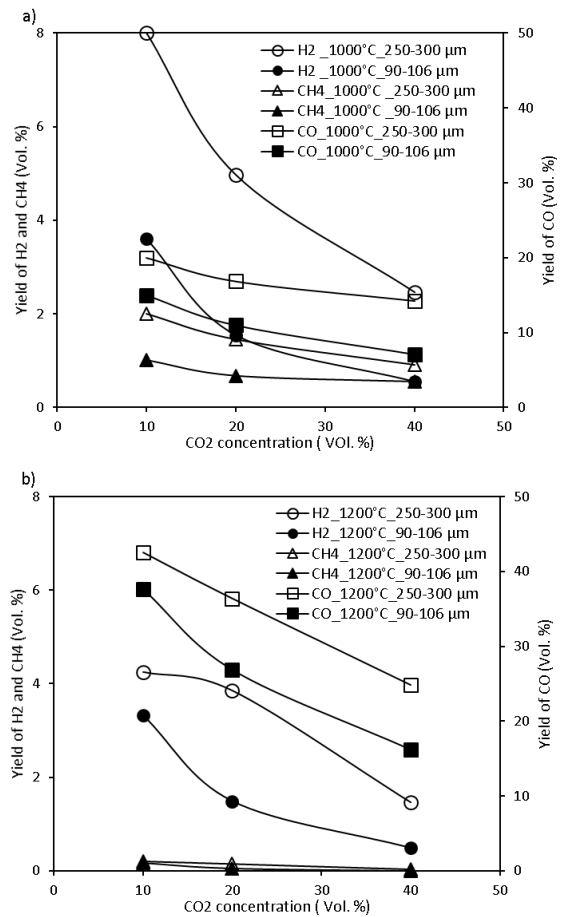


Fig. 3 Effect of temperature and CO₂ partial pressure on gas yield from two different particle sizes of 90-106 μm and 250-300 μm; a) 1000°C, b) 1200°C (N₂ and feed CO₂ free basis).

The ratio between CO and H₂ carries paramount importance, especially for chemical synthesis. Hence, gasification plants for chemical production require downstream treatment to adjust the gas composition in order to produce desired chemicals. However, this ratio does not necessarily play a pivotal role in terms of altering the heating value of the product gases, which is essential for the power generation. Table 2 and 3 show the ratio between CO and H₂ under different operating conditions for two particle sizes. It is seen that CO/H₂ ratio differs markedly under different operating conditions. As expected, the production of CO as compared to that of H₂ is higher under higher carbon conversion resulting in the ratio being higher for the corresponding condition. Furthermore, higher CO₂ concentration led to increasing the yield of CO, resulting in the higher ratio between CO and H₂.

Table 2. The ratio between CO and H₂ from two particle sizes at various temperatures and CO₂ concentrations (excluding N₂ and feed CO₂).

CO ₂ Concentration (Vol.%)		CO/H ₂ ratio		
		1000 °C	1200 °C	1400 °C
250-300 μm	10	2.50	10.01	12.75
	20	3.39	9.44	10.22
	40	5.79	16.92	-
90-106 μm	10	4.16	11.36	-
	20	7.10	18.10	-
	40	12.79	-	-

The lower heating value (LHV) presented in Table 3 was calculated using Eq. 10 under different operating conditions. It can be seen that increasing the temperature increases the heating value, which is opposed by the increasing CO₂ concentration. A maximum heating value under three temperatures and lowest CO₂ concentration of 10% were calculated to be 4.1, 5.9 and 6.87 MJ/m³ for larger particle size. When LHV is compared between the particle sizes, it is depicted that, the heating values from larger particle size are higher than the smaller particle size between the range of 14 and 107%. The result can be interpreted as the fact that the yield of all gases from larger particle size was considerably higher than the smaller particle size.

$$LHV(MJ / M^3) = 10.78X_{H_2} + 12.63X_{CO} + 35.81X_{CH_4} \quad (10)$$

Table 3. The heating value of the product gases from two particle sizes under different temperatures and CO₂ concentrations (excluding N₂ and feed CO₂).

CO ₂ Concentration (Vol.%)		Lower Heating Value (MJ/M ³) ²		
		1000°C	1200°C	1400°C
250-300 μm	10	4.10	5.90	6.87
	20	3.19	5.06	6.07
	40	2.39	3.30	-
90-106 μm	10	2.65	5.18	-
	20	1.80	3.57	-
	40	1.15	-	-

The heating value presented in the Table 3 was calculated excluding the feed N₂ and CO₂ from the outlet stream. However, calculating LHV based on CO₂ free basis results in the heating value between the range of 12-14 MJ/m³, which are closer to the heating value of pure CO, because of the dominant concentration of CO in the outlet stream. Therefore, in order to increase the heating value of the syngas, a CO₂ separation unit should be installed. In addition, a choice of optimum CO₂ concentration in the feed can be considered without penalising the carbon conversion efficiency.

4. Conclusion

In this research, CO₂ gasification characteristics of pine bark biomass were carried out using different

temperatures, CO₂ concentrations and particle sizes under entrained flow conditions. The results of this study show that increasing temperatures and CO₂ concentration increases the carbon conversion, though the effect of CO₂ concentration is not much significant, especially above 20% CO₂. Furthermore, the particle size has a strong influence on carbon conversion, gas yield and heating values. Decreasing particle increases the carbon conversion significantly. Smaller particle size (factor = ~ 2.8) resulted in a higher carbon conversion between the range of 1-12% percentage point. The gas composition results show that increasing the temperature increases the yield of CO but decreases H₂ and CH₄. In addition, larger particle size results in a higher syngas yield and heating value thereby. Further study, including solid residue characterisation by XRD, and SEM are sought for a better understanding of the pine bark gasification under CO₂ atmosphere, and these studies are in progress. The detailed analysis including solid phase characterisation and thermodynamic calculations will be published in future publications.

Acknowledgement

The authors would like to acknowledge the experimental facility provided by the department of chemical engineering, Monash University, Australia. Also, the financial support through MIPRS and MGS scholarships for PhD study of the first author is greatly acknowledged.

References

- [1] International Energy Agency (IEA) report 2017, Available at <http://www.iea.org/publications/>. Accessed on 12. 09. 2018.
- [2] M. Ni, D. Y. Leung, M. K. Leung and K. Sumathy, An overview of hydrogen production from biomass, *Fuel processing technology*, Vol 87, pp 461-472 (2006).
- [3] Federal Institute for Geosciences and Natural Resources (BGR) energy study, (2016).
- [4] C. Guizani, F. E. Sanz and S. Salvador, Influence of temperature and particle size on the single and mixed atmosphere gasification of biomass char with H₂O and CO₂, *Fuel Processing Technology*, Vol 134, pp 175-188 (2015).
- [5] K. Kirtania and S. Bhattacharya, CO₂ gasification behavior of biomass chars in an entrained flow reactor, *Biomass Conversion and Biorefinery*, Vol 6, pp 49-59 (2016).
- [6] P. P. Sripada, T. Xu, M. Kibria and S. Bhattacharya, Comparison of entrained flow gasification behaviour of Victorian brown coal and biomass, *Fuel*, Vol 203, pp 942-953 (2017).
- [7] J. Tanner and S. Bhattacharya, Kinetics of CO₂ and steam gasification of Victorian brown coal chars, *Chemical Engineering Journal*, Vol 285, pp 331-340 (2016).

- [8] J. Tanner, M. Bläsing, M. Müller and S. Bhattacharya, High temperature pyrolysis and CO₂ gasification of Victorian brown coal and Rhenish lignite in an entrained flow reactor, *AIChE journal*, Vol 62, pp 2101-2111 (2016).
- [9] J. Tanner, M. Bläsing, M. Müller and S. Bhattacharya, Reactions and transformations of mineral and nonmineral inorganic species during the entrained flow pyrolysis and CO₂ gasification of low rank coals, *Energy & Fuels*, Vol 30, pp 3798-3808 (2016).
- [10] J. Yu, J. A. Lucas and T. F. Wall, Formation of the structure of chars during devolatilization of pulverized coal and its thermoproperties: A review *Progress in energy and combustion science*, Vol 33, pp 135-170 (2007).
- [11] K. Qin, W. Lin, P. A. Jensen and A. D. Jensen, High-temperature entrained flow gasification of biomass, *Fuel*, Vol 93, pp 589-600 (2012).

Economic Viability of Biomass Power plant in Bangladesh

Tamal Chowdhury^{a*}, Hemal Chowdhury^b, Piyal Chowdhury^c, Pranta Barua^a, Monirul Islam Miskat^a

^{aa*}Department of Electrical & Electronic Engineering, Chittagong University of Engineering & Technology, Chittagong, BANGLADESH

^bDepartment of Mechanical Engineering, Chittagong University of Engineering & Technology, Chittagong, BANGLADESH

^cChittagong Collegiate School & College

ABSTRACT

Combustion of fossil fuels results in high emission of green house gas. Besides it also results in shortage of fossil fuels. So, it is necessary to look for alternate solution. Biomass is a renewable source which is abundant in nature. Combustion of biomass produces gas which can be used to generate electricity. In this study, a simulation has been done by RETScreen software to find out the economic viability of 3MW biomass based power plant in Chittagong. From simulation it is found that electricity export to grid from plant is 23,915 MWh and revenue earned by selling electricity is \$2,391,480. It was also observed that the proposed system reduces 13000 tonne CO₂ annually.

Keywords: Renewable energy, Organic waste, Solid waste, RETScreen.

1. Introduction

Approximately 80% people of Bangladesh live in rural area and 40% of people have access to electricity. The biggest portion of her energy demand is met up by fossil fuels such as natural gas, coal etc. As her population is increasing, the demand for electricity is increasing continuously. As a result, fossil fuels consumption is also increasing. According to World Bank, fossil fuel energy consumption (% of total) in Bangladesh was reported at 73.77% in 2014. Combustion of fossil fuels to produce electricity emits various dangerous gases. These gases are harmful for environment. It is also estimated that because of high cost grid connection, dispersed population 44% of the world population do not have access to grid electricity [1]. The only solution for this problem is to utilize renewable energy as they are environment friendly. Biomass which is abundant in nature can play an effective role here. They can be burned to produce steam or gas. This gas can drive turbine which will generate electricity.

In this study an attempt has been made to find out the economic viability of biomass power plant in Chittagong district. Meanwhile the effects of biomass power plant on greenhouse gas reduction are also shown in here. From the existing literatures it can be found that there is no study on economic viability of biomass based power plant in Bangladesh. So this study will focus on the economic viability and environmental impact of biomass power plants in Bangladesh. We hope that the current study will help the authority to evaluate biomass power plants for power generation in Bangladesh.

2. Present Situation of Energy in Bangladesh

Natural gas:

Being the 19th largest producer of natural gas, Bangladesh economy mostly depends on it. It provides

75% of commercial energy of this country [2]. So far 24 gas fields have been discovered. Among 24 gas fields, two of them are located in offshore area. Now-a-days gas is being extracted and produced from 79 gas wells [3]. Figure 1 states that between 1993 and 2013, natural gas production of Bangladesh increase significantly from 215.77 to 807.3 billion cubic feet while Figure 2 states that between 1995 and 2014, dry natural gas consumption of Bangladesh grew substantially from 260 to 844 billion cubic feet.

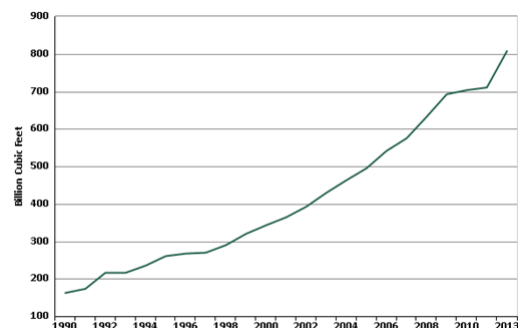


Fig.1: Natural gas production of Bangladesh up to 2013

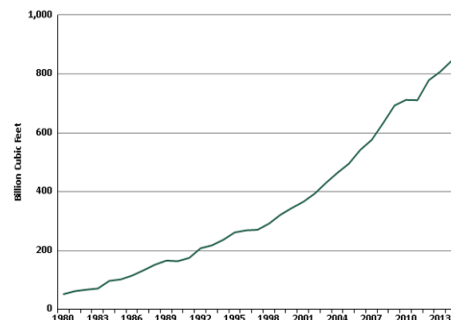


Fig. 2 Natural gas consumption of Bangladesh up to 2013

* Corresponding author.

E-mail addresses: tamalshanto@gmail.com

Coal Sector:

Coal has played an important role in this country's economy. The impact of this sector in national economic security is huge. In 2009-10, for electricity generation, this sector contribution was 3.5% [5]. Coal could have been a good alternative to natural gas but it is not due to proper management, lack of infrastructure.

Energy from tannery:

Table 1 shows the waste water component generated when each steps of tanning process occurs. Besides this a huge amount of soda ash, sulphuric acid, formic acid, resins etc are also used different stages of the tanning process [15].

Table 1: Contents of waste water generated during tanning process [16]

CONTENTS	PROCESS
Salts, fat, protein, preservatives	Soaking
Lime and ammonium salts, ammonia, protein (hair), and sulphides	Fleshing, trimming and bating
Chromium (salts), vegetable tannins and polyphenolic compounds	Tanning
Dye and solvent chemicals	Finishing

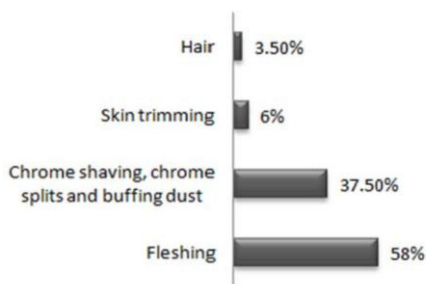


Fig. 3: Components of the solid waste produced during the tanning process [6].

3. Calculation of Biomass Energy

The energy content of the solid waste produced from the tanneries can be calculated by using the following references [7-11]. The findings are listed in table 2.

Table 2: Energy generation from tannery waste

% of organic waste	Solid waste	Amount of methane & produced Electricity
64%	96×10 ⁶ Kg	53.86×10 ⁶ m ³ of methane & 538.603 GWh of electricity annually

Energy from Dung:

Table 3 denotes the biogas production from animal dung.

Table 3: Biogas from animal manure.

No of animals	Manure per day and availability (%)	Biogas per kg	Total biogas
24.9 million [12]	8-10 kg and 50	0.036 [13-14]	4.482 million per day

4. Results and Simulation

4.1. Simulation

In this study a simulation has been done to find out how much electricity can be generated from biomass. Simulation has been by software RETScreen [17]. Biomass will be converted into gas as it will drive a gas turbine which will generate electricity. Table 4 shows the parameter of gas turbine considered for simulation. In this study Chittagong city has been considered for setting up biomass power plant. Project life has been considered 20 year for simulation.

Table 4: Simulation parameters for gas turbine

Item	Specification
Fuel type	Biomass
Fuel rate (\$/t)	.30
Power Capacity	3MW
Availability	91%
Manufacturer	Capstone
Model	C30
No of units	100
Heat rate(kj/kWh)	13000
Fuel required(Gj/h)	39

Here heat rate or lower heating value has been taken from RETScreen database. All of the input parameters are taken from RETScreen database.

Table 5 shows financial parameters considered for simulation.

Table 5: Financial Parameter

Parameter	Value
Inflation rate	2%
Discount rate	9%
Debt ratio	70%
Debt interest rate	7%
Debt term	15
Electricity export escalation rate	2%
Electricity export rate (\$/kWh)	0.10
Initial cost(\$/kW)	2200
Operation and maintenance cost(\$/kW-year)	133
Fuel cost (\$)	4720
Fuel Consumption (ton)	15734

4.2. Result Analysis:

Financial analysis:

From simulation it has been observed that electricity export to grid is 23,915 MWh and revenue earned by selling electricity is \$2,391 480. Table 6 shows the financial viability of biomass based power plant in Chittagong.

Table 6: Financial viability of biomass based plant

Parameter	value
Simple Payback Period (year)	3.3
Benefit to cost ratio	8.7

From simulation result it can be seen that it takes 3.3 years to get back the cost incurred on setting up power plant.

From [18] it can be seen that in Kenya for medium scale biogas plant the payback period is 6 years under very favourable conditions and for unfavourable conditions it is 9 years. But in our study it was found that the payback period is 3.3 years which is quite low considering the others.

4.3. Green house gas reduction:

Figure 4 shows that the proposed power plant reduces the emission of CO₂. It reduces approximately 13000 tonne of CO₂ annually.

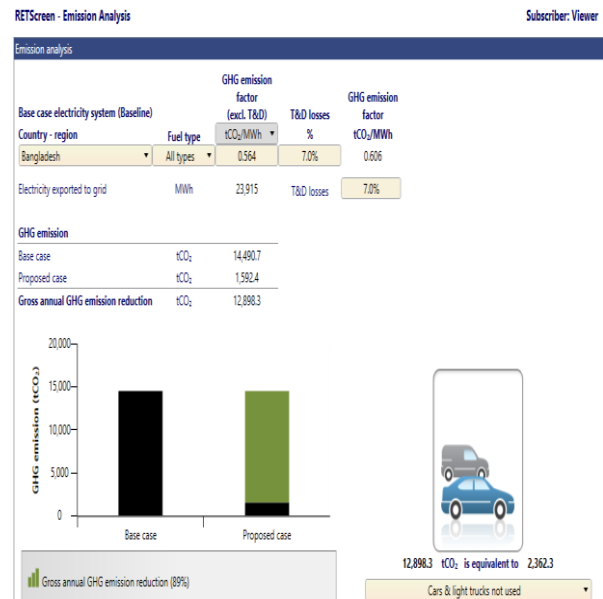


Fig. 4: Annual green house gas reduction

5. Conclusion:

The major findings of the study is

- Annually 538.603 GWh of methane can be generated from tannery waste.
- Approximate biogas generation from dung is 4.482 million per day.
- From simulation it is found that electricity export to grid from biomass pant is 23,915 MWh and revenue earned by selling electricity is \$2,391 480.
- It was also observed that the proposed system reduces 13000 tonne CO₂ annually.

REFERENCES

- [1] R.Sen, S. Bhattacharyya, “Off – grid Electricity generation with renewable energy technologies in India: An application of Homer”, *Renewable Energy*, pp 388-398, Vol 62, February 2014.
- [2] Saif Khan Alen, “Present Scenario and Prospect of the Power and Energy Sector in Bangladesh” http://www.academia.edu/8067842/Present_Scenario_and_Prospect_of_the_Power_and_Energy_Sector_in_Bangladesh. [Accessed: 18-Feb-2018].
- [3] “Country Profile: Bangladesh” (2010) [Online]. Available:http://www.pub.iaea.org/MTCD/publications/PDF/CNPP2011_CD/countryprofiles/Bangladesh/Bangladesh2011.htm [Accessed: 20-Feb-2018].

- [4] "Entering an era of coal based power." [Online]. Available:http://www.thedailystar.net/print_post/entering-an-era-of-coal-based-power-10075. [Accessed: 20-Feb-2018].
- [5] "Coal News of Phulbari - Bangladesh on WordPress.com." [Online]. Available:<https://phulbarinews.wordpress.com/>. [Accessed: 20-Feb-2018].
- [6] Salman Zafar, 'Renewable Energy Production from Tannery Wastes', <http://bioenergyconsult.wordpress.com/salman-zafar/>
- [7] 'How to estimate biogas from anaerobic digestion of organic solidwaste', from the web site of Anaerobic-Digestion.Com
- [8] UNEP Working Group for Cleaner Production, NSW, 'The potential for generating energy from wet waste streams in NSW', SustainableEnergy Development Authority, Sydney, 1999.
- [9] Brian A. Schumacher, 'Methods for the determination of TotalOrganic Carbon (TOC) in soils and sediments', US Environmental Protection Agency, Exposure Research Laboratory, 2002
- [10]H. G. Bingemer and P. J. G. Crutzen, ' The Production of Methane from Solid Wastes', Journal of Geophysical research, Vol. 92, No. D2, Pages 2181-2187, February 20, 1987
- [11] 'Difference between lpg and natural gas, Introduction', edurite, Pearson on <http://www.edurite.com>
- [12]<https://knoema.com/atlas/Bangladesh/topics/Agriculture/Live-Stock-Production-Stocks/Number-of-cattle-and-buffaloes>[Accessed: 20-April-2018].
- [13]Bangladesh Bureau of Statistics.[www.bbs.gov.bd] [Accessed: 20-April-2018].
- [14]MA Gofran, Biogas Projukti, Chapter 3 ,ISBN 984-32-1781-5 .
- [15]S.M. Imamul Huq, 'Critical Environmental Issues Relating to Tanning Industries in Bangladesh', Department of Soil Science, University of Dhaka.
- [16]L.A.H.M. Verheijen, D. Wiersema, L.W. Hulshoff Pol, 'Management of Waste from Animal Product Processing', J. De Wit Intl. Agriculture Centre, TheNetherlands, January, 1996
- [17]RETSscreen software. 2013. (Available online at <http://www.retscreen.net/th/home.php>) [Accessed: 20-July 2018].
- [18]https://energypedia.info/wiki/Electricity_Generation_from_Biogas [Accessed: 10 November 2018]

Finned-tube Heat Exchanger with Circular, Elliptical & Rectangular Tubes with Water-vapor as Working Fluid

Md. Hasibul Hasan*, Dipayan Mondal

Department of Mechanical Engineering, Khulna University of Engineering & Technology, Khulna 9203, Bangladesh

ABSTRACT

3D numerical study has been conducted on the finned-tube heat exchanger with multiple rows of tubes using ANSYS. The objective of this study is to numerically investigate finned tube heat exchanger for multiple rows of tube with several types of tubes such as circular, elliptical and rectangular tubes with water-vapor. Heat transfer performance analysis has been performed for three and six rows of tube. Heat transfer characteristics were studied with various inlet air velocities. The results show that in the case of water-vapor, modified heat exchanger (HX) 1 & 2 have 3.48% decrease in heat transfer from conventional circular tube heat exchanger. Also modified HX 1 & 2 have 2.11% decrease in heat transfer from conventional elliptical tube heat exchanger. On the contrary, at high inlet velocity, modified HX 2 have 10.45% higher from grouped elliptical tube heat exchanger, for modified HX 6 gives 5.80% higher heat transfer from grouped elliptical tube heat exchanger when $N=3$. Again in case of water vapor when $N=3$ modified HX 2 gives 2.38% higher heat transfer than baseline HX 2. When $N=6$, for water-vapor, all modified heat exchanger have a lower heat transfer than the conventional heat exchanger. For water-vapor, when $N=3$, all modified heat exchanger has a lower pressure drop than the conventional elliptical heat exchanger.

Key Words: Finned-tube heat exchanger, Darcy friction factor, Nusselt Number, Heat transfer, Pressure Drop

1.0 Introduction

Fin Tube Heat Exchanger (FTHX) are most used for forced air heating and cooling system. Usually, liquid passing through the tube and water-vapor flows over fin and tube. Tubes have been taken as a staggered arrangement in this work. Circular cross-section tubes are widely used in FTHX. Elliptical tubes have been using in recent years. For having a better aerodynamic shape of an elliptical tube, there has some advantage in compactness, high heat transfer coefficient, and lower pressure drop. In this present analysis, for the first time, the rectangular tube has considered for numerical investigation. Many geometric parameters are related with FTHX like fin pitch, tube pitch, tube size & fin thickness. It is difficult to find out the best performance considering all parameters. Hence, early experimental studies conducted by Rich et al. [1] who investigated a total of fourteen tubes, in which the tube size was 13.34 mm. The corresponding longitudinal and transverse tube pitches were 27.5 and 31.75 mm, respectively. He examined the effect of fin spacing and the number of tube row and concluded that the heat transfer coefficient was essentially independent of the fin spacing's and the pressure drop per row are independent of the number of tube rows [2]. 2D heat transfer analysis was performed by with one & two rows tube where only circular & elliptical tubes have been examined with experimentally determined heat transfer coefficient from heat & mass transfer analogy. Temperature distribution on the fin & air stream were determined Rocha et al. [3].

2.1 Problem statement

Plate-fin with staggered tube arrangement has taken to study with water-vapor heat transfer and pressure drop characteristics. To closely represent the real-time heat exchanger, multiple tube rows (number of tube rows, $N = 3, 6$) are considered. The effect of a number of tubes has also been studied. When the tube number exceeds six, the corresponding increase in heat transfer is negligible [4], therefore present work concerns up to six rows of tube.

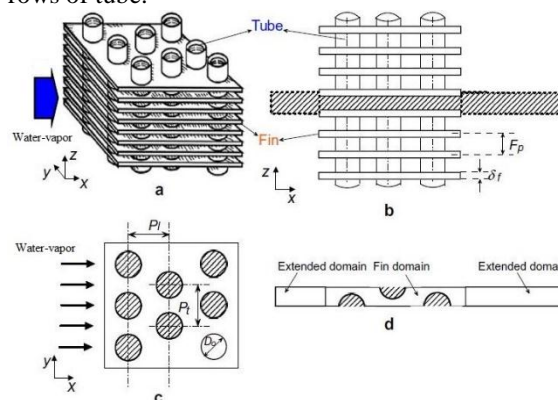


Fig 1: Schematic configuration of a heat exchanger (a) The overall core: air flows across the finned bundle. (b) Cross-section in $z-x$ plane surfaces (c) Cross-section in $y-x$ plane (d) Cross-section of computational domain in $y-x$ plane [4].

The circular and elliptical tubes are designed in such a way that perimeter of the tubes are same, which allows ease of manufacturing and ensures same heat transfer

Area for the circular, elliptical and rectangular tube. The eccentricity of the elliptical tube is taken as which is closer to Rocha et al [3]. As the region of interest of the present work is focused on to identify the tube geometric effect, the fin surface is assumed to be a constant wall temperature. Geometric parameters are taken from Deepakkumar et al. [5] where fin length is a product of number of tubes and longitudinal pitch.

2.2 Geometric Details

In this present investigation, there is three type of tube, so total $3P_3=6$ combinations are possible as shown in Table 1. But for 6 rows of tube, those combinations are doubled in a staggered arrangement.

Designation	Schematic Representation	Category
N3B1		Baseline-1
N3B2		Baseline-2
N3M1		Modified-1
N3M2		Modified-2
N3M3		Modified-3
N3M4		Modified-4
N3M5		Modified-5
N3M6		Modified-6
N6B1		Baseline-1
N6B2		Baseline-2
N6M1		Modified-1
N6M2		Modified-2
N6M3		Modified-3
N6M4		Modified-4
N6M5		Modified-5
N6M6		Modified-6

Table 1: Combination of the tube in the various arrangement.

2.3 Grid Generation and Solution Methodology

The computational domain is discretized into a finite number of control volume. In fin region, inflation mesh control is done with four edges of circular and elliptical in both sides. First layer thickness inflation option is selected as shown in Fig 2. After that body sizing is

done on fin region. In the upstream and downstream region, several edge sizing is done in various direction.

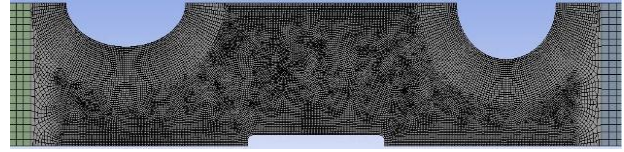


Fig 2: Schematic representation of the grid.

The finite volume based CFD code ANSYS Fluent 16.2 is used to calculate the flow and temp fields and by applying SIMPLEC algorithm. Fluid properties has been selected as water vapor from ANSYS fluent database. Under relaxation factor for pressure correction is taken as 1 for faster convergence. Boundary Condition has taken from the paper of Han et al [6]. Inlet has taken as velocity inlet and outlet as outflow boundary condition. Fin region portion has taken as wall with constant temp. Tube surface has also taken as constant wall temperature. To obtain improved accuracy of the solution, second-order spatial discretization of pressure is employed. As the grids are structured hexahedral and are aligned with flow direction, QUICK scheme is used for discretizing higher-order convective terms in the momentum equation. The residual is 10^{-6} for continuity and momentum, 10^{-8} for energy equation.

2.4 Definition Parameter

The definitions of non-dimensional parameters such as Reynolds number (Re), Nusselt number (Nu) and Darcy friction factor (f) are defined as follows [7],

$$LMTD = \frac{(T_w - T_{in}) - (T_w - T_{out})}{\ln \frac{(T_w - T_{in})}{(T_w - T_{out})}} \quad (1)$$

Heat Transfer rate

$$Q = m C_p (T_{out} - T_{in}) \quad (2)$$

$$h_m = \frac{Q}{LMTD \times A_s} \quad (3)$$

$$f = \frac{\Delta P}{0.5 \rho U_{in}^2 \frac{H}{L}} \quad (4)$$

3.1 Result Validation

The present results are validated with the experimental work of Wang and Chi [8] and a close agreement has been observed as shown in Fig 3.

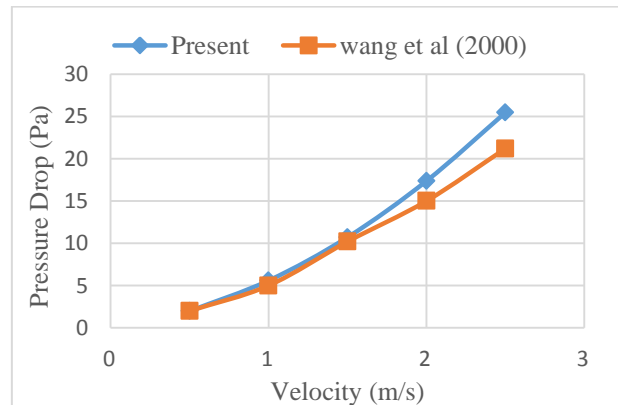


Fig 3: Validation results for N=2

3.2 Mesh dependency

For checking mesh dependency baseline N3B1 has taken for consideration. Grid 1 = 264935 nodes, Grid 2 = 361911 nodes, Grid 3 = 498982 nodes. Mesh dependency has been checked for heat transfer coefficient at different inlet velocity. From Fig 4, it is observed that at grid 1 and grid 3 gives almost the same heat transfer coefficient. For further calculation, grid 1 has taken as the best option considering time for a solution to converge.

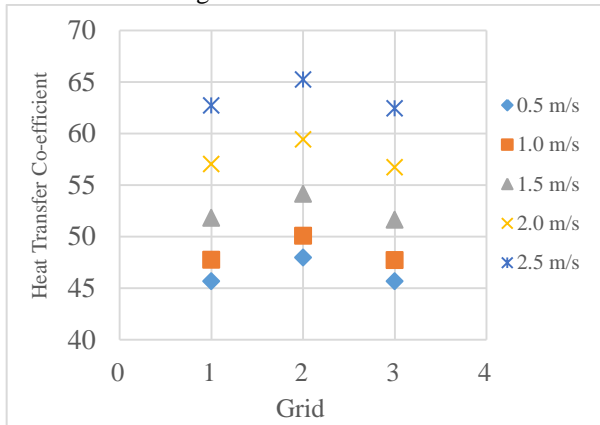


Fig 4: Grid independence results (N=3)

3.3.1 Heat Transfer rate for water-vapor

The result has been presented on Normalized Nu number and friction factor. The results are normalized (X_i/X_o), where i stands for modified cases and o stands for baseline cases. Water vapor is also taken in steads of air with all those combinations. Due to having different properties of water vapor, there is the difference in heat transfer and Nusselt number rather than air. The circular tube has a higher heat transfer rate than elliptical and rectangular tubes. Heat transfer for elliptical tube almost half than circular tubes [9].

From Fig 5, Heat transfer for N3M1 is lower at all inlet velocity than N3B2 for this reason slope of the curve is downward. But reverse action is shown for N3M2 when compared with N3B2. From Fig 6, for water-vapor N3M3 and N3M4 both have low heat transfer rate from low inlet velocity to high inlet velocity when compared with N3B1. Similar things happen for N3M3 and N3M4 when compared with N3B2. From Fig 7, these combinations are better than previous two named as N3M3 and N3M4. For water-vapor N3M5 and N3M6, both have low heat transfer rate from low inlet velocity to high inlet velocity when compared with N3B1. Similar things happen for N3M5 and N3M6 when compared with N3B2.

From Fig 8, this case is for six rows of tube. N6M1 and N6M2 are compared with N6B1, at that time heat transfer are so much lower in high inlet velocity. But N6M1 and N6M2 have also compared with N6B2 which is better than N6B1. From Fig 10, this is also similar to the previous two combination Heat transfer rate for N6M5 and N6M6 when compared with N6B2

decreases up to velocity 2 m/s is similar when velocity 2.5m/s N6M6 decreases more than N6M5.

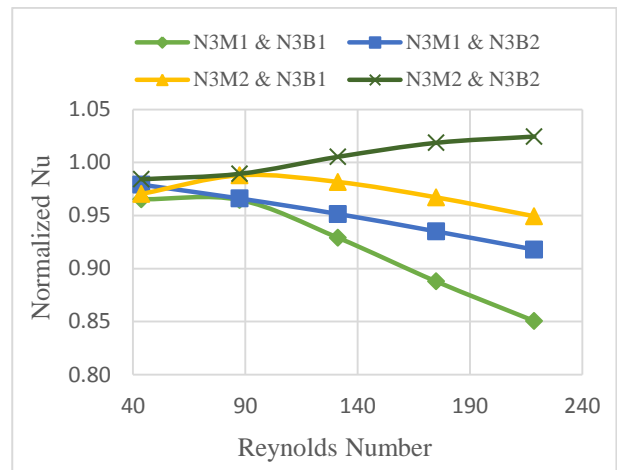


Fig 5: Normalized Nu VS Re number for N3M1 & N3M2 w.r.t N3B1 & N3B2

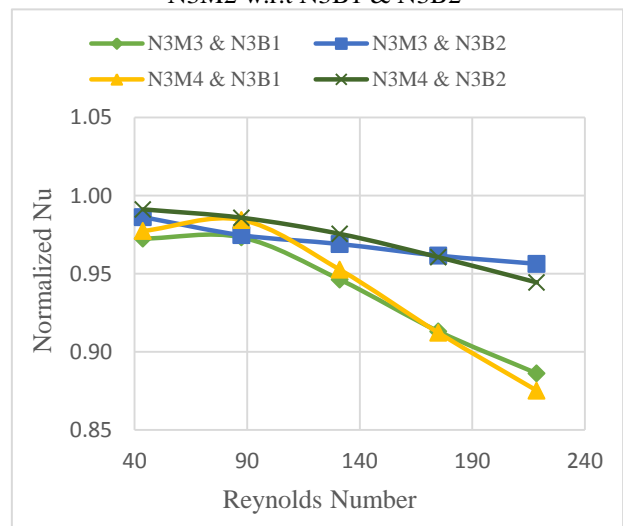


Fig 6: Normalized Nu VS Re number for N3M3 & N3M4 w.r.t N3B1 & N3B2

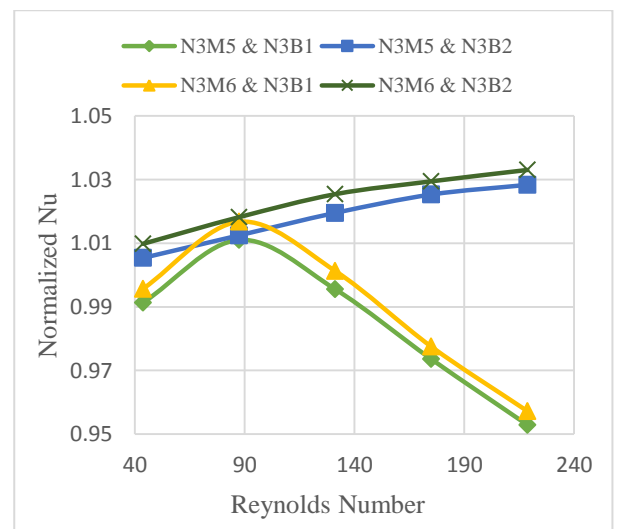


Fig 7: Normalized Nu VS Re number for N3M5 & N3M6 w.r.t N3B1 & N3B2

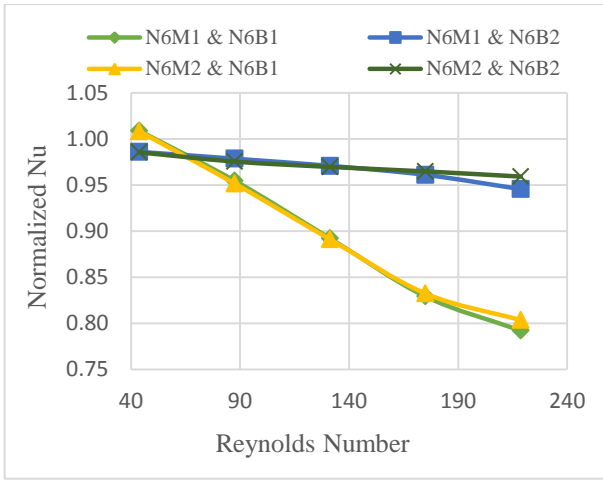


Fig 8: Normalized Nu VS Re number for N6M1 & N6M2 w.r.t N6B1 & N6B2

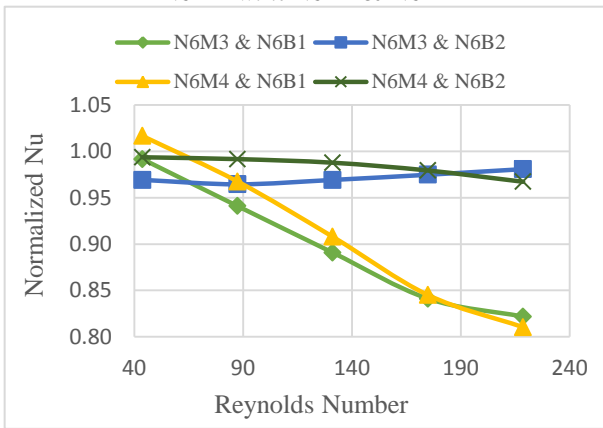


Fig 9: Normalized Nu VS Re number for N6M3 & N6M4 w.r.t N6B1 & N6B2

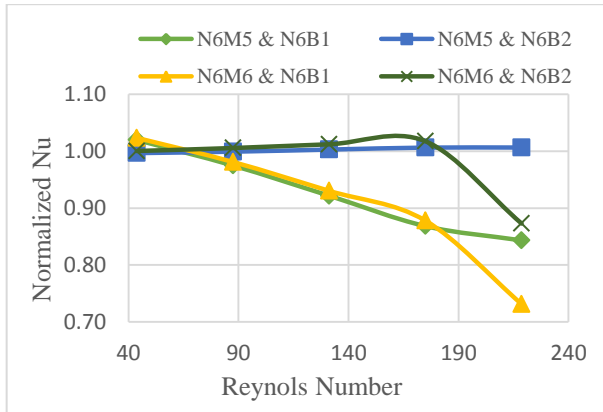


Fig 10: Normalized Nu VS Re number for N6M5 & N6M6 w.r.t N6B1 & N6B2

3.3.2 Friction factor for water-vapor

From Fig 11, N3M1 is better when compared with N3B2 because it has a lower friction coefficient. It is shown that friction for N3M2 increases having high friction factor. In contrast, the friction factor for N3M1 decreases when compared with N3B2. N3M1 combination is better when compare with N3B1. From Fig 12, it is observed that at low inlet velocity for N3M3 and N3M4, as velocity increases pressure drop reduces when both are compared with N3B1. From Fig 13, it is

shown that for N3M5 and N3M6 pressure drop reduces as velocity increases when compared with N3B1.

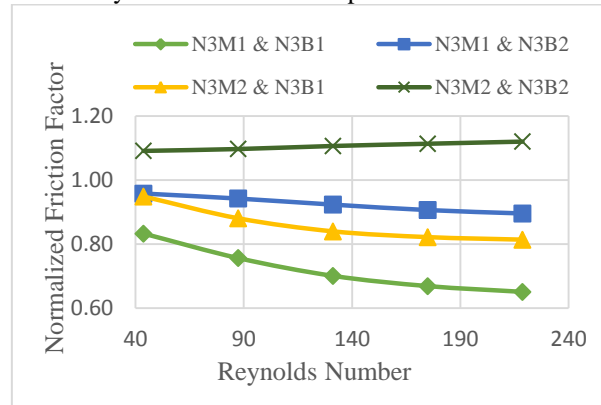


Fig 11: Normalized friction factor VS Re number for N3M1 & N3M2 w.r.t N3B1 & N3B2

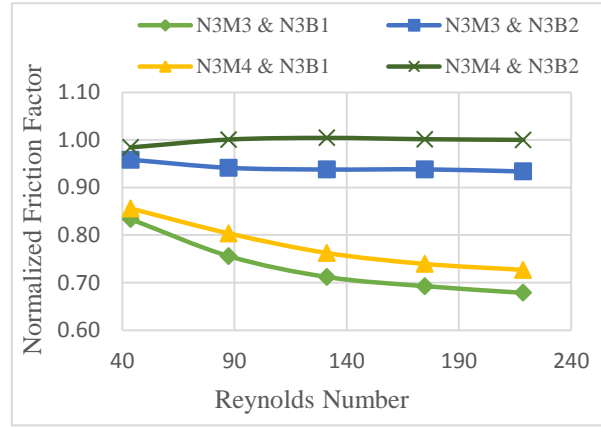


Fig 12: Normalized friction factor VS Re number for N3M3 & N3M4 w.r.t N3B1 & N3B2

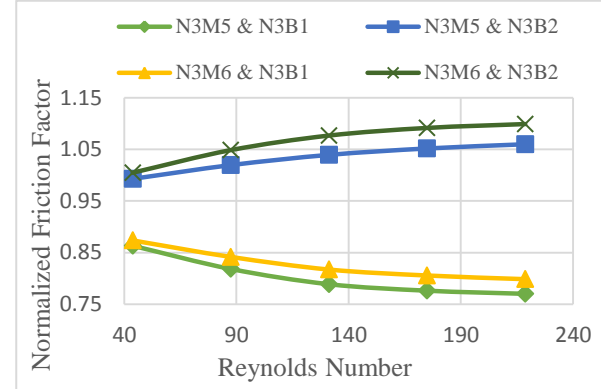


Fig 13: Normalized friction factor VS Re number for N3M5 & N3M6 w.r.t N3B1 & N3B2

From Fig 14, it is shown that N6M2 is one of the best combinations because it has much lower friction factor. For N6M2 pressure drop is higher when compared with N6B2 but friction factor decreases as velocity increases. N6M1 also have lower pressure drop when compared with N6B1 than N6B2. From Fig 15, it is inspected that, with increasing velocity, friction factor for N6M3 & N6B1 reduces while friction factor for N6M3 & N6B2 increases. N6M3 & N6B1 and N64 & N6B1 are similar their value of friction factor increases from 0.98 and 0.94 respectively. From Fig 16, it is shown for six rows

of tube that for N6M5 and N6M6 pressure drop reduces as velocity increases when compared with N6B1. Reverse action occurs when compared with N6B2.

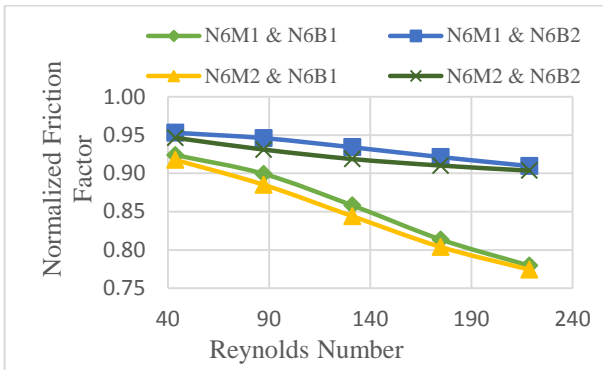


Fig 14: Normalized friction factor VS Re number for N6M1 & N6M2 w.r.t N6B1 & N6B2

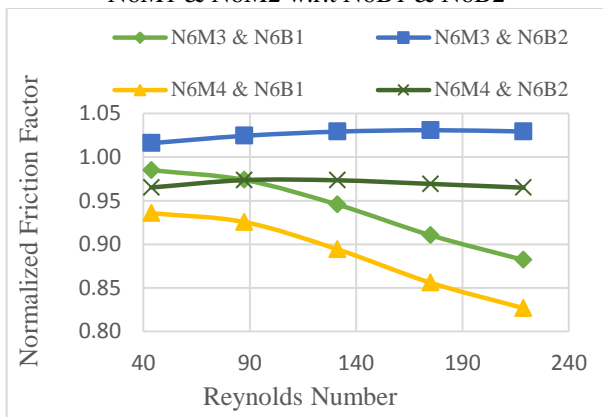


Fig 15: Normalized friction factor VS Re number for N6M3 & N6M4 w.r.t N6B1 & N6B2

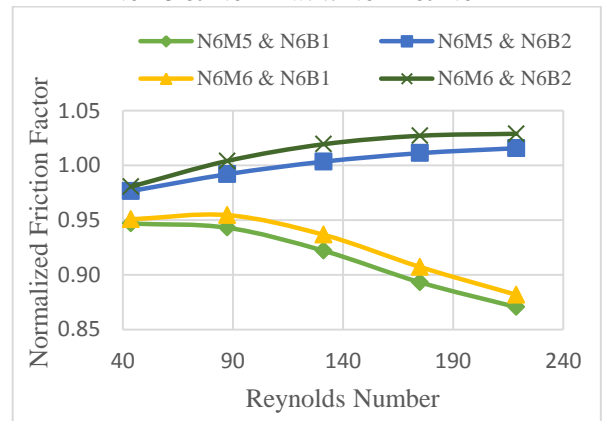
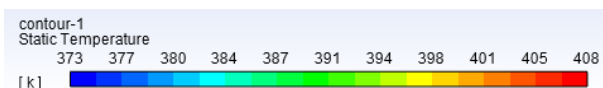


Fig 16: Normalized friction factor VS Re number for N6M5 & N6M6 w.r.t N6B1 & N6B2

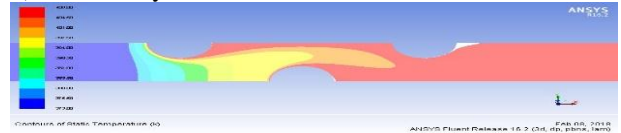
3.4.1 Temperature contour of water-vapor

The temperature distribution is shown for water-vapor for three rows of tube. There is little difference in the outlet temp of water-vapor than air.

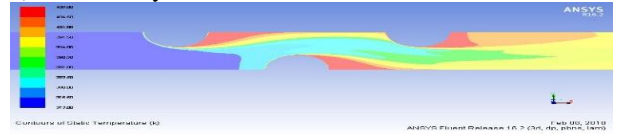
a) Temperature contour color legend



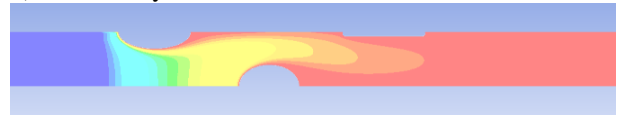
b) Geometry N3B1 0.5 m/s



c) Geometry N3B1 2.5 m/s



d) Geometry of N3M3 at 0.5 m/s



e) Geometry of N3M3 at 2.5 m/s

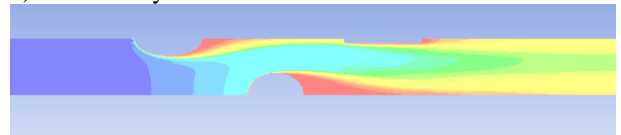


Fig 17: Temperature contour of water-vapor a) Temperature contour color legend b) N3B1 at 0.5 m/s c) N3B1 at 0.5m/s d) N3M3 at 0.5 m/s e) N3M3 at 2.5 m/s

3.4.2 Pressure contour of water-vapor

Static pressure distribution is shown for water-vapor are presented for one baseline case another for the modified case.

a) Geometry N3B1 for 0.5 m/s



b) Geometry N3B1 for 2.5 m/s



c) Geometry of N3M3 at 0.5 m/s



d) Geometry of N3M3 at 2.5 m/s



Fig 18: Pressure contour for water-vapor a) N6B1 at 0.5 m/s b) N6B1 at 2.5 m/s c) N3M3 at 0.5 m/s d) N3M3 at 2.5 m/s

3.5 Discussion

In this present simulation, water-vapor has been used as a fluid which passes over the tube. Several types of tubes have been considered for an investigation like circular, rectangular and elliptical. Several types of geometries named as a baseline and modified have been simulated. A number of tubes of rows have taken as three and six. There are some geometries which give lower friction factor than the conventional heat exchanger. On the other hand, gives a higher heat transfer coefficient than the conventional heat exchanger. Modified case 1 & 2 have 3.48% decrease in heat transfer from conventional circular tube heat exchanger. Also modified case 1 & 2 have 2.11% decrease in heat transfer from conventional elliptical tube heat exchanger. On the contrary, at high inlet velocity, modified case 2 have 10.45% higher from grouped elliptical tube heat exchanger, for modified case 6 gives 5.80% higher heat transfer from grouped elliptical tube heat exchanger when $N=3$. Again in case of water vapor when $N=3$ modified case 2 gives 2.38% higher heat transfer than baseline case 2 When $N=6$, for water-vapor, all modified heat exchanger have lower heat transfer than conventional heat exchanger 1.41 % of error occurred with the actual co-relation result. This has been due to flow separation point of the fluid over the tube surface. As long as flow adhered to the tube surface, fluid was heated up. Vortex generator could have been used to delay flow separation.

4.0 Conclusion

Water-vapor heat transfer characteristics for a different arrangement of circular, elliptical and rectangular tubes, has been numerically investigated in the laminar flow region for multiple rows. The heat exchanger with geometry N3M1 and N3M2 has been performed quite better than both circular and elliptical tubes. Similar performance has been observed for geometry N6M5 and N6M6 when compared with a conventional heat exchanger. The frictional resistance for water-vapor N3M1 N3M3 and N3M4 all have performed better than grouped circular and elliptical tubes. N6M1 and N6M2 have acted better than grouped circular tubes heat exchanger. N6M4 also performed better than grouped elliptical tubes.

Nomenclature

Symbol	Description
C_p	Specific heat capacity in J/Kg K
D	Diameter of the circular tube in m
f	Darcy Friction factor
H	Fin Height in m
h	heat transfer coefficient in W/m^2k
j	Nusselt number
k	Thermal conductivity in W/m-k
L	Length of fin in m
m	Mass flow rate of air in Kg/s
N	number of tube rows
Nu	Nusselt number

Pr	Prandtl number
Q	Heat transfer rate in W
Re	Reynolds number
T	Temperature in K
U	x -component velocity at inlet in m/s
Δp	Pressure drop in N/m^2
ΔT_{lm}	Logarithmic mean temperature difference
B	Conventional Heat Exchanger
M	Modified Heat Exchanger

References

- [1] Rich DG. The effect of fin spacing on the heat transfer and friction performance of multi-row, smooth plate fin-and-tube heat exchangers. ASHRAE Trans 1973; 79(1):137–45.
- [2] Lu CW, Huang JM, Nien WC, Wang CC, “A numerical investigation of the geometric effects on the performance of plate finned-tube heat exchanger”, Energy Conversion Manage 2011; 52:1638-43.
- [3] Rocha LAO, Saboya FEM, Vargas JVC, “A comparative study of elliptical and circular sections in one- and two-row tubes and plate fin heat exchangers” International Journal Heat Fluid Flow 1997, 18:247-252.
- [4] Xie G, Wang Q, Sunden B, “Parametric study and multiple correlations on air-side heat transfer and friction characteristics of fin-and-tube heat exchangers with large number of large-diameter tube rows”, Applied Thermal Engineering 2009; 29:1-16
- [5] R. Deepakkumar, S. Jayavel, “Airside performance of finned-tube heat exchanger with combination of circular and elliptical tubes”, Applied Thermal Engineering (2017),
- [6] Hui Han, Ya-Ling He, Yin-Shi Li, Yu Wang, “A numerical study on compact enhanced fin-and-tube heat exchangers with oval and circular tube configurations”, International Journal of Heat and Mass Transfer 65 (2013) 686–695
- [7] F. Kreith, Raj M. Manglik, Mark S. Bohn, “Principles of Heat Transfer”, Seventh Edition, Cengage Learning Inc. 2011
- [8] Wang CC, Chi KY, Chang CJ, “Heat transfer and friction characteristics of plain finned- tube heat exchangers, part II: Correlation”, International Journal Heat Mass Transfer 2000; 43:2693-700.
- [9] Jang JY, Yang JY, “Experimental and 3-D Numerical Analysis of the Thermal-Hydraulic Characteristics of Elliptic Finned-Tube Heat Exchangers”, Heat Transfer Engineering 1998, 19:55-67.

Experimental Study on NACA 2415 Airfoil with Rotating Cylinder at Leading Edge

Nashidul Islam*, Md. Mamun Islam, Mohammad Mashud, Abdullah Al Faruk

Department of Mechanical Engineering, Khulna University of Engineering & Technology, Khulna-9203, BANGLADESH

ABSTRACT

An aircraft's aerodynamic efficiency largely depends on lift and drag forces, stall angle at different stages of flight. The increase of lift and stall angle improve maneuverability and performance of any fixed wing aircraft. An experimental investigation has been conducted on a two dimensional NACA 2415 airfoil equipped with a rotating cylinder at leading edge. Rotating cylinder serve as active control device for boundary layer flow separation, thus increasing airfoil's lift and stall angle of attack. The effect of angle of attack, momentum injection ratio (ratio of cylinder linear motion to free stream air velocity) on the lift coefficient, drag coefficient and stall angle of attack are investigated in this study. The use of rotating cylinder at the leading edge of the airfoil increases the lift coefficient compared to the conventional NACA 2415 airfoil about 38.63% and stall angle increases to 16° from 12° at momentum injection ratio of 0.1173.

Keywords: NACA 2415, Coefficient of Lift, Momentum Injection Ratio, Rotating Cylinder, Stall Angle.

1. Introduction

Most common problem to solve of every aerodynamic research is to increase lift and decrease drag forces of the wing without decreasing stall angle of attack. Higher lift to drag ratio is useful in raising heavier payload and to improve maneuvering performance of fixed wing aircraft. If boundary layer separation over an airfoil is avoided this higher lift to drag ratio can be achieved [1]. The classification of boundary layer control methods into active and passive categories is one of the most common schemes. Vortex generators, distributed roughness, streamlining, and uniform blowing and suction are among various devices that are employing for the passive flow control technique. On the other hand, some of the active flow control methods are heating wall, movement of surface elements, oscillatory blowing and suction, and synthetic jets[2].

Hassan and Sankar [3] investigate the effect of fore-body boundary-induced vorticities on the generation of laminar or turbulent boundary layers over modified NACA 0012, NACA 63-218 airfoil with leading edge rotating cylinder. They use an implicit finite difference procedure to solve the two-dimensional compressible full Reynolds-averaged Navier-Stokes equation. According to investigation for subcritical flow rotating cylinder create a wall jet like effect resulted in the decline or complete elimination of surface separated flow region. Thus increasing sectional lift force by using leading edge rotating cylinder.

Tennant [4] tested a symmetrical airfoil model with a trailing edge cylinder in a low speed wind tunnel. Here lift produced as a function of cylinder speed when cylinder speed is three times higher than free stream speed. And lift produced at 0° angle of attack is 1.20 when speed ratio is 3.

X. Du and T. Lee[5] investigated the leading edge rotating cylinder (LERC) as a boundary layer control device on NACA 0015 airfoil. Here effect of a LERC on the growth, development and separation of boundary layer along with wake structure development on the

behind of symmetrical airfoil NACA 0015 airfoil had been demonstrated.

Ahmed Z. Al-Garni [6] experimentally studied a two dimensional NACA 0024 airfoil mounting a leading edge cylinder at leading edge. This experiment showed that lift coefficient of NACA 0024 airfoil increases from 0.85 to 1.63 and delay stall angle of attack by about 160%.

V. J. Modi[7] uses concept of moving surface boundary layer control applied to Joukowski airfoil throughout an experimental study by flow visualization technique. Here maximum lift coefficient achieved as around 2.73 which is approximately three times of the original airfoil.

The focus of this paper is to provide an effective- active control method of the boundary layer. This was accomplished by replacing the normally static leading edge of NACA 2415 airfoil with an input controlled rotating cylinder. Sometimes this process is known as moving surface boundary layer control (MSBLC). This investigation explains the effect of angle of attack, α and momentum injection ratio, $r=U_c/U_\infty$ on the lift, drag and stall angle of NACA 2415 airfoil.

2. Experimental Setup

First NACA 2415 airfoil surface has been generated by using C++ programming language by applying basic airfoil surface equation. Then surface has been created using SolidWorks with appropriate dimension suitable for wind tunnel testing. A cylinder groove has been cut in front of the airfoil so that external cylinder can rotate within the groove. Details dimension is given in Fig.-1. Actual model of modified NACA 2415 airfoil has been created using wood and a 24V DC motor has been directly coupled with cylinder which is to be rotated. A holding mechanism for this rotating cylinder and airfoil on wind tunnel is created which is shown in fig 2 along with wind tunnel setup. For this experiment subsonic wind tunnel of $1\text{ m} \times 1\text{ m}$ test section dimension has been used. Experiment was conducted at free stream velocity

*Corresponding Author Tel.: +88-01

E-mail addresses: i.nashidul72@gmail.com

25m/s and 30 m/s. And cylinder rotation has been used 4000 rpm. This gives momentum injection ratio, $r=0.1173$ for 25m/s free stream velocity and $r=0.097$ for 30 m/s free stream velocity. For determining static pressure on upper and lower surface of airfoil 27 pressure tube has been used distributed chord wise along a distance 10 mm. Reynolds number was 4.7×10^5 based on airfoil chord. Aerodynamic forces have been measured by integration of static pressure over the surface of airfoil assuming skin friction drag is small compared to the pressure drag.

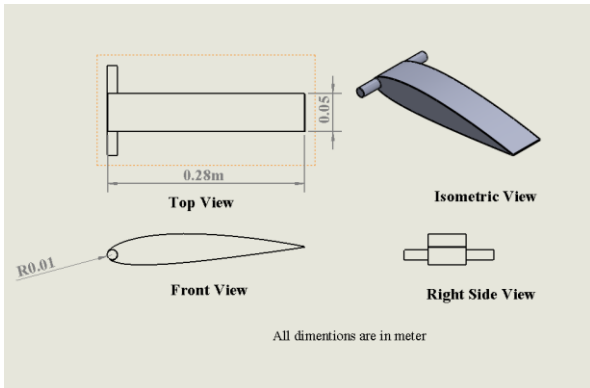


Fig.1 Dimensions of modified NACA 2415 airfoil



Fig.2 Airfoil mounted on wind tunnel.

3. Result & Discussion

Using static pressure over the airfoil, pressure coefficient at 0, 4, 8, 10, 12, 16, 20-degree angle of attack has been measured for both original NACA 2415 airfoil and with cylinder rotation at leading edge of modified NACA 2415 airfoil. From the experiment it is observed that actual NACA 2415 airfoil shows attached flow over it until 12° angle of attack. Thus stall angle, α_{stall} for NACA 2415 airfoil is 12° angle of attack. When cylinder rotation at the leading edge has been used, at 16° angle of attack flow becomes fully separated for both momentum injection ratio $r=0.1173$ and $r=0.0973$. Thus stall angle for both momentum injection ratio is $\alpha_{stall} \text{ (with momentum injection)} = 16^\circ$. This phenomenon is shown in Fig.-03 and Fig.-04 for NACA 2415 actual airfoil and

both momentum injection case in terms of pressure coefficient, C_p .

For both Fig.-03 and Fig.-04 original NACA 2415 airfoil upper surface pressure coefficient is indicated by label “original airfoil upper” and lower surface pressure coefficient as label “original airfoil lower”.

Using same technique pressure coefficient at both upper and lower surface of modified NACA 2415 airfoil is indicated using label “ $r=0.1173$ upper” and “ $r=0.097$ lower” for momentum injection ratio 0.1173 and 0.097 respectively.

From Fig.-3 it is clear that original NACA 2415 airfoil shows flow separation at 0.35C position but when momentum injection was applied then flow didn't separate in 12° AOA.

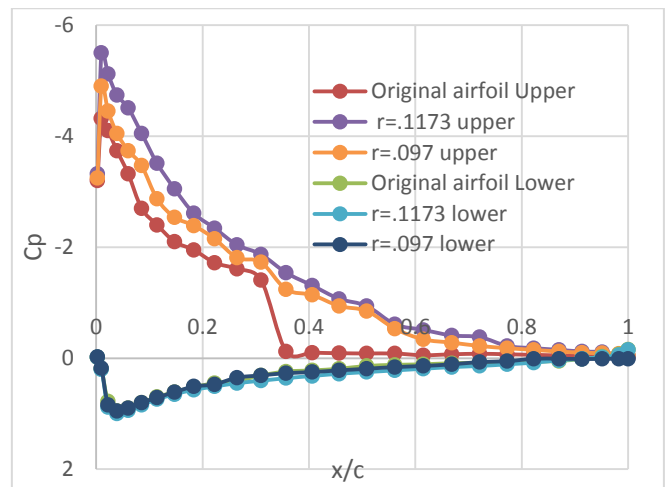


Fig.3 Effect of leading edge rotating cylinder on pressure coefficient, C_p at 12° AOA.

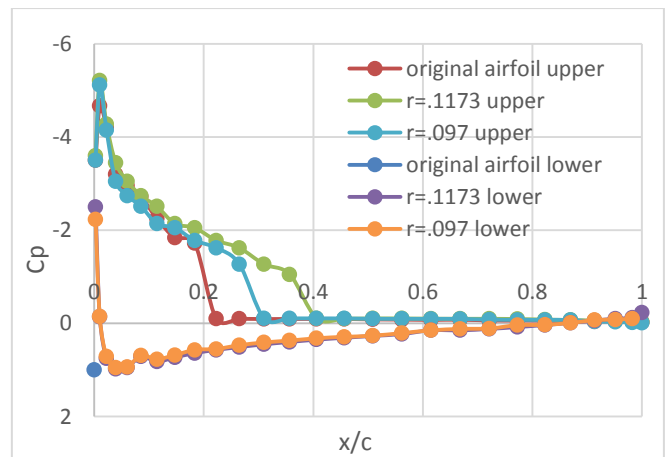


Fig. 4 Effect of leading edge rotating cylinder on pressure coefficient, C_p at 16° AOA

Fig.-4 shows separation phenomenon for all three cases without cylinder, with cylinder supplying momentum injection ratio $r=0.1173$ and $r=0.097$ at 16° AOA.

Flow separation occur 0.2C, 0.3C, 0.4C position from leading edge when using actual NACA 2415 airfoil,

Momentum injection ratio $r=0.097$ and $r=0.1173$ respectively at 16° AOA.

Fig.-5 shows lift coefficient, C_l varied when cylinder rotation is used at momentum injection ratio $r=0.1173$ and $r=0.093$ and without leading edge rotating cylinder using label “ $r=0.1173$ ”, “ $r=0.097$ ” and “original airfoil” respectively. It is clear that stall angle delayed from 12° for actual airfoil to 16° for modified airfoil when rotating cylinder is used in front of airfoil. Maximum lift coefficient increases about 38.63% for $r=0.1173$, 20.88% for $r=0.097$ than the lift coefficient of actual NACA 2415 airfoil. This increased lift coefficient helps airplane to carry more payload and increases maneuverability greatly.

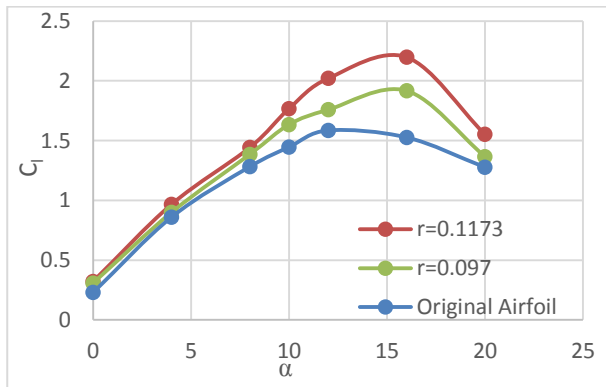


Fig. 5 Effect of rotating cylinder on lift coefficient, C_l

Lift coefficient increases with increased momentum injection rate. From Fig-5 it is evident that maximum lift coefficient at $r=0.1173$ is 2.2 and at $r=0.097$ maximum lift coefficient is 1.91 at 16° angle of attack for modified NACA 2415 airfoil. Maximum lift coefficient is 1.58 at 12° angle of attack for original NACA 2415 airfoil.

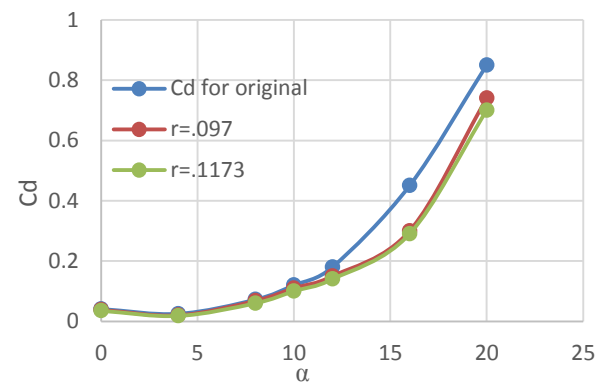


Fig. 6 Effect of rotating cylinder on drag coefficient C_d

It is clear that pressure drag decreases with the increase of momentum injection ratio. For actual NACA 2415 airfoil drag coefficient is $C_d=0.85$ at 20° AOA and when momentum injection ratio, $r=0.1173$ C_d is 0.7 at 20° AOA.

4. Conclusion

The wind tunnel test program shows that leading edge rotating cylinder with airfoil is a successful device that produce more section lift than normal airfoil at the same angle of attack hence reducing the need for higher angle of attack to achieve more lift. With high momentum injection ratio in the leading edge lift coefficient increases and stall angle of attack delayed. The increase in lift coefficient and stall angle of attack for momentum injection ratio, $r = 0.1173$ is about 38.63% and 4° angle of attack respectively. This increase in the lift coefficient and stall angle of attack would make an airplane fitted with such an airfoil more maneuverable and improve its performance in terms of STOL. And C_d decreases slightly when using momentum injection. This also helpful in airplane economy.

NOMENCLATURE

- C : Chord Length
- C_l : Lift Coefficient
- C_d : Drag coefficient
- C_p : Pressure coefficient
- r : Momentum injection ratio
- α : Angle of attack

REFERENCES

- [1] H. Schlichting, K. Gersten, *Boundary-layer theory* (New York: McGraw-Hill) (2017)
- [2] T. Moghaddamand, N.B. Neishabouri, The Active and Passive Flow Separation Control Techniques over Airfoils, *IOP Conference Series: Material Science and Engineering*, Vol. 248 (2017)
- [3] A.A. Hassan, L.N. Sankart, Separation Control Using Moving Surface Effects: A Numerical Simulation, Vol. 29 (1991)
- [4] J.S. Tennant, W.S. Johnson, A. Krothapalli, Rotating cylinder for circulation control on an airfoil, *Journal of Hydronautics*, Vol. 10, pp: 102–5 (1976)
- [5] T. Lee, F. Mokhtarian, F. Kafyeke, Flow Past an Airfoil with a Leading-Edge Rotation Cylinder, *Journal of Aircraft*, Vol. 39, pp: 1079–84 (2002)
- [6] A. Z. Al-Garni, A.M. Al-Garni, S. A. Ahmed, A. Z. Sahin, Flow Control for an Airfoil with Leading-Edge Rotation: An Experimental Study, *Journal of Aircraft*, Vol. 37, pp: 617–22, (2000)
- [7] V.J. Modi, F. Mokhtarian, T. Yokomizo, Moving Surface Boundary-Layer Control as Applied to Two-Dimensional Airfoils, *Journal of Aircraft*, Vol. 28, pp: 104–12 (1990).

Numerical Solution of One-Dimensional Heat Equation by Crank Nicolson Method

Md. Amirul Islam^{1,*}, S.M. Kamal Hossain², Abdur Rashid³

^{1,2}Department of Mathematics, Uttara University Dhaka-1230, Bangladesh

³Department of Mathematics, Jahangirnagar University, Savar, Dhaka-1342, Bangladesh

Corresponding author: amirul.math@gmail.com

ABSTRACT

In this paper we consider a Crank Nicolson algorithm for solving one-dimensional heat equation. In numerical analysis, the Crank–Nicolson method is a finite difference method used for numerically solving the heat equation and similar partial differential equations. The proposed method is quite efficient and is practically well suited for solving this problem. We compare numerical solution with the exact solution. The numerical solution is in good agreement with the exact solution. Finally, we investigate and compute the numerical results of proposed method for different step size. Several examples are given to verify the applicability and efficiency of the proposed method.

Keywords: Heat equation, Crank–Nicolson method, Numerical Solution Schemes, Application examples.

1. Introduction

The majority of practical design problems fall outside the reach of closed form solutions due to the complex and irregular form of structures, complexity of loading conditions, non-linearity and in homogeneity in properties of materials. For this reason, there is a growing interest in numerical methods for the solution of continuum mechanics problems. In such instances Finite difference Method (FDM) were used extensively in the 1960s. Now a day the FDM is a powerful tool for the approximate solution of differential equations governing diverse physical phenomena. Its use in industry and research is extensive, and indeed without it many problems in science and engineering would be incapable of solution. In finite difference, the mesh consists of rows and columns of orthogonal lines. In this paper we have used Crank Nicolson method to find numerical solution of heat equation. The Crank–Nicolson method is a finite difference method (FDM). It is used for finding numerical solution of engineering problems. Finite difference method is one of the numerical methods that are known as a highly applicable method in a lot of scientific fields. In many situations, finding an analytic solution to partial differential equations (PDE) is impossible, where numerical method are used to find approximate solutions. In real world, most of the problems in science and engineering are complicated enough that they can only be solved numerically. The heat equation plays a significant role in various physical problems.

Dehghan [1] developed numerical schemes for obtaining approximate solutions to the initial boundary-value problem for one-dimensional second-order linear parabolic partial differential equation with non-local boundary specifications replacing boundary conditions. Mebrate [2] discussed Finite difference method and Finite element methods to compute the numerical solutions of a one dimensional heat equation together with initial condition and Dirichlet boundary conditions.

Jamet [3] analyzed Stability and Convergence of a Generalized Crank-Nicolson Scheme on a Variable Mesh for the Heat Equation. Szyszka [4] presented an implicit finite difference method (FDM) for solving initial-boundary value problems (IBVP) for one-dimensional wave equation. He [5] applied the homotopy perturbation method to the search for traveling wave solutions of nonlinear wave equations. Abbasbandy [6] analyzed He's variational iteration method to the wave equations in an infinite one-dimensional medium and some non-linear diffusion equations. Noor and Mohyud-Din [7] applied Variational iteration method for solving higher-order nonlinear boundary value problems using He's polynomials. Han *et al.* [8] proposed a finite-difference scheme for the one-dimensional time-dependent Schrödinger equation. In this paper, we have applied developed Crank Nicolson method to solve one dimensional heat equation.

This paper is organized as follows. In section 2 problem formulations, in section 3 numerical solution schemes, in section 4 Application examples, in section 5 discussion of results and in the last section the conclusion of the paper is presented.

2. Problem formulation

The one dimensional heat flow equation is defined by

$$\frac{\partial u(x,t)}{\partial t} = \beta \frac{\partial^2 u(x,t)}{\partial x^2} \quad (1.1)$$

with initial and boundary conditions(IBC)

$$u(0,t) = T_0, u(l,t) = T_1, u(x,0) = f(x) \quad (1.2)$$

where $u = u(x,t)$ is the dependent variable, T_0 is a constant temperature along time axis, T_1 is a constant Temperature along $x = l$ and β is a constant coefficient. We have to solve equation (1.1) to replace

* Corresponding e-mail address: amirul.math@gmail.com

the partial differential coefficients by the finite difference approximations: At the point u_j^i the finite

difference approximation for $\frac{\partial^2 u(x,t)}{\partial x^2}$ is

$$\frac{\partial^2 u(x,t)}{\partial x^2} = \frac{u_j^{i+1} - 2u_j^i + u_j^{i-1}}{h^2} \quad (1.3)$$

At the point u_{j+1}^i the finite difference approximation

for $\frac{\partial^2 u(x,t)}{\partial x^2}$ is

$$\frac{\partial^2 u(x,t)}{\partial x^2} = \frac{u_{j+1}^{i+1} - 2u_{j+1}^i + u_{j+1}^{i-1}}{h^2} \quad (1.4)$$

Taking the average of (1.3) and (1.4) we have

$$\frac{\partial^2 u(x,t)}{\partial x^2} = \frac{u_{j+1}^{i+1} - 2u_{j+1}^i + u_{j+1}^{i-1} + u_j^{i+1} - 2u_j^i + u_j^{i-1}}{2h^2} \quad (1.5)$$

the forward difference approximation for $\frac{\partial u(x,t)}{\partial t}$ is

$$\frac{\partial u(x,t)}{\partial t} = \frac{u_{j+1}^i - u_j^i}{k} \quad (1.6)$$

Substituting (1.5) and (1.6) in (1.1) we get the following equation

$$\begin{aligned} & \delta(u_{j+1}^{i+1} + u_{j+1}^{i-1}) - (2\delta + 2)u_{j+1}^i \\ & = (2\delta - 2)u_j^i - \delta(u_j^{i+1} + u_j^{i-1}) \end{aligned} \quad (1.7)$$

Where $\delta = \frac{k}{h^2 \beta}$ and equation (1.7) is called the

Crank-Nicolson finite difference scheme for heat flow equation.

3. Numerical Solution Schemes

Partial differential equations with specified initial and boundary conditions can be solved in a given region by replacing the partial derivatives by their finite difference approximations (FDA). The finite difference approximations to partial derivatives at a point (x_i, t_j) are described as : The xy -plane is divided into a network of rectangles of length $\Delta x = h$ and breadth $\Delta t = k$ by drawing the lines $x_i = ih$ and $t_j = jk$ parallel to x and y axes. The points of intersection of these lines are called grid points or mesh points or lattice points. The grid point (x_i, t_j) are denoted by u_j^i . The approximate value of u_j^i can be obtained by using equation (7) for all values of i and j .

4. Application Examples

In this section, we consider two linear heat flow problems to verify accuracy of the proposed Crank Nicolson Method. Numerical results are computed and the outcomes are represented by graphically.

Example 1: We consider one dimensional heat flow equation, $u_t = 2u_{xx}$ with initial and boundary conditions (IBC): $u(x,0) = 3\sin(\pi x) - 2\sin(5\pi x)$, $u(0,t) = 0, u(4,t) = 0$ on the interval $0 \leq x \leq 4$ and $0 \leq t \leq 4$. The exact solution of the given problem is $u(x,t) = 3e^{-2\pi^2 t} \sin(\pi x) - 2e^{-50\pi^2 t} \sin(5\pi x)$. The exact solution is obtained and shown in figure.1 (a) and approximate results are obtained and shown in figures 1(b) and 1(c) and 1(d).

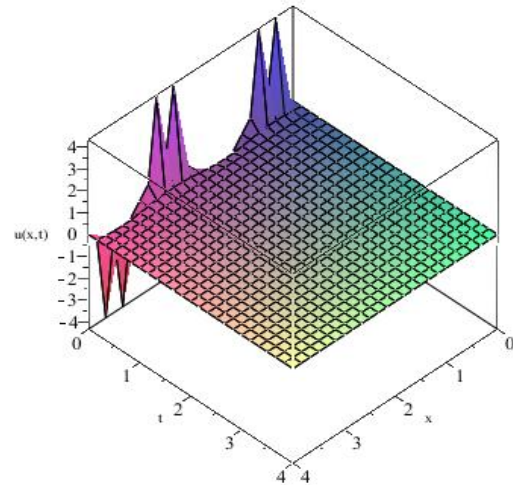


Fig1 (a): Exact solution $u(x,t)$ for different values of x and t of the given problem.

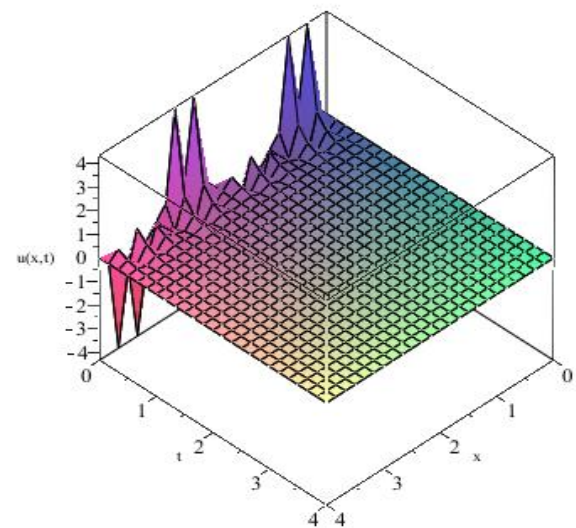


Fig1 (b): Approximate solution $u(x,t)$ for space step, $h=0.04$ and time step, $k=0.04$.

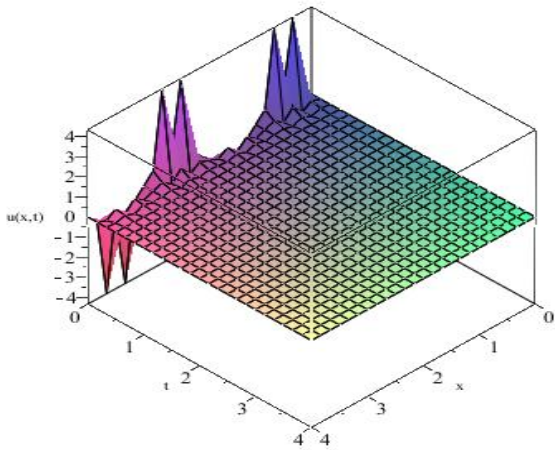


Fig1 (c): Approximate solution $u(x,t)$ for space step, $h=0.03$ and time step, $k=0.03$.

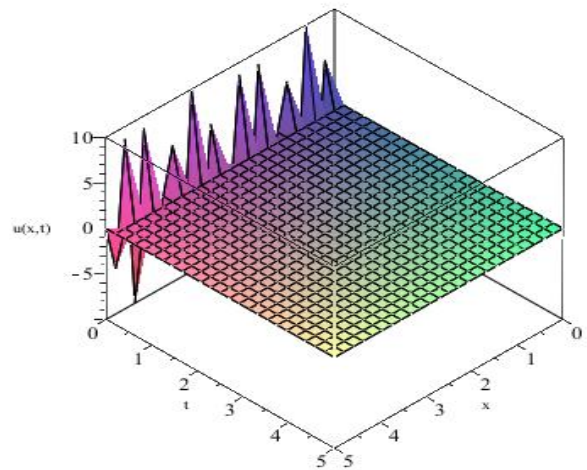


Fig2 (a): Exact solution $u(x,t)$ for different values of x and t of the given problem.

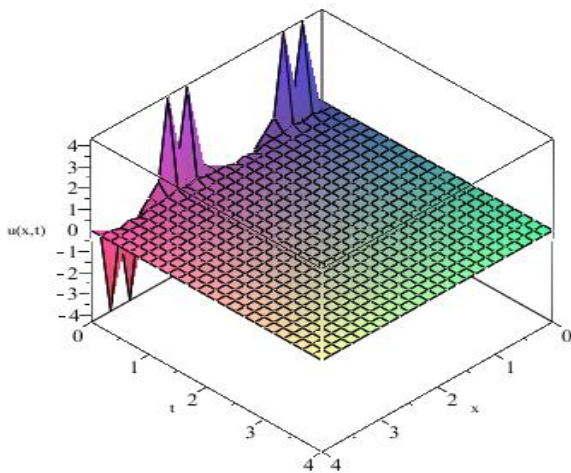


Fig1 (d): Approximate solution $u(x,t)$ for space step, $h=0.025$ and time step, $k=0.025$.

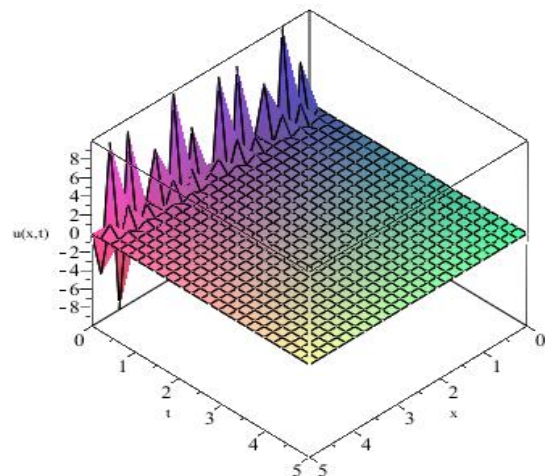


Fig2 (b): Approximate solution $u(x,t)$ for space step, $h=0.04$ and time step, $k=0.04$.

Example 2: We consider one dimensional heat flow equation, $u_t = 2u_{xx}$ with initial and boundary conditions (IBC):

$u(x,0) = 10\sin(4\pi x), u(0,t) = 0, u(5,t) = 0$ on the interval $0 \leq x \leq 5$ and $0 \leq t \leq 5$. The exact solution of the given problem is given by $u(x,t) = 10e^{-32\pi^2 t} \sin(4\pi x)$. The exact solution is obtained and shown in figure 2(a) and approximate results are obtained and shown in figures 2(b) and 2(c) and 2(d).

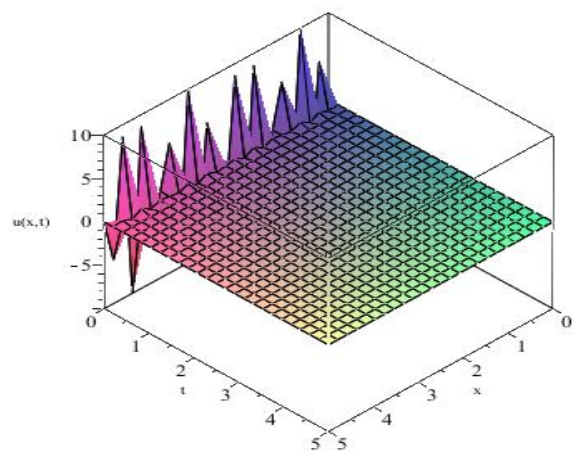


Fig2 (c): Approximate solution $u(x,t)$ for space step, $h=0.03$ and time step, $k=0.03$.

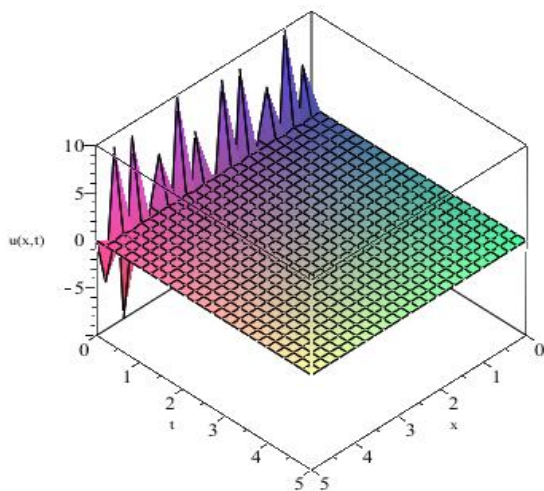


Fig2 (d): Approximate solution $u(x,t)$ for space step, $h=0.025$ and time step, $k=0.025$.

5. Discussion of results

The accuracy of the solution will depend on step size, h and k . In order to compare the approximate solution with the exact solution we consider two numerical examples. The effect of the space step h and time step k in the solution is shown in all figures: 1(a)-1(d) and figures: 2(a)-2(d). To obtain more accurate results, h should be small and k is necessarily very small. A numerical method is said to be convergent if

$$\lim_{\substack{h \rightarrow 0 \\ k \rightarrow 0}} \max_{1 \leq n \leq N} |U(x_n, t_n) - u(x_n, t_n)| = 0.$$

Where $U(x_n, t_n)$ denotes the exact solution and $u(x_n, t_n)$ denotes the approximate solution. The approximated solution is evaluated by using Maple software for proposed numerical method at different step sizes. Finally we observe that the proposed Crank Nicolson method is converging faster if $\Delta x = h \rightarrow 0$ and $\Delta t = k \rightarrow 0$ and it is the most effective method for solving initial boundary value problems for partial differential equations (PDE).

6. Conclusion

In this paper, we have applied the Crank Nicolson algorithm to develop numerical solution scheme for the heat equation. We present two numerical tests to show the convergence and efficiency of the proposed numerical method. To find more accurate results to need the step sizes smaller for this proposed method. From the figures we can see the accuracy of the method for decreasing the step size h and k the graph of the approximate solution approaches to the graph of the exact solution. The numerical solutions obtained by the proposed method are in good agreement with exact solutions. From the study the proposed method was found to be generally more accurate and also the approximate solution converged faster to the exact

solution. It may be concluded that the Crank Nicolson method is powerful and more efficient in finding numerical solutions of initial boundary value problems (IBVP) of heat equation.

ACKNOWLEDGEMENTS

The authors would like to express their sincere thanks to the referees for their valuable suggestions which helped to improve the presentation of the paper. We would also like to show our gratitude to the Professor Dr. Nurul Alam khan and Dr. Shahansha khan for sharing their pearls of wisdom with us during of this research work.

REFERENCES

- [1] M. Dehghan, Numerical solution of a parabolic equation with non-local boundary specifications, *Appl. Math & Comp*, Vol. 145(1), pp. 185-194 (2003).
- [2] B. Mebrate, Numerical Solution of a One Dimensional Heat Equation with Dirichlet Boundary Conditions, *Amer. Jour. Appl. Math.*, Vol. 3(6), pp. 305-311 (2015).
- [3] P. Jamet, Stability and Convergence of a Generalized Crank-Nicolson Scheme on a Variable Mesh for the Heat Equation, *SIAM Jour. Num. Anal*, Vol. 17, No. 4, pp. 530-539 (1980).
- [4] B. Szyszka, A nine-point finite difference scheme for one-dimensional wave equation", *AIP Conference Proceedings*, Vol.1863, No.1, pp.56-78 (2017).
- [5] J.H. He, Application of homotopy perturbation method to nonlinear wave equations, *Chaos Solitons Fractals*, Vol.26 (3), pp.695-700(2005).
- [6] S. Abbasbandy, Numerical method for non-linear wave and diffusion equations by the variational iteration method, *Int. J. Numer. Mech. Engrg.*, Vol. 73, No.12, pp.1836-1843(2008).
- [7] M.A. Noor, S.T. Mohyud-Din, Variational iteration method for solving higher-order nonlinear boundary value problems using He's polynomials, *Int. J. Nonlinear Sci. Numer. Simul.*, Vol.9, No.2, pp.141-156(2008).
- [8] HAN, H., JIN, J., WU, X., A Finite-Difference Method for the One-Dimensional Time-Dependent Schrödinger Equation on Unbounded Domain, *Comp. & Math. With Appl.*, Vol.50, pp.1345-1362(2005).

Air Pollutants Emission from Coal Fired Kiln and Its Variation for Use of Different Fuel Types

Md. Riad-Ul-Hasan*, Kazi ABM Mohiuddin

Department of Civil Engineering, Khulna University of Engineering & Technology, Khulna-9203, BANGLADESH

ABSTRACT

Air pollution due to brick kiln has been an increasing environmental concern in Bangladesh. This study investigates the emission from Coal fired brick kiln in Rupdia, Jessore. The emission of air pollutants such as PM₁₀, SO₂, CO, NO_x, and VOC_s are calculated using the Emission Factor Method. Brick kiln emission was found for PM₁₀ (9.45 ton/yr), SO₂ (8.1 ton/yr), CO (5.4 ton/yr) and NO_x (3.037 ton/yr). Total amount of VOC_s emission is calculated as 9.91 kg/yr. There are also some metal emissions from the brick kiln which emitted in the form of particulate matter. It is observed that emission of PM₁₀, SO₂, and NO_x is higher in coal fired kiln whereas CO and VOC_s are dominant in Natural gas fired kiln. This emission assessment of brick kiln is significant for emission reporting, and emission database for the brick kiln in Bangladesh.

Keywords: Air pollutants, Emission estimation, Particulate matter, Volatile organic content.

1. Introduction

Brick as popular construction material has been using since ancient times. Like other developing countries Bangladesh has its major priority is on infrastructure development which poses increasing demand of bricks. Brick manufacturing industry is a significant industrial sector in Bangladesh which contributes about one per cent to the country's gross domestic product (GDP). [1] About one million people in this country are working in brick manufacturing industry. As there are some paucity of stone aggregate in this country, brick has become the main building material for the country's construction industry. It's grew an average of about 5.6 per cent per year [2]. The current population of the country is assessed at around 160.8 million [3]. A large portion of this huge population is migrating to the urban areas for better living condition. This trend eventually directed the brick sector to increase annually at a projected 2-3 per cent over the next decade for housing construction and commercial sector development [4]. For long time the brick kilns and technology which are used in this country remained unchanged and still consumes energy inefficiently. Most of the kilns are using Biomass, mainly firewood and rice husk as their major energy sources [5]. Manufacture of brick is traditionally a cottage industry which produces bricks only for local consumption in this country. But its technological development is inadequate. Though brick making is a significant industry in this country, most of the kilns use outdated, energy intensive technologies. They are greatly harmful for the environment. Brick kilns are the main sources of fine particulate pollution. It leads to harmful impacts on human health, animals, agricultural yields and global warming. Fixed chimney kiln (FCK) are currently used all over the country. But there are some new technologies such as Vertical Shaft Brick Kiln (VSBK) and the Hybrid Hoffmann Kiln (HHL), which are substantially cleaner than the previous one. These improved technologies consume less energy and emit lower levels of pollutants and greenhouse gases (GHGs) [1, 6]. In Bangladesh, existing brick kilns are mainly

responsible for fine particulate pollution. The total greenhouse gas (GHG) emission in this country is estimated to be 15.67 million tons of carbon dioxide (CO₂) equivalents (tCO₂e) per annum. In Bangladesh, 92% of the 4880 [7] brickfields are highly polluting Fixed Chimney Kilns (FCKs) because of a combination of low capital cost requirement and high investment return. However, these kinds of kiln use more coal/wooded fuel, which emits more carbon. Brick manufacturing causes the emission of various harmful gases such as Sulphur oxides (SO_x), Nitrogen Oxides (NO_x), Carbon dioxide (CO₂) and Suspended Particulate Matter (SPM) and PM₁₀ [8]. These gases have major contribution to the local air pollution. In Bangladesh, about 50 per cent of the brick kiln use coal to bake brick. Now a day's coal is considered the source of some 20 per cent of global greenhouse gas emissions [9]. The poor quality of coal and uses of biomass cause poor emission from brick kilns. The main pollutants which emitted from the brickfields are particulate matter (PM), some hazardous gas like CO₂, CO, NO_x, NO and SO₂. Though the PM concentration appears to be low but it is expected to have long term massive impact on global environments as well as on human health. The particulate matter consists of dust, smoke, fumes and fly ash [10]. It was found that particulate matter was a major pollutant in the cluster region of brick kilns in Bangladesh when studied the pollutant load within that region. The objectives of this study is to estimate the emission of air pollutants from brick kiln and compare the emission of air pollutants due to different fuel types (coal, natural gas, sawdust) used in brick kiln.

* Md. Riad-Ul-Hasan Tel.: +88-01776097677
E-mail address: riad11248@gmail.com

2. Research Method

This study is to be based mostly on information that has been collected from field survey and hand calculation.



Fig. 1: The selected brick field for the study

2.1 Emission Estimation

An emission factor is a tool that is used to estimate emissions to the environment. In this Manual, it relates the quantity of substances emitted from a source to some common activity associated with those emissions. Emission factors are obtained from US, European, and Australian sources and are usually expressed as the weight of a substance emitted multiplied by the unit weight, volume, distance, or duration of the activity emitting the substance. These emission factors are developed from measurements for a specific brick kiln. But they may sometimes be used to estimate emissions at other sites also. A company needs not to operate several units of similar size and configuration. When emissions were measured from one brick kiln or kiln process, an emission factor could be developed and applied to similar kilns and processes. As previously mentioned, it is advisable to have the emission factor reviewed and approved by your local environmental authority prior to its use for NPI estimations. There are various methods for estimating brick kiln emission. Here we will follow emission factor and fuel analysis data method from Emission Estimation Technique Manual for Brick, Ceramics & Clay Product Manufacturing which is under National Pollutant inventory (NPI) of Australia 1998. [11]

Air pollutants like PM₁₀, CO, SO₂, NO_x and VOC_s from brick kiln can be estimated directly by using emission factors with the following equation (i)

$$E = A * T * EF * [1 - (ER/100)] \dots\dots\dots (i)$$

Where:

- E = emissions;
- A = activity rate (usually production rate);
- T = time (or another variable);
- EF = uncontrolled emission factor; and
- ER = overall emission reduction efficiency, %.

From the above equation we have calculated the amount of air pollutants emission from the brick kiln. In this equation there are four variables. Among the four variables activity rate or production rate and annual operating time of the brick kiln have to be collected from field visit. And if the brick field use any emission reduction techniques then the overall percent emission reduction efficiency should also have to be collected from the field visit. All the uncontrolled emission factor are collected from Emission Estimation Technique Manual for Brick, Ceramics & Clay Product Manufacturing which is under National Pollutant inventory (NPI) of Australia 1998. [11] Emission factor for various air pollutants are given below on the Table-1.

Table 1: Emission Factor for Brick Manufacturing

Process	PM ₁₀	SO ₂	CO	NO _x
Natural gas fired kiln	0.435	0.39	0.6	0.175
Uncontrolled coal fired kiln	0.7	0.6	0.4	0.255
Sawdust fired kiln	0.425	0.435	0.8	0.185

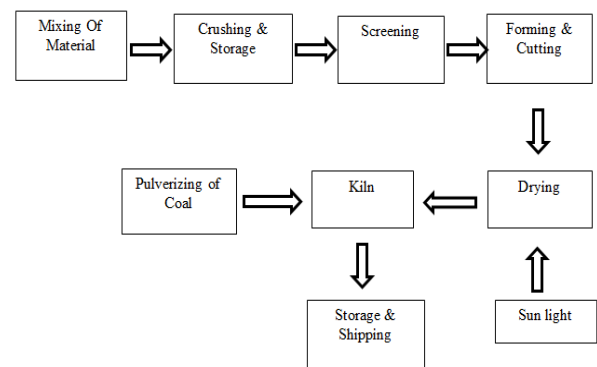


Fig. 2: Process Flow Diagram of a Brick Manufacturing

3. Results and Discussion

The brick kiln is a moderate size kiln. It is 200 ft in length and about 70 ft in width. It has 46 burning chamber in which the brick are burnt. The smoke which emits from the burning of coal was collected by a pump and released by the chimney. The chimney is about 120 ft in height. Its radius is 16 ft in bottom and 3 ft in the top. The mold of soil and water is mixed first then it is formed in the shape of desired size and dried in the sun light. After drying the brick is brought to the kiln and burnt there. Meanwhile the coal is pulverized and used in the kiln as fuel. After burning the brick are unloaded.

3.1 Emission from Brick Kiln

Table 2: Emission from Brick Kiln at Rupdia, Jessore

Process	PM ₁₀ (ton/yr)	SO ₂ (ton/yr)	CO (ton/yr)	NO _x (ton/yr)	VOC _s (ton/yr)
Uncontrolled coal fired kiln	9.45	8.1	5.4	3.037	9.9 × 10 ⁻³

The following figures (fig 3 to 7) show various types of emission and their specification due to use of different fuel types. Such as coal fired kiln, natural gas fired and sawdust fired. Such fuels have their own criteria for emission of different element. The main elements that emits from a brick kiln are PM₁₀, SO₂, CO, NO_x and VOC_s.

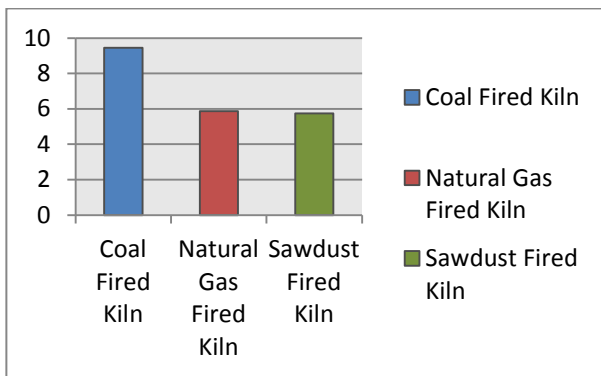


Fig 3: PM₁₀ Emission (Ton/yr)

From this figure (fig 3) it is visible that emission of PM₁₀ in coal fired kiln is very high than other kiln. In case of Natural Gas and Sawdust fired kiln its emission is quite same. As because coal emits lots of Black Carbon and other micro particle as the kiln use very fine coal. Chance of emission of fine particle is very much less in Natural gas and Sawdust fired kiln.

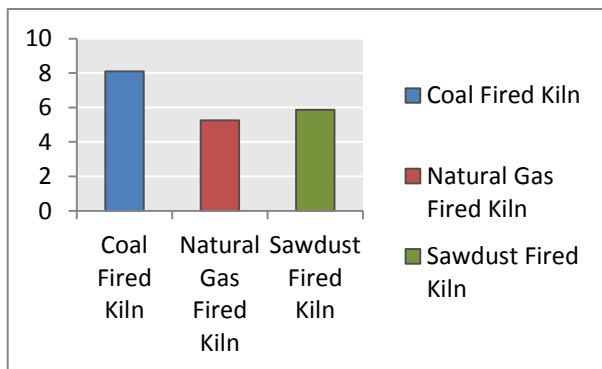


Fig 4: SO₂ Emission (Ton/yr)

This figure (fig 4) shows that in Natural gas and Sawdust fired kiln there is a little difference in SO₂ emission but in case of Coal fired kiln the deviation is very high and it emits a large amount of SO₂ than the other as the coal

have a greater proportion of Sulphur than any other gas or dust particle.

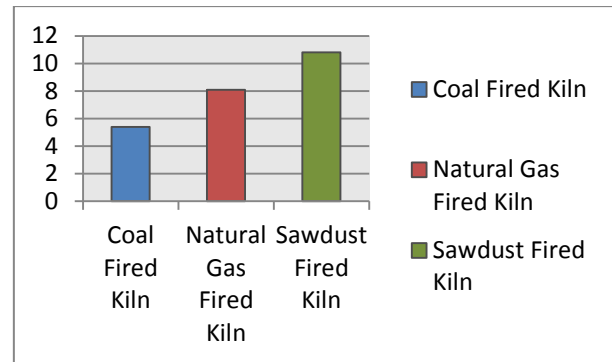


Fig 5: CO Emission (Ton/yr)

Natural gas and Sawdust possess larger amount of organic content. Combustion of this organic content produces a huge amount of carbon monoxide. Coal has other inorganic content also so a coal fired kiln emits less amount of CO than other. Meanwhile Sawdust and Natural gas fired kiln emits huge amount of CO.

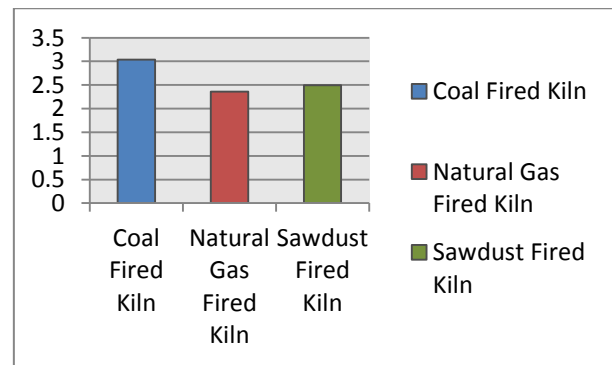
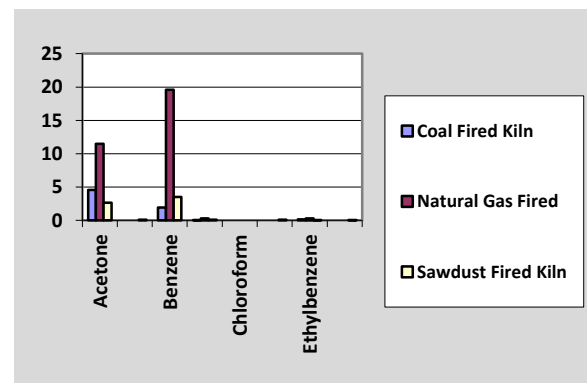


Fig 6: NO_x Emission (Ton/yr)

Emission of NO_x fluctuates very less for different fuel. It is clearly visible in the above figure. All types of fuel generate about same amount of NO_x.



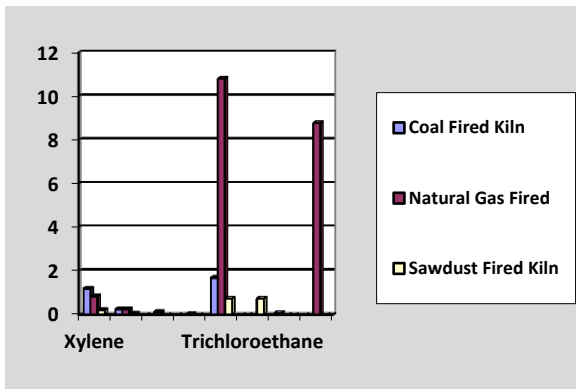


Fig 7: Typical VOCs Emission (kg/yr)

Emission of VOC_s is almost same for all type of fuel excluding some particle such as Acetone, Benzene, toluene and Chlorine. In every case it has been shown that Natural gas fired kiln emits the maximum amount of VOC_s. from the following figure it can be seen that emission of Acetone, Benzene, toluene and Chlorine are larger and maximum emission occurred in case of Natural gas fired kiln. In Natural gas there are a lot of organic content which decomposed and produce different hydrocarbon.

The following figure (fig 8) shows the other types of emission like Arsenic, Beryllium, Manganese and Mercury. Arsenic is emitted much by Coal fired kiln but the maximum amount of manganese is emitted by Natural gas fired kiln.

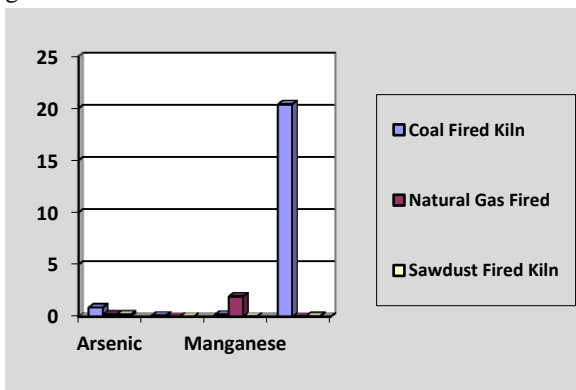


Fig 8: Metal Emissions (kg/yr)

4. Conclusion

Air pollution due to brick kiln emission is an increasing environmental concern in Bangladesh. This study was visualized the current state of air pollution from brick kiln , major sources of air pollutant, and suggests future strategies to reduce the air pollution in Jessore city and throughout the country. The emission from brick kiln were found for PM₁₀ (9.45 tone/yr), SO₂ (8.1 tone/yr), CO (5.4 tone/yr), NO_x (3.037 tone/yr) and various type of VOC_s as respectively. comparison between emission due to use of different fuel types was shown where it is visible that Coal fired kiln emits more amount of PM₁₀, SO₂ and NO_x but

less amount of CO than Natural gas and Sawdust fired kiln. Maximum amount of CO emission occurred at sawdust fire kiln. Whereas VOC_s is dominant in natural gas fired kiln.

REFERENCES

- [1] BUET. (2007). Small study on air quality of impacts of the North Dhaka brickfield cluster by modeling of emissions and suggestions for mitigation measures including financing models. Prepared by the Chemical Engineering Department, vol. 11. pp. 55-61.
- [2] Arifur, R. (2006). Introduction of brick kiln and their carbon emission in Bangladesh. CASE Project. Funded by the Energy Sector Management Assistance Program (ESMAP) of the World Bank. Final project report. vol.6. pp. 14-29.
- [3] Bangladesh Economic Review. (2018). Finance Division, Ministry of Finance, Government of Bangladesh.
- [4] WB (2010). Introducing Energy-Efficient Clean Technologies in the Brick Sector of Bangladesh, Report No. 60155-BD, Environment, Climate Change and Water Resource Unit, World Bank (WB), Washington DC.
- [5] Alam GJ (2009). Environmental pollution of bangladesh–it’s effect and control, Pulp and Paper , 51, 13-7.
- [6] Heirli, U. and Maithel, S. (2008). Brick kiln by emission: the Herculean task of cleaning up the Asian brick industry. Swiss Agency for Development and Cooperation. Report no. 14. pp. 11-19.
- [7] Butler, T.M., Gurjar, B.R., Lawrence, M.G. and Lelieveld, J. (2004). “Evaluation of emissions and air quality in megacities,” Atmospheric Environment, vol. 42. pp. 59-72.
- [8] Iqbal, A. and Hasan, I. (2007). Modeling for minimizing the emitted CO₂ from brick kilning through afforestation in Bangladesh, *J. Environ. Sci.* 5 (11): 21-29.
- [9] Enters, T.E. (2000). Report book on carbon emission monitoring and estimation in Asia. vol.8. pp. 7-24.
- [10] Ahmed S, Hossain I (2008). Applicability of Air pollution Modeling in a Cluster of Brickfields in Bangladesh, *Chemical Engineering Research Bulletin* , 12, 28-34.
- [11] National Pollutant Inventory, Australia (1998). Emissions Estimation Technique Manual for Bricks, Ceramics & Clay product manufacturing.

ICMIEE18-206

Numerical Investigation of Low Velocity Impact on Polystyrene Foam Core Based Sandwich Composites

Md. Ahatashamul, Haque Khan Shuvo*, Md. Arifuzzaman

Department of Mechanical Engineering, Khulna University of Engineering & Technology, Khulna-9203, BANGLADESH

ABSTRACT

A numerical study on a low-velocity impact on polystyrene foam core based sandwich structure was conducted. Sandwich composite with polystyrene foam core and mild steel sheet as skin was considered for modelling in Abaqus CAE 6.14 platform. Low velocity impact simulation was performed on the sandwich structure by varying impactor mass for constant impact velocity and by varying impact velocity for constant impactor mass. The primary focus was to investigate the variation of contact force, contact time, displacement and principal strain with respect to both variables and to find out the impact energy threshold for damage initiation. The model was validated by using existing literature for contact force history. Theoretical results were found to be well predicted by simulation. The variation of impact velocity for constant impactor mass does not have any effect on contact time. No damage in the sandwich was found up to impact energy of 8J.

Keywords: Low velocity Impact, Composite, Sandwich, Polystyrene Foam, Simulation

1. Introduction

Sandwich structure is a special type of composite material tailored with two thin but high strength facings and a core in between them which is a relatively soft material. Even though the core material is low in strength, but its higher thickness furnishes the material with high bending stiffness with low density [1, 2]. The purpose of sandwich structure is to achieve a stiff as well as light component. Many alternative forms of sandwich construction may be obtained by combining different facing and core materials. The facings consist of steel, aluminum, wood, fiber-reinforced plastic or even concrete and the core material may be made of rubber, balsa wood, cork, rigid foam material (polyurethane, polystyrene, phenolic foam), solid plastic material (polyethylene), mineral wool slabs or from honeycombs of metal or even paper [3]. Sandwich structures usually find their applications in fabricating aircraft, ships, automotive vehicles, building walls and ceilings and many other lightweight constructions. Many noticeable characteristics of sandwich composites such as light weight, high strength, high stiffness, good fatigue resistance, good corrosion resistance and manufacturing complex geometries with fewer components lead to increasing demand day by day in wide range of fields [4].

Polystyrene is a thermoplastic material which can be formed by heating. It is a good thermal insulating material but it is rather less significant in terms of application to sandwich panels as it possess low self-bonding properties with the faces. Hence, Polystyrene is attached to the facing material with adhesives. It is usually used where small quantities of relatively simple design are required [3] because of the inexpensive production equipment. Foamed polystyrene which is a low cost, easily available, lightweight, and good energy absorption and thermal insulator material may be a

potential candidate core material for manufacturing sandwich composites.

Sheet metal is manufactured by industrial process such as forging, extrusion etc. into thin, flat pieces. It is one of the most common structures utilized in metalworking and can be cut and bent into an assortment of shapes. Thickness can differ significantly, too thin sheets are considered as foil or leaf, and pieces thicker than 6 mm are considered as plate. Mild steel contains a very small percentage of carbon about 0.05–0.25% carbon. It is strong and tough but not readily tempered and also known as plain-carbon steel and low-carbon steel. This form of steel is most recognized and used as it is relatively cheap while providing material properties that are suitable for many applications. Low carbon in mild steel allows making it malleable and ductile. Mild steel has a relatively low tensile strength, it is easy to form and its surface hardness can be increased through carburizing [5]. Mild steel sheet may be a good facing material for the construction of sandwich structure because of its low cost, high stiffness and availability.

During manufacturing or in service, sandwich structures are often subjected to low velocity impact resulting from tool drop and unintentional striking. In case of sandwich structures, numerous studies have shown that a low-energy-impact caused by dropped tools, runway debris, hailstones etc., may result in a small indentation that is barely detectable or undetectable by visual inspection. Though the indentation is undetectable, the impact on the object may cause internal damage in the form of face sheet delamination, fiber fracture, matrix cracking, and core crushing. The presence of such undetected damage in load-carrying components may lead to severe structural failure at a fraction of design load through several mechanisms including unstable indentation growth, face-sheet kink band formation and propagation, delamination buckling, and fiber failure.

* Corresponding author. Mob. : +88-01680089760
E-mail addresses: mahsk1320@yahoo.com

Therefore, the behavior of sandwich structures under low-velocity impact has been receiving increasing attention. To investigate the impact damage resistance of composite sandwich structures many experimental studies have also been proposed [6-8].

Finite element analysis (FEA) method has been used for predicting absorbed energy, failure strain, contact force, displacement, stress, deformation etc. during impact loading. The most important advantage of FEA is that it is possible to model any object having complex geometry and several number of variables can be studied at low cost and within short period of time by reducing number of experiments involving money and time. There are many FEA studies on foams in literature and new constitutive models are being implemented into finite element codes.

In this study, a sandwich structure consisting of polystyrene foam as core material and mild steel sheet as facing is considered. A numerical model is developed in Abaqus CAE 6.14 to study the effects of low velocity impact on the sandwich structure. The concentration was on impact force limit, displacement, contact time, energy absorption, and principal strain for various impact velocities at constant impactor mass and for various impactor masses at a constant impact velocity.

2. Numerical Modeling

The dimensions of the core and skin were 150 mm × 150 mm × 15 mm and 150 mm × 150 mm × 0.8 mm respectively as shown in Fig.1. The impactor having 10 mm diameter and 19 mm height was assigned with rigid body behaviour to it. The experimental stress-strain curve and other properties for polystyrene foam were taken from Ref. [2] as mentioned in Table 1.

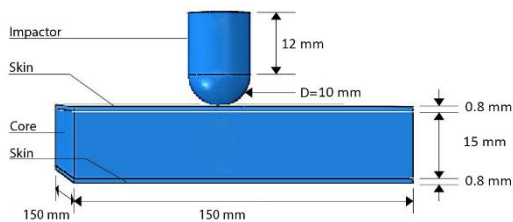


Fig.1 Setup for analysis

For MS sheet, the properties were assigned according to AISI standards as mentioned in Table 1 [4]. After assembly the impactor was kept offset from surface 0.02 mm. The contact between the face and core was provided by merging the assembled part since the elastic behaviour was studied and the contact between the sandwich and impactor was simulated using GENERAL CONTACT ALGORITHM. Linear brick elements were used with reduced integration and hourglass control options (C3D8R). The sides of the sandwich composite were fully constrained. The contact friction coefficient between the face and the impactor was set as $\mu = 0.3$ as

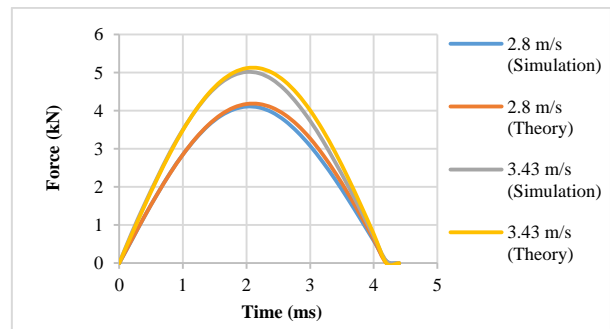
the friction coefficient of polystyrene and mild steel is ranged from 0.3-0.35. The velocity of the impactor was set only in z-direction with predefined field velocity. The appropriate mesh size is selected based on mesh dependency test and computational time.

Table 1 Material properties of foam core sandwich component

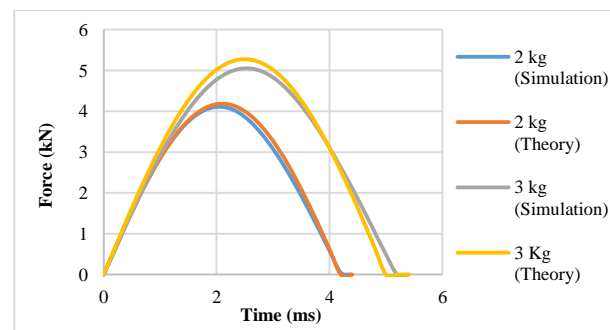
Material	Young's Modulus (GPa)	Poisson's Ratio	Density (kg/m ³)
Mild Steel	205	0.29	7780
Polystyrene	8.1E-3	0.1	30

3. Results and Discussion

For constant impactor height i.e. impact velocity analysis, the mass of the impactor was varied from 1 kg to 3 kg with an increment of 0.5 kg and for constant mass analysis, the height of the impactor was varied from 200 mm to 600 mm with an increment of 100 mm. Constant velocity and constant mass impact were simulated by varying the impactor mass (1.0 kg, 1.5 kg, 2.0 kg, 2.5 kg, and 3.0 kg) at a constant impactor velocity of 2.8 m/s and by varying the impact velocity (1.98 m/s, 2.43 m/s, 2.80 m/s, 3.13 m/s, and 3.43 m/s) for a constant mass of 2.0 kg respectively. The effect of these two types of impact



(a)



(b)

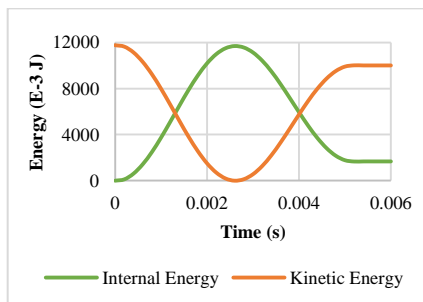
Fig.2 Force vs time comparison between simulation and theoretical results for (a) various impactor velocities for a constant impactor mass and (b) various impactor masses at a constant velocity.

phenomena on energy, contact force, displacement and principal strain were investigated.

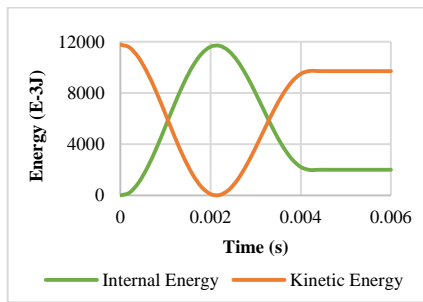
The verification of this numerical analysis was performed using the analytical model of force-time history. Choi [9] approximated the impact force history as –

$$F_l(t) = \frac{2\pi m_l v}{T_l} \sin \frac{2\pi t}{T_l} \quad (0 \leq t \leq T_l/2) \quad (1)$$

Where, F_l , m_l , v , T_l , and t are linear impact force, mass of the impactor, impact velocity, twice of impact duration and contact time respectively. The comparison of force vs time curve between simulation and theoretical (Eq. (1)) results at different impact velocities for a constant mass and for various impactor masses at a constant impact velocity is given in Fig.2. Theoretical results appear to be closely predicted the simulation results although a slight variation between simulation and theoretical results are noticed.



(a)



(b)

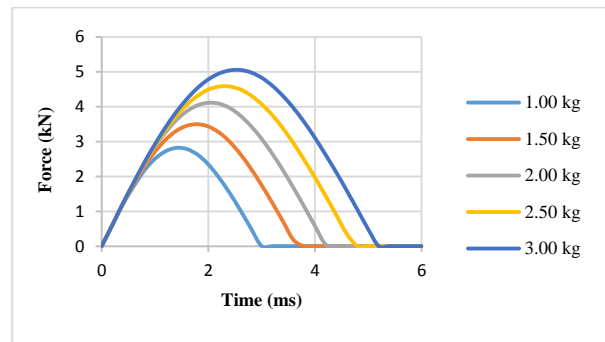
Fig.3 Typical energy vs time curves for (a) impact velocity of 2.8 m/s with impactor mass of 3 kg and (b) impactor mass of 2 kg with impact velocity of 3.43 m/s.

This is not unusual because the rebound velocity of the impactor is assumed to be equal to the impact velocity in the theory and losses are not considered due to friction. Nonetheless, the numerical results can be considered reliable for further analysis.

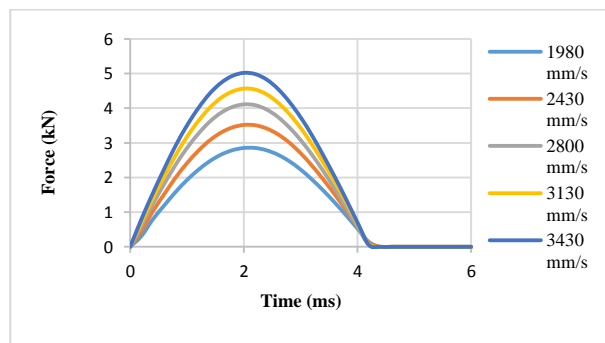
Fig.3 shows the typical variation of internal and kinetic energy with time for impact velocity of 2.8 m/s with impactor mass of 3 kg (see Fig.3(a)) and impactor mass

of 2 kg with impact velocity of 3.43 m/s (see Fig.3(b)). The internal energy appear to increase non-linearly with increasing time until a maximum then decrease gradually to a constant value when the impactor is detached from sandwich and the kinetic energy of the impactor follows a completely opposite trend as expected in both type of impact phenomena. A small amount of energy absorption is noticed due to friction during impact in each case.

Contact force is plotted as a function of time in Fig.4 for various impactor masses with a constant impact velocity of 2.8 m/s (see Fig.4(a)) and for various impact velocities with a constant impactor mass of 2 kg (see Fig.4(b)). The contact force seems to increase linearly at the start of the impact then gradually until the pick and then the force decreases to zero but with an opposite trend at the end in both cases. The slope of force vs time curved for constant velocity impact appeared to be constant irrespective to the impactor mass change (see Fig.4(a)) while the slope increases with increasing impact velocity for a constant impactor mass (see Fig.4(b)).



(a)



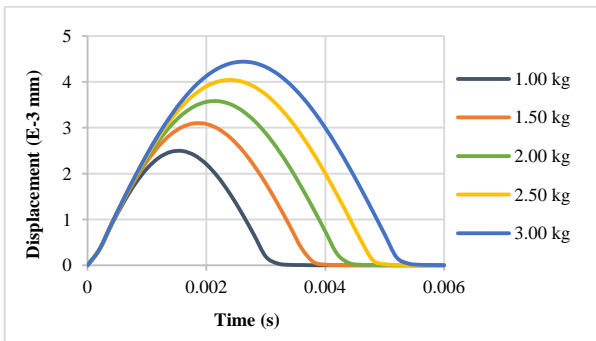
(b)

Fig.4 Contact force as a function of time for (a) various impactor masses with a constant impact velocity of 2.8 m/s and (b) various impact velocities with a constant impactor mass of 2 kg.

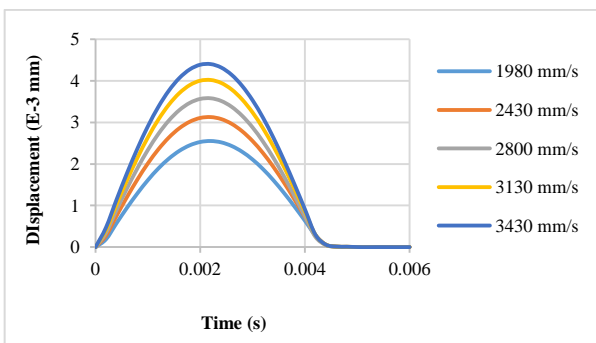
Displacement of the impact zone which comes in contact with the impactor from the beginning is found to be the maximum expectedly. The displacement vs time

curve for different impactor mass with constant velocity and for different impactor velocity with constant mass is given in Fig.5. The curves show similar pattern as contact force vs time curves.

The force vs displacement curves for different analysis are shown in Fig.6. The slope of the force vs displacement curves during loading and unloading appeared to be same irrespective to the impactor mass change for constant impact velocity (see Fig.6(a)). On the other hand, the slope of the force vs displacement curve increases with increasing impact velocity for constant impactor mass (see Fig.6(b)). In both type of impact cases, the force increases/decreases linearly with displacement although a small deviation is noticed at the beginning of impact because of the contact establishment. The area bounded by the force vs displacement curves represents the amount of energy absorbed which increases with increasing impactor mass for constant impact velocity (see Fig.6(a)) and also increases with increasing impact velocity for constant impactor mass (see Fig.6(b)). It is also seen that energy absorption increases with increasing impactor mass for constant impact velocity and with increasing impact velocity for constant impactor mass.



(a)

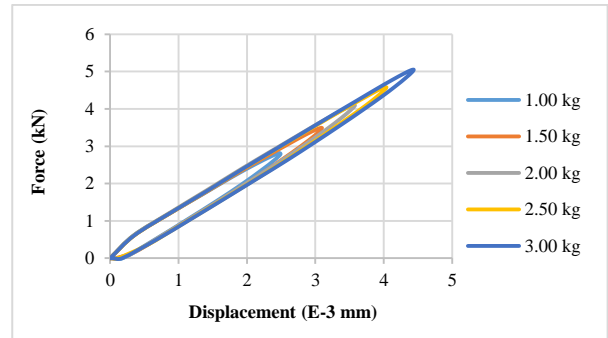


(b)

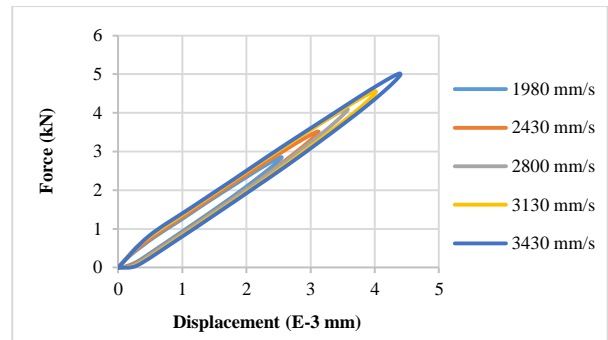
Fig.5 Displacement as a function of time for (a) various impactor masses with a constant impact velocity of 2.8 m/s and (b) various impact velocities with a constant impactor mass of 2 kg.

Maximum contact force is plotted as a function of total impact energy for constant velocity and constant mass

impact in Fig.7. The maximum contact force increases non-linearly with increasing impact energy for both analyses and no significant difference in maximum contact force for constant impact energy is seen between these two analyses. Non-linear behavior of contact force is also reported by Akil and Cantwell [10] for foam core sandwich structure. Displacement vs impact energy curves show similar behavior as contact force vs impact energy curves as shown in Fig.8.



(a)



(b)

Fig.6 Force vs displacement curves for (a) various impactor masses with a constant impact velocity of 2.8 m/s and (b) various impact velocities with a constant impactor mass of 2 kg.

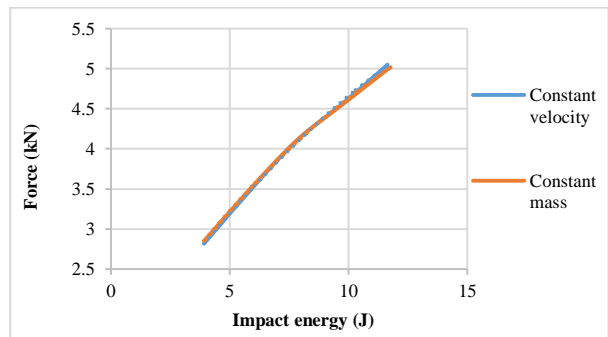


Fig.7 Maximum contact force as a function of impact energy for constant velocity and constant mass impact.

Contact time is plotted as a function of impact energy for both analyses in Fig.9. As the impact energy increases keeping the impact velocity constant, the

contact time of the impactor increases linearly but when impact energy increases keeping the impactor mass constant, the contact time remains constant. This is because the duration and the shape of the contact force history are dependent on the mass ratio between impactor and sandwich but not on the velocity as stated in Ref. [11].

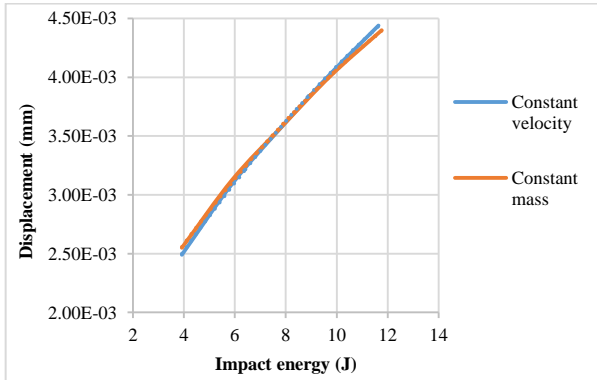


Fig.8 Maximum displacement as a function of impact energy for constant velocity and constant mass impact.

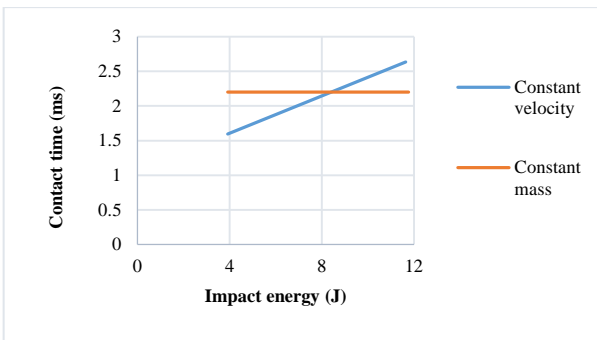


Fig.9 Contact time of impactor vs impact energy.

Maximum principle strain as a function of impact energy for both analyses is given in Fig.10. The maximum principle strain in the sandwich core increases linearly with increasing impact energy in both constant velocity and constant mass impacts and no significant difference

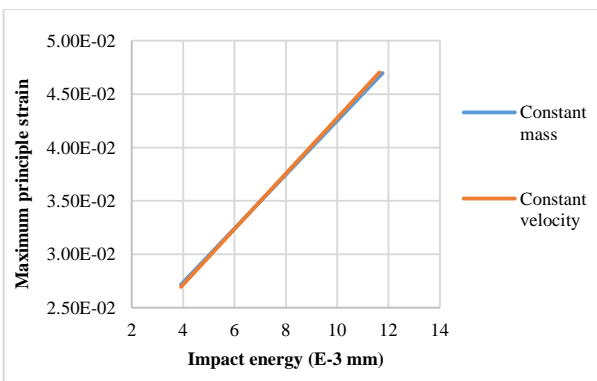


Fig.10 Maximum principle strain as a function of impact energy for constant velocity and constant mass impact.

is seen in maximum principle strain for constant impact energy between two analyses. Elastic limit of polystyrene foam is $4E-2$ mm. From the curve (see Fig.10) it is seen that at impact energies higher than 8J the value of maximum principle strain is over the limit which indicates the failure of core when maximum principle strain failure is considered.

4. Conclusion

Low-velocity impact on sandwich panels with polystyrene foam core and mild steel face sheets were modelled numerically using Abaqus CAE 6.14 and the model was validated using existing theory in literature. The analysis was performed based on the energy of impact which was varied by changing impactor mass and impact velocity. The findings of the study are summarized below:

- The contact force and displacement increases non-linearly with increasing impact energy with no significant variation between two analyses.
- For constant mass analysis the contact time of the impactor with the sandwich remains constant but for constant velocity analysis the contact time increases linearly with increasing impact energy.
- The maximum principle strain increases linearly with increasing impact energy irrespective to constant mass or constant velocity analysis.
- The maximum impact energy limit for sandwich core damage initiation is found to be 8J independent of height of impactor and mass of impactor.

REFERENCES

- N. Gupta, Characterization of syntactic foams and their sandwich composites: modeling and experimental approaches, *A Dissertation submitted to the Louisiana State University and Agricultural and Mechanical College in partial fulfillment of the requirements for the degree of Doctor of Philosophy in The Interdepartmental Program in Engineering Science, USA* (2003).
- U. Caliskan, and M. K. Apalak, Bending impact behaviour of sandwich beams with expanded polystyrene foam core: Analysis, *Journal of Sandwich Structures and Materials*, Vol. 1, (2017).
- J. M. Davies, Lightweight sandwich construction, *Blackwell Science Ltd.*, (2001).
- V. S. Hoa, Principles of the manufacturing of composite materials, *DEStech Publications, Inc.*, Pennsylvania, (2009).
- AISI 1018 Mild/Low Carbon Steel standard.
- M. Rout, and A. Karmakar, Low velocity impact performance of delaminated composite

- stiffened shell, *Procedia Engineering*, Vol. 173, (2017).
- [7] S.M.R. Khalili, M. Soroush, A. Davar, and O. Rahmani, Finite element modeling of low-velocity impact on laminated composite plates and cylindrical shells, *Composite Structures*, Vol. 93, (2011).
- [8] L. Aktay, A.F. Johnson, and M. Holzapfel, Prediction of impact damage on sandwich composite panels, *Computational Materials Science*, Vol. 32, (2005).
- [9] H. Choi, and C. S. Hong, New Approach for Simple Prediction of Impact Force History on Composite Laminates, *AIAA Journal*, Vol. 32, (1994).
- [10] H. M. Akil and W.J. Cantwell, The low velocity impact response of foam core sandwich structure, *AZO Materials*, Vol. 2, (2006).
- [11] S. Antonyuk, S. Heinrich, J. Tomas, N. G. Deen, M. S. V. Buijtenen, J. A. M. Kuipers, Energy absorption during compression and impact of dry elastic-plastic spherical granules, *Granular Matter*, Vol. 12, (2010).

Dyeing of 100% Cotton Fabric using Natural Dye, Mordant and Natural Finish

A. K. M. Nayab-Ul-Hossain^{1*}, Mohammad Naim Hassan¹, Aniruddha Sarkar², S. M. Kamrul Hasan², Kaniz Fatima Mishfa²

¹Lecturer, Department of Textile Engineering, Khulna University of Engineering & Technology Khulna-9203, BANGLADESH

²Department of Textile Engineering, Khulna University of Engineering & Technology, Khulna-9203, BANGLADESH

ABSTRACT

Normally fabric is dyed with synthetic dyes, along with chemical fixing agent. In few cases fabric is dyed with natural dyes using synthetic mordant. Here this is clarified that 100% cotton fabric is dyed with natural dyes using natural mordant and at the same time applied natural finish (Neem, *Aloe vera* and Holy Basil (Tulsi) exudates). Ingredients which are applied, collected from surrounding environment that leads to a cost effective dyeing process. Moreover this is advantageous in easy application process as well as harmful free substances. Natural saps were collected from respective ingredients and at the same time the sample fabrics were conditioned for the purpose of easy penetration of dye molecules. Here as usual technique was applied for uniform and level dyeing and subsequently natural finishes were applied. The quality of the dyed fabric levelness is good. The fastness properties are also satisfactory. In comparison with chemical procedure, the applied dyeing process is easy to operate as well as less time consuming which meets all the necessary requirements of a perfect dyed fabric.

Keywords: Red Spinach, Betel Nut, Neem & Holy Basil (Tulsi) exudate, Anti-microbial finish, Natural ingredients.

1. Introduction:

The use of dye stuffs is as old as textiles themselves and pre-dates written history. Dyes are obtained from two main sources; the natural dyes and synthetic dyes.[1] Natural dyes can be defined as those organic materials that have the ability to impart color to any substrates which they must have had affinity for.[2] Until the mid-19th century, all dye stuffs were made from natural materials, mainly vegetable matters.[2] Research findings have reported that synthetic dyes are harmful to the body and thus the increased search into the arrays of plants for natural dyes which is more environmental friendly.[4] Natural dyes are biodegradable and very compatible with the environment.[5] These dyes can be obtained either from plants, animals, and minerals.[3] In this article work, no inorganic textile chemicals, auxiliaries & inorganic textile dyes were used & even the mordant is also natural as well as the natural finisher. Everything was collected from nature & our surrounded area and the full dyeing process was completed by using these natural items. The whole dyeing process is easier process and also have satisfactory result on color fastness test.

2. Material and fabric used:

2.1 This fabric was used for dyeing:

Composition : 100% Cotton
Construction : Single Jersey
Condition : Bleached

Natural ingredient: These natural ingredients Red Spinach, Henna, Sajina, Betel nut, Banana stem, and Tamarind leaf were used.

Aloe vera, Neem, Holy Basil (Tulsi) leaves were used for natural finishing.

2.2 Extraction of dye & finishing solution from natural ingredients:

- (i) Firstly, the required ingredients were collected and cleaned properly by using water.
- (ii) Ingredients were blended and turned into paste form.
- (iii) These pastes were boiled at a certain temperature.
- (iv) After boiling the exudates were filtrated.

3. Identification of sample and dyeing recipe:

We dyed sample by varying the recipe:

Sample 1:

Red spinach : 60%
Henna : 20%,
Sajina : 20%
Mordant : Betel nut
Finisher : *Aloe vera*

Sample 2:

Henna : 70%
Red spinach : 20%
Sajina : 10%
Mordant : Tamarind leaf solution
Finisher : Neem leaf

Sample 3:

Sajina : 50%
Henna : 30%
Red spinach : 20%
Mordant : Banana bark sap
Finisher : Holy Basil (tulsi)

4. Fabric preparation:

100% cotton fabric(bleached) has been used. Prior to dyeing, the sample fabric has been washed properly to maintain the proper absorbency for dyeing.

5. Procedure of dyeing:

We have selected three nozzles and input the collected saps of different colors in the nozzles as per materials. We kept the nozzles to run for 30 minutes at 60°C. After that we added the natural fixer and kept additional 30 minutes at 60°C for proper & adequate take up of dye by the fabric. Here the total dyeing time was approximately 3 hours.

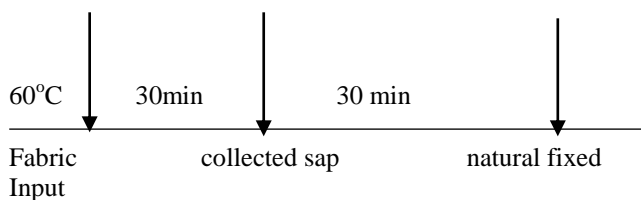


Fig: Dyeing Curve

5.1 Treatment after dyeing:

After dyeing the dyed fabric samples were washed properly to remove the unfixed surface color. We also used detergent to wash for good fastness result.

5.2 Finishing:

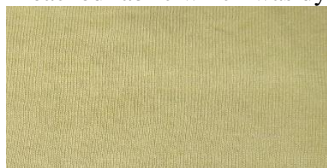
For finishing purpose, we used *Aloe vera* for sample 1, Neem paste for sample 2, Holy Basil (Tulsi) paste for sample 3. Firstly, the required ingredients were turned into paste form, then adequate amount of water has been added to turn the paste into juicy liquor so that the finishers can easily penetrate into the dyed fabric sample. The finishing treatment was continued for 1 hour at 60°C. After finishing treatment, the samples were rinsed with water for three times so that the surface particles (of the liquor) may be removed. Then the samples were allowed to dry.

5.2 Color of dyed fabric:

Different tones of color were achieved by using different natural ingredients in different proportions. Various shades were found after dyeing the bleached fabric.



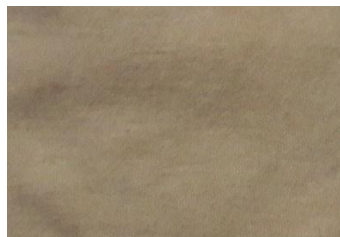
Bleached fabric which was dyed



Dyed sample 1:



Dyed sample 2:



Dyed sample 3

6. Different tests:

Different tests were carried out to check the fastness properties & dyeing accuracy. All the samples were tested in a third party testing company A-ONE POLAR Limited, which is a sister concern of the Micro Fibre group. Test results of different tests are provided below. Here different tests of dyed sample 2 are specially clarified with a picture to illustrate the testing procedure-

Test	Dyed Sample 01	Dyed Sample 02	Dyed Sample 03
Color fastness to wash	4	4	3-4
Color fastness to water	4	4	4
Color fastness to rubbing	3-4 both Wet & dry rub	4-5 both Wet & dry rub	3-4 both Wet & dry rub
Color fastness to perspiration	4	4-5	3-4

6.1 Color fastness to wash: (ISO-105-C06)

The color fastness to wash test was carried out by the ISO-105-C06 method.

After carrying out testing, multi-fiber fabric illustrates that the result is **satisfactory**.

Color staining in dyed sample during this test is 4-5 & change in color is 4, which is in **acceptable range**.



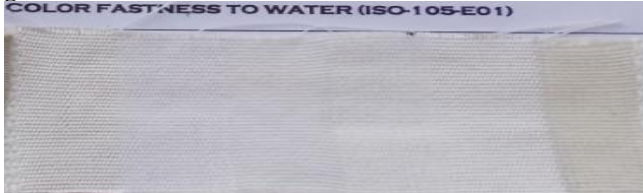
Picture:1- Color fastness to wash

Acetate	Cotton	Polyamide	Polyester	Acrylic	Wool
4-5	4-5	4-5	4-5	4-5	4-5

Table:1- Color fastness to wash test result

6.2 Color fastness to water: (ISO-105-E01)

The color fastness to water test was carried out by ISO-105-E01 method. Multi fiber fabric shows that the result is **good**. Change in color in this test is 4 which is **good**.



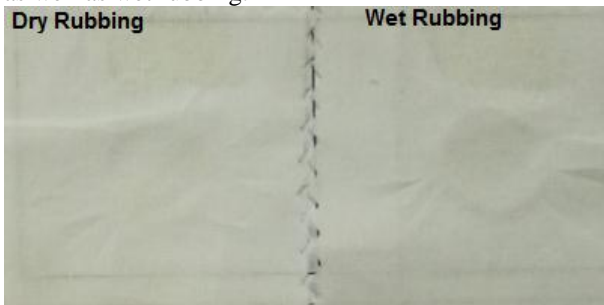
Picture:2- Color fastness to water

Acetate	Cotton	Polyamide	Polyester	Acrylic	Wool
4-5	4-5	4-5	4-5	4-5	4-5

Table:2- Color fastness to water test result

6.3 Color fastness to Rubbing: (ISO-105-X12)

The color fastness to rubbing test was carried out by ISO-105-X12 method & result is **good** both for the dry as well as wet rubbing.



Picture:3- Color fastness to dry & wet rubbing

SL. no	Test name	rating
01.	Dry Rubbing	4-5
02.	Wet Rubbing	4-5

Table:3- Color fastness to rubbing test result

6.4 Color fastness Perspiration (ISO-105-E04):

The color fastness to perspiration test was carried out by ISO-105-E04 method. Both the acid & alkali tests were carried out. In every case the test result is **satisfactory** & change in color is 4 which is also **good**.



Picture:4- Color fastness to perspiration in acidic medium.

Acetate	Cotton	Polyamide	Polyester	Acrylic	Wool
4-5	4-5	4-5	4-5	4-5	4-5

Table:4- Color fastness to perspiration test result in acidic medium



Picture:5- Color fastness to perspiration in alkali medium.

Acetate	Cotton	Polyamide	Polyester	Acrylic	Wool
4-5	4-5	4-5	4-5	4-5	4-5

Table:5- Color fastness to perspiration test result in alkali medium

7 Dyeing quality:

We have come to know that the fastness properties are really **satisfactory**. The visual appearance of dyed samples is **good** as well as the physical appearance.

- (i) No uneven shade was found in between the sample and within the sample.
- (ii) Possibility of crease mark formation was more as the fabric was single jersey but actually nothing was happened.
- (iii) All the dyed samples are free from any color spot.

8. Conclusion:

The result of this study has revealed that fully natural dyeing is possible without the use of inorganic mordant & the dyeing time is satisfactory. All the natural catalysts as well as the natural finishers were used for this dyeing suited perfectly with maintaining good dyeing quality & color fastness properties. In addition, the result of this experiment will add a bust to environmentally conscious consumers with growing need for organic clothing. This is just the step to dye naturally using fully natural ingredients but need more research to make this more convenient.

REFERENCE

- [1] www.researchgate.net/publication/308035255
- [2] Journal of Textile Engineering and Fashion Technology, volume 3, Issue3-201
- [3] International journal of chemical studies 2017:5(6): 187-191
- [4] Binitha kali, Gogai N. Cationic fixing agent. Indian Textile J. 1998;108(9-12):42-46
- [5] Paul R, Jayes MV, Nayak SR. Natural dyes Classification, extraction and fastness properties. Textile Dyer & Printer. 1996;29(22):16-24

Enhancement of Tube Side Heat Transfer using Twisted Stainless-Steel Angle

Md. Tarif Raihan

Fire Safety Engineer, Stichting Bangladesh Accord Foundation, Level - 13, AJ Heights, Cha-72/1/d, North Badda, Pragati Sarani, Dhaka-1212, BANGLADEH

ABSTRACT

The current research was carried out to investigate conventional heat transfer enhancement inside the tube by using twisted stainless-steel angle insert. Main objectives were to find the percentage of increment of heat transfer enhancement using twisted stainless-steel insert and to find the relation between Reynolds number and Nusselt number. A 940mm long copper tube of 26.6 mm internal diameter and 30 mm outer diameter, of which length of 762 mm has been used as the test section. A constant heat flux condition has been maintained by wrapping Nichrome wire around the test section and fiber glass insulation over the wire. K-type thermocouples and rotameter were used to measure temperature and rate of flow. With insert, heat transfer rate has been increased up to 140 percent. This technique does not rely on external power or activation. This experiment has shown simultaneous effects on Reynolds number and Nusselt number too.

Keywords: Heat transfer rate, Convective heat transfer co-efficient, Friction factor.

1. Introduction

1.1 Literature review:

The measurement of tube side heat transfer coefficient is an important part of heat transfer. Heat exchangers dealing with fluids of low thermal conductivity (gases or oils), there is a need to increase the heat transfer rate. Mesh or spiral brush inserts were used by Megerlin et al. (1974) to enhance turbulent heat transfer in short channels subjected to high heat flux. Variable roughness can be obtained by using a wire-coil insert made of a shape memory alloy (SMA) that alters its geometry in response to change in temperature proposed by Bergles and Champagne, 1999. This study mainly focuses on Reynolds number, Nusselt number, and especially on heat transfer coefficient by using stainless steel insert.

1.2 Applications:

Climate Engineering, Greenhouse effect, Evaporative Cooling, Laser Cooling, Magnetic Cooling, Radiative Cooling, Thermal Energy Storage.

1.3 Objectives:

- To find the tube side heat transfer co-efficient and friction factor.
- To find the percentage of increase of heat transfer enhancement using twisted stainless-steel angle insert and compare it to the plain tube.
- To find the relation between Reynolds number and Nusselt number.
- To find the pressure drop in tube side with twisted stainless-steel angle insert.

1.3 Methodology:

- A 940mm long copper tube of 26.6 mm internal diameter and 30 mm outer diameter, of which length of 762 mm has been used as the test section.
- A constant heat flux condition has been

maintained by wrapping nichrome wire around the test section and fiber glass insulation over the wire. This was used to heat the test section.

- Outer surface temperature of the tube has been measured at five points of the test section maintaining equal distance from one point to another point by K-type thermocouples.
- Two thermometers have been used at the inlet and outlet section of the tube for measuring the bulk temperatures. At the outlet section the thermometer was placed in a mixing box.
- Pressure drop has been measured at five points of the test section by using manometer. Open loop system of water supply was used.
- The rate of flow was measured with the help of Rota meter in the travelling path of inlet water.
- Two types of temperature have been measured during the experiment. One regarding tube outer surface temperature and another regarding water inlet-outlet temperature.
- Data has been taken for only plain copper tube without insert and with insert.

2. Experimental Setups:

2.1 Insert:

Length=0.762m

Angle of twisted=18 degree

Thickness=2.9 mm

Pitch length=12 cm.



Fig. 2.1: Twisted stainless steel angle insert

Setup:

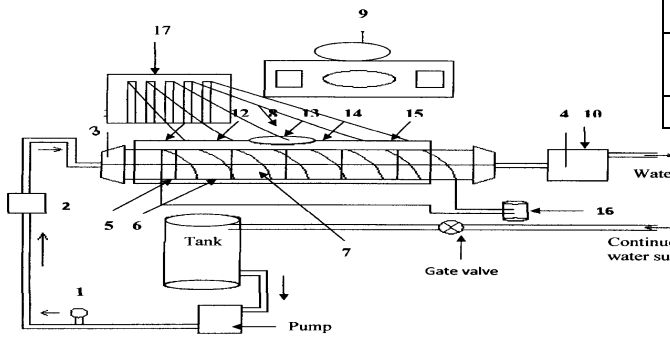


Fig. 2.2: Experimental Setup

- | | |
|-------------------------------|-----------------------|
| 1. Gate valve | 13. Thermocouple |
| 2. Rota meter | 14. Thermocouple |
| 3. Inlet Thermometer | 15. Thermocouple |
| 4. Outlet Thermometer | 16. Voltage regulator |
| 5. Insulation | 17. Manometer |
| 6. Test Section (copper tube) | |
| 7. Nichrome-wire coil | |
| 8. AC source | |
| 9. Thermo-electric monitor | |
| 10. Mixing box | |
| 11. Thermocouple 1 | |
| 12. Thermocouple 2 | |

(For detailed image please see Appendix)

3. Data collection and analysis

3.1 Necessary information and equation for calculation process:

- Tube inside diameter=0.026 m
- Tube outside diameter=0.03 m
- Tube test length=0.762 m
- Thermal conductivity of copper=379W/m⁰C
- Viscosity of water μ =0.00087 kg/m.s
- Density of water ρ =1000 kg/m³
- Thermal of conductivity of water, kW=0.62 w/m⁰C
- Specific heat of water (at 28⁰C), Cp =4177 J/kg ⁰C
- Thickness of Stainless-steel insert =0.0029 m
- Angle of twisted of insert =18⁰
- Thermal conductivity of copper, k=379 W/m ⁰C

Equations:

Outer surface area, $A_0 = \pi d_0 L$
Inner surface area, $A_i = \pi d_i L$
Heat transfer rate, $Q = m C_p (T_o - T_i)$
Cross sectional area = $\pi d_i^2 / 4$
Velocity, $V = m / A_i$, where m is the flow rate
Reynolds number, $Re = \rho V d_i / \mu$
Nusselt number, $Nu = h d_i / k$
Prandtl number, $pr = \mu C_p / k$
Convective heat transfer coefficient = $Q / A (T_{inner\ surface} - T_{bulk})$
$Nu_d = 0.023 Re_d^{0.8} Pr^{0.4}$ (By Dittus and Boelter)
The rate of heat Transfer through the tube wall by conduction is, $Q = 2\pi L K (T_{outer\ surface} - T_{inner\ surface}) / \ln (r_o / r_i)$
Bulk temperature = $T_b = (T_i + T_o) / 2$
Entrance length = $0.623 d_i Re^{0.25}$

Outer surface temperature = $(\text{Thermocouple 1} + \dots + \text{Thermocouple 5}) / 2$
Inner surface temperature = Outer surface temp - Wall temp difference
% of error = $(Nu_{exp} - Nu_{th}) / Nu_{th} \times 100$

NOMENCLATURE

- c_p : Specific heat at constant pressure, $\text{kJ} \cdot \text{kg}^{-1} \cdot \text{K}^{-1}$
- d_o : Outer diameter
- d_i : Inner diameter.
- m : Mass flow rate.
- T_o : Outer surface temp.
- T_i : Inner surface temp.
- A_i : Tube inside area
- μ : Kinematic viscosity.
- ρ : Density.
- h : Convective heat transfer coefficient
- k : Thermal conductivity.
- Nu_{exp} : Experimental nusselt no.
- Nu_{th} : Theoretical nusselt no.
- p : Pressure, kPa
- T : Temperature, K
- t : Celsius temperature, ⁰C
- V : Velocity.

3.4 Data calculation: (Full data calculation have been shown in detail at Appendix)

4. Results and Discussion

4.1 Summary of results:

Reynolds no. $Re = 4318.46 \sim 17446.59$

For plain tube:

Heat transfer rate = 626.85 ~ 3038.97 W

Convective heat transfer coefficient = 488.34 ~ 2056.99 $\text{w/m}^2 \text{ } ^\circ\text{C}$

Nusselt no. $Nu = 20.99 \sim 80.17$

Friction factor = 0.327 ~ 0.05162118

For plain tube with insert:

Heat transfer rate, $Q = 1504.44 \sim 3672.09 \text{ W}$

Convective heat transfer co-efficient, $h = 709.48 \sim 2576.58 \text{ w/m}^2 \text{ } ^\circ\text{C}$

Nusselt no. $Nu = 30.49 \sim 87.94334461$

Friction factor = 0.448 ~ 0.07420545

4.2 Discussion on results:

1. Here the heat transfer rate increases because of increasing flow rate.
2. Convective heat transfer co-efficient
Here the convective heat transfers co-efficient increases because of increasing heat transfer rate.
3. Error analysis: The reading increasing from thermocouple-1 to thermocouple-5 respectively. For minimum reading of thermocouple-1, average outer temperature decreases, wall temperature difference decreases, and inner surface temperature also decreases, and convective heat transfer coefficient also increases then experimental Nusselt number increases.

4.3 Graphical representation of different related values:

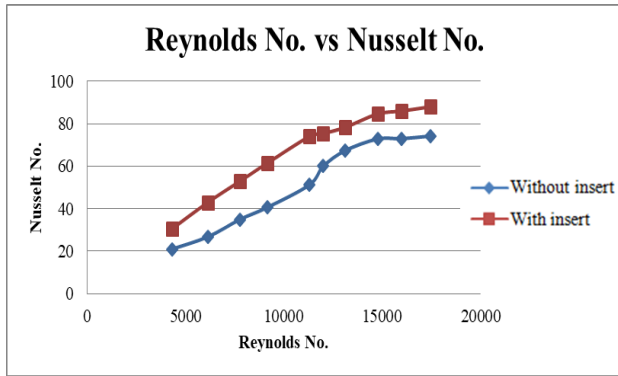


Fig. 4.1: Comparison of Nusselt no. with Reynolds no. using with insert and without insert. From the above graph it is found that for the increasing Reynolds no. Nusselt number increases both with insert and without insert. But the increasing Nusselt no. with insert is higher than without insert. Because convective heat transfer coefficient is increased for using insert.

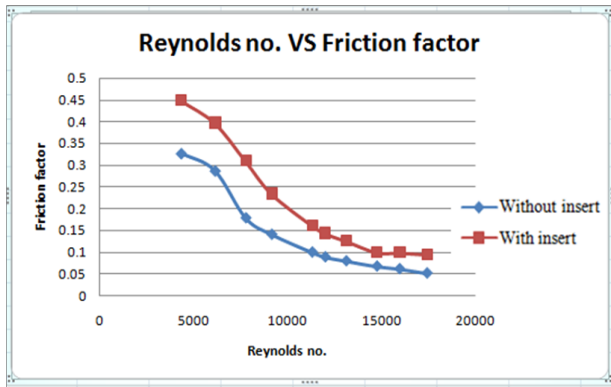


Fig. 4.2: Comparison friction factor with Reynolds no. using insert and without insert.

5. Conclusion:

The application of single-phase enhancement techniques is evaluated for tube side. Several active techniques have been identified as possibilities for tube enhancement. These techniques do require external power. But there is a power cost that needs to be considered. The present experimental study has made the simultaneous effects on Re, Nu and h which doesn't require any external power.

6. Recommendation:

1. The resistance of the heater must be known perfectly, because voltage should be controlled according to resistance.
2. Temperature reading should be taken after the flow reaches a steady state condition.

Acknowledgement:

Foremost, I would like to express my sincere gratitude to my advisor Prof. Dr. Bodius Salam (Dean, Mechanical Department of CUET) for the continuous support of my research, for his patience, motivation,

enthusiasm, and immense knowledge. His guidance helped me in all the time of research and writing of this paper.

REFERENCES

- [1] Megerlin et al, Murphy and Bergles A.E (1974), "Augmentation of heat transfer in tubes by use of mesh and brush inserts". J. Heat Transfer, pp-145-151
- [2] Champagne and Bergles (2001), "Augmentation of heat transfer in tubes by use of mesh and brush inserts". J. Heat Transfer, pp-145-151.
- [3] Garimella and Christensen, 1995 'Techniques to augment heat transfer readings.' Handbook of heat transfer applications, McGraw Hill; Chapter 3.
- [4] S.K.Saha, A.Dutta ' Thermo hydraulic study of laminar swirl flow through a Circular tube fitted with twisted tapes' ASME J. Heat Transfer 123 (2001) 417-427.

Appendix Explanatory Material

1 Experimental setups:



Fig 2.3: Rotameter



Fig. 2.4: Manometer



Fig 2.5: Voltage regulator



Fig. 2.6: Thermocouple monitor



Fig. 2.7: Copper tube



Fig. 2.8: Test section

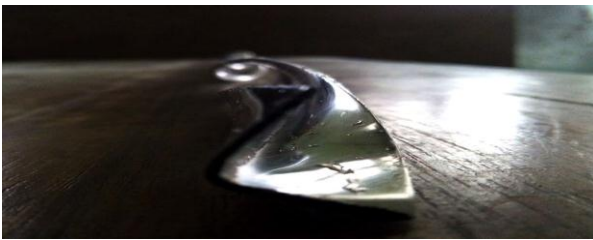


Fig. 2.9: Twisted stainless steel angle insert.

3.4 Data calculation:

3.4.1 Thermometer and thermocouple reading at various flow rates (plain tube): All temp. are in °C (Table 3.1)

Sr.	Inlet, T_i	Outlet, T_o	1	2	3	4	5
1	36	38	37	44	46	79	82
2	36	37.8	37	44	46	79	81
3	36	37.8	37	43	46	78	80
4	36	37.6	36	43	45	77	80
5	36	37.4	36	42	45	77	80
6	36	28	26	40	43	70	71
7	36	27.8	26	40	42	70	71
8	36	27.8	25	40	42	70	71
9	36	27.6	25	39	41	68	69
10	36	27.4	25	39	41	68	69

**First five data were taken at morning and last five data were taken at afternoon.

Calculation:

For without insert:

Tube outside diameter, $d_o = 30 \text{ mm} = 0.03 \text{ m}$

Tube inside area, $A_i = \pi d_i^2 / 4 = 0.000531 \text{ m}^2$

Mass flow rate, $m = 0.075 \text{ kg/s}$

Heat transfer rate, $Q = mc_p(T_o - T_i) = 626.85 \text{ W}$

Velocity, $v = m/A_i = 0.14 \text{ m/s}$

Reynolds no. = $\rho v d_i / \mu$
 $= 4318.46$

Here,

$\mu = 0.00087 \text{ kg/m}\cdot\text{sec}$

$\rho = 1000 \text{ kg/m}^3$

Wall temperature difference $\Delta T = Q \times \ln(r_o/r_i) / 2\pi L k = 0.042$

Outer surface temperature = $(37 + 44 + 46 + 79 + 80) / 5 = 57.20$

Inner surface temperature = $(57.20 - 0.042) \text{ }^\circ\text{C} = 57.16 \text{ }^\circ\text{C}$

Bulk temperature = $(T_i + T_o) / 2 = (36 + 38) / 2 = 37 \text{ }^\circ\text{C}$

Heat transfer co-efficient, $h = \frac{Q}{A(T_{\text{inner surface}} - T_{\text{bulk}})}$
 $= \frac{626.85}{0.000531 \times (57.16 - 37)}$
 $= 488.34 \text{ w/m}^2$

Nusselt number, $N_u = (h d_i) / k = 20.95$

Friction factor, $f = \frac{\Delta p \times 2 \times d_i}{\rho \times V^2 \times L}$

$L = 0.762 \text{ m}$

$d_i = 0.026 \text{ m}$

$\rho = 1000 \text{ Kg/m}^3$

$\Delta p = 133.42 \text{ N/m}^2$, $f = \frac{93.4 \times 2 \times 0.026}{1000 \times 0.14^2 \times 0.762} = 0.327$

With insert:

Tube outside diameter, $d_o = 30 \text{ mm} = 0.03 \text{ m}$

Tube inside area, $A_i = \pi d_i^2 / 4$

$= 3.14 \times (0.026)^2 / 4 = 0.000531 \text{ m}^2$

Mass flow rate,

$m = 5 \times 15 = 75 \text{ ml/s} = 0.000075 \text{ m}^3/\text{s} = 0.075 \text{ kg/s}$

Heat transfer rate, $Q = mc_p(T_o - T_i)$

$= 0.075 \times 4177(39.8 - 35)$

$= 1504.44 \text{ W}$

Velocity, $v = m/A_i = 0.000075 / 0.000531 = 0.14 \text{ m/s}$

Re.no. = $\rho v d_i / \mu = 318.46$ Here, $\mu = 0.00087 \text{ kg/m}\cdot\text{sec}$, $\rho = 1000 \text{ g/m}^3$

Wall temperature difference $\Delta T = Q \times \ln(r_o/r_i) / 2\pi L k$
 $= 1504.44 \times \ln(0.03/0.026) / (2\pi \times 0.762 \times 379)$
 $= 0.100 \text{ }^\circ\text{C}$

Outer surface temperature = $70.80 \text{ }^\circ\text{C}$

Inner surface temperature = $70.80 - 0.100 = 70.70 \text{ }^\circ\text{C}$

Bulk temperature = $(T_i + T_o) / 2 = 37.4 \text{ }^\circ\text{C}$

Heat transfer co-efficient, $h = 709.48 \text{ w/m}^2$

Nusselt number, $N_u = (709.48 \times 0.026) / 0.62 = 30.44$

Friction factor, $f = \frac{\Delta p \times 2 \times d_i}{\rho \times V^2 \times L} = 0.448$

3.4.2 Flow rate for various Rotameter reading (plain tube):

Exp. No.	Rotameter reading (cm)	Flow rate (ml/s)	Flow rate (m^3/s)	Flow rate (kg/s)
1	5	75	0.000075	0.075
2	7.1	106.5	0.0001065	0.107
3	9	135	0.000135	0.135
4	10.6	159	0.000159	0.159
5	13.1	196.5	0.0001965	0.197
6	13.9	208.5	0.0002085	0.209
7	15.2	228	0.000228	0.228
8	17.1	256.5	0.0002565	0.257

9	18.5	277.5	0.0002775	0.278
10	20.2	303	0.000303	0.303

Table 3.2: Value of Flow rate for various Rotameter reading (plain tube)

3.4.3 Determination of Q for various velocities (plain tube):

Exp no	Cross sectional area (m ²)	Velocity(m/s) Eq-5	Heat transfer rate Q(W)Eq-3
1	0.000531	0.14	626.85
2	0.000531	0.20	801.11
3	0.000531	0.25	1015.50
4	0.000531	0.30	1063.14
5	0.000531	0.37	1149.64
6	0.000531	0.39	2613.96
7	0.000531	0.43	2667.87
8	0.000531	0.48	3001.36
9	0.000531	0.52	3015.15
10	0.000531	0.57	3038.97

Table 3.3: Value of Q for various velocities (plain tube)

3.4.4 Determination of heat transfer coefficient and Reynolds number (plain tube):

Sr.	Eq-11	Eq-14	Eq-15	Eq-12	Eq-9	Eq-6
1	0.04	57.20	57.16	37	488.3	4318.4
2	0.05	57.20	57.15	36.9	621.3	6132.22
3	0.06	56.60	56.53	36.9	812.2	7773.23
4	0.07	56.00	55.93	36.8	972.7	9155.14
5	0.07	55.60	55.52	36.7	1259	11314.3
6	0.17	50.00	49.83	26.5	1459	12005.3
7	0.17	49.80	49.62	26.4	1604	13128.1
8	0.19	49.80	49.60	26.4	2031	14769.1
9	0.20	48.40	48.20	26.3	2040	15978.3
10	0.20	48.4	48.20	26.2	2056	17446.5

Table 3.4: Value of heat transfer coefficient and Reynolds number (plain tube)

3.4.5 Determination of experimental N_u, P_r and theoretical Nu (plain tube):

Sr.	Eq-7	Eq-8	Eq-10
1	20.99	5.31	31.30
2	26.70	5.33	45.04
3	34.91	5.34	56.70
4	37.57	5.35	66.15
5	41.28	5.37	80.43
6	65.97	5.40	85.04
7	67.37	5.42	92.29
8	72.8	5.45	102.7388363
9	72.98	5.47	110.3195344
10	74.17	5.48	119.3009372

Table 3.5: Value of experimental N_u, P_r, and theoretical Nu (plain tube)

3.4.6 Determination of friction factor (f) for various pressure drop with rotameter height, h (plain tube):

Exp no.	h(cm)	P(N/m ²)	f
1	0.1	133.4	0.327
2	0.11	146.8	0.287
3	0.11	146.8	0.179
4	0.12	160.1	0.141
5	0.13	173.4	0.1
6	0.13	173.4	0.089
7	0.14	186.7824	0.079772202
8	0.15	200.124	0.067532023
9	0.16	213.4656	0.061544216
10	0.16	213.4656	0.051621184

Table 3.6: Value of friction factor (f) for various pressure drop (plain tube)

3.5 Data Calculation for plain copper tube with insert:

3.5.1 Thermometer and thermocouple reading at various flow rates:

Sr.	T _i	T _o	1	2	3	4	5
1	35	39.8	47	55	59	95	98
2	35	39.7	46	55	58	95	98
3	35	39.5	46	54	58	94	97
4	35	39.3	45	53	57	93	96
5	35	39	44	51	55	91	95
6	35	38.8	44	51	55	90	94
7	35	38.5	43	50	54	89	93
8	35	38.3	42	50	54	88	92
9	35	38.1	42	49	53	88	92
10	35	37.9	41	48	52	87	91

Table 3.7: Thermometer and thermocouple reading at various flow rates with insert.

3.5.2 Flow rate for various Rotameter reading with insert:

Exp no	(cm)	(ml/s)	(m ³ /s)	(kg/s)
1	5	75	0.000075	0.075
2	7.1	106.5	0.0001065	0.107
3	9	135	0.000135	0.135
4	10.6	159	0.000159	0.159
5	13.1	196.5	0.0001965	0.197
6	13.9	208.5	0.0002085	0.209
7	15.2	228	0.000228	0.228
8	17.1	256.5	0.0002565	0.257
9	18.5	277.5	0.0002775	0.278
10	20.2	303	0.000303	0.303

Table 3.8: Flow rate for various Rotameter reading with insert.

3.5.3 Determination of Q for various velocities with insert:

Exp no	(m ²)	Eq-5	Eq-3
1	0.000531	0.14	1504.44
2	0.000531	0.20	2091.80
3	0.000531	0.25	2538.74
4	0.000531	0.30	2857.18
5	0.000531	0.37	3284.69
6	0.000531	0.39	3311.02
7	0.000531	0.43	3334.84
8	0.000531	0.48	3537.31
9	0.000531	0.52	3594.98
10	0.000531	0.57	3672.09

Table 3.9: Value of Q for various velocities with insert.

3.5.4 Determination of heat transfer coefficient and Reynolds number with insert:

Exp no	Eq-11	Eq-14	Eq-15	Eq-12	Eq-9	Eq-6
1	0.100	70.8	70.7	37.4	709.4	4318.46
2	0.139	70.4	70.3	37.35	998.1	6132.22
3	0.168	69.8	69.6	37.25	1231	7773.23
4	0.189	68.8	68.6	37.15	1426	9155.14
5	0.218	67.2	66.9	37	1720	11314.3
6	0.219	66.8	66.5	36.9	1751	12005.3
7	0.221	65.8	65.5	36.75	1816	13128.1
8	0.234	65.2	64.9	36.65	2461	14769.1
9	0.238	64.8	64.5	36.55	2493	15978.3
10	0.243	63.8	63.5	36.45	2576	17446.5

Table 3.10: Value of heat transfer coefficient and Reynolds number with insert.

3.5.5 Determination of experimental N_u , P_r , and theoretical N_u with insert:

Exp no.	Eq-9	Eq-8	Eq-17
1	31.30	5.31	30.49
2	45.04	5.33	42.89
3	56.70	5.34	52.91
4	66.15	5.35	61.39
5	80.43	5.37	74.05
6	85.04	5.40	75.40
7	92.29	5.42	78.32
8	102.7388363	5.45	84.57835021
9	110.3195344	5.47	85.95726359
10	119.3009372	5.48	87.94334461

Table 3.11: Value of experimental N_u , P_r , and theoretical N_u with insert.

3.5.6 Determination of friction factor (f) for various pressure drop with insert:

Exp no.	h(cm)	P(N/m ²)	f
1	0.18	240.1	0.448
2	0.19	253.5	0.396
3	0.19	253.5	0.309
4	0.2	266.8	0.234
5	0.21	280.2	0.161

6	0.21	280.2	0.143
7	0.22	293.5152	0.12535632
8	0.22	293.5152	0.09904697
9	0.23	306.8568	0.09846981
10	0.23	306.8568	0.09420545

Table 3.12: Value of friction factor (f) for various pressure drops with insert.

3.6 Percentage increase on Nusselt no. (with insert):

no.	Eq-7	Eq-7	%Of increase	% of increase
1	20.99	30.49	45.26	
2	26.70	42.89	60.64	
3	34.91	52.91	51.56	
4	37.57	61.39	63.4	38.346
5	41.28	74.05	79.4	
6	65.97	75.40	14.3	
7	67.37	78.32	16.3	
8	72.8	84.57835021	16.2	
9	72.98	85.95726359	17.8	
10	74.17	87.94334461	18.6	

Table 3.13: Percentage increase on Nusselt no. (With insert).

** First five data were taken at morning and last five data were taken at afternoon.

Biomaterials Serving the Purpose of Drug Delivery in Human Body

Talukdar Raian Ferdous, Tahsin Solaiman*

Department of Biomedical Engineering, Khulna University of Engineering and Technology, Khulna, Bangladesh
Email: raianferdous1415020bme@gmail.com, tahsinsohan@gmail.com

ABSTRACT

Today is an era when we overcome all constraints concerning our health. Drug is a substance that when inhaled, injected, smoked, consumed, absorbed via a patch on the skin or dissolve under the tongue causes a temporary physiological change in the body. Total number of approved drugs is 3254. Delivering drugs on the body should be efficient enough. Different types of drug carriers are used for delivering these drugs into body. These carriers are more specialized in biocompatibility apart from other materials. Sometimes the carriers have good effective area coverage but it takes much time to affect and vice-versa. As a consequence several prolific researchers have been asked to contribute unique research findings and reviews that could stimulate continuing effort to look for or to understand new biomaterials with biocompatibility, desired residence time, larger area coverage. This text focuses on the recent and far attempts in drug delivery biomaterials that would allow people to have a clear view of materials role in health site. The discussion comprises of metal-organic frameworks, carbon materials, microporous mesoporous materials and Mechanoresponsive materials for drug delivery system.

Keywords: Metal Organic, Photopolymerized , Mesoporous, Carbon, Protein.

1. Introduction: In recent years progressive health care facilities have been aggrandized to increase the possibility of eradicating any health related problems. Different types of drugs are being used worldwide to prevent and cure diseases. Development of new drug molecule is expensive and timeconsuming [1]. The drugs are delivered to the body by several systems serving particular purpose. There are basically three types of novel drug delivery systems. They are (i) targeted drug delivery system (ii) controlled drug delivery system (iii) modulated drug delivery system. Each of them have distinguishable features with advantages and limitation. The field of drug delivery focuses on the development of technologies to deliver biomolecules to the site of the disease so as to maximize therapeutic benefits, minimize side effects and enhance patient compliance [2]. It depends on the system and its features how efficiently the drug is working. Many of the pharmacological properties of conventional drugs can be improved through the use of drug delivery systems (DDS), which include particulate carriers, composed primarily of lipids and/or polymers, and their associated therapeutics [3]. Delivery of drugs to specific locations in the human body using materials-based systems has been approaching the forefront of biomedical research for the past few decades. The concept has arisen from our advancing knowledge of materials for example, biocompatible nanoparticles that encapsulate drugs and respond to environmental stimuli, biodegradable hydrogels with tunable drug-release profiles, and implanted depots that control the spatiotemporal presentation of a therapeutic and has been enabled by our increased understanding of disease and the biochemical pathways involved [4]. Different materials hold the interest of being used in delivering drugs into the human body. We can mention

mesoporous, microporous, mechanoresponsive, metal framework, protein based materials serving this cause. These limitations can be potentially overcome by designing carriers that perform multiple tasks including encapsulation and controlled release, minimization of immune-clearance, penetration of biological barriers and targeting the disease site [2]. The objectives of this paper is to review the previous works and literatures of the materials that include the usages of drug delivery materials and helps providing necessary information about increasing effective area, shortening the duration to impact, alleviate the hazardous impact on human health as well as briefing the delivery systems of each type materials incorporated. Considerable literature was studied and gathered information on previous research and development of drug delivery materials. The most focused aspect of this paper is to accumulate these multiple works into a single sight so that the maximum benefits can be obtained at the time of selecting drug delivery materials simultaneously as all the available drug delivery materials are described.

2. Methodology and Materials: The key ingredient of any drug delivery system lies in the application of stable, attractive and biologically responsible materials. Materials having severe destructive impacts to the body internal affairs by releasing infectant, toxicity and depletion of natural resources are to be avoided. To check these destructive impacts precautionary steps are initiated during acquisition of drug delivery materials, their production and manufacturing processes and along with their transportation process. The manufacturing processes of these materials are to be conducted by taking some intensive cares. Selection of the materials depends on some factors (e.g. aesthetically preferable to

* Corresponding author. Tel.: +88-01748692078

E-mail addresses: raianferdous1415020bme@gmail.com

the habitants, cost effective and inserting to the living subject, surface area, volume etc.).

2.1 Mesoporous Materials: The mesoporous drug delivery system has contributed to turn the drug delivery system for its unique pore size, desired surface area, higher pore volume to carry out the drug. The drug incorporation is carried out by two ways. One is soaking of the matrix in a highly concentrated drug solution and another is subsequent drying [5]. The several structural and functional mesoporous-silica systems for sustained release of various drugs are being developed day by day. These systems include MCM-41 or M-41, MSU, SBA, HMA. MCM-41 as one of the importantly synthesized mesoporous materials, M41S [45], has been firstly employed as drug deliveryMatrix. The hexagonal structure of the wall of the cylindrical pores consists of a disordered network made up of siloxane bridges and free silanol groups acting as reacting nuclei against appropriate guest chemical. The M-41 has the slow rate of loading of the drug. The MSU mesoporous silica is another type of drug carrying system which is in under development. Tourne-Peteilh et al. [6]employed MSU to store pentapeptide. They found that pentapeptide could be encapsulated in the mesoporous silica and would be released instantly upon the solid washing with dimethylformamide (DMF). SBA-15 is another important mesoporous material which has a large, controlled pore size and highly ordered hexagonal topology [7].The SBA groups consist larger pore size of about 6nm than the M-41 considered more carrying capabilities of the bulky molecules. The subsumed amount of drug strongly depends on the amoxicillin concentration, solvent, pH, and amoxicillin concentration. It has the largest diameter. Hollow mesoporous spheres (HMS) are considered unique group of essential mesostructured materials, which exhibit much more advantages in mass diffusion and transportation compared with conventional hollow spheres of solid shells. They compared the drug loading with MCM-41 and found that the HMS exhibited much more storage capacity than MCM-41 [8].This group has the highest loading wt% of the all.

2.2 Carbon Materials: One of the most recent strategies proposed to incorporate nanotechnology principles is through the application of carbon nanotubes (CNTs). It has the unique properties of biocompatibility in the drug delivery system and their indispensable role in the carrying of drug to the highly selective and sensitive area. It leads to the modulation of undesired effects and creating new conjugates with promising and developed pharmacological profiles. The CNTs are two of types single-walled (SWNTs) and the multi-walled (MWNTs), both has the optical absorption around 700-1000 nm which is in the range of NIR, having great opportunities in the therapeutic cancer treatment drug delivery. Differing from small drug molecules which are usually able to diffuse across cell

membranes, biomacromolecules such as proteins, DNA, and RNA cannot penetrate the cell membrane by themselves, instead requiring delivery vehicles to help in their cellular entry. Proteins transported into cells via CNTs was achieved in a few early reports, where it was shown that proteins could either be conjugated or non covalently absorbed on CNTs for intracellular delivery [9-11]. Several other CNT-based photo-therapies is also reported. The photoacoustic effect of CNTs, showing great promise as a contrast agent for photoacoustic molecular imaging in vivo [12]. Carbon-nanotubes are preferable drug carriers for the purpose of cancer drug delivery and therapeutic treatment as well as imaging of tumors.

2.3 Mechanoresponsive Materials: To date, different physical and chemical based stimulus drug delivery systems had been found. Among those the emerging mechanical force-based stimulus is up to date and has a vast research area which offers a suitable and robust controlled drug delivery systems. Mechanical activated delivery systems comprise three delivery systems compression, tension, shear though the process is still under developing. Compressive delivery systems require substrates which withstand compressive loading and respond to it (Elastomers). In example, Yang et al. describe another example of cyclical compressive release demonstrating controlled release of bovine serum albumin (BSA) from porous matrices [13]. Lee et al. report one of the earliest hydrogel compressive systems, composed of calcium cross linked alginate, as a device to stimulate neovascularization through the delivery of physically entrapped vascular endothelial growth factor (VEGF) [14,15]. Tension responsive drug delivery is another method. The method uses tension to activate and control the rate of drug flow. Tension property is used because it is the dynamic nature of the human body. While most hydrogels are capable of compressive loading, hydrogels often yield at low tensile strains (i.e., <50% strain, [16]). From a highly stretchable interpenetrating alginate polyacrylamide hydrogel, first developed by Sun et al. [17], Zhang et al. release horseradish peroxidase and *Candida antarctica* lipase B by stretching [18]. The shear-responsive system has the potential to use in the cardiovascular system where narrowing blood-vessel increases the shear stress. This system includes liposome deformation, particle aggregation and dispersion, supramolecular disassembly.

2.4 Metal Organic Frameworks as Material: Great effort is being applied devoted to the development of methods to control drug release to satisfy the ever-growing demand for prolonged and better control of drug administration [19].Two methods are introduced. The first one titled "organic route" which uses either biocompatible dendritic macromolecules or polymers [20]and the second one is "inorganic route" in which the hosts are inorganic porous solids such as zeolites and mesoporous silicate materials. In case of organic route a wide range of drugs can be encapsulated but controlled

release is difficult. On the contrary for inorganic route release is performed by grafting organic molecules on pore walls but implies a decrease in drug loading capacity [21,22]. A third way: the “hybrid” route a combination of high and regular porosity with the presence of organic groups within the framework may cumulate the advantages to achieve both a high drug loading and a controlled release [19]. But microporous is a restriction here that has been observed. To overcome this major problem, researchers developed a method that combines targeted chemistry and structural computer predictions to obtain mesoporous hybrids with large pores. This approach leads to the characterization of two new cubic (Fd3m) zeotypic metal carboxylates, denoted MIL-100 and MIL-101 (MIL=Materials of Institut Lavoisier) and built up from trimers of metal octahedra and di- or tricarboxylic acids [23]. The drug content of MIL-101 is four times larger than in MCM-41 and the delivery rate tends to be slower, thus taking 6 days for MIL-101 relative to 2 days for MCM-41 [19]. Thus, MIL-101 is allowed a higher dosage of drug and a longer controlled delivery, which is supposed advantages for larger pharmacological molecules.

2.5 Chiral Nanoporous Metal-Organic Frameworks with High Porosity as Material: For drug delivery, chiral nanoporous metal-organic framework (MOF) with high porosity has been synthesized based on nontoxic zinc and achiral hexadentate ligand. The high drug loading and slow release of the loaded drug of the material is desired function for many drug delivery. Sometimes there is a complete delivery time of about one week being used as a material for adsorption and delivery of anticancer 5-fluorouracil. The delivery of bioactive gas molecules such as NO from MOFs as an antithrombosis and vasodilation agent, Gd III -based nanoscale MOFs being used as magnetic resonance imaging (MRI) contrast agents, [24] and lanthanide-based MOFs being efficient multimodal cellular probes materials [25]. 5-FU containing methanol solution is helpful for different spectroscopy.

2.6 Photopolymerized Hydrogel Material: Matrices of hydrophobic polymers such as ethylene-vinyl acetate copolymers is used for sustained release of proteins, polysaccharides, oligonucleotides [26] but it is difficult to homogeneously disperse hydrophilic materials within a hydrophobic copolymer matrix resulting in unpredictable release profiles. However there is a need of hydrophilic polymer which have potential to be used for sustained release. A hydrogel material is developed which may be suitable for delivery of proteins, peptides, oligonucleotides [27]. The hydrogel is generally formed by photopolymerization of an aqueous solution of a macromolecular precursor. The precursor is consisted of a central polyethylene glycol (PEG) chain with oligomeric blocks of a hydrolysable α -hydroxy acid, or other degradable moiety on each side. The hydrogel materials have also been used to prevent thrombosis and vessel narrowing following vascular injury [28]. The

synthesis of hydrogels appropriate for a wide variety of drug delivery options is allowed by this versatile design of precursor. A small drug would require a low molecular weight PEG in the precursor to achieve release mediated by hydrogel degradation. It is possible to control the release of macromolecular drugs from these photopolymerized hydrogels through the design of the precursor. Drug which is released from this type of hydrogel has been maintained for as long as 2 months in vitro [27]. Numerous variations on the acrylated PEG-co- α -hydroxy acid format can be synthesized, thus allowing one to essentially tailor the hydrogel to the requirements of a specific drug delivery application.

2.7 Protein Based Materials: Interests in protein-based biopolymers for drug delivery have been being increased in recent years. While comparing to synthetic polymers, they have advantages of being water-soluble, biocompatible, biodegradable and non-toxic [29]. Many fibrous protein materials such as keratin, collagen, elastin and silk have been widely used in drug-delivery related research [30]. Keratin could be derived from the outer layer of human skin and the epidermal appendages of animals such as feathers, hair, hooves, horns, nails, scales and wool [31]. At molecular level, keratin shows three different configurations: α -, β -, γ -Keratin. Collagen is a protein imperative to the structural integrity of tissues and cell growth in vertebrates and other organisms [32]. It can be processed into various forms suitable for drug delivery (such as hydrogels, microparticles and films) [33]. There are two categories to chemically crosslink collagen molecules: bi-functional and amide-type. By selecting and employing safe crosslinking modification methods to collagen, drug stability and retention times can be increased [30]. Similar to collagen, elastin is a protein within the extracellular matrices comprises different flexible tissues [34]. Elastin is a heavily crosslinked structure with beta-spiral secondary structure, making up a major component in elastic fibers [34]. Various forms of thermoresponsive elastin, such as animal-derived soluble elastin, recombinant human tropoelastin (rhTE), and elastin-like polypeptides (ELPs), have been synthesized and utilized to engineer promising synthetic tissue scaffolds [35]. Silk is a protein of long historical use in biomedical applications, such as tissue and ligament repair, nerve regenerators, and artificial blood vessels [36]. Different silkworm silks have been used for drug-delivery applications including *Bombyx mori*, Tussah, and Eri silks [37]. Silk proteins can be prepared in various ways, such as films [38], 3D porous scaffolds [39], and micro and nanoparticles [40], with controlled degradation rates. They have a great contribution to biotechnical applications like drug delivery and tissue scaffolds. Resilin is an elastomeric protein which was first found existing in jumping insects' cuticles of many species [41]. Resilin exhibits high extensibility, low stiffness, efficient energy storage and extraordinary resilience, which enables some jumping insects to take jump many times' their body length. The resilin's

rubber-like elasticity possesses excellent biocompatibility and mechanical properties, which can be used for a broad range of biomedical applications such as drug delivery and tissue scaffolds [41,42][46]. Zein is a major plant-based storage protein rich in prolamine generally found in the endosperm of the corn kernel [43]. It has four classes, α -, β -, γ -, δ -zein, varies on molecular weights and modes of extraction [44]. All zein fractions have hydrophobic and hydrophilic domains but zein is frequently considered to be a hydrophobic protein as it has insolubility in water and solubility in ethanol, acetone, and acetylacetone. Zein shows to form aggregates and entrap solutes like drugs or amino acids which make it an excellent matrix material for sustained release [30].

3. Conclusion: In this paper we have discussed about drug delivery biomaterials that are used and may have the possibility of being developed efficiently for effective health standard. Implementation of these materials depends largely on the type of patient, conditions, symptoms, environment etc. Better drug delivery will result in better standard of life eradicating diseases. Manufacturer companies should adopt steps for researching these materials in order to develop a hybrid one which must be cost efficient at the perspective of Bangladesh. This will elevate the drug delivery system and people will be the most advanced technology's beneficiaries. This will contribute a lot in the advancement of health sector of Bangladesh.

REFERENCES:

- [1] Tiwari G, Tiwari R, Bannerjee S, Bhati L, Pandey S, Pandey P and Sriwastawa B 2012 Drug delivery systems: An updated review *Int. J. Pharm. Investig.* **2** 2
- [2] Mitragotri S and Lahann J 2012 Materials for drug delivery: Innovative solutions to address complex biological hurdles *Adv. Mater.* **24** 3717–23
- [3] Allen T M and Cullis P R 2004 SUPPLEMENTARY MATERIAL Drug delivery systems: entering the mainstream. *Science* **303** 1818–22
- [4] Pàmies P and Stoddart A 2013 Materials for drug delivery *Nat. Mater.* **12** 957
- [5] Vallet-Regí M, Balas F and Arcos D 2007 Mesoporous materials for drug delivery *Angew. Chemie - Int. Ed.* **46** 7548–58
- [6] Tourné-Péteilh C, Lerner D A, Charnay C, Nicole L, Bégu S and Devoisselle J-M 2003 The potential of ordered mesoporous silica for the storage of drugs: the example of a pentapeptide encapsulated in a MSU-tween 80 *Chemphyschem* **4** 281–286
- [7] Zhao D, Feng J, Huo Q, Melosh N, Fredrickson G H, Chmelka B F and Stucky G D 1998 Triblock copolymer syntheses of mesoporous silica with periodic 50 to 300 angstrom pores *Science (80-.)*. **279** 548–52
- [8] He Q and Shi J 2011 Mesoporous silica nanoparticle based nano drug delivery systems: Synthesis, controlled drug release and delivery, pharmacokinetics and biocompatibility *J. Mater. Chem.* **21** 5845–55
- [9] Kam N W S and Dai H 2005 Carbon nanotubes as intracellular protein transporters: Generality and biological functionality *J. Am. Chem. Soc.* **127** 6021–6
- [10] Kam N W S, Liu Z and Dai H 2006 Carbon nanotubes as intracellular transporters for proteins and DNA: An investigation of the uptake mechanism and pathway *Angew. Chemie - Int. Ed.* **45** 577–81
- [11] Kam N W S, Jessop T C, Wender P A and Dai H 2004 Nanotube molecular transporters: Internalization of carbon nanotube-protein conjugates into mammalian cells *J. Am. Chem. Soc.* **126** 6850–1
- [12] De La Zerda A, Bodapati S, Teed R, May S Y, Tabakman S M, Liu Z, Khuri-Yakub B T, Chen X, Dai H and Gambhir S S 2012 Family of enhanced photoacoustic imaging agents for high-sensitivity and multiplexing studies in living mice *ACS Nano* **6** 4694–701
- [13] Yang Y, Tang G, Zhang H, Zhao Y, Yuan X, Fan Y and Wang M 2011 Controlled release of BSA by microsphere-incorporated PLGA scaffolds under cyclic loading *Mater. Sci. Eng. C* **31** 350–6
- [14] Lee K Y, Peters M C, Anderson K W and Mooney D J 2000 Controlled growth factor release from synthetic extracellular matrices *Nature* **408** 998–1000
- [15] Lee K Y, Peters M C and Mooney D J 2001 Controlled drug delivery from polymers by mechanical signals *Adv. Mater.* **13** 837–9
- [16] Calvert P 2009 Hydrogels for soft machines *Adv. Mater.* **21** 743–56
- [17] Sun J Y, Zhao X, Illeperuma W R K, Chaudhuri O, Oh K H, Mooney D J, Vlassak J J and Suo Z 2012 Highly stretchable and tough hydrogels *Nature* **489** 133–6
- [18] Zhang Y, Chen Q, Ge J and Liu Z 2013 Controlled display of enzyme activity with a stretchable hydrogel *Chem. Commun.* **49** 9815–7
- [19] Horcajada P, Serre C, Vallet-Regí M, Sebba M, Taulelle F and Férey G 2006 Metal-organic frameworks as efficient materials for drug delivery *Angew. Chemie - Int. Ed.* **45** 5974–8
- [20] Soppimath K S K, Aminabhavi T M T M, Kulkarni A R A R and Rudzinski W E 2001 Biodegradable polymeric nanoparticles as drug delivery devices *J. Control. Release* **70** 1–20
- [21] Muñoz B, Rámila A, Pérez-Pariente J, Díaz I and Vallet-Regí M 2003 MCM-41 organic modification as drug delivery rate regulator *Chem. Mater.* **15** 500–3
- [22] Horcajada P, Rámila A, Férey G and Vallet-

- Regí M 2006 Influence of superficial organic modification of MCM-41 matrices on drug delivery rate *Solid State Sci.* **8** 1243–9
- [23] Férey G, Serre C, Mellot-Draznieks C, Millange F, Surlé S, Dutour J and Margiolaki I 2004 A hybrid solid with giant pores prepared by a combination of targeted chemistry, simulation, and powder diffraction *Angew. Chemie - Int. Ed.* **43** 6296–301
- [24] Mckinlay A C, Xiao B, Wragg D S, Wheatley P S, Megson I L and Morris R E 2008 Exceptional Behavior over the Whole Adsorption - Storage - Delivery Cycle for NO in Porous Metal Organic Frameworks 10440–4
- [25] Rieter W J, Taylor K M L and Lin W 2007 Surface Modification and Functionalization of Nanoscale Metal-Organic Frameworks for Controlled Release and Luminescence Sensing **27599** 9852–3
- [26] Anon 1976 © 1976 Nature Publishing Group
- [27] Hubbell J A 1993 Bioerodible Hydrogels Based on Photopolymerized Poly(ethylene 581–7
- [28] Hill-west A J L, Chowdhury S M, Slepian M J and Hubbell A 2015 and intimal Inhibition of thrombosis thickening by in situ photopolymerization of thin hydrogel barriers
- [29] Garrait G, Beyssac E and Subirade M 2014 Development of a novel drug delivery system : chitosan nanoparticles entrapped in alginate microparticles **2048** 363–72
- [30] Jao D, Xue Y, Medina J and Hu X 2017 Protein-based drug-delivery materials *Materials (Basel)*. **10** 1–24
- [31] Ferraro V, Anton M and Santé-lhoutellier V 2016 The “sisters” α -helices of collagen, elastin and keratin recovered from animal by-products: functionality, bioactivity and trends of application *Trends Food Sci. Technol.*
- [32] Xiaoxin Z, Jiayin Z and Bin S H I Mesoporous Bioglass / Silk Fibroin Scaffolds as a Drug Delivery System : Fabrication , Drug Loading and Release in vitro and Repair Calvarial Defects in vivo 401–6
- [33] Friess W 1998 Collagen – biomaterial for drug delivery 1 **45** 113–36
- [34] Ulijn R, Woolfson D, Almine J F, Bax D V, Mithieux S M, Nivison-smith L, Rnjak J, Waterhouse A, Wise S G and Weiss A S 2010 Peptide- and protein-based materials themed issue Elastin-based materials w
- [35] Annabi N, Mithieux S M, Camci-unal G, Dokmeci M R, Weiss A S and Khademhosseini A 2013 Elastomeric recombinant protein-based biomaterials *Biochem. Eng. J.* **77** 110–8
- [36] Mobini S Bioactivity and Biocompatibility Studies on Silk-Based Scaffold for Bone Tissue Engineering **33** 207–14
- [37] Vollrath F and Porter D 2006 Spider silk as archetypal protein elastomer 377–85
- [38] Pritchard E M, Hu X, Finley V, Kuo C K and Kaplan D L Effect of Silk Protein Processing on Drug Delivery from Silk Films 311–20
- [39] Seib F P and Kaplan D L 2013 Silk for Drug Delivery Applications : Opportunities and Challenges **02155** 756–66
- [40] Kaplan D L and Meinel L 2013 (12) Patent Application Publication (10) Pub . No . : US 2013 / 0195831 A1 1
- [41] Qin G, Hu X, Cebe P and Kaplan D L 2012 Mechanism of resilin elasticity *Nat. Commun.* **3** 1003–9
- [42] McGann C L, Levenson E A and Kiick K L Resilin-Based Hybrid Hydrogels for Cardiovascular Tissue Engineering 203–13
- [43] Sousa F F O, Luzardo-álvarez A, Blanco-méndez J and Martín-pastor M 2012 NMR techniques in drug delivery : Application to zein protein complexes *Int. J. Pharm.* **439** 41–8
- [44] Bouman J 2016 Controlled Release from Zein Matrices : Interplay of Drug Hydrophobicity and pH *Pharm. Res.* 673–85
- [45] Kresge C T, Leonowicz M E, Roth W J J C, and Beck J S 1992 Ordered mesoporous molecular sieves synthesized by a Liquid template mechanism *Nature* **359**
- [46] Li L, Tong Z, Jia X and Kiick K 2013 Resilin-like polypeptide hydrogels engineered for versatile biological function *Soft Matter* **9** 665-673

ICMIEE18-215

Influence of Industrial Bleach Wash on the Physical and Comfort Properties of Denim Garments

Niaz Morshed Rifat, Joy Sarkar*

Department of Textile Engineering, Khulna University of Engineering & Technology, Khulna-9203, BANGLADESH

ABSTRACT

As the faded denim or old look denim is preferred by the today's youth, washing has become a crucial issue for the technologists to modify denim apparel to fulfill the demand of existing trend. The main factors affecting consumers when selecting garments are aesthetic appearance and fashion. Denim garments are subjected in industrial washing to obtain specific appearance and handle. The washing and finishing processes are utilized for the purpose of fashion and different recipes are applied for different effects which are quite significant for marketing. Washing is a novel process to impart worn-out look, to modify the appearance and to improve the comfort ability of apparel. Bleach wash is used to fade the color of denim as well as it has an effect on the physical and comfort properties of the denim also. This project represents the impact of bleach wash and subsequent softening treatment on 98.88% cotton, 1.12% spandex denim dyed with Sulphur bottom Indigo top (SBIT). Garments are washed using a different bleach concentration i.e. 3 g/l, 5g/l and 10 g/l for the constant time and temperature i.e. 30 minutes and 60°C and then softened using standard recipe. The physical and comfort properties are analyzed in before wash, after bleaching and after softening. The properties that are analyzed include GSM, shrinkage, EPI and PPI, stiffness, tensile strength, tear strength, drape test and comfort properties. Bleach washed and softened garments exhibit a great difference in the physical and comfort properties than the unwashed garments.

Keywords: Denim, Bleach wash, Physical properties, Comfort

1. Introduction

Among all the textile products, no other fabric has received such a wide acceptance as denim garments [1]. It can be considered as the most widely used garment in the fashion business. It is well known that denim and jeans have had a major influence on the lives of consumers since their inception [2].

Denim has a lot of demand in the market of regular garments as well as in the fashion market. People of all ages, especially the youth have a great interest on the denim. Different values by adding processes like industrial washing make denims not only look beautiful but also impart some functional properties to the garments [3].

In the readymade garments industry sector garments washing is a new technology. After making garments from solid color from dyed or pigment printed fabrics, the garments are washed by garments washing, color and outlook of the garments are modified. As a result, new outlook and appearance is produced in the garments, which is not possible in any other method [4]. Among different techniques of garments washing, bleach wash is chosen to fade a higher degree of color. It is very difficult without bleach wash, to fade the color from all over the garments at one wash in such a higher degree. That's why despite of having some drawbacks like- bleach decomposes the cellulose hence destroys the fabric, tends to make the fabric yellowish, needs to be neutralized hence increases cost and adds a more step to the processing time the bleach wash cannot be avoided. Besides these drawbacks, bleaching agents especially chlorine bleaches are health hazardous and the effluents are hazardous to the environment [5], the process controlling is very tough and same results

cannot be achieved in every batch even after following the same recipe [6]. Bangladesh is a country where ready-made garments are the top export item and among ready-made garments the share of woven items is maximum [7].

The aim of this project work was to analysis of comfort, tensile strength, tear strength, drape ability, GSM, stiffness, shrinkage, EPI and PPI of denim garments. The findings of this research work will help the technologists to explore the consequence of bleach wash on 98% cotton with 1.12% spandex denim apparel at different concentration while the washing time and temperature remain same.

Objectives:

The objectives of this project were-

- i. To study of various types of washing process.
- ii. To study and analysis of different physical and comfort properties of denim garments after bleach washing and softening.
- iii. To comparison of physical and comfort properties of denim garments between before washing and after bleach washing and softening.
- iv. To characterize the effect of concentration of bleaching powder on the physical and comfort properties of denim garments.
- v. To characterize the effect of softening process on the physical and comfort properties of denim garments.

2. Methodology

Sample collection:

Sample collected from apparel washing laboratory

* Corresponding author. Tel.: +88-01684326094

E-mail addresses: niazrifat999@gmail.com

Type: Denim garments.
 Fabric: 98.88% cotton, 1.12% spandex twill (3/1)
 Construction: (12OSL+12oe) × 12L40D/85×55
 Dye type for warp yarn: We used Sulphur bottom
 Indigo top (SBIT) fabric of different concentration.
 Bleaching powder: Chlorine Bleach: 35% chlorine.
 Origin: China.
 Experimental Condition:

Table 1 Experimental Condition of Bleach wash.

	Condition 1	Condition 2	Condition 3
Sample	1kg	1kg	1kg
M:L	1:8	1:8	1:8
Bleach	3g/l	5g/l	10g/l
Temp	60°C	60°C	60°C
Time	30min	30min	30min

Procedure of Bleach Wash:

Calcium Hypochlorite Bleaching was used to perform the bleach wash due to its availability rather than Sodium Hypochlorite. The following steps were involved in bleach wash procedure.

Desizing procedure:

The initial treatment of bleach wash was desizing process which was carried out by desizing agent (DP-7). The purpose of desizing process was to remove the starch materials present in the garments fabric.

Table 2 Recipe of desizing procedure.

Recipe	Sample 1	Sample 2	Sample 3
Lot size	1kg	1kg	1kg
Water@ of 1:8	8 litre	8 litre	8 litre
Desizing agent	15g	15g	15g
Temperature	55°C	55°C	55°C
Time	15 min	15 min	15 min

Then dropped the liquor and cold washed for 3 minutes. This process of cold was done for three times.

Bleaching procedure:

Calcium hypochlorite bleaching is carried out to increase the fading effect of overall garments.

Table 3 Recipe of bleaching procedure.

Recipe	Sample 1	Sample 2	Sample 3
Liquor ratio	1:8	1:8	1:8
Calcium Hypo chloride	3g/l	5g/l	10g/l
pH	8	8	8
Temperature	60°C	60°C	60°C
Time	30 min	30min	30 min

Then drop the liquor and cold wash of 3 min at 2 times.

Neutralization:

After the beaching treatment the neutral wash was completed by the reducing agent sodium hyposulphite.

Table 4 Recipe of neutralization process.

Recipe	Sample 1	Sample 2	Sample 3
Liquor ratio	1:7	1:7	1:7
Sodium Hyposulphite	0.714g/l	0.714g/l	0.714g/l
Temperature	60°C	60°C	60°C
Time	5 min	5 min	5 min

Then drop the liquor and cold wash of 3 min at 2 times.

Softening process:

To improve fabric handle and other valuable properties, softeners are widely used in the finishing process.

Table 5 Recipe of Softening process.

Recipe	Sample 1	Sample 2	Sample 3
Liquor ratio	1:10	1:10	1:10
Softener	8.33g/l	8.33g/l	8.33g/l
Temperature	40°C	40°C	40°C
Time	5min	5min	5min

Then dropped the liquor and unloaded the garments from the washing machine into a perforated trolley.

Hydro-extraction process:

After unloading garments from the washing machine garments were sent to hydro extractor machine for removing excess water from the washed garments.

Drying process:

Then the garments were dried with the help of garments drying machine at 100°C for 15 min following a cold dry of 10 min to return the garments in normal position.

3. Results and Discussion:

A comparative study and analysis of physical and comfort properties of denim garments between before wash and after wash.

3.1 Shrinkage Test:

Shrinkage percentage= (change in length after wash / original length) × 100%.

Sample size: 35cm×35cm

Equipment: (i) Scale (ii) Template (iii) Scissor (iv) Chalk

Table 6 Effect of bleach washing on Shrinkage.

Concentration	Shrinkage (%)	
	Warp way shrinkage (%)	Weft way shrinkage (%)
3gpl, Bleach	2.77	12.85
3gpl, Bleach & softening	2.57	13.82
5gpl, Bleach	3.14	14.97
5gpl, Bleach & softening	3.14	14.77
10gpl, Bleach	3.14	13.71
10gpl, Bleach & softening	3.14	14.28

From the above table 6 it is seen that shrinkage increased gradually in warp way both for bleaching and softening as concentration of bleaching powder increased. In weft way shrinkage was increased for 3gpl and 5gpl both for bleaching and softening. But for 10gpl, shrinkage was decreased for bleaching in weft way than 5gpl.

GSM Test

Equipment: (i) GSM cutter (ii) Electronic balance

Table 7 Effect of bleach washing on GSM.

Concentration	Condition	GSM
3gpl	Before Wash	333
	Bleach	359
	Bleach & Softened	372
	Bleach	355
5gpl	Bleach & Softened	372
	Bleach	351
10gpl	Bleach & Softened	375

From the above table7 it can be said that GSM increased gradually for bleaching and softening as concentration of bleaching powder increased comparing with the unwashed garments. But for 10gpl GSM was decreased for bleaching than 3gpl and 5gpl.

EPI & PPI Test:

Sample size: 1 inch × 1 inch

Equipment: (i) Counting glass (ii) Scale (iii) Needle (iv) Scissor (v) Chalk

Table 8 Effect of bleach washing on EPI and PPI.

Concentration	Condition	EPI	PPI
3gpl	Before wash	85	55
	Bleach	96	56
	Bleach & Softened	100	55
	Bleach	92	57
5gpl	Bleach & Softened	96	51
	Bleach	104	56
10gpl	Bleach & Softened	112	54

From the above table 8 it is clear that EPI is increased as concentration of bleaching powder increased in both for bleaching and softening comparing with the unwashed

garments. But PPI is increased only for bleach as concentration of bleaching powder increased.

Stiffness Test:

Sample size: 204mm×102mm

Equipment: (i) Scissor (ii) Chalk (iii) Template (iv) Stiffness tester

Table 9 Effect of bleach washing on Stiffness.

Concentration	Condition	Stiffness
3gpl	Before wash	10.5 N
	Bleach	5.2 N
	Bleach & Softened	3.8 N
	Bleach	4.3 N
5gpl	Bleach & Softened	3.6 N
	Bleach	3.8 N
10gpl	Bleach & Softened	3.6 N

From the above table 9 it is clear that stiffness has diminishing characteristics in both for bleaching and softening as concentration of bleaching powder increased.

Tensile Strength Test

Sample size: (i) 20cm × 10cm (for warp) (ii) 10cm × 20cm (for weft)

Equipment: (i) Titan-5 (vertical strength tester) (ii) Scale (iii) Template (iv) Scissor (v) Chalk Method: ASTM-D 5034

Table 10 Effect of bleach washing on Tensile strength.

Concentration	Tensile Strength (Newton)	
Before wash	Warp	696.23
	Weft	504.56
3gpl, Bleach	Warp	673.36
	Weft	429.45
3gpl, Bleach and softened	Warp	612.47
	Weft	395.41
5gpl, Bleach	Warp	617.63
	Weft	399.32
5gpl, Bleach and softened	Warp	456.39
	Weft	338.95
10gpl, Bleach	Warp	448.36
	Weft	289.06
10gpl, Bleach and softened	Warp	363.02
	Weft	261.99

From the above table 10 it is seen that strength of the denim garments decreased in both warp and weft way as concentration of bleaching powder increased both for bleaching and bleaching & softening.

Tear Strength Test:

Sample size: 100mm × 63mm

Equipment: (i) Elma Tear Tester (ii) Scale (iii)

Template (iv) Scissor (v) Chalk Method: ASTM-D 1424

Table 11 Effect of bleach washing on Tear strength.

Concentration	Tear Strength (Newton)	
Before wash	Warp	63.10
	Weft	64.76
3gpl, Bleach	Warp	44.99
	Weft	46.62
3gpl, Bleach and softened	Warp	44.53
	Weft	44.14
5gpl, Bleach	Warp	39.59
	Weft	41.45
5gpl, Bleach and softened	Warp	39.07
	Weft	38.68
10gpl, Bleach	Warp	25.56
	Weft	27.33
10gpl, Bleach and softened	Warp	26.03
	Weft	33.83

From the above table 11 it is seen that tear strength of the denim garments decreased both for bleaching and softening in warp and weft way as concentration of bleaching powder increased.

Drape Test:

Sample size: 18cm in dia

Equipment: (i) Drape Tester (ii) Scale (iii) Template

(iv) Scissor (v) Chalk

Table 12 Effect bleach washing on Drapability.

Concentration	Static Drape Coefficient %	Dynamic Drape Coefficient (%)
Before Wash	100	100
3gpl, Bleach	96.95	93.32
3gpl, Bleach & Softened	95.91	93.93
5gpl, Bleach	90.74	93.03
5gpl, Bleach & Softened	89.59	92.80
10gpl, Bleach	87.95	90.35
10gpl, Bleach & Softened	87.22	90.11

From the above table 12 it is obvious that drapability of the denim garments increased with the increasing of concentration of bleaching powder.

4. Conclusion

To complete this research work 3/1 right hand twill stretch fabric was used. The construction of the fabric was (12OSL+12oe) ×12L40D/85×55 where lycra was inserted with weft at the percentage of 1.12. Due to the presence of lycra in the fabric, shrinkage was increased both in warp way and weft way but weft way shrinkage was higher than warp way direction. As shrinkage occurred, GSM and EPI×PPI were gradually increased with the increasing of concentration of bleaching powder. But Tear strength, Tensile strength and Stiffness were gradually decreased with the increasing of concentration of bleaching powder comparing with unwashed fabric. From this experiment it is concluded that, for 5gpl concentration comfort property was not up to the mark. But physical properties were good enough comparing with consumers recommendation.

REFERENCES

- [1] E. Khalil, *Sustainable and Ecological Finishing Technology for Denim Jeans*, AASCIT Communication, 2015, 159-163.
- [2] R. Paul, *Denim and jeans: an overview. Denim: Manufacture, Finishing and Applications*, Pp. 1-5.
- [3] J. Sarkar, K. Elias, *Effect of Industrial Bleach Wash and Softening on the Physical, Mechanical and Color Properties of Denim Garments*, IOSR Journal of Polymer and Textile Engineering, Vol.1, Issue 3, May-Jun.2014.
- [4] M.A. Kashem, *Garments merchandising*, Lucky- One Traders, Dhaka, 2008.
- [5] M. T. Islam, *Garments washing & dyeing*, Ananto Publications, Dhaka, 2010.
- [6] S. Pal, *Technology of denim production: Part VI*. Retrieved from <http://www.fibre2fashion.com/>.
- [7] Retrieved June 1, 2014 from http://www.bgmea.com.bd/chart_test/exportOfWovenAndKnit/ 2013.

Investigation of Mechanical Properties of Jute-Betelnut Husk Fiber (BHF) Reinforced Epoxy Composite

Tanvirul Islam*, Md.Shakhwat Hossain, Md.Mahmudul Hasan

¹ Department of Textile Engineering, Khulna University of Engineering & Technology, Khulna-9203, BANGLADESH

ABSTRACT

The importance of natural fiber reinforced composite material is increasing in the field of engineering and technology due to their outstanding promising properties. Here we investigate the mechanical properties of alkali treated jute betel-nut husk reinforced epoxy composite with respect to variation of BHF & epoxy. The composite sample was prepared by hand layup method. Different jute-betel nut reinforced epoxy composite was prepared in the ratio of fiber content 10:5, 10:10, 10:15 and 10:20 wt% with 85% epoxy, 80% epoxy, 75% epoxy and 70% respectively. The composite samples were prepared by hand layup process. Mechanical properties including tensile strength, yield strength, young modulus, elongation at break percentage and impact strength of the composites were investigated. The result showed that mechanical properties of 10:10 ratio of jute-betel nut and 80% epoxy was maximum. The effect of alkali treatment of fibers were verified by FTIR analysis.

Keywords: BHF, alkali treatment, mechanical properties, UTM, FTIR.

1. Introduction

The researchers and scientists have been interested to find suitable alternative materials in order to replace traditional polymer composites made with synthetic fibers. Hence using natural fiber as reinforcement in composite preparation due to its environmental and economic concerns is called eco-friendly composite. Eco-friendly composites are natural fibers such as jute, hemp, betelnut, sisal, flax, kenaf, etc.[1-3]. The main advantages of the eco-friendly composite materials are recyclable, biodegradable, sustainable and renewable. [4-7]. There are many other reasons that make natural fibers superior to use instead of synthetic fibers i.e. lightweight, superior strength, good mechanical properties, low energy consumption and high specific modulus. They are naturally non-toxic, nonhazardous, recyclable, flexible in usage, low cost and that allow clean energy recovery, etc.[8-10]. The properties of composite largely depends on adhesion of matrix and fiber. The adhesion of fiber and matrix are severely affected due to incompatibility of fiber and matrix. The degree of adhesion between the natural fiber and matrix determine the mechanical properties of natural fiber-reinforced composite [11]. The degree of adhesion depends on fiber surface. Naturally untreated natural fiber like betelnut [12], oil palm [13,14,15], banana [16], sugarcane [17,18] and coir [19] poses very weak interfacial adhesion strength with the matrix. Foreign substrate on the fiber surface of the natural fiber prevent the matrix to create strong bonding with the fiber. Hence some physical and chemical treatment were done to increase the adhesion between the fiber and matrix. Hence, it helps to increase the fiber properties, wettability and bondability between fiber and matrix. Physical process comprise treatments by laser, ionized gas (plasma or corona), steam explosion etc. [20]. There are many chemical process to remove foreign material and impart hydroxyl properties of the natural fiber. The aim of these treatments to improve adhesion between

fiber and matrix and hence increase the fiber strength and reducing water absorption [21]. Here alkalization was done to remove the foreign material and increase bondability. There has difference in mechanical properties between the treated and untreated jute-betelnut composite. In the past the investigational results of researchers indicates that chemically treated jute-betelnut composites poses better mechanical properties than untreated composites[22].

From various natural fiber, betelnut husk fibers poses outstanding mechanical properties. BNHF is extracted from the leave of plant *Aeraca Catechu*. Another blessing natural fiber jute has better performance than other natural fiber. It is inexpensive and available in the Asian subcontinent. Jute exhibits better mechanical properties and a suitable replacement for wood [23]. Mechanical properties of jute-betelnut husk fiber composites are highly depends on the maturity of fiber.

The main objectives of the research work is to test the mechanical properties of the jute-betelnut husk reinforced epoxy composite at different content of betelnut husk fiber and epoxy resin. We focus on betelnut husk fiber as it is treated as wastage and sometimes it just use as fuel in some region of Bangladesh and Asian subcontinent. The jute-betelnut husk fiber reinforced epoxy composite can be a good replacement of wood hence it prevent the deforestation.

2. Materials and Methods

2.1 Materials

Epoxy resin (Araldite LY556) and Hardener (Aradur HY951) were purchased from Lucky Acrylic and Fiber from Dhaka, Bangladesh. Betelnut husk fiber was collected from Goripur, Noakhali Bangladesh and jute fiber (hessian cloth) was collected from Bangladesh Jute Research Institute Dhaka, Bangladesh.

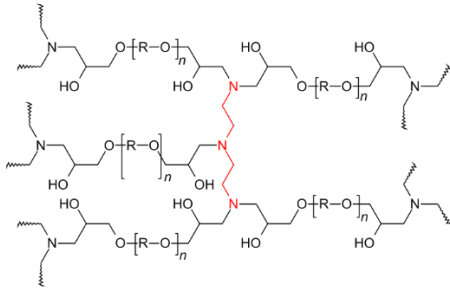


Fig.1 Molecular structure of epoxy resin

2.2 Methods

Weight of the samples were recorded by electric balance. Betelnut fiber content were varied for each composite sample.

Table 1 Sample Identification

Sample Name	Jute	Betelnut Fiber	Epoxy
Sample A	10	5	85
Sample B	10	10	80
Sample C	10	15	75
Sample D	10	20	70

3. Preparation of Composites

Composites were prepared by following steps

3.1 Fiber Extraction

Ripe betelnut husk was selected for fiber extraction. Selected betel nut husk was soaked in water for 20 days to rotten. Then the rotten husk was stripped manually by hand and rinsed in distilled water for several times. The extracted fiber was than dried for 15 days.

3.2 Alkali Treatment

The extracted betelnut was untreated. As it is natural fiber and its surface contain oil, wax and others foreign material so it was treated with coustic soda. 5% NaOH solution was prepared and betel nut husk fiber was immersed for 36 hr at 30oC. The fiber was than washed 10 times in distilled water and 2% acetic acid was used for neutralization. It was than washed again and the final Ph was near about to 7. Than they were dried at room temperature for 15 days.

3.3 Fabrication of Composite

Jute and betelnut husk fiber were taken for sample preparation according to sample identification. Butelnut husk fiber was in fiber stage. So the fiber was made in sheet like material and Jute hessian cloth was used for composite fabrication. Desired amount of betelnut husk fiber was measured in weight and 450KN was applied to make it a sheet like material. This force was applied

by UTM machine in Strength of Material Lab, Department of Civil Engineering, KUET. Epoxy resin and epoxy hardener were mixed properly in 2:1 ratio. Jute-betelnut husk fiber reinforced epoxy composites were prepared by hand layup process. Jute and betelnut husk fiber sheet were cut in 22cm*22cm and placed on a 30cm*30cm metal plate. A mylot paper was placed on the metal plate with the same dimension of the metal plate. According to jute and betelnut fiber content epoxy resin and epoxy hardener were mixed in 2:1 ratio and agitate properly to mix up. Some of the matrix solution was spread over the mylot paper and a jute fabric sheet and betelnut husk fiber sheet were placed and rolled. By this process 3 jute fabric sheet and 2 betelnut husk fiber sheet were required for each composite sample. Than complete matrix solution was poured and rolled properly. A dead weight of 15 kg was given on the arrangement for 8 hr. Finally the load was removed and mylot papers were separated from composite sample. Thus our required composite samples were obtained.

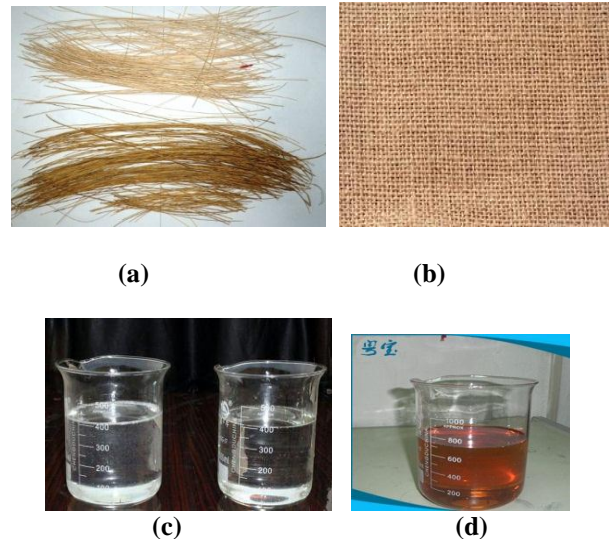


Fig 2. (a) Raw Betenut fiber, (b) Jute Fiber, (c) Epoxy Resin, (d) Epoxy Hardener

4. Testing of Composite Material

Mechanical properties such as Tensile properties (TS), Elongation at Break (EB), Young Modulus (YM), Yield Strength (YS), Impact Strength (IS) of the prepared composite sample were investigated by UTM at Bangladesh Atomic Energy Commission, Dhaka, Bangladesh. The samples were prepared for testing according to ASTM D638 standard. The specimen were cut in warp direction. The specimen size was 80mm*8mm*7mm. Here we maintained gauge length 35 mm and crosshead speed 10 mm/min. Three specimen were tested for each test from each sample A,B,C & D. Following equation 1, 2 and 3 were used for measuring the tensile strength, elongation at break percentage, Young’s modulus respectively. Impact strength was measured from isode table.

$$\text{Tensile strength (TS)} = \frac{F_{\max}}{A} \quad (1)$$

Where, F_{\max} = Load applied to the sample and, A = Cross-sectional area of the sample.

Percentage of elongation-at-break was obtained by the following relation:

$$\text{Elongation at Break EB (\%)} = \left(\frac{\Delta L_b}{L_0} \right) \quad (2)$$

Where, ΔL_b = Extension at break point of the sample and L_0 = Gage length or original length of the sample.

Yield modulus were measured by the following equation-

$$\text{Yield Modulus (YM)} = \frac{d\sigma}{d\epsilon} \quad (3)$$

Where, $d\sigma$ = Stress at yield point, $d\epsilon$ = Strain at yield point.

Impact strength of the the composite samples were measured by Izod impact testing machine (HT8041B) according to the ASTM standard.

5. Result and Discussion

5.1 Tensile Strength

The tensile strength of epoxy and jute, Betelnut-husk & epoxy composite are given in Table 2 and its corresponding data are plotted in Fig. 3. It was observed that tensile strength increased from sample A to B, which means that with increasing percentage of Betelnut-husk tensile strength increased. In this case, due to 5% Betelnut-husk percentage increasing tensile strength increase. With further increasing percentage of Betelnut-husk from sample B to C and C to D Tensile strength of the composite is decreasing. This because of the decreasing percentage of Epoxy. Sample B having the most tensile strength 26.96 MPa and while sample C having the least 9.97 MPa.

Table 2 Effect of fiber content on Tensile Strength of the composites

Sample	Tensile Strength (Mpa)
A	22.45
B	26.96
C	15.437
D	9.97

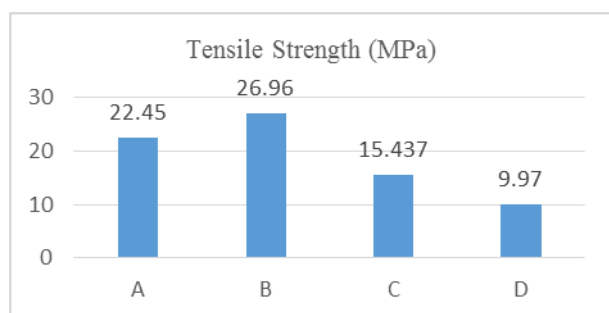


Fig 3. Effect of fiber content on Tensile Strength of the composites

5.2 Elongation at break (%)

Four samples were tested to observe their elongation behavior under tensile load. Elongation percentage are presented below in table 3 and fig 4. Elongation percentage of the four samples are not showing any proportional relation to the consisting materials of the composites. Sample B (10%betelnut-husk & 80% epoxy) having the least percentage of elongation and Sample C (15% Betelnut-husk & 75% epoxy) having the most amount of elongation percentage.

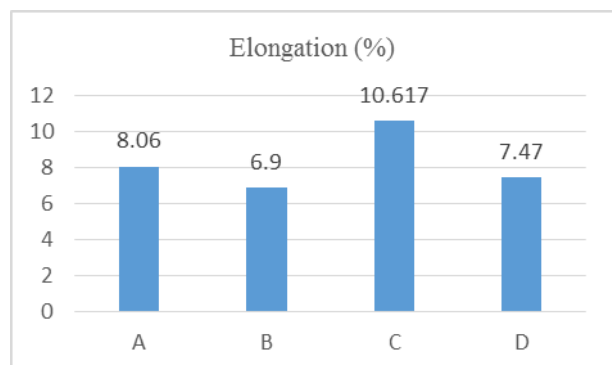
Table 3 Effect of fiber content variation on Elongation at break (%) of the composites sample

Sample	Elongation (%)
A	8.06
B	6.9
C	10.617
D	7.47

Fig 4. Effect of fiber content variation on Elongation at break (%) of the composites sample

5.3 Young's Modulus

Young's modulus means measure of the stiffness of a



solid material. It shows the relationship between stress (force per unit area) and strain (proportional deformation) in a material. From table 4 it was observed that sample B exhibit most Young's Modulus 607 Mpa and sample C exhibit least Young's Modulus 309.2 Mpa. Epoxy resin has good bonding capacity with natural fiber. As the fibers were alkali treated hence there have strong covalent bonds between fiber and epoxy resin and made it strong. This due to the effect of strong bonding between matrix and resin material.

Table 4 Effect of fiber content variation on Young's modulus of the composite sample

Sample	Young's Modulus(Mpa)
A	592.67
B	607
C	309.2
D	393.73

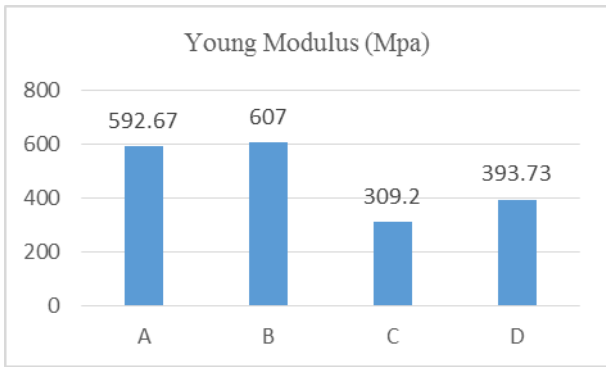


Fig 5. Effect of fiber content variation on Young's modulus of the composite sample.

5.4 Impact Strngth

The impact strength of jute-BHF reinforced epoxy composite are given in Table 5 and its corresponding data are plotted in Fig. 6. The impact properties of the composite sample were increased by the reinforcement of betelnut husk fiber. The maximum impact strength was found for sample D.

Table 5 Effect of fiber content variation on impact strength of the composite sample

Sample	Impact Strength(KJ/Cm ²)
A	13.848
B	12.842
C	16.968
D	22.485

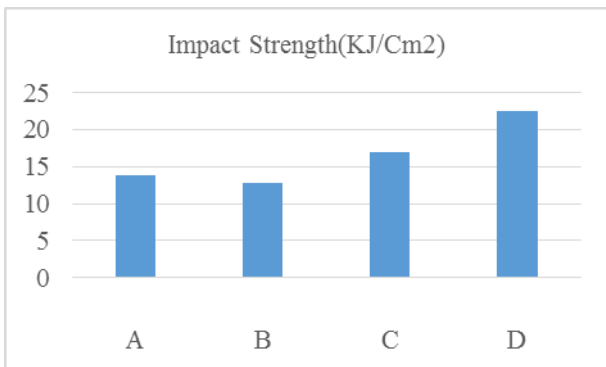


Fig 6. Effect of fiber content variation on impact strength of the composite sample

5.6 FTIR Spectra of Composite Sample

As the fibers were alkali treated, the peak 1722.43 cm⁻¹ corresponding to C=O stretching vibration of hemicellulose disappeared owing to structural change [24]. In chemical solution this may be imposed to dissolution of hemicelluloses. The hydrogen of droxyl group was substituted by acetyl groups in chemical treatment, resulting in little hydroxyl groups able to carry through hydrogen bonds. OH band was decreased after alkali treatment and its displacement from 3400-3700 cm⁻¹[25]. Most of the lignin and hemicellulose component were removed by the treatment and the changed the hydrophilic nature of the fibers to hydrophobic nature. FTIR spectra of composite samples

are given below. They show that the bonding between the matrix and reinforcement. As the jute and betelnut husk fiber were alkali treated so the foreign material were removed .Hence the bonding were prime.

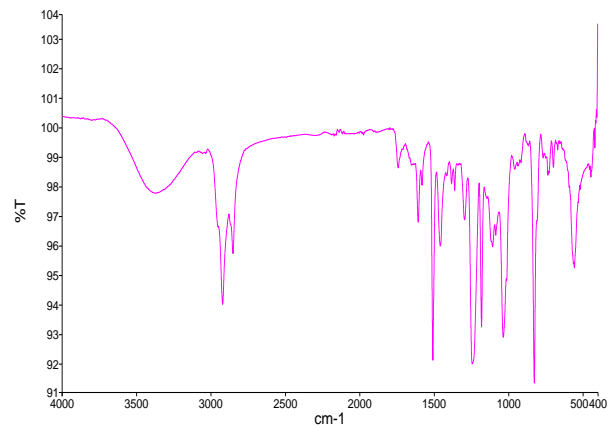


Fig 7. FTIR spectra of Jute-BHF reinforced epoxy composite sample A

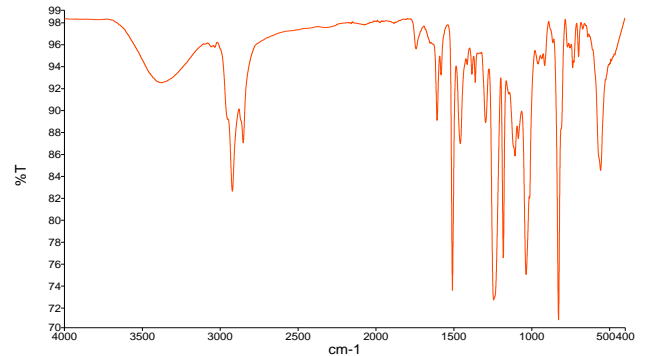


Fig 8. FTIR spectra of Jute-BHF reinforced epoxy composite sample B

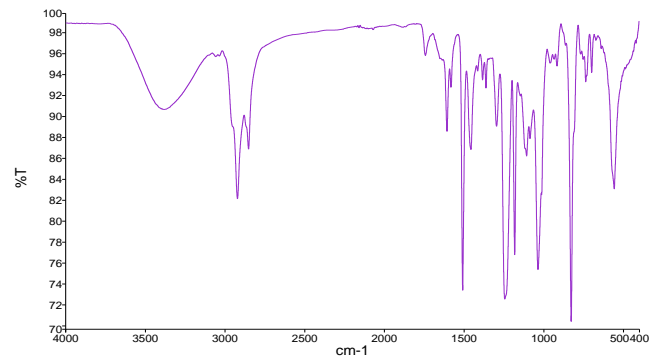


Fig 9. FTIR spectra of Jute-BHF reinforced epoxy composite sample C

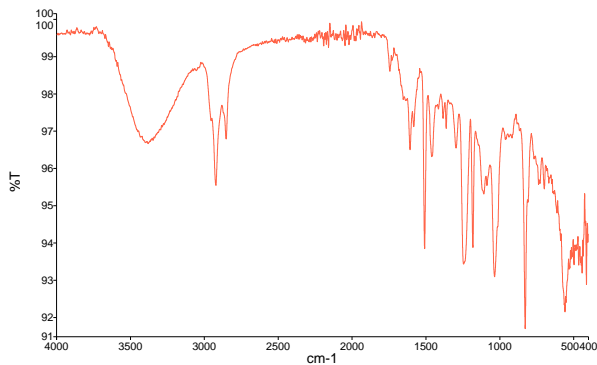


Fig 10. FTIR spectra of Jute-BHF reinforced epoxy composite sample D

5.7 Comparative Analysis

It was clearly evident that sample B exhibited better mechanical properties without impact strength. Tensile strength increased from sample A to sample B by 20.96%. But after that the tensile strength fall from sample C to sample D. This due to the strong interfacial bonding between matrix & reinforcement. Elongation at break percentage was better for sample B. It showed better elongation at break percentage property under tensile load. Sample B showed better Young's Modulus than sample A, C and D. Impact strength showed different phenomenon. Sample D showed better impact strength. As fiber content was more in sample D than sample A, B, and C so the capacity of withstand applied load was more and impact strength was more.

6. Conclusion

In this study mechanical properties of Jute-BHF reinforced epoxy composites were investigated. From above experiment we found that 10:10:80 ratio of jute, betelnut husk fiber and epoxy composition showed good mechanical properties. From the characterizations of the composites it can be suggested that jute-betelnut husk fiber reinforced epoxy composites can be used as engineering, automobile industry, building and construction materials and household utensils such as table, basket, shelve, partition board, ceiling etc. These are the potential application of this composite material as it has good mechanical properties. Further experiment will be done to improve processing to expand the application fields for jute and betelnut husk fiber reinforced epoxy composites.

REFERENCES

[1] Lee B-H, Kim H-J, Yu W-R. Fabrication of long and discontinuous natural fiber reinforced polypropylene biocomposites and their mechanical properties. *Fibers and Polymer* 2009;10(1):83-90.

[2] Lu N, Oza S. Thermal stability and thermo-mechanical properties of hemphigh density polyethylene composites: effect of two different chemical modifications. *Composites Part B Eng.* 2013;44(1):484e90.

[3] Alamri H, Low IM, Alothman Z. Mechanical, thermal and microstructural characteristics of

cellulose fibre reinforced epoxy/organoclay nanocomposites.

[4] M. Pakanita, K. Thiranan, P. Menutc, S. Suwit, (2011) Effect of lignin removal on the properties of coconut coir fiber/wheat gluten biocomposite, *Composites Part A: Applied Science and Manufacturing*, 42(2): 173-179.

[5] C. V. Srinivasa, A. Arifulla, N. Goutham, T. Santhosh, H. J. Jaeethendra, R. B. Ravikumar, S. G. Anil, D. G. Santhosh Kumar, J. Ashish, (2011) Static bending and impact behaviour of areca fibers composites, *Materials & Design*, 32(8-9): 4658-4663.

[6] K. G. Satyanarayana, G. G. C. Arizaga, F. Wypych, (2009) Biodegradable composites based on lignocellulosic fibers - An overview, *Progress in Polymer Science*, 34(9): 982-1021.

[7] S. A. Paul, K. Joseph, G. D. G. Mathew, L. A. Pothena, S. Thomasd, (2010) Influence of polarity parameters on the mechanical properties of composites from polypropylene fiber and short banana fiber, *Composites Part A: Applied Science and Manufacturing*, 34(9): 982-1021.

[8] N. S. Gill, B. F. Yousif, (2009) Wear and frictional performance of betelnut fibre-reinforced polyester composite, *Proceedings of the Institution of Mechanical Engineers, Part J: Journal of Engineering Tribology*, 223(2): 1983-1994.

[9] W. L. Lai, M. Mariatti, J. S. Mohamad, (2008) The properties of woven kenaf and betel palm (Areca catechu) reinforced unsaturated polyester composites, *Polymer-Plastics Technology and Engineering*, 47(10-12): 1193-1199.

[10] M. M. Hassan, M. H. Wagner, H. U. Zaman. M. A. Khan, (2011) Study on the performance of hybrid jute/betel nut fiber reinforced polypropylene composites, *Journal of Adhesion Science and Technology*, 25(6-7): 615-626

[11] T. Yu, J. Ren, S. Li, H. Yuan, and Y. Li, "Effect of fiber surface-treatments on the properties of poly (lactic acid)/ramie composites," *Composites Part A: Applied Science and Manufacturing*, vol. 41, pp. 499-505, 4// 2010

[12] S.C.Venkateshappa, B.Bennehalli, M.G.Kenchappa and R.P.G.Ranganagowada Flexural behavior of Areca fiber composite.

[13] B.F. Yousif, N.S.M. El-Tayeb, High-stress three-body abrasive wear of treated and untreated oil palm fiber reinforced polyester composite, *Proc. IMechE J: J. Eng. Tribol.*, 222 (2008).

[14] B.F. Yousif, N.S.M. El-Tayeb, Wet adhesive wear characteristics of treated and untreated oil palm fibres reinforced polyester composites using two POD and BOR techniques, *Proc. IMechE J: J. Eng. Tribol.* 224 (2010) 123–131.

[15] B.F. Yousif, N.S.M. El-Tayeb, The effect of oil palm fibres as reinforcement on tribological performance of polyester composite, *Surf. Rev. Lett.* 14 (6) (2007) 1095–1102.

[16] L.A. Pothana, Z. Oommenb, S. Thomas, Dynamic

- mechanical analysis of banana fibre reinforced polyester composites, *Compos. Sci. Technol.* 63 (2) (2003) 283–293.
- [17] N.S.M. El-Tayeb, Abrasive wear performance of untreated SCF reinforced polymer composite, *J. Mater. Process. Technol.* 206 (2008) 305–314.
- [18] N.S.M. El-Tayeb, A study on the potential of sugarcane fibers/polyester composite for tribological applications, *Wear* 265 (June (1–2)) (2008) 223–235.
- [19] B.F. Yousif, Frictional and wear performance of polyester composites based on coir fibers, *Proc. IMechE J: J. Eng. Tribol.* 223 (2009) 51–59.
- [20] K. G. Satyanarayana, G. G. C. Arizaga, and F. Wypych, "Biodegradable composites based on lignocellulosic fibers—An overview," *Progress in Polymer Science*, vol. 34, pp. 982-1021, 9// 2009.
- [21] Elammaran Jayamani, Sinin Hamdan, Md Rezaur Rahman and Muhammad Khusairy Bin Bakri, "Investigation of Fiber Surface Treatment on Mechanical, Acoustical and Thermal Properties of Betelnut Fiber Polyester Composites", *Procedia Engineering* 97 (2014) 545 – 554.
- [22] Priyadarshi Tapas Ranjan Swain and Sandhyarani Biswas, "Influence of fiber surface treatments on physico-mechanical behavior of jute/epoxy composites impregnated with aluminium oxide filler," *Journal of Composite Materials* 0(0) 1–14
- [23] Reddy, M.I., Kumar, M.A. and Raju, C.R.B., 2016. Tensile and Flexural properties of Jute, Pineapple leaf and Glass Fiber Reinforced polymer Matrix Hybrid Composites. *International Conference on Processing of Materials and Energy*, pp. 1-5.
- [24] M. K. Hossain, M. W. Dewan, M. Hosur, and S. Jeelani, "Mechanical performances of surface modified jute fiber reinforced biopolymer nanophased green composites," *Composites Part B: Engineering*, vol. 42, pp. 1701-1707, 9// 2011.
- [25] S. M. Luz, J. Del Tio, G. J. M. Rocha, A. R. Gonçalves, and A. P. Del'Arco Jr, "Cellulose and lignin from sugarcane bagasse reinforced polypropylene composites: Effect of acetylation on mechanical and thermal properties," *Composites Part A: Applied Science and Manufacturing*, vol. 39, pp. 1362-1369, 9// 2008.

Thermal Hydraulics Simulation of Fuel Sub-Assembly for 1200 MWe Nuclear Power Reactor

Taosif Alam^{1,*}, Dr. M. A. R. Sarkar²

^{1,2}Department of Mechanical Engineering, Bangladesh University of Engineering & Technology, Dhaka-1000,
BANGLADESH

ABSTRACT

This study illustrates the turbulent flow simulation of coolant water through the three sub-channels of a fuel sub-assembly at a pressure around 16 MPa. The geometry details of the fuel rods, coolant sub-channels and operating parameters are similar to those of Rooppur Nuclear Power Reactor under construction in Bangladesh. The fuel sub-assembly is modeled using seven fuel rods where $k-\epsilon$ turbulence model is used for turbulent flow simulation. The effect of turbulent flow on temperature, velocity, pressure drop, friction factor and Nusselt number in interior, edge and corner sub-channels have been discussed for various axial locations ($z=0-45Dh$). Thermal hydraulic properties of the coolant water are studied for safety analyses such as: i) Hot spot in coolant channel and ii) Departure from Nucleate Boiling (DNB)

Keywords: Subchannel, $k-\epsilon$, Turbulent Flow, Nusselt number, DNB

1. Introduction

Nuclear Reactor is used to generate thermal energy in a nuclear power plant. The thermal energy is generated from nuclear fission in fuel rods and it is transferred to a liquid coolant that flows through the space between the fuel rods. For a pressurized water reactor (PWR) turbulent flow of water is required which causes convective heat transfer from fuel rods to coolant. Turbulent flow properties have a major influence on thermal hydraulics of the coolant. Thermal hydraulics needs to be studied for reactor to operate within safety limits. Numerical investigations of turbulent flow in fuel sub-assembly have been carried out previously.

Rehme [1] described the turbulent nature in rod bundle sub-channels and natural mixing between inter-connected sub-channels. He concluded macroscopic flow pulsations between sub-channels are the main reason behind high mixing rates between them rather than secondary flow. Rehme [2] also had an experimental of turbulent flow through sub-channels of a rectangular core with four fuel rods. Jian et al. [3] modeled a simple analytical model for prediction of friction factor f , and nusselt number Nu , for fully developed turbulent flow in square and hexagonal channel. Bottcher [4] investigated a CFD model of complete reactor vessel of 1000 MWe reactor. But due to computational constraints detailed sub-channel study is not done. H. Ganjiani [5] et al. did 3-D CFD analysis of turbulent flow around 3 fuel rods with spacer grids for 1200 MWe pressurized water reactor. Saxena [6] carried out a numerical simulation of Sodium flow in wire-wrapped Sub-assembly of Sodium cooled Fast Reactor (SFR) by RANS, LES and DNS approach. Mohammad Mizanur Rahman et al. [7] carried out a thermal hydraulic and safety analyses of 3 MW TRIGA MARK-II reactor by COOLOD-N2 and PARET codes. It was concluded that the thermal hydraulic models through the hot channel fuel

center-line temperature in steady-state condition are validated within error margins. S. S. Mirafzal et al [9] examined the steady state and transient parameters of VVER-1000 fuel assembly using Drift-Flux Model. Ajoy et al [10] studied the thermal-hydraulic behaviour in the subchannels of High performance Light Water Reactor (HPLWR) fuel assembly. It is seen in the study the temperature rise in the corner channel is faster than other subchannels. It also concluded that the wire-wrapped spacer provide less pressure drop and good mixing than spacer grid. The fuel clad surface temperature also remain within limits by wire-wrapped spacers.

So it's seen that numerical study of sub-channels fuel sub-assembly has been carried out with great importance. In our study $k-\epsilon$ turbulence model is used. The model computes four variables to determine the turbulence nature of the flow field. Turbulent kinetic energy (k), turbulence dissipation rate (ϵ) and turbulent eddy viscosity (μ_t) and production of turbulent kinetic energy (P_k). Turbulent kinetic energy is the measure of the energy of the fluctuations in the flow field. When turbulent occurs large eddies form which then dissipate as they break up into smaller eddies. The rate of dissipation of turbulence is measured by μ_t . Also turbulent eddy viscosity adds up to internal fluid friction when turbulent transfer of energy and momentum happens by forming and breaking of eddies. In this study these characteristics along axial flow in three subchannels (interior, edge and corner) and its effect on the flow structure has been studied. The objectives of this study are as follows:

- 1) To determine turbulent properties and its effect on velocity, temperature and nature of convective heat transfer in the subchannels of the fuel subassembly.
- 2) Study of velocity and temperature distribution profiles

- 3) Analysis of the variations of pressure drops, friction factor along the axial length of the sub-assembly
- 4) Examining local Nusselt number and finding the minimum length for attaining a fully developed Nusselt number in the sub-channels
- 5) Probability of Departure from Nucleate Boiling (DNB) and finding the location of maximum temperature of coolant.

2. Geometry and Mesh

The fuel sub-assembly modeled here contains seven fuel rods where actually there are 163 fuel assemblies each having 312 fuel rods in the reactor core. The computational domain developed for the study contains only 10% of the actual fuel rod length and effect of spacer grids is neglected. The model was created in SolidWorks 2013. The geometrical parameters of the model is shown in the table below:

Table 1: Geometry of the computational domain

Parameter	Value	Unit
D_p	9.1	mm
P	12.75	mm
L	37.5	cm
N_{rings}	1	-
N_{pin}	7	-
a	20.95	mm

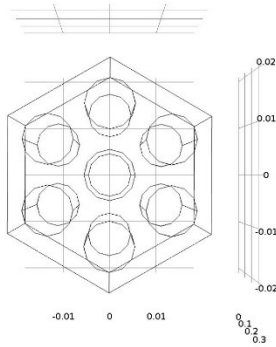


Fig. 1. (a) Computational domain of the fuel sub-assembly

Hydraulic diameter of the fuel sub assembly is defined as Eq. (1)

$$D_h = 4A_f / P_w \quad (1)$$

Where A_f is coolant flow area of the sub assembly and P_w is wetted perimeter by the flow in traverse direction. The hydraulic diameter found here is 8.4099 mm. There are three sub channels:

- (1) Interior sub-channel
- (2) Edge sub-channel

- (3) Corner sub-channel

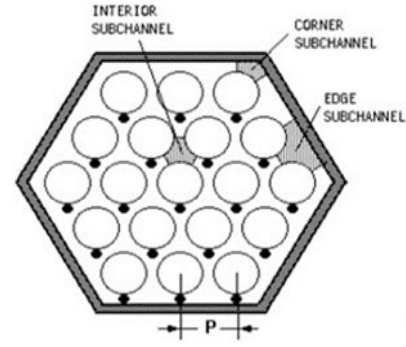


Fig. 2. Sub-channels of the fuel sub-assembly

Completed mesh contains 599119 domain elements including 331929 tetrahedral domains and 267190 prism domains. Figures of meshing domains are given below:

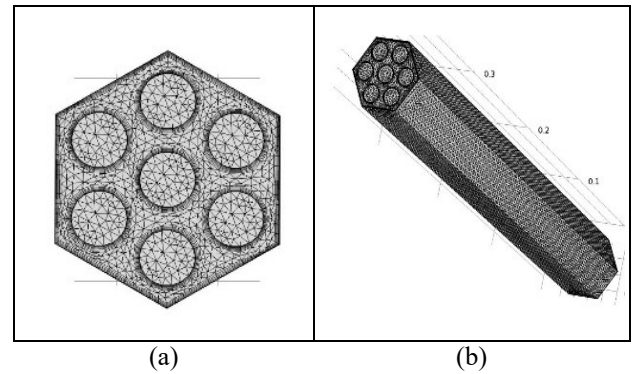


Fig. 3. a) and b) Meshing of the of the computational domain

3. Governing Equation

The equations for the fluid flow and heat transfer in the sub-channels used in the study are as follows:

Momentum equation:

$$\rho (\mathbf{u} \cdot \nabla) \mathbf{u} = \nabla \cdot [-p\mathbf{I} + (\mu + \mu_t) (\nabla \mathbf{u} + (\nabla \mathbf{u})^T) - \frac{2}{3} (\mu + \mu_t) (\nabla \cdot \mathbf{u}) \mathbf{I} - \frac{2}{3} \rho k \mathbf{I}] + \mathbf{F} \quad (2)$$

Continuity equation:

$$\nabla \cdot (\rho \mathbf{u}) = 0 \quad (3)$$

Heat transfer in fluids:

$$\rho C_{pu} \cdot \nabla T = \nabla \cdot (K \nabla T) + Q + Q_{vh} + W_p \quad (4)$$

Transport equations: The standard k- ϵ model equations:

For turbulent kinetic energy :

$$\rho (\mathbf{u} \cdot \nabla) k = \nabla \cdot [(\mu + \mu_t / \sigma_k) \nabla k] + P_k - \rho \epsilon \quad (5)$$

For dissipation:

$$\rho(u \cdot \nabla) \varepsilon = \nabla \cdot [(\mu + \mu_t/\sigma_\varepsilon) \nabla \varepsilon] + C_{\varepsilon 1} \frac{\varepsilon}{k} P_k - C_{\varepsilon 2} \rho \frac{\varepsilon^2}{k} \quad (6)$$

Here, Turbulent Eddy viscosity

$$\mu_t = \rho C_\mu (k^2/\varepsilon) \quad (7)$$

production of turbulent kinetic energy:

$$P_k = \mu_t [\nabla u : (\nabla u + (\nabla u)^T)] - 2/3 \rho k \nabla \cdot u \quad (8)$$

Where values of constants in the k - ε turbulence model are $C_\mu = 0.09$, $C_{\varepsilon 1} = 1.44$, $C_{\varepsilon 2} = 1.92$, $\sigma_k = 1.0$ and $\sigma_\varepsilon = 1.3$

Relative pressure drop :

$$P_r = (P - P_{in}) / P \quad (9)$$

Friction factor:

$$f = 2D_h \Delta P / (\rho L v^2) \quad (10)$$

Reynolds Number,

$$Re = \rho u D_h / \mu \quad (11)$$

Nusselt number : The Dittus-Boeltler equation-

$$Nu = 0.023 Re^{0.8} Pr^{0.4} \quad (12)$$

4. Boundary Condition

The Boundary conditions for flow field and thermal field are as follows:

Thermal Insulation:

$$-n \cdot (-K \nabla T) = 0 \quad (13)$$

At solid boundary surface the fluid will have zero velocity relative to the boundary

$$u = 0 \quad (14)$$

Inlet:

$$u = -u_0 \cdot n \quad (15)$$

Outlet:

$$[\rho I + \mu + \mu_t (\nabla u + (\nabla u)^T) - 2/3 \mu (\nabla \cdot u) I] \cdot n = -p_0 n \quad (16)$$

Also, uniform heat flux of 278 KW/m² has been set at the fuel rod walls. For $Re = 3.55 \times 10^5$, the inlet velocity and temperature are 5.66 ms⁻¹ and 570° K respectively. The outlet pressure has been fixed to 16.06 MPa. The fluid flows upward inside the sub-channels of the fuel rod assembly.

5. Result and Discussion

5.1 Turbulent Properties Distribution

Due high Reynolds number the coolant water flowing axially is turbulent. Turbulent characteristics like turbulent kinetic energy, turbulence dissipation rate and turbulent eddy viscosity play a major role in the flow structure and temperature of the fluid. From Figure 1 it is seen that all the properties are more dominant in corner subchannel than interior and edge subchannel. Velocity fluctuations and formation of eddies in corner subchannel influence its flow characteristics and dissipation of turbulence affects its fluid's temperature and convective cooling which will be discussed in the later sections.

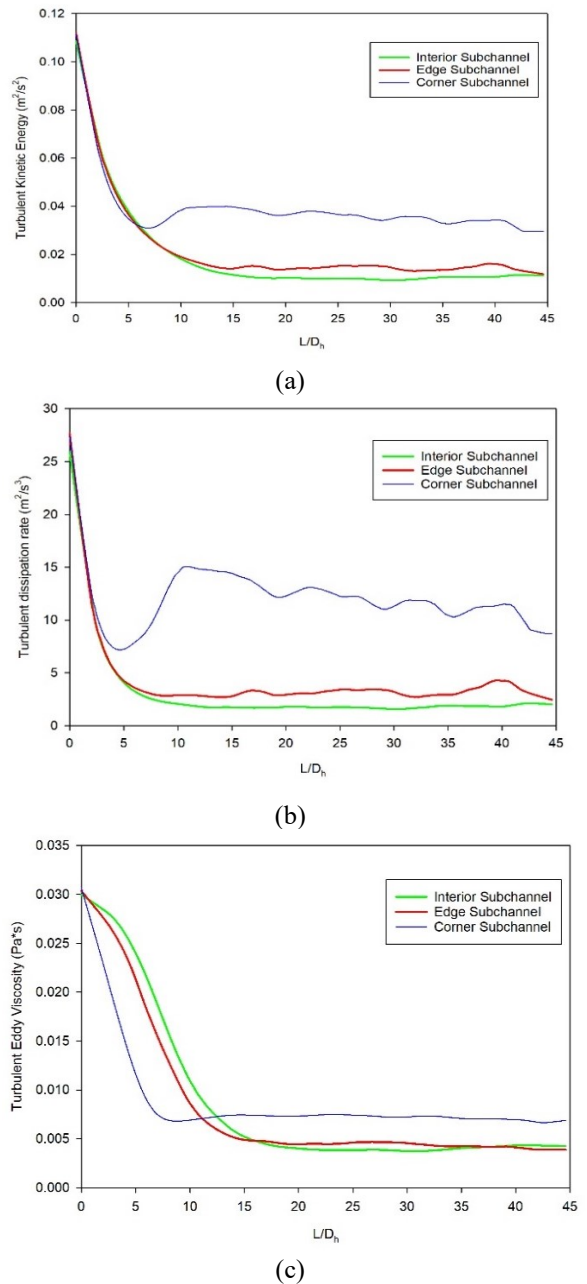


Fig. 4 (a) Turbulent kinetic energy, (b) Turbulence dissipation rate, (c) Turbulent eddy viscosity along 3 sub-channels in the axial direction

5.2 Velocity Distribution

The velocity distribution along 3 sub channel along the axial distance is shown in the Figure 5. Inlet velocity is fixed at 5.66 m/s. Up to an axial distance of $4D_h$ the velocity in all the sub channels has a sharp increase. Then the velocity along interior and edge sub channel gradually increased whereas in the corner sub channel it decreased. As seen in Figure 1 corner subchannel has more turbulent viscosity and turbulence dissipation rate. These are caused by forming of large eddies and their breaking of large eddies into smaller eddies. In these processes internal fluid friction rises here more than other subchannels and as a result flow velocity in the corner decreases.

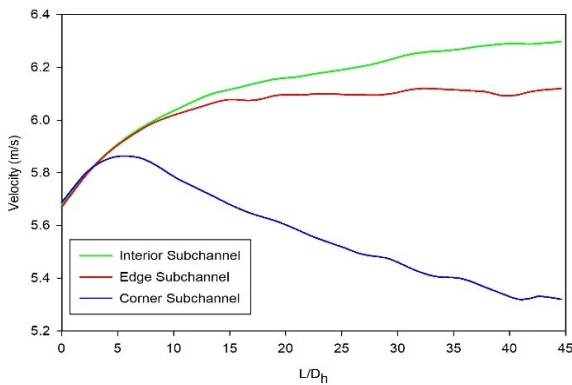


Fig. 5. Variation of velocity along 3 sub-channels in the axial direction

5.2 Temperature Distribution

The temperature distribution along 3 sub channel along the axial distance is shown in the graph where temperature of the cooling water at the inlet is fixed at 570K. Increase in temperature in the interior sub-channel is greater due to being surrounded by fuel rod walls which has uniform heat flux. From Figure 6 it is seen that in the corner subchannel fluid is adjacent to only one fuel rod and edge subchannel is adjacent to two fuel rods. But increase in temperature is more in the corner because of more dissipation of turbulent kinetic energy than the other. Here average temperature rise in the sub-channel is about 1K because the model is .001% of the whole core volume. For full reactor volume this temperature increase is about 30 K.

5.3 Local Nusselt Number Variation

Nusselt number is a function of Reynolds number according to equation no 12. Reynolds number depends on hydraulic diameter, D_h which is a varying quantity in the three subchannels. From equation 1 we found D_h of interior Subchannel to be 6mm, for edge subchannel 10 mm and for corner subchannel 4 mm. From figure 7 and 8 the difference in Reynolds number and local nusselt number is shown. In edge subchannel, greater local nusselt number suggest that the convective heat transfer is more here than other two subchannels. Also temperature gradient is seen to be less than two

subchannels in figure 6. The slope in figure 7 for edge and interior subchannel comes to zero at $20 D_h$ which suggests that the nusselt number has reached its fully developed state. For proper heat removal the length the sub-channel must be fixed considering the minimum length for attaining a fully developed nusselt number. In the corner subchannel nusselt number reaches it peak in $5D_h$ and continuously decrease along the axial length. This suggests that the convective heat transfer in this subchannel is decreasing but from figure 9 it can be seen that the local fluid enthalpy in corner subchannel is increasing. So, for having a low nusselt number and high fluid enthalpy there is a probability of nucleate boiling (DNB) occurring at the corner sub-channel. Due to nucleate boiling a two phase flow may occur which will decrease the convective heat transfer coefficient.

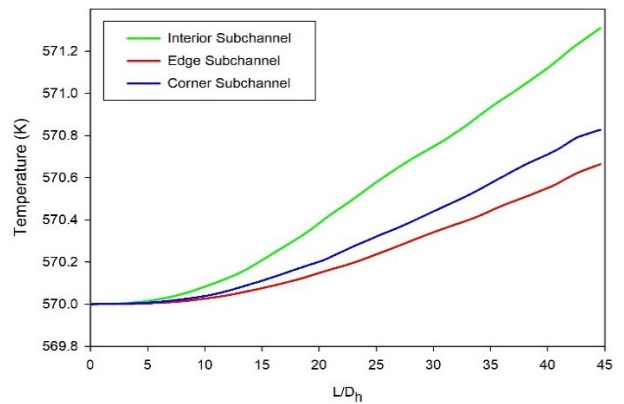


Fig. 6. Variation of temperature along 3 sub-channels in the axial direction

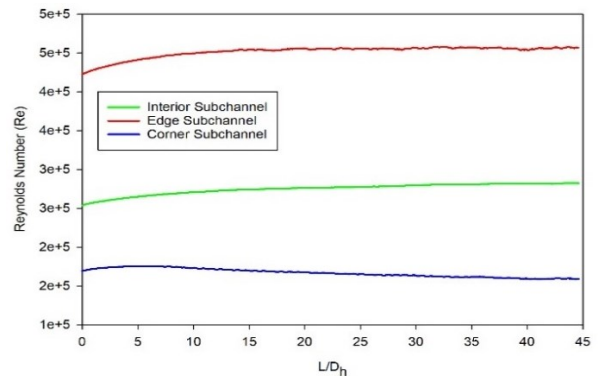


Fig. 7. Variation of Reynolds number along 3 sub-channels in the axial direction.

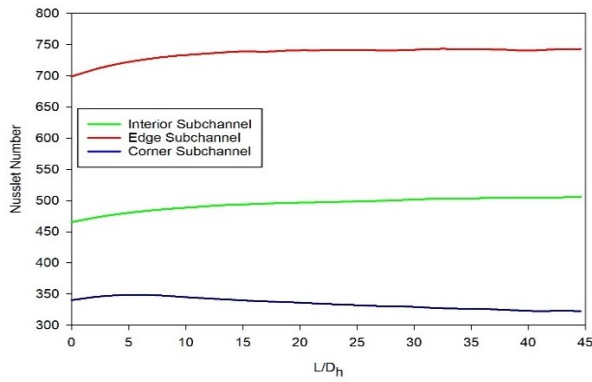


Fig. 8. Variation of local Nusselt number along 3 sub-channels in the axial direction

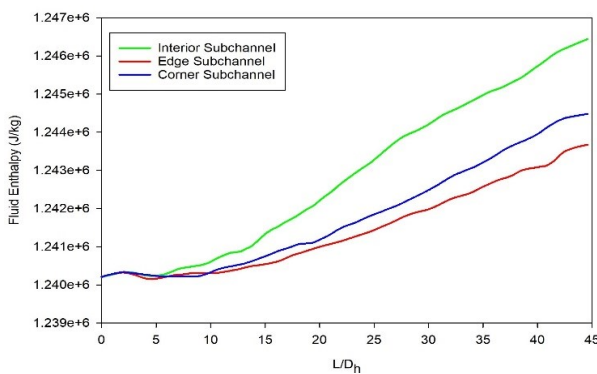
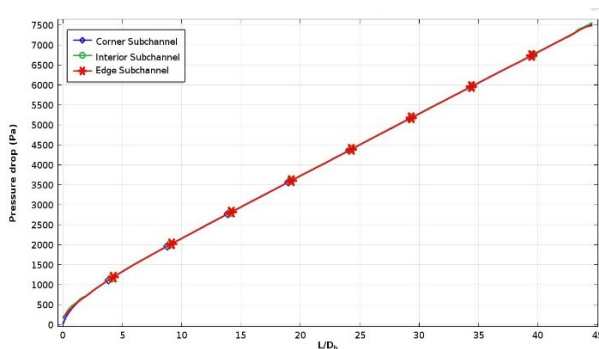


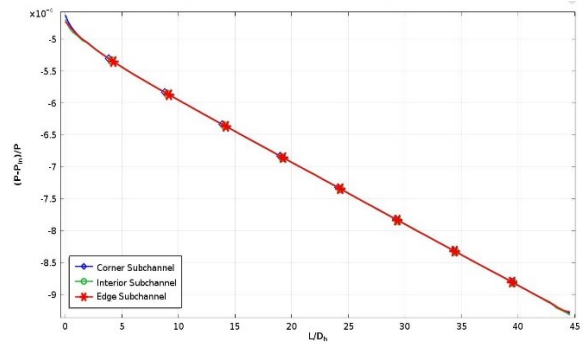
Fig. 9. Variation of Fluid Enthalpy along 3 sub-channels in the axial direction

5.4 Pressure drop variation

Pressure at outlet is set to 16.06 MPa and average pressure at inlet is 16.07 MPa. Here the total pressure drop of 7.5 KPa. Pressure drop is higher at the inlet and gradually decreases along the axial direction in all three subchannels. The figures for pressure drop and relative pressure drop along axial length is given:



(a)



(b)

Fig. 10: (a) Pressure drop (b) Relative Pressure drop along axial direction

5.5 Variations of friction factor

Local friction factor is calculated from local velocities in different sub-channels. The variation between friction factor along the axial direction in 3 sub-channels is shown in the following graph. Friction factor is more in edge subchannel because of larger coolant flow area. Interestingly while having smaller flow area coolant subchannel's friction factor gradient along axial length is more than interior subchannel because of added turbulent viscosity in its flow area.

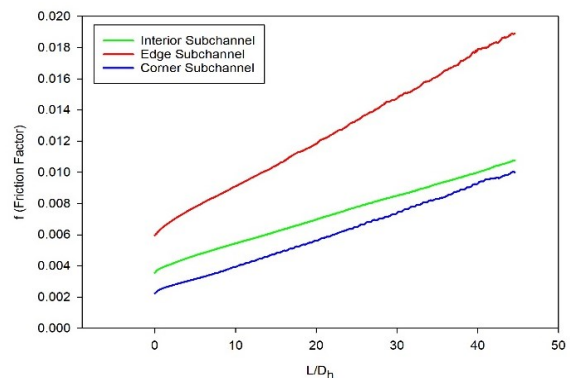


Fig. 11. Variation of friction factor along axial direction in 3 sub-channels

6. Conclusion

A three-dimensional Computational Fluid Dynamics (CFD) analysis for turbulent flow in the interior, edge and corner sub-channels of hexagonal fuel sub-assembly of a 1200 MWe nuclear power reactor is carried out. Having different geometrical shapes and boundary conditions, the effect of operational parameters in the three sub-channels varies accordingly. The following remarks may be drawn from the study-

- 1) In Corner sub-channel turbulent properties like turbulent kinetic energy, turbulence dissipation rate and turbulent eddy viscosity along the axial length is significantly large than other two subchannels. The flow

velocity decreases in the corner subchannel due to this eddy viscosity.

2) For having higher Nusselt Number in the edge subchannel region the fluid temperature is lower than that of other two subchannels. But in the corner subchannel because of the decreasing of nusselt number and increasing temperature and fluid enthalpy along its axial length probability of DNB and occurrence of hot spot in fuel rod adjacent to this subchannel is more than other two subchannels.

3) For proper heat removal from the fuel rod surface the length of the fuel sub-assembly should be such that the nusselt number should can reach its fully developed state. In this simulation the fully developed nusselt number is attained in edge and interior subchannel. The length of the fuel sub-assembly should more than taken here for computation to find fully developed nusselt number in the corner subchannel.

4) In the corner sub-channel along the direction of fluid flow slope of friction factor increase is more due added turbulent viscosity. Friction factor is greater in edge because of larger coolant flow area.

5) Relative pressure drop is almost the same for various Reynolds numbers in all the three sub-channels.

Nomenclature

A_f	: Coolant flow area, m ²
a	: Side of a hexagonal wall, m
C_{pu}	: Heat capacity at constant pressure, kJ·kg ⁻¹ ·K ⁻¹
D_h	: Hydraulic diameter, m
I	: Identity matrix
K	: Thermal conductivity, W/m·k
k	: Turbulent kinetic energy, m ² /s ²
L	: Length, m
Nu	: Nusselt Number, dimensionless
P	: Pressure, Pa
P_{in}	: Inlet Pressure, Pa
Pr	: Prandtl Number, dimensionless
P_w	: Wetted Perimeter, m
Q	: Heat generation, J
Q_{vh}	: Heat generation due to viscous heating, J
Re	: Reynolds Number, dimensionless
T	: Temperature, K
u	: Velocity, m/s
W_p	: Work done by Pressure, J

ρ	: Density, kg/m ³
μ	: Viscosity, Pa*s
μ_t	: Turbulent eddy viscosity, Pa*s
ε	: Turbulence dissipation rate, m ² /s ³

REFERENCES

- [1] Rehme, K., "The structure of turbulence in rod bundles and the implications of natural mixing between the subchannels", *Int. J. Heat Mass Transfer*, **35**(2), pp. 567-581 (1992)
- [2] Rehme, K., "The structure of turbulent flow through rod bundles", *Nucl. Eng. Des.*, **99**, pp. 141-154 (1987).
- [3] Jian, S., Atila, P. and Silva, F., "Analytical prediction of friction factors and Nusselt numbers of turbulent forced convection in rod bundles with smooth and rough surfaces", *Nucl. Eng. Des.*, **215**, pp. 111-127 (2002).
- [4] Bottcher, M., "Detailed CFX-5 study of the coolant mixing within the reactor pressure vessel of a VVER-1000 reactor during a non-symmetrical heat-up test", *Nucl. Eng. Des.*, **238**(3), pp. 445-452 (2008).
- [5] H. Ganjiani and B. Firoozabadi, "Three Dimensional Simulation of Turbulent Flow in 3 Sub-channels of a VVER-1000 Reactor", *Transaction B: Mechanical Engineering* Vol. 17, No. 2, pp. 83-92.
- [6] Aakanksha SAXENA., "Thermal-hydraulic numerical simulation of fuel sub-assembly for Sodium-cooled Fast Reactor".
- [7] Mohammad Mizanur Rahman, Mohammad Abdur R. Akond, Mohammad Khairul Basher, Md. Quamrul Huda, "Steady-State Thermal Hydraulic Analysis of TRIGA Research Reactor," *World Journal of Nuclear Science and Technology*, 2014, **4**, 81-87.
- [8] Endiah Puji Hastuti, Akira Yamaguchi, Takashi Takata, "Comparative Study of Turbulence Models on PWR Fuel Bundle Thermal Hydraulics Usi FLUENT Code".
- [9] S. S. Mirafzal, M. Khaleghi, M. Rahgoshay and M. Hashemi-Tilehnoee, "Sub-Channel Analysis in Hot Fuel Assembly's of VVER-1000 Reactor using Drift-Flux Model", *Indian Journal of Science and Technology*, Vol **8**(33), DOI: 10.17485/ijst/2015/v8i33/81001, December 2015
- [10] Ajoy Debbarma, K.M Pandey, "Numerical Analysis of Flow and Heat transfer in Sub-Channels of Supercritical Water Reactor", *International Conference on Design and Manufacturing 2013*
- [11] N. E. Todreas, M. Kazimi, *Nuclear Systems Volume I: Thermal Hydraulic Fundamentals*.
- [12] N. E. Todreas, M. Kazimi, *Nuclear Systems Volume II: Elements of Thermal*.

Investigation on Performance of Grass, Orange and Potato as Substrate of Microbial Fuel Cell

Nawrin Rahman Shefa¹, Ismat Ara Eti¹, Md. Jony Reza¹, Sonaton Biswas¹, Md. Abdul Halim^{2*}

¹ Student, Department of Chemical Engineering,
Jessore University of Science & Technology, Jessore-7408, BANGLADESH

² Assistant Professor, Department of Chemical Engineering,
Jessore University of Science & Technology, Jessore-7408, BANGLADESH

ABSTRACT

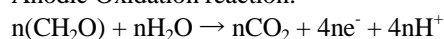
The dependence on fossil fuels is unsustainable because of its finite, depleting supplies and impact on environment. It is crying to find not only alternative energy source but also environment friendly energy source. The development of Microbial Fuel Cell (MFCs) is important to the advancement of alternative fuels. Microbial Fuel Cells (MFCs) are an emerging technology that uses bacteria to generate electricity from organic waste. The objective of this study was to observe different substrate which varies in major chemical content and compare the extracted energy to choose the best to extract energy as electricity. In this case, we used carbon felt as anode and copper wire as cathode, 0.1M NaCl solution as catholyte and sedimentary mud with a mixture of compost used microbe source in a double chambered mediator less type MFC. Studied substrates are grass, rotten orange and potato. We obtained maximum 368mV, 517mV and 454mV in a run of 15 days respectively from grass, orange and potato. The power density we got respectively 43.5mW/m², 102.9mW/m² and 73.7mW/m².

Keywords: Microbial Fuel Cell, Substrate, Catholyte, Power density

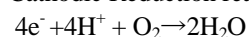
1. Introduction

Dependence on fossil fuel is leading us to the era of energy crisis. Combustion of fossil fuel also has negative impact on environment due to carbon-di-oxide emission [1]. To cope with this situation of energy scarcity and environment pollution finding of some alternative renewable energy sources is a first and foremost task to do. As an upshot of this finding is fuel cell (FC) which generates energy using high value metal catalysts according to general version [2]. Microbial fuel cell (MFC) is a type of FC. Microbial fuel cells (MFCs) employ microbes to generate electricity from organic substrates. MFC consists of anode and cathode which are by an external circuit and separated by proton exchange membrane (PEM). In anode chamber, organic substrates decomposed by microbes by which electrons (e⁻) and protons (H⁺) are generated. Electrons and protons transferred to cathode through circuit and membrane respectively [3]. The reactions occur are given below [4].

Anodic Oxidation reaction:



Cathodic Reduction reaction:



This technology initiated by Potter in 1911 [5]. Now it has turned into a great matter of interest for the researchers. Substrate is an important component for any biological process as it serves as carbon (nutrient) and energy source. The efficiency and economic viability of converting substrate to bioenergy depend on the characteristics and components of the substrate. The chemical composition and concentrations of the substrate can be converted into products as fuels [6]. For this reason, in this research we have observed weeded out grass from field, rotten orange from fruit

market and rotten potato from vegetable market as substrate of MFC. All of these are organic type of waste. MFCs can be described by electrochemical parameters such as current density, power density and cell voltage in continuous systems [7]. We studied the substrates under same conditions and compared the electrochemical parameters to gather information on performance of these organic wastes to evaluate suitability as substrate of MFC.

2. Application

The application of MFC technology still limited due to a bunch of limitations. MFCs can be turned into biosensors, because microbial activity on the electrode, depending on environmental parameters, produces an electrical signal [8]. A new form of MFC is microbial electrolysis cell (MEC) by which assisting the potential generated by the bacteria at the anode with a small potential by an external power source (>0.25 V), it is possible to generate hydrogen at the cathode. In typical electrolysis more than 1.5 volt is needed [9,3]. The microbial desalination cell (MDC) is a newly developed technology which integrates the microbial fuel cell (MFC) mechanism and electro dialysis for wastewater treatment, water desalination and production of renewable energy [10]. In this way application of MFC technology is entering in practical application sector.

3. Materials and Method

There are varieties of design for MFC. For this experiment we choose dual chamber mediator less MFC.

3.1 Experimental setup

For the construction of dual chamber mediator less MFC plastic jars of 200ml are used as anode and cathode chamber. Salt bridge used as proton exchange membrane (PEM). Cotton fabric soaked in 0.5M NaCl

solution and inserted into a 5cm PVA pipe having diameter 1.5 cm. Then the salt bridge inserted into drilled holes of plastic jars and attached with general purpose epoxy compound. Collected substrate samples from field and local market are cut into small pieces and then blended in blender. Sedimentary mud as microbe source collected from pond and screened after mixing with. Adding 0.5g sugar per liter mud to feed the microbes the mud kept covered for a day long. Carbon felt of dimension 6cm x 1.5cm x 1cm used as anode.

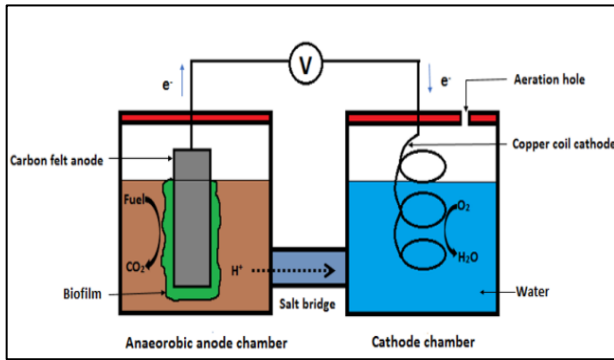


Fig.1: Experimental setup for dual chambered mediatorless MFC

Copper wire coiled of length 30 cm and diameter 0.075cm used as cathode. Maintaining 30% substrate concentration and 150 ml mixture of mud and substrate poured in anaerobic anode chamber after adjusting pH 7. As catholyte 0.1M NaCl solution poured in cathode chamber. Lids attached with electrodes place on to the jars. Then the MFCs rested for a day long to initiate the reactions.

3.2 Electrochemical monitoring

Output voltage, current density and power density were adopted to analyze experiment. All measurements have taken at room temperature and ambient pressure.

Output voltage (V) measured with a digital multimeter of model DT-9205A. The voltage obtained by multimeter through an external resistor, without external resistor and internal resistance are respectively V , E and R . We've used external resistance of 100k Ω . Internal resistance calculated by equation (1). Current density (I) calculated by equation (2) and (3).

$$E/V = R_{ext}/(R + R_{ext}) \quad (1)$$

Where, R_{ext} = external resistance.

$$i = E/R \quad (2)$$

$$I = i/A \quad (3)$$

Where, i = current, R = internal resistance and A = surface area of anode.

Power density (P) calculated by equation (3).

$$P = EI \quad (4)$$

Thus all electrochemical parameters are measured and calculated [2,3,11].

4. Result and Discussion

The observation of 15 days summarized in Fig.2,3 and 4.

The internal resistance of MFCs with substrate orange potato and grass are respectively 787 Ω , 848 Ω and 943 Ω . The maximum voltage obtained from the MFCs is respectively 517mV, 454mV and 368mV. The change in output voltage has gone through many ups and downs with time due to change in room temperature [12]. The maximum current density obtained respectively 199mA/m², 162mA/m² and 118mA/m². The maximum power density obtained respectively 102.9mW/m², 73.7mW/m² and 43.5mW/m². Comparatively orange performed better than potato and grass. Potato performed quite well too. Comparing with other researches overall these three substrates are quite potential.

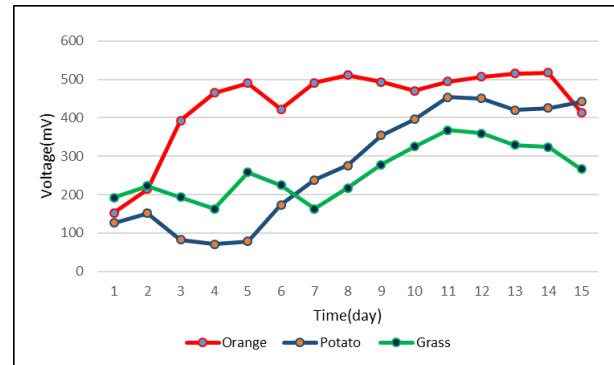


Fig.2: Voltage as function of time

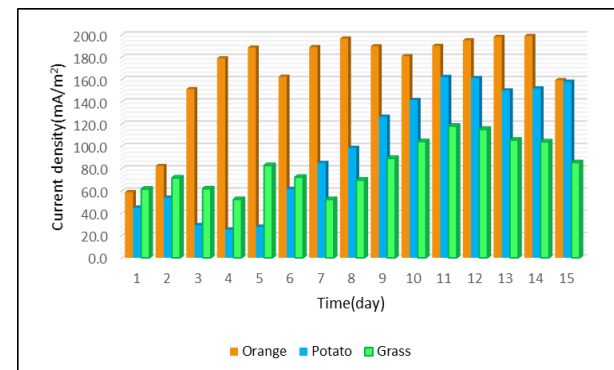


Fig.3: Current density as function of time

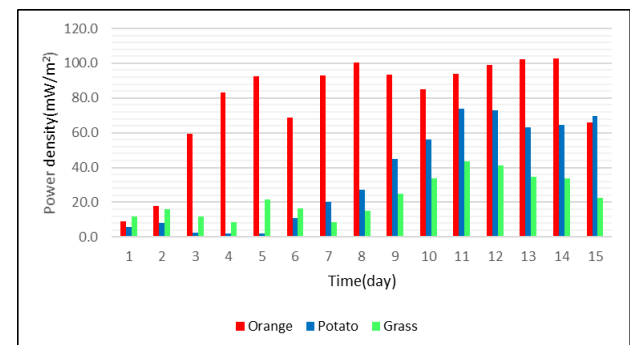


Fig. 4: Power density as a function of time

Liu et al. (2016) reported that with an effective volume 1260ml, carbon cloth cathode covered with Pt/C

catalyst. carbon rod anode got maximum 14.7mW/m^2 from a single cell with $3000\ \Omega$ internal resistance [11]. But in comparison we jumped ahead with MFCs of 150ml effective volume. Researches using pure glucose as substrate and carbon paper anode obtained maximum power density $40.3\pm 3.9\text{mW/m}^2$ [13,14]. Our substrates performed far better. Qian et al. (2009) using carbon felt as cathode obtained maximum power density 77mW/m^2 , maximum current density $0.006\ \text{mA/m}^2$ and maximum voltage 575mV [15]. Comparing with this our MFCs has given better power density and current density with carbon felt anode.

5. Limitation

At present because of prohibitive costs, MFC technology is economically competitive [16]. There is a lot lack of information about structure & catalytic activity of microbial communities. This limits the understanding the behavior of MFC too. MFC produces a very low voltage output. In a study the maximum achieved voltage was $0.62\ \text{V}$. It was significantly less than the maximum theoretical voltage output of $1.1\ \text{V}$, resulting in a voltage output difference of 44% [3]. With or without the PEM, the internal resistance still remains as a major a limiting factor [16].

6. Conclusion

To cope with upcoming crisis of energy source and manage the bio wastes MFC technology can be an arm to survive. But to take this technology at that height we have to overcome the drawbacks. Without overcoming these limitations MFC will not be capable to stand like knight to save us from energy crisis. To explore more efficient substrate and overcome the limitations more and more research is needed.

NOMENCLATURE

E : voltage without external load, mV
 V : voltage with load, mV
 R : internal resistance, Ω
 i : current, mA
 I : current density, mA/m^2
 P : power density, mW/m^2
 R_{ex} : external load, Ω
 A : surface area of anode, m

REFERENCES

[1] M. Rahimnejad, A.A. Ghoreyshi, G. Najafpour, Power generation from organic substrate in batch and continuous flow microbial fuel cell operations, *Appl. Energy* Vol. 88, pp. 3999–4004, (2011).
[2] M. Rahimnejad, A. Adhami, S. Darvari, A. Zirepour, Microbial fuel cell as new technology for bioelectricity generation: A review, *Alexandria Engineering Journal* Vol. 54, pp. 745–756, (2015).
[3] B. E. Logan, B. Hamelers, R. Rozendal, U. Schroder, J. Keller, S. Freguia, P. Aelterman, W. Verstraete, K. Rabaey, Microbial fuel cells:

methodology and technology, *Environ Sci Technol*, Vol. 40, 5181–5192, (2006).
[4] P. Jahangeer, K. Gupta, A. Shaktibala, S. Rayani, Review and Concept Development for Electricity Generation from Municipal Solid Waste Using MFCs, *Curr. World Environ.*, Vol. 11(2), pp. 406–412, (2016).
[5] M. C. Potter, Electrical effects accompanying the decomposition of organic compounds. *Proc. R. Soc. London Ser.*, Vol. 84, pp. 260–276, (1911).
[6] D. Pant, G. V. Bogaert, L. Diels, K. Vanbroekhoven, A review of the substrates used in microbial fuel cells (MFCs) for sustainable energy production, *Bioresource Technology* xxx (2009) xxx–xxx.
[7] K. Rabaey, G. Lissens, S. Siciliano, W. Verstraete. A microbial fuel cell capable of converting glucose to electricity at high rate and efficiency, *Biotechnol Lett.* Vol. 25, pp. 1531–5, (2003).
[8] Jianing Dai, Application of microbial fuel cells in a forested wetland, *Clemson University*, jdai@clemson.edu.
[9] A. Kadier, Y. Simayi, P. Abdesahian, N. F. Azman, K. Chandrasekhar, M. S. Kalil, A comprehensive review of microbial electrolysis cells (MEC) reactor designs and configurations for sustainable hydrogen gas production, *Alexandria Engineering Journal*, Vol. 55, pp. 427–443, (2016).
[10] A. A. Fara, A. Adian, H. M. Saeed, J. Saif, Rehab Khawanga, Sameer Al Asheh, Sara Azzam S. Yousef; Microbial Desalination Cell Technology: A review and a case study, *Desalination*, Vol. 359 pp. 1–13, (2015).
[11] L. Xinmin, W. Jinajun, G. Benyue, Series and parallel connection of anaerobic fluidized bed microbial fuel cells (MFCs), *IJAMBR* Vol. 4, pp. 7–14, (2016).
[12] G. S. Jadhav, M. M. Ghangrekar, Performance of microbial fuel cell subjected to variation in pH, temperature, external load and substrate concentration. *Bioresour. Technol.* Vol. 100, pp. 717–723, (2009).
[13] C. Bettin, Applicability and Feasibility of Incorporating Microbial Fuel Cell Technology into Implantable Biomedical Devices, 2006.
[14] S. Jung, J.M. Regan, Comparison of anode bacterial communities and performance in microbial fuel cells with different electron donors, *Appl. Microbiol. Biot.* Vol. 77, pp. 393–402, (2007).
[15] Q. Deng, X. Li, J. Zuo, A. Ling, B.E. Logan, Power generation using an activated carbon fiber felt cathode in an upflow microbial fuel cell, *J. Power Sources*, Vol. 195, pp. 1130–1135, (2009).
[16] H. Pham, K. Rabaey, P. Aelterman, P. Clauwaert, L. De Schampelaire, N. Boon, W. Verstraete, Microbial Fuel Cells in Relation to Conventional Anaerobic Digestion Technology, DOI: 10.1002/elsc.200620121

ICMIEE18-222

Experimental Investigation on Three Different Natural Convection Cabinet Solar Dryer for Food Drying Applications

Md. Imrul Islam¹, Mehedi Hasan Tusar^{1*}, Amir Hamza Limon¹, Majedul Islam^{1,2}

¹Department of Mechanical Engineering, Chittagong University of Engineering & Technology, Chittagong, BANGLADESH

²Post-Doctoral Research Fellow, Queensland University of Technology, Brisbane, Australia

ABSTRACT

The development and investigation of efficient solar drier, particularly meant for drying vegetables and fruit is described in this paper. Considering the importance of solar drying three different types of natural convection cabinet solar dryers are constructed and their performance are evaluated at natural conditions. To do so moisture removal rate, moisture ratio of various foods (Apple, Banana, pineapple, Guava) are evaluated from 10AM to 4PM for many days in different season. After analyzing the dehydration rate of three different chambers it is appeared that total dehydration of thin tube chimney type chamber is 44.5%, for attic space type chamber dehydration is 33.3% and for natural draft chamber it is 58.9% in 6 hours. So, it is clear from this analysis that the performance of natural draft chamber is best than other two chambers and performance of attic space type chamber is worst. This is due to the reflection loss in inclined glass of attic space type dryer compared to other chambers. Besides, the performance of chimney chamber is better than attic space type chamber. It is also seen that dehydration rate after 1pm is higher than before 1pm as solar irradiation was higher after 1 pm in best performance days. Besides, dehydration rate of Pineapple is the highest as water level and porosity is so much high and for guava is the lowest as water level and porosity is low. Dehydration rate of banana is higher than guava but lower than apple.

Keywords: Solar drying, Thin tube chimney type dryer, Attic space type Dryer, Natural convection solar dryer, Dehydration

1. Introduction

World's population is increasing in a faster rate and demand of food is increasing as well. With the developments of agricultural technology, production of food is expanding to meet the demand. Solar drying is one of the renewable forms of food storage that can reduce processing cost for storage. However, it has some problem of product discoloration in drying, might cause microbial infestation, and requires longer time for dehydration, loss of product in the process. Production of certain agricultural goods is higher in a particular season than demand but scarce in another season in Bangladesh. As a result, price falls in production season but rises higher in scarce time. Peasants cannot store their products due to lack of storage and high cost affiliated with it. So, food is wasted every year which might have been utilized to serve the countries growing population. Similar things happen in our fisheries sector. But solar drying in open environment which is naturally carried on can pollute the product, product loss due to wastage is common thing. Besides solar energy is not available at night and its intensity fluctuates with time. So, improvement in drying performance is necessary to reduce its drying time. For proper distribution of food around the globe their need a proper food production, supply and storage management for favor of mankind. Every year a huge amount of produced food is wasted due to proper storage of foods. This occurs for limited storage capacity, high charge of storage, lower price of produced food, transportation problem. So, farmers make waste of the food when it is loss for them. In developed countries they produce biofuel from the excess of produced food, but it is a

controversial fact as it effects human and animal food supply. Most of the developing countries are facing difficulty in solving their food problems as their population are vastly increasing but food quality and quantity is deteriorating due to inferior processing capability and storage shortage. For proper circulation of food among the population, reduction of food losses during harvesting season is necessary [1]. During the production season of any food its quantity is abundant so it's more than demand and as a result price drop. So, farmers need to preserve food for a longer period to supply it later the market when price rises and to meet the demand. There are many methods available for preservation of food like canning, chemical treatment, dehydration, refrigeration, controlled atmospheres use of subatomic particles of which dehydration is the tolerable approach providing solar radiation as the major energy source [2]. Ziafooghi et al. [3] presented an indirect solar assisted intermittent infrared dryer to investigate the effective parameters in the drying system. But in this case high amount of electric energy is needed which might not be afforded for the rural people of Bangladesh. Dehydration is most suitable for foods which have high moisture content, prone to microbial infestation. Different foods have maximum temperature and heating rate limitation as drying is a slow energy consuming process otherwise its quality will be ruined [4-5]. Solar drying is a promising alternative for food drying in Bangladesh, because mechanical drying is largely used in industrial countries and is not applicable to little farms in developing countries due to high investment and operating costs. A mixed mode type

* Corresponding author. Tel.: +8801852610004
E-mail addresses: meheditusar95@gmail.com

solar dryer consisting of dryer and collector was studied by Hossain et al. [6]. The dryer is composed of drying chamber, drying tray, and vent and used for chilly drying. An energy analysis of solar drying of jackfruit in a solar tunnel dryer was presented by Chowdhury et al. [7]. Jackfruit was dried from an initial moisture content of about 76% (w.b.) to 11.88% moisture content (w.b.). Kaewkiew et al. [8] studied the performance of a large-scale greenhouse dryer to dry red chili in Thailand. They dried 500 kg of red chili using this dryer and reduced the moisture content from 74% to 9% in 3 days. Use of solar energy is a viable solution for dehydration. Drying foods using solar energy are carried by open sun drying and solar drying. Products are directly subjected to sun in open sun drying. This method is the cheapest and economical option for drying foods, but it is a labor intensive process, leads to contamination of the food, requires larger area, slower drying rate and sudden exposure to rain, may result in discoloration of the product, lead to microbial infestation and product loss due to contamination, animal or bird eating [9-10]. Various types of open sun drying are specified based on the location, procedure of processing or the way solar radiation is utilized. For these reasons solar drying is a feasible alternative which can provide clean, hygienic drying of food maintaining national and international standards. Solar dryers can be classified according to their structure, mode of solar energy collection, drying method (Fig. 1)[11].

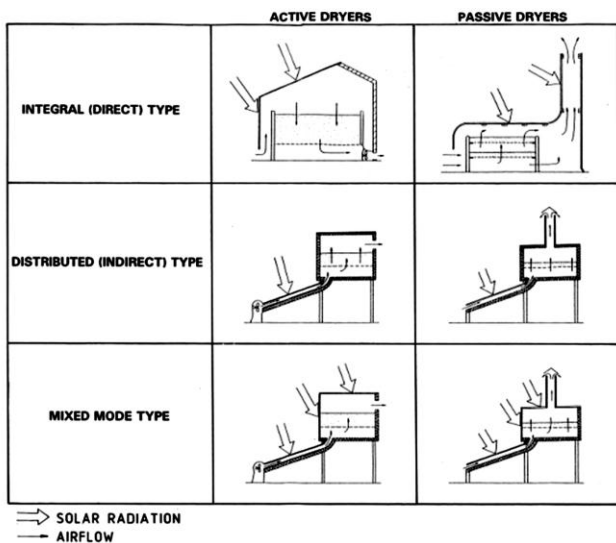


Fig. 1 Classification of drying using solar energy

In this study performance of three different types of natural convection cabinet direct solar dryer chambers, i.e. thin tube chimney type chamber, attic space type chamber, natural draft chamber was evaluated. In direct solar dryers foods to be dried are placed in an enclosed chamber, with a transparent cover over the chamber. Heat is generated by absorption of solar radiation on the product itself as well as on the interiors of the drying chamber [12].

2. Methodology

2.1 Experimental Setup

These dryer setups are fabricated using Mahogany wood and conventional glass. It has a base length and width of 28 Inch and 19 Inch. The base is supported in four 2×2 Inch columns made from Mahogany wood and has a fixed inclination of 18.5° to capture maximum amount of solar radiation at the Chittagong latitude of 22.3475° N. The length and shape of the supporting columns are kept providing the desired inclination of base. These experimental dryers are composed of three chambers (three different types of dryer) each having an internal dimension of 18×8 Inch and separated by 1-inch thick wall. The thin tube chimney type chamber has a hole of 1-inch diameter in the bottom where a flexible rubber pipe of 20 feet length and 1-inch diameter is fitted. The pipe hangs from the rooftop of a three storied building where solar cabinet dryer is placed and it acts as a chimney to provide natural draft. This chimney type chamber is covered with 18×8-inch glass panel (3 mm thick) and a hole of 1.5-inch diameter is made in the top side of the cover. Attic space type chamber has an attic shape provided by two glass covers both inclined at 50° with the horizontal of 18×6 inch and 18×8-inch dimension. These two inclined glass pieces are surrounded with two glass pieces which have a 1.5-inch hole on it. There is an open space above the cover for passing out hot air. Natural convection cabinet is a solar dryer covered with 18×8-inch glass panel. It has two rectangular ventilation port (15×1 inch on the side for air in and 6×1 inch for air out) to provide natural circulation of air across the chamber. Since performance evaluation of these dryers is one of the main concerns so joints and contacts of wood and glass or rubber is properly sealed.



Fig. 3 Experimental Setup (a) Top view; (b) Side view

2.2 Working Mechanism

In direct solar drying, fruits are placed inside a glazing roof box which has two openings (hot air exit and cold air inlet). It can be called cabinet drying. Some part of solar radiation incident on the glass plate is reflected back to surroundings. The rest part of solar radiation is transmitted into the chamber [12]. The only heating mechanism of these dryers was solar energy. Irradiated solar energy transmitted from sun passes through transparent glass covers of these dryers and is absorbed by the base and foods. So, the temperature of the surface of absorber and food rises. It heats up the adjacent air

enclosed in the dryer thus reduces its density. So, hot air rises in the upward direction and leaves the chamber entraining moisture from food to be dried resulting in suction using another port in the lower side. Since radiated energy from sun is absorbed in the dryer but cannot dissipate outside due to greenhouse effect in the chamber, temperature in the dryer rises. So, air in the chamber is less dense. As, this dryer is placed in the roof of a 3 storied building a pipe is used as chimney in dryer 1. The suspended inlet of the pipe is positioned in cool place. So, air flows upward in the pipe due to the pressure difference between drying chamber and pipe inlet. Since no other opening is provided in this chamber thus air flow is only due to pressure difference. In dryer 2 air enters through the circular holes as shown in figure 2 and exits using the gap of two inclined glass plates. As air inlet size is comparatively small wind velocity have minimum effect for this chamber. For dryer 3 air enters using the side opening and exits using through upward opening. Dryer 3 has privilege of natural wind velocity as it has larger openings. Wind velocity has a significant effect in moisture removal from food. In the dehydrating process food losses moisture to adjacent air and air reaches equilibrium with food so moisture removal ceases. Circulating air breaks the equilibrium by carrying the adjacent air away and increase moisture removal rate.

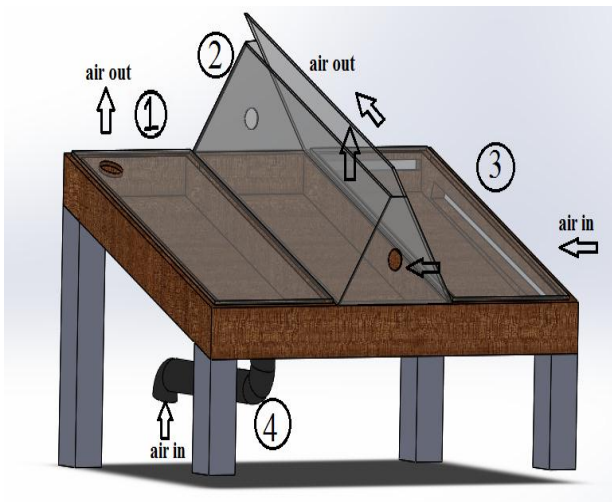


Fig. 4 Constructed dryer 1) Thin tube chimney type dryer 2) Attic space type dryer 3) Natural convection type dryer 4) Chimney.

In order to simplify the evaluation, heating source of this dryers was solar energy during day time (10am to 4 pm). The objectives of the trials are:

- To evaluate dehydration rate of different fruits i.e. apple, banana, guava, pineapple and moisture content at different drying period.
- To evaluate drying rate of different fruits in different chamber at different drying time interval.
- To evaluate the performance of three different types of natural convection cabinet direct solar dryers chamber

3. Data Reduction

The dryer was constructed and tested in the rooftop of Department of Mechanical Engineering, Chittagong University of Engineering & Technology, Raozan, (22.4600° N, 91.9710° E) Bangladesh. The performance of these dryers were evaluated during July-August 2017. For these assessment thirteen data were collected at these intervals from which three data were chosen as follows: first day, highest performance day and last day. All the experiments were done from 10 AM to 4 PM. Apple, Banana, Guava and Pineapple are chosen to compare the different dryer performance and also to check their drying performance. Three pieces of each sample were placed in individual compartments after weighing at 10 AM. At 1 PM and 4 PM the dehydrated samples were weighted again. From these data percentage of moisture lost, drying rate, moisture ratio of Apple, Banana, Guava and Pineapple during drying experiment in different chambers were calculated using the following equation:

Dehydration rate (gm/gm)

Drying rate (gm water/gm dry matter. min)

$$\frac{W_i - W_f}{W_i} \times 100 \quad (1)$$

Moisture ratio

$$\frac{M_t - M_{t+dt}}{M \times DMC \times dt} \quad (2)$$

$$\frac{M - M_e}{M_0 - M_e} \quad (3)$$

Where W_i , W_f , are the initial and final weight of the sample. M , M_0 , M_e , M_t and M_{t+dt} are the moisture content, initial moisture content, equilibrium moisture content, moisture content at ‘t’ and moisture content at ‘t+dt’, respectively. The moisture ratio was simplified to (M/M_0) of the $(M-M_e / M_0-M_e)$ [13].

4. Results and Discussion

The data collection period was started 9th April 2017. Usually data was taken in sunny day for getting proper dehydration rate. Some data were avoided because of erroneous data collection technique at the beginning from 9th April 2017 to 23th May 2017. Then the data collecting technique was corrected and data was taken three times in a day such as 10am, 1pm and 4pm. After analyzing dehydration rate of before 1pm and after 1pm the performance of each chamber can be identified.

Banana, pineapple, apple and guava were the food samples. In induced draft chamber, the dehydration rate of pineapple is 56% in which 21% dehydration is occurred before 1pm and 35% dehydration is happened after 1pm. Total dehydration rate of Apple is 54.2% in this chamber in which 20.2% dehydration is completed before 1pm and 34% dehydration is occurred after 1pm. For banana dehydration rate is 46.8% in where 15.6% dehydration is completed before 1pm and 31.2%

dehydration is completed after 1pm. In this chamber, dehydration rate of guava is 46.75% in which 17% dehydration is occurred before 1pm and 29.75% dehydration is completed after 1pm. After analyzing the dehydration rate of the samples of induced draft chamber it is seen that the dehydration rate of pineapple is the highest as water level in pineapple is highest among these four samples and it is 87%. Besides, for guava dehydration rate is lowest as water level of guava is lowest than other samples and it is around 58%. Dehydration rate of apple is lower than pineapple but higher than banana. 84% water is contained in apple and 74% water is existed in banana. Besides, dehydration rate of banana is higher than guava but lower than apple. It is also appeared that total dehydration rate of induced draft chamber is 44.5% in which 13.2% is occurred before 1pm and 31.3% is completed after 1pm.

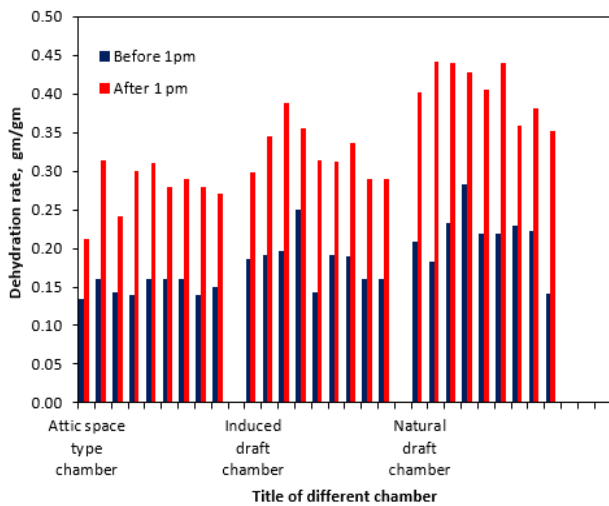


Fig. 5 Dehydration rate of three different direct solar dryer.

After analyzing the dehydration rate of the samples of attic space type chamber it was also seen that the dehydration rate of pineapple is the highest as water level in pineapple is highest among these four samples and it is 87%. Besides, for guava dehydration rate is lowest as water level of guava is lowest than other samples. Dehydration rate of apple is lower than pineapple but higher than banana. Besides, dehydration rate of banana is higher than guava but lower than apple. It is also appeared that total dehydration rate of attic space type chamber is 33.3% in which 11.2% is occurred before 1pm and 22.1% is completed after 1pm. In natural draft chamber, the dehydration rate of pineapple is 66.33% in which 23.3% dehydration is occurred before 1pm and 43.03% dehydration is happened after 1pm. Total dehydration rate of Apple is 63.8% in this chamber in which 22.4% dehydration is completed before 1pm and 41.4% dehydration is occurred after 1pm. For banana dehydration rate is 53.6% in where 19.8% dehydration is completed before 1pm and 33.8% dehydration is completed after 1pm. In this chamber, dehydration rate of guava is 54.75% in

which 20.62% dehydration is occurred before 1pm and 34.13% dehydration is completed after 1pm. After analyzing the dehydration rate of the samples of natural draft chamber it is also appeared that the dehydration rate of pineapple is the highest as water level in pineapple is highest among these four samples. Besides, for guava dehydration rate is lowest as water level of guava is lowest than other samples and it is around 58%. Dehydration rate of apple is lower than pineapple but higher than banana. Besides, dehydration rate of banana is higher than guava but lower than apple. It is also appeared that total dehydration rate of natural draft chamber is 58.9% in which 20.5% is occurred before 1pm and 38.4% is completed after 1pm. It is appeared that total dehydration rate of induced draft chamber is 44.5%, for attic space type chamber dehydration rate is 33.3% and for natural draft chamber it is 58.9%. So, it is cleared from this analysis that the performance of natural draft chamber is best than other two chambers and performance of attic space type chamber is worst. Besides, the performance of induced draft chamber is better than attic space type chamber. It is also seen that dehydration rate before 1pm is lower than after 1pm. Besides; dehydration rate of pineapple is the highest as water level is so much high and for guava is the lowest as water level is low. Dehydration rate of apple is lower than pineapple but higher than banana. Different fruits have different rate of moisture loss percentage in a day. As shown in Fig. 6 (a) moisture loss rate of each fruits is maximum in natural draft chamber and minimum at attic space type chamber in each of the three days. Moisture loss percentage is minimum for pineapple as it contains maximum amount of water among these four items. Moisture loss percentage is maximum for Guava as it contains less amount of water among these four items.

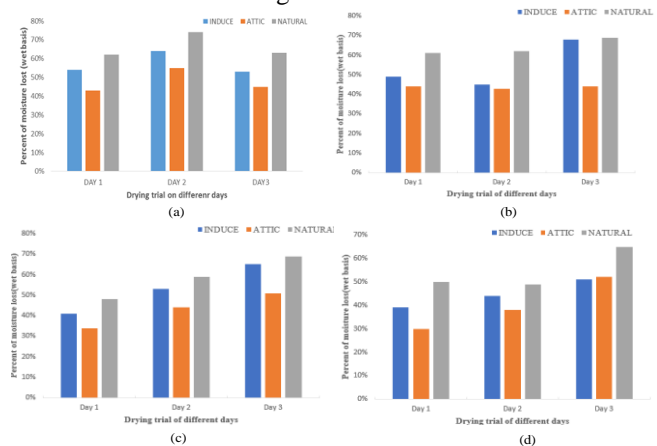


Fig. 6 Moisture loss rate for (a) Apple; (b) Banana; (c) Pineapple; (d) Guava.

Fig.7 shows the drying rate of different fruits (Apple, Banana, Guava) in different chambers with time. First drying rate analyzed from 10am to 1pm and then 1pm to 4pm. It is seen from Fig.7 that drying rate is maximum in natural draft chamber for all the sample. Because maximum air can be passed through natural draft chamber. Drying rate is found maximum at 2nd period of

drying time(1pm-4pm). Because temperature was keep rising from 10am and become maximum at mid noon of those days. Drying rate of Apple is maximum as it contains highest level of water and this rate is maximum between 1pm to 4 pm. Drying rate of guava is minimum as it contains lesser level of water. Its drying rate is maximum between 1pm to 4pm. Drying rate of Banana is higher than Guava but lower than Apple because it contains higher quantity of water than Guava but lower amount of water than Apple.

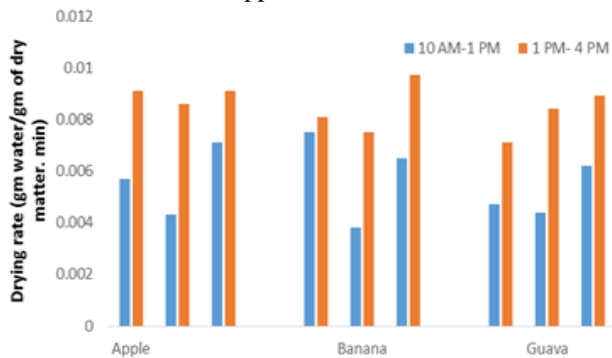


Fig. 7 Drying rate of different fruits in different chambers with time.

Fig. 8 shows the moisture ratio of different fruits (Apple, Banana, Guava) in two different times of 1pm and 4pm. Moisture ratio of the samples was lower at 4pm and higher at 1 pm. Because dehydration rate was increasing higher after 1 pm. Fig.8 indicates more moisture was removed during 1pm to 4pm instead of 10am to 1pm. As well as more convenient chamber was natural draft chamber at which most moisture content was removed from those fruits. Attic type chamber was found less efficient among the three chambers in which moisture ratio was higher for every sample. Induced draft chamber was less efficient than natural type chamber but more efficient than attic type chamber.

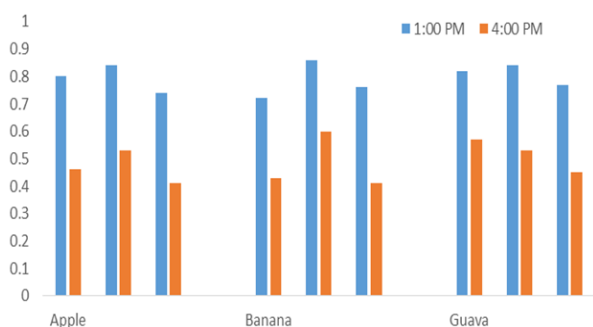


Fig. 8 Moisture ratio of different fruits in different chamber.

5. Conclusion

In the study three different types of natural convection cabinet direct solar dryers chamber, i.e. induced draft chamber, attic space type chamber, natural draft chamber, were used. Performance of natural draft chamber was the best and attic space type chamber was the worst among three chambers. Because the total

dehydration rate of natural draft chamber was 58.9% which was highest among the three chamber and 33.3% for the attic space type chamber which was lowest among them. The performance of induced draft chamber was better than attic space type chamber with total dehydration rate of 44.5%. Dehydration rate of pineapple was the highest and lowest for guava among four samples. Dehydration rate of apple was lower than pineapple but higher than banana. Besides, dehydration rate of banana was lower than apple but higher than guava. Drying rate after 1pm was higher than rate of before 1pm. As natural draft chamber was a wooden chamber, so much cheap to make and performance is the best among three chambers, so it can be told that natural draft chamber will be most effective for the coastal area of Bangladesh.

References

- [1] A. G. M. B. Mustayen, S. Mekhilef, and R. Saidur, Performance study of different solar dryers: A review, *Renew. Sustain. Energy Rev.*, vol. 34, pp. 463–470, (2014).
- [2] V. K. Sharma, S. Sharma, R. A. Ray, and H. P. Garg, Design and performance studies of a solar dryer suitable for rural applications, *Energy Convers. Manag.*, vol. 26, no. 1, pp. 111–119, (1986).
- [3] A. Ziafroughi, A. J. Esfahani, A salient reduction of energy consumption and drying time in a novel PV-solar collector-assisted intermittent infrared dryer, *Sol Energy* vol. 136 pp. 428–36, (2016).
- [4] A. Sharma, C. R. Chen, and N. Vu Lan, Solar-energy drying systems: A review, *Renew. Sustain. Energy Rev.*, vol. 13, no. 6–7, pp. 1185–1210, (2009).
- [5] V. K. Sharma, A. Colangelo, and G. Spagna, Experimental performance of an indirect type solar fruit and vegetable dryer, *Energy Convers. Manag.*, vol. 34, no. 4, pp. 293–308, (1993).
- [6] M. Hossain, M. Z. Hossain, M. A. Hossain, M. A. Awal, M. M. Alam, and A. H. M. M. Rabbani, Design and Development of Solar Dryer for Chilli Drying, *Int. J. Res.*, vol. 2, no. 1, pp. 63–78, (2015).
- [7] M. M. I. Chowdhury, B. K. Bala, and M. A. Haque, Energy and exergy analysis of the solar drying of jackfruit leather, *Biosyst. Eng.*, vol. 110, no. 2, pp. 222–229, (2011).
- [8] J. Kaewkiew, S. Nabnean, and S. Janjai, Experimental investigation of the performance of a large-scale greenhouse type solar dryer for drying chilli in Thailand, *Procedia Eng.*, vol. 32, pp. 433–439, (2012).
- [9] Tiwari, G. N. Analytical studies of crop drying cum water heating system. *Center of energy studies, IIT* (1995), “Tiwariana97.Pdf.” .
- [10] P. H. Oosthuizen, The selection of simple indirect solar rice driers. *Drying* (1992).

- [11] O. V. Ekechukwu, Review of Solar Energy Drying Systems I - An Overview of Drying Principles and Theory, *Energy Convers. Manag.*, vol. 40, no. 6, pp. 593–613, (1999).
- [12] S. Tiwari, G. N. Tiwari, and I. M. Al-Helal, Development and recent trends in greenhouse dryer: A review, *Renew. Sustain. Energy Rev.*, vol. 65, pp. 1048–1064, (2016).
- [13] I. Ceylan, M. Aktaş, and H. Doğan, Mathematical modeling of drying characteristics of tropical fruits, *Appl. Therm. Eng.*, vol. 27, no. 11–12, pp. 1931–1936, (2007).

Dust Effect on Glass Transmittance and Mirror Reflectance of Solar Collectors

Mehedi Hasan Tusar*, Amir Hamza Limon, Abdullah Al Noman, Goutam Das

Department of Mechanical Engineering, Chittagong University of Engineering & Technology, Chittagong-4349,
BANGLADESH

ABSTRACT

Almost every country in the world is leaning towards renewable energy and installation of solar power systems are increasing day by day. But, solar power systems are affected by dust deposition as it reduces optical efficiency of these systems. So, evaluation of dust deposition effect for a particular location needs to be carried out to predict the performance and installation of different solar power systems. In this experiment transmittance and reflectance loss of glass and mirrors are examined respectively at seven days interval for a period of three month in maximum solar irradiation season of Bangladesh to evaluate dust deposition effect on optical performance of them. It is found that glass and mirror suffered from 3% to 6% transmittance and 8% to 16% reflectance loss respectively over the experiment period.

Keywords: renewable energy, solar collectors, dust effect, optical efficiency

1. Introduction

The world is passing through energy crisis and demand of energy is increasing day by day. However, our fossil fuel stocks are decreasing and will diminish fully within this century. Nonrenewable energy reserves like oil, coal, gas will be depleted fully within 35, 107, 37 years respectively [1]. So, renewable energy sources are taking place in energy production and will be one of the major sources within few decades. Solar energy is one of the leading renewable energy resources. Photovoltaics (includes both concentrating and non-concentrating systems) and concentrating solar thermal systems (CST) are developed technologies to harvest solar energy. Both of these technologies suffer from dust deposition effect that reduces the energy performance of the system, causes degradation of the system, cuts down power generation and increases production and maintenance cost and lowers benefit. A lot of research is ongoing about what is the composition of dust, how dust effects the energy generation, how it degrades a system and its performance, what are the remedies, how to clean the systems for better performance with cutting water consumption at minimized cost. Dust mainly consists of quartz and silica components. Accomplishing elemental and mineralogical analysis, Eliminiir et al. [2] found that dust accumulated on transparent covers of solar cells were composed mostly of quartz and calcite with smaller amount of dolomite and clay minerals. Dust deposited on solar panel or concentrator is fully site specific as dust concentration in greenery is less than dust concentration in the roadside or heavy industrial area in the same location. Dust particle available in air also differs in size with location, geography, wind, temperature etc. If dust deposition happens due to airborne dust particle then particle diameter is less than 70 micrometers [3]. Dust deposited on the solar panel scatters the light in random direction and provides shading in the panel prohibiting the transmission of incident solar energy in solar cells. Many researchers investigated the dust effect on output power for solar panels and collectors in different countries [4-6]. Nimmo, Saed [7] recorded 26% and 40% loss of

efficiency respectively in solar collectors and PV modules at dry conditions in a period of 6 months in Saudi Arabia. Jiang et al. [8] experimented that when dust density increases from 0 to 22 g/m² the corresponding reduction of PV output efficiency grew from 0 to 26% and reduction has a linear relationship with dust deposition density. Vivar et al. [9] found soiling reduced 4% electrical output on average in flat PV module and concentrating photovoltaic (CPV) systems are more sensitive to soiling than flat plates. Solar energy converting systems use glass and mirror and dust reduces their transmittance and reflectance respectively. Due to this reason fraction of incident solar energy is lost that reduces system efficiency. Deposition of dust also depends on tilt angle and orientation of glass and mirror panels. A lot of investigator experimented effect of orientation and tilt angle for dust deposition in glass and mirror plates all over the world [10-12]. Garg reported 30% and 2% transmittance loss in one month for horizontal and vertical plates respectively for solar collectors (glass) in India [13]. Sayigh et al. [14] in Kuwait found 64%, 48%, 38%, 30%, 17% transmittance reduction after 38 days for 0°, 15°, 30°, 45°, 60° tilt angles respectively for different types of glass. It has been seen that horizontal plates have more dust deposition than vertical plates. So, more energy is lost in horizontal plate than vertical plate and accumulation of dust on photovoltaic modules is of more concern in tropics than other region because of the lower tilt angles [15]. Since, Bangladesh is situated in tropical region thus lower tilt angle for PV panels, concentrators it is important to investigate the effect of dust on energy output for different solar modules. Solar modules use glass, glass mirror (one of the glass surfaces coated with reflecting material), polished mirror surface. Energy loss of these modules depends on the transmittance and reflectance loss of glass and mirror. In nearly similar experiment of this study a transmittance and reflectance loss of 22% and 19% for glass and mirror are recorded by Hasan et al. [16] for dust accumulation at different orientation and inclination at CUET, Chittagong from August to

* Corresponding author. Tel.: +88-01852610004
E-mail addresses: meheditusar95@gmail.com

September. However, evaluation of transmittance and reflectance using LASER lite is not a perfect technique for dust deposited plates because dust accumulates discretely and is not uniform throughout the plates. Since, LASER light does not diffuse so it measures localized effect of dust on glass and mirror plates. It will show greater loss for dust accumulated region while less for dust free region. So, better result comes if overall effect can be evaluated. In this experiment transmittance and reflectance loss of glass and mirror plates are studied at CUET, Chittagong region for 3 months (March-May) using diffuse light from LED source which is more realistic than LASER to study overall transmittance and reflectance loss.

2. Methodology

2.1 Test Facilities

For this experiment 22 pieces of $10 \times 10 \text{ cm}^2$ glass and mirror samples in total were cut in equal dimensions from their respective large sections. Two pieces of the glass and mirror samples are stored carefully in the laboratory that are used as reference samples and the rest of the cut samples are used as the test samples. The loss of transmittance and the reflectance of the test samples are compared with that of the reference samples. A light is used as a source of LED. “Mastech” digital lux meter is used to measure the intensity of the incident light on the samples. It gives output in three ranges 0-1999, 2000-19990, 20000-50000 lux with 5% tolerance using one silicon photo diode with filter operating at 9V. Two timber frames (in Fig. 3. (a)) were fabricated, which has four 45° inclined sides in four earth direction (i.e. North, South, East, West) and one horizontal side. Each of the sides has two slots to hold and expose the test samples to outdoor condition at the investigation site. On the other hand, in order to ensure precautions handling of the test samples between the laboratory and the investigation site during data collection, two timber carriers (in Fig. 3. (b)) with ten slots each were fabricated. Two dark boxes (boxes with top covers and black walls) were used for glass and mirror samples to collect data in dark condition. The schematic of the boxes is shown in Fig. 1 and 2. There are slots to attach the LED lite, Lux meter and the test samples inside the boxes. Top cover of the box ensures no interference between the Lux meter and the external light.

2.2 Experimental procedure

In this experiment five orientation are selected i.e. east side, west side, north side, south side and horizontal to the floor. Two sample holders are placed in each of five orientation for dust deposition. Total ten glass and ten mirror sample holders are placed in these five orientations for depositing dust. The sample holders of each side are placed on timber frames 45° inclined corresponding to horizontal. Then whole setup is exposed to the environment and let the dust to deposit on them over time. Care is taken to ensure that the dust is accumulated on the sample holder freely and this dust

and dirt are not removed by any agents other than wind and rain. Then the dust deposited glass and mirror samples are carried to the laboratory at every seven days interval using sample carrier for data collection.

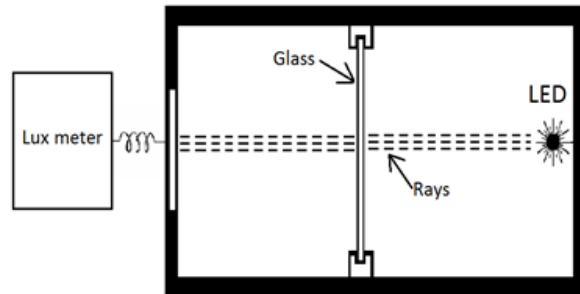


Fig. 1 Schematic diagram of experimental setup for glass transmittance measurement (top view).

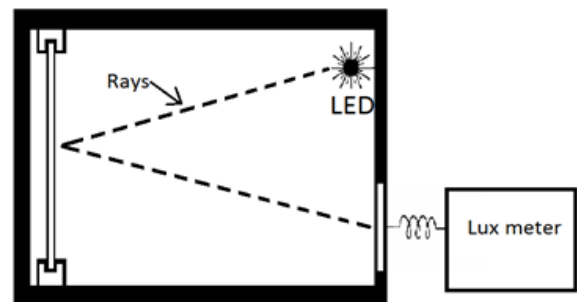


Fig. 2 Schematic diagram of experimental setup for mirror reflectance measurement (top view).

Every dust deposited glass samples are placed in experimental setup or dark box (in Fig. 1.) exposed to bright light to measure the illuminance of them using lux meter. Meanwhile illuminance of the clean reference glass sample prepared from same glass and stored in the lab is measured. Then normalized transmittance is found by dividing dust deposited glass illuminance by clean reference glass illuminance. Similar procedure is followed for measuring normalized reflectance of the mirror sample in another dark box prepared for mirror (in Fig. 2.).



Fig. 3: (a) Timber frame; (b) sample carrier [16].

3. Data analysis and discussion

The performance of solar collector drops gradually as dust is accumulated on its surface. The rate of decrease in the performance depends on the rate of dust deposition. The amount of accumulated dust increases with time which reduces transmittance and reflectance. As two glass sample holders are placed each side (east, north, west south and horizontal to the floor), the average of the two samples are considered for each side. Since illuminance of both dust deposited and reference glass sample are measured in same setup at same conditions the ratio of them gives normalized transmittance of glass samples. That expresses the resultant transmittance of dust deposited glass sample with respect to clean glass sample. Similar procedure goes for normalized reflectance measurement for mirror. Fig. 4 and 5 shows the normalized transmittance and reflectance of glass samples held at different orientation (East, West, North, South and horizontal orientation of earth) over time. From the Fig. 4 and Fig. 5 it is shown that the Normalized transmittance and normalized reflectance is first reduced as deposited dust is increasing on the samples, then transmittance and reflectance are increasing after some days and so on. It follows decreasing and increasing trend as time passes. The study conducted in summer season in Chittagong, Bangladesh and data was collected in seven days interval. There was uncertainty in weather at this period because sudden rain came anytime, and wind velocity was varied as well. For these reasons dust which is deposited on the glass plate was removed in some portion. When dust deposition was increasing transmittance and reflectance were decreasing for all samples, after some day's rainfall or heavy wind speed removed some portion of deposited dust and for this reason transmittance and reflectance was increasing and so on. From the Fig. 4 and Fig. 5 it also be shown that the decreasing rate of transmittance and reflectance is maximum for horizontal sample holders because of maximum dust deposition rate. Dust deposition rate is lower for other samples tilted 45° from horizontal as dust particles might be rolled downwards, washed by dew at night or these tilted plates captures more wind than horizontal samples. After horizontal sample average transmittance and reflectance decrease is maximum for south samples. it means dust deposition rate is maximum in south orientation after horizontal orientation. From Fig. 3 and Fig. 4 dust deposition rate in this location is found in following trend:

Horizontal > South > North > West > East

After studying three month's data it is found that dust deposition rate is minimum in East and West side samples. The main reason behind this attitude is wind direction in Chittagong during pre-summer season when dry air moves south from north and during post summer season warm air moves towards the land from the south (sea) [17]. Particulates which are mixed with this moving air is then deposited, when the air is introduced to any obstacle along its direction of motion.

Normalized transmittance, reflectance of glass and mirrors respectively varies with different orientations. Mirror has more reflectance loss than transmittance loss of glass plate. For better understanding of dust effect on glass and mirror samples these values are averaged and expressed in Fig. 5. As shown in Fig. 5 normalized transmittance and reflectance of glasses is first decreasing as amount of deposited dust is increasing then increasing as the amount of dust is removed by rain or strong wind effect and so on. Decrease of transmittance and reflectance is higher in March and lower in May. That indicates dust deposition rate is higher in March and lower in May in this location. The main reason is more rainfall in May than March.

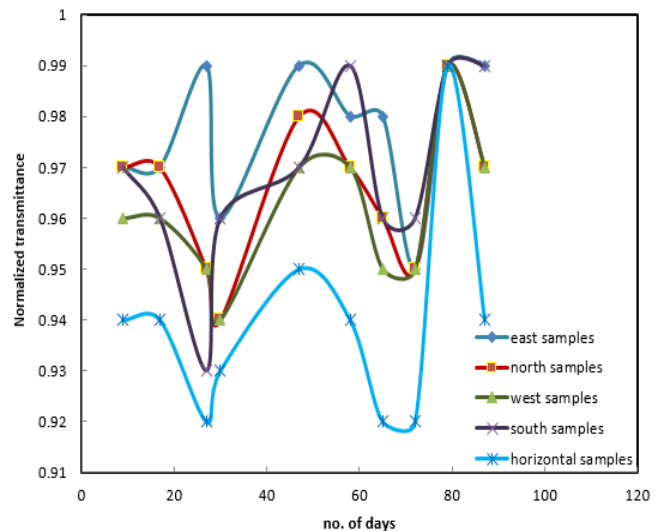


Fig. 4 Dust effect on the normalized transmittance of glass samples over time

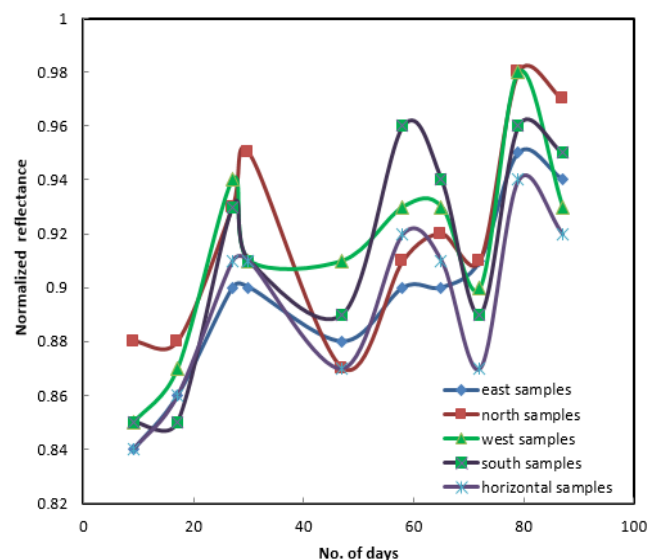


Fig. 4 Dust effect on the normalized reflectance of glass samples over time.

PV solar panels are protected with glass covers thus normalized transmittance gives the relative percentage

of incident energy transmitted through dust deposited glass panel with respect to clean glass panel. Since mirrors are used in concentrating systems normalized reflectance is important in concentrating systems to understand energy loss and fraction of incident energy concentrated on receiver.

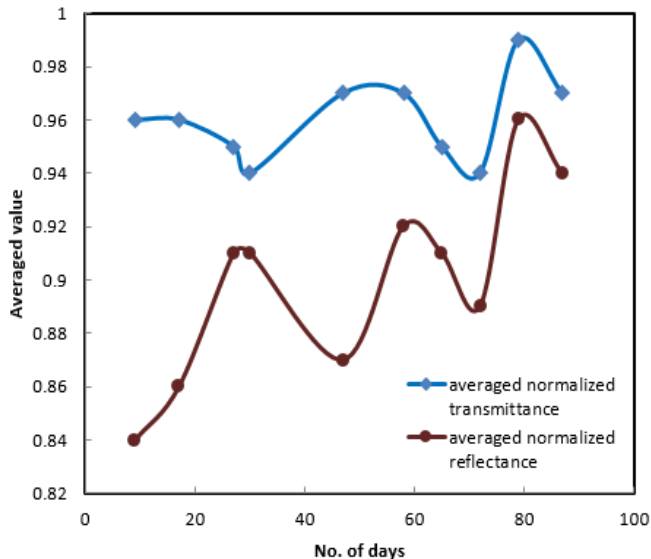


Fig. 5 Dust effect on the averaged normalized transmittance and reflectance of glass and mirror samples respectively over time

4. Results & Conclusion

4.1 Summary

An experimental investigation is done in CUET, Chittagong to find the loss of transmittance, reflectance of glass and mirrors respectively to predict the potential of different solar power systems. The findings of the study are listed below:

- Average values of normalized transmittance and reflectance varied in between 94% to 97% and 84% to 92% for exposed glasses and mirrors respectively. That is the transmittance of glass and reflectance of mirror dropped in between 3% and 6%, and 8% and 16% respectively.
- Mirror has more reflectance loss than transmittance loss of glass since the mirror used in this experiment was silvered on the opposite side of dust accumulated surface. So, incident light was affected twice for same dust deposition density.
- During the period of experiment in March, April and May raining occurred for many times in every month. In periodic checking it is observed that glass and mirror is cleaned up to

98% and 92% by raining, so requires less cleaning in these months.

- Decrease of transmittance and reflectance for glass and mirrors is higher in March and lower in May during summer season in this location.

4.2 Limitation & Further Research

Many of the state-of-the-art concentrating power plants use surface polished mirror where dust deposits whereas silvered glass mirror was used in this experiment. So, incident light will be affected only single time in state-of-the-art technology. For this, ongoing research focuses on reflectance loss of surface polished mirror.

REFERENCES

- [1] S. Shafiee and E. Topal, "When will fossil fuel reserves be diminished?," *Energy Policy*, vol. 37, no. 1, pp. 181–189, 2009.
- [2] H. K. Elminir, A. E. Ghitas, R. H. Hamid, F. El-Hussainy, M. M. Beheary, and K. M. Abdel-Moneim, "Effect of dust on the transparent cover of solar collectors," *Energy Convers. Manag.*, vol. 47, no. 18–19, pp. 3192–3203, 2006.
- [3] Y. Shao, "Physics and Modelling of Wind Erosion," *Phys. Model. Wind Eros.*, vol. 37, no. January 2008, pp. i–xv, 2009.
- [4] F. Wakim, *Introduction of PV power generation to Kuwait*. Kuwait City: Kuwait Institute for Scientific Research, 1981.
- [5] M. Louy, Q. Tareq, S. Al-Jufout, Q. Alsafasfeh, and C. Wang, "Effect of dust on the 1-MW photovoltaic power plant at Tafila Technical University," *2017 8th Int. Renew. Energy Congr. IREC 2017*, no. Irec, 2017.
- [6] C. P. Ryan, F. Vignola, and D. K. McDaniels, "Solar cell arrays: Degradation due to dirt.," *Proc. Solar 1989, Proceedings of the American Section of the International Solar Energy Society, Denver, CO*. 1989.
- [7] B. Nimmo and S. A. Said, "Effects of dust on the performance of thermal and photovoltaic flat plate collectors in Saudi Arabia-Preliminary results," *Altern. Energy Resour. II*, vol. 1, no. 1, pp. 145–152, 1981.
- [8] H. Jiang, L. Lu, and K. Sun, "Experimental investigation of the impact of airborne dust deposition on the performance of solar photovoltaic (PV) modules," *Atmos. Environ.*, vol. 45, no. 25, pp. 4299–4304, 2011.
- [9] M. Vivar *et al.*, "Effect of soiling in CPV systems," *Sol. Energy*, vol. 84, no. 7, pp. 1327–1335, 2010.
- [10] N. M. Nahar and J. P. Gupta, "Effect of dust on transmittance of glazing materials for solar collectors under arid zone conditions of India," *Sol. Wind Technology*, vol. 7, no. 2–3, pp. 237–243, 1990.
- [11] A. El-Nashar, "The effect of dust accumulation

- on the performance of evacuated tube collectors,” *Sol. Energy*, vol. 53, no. 1, pp. 105–115, 1994.
- [12] L. Boyle, H. Flinchpaug, and M. Hannigan, “Impact of natural soiling on the transmission of PV cover plates,” in *2013 IEEE 39th Photovoltaic Specialists Conference (PVSC)*, 2013.
- [13] H. Garg, “Effect of dirt on transparent covers in flat-plate solar energy collectors,” *Sol. Energy*, vol. 15, no. 4, pp. 299–302, 1974.
- [14] A. A. . Sayigh, S. Al-Jandal, and H. Ahmed, “Dust effect on solar flat surfaces devices in Kuwait.,” in *In Proceedings of the workshop on the physics of non-conventional energy sources and materials science for energy*, 1985, pp. 353–367.
- [15] J. Kern and I. Harris, “On the optimum tilt of solar collector,” *Sol. Energy*, vol. 17, no. 2, pp. 97–102, 1975.
- [16] M. M. Hasan, A. A. Noman, M. H. Tusar, and M. Islam, “Effect of dust on the optical properties of the glazing materials of solar collectors: a case study.” in *Proceedings of International Conference of Mechanical Engineering & Renewable Energy, 2017, Chittagong*.
- [17] M. A. Khatun et al., “MET report on Climate of Bangladesh”, *Norwegian meteorological institute*, no. 08/2016 ISSN 2387-4201

ICMIEE18-227

Experimental Investigation of an Air to Air Heat Pipe Heat Exchanger for Moderate Temperature Waste Heat Recovery

Saddam Hossen*, Mahmud-Or-Rashid, Mantaka Taimullah, Farhan Ahmed Shakil, and Dr.A K M Monjur Morshed

Department of Mechanical Engineering, Bangladesh University of Engineering & Technology, Dhaka-1000, BANGLADESH

ABSTRACT

Due to environmental concern and high price of the fuel, waste heat recovery has become a central issue for industrial and commercial energy users. Heat pipe heat exchanger (HPHE) could be employed in this regard economically. In this study, an HPHE consisting of heat pipes arranged in stages has been developed. Water was used as the heat carrying fluid inside the heat pipe and square fins were used in the cooling and heating zone of the heat pipe. The constructed HPHE was placed between two ducts carrying hot and cold air. The hot fluid temperature was varied from 60 to 80°C which resembles waste heat and cold air was atmospheric air. The hot and cold air's mass flow rate was varied between 0.037 and 0.087 kg/s and heat transfer between two air streams were measured as 228.5 to 362.2W and heat transfer coefficient varies from 4.22 to 8.09 W/m²-K.

Keywords: Heat pipe, Heat pipe heat exchanger, Air to air heat exchanger, Waste heat recovery

1. Introduction

Energy is the key element in modern life and at the same time is responsible for environmental pollution and global warming. To keep pace with modern life and at the same time to reduce environmental footprints, efficient utilization of the energy resources has become a key concern. A large amount of energy is being wasted while converting the energy into useful work. At present, about 20% to 50% of energy used in the industry is rejected as waste heat [1]. Recovering the waste heat from the industrial processes is one of the ways to reduce energy consumption without hampering the quality of the processes. With the increase of fuel price and environmental concern, waste energy recovery is becoming popular. Waste heat from processes comes in both high quality energy, where the temperature varies between 220°C and 700°C (e.g. generator exhaust, boiler exhaust, reheating furnace exhaust, etc.) and low quality energy, where the temperature is less than 100°C (e.g. compressed air cooling, stenter machine exhaust, bakery dryer, HVAC system, etc.). Waste heat recovery system and technology is well established for the high quality waste energy sources whereas for the low grade waste energy sources, heat recovery is not popular due to technological and economical limitations.

To recover the waste heat from the low temperature sources, heat pipe heat exchanger (HPHE) is an efficient way [1-10], where heat can be extracted at a very low temperature difference. Heat pipe is a known technology. The idea of heat pipe was first presented by Gaugler in General Motor Company in 1942. The first heat pipe was designed and manufactured by Grover in National Lab, Los Alamos, in the US in 1964 [1]. Since then, heat pipes are being used in many applications such as, heat exchangers (air pre-heaters or systems that use in economizers for waste heat recovery), HVAC system, cooling of electronic components, solar energy conversion systems, spacecraft thermal control, cooling of gas turbine rotor blades etc. In recent days, some common applications of HPHE are in medicine and

human body temperature control [2], spacecraft cooling [3], electrical and electronics equipment cooling [4, 5], waste heat recovery applications [6-11] etc.

In a heat pipe heat exchanger (HPHE), a group of vertical heat pipes is arranged in such a manner that two streams of fluid can flow over them through two separate ducts or pipelines. A high temperature fluid flows on one end of the HPHE (known as evaporation section) and a low temperature fluid flows on the other end (known as condensation section), thereby transfers heat from the high temperature fluid to the low temperature one using the fluid sealed in heat pipes as heat carrier. The heat pipes in a heat pipe heat exchanger are arranged in stages, each stage consisting of a single row of heat pipes, all of which are at the same temperature. Hagens et al. [12] studied experimentally the heat exchanger consisting of heat pipes with two different filling ratios of R-134a: 19% and 59% which demonstrated that a heat pipe heat exchanger is a good alternative for air-air exchangers in process conditions when air-water cooling is not possible. S.H Noie-Baghban and Majideian [13] studied experimentally the performance of distilled water filled heat pipe equipped heat exchanger at low temperatures (15-55°C) and concluded that appropriate method of vacuum, filling ratio and sealing of the heat pipe are necessary for increasing the effectiveness of heat pipe heat exchanger. Nguyen-Chi et al. [14] investigated experimentally the performance of vertical two-phase closed thermosiphon and used water as a working fluid. They investigated the influence of operating parameters on the maximum performance either by dry out or burn out limits. Li et al. [15] investigated experimentally the steady-state heat transfer characteristics of a vertical two-phase closed thermosiphon at low temperature differences with R-11, R-22 and water as working fluids. Park and Lee [16] made an experimental study on the performance of stationary two-phase closed thermosiphon with three working fluid mixtures (water-glycerin, water-ethanol, and water-ethylene glycol).

* Corresponding author. Tel.: +88-01

E-mail addresses: saddamme170@gmail.com

Shiraishi et al. [17] investigated experimentally a critical heat transfer rate in thermosiphons by taking into account the aspect ratio, filling ratio, working fluid property, and operating pressure.

In this paper, a vertical heat pipe (thermosiphon) heat exchanger is designed to recover heat from low temperature region (from 55°C air to ambient temperature air). The design of the HPHE is presented and the results for experimental investigations are reported. The performance of the HPHE is evaluated by varying the filling ratio of the heat pipes and mass flow rates of hot and cold air for an optimum operating condition thus optimizing the effectiveness of the HPHE.

2. Experimental apparatus and procedure

To investigate the heat transfer performance and evaluate the effectiveness of a HPHE and also to determine the optimum filling ratio and operating conditions of HPHE system for low temperature waste heat recovery application, an experimental setup was designed and constructed. The test system consisted of a HPHE, a data collection system, two fans for cold and hot air passing, an air pre-heater, four k-type thermocouples etc. as showing in the figure: 1 (a), (b), (c) and (d). In this study the designed HPHE was consisting of thirty eight heat pipes that are arranged vertically on the separation plate with two different rows and in seven columns, where 1st row consists of five tubes and 2nd row consists of 6 tubes total $(5+6+5+6+5+6+5) = 38$ tubes. Tubes are arranged in triangular formation for creating the turbulent flow in both condensation and evaporation section. Each heat pipes consists of a seven square fins (1.5 × 1.5 inch) of copper plate. Fins are arranged in the heat pipes in such way that, the flow becomes zigzag and create more turbulence and thus increase the heat transfer rate.

The working fluid selected for the heat pipes is water as it is cheap and has high latent heat of evaporation. Water is inserted into the copper pipe after sealing its one end, then it is heated up to its boiling point to make it air free and then the other end is sealed up. When the steam condense; vacuum is created by the vacuum inside the tube. The filling ratio of the working fluid (distilled water) in the heat pipe is varied form 33% and 50% of the heat pipe volume and then performance of the heat pipes were tested under those filling ratios. Thus an optimum filling ratio is obtained that ensures the maximum performance of heat pipe. The length of heat pipe 558 mm with inner and outer diameter of 13 and 15 mm. The lengths of the evaporator and condensation section in HPHE are 277 mm and 277 mm respectively.

Two ducts were arranged with the constructed HPHE in both condensation and evaporation section for passing the cold and hot air receptively with the help of two fans that are fitted at the two ends of the ducts. An air-preheater of 4500 W is used in the duct of evaporation side for heating the air. The temperature of air is controlled to 40°C to 75°C by a temperature controller.

The cold air in the condensation section is taken from the atmosphere.

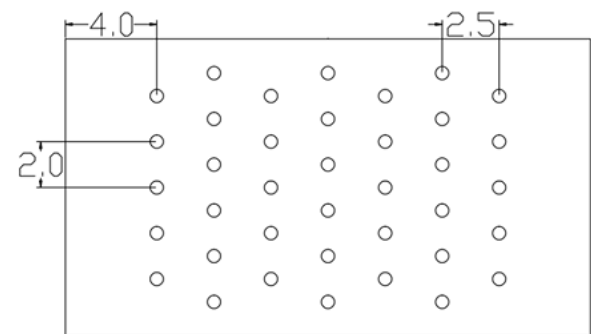
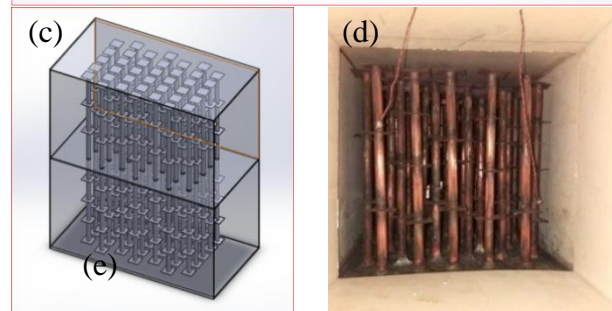
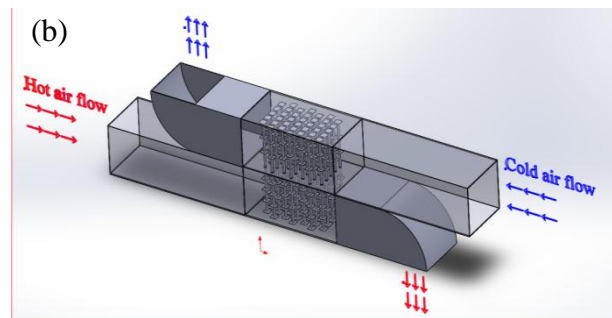


Fig.1 (a) Experimental setup; (b) Drawing for the experimental setup; (c) Drawing of the heat exchanger; (d) Front view of the heat exchanger; (e) Heat pipe arrangement.

For measuring the temperature of hot and cold air in condensation and evaporation inlet, outlets there are four k-type thermocouples were used. The mass flow rate of air is measured by anemometer.



Fig.2 Anemometer

3. Data reduction

The heat transfer rate for the HPHE from the hot flow air can be calculated by the following equation:

$$\dot{Q} = \dot{m}_{HA} C_{pHA} (T_{HA,in} - T_{HA,out}) \quad (1)$$

Where, \dot{m} is the mass flow rate of hot air, C_p is the specific heat capacity, $T_{HA,in}$ and $T_{HA,out}$ refer to the inlet and outlet temperature of hot air respectively.

Similarly, \dot{Q} can be also obtained by the cold air from the following formula,

$$\dot{Q} = \dot{m}_{CA} C_{pCA} (T_{CA,in} - T_{CA,out}) \quad (2)$$

This heat is not same to previously calculated heat transfer from the hot air due to uncertain heat loss. The overall heat transfer coefficient, U of the HPHE is defined as follows, $W / (m^2 K)$:

$$U = \dot{Q} / A \cdot \Delta T_{lm} \quad (3)$$

Where, A is the overall heat transfer area of the HPHE, (m^2) and logarithmic mean temperature difference ΔT_{lm} (K), which is calculated for a counter-flow arrangement as follow:

$$\Delta T_{lm} = \frac{(T_{HA,in} - T_{CA,out}) - (T_{HA,out} - T_{CA,in})}{\ln \left[\frac{(T_{HA,in} - T_{CA,out})}{(T_{HA,out} - T_{CA,in})} \right]} \quad (4)$$

The effectiveness of HPHE is defined as the ratio of the actual heat transfer rate \dot{Q} in a given heat exchanger to the maximum possible heat transfer rate \dot{Q}_{max}

$$\varepsilon = \dot{Q} / \dot{Q}_{max} \quad (5)$$

The following equation can be used to calculate the maximum theoretical heat transfer rate:

$$\dot{Q}_{max} = C_{min} (T_{HA,in} - T_{CA,in}) \quad (6)$$

Where, C_{min} is the smaller one of the heat capacities of hot air (C_{HA}) and cold fresh air (C_{CA}), kJ/K . C_{HA} and C_{CA} are calculated by following relations:

$$C_{HA} = \dot{m}_{HA} C_{pHA} \quad (7)$$

$$C_{CA} = \dot{m}_{CA} C_{pCA} \quad (8)$$

C_{max} is the larger one of the hot (C_{HA}) and cold air (C_{CA}) specific heat capacities. R is the ratio of the minimum and maximum heat capacity of the two fluid streams:

$$R = C_{min} / C_{max} \quad (9)$$

The number of heat transfer units (NTU), an important parameter for the heat exchanger, is expressed as follows:

$$NTU = UA / C_{min} \quad (10)$$

Where, U is the overall heat transfer coefficient, A is heat transfer surface area. The ε - NTU method is a thermodynamic calculation method of dividing wall type of heat exchanger, which is derived by the dimensionless equation when the logarithmic mean temperature difference is discussed. The relationship between ε and NTU can be expressed by:

$$\varepsilon = \frac{1 - \exp[-(1-R)NTU]}{1 - R \cdot \exp[-(1-R)NTU]} \quad (11)$$

4. Results and discussions

4.1 Performance of the Heat Pipe

In this experiment water is selected as working fluid because of its availability, low cost and also depending on its performance. Tests were performed and performances of a water filled heat pipe, an ethanol filled heat pipe and an empty copper tube were compared. The performance results reveal that water filled heat pipe shows better heat transfer performance over the other two. The test results are presented the following figures.

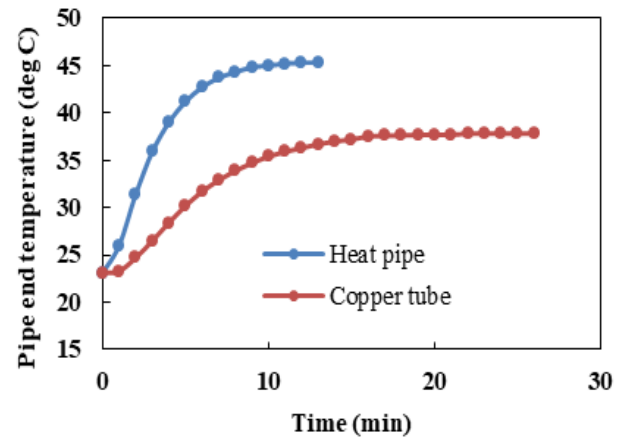


Fig.3 Variation of pipe end temperature with time when pipes other ends inserted into water initially at 57 °C

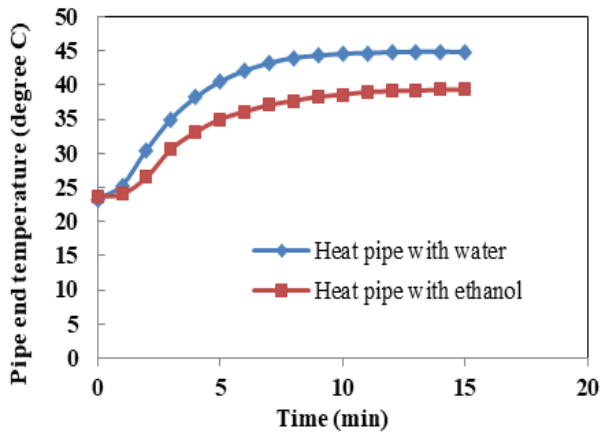


Fig. 4 Variation of pipe end temperature with time when pipes' other ends inserted into water initially at 53°C

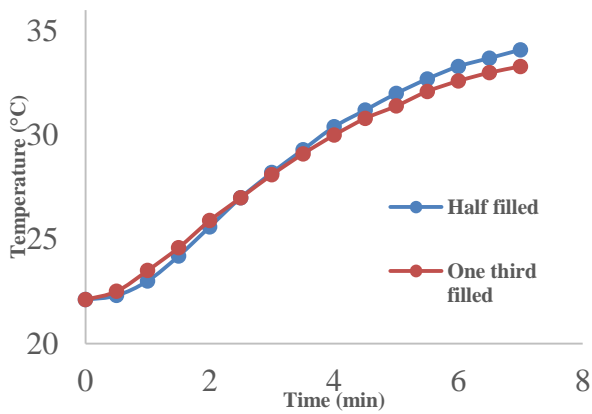


Fig.5 Variation of heat pipe performance with filling ratio

The filling ratio has a significant effect on the performance of the HPHE. For analyzing the performance of heat pipe by varying the filling ratio, a heat pipe is selected which length is 568 mm with 15 mm outer diameter and 1mm thickness. Working fluid was filled to 50% and 33% of total heat pipe volume for the performance test. The performance results are expressed with respect to the increase of top end temperature of heat pipe with time. In the initial period, the one-third filled heat pipe showed better performance than the half-filled heat pipe. But after a certain period of time, the situation had reversed. The half-filled heat pipe showed better performance than the one-third filled heat pipe. So in this experiment 50% filling ratio is taken as optimal filling ratio, then all heat pipes are constructed and assembled for HPHE.

4.2 Analysis on the performance of the HPHE

The variations of heat transfer rate, overall heat transfer co-efficient and effectiveness with hot air mass flow rates at different cold air mass flow rates are presented in Fig. 6, Fig.7 and Fig. 8. From the results, it is clear that both the heat transfer rate and overall heat transfer

coefficient increase with the increase of hot and cold air mass flow rates and effectiveness decrease.

In the experiment, the heat transfer rate changes between 228.5 and 1003.4 W and the overall heat transfer coefficient varies between 4.22 and 13.88 W/m²-K. The heat transfer rate and overall heat transfer coefficient gets the minimal value, when the hot air mass flow rate is 0.034 kg/s, maximum values when the hot air flow rate is 0.124 kg/s. The pattern is nearly similar for comparison with cold air mass flow rate also. The heat transfer coefficient is very low when the air flow rate is small. There are several reasons behind this phenomenon. One of the main causes is the turbulence. When the air flow rate is small, laminar flow is predominant and under laminar flow condition heat transfer coefficient is small because of lack of mixing of the fluid. When flow rate is high, turbulence is created and proper mixing takes place and thus heat transfer coefficient is also increased. The same reason is for the variation of heat transfer rate. So heat transfer can be increased by increasing the air flow rate.

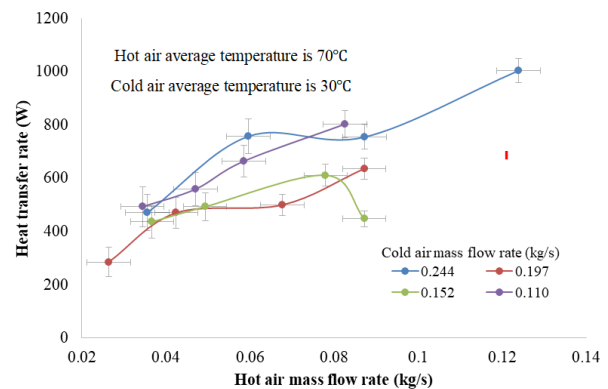


Fig.6 Effect of hot air and cold air mass flow rates on heat transfer rate.

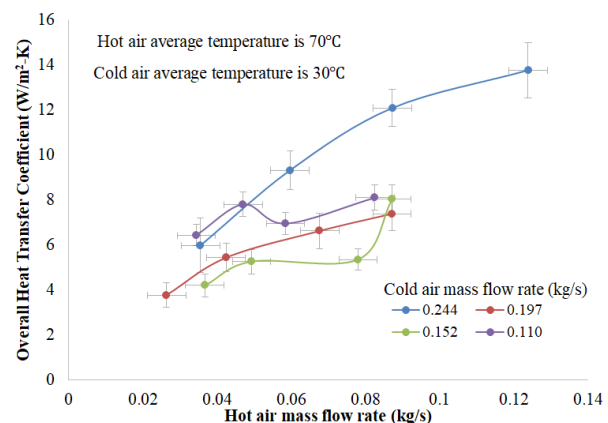


Fig.7 Effect of hot air and cold air mass flow rates on overall heat transfer coefficient.

The relationship between effectiveness and mass flow rate was different from previous patterns. Here effectiveness decreased with increasing of hot air mass

flow rates at a constant cold air mass flow rate. It was summarized from analyzing data of an experiment that for cold air mass flow rate 0.244 kg/s, effectiveness was decreased from 0.19 to 0.13 when hot air mass flow rate increased from 0.04 to 0.124 kg/s. So it was concluded that this HPHE was more effective and suitable for lower mass flow rate.

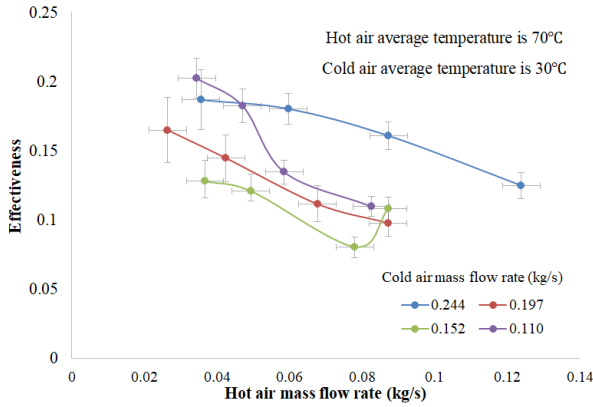


Fig.8Effect of hot air and cold air mass flow rates on effectiveness of HPHE.

In this paper, the effectiveness-NTU method regarding heat exchanger operation has been applied, and the nature of the relationship between effectiveness and NTU at different air mass flow rates is shown in Fig 9. From the figure, it is clear that that the effectiveness of HPHE increases with the increasing of NTU and the pattern of the relationship between effectiveness and NTU is nearly linear. It is because NTU is directly proportional with heat transfer coefficient and as heat transfer co-efficient increases with increasing air mass flow rates, NTU is also increased and when NTU increases effectiveness of HPHE also increases as the nature of their relationship described in theory. Here the effectiveness varying from 0.08 to 0.202, and the relationship can be expressed as $\epsilon = 0.8183 \text{ NTU} + 0.008$ from the best fit straight line.

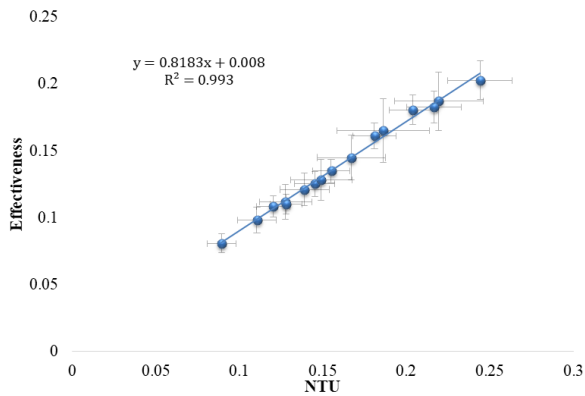


Fig.9Relationship between effectiveness and NTU

5. Conclusions

In this study, experimental work was carried out to investigate the effectiveness of a low cost HPHE in recovering low grade waste heat. From the results of the experimental investigation following conclusions can be drawn:

1. Low cost HPHE can be constructed without any sophisticated equipment at laboratory with water as the working fluid.
2. The performance of heat pipe in steady state is better for half-filled heat pipe than one-third filled heat pipe.
3. The heat transfer rate and overall heat transfer coefficient increases with increasing mass flow rate of air but the effectiveness of the HPHE decreases.
4. The relation between effectiveness and NTU is linear, where the effectiveness varying from 0.08 to 0.202. The relationship can be expressed as $\epsilon = 0.8183 \text{ NTU} + 0.008$.
5. The heat exchanger is very sensitive to the dust accumulation and automatic cleaning of the heat exchanger would be necessary to get the maximum performance.

NOMENCLATURE

<i>WHRS</i>	waste heat recovery system
<i>HPHE</i>	heat pipe heat exchanger
<i>NTU</i>	number of heat transfer units
<i>HVAC</i>	heating, ventilation and air conditioning.
<i>WHRS</i>	waste heat recovery system
\dot{Q}	heat transfer rate (kW)
\dot{m}	mass flow rate (kg/h)
\dot{m}_{HA}	hot air mass flow rate (kg/h)
\dot{m}_{CA}	cold air mass flow rate (kg/h)
C_p	specific heat (kJ/(kg K))
C_{pHA}	specific heat of hot air (kJ/(kg K))
C_{pCA}	specific heat of cold air (kJ/(kg K))
T	temperature (K)
$T_{HA,in}$	inlet temperature of hot air (K)
$T_{HA,out}$	outlet temperature of hot air (K)
$T_{CA,in}$	inlet temperature of cold air (K)
$T_{CA,out}$	outlet temperature of cold air (K)
U	overall heat transfer coefficient (W/(m ² K))
A	overall heat transfer surface area (m ²)
ΔT_{lm}	logarithmic temperature difference (K)
C	heat capacity (kJ/K)
C_{HA}	heat capacity of hot air (kJ/K)
C_{CA}	heat capacity of cold air (kJ/K)
ϵ	heat exchanger effectiveness
C_{min}	Minimum heat Capacity(kJ/K)
C_{max}	Maximum Heat capacity(kJ/K)

REFERENCES

- [1] BCS, Waste Heat Recovery: Technology and Opportunities in US industry, March 2008, www1.eere.energy.gov/industry/intensive_processes/pdfs/waste_heat_recovery.pdf
- [2] A. Faghri, 1993. Temperature Regulation System for the Human Body Using Heat Pipes, US Patent 5,269,369 Issued Des. 14.
- [3] R. Brown et al., 1990. Performance evaluation of the grumman prototype space erectable radiator system, AIAA Paper No. 90-1766.
- [4] L.L. Vasilier, et al., 1990. Heat pipes for electronic equipment cooling systems, in: Proc. 7th Int. Heat Pipe Conference, Minsk, USSR.
- [5] A. Basiulis, et al., 1987. Heat pipes for cooling of high density printed wiring board, in: Proc. 6th Int. Heat Pipe Conf., Grenoble, France, pp. 685-691.
- [6] M.S. Soylemez, 2003. On the thermoeconomical optimization of heat pipe heat exchanger HPHE for waste heat recovery, *Energy Convers. Manage.*, vol. 44, pp. 2509–2517.
- [7] Hongting Ma, Lihui Yin, Xiaopeng Shen, Wenqian Lu, Yuexia Sun, Yufeng Zhang, Na Deng, 2016. Experimental study on heat pipe assisted heat exchanger used for industrial waste heat recovery, *Applied Energy*, vol. 169, pp. 177–186.
- [8] W. Srimuang, P. Amatachaya, 2012. A review of the applications of heat pipe heat exchangers for heat recovery, *Renewable and Sustainable Energy Reviews*, vol. 16, pp. 4303–431.
- [9] Abd El-Baky MA, Mohamed MM, 2007. Heat pipe heat exchanger for heat recovery in air conditioning, *Applied Thermal Engineering*, vol. 27, pp. 795–801.
- [10] Leonard L. Vasiliev, 2005. “Heat pipes in modern heat exchangers, *Applied Thermal Engineering*, vol. 25, pp. 1–19.
- [11] Hongting Maa, N. Dua, Zeyu Zhanga, Fan Lyua, Na Denga, Cong Lia. And Shaojie Yua, 2017. Assessment of the optimum operation conditions on a heat pipe heat exchanger for waste heat recovery in steel industry, *Renewable and Sustainable Energy Reviews*, vol. 79, pp. 50–60.
- [12] H. Hagens, F.L.A. Ganzevles, C.W.M. van der Geld, 2007. Air heat exchangers with long heat pipes: experiments and predictions, *Applied Thermal Engineering*, vol. 27, pp. 2426–2434.
- [13] S.H. Noie-Baghban, G.R. Majideian, 2000. Waste heat recovery using heat pipe heat exchanger (HPHE) for surgery rooms in hospitals, *Applied Thermal Engineering*, vol. 20, pp. 1271–1282.
- [14] H. Nguyen-Chi, M. Groll, Th. Dang-Van, 1979. Experimental investigation of closed two-phase thermosiphons. AIAA 14th Thermophysics Conference, Orlando, Florida, pp. 239–246.
- [15] H. Li, A. Akbarzadeh, P. Johnson, 1991. The thermal characteristics of a closed two-phase thermosiphon at low Temperature difference, *Heat Recovery Systems & CHP* 11:6, pp. 533–540.

CFD Analysis of Two-Phase (Oil-Water) Flow in Horizontal Pipe

Md. Abir Hasan*, Mohammad Ilias Inam

Department of Mechanical Engineering, Khulna University of Engineering & Technology, Khulna-9203, Bangladesh

ABSTRACT

In this paper, the behaviors of two-phase (oil-water) flow in horizontal pipe have been investigated numerically using ANSYS Fluent 16.1. For these simulations for oil-water stratified flow, Volume of Fluid (VOF) model and RNG k- ϵ turbulence model is adopted. A number of simulations have been carried out for different inlet velocity (0.5m/s, 1.0m/s, 1.5m/s, 2.0m/s, 2.5m/s and 3.0m/s) and for different volume fraction (ν_f) of oil (10%, 20%, 30%, 40%, 50%, 60%, 70%, 80% and 90%). Numerical results demonstrate that pressure drop (ΔP) and wall shear stress (σ), both, are increasing with respect to inlet velocity and volume fraction of oil. A series of empirical relations were also developed to show the effect of inlet velocity and volume fraction of oil on the pressure drop and wall shear stress.

Keywords: CFD Simulation, VOF model, Two-phase flow, Oil-water, Pipe flow.

1. Introduction

Analysis of immiscible liquid-liquid two-phase flow in pipes has been a subject of intense research for several decades due to its fundamental significance as well as much related industrial application, especially in the petroleum and process industries. Though liquid-liquid flow systems play very significant roles in the petroleum and other industries, however very less attention has given as compared to the gas-liquid flow systems. Now-a-days, liquid-liquid flow systems have attracted more and more interest in the offshore oil industry. Typically immiscible liquid-liquid two-phase, i.e. oil-water, flow occurs in the co-current manner of in petroleum products transportation since oil and water are mostly produced at the same time. The transportation of crude oil is very important in the offshore facilities, where the oil is transported using pipelines to the processing facility.

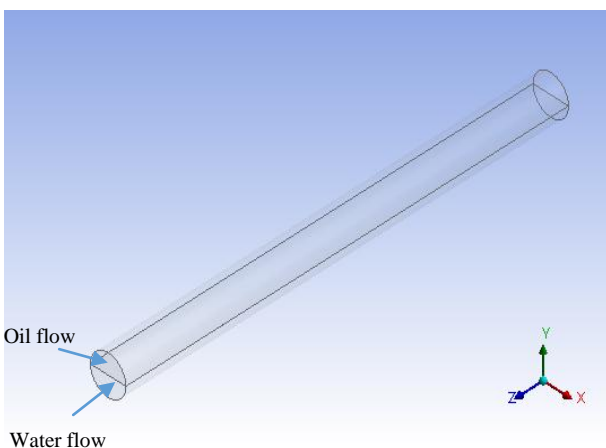


Figure 1.1: Oil Water two phase flow in horizontal pipe.

The water present in the crude oil significantly affects the transportation of petroleum oil from the well to an onshore platform [1]. The oil transportation pipes lie on

the seabed in either horizontal or inclined way. During the transportation process, the variation in water or oil volume fraction in the pipes can have a significant influence on pumping power required to pump the fluid, due to the change in the pressure drop across the pipeline. The presence of water in the pipe has a significant effect on the transportation of mixture of oil and water from the reservoir to the onshore or processing platform since the behavior of liquid two-phase flow in tubes behaves differently from single-phase flow [2]. For variable mixture velocities and the water volume fraction, the fluid might have different flow regimes in the pipe, which might influence the input power requirement during the pumping of the mixture.

2. Literature Review

Lots of works have been carried on water and oil two-phase flow in straight horizontal pipes in last two decades. Angeli *et al.* (1998) experimentally studied the pressure gradients for the co-current flow of low viscosity oil-water in horizontal pipes ($D = 0.0254$ m), made of stainless steel and acrylic resin, for different velocities and water volume fractions. It was found that at high Reynolds number, where dispersed flow patterns occur, there was a peak in pressure gradient during phase inversion and an apparent drag reduction affect when oil is the continuous phase [3]. Gao *et al.* (2003) numerically studied the pressure drop, liquid holdup, the axial velocity, and slippage, for the oil-water two-phase flow in the straight horizontal pipe and also verified with experimental data in the literature. Stratified water oil oil-water flow in a straight horizontal pipe is simulated numerically with VOF model. The simulation is done in a time-dependent way and the final solution which relates to steady-state flow is studied [4]. Elseth *et al.* (2001) experimentally study the behavior of flow of oil-water in the horizontal straight pipe ($D = 0.0508$ m). Pressure drops, slip ratio, velocity profiles, turbulence distributions and liquid holdup are measured

* Corresponding author. Tel.: +88-01761919895
E-mail addresses: abir.hasan.kuetme@gmail.com

for a various number of flow-conditions. A typical flow parameters measuring instrument laser Doppler anemometer (LDA) is used and applied as a transparent part of test pipe. Stratified and dispersed types of flow are observed [5]. Walvekar *et al.* (2009) have been studied volume phase fraction profiles and average in-situ phase fraction on the 3D flow of liquid-liquid immiscible fluids in a horizontal pipe using computational fluid dynamics models. The unsteady state numerical simulations of liquid-liquid two-phase dispersed type flow in a pipe of inner diameter is equal to 0.0024 m have been done using commercial Computation fluid dynamics software FLUENT with the multiphase model. Oil–water system is selected as the two-phase system in this work. The $k-\epsilon$ viscosity model was implemented to explain the turbulence characteristics in the continuous phase [6]. Al-Wahaibi *et al.* (2012) pressure drop per unit length correlation for straight horizontal oil-water separated flow (stratified and dual continuous flows) was reported based on the experimental work of Angeli and Hewitt (1998). Zigrang and Sylvester friction factor correlation were changed and modified for oil-water multiphase flow. The pressure gradient equation was validated with the experimental pressure gradient results. This is the first pressure drop/gradient work that published for oil-water flow which includes a good range of working conditions, fluid properties, pipe diameters and materials. The proposed equation predicts the pressure drop per unit length with larger accuracy than the two-fluid model [7].

3. Methodology

ANSYS Fluent 16.1 is used for these simulations, which is most widely used simulation software. For these simulations Volume of Fluid (VOF) model and RNG $k-\epsilon$ turbulence model is adopted. These simulations were conducted in 3-D. It was assumed for these simulations that temperature remains constant (means no Energy equation) and all physical properties also remain constant. The Navier-Stokes equations and the Continuity equation are the main governing equations.

The geometry has been created creating by ANSYS Design module, shown in Figure 1.1. The length of the pipe is 500mm and diameter is 40mm. For using volume fraction here used slice tool for parting the inlet region. Mesh generation have been done in Meshing Module. For mesh dependency test, different types of mesh have been created by changing element size from $2.5081e-004$ meter to $5.0162e-002$ meter. To create fine mesh near the wall, Inflation option is selected to smooth transition and transition ratio is 0.272. A maximum layer of inflation is 5. And growth rate is 1.2. For doing precision result face sizing and inflation were done in the inlet and outlet of the pipe. Maximum thickness for inflation is $2e-003$ and element size for face sizing is taken $1e-003$. Body sizing is also done in the whole pipe. After using all that features, number of nodes varies from 19684 to 190627.

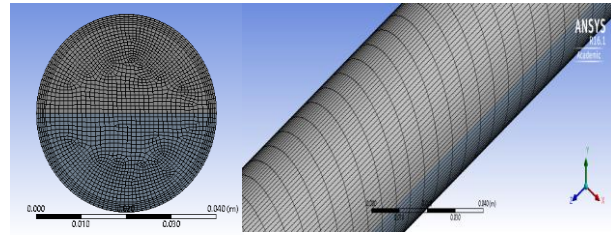


Figure 3.1: Generated mesh in outlet and wall.

The properties water and oil are shown in Table 3.1.

Table 3.1: The properties water and oil.

Property	Water	Oil(Crude oil)
Density(kg/m^3)	998.2	780
Dynamic viscosity(Pa.s)	0.001003	0.00157
Interfacial tension(N/m)	0.17	0.17

Solver settings for these numerical analysis is listed in Table 3.2.

Table 3.2: Solver setting for these numerical analysis.

Items	Inputs
CFD Simulation	3-D Double precision
Solver	Pressure-Based
Time	Steady
Gravity	9.81 m/s^2
Modeling	Multiphase(VOF)
Turbulence model	$k-\epsilon$ (2 equation)
$k-\epsilon$ model	Standard
Near-Wall Treatment	Standard Wall Function
Material type	Oil, Water
Turbulent Intensity	5%
Turbulent Viscosity	10%

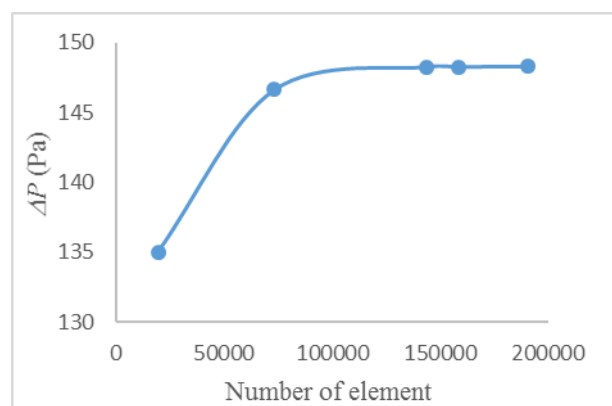


Figure 3.2: Pressure drop vs number of element for 50%-50% oil-water at constant velocity of 1m/s.

A series of numerical simulations for different meshes with varying nodes have been conducted for the mesh independency test. Figure 3.2 depicts the variation of pressure drop (ΔP) for different mesh with different number of elements, which varies from 19684 to 190627. And here the two contours 158316 and 190627 are looks like same. It is clearly observed from figure that numerical results for meshes with nodes 158316 and 190627 have almost identical values. This indicates that mesh with 190627 nodes can generate more accurate result. As a result, following simulations were conducted with this mesh to confirm the numerical results are meshes independent.

4. Results and Discussion

4.1 Effect of velocity on pressure drop and wall shear stress

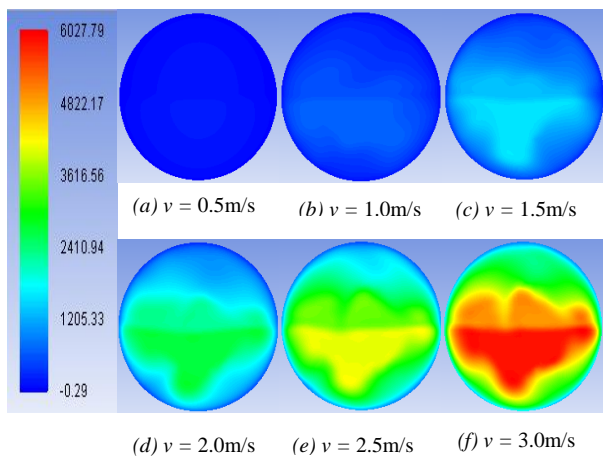


Figure 4.1: Pressure contour at outlet for 50%-50% oil-water two phase flow at different flow velocity.

Figure 4.1 depicts pressure contours at outlet for different inlet velocities (varies from 0.5m/s to 3.0m/s) at 50%-50% oil-water. It is observed that pressure intensity at outlet is increasing from lower velocity to higher velocity.

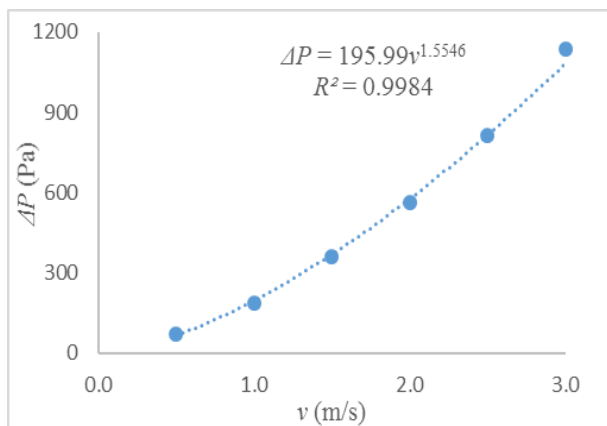


Figure 4.2 Variation of Pressure drop respect to velocity for 50%-50% oil water.

Figure 4.2 shows that the variations of pressure drop respect to inlet velocities. It is observed from Figure 4.2

that Pressure drop varies non-linearly respect to velocity, according to the following equation:

$$\Delta P = 195.99 v^{1.5546} \dots\dots\dots (1)$$

The value of R^2 , is equal to 0.9984, indicates that the numerical result follows a very approximation according to the equation (1).

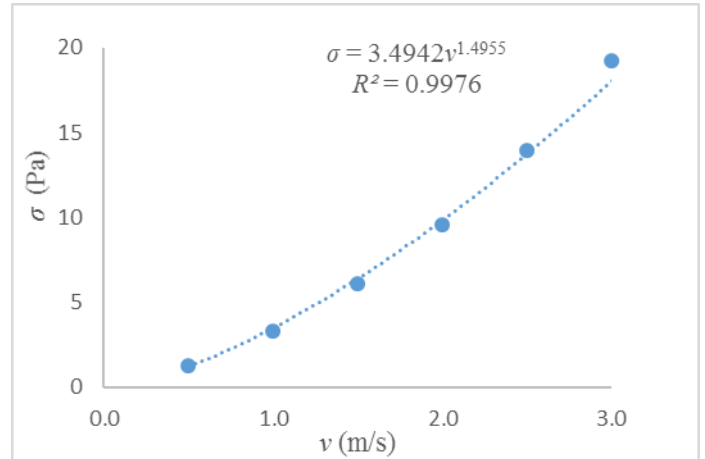


Figure 4.3: The Wall shear stress variation respect velocity for 50%-50% oil water.

Figure 4.3 depicts that the wall shear stress variation respect to inlet velocities. It is observe from Figure 4.3 that wall shear stress increase non-linearly respect to velocity, which follows like as the following equation:

$$\sigma = 3.4942v^{1.4955} \dots\dots\dots (2)$$

The value of R^2 is equal to 0.9976 also indicate very good curve fitting.

4.2 Effect of volume fraction on pressure drop and wall shear stress

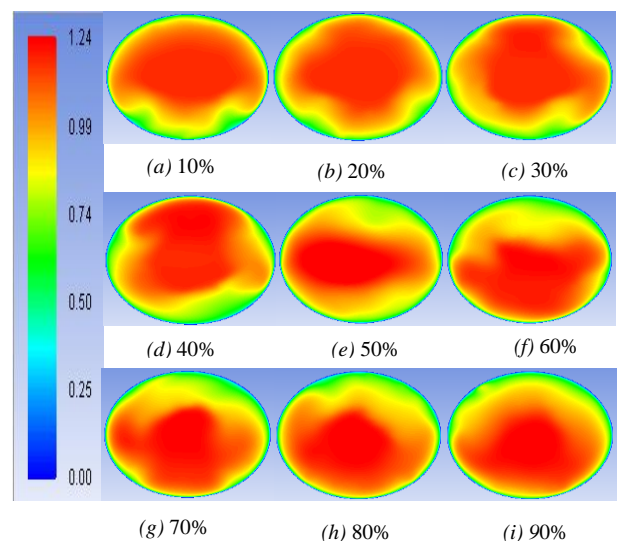


Figure 4.4 Velocity contour at outlet for different volume fraction of oil constant flow velocity of 1m/s.

Figure 4.4 shows that the velocity contour at outlet for different volume fraction of oil like 10%, 20%, 30%, 40%, 50%, 60%, 70%, 80% and 90% for inlet velocity 1 m/s. It is observed from figure that maximum velocity region, indicate by red color, and translate from upper region to lower region by increasing volume fraction of oil.

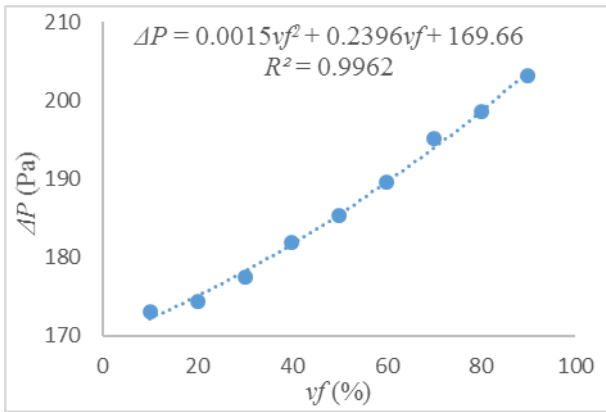


Figure 4.5: Pressure drop vs Volume fraction of oil at velocity 1m/s.

In Figure 4.5, pressure drop is plotted for different volume fraction of oil. It is observed from the figure that pressure drop increase non-linearly with volume fraction of oil, like as the following equation

$$\Delta P = 0.0015vf^2 + 0.2396vf + 169.66 \dots\dots\dots (3)$$

And the value of R^2 is 0.9962.

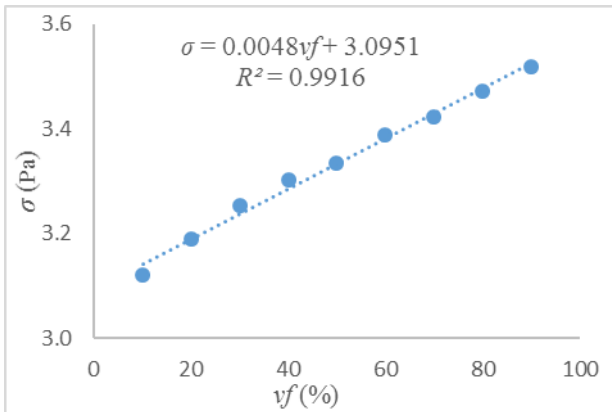


Figure 4.6: Wall shear stress vs Volume fraction of oil at velocity 1m/s.

In Figure 4.6, wall shear stress is plotted for different volume fraction of oil. It is observed from figure that wall shear stress increase linearly respect to volume fraction of oil. In here it is maintained a linear equation like

$$\sigma = 0.0048vf + 3.0951 \dots\dots\dots (4)$$

And the value of R^2 is 0.9916.

5. Conclusion

In the present work oil-water two phase flow in horizontal pipe was numerically simulated using commercially software ANSYS Fluent 16.1. Numerical results shows that the pressure drop and wall shear stress, both, increase with respect to inlet velocity and volume fraction of oil.

NOMENCLATURE

- P_i : Inlet Pressure
- P_o : Outlet Pressure
- ΔP : Pressure Drop
- σ : Wall shear Stress
- μ : Viscosity
- v : Velocity
- ρ : Density
- L : Length
- D : Diameter
- vf : Volume Fraction of Oil

REFERENCES

- [1] Al-Yaari, Abu-Sharkh, F., 2005. CFD prediction of stratified oil-water flow in a horizontal pipe. Asian Trans. Eng. 1 (5), 155-162
- [2] Beggs, H.D., Brill, J.P., 1973. A study of two-phase flow in inclined pipes. J. of Petroleum Technol. 607-617.
- [3] Angeli, P., Hewitt, G.F., 1998. Pressure gradient in horizontal liquid-liquid flows. Int J.of Multiphase Flow 24(7), 1183-1203.
- [4] Hui Gao, Han-Yang Gu, Lie-Jin Guo, 2003. Numerical study of stratified oil-water two-phase turbulent flow in a horizontal tube. Int. J. of Heat and Mass Transfer, 46, 749-754.
- [5] Geir Elseth, 2001. An experimental study of oil / water flow in horizontal pipe. Doctoralthesis, Department of Technology (HiT-TF) Telemark University College Kjolnes Ring, N-3914 Porsgrunn Norway.
- [6] Walvekar R, 2009. Numerical study of dispersed oil-water turbulent flow in horizontal tube. J. of Petroleum Science and Eng. 65, 123-128
- [7] Yusuf N., Al-Wahaibi Y., Al-Wahaibi T., Al-Ajmi, A.S. Olawale, I.A. Mohammed, 2012. Effect of oil viscosity on the flow structure and pressure gradient in horizontal oil-water flow. Chemical Engineering Research and design 90 1019-1030.

Development of Surface Mounted concentrator for Photovoltaic solar cell

Md Anwar Hossain^{1*}, YiHong Zhang^{1,2}

¹College of Information Science & Technology, Donghua University, Shanghai, P. R. China

²State key University, Ministry of Education, P. R. China

ABSTRACT

This paper will provide a design of Surface Mounted concentrated photovoltaic (SMCPV) at low cost. First work on finding the best and suitable concentrator that can increase the efficiency of PV cell near about 20% of its traditional efficiency. At the accurate combination point of concentrator and PV cell, the focus point is set behind the PV cell. As the distance between concentrator and PV cell is X , the focus of concentrator is $4X$ to ensure close contact between concentrator and PV cell and prevent from burning cell sections. To ensure the targeted result, the optical modeling of this system and performance analysis through experimental tests has done. The experimental validation allows concluding that, high accurately controlled application of SMCPV is very important since the big density of the solar radiation leads to important losses of system efficiency or system failure. On the other hand, it is found that the external factors can affect the final results which include the optical and geometrical properties of the concentrators, the absorptivity as well as the weather conditions (especially the wind speed and clouds). Thus, the paper aims to present the advantages and benefits of this technology.

Keywords: Renewable Energy Resources, Solar Concentrator, Surface Mounted Solar Concentrator, Improved Solar Cell.

1. INTRODUCTION

The photovoltaic industry is growing rapidly today. Even though photovoltaic (PV) technology offers great potential in terms of supplying the world's energy needs, its current contribution to the world is still limited. The main factor is related to the high initial cost of building the system. However solar energy is one of the most economic and freely available energy sources in today's world [1-2].

The development of photovoltaic (PV) concentrator innovation started adequately in 1976 at national Sandia laboratories. This early work was the first line of solution related to solar cell and concentration system. Utilizing optics such as mirror or lenses to concentrate sunlight radiation is the basic purpose of Photovoltaic (PV) concentrator [3].

Now days, the use of cost-efficient concentrating optics that severally diminish the cell area is the standard of concentration photovoltaic (CPV), taking into consideration the utilization of more cost efficiency, high-efficiency cells and possibly a leveled cost of electricity competitive with concentrated solar oriented power and standard flat-plate photovoltaic (PV) technology in certain sunny zones with high direct normal irradiance (DNI) [4].

For SMCPV systems to be cost-effective, the complete cost of the optics, assembly and mechanical tracking must not exceed the cost savings gained from using small area PV cells. Solar ray tracing programs was used to find new types of solar lens concentrator to save the cost by reducing the area of PV cells [5].

For many years in the field of the concentrator, the Fresnel lens is being used. Despite the simplicity and uniform illumination on a cell of this concept, due to its

low acceptance concentration product, their application is still a big challenge to low concentrations.

For traditional Fresnel concentrator, however, the proposed model for the focal length of SMCPVs will be enlarged with the geometric concentration [6]. Such a module will also be of interest when solar energy utilization is in higher demand. To date, such an SMCPV module has not yet been experimentally demonstrated. In this study, we proposed this concept using a prototype Fresnel lens based SMCPV module with an additional low-cost solar cell.

2. CONCENTRATOR GEOMETRY

The concentration ratio is used to describe the intensity of energy concentration achieved by a given collector.

The geometrical concentration ratio (CR_g) of a solar concentrator over a typical absorber surface is calculated as the ratio of the entrance aperture area (A_a) to that area of the absorber (A_r) which is capable of collecting all the radiation reflected from the concentrator and which takes part in the emission of thermal radiation at the absorber temperature [7].

$$CR_g = \frac{A_a}{A_r} \quad (1)$$

The aberration-free solar image height was calculated using $2f \tan \theta$ where f is the lens focal length and θ is the acceptance half-angle. Lens element has its own two-dimensional geometric concentration defined by, [8].

$$C_{lens} = \frac{1}{(2f \tan \theta)^2} \quad (2)$$

The lens aperture to image area is expressed in terms of the lens focal length to diameter ratio, or F-number, and acceptance half-angle.

2. 1 CONCENTRATOR APERTURES and COMPARISON

A ray tracing software for Complex Solar Optical Systems, ‘SolTrace’ was used to design and optimize the efficiency of the optic concentrator [9]. The analysis simulated circular, triangular, rectangular, hexagonal aperture lenses forming a focus on a slab of the PV. Ray intersection for each aperture with flat, parabolic and spherical surfaces was examined with direct normal irradiance (DNI) of 1000. Encircled energy, illumination distribution on the PV cell was included in optical efficiency calculations [10].

Table 1 Baseline parameters for the comparison study.

Sun Parameter	Target Parameter
Buie Sunshine	Lens facing north (no tilt)
Day 80 at solar noon	Size: 8x5 mm
Latitude 34.96	Aperture: Circular, Triangle, Rectangular, and Hexagonal
Insulation 1000 k-m ² /w	

Table 2 Simulation runs with “Soltrace”.

Parameters/ Aperture	Circular	Triangular	Rectangular	Hexagonal
DNI	1000	1000	1000	1000
Sun ray count	32077	33561	32019	39090
Power per ray (W)	1.247	0.52797	1.60704	1.02328
Number of plotted rays	20000	20000	20000	20000
Power of plotted rays (W)	12470	10559.5	32140.8	20465.6
Peak flux	3212.27	1429.75	4184.73	2586.85
Average flux	124.7	52.7973	160.704	102.328

Table 3 Specification of the test for SMCPV system.

Parameters	Value
Irradiation power source	Buie Sunshine
Irradiance (DNI)	1000
Solar cell	monocrystalline Si solar cell
Cell efficiency	18.13% at (STC)
Open-circuit voltage (Voc)	10.8V
Short-circuit current (Isc)	0.98 A (at 1000W/m2)
Module size	290 cm×190cm

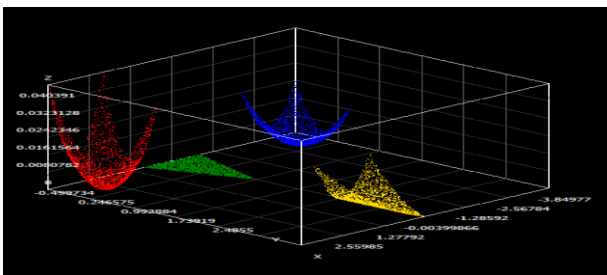


Fig.1 Ray intersection for triangular aperture with flat, parabolic and spherical surfaces

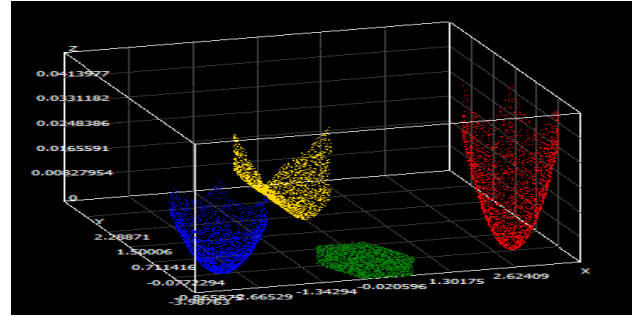


Fig.2 Ray intersection for hexagonal aperture with flat, parabolic and spherical surfaces

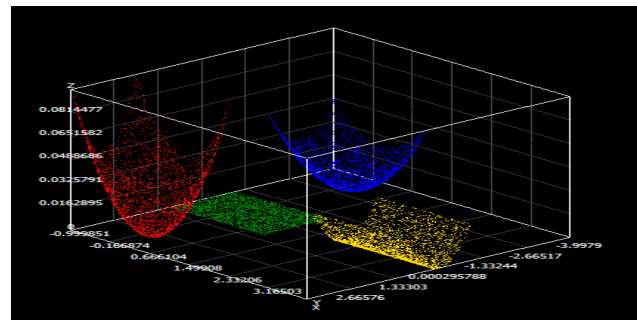


Fig.3 Ray intersection for rectangular aperture with flat, parabolic and spherical surfaces

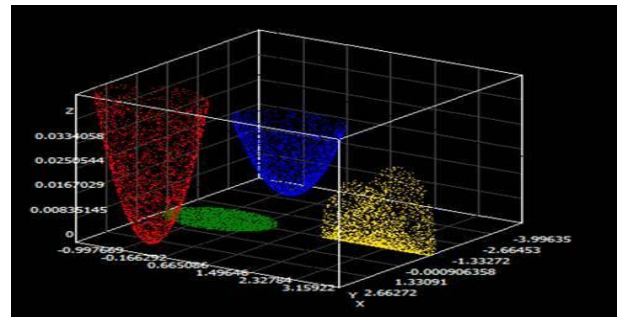


Fig.4 Ray intersection for circular aperture with flat, parabolic and spherical surfaces

3. PROPOSED SMCPV MODEL

The SMCPV optics constitute a typical design problem that contains both the bundle coupling problem for obtaining maximum acceptance-concentration product and the prescribed irradiance to obtain uniform irradiance distribution on the solar cell area [11]. The solar cell is adhered at the bottom of the lens directly, making it simple to seal against moisture and prevent misalignment. Figure 5 shows the cross-sectional sketch of this compound Fresnel-R concentrator for SMCPV system. The design method includes two parts: design of Fresnel lens with the close setup of base photovoltaic (PV) cell and design of secondary or extended PV cells of SMCPV system. This design also includes two parts: design of the outer saw teeth of Fresnel lens that work by total internal reflection and design of the inner saw teeth that work by refraction.

3.1. PROPOSED MODEL DESIGN

A crystalline silicon solar cell with an extended rectangular module also might be installed onto a Fresnel-lens SMCPV module. In this configuration, incident direct solar radiation is concentrated by the Fresnel lens onto direct contact solar cell module. The Si solar cell does not capture total radiation of the concentrating rays. Incident diffuse and reflected solar radiation through the Fresnel lens is then captured by the extended Si solar cell. The Si solar cell was encapsulated by EVA with a glass cover. With both base PV cell module and extended PV cell module in order to keep them safe from heat damage heatsink is being used.

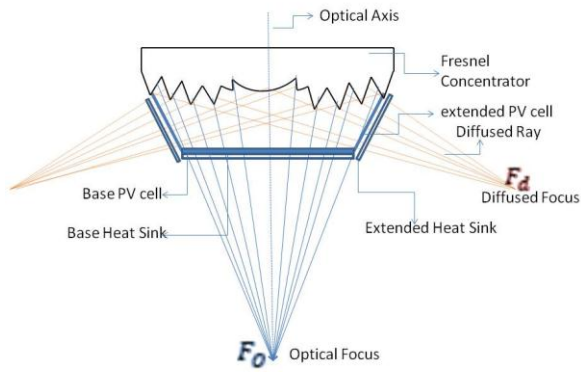


Fig.5 Compound Fresnel-R concentrator for SMCPV system.

The proposed system shows the optical configurations of an SMCPV module for harvesting diffuse solar radiation through an additional low-cost cell, as described in a patent document [12]. To overcome Optical aberration photovoltaic (PV) cell should set as close as possible. The geometrical concentration ratio for the low-cost cell should be close to unity in order to fully capture diffuse radiation and for maximum acceptance angle. For a given acceptance angle θ , for a point-focus concentrator, the maximum concentration possible, C_{max} is given by,

$$C_{max} = \frac{n^2}{\sin \theta} \quad (3)$$

Where n is the refractive index of the medium in which the receiver is immersed [13]. In practice, real concentrators either have a lower than ideal concentration for a given acceptance or they have a lower than ideal acceptance angle for a given concentration. This can be summarized in the expression $CAP = \sqrt{C} \sin \theta \leq n$ (4)

This defines a quantity concentration acceptance product (CAP), which must be smaller than the refractive index of the medium in which the receiver is immersed. The Concentration Acceptance Product is a consequence of the conservation of etendue. The higher the CAP, the closer the concentrator is to the maximum possible in concentration and acceptance angle [14].

Test modules based on Fresnel lenses are easily fabricated by installing an additional low-cost cell. Although the proposed module in this study is a single-lens module, a practical multiple-lens-array module could in principle be constructed according to the schematic.

3.2 PROPOSED SMCPV SYSTEM EXPERIMENT

To verify the effectiveness of the SMCPV system proposed in this study, a power-measurement test was performed using a non-commercial Fresnel lens. Table 3 lists the specifications of the test used in this study. The test consists of a polycrystalline Si solar cell with a conversion efficiency of 20%, a sunny day with an illumination intensity of $1,388 \text{ W/m}^2$ was an irradiation source. For current - voltage measurement, a Keithly-616 digital electrometer, Tektronics CDM 250 multimeter and a dual Farnel LT30/2 (-3 to 3) V power supply were used. We measured Open circuit voltage V_{OC} and short circuit current I_{SC} to calculate the fill factor (FF) and the efficiency ($\eta\%$) of the proposed SMCPV model using the relations [15].

$$FF = \frac{I_m V_m}{I_{sc} V_{oc}} \quad (5)$$

$$P_{max} = I_{sc} V_{oc} FF \quad (6)$$

$$\eta = \frac{FF I_{sc} V_{oc}}{P_{in}} \% \quad (7)$$

Where V_m is maximum voltage and I_m is maximum current, and P_{max} represents the maximum power output of the solar cell. The current voltage characteristics for the PV were measured with and without concentrator by using the electric circuit shown in Figure-6.

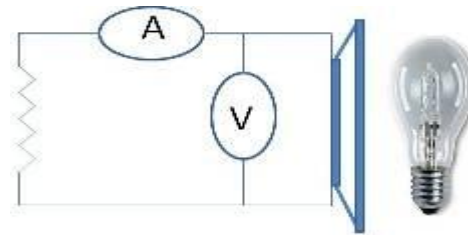


Fig.6 Electrical diagram represent I-V characteristic measurements circuit.

4. RESULTS and DISCUSSION

The analysis of concentrators for solar power has been investigated using simulation software 'Soltrace' along with theoretical studies. The analysis is done for four different types of apertures and three different types of surfaces. It has been found that; concentrator is a most important role for any CPV system.

Proposed SMCPV system is a most effective system for tradition photovoltaic solar cell for general use. And some test has been done using the best aperture for Fresnel lens for proposed SMCPV model.

Analyzing test data shows the improvement of the efficiency of the solar cell system.

4.1 Concentrator lens aperture

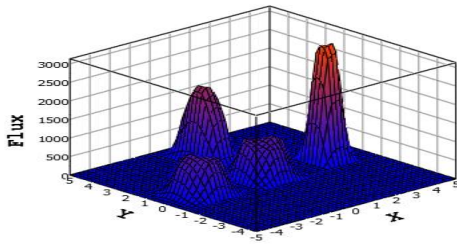


Fig.7 Surface plot of the flux density of circular aperture

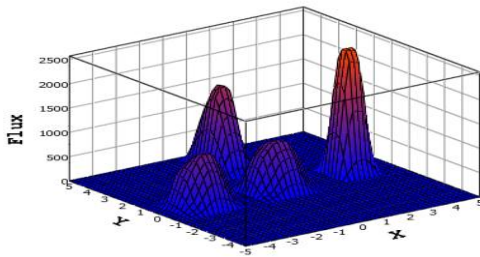


Fig.8 Surface plot of the flux density of hexagonal aperture

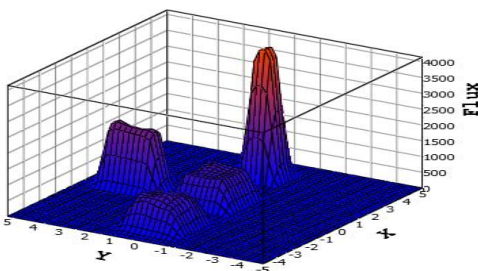


Fig.9 Surface plot of the flux density of rectangular aperture

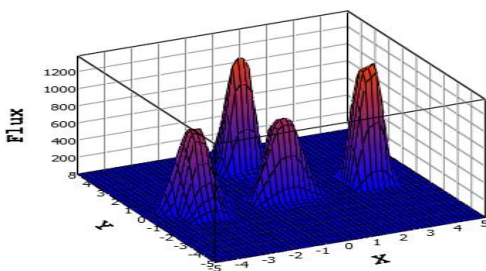


Fig.10 Surface plot of the flux density of triangular aperture

Table 4 Investigated the flux density of the concentrator.

Aperture	Most Flux density
Circular	3200
Triangular	1350
Rectangular	4050
Hexagonal	2600

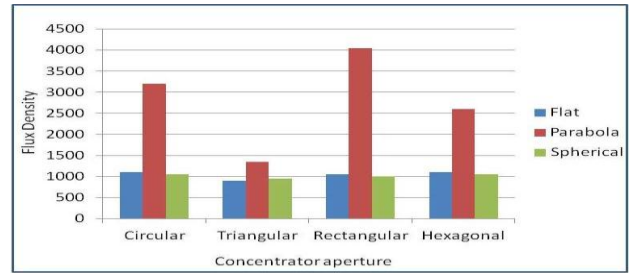


Fig.11 Comparison study for different aperture with different surface

The concentrator lens is approximated in SolTrace using 4 aperture and three types of surfaces (flat, parabolic, spherical) total 12 types of surfaces since SolTrace can only plot flux maps for surfaces and cylinders, but not spheres. Figure 7-10 shows examined flux maps of these surfaces. Figure 11 is representing the comparison of different types of concentrator aperture with a different surface. In SolTrace, specular errors in the range of 0 to 15 mrad are investigated and slope errors in the range of 0 to 15 mrad are considered, to determine the effect on the performance of the receiver. According to SolTrace, this is an optical error range of 0 to 33.5 mrad.

A tracking error range of 0° to 3° is also considered. The concentrator surface is modeled with a reflectivity of 85%. A direct normal irradiance of 1000 W/m² and a pillbox sun shape are assumed in the analysis. The optimized receiver using entropy generation minimization has concentrator diameter of 5x8 mm. This receiver geometry was investigated in SolTrace. Examined data is shown in Table 4. Analyzing these data indicates rectangular aperture the best concentrator.

4.2 PROPOSED SMCPV MODEL TEST

The FF is the parameter which, in conjunction with V_{OC} and I_{SC} , determines the P_{max} from a PV solar cell (equation 5). Since I_{SC} , V_{OC} and FF are used directly in characterizing the performance of the PV modules and are defined as equation 6, improvement of output power i.e. P_{max} of a PV module is depended on the improvement of I_{SC} , V_{OC} and FF. Data comparing include and exclude of concentrator indicates the improvement of I_{SC} , V_{OC} , FF, maximum output power P_{max} , and the efficiency (η) by significant amount (table-5). There is $\Delta\eta = 26.61\%$ improvement in the efficiency of SMCPV with concentrator (here the efficiency (η) is calculated by equation 7). By analyzing data's of table 5, we conclude that there is an improvement in PV module by using the proposed system. Another way is, it is also reduction of cost, by reducing the high cost of Si material, proposed SMCPV can be used for traditional household appliances. Figure 12 represents the current-voltage characteristics curve of PV cell without and with the new concentrators. This figure shows the improvement in solar cell performance.

Table 5 Performance parameters for PV cell without and with a concentrator (930 DNI).

Parameters	Without concentrator	With Concentrator	Improvement %
Isc in A	0.98	1.23	25.55
Voc in V	10.80	11.10	2.8
Pmax in W	8.012	10.144	26.61
FF	0.757	0.743	
$\eta\%$	18.13	21.63	17.81

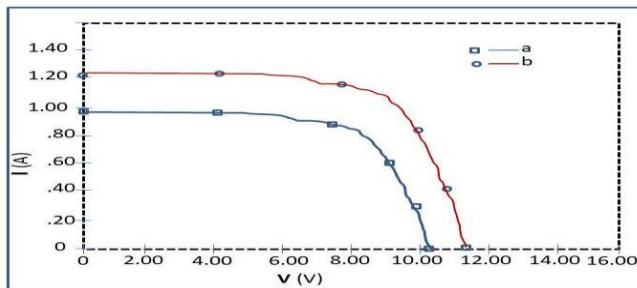


Fig.12 The current-voltage characteristics for PV Si cell without (a) and with (b) Fresnel lens.

CONCLUSION

The optical properties of used Fresnel lens were measured using simulation software “Soltrace”. The Fresnel lens was used practically to concentrate sunlight components on the solar cell. The electrical output parameters of the used solar cell were measured practically where the used Fresnel lens was found to increase the electrical output power from the solar cell which was related to the action of used Fresnel lens and properties of the used solar cell. An increase in the output power is observed about 29.01% of total output. The proposed SMCPV system is designed for direct normal irradiance, diffused light and reflected light from base PV cell. Focus length is set behind the solar PV cell to mount the concentrator on the base PV cell and the improved characteristic with concentrator was found. Our future work will include the cost analysis of the proposed model. Our primary focus will be on details electrical parameter experiment of SMCPV.

ACKNOWLEDGMENT

The authors gratefully acknowledge the constant encouragement of administration of Donghua University, and very good research environment. Thanks to supervisor for inspirational supervision. This work is supported by the Fundamental Research Funding for the Central Universities of Ministry of Education of China, Project Number: [18D110408] and the Special Project Funding for the Shanghai Municipal Commission of Economy and Information Civil-Military Inoculation Project “Big Data Management System of UAVs”, Project Number: [JMRH-2018-1042].

REFERENCES

[1] Nowak S, the IEA PVPS Programme: Towards Sustainable Global Deployment of PV“.

Proceedings 20th European Photovoltaic Solar Energy Conference, June 6-10, 2005, Barcelona, Spain. Volume III of 3, pp. 2827.

- [2] R. Singh, and Y.R. Sood, “Transmission tariff for restructured Indian power sector with special consideration to the promotion of renewable energy sources”, *The IEEE Conference TENCON-2009*, pp. 1-7, 2009.
- [3] Reis A.M., Coleman N.T., Marshall M.W., Lehman P.A. Comparison of PV Module Performance before and after 11-Years of Field Exposure, *The Proceedings of the 29th IEEE Photovoltaics Specialists Conference, New Orleans, Louisiana* May, 2002.
- [4] Mehrdad khamooshi, hanasalati, fuategelioglu, alihooshy arfaghiri, judytarabishi, and saeedbabadi," a review of solar photovoltaic concentrators", *international journal of photo energy*, 2014, pp: 17.
- [5] Al-Hamdani, Ali H., Al-Ani S.K. and Blawa B.D. Performance of two - stages solar concentrator. *Journal of Um-Salama for science.* 1(2): 317-320.
- [6] R. Leutz and A. Suzuki, *Nonimaging Fresnel Lenses: Design and Performance of Solar Concentrators*, Springer Series in Optical Sciences, Springer, New York, NY, USA, 2001.
- [7] Jason H. Karp, Eric J. Tremblay and Joseph E. Ford. 2010. Planar micro-optic solar concentrator. *Optics express.* 18(2): 1122-1133.
- [8] Rabl A. *Active solar collectors and their applications.* Oxford university press, New York, USA.1985.
- [9] Tim Wendelin and Aron Dobos. October 2013. SolTrace: A Ray-Tracing Code for Complex Solar Optical systems. *Technical Report. NREL/TP-5500-59163. Prepared under Task No. ST11.3070.*
- [10] M. Thirugn anasam bandam, S. Iniyan, and R. Goic, “A review of solar thermal technologies,” *Renewable and Sustainable Energy Reviews*, vol. 14, no. 1, pp. 312–322, 2010
- [11] Garcia, P., Ferriere, A., and Bezian, J-J, “Codes for solar flux calculation dedicated to central receiver system applications: A comparative review,” *Solar Energy* 82(3), 189-197 (2013).
- [12] L. W. James, “Use of refractive secondaries in photovoltaic concentrators,” *Tech. Rep. SAND89-7029, Sandia National Laboratories, Albuquerque, NM, USA*, 1989.
- [13] P. Benitez, J. C. Minano, and R. Alvarez, Photovoltaic concentrator with auxiliary cells collecting diffuse radiation, *US patent application publication, Pub. No.: US 2010/0126556 A1* (2010).
- [14] Chaves, Julio (2015). Introduction to Non-imaging Optics, Second Edition. *CRC Press.* ISBN 978-1482206739.
- [15] Tuzun S.O. Altindal and T. S. Mammadov. 2006. Electrical characterization of novel Si solar cells. *Thin Solid Films.* 511-512, pp. 258-264.

Reduction of Chatter in Turning by Using A Tool Holder with High Damping Coefficient

A H M Shahjahan*, Amin Hasan Khan, Jannatun Naeema and A.K.M. Nurul Amin

Department of Mechanical and Production Engineering, Ahsanullah University of Science and Technology, Dhaka
BANGLADESH

ABSTRACT

Machining of metals is generally accompanied by an intense relative vibration between tool and work, known as chatter. Chatter is unwanted because of its many adverse effects during machining. This paper presents a new method of chatter suppression during turning operation of stainless steel - AISI 201 using tool holders with high damping coefficient. Turning operation of the given work material was conducted using a medium carbon steel tool holder along with two fabricated tool holders made of two types of gray cast iron. Response Surface Methodology (RSM) was used for the design of this experiment. Simulations of total deformation, modal and harmonic response analyses of the tool holders were conducted using ANSYS. Fast Fourier Transform (FFT) was later used to transform the vibration data to a function in frequency domain. The experiments focused on monitoring the surface roughness, sound level and analysis of chips formed during metal cutting. It was observed that both the gray cast iron tool holders contributed to reduction of chatter amplitudes but the annealed gray cast iron tool holder contributed most to the improvement of surface finish and reduction of noise level.

Keywords: Chatter, Gray Cast Iron, Stainless steel, Surface roughness, Sound Level.

1. Introduction

Chatter is an unusual tool behavior and is one of the most critical problems in machining processes. Chatter is unwanted because of its adverse effects on machining accuracy, product quality, operation cost, tool life, and productivity. It must be avoided in order to improve the dimensional accuracy and surface quality of the product [1]. Chatter phenomenon was first observed by Taylor [2] during metal cutting. He stated that element chip formation is responsible for chatter. Wiercigroch et al. [3] stated that the mode coupling resulted when the vibration in the thrust force direction generated oscillations in the thrust and cutting force directions. Tobias et al. [4] mentioned about the regenerative effect which occurs with single-edged tools, such as lathe tools, when the cutting edge of the tool traverses a wavy surface on the work generated by the previous cut. Experimental works of Eliasberg [5] and Amin [6] showed some contradiction with the regenerative chatter theory. Patwari et al. [7] found that the root cause of chatter was in the coincidence of the frequency of the instability of chip formation with one of the natural mode frequencies of the machine-spindle-tool system during end milling operations. Several researchers have tried to address the chatter phenomenon. In this study, the influence of tool holders with high damping coefficient in suppressing chatter in turning operations on stainless steel - AISI 201 using coated WC-Co insert was investigated. It has been observed that tool holders with high damping coefficient did reduce the chatter vibration and improve the surface finish.

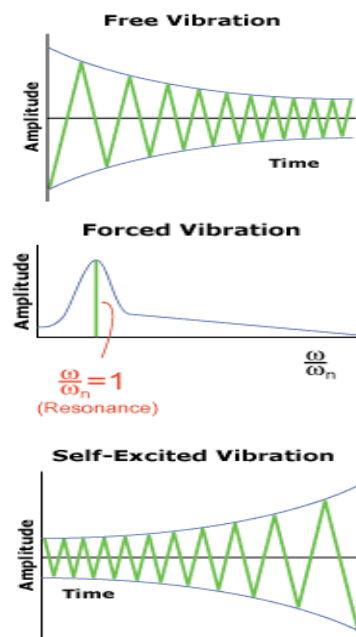


Fig. 1 Types of chatter vibration

2. Experimental Details

Experimental machining was conducted on Engine Lathe Machine, model: CS6266B powered by a 7.5KW motor with a maximum spindle speed of 1600 rpm. Machining was done using three tool holders having different materials and properties i.e. carbon steel, pearlitic gray cast iron and annealed gray cast iron. Both the gray cast iron tool holders were fabricated from pearlitic gray iron. One of them was later annealed using a furnace. Fig.2 displays schematic diagram of temperature distribution for annealing process of the gray cast iron tool holder.

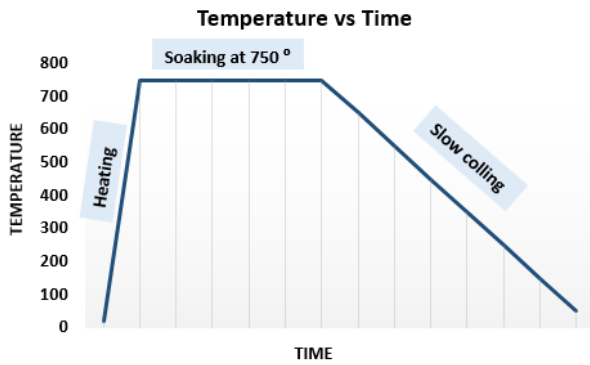


Fig. 2 Temperature vs. time curve in the annealing process of the gray cast iron tool holder

The specimen has been heated for about 2 hours at 750⁰ C and then it was slowly cooled to the room temperature. Fig.3 shows the tool holder inside the furnace at 750⁰ C

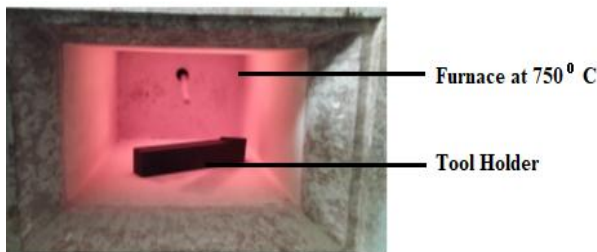


Fig. 3 Gray cast iron tool holder inside the furnace

There were 45 machining runs and these were taken using six coated WC-Co inserts (dimension 1.2mm X 1.2mm). Each cutting edge was used for two consecutive runs. A microphone was used for monitoring the vibrations, which was later investigated using Fast Fourier transformation. A sound level meter was also used for further verification of the accuracy of this method. Fig.2 displays the schematic diagram and photograph of the experimental setup.

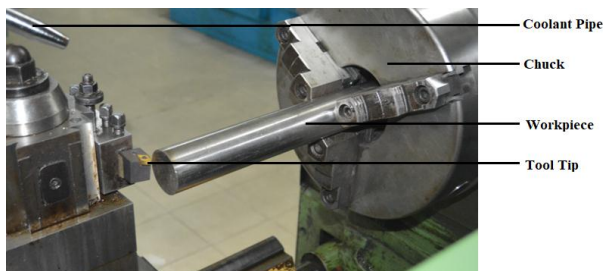


Fig.4 Experimental set up for turning operation

Central Composite Design (CCD) of Response Surface Methodology (RSM) was used for the design of experiments (DOE) and Design Expert software version 11.0 was used for this purpose. CCD can run sequentially, it naturally gives severance of two subsets of points where the first subset estimates the linear and two factor interaction effects while the second subset

estimates curvatures effects. The second subset need not be run when the data is analysed from the first subset points indicates the absence of significant curvature effects. RSM discovers a relationships between several descriptive variables and one or more response variables. In this project RSM has been used to develop the relation between cutting parameters and responses, which were surface roughness and sound level. The design structure is shown in Table 1 along with the results on surface roughness.

3. Results and Discussions

Surface roughness of three different tool holders has been measured by using a contact type Phase II SRG-4500. Fig. 6 shows the surface roughness tester equipment. Table 1, below, compares the resultant surface roughness for the three cases. It also shows the percentage reduction of those cases.



Fig. 5 Surface roughness tester

Table 1: Comparison of surface roughness for the three cases

Run	Cutting speed (m/min)	Feed (mm/min)	Depth of Cut (mm)	Surface roughness, Ra (µm)			Percentage Reduction (%)
				Carbon Steel	Pearlitic Gray Cast Iron	Annealed Gray Cast Iron	
1	108.07	0.3	1	2.482	2.244	2.162	12.89%
2	141.37	0.49	0.5	3.95	3.63	3.067	22.35%
3	168.86	0.3	1	3.95	3.339	2.12	46.33%
4	108.07	0.09	1	1.077	0.815	0.756	29.81%
5	108.07	0.3	1	3.303	2.484	1.965	40.51%
6	108.07	0.3	1	2.524	2.229	1.64	35.02%
7	108.07	0.3	1	2.221	2.14	1.22	45.07%
8	54.03	0.1	0.5	0.821	0.564	0.562	31.55%
9	29.68	0.3	1	3.185	1.8	1.46	54.16%
10	108.07	0.3	0.29	3.001	2.177	2.056	31.49%
11	108.07	0.58	1	5.442	4.831	3.11	42.85%
12	108.07	0.3	1	2.327	2.073	2.03	12.76%
13	141.37	0.1	1.5	1.351	0.937	0.672	50.26%
14	108.07	0.3	1.7	4.62	2.662	2.48	46.32%
15	54.03	0.49	1.5	5.756	3.948	3.111	45.95%

From Table 1, it can be observed that with the use of annealed gray cast iron tool holder surface roughness improves remarkably. Surface roughness is also dependent on the cutting parameters. From table 1, the highest percentage reduction for roughness was observed when cutting the work material at 29.68 m/min speed, 0.3 mm/rev feed, and 1 mm depth of cut

(run number 09) and the effect of different tool holder material on surface roughness (Ra) is shown on Figure 6. The corresponding surface roughness reduction percentage was about 54.16%. This is followed by run number 13 (cutting speed 141.37 m/min speed, feed 0.10 mm/tooth, and depth of cut 1.5 mm) where the reduction is roughly 50.26%. These reductions observed in surface roughness were caused by the damping characteristics of the materials on oscillatory motion of the tool.

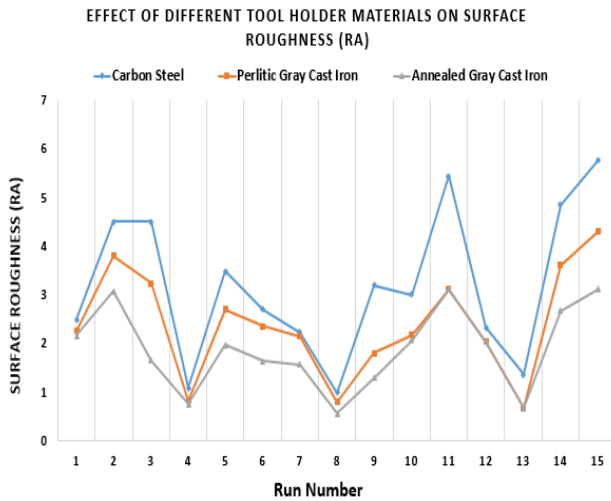


Fig. 6 Influence of different tool holder materials on surface roughness

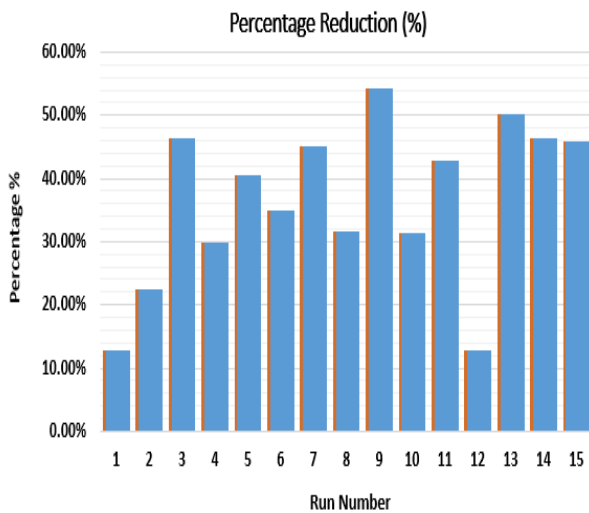


Fig. 7 Percentage reduction of surface roughness due to the change of tool holder materials

The chip reduction coefficient was calculated for the three tool holder materials. The value of the chip reduction coefficient was lower when annealed gray cast iron tool holder was used.

Table 2 Chip Reduction Coefficient of three different tool holder materials.

Run	Chip Reduction Coefficient (ζ)		
	Carbon Steel	Pearlitic Gray Cast Iron	Annealed Gray Cast Iron
1	1.42	1.48	1.35
2	1.17	1.13	1.08
3	1.49	1.38	1.32
4	1.48	1.29	1.18
5	1.46	1.38	1.10
6	1.49	1.41	1.35
7	1.46	1.42	1.39
8	1.35	1.33	1.29
9	1.49	1.42	1.30
10	1.12	1.08	1.02
11	1.43	1.41	1.38
12	1.38	1.32	1.20
13	1.49	1.40	1.20
14	1.37	1.35	1.10
15	1.45	1.42	1.27

Figure 8 shows the graphical comparison chip reduction coefficient of three different tool holder materials

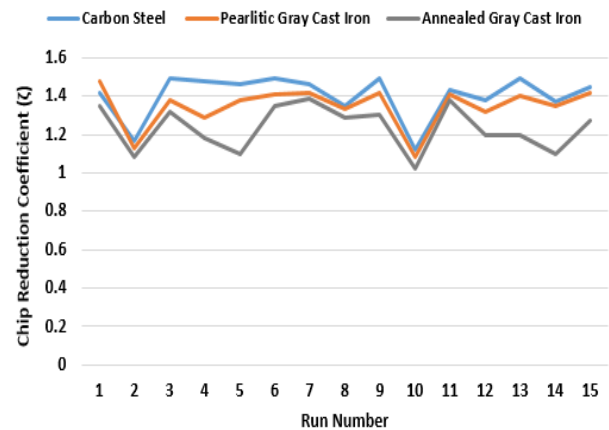
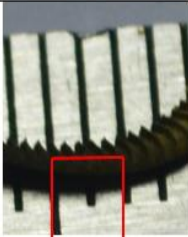




Fig. 8 Comparison of chip reduction coefficient of three different tool holder materials

3.1 Chip Morphology

The effect of different cutting parameters on chip serration frequencies and its interaction with the mode frequencies of the lathe components has been investigated, considering the vibration data that are recorded during machining using a microphone and a sound level meter. The detail calculation for the (09 number run) procedure is shown in Table 3 below.

Table 3 Chip serration frequency calculation for 09 number run

Carbon Steel	Pearlitic Gray Cast Iron	Annealed Gray Cast Iron
		
Cutting Speed(V)=29.289m/min No of serrated teeth(n) = 5 Length = 0.02mm Chip shrinkage coefficient (K) = 1.49	Cutting Speed(V)=29.289m/min No of serrated teeth(n) = 7 Length in = 0.02mm Chip shrinkage coefficient (K) = 1.42	Cutting Speed(V)=29.289m/min No of serrated teeth(n) = 6 Length in = 0.02mm Chip shrinkage coefficient (K) = 1.30
Determination of chip serration frequency		
$fc = \frac{29.289 \cdot 1000 \cdot 5}{60(0.2 \cdot 1.49)} = 8191$	$fc = \frac{29.289 \cdot 1000 \cdot 7}{60(0.2 \cdot 1.42)} = 10313$	$fc = \frac{29.289 \cdot 1000 \cdot 6}{60(0.2 \cdot 1.30)} = 11265$

3.2 Analysis of sound level

The analysis the sound levels of each run of three different tool holder, are shown on the following Table 4.

Table 4 Comparison of sound levels of three different tool holder materials

Run	Carbon Steel (dB)	Pearlitic Gray Cast Iron (dB)	Annealed Gray Cast Iron (dB)	Percentage Reduction (%)
1	94.3	93.6	90.8	4%
2	99.3	93.3	92.3	7%
3	95.7	94	90.4	6%
4	91	87.2	85.7	6%
5	94.9	91.6	89.6	6%
6	95	93.4	89.1	6%
7	94.2	93.5	89.6	5%
8	85.2	84.2	83.8	2%
9	84.3	80.5	77.9	8%
10	88.1	87.3	86.6	2%
11	98.8	97.4	89.1	10%
12	95.7	94.7	91	5%
13	94.1	89.9	87.4	7%
14	97.9	97.8	95.9	2%
15	104.6	99.6	97.3	7%

Figure 9 shows the graphical comparison of sound level of three different tool holder materials

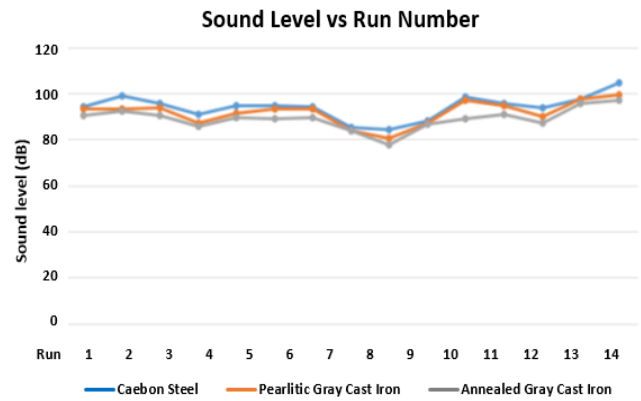


Fig. 9 Comparison of sound level of three different tool holder materials

So from the graph it is clear that for annealed gray cast iron, minimum sound level is found. For further verification, FFT function was done. After plotting amplitude Vs frequency bins graphs with the help of FFT the highest peak value of the amplitude of each run was selected for measuring the sound level for three different tool holders. Figure 10 shows the Fast Fourier transformation for run number 09.

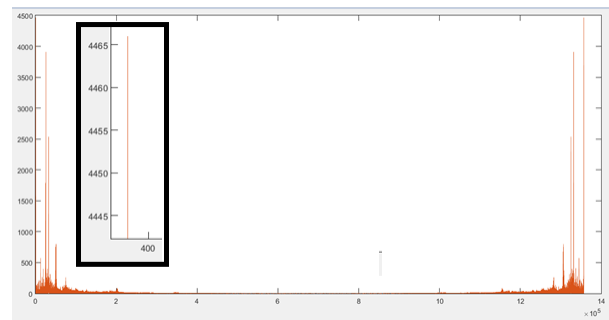


Fig. 10 FFT (Fast Fourier transformation) and maximum peak point of amplitude vs frequency bin for run number 09

4. Conclusions

The following specific conclusions were drawn from the research results:

1. The change of tool holder material to annealed gray cast iron resulted in a maximum reduction of 54% in average surface roughness; the average reduction being 36.49%. This significant improvement in surface finish would likely eliminate the cost of operations for grinding and polishing in machining of AISI 201.
2. Both primary and secondary serrated teeth were formed in turning of AISI 201 work material using coated WC-Co.
3. The chips were more stable when Annealed gray cast iron tool holder was used and the chip serration frequencies are higher than the other two. This phenomenon occurred because of the greater damping effect of the annealed gray cast iron tool holder.

5. Recommendations

- [1] Scanning Electron Microscope (SEM) could be used for further analysis of the chips and tool wear.
- [2] To conduct the experiments using data acquisition system i.e. accelerometer for measuring frequency and amplitude accurately.
- [3] CNC lathe machine is recommended to be used for getting more accurate results.

NOMENCLATURE

- f_c : frequency of the serrated teeth formation, Hz
 L : length of the portion of the chip, mm
 K : coefficient of chip shrinkage
 V : cutting speed, m/min
 n : number of serrated teeth

REFERENCES

- [1] F.J. Campa, L.N.L. Lacalle, A. Lamikiz, J.A. Sanchez, Selection of cutting conditions for astable milling of flexible parts with bull nose end mills, *J. Materials Processing Technology* 191 (2007) 279-282.
- [2] Taylor, F.W. (1907). On the art of cutting metals, *Trans. Amer. Soc. Mech. Eng.* Vol. 28 pp.31-35.
- [3] M. Wiercigroch, Budak, Source of nonlinearities and suppression of chatter in metal cutting, *Phil Trans R. Soc. Lond.* A359 (2001) 663-693.
- [4] Tobias, S. A. and Fishwick, W. The chatter of lathe tools under orthogonal cutting conditions, *Transactions of the ASME: B*, 1958, 80: 1079–1088 20
- [5] Eliasberg, M.E. (1962). *Fundamentals of the theory of chatter during metal cutting process*, *Journal of Machine-Tool.* (1) pp. 3-4.
- [6] Amin, A.K.M.N., (1983). *Investigation of the mechanism of chatter formation during the metal cutting process*, *Mech. Eng. Res. Bulletin*, 6 (1), pp. 11 18.
- [7] Wiercigroch, M. and Budak. (2001). Sources of nonlinearities and suppression of chatter in metal cutting, *Phil Trans R. Soc. London*, A359, pp. 663-693.

Difficulties to Develop a Four Legged Robot

Mohammad Harun-Or-Rashid, Mostafijur Rahman, Sabrina Rashid

Department of Mechanical and Production Engineering, Ahsanullah University of Science and Technology, Dhaka-1208, BANGLADESH

ABSTRACT

Development process of a four legged robot is discussed in this paper. During making the robot many difficulties are faced. This paper is mainly focused on difficulties and their remedies. In 20th century many mathematical methods are introduced for smooth control of linear as well as nonlinear motion of dynamic system. Sensor, actuator and control algorithm are commonly used to build up field, aerial as well as under water robot. Among different types of field robots wheeled robots are commonly built because compare to aerial and under water robot these are easier to control. On the other hand, there are various limitations of wheeled robot such as move on stairs and rough topography. Therefore, to overcome these problems, in the present study, a four legged robot is developed. During development of a four legged robot many difficulties are arisen such as proper electric motor selection, leg mechanism and motion control as well as synchronization of movement of four legs for steady motion of the robot.

Keywords: Field robot, Gear motor, Leg mechanism.

1. Introduction

Robot is a programmable machine. It is designed on the basis of the task perform and controlled by the microcontroller board. In recent years many people are studying and working on field robot. It includes wheel controlled robot as well as legged robot. Even though it is easier to develop wheeled robot than legged robot but it has various disadvantages such as walk on stairs and rough terrain. On the other hand, quadrupedal robot also known as four legged robot is difficult to develop and motion control but it can move on rough surfaces and stairs without any trouble. Therefore, in the present study, it is planned to develop a four legged robot.

Khaled M. Goher and Sulaiman O. Fadlallah [1] developed a two legged portable system, which allows patients with lower-limb disabilities to perform leg and foot rehabilitation exercises anywhere without any embarrassment. The system is modeled by applying Lagrangian approach. Jing Liu et al. [2] studied different types of legged robot, their problems and future trend. Lee & Shih, work on a quadruped walking vehicle constructed at the National Chiao Tung University which is referred as NCTU quadruped-1. For controlling the motion and position of legs, first of all, they used non linear feedback and after that model reference adaptive control. Its total weight and length of each leg is 50 kg and 0.6 m respectively [3]. Marc Raibert et al. developed a rough-terrain robot that is able to move in outdoor steep, rocky and muddy as well as in house [4]. They found that further attention is necessary on several areas like quieter operation, self righting, more autonomy and travel in rougher terrain.

The main objective of this work is to develop the leg mechanism and control the movement of the robot. Fig. 1 shows the 3D model and Fig. 2 shows the constructed model of the four legged robot. Length, width and

height of the robot are 14 in, 8.5 in and 8 in respectively. Conversely, total weight of the robot is 3 kg.

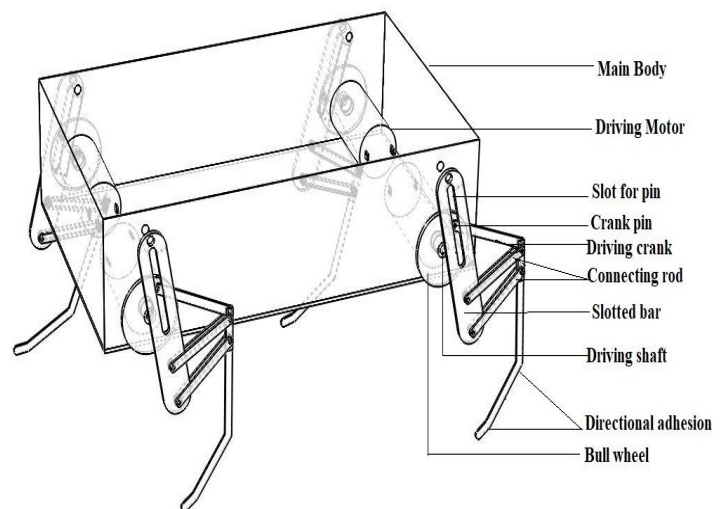


Fig. 1 3D model of the four legged robot



Fig. 2 Four legged robot (constructed model)

2. Leg Mechanism

Design and development of the leg mechanism is one of the major issues of four legged robot. First of all, one leg was designed and fabricated. In that design, there were two motors for each of the legs. One motor was used to rotate the lower part of the leg and another had the function of move the whole leg. But the whole leg was such heavy weight that the main motor was not able to lift the weight. In this case, eight motors were needed for four legs, which made the whole structure too much heavier. Thus, it might become slower with movement. Replacing this with a high torque motor was not possible as it would make the system weightier and consequently, target of minimizing the weight would be failed. On the other hand, it is a load carrying robot; if the body has too much weight then it would be difficult to carry additional loads. Therefore, the first attempt [Fig. 3 (a)] went wrong.

At the second case, a mechanism with linear tubular actuator was being considered. It was designed by using SolidWorks. The design was looked good and satisfactory. It was also checked if it would give proper motion to the leg. In this design, actuator was used for holding the heavy weight of the body. It was the simplest mechanism of motion of the leg. The leg was constructed according to the design. Fig. 3 (b) shows the fabricated model of a leg. However, after the

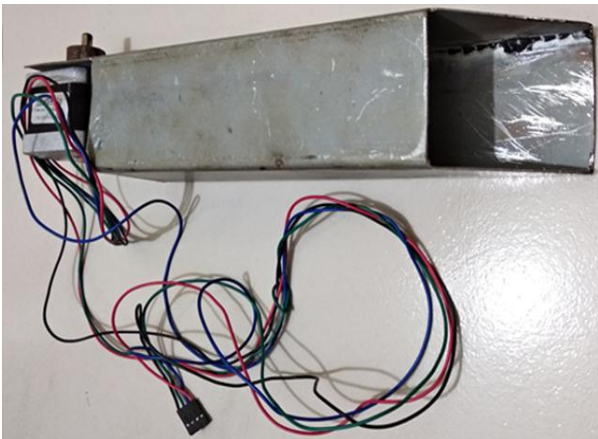


Fig. 3 (a): Fabrication of the leg (First attempt)



Fig. 3 (b): Fabrication of the leg (Second attempt)



Fig. 3 (c): Fabrication of the leg (Third attempt)

construction, a new problem was found. The actuator itself had heavy weight. After attaching with the leg, the leg was too heavy to rotate with the driving motor. It was very difficult to rotate the leg with stepper motor (NEMA 17). Furthermore, the actuator was very slow during giving feed. Since there was lack of availability of actuator in Bangladesh it was not possible to replace and recheck the mechanism. Thus, second design was failed to fulfill requirement.

Since first two designs were too weighty, therefore, at the third attempt, main objective was to reduce the weight of the leg. It need to be less weight so that, the driving motor can easily move it. Hence, a new design with a new mechanism was made. It was a four bar linkage mechanism using one motor. Fig. 3 (c) shows the four bar linkage mechanism. Aluminum sheet was used to construct the leg. Therefore, weight was dramatically reduced. In addition, it does not need any secondary motor to rotate the lower portion of the leg. One motor was enough for the rotation the entire leg. But during the test run of the leg, it was being stuck at the linkages. Further more, the leg was just bending in one position, hence, it was not possible to give a forward feed to the robot. As few problems were being solved in this design, therefore, some hope was gained from this work. Thus, further design and development of the leg was encouraged using one motor for each leg.



Fig. 3(d): Fabrication of the leg (Selected for use)

At the third attempt, the weight problem was solved and found a way to design the leg with one motor and mechanical linkage. Therefore, during the fourth attempt the target was to make the linkages smooth and clear. Finally, crank-slider mechanism [Fig. 3(d)] was considered to give motion to the leg. For this a bull wheel was needed. The wheel was made of iron. The wheel is connected to the motor shaft and a crankshaft. Therefore, it was the main part after the motor shaft to maintain the proper motion. It needs to be strong so that, it would not bend or break down.

2.1 Walking Mechanism

The walking mechanism of the leg was not so much easy. Leg was manufactured in four different ways. However, in first three cases, there were problems, and hence fail to run the robot. At last, come out with an idea of bull wheel crankshaft, connecting rod and crank slider mechanism. The motion of the leg is controlled by a gear motor. Fig. 4 shows the flow chart of the leg motion.

Here, the motor shaft is connected with the bull wheel. The pin of the bull wheel is connected with the crankshaft. The crankshaft is connected with the lower leg. The connecting pin can slide through a slot in a slotted bar. The slotted bar is attached with the main body through a pin in such a way that pin is fixed and slotted bar can rotate. The slotted bar is connected with the lower leg by using connecting rods.

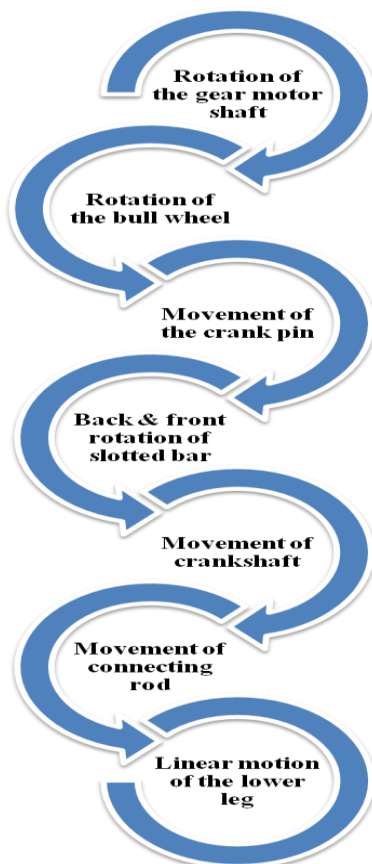


Fig. 4 Flowchart of the leg motion

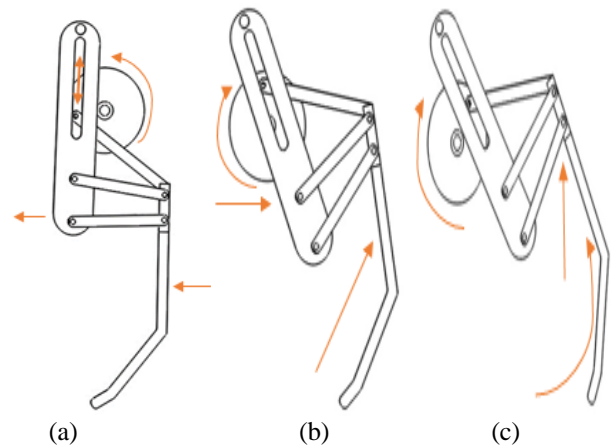


Fig. 5 Walking positions: (a) position 1, (b) position 2, (c) position 3



Fig. 6 position of legs during moving of the robot

The wheel rotates with the motor shaft, thus the crankshaft moves backward & forward. The crank pin moves through the slot in the slotted bar.

The movement of the wheel gives feed to the crankshaft then pin slides into the slotted bar and convert the rotational motion into linear motion to move the lower part of the leg. With the forward movement of the slotted bar, the lower leg moves forward and the backward movement of the slotted bar moves the lower leg backward. The more the slider can move forward the more the lower leg can pass the distance. Fig. 5 shows the motion of different components as well as walking positions of the leg. On the other hand, Fig. 6 shows the movement of four legged robot during experiment.

3. Selection of electrical devices

Electric motor is a device that is used to convert electric energy to mechanical energy. A gear motor is an explicit type of motor that is designed to produce high torque and low speed to the output shaft at low input power. In the present study, initially stepper motor was selected. However, the stepper motor was not able to produce needed torque and its very weighty. As a result, stepper motor was replaced by gear motor. The RPM of the gear motor is 200.

Four brushed gear motor is used for the four legs of the robot. Each motor is connected with the bull wheel of the leg and the motor is attached to the main body of the



Fig. 7 Gear motor



Fig. 8 Arduino uno board

robot. A gear motor is shown in Fig. 7. Rated torque of the motor is 0.1765 N-m.

A 6000 mAh, 11.1V battery is used as power source. Weight of the battery is 442 gram. From this battery power is supplied to the microcontroller board and four gear motors.

An Arduino UNO (AU) is used for this robot as the main control board. It has a physical programmable circuit board called micro controller and several input and output pins in it. It has Special software called integrated development environment (IDE) is used to write code and upload to the Arduino. An Arduino uno board is presented in Fig. 8.

Two L298N motor shields are used to connect four motors with the micro controller board. L298 IC is utilized in the motor shield which is a dual H-bridge driver designed to drive inductive loads such as DC and stepper motors. A L298N motor shield is presented in Fig. 9.



Fig. 9 L298N motor shield

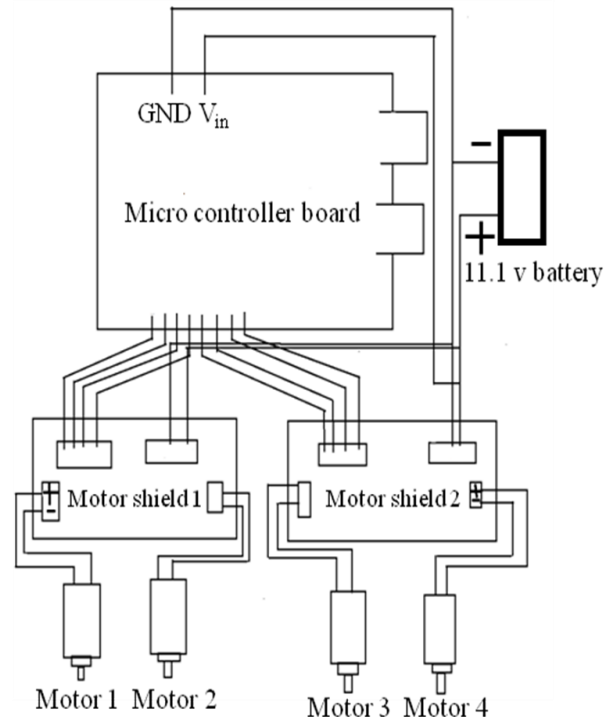


Fig. 10 Circuit Diagram of the electrical setup

Fig 10 shows the circuit diagram of the electrical setup. Power is supplied from the battery to the AU board as well as to the motor shields. Signal from the AU goes through the motor shield to the motor.

4. Result and Discussion

At the beginning of the experiment motors are disconnected from power supply and bull wheel is rotated manually. During experiment, for a given angular displacement of the bull wheel, leg's forward and backward displacement as well as slotted bar's angular displacement is measured. Fig. 11 shows the movement of different components of the leg and Experimental data is presented in Table 1.

Table 1: Linear and angular displacement of the leg and slotted bar respectively for different angular displacement of the bull wheel

Rotation of Bull wheel (Degree)	Rotation of slotted bar (Degree)	Linear movement of the leg (Inches)
30	5.294	1.147
60	10.588	2.294
90	15.882	3.441
120	21.76	4.588
150	26.471	5.735

Longest, shortest and cross distances between front and rear legs are also examined. Longest and shortest distances are 16 in and 6 in respectively (Fig. 12). On the other hand, Fig. 13 shows the rotational path and motion of the leg.

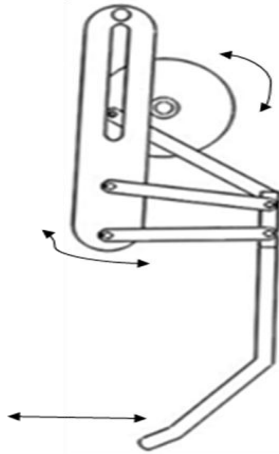
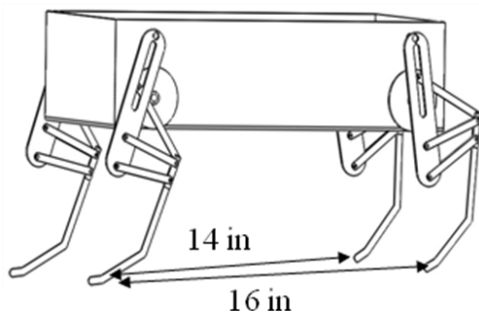
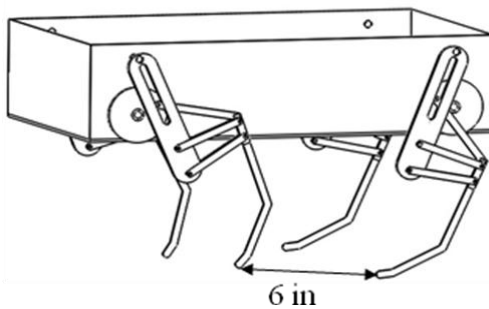


Fig. 11 Movement of different components of the leg



(a)



(b)

Fig. 12 Distance between front and rear leg: (a) longest, (b) shortest

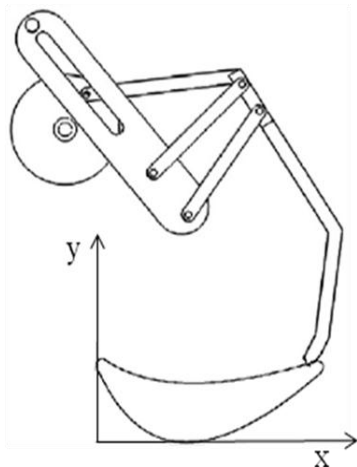


Fig. 13 Movement path of the leg.

5. Conclusion

Objective of this research was to develop a four legged robot. Finally a robot was built. During movement of the robot it was found that there was a lot of friction at different components of leg. Furthermore, after walking few steps two motors stopped working. This was happened because of weight of the robot and frictional loss in legs. Therefore, it is necessary to reduce the friction and weight of the robot. Addition of more powerful motor can be another option to solve the problem.

Acknowledgement

Thanks to Ahsanullah University of Science and Technology for all kind of support.

REFERENCES

- [1] Khaled M. Goher, Fadlallah S. O., Design, Modelling, and Control of a Portable Leg Rehabilitation System, *Journal of dynamic system, Measurement and Control*, doi:10.1115/1.4035815 (2017).
- [2] Jing Liu et al., Legged robots –an overview, *Transactions of the Institute of Measurement and Control* 29, pp.185-202 (2007).
- [3] Tsu- Tian Lee, Ching-long Shih, Real Time Computer Control of a quadruped walking robot, *Transactions of the ASME*, Vol .108. pp. 346-353 (1986).
- [4] Marc Raibert et al., Big Dog, the Rough- Terrain Quadruped Robot, *Proceedings of the 17th World Congress (IFAC '08)*, Seoul, Korea, pp 10822-10825 (2008).
- [5] Seyed Fakoorian et al., Ground Reaction Force Estimation in Prosthetic Legs with Nonlinear Kalman Filtering Methods, *Journal of dynamic system, Measurement and Control*, doi:10.1115/1.4036546 (2016).
- [6] M. Buehler et al., SCOUT: A simple quadruped that walks, climbs, and runs, *International Conference on Robotics & Automation*, pp 1707-1712 (1998).
- [7] Tetsuo Kinoshita et al., Control of Four-Legged Robot, *SCIE Annual Conference*, pp 571-575 (2011).

Numerical Study of Heat Transfer and Flow Characteristics in a Rectangular Channel with Rib Type Turbulent Promoters

Sunanda Kumar Saha*, Md Mosarof Hossain, Dr. Mohammad Ali

Department of Mechanical Engineering, Bangladesh University of Engineering & Technology, Dhaka, BANGLADESH

ABSTRACT

Numerical simulation is carried out to study turbulent forced convection heat transfer and friction loss for flow through a rectangular channel having a constant heat flux with different rib type turbulent promoters. The rib shapes used in this study are rectangular, triangular, trapezoidal, wedge rib upstream and wedge rib downstream. Two rib configurations: (i) ribs mounted on bottom wall and (ii) ribs mounted on both wall (staggered rib array) are simulated. Standard $k-\epsilon$ turbulence model and enhanced wall treatment are used to perform the simulation. The inflow Reynolds number is varied from 5000 to 10000. Simulation is performed for a rectangular channel with aspect ratio 13, pitch to height ratio of 4 for configuration (i) and 8 for configuration (ii), rib width to rib height ratio of 2, blockage ratio of 1/3 for configuration (i) and 1/6 for configuration (ii). The results indicate that the heat transfer performance and the friction loss are strongly affected by different rib shapes. The highest heat transfer performance is achieved for wedge rib upstream for configuration (i). For configuration (ii) highest value of heat transfer performance is obtained for triangular rib. The lowest value of heat transfer performance is obtained for wedge rib downstream for both configurations. For ribs mounted in bottom surface wedge rib downstream has the highest frictional loss and for staggered rib arrays highest frictional loss is found for wedge rib downstream. Triangular ribs mounted on both wall with staggered rib array configuration shows the highest thermal performance among the rib shapes.

Keywords: Numerical simulation, Heat transfer, Friction loss, Reynolds Number, Rib type turbulent promoter.

1. Introduction

The usage of ribs in the cooling channels or heat exchangers is one of the commonly used passive heat transfer enhancement technique. Heat transfer augmentation with turbulent promoters has become significantly important in many aspects of engineering. Different shaped ribs are used so far and their effects are analyzed. Laminar flow is comparatively easy to analyze with governing equations but turbulent flow is beyond analytical analysis depends massively on physical intuition and dimensional arguments. It is also necessary to consider their relations that describe the manner in which they influence the velocity distributions which in turn affects temperature fields. Numerical simulations are used to analyze turbulent flow and their behavior while flowing through a channel with ribs. Enhancing heat transfer on a surface is done by making the surface rough and by the use of repeated ribs to act as turbulent promoters. These turbulent promoters break the laminar sub layer and or buffer layer and create local wall turbulence due to flow separation and reattachment between the ribs, which greatly enhance the heat transfer and increase the pressure drop. Liu Pingan, Gao Ye et al. [1] get highest heat transfer for square ducts with triangular ribs applying high Reynolds no.. In the work of Kamali R et al. [6] the highest heat transfer occurs in the case of trapezoidal ribs with decreasing height in the flow direction. Francesca, Danielle et al. [2] used 45° ribs in a rectangular channel for their simulation. In our present work, the effect of turbulence promoters on fluid flows and heat transfer in a square duct for Reynolds numbers varying from 5000 to 10000 will be investigated. While

traditional approaches use high Reynolds no. but using flow of low Reynolds no. is becoming very important in non-circular ducts flow and practical usages like micro cooler, automotive cooler and cold plates. In conversion and reclamation devices, also there is significant usage of low Reynolds no. flow. A two-dimensional domain of a square channel is considered and a constant heat flux boundary condition is applied to the ribs section of the channel. Air is considered as the medium flowing in the channel with varying velocity. Inlet air temperature is 298K. A constant heat flux of 100 W/m^2 is provided in the whole channel length section. It is assumed that the flow is a steady, turbulent, incompressible and fully developed flow. Numerical simulations are performed using the finite volume method. Standard $k-\epsilon$ turbulence model and enhanced wall treatment are used to produce the numerical simulations. Archarya et al. [3] applied $k-\epsilon$ models to straight and inclined ribs for two-dimensional rectangular ribs and found similar performance for these two cases. Iacovides and Raisee [7] examined the capabilities of low-Reynolds number versions of Launder & Sharma $k-\epsilon$ model [8] in predicting convective heat transfer for pipes and ducts. They obtained a more realistic heat transfer variation in the separation region and reasonable Nusselt number levels. $k-\epsilon$ model was also selected due to its good convergence rate and relatively low memory requirements. Another advantage of the model is it does perform well for external flow problems around complex geometries. It is the most common model used in Computational Fluid Dynamics (CFD) to simulate mean flow characteristics. Also, it provides good initial guess as well.

* Corresponding author. Tel.: +88-01772439344

E-mail addresses: shunondosahabuet@gmail.com

The main objective is to study the effect on the heat transfer of a square channel with different ribs with pitch (P) to rib height (k) ratio as 4 and width (b) to rib height (k) ratio as 2 for various Reynolds number with dimensions as shown below. The two-dimensional detailed view of the channel is shown below:

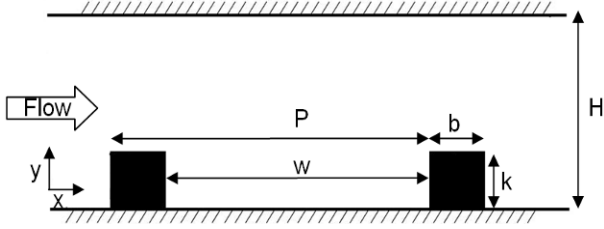


Figure 1: Detailed view of the rectangular channel with rectangular ribs from the work of R. Kamli et al., [6]

Various parameters of the channel are as follows: P/k is 4, b/e is 2, H/e is 3, the length of channel (L) is 39cm. In all these simulations, k is considered as 1cm. Hence, H is 3cm, b is 2cm, w is 2 cm and p is 4cm. The inlet velocity of the air is uniform and is calculated as per the required inflow Reynolds number. Similar simulation is carried out for staggered rib arrays. In this arrangement, ribs are also present in upper surface and each rib at upper surface is positioned in the middle of two ribs at lower surface. Reynolds number range is kept same for the experiment and a constant heat flux of 100 W/m² is also provided in the upper surface. The purpose of the study is to reconnoiter numerically the effect of heat transfer through a rectangular channel with different type of ribs. The shapes of ribs that are used in the numerical simulation are: rectangular, triangular, trapezoidal, wedge rib upstream and wedge rib downstream. Air is considered as the medium flowing in the channel and inlet air temperature is 298K. Hence the specific objectives of present study are as follows: 1) To measure average Nusselt number for the channel with different shaped ribs mounted on the bottom side of the channel. 2) With analyzed data graph will be plotted for average Nusselt number vs Reynolds number. 3) Simulations will be carried out to study the effect of ribs in both sides of the rectangular channel and a similar graph will be plotted. 4) For each cases, variation of Nusselt number, Friction factor and Enhancement factor with Reynolds number will be shown in graph. 5) The results obtained from this investigation are to be compared with the published data available in the literature. 6) Conclusions will be drawn and recommendation will be made based on the discussion of the results.

2. Computational framework

In this work, Commercial CFD Software for Numerical Solution. Finite Element Method (FEM) was used for solving Incompressible Navier-Stokes. Momentum equations was solved (with or without pressure/either implicit or explicit) to obtain a

predicted velocity. Then to solve pressure poisson equation to obtain a pressure correction that can be used to update velocity so that continuity is satisfied. The grid independency test was performed. It was done for computing the solution on successively finer grids. The difference between two refinements was taken as a measure of the accuracy of the coarser of the two.

2.1 Governing Equation

The cornerstone of computational fluid dynamics is the fundamental governing equation of fluid dynamics, the continuity, momentum and energy equations. They are the mathematical statements of three fundamental physical principles upon which all of the fluid dynamics is based. 1) Mass is conserved 2) F=ma (Newton's second law) 3) Energy is conserved. Our study deals with all three of the above mentioned equations as it is concerned with both heat transfer and fluid flow.

Continuity conservation:

$$\frac{\partial \rho}{\partial t} + \nabla \cdot (\rho \mathbf{v}) = 0 \quad (1)$$

Momentum conservation:

$$\frac{\partial (\rho \mathbf{v})}{\partial t} + \nabla \cdot (\rho \mathbf{v} \mathbf{v}) = \rho \mathbf{g} - \nabla P + \nabla \cdot (\boldsymbol{\tau}) \quad (2)$$

Energy conservation:

$$\frac{\partial (\rho E)}{\partial t} + \nabla \cdot (\mathbf{v} (\rho E + p)) = \nabla \cdot (k_{eff} \nabla T + (\boldsymbol{\tau}_{eff} \cdot \mathbf{v})) \quad (3)$$

Where,

$$\boldsymbol{\tau} = \mu \left((\nabla \mathbf{v} + \nabla \mathbf{v}^T) - \frac{2}{3} \nabla \cdot \mathbf{v} \mathbf{I} \right) \quad \text{and} \quad E = h - \frac{p}{\rho} + \frac{v^2}{2}$$

Here, v is the velocity vector of the flow, ρ is the density of the flow.

2.2 Performance Parameter

The main dimensionless parameters governing this problem are Reynolds number and Nusselt number.

$$Re = \rho \mathbf{u} D / \mu \quad (4)$$

Where, ρ is the density, μ is the dynamic viscosity and the velocity of the air.

$$Nu_x = \frac{h_x D}{k} \quad (5)$$

And the average Nusselt number is obtained by,

$$Nu = \frac{1}{A} \int Nu_x \partial A \quad (6)$$

Friction factor is calculated by,

$$f = \frac{2}{(L/D_h)} \frac{\Delta P}{\rho U^2} \quad (7)$$

Where ΔP is the pressure drop across the test section u is the mean air velocity in the channel. All of thermo-physical properties of the air are determined at the overall bulk air temperature. The thermal enhancement factor (TEF) is defined as the ratio of the heat transfer coefficient of an augmented surface (h) to that of a smooth surface (h_0) at an equal pumping power and given by,

$$TEF = \frac{h}{h_0} \Big|_{pp} = \frac{Nu}{Nu_0} \Big|_{pp} = (Nu / Nu_0) / (f / f_0)^{\frac{1}{3}} \quad (8)$$

Where, Nu_0 and f_0 stand for Nusselt number and friction factor for the smooth duct respectively.

2.3 Physical Model

Fig.1 and Fig.2 shows the geometry which has been considered in this simulation to study effect of ribs on heat transfer and friction factor. The total length of channel is 39cm and 3cm in height. The space between the ribs is 4cm. The height of the rib is considered to be 1cm for ribs mounted in bottom surface and 0.5 cm for staggered rib arrays. A two-dimensional detailed view of the channel for both rib configurations is shown in Fig.1 and Fig.2.

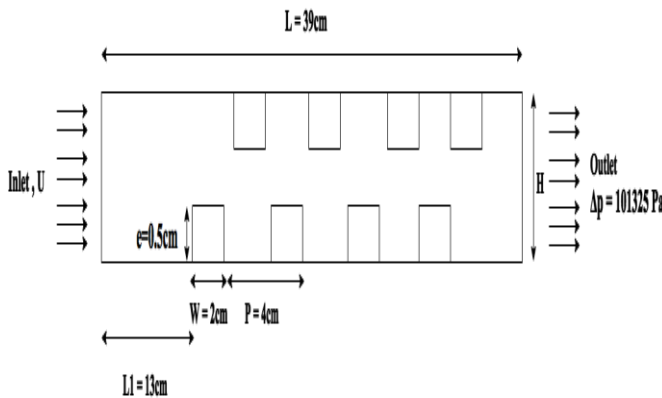


Figure2: Schematic Diagram of Rectangular channel with staggered rib arrays

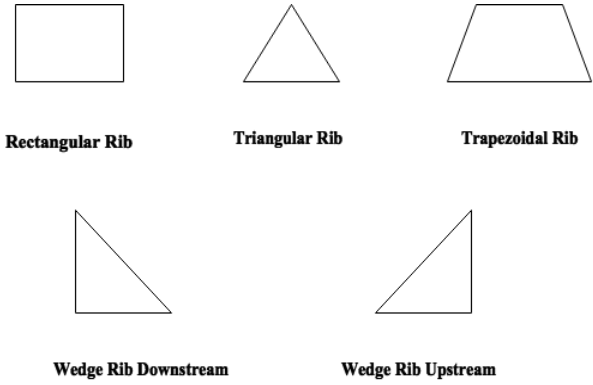


Figure 3: Different rib shapes used which are used in study

2.4 Boundary Condition

The Flow enters the domain from the left side with a velocity of U , which varies with the Reynolds number used in the study. An outlet pressure condition is imposed for the outflow at the right side of the domain. The inlet temperature of the air is 298K. A constant heat flux of $100W/m^2$ is supplied to the bottom for ribs mounted on the bottom surface and for on both side of the channel for staggered rib array configuration.

Table 1: Inlet velocity as per the inflow Reynolds number

Reynolds Number	Inlet Velocity
5000	2.595
5500	2.854
6000	3.114
6500	3.373
7000	3.633
7500	3.892
8000	4.152
8500	4.411
9000	4.671
9500	4.930
10000	5.190

2.5 Mesh Generation

In our present study the whole computational domain is discretized into free triangular. The free triangular structure is most popularly used for mesh generation in numerical modeling. In Fig.4, meshing for the whole domain for rectangular rib is shown. Dense meshing is done near the wall where ribs are mounted. For

staggered rib array configuration, no of elements generated is more than ribs on lower side and also dense meshing is done on both sides (in Fig.5)

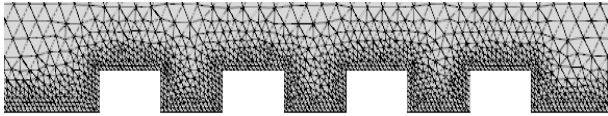


Figure 4: Triangular mesh structure of the domain for ribs mounted on lower side

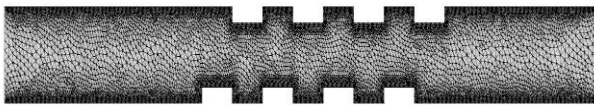


Figure 5: Triangular mesh structure of the domain for ribs mounted on lower side for staggered rib arrays

Table 2: Meshing Details for both rib configuration

	Ribs mounted on lower	Staggered rib array
Number of elements	4875	18508
Number of edge elements	465	1268
Number of vertex elements	20	36
Number of nodes	2671	9889

3. Result

The results are presented step by step, first the results of heat transfer and friction characteristics in a smooth channel are compared in terms of Nusselt number and friction factor. The data are post processed to find the variation of Nusselt number and friction factor for a range of Reynolds number.

3.1 Effect of Reynolds Number

Fig.6 shows variation of average Nusselt number with Reynolds numbers for rectangular channel and staggered rib arrays configuration. It is found that Nusselt number increases with the increase of Reynolds number which is similar to conclusion found by V.D.

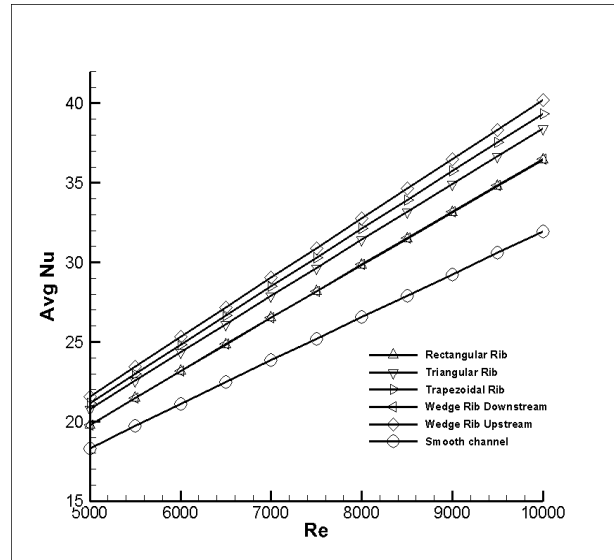


Figure 6: Average Nusselt number plot for ribs mounted on the bottom of square channel.

Boga and S.Jayave [4]. It happens because ribs interrupt the development of laminar boundary layer of the fluid flow and increase the turbulence and heat flow.

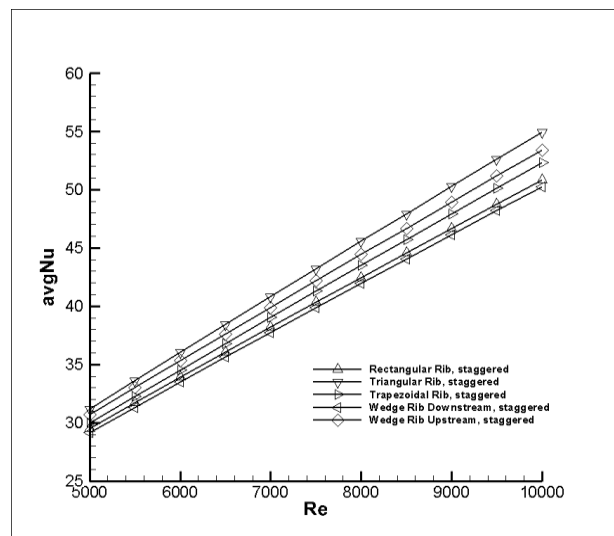


Figure 7: Average Nusselt number plot for channel with staggered rib arrays

The Nusselt number obtained under turbulent flow conditions for all five types of rib shapes are presented in the Fig.6 and Fig.7. The highest value of Nusselt number is found for wedge rib pointing upstream for ribs mounted in bottom wall and for ribs mounted on both wall it is found for triangular ribs. For both configurations wedge rib downstream has the lowest value of Nusselt number.

The wedge rib upstream and triangular ribs yield higher value of Nusselt number than rectangular ribs for all value of Reynolds number similar to the conclusion by

Ahn [5], who found that the triangular shape is more efficient for heat transfer than rectangular shaped

3.3 Average heat transfer and friction characteristics

The present result of heat transfer and flow friction characteristics in a rectangular channel equipped with different shapes of ribs are presented in the form of Nusselt number ratio and friction factor ratio. Both Nusselt number and friction factor are normalized by following factors:

$$Nu_0 = 0.023Re^{0.8}Pr^{0.4} \quad \text{and} \quad f_0 = 0.0791Re^{0.25}$$

For ribs mounted on bottom wall it is found that Nusselt number ratio increases with the increase of Reynolds number for all type of rib shapes. It shows highest value for wedge rib upstream and lowest for rectangular rib. Though rectangular rib has higher surface area for heat transfer than wedge rib upstream, but having lower recirculation zone results in lower heat transfer.

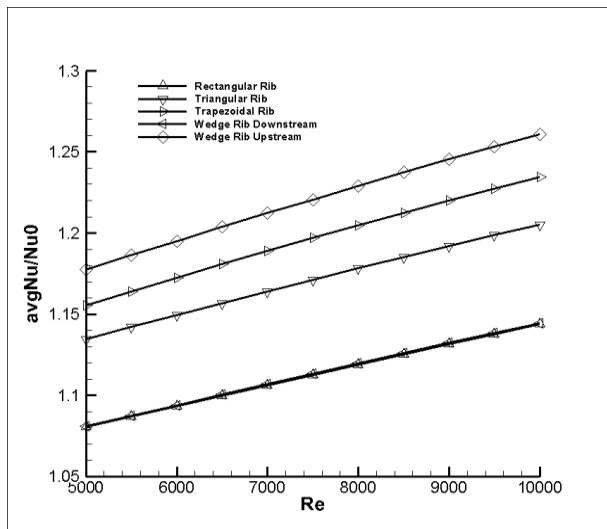


Figure 8: Variation of Nusselt number ratio with Reynolds number for ribs mounted on the bottom of rectangular channel.

Triangular rib has small recirculation zone compared to the other rib shapes except wedge rib downstream, it gives more heat transfer. Because when recirculation zone becomes larger, it reduces the flow velocity in that area which nullifies the effect of fluid mixing. Heat transfer enhancement decreases due to this phenomenon in those areas.

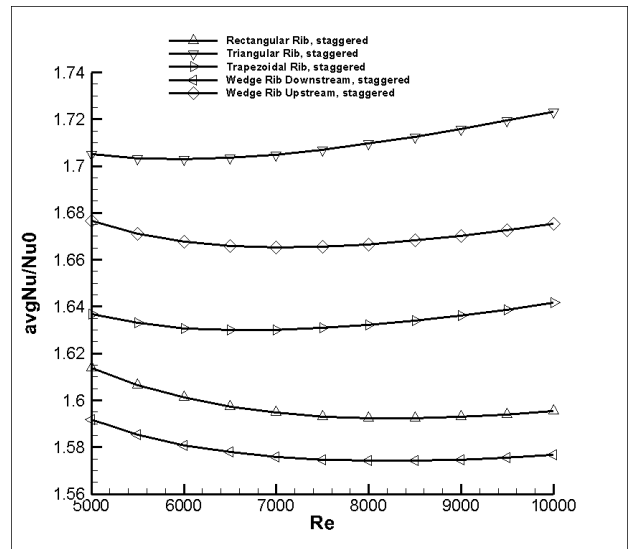


Figure 9: Variation of Nusselt number ratio with Reynolds number for channel with staggered rib arrays



Figure 10: Small recirculation zone for triangular ribs in staggered rib arrays

The effect of ribs on pressure drop across the channel is presented in the Fig.11 and Fig.12 for both rib configurations in the form of friction factor ratio with Reynolds no. For both rib configurations wedge rib downstream has the highest frictional loss. For ribs mounted on bottom wall rectangular ribs gives the lowest frictional loss. And for ribs mounted on both wall at low Reynolds number wedge rib upstream gives the lowest frictional loss and at higher Reynolds number trapezoidal rib gives the lowest frictional loss. Friction loss across the wall section is found to increase with Reynolds number because the velocity of flow increasing with Reynolds number as well. It has a direct impact on the pressure drop which reaches higher value at higher Reynolds number. The loss is mainly due to dissipation of dynamic pressure caused by head loss due to viscosity near the wall region and blockage because of the ribs. Also, friction factor increases with Reynolds number because a high amount of fluid remains at low velocity in the recirculation region past the rib shapes. This implies high flow velocity at the center of channel, resulting increased pressure drop. For this reason, at higher Reynolds number wedge rib upstream shows more frictional loss than trapezoidal rib.

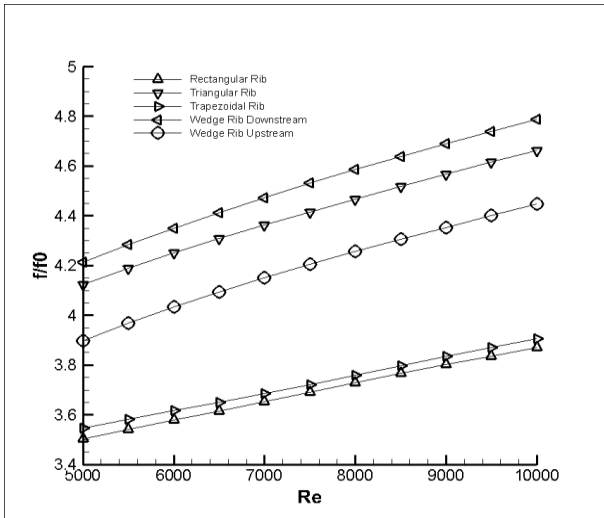


Figure 11: Variation of friction factor ratio with Reynolds number for ribs mounted on the bottom of rectangular channel

4. Conclusion

For both cases rectangular rib and wedge rib downstream gave the worst heat transfer performance and wedge rib downstream shows the highest friction loss among the investigated shapes. Rectangular ribs also show significant friction loss. Thus, rib shapes having slopes on the front proved to be a critical factor in determining heat transfer performance as it affects the recirculating zone. But friction loss doesn't depend only on the recirculation zone but mainly on the shape of the ribs. It is seen that both heat transfer performance and friction loss are dependent of Reynolds no.

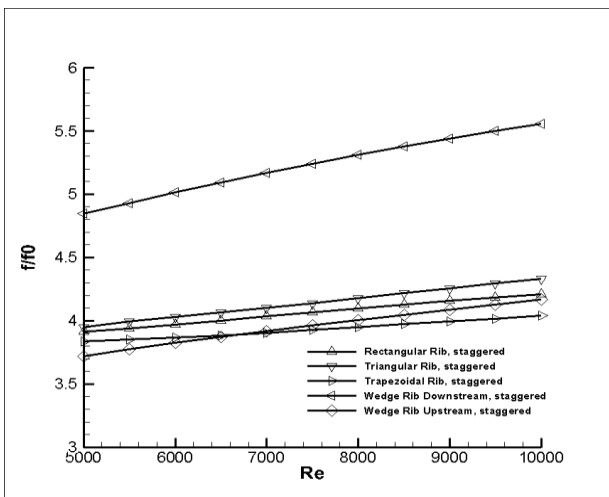


Figure 12: Variation of friction factor ratio with Reynolds number for channel with staggered rib arrays

For staggered rib arrays, triangular ribs show best heat transfer performance with average friction loss and for one sided rib arrays, wedge rib upstream ribs show best

heat transfer performance. But friction loss doesn't depend only on the recirculation zone but mainly on the shape of the ribs. It is seen that both heat transfer performance and friction loss are dependent of Reynolds no

NOMENCLUTURE

D_h	Hydraulic diameter
C_p	Specific heat capacity of air
e	Rib height
f	Friction factor
H	Channel height
h	Average heat transfer co-efficient
K	Thermal conductivity of air
k	Turbulent kinetic energy
Nu	Nusselt number
P	Pitch
ΔP	Pressure drop
Pr	Prandtl number
Re	Reynolds number

REFERENCES

- [1] Liu Pingan, Gao Ye and et. al., 2010, Numerical Simulation of Heat Transfer and Resistance Pattern in Channels with Different Ribs, ICCDA
- [2] Francesca Satta, Daniele Simoni and et. al, 2012, Experimental investigation of flow and heat transfer in a rectangular channel with 45°angled ribs on one/two walls, Experimental Thermal and Fluid Science 37, 46–56.
- [3] S. Acharya, S. Dutta, T.A. Myrum and R.S.Baker. Periodically developed flow and heat transfer in ribbed duct. Int. J. Heat Mass Transfer 36: 2069–2082, 1993.
- [4] V.D. Boga and S.Jayave, "Numerical Simulation of Heat Transfer in Channels with Different Ribs." Int J Mech Prod Eng ISSN 2320-2092., vol. 2 ,pp.79-82,2014.
- [5] S.W. Ahn, The effects of roughness types on friction factors and heat transfer in roughened rectangular duct, International Communications in Heat and Mass Transfer 28 (7) (2001) 933–942.
- [6] R. Kamali and A.R. Binesh, " The importance of rib shape effects on the local heat transfer and flow friction characteristics of square ducts with ribbed internal surfaces"International Communications in Heat and Mass Transfer, Volume 35, Issue 8, October 2008, pages 1032-1040.
- [7] H. Iacovides and M. Raisee. Computation of flow and heat transfer in two-dimensional ribroughened passages, using low-Reynolds number turbulence models.Int J Numerical Method for Heat and Fluid Flow.11. 138-155, 201.
- [8] B.E. Launder and B.I. Sharma. Application of the energy dissipation model of turbulence to the calculation of flow near a spinning disc. Lett. Heat Mass Transfer. 1: 131-138, 1974.

Effect of Tip Speed Ratio on the Flow Characteristics of Single-bladed Darrieus Wind Turbine

Md. Tanvir Khan, Mohammad Ilias Inam, Abdullah Al-Faruk

Department of Mechanical Engineering, Khulna University of Engineering & Technology, Khulna-9203, BANGLADESH

ABSTRACT

Wind energy is considered as one of the most realizable sources of renewable energy on the eve of fossil fuel energy depletion. Vertical axis wind turbines such as the Darrieus turbines appear to be promising for the condition of low wind speed though it has a low efficiency compared to horizontal axis turbines. The aim of this study is to investigate the flow development of a single bladed vertical axis wind turbine using CFD at different tip speed ratios. The blade is designed using the NACA 0015 profile and is operating under stalled conditions. Two dimensional simulations are performed using ANSYS Fluent 16.2, employing the realizable k-epsilon turbulence model and scalable wall function. Simple pressure-based solver is selected along with the second order implicit transient formulation. The CFD results under dynamic cases are presented and the resulting aerodynamic forces are evaluated. The turbine is observed to generate both positive and negative power at certain azimuthal angles. The pressure contours, velocity profiles as well as the velocity streamlines are illustrated and the powers and the power coefficients are calculated. Results show that force as well as the power is proportional to the tip speed ratio and at every case net average power is positive. Moreover, force as well as power varies periodically with the azimuthal angles. Finally, the average power and power coefficient are calculated after the turbine has come to steady state condition—that increase with the tip speed ratios.

Keywords: Darrieus wind turbine, power coefficient, pressure coefficient, tip speed ratio, vortex.

1. Introduction

The focus on Renewable Energy Resources has increased significantly in the recent years in the wake of growing environmental pollution, rising energy demand and depleting fossil fuel resources. Different renewable energy sources include solar, biomass, geothermal, hydroelectric, wind etc. Among these the Eolic energy source (wind power) has proved to be a cheaper alternative energy resource and hence extensive research efforts have been put to improve the technology of electricity generation through it [1]. The world has enormous potential of wind energy that can be utilized for electricity generation [2]. Wind power is now world's one of the fastest growing energy resources [2]. Although the vertical axis wind turbine (VAWT) was the first ever wind turbine to be used for harnessing wind energy [3], researchers of the modern era lost interest in it for the initial perception that VAWT cannot be used for large scale electricity generation. Horizontal axis wind turbine (HAWT) remained the focus of all wind energy related research activity for last few decades. However, research work on VAWT continued in parallel at a relatively smaller scale. Scientists and Engineers developed various wind turbine configurations and utilized different approaches for their analysis. Optimum conditions for the working of VAWTs were determined. Some of these techniques and configurations of researchers on vertical axis wind turbines are reviewed in this paper. A closer look on the concepts leads towards the fact that VAWTs are suitable for electricity generation in the conditions where traditional HAWTs are unable to give reasonable efficiencies such as high wind velocities [3], and turbulent wind flows [3]. Moreover, vertical axis wind

turbines are convenient for power generation in the built environment like urban, suburban or remote areas [3]. Another major advantage is that VAWTs are Omni-directional, accepting wind from any direction without any yawing mechanism [3]. VAWT has a number of promising features which if exploited properly can make it a better alternative to fulfill the world's energy demand [4]. Although currently large scale VAWTs are not economically attractive, they offer energy solutions for remote places away from the main distribution lines and places where large wind farms cannot be installed for environmental concerns and small-scale dispersed generation units are preferred [4]. That is why mass production of VAWTs has recently been started as small scale wind power generating units [5].

Two types of VAWTs, namely, Savonius wind turbine (SWT) and Darrieus wind turbine (DWT) are available. Among them DWT is more suitable for power production for high rotating speed [6]. Darrieus is a lift type wind turbine of which the blades are of airfoil shaped. A huge amount of research has been done on Darrieus wind turbine and still continuing. Castelli and Benini [7] presented the effect of blade thickness on the operation of a straight-bladed vertical axis wind turbine (SVAWT) in a 2D, time accurate, numerical simulations. Castelli and Ardizzone [8] performed a numerical analysis on a small DWT to make a systematic comparison with wind tunnel experimental data. Result proved that the best near-blade grid element dimension can be determined through statistical analysis of some indicators, such as the Y^+ parameter, to maximize the accuracy of the numerical prediction of rotor performance while maintaining a reasonable computational effort. Ferreira [9, 10] investigated the

effect of the dynamic stall in a 2D single-bladed SVAWT, which reports the influence of the turbulence model in the simulation of the vertical structures spread from the blade itself. Vassberg [11] tried to improve the efficiency of a VAWT by applying the emerging CFD capabilities through the simulation of the dynamic motion of a turbine blade including the parametric study of turbine solidity, turbine tip speeds and a variation of NACA 0015 section. Owing to the occurrence of most structural failures of wind turbines in the blade root section, a 3D analytical model of HAWT, blades constructed of NACA 0015, was proposed by Chazly [12] using bending triangular plate finite elements to compute the deflection, stresses, and eigenvalues in the rotor blades. Compendium of the proposition is—maximum stresses occurred at the root of the blades in the span wise direction and in addition to saving material weight—a tapered blade—diminished the stresses obtained. Moreover, the twisting blade leads to enhance stiffness and decrease stresses. A CFD model was presented by Castelli and Englaro [13] for the evaluation of energy performance and aerodynamic forces acting on a SVAWT of Darrieus type. In which the basic principles that are currently applied to Blade Element-Momentum (BE-M) theory for rotor performance prediction are transferred to the CFD code, that allow the correlation between flow geometric characteristics (such as blade angles of attack) and dynamic quantities (such as rotor torque and blade tangential and normal forces). Energy performance and aerodynamic forces acting on a helical SVAWT was evaluated by Castelli and Benini [14] depending on the blades inclined to the horizontal plane to generate a phase shift angle of 0°, 30°, 60°, 90° and 120° between lower and upper blade sections, for a rotor with an aspect ratio of 1.5.

The tip speed ratio is the relationship between rotor blade velocity and relative wind velocity which is defined by, $\lambda = \frac{\omega R}{U}$, where, ω = Rotor rotational speed in radian/second, R = Rotor radius in meter, U = Wind velocity. It is the foremost design parameter around which all other optimum rotor and blades dimensions are calculated. Higher tip speeds result in higher noise levels and require stronger blades due to large centrifugal forces [15]. The tip speed ratio is a very important aspect; therefore, efficiency, torque, mechanical stress, aerodynamics and noise should be considered in selecting the appropriate tip speed. Besides, it has been found to produce efficient conversion of the wind's kinetic energy into electrical power [15]. This paper aims to investigate the flow development of a single bladed vertical axis Darrieus wind turbine using CFD methods under different tip speed ratios. The turbine blade was constructed of NACA 0015 airfoil shape. Two dimensional simulations were performed using ANSYS Fluent software 16.2 version, employing the Realizable K-epsilon turbulence model [16] with scalable wall function. The CFD results from the dynamic case were presented and the resulting

aerodynamic forces were evaluated. Also, The Power coefficients for different tip speed ratios were calculated.

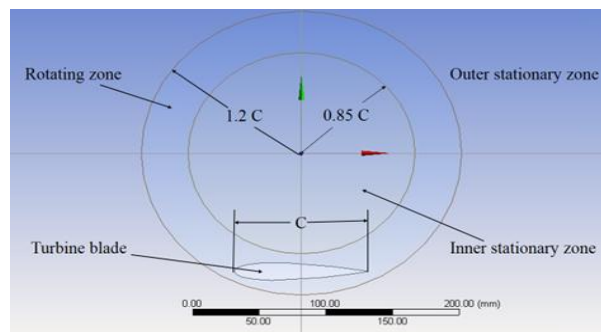
2. Numerical model development

ANSYS FLUENT provides the opportunity to solve both

steady state and transient flow analyses with a variety of turbulence modeling. Continuity equation and Navier Stokes equation are solved in all CFD analysis, and in compressive flow or heat transfer cases. A numerical model was developed for this simulation, where the governing equations were employed to describe the flow over the turbine. Continuity and momentum equations were included in the models the model as the model neglects heat transfer. All the governing equations are described in the literature [16].

3. Computational set up

The computational domain was constructed of two different zones, namely, stationary zone and rotating zone including the turbine blade [17]. The rotating zone, generated bi-directionally from the blade surface resulting in an annulus shaped zone, rotates at a



predefined angular velocity as shown in Fig.1. The square shaped domain dimension is 50C by 50C, based on chord length (C) and the center of the rotating zone is placed at the middle of the square, which is also chosen by Mohamed [16]. Before finalize the domain, different domain sizes were taken and the domain independence test was done.

Fig.1 Domain of numerical analysis

Different sizes of unstructured mesh were employed in this analysis, combining element size of 0.003 mm near the blade for precisely analyzing the flow characteristics and 0.008 mm further from the blade. 20 inflation layers were used with 5 mm thickness in the vicinity of the blade surface to better resolve the boundary layer as illustrated in Fig.2. The selected node and element numbers were 1232362 and 2459030, respectively, after executing grid independence test. The combined grid was chosen instead of single grid to reduce the complexity of the mesh generation. The similar technique was employed in the literature [17, 18, and 19] and good agreements with the measurements were shown. The stationary and rotating zones were linked via the sliding interface boundary condition.

Velocity inlet and pressure outlet boundary conditions were used at the upstream and downstream section, respectively, and symmetry condition was used at the other two sides to reduce the computational effort as done

by Castelli [20, 21]. The blade was placed in the rotating zone that can rotate with the rotating zone of the same angular velocity between the stationary zones. No slip wall is set as the boundary condition on the blade surface.

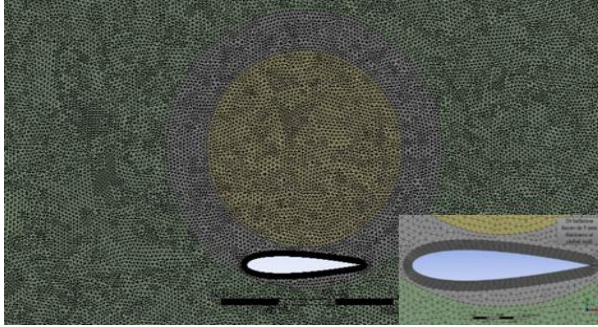


Fig.2 Generated mesh around the domain

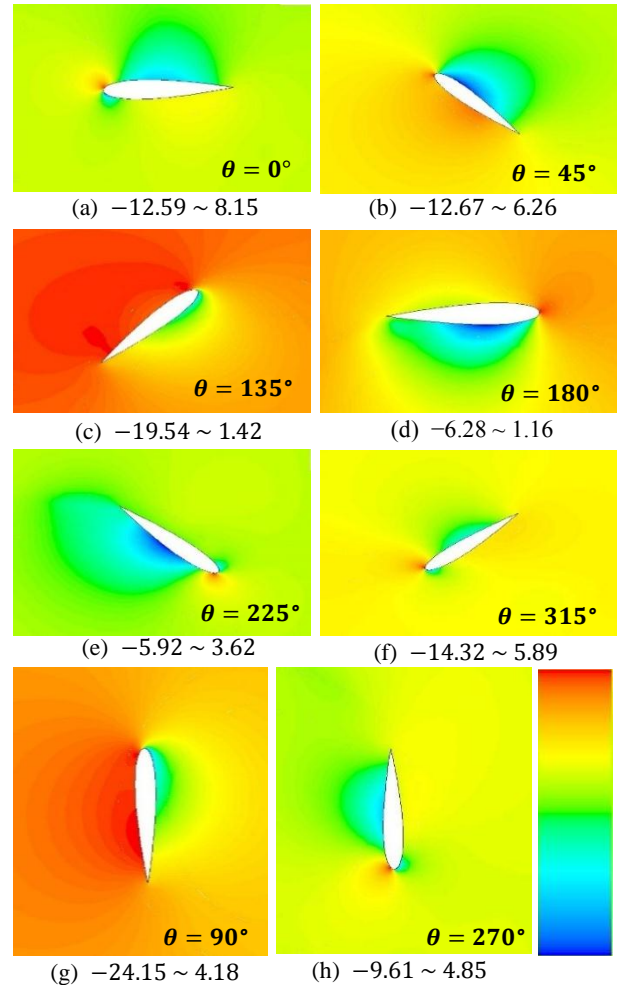
To capture the flow phenomena around the blade precisely, as minimal as 0.005 time step size was used after time independence verification. The turbine blade was set with an initial clockwise rotation and the air was allowed to flow around the turbine blade at a known velocity (2.5 m/s). Due to wind velocity, a net torque was developed for the combined effect of the air kinetic energy and the blade rotation. The normal and tangential force as well as the power had been calculated from the developed lift and drag force on the blade at each azimuthal position. Realizable $k-\epsilon$ turbulence model, referred by Mohammed [16], was used for rotating zones due to improved performance in flow circulation, strong pressure gradients, flow separation, and non-reliance on an assumed relationship between the Reynolds stress tensor and the strain rate tensor. Simple pressure based solver was selected along with second order implicit transient formulation. All solution variables were solved via the second order upwind discretization scheme that is also followed by Bangga [17]. Scalable wall function was used and $Y^+ \geq 11.126$ was ensured for the analysis.

4. CFD results

The simulations were carried out for 10 blade revolutions and the last three revolutions were extracted and averaged which is also done by Bangga [17]. Flow characteristics around the blade are observed and different types of vortex, generated for dynamic stall and the blade vortex interaction, are analyzed. The tangential (F_T) force, normal (F_N) force and the average power coefficient for different tip speed ratios had been calculated from the simulation data.

4.1 Flow field analysis of DWT

Flow characteristics such as pressure coefficient contour, velocity contour and streamline has been determined after every 45° interval of azimuthal angle (θ) in the analysis. Pressure coefficient is a dimensionless number that describes the relative pressure throughout a flow field and is defined by, $C_p = \frac{P - P_\infty}{1/2 \rho_\infty V_\infty^2}$ [22]. It is a vital factor for wind turbine aerodynamics which causes a significant change in the lift and drag as well as the power generation. It is observed from **Fig.3(a)** pressure at the upper surface of the blade is less than the lower surface at the beginning of the turbine rotation when $\theta = 0^\circ$. Air strikes at the turbine tip and



maximum pressure occurs there which is called the stagnation point. Velocity at the upper surface is higher than the lower surface as shown in **Fig.4(a)**. Theoretically, no lift force is generated at

Fig.3 Contour of pressure coefficient with different azimuthal angle θ at 2.5 m/s wind velocity and tip speed ratio 2. The minimum and maximum values of the color legend are mentioned below the figure.

this position of the blade. Flow separates from the trailing edge and a negative (anticlockwise) vortex is visible at the lower surface **Fig.5 (a)**. The more the turbine rotates the more flow separation starts from the leading edge and Stall formation occur after the flow

separation. Maximum pressure occurs at the lower surface at $\theta = 45^\circ$ where the air strikes **Fig.3(b)**. Pressure at upper surface is lower than the lower surface. Velocity near the tip is very high from where the flow separates. Velocity at the upper surface is greater than the lower surface according to the Bernoulli equations as illustrated in **Fig.4(b)**. A positive (clockwise) trailing edge vortex (TEV) forms at the lower surface of the blade **Fig.5(b)**. High pressure drag occurs at the upstream of the blade at $\theta = 90^\circ$ due to high air kinetic energy as shown in **Fig.3(g)**. Separation occurs from both the leading and the trailing edge of the blade and Maximum velocity occurs at the leading edge of the blade **Fig.4(g)**. Positive vortex occurs at the middle of the upstream of the blade and at the downstream near the blade as observed in **Fig.5 (g)**. Flow separations occur both from the leading edge and the trailing edge at $\theta = 135^\circ$. A positive TEV is visible

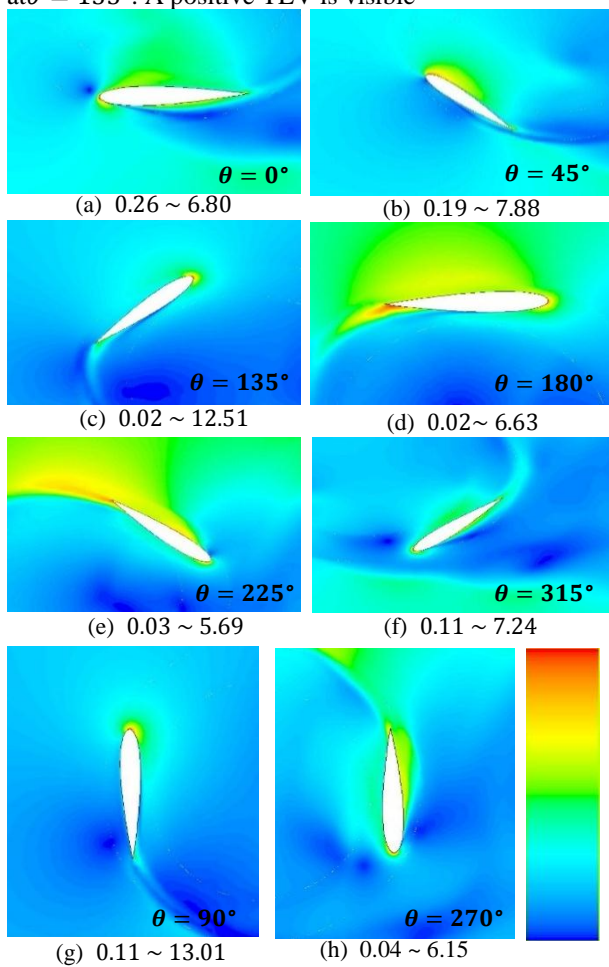


Fig.4 Contour of velocity profile with different azimuthal angle θ at 2.5 m/s wind velocity and tip speed ratio 2. The minimum and maximum values of the color legend are mentioned below the figure.

at this position which tends to separate **Fig.5(c)**. Pressure is higher at the upstream than the downstream of the blade and maximum velocity occurs at the leading-edge **Fig.3(c)**. Another negative vortex (LEV) formation starts at the leading edge of the blade due to the

dynamic stall (DS). Low pressure occurs below the blade and maximum pressure is at the leading edge of the blade at $\theta = 180^\circ$ **Fig.3(d)**. Velocity at the trailing edge is maximum and higher velocity occurs at the upper surface than the lower surface of the blade **Fig.4(d)**. Different types of vortex are visible at this position of blade. Positive LEV and TEV and another negative vortex are visible at a little distance from the blade as shown in **Fig.5(d)**. The lower pressure zone does not separate from the lower surface of the blade at $\theta = 225^\circ$ **Fig.3 (e)** due to the high speed of the turbine blade. Velocity at the trailing edge is higher than another zone as illustrated in **Fig.4(e)**. Different negative vortices are visible near the blade's leading edge and trailing edge due to the dynamic stall and blade vortex interaction **Fig.5(e)**. Pressure at the leading edge is maximum at $\theta = 270^\circ$ **Fig.3 (h)** and velocity at the downstream is higher than the upstream **Fig.4(h)**. Flow separation occurs from both the leading and the trailing

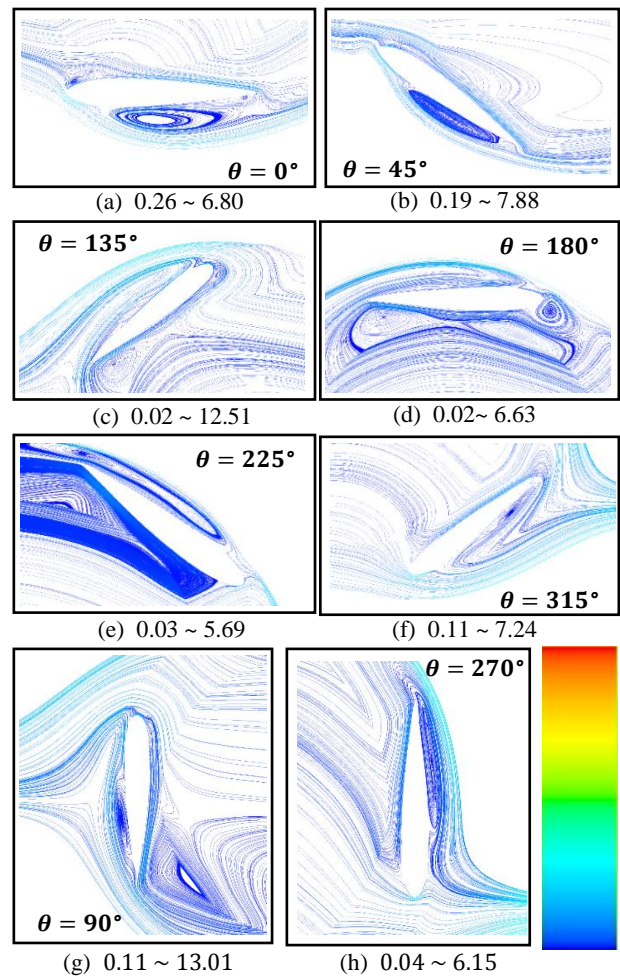


Fig.5 Contour of stream line with different azimuthal angle θ at 2.5 m/s wind velocity and tip speed ratio 2. The minimum and maximum values of the color legend are mentioned below the figure.

edge and a small negative TEV is formed and tends to separate from the blade **Fig.5(h)**. Pressure at lower

surface of the blade is greater than the upper surface and maximum Pressure occur at the blade tip at $\theta = 315^\circ$ as shown in **Fig.3 (f)**. The previously formed TEV becomes smaller. Flow separates from both the leading edge and the trailing edge and reattachment occur at a little distance from the blade **Fig.5(f)**. In the presence of laminar-turbulent transition, flow may reattach in such a way that, initially laminar boundary flow may separate because of an adverse pressure gradient. Then the flow becomes strongly unstable and hence turbulent. Hence, it reattaches further downstream because of the stronger resistance of turbulent boundary-layer flow against separation. After the cycle complete the flow phenomena repeats as the turbine come to a steady state.

4.2 Tangential (F_T) and Normal (F_N) force

The tangential and normal forces vary periodically after the 7th revolution of the rotor blade in the simulation. Both the forces are proportional to the tip speed ratios. Tangential force occurs due to the wind flow tangent to the blade surface whether normal force occur perpendicular to the blade. Lift and drag forces were calculated from the lift (C_L) and drag (C_D) coefficient and then tangential and normal forces were calculated from the lift and drag forces.

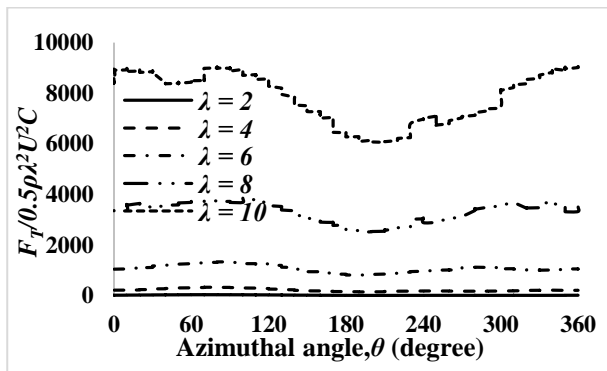


Fig.6 Variation of Tangential Force with Azimuthal Angle for different Tip Speed Ratios

It is observed from **Fig.6** that, tangential force in the total cycle is positive. F_T increase from $\theta = 0^\circ$ to $\theta = 90^\circ$ and then decreases for the generation of a vortex (TEV) at the trailing edge. As the TEV stays till $\theta = 200^\circ$ the tangential force tends to decrease. When the TEV separates, force starts increasing and continues for the rest of the cycle. It is discerned that the tangential force decreases due to the TEV.

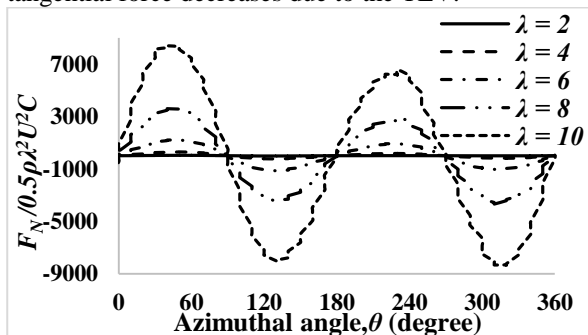


Fig.7 Variation of Normal Force with Azimuthal Angle for different Tip Speed Ratios

The normal force around the blade is zero when the turbine is at $\theta = 0^\circ$ as illustrated in **Fig.7**. However, F_N starts increasing with the increment of the azimuthal angle and gain a maximum value at $\theta = 45^\circ$. Then F_N tends to decrease till $\theta = 135^\circ$ and from $\theta = 90^\circ$ the value of the force become negative. However, F_N starts increasing at $\theta = 135^\circ$ up to $\theta = 225^\circ$ and from $\theta = 180^\circ$ the values become positive. Again the force decrease till $\theta = 315^\circ$ and at $\theta = 270^\circ$ the value becomes negative. Finally F_N increase for the rest of the cycle. For the variation of azimuthal angle with the flow direction the normal forces show these natures. It is observed that F_N is positive at the 1st and the 3rd quarter and the rest of the cycle F_N is negative.

4.3 Angle of attack (α)

The angle of attack varies periodically with the azimuthal angle (θ) by, $\alpha = \tan^{-1} \left[\frac{\sin \theta}{(\lambda + \cos \theta)} \right]$. The magnitude of α change as the sine curve as illustrated in **Fig.8**.

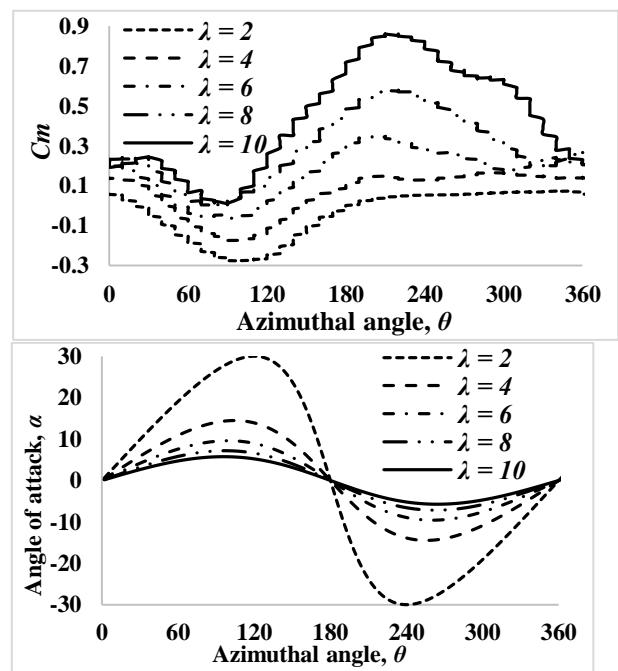


Fig.8 Variation of angle of attack with azimuthal angle at different tip speed ratio

4.4 Torque coefficient (C_m)

Torque/moment coefficient (C_m) is varying periodically with the azimuthal angle (θ). Torque coefficient is decreasing up to $\theta = 90^\circ$ but after that C_m increasing

and attain a maximum value between $\theta = 180^\circ$ and $\theta = 240^\circ$ as shown in **Fig.9**.

Fig.9 Variation of moment coefficient with azimuthal angle at different tip speed ratio

4.5 Power coefficient

Power coefficient is the ratio of the generated output power (P) to the theoretical input power (P_{in}). As the turbine rotates clockwise direction the negative tangential force (F_T) generate the positive power which can be defined by, $P = -\omega R F_t$ [17]. The theoretical input power is $P_{in} = \frac{1}{2} \rho A V^3$, where A is the swept area, V is the air velocity and ρ is air density. The variation of power coefficient is similar to the variation of F_T with azimuthal angle. The values of power coefficients are 2.95, 17.42, 53.14, 128.59, and 267.37 for the tip speed ratios which indicate that average power coefficient is gradually increasing with the tip speed ratios. Variation of average power with the tip speed ratio follows 2nd order polynomial curve as shown in **Fig.10**.

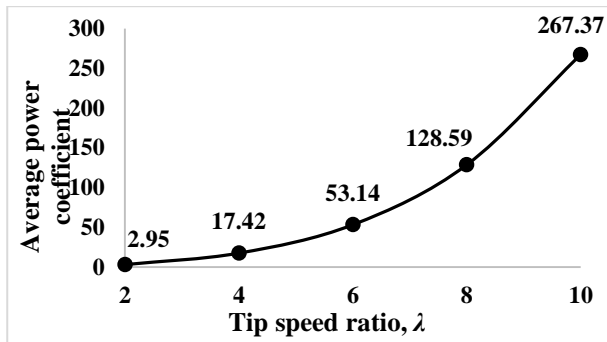


Fig.10 Average power coefficient at different tip speed ratios

5. Conclusions

Numerical analysis has been carried out to study a single-bladed Darrieus wind turbine at different tip speed ratios (2, 4, 6, 8, 10). The studied turbine blade was constructed of NACA 0015 airfoil profile and operating under the dynamic stalled condition. Investigation of the flow characteristics around the bladed surface were highlighted as the main focus of the paper. The tangential and normal force and the average power coefficient had been calculated. Moreover, the torque coefficient around the blade was determined. It is observed that positive and negative vortices generate around the blade surface as a consequence of dynamic stall. As a result, pressure varies considerably that affect the tangential forces as well as power production. The forces and the power coefficients, varying positively and negatively with the azimuthal angle, are periodic and proportional to the tip speed ratios. The average power coefficients at the steady state are positive which indicate that the turbine can produce net positive power.

NOMENCLATURE

λ : tip speed ratio

C_p : pressure coefficient
 F_T : tangential force, N
 F_N : normal force, N
 C_m : torque coefficient

REFERENCES

- [1] Batista, N. C., Melício, R., Mendes, V. M., Figueiredo, J., & Reis, A. H. (2013, April). Darrieus Wind Turbine Performance Prediction: Computational Modeling. In *Doctoral Conference on Computing, Electrical and Industrial Systems* (pp. 382-391). Springer, Berlin, Heidelberg.
- [2] Ponta, F. L., Seminara, J. J., & Otero, A. D. (2007). On the aerodynamics of variable-geometry oval-trajectory Darrieus wind turbines. *Renewable Energy*, 32(1), 35-56.
- [3] Chaichana, T., & Chaitep, S. (2010). Wind power potential and characteristic analysis of Chiang Mai, Thailand. *Journal of mechanical science and technology*, 24(7), 1475-1479.
- [4] Bishop, J. D., & Amaratunga, G. A. (2008). Evaluation of small wind turbines in distributed arrangement as sustainable wind energy option for Barbados. *Energy Conversion and Management*, 49(6), 1652-1661.
- [5] Islam, M., Fartaj, A., & Ting, D. S. K. (2004). Current utilization and future prospects of emerging renewable energy applications in Canada. *Renewable and Sustainable Energy Reviews*, 8(6), 493-519.
- [6] Bhutta, M. M. A., Hayat, N., Farooq, A. U., Ali, Z., Jamil, S. R., & Hussain, Z. (2012). Vertical axis wind turbine—A review of various configurations and design techniques. *Renewable and Sustainable Energy Reviews*, 16(4), 1926-1939.
- [7] Castelli, M. R., & Benini, E. (2011, September). Effect of blade thickness on Darrieus Vertical-Axis Wind turbine performance. In *CSSim 2011, 2nd International Conference on Computer Modelling and Simulation* (pp. 5-7).
- [8] Castelli, M. R., Ardizzon, G., Battisti, L., Benini, E., & Pavesi, G. (2010, January). Modeling strategy and numerical validation for a Darrieus vertical axis micro-wind turbine. In *ASME 2010 International Mechanical Engineering Congress and Exposition* (pp. 409-418). American Society of Mechanical Engineers.
- [9] Ferreira, C. S., Bijl, H., Van Bussel, G., & Van Kuik, G. (2007). Simulating dynamic stall in a 2D VAWT: modeling strategy, verification and validation with particle image velocimetry data. In *Journal of physics: conference series* (Vol. 75, No. 1, p. 012023). IOP Publishing.
- [10] Simao Ferreira, C., Van Bussel, G., Van Kuik, G., & Scarano, F. (2007, January). 2D PIV visualization of dynamic stall on a vertical axis wind turbine. In *45th AIAA Aerospace Sciences Meeting and Exhibit* (p. 1366).
- [11] Vassberg, J., Gopinath, A., & Jameson, A. (2005). Revisiting the vertical-axis wind-turbine design using advanced computational fluid dynamics. In *43rd AIAA Aerospace Sciences Meeting and Exhibit* (p. 47).
- [12] El Chazly, N. M. (1993). Static and dynamic analysis of wind turbine blades using the finite element method. *International journal for numerical methods in engineering*, 36(16), 2791-2804.
- [13] Castelli, M. R., Englaro, A., & Benini, E. (2011). The Darrieus wind turbine: Proposal for a new performance prediction model based on CFD. *Energy*, 36(8), 4919-4934.
- [14] Castelli, M. R., & Benini, E. (2012). Effect of blade inclination angle on a Darrieus wind turbine. *Journal of turbomachinery*, 134(3), 031016.
- [15] Wind Turbine Tip Speed Ratio | REUK.co.uk". www.reuk.co.uk. Retrieved 14 May 2017

- [16] Mohamed, M. H., Ali, A. M., & Hafiz, A. A. (2015). CFD analysis for H-rotor Darrieus turbine as a low speed wind energy converter. *Engineering Science and Technology, an International Journal*, 18(1), 1-13.
- [17] Bangga, G., Hutomo, G., Wiranegara, R., & Sasongko, H. (2017). Numerical study on a single bladed vertical axis wind turbine under dynamic stall. *Journal of Mechanical Science and Technology*, 31(1), 261-267.
- [18] Qin, N., Howell, R., Durrani, N., Hamada, K., & Smith, T. (2011). Unsteady flow simulation and dynamic stall behaviour of vertical axis wind turbine blades. *Wind Engineering*, 35(4), 511-527.
- [19] Hutomo, G., Bangga, G., & Sasongko, H. (2016). CFD studies of the dynamic stall characteristics on a rotating airfoil. *Applied Mechanics and Materials*, 836, 109-114.
- [20] Castelli, M. R., Englaro, A., & Benini, E. (2011). The Darrieus wind turbine: Proposal for a new performance prediction model based on CFD. *Energy*, 36(8), 4919-4934.
- [21] Castelli, M. R., Dal Monte, A., Quaresimin, M., & Benini, E. (2013). Numerical evaluation of aerodynamic and inertial contributions to Darrieus wind turbine blade deformation. *Renewable Energy*, 51, 101-112.
- [22] Anderson Jr, J. D. (2010). *Fundamentals of aerodynamics*. Tata McGraw-Hill Education.

Environmental Impact of Nuclear Power Plant (Rooppur Nuclear Power Plant) on Third World Country like Bangladesh

Md. Nesar Ali^{1}, Md. Ridwan Ullah² and Shuva Sarkar³*

^{1,3}Department of Mechanical Engineering, Chittagong University of Engineering & Technology, Chittagong-4349, BANGLADESH

²Department of Electrical & Electronics Engineering, Khulna University of Engineering & Technology, BANGLADESH

ABSTRACT

Nuclear power is the use of nuclear reactions nuclear that release nuclear energy to generate heat which most frequent is then used in steam turbines to produce electricity in a nuclear power plant. Bangladesh first conceived building a nuclear power plant in 1961. Bangladesh Atomic Energy Commission was established after independence in 1973. The country currently operates a TRIGA research reactor at the Atomic Energy Research Establishment in Savar. More recently, in 2001 Bangladesh adopted a National Nuclear Power Action Plan. On 24 June 2007, Bangladesh government announced plan to build a Nuclear Power Plant to meet electricity shortage. In May 2010, Bangladesh entered into a civilian nuclear agreement with the Russian Federation. This research paper also deals about the safety aspects of this power plant & RNPP Project Timeline, Overall Safety Management including Effluent treatment and Human safety & Protection from external impacts as well.

Keywords: Nuclear Power, Atomic energy, Electric Energy, RNPP Project Timeline, Safety Management and Radio-Active Waste Management of Nuclear power plant.

1. Introduction

Nuclear energy is the abundant source of heat energy which can be transferred into many useful form of energy like Electrical energy or Electricity. The heart of nuclear energy Uranium was discovered in 1789 by Martin Klaproth, a German chemist, and named after the planet Uranus. Nuclear provides about 6% of the world's energy and 13–14% of the world's electricity.^[1] U.S., France and Japan together account for about 50% in nuclear generated electricity. The IAEA (International Atomic Energy Agency) reported there were 439 nuclear power reactors in operation in the world. These nuclear power reactors are operating in 31 countries. The safety record of nuclear power is good when compared with many other energy technologies. Research into safety improvements is continuing. Besides this there are also some major accidents in Nuclear Power plants. The Chernobyl disaster was a nuclear accident that occurred on 26 April 1986 at the Chernobyl Nuclear Power Plant in Ukraine (officially Ukrainian SSR), which was under the direct jurisdiction of the central Moscow's authorities.^[1,5] A proposed site for the first nuclear power plant in Bangladesh, was selected in a remote village called Ruppur in Pabna district in the western zone of Bangladesh near the state of West Bengal in India. The site at Ruppur, downstream of the Hardinge Bridge over the Ganges (Padma), was thus a natural choice for a nuclear power plant. After

receiving the positive response of IAEA, Bangladesh Government decided the Ruppur power plant on its own concept. At last 24th February, 2011 Bangladesh government signed a primary deal with Russia for installing a 2000 MW nuclear power plant at Ruppur in Pabna. By signing the deal, the government launched country's first Nuclear Power Plant project (NPP) which would be completed in 2017-18 at the cost of US\$ 1.5 to 2 billion.

2. Theoretical Redaction

Ruppur Nuclear Power project conceives in 1961 to meet the deficiency of future electric shortage. A number of feasibility studies had done before the liberation war of Bangladesh. After the liberation war selected site was taken for nuclear power plant project in Ruppur, Pabna. The selected land for the plant was 103.5 ha and the land for the rehabilitated people was 12.15 ha. There were three different projects approved by National Economic Council. They were 70MW in 1963, 140MW in 1966 and 200MW in 1969. Initial negotiations started in the early 1960s with USAID for a 70 MW nuclear power Plant at Ruppur in 1963. As time passed, the reactor vendors were changed, the size of the power plant was increased and some feasibility reports were prepared, but no contract was signed. It is because the government of Pakistan was not concerned about the project. By this time in 1965 the contract for the con-

struction of a 125 MW Pressurized Heavy Water Reactor(CANDU) in Karachi in West Pakistan, was signed with Atomic Energy of Canada Ltd. (AECL) without any feasibility study, even though there was a cabinet decision to build the first nuclear power plant in Pakistan at Ruppur.^[2] Several senior engineers and the Project Manager of the Ruppur Nuclear Power Project were transferred to the Karachi Nuclear Power Plant (KANUPP), thus crippling the Ruppur project. In 1968, PAEC received a proposal from V/o Techno prom export of Moscow to supply a 400 MW Pressurized Water Reactor (PWR) nuclear power plant with two turbines of 200MW each for Ruppur. At the same time a Beigial firm submitted a project proposal for a 200MW PWR plant in 1969.This offer appeared to be more attractive than the Russian one in view of the small size of the grid in the western zone of East Pakistan and some unresolved safety issues of the Russian reactor. It may be mentioned here that the proposed Russian reactor did not have any containment building, an essential safety feature designed to contain any release of radioactivity to the atmosphere in case of a nuclear accident. All the terms and conditions of the supply, construction and erection of the nuclear power plant were finalized with WENESE and the contract was due to be signed in early 1971.But after the liberation war the project was not in service due to the effect of after war financial crisis. A French consulting firm started a feasibility study in 1977 and finished it in 1978 with a conclusion that Ruppur project is suit-able for 125 MW Reactor. The contract was signed in 1979.The executive committee of national economic council gave approval of 125 MW project. But the funding source from Saudi Arabia was failed to finance the project due to some reasons. Latter on from 1987-1988 M/S Lahmeyer of Germany and M/S Motor Columbus of Switzerland conducted the latest study and unfortunately this project was also failed. After receiving the positive response of IAEA, Bangladesh Government decided the Ruppur power plant on its own concept. At last 24th February, 2011 Bangladesh government signed a primary deal with Russia for installing a 2000 MW nuclear power plant at Ruppur in Pabna.

3. Methodology

3.1 Reactor Coolant System Analysis:

The reactor coolant system removes the heat from the reactor core by coolant circulation in a closed circuit and provides heat transfer to the secondary side. The reactor coolant system comprises a reactor, a pressurizer and four circulation loops, each one comprising a steam generator, reactor coolant pump set and main coolant pipelines that provide the loop equipment-to-reactor connection.

3.2 Reactor Core and Fuel Design:

The reactor cores contain 163 fuel assemblies (FA). The FAs are intended for heat generation and its transfer from the fuel rod surface to coolant during the design service life without exceeding the permissible design limits of fuel rod damage. The FAs are 4570 mm high (nominal value). When the reactor is in the hot state the height of the power generating part of the fuel rod is 3750 mm. Each FA contains 312 fuel rods. The FA skeleton is assembled of 18 guide channels, 13 spacer grids welded to them, an instrumentation channel and a support grid. The fuel rod cladding is a zirconium alloy tube. Sintered UO₂ pellets with a 5% (4.95±0.05) maximum enrichment are stacked inside the cladding. The average linear heat rate of a fuel rod is 167.8 W/cm.^[5, 13]

3.3 Nuclear Fuel Storage and Handling Systems:

The nuclear fuel storage and handling system complex& complicated system which is a set of systems, equipment and components designed for nuclear fuel storage, loading, unloading, monitoring and transfer. The complex comprises a number of systems and equipment to implement all the fuel handling procedures on the site.

3.4 Reactor Type:

This is a pressurized water reactor. Pressurized Water Reactors keep water under pressure so that it heats, but does not boil. This heated water is circulated through tubes in steam generators, allowing the water in the steam generators to turn to steam, which then turns the turbine generator. Water from the reactor and the water that is turned into steam are in separate systems and do not mix.This reactor type consists of Steam Generator, feed water supply and distribution systems, distribution perforated plate, submerged perforated plate, chemical feeder, reactor Coolant Pump, main coolant pipeline, a vertically positioned pressurized cylindrical vessel with elliptic bottoms, auxiliary systems (pneumatic valves) and Alternative Fuel like MOX (Mixed Oxide) fuel.^[3]

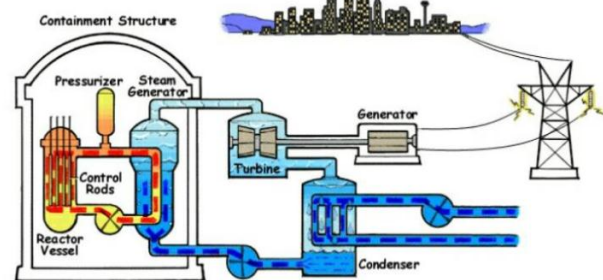


Fig 1: Nuclear power plant using pressurized water reactor

3.5 Spent Fuel (Sf) and Sf Handling Schedule:

Spent fuel is taken out of the reactor to be installed for storage in the spent fuel pond. It is located in the reactor hall inside the containment close to reactor cavity. During reactor refueling the fuel cooled in the spent fuel pond is taken to the spent fuel storage. The spent fuel storage is designed for dry storage on the NPP site in double purpose casks designed both for transport and storage. The spent fuel storage tank is designed for long-time storage of the spent fuel accumulated for 10 years of operation of two units with a possibility for the capacity of the building to be expanded in the future to keep the fuel accumulated during the Unit service life.^[9]

4. Turbine-Generator Systems:

4.1 Turbine Generator:

Turbine is a single-shaft five-cylinder set and comprises a double-flow high pressure cylinder (HPC) and four double-flow low pressure cylinders (LPC). Without the generator the turbine is 52.3 m long, and with the generator it is 74.5 m long. The schematic thermal diagram of the turbine plant comprises four stages of low pressure heaters, a deaerator, and two stages of high pressure heaters. The main parameters of the turbine plant operation under nominal conditions with reactor plant thermal power 3212 MW are presented in Table 1.

Table 1: Main parameters of the turbine plant operation

Parameter	Value
Nominal pressure of steady state conditions, MPa	16.1
Nominal temp. of steady state conditions, °C	347.9
Design pressure(gauge pressure), MPa	1764
Design wall temperature, °C	350
Internal diameter, mm	3000
External diameter, mm	3330
Capacity(full volume), m ³	79
Water level of nominal power operation, m ³	55
Water level under steady state conditions, m	8.17±0.15
Working medium	Steam & water; N ₂ under heatup/cool-down conditions
Quantity of TEH groups, pcs.	4
Total power of PRZ TEHs, kW	2520

4.2 Feed Water System:

Feed water system is consists of two main parts. They are: Main feed water system (continuous water supply at a rate of 300 – 6480 t/h through the main control feed water valves and at a rate of not less than 350 t/h) and Auxiliary feed water system (anticipated operational occurrences in case of a shutdown and subsequent cool down, under the conditions of loss of normal heat removal through the secondary side).

4.3 Power Supply Systems:

There two accepted electric wiring circuitry proposed in RNPP (**R**uppur **N**uclear **P**ower **P**lant) are the 500 kV switchgear “breaker-and-a-half” scheme and the 220 kV switchgear – two working bus bar systems.

5. Power Plant Safety & Waste Management:

5.1 Safety Requirements & Principles:

The VVER-1200 (AES-2006) plant was designed to meet the Russian general safety requirements issued in 1997, which were consistent with the IAEA’s International Nuclear Safety Group (INSAG) recommendations. Thus all new VVER-1200 plants under construction already have design features that take fully into account the main “Fukushima lessons learned”, including: long term cooling of reactor core without electrical power, long term decay heat removal that does not rely on primary ultimate heat sink, protection of reactor containment integrity with dedicated systems after a core meltdown accident, the inherent-safety principle, that is, the ability of the reactor to ensure safety based on natural, feedback processes and characteristics and defense in depth principle, that is, use of successive barriers preventing the release of ionizing.^[4]

5.2 Provision of Fundamental Safety Functions:

Reliable provision of the three fundamental safety functions has been the leading principle in the design of VVER-1200(AES-2006) plants.

5.3 Control of Reactivity:

All VVER-1200 reactors have a unique safety features, when compared with other PWR types or older VVERs: if the control rods are inserted into the core the reactor will stay in shutdown state even at low temperature over the long term.

5.4 Decay Heat Removal:

In the VVER-1200, decay heat can be removed in three different ways Firstly, by active systems to the main ultimate heat sink or to a separate dedicated “spray pond”. Secondly, by active systems to atmosphere (feed and bleed from steam generators). Finally, by passive systems to atmosphere. On the other hand, passive decay heat removal is an important advanced feature for ensuring safety of the VVER-1200.^[10]

5.5 Containment of Radioactive Material:

Ensuring VVER-1200 containment integrity in the event of these circumstances is based on systems that are completely independent and separated from the

systems that are intended to prevent severe reactor core damage. Containment overpressure is prevented by the **Containment Passive Heat Removal System (CPHRS)**.^[8] Accumulation of hydrogen is prevented by passive hydrogen re-combiners, with some contribution from the core catcher, which is also the main system for elimination of steam explosion, containment bottom penetration and re-criticality of the molten core.

5.6 Radioactive Waste Management:

A complex of spent fuel handling systems was realized in the RP AES-2006 and V-392M design. The in-containment spent fuel storage system is designed to cool the spent fuel taken out of the reactor in order to reduce the former's activity and residual heat to the values that are permissible at transportation. When the service life of a NPP Unit has expired and it is decommissioned, the spent fuel handling equipment is subjected to the procedures that are in preparation stage: removal of spent fuel from the NPP Unit, coolant discharge and reactor and spent fuel pond drying, coolant treatment in the dedicated water purification unit, equipment decontamination as per standard process procedure, At the stage of the Unit preparation for the observation period, equipment conservation at the standard places.^[6]

6. Environmental Impacts:

6.1 Population Density:

The first and major consideration to set a RNPP is the area and density of the people. According to the international law the radius of the area of nuclear power station is 30Km. The area is divided into three circular zone with $3.14(30)^2=2,826\text{Sq Km}$ area. According to the zone, zone-1 is reactor area, zone-2 is security area and zone-3 is for planning disaster. The area of zone-1 is a circular area of 3.14 Sq. Km. This area is only for the people who are working with reactors, others entrance is strictly prohibited. The distance of zone-2 is 5 Km away from the center and the total area of is $3.14(5)^2=78.5\text{ sq. Km}$. This area is prohibited for agriculture and industries and only 3 people can leave per sq. Km that is the total people of that zone will be only 200. The distance of zone-3 is 30 Km from the center.^[7] This 30 Km area must be free of population. If there are more people than there will be obstacles for rescuing the people. Developed countries nuclear power stations are free of population. That is for those reactors among 30Km is free from population. For example if there is an explosion in RNPP like Three Miles Island than people leaving there must be transferred $3.14(40)^2=5024\text{ sq. Km}$ area. So if 1000 people leave

per Sqr Km then almost 1000000 people must be transferred from that area. It is quiet impossible. But the problem can be solved through changing some regulation. According to the international law some changes is applicable depending the situation. For example India has changed some regulation to build their nuclear powerplant.^[12] They have changed the zonal area. They do this because they have the same problem of large population like Bangladesh. But there is a considerable think that as per there total country area the population is to very big. Therefore Bangladesh can their policy can be a little bit safe.

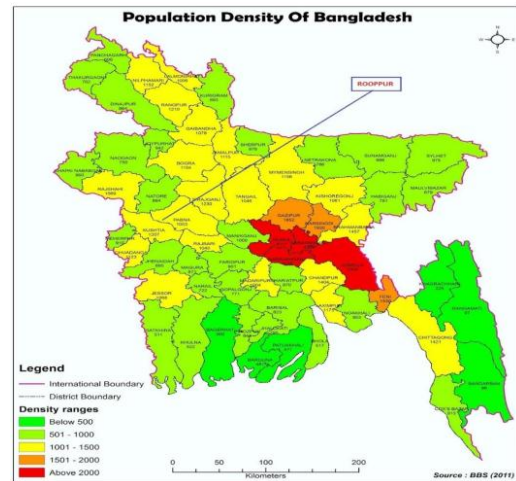


Fig 2: Population density map of Bangladesh

6.2 Earthquake & Natural Disasters:

The second major problem is earthquake and natural disaster. From the experience of Fukushima Daiichi Nuclear Power plant in Japan 9.0 MW earthquake occurred at 14:46 JST on Friday, 11 March 2011 with epicenter near the island of Honshu. It resulted in maximum ground accelerations of 0.56, 0.52, 0.56 g (5.50, 5.07 and 5.48 m/s²) at Units 2, 3 and 5 respectively, above their designed tolerances of 0.45, 0.45 and 0.46 g (4.38, 4.41 and 4.52 m/s²), but values within the design tolerances at Units 1, 4 and 6. When the earthquake occurred, the reactors on Units 1, 2, and 3 were operating, but those on Units 4, 5, and 6 had already been shut down for periodic inspection. Units 1, 2 and 3 underwent an automatic shutdown when the earthquake struck. When the reactors shut down, the plant stopped generating electricity, stopping the normal source of power for the plant. The subsoil investigations, geotechnical, site specific seismic hazard assessment investigation, any heavy structure like RNPP with the design basis H PGA values above 0.2g-0.25g could withstand a 7.5-9.5 Mw earthquake and can damage the RNPP in future. RNPP will be located in Pabna which is

situated in the South-Western Region of Bangladesh and there is no big and wide river which will affect the nuclear power plant even though there is tsunami.^[15]

6.3 Nuclear Waste:

The waste from nuclear power plant in Ruppur is a major consideration. The waste from nuclear power plant will be radioactive and the wastes will be radioactive. Radioactive wastes are wastes that contain radioactive material. Around 20–30 tons of high-level wastes is produced per month per nuclear reactor. There are some 65,000 tons of nuclear waste now in temporary storage throughout the U.S., but in 2009, President Obama “halted work on a permanent repository at Yucca Mountain in Nevada, following years of controversy and legal wrangling”. There are three types of waste. High-level, Mill Tailings and Low level waste. Among these high level waste is most dangerous. During fission, very harmful radiation rays are released. The most harmful of which are gamma rays. When the human body is exposed to radiation, it can cause tumors and can do extreme damage to the reproductive organs. For this reason, problems associated with radioactivity can be passed on to the victim’s children as well. That is why radioactive waste produced by nuclear power plants is so toxic & dangerous. Radioactive fission products could pose a direct radiation hazard, contaminate soil and vegetation, and be ingested by humans and animals. Human exposure at high enough levels can cause both short-term illness and death, and longer-term deaths by cancer and other diseases. So it has seen that radioactive waste can cause a great harm in Bangladesh if any disaster is occur in the future nuclear power plant. But there is nothing to be worried about it.^[11] Because there are new waste disposal technologies invented now a days. Bangladesh can use Experimental Breeder Reactor II. A breeder reactor is a nuclear reactor that generates more fissile material in fuel than it consumes. Breeder Reactor II is being developed by Argonne National Laboratory in the US; almost 100% of the transuranic nuclear wastes produced through neutron capture can be caused to fission. Generally, the fission products created have shorter half-lives and are not as dangerous. This reactor, dubbed EBR-II, uses liquid sodium as a coolant, which means that the internal reactor temperature is much, much hotter than that of a normal PWR reactor, which uses water as a coolant. Another advantage of EBR-II (Experimental Breeder Reactor) is that its fuel is not

weapons grade quality. When the transuranic wastes are separated from the other wastes in the spent fuel rods, the resultant mix of isotopes cannot be used in a bomb. Thus, the mix can be used as fuel for EBR-II without a chance of it getting stolen by a terrorist group for use in an explosive device. Breeder reactors “breed” fuel. That is, they are designed to create ^{239}Pu from ^{238}U through neutron capture. This “waste” can then be used as fuel.

7. Conclusion:

At present, Bangladesh is facing energy and power crisis. The natural energy resources of Bangladesh mainly gas, coal and hydro are decreasing very rapidly due to higher population growth. Gas, being the main energy resources of the country is used mainly in three categories: power generation, fertilizer production, and household. According to Patrobangla, it would not possible to supply gas to new power plant after 2011. Due to lack of reserve of gas, government is trying to generate power from coal in large scale. But depending on different type of coal mining, the amount of recoverable coal will be different. For the higher transportation cost, fuel cost and environmental pollution, the coal based power generation is not safe for long term plan.^[14, 15] Also skyrocketing oil price is a major obstacle for power generation. Water head is not available through the country which can solve power shortage by Hydro power plant. Again renewable energy sources of Bangladesh like solar, windmill and traditional biomass could not be able to fulfill the huge power and energy shortage. In that situation nuclear power plant will be a good option. The advantage of nuclear power plant over other options include: absence of greenhouse gases, lower operating cost, less fuel consumption, less sensitivity to fluctuations in the fuel price, cheaper generation cost with respect to higher capacity cost. Bangladesh has gone a long way in getting ready for nuclear power. Manpower has been trained, radiation safety bill has been passed, land for the nuclear power station has been acquired, and many feasibility studies have been made. Energy policy has clearly stated the necessity for energy security and keeps all options for power production.

REFERENCE

- [1] <http://www.world-nuclear.org/info/inf54.html>
- [2] World Nuclear Association. Safety of Nuclear Power Reactors.
- [3] “Explainer: What went wrong in Japan’s nuclear reactors,” IEEE Spectrum. 4 April 2011.
- [4] V. Mokhov, N. Trunov, “VVER reactors: clean and reliable source of energy in the past and in the future,” International Conference on

- Opportunities and Challenges for Water Cooled Reactors in the 21st Century, Vienna, Austria, October 27–30 2009.
- [5] Dan, G. C., Handbook of nuclear engineering, Springer, Germany (2010).
- [6] “The State Atomic Energy Corporation ROSATOM: Russian NPPs under construction,” [7]http://www.rosatom.ru/en/areas_of_activity/npp_design_engineering_construction/russian_npp_under_construction/ (2014)
- [7] “The State Atomic Energy Corporation ROSATOM: NPPs under construction in foreign countries,”
- [8] NEA- OECD: VVER-1000 LEU and MOX Assembly Computational Benchmark: Specification and Results. Nuclear Energy Agency, Nuclear Science, Organization for economic co-operation and development, Paris, France (2002)
- [9] Mollah AS, Rahman MM, Hussain SR (1985) Preoperational background radiation level in and around 3 MW TRIGA Mark II research reactor, Report INST-19/HPRPD-3.
- [10] LEE MH and LEE CW (1997) Distribution and characteristics of ^{239}Pu , ^{240}Pu and ^{137}Cs in the soil of Korea, J. Environ Radioactivity, 1: 1–16.
- [11] Beretka J and Mathew PJ (1985) Natural radioactivity of Australian building materials, industrial waste and by-products. Health Physics, 48(1): 87-95.
- [12] Noordin I (1999) Natural activities of ^{238}U , ^{232}Th and ^{40}K in building materials. Journal of Environmental Radioactivity, 43: 255-258
- [13] http://www.rosatom.ru/en/areas_of_activity/npp_design_engineering_construction/npps_under_construction_in_foreign_countries/ (2014)
- [14] <http://www.poribesh.com>

Prediction of Weld Quality by Artificial Neural Network Modeling of Parameters of MIG Welding Process

Israt Zarin Era*, Dr Nikhil Ranjan dhar

Department of Industrial & Production Engineering, Bangladesh University of Engineering & Technology, Dhaka-1000,
BANGLADESH

ABSTRACT

The study aims to predict the weld quality of MIG welding by Artificial Neural Network Modeling of the process parameters. Due to the lack of any direct analytical mathematical relation among the welding factors, the paper focused on establishing a co-relation among the welding parameters and responses. Tensile strength and Hardness of the welding joints are taken as welding responses. Welding current, welding voltage and wire feed rate are selected among the MIG welding parameters as the inputs to form a multilayer perception (MLP) neural network. The training of the model has been done through Back-propagation (BP) algorithm. The result shows that with the rise of welding current and voltage, the Tensile strength and Hardness of the weld joints have been increased but the best result is obtained at moderate wire feed rate. It is found that the proposed adaptive Artificial Neural Network is capable of mapping the complex relationship among the welding parameters and corresponding weld quality as output.

Keywords: MIG welding, Artificial Neural Network, Multilayer Perception Neural Network, Back-propagation, Welding response.

1. Introduction

Metal joining processes are really very much used processes by the manufacturers now-a-days. Welding is a fabricating process of joining materials which includes basically metal and thermoplastics by fusion of heated and molten materials. Gas Metal arc welding (GMAW) is a welding process in which an electric arc forms between a consumable wire electrode and work piece metals, which heats the work piece metals, causing them to melt and join [12]. Manufacture Engineers often face the problems of process optimization, most of them are multiple response process optimization. And in many manufacturing systems and processes boundary conditions and physical phenomena are so complex that they exceed the current technical capability of system to perform satisfactory analytical or numerical models or approaches which make these problems more complicated [1]. In these cases experimentation is necessary to describe the optimal behavior of the system. One such example of multiple responses is optimization of GMAW parameters. There are lots of tools for optimizing tools for GMAW like Taguchi methods, Response Surface Methods, Artificial Neural networking, Among them Artificial Neural networking is used for more complex problems and reliable solutions.

K. Abbassi et.al studied the effect of MIG welding parameters on the weld bead and shape factor characteristic of bright drawn mild steel specimen of dimensions 144 31 10 mm. The welding current, arc voltage, welding speed, heat input rate are chosen as welding parameters. MIG welding parameters are the most important factors affecting the quality, productivity and cost of welded joint [2]. Metal transfer in MIG welding refers to the process of transferring

material of the welding wire in the form of molten liquid droplets to the work-piece [2,4]. The input variables directly affect the shape factor.

Welding current is the most important variable for welding, because it controls the burn off rate of electrodes, fusion depth and weld geometry [2].

Welding voltage determines the shape of fusion zone and weld reinforcement height. Welding speed is defined as the rate of travel work piece under electrode.

Speed of welding(s) = Travel of electrode/ arc time mm/min. Heat input rate = $(V \times A \times 60) / S$ joules per mm, Where, V is arc voltage in volts, A is welding current in ampere, S is speed of welding in mm/min [2, 11].

Shape Factor is the ratio of Penetration Depth to Weld Width. Width The above factor i.e. arc current, arc voltage and welding speed and their interactions play a significant role in determining the weld bead shape characteristics [9,10].

Process optimization is the discipline of adjusting a process so as to optimize some specified set of parameters without violating some constraint. The most common goals are minimizing cost and maximizing throughput and/or efficiency. This is one of the major quantitative tools in industrial decision making. In their study, Aktepe et.al used Pareto Analysis for determining uncontrollable input parameters of the welding process based on expert views. With the help of these analyses, 9 uncontrollable parameters are determined among 22 potential parameters. Then, the welding process of ammunition is modeled as a multi-input multi-output process with 9 input and 3 output parameters [5]. The study of K. Anand et.al focuses on friction welding process parameter optimization using a hybrid technique of ANN and different optimization algorithms. This optimization techniques are not only for the effective

* Corresponding author. Tel.: +88-01

E-mail addresses: isratzarin1208022@gmail.com

process modelling, but also to illustrate the correlation between the input and output responses of the friction welding of Incoloy 800H. In addition the focus is also to obtain optimal strength and hardness of joints with minimum burn off length [6]. Asif Iqbal et al, investigated the weld bead geometry (front bead width and height, and back bead width and height) is a significant physical characteristic of a welding [7]. Several welding parameters such as welding speed, weld current, voltage, and shielding gas flow rate affect the weld bead geometry [8].

2. Methodology

2.1 Problem Definition

All welding processes are non-linear and highly coupled multivariable systems. The task of determination of weld quality is difficult because the welding process is a complex process with a lack of analytic mathematical description [1]. The present welding theories are inadequate to model the weld quality (penetration, tensile strength and hardness). In addition, not all the process variables affecting the weld quality are known, nor easily quantified, e.g. contamination, heat absorption and environmental conditions. Unfortunately, few of these factors are simply related to weld quality or to one another. It is seldom possible to establish a simple mathematical equation for weld quality as a function of these variables [12]. In order to solve this inherent weld quality complexity, a new tool is required to find an 'equation' to relate these various parameters to determine weld quality.

2.2 Artificial Neural Network

Artificial Neural Network or **connectionist systems** are computing systems inspired by the biological neural system that constitutes animal brains. Such systems learn (progressively improve performance) to do tasks by considering examples, generally without task-specific programming [12].

Artificial Neural Networks (ANN) are programs designed to solve any problem by trying to mimicking the structure and function of our nervous system. An Artificial Neural Network consists of following components-

- A set of processing unit (cell).
- A set of activation unit (inputs) for each unit.
- Connection between every units, generally marked by weights, w_{ji}
- A propagation rule.
- An activation function, $f()$
- A learning rule.
- An environment where the system must operate providing input signals and error signals if required.

The working principle of an artificial neuron is shown in the figure 1-

1. The inputs are the activity of collecting data from the relevant sources. These data are fed to the neural network. A set of synapses (i.e.

connections) brings in activations from other neurons.

2. A processing unit sums the inputs, and then applies a non-linear activation function (which is also often called a threshold or transfer or squashing function). An ANN saves its information in its links and each link has weight (w_{jk}). The weights are constantly varied while trying to optimize the relation between inputs and outputs.
3. An output line transmits the result to other neurons.

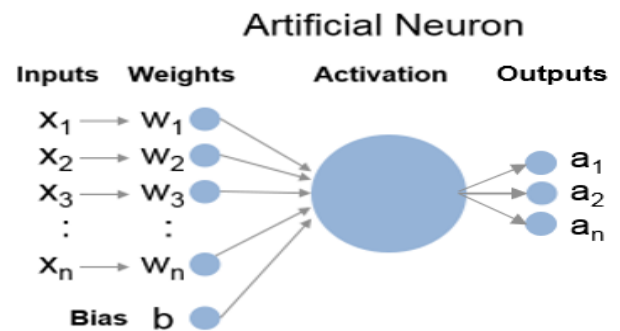


Fig.1 Structure of an Artificial Neuron

2.3 Architecture of Artificial Neural Networking

The architecture of an artificial neural network defines how its several neurons are arranged, or placed, in relation to each other. Training a particular architecture involves applying a set of ordinated steps to adjust the weights and thresholds of its neurons. The network required for our study is constructed with the following components-

Table 1 Architecture of ANN

Type	Multilayer Perception free forward ANN
Input Neurons	Current, Voltage and Wire feed rate
Output Neurons	Tensile strength and Hardness of specimen
Performance function	MSE
Activation function	'relu', 'tanh'
Solver	'lbfgs'
Test function	Test
Software and language	Anaconda Prompt and Python

2.4 Steps of formulating the model

- Using the experimental data as the inputs to train the mode.
- Finding out the smallest mean square error (mse) from input data by altering the combinations of the number of weights, activation function type and iteration number.

- Using the set of weights, activation functions and mean square error the result is predicted by the model.
- The deviation of the predicted values from the real data is determined by graphs.

3. Experimental Investigation

By the present setup of the foundry lab, three parameters of MIG welding were available to vary. These parameters are welding current, welding voltage and wire feed rate. As welding responses tensile strength and hardness of the weld pieces were investigated. For the experimental investigation we have prepared V shaped groove in a square bar.

3.1 Preparation of work piece

After selecting the material types the work piece dimension and types of joint for the experimental welding are fixed. The dimensions are given below:
 Work piece dimension: 200mm × 10mm × 10mm.
 Types of joint: V Type Butt Joint of 45° angle.



Fig.2 Prepared Work-piece.

3.1.1 Process of work piece preparation

After selecting the material and dimensions of the work piece there need to be started to prepare it. The preparation is done by three steps and three types of machines were used here and shown in figure 3.

1. At first the work piece is cut according to their dimension in disc cutter.
2. The grinded the work piece in grinding machine.
3. The aligned the vertical milling machine at 22.5° for cutting the V shape in work piece. Here end mill cutter is used for this operation.



Fig.3 Prepared Work-piece after grinding, surface finishing and milling.

3.2 Data collection

3.2.1 Mean square value

Mean square error (MSE) is the performance function which determines the best solution for the problem from the data.

Table 2 Determination of smallest Mean Square Value.

Serial	a	b	c	d	Activati on	Iterations	MSE
1	10	5	5	10	relu	100	38.96712
2	5	5	5	15	relu	100	44.202
3	5	5	5	5	relu	200	37.670
4	5	5	5	5	relu	100	33.67
5	5	5	5	5	relu	300	33.51

Here a,b,c,d denote the weights. And the smallest mse value obtained is 30.94 with weights (10, 5, 5, 10) and activation function relu with 260 iterations.

3.2.2 Welding Responses

Welding responses are those who can show the result of the effect of the varying of the parameters. In this experimentation, only three parameters were possible to vary within their range. As mentioned earlier they are welding current, arc voltage and wire feed rate. And the two welding responses are considered. They are **Tensile Strength** and **Hardness**. In current setup, welding current was varied from 100amp-120amp, voltage was (20V-25V) and Welding speed (8cm/m-14 cm/m).

Table 3 Data collection for Tensile Strength.

Sample number	current ampere	voltage volt	wire feed rate cm/min	output Tensile Strength MPa	Predicted values MPa
1	100	20	8	289.5	295.599
2	100	20	12	315.7	316.299
3	100	20	14	303.8	306.721
4	110	20	8	389.65	384.647
5	110	20	12	404.3	404.744

Table 4 Data collection for Hardness.

Sample no	current ampere	Voltage volt	wire feed rate cm/min	Hardness HRB	Predicted values HRB
1	100	20	8	69	68.579
2	100	20	12	73	72.858
3	100	20	14	70.5	69.512
4	110	20	8	389.65	384.647
5	110	20	12	404.3	404.744

All data from the experiment of Tensile Strength and Hardness test of the weld joints weren't possible to be shown in the Table 3 and Table 4 for convenience of the paper. They are shown in the graphs later.

3.2.3 Graphical representation of the deviation of the predicted value from the actual value for tensile strength and hardness

Almost forty samples were used to check the real obtained values for weld responses and real and predicted values are plotted against sample numbers.

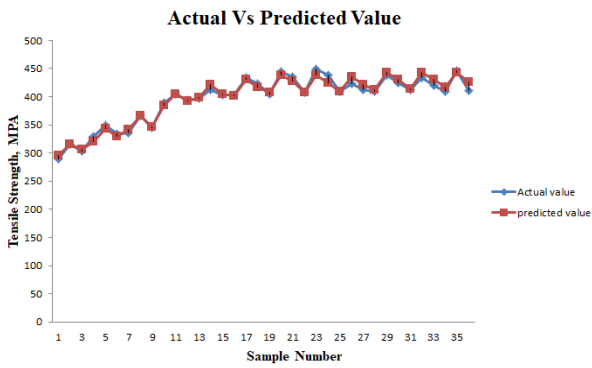


Fig.4 Deviation of predicted values from actual values (Tensile strength)

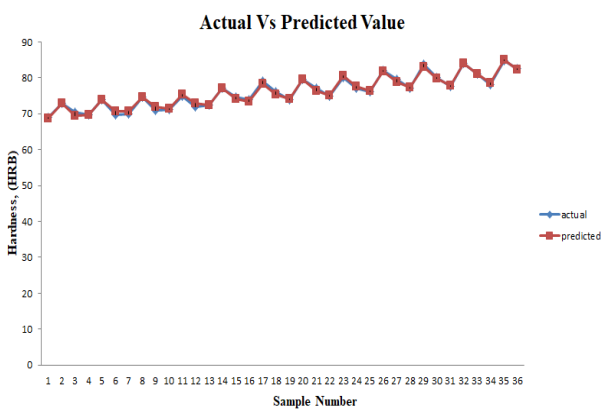


Fig.5 Deviation of predicted values from actual values (Hardness)

In Fig.4 and Fig.5 the blue lines represent the actual values and the red ones do the predicted values. It's clearly seen that the values of both real and predicted results are rising as the sample numbers. Because from the tables containing the values it gets to know that the welding current and voltage have been increased by the way the sample numbers go forward. But fluctuations happened because in these experiments three varying wire feed rates e.g. 8, 12 and 14 cm per minute have been used. And the result is satisfactory when the moderate wire feed rate was in use. So it is clearly evident that with the rise of the welding voltage and current and with a moderate wire feed rate the tensile strength of MIG weld joints increases. And the graph shows a very negligible deviation of the predicted values from the actual ones. In the Fig 3.4, like tensile strength, both the real and predicted values of hardness are plotted against sample numbers. This graph behaved in the same way like tensile strength. But the deviation is more negligible, the line of predicted values almost coincides with the line of real values.

3.2.4 Error Calculation

The differences between the actual and predicted value of are showed in percentage value to demonstrate the error. The percentage of error is showed in the Table 5.

Table 5 The percentage of error (%)

Sample Number	Tensile Strength (%)	Hardness (%)
1	2.1067	1.25
2	0.1897	0.852
3	0.9614	0.0190
4	1.2839	0.734
5	0.1098	0.758

3.2.5 Graphical representation of the percentage of error for tensile strength and hardness.

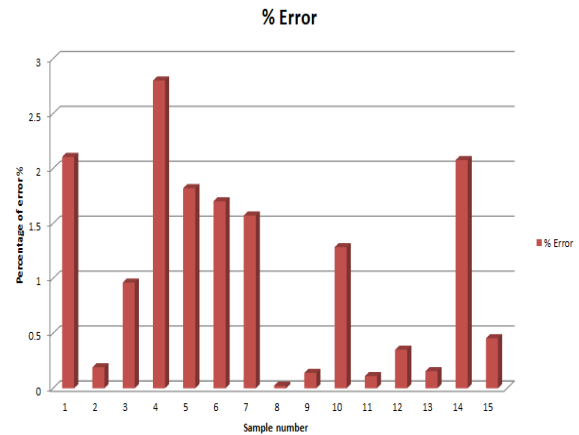


Fig.6 Percentage of error % for Tensile strength.

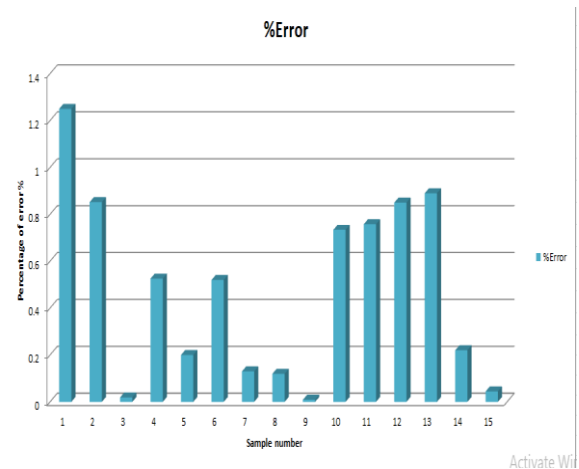


Fig.7 Percentage of error % for Hardness

The figures 6 and 7 show that the accuracy of the model while predicting the results after being trained. The range remains 0.0019%-3.89%.

3.3 Destructive Tests

For finding the welding quality and performance of the welded work piece, two types of destructive test was performed in the laboratory. These are:

- 1) Macro etching tests
- 2) Nick break tests

3.3.1 Macro Etching Test

For this test the work piece need to be prepared. The steps involved in preparation of the work piece are described below:

1. At first grind the work piece in the grinding machine
2. Than shaped the work piece in shaper machine
3. At last finished the surface with surface grinding machine

After preparation of work piece for testing than applied 5% nitrile solution in it so that it can be seen the shape and defects of welding. 5% nitrile solution contains 5% nitric acid and 95% methanol. Than observed the welding with the help of magnifying glass.



Fig.8 at 110 A, 20 V, 8 cm/min



Fig.9 at 110 A, 20 V, 12 cm/min



Fig.10 at 110 A, 20 V, 14 cm/min

Results of the macro Etching tests for figure 8, 9 and 10 are mentioned in Table 6 later.

3.4 Nick break test

This type of testing involves breaking a sample fillet weld that is welded on one side only. The sample has a load applied to its unwedded side, typically in a press, and the load is increased until the weld fails. The failed sample is then inspected to establish the presence and extent of any welding discontinuities. This type of weld inspection can detect such items as lack of fusion, internal porosity, and slag inclusions

To compare the results and of four tests together, three samples keeping welding current 110A, voltage 20 V constant and at the three varying wire feed rates are taken. Thus the optimized conditions for these

parameters are obtained by comparing the results. During the experiments, the defects those are detected are shown in Fig.11.



110 A, 20 V,
8 cm/min

110 A, 20 V,
12 cm/min

110 A, 20 V,
14 cm/min

Fig.11 Nick Break Test.

3.5 Result

The results found from all destructive tests are given bellow-

Table 6 Results of tests

Type of tests	Specimen 1 110A, 20 V, 8cm/min	Specimen2 110A, 20V, 12cm/min	Specimen 3 110A, 20 V, 14 cm/min	Remarks
Tensile Strength	389.65	404.3	395.5	Specimen 2 is better
Hardness test	71.23	75	72	Specimen 2 is better
Marco Etching test	Cracks with burnt areas.	No cracks, only heat affected zones.	Blow holes with cracks.	Specimen 2 is better
Nick break test	Cracks and slag inclusions	No cracks and little spatter	Voids with slag and porosity.	Specimen 2 is better

3.6 Discussion

- It is clearly seen that specimen 2 in each case of having the wire feed rate 12 cm per min has the highest tensile strength and better hardness value.
- In case of Macro Etching test, showing no cracks and only little heat affected zone. And the results of the Nick break test reveal also that at 12 cm per min they have no cracks and little spatter.
- The highest and lowest percent error from the predicted values of the tensile strength and hardness are found 3.89% for Tensile Strength and 0.0019% for hardness tests.

4. Recommendation and Conclusion

4.1 Recommendation

- There are a number of parameters which can be varied for MIG welding. But in our current setup only three parameters i.e. welding

- current, welding voltage and wire feed rate were possible to vary for experimentation.
2. If The number of inputs can be increased than present, the Mean Square Error will be less than the results obtained in this experiment
 3. The available inputs of our current set up (current, voltage and wire feed rate) can provide limited sets of data. If the range of variation could be increased, more data would have been collected.
 4. As we know, Artificial Neural Network Modeling can predict closer results to actual ones only when a huge set of data is available. That's why increasing the size of data can provide a more accurate and reliable prediction than the present model.

4.2 Conclusion

This model was able to demonstrate the successful use of Artificial Neural Network in predicting the weld responses i.e. tensile strength and hardness of the weld joints of mild steel by MIG welding and the result reported are in good agreement with other researches. The mean square error for tensile strength and Hardness obtained are 30.004 and 0.295354 respectively. And the highest and lowest percentages of error among the actual and predicted data are obtained. These values are in good agreement within the range of errors predicted by other researches though they were conducted under different conditions and media. Predicted values show that Tensile strength and Hardness values obtained are in range and can be achieved by combination of certain factors shown in the model. Thus the set of factors have been found which are capable of obtaining quality weld joints.

REFERENCES

- [1] Tay KM. and Butler C., Modeling and optimization of a MIG welding process, a case study using experimental design and neural networks, *Quality and Reliability International*, Vol 13, 61-70, 1997.
- [2] Abbasi K., Alam S. and Dr Khan M.I., An experimental study on the effect of MIG welding parameters on the weld bead shape characteristics, *IRACST-Engineering Science and Technology, An International Journal (ESTIJ)* , ISSN, 2250-3498, Vol 12, No. 4, August 2012.
- [3] Ghazvinloo H.R., A. Raouf H. and Shadfar N, Effect of arc voltage, welding current and welding speed on fatigue life, impact energy and bead penetration of AA6061 joints produced by robotic MIG welding, *Indian Journal of Science and Technology*, Vol. 3 No. 2, pp 156-162, February 2010.
- [4] St. Węglowski M., Huang Y., Zhang Y.M., Effect of welding current on metal transfer in GMAW, *Archives of Materials Science and Engineering*, Vol 33 Issue 1, pp 49-56, September 2008.
- [5] Aktepel, An Artificial Neural Network on welding process control of 155mm Artillery Amunition, *6th*

- International Advanced Technologies Symposium*, 2011.
- [6] Anand K., Kumar B.B., Tamilmannan K., Sathia P., Artificial Neural Network modeling studied to predict the function welding process parameters of Incoloy 800H joints, *Engineering Science and Technology, an International Journal*, Vol 18, Issue 3, Page 394-407, September 2015.
 - [7] Iqbal A., Saeed Khan M., and Mukhtar Sahir H., ANN Assisted Prediction of Weld Bead Geometry in Gas Tunston Arc Welding of HSLA Steels, *Proceedings of the World Congress on Engineering*, Vol I WCE 2011, July 6 - 8, London, U.K, 2011.
 - [8] Kolahan F., Heidari M., A New Approach for Predicting and Optimizing weld bead geometry in GMAW, *World Academy of Science, Engineering and Technology*, 59, pp 138-141, 2009.
 - [9] Raghu Babu G., Murti K. G. K. and Janardhana G. R., An experimental study on the effect of welding parameters on mechanical and microstructural properties of AA 6082-T6 friction stir welded butt joints, *ARPN Journal of Engineering and Applied Sciences*, Vol. 3, No. 5, pp 68-74, October 2008.
 - [10] Abbasi K., Alam S. and Khan M.I., An Experimental Study on the Effect of Increased Pressure on MIG Welding Arc, *International Journal Of Applied Engineering Research*, Dindigul, Vol 1, No 3, pp 22-27, 2010.
 - [11] S. Alam and M.I.Khan, Prediction of Weld Bead Reinforcement Height for Steel using SAW Process Parameters, *International Journal Of Applied Engineering Research*, ISSN 0973-4562, Volume 6, No 15, pp 1857-1871, 2011.
 - [12] Wikipedia

ICMIEE18-248

Comprehensive Hazard Identification and Safety Evaluation for Shahjalal Fertilizer Industry Limited

*Shanzida Sultana Ema**, Anamika Roy, Md Tanvir Sowgath

Department of Chemical Engineering, Bangladesh University of Engineering and Technology, Dhaka, BANGLADESH

ABSTRACT

The objective of the paper was to identify the relative hazard index for all the main ammonia process units of Shahjalal Fertilizer Company limited and calculate hazard area for probable toxic release of the ammonia storage tank. Various indices were extensively used for ranking various units of a chemical process industry on the basis of the hazards they pose of the accidental probability of fires, explosions or toxic release with some restrictions and limitation. So, a new, user-friendly tool for swift yet comprehensive hazard identification and safety evaluation index called Safety Weighted Hazard Index (SWeHI) was introduced for representation of overall comprehensive hazard identification and safety evaluation factors SFCL plant. The Dow chemical exposure index (CEI) was also calculated for the process units handling flammable and toxic materials respectively. The hazard area of the ammonia storage tank for probable toxic release with the atmospheric conditions data of the plant location was also determined using ALOHA software and CEI value. The SWeHI ranking was between 1.74 (NG loading) and 10.61 (primary reformer).

Keywords: hazards, SWeHI, Dow CEI.

1. Introduction

Industrial safety is important as it safeguards human life, especially in high risk industries like ammonia-urea plant operating under high pressure and temperature. The first step in any risk assessment procedure for industrial safety involves hazard identification, or answering the question: what can go wrong [1]? However, hazard identification is easier said than done, and it is becoming more difficult as the complexity and variety of the technologies which pose risk continually increases. Some key facts are needed to understand the process of making a chemical safety assessment. The communication system and tasks within the supply chain are related to the chemical safety assessment [2]. The roots of the hazards, as well as the strategies for reducing them, lie in the man-machine management system that runs any chemical plant and it is not always easy to discover the weaknesses in such a system. The hazards are rarely obvious, or accessible to simple visual inspection, [3] but it is very important to evaluate safety of the plant and surrounding lives and properties. In this paper, hazard identification and safety evaluation for the ammonia process plant of Shahjalal Fertilizer Industry Limited is presented. The best possible indices for the purpose are used for ranking and hazard area for accidental toxic release (ammonia release) such, SWeHI as SWeHI method [4] and Dow fire and explosion index (FEI) [5], Dow chemical exposure index (CEI) [6]. ALOHA software was also used for simulating the hazard area with environmental conditions [7]. The safety measures in industries such as use of pressure valves, flare systems, venting systems, alarms, and emergency shutdowns are to be designed for development of unusual situations during operation at the design stage of any industrial project. It is very important in case of approval of plant design, legal documents and installment of insurance. These are

called means of inherently safer design [8-11]. In spite of that there remains some factors like model inaccuracy, human error, sensitivity of the process etc., which may cause failure of safety systems and accidents. That's why to ensure safety the process industry periodically needs the attention of safety audits [12]. But, how should it be measured that a plant has risk or is sufficiently safer? This is where safety indices come. Different kinds of safety indices are there to rank the safety of process or equipments of any industry, such as Dow fire and explosion index, Dow chemical exposure index, the Mond fire, explosion and toxicity index [13,14], the IFAL index [15], the mortality index [16], HIRA method [17], SWeHI method, extras. There are some safety indices that provides few rapid ranking techniques and databases such as the substance hazard index [18] and the NFPA ranking [19, 20], but they have different applicative sides. Each of them is used for different purpose.

The available indices, including the well-known Dow and Mond indices, and HIRA rank chemical process units mainly works in terms of the hazardous substances and operating conditions associated with the concerned units or process equipment. Most of them do not count in existing safety measures and human communication. Though Dow and Mond indices do consider some factors such as 'offsetting index values' in the case of the Mond Index and 'credits factor' in the case of the Dow index to account for the safety measures existing or planned in the unit [21, 22] but much greater rigorous, accuracy, and precision are needed in quantifying the impact of safety measures on the values of the hazard indices. Besides they are used for different purpose with different calculative method.

The Dow FEI relies on the calculation of a fire and explosion index which is then used to determine fire protection measures and, in combination with a damage

* Shanzida Sultana Ema. Tel.: +88-01954907763

E-mail addresses: emashanzida@gmail.com

factor, to derive the base maximum probable property damage [10]. Obviously, it is used for flammable materials, specially gas and liquid [22].

The Mond index and Dow CEI are used for exposure ranking of toxic materials [11-13]. They have fairly similar calculation procedures. Dow CEI is relative ranking system where the Mond index gives a briefer view of the damage [21].

The IFAL index is too complex for manual calculation and used both to calculate damage due to accidents of major units of a process plant. It used to be the primarily for insurance assessment purposes [23].

This the mortality index is a measure of the lethality which is computed on the basis of the number of deaths per ton of material involved [15].

HIRA method is more systematic, comprehensive and reliable than previous index systems. It provides more brief data on safety matters. Some calculations were done according to this method.

SWeHI provides a 'single frame' view of the industry or the desired process unit the hazards posed by it under a given set of external forcing factors. It simultaneously integrates this HAZOP information with the safety measures to represent the radius of the hazard area under moderate hazard (50% probability of fatality/damage) due to the operation to installed safety features. It also accounts for the environmental setting. It accounts for almost all factors of the process industry [17]. It a complete and easy index to rank relative hazardous units of a process industry including all possible risk factors. In this paper, SWeHI was calculated for main units of ammonia plant of SFCL. For NG loading, primary reformer, secondary reformer, ammonia storage tank and ammonia reactor were calculated to be 1.74, 10.61, 4.32, 7.12 and 2.59. The numbers indicate if the units are low, moderate or highly hazardous. The CEI and hazard area was also calculated for ammonia storage tank under SFCL environmental condition as it can greatly affect the human health surrounding the area.

2. Methodology

For ammonia plant of Shahjalal Fertilizer Industry limited hazardous units of industry can be classified in two groups-

- a) Fire Hazards
- b) Toxic Hazards

For fire hazards, Dow fire explosion index (FEI) is calculated and for toxic release, Dow chemical exposure indexes (CEI) are calculated only for ammonia storage tank due to frequent accident in this unit. Primary and secondary reformer have the highest probability of fire explosion. At the same time, ammonia storage tank and ammonia reactor have the probability of toxic release of ammonia and CEI (chemical exposure index) have been calculated. This is also been simulated by ALOHA software to show the affected hazard area of toxic release of storage tank at plant's average atmospheric condition. For hazard ranking SWeHI method is used.

2.1 SWeHI method

The SWeHI methodology was collected from reference 4. In mathematical term of SWeHI is represented as,

$$SWeHI = B/A \quad (1)$$

Where, B is the quantitative measure of the damage that may be caused by a unit. It is measured in terms of area under 50% probability of damage, A represents the credits due to control measures and safety arrangements made to counter the undesirable situations.

$$B = B1 + B2 \quad (2)$$

B1 represents damage due to fire and explosion, while B2 considers damage due to toxic release.

2.1.1 B1 methodology

B1 has different a methodology for storage units; units involving physical operations such as heat transfer, mass transfer, phase change, pumping and compression; units involving chemical reactions; transportation units and other hazardous units such as furnaces, boilers, direct-fired heat exchangers, extraa.

For the storage tank, there were three energy factors to be calculated, F1 (only for chemical energy release), F2 and F3. Their corresponding equation are given below-

$$F1 = 0.1M \times H_c / K \quad (3)$$

$$F2 = 1.304 \times 10^{-3} \times PP \times V \quad (4)$$

$$F3 = 1.0 \times 10^{-3} \times (1/T + 273) \times (PP - VP)^2 \times V \quad (5)$$

The impact of pressure (presented by F2 and F3) were quantified as follows,

$$F = F2 + F3 \quad (\text{if } VP > AP \text{ and } PP > VP) \quad (6)$$

$$\text{or, } F = F2 \quad (7)$$

$$\text{or, } F = F3 \quad (\text{if } AP > VP \text{ and } PP > AP) \quad (8)$$

So, total Hazard potential = $(F1 \times pn1 + F \times pn2) \times pn3 \times pn4 \times pn5 \times pn6 \times pn7 \times pn8$ (9)

Here pn1-pn8 are penalty factors. They represent the impact of temperature, pressure, distance, quantity in ton, flammable and/or reactive characteristics of a chemical, the density of the units at the site, external factors such as earthquake and vulnerability of the surroundings accordingly. They are calculated according their potential risk due to temperature, pressure, distance extra with probabilistic analysis of HIRA method [4].

For units involving physical units, hazard potential can be calculated using equation 9, but penalty calculation will be different.

For, units involving chemical reactions (for ammonia reactor), new factors must be calculated, F4 is energy factor for reaction energy.

$$F4 = M \times H_r / K \quad (10)$$

The nature of the reactions is presented as pn9 and related to the probability of 'side reactions' or 'runaway reactions' is represented as pn10 [4]. So,

$$\text{hazard potential} = (F1 \times pn1 + F \times pn2) + F4 \times pn9 \times pn10 \times pn3 \times pn4 \times pn5 \times pn6 \times pn7 \times pn8 \quad (11)$$

For other hazardous units B1 can be calculated as

$$\text{Hazard potential} = F1 \times pn1 \times pn2 \times pn3 \times pn4 \times pn5 \times pn6 \times pn7 \times pn8 \quad (12)$$

All the hazard potential mentioned above can be represented by B1 (as they are for flammable material).

2.1.2 B2 methodology

The estimation of B2 was done with one core factor, named as the 'G factor', and several penalties. The G factor was accounted for the accidental release of super-heated liquid from the unit, the release of gases would directly lead to dispersion in the atmosphere and causing build-up of lethal toxic load and liquefied gases having two-phase release. All are responsible for toxic release disasters. The G factor is represented by,

$$G = S \times m \quad (13)$$

m is the anticipated mass release rate of materials present in the unit and S is dependent on the physical state of the materials of the unit. It is calculated through the NFPA ranking shown in table 1.

Table 1 NFPA rank for evaluating S

NFPA rank	Liquefied gas	Gas	Ref
4	8.0	13.40	
3	0.80	1.34	20
2	0.40	0.67	
1	0.10	0.25	

After calculating G, B2 was calculated by equation 14 where a=25.35 and b = 0.425.

$$B2 = a \times (G \times pnr1 \times pnr2 \times pnr3 \times pnr4 \times pnr5 \times pn6 \times pn7)^b \quad (14)$$

pnr1-pnr5 are penalty factor represented operating temperature, operating pressure, vapor density, toxicity of the chemical that are being handled, and site characteristics and soil type [20,24-26]. They were calculated differently. Some of their values were fixed based on the characteristics of the unit.

2.1.3 A methodology

Hazard control index, A represents present credits for the safety arrangements planned or exist on the unit as numbers.

$$A = 0.15 \times (1 + cr1)(1 + cr2)(1 + cr3)(1 + cr3)(1 + cr4)(1 + cr5)(1 + cr6)(1 + cr7)(1 + cr8) \quad (15)$$

cr1-cr8 are credits for safety measurements already exist in the unit or emergency response system (ERS). They were calculated specifically for SFCL plant. cr1 stands for ERS; cr2 for disaster management plan (DMP); cr3 for other damage control measures; cr4 for general control system like temperature, pressure, level control; cr5 for installation of detecting devices; cr6 for emergency control systems like interlock; cr7 are for general human characteristics and probable human errors and cr8 for quantification of credit for equipment reliability [4, 27-31]. Most of the information regarding credit calculation for SFCL, were collected personally from some of the employees of SFCL and students of BUET who were internee of SFCL. Some data was also collected from the literature review [32,33]. Most of the calculation was proceeded with statistical data and probabilistic equations in plotted graph [4].

After calculating B and A, SWeHI numbers were arranged. The ranking was done accordingly fig 1.

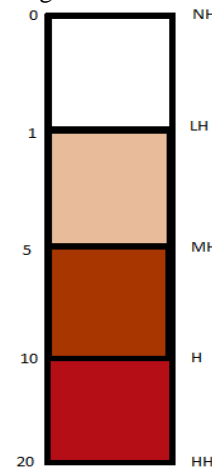


Fig.1 SWeHI Hazard Ranking where HH: Highly Hazardous, H: Hazardous, MH: Moderately Hazardous, LH: Less Hazardous

2.2 Dow CEI

The Chemical Exposure Index (CEI) provides a simple method of rating the relative acute health hazard potential to people in neighboring plants or communities from possible chemical release incidents. For ammonia storage tank, CEI was calculated. It can be expressed by the equation,

$$CEI = 655.1 \times \sqrt{(AQ/ERPG-2)} \quad (16)$$

Where, AQ is airborne quantity (kg/sec), ERPG-2 value (mg/m3) [The value is taken from AIHA guideline]. ERPG is abbreviation of emergency response system guideline. [34] It is fixed for a toxic material ERPG are same for the operating pressure and temperature. If the gas releases from the storage tank,

$$AQ = 4.751 \times 10^{-6} \times D^2 P_a \times \sqrt{\{MW/(T+273)\}} \quad (17)$$

Where, P_a absolute pressure, MW molecular weight of the ammonia, D diameter of the probable hole of the storage tank in millimeter. For ammonia storage tank liquid ammonia may release and then vaporize in atmospheric conditions. So equation will be,

$$AQ = 5 F_v \times L + 9.0 \times 10^{-4} \times A^{0.95} \{MW \times P_v / (T+273)\} \quad (18)$$

$$F_v = (C_p / H_v) \times (T_s - T_b) \quad (19)$$

$$L = 9.44 \times 10^7 \times D^2 p_1 \times \sqrt{(1000 P_g / p_1)} + 9.8h \quad (20)$$

The symbols have their usual meaning. [35, 36]

2.3 Hazard area using Aloha Software

ALOHA which is elaborated as Areal Locations of Hazardous Atmospheres, is the hazard modeling software program for the CAMEO software suite. It is used widely to plan for and respond to chemical/hazardous materials emergencies. Details about a real or potential chemical/hazardous materials release can be entered into ALOHA for generating threat zone (hazard area) estimated for various types of hazards. This software can also be used for modeling hazard area for toxic gas clouds, flammable gas clouds, Boiling Liquid Expanding Vapor Explosions (BLEVEs), jet fires and vapor cloud explosions. The estimated hazard area are shown on a grid in ALOHA. The red threat zone represents the worst hazard level; the orange and yellow threat zones represent areas of decreasing hazards [37, 38].

3. Results and Discussion

The results found from the calculation is expressed below.

3.1 SWeHI Ranking

Table 2 SWeHI ranking for main units of ammonia section of SFCL

Units	B1	B2	B	A	SWeHI =B/A	Rank
NG loading	202.55	13.34	202.55	116.20	1.74	LH
Primary reformer	669.47	5.56	669.47	101.36	10.61	HH
Units	B1	B2	B	A	SWeHI =B/A	Rank
Secondary reformer	397.90	105.22	397.90	108.06	4.32	MH
Ammonia Storage Tank	255.18	296.27	296.27	115.29	7.12	H
Ammonia Reactor	112.64	138.64	138.64	110.2	2.59	LH

3.2 CEI value

After calculation using excel, CEI value for ammonia storage has been found 89.9. This indicates that it is moderately toxic but it only depends on operating temperature and pressure. So, nothing else can be predicted from this analysis.

3.3 ALOHA software

In ALOHA, for SFCL average environmental condition for the ammonia storage tank, two kinds of hazard area were simulated; one for toxic vapor release and another for blast area of a vapor cloud. The simulated area shows that how much area will be mostly affected if any accident takes place

3.3.1 Toxic area of vapor cloud

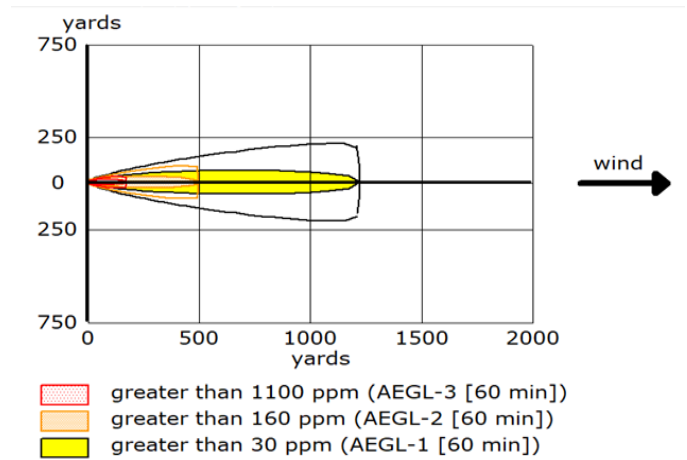


Fig.2 Hazard area calculation of ammonia storage tank for toxic release

3.3.2 Blast area of vapor cloud

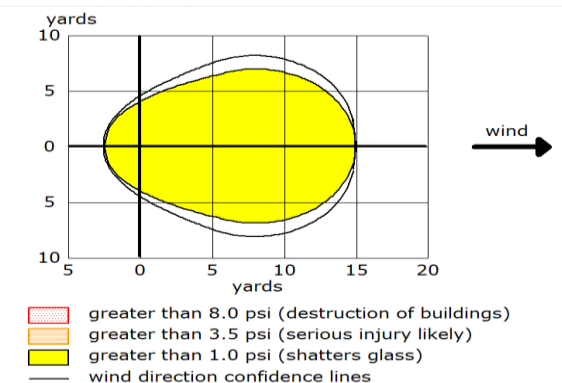


Fig.3 Hazard area calculation of ammonia storage tank for blast area of vapor cloud

4. Conclusion

To identify the hazard of SFCL through an index (SWeHI) for assessing hazards in chemical process industries. As there are locals around the plant, CEI and

ALOHA software simulation were also used (as mostly used) for Ammonia storage tank. The purpose of the study was to acknowledge the SWeHI method for the contribution of safety measures in its final hazard assessment score with greater rigor, accuracy, and precision than that achieved in the prevailing indices. The SWeHI has also been based on more systematic and reliable methods for hazard identification as it considers a larger number of parameters for hazard quantification. It is so complete, simple and rigorous that it can help in insurance procedure too. A 'snap-shot picture' of ammonia process units of SFCL is presented through indices. In near future, the SFCL authority can use the data for further safety measures.

NOMENCLATURE

cr	Credit factor
pn	penalties for damage index estimation
pnr	penalties for toxic damage index estimation
PP	processing pressure, kPa
T	temperature, °C
TP	transportation pressure, kPa
V	volume of the chemical, cu m
Fv	Flash fraction
Pv	Vapor Pressure
pl	Liquid Pressure

REFERENCES

- [1] ECHA, May. "Guidance on information requirements and chemical safety assessment." Chapter R 8 (2008)
- [2] Carmichael, Neil G., Hugh A. Barton, Alan R. Boobis, Ralph L. Cooper, Vicki L. Dellarco, Nancy G. Doerrer, Penelope A. Fenner-Crisp, John E. Doe, James C. Lamb Iv, and Timothy P. Pastoor. "Agricultural chemical safety assessment: a multisector approach to the modernization of human safety requirements." *Critical reviews in toxicology* 36, Vol. 1. pp 1-7, (2006).
- [3] Sugiyama, Hirokazu, U. Fischer, K. Hungerbühler, M. Hirao, Decision framework for chemical process design including different stages of environmental, health, and safety assessment." *AICHE Journal* 54, Vol. 4, pp 1037-1053, (2008).
- [4] F. I. Khan, T. Husain, and S. A. Abbasi, Safety weighted hazard index (SWeHI): a new, user-friendly tool for swift yet comprehensive hazard identification and safety evaluation in chemical process industrie, *Process Safety and Environmental Protection* 79, Vol 2, pp 65-80, (2001).
- [5] Dow, Dow's Fire and Explosion Hazard Classification, Midland, US, (1994).
- [6] Dow, Dow's Chemical Exposure Index, AIChE, New York (1994).
- [7] N. Abramson, THE ALOHA SYSTEM: another alternative for computer communications. *fall joint computer conference*, pp. 281-285. ACM, (1970).
- [8] M. Bartley, B. David, and M. Scott, Socioeconomic determinants of health: Health and the life course: why safety nets matter. *Bmj* 314, Vol. 7088, pp 1194, (1997).
- [9] AM. Heikkilä, M. Hurme, M. Järveläinen, Safety considerations in process synthesis, *Computers & chemical engineering*, Vol 20, pp S115-S120, (1996)
- [10] M. Gentile, WJ Rogers, MS Mannan, Gentile, Development of a fuzzy logic-based inherent safety index, *Process Safety and Environmental Protection*, Vol 81, pp.444-456, (2003).
- [11] H.O. Madsen, S. Krenk, and N.C. Lind, *Methods of structural safety*. Courier Corporation (2006).
- [12] Am. Heikkilä, Inherent safety in process plant design: an index-based approach. *VTT Technical Research Centre of Finland*, (1999).
- [13] D. J. Lewis, The Mond fire, explosion and toxicity index development of the Dow Index, *AIChE on Loss Prevention*, New York, (1979).
- [14] B. J. Tyler, A. R. Thomas, P. Doran, and T. R. Grieg, A toxicity hazard index, *Hazards XII, IChemE Symposium*, Vol. 141, pp 351-366, (1994)
- [15] H. B. Whitehouse, IFAL—a new risk analysis tool *In Institution of Chemical Engineers symposium series*, vol. 309. (1985).
- [16] J. G Marshall, and J. H. Burgoyne. The size of flammable clouds arising from continuous releases into the atmosphere, *In Inst. Chem. Symp*, Vol. 49, p. 103. (1977).
- [17] F. I. Khan, and S. A. Abbasi, Techniques and methodologies for risk analysis in chemical process industries, *Journal of loss Prevention in the Process Industries 11*, Vol 4, pp 261-277, (1998).
- [18] API, Management of process hazards, *American Petroleum Institute Recommended Practice 750 (1st Ed.)*, Washington DC. (1990)
- [19] NFPA, Identification of hazardous material, *National Fire Protection Agency-Code 704, Quincy, Massachusetts*, (1989)
- [20] NFPA, Hazardous Materials Response Handbook, *National Fire Protection Association, USA*, (1992)
- [21] P. Andreasen, & B. Rasmussen, Comparison of methods of hazard identification at plant level. *Journal of Loss Prevention in the Process Industries*, Vol 3(4), pp 339-344, (1990).
- [22] J. E. Ricart, M. Á. Rodríguez, P. Sánchez, Sustainability in the boardroom: An empirical examination of Dow Jones Sustainability World Index leaders, *Corporate Governance:*

- the international journal of business in society*, Vol 5(3), pp.24-41, (2005).
- [23] J. Singh, and G. Munday, IFAL: a model for the evaluation of chemical process losses. *In Design 79 Symposium. Institute of Chemical Engineering Midlands Branch London*, (1979)
- [24] F. I. Khan, and S. A. Abbasi, Major accidents in process industries and analysis of their causes and consequences, *J Loss Prevention in Process Industries*, vol 12, pp 361-378, (1999).
- [25] F. I. Khan, and S. A. Abbasi, Accident hazard index: a multiattribute method for process industry hazard rating, *Trans IChemE Part B, Proc Safe Env Prot*, vol 75, pp 217-224, (1997)
- [26] F. I. Khan, and S. A. Abbasi, Accident simulation as a tool for assessing and calculation environmental risk in CPI: a case study, *Korean J Chem Eng*, vol 11, pp 12-19, (1998).
- [27] G. P. Williams, Safety performance in ammonia plants: survey VI, *Process Safety Progress*, vol 18, pp 78-81, (1999).
- [28] T. A. Kletz, Process safety and engineering achievement, *Proc IMechE*, vol 205: pp 11, (1991).
- [29] M. D. Topf, Improve employee morale to reduce injuries, *Chem Eng Progress*, pp 56-58. (1998)
- [30] F. I. Khan, and S. A. Abbasi, The worst chemical industry accident of 1990s, what happened and what might have been: a quantitative study, *Process Safety Progress*, vol 18, pp 135-145, (1999).
- [31] V.A. Ciliberti, Use criticality-based maintenance for optimum equipment reliability, *Chem Eng Prog*, vol 1, pp 63-67, (1998)
- [32] M.M. Hasan, Al Mahmud and M.F. Howladar, Rules and Regulation of Transmission and Distribution of Natural Gas and its Application in Bangladesh. *In ICPE* , Vol. 2016, pp 019. (2016)
- [33] A. E. Haque, Natural Gas Management of Bangladesh: Future Powerhouse of South-East Asia?. *In The 1st International Applied Geological Congress, Department of Geology*, pp. 26-28, (2010).
- [34] R. W. Perry, & M. K. Lindell, Preparedness for emergency response: guidelines for the emergency planning process. *Disasters*, vol 27, pp 336-350, (2003).
- [35] G. J. Ruiz-Mercado, R. L. Smith., & M. A. Gonzalez, Sustainability indicators for chemical processes: I. Data needs. *Industrial & Engineering Chemistry Research*, vol 51(5), pp 2309-2328. (2012).
- [36] G. J. Ruiz-Mercado, R. L. Smith., & M. A. Gonzalez, Sustainability indicators for chemical processes: II. Data needs. *Industrial & Engineering Chemistry Research*, vol 51(5), pp 2329-2353. (2012).
- [37] X. Liu, J. Kountouriotis, A. P. Petropulu, & K. R. Dandekar, ALOHA with collision resolution (ALOHA-CR): theory and software defined radio implementation. *IEEE Transactions on Signal Processing*, vol 58(8), pp 4396-4410, (2010).
- [38] M. J. Gharabagh, H. Asilian, S. B. Mortasavi, A. Z. Mogaddam, E. Hajizadeh, & A. Khavanin, Comprehensive risk assessment and management of petrochemical feed and product transportation pipelines. *Journal of Loss Prevention in the Process Industries*, vol 22(4), pp 533-539, (2009).

Numerical Study on Aero-Acoustic Behavior for Flow over a Supercritical Airfoil at Low Reynolds Number

Syed Angkan Haider, Tanveer Islam Joy, Md. Fazlur Rahman Akanda

Department of Mechanical Engineering, Bangladesh University of Engineering & Technology, Dhaka-1000, BANGLADESH

ABSTRACT

A two-dimensional supercritical RAE-2822 airfoil cross-section with 100 mm chord length was analyzed at low Reynolds number (Re) flow and the resulting aero-acoustic parameters were investigated. A Reynolds number of approximately 168,000 (based on airfoil chord length) was used for the analysis. The study was conducted for three different angles of attack, namely 0° , 6° and 12° . For the computational analysis, 2-D transient Reynolds Averaged Navier-Stokes (RANS) equations were used, coupled with the two equation $k-\omega$ shear stress transport (SST) turbulence model and broadband noise source settings. The pressure, turbulent intensity, acoustic power level and LEE self- and shear-noise were analyzed in the vicinity of the airfoil surface and wake; possible explanations behind noise generation and their relation to turbulence, flow separation and vortex formation at different angles of attack were discussed. It was observed that the aero-acoustic noise increased with angle of attack as the vorticity and turbulence effects got stronger.

Keywords: Supercritical airfoil, Reynolds number, shear-noise, self-noise.

1. Introduction

Aircraft noise has become a major concern because of its detrimental effects on communities living in the vicinity of airports while also registering itself as a significant loss of energy during flight. Aerodynamic noise is one of the most important sources of aircraft noise arising from the airflow around the airfoil. This becomes more noticeable when aircrafts fly at low altitudes near the airports. This noise, while being a loss in the flow, is also known to be a health hazard, with many different physical and psychological effects. So knowledge about acoustic noise is vital for being able to not just find how it is produced but also possible ways on how it can be minimized.

Sandberg *et al.* [1] conducted DNS of the flow at low Re around NACA-0006 and NACA-0012 airfoils and studied airfoil self-noise and noise reduction of trailing edge (TE) serrations. Interaction of the disturbance with the trailing edge was the main source of self-noise. He also showed that laminar boundary layer separation, laminar-turbulent transition and turbulent reattachment led to additional sources which became dominant at high frequencies, while trailing edge noise was dominant at low frequency.

Doolan *et al.* [2] described the mechanism of trailing edge noise generation. Empirical methods, direct methods and hybrid methods of computing trailing edge noise were also described. The importance of modelling a turbulent flow field for TE noise prediction were discussed. LES, being more accurate than RANS for modelling a turbulent flow field, required better SGS models to be developed if the turbulence scales were smaller than grid size. Different analytical and numerical methods to estimate the noise from turbulent flow data were described.

Jackson *et al.* [3] investigated the airfoil self- and shear-noise for a NACA 0012 airfoil section at three angles of

attack. The results were analyzed for the trailing edge noise effects and on how noise sources varied with different angles of attack. A direct correlation between turbulent intensity and the acoustic power level was formulated. Self-noise became more dominant as angle of attack was increased. At larger angles of attack y-sources of self- and shear- noise contributed more as noise compared to the x-sources

In the present study, a supercritical airfoil cross-section was studied at low-Re flow for aero-acoustic parameters such as acoustic power level and LEE noise, and effects of turbulence and vorticity were explained. Angles of attack of 0° , 6° and 12° were considered to give a clear idea of the influence of angle of attack on flow noise.

2. Computational Method

2.1 Mathematical Model

The most complete model available for the flow of air is the Navier-Stokes equations. They, however, represent a model, not physical truth. They represent three conservation laws:

Conservation of mass:

$$\frac{\partial(\rho u)}{\partial x} + \frac{\partial(\rho v)}{\partial y} = 0 \quad (1)$$

Conservation of momentum:

$$\rho(u \frac{\partial u}{\partial x} + v \frac{\partial u}{\partial y}) = -\frac{\partial p}{\partial x} + \mu(\frac{\partial^2 u}{\partial x^2} + \frac{\partial^2 u}{\partial y^2}) \quad (2)$$

$$\rho(u \frac{\partial v}{\partial x} + v \frac{\partial v}{\partial y}) = -\frac{\partial p}{\partial y} + \mu(\frac{\partial^2 v}{\partial x^2} + \frac{\partial^2 v}{\partial y^2}) \quad (3)$$

* Corresponding author. Tel.: +88-01789-908629, +88-01757-001196, +88-01626-501889.

E-mail addresses: angkanhaider@gmail.com, joytanveer796@gmail.com, md.fazlurrahmantonmoy@gmail.com

Conservation of Energy:

$$\frac{\partial(\rho u E)}{\partial x} + \frac{\partial(\rho v E)}{\partial y} = \frac{\partial(\rho u q)}{\partial x} + \frac{\partial(\rho v q)}{\partial y} + \frac{\partial}{\partial x}(u\tau_{xx} + v\tau_{xy}) + \frac{\partial}{\partial y}(u\tau_{xy} + v\tau_{yy}) \quad (4)$$

2.2 Solver Settings

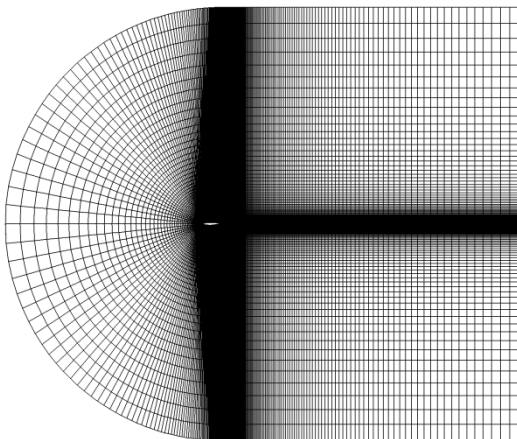
The solver used was ANSYS Fluent. The settings are given in Table 1.

Table 1 Solver, viscous model and noise sources

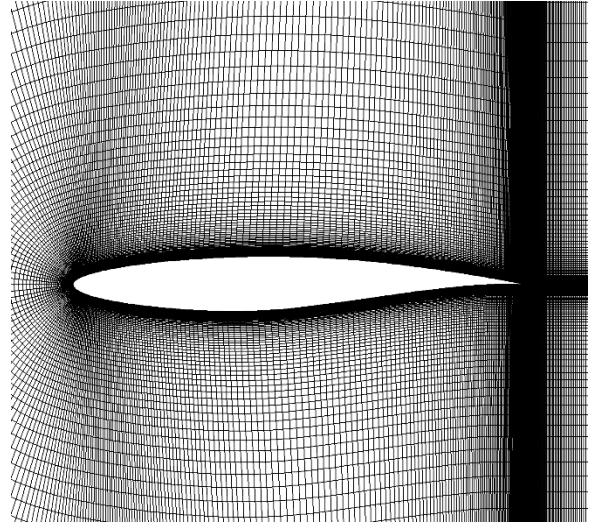
Function	Option
Model	<i>k-ω</i> (2 equation)
<i>k-ω</i> model	SST
<i>k-ω</i> option	Low Re Corrections
Turbulent Viscosity	None
Options	Viscous Heating Curvature Correction
Solver	Pressure-based
Space	2D
Gradient Option	Least Squares Cell-Based
Formulation	Implicit
Time	Transient
Acoustics	Broadband Noise Sources

3. Computational Domain

The computational domain was discretized with a user-defined structured mesh. The total number of cells used was 96,090. In the wall normal direction, the first node after the wall was selected in such that the value of wall y^+ was around 1. The mesh around the airfoil wall was made dense to ensure higher accuracy.



(a) Mesh of the complete domain



(b) Relatively denser mesh around airfoil

Fig. 1 Discretization and Mesh

4. Boundary Conditions

The boundary of the domain consisted of a domed inlet with velocity of 30 m/s and a pressure outlet. The airfoil surface was taken to be a no-slip wall. The flowing fluid was air with constant density and viscosity at 300K and a Reynolds number of about 168,000 (based on chord length) was maintained. Three different cases of flow were considered by varying the angles of attack. The three angles used were 0° , 6° and 12° .

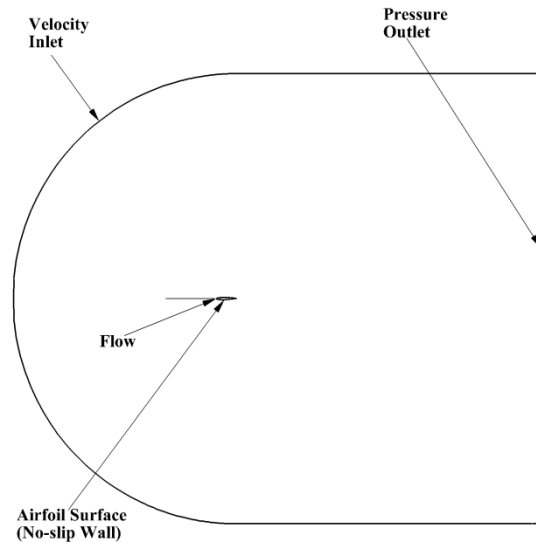


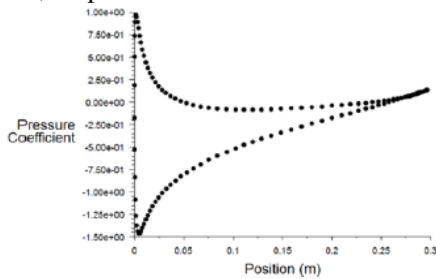
Fig. 2 Boundary Conditions

Table 2 Three cases of flow

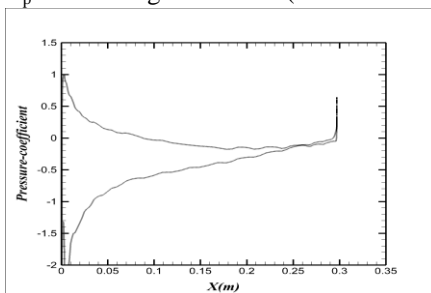
<u>Case</u>	<u>Angle of attack</u>
Case – 1	0°
Case – 2	6°
Case – 3	12°

5. Validation of Computational Method

Since very little computational or experimental work is done on supercritical airfoils at low Re, the computational method was validated for a NACA 0012 airfoil profile and pressure coefficient values were compared to those obtained by Jackson *et al.* [3]. As can be seen in Fig. 3, the values obtained were quite reasonable, despite some fluctuations.



(a) C_p for 10° angle of attack (Jackson *et al.*)



(b) C_p for 10° angle of attack (present method)

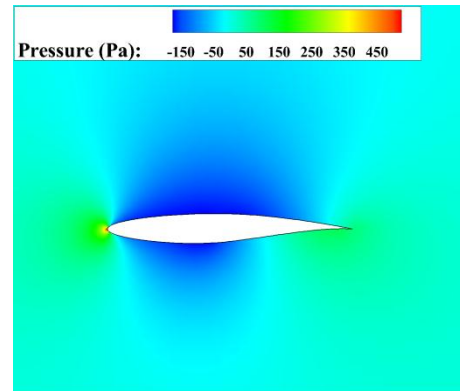
Fig. 3 Validation of computational method

6. Results and Discussions

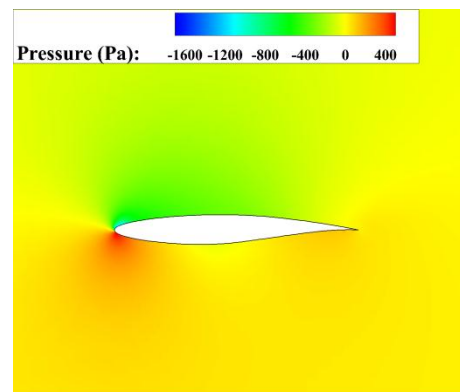
The pressure contours for Cases - 1, 2 & 3 angles of attack are shown in Fig. 4. From Fig. 4. (a) and 4. (b), it can be seen that at 0° angle of attack there was an adverse pressure gradient towards the vicinity of Trailing Edge (TE) but at 6° angle of attack adverse pressure gradient occurred just downstream of the Leading Edge (LE). The adverse pressure gradient was correlated with the transition length and the formation of turbulent boundary layer as given by Fahy *et al.* [4]. These phenomena were substantiated by the demonstration of turbulent intensity for 0° and 6° angle of attack (Fig. 6. (a) and 6. (b)) as these figures showed that turbulence started earlier in case of 6° angle of attack in comparison to the case of 0° angle of attack due to separation of flow, resulting in negative pressure

at LE for 6°. At 12° angle of attack vortex shedding occurred which was evident in Fig. 4. (c), characterized by circular negative pressure regions. Turbulent intensity for 12° angle of attack shown in Fig. 6. (c) was in complete agreement with the occurrence of vortex shedding.

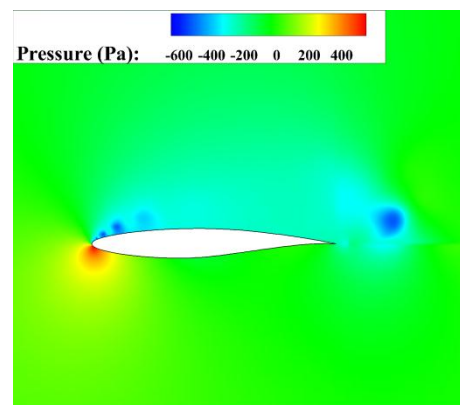
The comparison between turbulent intensity in Fig. 6 and contours of acoustic power level in Fig. 5 suggested a direct correlation between them. Both acoustic power level and turbulent intensity increased as the angle of attack was increased.



(a) Case - 1

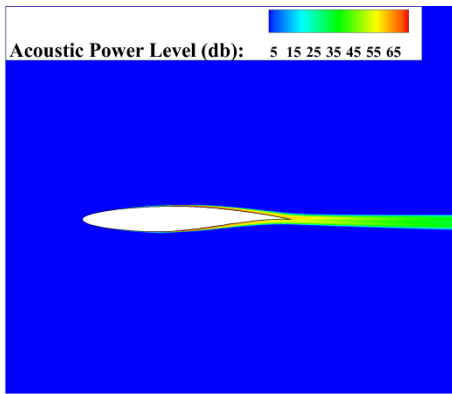


(b) Case – 2

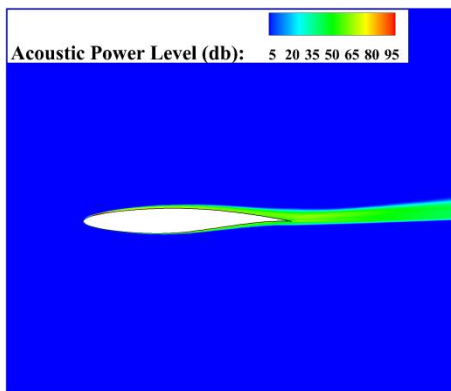


(c) Case - 3

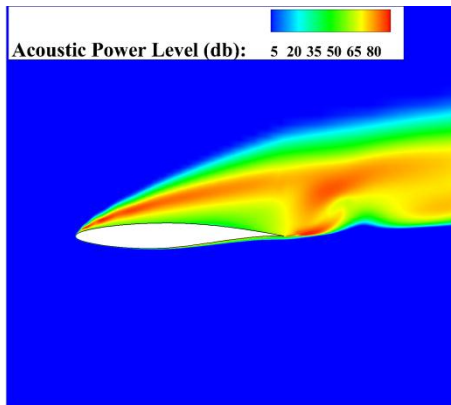
Fig. 4 Pressure Contours at different cases



(a) Case - 1



(b) Case - 2

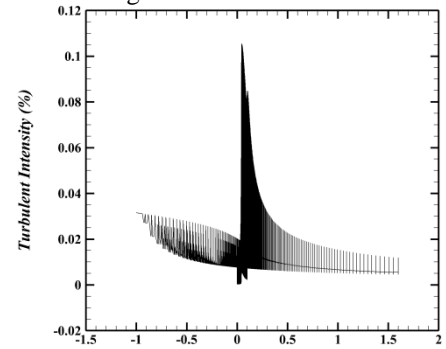


(c) Case - 3

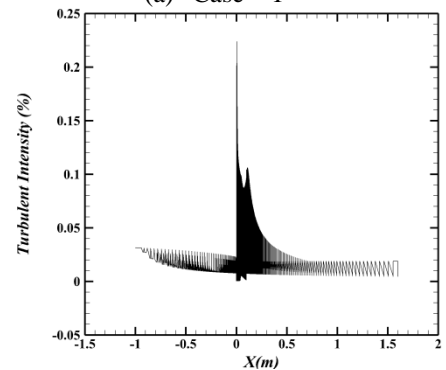
Fig. 5 Contours of Acoustic Power Level

For this study, Broadband Noise Source Model was used to compute aerodynamic noise. Source terms in Linearized Euler Equations (LEE) were used as source model to quantify different sources (self-noise and shear-noise) contributing to the generation of noise. Self-noise arose from the interaction between turbulent fluctuations with the surface of the airfoil and shear-noise arose from the interaction between mean shear and velocity fluctuation as proposed by Crighton *et al.* [5]. Graphs of self-noise and shear-noise sources were plotted for 0° , 6° , 12° angle of attack. It was seen that

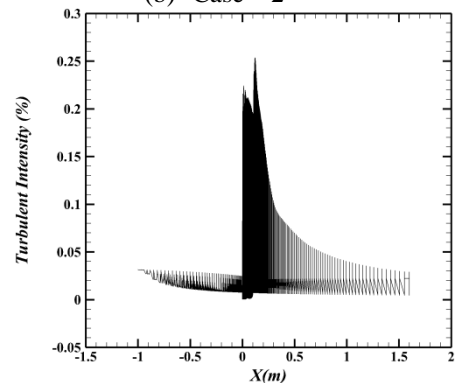
graphs of x and y sources of self-noise (Fig. 7 & 8) were quite similar for each angle of attack and it indicated that the contribution of x and y sources to the self-noise were almost equal. Even though the pattern of local distribution of x and y sources of shear-noise (Fig. 9 & 10) were quite similar, y-source of shear noise dominated the x-source of shear noise. Increase in angle of attack caused increase in both x and y sources of self-noise and shear-noise. Shear-noise sources were greater than self-noise sources for each angle of attack. But contributions of self-noise sources became higher at higher angle of attack. Both x and y sources of self-noise and shear-noise had higher value near the LE at 6° angle of attack than the values obtained at 12° angle of attack. One possible reason behind this result was that at the end of flow time, a separated low pressure region was generated only at LE for 6° but for 12° two separate vortices were being shed from the two edges as studied by Lam *et al.* [6], resulting in two peaks, both having lower noise source magnitudes than for the 6° case.



(a) Case - 1

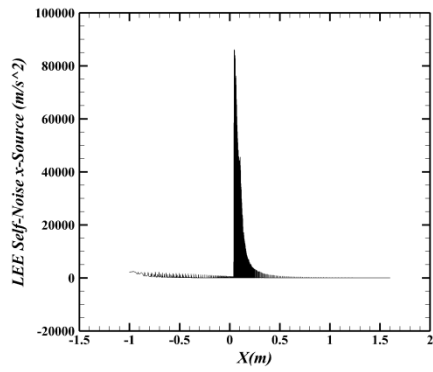


(b) Case - 2

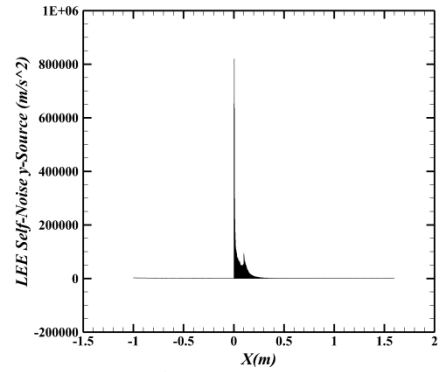


(c) Case - 3

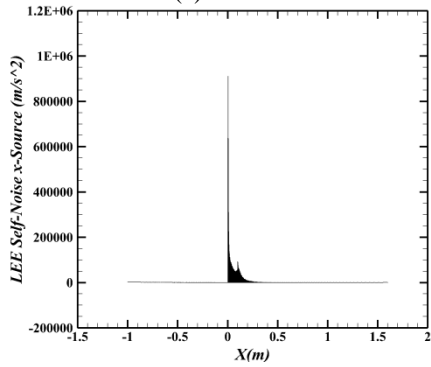
Fig. 6 Turbulent intensity at different cases



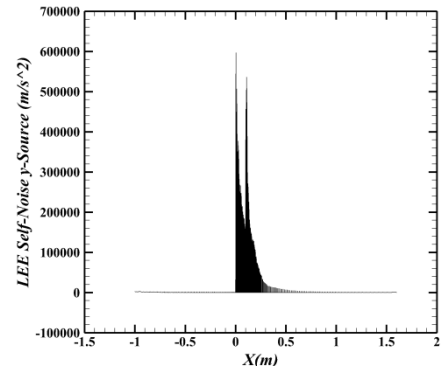
(a) Case - 1



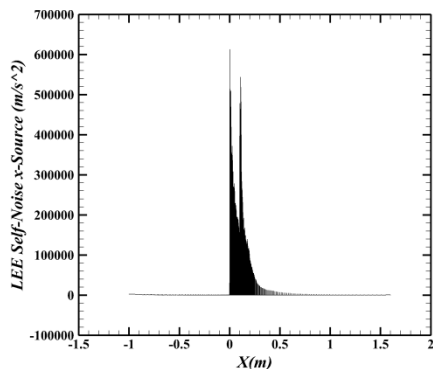
(b) Case - 2



(b) Case - 2



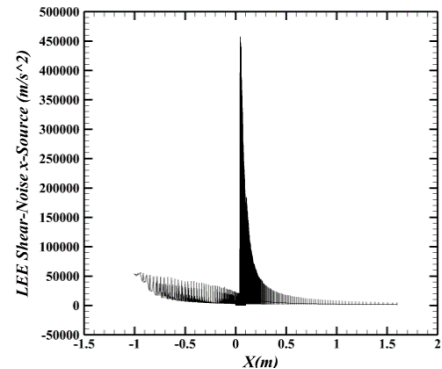
(c) Case - 3



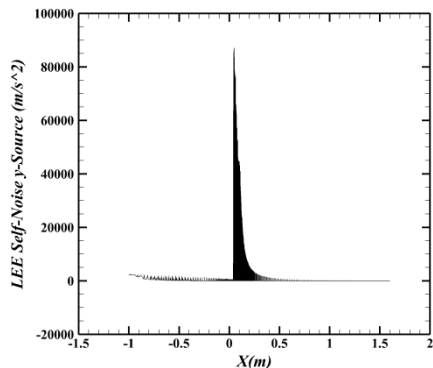
(c) Case - 3

Fig. 8 LEE Self-noise (y-sources) at different cases

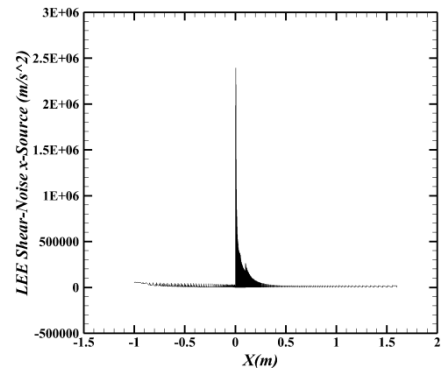
Fig. 7 LEE Self-noise (x-sources) at different cases



(a) Case - 1



(a) Case - 1



(b) Case - 2

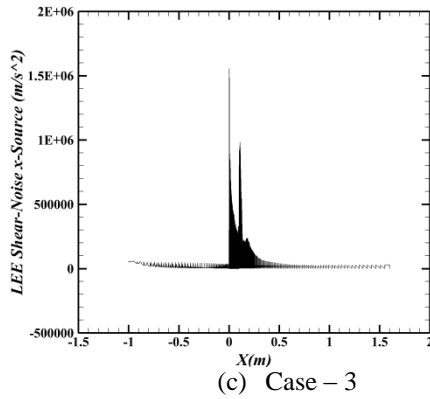


Fig. 9 LEE Shear-noise (x-sources) at different cases

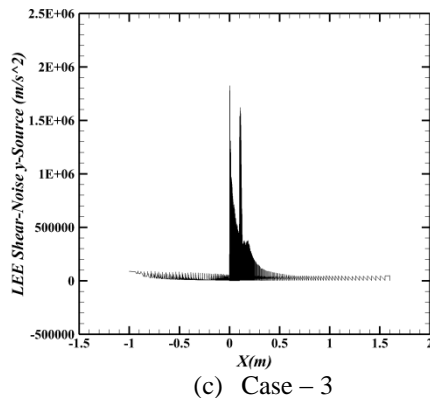
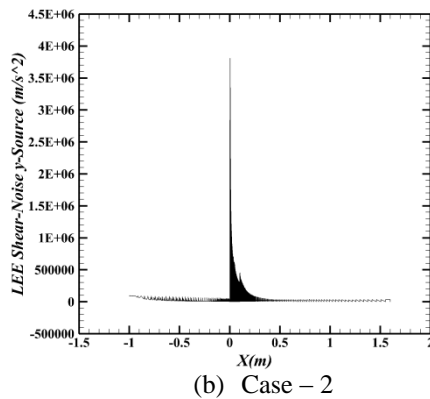
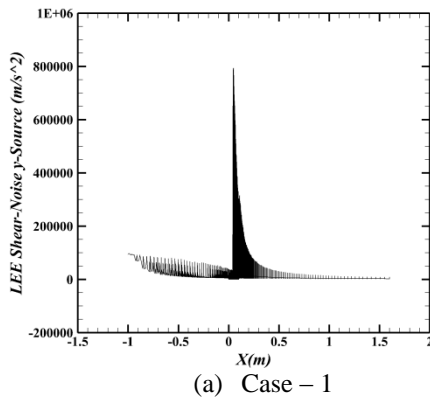


Fig. 10 LEE Shear-noise (y-sources) at different cases

7. Conclusions

In this study, a numerical study of low Reynolds number flow at 3 angle of attack over a supercritical RAE-2822 airfoil cross-section was done.

It was found that with the increase of angle of attack, the acoustic power level increased as a direct result of increase in turbulence with flow separation at the lower angles (0° and 6°) and vortex shedding at higher angle (12°). For the 6° case adverse pressure gradient close to the LE caused flow to separate and become turbulent. Vortex formation and shedding as observed in the 12° case introduced greater turbulence and hence more potent noise.

Shear-noise source terms were higher in magnitude compared to self-noise sources for each angle of attack. But contributions of self-noise sources became higher at the higher angle. Both x and y sources of self-noise and shear-noise had higher value near the LE at 6° angle of attack than the values obtained at 12° angle of attack which could be due to the shedding of two separate vortices from both LE and TE for 12° as opposed to a single low pressure separated region at the vicinity of the LE for the 6° case. This formation of two different vortices also explained the two distinct peaks observed in all the noise source graphs for the 12° but only a single peak for the noise source graphs of the 0° and 6° cases.

REFERENCES

- [1] Sandberg, R.D. and Jones, L.E., 2010. Direct numerical simulations of airfoil self-noise. *Procedia Engineering*, 6, pp.274-282.
- [2] Doolan, C., 2008. A review of airfoil trailing edge noise and its prediction.
- [3] Jackson, B.R. and Dakka, S.M., 2018. Computational fluid dynamics investigation into flow behavior and acoustic mechanisms at the trailing edge of an airfoil. *Noise & Vibration Worldwide*, 49(1), pp.20-31.
- [4] Fahy, F. and Walker, J. eds., 2004. *Advanced applications in acoustics, noise and vibration*. CRC Press.
- [5] Crighton, D.G., 1975. Basic principles of aerodynamic noise generation. *Progress in Aerospace Sciences*, 16(1), pp.31-96.
- [6] Lam, K.M. and Wei, C.T., 2010. Numerical simulation of vortex shedding from an inclined flat plate. *Engineering Applications of computational fluid mechanics*, 4(4), pp.569-579.

Construction and Performance Test of a Manual Pipe Bending Machine

S. M. Moinur Rahman and A. N. M Mizanur Rahman*

Department of Mechanical Engineering, Khulna University of Engineering & Technology, Khulna 9203, Bangladesh

Abstract- In modern manufacturing, different type of structures are used that need pipe bending. In today's life SS pipes are frequently used in furniture and decorative works. Pipe bending is quite different from rod bending and it needs special technique otherwise there will be distortion at the bends. Thus, pipe bending machines are used to bend different types of pipe. They can be automatic, semi-automatic or manual type. Manual pipe bending machines are used to bend small diameter pipes and particularly in small entrepreneurs. This paper presents the design, construction and performance test of a 3-roller manual pipe bending machine that could be used to bend a 25mm diameter pipe. The lower two rollers are kept at fixed height and the top middle one could move up and down to give the required shape and bending radius. A lead screw and hand wheel is used to force the middle roller down and give different deflections in the pipe. The rollers were made of cast iron and the base and the structure were made of MS plate. In the performance test 15 and 20 mm GI pipe was used and their bending radiuses were measured for various vertical displacement of the middle roller. It is found that bending diameter depends only on the vertical displacement of the middle roller. The project result shows that for increased displacement in the middle roller, the pipe bending is more accurate and deviation between the theoretical value and the experimental value of bending diameter is reduced.

Key words: Pipe bending, bending machine, roller bender, manual bending.

1. Introduction

For various applications, bent tube or pipe products are employed in manufacturing of many kinds of high-end industries such as aviation, aerospace, ship building, automobile, steel structures, furniture and decorative works, transport appliances, fluid arrangements and in various mechanical parts. This may be because of reduction in the production cost and weight of the structure. But pipe bending is not as simple as rods because there is chance of distortion at the bends, if sufficient care is not taken. Also, for precision works, accurate dimensioning and shape is essential. This needs the requirement of a proper bending machine that could satisfy the above requirements. To reduce the power needed to driving a machine proper arrangement and design is strictly necessary. In modern pipe bending machineries the operation is maintained with accuracy and a wide range of bend operation is performed. There is semi-automatic and automatic version of pipe bending machines that requires minimal need for the presence of an operator. The semi-automatic pipe bending machine seems to be most preferred due to its low running cost, flexibility and requirement of less operator interface. In developed and developing countries automatic or semi-automatic system is widely used while in under-developed countries manual bending machine is useful because of its simplicity and small scale production, particularly for a small entrepreneur.

There are various types of bending machines. For basic pipe bending methods, rotary-draw bending, press bending and roll bending are commonly used. The rotary-draw bending is the most standard method used on rotary type bending machines which are powered

either manually or by numerically controlled devices. The rotary-draw bending consists of the rotating bending form, clamping die and pressure die. The work-piece is secured to the bending form by a clamping die. As the bending die rotates, it draws the work-piece against the pressure die.

The press bending method uses simple tooling and is quick and easy to set up. The press bending draws power from a hydraulic power source. The pipe is situated in the die and then pressed; for this the pipe takes the shape of the die. Roll bending is used for producing work pieces with large bending radii. The method is similar to the ram bending method, but the working pulley and the two-stationary counter pulley rotate, thus forming the bend. Normally, there are two fixed pulleys and one moving pulley and the work-piece is passed forward and backward through the pulley while gradually moving the working pulley closer to the counter pulley which changes the bend radius in the pipe. This method of bending causes very little deformation in the cross section of the pipe and is suited to producing coils of pipe as well as long sweeping bends like those used in powder transfer systems where large radii bends are required.

For industrial purpose and where rate of production is important, automated pipe benders are used. But in the developing countries and particularly in rural areas where electricity and other power are not available, manual pipe bender should be the only alternative. Also, for pipes with smaller diameter can easily be bent without the external electric power rather by manual power.

H. Yang et. al. [1] developed one kind of pipe bending machine with the key components having enormous

*Corresponding Author: Tel. +8801714002333
E-mail addresses: drmizan84@gmail.com

quantities and diversities. The bent tube parts satisfy the increasing needs for light-weight and high-strength products from both material and structural aspects. The tube bending has become one of the key manufacturing technologies for lightweight product forming. Through the analysis of bending characteristics and multiple defects, advances on exploring the common issues in tube bending are summarized regarding wrinkling instability at the intrados, wall thinning (cracking) at the extrados, spring buck phenomenon, cross-section deformation, forming limit and process/tooling design/optimization. Some currently developed bending techniques are reviewed in terms of their advantages and limitations. Finally, in view of the urgent requirements of high-performance complex bent tube components with difficult-to deform and light weight materials in aviation and aerospace fields, the development trends and corresponding challenges are presented for realizing the precise and high-efficiency tube bending deformation.

Hiroyuki Goto et al. [2] present a new flexible bending machine and its practical applications. The proposed machine uses a new method. When tubes are fed into the fixed and mobile dies, they are bent by shifting the relative position of the mobile die. The bending radius is controlled by the relative distance and orientation between the mobile die and the tube. The bending angle is controlled by the length of the fed tube. This forming process has a big advantage. A change of the expected bending shape will need no change in the tooling system but only a new definition of the motion of the active die and the length of the fed tube. The active die movements are controlled by a 6-DOF Parallel Kinematics Mechanism (PKM) with hydraulic servo drive. Making use of the PKM serves not only to achieve a complete motion along 6-axes but also to obtain a high dynamic motion of the bending machine. Application examples show that the bending machine can be applied to designer's interiors, universal designed products, and automotive parts. Until now these processes have been difficult to achieve using a conventional bending machine.

H. A. Hussain [3] designed and developed a bicycle integrated pipe bending mechanism. The machine consists of a chain drive, compound gear train that is utilized for bending steel pipe of outside diameter 25 mm and having 2 mm thickness. The kinematic synthesis of bending mechanism is carried out. The dimensional analysis was carried out. The relations deduced predicts the performance of bicycle integrated pipe bending mechanism and all the parameter needs to be optimized to get the best performance of the machine.

N. Nirwan and A. K. Mahalle [4] found a portable rolling pipe bending machine that was used for reliability, ease of convenience and good quality purpose. But there were some difficulties like not to be

used for mass production and slow process due to hand operated device.

A. P. Kshar and A. P. Kshar [5] designed and fabricated a portable pipe bending machine considering the cost of machine and ease of use. The machine was based on fixed die and manually operated lever.

As reported in [5], A. Pandiyan of Saveetha School of Engineering, Chennai, India found a zigzag pipe bending machine that was used for making zigzag profile pipe. It was operated by hydraulic bottle jack. This bending machine is only used for zigzag profile. So, This is not used for other bending operations.

N. N. Jadeja [6] designed manually operated pipe bending machine that was used in small industries. This machine was generally used for low cost purchasing purpose. It has low accuracy of bending and force is not uniformly distributed over the whole length of the pipe so, this bending machine is not preferable for precision works.

B. Okafor and D. Obiora [7] found motorized pipe bending machine which was operated by a 2-hp motor. This machine can run in both upward and downward direction. Here, worm and wheel gear mechanism were used. Mandrel is used for less thickness pipes.

P. P. Khandare et. al., [8] has developed a project to design and construct a portable pipe bending machine which was used to bend steel pipes into curve and other curvature shapes. It was easy to carry and use at any time and any place with reduced human effort and less skilled manpower. It could bend up to 4-5 mm thickness of pipe; but it is for small workshop and fabrication shop only.

Considering small entrepreneurship and inconsistent electricity supply in our country, in this project, a manual pipe bending machine with three roller mechanism is considered. The upper middle roller, controlled by a hand wheel and lead screw, is movable in the up and down direction and the lower two rollers are at a fixed height framed with the structure and base. The horizontal distance between the two lower rollers is fixed. The objective of the project is to design, construct and performance test of a manual pipe bending machine.

2. Theoretical Aspects

It is envisioned that while bending a pipe, the material surfaces experiences two types of stresses that are developed in the outer and inner side of the pipe. The 3-roller bending of pipe is similar to a simple supported beam deflection. The middle roller gives the bending force to the pipe at the center of the two rollers and the lower two rollers support the pipe. The bending process may be considered as deflection of a simple supported beam similar to that shown in Fig. 1.

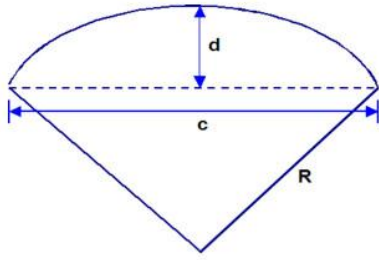


Fig.1: Simple supported beam deflection

For this type of bending according to [11], the radius is given by Eq. (1).

$$R = \frac{c^2 + 4d^2}{8d} \quad (1)$$

where, R is the bending radius, c is the distance between two fixed rollers and d is the deflection in the middle roller.

3. Design Consideration

Selection of pipe and other design considerations for the different components of the present project are briefly discussed in the following sub-sections.

3.1 Selection of Pipe

For the manually operated pipe bending machine it is necessary to consider that the machine could not bend pipes with higher diameter i.e., with higher wall thickness, that need very high pressure to bend it. Keeping this in mind, in this project only 15, 20 and 25 mm GI nominal pipe sizes (NPS) are considered. Assuming that if the machine could bend 25 mm diameter pipe, it could also bend 15 or 20 mm pipes as well. The design is based on 25 mm nominal pipe. For 25 mm NPS with schedule 5, from [11], the pipe specifications are: outer diameter (D_p) = 33.4 mm, inner diameter (d_p) = 30.1 mm. The pipe material is cold rolled, Mild Steel. According to [11], σ_{ut} = 350 MPa, σ_{yt} = 195 MPa.

3.2 Design of Rollers

As the outer diameter of pipe (D_p) is 33.4 mm, the material was selected for the roller as case-hardened steel. For fewer defects in bending, the larger roller diameter was taken as 5 (five) times the diameter of the pipe [12]. So, the large roller diameter is 167 mm. Roller dimensions are shown in Fig.2.

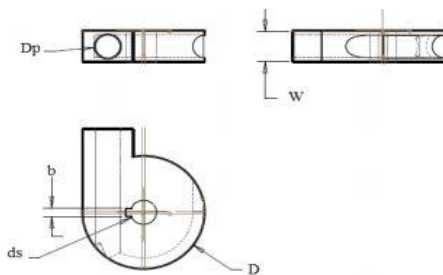


Fig. 2: Roller Dimensions

3.3 Design of Bending Die

The middle roller acts as the bending die. As mentioned before, the roller diameter is taken five times that of the pipe diameter. With the pipe outer diameter of 33.4 mm, the bending roller diameter is 167 mm.

3.4 Bending Moment and Force Calculation

As the selected pipe material is Cold rolled, Mild steel, So, as mentioned before, σ_{ut} = 350 MPa, σ_{yt} = 195 MPa. Assuming stress required for bending the pipe is equal to the yield stress (σ_{yt}); the bending stress is calculated according to [11], as,

$$\sigma_b = \frac{Mc}{I} \quad (2)$$

where, c is distance of outer fiber from the neutral axis = $33.4/2 = 16.7$ mm or 16.7×10^{-3} m, I is area moment of inertia = $\frac{\pi(D_p^4 - d_p^4)}{64} = 20794.40$ mm⁴ or 2.08×10^{-8} m⁴. Thus, the bending moment M is 242.87 Nm.

As mentioned earlier, assuming simple supported beam as shown in Fig.3 and the distance between the two supports $L = 254$ mm, according to [11], the relation between the maximum bending moment and force is given by the formula, $M = \frac{PL}{4}$. Thus, bending force, $P = 3824.8$ N.

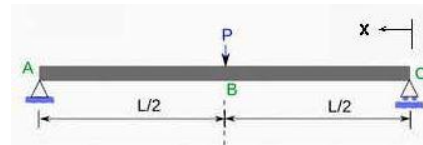


Fig. 3: Force diagram for simple supported beam

3.5 Design of Lead Screw

Assuming single threaded square lead screw. Let, the material of screw is grey cast iron (FG 200) and a factor of safety to be 3. Also, Assuming, nominal diameter, $D = 20$ mm, pitch, $p = 3$ mm, lead, $l = 3$ mm, outer diameter of collar, $D_o = 40$ mm, inner diameter, $D_i = 20$ mm, coefficient of friction $\mu = 0.15$ and torque coefficient, $C = 0.2$. In this case, the load, $P = 3824.8$ N.

According to [11], the relation between the torque to turn the screw and the load is given by equation,

$$T = \frac{PD(\tan\lambda + \mu)}{2(1 - \mu\tan\lambda)}$$

where, $\tan\lambda = \frac{\text{Lead}}{\pi D} = 0.05$, where λ is the lead angle. Thus, the torque to turn the screw $T = 7.71$ Nm. According to [12], shear stress developed by torque is given by the equation, $\tau = \frac{16T}{\pi D_i^3}$. Thus, shear stress produced due to torque, $\tau = 245.41$ MPa. A schematic of the lead screw is shown in Fig. 4.

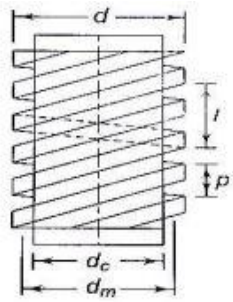


Fig.4: Schematic of the Lead Screw

3.6 Design of Shaft

Material selected for all shafts is C1045 steel (as rolled). According to [11], ultimate strength for C1045, $\sigma_{ut} = 662$ MPa, and yield strength $\sigma_{yt} = 407$ MPa. Here yield strength is considered.

While the bending force is applied, only the radial force is significant and axial force is not considered. So, shear stress due to bending moment is considered. According to [11], relation between bending moment and shear stress is,

$$\sigma_{yt} = \frac{32Mk_m}{\pi D^3}$$

For gradually applied force and rotating shaft, $k_m = 1.5$. Assuming length of the shaft $L = 25$ cm, maximum moment due to applied point load P , $M = \frac{PL}{4} = 239$ Nm.

Thus, the diameter of the shaft found from the above equation, $D = 0.021$ m or 21 mm. So, the nominal diameter 25 mm is taken. The schematic of shaft with load is shown in Fig. 5.

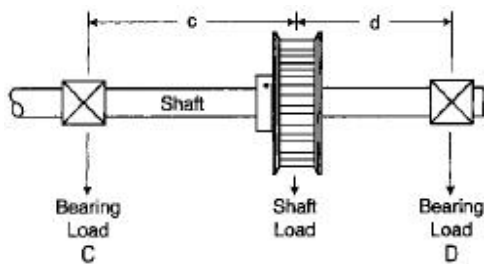


Fig.5: Schematic of the shaft with load

3.7 Design of Bearing

The bearings are used to support the radial loads only. So, the selected bearings are: Bearing no. 6205. The specification of the bearing is housing diameter, $D_b = 52$ mm, internal diameter, $d_b = 25$ mm and width of bearing, $w_b = 15$ mm and static load carrying capacity $= 7800$ N

3.8 Design of Key

A square key is assumed to be appropriate in this case. Only shear stress acts on the key. So, for the key design only shear stress is considered. The key dimensions are: width $b = D/4 = 6.25$ mm and height $h = D/4 =$

6.25 mm; For simplicity, both width and height is chosen as 7 mm. Length of the key: $L = 45$ mm [Assuming $L=1.8D$]. A schematic of a square key is shown in Fig. 6.



Fig. 6: Square key

The schematic diagram of the proposed manual pipe bending machine is shown in Fig. 7.

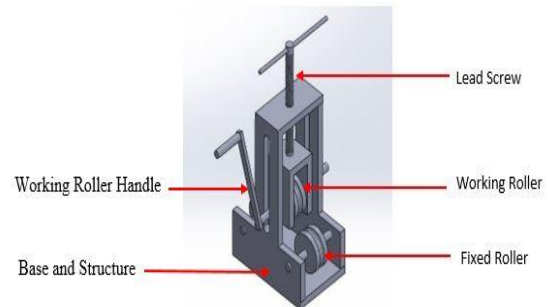


Fig. 7: Schematic of the manual pipe bending m/c.

4. Experimentation and Data Acquisition

The photographic view of the constructed Manual Pipe Bending machine is shown in Fig. 8. For the performance test, samples of three pipes with same dimensions were taken and the average values for each dimension is considered.



Fig. 8: Photographic view of the constructed pipe bending machine

In the performance test, the experiments were conducted with 15 mm and 20 mm GI pipe. The test with 25 mm pipe was not carried out as this size pipe was not available in the lab. For various midpoint deflections of the pipes the diameters were measured. The bending force was applied by giving torque on the

lead screw through the lever fitted with the lead screw. Then the pipe was moved forward and backward by using the handle of the middle roller and the required bending diameter was achieved through gradually increasing the bending pressure. By repetitive process, the required bending was achieved and a smooth bending was found. The pipe diameter and the deflection of the pipe were measured and they are shown in Table 1.

Table 1: Data for 15 and 20 mm pipe bending test.

Pipe Diameter (mm)	Deflection (mm)	Bending Diameter (mm)	Remarks
15	31.75	457.20	There was a small damage for 15 mm pipe initially. But no damage for 20 mm pipe.
	38.10	412.75	
	50.80	330.20	
20	31.75	495.30	
	38.10	444.50	
	50.80	361.95	

5. Results and Discussions

The measured data are analyzed and they are presented in the following subsections. In the experiment the length between two fixed rollers was $c = 254$ mm.

5.1 Results

By using Eq. (1), the theoretical bending radius was calculated. From the specimen, the same was measured practically after bending. The comparison between the theoretical and the experimental values are shown in Table 2.

Table 2: Comparison between theoretical and experimental values of bending radius:

Pipe dia. mm	Deflection mm	Bending dia. in mm		Deviation	
		Experimental (D_E)	Theoretical (D_T)	($D_E - D_T$) mm	% ($(D_E - D_T) / D_T$)
15	31.75	457.20	539.75	82.55	15.30
	38.10	412.75	461.52	48.77	10.56
	50.80	330.20	368.30	38.10	10.34
20	31.75	495.30	539.75	44.45	8.24
	38.10	444.50	461.52	17.02	3.69
	50.80	361.95	368.30	26.35	1.72

The comparison between theoretical and experimental values of the bending radius (diameter) is shown graphically for 15 and 20 mm pipes respectively in Fig. 9 and Fig. 10. From the Table, it is seen that the deviation reduces as the bending radius increases. While bending, the pipe is supported on the bottom

roller and pressure is created by the middle roller. In each case the two ends could not be bending properly.

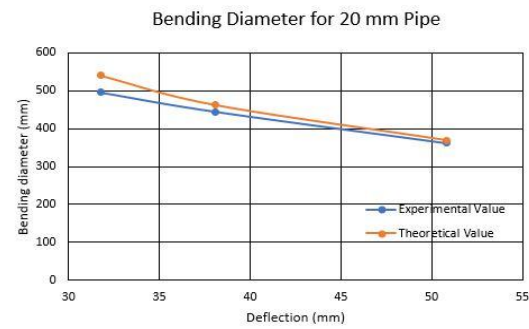


Fig.9: Graphical representation of experimental and theoretical value for 15 mm pipe bending.

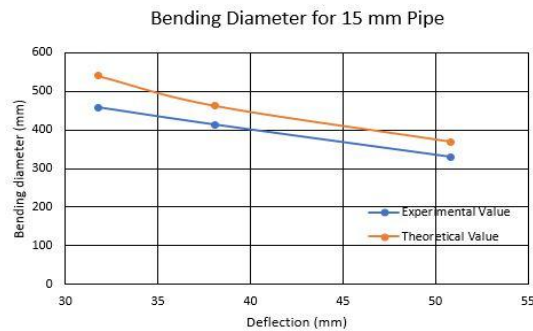


Fig.10: Graphical representation of experimental and theoretical value for 20 mm pipe bending.

5.2 Discussions:

In three-roller bending machine there are two methods for changing the bending angle and radius – one is changing the distance between two fixed rollers and another is changing the vertical displacement in the middle roller. To reduce the complexity in the design, in this project, the latter is considered. Thus, the bending radius is only dependent on the bending force exerted by the middle roller. The bending radius is found from the Eq. (1). As the distance between the two rollers is fixed, the only changeable variable in this case the distance 'd'. From Table 2, it can be envisioned that the experimental result of bending radius for various displacement in middle roller in two pipes. There is a little deviation in the results. By a slow and smooth operation this deviation could be reduced. Also, it is seen that for higher displacement of middle roller the deviation is reduced. From Figs. 9 and 10, one can see that the theoretical value is slightly higher than the experimental value. For 15 mm pipe the curves go in parallel. But for 20 mm pipe the two curves tend to intersect for higher deflection.

From the result it can be said that there is little deviation between theoretical and experimental value. By maintaining proper bending process and smooth operation the deviation could be reduced.

6. Conclusion:

Pipe bending is regular phenomena now-a-days. In mass production various automatic and semi-automatic bending mechanisms are used. But for small production automatic and semi-automatic pipe bending machine are costly. Also, where electricity is rare and costly they cannot be used. On the other hand, manual pipe bending is less expensive and can easily be made and operated. In this report the designs, construction and performance test are illustrated. From the performance test the result can be summarized as:

- 1) For two fixed rollers the bending diameter depends only on the deflection of the mid roller.
- 2) For the higher deflection the deviation in results is reduced.

Result shows that various diameter of the pipe bending can be achieved from the designed machine.

REFERENCES

- [1] Yang Hea, Li Henga, Zhang Zhiyonga, Zhan Meia, LIU Jinga, Li Guangjunb; Advances and Trends on Tube Bending Forming Technologies, Chinese Journal of Aeronautics, vol. 25, pp.1-12,2012.
- [2] Hiroyuki Goto, Ken Ichiryu, Hidenobu Saito, Yuu Ishikura, Yutaka Tanaka; Applications with a New 6-DOF Bending Machine in Tube Forming Processes, Proceedings of the 7th JFPS International Symposium on Fluid Power, Toyama, September, 2008, OS8-3.
- [3] H. A. Hussain, M. S. Pervez, M. N. Alam, A. P. Ganorkar; Design and Development of Bicycle Integrated Pipe Bending Machine, Journal of Mechanical and Civil Engineering (IOSRJMCE), e-ISSN: 2278-1684, p-ISSN:2320-334X,pp.24-28, 2014.
- [4] N. W. Nirwan, A. K. Mahalle, Design and Analysis of Portable Rolling and Bending Machine Using CAD and FEA Tool, International Journal of Engineering Research & Technology (IJERT), Vol. 2, Issue 4; April – 2013; ISSN: 2278-0181.
- [5] Avirat P. Kshar , Avantika P. Kshar; Improvement in Design and Fabrication of a Portable Pipe Bending Machine, International Journal of Mechanical Engineering and Information Technology; Vol.05; Issue 08, August; pp.1683-1687; ISSN-2348-196x, 2017.
- [6] N. N. Jadeja, Research Paper of Manually Operated Pipe Bending Machine; Indian Journal of Research, PARIPEX, vol. 3, Issue 5, ISSN- 2250-1991.
- [7] B. E. Okafor, D. O. Isiohia; Development of a Motorized Pipe Bending Machine, International Journal of Engineering and Technology; Volume 4 No. 5, May, 2014; ISSN: 2049-3444.
- [8] P. P. Khandare, D. N. Patel, M. K. Aher, R. S. Parbat and S. S. Patil; Study of Portable 3-Roller Pipe Bending, International Journal of Advanced Technology in Engineering and Science; Vol. 4, Issue 3, 2016.
- [9] Circle Radius from Chord Length and Depth. <http://mathforum.org/library/drmath/view/55146.html>.
- [10] https://en.wikipedia.org/wiki/Nominal_Pipe_Size; Visited: 27th October, 2018.
- [11] V. M. Faires, Design of Machine Elements; 4th Edition; The Macmillan Book Company, New York, USA.
- [12] S. S. Dhende, Design and Fabrication of Pipe Bending and Pipe Rolling, International Journal of Advanced Research, Ideas and Innovations in Technology, ISSN-2454-132X, Vol. 3, Issue2, 2017.

Development and Performance Test of Gearless Power Transmission System

Md. Jewel Rana¹ and A. N. M Mizanur Rahman^{2,*}

¹Department of Mechanical Engineering, KUET, Khulna 9203, BANGLADESH

²Professor, Department of Mechanical Engineering, KUET, Khulna 9203, BANGLADESH

Email: drmizan84@gmail.com;

Abstract

In modern machineries, the motion and power need to be transferred from one shaft to other for various and complex activities. Also, it is essential to achieve such objectives with maximum efficiency and minimum cost. For transmitting power between different orientations of shaft, various medium like belt, chain and especially gears are used. But due to cost of manufacture of gear, interchangeability in parts and very limited shaft orientations, need arises for an alternative system. In this project a Gearless power transmission system has been studied, a possible gearless power transmission layout is designed and developed where it can transmit power from one shaft to other without any gear being used. This project deals with transmission of power from one shaft to other at right angle by means of sliding links that form revolute pair with the hub. Links bent at right angle slide inside the holes in the hub and three links were used. Thus, as the holes in input hub rotate; it pushes the links and in turn output hub is rotated. Depending upon the power, the system was tested and it ran safely up to 985 rpm when the motor power was 1 hp and up to 246 rpm when the motor power was 0.25 hp. If the system was run higher than this permissible limit, the transmission system produces unwanted noise. Also, when the system was run lower than the mentioned rpm, it could not transfer motion from the input shaft to the output.

Key Words: Gearless drive, Power transmission, Sliding links, Elbow power transmission

1. Introduction

In modern world the living standard of human being were developed by adopting more and more equipment and technology. Today's world requires power or motion on each and every field. An essential requirement of the present world is to achieve the objectives with maximum efficiency at minimum cost. To achieve higher efficiency, proper power transmission is the prime concern of modern era. If someone wants to transfer power efficiently from its source of generation to the required place to obtain required task, then power transmission is vital concern. Different types of medium like chain-sprocket, belt-pulley, friction drive, hydraulic coupling and gears are used to transmit power between two shafts. Some of them are used to transmit power within a short distance like gears or couplings [1]. Belt-pulley or chain-sprocket is another type of transmitting mechanism where the power can be transmitted to a long distance. A belt is a looped strip of flexible material used to mechanically link two or more rotating shafts. Belt drives are used as the source of motion transfer efficiently or to track relative movement. Another type of transmitting drive exists which is known as friction drive. A friction drive or friction engine is a type of transmission that, instead of a chain and sprockets, uses two wheels in the transmission to transfer power to the driving wheels. But in friction drive system, the problem with this type of system is that they are not very efficient [2]. Normally gear is used to transmit power between two shafts in short distances. For transmitting power to adjacent shafts, various types of gear are normally

adapted. These gears can be used for transmitting power in various orientation of the shaft. For example, in parallel shaft helical gear, spur gear and herringbone gear are used. Again in non-parallel or intersecting shaft, bevel gear and worm gear are used and spiral gear and skew bevel gear are used in non-parallel shaft as well as non-intersecting shaft [1]. But there are some inherent disadvantages associated with bevel and worm gearing stated as complexity in manufacturing. Again gears are costly to manufacture, lubrication and cooling are more difficult, limited to transfer power for short distances, special machining process is required to produce, no freedom of interchangeability, replacement of the entire set of the gears, complex calculation in design are the limitation of the gear drive system [3].

An influential mechanism ought to be introduced which might be eliminated this sort of drawbacks. Therefore, gearless power transmission concept is introduced. As it replaces gears and transmits motion without the aid of gears it is also called as Gearless Power Transmission mechanism. Gearless transmission mechanism is capable of transmitting power at any angle without any gears being manufactured. Instead of using any gears, this technology elegantly convert's rotational motion using a set of cylindrical hubs, bent to 90°, in a clever, simple, smooth process that translates strong rotational force even in restricted spaces. A gearless power transmission is provided for transmitting rotational velocity from an input connected to three bent links. Both the input shaft and a hub have rotational axes. The rotational axis of the input shaft is disposed at an angle of 90° respect to the

* Corresponding author. Tel.: +88-01714002333
E-mail addresses: drmizan84@gmail.com

rotational axis of the hub. As a result, rotation of the input shaft results in a processional motion of the axis of the bent link. The rotary and reciprocating motion of bent link transmit rotation of prime mover to the 90° without any gear system to an output shaft without gears. The transmission includes input shaft, hub, links etc. [3].

In this project a gearless power transmission system has been developed for transmitting motion at right angle without using any gears. This method may be a rattling mechanism that carries force through 90° bends [4]. For that el-bow mechanism is used which is an ingenious link mechanism of kinematic chain principle and slide. Based on these ideas, the following objectives can be summarized for this project.

- To design and construct a model gearless power transmission mechanism.
- Performance test of the constructed model of gearless power transmission mechanism.

2.1 Gearless Power Transmission

This system is used to drive the machine without using any gear. The gearless transmission or El-bow mechanism is a device for transmitting motion at any fixed angle between the driving and driven shaft. This system consists of number of links that would be within three to nine. The more the number of links, the smoother is the operation. These links slide inside hollow cylindrical hub thus forming a sliding pair. This mechanism has three such sliding pair. These links are placed in a hole in the cylindrical hub and are fastened at 120° to each other [3].

The input shaft power is supplied by an electric motor. The working mechanism of the gearless power transmission system will be understood from the schematic diagram and photographic view as shown in Fig. 1 and Fig. 2. An unconventional form of transmission of power on shaft located at an angle. Motion is transmitted from driving to the driven shaft through the links which are bent to conform to the angles between the shafts. These links are located at the holes equally spaced around a cylindrical hub and they are free to slide in and out as the shaft rotates. This type of drive is especially suitable where quiet operation at high speed is essential but only recommended for low torque operation. The operation of this transmission will be apparent by the action of one link during a revolution. It is assumed that as the driving shaft is rotating clockwise, the driven shaft will rotate counter clockwise. As shaft turns through half revolution, the link slides out from both driving shaft and driven shaft and at that time the link will be at the top position between two shafts. Then during the remaining half this link slide inwards until it again reaches to inner most position as shown in Fig. 1. In the meanwhile the other links have of course passed through the same cycle of movements all links are

successively sliding inwards and outwards [3]. Although this illustration shows a right angle transmission, this drive can be applied also to shafts located at intermediate angle between 0° and 90 °.

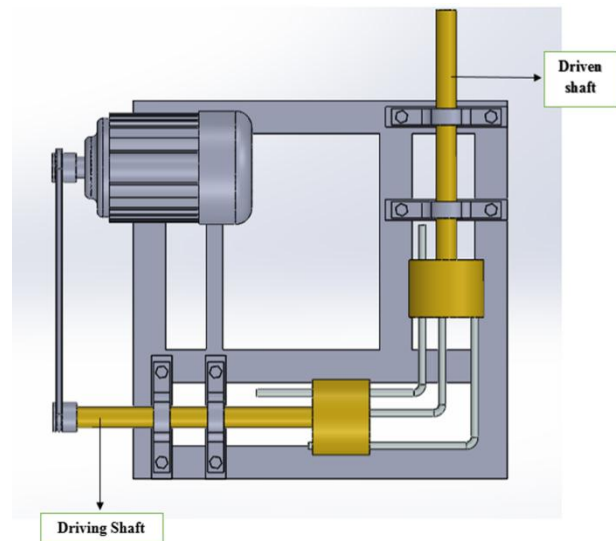


Fig. 1: Schematic arrangement of Gearless Power Transmission System



Fig. 2: Photographic view of Gearless Power Transmission

2.2. Comparison between Gear and Gearless drive

It is seen that gearless drive differs to a great extent not only in their manufacturing method or working principle but also in other aspect. These aspects are briefly discussed below:

Manufacturing method: Gears are made on special purpose machines. Hence, they are costly to manufacture and there is no interchangeability. The gearless drive has this advantage that it is machined and made on conventional machines and it gives freedom of interchangeability [3].

Causes of failure: The varied forms of failures like indentation, corrosion, erosion, fatigue etc. occurs in gear drive system. Cause of the wearing of the gear tooth resulting in the tooth leads to the replacement of the entire gear set, which is very expensive. The failure will be present in the gearless drive also but the result of those will be not be as severe as in the case of geared one [3]. Again only defected link/links replacement needs to be done.

Lubrication and Cooling: In gearless drive the lubrication and cooling system is simple and easy where as the lubrication system in gear drive system is complex. Again cooling is a big issue in gear drive system [3].

Others: Different speed at any angle is possible in gearless drive which is not possible in gear drive system [3].

2.3 Basic Components

The basic component required to establish the gearless power transmission system is: an AC motor, V-belt, Shaft and cylindrical hub, Elbow links and Bearings. A systematic arrangement of Gearless power transmission system having of all its component is shown in Fig. 3.

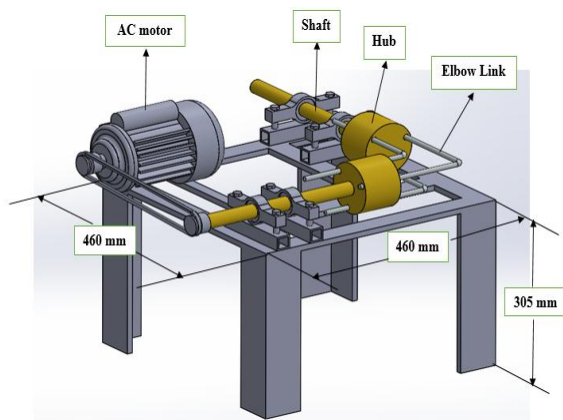


Fig. 3: Schematic arrangement of the final assembly.

3. Literature Review

The Gearless mechanism is a link mechanism of slider and pair, also known as El-bow mechanism. The component is exceptionally valuable for cornering or transmitting movements at right angle. However in certain mechanical application gearless transmission at right angle can likewise work at insensitive or exact edge plane and can be contrasted with worm and worm rigging or slant and pinion gear which are constantly utilized as a part of the business for various application. Similarly high proficiency between the info and the yield power shafts as to the rigging efficiencies [4].

The motion study and simulation of various mechanisms has been frequently studied for several years. Prof. MahanteshTanodi performed experiments on the gearless power transmission offset parallel shaft coupling [4]. Amit Kumar and Mukhesh Kumar developed the gearless power transmission between the skew shafts (SRRS mechanism) [5]. Hassanzadeh et. al. performed kinematic and kinetic study of Rescue Robot [6]. Gadhia Utsav D. has given the Quarter model of Wagon-R car's rear suspension by making analysis on ADAMS software [7]. However, there hasn't been

performed any study to sort out problems on gearless transmission mechanism. Gearless transmission for speed reduction through rolling motion induced by wobbling motion, Us [8]. Assad Anis carried out analysis of Slider Crank Mechanism on ADAMS Software package [9]. A. A. Yazdani performed Multi-body Dynamics Simulation of an Integrated Landing Gear System using ADAMS-MSC software [10]. Ranjbarkohan et. al. [11] made use of ADAMS software package and Newton's laws for analyzing the behavior of slider crank mechanism and investigated the effect of engine rpm on connecting link and crankshaft.

4. Design Details

Design consideration

According to [12], some parameters were assumed which are as follows:

Input motor power = 0.75 hp at 1440 rpm; hub diameter inner = 32 mm, Outer = 92 mm, Length of hub = 82 mm; Length of the elbow link = 204 mm and No. of Elbow links = 3. Shaft diameter = 25 mm.

For functioning of the machine and also for testing of the mechanism some calculation are necessary.

Torque Calculation

Assuming motor of 0.75 hp which was available in the laboratory and the torque available was 559.5 N.m.

With rated motor rpm of 1440 rpm, the required transmitted torque was calculated using the Eq. (1).

$$P = \frac{2\pi Tn}{60} \text{ ----- (1)}$$

The torque transmitted is 3.71 N.m.

Design of Shaft

The stresses normally adopted in shaft design [11] are: max. tensile stress = $60 \times 10^6 \text{ N/m}^2$ and max. shear stress = $40 \times 10^6 \text{ N/m}^2$. The shaft shear stress was evaluated using Eq. (2).

$$S_s = \frac{16 T}{\pi D^3} \text{ ----- (2)}$$

Considering 25 % overload, T_{\max} was 4.6375 N.m.

As the shaft is subject to torsional stress, the shaft diameter was calculated using Eq. (3).

$$T = \frac{\pi \times S_s \times D^3}{16} \text{ ----- (3)}$$

Taking factor of safety of 2.5, the shaft diameter was 21 mm. In actual construction 25 mm was taken.

Design of the Hub

Considering hub internal diameter is 32 mm and outer diameter is 92 mm and length is 82mm, the mass of the system is 28 kg.

It is known that force, $F = mg = 275 \text{ N}$. The bending stress of the hub was evaluated using Eq. (4).

$$\sigma_b = \frac{FDi^2}{Do^2-Di^2} \text{----- (4)}$$

So, the calculated value of bending stress is 37.84×10^3 N/m.

Design of the Elbow Link

It is known that the same torque will be transmitted to elbow link. So, torque on each elbow link will be total torque divided by 3 and it will be 1.5458 N.m. Thus, the elbow link diameter would be obtained by using Eq. (5).

$$T = \frac{\pi \times Ss \times D^3}{16} \text{----- (5)}$$

Considering factor of safety of 1.5, the diameter of the link will be 8.626 mm. In actual 8.5 mm was chosen. The bending stress on the link was evaluated using Eq. (6).

$$\sigma = \frac{PL}{4Z} \text{----- (6)}$$

It is known that, the section modulus for circular rod [13],

$$Z = \frac{\pi D^3}{32} \text{----- (7)}$$

The calculated value of section modulus can be obtained by using eq. (7) was $Z = 60.29 \times 10^6$ kg/m². So the calculated value of bending stress on the link [using Eq. (3)] was 473×10^6 N/m².

5. Construction of the Model

Finally all the components and parts of the project were constructed using locally available materials and are mounted on a frame. The motor available in the lab was used in this project. The hubs and links were fabricated in the lab. The bearings and pulleys were purchased from local market. Fig. 4, shows the final constructed model or assembly of the gearless power transmission system in right angles.

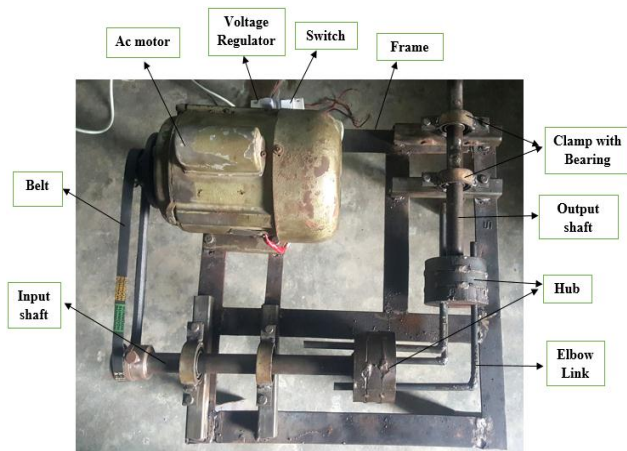


Fig. 4: Photographic view of Final setup of the project

6. Performance Test

Performance test of the gearless power transmission system consists of-

- Estimation of input motor speed, input shaft speed and output shaft speed at various power.
- Calculate speed loss between input and output shaft.
- Estimation of transmitted torque from motor at different motor speeds.
- Estimation of maximum speed for various powers at maximum torque.

The outcome of the performance tests are presented in Table 1.

Table 1 Experimental and calculated data

Power hp	Motor Speed rpm	Input shaft speed rpm	Out. shaft speed rpm	Speed loss %	Transmitted torque N.m
720.2	1367	1432	1425	0.48	5.03
712.4	1255	1325	1316	0.67	5.42
712.4	1214	1284	1273	0.85	5.60
707.2	1153	1225	1213	0.97	5.85
704.6	1113	1187	1174	1.09	6.04
702.0	1055	1130	1117	1.15	6.35
694.2	1017	1093	1055	3.47	6.51
691.6	963	1040	1010	2.88	6.85
689.0	928	1005	968	3.68	7.09
686.4	877	956	925	3.24	7.47
683.8	845	875	858	1.94	7.72
678.6	766	797	778	2.38	8.46
678.6	766	798	753	5.64	8.46
676.0	624	656	636	3.05	10.35
676.0	597	630	611	3.02	10.81
673.4	560	592	574	3.04	11.48
673.4	502	533	515	3.38	12.81
670.8	447	478	461	3.56	14.33
660.4	324	342	328	4.09	19.46
652.6	272	283	274	3.18	22.91

Maximum torque was evaluated using Eq. (8) and using the maximum stress, maximum torque is estimated and finally the maximum permissible speed is estimated. It is known that,

$$T_{max} = \frac{\pi \times \tau \times D_2^3}{16} \text{----- (8)}$$

Now the maximum stress $\tau = 60 \times 10^6$ N/m²

and with diameter $D_2 = 8.50$ mm, the maximum torque will be, $T_{max} = 7.23$ N-m

For this torque maximum permissible speed was achieved for various powers. The maximum permissible speeds are presented in Table 2.

Table 2: Maximum permissible speed estimation

Power hp	Torque (T_{max}) N.m	Maximum permissible speed rpm
1.00	7.23	985.30
0.75	7.23	738.97
0.50	7.23	492.65
0.25	7.23	246.32

7. Result and Discussion

Results: The constructed model works well as per the design but because of friction in the hub and vibration of the system some speed losses are found. The speed loss varies with changing of power because of vibration of the system varies with speed. The vibration is the result of unskilled workmanship and also the clearance between the hub and links was more. The maximum speed loss occurred when the power was 678.6 watt and the loss is 5.64%. With the help of this system, one could efficiently reduce the cost in power transmission. A certain initial torque is required to start the input shaft rotation and the minimum torque is 22.92 N.m. It is observed from the table that for various input power of motor the maximum permissible speed of the system varies. The maximum permissible limit for the 1.0 hp motor is 986 rpm and for 0.25 hp motor is 246 rpm. This value is the safest running speed of this gearless power transmission system. The input shaft speed, output shaft speed, motor speed, transmitted torque, speed loss all are estimated and shown in respective table.

Discussion: From the tabulation of all data, it can be said that the gearless power transmission system works smoothly when the system run with permissible speed limit. As speed loss is occurred in the system owing to frictional effect and vibration, it could be reduced by proper manufacturing and using lubrication. For that simple technique could be applied for lubrication to drill oil hole in the cylinder body and fill up with oil. As the surface finish cannot be done properly, so vibration often occurs when the power is transmitted in a right angle. So it can be reduced by providing surface finish.

In gearless power transmission system, the power can be transmitted at varied angle. But these are depending upon the angular limitation of the elbow joints. With more analysis and advanced analysis within the style wide-ranging applications of the drive may be discovered.

8. Conclusion

1. This projects looks very simple and easy to construct but actually was difficult to conceive and imagine without seeing an actual one. Hence, it has been

mould to present this project at 90° (El-bow mechanism) only.

2. This system runs well and transmits power in angular direction when appropriate links are used with little loss.
3. The system has the freedom of interchangeability and most important thing is its low manufacturing cost.
4. This system does not work at very low transmitting torque. Improper drilled hole may cause problem, and sudden load may break down the mechanism. The speed ratio of the mechanism is almost 1:1.

REFERENCES

- [1] Jagushte G. S, Kudalkar Hrishikesh Patil, Vikas Varak Vishal, "Design, Analysis and Fabrication of Gearless Transmission by Elbow Mechanism", International Journal for Scientific Research & Development; Vol. 4, Issue 02; 2016.
- [2] https://en.wikipedia.org/wiki/power_transmitting_Drive.
- [3] Rohit Sharma; "Gearless power transmission system in right angle"; seminar report; 2016.
- [4] MahanteshTanodi; "Gearless Power Transmission-offset Parallel Shaft Coupling", International Journal of Engineering Research and Technology; vol.3, No-3; pp.129-132, 2014.
- [5] Amit Kumar and Mukhesh Kumar; "The gearless power transmission between the skew shafts (SRRS mechanism)"; International Journal of Advanced Science and Technology; Vol.79, pp.61-72, 2015.
- [6] Elaheh Hassanzadeh Toreh, Mehdi Shahmohammadi and Nazim Khamseh; Kinematic and kinetic study of rescue robot by using Solid works software, Research Journal of Sciences, Engineering and Technology, Published May 20, 2013.
- [7] Gadhia Utsav D; Quarter Model of Wagon-R car's Rear Suspension, analyzed by using ADAMS; International Journal of Engineering Research & Technology; Vol.1;2012.
- [8] Gearless transmission for speed reduction through rolling motion induced by wobbling motion; US patent no. 6,113,511; 2000.
- [9] Assad Anis, Simulation of Slider Crank Mechanism using ADAMS software; International Journal of Engineering & Technology; Vol: 12 No: 04; 2012.
- [10] A. A. Yazdani, J. Jin, G. Lepage Jupiter and G. Cozzonlino; Multi-body Dynamics Simulation of an Integrated Landing Gear System using MSC ADAMS software; Users Conference Irvine, CA; May 7-8, 2013.
- [11] Mohammad Ranjbarkohan, Mansour Rasekh, Abdul Hamid Hoseini, Kamran Kheiralipour and Mohammad Reza Asadi; Kinematic and kinetic analysis of slider-crank mechanism in Otto linear four cylinder Z24 engine; Journal of Mechanical Engineering Research; Vol. 3(3), pp. 85-95;2011.
- [12] R. Somraj, B. Sailesh; "Design and Fabrication of Gearless Power Transmission for Skew Shafts";

International Research Journal of Engineering and Technology (IRJET); Volume: 04 No- 04; 2017.

[13] PSG Design data book.

[14] Andrew Pytel and Ferdinand L. Singer; 'Strength of Materials', 4th edition, Addison-Wesley Longman, Inc., 1999.

ICMIEE18-254

Development of an Izod Impact Test Machine for Non-Metals

Mohammad Emran Hossain and A.N.M. Mizanur Rahman*

Department of Mechanical Engineering, Khulna University of Engineering & Technology, Khulna 9203, Bangladesh

Abstract: Different type of tests that are conducted to know the various properties of metals and non-metals include tensile, compression, hardness, fatigue, flexural, torsional etc. There are many properties of metals and non-metals such as ductility, brittleness, toughness, hardness, fatigue strength, impact load etc. which are important for their uses. To identify metal or non-metals some characteristic properties are required. To differentiate any metal from another these characteristic properties should be known. Izod impact test is one of them where the finding is the impact strength of the material. Izod impact testing is an ASTM standard method of determining the impact resistance of materials. A pivoting arm is raised to a specific height and then released. The arm swings down hitting a notched sample, breaking the specimen. A part or material sustainability can be defined by Izod Impact test. The ability to identify the characteristics of the product helps to prevent the failure of the material on sudden load. The optimum value of this parameter for maximum value of Impact energy absorbed can be determined. In plastics and non-metals Izod impact test is required for stability against sudden load and internal strength. In this project an Izod Impact Test machine for non-metals has been designed, fabricated and its performance was tested. The comparison of impact properties of Polycarbonate was made. The machine performance is satisfactory.

Key Words: Material properties, Impact test, Izod impact test, Charpy test, Non-metal test.

1. Introduction

Impact is an important phenomenon in governing the life of a structure. In case of an aircraft, impact can take place by a flying bird hitting the plane; while it is cruising or during take-off and landing, the aircraft may be struck by debris that is present on the runway, and similar other causes. It must also be calculated for roads if speed breakers are present, in bridge construction where vehicles punch an impact load, etc. [1].

Impact tests are used in studying the toughness of material. The toughness of a material is a factor of its ability to absorb energy during plastic deformation. Brittle materials have low toughness, as a result a small amount of plastic deformation that they can endure. The impact value of a material can also change with temperature. Generally, at lower temperatures, the impact energy of a material is decreased. The size of the specimen may also affect the value of the impact test because it may allow a different number of imperfections in the material, which can act as stress risers and lower the impact energy on the specimen [1]. Notched bar impact test of metals provides information on failure mode under high velocity loading conditions leading to sudden fracture where a sharp stress riser (notch) is present.

The energy absorbed at fracture is generally related to the area under the stress-strain curve which is termed as toughness in some references. Brittle materials have small area under the stress-strain curve (due to its limited

toughness) and as a result, little energy is absorbed during impact failure. As plastic deformation capability of the materials (ductility) increases, the area under the curve also increases and absorbed energy and respectively toughness increase. Similar characteristics can be seen on the fracture surfaces of broken specimens. The fracture surfaces for low energy impact failures, indicating brittle behaviour, are relatively smooth and have crystalline appearance in the metals. On the contrary, those for high energy fractures have regions of shear where the fracture surface is inclined about 45° to the tensile stress, and have rough and more highly deformed appearance, called fibrous with increasing strain rate. A variety of testing methods are used to evaluate the toughness of a material, three of the most common are uniaxial tension, fracture toughness, and the Izod Impact test [1].

Two basic types of impact testing have been developed. One is bending which includes Charpy and Izod test; other one is Tension impact tests. Bending tests are most common and they use notched specimen that are supported as beams. In the Charpy test, the specimen is supported as a simple beam with the load at the centre. In the Izod Impact test, the specimen is supported as cantilever beam [1, 2].

Now-a-days, plastics, rubbers, glasses are using in many commercial purposes, so stress and impact analysis for such non-metals is essential for their sustainability against sudden load and stress conditions. For example, a plastic pipe, under the soil, need to absorb more pressure

* Corresponding author. Tel.: +88-01714002333
E-mail addresses: drmizan84@gmail.com

to sustain its durability. Izod Impact test is one of the basic tests for non-metals to check their durability against such condition.

Previous century was the initial time for realizing the impact test necessity. The impact test procedure seems to have become known as the Charpy test in the first half of the 1900's for similarity of their testing procedure. Mechanics of Notched impact test for polycarbonate was related to impact test of non-metals. The Charpy V-notched impact test to determine the ductile-brittle transition was another work on impact test. Most of these works were basically on the analysis on the impact test of non-metals and are on the basis of design and construction of the machine. The outcome of these works are to check the metals and non-metals sustainability, striking angle, amount of force required to create impact. Using notched specimens, the specimen is fractured at the notch. Stress is concentrated and soft materials fail as brittle fractures. Both Charpy and Izod Impact testing utilize a swinging pendulum to apply the load. ASTM has standardized the impact test with two testing approaches: the Charpy and Izod.

It is said (Harvey, 1984) that 'No man is civilized or mentally adult until he realizes that the past, the present, and the future are indivisible.' This statement applies equally to all fields of science and technology, including material testing. This contribution focuses on the development of material testing using the Charpy test method, which is based on the use of a pendulum to apply an impact force to a specimen. Some of the milestones in the development of this technique have been outlined in a conference on Fracture Mechanics in Design and Service - Living with Defects by the Royal Society in 1979. According to the paper 'Historical Background and Development of the Charpy Test' by H. P. L. Tóth et. al. [3], the important role of the impact pendulum test machine was highlighted. The present history-oriented contribution illuminates the development of impact testing from a material toughness characterization point of view. Historically, the impact-pendulum test method and associated apparatus were suggested by S. B. Russell in 1898 and G. Charpy in 1901. G. Charpy presented his fundamental idea in France in the June issue of the Journal Soc. Ing. Civ. De Francais and in the Proceedings of the Congress of the International Association for Testing of Materials, which was held in Budapest in September 1901. The impact-test procedure seems to have become known as the Charpy test in the first half of the 1900's, through the combination of Charpy's technical contributions and his leadership in developing the procedures to where they became a robust, engineering tool [3].

Marshall et. al. [4] developed a fracture mechanical analysis to account for the observed dependence of W (energy per unit area) on notch size. A correction factor had been derived to accommodate notch effects and this

allows for the calculation of the strain energy release-rate G directly from the measured fracture energies. Tests PMMA have shown that corrected results were independent of specimen geometry and the G_c for PMMA had been evaluated as $1.04 \times 10^3 \text{ J/m}^2$. The experimental results showed that there was an additional energy term which must be accounted for and that had been interpreted there as being due to kinetic energy losses in the specimens. A conservation of momentum analysis had allowed a realistic correction term to be calculated to include kinetic energy effects and the normalized experimental results showed complete consistency between all the geometries used in the test series. It was concluded that the analysis resolved many of the difficulties associated with notched impact testing and provided for the calculation of realistic fracture toughness parameters.

McMillan and Tesh (1975) experimentally investigated the impact failure in a glass, a glass-ceramic and two conventional ceramics. This revealed the occurrence of complex dynamic effects during impact as a result of vibrations induced in the test specimen. These effects were studied by using strain gauges fitted to the impactor and the specimen. To aid understanding of the observations, computer simulations of impact behavior was undertaken and the results were compared with the experimental data. A conclusion was drawn concerning the design and limitations of impact testing machines of the pendulum type for investigating impact failure of brittle materials - the value of instrumentation of the pendulum and of computer calculations of the type described was emphasized.

Hine (1986) studied the impact behavior of polyether sulphone using a specially constructed instrumented impact testing machine. This machine was of the pendulum type and the samples were fractured in three-point bend loading. It was shown that accurate force/deformation curves could be obtained in spite of complications due to flexural vibrations of the test sample. Measurements were made on both sharp-notched and blunt-notched specimens over a range of crack lengths. It was found that the sharp-notched samples could be analyzed in terms of fracture toughness, whereas the blunt-notched samples corresponded to a constant critical stress at the root of the notch. The importance of multiple crazes at the crack tip in blunt-notched specimens was emphasized. It was also shown that ageing reduces the fracture toughness; while on the other hand, the critical stress observed in blunt-notched specimens, who had been associated with the craze initiation stress, was not affected by ageing [5].

Ajit et. al. [6] investigated the impact resistance of silicon containing modified Cr-Mo steels within a temperature regime of - 40 to 440°C using the Charpy method. The results indicated that the energies absorbed in fracturing the tested specimens were substantially lower at temperatures of - 40°, 25° and 75°C compared to

those at elevated temperatures. Lower impact energies and higher ductile-to-brittle transition temperatures (DBTTs) were observed with the steels containing 1.5 and 1.9 wt. % Si. The steels containing higher Si levels exhibited both ductile and brittle failures at elevated temperatures. However, at lower temperatures, brittle failures characterized by cleavage and inter granular cracking were observed for all four tested materials.

Kinloch et. al. [7] conducted instrumented impact tests on both a simple unmodified and rubber-modified epoxy polymer over a range of impact velocities. Single-edge notched three-point bend and double-edge notched tensile specimens had been employed and from the measured force-time response, values of the fracture energy, G_{Ic} , and the fracture toughness K_{Ic} had been determined and shown to be independent of the geometry of the test specimen. However, the measured value of the toughness was found to be dependent upon the impact velocity of the pendulum-striker and this dependence appears to largely arise from dynamic effects presented in the test technique. The nature of these effects were discussed and modeled and the material impact resistance of the epoxy polymers determined. These studies clearly revealed that the multiphase microstructure of the rubber-modified epoxy leads to a significant improvement in the impact behavior of cross-linked epoxy polymers.

Giovanni [8] investigated the impact fracture toughness of sintered iron and high-strength sintered steels, with densities between 7.0 to 7.25 gm/cm³, by means of instrumented impact testing on fatigue pre-cracked as well as 0.17 mm-notched specimens. Experimental results showed that the fracture behavior was controlled by the properties of the resisting necks at the cracked notch tip. The materials with impact yield strengths of up to 700 MPa display an increase in fracture toughness as the yield strength was increased. These materials undergo continuous yielding during loading, and ductile fracture took place once the critical plastic strain was attained within a large process zone. A process-zone model, physically consistent with the fracto-graphic observations, correctly rationalized their impact fracture toughness. The materials with higher impact yield strengths display an impact curve which was linear up to fracture and were characterized by a fracture toughness which was independent of the yield strength. For these materials, the process zone reduced to the first necks at the cracked notch tip and fracture took place once the local applied stress-intensity factor reached the fracture toughness of the matrix. Based on the above information, the objectives of the present project are as follows:

- To design and construct an Izod Impact test machine for non metals.
- To test the performance of Izod Impact test machine.
- To analyze the properties obtained from the Izod Impact test machine.

3. Impact Testing Features and Principles

Testing of materials can be carried for various purposes and it may be either destructive or non-destructive. In destructive test, the specimen either breaks or remains no longer useful for future use, e.g., tensile test, torsion test. But in non-destructive test, the specimen does not break and even after being tested, it can be used for the purpose for which it is made, e.g., radiography, ultrasonic test. Impact test is a dynamic test in which a selected specimen, usually notched, is struck and broken by a single blow in a specially designed machine. It signifies the toughness of the material; i.e., ability to deform plastically and to absorb energy in the process before fracture. The key to toughness is a good combination of strength and ductility. A material with high strength and high ductility will have more toughness than a material with low strength and high ductility. The essential features of impact test are: suitable specimen, an anvil or support, a moving mass of known kinetic energy and a device for seaming the energy absorbed by the broken specimen. The schematic of an Izod Impact test machine is shown in Fig. 1.

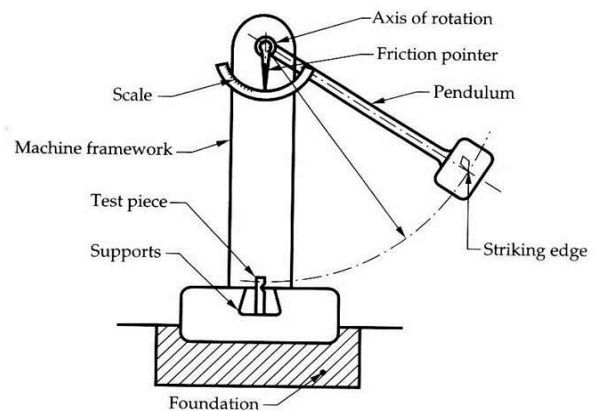


Fig.1: Schematic of Izod Impact Test Machine

4. Design of Izod Impact Testing Machine

The main objective of Impact test is to predict the likelihood of brittle fracture of a given material under impact loading. The test involves measuring the energy rammed in breaking a notched specimen when hammered by a swinging pendulum as shown in Fig.1. The energy can be calculated from the positions of the pendulum before and after struck the specimen. The detail of the calculations for designing the Izod Impact test machine is available in [9] but some of them are briefly described below:

Design of the Machine:

An MS base with dimensions of 46 × 30 × 9.5 cm was chosen to support the whole structure. The pendulum is chosen as a rectangular inverted U-shaped one as shown in Fig. 2. The gap between the two sides of the pendulum is 63.5 mm plus the clearance between clamp and sides. Assuming a clearance of 6.35 mm., the gap between two sides of the pendulum is = (63.5 + 2 × 6.35) mm = 76.2

mm. The pendulum sides are constructed from 12.7 mm thick MS plate. Hence, the dimension of the sides is $90 \times 90 \times 12.7$ mm.

The pendulum arm is made of 25.4 mm dia pipe with a length of 170 mm from the centre of swing. The total mass of the pendulum arm is 3.43 kg.

The maximum angle the pendulum can swing is 90° with vertical and the maximum energy stored in this position = $mgh_1 = m g \times r (1 - \cos\alpha) = 3.43 \times 9.81 \times 0.382 \times (1 - \cos 90^\circ) \text{ N.m} = 12.85 \text{ J}$.

Thus, the maximum velocity achieved, $V = \sqrt{2gh_1} = \sqrt{2 \times 9.81 \times 0.382 \times (1 - \cos 90^\circ)} = 2.74 \text{ m/s}$.

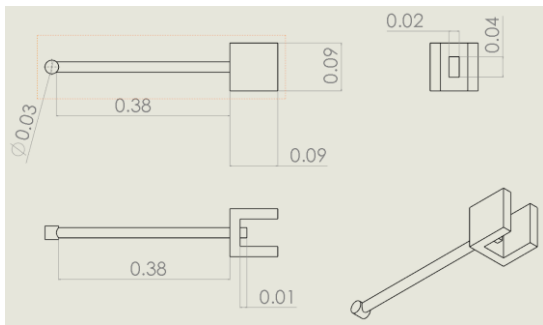


Fig 2: Schematic View of Rectangular Pendulum

After calculation of various parameters the specification of the designed Izod impact test machine is as follows and is shown in Fig.3: The clamp was purchased from the local market.

Machine Specification:

- Base dimension = 46 cm \times 30 cm \times 9.5 cm
- Clamp dimension = 10.1 cm \times 6.35 cm \times 7.5 cm
- Pendulum cross-section = 9 cm \times 1.27 cm
- Pendulum mass, $m = 3.43$ kg
- Pendulum radius, $r = 382$ mm
- Range of pendulum swing angle = 0° to 90°
- Tolerance angle or error angle = 2° .

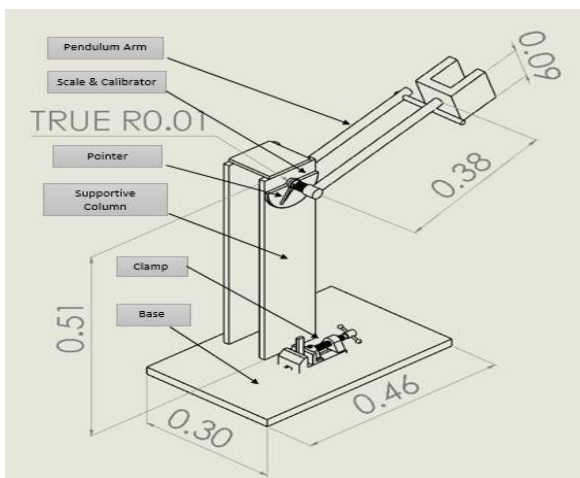


Fig. 3: Various Dimension of the Model.

5. Experimental Procedure

There are several standards for impact test. The ASTM standard for Izod Impact test for non-metals is ASTM

D256. The result is expressed as energy lost per unit thickness (say, J/cm) at the notch. The dimension of a standard specimen for ASTM D256 is $63.5 \times 12.7 \times 3.2$ mm. The test specimen varies on which material is being tested. Metallic samples are square in cross-section whereas polymeric specimens are often rectangular being struck parallel to the long axis of the rectangle. The specimen is held at one end and the other end is free. A 45° V-notch of depth 2 mm is cut at the middle. The experimental setup depends on the setting up of two things of the specimen on the clamp and the angle of the pendulum where it is freed. These are (i) Setup on the clamp and (ii) Angle graduation.

Setup on the Clamp: The specimen is set on the clamp tightly and rigidly. The middle section of the V-notch is situated at the centre of the clamp. As suggested in [5], the striking edge must strike the specimen 22 mm above the clamp as shown in Fig. 4.

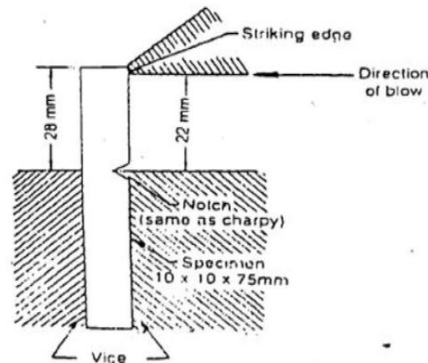


Fig. 4: Striking Edge and Striking Position

Angle graduation: First of all from an assumable angle, the pendulum is swung and then decreases it gradually onto the angle where the fracture actually occurred. The dial moves upward and the scale give the angle of the impact load. From the angular difference between initial angle and pointer angle absorbed energy and impact strength can be calculated. Fig. 5 and Fig. 6 show the photographic view of the experimental setup.



Fig. 5: Photo of Experimental setup from Front.



Fig. 6: Photo of Experimental setup from Top

6. Performance Test

The performance test was carried out with the constructed Izod Impact test machine with the following six samples whose specifications are as shown in Table 1.. For each test three samples were used and the average of the three results was taken.

Table 1: Specification of different samples for testing

Test No.	Specimen name	Length (mm)	Width (mm)	Thickness (mm)
01.	U-PVC pipe	63.5	12.7	2.0
02.	Thread pipe	63.5	12.7	3.2
03.	PPR pipe	63.5	12.7	6.0
04.	U-PVC pipe	63.5	12.7	6.3
05.	U-PVC pipe	63.5	12.7	8.0
06.	U-PVC pipe	63.5	12.7	10.0

The setting up of the specimens was closely monitored. It was ensured that the clamp should hold the specimen at the middle position and pendulum must be frictionless as much as possible. The free swing of the pendulum movement was ensured. The sensitivity of the dial was checked. In this experiment the specimen criteria follow the basic of ASTM D256 standard. For checking the experimental value of non-metals some polycarbonate characteristics were also examined.

7. Results and Discussion

The experimental data and some calculated parameters are presented in Table 2 to Table 3.

Table 2: Test Results for Minimum Fracture Angle and Absorbed Energy

Test No.	Specimen Material	Thickness (mm)	Minimum Fracture angle	Absorbed Energy (J)
01.	U-PVC pipe	2.0	10°	0.042
02.	Thread pipe	3.2	21°	0.333
03.	PPR pipe	6.0	30°	0.7524
04.	U-PVC pipe	6.3	24°	0.3090

05.	U-PVC pipe	8.0	29°	0.5164
06.	U-PVC pipe	10.0	43°	1.144

Table 3: Test Results for Minimum Impact Force and Impact Strength

Test No.	Specimen Material	Thickness (mm)	Force (N)	Impact strength (J/m)
01.	U-PVC pipe	2.0	18.20	92.48
02.	Thread pipe	3.2	79.43	239.41
03.	PPR pipe	6.0	160.28	204.37
04.	U-PVC pipe	6.3	103.60	97.72
05.	U-PVC pipe	8.0	150.18	104.37
06.	U-PVC pipe	10.0	322.64	115.21

To compare the results from the constructed machine, some tests were carried out with polycarbonate specimen. Table 4 shows the breaking and fracture energy for polycarbonate specimen. Four specimens of 63.5 × 12.7 × 6.35 mm were tested. The fracture energy is calculated by dividing the experimentally obtained breaking energy by the specimen thickness.

Table 4: Test Result for Polycarbonate Sample

Test No.	Maximum pendulum energy(J)	Breaking energy (J)	Fracture energy per thickness (J/m)
01.	2.82	0.7873	123.98
02.	2.82	0.7399	116.52
03.	2.82	0.7942	125.07
04.	2.82	0.7257	114.29

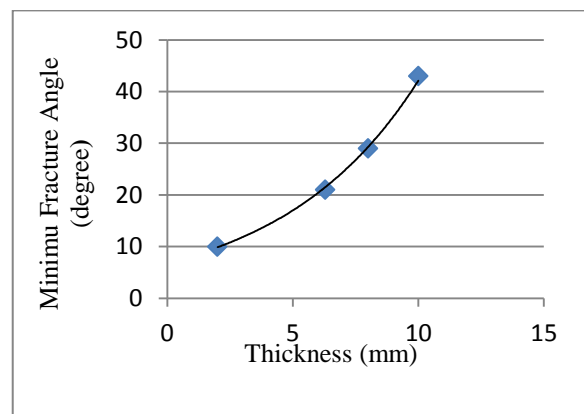


Fig 7: Best fit curve for thickness vs minimum fracture angle .

The equation from the best fit curve for Fig. 7 is an exponential line and the equation is: $Y = 6.860e^{0.1815X}$.

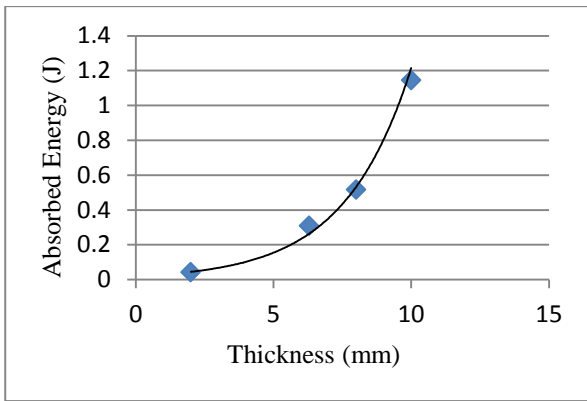


Fig 8: Best fit curve for thickness vs absorbed energy.

The equation from the best fit curve for Fig. 8 is an exponential line and the equation is: $Y = 0.0197e^{0.4215X}$.

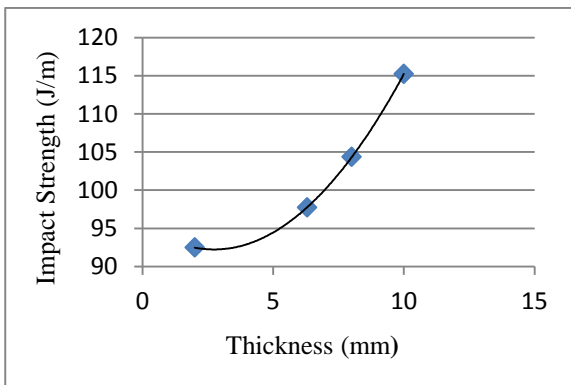


Fig.9: Best fitcurve for thickness vs Impact strength.

The equation from the best fit curve for Fig. 9 is a polynomial and the equation is:

$$Y = 0.4326 X^2 + 2.3892X + 95.508$$

From the test results of Izod impact test and analyzing the properties of U-PVC specimen, it is clear that the toughness and minimum fracture angle, absorbed energy increases with the thickness of the specimen. The impact strength of non-metals gradually increases with the thickness as envisioned from Fig. 9.

The minimum fracture angles are 10°, 21°, 30°, 24°, 29° and 43° for 2-mm U-PVC, 3.2-mm Thread, 6-mm PPR, 6.3-mm U-PVC, 8-mm U-PVC and 10-mm U-PVC pipes respectively.

From Table 2, it is evident that the absorbed energy for various size specimens are: 0.04204 J, 0.333 J, 0.7524 J, 0.354 J, 0.5164 J and 1.114 J for 2-mm U-PVC, 3.2-mm Thread, 6-mm PPR, 6.3-mm U-PVC, 8-mm U-PVC and 10-mm U-PVC pipes respectively; whereas, the absorbed energy for polycarbonate is 0.7617J as seen from Table 5. So, from the comparison of U-PVC and polycarbonate specimen it can be concluded that polycarbonate required two times more energy to

breaking the similar specimen.

8. Conclusion

Izod Impact test machine is constructed for testing absorbed energy and material strength. The constructed machine will be used for checking absorbed energy and strength of non-metals (plastics) of various thicknesses. In this machine maximum 12.84J of energy could be achieved with the pendulum velocity of 2.73 m/s. Different types of U-PVC pipe samples were tested and compared with the corresponding values of polycarbonate. The polycarbonate specimen's absorbed energy, impact strength are greater than U-PVC pipe. The result of the tests are based on the thickness, minimum fracture angle, force required to break the specimen, absorbed energy, impact strength etc.

References

- [1] M. N. Silberstein; Mechanics of Notched Izod Impact Testing of Polycarbonate; Massachusetts Institute of Technology June 2005.
- [2] C. Glocker; On Frictionless Impact Models in Rigid-body Systems; April 2012.
- [3] L. Tóth, H. P. Rossmanith and T. A. Siewert Bay Zoltán; Historical Background and Development of the Charpy Test.; Applied Research Foundation, Institute for Logistics and Production Systems, Miskolc, Hungary.
- [4] G. P. Marshall, J. G. Williams and C. E. Turner; Fracture Toughness and Absorbed Energy Measurements in Impact Tests on Brittle Materials; Journal of Materials Science, Vol. 8., issue 7, pp. 949-956, 1973.
- [5] Narinderpal Singh; Experimental Study and Parametric Design of Impact Testing Methodology; M. Eng. Thesis Report, 2009.
- [6] Ajit Roy, Pankaj Kumar and Debajyoti Maitra; The Effect of Silicon Content on Impact Toughness of T91 Grade Steels; Journal of Materials Engineering and Performance, Vol. 37, 2008.
- [7] A. J. Kinloch, G. A. Kodokian, M. B. Jamarani; Impact Properties of Epoxy Polymers, Journal of Materials Science, Vol. 22, Issue 11, pp. 4111-4120, 1987.
- [8] G. Straffelini; Impact Fracture Toughness of Porous Iron and High-Strength Steels; Metallurgical and Materials Transactions, Vol. 31(a). 2000.
- [9] M. Emran Hossain, Design, Construction and Performance Test of a Izod Impact Test Machine for Non-Metals, UG Research Report, Dept. of Mechanical Engineering, KUET, Khulna, 2018.

Construction and Performance Test of a Pedal Operated Double Cylinder Reciprocating Pump

Abdullah al Musabbir¹ and A.N.M Mizanur Rahman^{2,*}

¹UG Student; ²Professor

Department of Mechanical Engineering, Khulna University of Engineering & Technology, Khulna, BANGLADESH
email: drmizan84@gmail.com

Abstract- Bangladesh is an agricultural country, so irrigation or watering of the cultivable land is a great concern for the farmers. Capable farmers use motorized centrifugal pumps for the purpose of irrigation or lifting water. On the other hand, poor farmers, particularly those have small lands, cannot afford motorized pumps. Also, electricity problem has become a big issue during the irrigation season and many areas of the country are still deprived of electricity. As most of the farmers in rural areas are below the poverty line, so the electricity bill of these motorized pumps become a burden for them. In this circumstance, a manually operated, cost effective and high efficient water pumping system is going to be a great importance. So, this project emphasizing the design and construction of a pedal operated double cylinder reciprocating pump that may be an amazing solution to this irrigation problem of poor farmers. At this moment, some farmers are using treadle pump in place of motorized centrifugal pump. But it is proven that bicycling pedaling is much more comfortable and efficient, so a pedal operated double cylinder reciprocating pump system would be more convenient than the treadle pump. A model of the proposed pump was constructed and tested. The results show that the pedal operated double cylinder reciprocating pump system is cost effective, easy maintenance and gives an average discharge of about 1250 liter/hr. So, the poor farmers of the remote areas where electricity problem is acute can be benefitted by using this pedal operated pump.

1. Introduction

Bangladesh is an agricultural country and therefore irrigation plays a vital role in production of food grains and cereals for the people of the country. The productivity of any species depends upon the fertility of land and of course on other inputs such as improved seed, fertilizer and largely on the availability of ensured water supply in the fields. With the supply of irrigation water, most of the agricultural lands can be brought under cultivation of high yielding crops. The productivity of the land, which is now producing food under natural condition, can be increased considerably by the application of supplemental irrigation. The socio-economic condition of Bangladeshi farmer does not permit large scale irrigation investment. Hence, introduction of small scale irrigation using treadle pumps or pedal pumps can play a vital role for increasing food production in Bangladesh. Capital intensive technology like deep tube-wells, shallow tube-wells are beyond the purchasing capacity of the poor farmers, while they can afford labor intensive technologies such as pedal pump, hand pumps, rower pumps, treadle pumps etc. due to their lower cost, easy maintenance and user friendly technology. In the context of Bangladesh, where labors are abundant and most of the farmers are poor, the pedal pump seems to be an appropriate irrigation technology. Such kind of irrigation technologies are operated and maintained by farmers themselves from their own capital for producing crop in the small fragmented lands. The average small farm sizes spreading over a number of scattered plots are unsuitable to irrigate with a large size of stream.

But the manually operated technology with a small stream size is suitable for small and fragmented farm holding and involves less mechanical and maintenance problems. From [1], it is seen that, according to statistics of the Peoples' Republic of Bangladesh 1986; the poor farmers represent 70% of the population in the country and they own only 20% of total land. Due to their extreme poverty, they are gradually joining the landless group. In this context, manually operated pedal pump is helpful for poor farmers to reduce poverty. The current success of manually operated pump can be explained in terms of factors like appropriate design, low cost, effective marketing, and high cash returns [1].

Some researchers had focused their endeavor on the development of low lift labor-intensive devices and had succeeded to develop some devices of such characters like treadle pump, rower pump, wheel pump, diaphragm pump, blower pump, etc. But these pumps still are not popular in the country due to their low efficiencies and discharges, short service lives, high friction losses and many other mechanical troubles. Operation of the devices is very laborious and operators often complain about their suffering from various health hazards [2].

Nobody can work at much over $\frac{1}{5}$ th of a horse power for very long period. As mentioned before [2], many users of these devices complained about their health troubles and desired to get a better technology requiring less manual power and mechanical troubles. High initial maintenance cost, non-availability of spare parts, requirements of large irrigable land and similar other restrictions make the poor illiterate farmers reluctant to

* Corresponding author. Tel.: +88-01714002333
E-mail addresses: drmizan84@gmail.com

use even the shallow tube-wells. But the components of pedal pumps can be locally produced with low-cost and all spare parts are available in the country. Hence, a study is needed to design and develop the pedal pump to make it simple to ensure automatic participation of farmers [3].

A minor revolution is taking place in the field of manual irrigation in Bangladesh. Low-cost bamboo and PVC tube-wells introduced in the late 1970s have brought irrigation within the reach of millions of small and marginal farmers for the first time.

The history of positive displacement reciprocating pumps goes back as far as 275 BC in Ancient Rome. In the sixteenth century, great lift and force pumps, driven by water wheels became the effective method for pumping water to be piped in Europe [4]. As late as 1987, the World Bank estimated that, throughout the world, 1.8 billion people would need improved water supplies, and that wells equipped with hand pumps would be an appropriate choice to meet the needs of this number of people. Most of the reciprocating hand pumps commonly used in developing countries have their origins in designs developed during the late 19th and early 20th centuries in the United States and in Europe [5].

What is needed in a developing country is a manually operated pump which can be easily operated by a person for relatively longer period of time and which lifts significant volumes of water with as little effort as possible. Because of the high usage requirements and because the pump must operate as a practical device far from cities having maintenance facilities and personnel, the pump must be both reliable and easily repaired. So this project has some specific objectives. These are:

- To design and construct a cost effective reciprocating pump for irrigation and water lifting.
- To add pedaling system instead of conventional manual water pumping arrangement.
- To test the performance of the proposed pedal operated double cylinder reciprocating pump.

2. Theoretical Aspects

Various motorized water pumping system for irrigation and household purposes is introduced in the urban areas of Bangladesh, but in the rural areas of the country where electricity is hardly available hand powered tube-wells are used for lifting water and irrigation purposes. In recent years treadle pump is also introduced in Bangladesh instead of motorized water pumping. There are also various types of centrifugal pump, submersible pump available for water lifting or sewage purposes.

Hand Pump

Hand pumps are manually operated, where mechanical advantage of lever action is used to move fluids from one place to another. They are widely used in every country in the world for a variety of industrial, marine, irrigation and leisure activities. There are many different types of hand pump available, mainly operating on a piston, diaphragm or rotary vane principle with a check valve in opposing directions. Most hand pumps have plungers or valve on the entry and exit ports to the chamber operating reciprocating pistons, and are positive displacement type.

Centrifugal Pump

Centrifugal pumps are used to induce flow or raise pressure of a liquid. At the heart of the system lies impeller which is a series of curved vanes fitted inside the shroud plates. The impeller is always immersed in the water. When the impeller is made to rotate, it makes the fluid surrounding it to rotate [5]. This imparts centrifugal force to the water particles and water moves radially out. Since the rotational mechanical energy is transferred to the fluid, at the discharge side of the impeller, both the pressure and kinetic energy of water will rise. At the suction side, water is getting displaced, so a negative pressure will be induced at the eye. A low pressure in it helps to suck fresh water stream into the system again and the process continues.

Treadle Pump

A treadle pump is a human-powered suction pump that sits on top of a well and is used for irrigation. It is designed to lift water from a depth of 7 meters or less. The pumping is activated by stepping up and down on a treadle, which is nothing but a lever that drives piston, creating cylinder suction that draws ground water to the surface. Treadle pumps free farmers from dependence on rain-fed irrigation and helps farmers maximize return on their small plots of land. The treadle pump can do most of the work of a motorized pump, but costs considerably less. Pump prices including installation range between \$20 and \$100 [6]. Because it needs no fossil fuel, it can also cost less (50%) to operate than a motorized pump.

2.1 Limitations of Conventional Water Pump

A hand pump connected with a typical well is driven by pressing the end of a lever and by either pulling it upward or permitting it to return upward due to the weight of the well. The work of lifting the water occurs as the lever is pushed down. This requires large amount of human effort and the quantity of water lifted through this process is unsatisfactory. Again in case of centrifugal pump due to cavitation and insufficient NPSH, people face some acute problem in the irrigation period [7]. Moreover, they can hardly bear the expense of these pumps utilities. On the other hand, where electricity is unavailable motorized water pumps

whether it is centrifugal or reciprocating is of no use. So, there are various types of barrier or limitations existed in the conventional water pumping system.

2.2 Development of Pedal Operated Pump

Due to some limitations of conventional water pumps and in capacitance of the poor farmers to buy a conventional pump there is a need of developing a reciprocating pump which could be run without electricity and also cost effectively. In this respect a pedal powered reciprocating pump is the best suitable solution.

One problem with most reciprocating pumps is caused by the fact that the lever is used to operate the pump, while providing an exceedingly simple mechanism, does not make particularly good use of the ability of the human body. Another problem with most reciprocating pump arises from the fact that the work of lifting water and the pump mechanism occurs only as the lever is pushed down. For example, a conventional reciprocating pump requires a force of about 20 kg as the lever is pushed down, while a force of only about 4 kg is required to move the lever. Thus, uneven demands are placed on the user to supply energy to the pumping process. But in case of pedal powered reciprocating pump, such kind of problems will not arise. As treadle pump is making a great impact in the rural areas where electricity is unavailable, so it can be said that the manual pumps which are powered by the legs are much more convenient. But in the type of pump where legs are not moved in circular direction, makes the user uncomfortable and tedious. So, efficiency is decreased when it works for a longer duration. So, a pedaling system containing a seat to sit down on it, in order to operate the pump, makes the user more comfortable. On the other hand, if two cylinders are used for the suction of the water from the sump while rotating the crank, the two pumps might be adjacent so that each one will work for 180° of the crank rotation. Thus, the power required could be reduced at the same time balancing of load will be minimized. But the resulting system would deliver almost double water with same input effort.

A schematic view of the proposed pedal operated double cylindered reciprocating pump is shown in Fig. 1.

3.1 Design Consideration

There are several requirements for a pedal operated reciprocating pump. The area which is beyond electricity is badly in need of a pump for irrigation and other purposes. Some assumptions are considered during designing the pedal operated reciprocating pump. This kind of reciprocating pump is suitable in the remote areas where there is an acute problem of electricity and the farmers who cannot afford the expenses of the motorized pump. The double cylinder reciprocating pump will be connected with the crank as shown in Fig. 4. These cranks are slightly different from

conventional cranks. They also work as flywheel. The cranks are supported on a common shaft to which power is transferred through chain and sprocket. The sprocket is fixed at the middle of the shaft and is connected with the pedal through a chain. When the force is applied on the pedal, the sprocket will start rotating and the valves of the cylinders move forward and backward at the same time. The connecting rod is connected with the crank in such a way that when one pushes up one valve, the other one pushes down the other valve. The cylinders are supported on a frame. The suction pipes to the cylinders should be separate. There should be a sitting arrangement to operate the pump. Considering these facts, the design is made. The design considerations are based on general and mechanical view points. The two types of considerations are briefly described below-

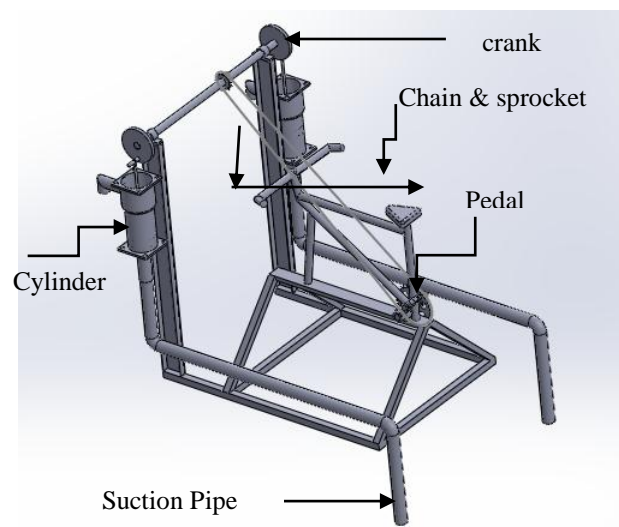


Fig. 1: Schematic of the proposed Pedal Operated Reciprocating Pump

General Consideration

The general considerations include:

- The design and construction should be as simple as possible.
- The assembly and disassembly of components should be easy and convenient
- The construction materials should have local availability as much as possible.
- Maintenance process should be simple.
- The cost of the construction should be as low as possible.

Mechanical Consideration

The mechanical considerations are:

- The main structure should be light weighted but rigid and should withstand the forces while in action.
- The parts should be easily assembled and replaceable.

- The sprocket should be sharp edged for transmitting power effectively.
- The force should be uniformly distributed to the double cylinder pump.
- The two cranks should be positioned in an accurate distance so that the upward and downward movement of the piston in the cylinder remains uniform.

3.2 Selection of Components

The components are selected according to the assumptions and design considerations. The components are designed in such a way to make the pedal operated reciprocating pump simpler and easy to handle.

Piston with Connecting Rod

Piston is used as pressure creating component. It is made of steel. It reciprocates within the cylinder. It is attached with a connecting rod and very close tolerance is maintained with the cylinder. A rubber bucket surrounds the piston while the pump is in operation. The piston develops the maximum pressure inside the cylinder.

Cylinder

A hand-tube well, having 304.8 mm outer diameter and 284.8 mm inner diameter, is used as a cylinder and is set up at the front-side of the main structure. The hand-tube will work as a reciprocating pump. It is connected with the structure, which is made of GI pipe. It is two in number as the whole system is acting as a double cylinder reciprocating pump. Fig. 2 shows the CAD model of the cylinder of this pedal operated reciprocating pump which is available in the market. The suction pipe is fixed at the lower portion of the cylinder. Again the discharge pipe is fixed at the front side of the cylinder.

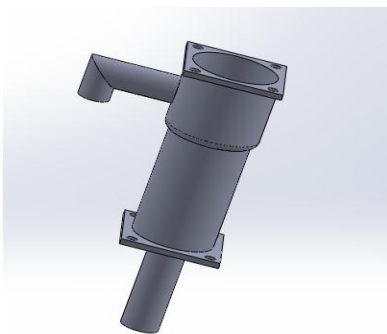


Fig. 2: Cylinder

Pedal link

A pedal is used to connect the piston rod and foot step mechanism. A chain is connecting the sprocket and the pedal. When force is applied on pedal, the power transmitted through this chain and sprocket to rotate the shaft of the circular crank. The pedal is so sturdy that it could withstand cyclic load.

Crank

A crankshaft which is connected to cranks is a mechanical part able to perform a conversion between reciprocating motion and rotational motion. In a reciprocating engine, it translates reciprocating motion of the piston into rotational motion; whereas in a reciprocating compressor, it converts the rotational motion into reciprocating motion. In order to do the conversion between two motions, the crankshaft has "crank throws" or "crankpins". This kind of crank has the special feature of working as a flywheel. Fig. 3 exposes the CAD model of the crank.

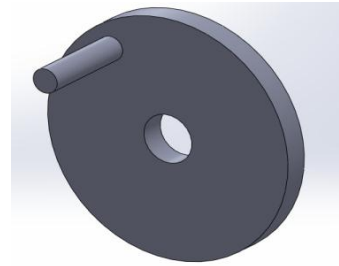


Fig. 3: Crank (designed)

Connecting Rod

It is used for connecting the piston and foot pedal. It is also used to push the piston according to the foot pedal action. The maximum pressure is achieved due to pumping lift height. It will convert angular motion to linear motion.

4.1 Construction and Performance Test

The pedal operated double cylinder reciprocating pump was constructed and tested in the laboratory of Mechanical Engineering department of KUET. The barrels of two small hand tube wells were used as cylinders. The crank was constructed with mild steel plate. MS rod was used as the shaft. An old bicycle frame was used as part of the frame. The frame was constructed so that it can be installed over a sump. Two foot valves were used in the suction lines. The delivery line was united to a single point, so that discharge can be collected in a single reservoir. Finally all the components and parts of the project have been assembled and mounted on the frame.

4.2 Performance Test:

The performance test of the constructed pedal operated double cylinder reciprocating pump was carried out in a small size of sump. Because of fund limitation the test was not carried out with underground water. For underground water lifting, both the suction line should be in the same water reservoir. It was possible to conduct the performance test with a considerable period of time. A water drum of 150 liter capacity was used to measure the discharge of water. The discharge time was

estimated with a stop watch. Finally the discharge rate was calculated.



Fig.4: Photographic view of Proposed Pump

The following observations were made during the performance test. The results of the test, when both the cylinders were acting, are presented in Table 1, Table 2 and Table 3. The result with single cylinder is also shown in Table 4.

Table 1: Data for Performance Test at day-1

No. of Obs.	Water discharged (liter)	Time Required (min)	Discharge rate (liter/min)
01	143.90	6.43	22.43
02	142.55	6.63	21.48
03	144.70	7.07	20.47
04	143.64	6.87	20.91
05	142.80	6.58	21.69
06	144.30	7.43	19.98
07	143.70	6.50	22.10
Average discharge rate			21.28

Table 2: Data for Performance Test at day-2

No. of Obs.	Water discharged (liter)	Time Required (min)	Discharge rate (liter/min)
01	144.90	6.54	22.15
02	143.75	6.80	21.48
03	144.70	7.07	20.32
04	141.64	6.23	21.52
05	143.88	6.70	21.47
06	142.35	6.43	22.14
07	143.38	7.03	20.39
Average discharge rate			21.35

Table No.3: Data for Performance Test at day-3

No. of Obs.	Water discharged (liter)	Time Required (min)	Discharge rate (liter/min)
01	141.50	6.26	22.60

02	143.39	6.50	22.06
03	142.78	6.87	20.78
04	144.54	6.80	21.25
05	142.54	6.23	22.87
06	143.60	7.07	20.31
07	142.32	6.53	21.79
Average discharge rate			21.66

Table No.4: Data for Performance Test at day-4

No. of Obs.	Water discharged (liter)	Time Required (min)	Discharge rate (liter/min)
01	143.72	10.93	13.15
02	141.78	11.28	12.57
04	142.38	11.67	12.20
05	145.90	11.39	12.82
06	142.40	12.53	11.28
07	144.2	11.05	13.05
Average discharge rate			12.45

The results of the performance test showed that the average discharge of pedal operated double cylinder reciprocating pump at day 1 was 21.28 liter/min, at day-2 was 21.35 liter/min and at day-3 was 21.66 liter/min. The result of the test with single cylinder at day-4 was 21.54 liter/min. So, the 4 (four) days average discharge was 21.45 liter/min. On the other hand, the average discharge of pedal operated single cylinder reciprocating pump is 12.45 liter/min. It is to be mentioned that this test was carried out by closing one of the cylinders of the main setup.

5. Result and Discussion

5.1 Results

Analyzing the data from Table 1, 2, 3 & 4, it is seen that the discharge varies with the quantity of water that means for different observation it shows different discharge. It is because of the human effort that produces power by pedaling is not remain same all the time. Again from the calculation of the average discharge it is seen that there is a difference between the discharge of double cylinder and single cylinder. In comparison the difference of average discharge between them is almost 1.70 liter/minute. That means a double acting pedal operated reciprocating pump is 1.70 times more efficient than the pedal operated single acting reciprocating pump.

5.2 Discussion

The pedal operated double acting reciprocating pump is designed to reduce the human effort in the daily purposes of water. It discharges more water than the hand powered pump. On the other hand the double cylinder pump is more efficient than the single acting

pump. In the remote area of Bangladesh where electricity is unavailable or where supply is not consistent, people who are facing problem during irrigation & agricultural purposes, this kind of pedal operated water pumping system would be of great importance. It does not require electricity for operation like the conventional motorized water pump. Again this kind of manual but efficient water pumping system helps to reduce the expense for the irrigation, as any kind of fuel isn't required; any kind of electricity bill isn't required. The maintenance cost of this pedal operated water pump is very small. The easy design of the pedal operated water pump system makes it comfortable; people can easily sit on the seat of the bicycle and can pedal as much as they can.

4. Conclusion

The Pedal operated double acting reciprocating pump, which is environmental friendly and less power consuming, is designed, constructed and tested in the laboratory. The following conclusions could be made:

- It is simple, user-friendly design, easy to carry and easy to assemble and disassemble.
- It reduces human effort, so cost of lifting water and energy consumption is less.
- Could be used in all seasons specially in winter for watering in the vegetable fields.
- Could be used to irrigate at different land at the same time with special attachment.

REFERENCES

- [1] M. Serajul Islam, M. Zakaria Hossain, M. Abul Khair; 'Design and Development of Pedal Pump for Low-lift Irrigation', ISSN 1810-1860; Journal of Agriculture Rural Development vol. 5 (1&2); pp.116-126; 2007.
- [2] M. Sermaraj, 'Design and Fabrication of Pedal Operating Reciprocating Water Pump', IOSR Journal of Mechanical and Civil Engineering (IOSR-JMCE); e-ISSN: 2278-1684; p-ISSN: 2320-334X, pp.64-83.
- [3] A. Orr, A. S. M. Nazrul Islam, G. Barnes; 'The Treadle Pump', Seminar Report; 2004.
- [4] https://en.wikipedia.org/wiki/Bicycle_pedal
- [5] <http://www.learnengineering.org/2014/01/centrifugal-hydraulic-pumps.html>
- [6] https://en.wikipedia.org/wiki/Treadle_pump
- [7] James David Ellen; 'Water System With Pedal Powered Reciprocating Pump'; United States Patent, Patent No.: 5, pp.772, 405, 1998.

Numerical Simulation and Analysis of Supersonic Flow over a Circular Cylinder

Shawon Kumar Saha

Department of Mechanical Engineering, Bangladesh University of Engineering & Technology, Dhaka-1000, BANGLADESH

ABSTRACT

The purpose of this study is to investigate a two dimensional supersonic flow over a circular cylinder numerically. The calculations are performed on a boundary fitted co-ordinate system. Time dependent Navier-Stokes equations is used to evolve the correct steady-state solution. The analysis is conducted by assuming a rigid circular cylinder with a wide range of Mach number (2,4,6,7) and two different temperatures (300K and 373K) by Ansys Fluent We consider air as calorically perfect gas, with constant Prandtl number and Sutherland's law for the viscosity. The two dimensional Navier-Stokes equations for a unsteady flow, with no body forces, no mass diffusion are solved. Flow fields are obtained. The pressure along the entire surface is computed over a wide range of Mach number and two different temperatures. The temperature variation due to dissipation of kinetic energy has been analyzed numerically.

Keywords: Computational fluid dynamics, Supersonic Flow, Numerical Investigation, Sutherland's Law, Circular Cylinder

1. INTRODUCTION

The flow field of a velocity greater than that of a sound, in which a circular cylinder is mounted, is very complicated, because a detached shock wave is originated ahead of the cylinder and behind it a rotational flow field of mixed type, that is, containing super and sub-sonic regions appear. It is quite important to analyze the Supersonic flow over various objects as it has a great importance in aerodynamics and theoretical aspects in fluid mechanics. In order to evaluate such phenomena, the 2-D viscous flow over a calorically perfect gas (we consider air with constant Prandtl number and Sutherland's law for viscosity) a wide range of Mach number over a cylinder was simulated. Flow motion is represented by the compressible Navier-Stokes equations, and they are solved with Finite Volume techniques. Among the different approaches existing in the literature for the numerical fluxes discretization, a hybrid initialization is preferred. This type of numerical schemes preserve kinetic energy of turbulent scales. Hybrid initialization is a collection of recipes and boundary interpolation methods. The pressure along the entire surface has been computed over a wide range of Mach numbers and two different temperatures. The temperature variation due to dissipation of kinetic energy has been analyzed numerically. The two dimensional Navier-Stokes equation for non-steady flow, with no-body forces, no volumetric heating and no mass diffusion are solved.

Deng-Pan *et al.* [1] investigated the flow structure of a supersonic flow over a cylinder by method of flow visualization and with nanoparticle-based planar laser scattering in a supersonic quiet wind tunnel at Mach number of 2.68. Based on the time correlation of NPLS Images the time space evolutionary characteristics of the structure in the supersonic flow over a finite cylinder has

been studied and the characteristics of the structure in the

Flow direction are obtained.

Poplavskaya *et al* [2] studied the supersonic flow around a stream wise aligned cylinder with a frontal gas permeable insert made of a high porosity cellular material are presented. The computed results were compared with the data of wind tunnel experiments performed in T-327B supersonic continuous flow wind tunnel at the flow Mach number 4.85. Experimental and computed data for the normalized drag co-efficient of the model versus the normalized length of the porous insert and versus the Reynolds number are analyzed.

Bashkin *et al* [3] investigated the supersonic flow of perfect gas past a circular cylinder with an isothermal surface at the Mach number 5 and Reynolds Number ranging from (30 to 500000). He showed that two branches of numerical solution of the problem can exist. Pressure coefficient distribution on the rear of an isothermal surface at Mach number 5 was analyzed. Velocity profile in the plane of symmetry downstream of an isothermal cylinder at Mach number 5 was also analyzed.

Rajani *et al* [4] focused on the two and three dimensional flow past a circular cylinder in different flow regimes. He used an implicit pressure based finite volume method for time accurate computation of incompressible flow. Both experimental measurements and numerical computations were done. Temporal variation of lift coefficient on time and frequency domain at different Reynolds number were analyzed also.

In the present study a circular cylinder is studied at two different temperature (300K and 373K) at a wide range of Mach No. (2, 4, 6, 7) and pressure and temperature distribution are computed. This study also includes the comparison of static temperature and pressure distribution for two different temperatures at a fixed Mach number. This is done to analyze the effect of stagnation temperature.

2. COMPUTATIONAL METHOD

2.1 Mathematical Model

This problem is considered with interesting fluid phenomena. The most complete model available for the flow of air is the Navier-Stokes equations. The advantage of using time-dependent Navier-Stokes approach is its inherent ability to evolve to the correct steady-state solution. However, they represent a model not a physical truth. They represent the three conservation laws. Neglecting body Forces and volumetric heating and mass diffusion the two dimensional forms of the Navier-Stokes equations are

Continuity Equation:

$$\frac{\partial \rho}{\partial t} + \frac{1}{r} \frac{\partial}{\partial r} (\rho r u_r) + \frac{1}{r} \frac{\partial}{\partial \theta} (\rho u_\theta) = 0 \quad (1)$$

r- Momentum:

$$\frac{\partial(\rho u_r)}{\partial t} + \frac{\partial}{\partial r}(\rho u_r^2 + P) + \frac{1}{r} \frac{\partial}{\partial r}(r \tau_{rr}) + \frac{1}{r} \frac{\partial}{\partial \theta}(\rho u_\theta u_r + \tau_{\theta r}) + \frac{1}{r}(\tau_{\theta \theta} - u_\theta^2) = 0 \quad (2)$$

θ - Momentum:

$$\frac{\partial(\rho u_\theta)}{\partial t} + \frac{1}{r} \frac{\partial}{\partial \theta}(u_\theta^2 + P + \tau_{\theta \theta}) + \frac{\partial}{\partial r}(\rho u_r u_\theta) + \frac{1}{r^2} \frac{\partial}{\partial r^2}(r^2 \tau_{r\theta}) = 0 \quad (3)$$

Energy Equation:

$$\begin{aligned} \frac{\partial(\rho c T)}{\partial t} + u_r \frac{\partial(\rho c T)}{\partial r} + \frac{u_\theta}{r} \frac{\partial(\rho c T)}{\partial \theta} \\ = \varphi_v + k \left\{ \frac{1}{r} \frac{\partial}{\partial r} \left(r \frac{\partial T}{\partial r} \right) + \frac{\partial^2 T}{\partial \theta^2} \right\} \end{aligned} \quad (4)$$

Where $t, \rho, u_r, u_\theta, P$ are the time, density, velocity in r-direction and θ -direction respectively and $\tau_{r\theta}, \tau_{rr}, \tau_{\theta\theta}$ are the stresses. This forms a four basic equations (Ref [5]). For solving these equations four additional equations used are the equation of state for a perfect gas.

These additional four equations are

$$\tau_{rr} = -\mu \left\{ 2 \frac{\partial u_r}{\partial r} - \frac{2}{3} (\nabla \cdot \vec{u}) \right\} \quad (5)$$

$$\tau_{\theta\theta} = \mu \left\{ 2 \left(\frac{1}{r} \frac{\partial u_\theta}{\partial \theta} + \frac{u_r}{r} \right) - \frac{2}{3} (\nabla \cdot \vec{u}) \right\} \quad (6)$$

$$\tau_{r\theta} = \tau_{\theta r} = -\mu \left\{ r \frac{\partial}{\partial r} \left(\frac{u_\theta}{r} \right) + \frac{1}{r} \frac{\partial u_\theta}{\partial \theta} \right\} \quad (7)$$

And φ_v is the dissipation rate of energy and it is represented as

$$\varphi_v = \mu \left[2 \left\{ \left(\frac{\partial u_r}{\partial r} \right)^2 + \left(\frac{1}{r} \frac{\partial u_\theta}{\partial \theta} + \frac{u_r}{r} \right)^2 \right\} + \left\{ r \frac{\partial}{\partial r} \left(\frac{u_\theta}{r} \right) + \frac{1}{r} \frac{\partial u_r}{\partial \theta} \right\}^2 \right] \quad (8)$$

Where,

$$\nabla \cdot \vec{u} = \frac{1}{r} \frac{\partial}{\partial r} (r u_r) + \frac{1}{r} \frac{\partial u_\theta}{\partial \theta}$$

2.2 Solver Settings

The solver setting used was ANSYS Fluent. The settings are given in Table 1.

Function	Option
Model	k- ω (2 eqn), Energy
K- ω model	SST
Turbulent viscosity	None
Options	Curvature Correction
Solver	Density-based
Space	2D
Velocity Formulation	Absolute
Formulation	Implicit
Flux Type	Roe-FDS
Gradient	Least Square Cell Based
Flow	Second Order Upwind

3. Computational Domain

As shown in Figure 1 the computational domain was discretized with a user defined structured mesh. Maximum face size was taken (5.3852e-003 m) with a growth rate of 1.20 and defeaters size of (2.6926e-005 m) where the minimum face size was considered as (5.382e-005). Element Order was taken as quadratic. Free mesh face type was kept quadratic or triangular. The mesh around the cylinder was made denser to ensure high accuracy.

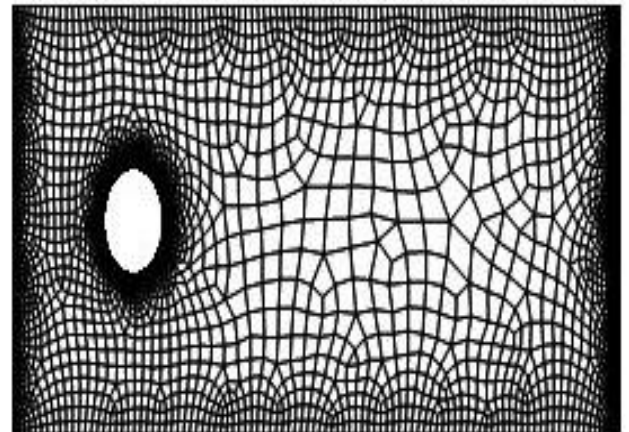


Fig.1 Mesh of the complete domain

4. Boundary Conditions

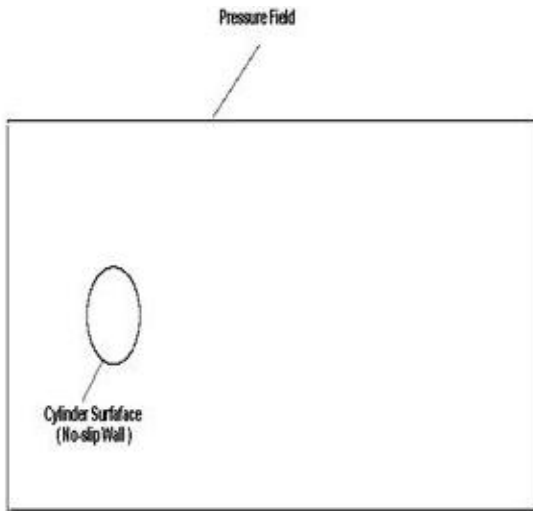


Fig.2 Boundary Conditions

As shown in Figure 2 the boundary of the domain is consisted of a pressure far field. The cylinder wall was taken to be no slip wall and standard roughness model with a roughness constant of 0.5. The flowing fluid was air with constant density, specific heat thermal conductivity. Sutherland Law is used for the viscosity of flowing fluid. Four different cases was considered by varying the Mach number at two different temperature of 300K and 373K. The Mach number used were 2, 4, 6, 7.

Table 2 Cases of Flow

Cases	Mach Number	Temperature
Case-1	2	300K 373K (for all cases)
Case-2	4	
Case-3	6	
Case-4	7	

5. RESULT AND DISCUSSIONS

The static surface pressure distribution in the entire flow field was plotted in Fig (3 & 4) as a function of distance from the inlet of the flow field. Static Surface pressure was computed for Mach numbers (2, 4,6,7) and two different temperature of 373K and 300K. As shown in (Figure 3) initially oscillators were observed showing higher increase in pressure in the region near the cylinder wall. The result was relatively lower density and hence thick boundary layer therefore it create a strong leading edge shockwave thus increase in the pressure within the shock layer. However, the oscillator disappeared past the cylinder wall and stable result was obtained. With the increase in Mach number there was a consequent increase in the static surface pressure. The pressure in both the cases was gradually decreasing after the cylinder wall along the entire field and result in almost stable value.

It was seen that the pressure was maximum at the stagnation point and decreases as a function of distance away from the stagnation point- a variation that we would expect[6].After reaching the peak value the static pressure decrease and approached at a steady value.

The temperature distribution in the entire flow field was computed.The static temperature over the entire flow field for the inflow velocity for different Mach numbers and two different temperature were plotted in Fig (5 & 6). It was observed that due to the formation of shock layer the temperature increased as shown by the plot. Again in this case like the Pressure distribution profile the temperature was decreased after a certain point, actually after passing the cylinder wall and comes to almost constant temperature.It was seen in (Figure5 and 6) like pressure distribution profile here also with the increased of Mach numbers the temperature was increasing. It can be seen that the static temperature was higher for stagnation temperature of 373K than the stagnation temperature of 300K. Like the static pressure, static temperature also decreased and approached at a steady value.

It can be seen that similar curves was found for the static temperature distribution. Here the static temperature was maximum at the stagnation point and lately decreased as a function of distance away from the stagnation point.

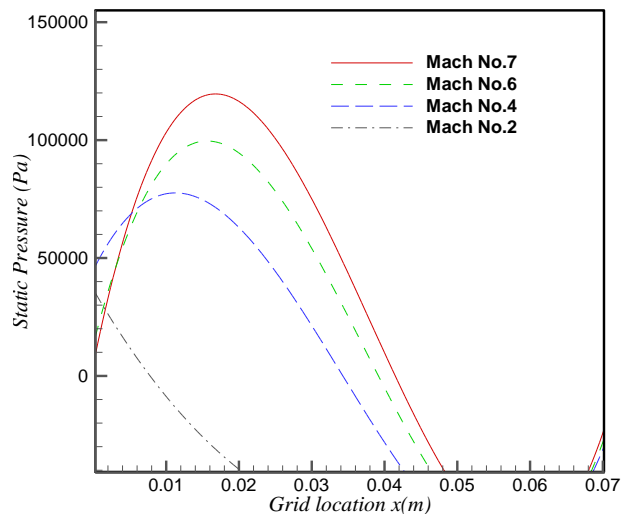


Fig. 3 Variation of Static Surface Pressure at 373K for different Mach numbers.

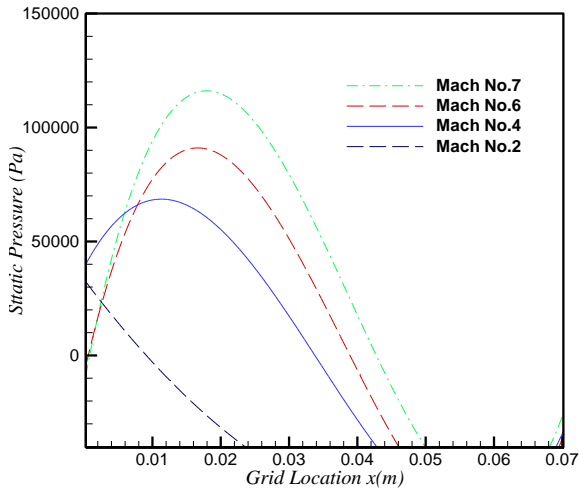


Fig. 4 Variation of Static Surface Pressure at 300K for different Mach numbers.

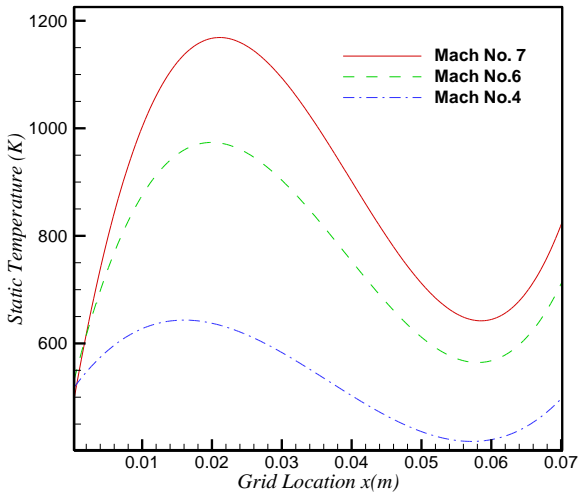


Fig. 5 Variation of Static Temperature at 373K for different Mach numbers.

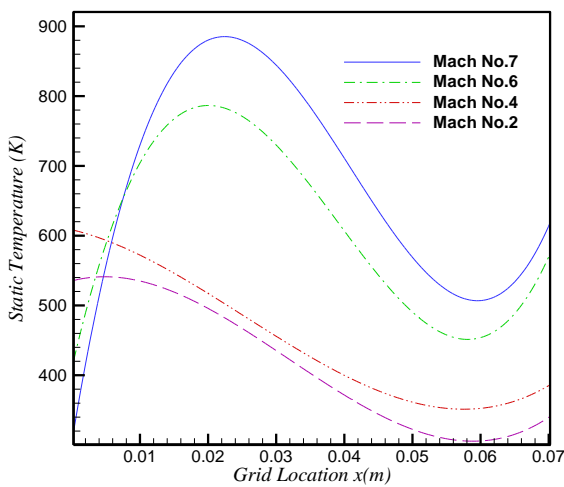


Fig. 6 Variation of Static Temperature at 300K for different Mach numbers.

The comparison of static pressure and static temperature for different temperature at Mach No. 6 were computed. The variation for these two temperatures (373K and 300K) were plotted against the grid location in (Figure 7 and 8). It can be seen that static temperature and static pressure was higher for 373K than 300K. If stagnation temperature increased static pressure and temperature will increase [7]. Similar results were found in this study.

The relation between stagnation temperature and static temperature is

$$\frac{T_0}{T} = 1 + \frac{k-1}{2} M^2 \quad (9)$$

$$\text{Mach Number, } M = \frac{V}{\alpha} ;$$

Where the speed of sound, $\alpha = \sqrt{kRT}$

$$\text{and } c_p = \frac{kR}{k-1}$$

So, the relation becomes,

$$\frac{T_0}{T} = 1 + \frac{(kR)V^2}{2c_p(kRT)} \quad (10)$$

And the relation between static pressure and stagnation pressure is

$$\frac{P_0}{P} = \left\{ 1 + \frac{(kR)V^2}{2c_p(kRT)} \right\}^{\frac{k}{k-1}} \quad (11)$$

Here P_0, T_0 is the stagnation pressure and temperature where P and T are the static pressure and temperature and c_p, k are the specific heat at constant pressure and ratio of specific heat. From the above relations it can be observed that if stagnation temperature increased static pressure and temperature will increase.

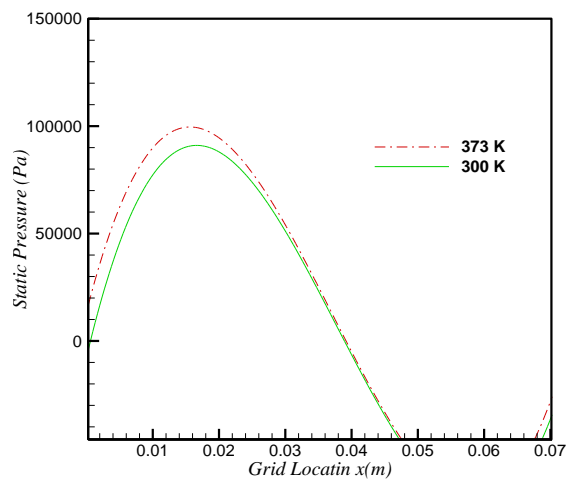


Fig. 7 Variation of Static Pressure for two different stagnation temperature (Mach No. 6).

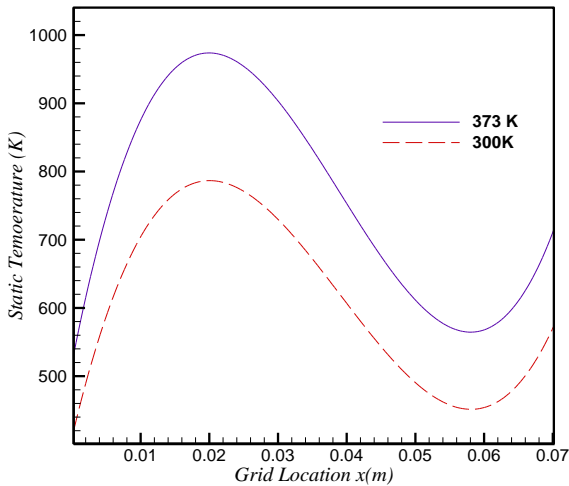


Fig.8 Variation of Static Temperature for two different stagnation temperature (Mach No. 6).

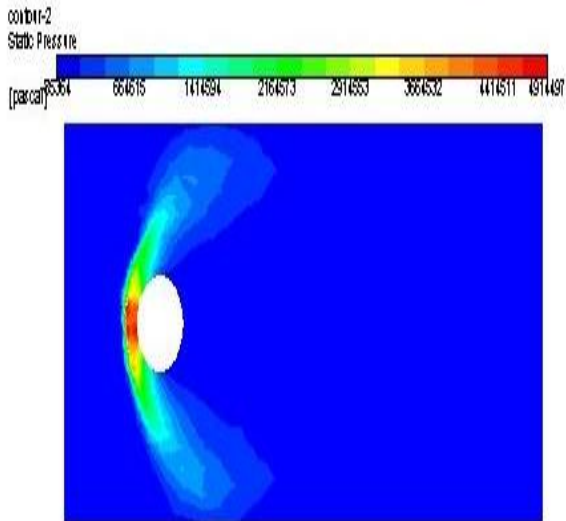


Fig.9 Pressure Contours at Mach No. 6 for flow over a Circular Cylinder (Temperature 373K)

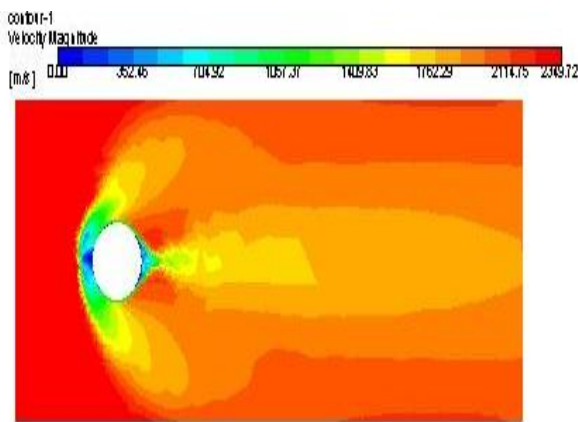


Fig.10 Velocity Contours at Mach No. 6 for flow over a Circular Cylinder (Temperature 373K)

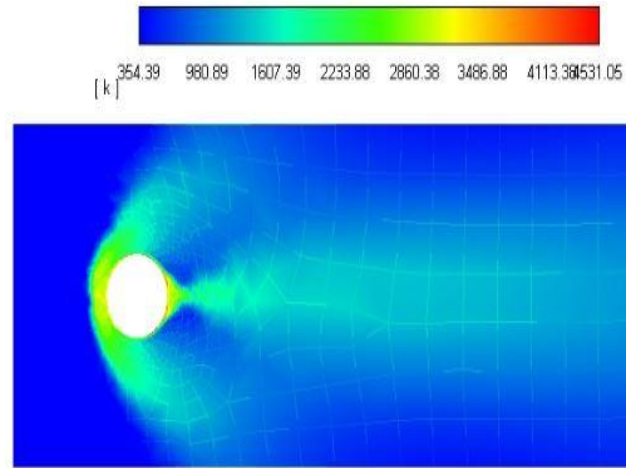


Fig.11 Temperature Contours at Mach No. 6 for flow over a Circular Cylinder (Temperature 373K)

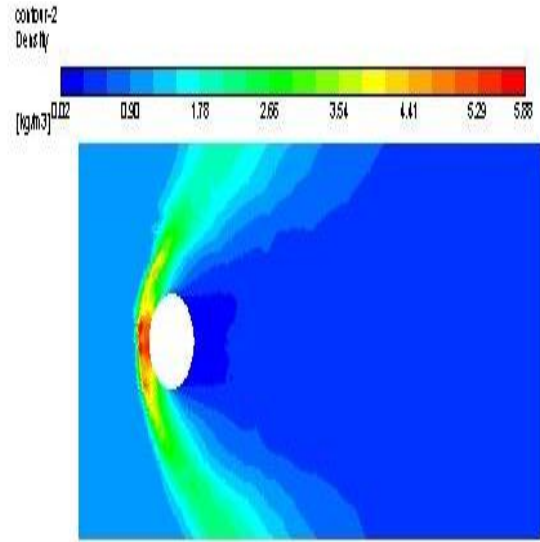


Fig.12 Density Contours at Mach No. 6 for flow over a Circular Cylinder (Temperature 373K)

The velocity, pressure, density and temperature contours were obtained at Mach No. 6 at temperature of 373K. In the pressure contour, it can be seen that, the static pressure upstream the cylinder was higher and gradually decreased downstream the cylinder which we would expect for the pressure distribution of a supersonic flow over any blunt bodies.

In the study of temperature contour, similar results were found which showed the high temperature upstream the cylinder and decreasing temperature downstream the cylinder. Even though similar result were found for density contours it can be observed that density contour had higher gradient than the temperature contour.

Shock waves are formed when a pressure front moves at a supersonic speed and pushes on the surrounding air [8]. At the region where this occurs sound wave travelling against the flow reaches at a point where they could not travel any further upstream and the pressure

progressively builds up in this region. Shock waves are very small region in the gas where the gas properties changes by a large amount. Across the shock wave the static pressure, static temperature and the gas density increases almost instantaneously. Similar results were found in our study. From the study it can be seen that the static temperature and static pressure increase instantaneously downstream the cylinder. The contours of the velocity, pressure, temperature and density showed the results similar to the actual results. Because the shock wave does no work, there is no heat addition. So the total temperature and total enthalpy are constant. But because the flow is non-isentropic, the total pressure downstream the shock wave is less than the total pressure upstream the shock wave. There is a loss of total pressure associated with the shock wave. But a change of static temperature, static pressure and density change was happened.

6. CONCLUSION

In this study, a numerical study of supersonic flow over a circular cylinder at two different temperature(300K and 373K) with a wide range of Mach number(2, 4, 6, 7) was done.

Study of the following things, i.e. variation of static pressure for different surface temperature and different Mach numbers, variation of static temperature for different surface temperature and pressure and comparison of static temperature and pressure for two different surface temperature at a constant Mach number was done. It was found that static pressure and static temperature increases almost instantaneously upstream the cylinder and after the peak value both pressure and temperature decreases and tends to a steady value.

NOMENCLATURE

c_p : Specific heat at constant pressure, $\text{kJ} \cdot \text{kg}^{-1} \cdot \text{K}^{-1}$
 P : Pressure, Pa
 T : Temperature, K
 k : Ratio of specific heat
 M : Mach number
 α : Speed of sound, ms^{-1}
 R : molar gas constant, $\text{J} \cdot \text{mol}^{-1} \cdot \text{K}^{-1}$
 μ : Dynamic viscosity, Ns/m^2

REFERENCES

- [1] Deng-Pan, W., Yu-Xin, Z., Zhi-Xun, X., Qing-Hua, W. and Zhen-Bing, L., 2012. Flow visualization of supersonic flow over a finite cylinder. *Chinese Physics Letters*, 29(8), p.084702.
- [2] Poplavskaya, T.V., Kirilovskiy, S.V. and Mironov, S.G., 2016, October. Supersonic flow around a cylinder with front gas-permeable insert which modeled by skeleton of porous material. In *AIP Conference Proceedings* (Vol. 1770, No. 1, p. 030067). AIP Publishing.
- [3] Bashkin, V.A., Egorov, I.V., Egorova, M.V. and Ivanov, D.V., 2001. Supersonic flow past a

circular cylinder with an isothermal surface. *Fluid Dynamics*, 36(1), pp.147-153.

- [4] Rajani, B.N., Kandasamy, A. and Majumdar, S., 2009. Numerical simulation of laminar flow past a circular cylinder. *Applied Mathematical Modelling*, 33(3), pp.1228-1247.
- [5] Fox, R.W. and McDonald, A.T., 1994. Introduction to Fluid Mechanics, John Wiley&Sons. Inc., New York.
- [6] Anderson Jr, J.D., 2010. *Fundamentals of aerodynamics*. Tata McGraw-Hill Education.
- [7] Potter, M.C., Wiggert, D.C. and Ramadan, B.H., 2016. *Mechanics of fluids*. Nelson Education.
- [8] Settles, G.S., 2006. High-speed imaging of shock waves, explosions and gunshots: New digital video technology, combined with some classic imaging techniques, reveals shock waves as never before. *American Scientist*, 94(1), pp.22-31.

Metal Surface Defect Inspection through Deep Neural Network

Md. Fantacher Islam^{1,*}, Md. Mahbubur Rahman²

¹Department of Industrial Engineering and Management, Khulna University of Engineering & Technology, Khulna-9203, BANGLADESH

² Assistant Professor, Department of Industrial Engineering and Management, Khulna University of Engineering & Technology, Khulna-9203, BANGLADESH

ABSTRACT

Visual inspection of a metallic surface has taken thriving attention for the metal product quality control. Deep convolution neural networks have got impressive recommendation rates recently to effectively inspect defects for metallic products. Here, we proposed a deep neural network model to analyze the image data for inspecting metal surface defects and also their respective classes. The designed deep neural network was trained on 1800 images of six different kinds of typical surface defects of 200×200 pixel resolutions. The image datasets were obtained from North Eastern University (NEU) surface defect database. And to predict the model performance we had tested 17 images and found 64.7% accuracy. The results manifested that the proposed method gives a good outcome though we used small datasets and it can indeed trace metal surface defects in realistic situations.

Keywords: Metal surface inspection, deep neural network, defect classifier

1. Introduction

Quality is an important issue for industrial product and it's very important to look after the machine that associated with the production process. So for assuring the best quality of product machine should be in right kind and also if the product is metallic, it's also important to look after the metallic product. Actually metal quality more dependent on its surface first as well as its composition and another germane issue. Surface defect inspection is now have possessed great impact for assuring good quality for metallic product or machine. Now visual inspection system has got more attention for the measuring accuracy and correctness. Human visual inspection defends on the fatigue and stress level wherein vision system is fast enough.

As the technology growing fast the application of intelligence system grew more attention in manufacturing and quality consideration for a product [1, 2]. Visual system and other computer vision technology getting more popular for inspection base fields such as surface quality and textured surface [3, 16]. In molecular biology and genetics thousands of potential network architectures and parameter instantiations, screening object recognition performance can be solved now [10]. The Convolutional Neural Networks (CNN) Architecture is used now to determine the Automatic Localization Casting Defects inspection [16]. Image classification has got more attention at present and there have more methods that are classified the image into their relevant classes. Olivier Chappelle et.al introduced Support Vector Machines for Histogram-Based Image Classification [5] and Nearest-Neighbor Based Image Classification technique is used to classify image [4]. Convolution Neural Network

(CNN) method shows the surprising result for classifying images because of short time requirements and the redundancy of data for feature learning [9, 6]. Backpropagation is used for learning the feature in CNN which has done by updating the weights and bias. CNN can extract features from the images automatically and need fewer connection compared to standard feedforward neural networks. K Jarrett and K Kavukcuoglu showed a Best Multi-Stage Architecture for Object Recognition [7]. High-dimensional images are difficult for computation, a hierarchical generative model [8] was developed which scales to realistic image sizes by convolutional deep belief network. For image defect inspection of the metallic surface, we used a Convolution neural network (CNN) as it's needed lesser time and computation.

2. CNN defect inspection method

The detection method consists of two part one is training the datasets by mapping with their relevant class and another process is testing a new image to find the relevant classes shown in the Fig.1. In training process images and their respective labels are set correctly as the procedure followed in a purely supervised learning manner. Then feature extraction process needed as CNN is a feature-based learning which the process is discussed briefly in 2.1 section. After feature extraction, the CNN algorithm finds the relationship between the input features and the output labels which is discussed in 2.2 section. Gradient descent algorithm used for updating weight and bias for minimizing the error. The training procedure works in an offline manner [12]. In the testing, procedure images need preprocessing and feature extraction also need for

* Corresponding author. Tel.: +88-01823020618
E-mail addresses: fantacherjoy@gmail.com

synchronizing with the classifier model. The classifier model predicts the output labels from the learning of training procedure.

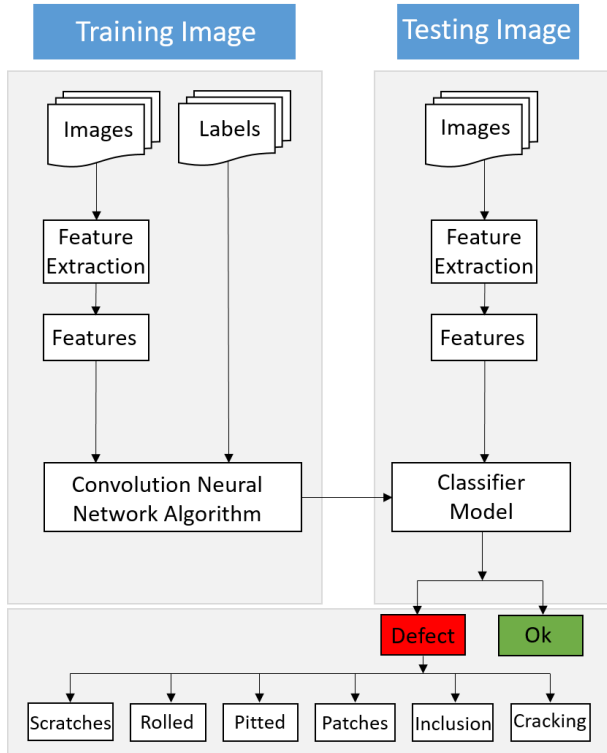


Fig.1 Classifier Model

2.1 Feature Extraction

The training images consider as a pixel value of the matrix and a filter is sliding over the matrix. The input image patch $\times A_i^j$ is convoluted by J_i number of maps with the size of $A_i^j \times A_i^j$ and is produced J_o number of output maps with the size of $A_o^j \times A_o^j$ where g^{j-1} and g^j are represent the input and output of the layer and g^L is representing the output of the last layer L . The j^{th} feature maps of l^{th} convolution layer g_j^l , is calculated by:

$$g_j^l = \sum_{i=1}^{N^{l-1}} K_{ij}^l * g_i^{l-1} + r_j^l$$

Where $0 \leq i \leq J_i^{l-1}$, $0 \leq i \leq J_o^{l-1}$, K_{ij}^l is the convolution kernel corresponding to j^{th} map between l^{th} layer and i^{th} map in $(l-1)^{th}$ layer, r_j^l is the bias term of the above kernel. And the convolution process is indicated by symbol (*) [13, 14]. And then it fed to an activation function which will decide which neuron should fire and also decides, given the inputs into the node. Here nonlinear activation function used as RELU:

$$f(x) = \max(x, 0)$$

And then Pooling operation is used to reduce the number of parameters and amount of computation in the network and it also controls the over fittings. Here we used mean pooling. Downsampling is performed for pooling layer by mean pooling the (x, y) element output of feature map j of layer is expressed as:

$$z_j^l(x, y) = \frac{\sum_{m=0}^{s-1} \sum_{n=0}^{s-1} z_i^{l-1}(s \times x + m, s \times y + n)}{s^2}$$

Where $0 < x, y < c_i^l$ and s is expressed as Downsampling factor [14]. After pooling, the high-level reasoning in the neural network is done via fully connected layers. Neurons in a fully connected layer have connections to all activations in the previous layer, as seen in regular neural networks. Their activations can hence be computed with a matrix multiplication followed by a bias offset [13].

2.2 Classifier Model

Artificial Neural Network (ANN) which is formulated as:

$$a_j^l = \sum_{i=1}^{p^{l-1}} x_i^{l-1} * w_{ij}^l + r_j^l$$

Where w_{ij}^l and r_j^l are the weight vector and bias term of the i^{th} filter of the l^{th} layer. ANN is actually liable for predicting the output label for input data. Let o_k and y_k denote the output label and expected label for input samples individually. The Mean Squared Error (MSE) function is usually formulated as:

$$E = \frac{1}{2} \sum_{k=1}^{p^{l-1}} \|y_k - o_k\|^2$$

The gradient descent method is used to minimize this error by updating weight vectors and bias term layer by layer. Softmax activation used to find the probability of the output of the ANN model which actually used at the last layer [13]. Softmax function is usually formulated as:

$$\sigma(a_j^l) = \frac{e^x}{\sum_{k=1}^K e^x}$$

It gives the probability from 0 to 1 and then from the best probability fraction relevant class can be detected [15].

3. Inspection analysis

3.1 Datasets

Datasets had collected from North Eastern University (NEU) Surface Defect Database. This database contains 1800 images of different types of defect of the metal surface defects shown in the Fig.2. Each image has 200x200 pixels and there have six types of defect images in this database. Each class has contained 300 Images and the classes are Scratches, Patches, Rolled, Pitted, Cracking and Inclusion.

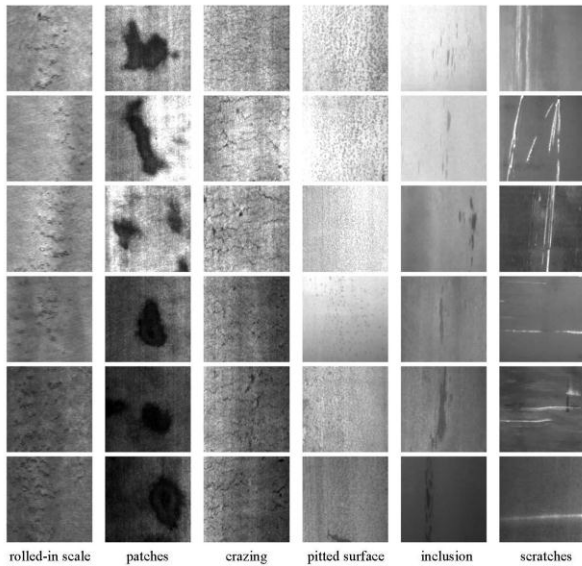


Fig.2 Six types of defect images.

3.2 Model implementation

To identify defect types of images we used two convolutions and pooling operation in our CNN model. Kernel striding through the images of 200x200 pixel values of the matrix is taken 3x3 and the pooling filter has taken 2x2. As our datasets labels contain more than two classes we used categorical cross-entropy as loss function. All 1800 images of different types defect use as training datasets but for validation 180 sample is taken by default by the program.

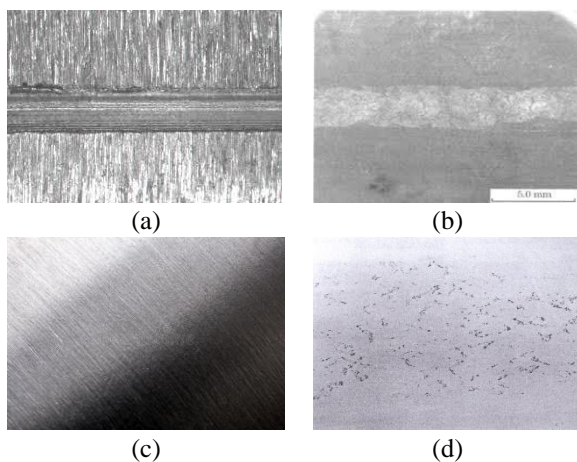


Fig.3 Test Images before implement to the model.

The batch size is chosen 90 and epoch taken 30 as having the low number of datasets. And for calculating the test image probability we used Softmax function which gives 0 to 1 probability. The output probabilities then compared to a specific threshold. Seventeen test images fed into the classifier model to find the relevant classes. And here four of them are shown in the Fig.3. Before implementing test images into the classifier model a preprocessing method is required where images resize to synchronize with the building model. And decided the test image as a defect of any types belonging or defect less.

3.3 Experimental result

The classifier model predicts the 17 test images based on probability and finds the relevant classes. Four of them shown in the Fig.4 along with the probability. Model classification accuracy for 17 images is 64.7% which is calculated from the confusion matrix.

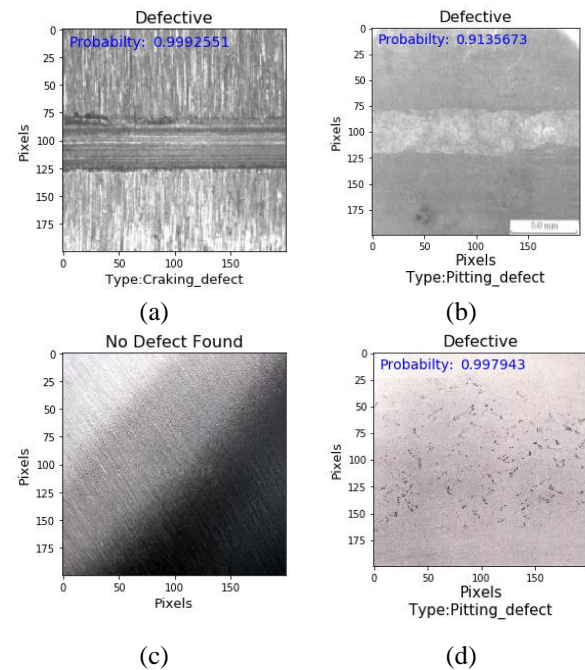


Fig.4 Test Images after implement to the model.

In the Confusion matrix for 17 images 11 are found as TP (True Positive), 2 as TN (True Negative), 4 as FP (False Positive), and 1 as FN (False Negative). And the accuracy calculated by $(TP+TN) / (TP+TN+FP+FN)$ this equation.

3. Conclusion

In this work, we proposed a CNN architecture with two convolution layer for detecting the surface defect. We used categorical cross-entropy as loss function as our model output labels are six types. The result of the inspection is better than the proposed model expected. The model shows 64.7% accuracy which is best in sense

of such small training datasets. The model evaluation will be more reliable if the model can be fed approximate 10,000 training datasets. In the future, the model will compare with other image classifier models like Nearest-Neighbor Based Image Classification technique or any other technique.

REFERENCES

- [1] Tao F, Cheng Y, Da Xu L, Zhang L, Li BH Cciot-cmfg:cloud computing and internet of things based cloud manufacturingservice system,*IEEE Trans IndInf* 10(2):1435–1442 (2014).
- [2] Tao F, Zuo Y, Da Xu L, Zhang L Iot-based intelligentperception and access of manufacturing resource toward cloudmanufacturing,*IEEE TransIndInf* 10(2):1547–1557 (2014).
- [3] Zhao YJ, Yan YH, Song KC, Vision-based automatic detection of steel surface defects in the cold rolling process: consideringthe influence of industrial liquids and surface textures,*Int J AdvManufTechnol* 90(5-8):1665–1678 (2017).
- [4] Olivier Chapelle, Patrick Haffner, and Vladimir N. Vapnik,In Defense of Nearest-Neighbor Based Image Classification. *IEEE, Anchorage, AK, USA DOI: 10.1109/CVPR.2008.4587598* (2008).
- [5] Olivier Chapelle, Patrick Haffner, and Vladimir N. Vapnik,Support Vector Machines forHistogram-Based Image Classification,IEEE Computational Intelligence Society DOI: 10.1109/72.788646(1999).
- [6] Y. LeCun, F.J. Huang, and L. Bottou, Learning methods for generic object recognition with invariance topose and lighting. *In Computer Vision and Pattern Recognition, 2004, CVPR 2004. Proceedings of the2004 IEEE Computer Society Conference on, volume 2, pages II–97. IEEE,* (2004).
- [7] K. Jarrett, K. Kavukcuoglu, M. A. Ranzato, and Y. LeCun, What is the best multi-stage architecture forobject recognition? *In International Conference on Computer Vision, pages 2146–2153. IEEE, 2009.(ImageNet Classification with Deep ConvolutionalNeural Networks) Krizhevsky, Convolutional deep belief networks on cifar-10. Unpublished manuscript,* (2010).
- [8] H. Lee, R. Grosse, R. Ranganath, and A.Y. Ng, Convolutional deep belief networks for scalable unsupervised learning of hierarchical representations,*In Proceedings of the 26th Annual International Conferenceon Machine Learning, pages 609–616. ACM,* (2009).
- [9] Y. Le Cun, B. Boser, J.S. Denker, D. Henderson, R.E. Howard, W. Hubbard, L.D. Jackel, et al, Handwritten digit recognition with a back-propagation network,*In Advances in neural information processingsystems,* (1990).
- [10] N. Pinto, D. Doukhan, J.J. DiCarlo, and D.D. Cox. A high-throughput screening approach to discoveringgood forms of biologically inspired visual representation. *PLoS computational biology, 5(11):e1000579,* (2009).
- [11] S.C. Turaga, J.F. Murray, V. Jain, F. Roth, M. Helmstaedter, K. Briggman, W. Denk, and H.S. Seung, Convolutional networks can learn to generate affinity graphs for image segmentation, *Neural Computation,22(2):511–538, 2010* (2010).
- [12] D. Weimera, H. Thamera, B. Scholz-Reiterb, Learning defect classifiers for textured surfaces using neural networks and statistical feature representations,*Intelligent Production Systems (BIBA), University of Bremen, Hochschulring 20, 28359 Bremen, GermanyUniversity of Bremen, Bibliotheksstraße 1, 28359 Bremen, Germany 1-s2.0-S2212827113002667-main_2* (2013).
- [13] DongmeiHana ,QigangLiu ,WeiguoFan , A New Image ClassificationMethod Using CNN transfer learning and Web Data Augmentation, *Expert Systems With Application ,doi: 10.1016/j.eswa.2017.11.028* (2017).
- [14] PushparajaMurugan, Implementation of Deep ConvolutionalNeural Network in Multi-class CategoricalImage Classification. *School of Mechanical and Aerospace Engineering, Nanyang Technological University, Singapore 639815* (2018).
- [15] D. Weimera, H. Thamera, B. Scholz-Reiterb, Learning defect classifiers for textured surfaces using neuralnetworks and statistical feature representations,Forty Sixth CIRP Conference on Manufacturing Systems 1-s2.0 S2212827113002667-main (2013).
- [16] Max Ferguson, RonayAk, Yung-Tsun Tina Lee, Kincho H. Law, Automatic Localization of Casting Defects with Convolutional Neural Networks,*IEEE International Conference on Big Data (Big Data)DOI: 10.1109/BigData.2017.8258115* (2017).
- [17] Tian Wang, Yang Chen, MeinaQiao, HichemSnoussi, A fast and robust convolutional neural network-based defectdetection model in product quality control,*Int J AdvManufTechnolDOI 10.1007/s00170-017-0882-0* (2017).

Aerodynamic Shape Optimization of Vehicles Using CFD Simulation

Ahmed Zawad Ul Hoque*, Mohammad Ariful Islam, Md. Ahatashamul Haque Khan Shuvo

Department of Mechanical Engineering, Khulna University of Engineering & Technology, Khulna-920, BANGLADESH

ABSTRACT

With the significant improvement of battery technology and manufacturing methods in the last two decades, the automotive industries worldwide are shifting towards more environment-friendly electric and hybrid-electric vehicles rather than fuel based combustion engine vehicles. Aerodynamic shape optimization of vehicles still holds a large potential for cuts in emissions. Drag and lift characteristics of a vehicle play a key role in vehicle aerodynamics and therefore, an active area of research for automobile manufacturers. This paper approaches computational fluid dynamics (CFD) simulation for some of the major design parameters that affect the vehicle aerodynamics. Geometrical bodies of “Ahmed body” and 3 common vehicle types i.e. Sedan, Compact Utility Vehicle (CUV), Truck had been created. Then airflow around the vehicles was simulated to calculate lift and drag coefficients. Also, experimental drag coefficient value for “Ahmed Body” had been validated by CFD simulation before performing design modifications and further simulations. Finally, obtained values of drag and lift coefficients were compared with the benchmark value.

Keywords: Aerodynamics, Shape Optimization, Vehicle, Drag, Lift, CFD, Simulation

1. Introduction

Since the invention of automobile, there had been tremendous developments in the automotive industries. And yet, climate change due to the emissions of automobiles remains one of the key concerns of the 21st century. As drastic changes occurred in the climate due to the increased emissions of CO₂ in the recent years, an act passed by the European Union in 2009 urged to reduce the emissions of greenhouse gases by 20% within 2020 compared to the levels of 1990 [1]. This act has pushed the automotive industries to further development of economical vehicles which are both environment friendly and fast. At highway speeds, overcoming aerodynamic drag is responsible for more than 50 percent of fuel consumption [2]. Hence, improving the aerodynamic shape will result in significant reduction in drag force and improved fuel economy & emissions.

Vehicle aerodynamics is a science in continuous development and research. In contrast to other technical disciplines which are mainly governed by well-established theoretical and experimental methods of fluid mechanics, there are no consistent design procedures available for road vehicles yet. The flow fields around a car characterized by separation are so complex that the vehicle aerodynamicist must make references to a large amount of data from earlier works and his triumph resides on his ability to transfer and combine results originating from many different earlier developments into his own problem for a consistent solution.

For the proper understanding of vehicle aerodynamics, first it's needed to identify the common design parameters. Then the flow around the vehicle is

considered and from it the drag and lift coefficient of the vehicle comes into play. To improve aerodynamic characteristics, the drag coefficient of the vehicle must be reduced to such a limit that the other aerodynamic properties of the vehicle also remain at a considerable point. Aerodynamic drag (D) increases with the square of vehicle speed (V) as shown in Eq. (1).

$$D \sim V^2 \quad (1)$$

The complete expression of Eq. (1) is

$$D = C_D A \frac{\rho}{2} V^2 \quad (2)$$

Where, A is projected frontal area and ρ is the density of the surrounding air. The drag D of a vehicle is therefore determined by its frontal area A, and by its shape, the aerodynamic quality of which is described by the drag coefficient C_D . Generally the vehicle size, and hence frontal area, is determined by the design requirements, and efforts to reduce drag are concentrated on reducing the drag coefficient [2].

The objectives of this paper are to identify common design parameters that affect the vehicle aerodynamics, to simulate the air flow around the vehicle for obtaining an accurate value of its drag and lift coefficient and to make modifications to the vehicle geometry which could improve its lift and drag characteristics.

2. Optimization Method

There are a number of different methods for optimizing the aerodynamic shape of a vehicle but they all share some common aspects. The schematics of a general

* Corresponding author. Tel.: +88-01919303838, +88-01748714374

Email addresses: hoque.me.kuet@gmail.com, ariful@me.kuet.ac.bd, mahsk1320@yahoo.com

method which had been followed in this paper for optimizing the aerodynamic shape of the vehicles can be seen in Fig.1.

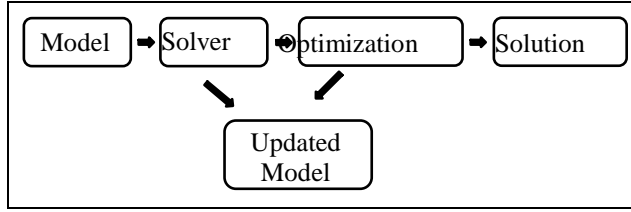


Fig.1 A schematic diagram of the general method for the aerodynamic shape optimization

CFD simulation is performed on an initial model. The result is analyzed by using some optimization algorithm. Some design parameters of the model are updated and a new CFD simulation is performed on the updated model. This iterative process continues until some stop condition is reached. Due to longer computational periods, only simplified models or coarse meshes are used in this method. The large computational cost associated with this method limits the real-world applications for the automotive industry at present day [3].

Simulation of vehicle shape optimization was performed on ANSYS Fluent which uses a Finite Volume Method (FVM) to solve the governing equations by discretization and integration over the finite volume [4]. Standard k-ε turbulent model was used. It is a semi-empirical, two-equation model, including two transport equations that represent the turbulent properties of the flow. The first transported variable is turbulent kinetic energy, k. The second transported variable in this case is the turbulent dissipation, ε. It is the variable that determines the scale of the turbulence, whereas the first variable, k, determines the energy in the turbulence [5].

4. Governing Equations

The continuity equation in Eq. (4) and momentum equations (also known as Navies - Stokes equations) in Eq. (5) – Eq. (7) with a turbulence model were used to solve the airflow

$$\frac{\partial u}{\partial x} + \frac{\partial v}{\partial y} + \frac{\partial w}{\partial z} = 0 \quad (4)$$

$$u \frac{\partial u}{\partial x} + v \frac{\partial v}{\partial y} + w \frac{\partial w}{\partial z} = -\frac{1}{\rho} \frac{\partial p}{\partial x} + \frac{1}{\rho} \left(\frac{\partial \tau_{xy}}{\partial y} + \frac{\partial \tau_{xz}}{\partial x} \right) + B_x \quad (5)$$

$$u \frac{\partial u}{\partial x} + v \frac{\partial v}{\partial y} + w \frac{\partial w}{\partial z} = -\frac{1}{\rho} \frac{\partial p}{\partial y} + \frac{1}{\rho} \left(\frac{\partial \tau_{xy}}{\partial y} + \frac{\partial \tau_{yz}}{\partial x} \right) + B_y \quad (6)$$

$$u \frac{\partial u}{\partial x} + v \frac{\partial v}{\partial y} + w \frac{\partial w}{\partial z} = -\frac{1}{\rho} \frac{\partial p}{\partial z} + \frac{1}{\rho} \left(\frac{\partial \tau_{xz}}{\partial y} + \frac{\partial \tau_{yz}}{\partial x} \right) + B_z \quad (7)$$

Where u is x -component of velocity vector, v is y -component of velocity vector and w is z -component of velocity vector. ρ is density of air, p is static pressure, τ is shear stress and B_x, B_y, B_z are body forces [6].

4.1 Transport equations for standard k - εturbulent model:

For turbulent kinetic energy k:

$$\frac{\partial}{\partial t}(\rho k) + \frac{\partial}{\partial x_i}(\rho k u_i) = \frac{\partial p}{\partial x_j} \left[\left(\mu \frac{\mu_t}{\sigma_k} \right) \frac{\partial k}{\partial x_j} \right] + G_k + G_b - \rho \epsilon - Y_M - S_k$$

For dissipation ε:

$$\frac{\partial}{\partial t}(\rho \epsilon) + \frac{\partial}{\partial x_i}(\rho \epsilon u_i) = \frac{\partial p}{\partial x_j} \left[\left(\mu \frac{\mu_t}{\sigma_\epsilon} \right) \frac{\partial \epsilon}{\partial x_j} \right] + C_{1e} \frac{\epsilon}{k} (G_k + C_{3e} G_b) - C_{2e} \rho \frac{\epsilon^2}{k} + S_\epsilon$$

In these equations, G_k represents the generation of turbulence kinetic energy due to the mean velocity gradients. G_b is the generation of turbulence kinetic energy due to buoyancy. Y_M represents the contribution of the fluctuating dilatation in compressible turbulence to the overall dissipation rate. C_{1e}, C_{2e} and C_{3e} are constants. σ_k and σ_ϵ are the turbulent Prandtl numbers for k and ε, respectively. S_k and S_ϵ are user-defined source terms [6].

The model constants $C_{1e}, C_{2e}, C_{3e}, \sigma_k$ and σ_ϵ have the following default values: $C_{1e} = 1.44, C_{2e} = 1.92, C_{3e} = 0.09, \sigma_k = 1.0, \sigma_\epsilon = 1.3$. These default values have been determined from experiments with air and water for fundamental turbulent shear flows including homogeneous shear flows and decaying isotropic grid turbulence [6]. They have been found to work fairly well for a wide range of wall- bounded and free shear flows [6].

5. Numerical Modeling

For the analysis, the geometry of vehicle was modeled using SolidWorks 2017, where the boundary of the vehicle was formed by tracing curves from the unofficial blueprints of the model. Then the model was converted to solid part and simplified before importing to ANSYS Design Modeler. In this study, 3 types of vehicle were analyzed where the experimental and computational results of “Ahmed Body” was used to validate the other results. The “Ahmed Body” was first created by S.R. Ahmed in 1984 [7]. In vehicle’s industry, Ahmed Car Body is the standard model that can be used as validating case, in industry and CFD simulation [8]. The other vehicle types were Sedan, CUV, Cargo Truck and their respective bodies after geometrical modifications.

A 12500 mm× 3000 mm× 3000 mm fluid flow field enclosure had been created where the enclosure acted as air. The front of the body is placed at a distance of 2 car lengths (2L) from the flow inlet and at a distance of 6 car

lengths (6L) from the flow outlet. A symmetry plane is introduced to model half of the model with an aim to reduce the computational time.

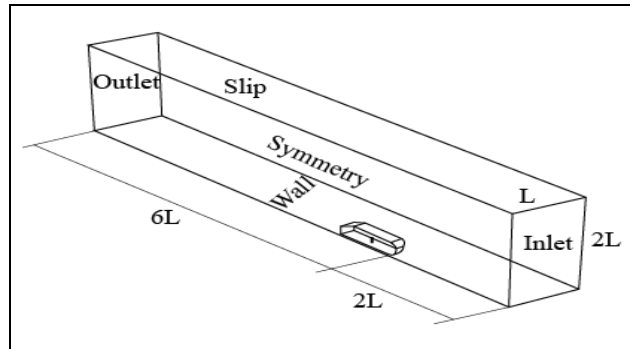


Fig.2 Computational domain for the simulation

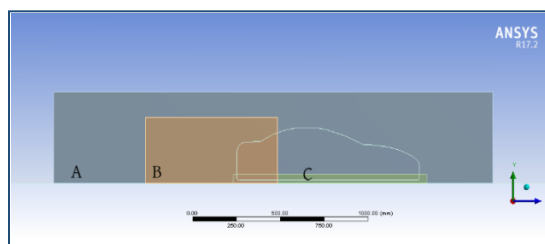


Fig.3 Fine mesh boxes inside the computational domain for Sedan type vehicle analysis (sample image)

Table 1 Cell sizes in each refinement box

Area	Cell Element Size (High Mesh)	Cell Element Size (Low Mesh)
Around Car (A)	10 mm	100 mm
Wake (B)	10 mm	100 mm
Under Car (C)	15 mm	150 mm

A finer mesh downstream of the model was used to capture the wake zone. The cell element size was varied from 10 mm to 150 mm at a growth rate of 1.2. While creating the mesh, 3 different sizing functions had been used to obtain accurate lift & drag characteristics. Three bodies (Box A, Box B and Box C) of refinements as shown in Fig.3 and Table 1 were added to properly capture the flow in the region closest to the vehicle and the flow in the wake. The total number of nodes and elements for corresponding high & low meshes are shown in Table 2.

For boundary conditions, the enclosure inlet plane was named “velocity-inlet”. Air coming through the inlet was given a velocity of 40 m/s. The road and the vehicle body were both made walls & corresponding enclosure surface was named symmetry plane having a “no slip” condition. The outlet was named a “pressure-outlet” with a constant

Table 2 Total number of nodes and elements

Geometry	Nodes (High)	Elements (High)	Nodes (Low)	Elements (Low)
Ahmed body	386856	1813949	72379	237868
Sedan	763911	2983666	238229	737570
Modified Sedan	707603	2805471	207009	644505
CUV	584947	2545238	138981	478941
Modified CUV	569018	2456256	122331	413021
Truck	1210102	4896517	199281	608368
Modified Truck	1267364	5120525	272219	872608

pressure equal to the atmospheric pressure. The flow is solved with a steady-state pressure-based Navier-Stokes solver in Fluent. As the strengths and weaknesses of the standard k-ε model have become known, modifications have been introduced to improve its performance. Two of these variants are available in ANSYS FLUENT: the RNG k-ε model and the realizable k-ε model. The term “realizable” means that the model satisfies certain mathematical constraints on the Reynolds stresses, consistent with the physics of turbulent flows. Neither the standard k-ε model nor the RNG k-ε model is realizable [5]. A realizable k-ε turbulence model is used together with a second-order discretization scheme for pressure and momentum and a first-order discretization scheme for k and ε.

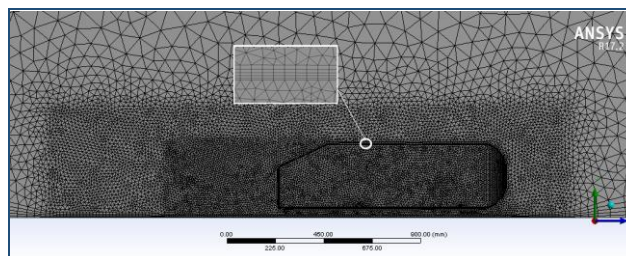


Fig.4 Final Mesh of Ahmed body 25 degree slant with different sizing functions (sample image of mesh)

5.1 Model Optimization Study:

A total of six studied design parameters were roof drop, underbody hoist, diffuser hoist, boat tailing, wing mirrors removal and addition of spoiler. The limits were chosen as the maximum changes that would still produce a realistic

Table 3 Design parameter limits

Parameter	Baseline	Maximum
Roof Drop	0	100 mm
Underbody Hoist	0	107 mm
Diffuser Hoist	0	100 mm
Boat Tailing	0	50 mm

car. Some of these design parameters had been experimented and optimized by Anton Lundberg [3] and were applied in this analysis with a mission to produce a satisfactory drag reduction rate.

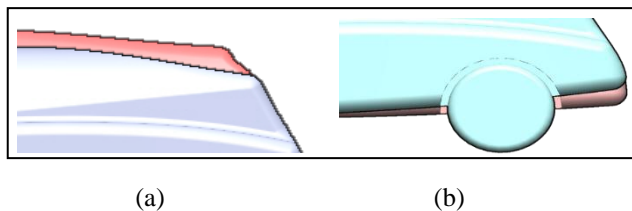


Fig.5 (a) Comparison of baseline (colored red in background) and fully morphed (colored blue in foreground) roof. (b) Comparison of baseline (colored red in background) and fully morphed (colored blue in foreground) diffuser.

A roof drop was achieved by compressing a portion of the roof from the highest point to the rear end. The compression had a linear variation with full compression at the highest point of the roof. A comparison of the baseline and the maximum roof drop of 100 mm can be seen in Fig.5. The diffuser was changed by moving the rear edge upwards by a maximum distance of 100 mm.

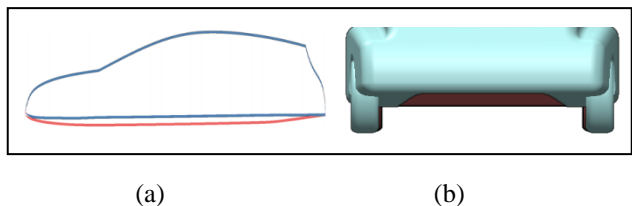


Fig.6 (a) Comparison of baseline (colored in red) and fully morphed (colored in blue) underbody contours. (b) Comparison of baseline (colored red in background) and fully morphed (colored blue in foreground) underbody as seen from the front.

The baseline underbody has a curvature along the car. The underbody was hoisted to achieve the latter profile. The maximum underbody hoist was 107 mm, at which point the underbody was flat as shown in Fig.6

The rear end was slimmed by moving the rear side edge of the car inwards. This is known as boat tailing. A comparison of the baseline and the maximum boat tailing of 50 mm can be seen in Fig.7.

Wing mirrors also known as side view mirrors do impact vehicle aerodynamics and fuel economy. But as an alternative to conventional wing mirrors, the use of cameras could help in reducing aerodynamic drag by an average of 2-7% [2]. This method had been applied by many of the modern automakers like Tesla, Volkswagen, Volvo, especially, in their electric vehicles and gaining popularity day by day.

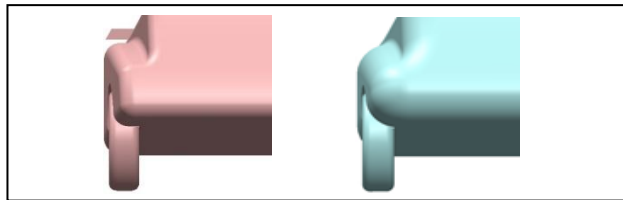


Fig.7 Comparison of baseline and fully morphed rear. In the fully morphed case a boat tailing is applied, i.e. the rear is slimmed by moving the rear edge inwards. The maximum boat tailing is 50 mm.

Spoilers are not only used on sedan type race cars and road cars to provide downward force, but also to resist the natural tendency of these cars to become “light” in the rear because of the lift generated by the rear body shape. They act like barriers to air flow which results into a buildup of higher air pressure in front of the spoiler, therefore, helping to stabilize the lighter rear portion of car stick to the road.

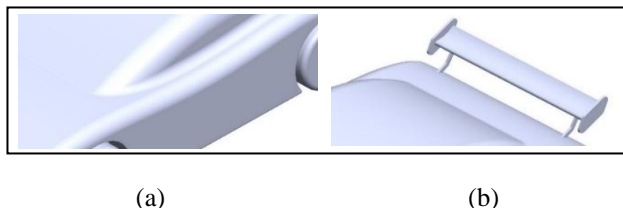


Fig.8 (a)Wing Mirror removed in Modified Sedan (b) Spoiler added to Modified Sedan

6. Results & Discussion

The computational drag and lift co-efficient values of the “Ahmed Body” was found in close agreement with the experimental values as shown in Table 5 [10] and Fig. 9

Table 4 Comparative C_D and C_L values of Ahmed Body

Ahmed Body ($\alpha=25^\circ$)	Experimental Value	Computational Value
C_D	0.299	0.286
C_L	0.345	0.381

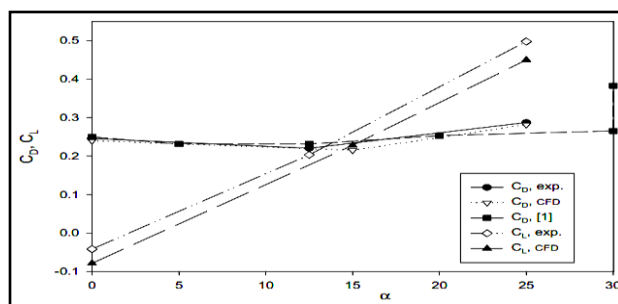


Fig.9 Comparisons of C_D and C_L from present computational and experimental (exp) studies and the experimental data from ref. [7] (Fig. ref. [11])

Therefore, the computational data of the “Ahmed Body” is validated by the mentioned experimental data which had been used as a benchmark value throughout rest of the CFD simulations.

Fig.10 depicts a series of comparative illustration of velocity streamlines between the initial and the modified bodies of the subject vehicles. These figures demonstrate that the air velocity decreases as it approaches the frontal

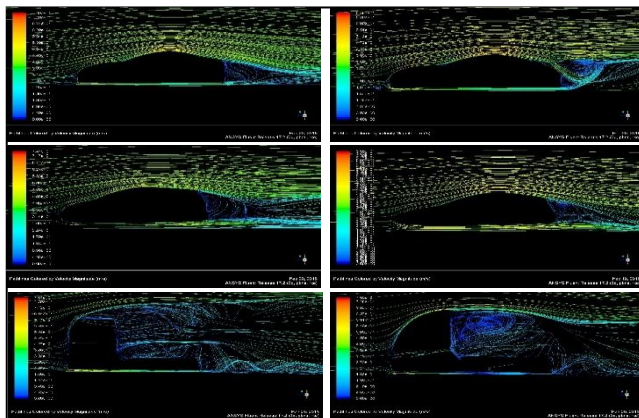


Fig.10 Streamlines of Velocity Magnitude (m/s)

section of the vehicles and then increases away from the front. In modified bodies, the velocity magnitude decreases from a higher gradient, therefore, indicating that the air resistance is smaller.

Table 5 Comparison of Velocity Magnitude (m/s) Gradients

Geometry	Initial Gradient Range (m/s)	Modified Gradient Range (m/s)
Sedan	0-7.49E+1	0-6.56E+1
CUV	0-7.47E+1	0-6.43E+1
Truck	0-7.91E+1	0-7.58E+1

Fig.11 illustrates the comparative static pressure contours of the subject bodies. It is evident from the images that there is a higher pressure concentration on the vehicle front, windshield and wing mirror in all cases. But this pressure concentration is dropped significantly when the wing mirrors of the vehicles had been removed and the frontal curve of the vehicles are less steeper after performing the geometrical modifications.

Particularly, the air slows down when it approaches the front of the car and results in that more air molecules are accumulated into a smaller space. Once the air stagnates in front of the car, it seeks a lower pressure area, such as the sides, top and the bottom of the car. As the air flows over the car hood, pressure is decreasing, but when it reaches the front windshield, it increases briefly [9]. As

the high pressure air glides over the windshield, it accelerates and causes a decrease of the pressure which results into a lift - force on the car roof as the air passes over it.

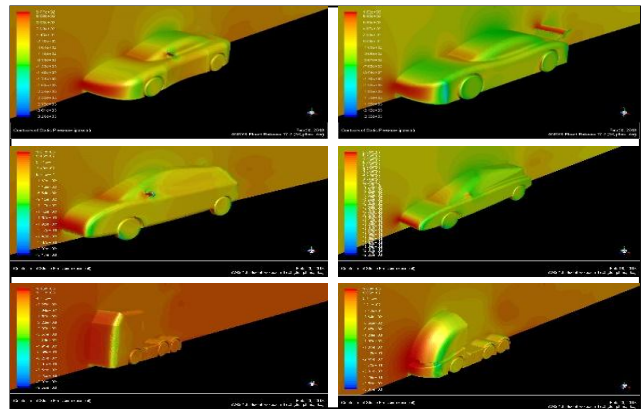


Fig.11 Contours of Static Pressure (Pa)

Fig.12 shows the contours of Wall y^+ for all cases. As the turbulence model wall laws have restrictions on the y^+ value at the wall. So, for each turbulence model it should be determined in appropriate way. It had been observed from contours that the y^+ values fall into the required range of $30 < y^+ < 300$ for $k-\epsilon$ turbulence model.

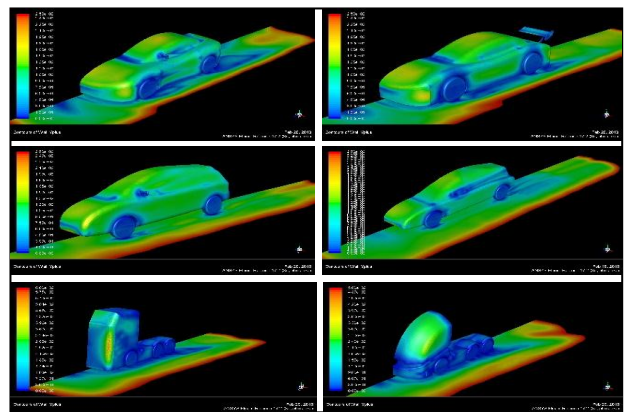


Fig.12 Contours of Wall y^+

Table 6 Comparative results of C_D and C_L between high and low meshes

Geometry	High Mesh	Low Mesh	High Mesh	Low Mesh
	C_D	C_L	C_D	C_L
Ahmed body	0.286	0.381	0.352	0.475
Sedan	0.364	0.303	0.476	0.369
Modified Sedan	0.262	0.488	0.328	0.546
CUV	0.22	-0.173	0.294	-0.113
Modified CUV	0.20	-0.719	0.291	-0.785
Truck	0.533	0.416	0.687	0.511
Modified Truck	0.35	0.184	0.492	0.216

Table 6 shows the comparative drag and lift co-efficient values between high mesh and low mesh geometries. By reducing cell element sizes (Table 1), it was possible to produce a more accurate drag & lift coefficient. Reducing the size of the mesh attached to the car surface and its growth rate has a significant effect on the solution and they are considered the most important parameters, nevertheless y^+ has to be within the valid range [11].

Table 7 Drag reduction rate comparison

Car Type	Modifications Performed	C_D (before)	C_D (after)	Drop rate %
Sedan	Roof Drop, Wing Mirror, Spoiler, Underbody Hoist	0.364	0.262	28.02 %
CUV	Roof Drop, Diffuser Hoist, Boat Tailing, Underbody Hoist	0.22	0.20	9.09 %
Truck	Roof Drop, Wing Mirror, Underbody Hoist	0.533	0.35	33.96 %

Table 7 shows the modifications performed on each vehicle and the rate of drag reduction after those modifications. The drag reduction rate in the Sedan and Truck type vehicle is significant compared to Crossover Utility Vehicle (CUV).

From Fig.13 it is apparent that the C_D conditions had been improved in the modified ones.

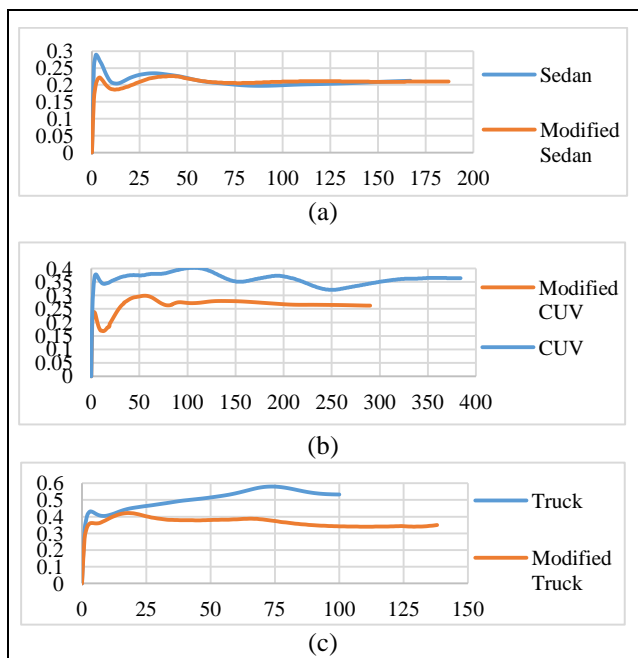


Fig.13 Comparative C_D (Y-axis) vs Iteration (X-axis) plots for (a) Sedan & Modified Sedan (b) CUV and Modified CUV (c) Truck and Modified Truck

7. Conclusion

Aerodynamic characteristics of several ground vehicles had been analyzed by CFD and the results were found to be in reasonable agreement with the computational value of Ahmed Body. As modifications in the geometries of the original models led to a significant drag reduction rate of 28.02% for Sedan, 9.09% for CUV, and 33.96% for Truck type vehicle, therefore, it can be concluded that the CFD simulations produced satisfactory results. Also, based on the mesh dependency study, it is safe to assume that more accurate results are obtainable if further mesh refinement can be continued. This will eventually lead to positive performance characteristics (lift and drag), therefore, improving the overall performance of the vehicles.

REFERENCES

- [1] European Commission. 2014b, *Innovation Union Scoreboard*, 2014
- [2] Bettes, WH. "The Aerodynamic Drag of Road Vehicles – Past, Present and Future" *Engineering & Science*, January 1982, 4-10.
- [3] Lundberg, A., Hamlin, P., Shankar, D., Broniewicz, A. et al., "Automated Aerodynamic Vehicle Shape Optimization Using Neural Networks and Evolutionary Optimization", *SAE Int. J. Passeng. Cars - Mech. Syst.* 8(1):242-251, 2015
- [4] "ANSYS FLUENT will", 18.1 Overview of Flow Solvers, 2009, January 23
- [5] Thet Mon Soe, San Yu Khaing, "Comparison of Turbulence Models for Computational Fluid Dynamics Simulation of Wind Flow on Cluster of Buildings in Mandalay", *IJSRP* 7(8) (ISSN: 2250-3153), 2017
- [6] Damjanovic, D., Kozak, D., Živić, M., Ivandic, Z., Baškarić, T., "CFD analysis of concept car in order to improve aerodynamics", *International Scientific and Expert Conference TEAM 2010*, Kecskemét, November 4-5, 2010
- [7] Ahmed, Syed R., G. Ramm, and G. Faltn. "Some salient features of the time-averaged ground vehicle wake." *SAE Transactions: p473-503*, 1984
- [8] Davis, N., "FLUENT Lab Exercise 10 - Ahmed Car Body", *Illinois: Computational Science and Engineering Illinois*, 2015
- [9] Jathar, L.D., Borse, S.L. , "Study of Flow over Car by Changing Different Parameters using Open Foam", *ISSN 0974-3138* Volume 6, Number 1, 2014
- [10] Meile, Walter & Brenn, Günter & Reppenhagen, Aaron & Lechner, Bernhard & Fuchs, Anton. "Experiments and numerical simulations on the aerodynamics of the Ahmed body", *CFD Letters* 3, 2011
- [11] Bayraktar, I., Landman, D., and Baysal, O., "Experimental and Computational Investigation of Ahmed Body for Ground Vehicle Aerodynamics," *SAE Technical Paper* 2001-01-2742, 2001.

Application of Lean and Six Sigma Tool to Waste Reduction and Productivity Improvement in Footwear Industry

Adhir Chandra Paul*, Noor-E-Imam, Shakhawath Hossain

Department of Leather Engineering, Khulna University of Engineering & Technology, Khulna-9203, BANGLADESH

ABSTRACT

Footwear sector is one of the promising sectors in our country as its raw material is almost available. As a result, we see many footwear industries have been set up in recent decades. This study assesses the current operational and management practices. By applying Lean and Six Sigma tools, green manufacturing holds potential economic benefits including long-term process efficiency benefits, cost saving, and waste reduction. It also assists in attaining the knowledge about different techniques of production improvement and environment-related factors. This analysis focuses on how environmental wastes are produced and analyses possible solutions in order to reduce cost. In this work, productivity has been improved from 13 pair/worker to 16 pair/worker through reducing standard time. In this competitiveness, the present and future will belong to those who can do both to achieve high productivity. The advantages of Lean Six Sigma (LSS) are reduction in defects, cycle time, work in progress etc., as well as increase in product quality, reliability, customer satisfaction, productivity etc., leading ultimately to excellent business results.

Keywords: Lean, Six Sigma, LSS, Time study and Footwear industry.

1. Introduction:

Economic competition for high quality products has increased. Manufacturers always look for systematic opportunities to eliminate energy and environmental wastes. Inter-linked and interrelationship among these factors are vital and should be balanced and variable relating to external and internal factors as well as environment-related factors. This study also focuses on waste producing across the manufacturing processes [1].

With the fast changing economic competition for high quality products has increased. Product variety, high lead time, minimal waste, green manufacturing adds a major impact to manufacturing industries. Thus methods like Enterprise Resource Planning, Business Process Reengineering, and Just in Time (JIT) manufacturing and Lean Management have been developed [2]. Quality Management and Improvement can be defined as the fitness for use or purpose at the most cost-effective level. LSS is a statistical measure of the performance of a process and measures the degree to which it deviates from the required value and then gives efforts to improve the operations. [2] The traditional DMAIC Six Sigma process, as it is usually practiced, which is focused on evolutionary and continuous improvement manufacturing or service process development, usually occurs after the initial system or product design and development have been largely completed. It starts from an understanding of the customer expectations, needs and Critical to Quality issues (CTQs) before a design can be completed [3].

Applying Lean Six Sigma (LSS) methodology and waste management in the footwear industry leads to many of the improvements demonstrated in other sectors—reduction of raw material use, and increasing reuse and recycling on site respecting Bangladesh. Such improvements in environmental

performance produce a directly beneficial effect on the profitability of business.

This work can be used to minimize work content as well as waste that also makes sense from a business perspective. In order to produce products like footwear, resources in the form of man, machine, materials, capital and other equipment are required. The more effective use of resources is ensured the more goods will be produced. By effective and efficient use of resources the economic system can attain self-sustained growth. Productivity improvement is not only just doing things better but also doing the right things better. The right things or more specifically factors influencing productivity is the prime concern for the productivity manner. Here, it was shown the improvement of productivity by reducing standard time through time study.

2. Method:

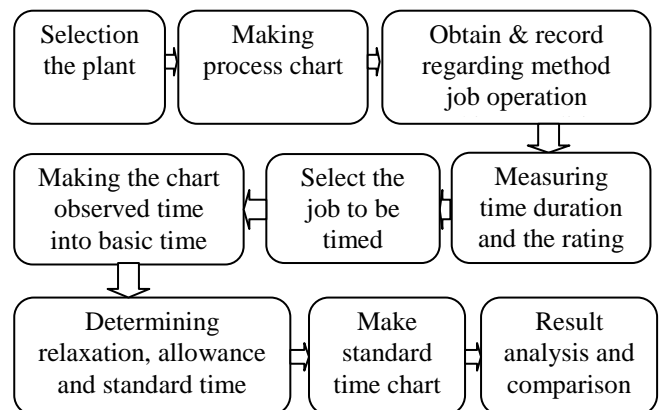


Fig.01: Overview of the study

2.1 Lean six sigma:

Lean Six Sigma is a methodology that relies on a collaborative team effort to improve performance by systematically removing waste; combining Lean

manufacturing and six sigma to eliminate the eight kinds of waste (muda): Time, Inventory, Motion, Waiting, Over production, Over processing, Defects, and Skills. Lean six sigma project comprise aspect of leans waste eliminations. Lean six sigma utilizes the DMAIC phase similar to that of six sigma.

2.2 Work Study:

Work study can be defined as techniques that analysis the elements of a specific process carefully to eliminate unnecessary operations & to determine better method for these operation. Employees are trained to follow standard method. Equipment's & working conditions are also standardized. Work study can be divided into the following two compositions: [6]

- ✓ Method study (Method design stage)
- ✓ Work measurement (Standard time setting phase)

2.3 Method Study:

The purpose of is to analyses the element of a given work i.e. raw materials process, machinery, operating sequences & layout & to plan better working method & operating system. [6]

2.3.1 Operation analysis, Motion analysis & example of application:

Operation analysis emphasis improvement in various lands of working operations performed by individual or several operations. [6]

2.4 Production Process Analysis:

Production process analysis primarily includes two types of analytical method:

- ✓ Process analysis
- ✓ Man process analysis

Production Process analysis is an analytical method applicable to various objectives & used to record & analysis specific process. This method includes five kinds of symbols denoting operation inspection transportation delay & storage to illustrate the various processes which appear during the course of production. It is used to investigate the structure of overall processing systems and used to determine improvement.

2.4.1 Production Process Chart:

Outline process chart (Simple Type)

- ✓ Simple type
- ✓ Assembly type
- ✓ Disassembly type

Flow Process Chart (Detail Type)

- ✓ Simple type
- ✓ Assembly type
- ✓ Disassembly type

The outline process chart is used to obtain a board understanding conditions. This is a short duration procedure performed through quick observation of workplaces in need of improvement. Only operation & inspection symbols are used at this stage. [6] [8]

2.5 Work Measurement:

Work measurement is also known as "Time study". Work measurement is absolutely essential for both the planning and control of operations. Without this we cannot determine the capacity of facilities or it's possible to quote delivery dates or costs. Calculate

proper working time for each optimum working thing system & to supervise output etc. The application of this techniques designed to establish the time for a qualified worker to carry out a specific job at a defined level of performance. [6]

2.5.1 Time study:

Time study for recording the times and rates of working for the elements of specified job carried out under specified conditions and for analysis the data so as to determine the time necessary for carrying out the job at the defined level of performance. [6] [11]

Steps in making time study- [6]

1. Select the work to be studied.
2. Obtain and record all the information available about the job, the operation, working conditions to affect the time study work.
3. Breakdown the operation into element.
4. Measuring the time by means of stop watch, taken by operator to perform each element of operation.
5. At the same time assess the worker effective speed of work called performance rating.
6. Adjust the observed time by rating factor to obtain normal time.
7. Add suitable allowance to compensate for fatigue, personal needs, contingencies etc.
8. Compute allowed time the entire job by standard time.
9. Make a detailed job description describing the method for which the standard time is established.
10. Test and review standards where necessary.

$$\text{Normal time} = \text{Observed time} \times \text{Performance Rating (\%)} / 100$$

$$\text{Basic Time} = \text{Cycle time (operation average time)} \times \text{Performance rating}$$

$$\text{Standard time} = \text{Basic time} + 15\% \text{ relaxation allowance} + 3\% \text{ contingency allowance [6]}$$

2.5.2 Step in time study:

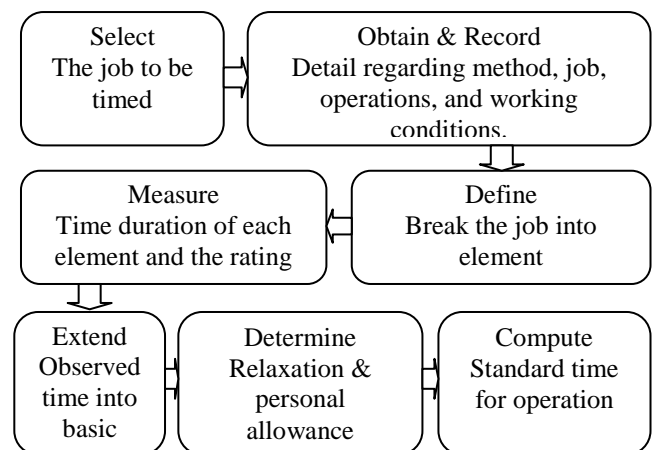


Fig. 02: Flow chart of time study

2.5.3 Observe time: The time taken to perform an element or combination of elements obtained by means of direct measurement. [6]

2.5.4 Selected time: The time chosen as being representative of a group of times for an element or group of elements by calculating means, median or mode. [6]

2.5.5 Rating:

Rating is the assessment of the worker's rate of working relative to the observer's concept of the corresponding to the pace. [6]

Rating Scale	Description
0	No activity
50	Very slow, clumsy, half sleep with no interest in job
75	Steady, deliberate, unhurried performance, looks slow but time is not being intentionally wasted while under observation.
100	Brisk, business like performance, as of an average qualified worker on piece work. It is standard rate.

2.5.6 Relaxation allowance:

Relaxation allowance is an addition to basic time intended to provide the worker with the opportunity to recover from physiological and psychological effects of carrying out specified work under specified conditions. [6] Generally relaxation allowance is about 15% of basic time.

2.5.7 Contingency Allowance:

Contingency allowance is a small allowance of time that may be included in a standard time to meet legitimate and expected items of work on delays, the precise measurement of which is uneconomical because of their infrequent or irregular occurrence. Contingency allowance is 3% of basic time. [6]

2.6 Selection of operators to observe:

When the purpose of the study is to establish standards, it is advisable to work with workers of medium or high skilled level in order to facilitate rating & file suspicious of other workers towards the standard time that is established. When improvement is the aim, it is best to select skilled workers with diligent personalities, in order to facilitate further improvement. [6]

2.6.1 Efficiency:

Efficiency = Present output / Standard output

Efficiency = Minutes output / Minutes input

Increasing Efficiency = [(the efficiency of proposed line - present efficiency) / Present Efficiency] × 100

% of work content reduction per pair = [(present work content / pair - proposed work content / pair) / Present work content / pair] × 100

Increasing Productivity (at 100% capacity) = [(Proposed standard output - Existing standard output) / Existing Standard output] × 100 [6]

3. Methodology:

3.1 Plant selection:

First, a suitable plant was selected for our thesis work. Thesis study was conducted at Bata Shoe Company (BD) Ltd. and its subsidiary Anonna footwear and FB Footwear Ltd. Dhaka, Bangladesh.

3.2 Time Study:

After selecting the lasting and finishing line for study, the cycle time into time study form named collected data from present production line was recorded.

3.3 Calculation:

The basic time and standard time of operations was calculated

Basic Time = Cycle time (operation average time) × Performance rating

Standard time = Basic time + Relaxation allowance + Contingency allowance

3.4 Modify the production line:

After calculating existing standard time and exploring, a modified production line was proposed through reducing standard time and man power.

4. Data collection and analysis:

After selecting the lasting and line for study, cycle time was measured by stop watch and recorded as collected data of existing production line as below:

4.2 Calculations:

Average production of line = 500

Total-Worker = 45

Working minutes per worker = 480 minutes

(8 hours)

Work Minutes per pair = 2120/60 = 35.34

S. N	Name of operation	Observed Time (sec)			Average cycle time (sec)	Standard deviation	Rating (sec)	Basic Time (sec)	Std. Time (sec)	System	Man power
1	Last collection & insole attaching	45	44	46	45	±1	75	34	40	Manual	4
2	Apply adhesive to insole lasting	210	200	215	206	±1	75	155	183	Manual	4
3	Mulling	30	33	34	32	±1	75	24	28	Machine	1
4	Toe lasting	215	220	224	217	±1	75	163	193	Machine	2
5	Side lasting	70	74	72	71	±1	75	53	63	Machine	2
6	Heel seat lasting	205	210	200	203	±1	75	152	180	Machine	2

7	Conditioning	65	65	65	65	±1	75	49	58	Machine	2
8	Wrinkle chasing	320	315	318	314	±1	75	236	278	Machine	2
9	Roughing	325	332	330	326	±1	80	260	292	Machine	2
10	Upper cleaning & sole preparation	89	91	97	91	±1	65	63	75	Manual	2
11	Apply adhesive	52	55	57	54	±1	75	41	48	Manual	2
12	Drying	45	45	45	45	±1	70	31	37	Machine	2
13	Attaching sole	120	118	115	116	±1	75	87	103	Manual	2
14	Sole pressing	62	60	65	62	±1	75	46	54	Machine	1
15	Cooling	35	35	35	35	±1	75	26	31	Machine	2
16	Ironing	115	125	130	122	±1	75	92	108	Machine	1
17	Cleaning	120	140	125	127	±1	65	83	98	Manual	4
18	Brushing with wax	150	145	155	149	±1	75	112	132	Machine	2
19	Delasting	38	40	36	38	±1	85	32	38	Machine	2
20	Inspection	90	95	92	92	±1	75	69	81	Manual	4
Total									2120		45

Standard output at 100% efficiency = $(480 \times 45) / 35.34$
= 611

Productivity = $611/45 = 13$ Pair/worker

Efficiency = $(500/611) \times 100 = 82\%$

4.1 Proposed modified line:

After analysed the collected data, a production line has been proposed as below-

4.1.1 Calculation:

According to collected data:

Average production = 500

Total Worker = 38

Working minutes per worker = 480 minutes (8hours)

Work Minutes per pair = $1738/60 = 28.96$

Standard Output at 100% efficiency = $(480 \times 38) / 28.96 = 630$

Productivity = $630/38 = 16$ Pair/ worker

Efficiency = $(500 / 630) \times 100 = 79\%$

5. Results and discussion:

Average production of line = 500

Total Worker = 45

Working minutes per worker = 480 minutes (8hours)

Work Minutes per pair = $2120/60 = 35.34$ Standard

Output at 100% efficiency = $(480 \times 45) / 35.34 = 611$

Productivity = $611/45 = 13$ Pair/ worker

Efficiency = $(500 / 611) * 100 = 82\%$

Here at below, the histogram shows the highest time consuming operation roughing and lowest time consuming operation mulling where X axis indicates operations and Y axis indicates standard time (second) according to present production line

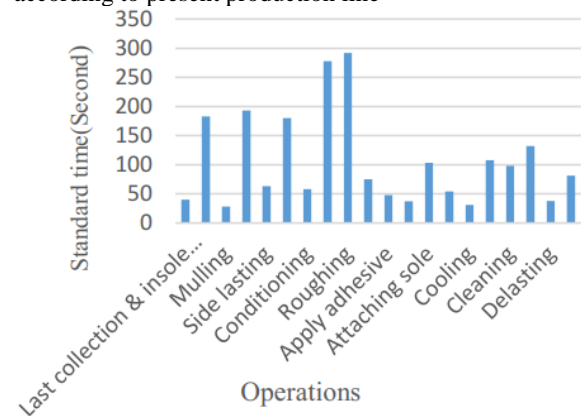


Fig. 03: Standard time in various operations of present line

According to modified line:

Average production = 500

Total Worker = 38

5.1 Proposed modified line:

S.N	Name of Operation	Operation/ Cycle time (sec)	Rating	Basic Time (sec)	Std. Time (sec)	System	Manpower
1	Last collection & insole attaching	40	65	26	31	Manual	3
2	Apply adhesive to insole lasting	185	65	120	142	Manual	3
3	Mulling	24	65	16	19	Machine	1
4	Toe lasting	200	70	140	165	Machine	2
5	Side lasting	65	70	45	53	Machine	2
6	Heel seat lasting	180	75	135	160	Machine	2

7	Conditioning	60	65	39	46	Machine	1
8	Wrinkle chasing	280	70	196	231	Machine	2
9	Roughing	300	65	195	230	Machine	2
10	Upper cleaning & sole preparation	80	70	56	65	Manual	2
11	Apply adhesive	50	75	38	45	Manual	2
12	Drying	40	70	28	33	Machine	1
13	Attaching sole	110	75	82	86	Manual	2
14	Sole pressing	60	65	39	46	Machine	1
15	Cooling	35	75	24	28	Machine	2
16	Ironing	110	60	66	78	Machine	1
17	Cleaning	100	60	60	70	Manual	2
18	Brushing with wax	135	65	87	102	Machine	2
19	Delasting	40	70	28	33	Machine	2
20	Inspection	85	75	64	75	Manual	3
Total					1738		38

5.2 Analysis of operation:

Name of the operation	Existing line		Proposed line	
	Existing method	Std. time	Suggested method	Std. time
Last collecting & Insole attaching	It has been observed that the workers waste their time by gossiping and their operation is done by 4 workers. Two of them attaching insole & others help them	40	If three workers involve in this operation and carefully done this work then productivity will increase	31
Apply adhesive on insole up to lasting margin	Four workers were doing this operation. Workers were talking adhesive very small amount by brush, so they repetitively take cement & apply to insole. As a result work content was increase	183	For applying cement, if three workers in this operation, take only one time they could able to save the time & productivity will increase	142
Drying	It has been observed that this operation was done by two workers were waste time by gossiping and wait for work during operation	37	If the operation is done by one worker, time and cost will save & Productivity will increase.	33
Cleaning	During upper marking they were using silver marker. To remove silver marking it was taking more time. Other two workers were waste time to wait for work during operation	98	If they will use proper pencil during marking then this problem solve easily. If two worker done this, then productivity will increase	70
Conditioning	It has been observed that this operation was done by two workers were waste time by gossiping and wait for work during operation	58	There is no need of two worker. If the operation is done by one worker, time and cost will save	46

			&Productivity will increase	
Inspection	Four workers were doing this operation. Workers waste their time by gossiping and remain idle waiting for next pair	81	If three workers involve in this operation and carefully done this work then productivity will increase and reduce cost	75

Figure 4.2: Operations analysis

Working minutes per worker = 480 minutes

(8hours)

Work Minutes per pair = $1738/60 = 28.96$ Standard Output at 100% efficiency = $(480*38) / 28.96 = 630$

Productivity = $630/38 = 16$ Pair/ worker

Efficiency = $(500 / 630) * 100 = 79\%$

Here at below, the histogram shows the highest time consuming operation wrinkle chasing and lowest time consuming operation cooling where X axis indicates operations and Y axis indicates standard time (second) according to proposed production line. This histogram also indicates the reduction of standard time of various operations.

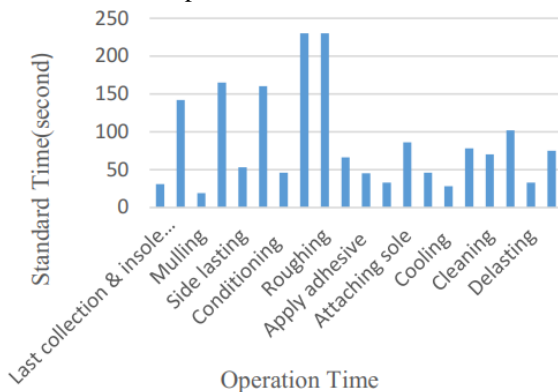


Fig. 04: Standard time in various operations in modified

Hence, Productivity improvement = $(16-13)$ pair/worker = 3 pair/worker

Work content (Minutes) reduction = $(82-79) = 3\%$

Here at fig: 5.2.1 histogram indicates improvement of productivity from 13 pair/worker to 16 pair/worker where Y axis indicates productivity.

At fig 5.2.2, this graph shows how standard time is reducing after modifying the production line where X axis indicates standard time and Y axis indicates operations

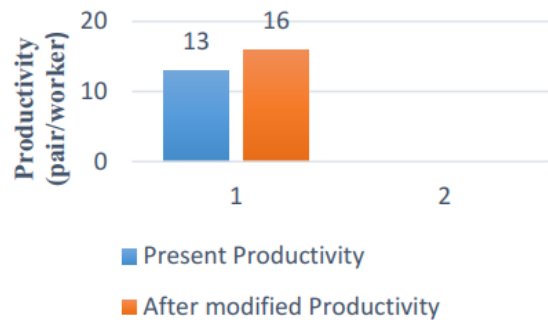


Fig. 05: Comparison of productivity between present and modified line

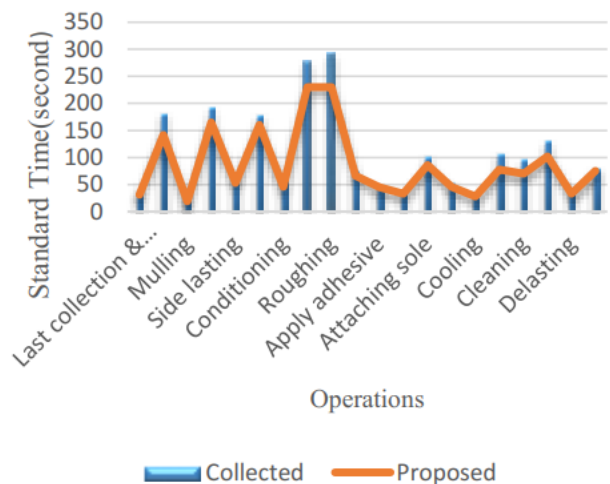


Fig. 06: Comparison of Productivity and standard time between Present and modified line

In proposed modified line Total work content reduction is 3% and worker could be reduced from 45 to 38. So the company can save 7 workers salary per month through proposed line and controlling labour Waste management is very difficult to provide a global image of the costs related to each practice; each country has its own costs and regulations. The environment is getting profit because the industry is generating wastes that can be more easily recycled. The garbage maybe the raw material of another industry. Sell it to another industry as by

product and get some profits. Avoiding the use of compressed air consume. The major common point is the costs regarding landfilling is the lowest everywhere and it is also environment friendly. In most cases, internal reduction solutions cannot reduce the quantities of waste very much and internal recycling solutions can only be applied in large scale.

6. Conclusion:

Productivity improvement is not only just doing things better but also doing the right things better. As a tool we use Lean six sigma to improve productivity and reducing waste. The methodology involves statistical analysis to quantify repeated common cause variations. Lean Six Sigma becomes a continuous process for quality improvement and cost reduction and developed the capability of reducing problems or issues effecting customer expectations on key business processes. This study also focus on waste producing across the manufacturing processes and act as an improvement and cost reduction process. Applying Lean Six Sigma (LSS) methodology and waste management in the footwear industry leads to many of the improvements demonstrated in other sectors. By going green manufacturers can realize savings and increased profits beyond wildest imagination. To be productive enterprise must be able to produce efficiently and effectively. To require this

Organization must focus in skill upgrading and focus on Lean strategies that involves customers, distributors and manufacturer to reduce cost and quality. By applying Lean and six sigma tool, green manufacturing holds potential economic benefits including long term process efficiency benefits, cost saving, waste reduction. Here, we improve productivity from 13 pair/worker to 16 pair/worker through reducing standard time. In this competitiveness, the present and future will belong to those whom can do both to achieve high productivity. The advantages Of LSS are reduction in defects, cycle time, work in progress etc. as well as increase in product quality, reliability, customer satisfaction, productivity etc. leading ultimately to excellent business result.

7. Future approach:

After completing this thesis work it can be included for further modification of production line by applying Lean Sigma tool. In this thesis, Productivity has been improved from 13 pair/worker to 16 pair/worker by reducing standard time and man power through time study. Productivity can also be improved by studying analytical estimating and predetermined motion. By continuing the inspection, standard time can be reduced in minimum cycle time as well as increasing productivity

Further study can be done on-

- ✓ Reduction of material consumption
- ✓ Cost reduction measures on power consumption

- ✓ Rework cost calculation
- ✓ Line balancing of the other line

8. References:

- [1] Syed Hasib Akhter Faruqui. (2013), Application of Lean and Six sigma tool to waste reduction in industry, Journal of Cleaner Production, (1-6)
- [2] https://en.wikipedia.org/wiki/Lean_Six_Sigma
- [3] https://en.wikipedia.org/wiki/Six_Sigma
- [4] https://en.wikipedia.org/wiki/Lean_manufacturing
- [5] Andrea Chiarini, (2014), Sustainable manufacturing-greening processes using specific Lean Production tools: an empirical observation from European motorcycle component manufacturers, Journal of Cleaner Production 85 (2014) 226-233
- [6] Martand Telsang (2011) - "Industrial Engineering and Production Management", S. Chand, Ramnagar, New Delhi.
- [7] https://en.wikipedia.org/wiki/Production_theory
- [8] <https://en.wikipedia.org/wiki/Production>
- [9] http://www.gdrc.org/sustbiz/green/doc-prod_introduction.html
- [10] Fourteenth Session of the Leather and Leather Products Industry, Zlin, Czech Republic (13-15 December 2000)
- [11] https://en.wikipedia.org/wiki/Time_and_motion_study
#Time_study
- [12] <http://www.slideshare.net/AdvanceIgroup/defect-reduction-six-sigma-green-belt-project-in-footwear>

Studies on Sewing Complication through Pareto Chart and Cause-Effect Diagram analysis of a Footwear Industry

Adhir Chandra Paul*, Md. Atikul Islam, Md. Shohag Hossain

Department of Leather Engineering, Khulna University of Engineering & Technology, Khulna-9203, BANGLADESH

ABSTRACT

Due to global competition, declining profit margin and customer demand for high quality product at low cost, push the manufactures to reduce their production cost without compromising quality in order to survive in business arena. The quality and productivity of footwear largely depends on various organized operations especially on the sewing operation. Defects minimization is the first condition of reducing production cost and improving the quality. In this study, information of different types of defects of sewing sections had collected and analyzed through Pareto chart and Cause-effect diagram. The main purpose of the work is to reduce the defects, which will also minimize the rejection and reworks rate. Here we were concentrating on five major defects in sewing process. Finally, these working policies able to % of defects decrease 79.28% to 17.5%. The study also facilitates the process performance of the critical operational processes. It will also reduce the cycle time by reducing reworks and finally result higher productivity.

Keywords: Profit margin, Sewing defects, production cycle time, Pareto chart and Cause-effect diagram

1. Introduction

Footwear is a human made outer covering of foot. When the human beings came into existence, they were required to protect themselves from, cold dampness, dust, heat, and roughness of ground while standing, walking or even running. So they originate shoes for the protection of their feet. Footwear sector is the most potential and booming export sector in Bangladesh after RMG. Besides that, Bangladesh is set to emerge as a next manufacturing hub for global footwear industry. In recent times, more than 50 foreign countries are the substantial export destination of Bangladesh's footwear. In addition, more than half of finished leather (54%) has exported to the EU market[1]. Germany, France, United Kingdom and Italy are the top four buyers among 10 global footwear but now, US buyers are showing intent for import footwear from Bangladesh [2]. According to the EPB, the first two months of the current fiscal year 2016-2017, the country posted 23.62% growth in footwear exports over than that of the last year. Bangladesh has received \$ 120.59 million foreign exchange from exports of finished leather and footwear in current years[3]. Global footwear industry is now at upward trajectory. Contemporary, rising global demand for footwear which is expected to reach \$ 211 billion by the end of 2018. Bangladesh has the potential to tap into the growing market by offering quality type footwear that depend on the manufacturing process like sewing, lasting, finishing and so on [4]. Sewing is the craft of fastening or attaching objects using stitches made with a needle and thread. Sewing is one of the oldest of the textile arts, arising in the Paleolithic era[5]. Before the invention of spinning yarn or weaving fabric, archaeologists believe Stone Age people across Europe and Asia sewed fur and skin clothing using bone, antler or ivory needles and "thread" made of various animal body parts including sinew, catgut, and veins [6]. For thousands of years, all sewing was done by hand. The

invention of the sewing machine in the 19th century and the rise of computerization in the 20th century led to mass production and export of sewn objects, but hand sewing is still practiced around the world [7]. The Inuit, for example, used sinew from caribou for thread and needles made of bone; the indigenous peoples of the American Plains and Canadian Prairies used sophisticated sewing methods to assemble tipi shelters [9]. The weaving of cloth from natural fibers originated in the Middle East around 4000 BCE, and perhaps earlier during the Neolithic Age, and the sewing of cloth accompanied this development [10]. Advances in industrial technology, such as the development of synthetic fibers during the early 20th century, have brought profound changes to the textile industry as a whole. According to the U.S. Department of Labor "employment of sewers and tailors is expected to experience little or no change, growing 1 percent from 2010 to 2020" [22].



Fig. 01: Global footwear demand

A Parito chart, also called a Pareto distribution diagram, contains a vertical bar graph in which values are plotted in decreasing order of relative frequency from left to right. Pareto Chart is used to graphically summarize and display the contribution of each type of defects. The lengths of the bars represent occurrence and are organized with longest bars on the left and the shortest

to the right [23]. Fishbone diagram is a one kind of cause-effect diagram which contains many causes for a specific effect or problem. It looks like the shape of a fish. That's why it is called fishbone diagram [24].

From Pareto Chart analysis we had identified top ten defects. By our own observation we had identified the causes for each specific defect types from the sewing lines operations through questionnaires. After that we had constructed the cause-effect diagram for each type of defect by using 4M (Man, Machine, Material and Method) bones. These Cause-Effect Diagrams are shown in figure for top three defects that had identified.

2. Methodology

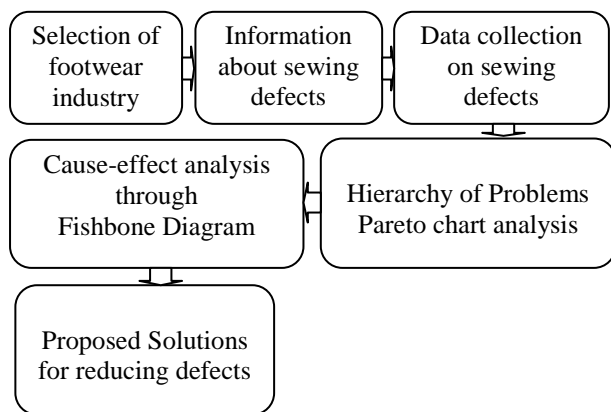


Fig.02: Overview of the study

2.1 Factory Selection

After gathering information we made contact with some footwear factories and tried to select a newly established factory where we can place or utilize our knowledge to make some contribution for the development of the factory. Finally we conduct our research work in two particular footwear factories named “X Footwear Industry” established in 2006 which situated in Tongi, Abdullahpur, Gazipur, Dhaka and “Y Footwear Industry” established in 1994 which situates in Safipur, Gazipur, Dhaka. In these organizations we worked in a particular section (i.e. sewing section) for a particular product (i.e. Derby Footwear). One days defect data has been collected from the management of each industry and Pareto Analysis is performed on them. So hierarchies of causes for individual defect types are organized and Cause-Effect Diagrams are constructed for those defect types. Then relative suggestions to those causes are also provided. In the end necessary clues and recommendations have been added for the advancement of the study.

Company Name	‘X’ Industry	‘Y’ Industry
Location	Dhaka	Dhaka
Establishment	2010	1990
Product Type	Footwear	Footwear
Total workers	1000	7000
Production capacity per day	4000	16000
Working hour per day	8	8

2.2 Gathering information about defects

We have gathered information on the Quality Control system of the sewing section of the selected footwear industry. Here we have collected data of various defects from the sewing section provided by the management which is used for the Analysis purpose of the study.

2.3 Identify the defects

Identification of the major concerning areas to minimize the defects was next step. According to the observation and using management data we have seen some repetitive defects occur in the sewing section. So we tried to do our research work on this section which is our major concern.

2.4 Analysis the defects

In this step Pareto chart Analysis is performed which is required to identify the top defects and it's major concerning areas of defects. After that Cause-Effect Diagrams have been constructed for top defect types. Then we have provided some respective suggestions to minimize the frequency of those defects.

3. Result and Discussion

During shoe production, we had identified ten types of defects like Stitch Slip, Stitch allowance uneven, Irregular Stitch and so on. In visited factory, various defect types of sewing department are denoted by some specific alphabetical defect codes.

S.L NO	DEFECTS	DEFECT CODES
01.	Stitch Slip	SA
02.	Stitch allowance uneven	SB
03.	Irregular Stitch	SC
04.	Wavy stitching	SE
05.	Leather cut	SH
06.	Loose leather	SO
07.	Color shade	SQ
08.	Wrinkle at upper	ST
09.	Pasting problem	SZ
10.	Needle Scratch	SL

Fig.03: Defect types with their corresponding codes

Quality Inspection (100% Sewing) in Royal Footwear Ltd: Observing product style number, order number, QC name, line number and date was OR-001, 005, ‘M’ 12 and 10.10.2016 respectively.

Quality Inspection (100% Sewing) in Apex Footwear Ltd: Observing product style number, order number, QC name, line number and date was Roho-003, 008, ‘N’ 16 and 10.01.2017 respectively.

Table 01: Data of 'X' Footwear Limited

	Jan	Feb	Mar	Apr	May	June	Total
No. of pieces checked	50	55	45	43	40	48	365
No. of rejected pieces	7	12	6	4	5	10	57
Total defects	250	300	215	205	195	240	1405

Table 02: Data of 'Y' Footwear Limited

	Jan	Feb	Mar	Apr	May	June	Total
No. of pieces checked	50	55	45	43	40	48	365
No. of rejected pieces	4	7	3	4	2	8	38
Total defects	165	154	185	176	169	151	1000

Calculation for 'X' Footwear Ltd.:

% of rejection rate (cause of defects) = Total no. of rejected pieces *100/ Total no. of pieces checked=57*100/365=15.6%

% of defects= Total defects*100/ Total no. of rejected pieces=1405*100/57=2464%

Calculation for 'Y' Footwear Ltd.:

% of rejection rate (cause of defects) = Total no. of rejected pieces *100/ Total no. of pieces checked=38*100/365=10%

% of defects= Total defects*100/ Total no. of rejected pieces=1000*100/38=2631%

3.1 Pareto Analysis for Defect:

A Pareto chart, also called a Pareto distribution diagram, contains a vertical bar graph in which values are plotted in decreasing order of relative frequency from left to right. Pareto Chart is used to graphic ally summarize and display the contribution of each type of defect. It is a bar graph. The lengths of the bars represent occurrence and are organized with longest bars on the left and the shortest to the right. In this way the chart visually shows which defects are more significant. By using Pareto Chart major types of defects were identified which is shown in in chart are those defect types are Skipped Stitch, Staggered Stitch, Unbalance Stitch, Variable Stitch Density, Frequent Thread Breakage, Seam Puckering Damage of Fabrics on Seam Line, Needle Heating and Needle Breakage. These types of defect occur due to some specific causes.

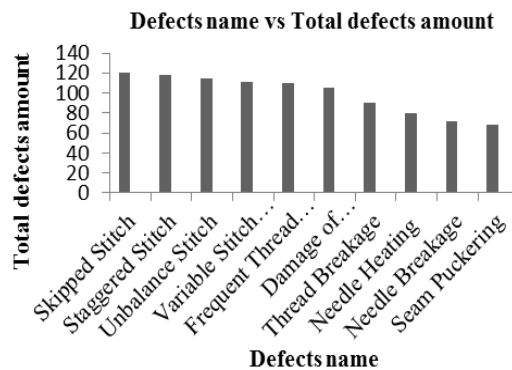


Fig.04: Pareto chart for defects of 'X' Footwear Ltd.

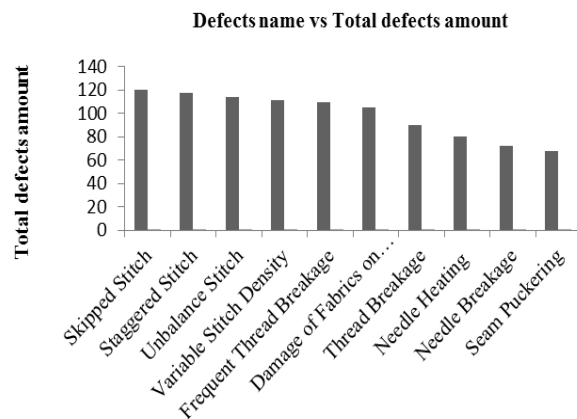


Fig.05: Pareto chart for defects of 'Y' Footwear Ltd.

Table 03: Data of 'X' & 'Y' Footwear Limited (Oct-16 to Mar-17)

	OCT	NOV	DEC	JAN	FEB	MAR	TOTAL
	(PRS)	(PRS)	(PRS)	(PRS)	(PRS)	(PRS)	(PRS)
No. of production PRS	21188	13515	15831	14661	17174	15551	97920
No. of rejected PRS	180.75	150.43	115.20	104.65	128.15	113.42	792.6
No. of rework products	633.86	404.31	473.60	438.59	513.77	465.22	2929.35
Defects Exist in Rework Items							
No. of Major Defects	9786	5958	6280	6971	7769	6483	43247
No. of Minor Defects	6756	3480	4162	4428	5017	3789	27632
Total No. Of Defects	16542	9438	10442	11399	12786	10272	70879

Table 04: Defects analysis of 'X' & 'Y' Footwear Ltd.

Month	Total no. of defects	Selected Top ten major Defect Codes in amount									
		SA	SB	SC	SE	SH	SO	SQ	ST	SZ	SL
OCT	16542	1450	2368	1368	1944	2850	1647	959	455	250	168
NOV	9438	656	1620	550	1264	1822	1208	356	188	198	175
DEC	10442	764	1405	455	1200	1905	1100	381	205	205	186
JAN	11399	809	1559	542	993	2108	1218	428	195	350	229
FEB	12786	1002	1706	614	1462	1806	1383	512	286	281	233
MAR	10272	966	1306	755	1123	1702	1554	757	105	409	250
Gross Total defects	70879	5647	9964	4284	7886	12193	8118	3393	1434	1693	1241

Table 05: Defects percentage of top ten defects ('X' & 'Y' Footwear Ltd.)

SL No.	Defects Name	Defects Code	Calculation	% of Defects
01	Stitch slip	SA	$5647 \times 100 / 70879$	7.96
02	Stitch allowance uneven	SB	$9964 \times 100 / 70879$	14.05
03	Irregular stitch	SC	$4284 \times 100 / 70879$	6.04
04	Wavy stitch	SE	$7886 \times 100 / 70879$	11.12
05	Leather cut	SH	$12193 \times 100 / 70879$	17.20
06	Loose leather	SO	$8118 \times 100 / 70879$	11.45
07	Color shade	SQ	$3393 \times 100 / 70879$	4.78
08	Wrinkle at upper	ST	$1434 \times 100 / 70879$	2.00
09	Pasting problem	SZ	$1693 \times 100 / 70879$	2.93
10	Needle scratch	SL	$1241 \times 100 / 70879$	1.80

Calculation:

Total % of defects of top ten defects= $7.96 + 14.05 + 6.04 + 11.12 + 17.20 + 11.45 + 4.78 + 2.00 + 2.93 + 1.75 = 79.28\%$

Rest of percentage of defects=20.72 %

We see, here is the total % of defects is not 100% because rest of % of defects is negligible.

Now, Major five defects code (SH, SB, SO, SE, SA) containing = $17.20 + 14.05 + 11.45 + 11.12 + 7.96 = 61.78\%$

If we reduced these five defects, then % of defects decrease 79.28% to 17.50%

So, we can focus on these five major defects. Actually this 61.78% is the amount of major five defects of 'X' & 'Y' Footwear Ltd. Which can be eliminated by taking necessary solutions. Then the amount of defects reduced to 17.50%

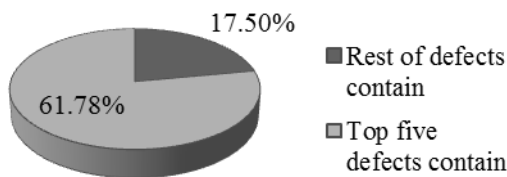
3.1 Categorization of Defects: Parito Chart analysis

A Parito Chart, also called a Pareto distribution diagram, contains a vertical bar graph in which values are plotted in decreasing order of relative frequency from left to right. Pareto Chart is used to graphically summarize and display the contribution of each type of defects.

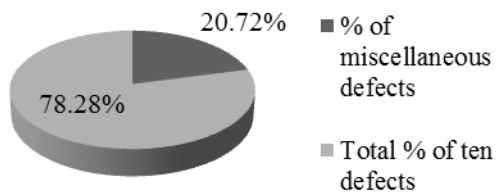
The lengths of the bars represent occurrence and are organized with longest bars on the left and the shortest to the right. In this way the chart visually shows which defects are more significant [5]. By using Parito Chart major types of defects are identified which were shown in chart. These types of defects occur due to some specific causes.

Parito Chart analysis regarding top ten defects of 'X' & 'Y' Footwear Ltd.

% of Top ten defect amount



Pie diagram of Total % of defects



Defects name vs. Total defects amount

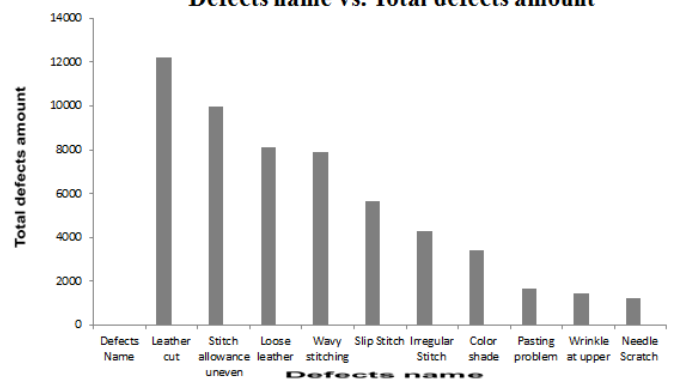
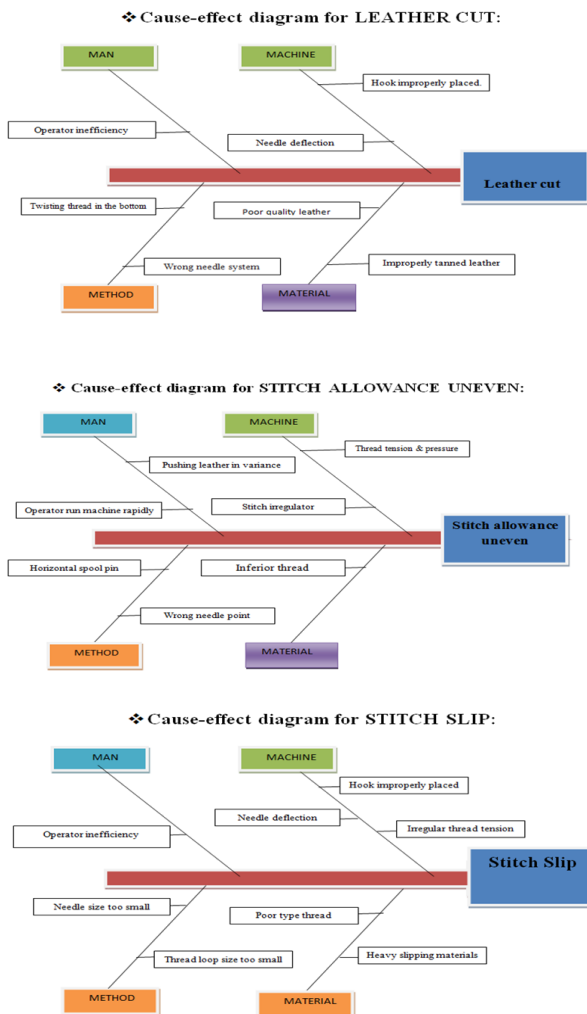


Fig.06: Defects name Vs. Total defects amount

3.2 Cause-Effect analysis with Fish-Bone Diagram:

Fishbone diagram is a one kind of cause-effect diagram which contains many causes for a specific effect or problem. It looks like the shape of a fish. That's why it is called fishbone diagram [6]. From Pareto Analysis we had identified top ten defects. By our own observation we had identified the causes for each specific defect types from the sewing lines operations through questionnaires.

After that we had constructed the cause-effect diagram for each type of defect by using 4M (Man, Machine, Material and Method) bones. These Cause-Effect Diagrams are shown in figure for top three defect that had identified [7].



4. Conclusion

Defect minimization are concerning for ensuring the quality of footwear which also helps to sustain global competitive market. This study try to find out the major defects through Pareto chart analysis and cause-effect diagram and suggests logical solutions in order to minimize defects. By the Pareto chart, top ten defects had identified with a descending order that were responsible for major defects occurring in sewing section of a factory . This study found that the sewing section of selected footwear factory was operating at a high defect percentage. The rate was very high at this present business context. So, it is very essential to minimize the defects and enhance productivity as well. Many footwear factories in Bangladesh are not conscious about the sewing defects and this study will start a positive impact across the footwear industries and make them more competitive.

5. References

- [1] Raluca BRAD, Eugen HĂLOIU and Remus BRAD.(2010), “Seam Puckering Evaluation Method for Sewing Process.
- [2] Islam, Md. Mazedul, Maroof Khan, Adnan and Khan, Md. Mashiur Rahman.(2013), Minimization Of Reworks In Quality And Productivity Improvement In The Apparel Industry, International Journal of Engineering and Applied Sciences, 1 (4):
- [3] Ahmed Tanvir, Narayan Acharjee Raj, Rahim MD.Abdur, Sikder Noman, Akther Taslima, Khan Mohd. Rifat, Rabbi, MD. Fazle and Saha Anup.(2013), An Application of Pareto Analysis and Cause-Effect Diagram for Minimizing Defect Percentage in Sewing Section of a Garment Factory in Bangladesh, International Journal of Modern Engineering Research (IJMER), 3 (6): 3700-3715
- [4] Parthasarathi V., Revathy, S., Praveena, R. and Saranya, S.(2014),Investigation of Fabric Sewability Problems And Solutions: An Overview,International Journal of Applied Engineering and Technology, 4 (1): 32-26
- [5]<https://www.scribd.com/document/319609202/MinimizingThread-BreakageSkips-2-5-10-pdf>
- [6]<https://www.scribd.com/document/319607830/Solution-to-Sewing-Problemstck35-166621-Pdf>.
- [7] https://www.coatsindustrial.com/en/images/Solution%20to%20Sewing%20Problems_tcm35-166621.Pdf
- [8] Abdul Quddus, Md. And Nazmul Ahsan, A.M.A.(2014), A Shop-floor Kaizen Breakthrough Approach to Improve Working Environment and Productivity of a Sewing Floor in RMG Industry, Journal of Textile and Apparel, Technology and Management, 8 (4)
- [9] C. Chen, James, Chen, Jeff.,and Su, Yung-Sheng.(2014), Simulation Modeling and Analysis for Stitching Line of Footwear Industry, Proceedings of the 2014 International Conference on Industrial Engineering and Operations Management ,Bali, Indonesia.
- [10] Md. Mazedul Islam, Adnan Maroof Khan and Md. Mashiur Rahman Khan, “Minimization of Reworks in Quality and Productivity Improvement in The Apparel Industry”, International Journal of Engineering and Applied Sciences, January 2013. Vol. 1, No.4,
- [11] K. L. Mak and Wei Li, “Objective Evaluation of Seam Pucker on Textiles by Using Self-Organizing Map”, IAENG International Journal of Computer Science, 35:1, IJCS_35_1_07. Available http://www.iaeng.org/IJCS/issues_v35/issue_1/IJCS_35_1_07.pdf
- [12] Dung, Nguyen Hoang Phuong, “Improving the quality of service, Case: International SOS Viet Nam”, Bachelor’s Thesis of Degree Programme in International Business, Lahti University of Applied Sciences, Winter 2010,
- [13] Mahto, D., & Kumar, A. (2008), “Application of Root Cause Analysis in Improvement of Product Quality and Productivity”,Journal of Industrial Engineering and Management, 01 (02), page: 16-53.

- [14] A&E Visual Examples of Stitch & Seam Defects - Garmento.org <http://www.garmento.org/quality/a&estitic hseamdefects.pdf> (date of retrieval: July 25, 2012)
- [15] O.H. Khan, "A Study of Six Sigma Implementation and Critical Success Factor", Pakistan's Ninth International Convention on Quality Improvement, Karachi, Pakistan, pp. 1-12, Nov. 2005
- [16] Saroj Bala, Factors Influencing Costing of woven Fabrics, The Indian Textile Journal, 2003
- [17] F.M. Gryna, J.A. DeFeo, "Quality Planning & Analysis for Enterprise Quality", Tata McGraw-Hill, Edition, 2008
- [18] Florida, R. "Lean and Green The Move to Environmentally Conscious Manufacturing." California Management Review 39, (1996) 80-105
- [19] M.Mahajan, "Statistical Quality Control", Dhanpat Rai & Co. (P) LTD. pp.186-206,
- [20] Hawken, Paul, Amory Lovins, and L. Hunter Lovins. Natural Capitalism: Creating the Next Industrial Revolution (New York Little, Brown and Company, 1999)
- [21] Khekalei, S. N., Chatpalliwar, A. S., & Thaku, N. (2010), "Minimization of Cord Wastages in Belt Industry Using DMAIC", International Journal of Engineering Science and Technology, 2 (8), page: 3687-3694.
- [22] Chandna, P., & Chandra, A. (2009), "Quality Tools to Reduce Crankshaft Forging Defects: An Industrial Case Study", Journal of Industrial and Systems Engineering, 3 (1), page: 27-37.
- [23] Defects of Sewing, http://www.jukiindia.com/item-list/defcts_of_sewing.pdf (date of retrieval: July 19, 2012)
- [24] Garmentdefects, <http://www.slideshare.net/2008000400034/garment-defects> (date of retrieval: July 19, 2012)
- [25] Abhishek Kumar, "Apparel Standards Specifications and Quality Control, Cutting, Sewing & Finishing Defects", National Institute of Fashion technology, <http://share.pdfonline.com/7926bbe6d71d4dcbb81ec5c1a603df26/Abhishek.htm> (date of retrieval: July 19, 2012)
- [26] Major/Minor/Critical defects: what are they? <http://www.asiaqualityfocus.com/blog/major-minor-critical-defects> (date of retrieval: July 25, 2012)
- [27] Learn About Sewing Problems/ Problems Of Sewing/Different Type Of Sewing Problems, <http://textileeducationtips.blogspot.com/2013/03/learn-about-sewing-problemsproblems-of.html> (date of retrieval: July 19, 2012)
- [28] Mohiuddin Ahmed and Nafis Ahmad, "An Application of Pareto Analysis and Cause-and-Effect Diagram (CED) for Minimizing Rejection of Raw Materials in Lamp Production Process", Management Science and Engineering, Vol. 5, No. 3, 2011, pp.87-95,
- [29] I. G. Mariolis & E. S. Dermatas, "Automated assessment of textile seam quality based on surface roughness estimation", Journal of Textile Institute, vol. 101:7, pp. 653-659, 2010
- [30] T. Aibara, T. Mabuchi, O. Kenji, "Automatic evaluation of the appearance of seam puckers on suits", Proc. SPIE, vol. 3652: 110, 1999.
- [31] Dr P Khanna: *Work study, time and motion study*, Dhanpat Rai and Sons, New Delhi, (pp 21-31).
- [32] Dean J W and Bowen D E., 1994, Management Theory and Total Quality: Improving Research and Practice and Theory Development, *the Academy of Management Review* 19, (3) PP 392-418.
- [33] Common Defects In Denim Jeans Sewing, <http://www.denimsandjeans.com/denim/manufacturing-process/common-defects-in-denim-jeans-sewing/> (date of retrieval: July 19, 2012)
- [34] I. G. Mariolis & E. S. Dermatas, "Automated quality control of textile seams based on puckering evaluation", 37th Int. Symp. on Nov. in Text., Ljubljana, Slovenia, June 2006.
- [35] Environmental Technology Best Practice Programmed. (1996). saving money through waste minimization raw material use, GG25, Crown Copyright.
- [36] F.M. Gryna, J.A. DeFeo, "Quality Planning & Analysis for Enterprise Quality", Tata McGraw-Hill, Edition, 2008

Planning for Budget Allocation in Digital Marketing

Md. Mahbubur Rahman, Al-Muktadir, and Samiya Rahman

Department of Industrial Engineering and Management, Khulna University of Engineering & Technology, Khulna-9203,
BANGLADESH

ABSTRACT

Globalization and increased internet usage have generated immense marketing opportunities as well as competitions. Marketing on the internet is now an ever growing practice. Digital Marketing, marketing through digital technologies is a new form of marketing with a few mixes of traditional marketing practices. The aim of this research was to propose a budget plan for digital marketing. In Bangladesh, digital marketing practices made its way as e-commerce and steadily grew from 2000 to 2008. RACE framework was followed to narrow down the digital marketing operations into four key stages to easily manage the expenditure. In this study, nearly 50% of marketing budget was allocated to digital marketing, an expense backed by companies surveyed. This study found that the most popular digital marketing strategy in Bangladesh was Social Media Marketing (SMM) and the most popular SMM platform was Facebook. This project concluded with a budget plan heavily focused on Facebook as found by surveys from both consumers and companies.

Keywords: Digital marketing, Email marketing, SMM, SEO, PPC.

1. Introduction

Digital marketing a global era phenomenon is the marketing of products or services using digital technologies, mainly through the internet but also including mobile phone, display advertising, and any other digital medium [1]. Since the late 1990s development in digital marketing has changed the way today businesses use technology for marketing purpose. As access to the internet is becoming more available to the world and digitalization is incorporated in every sector of this modern time people are shifting towards more digital platforms for everyday life i.e. communication, shopping, consultancy, dining, entertainment etc. Marketers exploit these opportunities for their marketing campaigns and digital marketing thus becoming more prevalent and efficient. Search engine optimization (SEO), Social Media Marketing (SMM), e-commerce marketing, Email marketing are common practices in digital marketing. Nowadays, digital marketing is expanded to offline channels that provide digital media, such as mobile phones (SMS and MMS), promotion calls, and on-hold mobile ring tones [2].

2. Literature review

Tiago (2014), the paper is about digital marketing and social media. In this paper, interrelating social media with companies for a good digital marketing has been discussed. How the internet based applications enhance marketing practices and improve, was discussed in this paper [3].

Corniani (2006) published a paper about digital marketing communications. It discusses the communications which can increase digital marketing approach. Communications are to be designed in a way that there should be a question-answer option where the consumers can ask any kind of their queries and an

immediate feedback is ensured to strong the bond between the consumer-seller [4].

3. Methodology and approach

Data and information required for this study were collected from both primary and secondary sources. Primary sources include structured questionnaires and data collected from different surveys done with startup companies and consumers. Secondary data was collected from the companies, agencies through websites, reports, historical and financial reports from internet and journals. As a means of budget allocation for digital marketing, the RACE framework was implemented. RACE is a digital marketing framework that simplifies the approach towards digital marketing by dividing into key steps or stages.

3.1 Data Collection Techniques

Data collection was done by

- a. Questionnaires
- b. Documents and Records

A total number of 7 companies and 30 random consumers as respondents were selected for survey questionnaires. Questionnaires for companies were to extract the data required for conducting a budget for digital marketing whereas questionnaires for consumers were mainly to understand their opinions.

3.2 Data analysis

Data relevant to this project are categorized into two sectors viz. companies who do the business and consumers who the companies do business too.

Data acquired from startup companies

- a. 87.5% companies' age is less than 2.5 years and rest of the companies age is more than 2.5 years.

- b. 87.5% of companies' plan their budget for 3 months and 12.5% of them for 6 months to avoid risk.
- c. 25% of the companies allocate (45-50) %, 50% of the companies allocate 50 %, 12.5% of the companies allocate (45-55) % and the rest 12.5% of the companies allocate (50-55) % of their firm's budget for doing the marketing. The weighted average is 4.68%.
- d. 55.6% of them rated SEO attraction level 3, 22.2% of them rated 2 and the rest 22.2% rated 4 on a scale of 5. The weighted average of attraction level is 3.
- e. 88.9% of them rated SMM attraction level 5 and other 11.1% of them rated 4 on a scale of 5. The weighted average of attraction level is 4.88.
- f. 100% of companies were favored towards Facebook while only 2% had an opinion on Twitter and another 2% had on Instagram along with Facebook.
- g. 11% of them rated PPC attraction level 1 and 55.6% of them rated 2 and the rest 33.3% reported a level of 3 on a scale of 5. The weighted average of attraction level is 1.89.
- h. 11% of them rated web optimization attraction level 1 and 55.6% of them rated 3 and the rest 33.3% reported a level of 4 on a scale of 5. The weighted average of attraction level is 3.11.
- i. 11% of them rated Email Marketing attraction level 1 and 55.6% of them rated 4 and the rest 33.3% reported a level of 3 on a scale of 5. The weighted average of attraction level is 3.33.
- j. 11% of them rated content marketing attraction level 3 and 77.8% of them rated 4 and the rest 11.1% reported a level of 5 on a scale of 5. The weighted average of attraction level is 4.

Table 1 Company profiles

Company	Products	Website
Offerage	Aggregated discount offers	www.offerage.com
Prix.com	Price comparison site	prix.com.bd
Aponzone	Consumer electronics	www.aponzone.com
Pulpy Park	Fashion items	www.pulpypark.com
Aboyob	Handcrafts	www.facebook.com/AboyobLifeStyle/
TailBird	Saree	www.facebook.com/Tailbirdfashion/
Ortha	Home décor	www.orthashop.com

Data acquired from consumers

- a. 66.7% of people checked ads while browsing internet mostly and 27.3% checked ads occasionally. Rest of the people checked ads hardly.
- b. 57.6% people click to next page in search engine result page whereas 36.4% of

them clicked occasionally and rest of them clicked hardly.

- c. 57.6% of the people regularly check message/email delivered from the company and 36.4% of them check mostly and rest of the people check them hardly.
- d. 60% of them visited a landing page from an online advertisement and rest of them didn't approach with that.

3.3 RACE approach implementation

To propose a recommendation on digital marketing budget allocation, RACE framework [5] is used to approach step by step which makes budgeting goal efficient and strategy oriented. It is a strategic planning process applied to digital marketing that allows an action plan to be structured for digital marketing. As for every marketing funnel, RACE starts with an initial phase called **Plan** where time horizon, targeted audience, goals, and strategies are being set. According to Plan agreement companies **Reach** to targeted audiences, gradually **Interact** with them to convert into their customers and then continues **Engaging** with them to make future frequent buyers.

Table 2 Proposed budget allocation plan.

Phase	Activities
Plan	<ul style="list-style-type: none"> • Set time horizon • Target audience • Increase brand awareness and drive sales • Allocate a firm's budget for Digital Marketing
Reach	<ul style="list-style-type: none"> • Via Facebook posts, pages. • Paid and organic advertisements • Paid and organic searches.
Act	<ul style="list-style-type: none"> • Content marketing through social media. • Improved web pages • searches
Convert	<ul style="list-style-type: none"> • Content marketing through social media • Enhanced web page • Facebook store • Email marketing • Guest posts
Engage	<ul style="list-style-type: none"> • Send Emails to prospective buyers • Display ads frequently • Ask for feedbacks on products

It is therefore, recommended that Facebook, SEO and PPC are best suited for Reach. Facebook, web optimizations, content marketing, SEO and email marketing are best suited for Act. Facebook, web optimizations, content marketing, SEO and email marketing are best suited for Convert phase. Facebook, Email marketing, web optimization and PPC are best suited for the phase of Engage.

Factoring the channels according to RACE.

Table 3 Factoring the channels(According to RACE)

Channels	Stage presented	Factors
SMM	RACE	4
Content marketing	ACE	3
Email marketing	ACE	3
Web optimization	ACE	3
SEO	RAC	3
PPC	RE	2

Ranking the channels according to attraction index (higher index represents better indication).

Table 4 Ranking the channels (According to attraction index).

Channels	Attraction index	Score
SMM	4.88	6
Content marketing	4.00	5
Email marketing	3.33	4
Web optimization	3.11	3
SEO	3.09	2
PPC	1.89	1

According to conversion rate (CVR), table 4 represents the ranking among the channels where higher rate represents better indication [6].

Table 5 Ranking the channels (According to CVR).

Channels	CVR	Score
SMM	9.21%	6
Email marketing	5%	5
Content marketing	3.75%	4
SEO	3.05%	3
Web optimization	2.95%	2
PPC	2.69%	1

According to cost per click (CPC), table 5 represents the ranking among the channels where lower cost represents a better indication [7].

Table 6 Ranking the channels (According to CPC)

Channels	CPC(BDT)	Score
SMM	1.66	6
Content marketing	9.50	5
Email marketing	9.96	4
PPC	10.458	3
SEO	44.654	2
Web Optimization	150	1

Table 7Totaling the score obtained by channels.

Channels	Total Score (Index score +CVR score +CPC score)
SMM	6+6+6=18
Content marketing	5+4+5=14
Email marketing	4+5+4=13
PPC	3+2+1=6
SEO	2+3+2=7
Web Optimization	1+1+3=5

4. Results

Following formula will be used to allocate budget for each channel.

Percentage of recommended budget allocation =

$$\left\{ \frac{\text{Total Score} \times \text{RACE Factor}}{\sum(\text{Total Score} \times \text{RACE Factor})} \right\} \times 100 \%$$

Table 8Percentage of recommended budget allocation.

Marketing channels	Percentage
SMM	36%
Content marketing	21%
Email marketing	19%
Web optimization	9%
SEO	10%
PPC	5%

5. Discussions

This paper was intended to propose a recommendation on an approximate budget allocation for digital marketing. The first thing to take into account while conducting this research is there is no exact budget allocation method for digital marketing and although in this research a recommendation based on data collected from various sources was proposed, it is not advised to implement this recommended budget directly without matching with goals and strategies undertaken by company policies. Bangladesh is emerging as a developing country so is in great need of start-up companies to boost commerce and trade. This paper was conducted following a typical methodology of collecting information through primary sources like surveys from companies and consumers and secondary sources such as journals, internet, annual reports etc. RACE framework approach was implemented to narrow down the vast digital marketing operations into four key stages to simplify strategies and thus budgeting. The main drawback for this research was that its planning horizon is very small and involved only tech companies. The surveys directed to companies was done with only 8 in total which of course led to a very small percentage of whole start-up companies and their budgeting information. Key information like conversion rate, how much revenue does one visitor brings, visits per page etc. was not available precisely as these are confidential data.

Opportunities for budgeting in digital marketing for other kinds of companies are still open. Although this research was done with new companies, a similar project on established companies is very much recommended.

One of the difficulties in proposing a general digital marketing budget recommendation is that not all companies are consisted of what they include in their marketing budget. With all the limited information gathered and drawback faced this research concludes a general proposal for digital marketing budget plan that is intended to be a helpful and effective guide to emerging young startup tech companies in Bangladesh.

REFERENCES

- [1] *Definition of digital marketing*. Retrieved 22 August, 2015, from Financial Times.
- [2] BEST Digital Marketing Course. Retrieved 28 June, 2018, from <https://www.wattpad.com/story/149293713-best-digital-marketing-course>
- [3] Teresa Tiago, *Digital Marketing and Social Media: Why Bother?*, (2014).
- [4] Margherita Corniani, *Digital Marketing Communication*, (2006).
- [5] *Introducing RACE: a practical framework to improve your digital marketing*. Retrieved June 28, 2018, from <https://www.smartinsights.com/digital-marketing-strategy/race-a-practical-framework-to-improve-your-digital-marketing/>
- [6] *Google Ads Benchmarks for YOUR Industry [Updated!]*. Retrieved June 28, 2018, from <https://www.wordstream.com/blog/ws/2016/02/29/google-adwords-industry-benchmarks>
- [7] *Average Conversion Rates by Industry*. Retrieved June 28, 2018, from <https://searchenginewatch.com/2016/03/15/google-adwords-average-conversion-rates-by-industry-study/>

Self-Balancing Autonomous Unicycle using Raspberry Pi

Pulok Tarafder^{1,*}, Moyukh Amin¹, Syed Samiul Alam Mehrab², Abdullah Al Maruf¹

¹Department of Electrical and Electronic Engineering, BRAC University, 66 Mohakhali, Dhaka 1212, BANGLADESH

²Department of Computer Science Engineering, BRAC University, 66 Mohakhali, Dhaka 1212, BANGLADESH

ABSTRACT

Traditionally mobile devices contain no balancing mechanism as they are already quasi static containing three or four wheels. Using gyroscopes to power human forwards and backwards only a single wheel is needed to make a vehicle which will be much smaller and lighter with less cost. Being an inverted pendulum design it is inherently unstable so it needs constant control to provide appropriate acceleration. Using Kalman filter algorithm on the gyroscopic data this problem can be solved. As the proposed model is automatically controlled it will help reduce our design cost bare bones. The model always ensures that the tilt factor is minimized. We were successfully able to implement balancing during movement and on lateral level during static state.

Keywords: Self balance, Unicycle, Kalman Filter, PID Control, Raspberry Pi.

1. Introduction

Imagine robots of the future cruising through space time with two or even a single wheel. Our effort is to seek a solution to this problem by taking on the challenge of balancing a unicycle in a single direction using the existing motors torque and forward-backward acceleration. An autonomous self-balancing vehicle i.e. a single wheel vertically stable transport is the future. Being an inverted pendulum design it is intrinsically not stable so it needs a steady control to maintain its movements. The single wheel explores the Linear-quadratic-Gaussian control problem. The solution can be found by using a series of Kalman filter algorithm on the gyroscopic data and then apply forward and backward acceleration to balance a load while moving in the rolling direction. The Self balancing unicycle uses raspberry pi to control the motor, process gyro and accelerator data and provide more features for further development. Using these methods we are able to balance it during its movement in the rolling direction.

1.1 Physical Model

The inspiration was Segway type vehicle but with a single wheel. As this is a classic inverted pendulum problem. The body needs a good balance and moment of inertia as not to lean and fall. The lateral balancing is done by measuring the tilt angle and setting and offset in the opposite direction and providing torque in that direction. There are four degrees of freedom for this vehicle as such balancing in the lateral direction is discussed in this paper. The concept of this type of PID control is quite popular and widely used in automated control systems. We get the current tilt and yaw, predict the next position and use this feedback to control the output. This process will prevent the robot from falling by providing acceleration in the wheels corresponding to its inclination from the neutral vertical. As the vehicle gets deviated by an angle, then in the frame of reference of the wheels and the center of mass will encounter a pseudo force and apply a torque opposite to the

direction of tilt. The project needs precision vector calculations done in seconds. Moreover, over the years the sensors data has been seen to be populated with noise data. This is where fusion algorithms come which require huge processing power. As such the reasonable choice for our project was a processor of GHz power. So the raspberry pi zero was the obvious choice of embedded controller. This project includes the RPi Zero. The mechanical design problem is solved by keeping the center of gravity (COG) at a single vector over any motion which is described on another section. The motor choice needed to be high RPM, high Torque and only a geared DC motor provided the requirement. Our project implements a 12VDC 120W motor. We needed a suitable motor driver to control both speed and direction. The RPi motor driver satisfied all those requirements and also solved the problem of supplying power to the pi by regulating 12V to 5V using LM2596. An MPU6050 sensor which contains a MEMS accelerometer and a MEMS gyro in a single chip which contains 16-bit analog to digital conversion hardware for each channel was sufficient for our project and it has I2C bus that helps communicate with it in a relevant and fast way.

1.1.1 Raspberry Pi Specification

The project uses Debian OS in Raspberry Pi zero (Linux raspberry pi 4.9.59+ #1047 Sun Oct 29 11:47:10 GMT -

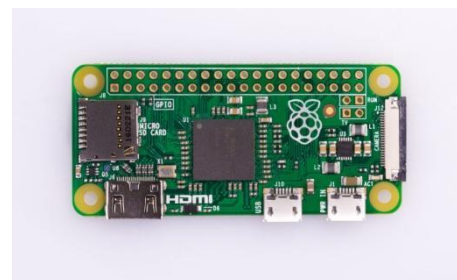


Fig.1 Raspberry Pi Zero

* Pulok Tarafder. Tel.: +88-01682510085

E-mail address: pulok.tarafder@g.bracu.ac.bd

2017 armv6l GNU/Linux). The code is done in Python3.6 and the dependencies are all under GNU. This single core 1.2GHz device with 512MB of RAM including unpopulated 40-pin GPIO connector is capable of applying this complex fusion of Kalman-filter Algorithm and predicts state almost at real-time. The physical look of this Raspberry Pi Zero is shown in Fig.1.

1.1.2 Motor Driving Principle

The main purpose of using a DC motor is to transfer electrical energy into mechanical energy. Whenever a current conductor is placed in magnetic field, it experiences a mechanical force. Although DC motors have low efficiency in our case it serves the best as we don't need servo mechanism to guess the wheel position they are inefficient and our gyroscope and accelerometer data acts as feedback. The RPi motor driver fits as overhead on the pi zero and also provides power. We don't need connecting anything separately. Although the motor is controlled through 3 pins. Table 1 states that the Pulse Width Modulated signal on pin 26 controls the speed and torque of the motor. Making M1 High and M2 Low moves the motor forward and on the other hand M1 Low and M2 High move the motor backward.

Table 1 Controlling Movements using Motor

Interface	WiringPi	BCM
M1	P28	20
M2	P29	21
PWMA	P25	26



Fig.2RPi Motor Driver

1.1.3 Interfacing with MPU6050

The MPU-6050 devices combine a 3-axis gyroscope and a 3-axis accelerometer on the same silicon die, together with an onboard Digital Motion Processor™ (DMP™), which processes complex 6-axis Motion Fusion algorithms. The device can access external magnetometers or other sensors through an auxiliary master I²C bus, allowing the devices to gather a full set of sensor data without intervention from the system processor. The devices are offered in a 4 mm x 4 mm x 0.9 mm QFN package. The Inter-integrated Circuit (I²C) Protocol is a protocol intended to allow multiple “slave” digital integrated circuits (“chips”) to communicate with one or more “master” chips. Like the

Serial Peripheral Interface (SPI), it is only intended for short distance communications within a single device. Like Asynchronous Serial Interfaces (such as RS-232 or UARTs), it only requires two signal wires to exchange information. Messages are broken up into two types of frame: an address frame, where the master indicates the slave to which the message is being sent, and one or more data frames, which are 8-bit data messages passed from master to slave or vice versa. Data is placed on the SDA line after SCL goes low, and is sampled after the SCL line goes high. The time between clock edge and data read/write is defined by the devices on the bus and will vary from chip to chip. The RPi reads the specific addresses and collects its data.

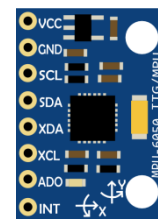


Fig.3MPU-6050 6-Axis MEMS Sensors

1.2 Mechanical Structure

The seat is sourced from a second hand bicycle. The shape of the seat is important as you need to be able to shift your center of gravity forward and backward on the seat. We attached it to the frame with a simple steel pipe. The wheel, sprocket axle all were welded in to the frame. We used 1x1 inch tubing for the frame and the foot pegs. A couple of plates across the middle of the frame served to mount the single motor with the frame to which we glued or screwed the electronics. The axle was set in a channel which allows the two sprockets of the motor and wheel to be moved so the chain can be easily fitted. A bolt above the axle stops it from suddenly upwards when in use. The whole package came to 30 x 7 inch excluding the 3 inch foot pegs. The Mechanical diagram is given in Fig.4.

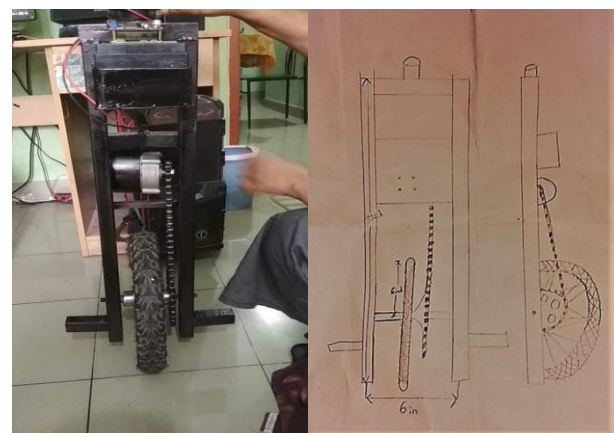


Fig.4Mechanical Diagram and Physical Product

1.3 Angle Measurement

To measure the angle of tilt we have the data from two sensors, accelerometer and gyroscope. The accelerometer measures the force with respect to gravity, thus we calculate angle of the vehicle. The accelerometer measures angle using the Eq. (1).

$$\theta = \arctan(Ay / \sqrt{Ax^2 + Az^2}) \quad (1)$$

The problem with this type of sensor is that it accounts for the rest of the forces the vehicle is experiencing i.e., it has a lot of error and noise. The gyroscope can measure the angular velocity by integrating the signal over time by using Eq. (2).

$$\theta_i = \theta_{i-1} + w * dt \quad (2)$$

but the problem is measurement is that is not perfect and has a deviation, such that in short run times the measure is valid, but for long time runs the value will start to deviate much from the real angle. To avoid this situation we integrate these measurements and can accurately obtain the angle of the vehicle at its current position in any instantaneous time. To combine of both sensors, which is called sensor fusion, we use Kalman Filter in this application, as it is an algorithm that gives an accurate data with low computation costs.

1.4 Kalman Filter

Kalman filtering also known as Linear Quadratic Estimation (LQE) is a widely used algorithm used to model data accurately in a series of measurements observed over time containing statistical noise and other inaccuracies. It finds the most optimum averaging factor for each consequent state. Also somehow remembers a little bit about the past states. Here the equation below is a basic model of Kalman filter. The Kalman gain eliminates the noise by applying co-variance principle between measured data and previous estimation and iterates the Kalman gain to be accurate over time which in turn accurately predicts future states. It treats each of the data in discrete time interval and calculates Kalman gain at each consequent state getting smarter gain each iteration using Eq. (3).

$$X_k = K_k \cdot Z_k + (1 - K_k) \cdot X_{k-1} \quad (3)$$



Fig.5 Sensor Data(RG) and Filter Data(B)

Fig.5 shows how Kalman filter works on the data. The red line shows how much noisy the acceleration data is. And the drift is clearly visible in the Gyroscope readings. The green line shows simple complimentary filter output while Kalman filter output is visible in blue. The blue data is quite accurate and noise less. As

such Kalman filter algorithm is fitted to our data by iterating through gyroscope and accelerometer readings.

1.5 Mathematical Model

1. If the tilt angle is to the right, the vehicle must decelerate to the left and vice versa.

2. The position of the vehicle relative to track center is stabilized by slightly modulating the null angle (the angle error that the control system tries to null) by the position of the vehicle, that is, (null angle = tilt angle + k * position) where k is small. This makes the pole want to lean slightly toward track center and stabilize at track center where the tilt angle is exactly vertical. Any offset in the tilt sensor or track slope that would otherwise cause instability translates into a stable position offset. A further added offset gives position control.

3. A normal pendulum subject to a moving pivot point such as a load lifted by a crane, has a peaked response at the pendulum radian frequency of $\omega = \sqrt{g / \ell}$. To prevent uncontrolled swinging, the frequency spectrum of the pivot motion should be suppressed near ω . The inverted pendulum requires the same suppression filter to achieve stability.

1.6 PID Control of the Motor

The PID controller is widely employed because it is very understandable and because it is quite effective. One attraction of the PID controller is that all engineers understand conceptually differentiation and integration, so they can implement the control system even without a deep understanding of control theory. Further, even though the compensator is simple, it is quite sophisticated in that it captures the history of the system (through integration) and anticipates the future behavior of the system (through differentiation). The output of a PID controller, which is equal to the control input to the plant, is calculated in the time domain from the feedback error as follows in Eq. (4).

$$u(t) = K_p * e(t) + K_i \int e(t) dt + K_d \frac{de(t)}{dt} \quad (4)$$

Increasing the proportional gain (K_p) has the effect of proportionally increasing the control signal for the same level of error. The fact that the controller will "push" harder for a given level of error tends to cause the closed-loop system to react more quickly, but also to overshoot more. Another effect of increasing K_p is that it tends to reduce, but not eliminate, the steady-state error.

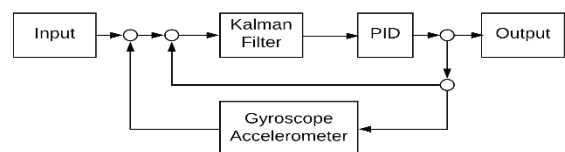


Fig.6 Control Diagram

The addition of a derivative term to the controller (K_d) adds the ability of the controller to "anticipate" error. With simple proportional control, if K_p is fixed, the only way that the control will increase is if the error increases. With derivative control, the control signal can become large if the error begins sloping upward, even while the magnitude of the error is still relatively small. This anticipation tends to add damping to the system, thereby decreasing overshoot. The addition of a derivative term, however, has no effect on the steady-state error.

The addition of an integral term to the controller (K_i) tends to help reduce steady-state error. If there is a persistent, steady error, the integrator builds and builds, thereby increasing the control signal and driving the error down. A drawback of the integral term, however, is that it can make the system more sluggish since when the error signal changes sign, it may take a while for the integrator to "unwind."

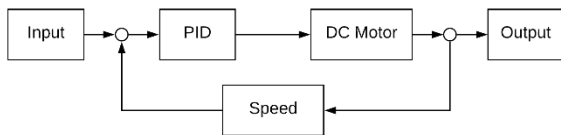


Fig.7Block diagram of feedback mechanism of PID controller.

1.7 Computation

The program starts by adjusting the optimum position for the first 5 iterations. Then reading and adjusting motor offset. The motor then keeps adjusting the speed of acceleration and deceleration to get the optimum torque and adjust tilt angle. The block diagram of Fig 8 shows the computation process.

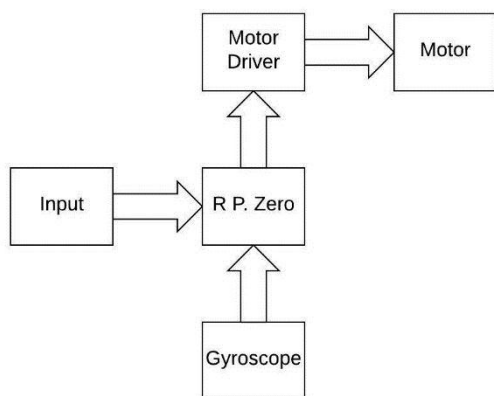


Fig.8 Computation process of the RPi Zero

2. Conclusion

In this paper, we proposed a model for solving the inverted pendulum problem on a single point of inertia. Using Kalman filter over gyroscope and accelerometer data to provide an optimum motor offset that the motor driver adjusts while correcting the Kalman gain over time. We designed and implemented this model considering factors like low cost, reliability and automatic control. As the proposed model is automatically controlled it will help reduce our design cost to bare bones reducing both motor, gear and wheel costs. The model always ensures that the tilt factor is minimized. We were successfully able to implement balancing during movement and on lateral level during static state. We hope that this control system will be perfected and everything will be single wheeled in the near future.

NOMENCLATURE

- X_k = Current estimation
- Z_k = Measured value
- K_k = Kalman gain
- X_{k-1} = Previous estimation
- K_p = Proportional gain
- K_i = Controller integral term
- K_d = Differential term
- $u(t)$ = Output of the PID controller

REFERENCES

- [1] M. Baloh & M. Parent, Modeling and model verification of an intelligent self-balancing two-wheeled vehicle for an autonomous urban transportation system, *The conference on computational intelligence robotics and autonomous systems* pp. 1-7 2003.
- [2] C. -N. Huang, The development of self-balancing controller for one-wheeled vehicles; *Engineering vol. 2 no.4* 2010.
- [3] J. Juan Rincon Pasaye, J. Alberto Bonales Valencia & F. Jimenez Perez Tilt measurement based on an accelerometer a gyro and a Kalman filter to control a self-balancing vehicle; *Power Electronics and Computing (ROPEC) 2013 IEEE International Autumn Meeting* on pp. 1-5 2013.
- [4] B. Mahler & J. Haase, Mathematical model and control strategy of a two-wheeled self-balancing robot"; *Industrial Electronics Society IECON 2013-39th Annual Conference of the IEEE* pp. 4198-4203 2013.
- [5] A. M. Mohtasib & M. H. Shawar, Self-balancing two-wheel electric vehicle (steve); *Mechatronics and its Applications (ISMA) 2013 9th International Symposium* on pp. 1-8 2013.
- [6] C. Sun, T. Lu & K. Yuan Balance control of two-wheeled self-balancing robot based on linear quadratic regulator and neural network; *Intelligent Control and Information Processing (ICICIP)*

2013 *Fourth International Conference* on pp. 862-867 2013.

- [7] L. Sun J. Gan Researching of two-wheeled self-balancing robot base on lqr combined with pid; *Intelligent Systems and Applications (ISA) 2010 2nd International Workshop* on pp. 1-5 2010.
- [8] R. Xiaogang, L. Jiang, D. Haijiang & L. XinYuan Design and lqr control of a two-wheeled self-balancing robot; *Control Conference 2008. CCC 2008. 27th Chinese* pp. 275-279 2008.
- [9] Q. Yong, L. Yanlong, Z. Xizhe et al. Balance control of two-wheeled self-balancing mobile robot based on tsfuzzy model; *Strategic Technology (IFOST) 2011 6th International Forum* on vol. 1 pp. 406-409 2011.
- [10] N. Yu, Y. Li, X. Ruan & C. Wang Research on attitude estimation of small self-balancing two-wheeled robot; *Control Conference (CCC) 2013 32nd Chinese* pp. 5872-5876 2013.

ICMIEE18-268

Available and Cost Reductive Materials in Bangladesh Having an Eye to Bone Treatment

Talukdar Raian Ferdous*

Department of Biomedical Engineering, Khulna University of Engineering & Technology, Khulna-9203, BANGLADESH
Email:raianferdous1415020bme@gmail.com

Abstract: Bangladesh have been announced as a developing country among the countries in the world in 2018. But poverty has not yet been eradicated properly. According to the World Bank, Bangladesh's poverty rate fell from 82% in 1972, to 18.5% in 2010, to 12.9% in 2016, as measured by the percentage of people living on the equivalent of US\$1.90 or less per day in 2011 purchasing power parity terms. People die due to lack of treatment every year. Labourer and old people cover a great amount of population in Bangladesh. These people are suffering or will be the sufferer of bone disease like osteoporosis, bone fracture, bone pain etc. As a result the economy of Bangladesh will be hampered greatly. Bone treatment is a material dependent technique. So the cost is dependent on the material whether it is expensive or not. People can't afford titanium but they can afford steel. If the purpose is served by using steel then these sufferers will be the beneficiaries at a low cost. In this treatment there are a several factors that should be looked into. This paper focuses on the features of cheap and very common materials that can be used for bone treatment. Steel, aluminium, zinc, ceramics are very common materials here in Bangladesh. This literature will aggrandize the bone treatment facility in Bangladesh at a low cost and will be inspiring the researcher in this sector.

Keywords: Bone treatment, Steel, Magnesium, Aluminium, Cobalt, Copper, Zinc.

1. Introduction: Bangladesh is a developing country among the 196 countries in the world. According to the survey of the year 2015 the early income per capita is 1314 USD here. Most people living here are associated to hardworking. They are vulnerable to bone related diseases such as osteoporosis, osteopenia, hip fracture etc. Most of the people living in this country can't afford higher standard medical care. It should be focused on the issue that the people get better treatment while the cost is reachable. Biomaterials are being developed all over the world with a great consensus value. There is a slight wall between materials and biomaterials. This determined that a biomaterial was 'a nonviable material used in a medical device, intended to interact with biological systems.' For bone treatment basically three type of biomaterials are used like metals, ceramics and polymers. Metals have unique and often useful bulk, surface, and biological properties, including biocompatible strain and heat transduction. Polymers often degrade by hydrolysis but metals degrade in the body by either oxidative corrosion or galvanic corrosion [1-3]. Metals are available comparing to the others materials in Bangladesh. In Bangladesh Steel, Magnesium, Aluminium, Cobalt, Copper, Zinc and other metals are cheaper and easy to get. Titanium is a significant material in bone treatment but as cheap and available metals are discussed this review will not highlight Titanium. Some prolific researcher have already worked on these materials covering the field of bone treatment as they are cheap enough. This literature will review these materials having potentials to be used in bone treatment as a biomaterial for the welfare of Bangladeshi people. The most contributory aspect of this paper is to accumulate these separate studies into a

single form so that the maximum benefits can be obtained at the time of selecting efficient materials simultaneously as all the available bone treatment materials are described.

2. Methodology and Materials: The key ingredient of any bone treatment system lies in the application of stable, attractive and biologically responsible materials. Biomaterials having severe destructive impacts to the body internal affairs such as functional disability, movement constraints etc by releasing infectant, toxicity and depletion of natural resources are to be avoided. The selection of the materials depends on some factors (e.g. highly efficient to the habitants, cost effective and inserting to the living subject, surface area, strength, stress etc.).

2.1 Stainless Steel: Stainless steel is a very available material in Bangladesh. It is used for different purposes. The use of stainless steel in surgical applications began in 1926. Stainless steel is considered the most common material among the metallic implants due to the low cost and the ease of fabrication [4]. It holds a benefit of being used as a cost effective biomaterial. Stainless steel is used for fracture fixation for most cases [3,5]. Stainless steel is mainly used when there is a requirement of stiffness [1]. It has higher stiffness than coral bone. In bone implant stiffness is a very important feature. The density of stainless steel is about 7.9 g/cm³ [6]. This is nearly twice the density of titanium, but this is not critical since the weight of relatively small-sized fracture fixation implants is not considered a major factor. Today's implant quality stainless steel contains 13 to 16 wt.% nickel although nickel ions are the most

* Corresponding author. Tel.: +88-01748692078
E-mail addresses: raianferdous1415020bme@gmail.com

widespread skin contact allergen [6]. The elastic modulus of stainless steel for being used as implants is about 200GPa [7]. Newly developed nickel-free implant quality stainless steels combine the advantages of excellent mechanical properties which are clearly better than today's standard implant stainless steels and the absence of nickel as an allergen [2]. The release of iron from stainless steel favors bacteria infections by acting as an iron source for their proliferation [8]. To avoid this consequence stainless steel is used in the body as short term implants or is used with coating. So this material is a perfect choice for using as bone implant material as well as fixation material comparing the financial aspect of this country's people.

2.2 Magnesium: Elemental magnesium (Mg) was discovered in 1808 and Mg and its alloys have shown generating significant interest for use in biomedical applications as implants, osteosynthesis devices, ligatures, and wires for aneurysm treatment and connectors for vessel anastomosis [9]. Magnesium is also used as biodegradable alloy which dissolves in aqueous solution containing chloride ion [10,11]. Magnesium based alloys are typically 1/3 as dense as titanium based alloys and only 1/5 as dense as stainless steel and chrome-cobalt alloys. Magnesium alloys, in contrast, have a modulus of elasticity of around 45 GPa, which is much more closely matched to that of bone, thus lessening the likelihood of stress shielding and the associated loss of bone density. This feature has inspired researchers to develop a biodegradable biomaterial. Magnesium can be used as Mg-Al alloy system and Mg-RE alloy system [12]. Aluminum is well known as a neurotoxicant and its accumulation has been suggested to be an associated phenomenon in various neurological disorders as dementia, senile dementia and Alzheimer disease [13]. We all know calcium is an important material in bone. Ca has a low density (1.55 g/cm³), which endues the Mg-Ca alloy system with the benefit of similar density to bone. Magnesium possesses good biocompatibility and relatively large amounts of magnesium are tolerated by the body without ill effect. Recently, there have progress made in the direction of better performance of bone screws leading to the study of magnesium (Mg) and Mg-coated screws. So it should be understood that magnesium can be an efficient material for the solution of bone related health problem.

2.3 Copper: Copper is a very common material in Bangladesh serving various purposes like industrial, ornamental, experimental etc. Orthodontic brackets and wires are widely used for long span of treatments. Researchers are trying to minimize the discomfort caused by it [14]. For this purpose copper can be used as a cheap material along with titanium, nickel and others. Copper has a great advantage of being used as coating material. Copper can also be used as metallic nanoparticles along with zinc showing antibacterial activity and non-toxicity for osteoprogenitor cells [15].

Copper with NiTi wire more resistant to permanent distortion than NiTi wires [16]. So copper has a great chance to be used in orthopaedic application and more research activities in copper should be inspired for the welfare of this country's people.

2.4 Zinc: Zinc has a very interesting role in bone formation and mineralization. The effects are specifically obvious for Zn-incorporated biomaterials including bone cements [17], bioglasses [18,19], ceramics [20], and coatings [21]. Despite the established roles of zinc in bone metabolism, the feasibility of Zn-incorporated biomaterials in clinical applications are relied on many factors especially safety issues associated with the zinc content and release kinetics. Uncontrolled fast release of Zn ion can disrupt zinc homeostasis, alter the concentrations of other metals for tracing such as calcium, iron, and copper causing deficiency, and bind to low affinity sites leading to protein dysfunction [22-24]. It has been reported that the influence of Zn²⁺ on the osteogenic differentiation of mesenchymal stem cells (MSCs) is dependent on dose [25,26]. Therefore, it is crucial to determine the tolerable and safe upper intake level and much work has been done to investigate the optimal zinc contents in various biomaterials. Hydroxyapatite is a very useful material when it comes to bone treatment related topic. Silicon substituted and silver substituted HA have been studied. But among the candidates zinc is a very potential candidate because of its abundancy as a trace metallic component of bone and has a very important role in bone biochemistry [27].

2.5 Aluminium: As a bio tolerant material, Aluminum is considered as the alternative solution for the natural bone for characteristics such as osteoinduction, osteoconduction, inflammation and mechanical integrity. Aluminum is used as the implant in the human bone as well as the dental implant. Ceramics from Aluminum also used as biomaterial. Alumina (Aluminum based ceramics) currently is used for orthopedic and dental implants, and has the ability to be polished to a high surface finish and high hardness. The compressive, tensile and bending strengths exceed the strength of compact bone by 3 to 5 times. These properties combined with high modulus of elasticity and especially with fatigue and fracture strength is resulted in specialized design requirements for this class of biomaterials [28]. Now, the applications for alumina encompass porous coatings for femoral stems, porous alumina spacers (specifically in revision surgery), knee prosthesis and in the past as polycrystalline and single crystal forms in dental applications as tooth implants. Alumina is also used in the head replacements of the bone. Aluminum, its alloys, ceramics are considered to be replaced in human body as a bone or dental implants. As aluminium is used abundantly in Bangladesh further research work can pave the way to make this a revolutionary bone treating material.

2.6 Cobalt: Cobalt is used as a biomaterial for its unique properties and characteristics which allow its validity in the human body. Basically Cobalt alloys are used highly in implants. There are commonly two types of Co-Cr alloys which are used as implant materials, (i) Co-CrMo alloy which is castable and (ii) Co-Ni-Cr-Mo. Cobalt (Co) based implants have higher wear resistance compared to Ti alloys, which warrants their extensive use in artificial hip joints, where the direct contact between femoral head and the bone or plate over time may lead to wear. Clinically, Co-Cr-Mo is one of the most commonly used alloy for having high strength and high ductility [29]. While compared to cast Co-Cr alloys, wrought Co-Cr alloys that contain Ni, e.g., Co-Ni-Cr-Mo, have higher strength, however since Ni is potentially toxic, it is only used in those applications where this additional strength is required. The elastic modulus of Co-Cr alloys is higher than Ti or Ti alloys [30]. Compared to that of bone, the Co-Cr alloys have higher elastic modulus and greater density and stiffness [31], which leads to greater stress shielding than in the case of Ti and Ti alloys or Mg [32]. So Cobalt is a very potential material in this field.

	estimated properly to skip medical hazard [43]. 3. Density and modulus of elasticity are slightly higher which may negatively influence the healing process due to non-uniform transfer of loading between implant and growing bone [44].
5. Aluminium	1. Bone Toxicity [45] 2. High propensity to participate in biological process [46] 3. Aluminium can cause premature cell death so it can cause bone apoptosis [47].
6. Cobalt	1. Expensive and quite hard to machine. [48] 2. Biological toxicity due to Co, Cr and Ni ions release. [49,50]

Table 1 Negative impacts of the described metals

Material Name	Negative Impacts
1. Stainless Steel	1. Having stress shielding effects. [33] 2. High modulus of elasticity. [34] 3. Poor corrosion and wear resistance. [35] 4. The release of iron from stainless steel favors bacterial infections and could cause allergy, toxicity and other symptoms. [36]
2. Magnesium	1. Poor corrosion resistance due to the presence of Cl ion. [37, 38] 2. Hydrogen evolution due to rapid degradation. [39] 3. Lower elastic modulus. [40]
3. Copper	1. Poor resistance and repeated stress. [41] 2. Susceptibility to corrosion [42]
4. Zinc	1. There is a possible toxicity that should be taken into account [43]. 2. Corrosion of zinc implant should be

3. Numerical Modeling

3.1 Comparison of elastic modulus is shown in figure 1. Elastic modulus is the ratio of the force exerted upon a substance or body to the resultant deformation. Elastic modulus plays a vital role for bone implantation process. The metals of which elastic modulus are close to bone's elastic modulus are more preferred.

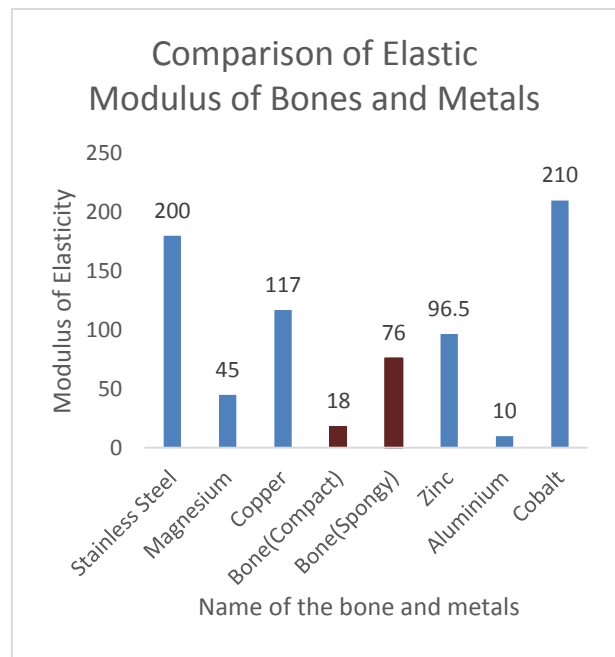


Fig.1 Elastic Modulus Comparison

3.2 The prices of above described metals are shown in figure 2. The price has been collected by International standard and the amount has been converted into BDT.

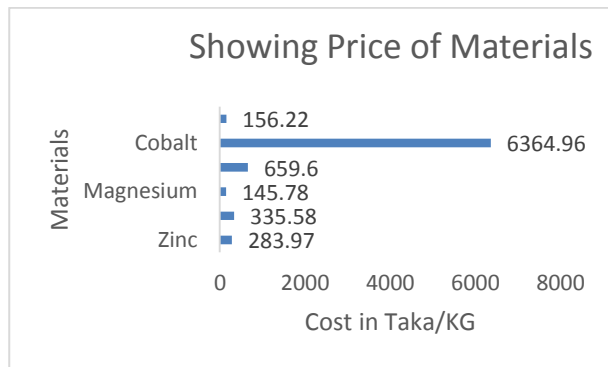


Fig.2 Price of materials described above for bone Treatment.

4. Conclusion: In this paper we have discussed about bone treating biomaterials specially metals which are very available in this country. These are used for various purposes. Implementation of these materials depends largely on the type of patient, conditions, symptoms, environment etc. Better treatment will result in better standard of life eradicating diseases while securing financial security. If Manufacturer companies adopt steps for researching these materials which are cost effective at the perspective of Bangladesh there may be a great scope

REFERENCES:

- [1] Rondelli G, Torricelli P, Fini M and Giardino R 2005 In vitro corrosion study by EIS of a nickel-free stainless steel for orthopaedic applications *Biomaterials* **26** 739–44
- [2] Uggowitz P J, Magdowski R and Speidel M O 1996 High Nitrogen Steels. Nickel Free High Nitrogen Austenitic Steels. *ISIJ Int.* **36** 901–8
- [3] Eglin D and Alini M 2008 Degradable polymeric materials for osteosynthesis: Tutorial *Eur. Cells Mater.* **16** 80–91
- [4] Cohen J 1998 Current concepts review. Corrosion of metal orthopaedic implants. *J. Bone Joint Surg. Am.* **80** 1554
- [5] Christensen F B, Dalstra M, Sejling F, Overgaard S and Bünger C 2000 Titanium-alloy enhances bone-pedicle screw fixation: Mechanical and histomorphometrical results of titanium-alloy versus stainless steel *Eur. Spine J.* **9** 97–103
- [6] Disegi J A and Eschbach L 2000 Stainless steel in bone surgery *Injury* **31**
- [7] Kubota K, Mabuchi M and Higashi K 1999 Processing and mechanical properties of fine-grained magnesium alloys *J. Mater. Sci.* **34** 2255–62
- [8] Cramers M and Lucht U 1977 Metal sensitivity in patients treated for tibial fractures with plates of stainless steel *Acta Orthop.* **48** 245–9
- [9] Seal C K, Vince K and Hodgson M A 2009 Biodegradable surgical implants based on magnesium alloys - A review of current research *IOP Conf. Ser. Mater. Sci. Eng.* **4** 8–12
- [10] Song G L and Atrens A 2000 Corrosion Mechanisms of Magnesium Alloys *Adv. Eng. Mater.* **1** 11–33
- [11] Staiger M P, Pietak A M, Huadmai J and Dias G 2006 Magnesium and its alloys as orthopedic biomaterials: A review *Biomaterials* **27** 1728–34
- [12] Li Z, Gu X, Lou S and Zheng Y 2008 The development of binary Mg-Ca alloys for use as biodegradable materials within bone *Biomaterials* **29** 1329–44
- [13] El-Rahman S S A 2003 Neuropathology of aluminum toxicity in rats (glutamate and GABA impairment) *Pharmacol. Res.* **47** 189–94
- [14] Yap J, Walsh L J, Naser-ud Din S, Ngo H and Manton D J 2014 Evaluation of a novel approach in the prevention of white spot lesions around orthodontic brackets *Aust. Dent. J.* **59** 70–80
- [15] Campana V, Milano G, Pagano E, Barba M, Cicione C, Salonna G, Lattanzi W and Logroscino G 2014 Bone substitutes in orthopaedic surgery: from basic science to clinical practice *J. Mater. Sci. Mater. Med.* **25** 2445–61
- [16] Jyothikiran H, Shantharaj R, Batra P, Subbiah P, Lakshmi B and Kudagi V 2014 Total recall: an update on orthodontic wires. *Int. J. Orthod. Milwaukee.* **25** 47–56
- [17] Pina S, Vieira S, Rego P, Torres P, da Cruz e Silva O, da Cruz e Silva E and Ferreira J 2010 Biological responses of brushite-forming Zn- and ZnSr- substituted beta-tricalcium phosphate bone cements *Eur. Cells Mater.* **20** 162–77
- [18] Saino E, Grandi S, Quartarone E, Maliardi V, Galli D, Bloise N, Fassina L, de Angelis M G C, Mustarelli P, Imbriani M and Visai L 2011 In vitro calcified matrix deposition by human osteoblasts onto a zinc-containing bioactive glass *Eur. Cells Mater.* **21** 59–72
- [19] Bini M, Grandi S, Capsoni D, Mustarelli P, Saino E and Visai L 2009 SiO₂ - P₂O₅ - CaO Glasses and Glass-Ceramics with and without ZnO: Relationships among Composition, Microstructure, and Bioactivity *J. Phys. Chem. C* **113** 8821–8
- [20] Zreiqat H, Ramaswamy Y, Wu C, Paschalidis A, Lu Z F, James B, Birke O, McDonald M, Little D and Dunstan C R 2010 The incorporation of strontium and zinc into a calcium-silicon ceramic for bone tissue engineering *Biomaterials* **31** 3175–84
- [21] Hu H, Zhang W, Qiao Y, Jiang X, Liu X and Ding C 2012 Antibacterial activity and increased bone marrow stem cell functions of

- Zn-incorporated TiO₂ coatings on titanium *Acta Biomater.* **8** 904–15
- [22] Willis M S, Monaghan S A, Miller M L, McKenna R W, Perkins W D, Levinson B S, Bhushan V and Kroft S H 2005 Zinc-induced copper deficiency: A report of three cases initially recognized on bone marrow examination *Am. J. Clin. Pathol.* **123** 125–31
- [23] Uthus E O and Zaslavsky B 2001 Interaction Between zinc and iron in rats *Biol. Trace Elem. Res.* **82** 167–83
- [24] Finney L A and O'Halloran T V 2003 Transition metal speciation in the cell: Insights from the chemistry of metal ion receptor *Science* **300** 931–6
- [25] Hoppe A, Güldal N S and Boccaccini A R 2011 A review of the biological response to ionic dissolution products from bioactive glasses and glass-ceramics *Biomaterials* **32** 2757–74
- [26] Wang T, Zhang J C, Chen Y, Xiao P G and Yang M S 2007 Effect of zinc ion on the osteogenic and adipogenic differentiation of mouse primary bone marrow stromal cells and the adipocytic trans-differentiation of mouse primary osteoblasts *J. Trace Elem. Med. Biol.* **21** 84–91
- [27] Chen Y, Zheng X, Xie Y, Ji H, Ding C, Li H and Dai K 2010 Silver release from silver-containing hydroxyapatite coatings *Surf. Coatings Technol.* **205** 1892–6
- [28] Wennerberg A and Albrektsson T 2009 On implant surfaces: a review of current knowledge and opinions. *Int. J. Oral Maxillofac. Implants* **25** 63–74
- [29] Niinomi M 2002 Recent metallic materials for biomedical applications *Metall. Mater. Trans. A* **33** 477–86
- [30] Hussein M A, Mohammed A S and Al-Aqeeli N 2015 Wear characteristics of metallic biomaterials: A review *Materials (Basel)*. **8** 2749–68
- [31] Li Y, Yang C, Zhao H, Qu S, Li X and Li Y 2014 New developments of ti-based alloys for biomedical applications *Materials (Basel)*. **7** 1709–800
- [32] Nayak S, Bhushan B, Jayaganthan R, Gopinath P, Agarwal R D and Lahiri D 2016 Strengthening of Mg based alloy through grain refinement for orthopaedic application *J. Mech. Behav. Biomed. Mater.* **59** 57–70
- [33] Nagels, J., Stokdijk, M. and Rozing, P.M., 2003. Stress shielding and bone resorption in shoulder arthroplasty. *Journal of shoulder and elbow surgery*, *12*(1), pp.35-39.
- [34] Daniels, A.U., Chang, M.K., Andriano, K.P. and Heller, J., 1990. Mechanical properties of biodegradable polymers and composites proposed for internal fixation of bone. *Journal of applied biomaterials*, *1*(1), pp.57-78.
- [35] Bagherifard, S., Hickey, D.J., de Luca, A.C., Malheiro, V.N., Markaki, A.E., Guagliano, M. and Webster, T.J., 2015. The influence of nanostructured features on bacterial adhesion and bone cell functions on severely shot peened 316L stainless steel. *Biomaterials*, *73*, pp.185-197.
- [36] Cramers, M. and Lucht, U., 1977. Metal sensitivity in patients treated for tibial fractures with plates of stainless steel. *Acta Orthopaedica Scandinavica*, *48*(3), pp.245-249.
- [37] Waizy, H., Seitz, J.M., Reifenrath, J., Weizbauer, A., Bach, F.W., Meyer-Lindenberg, A., Denkena, B. and Windhagen, H., 2013. Biodegradable magnesium implants for orthopedic applications. *Journal of Materials Science*, *48*(1), pp.39-50.
- [38] Bornapour, M., Celikin, M., Cerruti, M. and Pekgulyuz, M., 2014. Magnesium implant alloy with low levels of strontium and calcium: The third element effect and phase selection improve bio-corrosion resistance and mechanical performance. *Materials Science and Engineering: C*, *35*, pp.267-282.
- [39] Avedesian, M.M. and Baker, H. eds., 1999. *ASM specialty handbook: magnesium and magnesium alloys*. ASM international.
- [40] Davis, K.G., Marras, W.S. and Waters, T.R., 1998. Evaluation of spinal loading during lowering and lifting. *Clinical Biomechanics*, *13*(3), pp.141-152.
- [41] Cohen, D.M., Cohen Donald M, 1994. *Low resistance implantable electrical leads*. U.S. Patent 5,330,521.
- [42] Damon, G.H. and Cross, R.C., 1936. Corrosion of copper. *Industrial & Engineering Chemistry*, *28*(2), pp.231-233.
- [43] Vojtěch, D., Kubásek, J., Šerák, J. and Novák, P., 2011. Mechanical and corrosion properties of newly developed biodegradable Zn-based alloys for bone fixation. *Acta Biomaterialia*, *7*(9), pp.3515-3522.
- [44] VOJTĚCH, D., KUBÁSEK, J., ČAPEK, J. and POSPÍŠILOVÁ, I., Magnesium, zinc and iron alloys for medical applications in biodegradable implants.
- [45] Colussi, G., Rombola, G., De Ferrari, M.E., Minola, E. and Minetti, L., 1987. Vitamin D treatment: a hidden risk factor for aluminum bone toxicity?. *Nephron*, *47*(1), pp.78-80.
- [46] Martin, R.B., 1986. The chemistry of aluminum as related to biology and medicine. *Clinical Chemistry*, *32*(10), pp.1797-1806.
- [47] Hellström, H.O., Michaëlsson, K., Mallmin, H. and Mjöberg, B., 2007. The aluminium content of bone, and mortality risk. *Age and ageing*, *37*(2), pp.217-220.
- [48] Navarro, M., Michiardi, A., Castano, O. and Planell, J.A., 2008. Biomaterials in

orthopaedics. *Journal of the royal society interface*, 5(27), pp.1137-1158.

- [49] Öztürk, O., Türkan, U. and Eroglu, A.E., 2006. Metal ion release from nitrogen ion implanted CoCrMo orthopedic implant material. *Surface and Coatings Technology*, 200(20-21), pp.5687-5697.
- [50] Vidal, C.V. and Muñoz, A.I., 2009. Effect of thermal treatment and applied potential on the electrochemical behaviour of CoCrMo biomedical alloy. *Electrochimica Acta*, 54(6), pp.1798-1809.

Numerical Analysis of Energy Harvesting on a Wind Turbine Blade by Using Piezoelectric Material

Md. Faidid Ahasan¹, Mohammad Fuad Hassan¹, Dipayan Mondal²

¹Department of Mechanical Engineering, Khulna University of Engineering & Technology, Khulna-9203, BANGLADESH

²Assistant Professor, Department of Mechanical Engineering, Khulna University of Engineering & Technology, Khulna-9203, BANGLADESH

ABSTRACT

The main concern of this paper is to theoretically prove the absolute possibility of generating electricity from the wind turbine blades' vibration and natural frequency while using piezoelectric material as raw material for turbine blade construction. The reference piezoelectric material used in the design is Lead Zirconate Titanate (PZT-5H). Using design of experiments (DOE), a study was conducted to determine the sensitivity of power with respect to the geometric and material variables. By doing the fluid analysis over the blade, a pressure is obtained which is further used for static analysis and by this pressure mechanical stress is produced and natural vibration is obtained. Due to mechanical stress, electricity formation is 9.497×10^2 V and power produced is 1.1527 W in whole piezoelectric blade. While in thin piezoelectric blade, electricity formation is 1.138×10^3 V and power produced is 2.61 W. When stress is taken under consideration, with 4.14 Hz natural vibration, electricity will be produced up to 129.4 KW (maximum) for whole piezoelectric blade. For 3.4 Hz, at a small section of the blade with a small thickness (about 0.01 m) electricity will be produced up to 0.5 W.

Keywords: Wind Turbine Blade, Vibration, Piezoelectric Material, DOE, Electricity

1.0 Introduction

Wind energy is to be considered as one of the most viable sources of renewable energy when environmental issues such as acid rain, climate change, and imbalance of natural resources have been developed due to use of oil, gas and coal as fuel in power generation [1]. A wind turbine consists of three elements known as Towers, Nacelles and Turbine Blades. A wind turbine tower must be stiff and strong so that it can bear the load of turbine blades and generator. The stiffness is the most important factor to be considered because tower is also subjected to fluctuating wind loads due to rotation of blades. Nacelles are considered as a house of shafts, gearbox, generator and others supporting elements. In case of Nacelles weight is an important factor to be considered not the material. Turbine Blades are required to have an optimum cross section for aerodynamic efficiency to generate the maximum torque to drive the generators. Unused power exists in various forms such as industrial machines, human activity, vehicles, structures and environment sources. Among these, some of the promising sources for recovering energy are periodic vibrations and mechanical stress generated by rotating machinery or engines. Primarily, the selection of the energy harvester as compared to other alternatives such as battery depends on two main factors cost effectiveness and reliability. In recent years, several energy harvesting approaches have been proposed using solar, thermoelectric, electromagnetic, piezoelectric, and capacitive schemes which can be simply classified in two categories such as the power harvesting for sensor networks using MEMS/thin/thick film approach, and power harvesting for electronic devices using bulk approach. As wind turbine blade tolerate various types of loading and vibration extra energy can obtain from

this unused energy. Piezoelectric material can produce electricity from mechanical stress and vibration. If we set up this material into the wind turbine blade some electricity can be produced by the mechanical stress develops by the air and natural frequency of its own [3-4].

2.0 Mathematical Formulation

Continuity Equation:

According to the law of conservation,

$$\frac{\partial \rho}{\partial t} + \nabla \cdot (\rho V) = 0 \dots \dots (1)$$

Navier Stokes Equation:

Transient + Convection = Diffusion + Source

$$\frac{\partial \rho \phi}{\partial t} + \nabla \cdot (\rho u \phi) = \nabla \cdot \lambda \nabla \phi + Source_{\phi} \dots \dots (2)$$

There are two types of piezoelectric materials PZT and PVDF. When piezo electric materials are deformed or stressed, voltage appears across the materials. The mechanical and electrical behavior can be modeled by

$$\{S\} = S_E \{T\} + d \{E\} \dots \dots (3)$$

$$\{D\} = d \{T\} + \epsilon_T \{E\} \dots \dots (4)$$

Where, $\{S\}$ = Strain, $\{T\}$ = Stress $\{E\}$ = Electric

Field, $\{D\}$ = Electric Displacement S_E = Compliance,

d = Piezoelectric Coefficient ϵ_T = Permittivity

Summary of basic electrical equation

$$\text{Capacitance parallel, } C_{p(\text{parallel})} = 2K_3^T \epsilon_0 b \left(\frac{L}{t_p} \right) \dots \dots (5)$$

$$\text{Capacitance series, } C_{p(\text{series})} = K_3^T \epsilon_0 b \left(\frac{L}{2t_p} \right) \dots \dots (6)$$

* Corresponding author. Tel.: +88-01552306978

E-mail address: fuadhassan.kuet@gmail.com

$$\text{Energy, } W = \frac{1}{2} C_p V^2 \dots \dots \dots (7)$$

3.0 Design and Structural Analysis

Airfoil design:

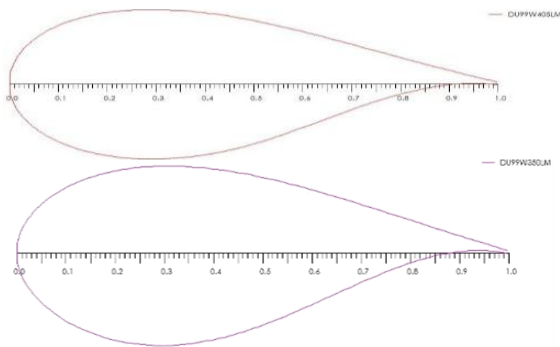


Fig. 3.1: DU99W405LM and DU99W350LM airfoil coordinate.

Model design:

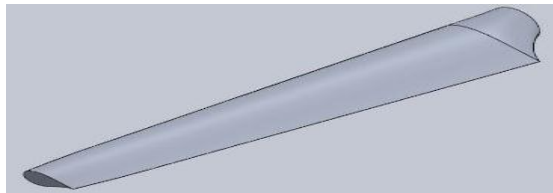


Fig. 3.2: Isometric view of wind turbine blade

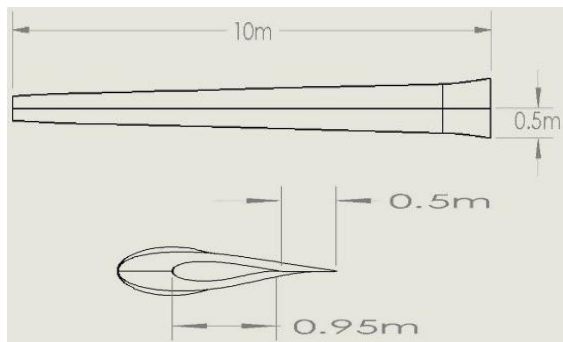


Fig. 3.3: Dimension of wind turbine blade

Material definition:

Properties	Description/ Value
Material	aluminum alloy 1100-H14
Density	2710 kg/m ³
Modulus of elasticity	70GPa
Poison ratio	0.31.

Piezoelectric Materials

Properties	Description/ Value
Material	PZT-5H
Density	7800 kg/m ³ ,
Modulus of elasticity	62 GPa
Poison ratio	0.31.
Dielectric Properties	3.89E-08 and 3.36E-08
K_3^T	3800

Permittivity	8.85E-12 F/m
--------------	--------------

Meshing for wind turbine blade:

For CFD analysis ANSYS simulation software is used and for CAE analysis ABAQUS simulation software is used. The meshing is very fine and sizing is much smaller than the default sizing. An inflation layer is created around the surface of the blade body for better contact of fluid. At inlet section fluid velocity is 12m/s and in the outlet the pressure is zero.

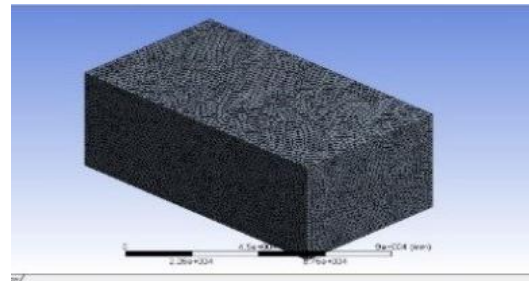


Fig. 3.4: Mesh for fluid analysis

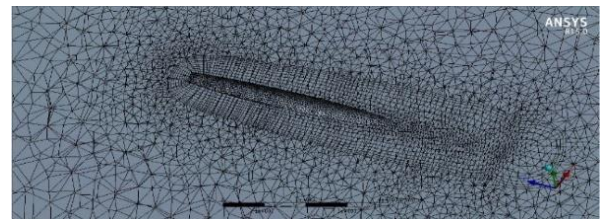


Fig. 3.5: Inflation layer on blade mesh for proper contact of fluid.

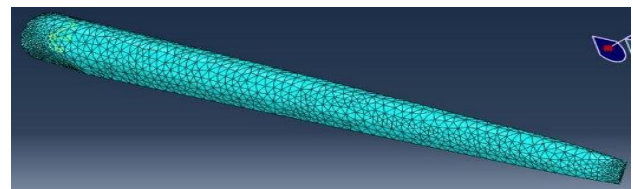


Fig.3.6: Mesh generation in ABAQUS for thin part of the blade for piezoelectric analysis

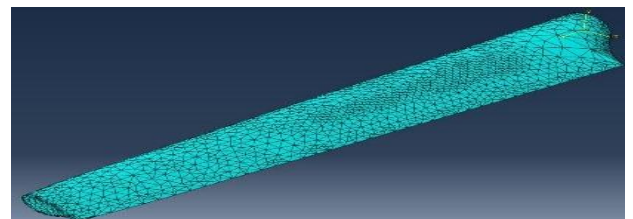


Fig. 3.7: Mesh generation in ABAQUS of the blade

4.0 Boundary condition:

CFD Solution Setup:

Blade body is set as wall. No slip is applied. Inlet is taken as Velocity-inlet. Specification Method is components and the velocity of fluid has only component at X

direction of a magnitude of 12 m/sec primarily. Outlet is described as Pressure-outlet with Gauge pressure as zero meaning the atmospheric pressure condition. Top and bottom surface is taken as wall and side surfaces are given symmetry for proper calculation.

CAE Solution Setup:

For static analysis in ABAQUS CAE material properties was given. The blade material is aluminum. Then static general step was selected where a uniformly distributed pressure was given which was obtain from CFD analysis. The value of pressure was 5954 Pa in the bottom surface of the blade. The pressure is given in the bottom surface as maximum positive pressure was given by the air in the bottom surface of the blade.

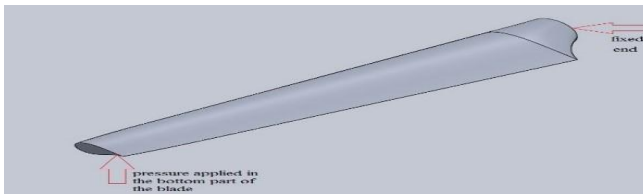


Fig. 4.1: The load and boundary condition

Piezoelectric analysis set up:

Load and Boundary Condition:

A uniform mechanical pressure of 5954 Pa was applied along the y-direction of the system on bottom of the piezoelectric surface. An electrical boundary condition is also imposed.

5.0 Simulation Results and Discussion

CFD Result

First simulation was done for getting pressure by the fluid flow over the blade. This was done by the use of ANSYS FLUENT analysis. The result is given below.

Pressure Contour

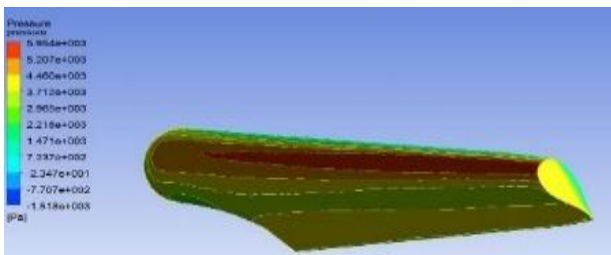


Fig. 5.1: Pressure contour of the wind turbine blade

Pressure Distribution on a Plane perpendicular to the Blade-This shows that the pressure at the upper surface of the airfoil has lower pressure than that of the lower surface of the blade. This generates the lift force that causes the rotation of the blade.

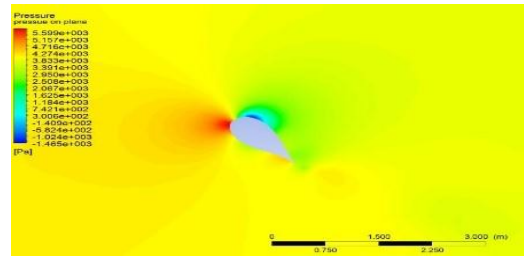


Fig.5.2: Pressure contour on a plane 3m distance from z axis

CAE result on aluminum blade:

From the obtain pressure of ANSYS fluent the next step is static analysis on blade. This was done in ABAQUS CAE. The maximum pressure on blade obtain from ANSYS fluent was 5954Pa and minimum pressure was -1518Pa. now the average pressure is taken as uniformly distributed pressure in case of static analysis.

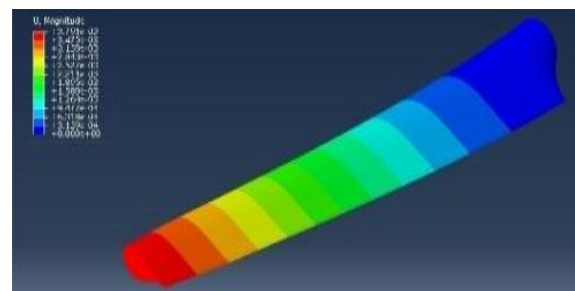


Fig. 5.4: Displacement of blade for applied pressure

As the blade acts as a cantilever beam, somaximum strain will be occurred in the fixed end.

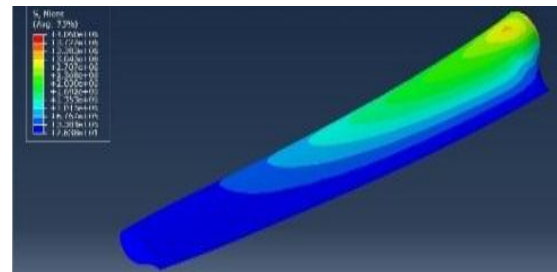


Fig 5.6: Stress on blade due to pressure

CAE result for whole piezoelectric blade:

The average stress magnitude denotes the total stress, we can say the stress is quite low in the free part of the blade but quite high in the fixed end.

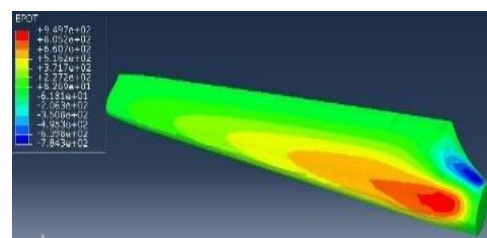


Fig 5.8: Electric potential of whole piezoelectric blade maximum 949.7V for applied pressure

The electric potential at the base state of whole piezo blade is quite low. The maximum electric potential

obtains in the fixed end as piezo electric material gives higher response in high mechanical stress

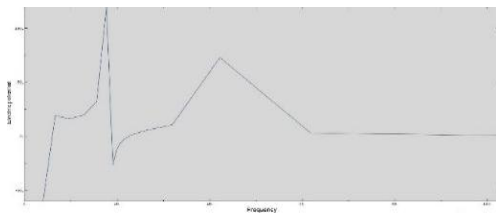


Fig. 5.10: Variation of Electric potential with respect to Frequency graph for whole piezoelectric blade

CAE result for thin piezoelectric blade where air pressure is maximum: For producing lift air will press the wind turbine in the front part of the blade, because of this maximum pressure displacement, stress and strain, efflux and EPOT is shown.

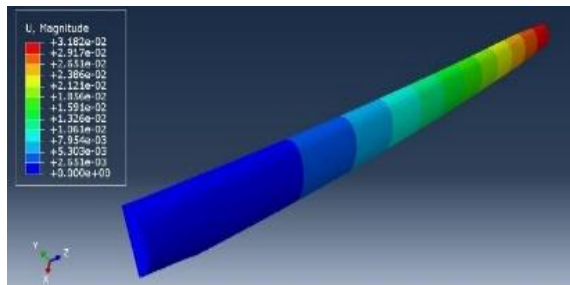


Fig 5.11: Displacement magnitude for thin section

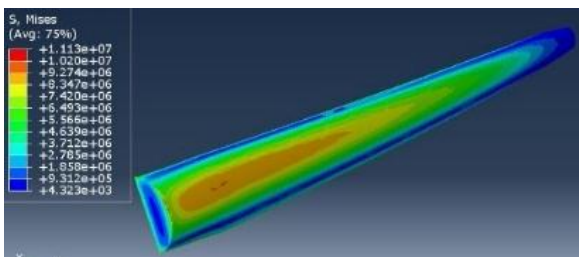


Fig 5.13: Stress magnitude for thin piezoelectric blade

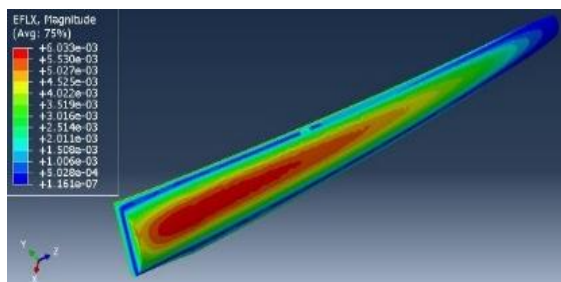


Fig 5.14: EFLUX magnitude for thin piezoelectric blade

The EPOT contour gives the electric potential where no natural frequency is considered and the maximum value is 1.13KV.

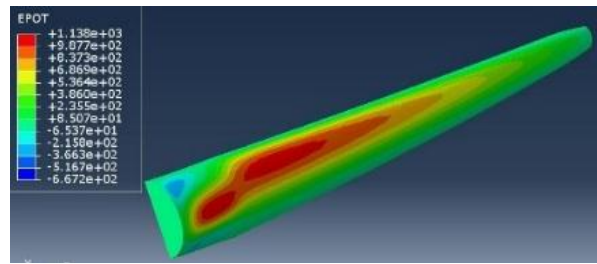


Fig 5.15: Electric potential magnitude

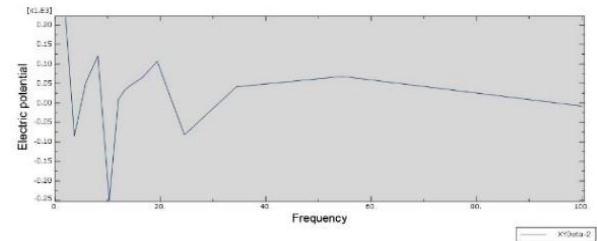


Fig. 5.16: Variation of Electric potential with respect to Frequency graph for thin piezoelectric blade

5.5 Result Calculation:

Power output for whole piezoelectric blade:

From summary of electrical equation in theory section, Due to applied pressure on the piezoelectric blade, in base state the electric potential is,

$$\text{Capacitance } C_{p(\text{parallel})} = 2K_3^T \epsilon_0 b \left(\frac{L}{t_p} \right) = 1.278 \times 10^{-6}$$

Length, $L=10\text{m}$, Width $b= 1.53\text{m}$, Thickness, $t_p=.81\text{m}$

$$\text{Resistance, } R = \frac{1}{\omega C_p} = 781472.614 \Omega$$

here, eigen frequency $\omega = 1$, at base state

$$\text{Now, from maximum output EPOT at base state, } V = 9.497 \times 10^2, \text{ Power, } P = \frac{V^2}{R} = 1.1527 \text{ W}$$

From the calculation, we can say the output voltage is quite low but we know the typical eigen frequency of wind turbine blade is the range between .83 to 10 Hz. in my model the first eigen frequency is 4.14Hz. Putting this in equation 22 we get, Resistive load,

$$R = \frac{1}{\omega C_p} = 195618.2 \Omega.$$

And, V at first eigen frequency is $=1.591 \times 10^5$

Now, power is $=129.4\text{KW}$

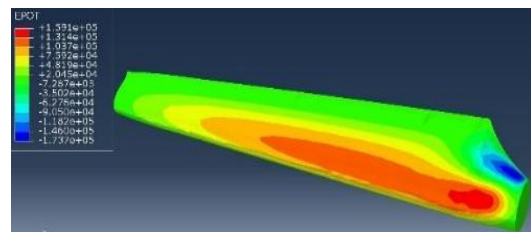


Fig 5.17: The electric potential for 4.147 Hz natural frequency.

Power output for thin piezoelectric blade:

From summary of electrical equation 19,21,22 in theory section, Due to applied pressure on the piezoelectric blade, in base state the electric potential is,

$$\text{Capacitance } C_{p(\text{parallel})} = 2K_3^T \epsilon_0 b \left(\frac{L}{t_p} \right) = 2.0178 \times 10^{-6}$$

Length, L=10m, Width, b= 0.6m, Thickness, t_p=.2m

$$\text{Resistance, } R = \frac{1}{\omega C_p} = 495589$$

here, *eigen frequency* $\omega = 1$, at base state

Now, from maximum output EPOT at base state, V=

$$1.138 \times 10^3, \text{Power, } P = \frac{V^2}{R} = 2.61 \text{ W}$$

When the blade is its first natural frequency the thin blade will be in the same natural frequency. Now for thin blade frequency 3.4 Hz and from the surface shown in the figure the power output will be,

$$\text{Capacitance } C_{p(\text{parallel})} = 2K_3^T \epsilon_0 b \left(\frac{L}{t_p} \right) = 1.022 \times 10^{-5}$$

$$\text{Resistance, } R = \frac{1}{\omega C_p} = 28778.6$$

here, *eigen frequency* $\omega = 3.4$. Now, from maximum output EPOT at base state, V= -1.12×10^3

$$\text{Power, } P = \frac{V^2}{R} = .5 \text{ w}$$

The surface is shown in the figure

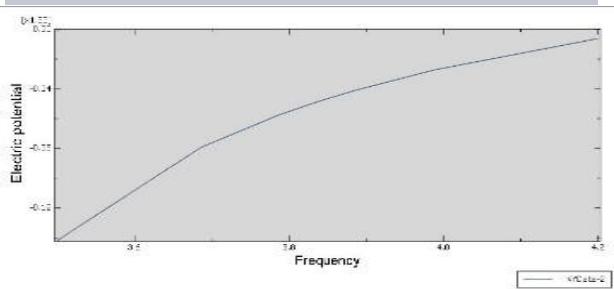
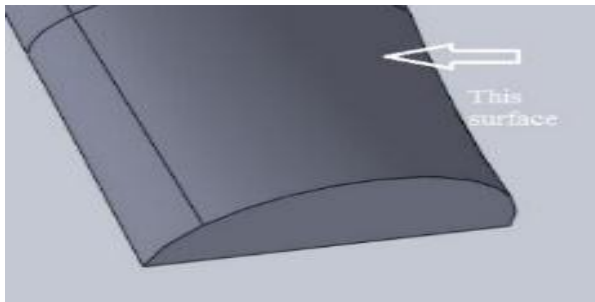


Fig.5.18: The selected surface near the fixed end and the electric potential in that surface

Result Verification:

from theory, the electric potential obtain by piezoelectric material is denoted by this equation 33.

$$V = E * t$$

Here,

V= electric potential [V], E = electric field [V/m]

t= thickness of the material

for datum CSYS and the applied load this equation can be written as

$$V_3 = E_3 * t = \frac{d_{333} * Y * E_{33} * t}{\epsilon_3}$$

Here E₃₃ is obtain from strain of thin blade and which is 1.358*10⁻⁴ for the selected node.

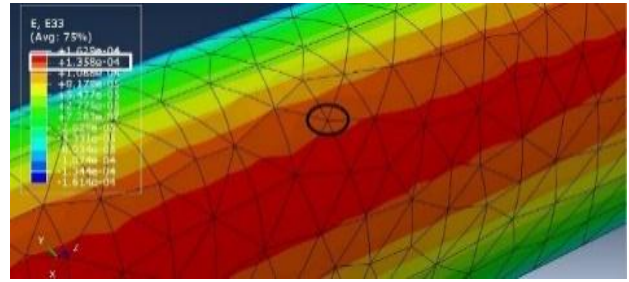


Figure 5.19: The required strain potential for base state

Now for input value and material properties of piezoelectric material the theoretical electric potential is $\frac{7.2e-10 * 49e9 * (-1.188e-9) * 0.01}{1.301e-8} = 1.2015527 \times 10^3$

Now the electric potential obtains from analysis:

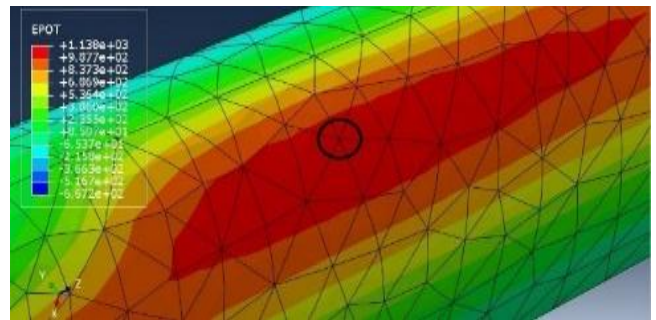


Figure 5.20: The maximum electric potential

Now CAE analysis value is 1.138*10³

Percentage of error:

theoretical value is =1.201552*10³, Experimental value is =1.138*10³, So, percentage of error=5.3%.

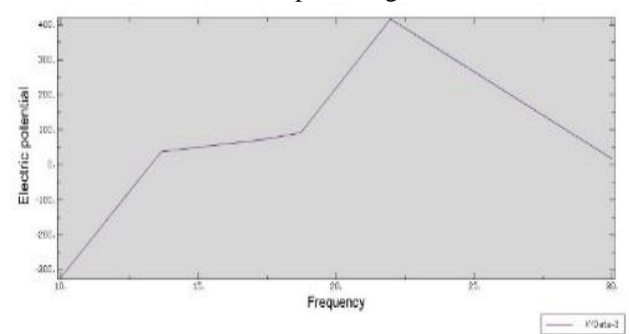


Figure 5.21: Electric potential vs Frequency graph for selected node

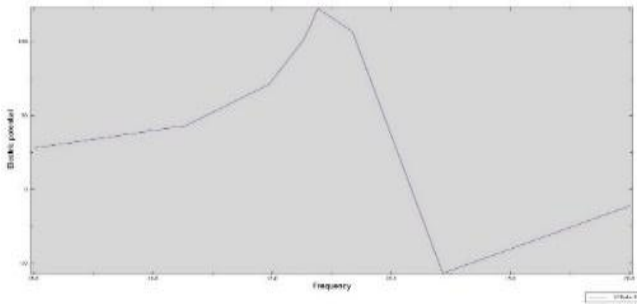


Figure 5.22: Electric potential vs Frequency graph for selected node

This graph represents the electricity produced in the section in various natural frequency [6].
Ideal graph for electric potential vs frequency [7]:

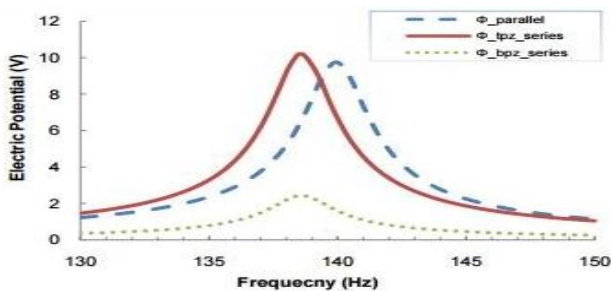


Figure 5.23: Electric potential vs Frequency graph

6.0 Discussion:

From the analysis and calculation, it is obtained that electric potential can be obtained from mechanical stress which is developed by the wind pressure and vibration. The piezoelectric material Lead Zirconate Titanate (PZT-5H) was applied firstly to whole wind turbine then it is applied into a thin section of wind turbine where pressure is maximum. From the calculation, due to mechanical stress 1.15 W power can be produced in the whole blade with piezoelectric materials. Piezoelectric materials are highly sensitive to natural frequency, so when the blade is at its first natural frequency, 129.3 KW power can be produced. For mechanical stress 2.61 W is produced by the thin section but when it is at its natural frequency a small surface can produce .5W which is very reasonable. By validating the result with the actual mathematical calculation 5.3% error is occurred. This is due to some deviation in taking dimension of curved shape wind turbine blade.

Compare with the ideal graph the main theme of the graph is totally same. If the circuit is closed then the experimental graph will take the shape of the ideal graph.

Last of all, it is quite arduous and costly to fabricate such a huge blade with PZT-5H. But the technology just keeps getting better. An ultra-efficient piezoelectric material that can convert up to 80 percent of mechanical energy into electricity [8]. This paper shows the theoretical possibility of getting voltage from wind turbine blade with PZT.

7.0 Conclusion:

Applying piezoelectric material into the blade and a section of blade electricity is produced. This electricity is produced without applying any external energy source. So, it will be very useful as no input is required. Though the initial cost is very high for the price of piezoelectric material, it can produce electricity for longer period of time. The results are shown as follows, For only mechanical stress electricity produced is $9.497 \times 10^2 \text{ V}$ and power produced is 1.1527 W for whole piezoelectric blade. For only mechanical stress electricity produced is $1.138 \times 10^3 \text{ V}$ and power produced is 2.61 W for thin piezoelectric blade. For stress with 4.14 Hz natural vibration will produce maximum 129.4 KW for whole piezoelectric blade. For natural vibration at 3.4 Hz of a small section with a small thickness about 0.01 m can produce .5W. with the help of voltage output of $0.12 \times 10^3 \text{ V}$.

REFERENCES

- [1] P.E. Ciolkosz Daniel, "What is Renewable Energy? Renewable and Alternative Energy"; Penn State Extension, doi:10.1016/j.rser.2008.09.017.
- [2] Free Vibration Analysis of A1 2024 Wind Turbine Blade Designed for Uttarakhand Region Based on FEA Ashwani Kumara , Arpit Dwivedia , Vipul Paliwala , Pravin P Patil a,bDepartment of Mechanical Engineering, Graphic Era University, Dehradun, Uttarakhand, India 248002 E-mail: kumarashwani.geu@gmail.com
- [3] Composite Blades of Wind Turbine: Design, Stress Analysis, Aeroelasticity, and Fatigue Ahmad Reza Ghasemi and Masood Mohandes.
- [4] Advances in energy harvesting using low profile piezoelectric transducers Shashank Priya. Sustainable Energy technologies (SET-2013) 26-29th August, 2013 Hong Kong.
- [5] Deepak Poria, Monika, Rajeev Sharma, Deepak Rohilla, Dr. Manoj kumar Pandey, "Modeling and Simulation of Vibration Energy Harvesting of MEMS Device Based on Epitaxial Piezoelectric Thin Film", International Journal of Advanced Research in Computer Science and Software Engineering, Conference Held in SRM University, NCR Campus, India, Oct 2012, pp: 20-25.
- [6] Effects of Geometric and Material Properties on Electrical Power Harvested from a Bimorph Piezoelectric Cantilever Beam Nataraj Chandrasekharan Graduate Research Assistant cchandr@g.clemson.edu Jaehyung Ju Research Associate jjju@clemson.edu Lonny Thompson Associate Professor lonny@clemson.edu Department of Mechanical Engineering, Clemson University Clemson, SC 29634-0921
- [7] ANSI/IEEE std 176-1987, An American National standard on Piezoelectricity
- [8] Ariel Schwartz. "Electricity Generating Dance Floors and Other Miracles of Piezoelectricity", articles, 2011. <https://www.good.is/articles/electricity-generating-dance-floors-and-other-miracles-of-piezoelectricity>, Accessed September 2016

Application of Extracted and Modified Gelatin from the Leather Solid Waste in Commercial Finishing Agents

Priyanka Saha Gita*, Zia Uddin Md. Chowdhury

Department of Leather Engineering, Khulna University of Engineering & Technology, Khulna-9203, BANGLADESH

ABSTRACT

Raw trimming has the potential to generate value-added product gelatin which produces the biodegradable film with low physical and mechanical properties. The chemical modifications by using the crosslinking agent improved the performance properties of the gelatin. Commercially produced leather finishing binders are mostly non-biodegradable which have an adverse environmental impact with high grain loading. The binders blended with extracted and modified gelatin can reduce the environmental burdens by replacing a part of non-biodegradable materials from leather finishing agent. In this study, the gelatin was undergone thermal hydrolysis in acidic and alkali conditions at 90°C hot water and after modification of gelatin with cross-linkers it was blended with available commercial binders in an optimized ratio and tests carried out to check whether there is any major change to the performance properties of the finished film. Prepared films showed promising results with the gelatin-protein (PG_m) and gelatin-acrylic (AG_m) formulation. This approach has the implication in leather finishing subject to the assessment of physical properties of the finished film.

Keywords: Gelatin, binders, biodegradable film, performance property.

1. INTRODUCTION

The leather is a valuable outcome of the tannery by processing raw hides and skins, which are the by-products of meat and meat product industry [1]. The finishing process is one of the crucial steps in the processing of leather by which the tanning industry transforms leather into end-product [2]. The purpose of finishing is to improve the use properties of the leather in general and to protect it from wetting and soiling, to level out patches and grain faults and to apply an artificial grain layer to split or corrected grain leather etc. The finishing materials used in leather finishing can be classified into two main groups such as the binders that is main film-forming materials and additives that include colorants, penetrators, fillers, lacquers, feel modifiers, plasticizers, and auxiliaries' etc. [3]. There are mainly two types of binders used in leather finishing such as natural and synthetic binders. Among the natural binders protein (casein, albumens), resin (shellac) and among the synthetic binders resin emulsions such as acrylics, butadiene, polyurethane, hybrids and compact are main. All of these binders have high grain loading, high volatile organic content (VOC). But all these types produce the non-biodegradable film with the artificial look. In that case, biodegradable films can replace existing synthetic non-biodegradable products at the lowest cost possible; focusing on improving quality and shelf life, protecting, and maintaining product integrity and enhancing product appearance. This biodegradable film can be prepared simply with low cost by utilizing solid waste generated from tannery during tanning operations [4]. Solid wastes generated in leather industries include skin trimmings, keratin wastes, fleshing wastes, chrome shaving wastes, and buffing wastes. [5]. Protein is the main component of most of these wastes [4]. The recovery of protein from various tannery residues can be done by hydrolysis at 80-130°C in aqueous acid or alkali [6]. Gelatin is a substantially pure protein obtained by the thermal denaturation of the protein [7]. Due to its functional properties, it has been utilized in the production of edible and/or biodegradable films; the practical use of gelatin extracted from leather waste, as a material, may be limited by its relatively poor physical properties whereupon the material may

disintegrate upon handling. To improve the product properties, it is often necessary to introduce exogenous crosslinking into the molecular structure of the gelatin. Crosslinking has shown to improve the physical performance of a film/coating [3]. The main target of this study is to blend the chemically modified gelatin with the commercially available binders to produce a low cost, less nonbiodegradable, low grain loading and comparatively eco-friendly film.

2. METHODOLOGY

2.1 Gelatin extraction

Gelatin was prepared by the treatment of acidic and alkali hydrolysis in hot water (90°C) with a slight modification of the referenced [4] process. The wet salted raw trimming offals were properly washed to remove the salt and chopped into a smaller size. The added water was 5 times more than the trimming weight and allowed to swell by sulfuric acid with proper maintenance of pH for 48 hours. The pH of the solution was 2.5 and it was adjusted by different installment of acid addition. After acidic swelling, the trimmings were divided into two parts. At one part, the pH of the solution was maintained 9.4 for alkaline hydrolysis and for acidic hydrolysis the pH of the solution was kept 4.7. Then, each of them was subject to thermal treatment at 90° C for 6 hours with continuous agitation. After thermal treatment, it was slowly brought to the normal room temperature and filtered. Next, the filtrates were shaken well and slowly stirred at room temperature for 40 minutes. Finally, the resultant solutions were centrifuged at 4000 rpm for 25 minutes and gelatin separated. A part of gelation was preserved at 4° C for measuring the gel strength and the rest was kept at normal temperature with an addition of 0.4% bactericide (BUSAN 30L) to prevent putrefaction.

2.2 Chemical Modification

The aldehyde-based crosslinker (LUXOFIX NH8) was used to modify the gelatin. The crosslinker contains 5% solid and added as a percent (10%) of the gelatin solutions. The mixture was left for curing at the room temperature for 2 hours. Here **Photo1** shows the

* Corresponding author. Tel.: +88-01759177263
E-mail addresses: gitapriyana18@gmail.com

centrifugation process and **Photo2** shows the prepared films.

2.3 The blending of modified gelatin with binders

Three binders such as acrylic, polyurethane, and polyamide protein were collected from a local agent of a reputed leather finishing chemical company. Then, all of them were blended with modified gelatin at a ratio of 70:30 (optimized) to prepare a 2gm film in a 55 mm diameter petri dish. Initially, the Petri dishes were cleaned up and castor oil was used as film releasing agent. After that, the properly mixed binders with modified gelatin were poured on the dish. Then the Petri dishes were stored and left out for drying at room temperature with proper ventilation for film formation.



Photo1: Centrifugation



Photo2: prepared films

The simplified study workflow is illustrated below in **Fig.1**

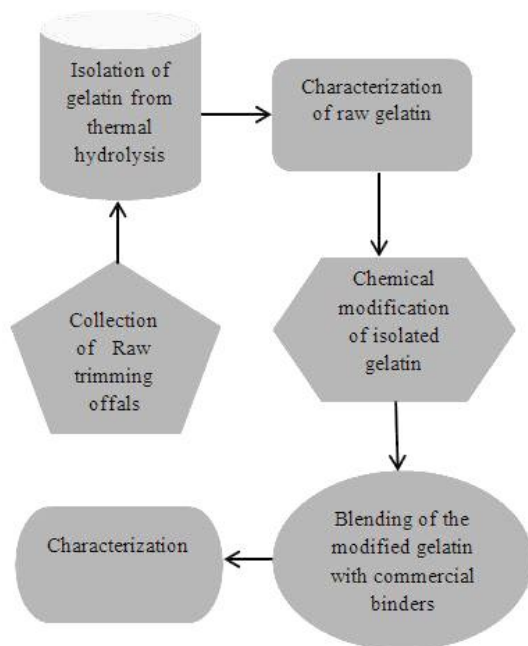


Fig.1 Process flow diagram

2.3 Characterization

Different performance properties of the prepared films with respect to original film such as swelling or

crosslinking, rheological property (viscosity at different shear rates), the melting point were analyzed.

2.3.1 Swelling property

Prepared films were analyzed for their water absorption or swelling. The films were weighed and immersed in a physiological solution for different periods of time. Wet samples were blotted with a tissue to remove excess liquid and re-weighed [4].

The amount of absorbed water was calculated as:

$$\text{Swelling (\%)} = 100 (W_{\text{wet}} - W_{\text{dried}}) / W_{\text{dried}}$$

Where W_{wet} is the weight of the wet sample and W_{dried} is the weight of the dry sample.

2.3.2 Viscosity property

The average viscosities of the samples with respect to different shear rates such as 1s^{-1} , 10s^{-1} , 100s^{-1} and 500s^{-1} were measured. This feature is important for different finishing stages or processes such as can stability, mixing and pumping, and coating application. Each of these processes requires certain viscosity to aid the overall finishing system. Analysis of viscosity helps to build a perspective of applicability of prepared finishing agents.

2.3.3 Thermal analysis

Thermal analysis was carried out by differential scanning calorimeter (DSC) that is a powerful and versatile thermal analyzer allows for property measurements on a broad variety of materials from -150 to 600°C with heat flow range $\pm 40\mu\text{w}$. It is basically a thermoanalytical technique in which the difference in the amount of heat required to increase the temperature of a sample and reference are measured as a function of temperature. Both the sample and reference are maintained at nearly the same temperature throughout the experiment.

Generally, the temperature program for a DSC analysis is designed such that the sample holder temperature increases linearly as a function of time. The reference sample should have a well-defined heat capacity over the range of temperature to be scanned. The main application of a DSC is in studying phase transitions, such as melting, glass transitions or exothermic decompositions, crystallization time and temperature etc. Samples were stored in a humidity chamber at the prescribed relative humidity (60%) for a minimum of 48 h and 20°C , and the machine needs to stabilize and purging prior to analysis. The dry film (10 mg) was hermetically sealed in an aluminum pan and subjected to a double scan in a differential scanning calorimeter. The scans were carried out at a heating rate of $10^{\circ}\text{C}/\text{minute}$ in the temperature range of 50°C to 200°C . All samples were run in triplicate [4]. The result of a DSC experiment is a curve of heat flux versus temperature or versus time. From the curve analysis, the melting temperature of different films can be determined.

3. RESULT AND DISCUSSION

The graphical representation of water uptake (swelling) of 100gm film, average viscosities and thermal analysis of original and modified films are given below. Also, **Table 1** shows the characterization property of the original and modified films.

Table 1 Characterization of original and modified films.

Sample	Swell (water per 100 gm film)	Melting point, °C	Average viscosity, mPa.s			
			Share rates			
			1	10	100	500
			s ⁻¹	s ⁻¹	s ⁻¹	s ⁻¹
A	29	167.11	127	17	30	52
P	2537	118	1129	124	110	224
PU	23	207.48	1104	1049	846	467
G	4000	65.06	11	9	24	34
G _m	193	85.42	112	13	19	36
AG _m	128	126.81	225	39	33	53
PG _m	229	122	28	61	66	104
PUG _m	92.47	101.7	8	30	62	87

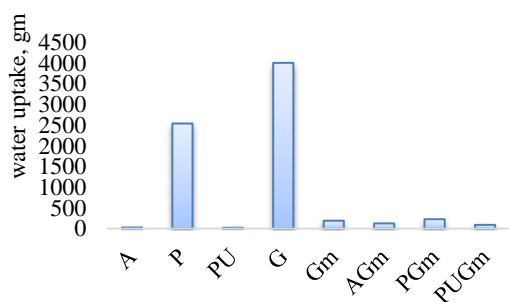


Fig.2 Water uptake of 100 g film

From the above **Fig.2**, the water uptake (swelling) of 100gm different films are shown. It is visible that the raw gelatin swelled much as expected whereas the modified gelatin absorbs only a little amount of water.

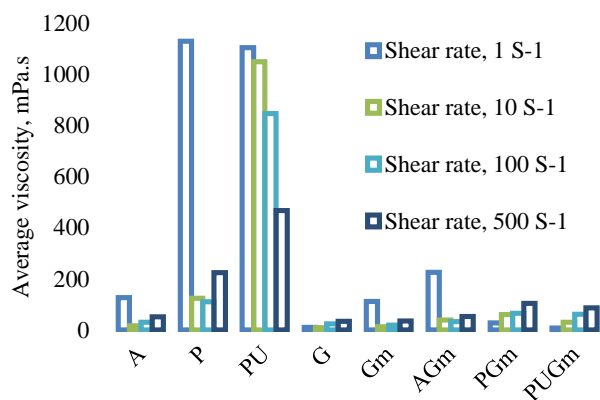


Fig.3 Average viscosity of different samples at the different shear rates.

The above **Fig.3** shows the average viscosity for different samples at different share rates. Viscosity is an important property for the binders when applied as a finishing agent on leather. Gelatin-protein (PG_m) and acrylic-protein (AG_m) blending show the reliable range of viscosity suitable for use as a finishing agent.

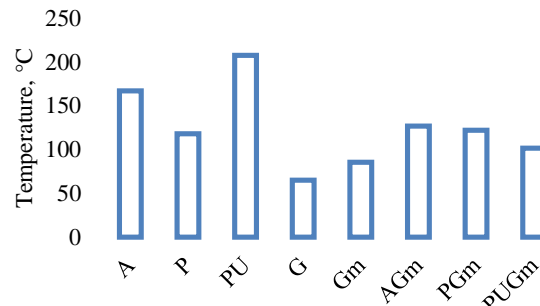


Fig.4 Comparison of thermal behavior of different samples

The above **Fig.4** shows the melting temperature of different sample films. After modification melting temperature increased for gelatin (G), and acrylic-gelatin (AG_m). However, protein-gelatin (PG_m) appears to same as the original films and PU declined sharply when mixed with the modified gelatin. The DSC analysis of original and modified films are illustrated in **Fig.5**. The onset temperatures (melting temperature) for different samples measured using these thermograms.

4. CONCLUSION

This study streamlined the utilization of leather solid waste (raw trimmings) to produce a less nonbiodegradable film without compromising performance properties of selected commercial binders except PU. It is evident that gelatin is more compatible with a protein-based binder and enhanced all the performance properties may be due to the similar chemical composition. On the other hand, acrylic-gelatin (AG_m) blending slightly differed from its original property. However, it will not create a problem in a time of application as the rheological features are within the range of acceptable limit of conventional finishing agents. This finding signifies that part of non-biodegradable commercial binders can easily be replaced partly by a biodegradable film producing modified gelatin without experiencing major changes in physical and mechanical performances. For future research, other performance property such as tensile strength, gel strength and percentage of biodegradation and glass transition property of the blended films can be determined to form a more conclusive remark. Besides, other binders such as butadiene, vinyl binders can examine in the same way. Importantly, prepared blending agents should be applied to leather and subsequently assessed for mechanical and chemical tests for verification.

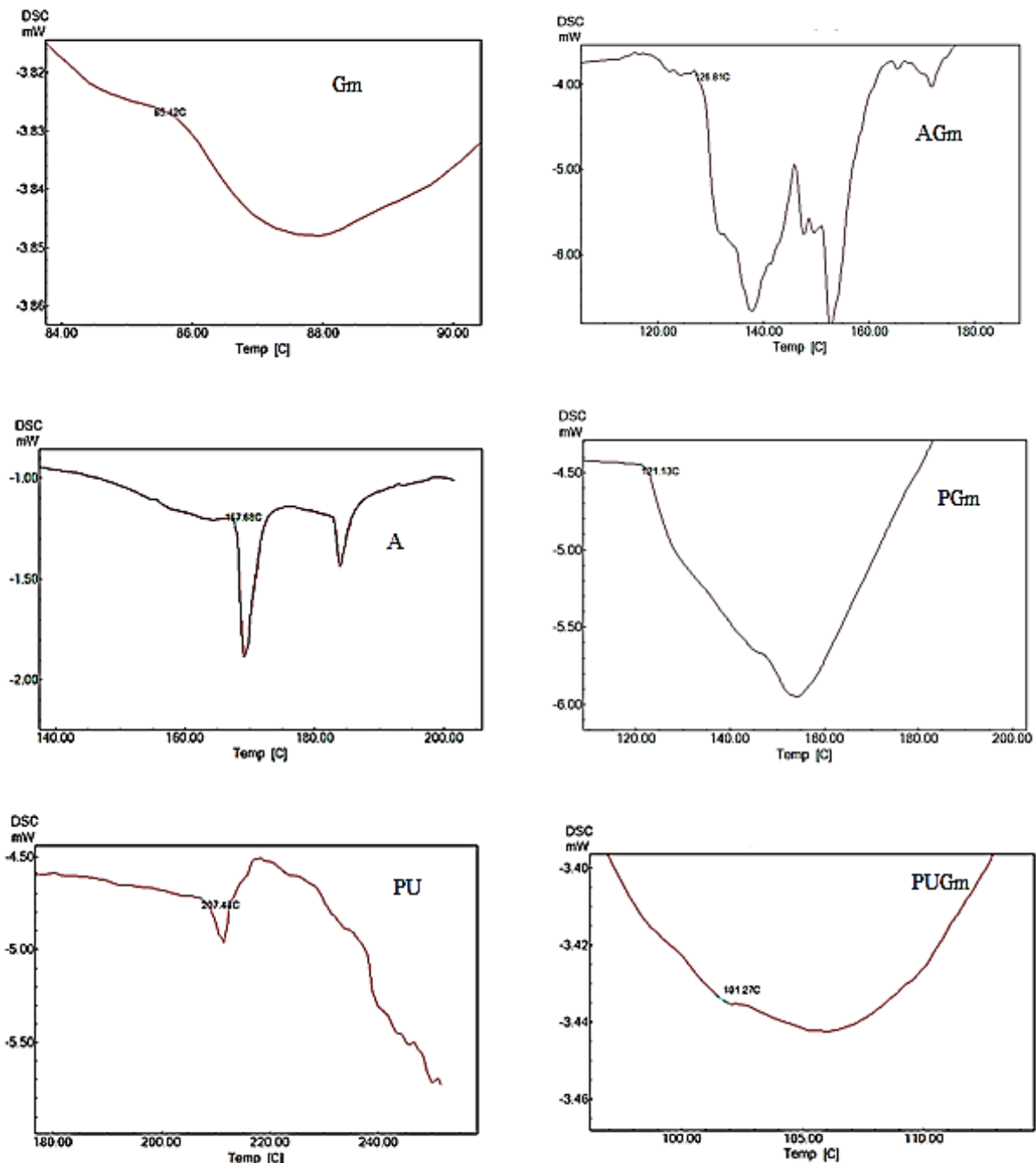


Fig.5 DSC analysis of different films

NOMENCLATURE

A	Acrylic binder
P	Protein binder
PU	Polyurethane binder
G	Gelatin
G _m	Modified gelatin
AG _m	Acrylic binder and modified gelatin blend
PG _m	Protein binder and modified gelatin blend
PUG _m	Polyurethane and modified gelatin blend

ACKNOWLEDGMENT

We are grateful to the department of leather engineering, Khulna University of Engineering & Technology, for providing amazing lab facilities.

REFERENCES

- [1] Ozgunay H., Colak S., Mutlu M.M., and Akyuz F., Characterization of leather industry wastes, *Polish J. Environ. Stud.*, 16(6): 867–873, (2007)
- [2] Bacardit A., Cobos M., Borr E. À. S., and Ollé L., Epoxy resin crosslinked binders in aqueous finishing, *Journal of the Society of Leather Technologists and Chemists*, vol. 94, p.1.

- (2009)
- [3] Ollé L., Cobos M., Solé O., and Bacardit A., Aqueous finishing with polyisocyanate crosslinked binders, *Journal of the Society of Leather Technologists and Chemists*, vol. 93, p.222, (2009)
 - [4] Antunes A. P. M., Catalina M., Attenburrow G. E., Cot J., and Covington A. D., Influence of Crosslinkers and Crosslinking Method on the Properties of Gelatin Films Extracted from Leather Solid Waste, *Polym. Polym. Compos.*, 21(7) : 449–456, (2013)
 - [5] Sundar V. J., Gnanamani A., Muralidharan C., Chandrababu N.K., and Mandal A. B., Recovery and utilization of proteinous wastes of leather making: A review, *Rev. Environ. Sci. Biotechnol.*, 10(2):151–163, (2011)
 - [6] Montoneri E., Rizzi G., Rizzi A., Mordenti A., Bauli A., Riolfatti M. and Pellegrini L., Hydrolysis of tannery wastes to protein meal for animal feedstuffs: A process and product evaluation, *J. Chem. Technol. Biotechnol.*, 59(1) : 91–99, (1994)
 - [7] Abdalbasit and Fadol H., Review : Gelatin, Source, Extraction and Industrial Applications, *Acta Sci. Pol. Technol. Aliment.*, pp. 135–147, (2013)

ICMIEE18-278

Investigation of Different Mechanical Properties on Various Hybrid Natural Fiber Based Polymer Composites

*Rahul Sarker**, *Md. Shahidul Islam*

Department of Mechanical Engineering, Khulna University of Engineering & Technology, Khulna-9203, BANGLADESH

ABSTRACT

The recent era of material belongs to the composite materials because of its numerous numbers of advantages. Several researches have been done on different natural fiber composites. But different mechanical properties on various hybrid natural fiber based polymer composites still uncovered to us. Therefore, in this present research work macrostructural analysis of different mechanical properties like tensile, flexural strength and water absorptivity on natural fibers (jute, murta and bamboo) as hybrid composite in three combinations (jute-bamboo, bamboo-murta and jute-murta) are studied. Each combination consists of two natural fibers where each has two layers of woven fiber. Epoxy resin as matrix material and hardener with natural fibers as the reinforcement material is used to make the specimens. Hand lay-up technique is used to fabricate the specimens. After testing the specimens it is found that the jute-bamboo hybrid composite has superior mechanical properties and better water absorption property as compared to the other hybrid composites.

Keywords: Hybrid, Matrix, Reinforcement, Tensile, Flexural.

1. Introduction

The advancement of mankind is defined in terms of the development in materials i.e. the stone age, the bronze age, and the iron age. The recent era of material belongs to the composite materials because of its numerous numbers of advantages. The word 'composites' derived from the Latin word *compositus*, which means put together signifying something made by putting together different parts or materials [1]. A composite is a material made when two or more different materials are combined together to create a superior and unique material. Composite material consists of strong carry-load materials which are embedded in a weaker material. The stronger material is commonly referred as reinforcement and the weaker material is referred as matrix. The two materials works together to give the composites unique properties. However, within the composites the material does not dissolve or blend into each other. The reinforcement provides the strength and rigidity which helps to support the structural load. The matrix or the binder helps to maintain the position and orientation of the reinforcement and is somewhat more brittle [2]. The reinforcement materials such as Fibers are thin and but integrity is not maintained. In matrix materials, strength values are less and hence fibers or matrix alone cannot find its application as a structural material but when these two materials are combined we get a composite materials which is light weight, stiff, strong and tough [3]. There are different types of composite. Fiber composite is one of them. When two or more type of fibers is used in composites as reinforcement fillers is called as hybrid fiber composites. These types of composites have great applications in mankind. It has achieved a major breakthrough in the construction of low weight structures. Moreover, it has high specific strength, toughness and stiffness. It is moderately heat and fire resistive. It is ecofriendly in nature as it is fully bio-degradable. It is costeconomic as atural fibers are abundantly available

and it is renewable. A lot of research work has been done by researchers on different natural fibers. Jacob Olaitan Akindapo, Umar Alhaji BINNI, Olawale Monsur have made roofing sheet by using groundnut sell particles and epoxy resin as composite Material. They have tested different tests like water absorptivity test, flexural strength, tensile Strength, impact strength [4]. Jochen Gassan and Andrzej K. Bledzki have investigated different properties of a jute-polypropylene composite. They also worked on improving different properties like tensile and impact strength [5]. Madhukiran.J, Dr.T.Venkateswara Rao, Dr.S.Madhusudan, Dr. R.Umamaheswara Rao have worked on jute-coir hybrid natural fiber composites. They have done different tests like tensile test, flexural tests and shown that jute-coir fiber hybrid composites exhibited superior properties when compared to pure composites [6]. So, several researches have been done on different natural fiber composites. But still there are different kinds of fibers which properties are not uncovered to us. In this paper different mechanical properties of jute, bamboo and murta fiber as hybrid composite in three different compositions have been revealed. So it is undoubtedly a new addition in research of composite material.

2. Materials and Methods

2.1 Materials and Equipments

Materials and equipments used in fabricating composite are given below:

2.1.1 Jute Fiber

Jute is a natural fiber which has many inherent advantages like high tensile strength, lustier, moderate heat, low extensibility, long staple lengths and fire resistance. It is one of the most available natural fibers in our country. Woven jute fiber is collected from the local shop.

* Corresponding author. Tel.: +88-01723370537
E-mail addresses: rahulsarker.akash@gmail.com

2.1.2 Bamboo fiber

In our country bamboo is another easily available natural fiber which is used in versatile products manufacturing. It has high compressive and tensile strength. It is collected as woven bamboo mat.

2.1.3 Murta fiber

Murta fiber also known as pati bet is one kind of natural fiber which is the raw material for making shitalpati, a traditional bed mat of Bangladesh. It is also known as 'patipata', 'mostak', 'paitara', in different parts of Bangladesh. [7]. It is collected as woven mat.

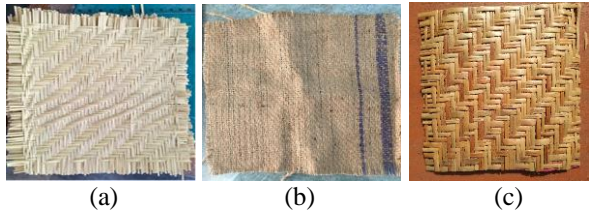


Fig. 1 (a) woven jute fiber (b) woven bamboo fiber (c) woven murta fiber.

2.1.4 Resin and Hardener

Resin acts as the matrix material in composite to bind the reinforcing fiber together. On the other hand hardener is a chemical substance which is added to something in order to harden it. In this experiment Araldite AW 106 is used as epoxy resin and HV 953 IN is used as hardener which is collected from local traders. The mixing ratio of resin and hardener is 1:1 by volume.

2.1.5 Mould

Generally a mould is used for making parts in hand lay-up process where the layers are placed to get desired shape. Two stainless steel plates of 30cm length and 27.5 cm width are used as mould.

2.1.6 Other Equipments

Some equipments like mug, polythene cover, hand gloves, lubricating oil, roller, acetone, laminating paper, some weights etc. are used in fabricating composite.

2.2 Laminate Fabrication Method

Hand lay-up process is used to fabricate the samples of hybrid composite. Each sample consists of two pairs of two different fibers.

2.3 Measurements

2.3.1 Mechanical Testing

Two different mechanical properties of the composites analysed in the present work are tensile and flexural strengths. Tensile test is conducted according to the ASTM D-638 standard while the flexural (three-point bending test) is conducted according to the ASTM D-790 standard on a universal testing machine.

2.3.2 Water Absorptivity Test

The percentage water absorptivity is calculated and recorded against each mass fraction.

$$m = (w - w_0) / w_0 * 100\%$$

Where m, w, w_0 are the moisture absorption content, weight of dried and wet composite material respectively.

3. Results and Discussion

3.1 Macrostructural analysis

In this analysis some typical cross-sectional view of different composite surface are investigated.

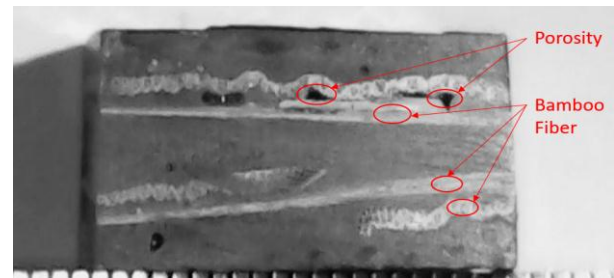


Fig. 2 Cross-sectional view of a jute-bamboo hybrid composite surface

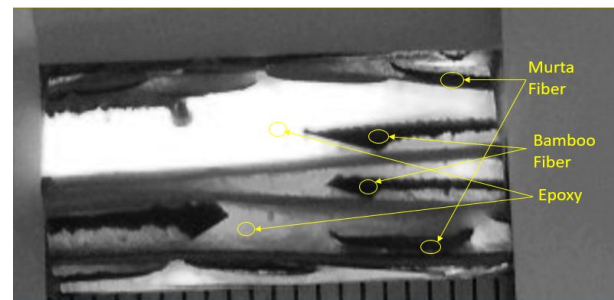


Fig. 3 Cross-sectional view of a bamboo-murta hybrid composite surface.

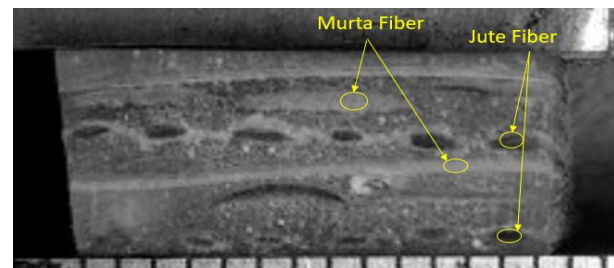


Fig. 4 Cross-sectional view of a jute-murta hybrid composite surface

From these figures fiber distribution in the epoxy matrix are seen. In fig. 2 bamboo fiber and some void areas are found in the jute-bamboo composite. But jute fiber is not seen properly in this structure. In figure 3 both bamboo and murta fiber are seen in the matrix material and in this case no void area is found. In figure 4 both jute and murta fibers are identified.

3.2 Volume fraction

Table 1 Volume fraction of the different constituents of composites.

Composite Name	Volume of jute fiber (%)	Volume of murta fiber (%)	Volume of bamboo fiber (%)	Volume of epoxy resin (%)	Volume of void space (%)
Jute-bamboo	11.65		30.2	56.95	1.2
Jute-murta	17.78	26.15		54.37	1.7
Murta-bamboo		22.62	24.23	52.48	0.67

From table 1 it is seen that jute-murta composite has highest void space and bamboo-murta composite has the least in it's composition. Again jute-bamboo composite has the highest amount of epoxy material and least amount of fiber in it's composition and bamboo-murta fiber has the least amount of epoxy material and highest amount of fiber in it's composition.

3.3 Water Absorptivity Test

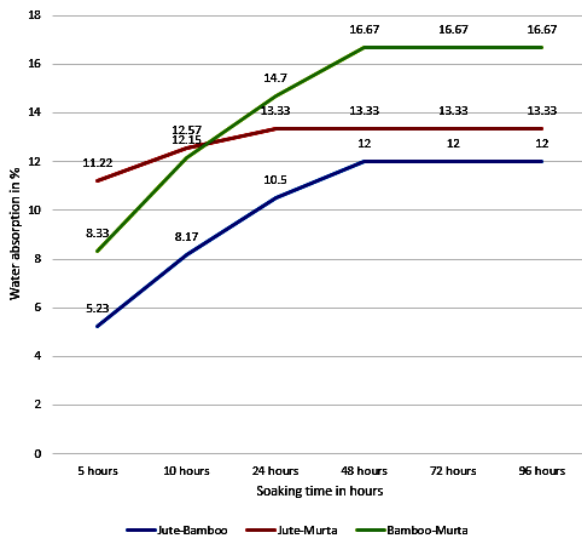


Fig. 5 Water absorption rate of different composites.

From fig 5 we can see jute-bamboo composite has absorbed lowest amount of water and bamboo-murta composite has absorbed the highest. Water absorption rate is high in both jute-bamboo and bamboo-murta composite but jute-murta composite has the lowest rate of water absorption.

3.6 Flexural Strength Test

Flexural stress-strain diagram and flexural strength are shown below.

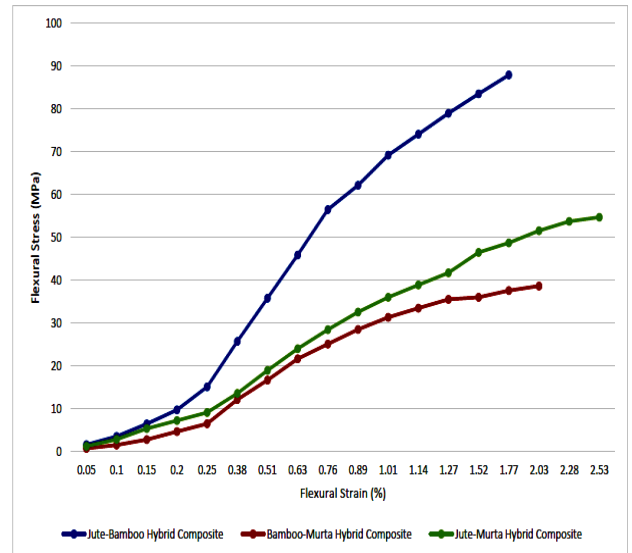


Fig. 6 Flexural stress-strain diagram for different composites

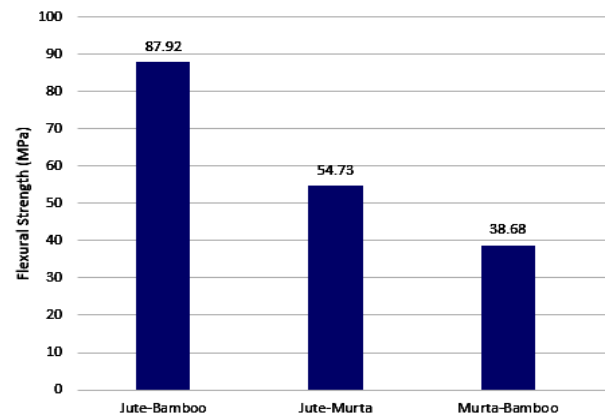


Fig. 7 Flexural strength of different composites

From fig 7 it is seen that jute-bamboo composite has the highest flexural strength and murta-bamboo composite has the lowest flexural strength.

3.7 Tensile Strength Test

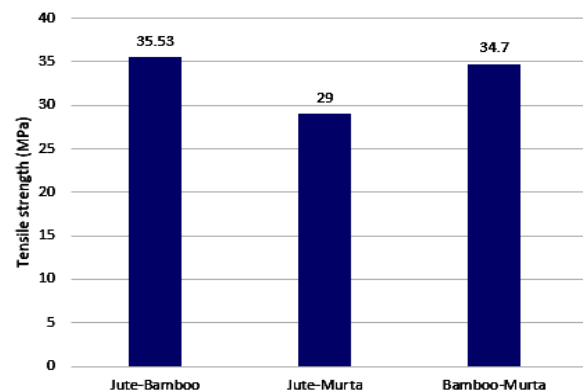


Fig. 8 Tensile strength of different composites

From fig. 8 it is seen that jute-bamboo composite has the highest tensile strength and jute-murta composite has the lowest tensile strength.

Engineering & Technology IJET-IJENS Vol:13
No:02.

4. Conclusion

From macrostructure analysis and volume fraction that the composite has some void areas inside it which is responsible for decrease of fatigue strength. So strength properties can be improved by reducing the void areas. From mechanical testing and water absorptivity test it can be concluded that jute-bamboo fiber reinforced hybrid composite has the best flexural and tensile strength but it has the highest water absorption rate.

REFERENCES

- [1] Animesh Borah, Duniwanhi Suchiang, Kallol Debnath, Md. Murtaza Alam, Manapuram Muralidhar, "Studies on Design and Fabrication of Polymer Based Composite Materials with Fish Scale Reinforcement." American Journal of Engineering Research (AJER) e-ISSN: 2320-0847 p-ISSN : 2320-0936 Volume-4, Issue-6, pp-165-173.
- [2] Maria Mrazova, "Advanced composite materials of the future in aerospace industry." Incas Bulletin, Volume 5, Issue 3/ 2013, pp. 139 – 150.
- [3] G. Kamali 1 , N. Ashokkumar 2 , K. Sugash3 ,V. Magesh, "Advanced Composite Materials of the Future in Aerospace Engineering." International Journal for Research in Applied Science & Engineering Technology (IJRASET) Volume 5 Issue II, February 2017 IC Value: 45.98 ISSN: 2321-9653.
- [4] Jacob Olaitan Akindapo, Umar Alhaji BINNI, Olawale Monsur Sanusi," Development of Roofing Sheet Material Using Groundnut Shell Particles and Epoxy Resin as Composite Material" American Journal of Engineering Research (AJER) e-ISSN: 2320-0847 p-ISSN : 2320-0936 Volume-4, Issue-6, pp-165-173
- [5] Jochen Gassan* and Andrzej K. Bledzki, "The influence of fiber-surface treatment on the mechanical properties of jute-polypropylene composites" Composites Part A 28A 100 1 – 1005 6 1997 Published by Elsevier Science Limited Printed in Great Britain.
- [6] Madhukiran,J, Dr.T.Venkateswara Rao, Dr.S.Madhusudan, Dr. R.Umamaheswara Rao, "Evaluation of The Mechanical Properties on Sisal-Coir Hybrid Natural Fiber Composites" International Journal Of Engineering Research And Development, e-ISSN: 2278-067X, p-ISSN: 2278-800X, www.ijerd.com, Volume 13, Issue 9, PP.4349
- [7] Rafia Akter, Rajia Sultana, Md. Zahangir Alam, Md. Rakibul Qadir, M. H. Ara Begum, Md. Abdul Gafur, "Fabrication and Characterization of Woven Natural Fibre Reinforced Unsaturated Polyester Resin Composites" International Journal of

Ergonomic Analysis of Bangladeshi Train Passengers

Sajia Afrin Shifa*, Md. Golam Kibria

Department of Industrial Engineering and Management, Khulna University of Engineering & Technology, Khulna-9203,
BANGLADESH

ABSTRACT

Though the train is a common mode of transportation in Bangladesh, it is imported for passengers without considering ergonomic design for the users. The objectives of this study were to identify performed activities and corresponding posture of the passengers, duration of the activities and to assess the comfort in respect of the performed activities and postures. Activities and duration were recorded with a smart phone. The postures were defined using coding technique. A comfort questionnaire was given to weigh the passengers comfort experiences in combination with the activities performed. Eight discrete postures were defined with four main activities: Staring, Sleeping, Talking and Listening to music or using mobile phone. The combination of activities and postures connected to comfort scores. For passenger seat design, it is very important to consider the postures. Vital consideration need to be taken for the long-performed activities (such as sleeping) to avoid musculoskeletal risks. The outcome can help to improve the existing seat design and interior facilities of train as to Bangladeshi passenger's ergonomic consideration.

Keywords: Train passenger comfort, activities, postures, seat design

1. Introduction

Most of the country prefer train as a safer and cheaper transportation mode than others. It is a common mode of transportation in Bangladesh also. Trains are imported for Bangladeshi passengers without considering ergonomic design for the users. As a result, people uncomfortably do their journey from one place to another. Particularly, passengers comfort during leisure and relaxation is important. These are the motivation to make ergonomic analysis of Bangladeshi train passengers. Dhaka-Khulna intercity trains were considered for this work. The study of corresponding postures is not involved though few studies in different countries on activities performed during train travel were carried out with survey or observations [1, 2]. The study assured that the postures and the muscle activities of the erector spinae and trapezius muscles rely more on the activities performed than on the use of a specific type of chair. [3]. To use as inputs for car seat design, the activities performed and the associated postures adopted were recommended [4]. In this study the experienced comfort is not considered. To create a comfort experience, it is necessary to consider the behavior, the perception and also the abundance of users. The comfort of rides has been identified as one of the top criteria that affect customer's satisfaction with public transportation systems, and it has been shown that comfort is a significant consideration for passengers that use public transportation [5, 6 and 7].

The article created some insight in activities, posture and comfort of seated train passengers and the outcome of the study can be used to design peaceful seating in the industry of transportation [8].

The objectives of the work were

1. To select mainly performed activities and resembling postures of train passenger

2. To identify the duration of the activities and assess the comfort in respect of the performed activity.

2. Methodology

The observations were made from different trains with same types of second class shovon chair over 200 passengers using smart phone.

2.1 Activities and Postures Observation

During real train rides in Bangladesh the activities and postures of train passenger were observed. The observations were made in two different train with same types of second class shovon chair. A portion of the observed travelers performed a brief questionnaire to assess the comfort experience with respect to their performed activities.

2.1.1 Momentary observation

It was performed in order to get highest performed activities of broad group of passengers. Total 200 observations were used including 66 females and 134 males where 182 persons of 18–60 years and 18 persons of greater than 60 years. Smart phone was used to record the observation.

2.1.2. Longer observation

A few group of passengers (23 passengers) was observed for longer period of time to study durations of performed activities and variation of activities in one journey. The observation duration lasted almost 7-8 hours. The passengers' activity and postures were determined at the beginning of the observation, and after that real-time activity changes and little movements were recorded.

2.2 Coding Technique:

In Table 1, the coding technique for defining postures are shown. Each posture was represented by a set of five figures for seat contact and three for body part postures: e.g. 34111212. The first figure refers to the contact of the head, the second to the backrest, the third to the seat, the fourth to the feet, the fifth to the arm, the sixth to the head position, the seventh to the trunk position and the eighth to the legs [8].

Table 1 Coding Technique for positions

	i. Head contact	ii. Backrest contact	iii. Seat contact	iv. Foot Contact
1	Back	Upper	Back	Footrest
2	Side	Middle	Middle	Floor
3	No contact	Lower back	Front part	Wall

	v. Arm contact	vi. Head	vii. Trunk	viii. Legs
1	Seat	straight	straight	Parallel
2	Arm rest	forward	forward	Not Parallel
3	Table	sideward	sideward	Crossed
4	No contact	asymmetric	asymmetric	Bended
5			slumped	

Along with this eight figures, the following variables were also recorded:

- Ride characteristics: train, bogies
- Person characteristics: seat number, sex, age
- Main activities: Using laptop, listening music or using mobile phone, reading book/paper/magazine, talking with people, making a call, writing, staring, sleeping, eating /drinking, other activities.

2.3 Comfort Questionnaire

A comfort questionnaire was made over 50 passengers who responded to assess the passengers comfort experiences in combination with the activities performed. On a 10-point scale (from 10 = high to 1 = low), the passengers were questioned about their seat comfort experience with their performed activity.

3.0 Data Analysis

3.1 Instantaneous Observation Analysis

This observation was performed to pick the most common activities that occurred with highest frequency. Low frequency activities were excluded for the ease of further analysis. Therefore, the following analysis steps were performed:

- 1) Generation of frequencies of all activities recorded;
- 2) Selection of the four main activities with the highest frequencies;

3) Selection of the main postures resembling to the four main activities using the top frequencies of the body part posture and seat part contact codes combination. The codes are head position, backrest contact, back posture, buttock seat contact and footrest contact which represent the most important body parts and contact areas in relation to seat design. For reducing the probable combination, arm and leg postures were trimmed as observed other criteria appear more relevant than these two.[8]

4) Identification of top eight of postures by selecting the posture-contact codes.

The top eight posture code with maximum frequencies are as follows:

Table 2 Top 8 postures code with frequency

No	Posture code	Frequency
1	21211351	11
2	33111211	9
3	21321352	8
4	33121212	8
5	21211352	7
6	31111151	7
7	34311351	7
8	21121341	6

3.2 Duration observation analysis

The average duration of activities over the subjects are shown in the table 3

Table 3 Activities with average duration

Activities	Average Duration (min)
1. Staring	116.27
2. Sleeping	198.87
3. Talking	25.67
4. Listening music or using mobile phone	47.93
5. Reading book/paper	15.5
6. Eating or Drinking	18.21
7. Making a call	14.53
8. Using laptop or notepad	76
9. Writing	15
10. Others	26.57

3.3 Comfort questionnaire analysis

The average comfort score for the seat and for the top eight postures was determined, from the data using the similar codes for observation and questionnaire per passenger. In this case, the data amount was not enough large to do a fine analysis.

4.0 Result and Discussion

4.1 Activities instantaneous observations

The Fig 1 depicts the percentages of various activities from which four top activities are found that are Staring, Sleeping, Talking and listening music or using mobile phone.

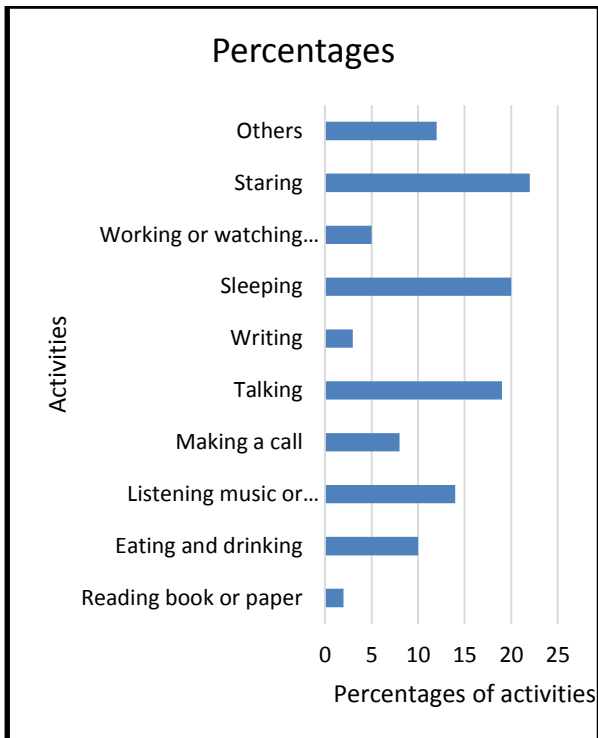


Fig 1 Percentages of activities

For the main activities staring, sleeping, talking and listening music or using mobile phone, the top eight most observed postures are shown in Table 4. Body part position were defined according to Groenesteijn [8] with addition to foot contact.

Table 4 Top eight of observed postures

	Body part position	Stick Diagram
1.	Head upright Trunk backwards Full seat contact Foot contact on floor	
2.	Head upright Trunk upright Full seat contact Foot contact on floor	
3.	Head forward Trunk upright Full seat contact Foot contact on footrest	

4	Head sideward Trunk backwards Full seat contact Foot contact on footrest	
5	Head forward Trunk backward Full seat contact Foot contact on floor	
6	Head sideward Trunk upright Full seat contact Foot contact on footrest	
7	Head sideward Trunk slumped Middle + Front seat contact Foot contact on floor	
8	Head sideward Trunk upright Full seat contact Foot contact on floor	

The posture with the head upright, the trunk backwards, full seat contact and foot on the floor was found in all four activities. In longer observation, sleeping was the activity with highest duration and the second highest is staring.

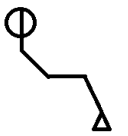
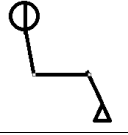

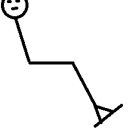
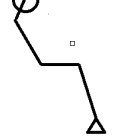
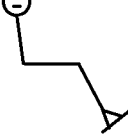
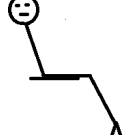

4.2 Resembling Postures and Perceived Comfort for Main Activities

Out of the responses of 50 (13 female and 37 male) passengers who completed the questionnaires, 20 subjects were staring, 11 subjects were sleeping, 2 subjects were listening music and 8 subjects were talking.

Table 4.2 shows the observed posture activity combinations and the corresponding comfort scores. Discrete postures were observed for each activity and comfort scores varied in respect of to the combination of posture and activity. Here in the first posture, staring,

sleeping, talking and listening music or using phone possess comfort 60%, 60%, 70% and 50% respectively. In the second posture staring, sleeping and listening music or using phone have comfort only 40%, 50% and 60% respectively and the rest can be explained as same.

Table 5 Main activities, corresponding postures and comfort score

postures	staring	sleeping	talking	Listening music or using mobile phone
	6	6	7	5
	4	5		6
	7	6	7	
	6.5	5	4	
	6	5		5
			8	
		6		5.5
			5	

5.0 Conclusion

The goals of this study were obtained eventually. Four mainly performed activities: staring, sleeping, talking and listening music or using mobile phone were found. Associated with these four activities, eight different

postures were found based on the variations in head position, back posture and seat pan contact. The posture with the head upright, the trunk backwards, full seat contact and foot on the floor was the observed posture that occurred in all four activities. Sleeping was the activity with longest duration and writing was the activity with shortest duration. The comfort in respect of the performed activities and postures were also determined. The comfort score was highest for talking with the posture of head sideward, trunk slumped, and middle + front seat contact, foot contact on floor.

The research work will be helpful for Bangladesh Railway (BR) to evaluate train environment considering passengers' performed activities, postures and construct ergonomically fit passenger train seat assessing comfort score. In this study along with the described postures and activities, more specification is needed to provide recommendations for train seats and train interior design. The manufacturer should produce train seat in such a manner that it can give comfort to the lion's share of the population. The study will be helpful for providing more features according to performed activities and corresponding postures. The study shows longest duration for sleeping and so special concern should be given for this activity.

6.0 Recommendations

A movable situation often influences the chosen activities. Vibrations and sudden movements of the train have an influence on the comfort feeling of passengers. As the data of this study was collected in running trains, there may be some biasness with vibrations and movements. So the recommendation is to consider the necessary calculation for vibration and movement. There may have some potential activities that passenger want to perform which should be explored. The train seat should be evaluated according to human anthropometry to check if there is any mismatch.

REFERENCES

- [1] Lyons, G., Jain, J., & Holley, D. (2007). The use of travel time by rail passengers in Great Britain. *Transportation Research Part A: Policy and Practice*, 41(1), 107-120.
- [2] Thomas, J. A. P. K. (2009). The social environment of public transport
- [3] Ellegast, R. P., Kraft, K., Groenesteijn, L., Krause, F., Berger, H., & Vink, P. (2012). Comparison of four specific dynamic office chairs with a conventional office chair: impact upon muscle activation, physical activity and posture. *Applied ergonomics*, 43(2), 296-307.
- [4] Kamp, I., Kilincsoy, Ü., & Vink, P. (2011). Chosen postures during specific sitting activities. *Ergonomics*, 54(11), 1029-1042.
- [5] Andaleeb, S. S., Haq, M., & Ahmed, R. I. (2007). Reforming innercity bus transportation in a developing country: A passenger-driven model.

- [6] Disney, J. (1998). Competing through quality in transport services. *Managing Service Quality: An International Journal*, 8(2), 112-118.
- [7] Viggiano, C., Koutsopoulos, H., & Attanucci, J. (2014). User Behavior in Multiroute Bus Corridors: Analysis by a Web-Based Survey. *Transportation Research Record: Journal of the Transportation Research Board*, (2418), 92-99.
- [8] Groenesteijn, L., Hiemstra-van Mastrigt, S., Gallais, C., Blok, M., Kuijt-Evers, L., & Vink, P. (2014). Activities, postures and comfort perception of train passengers as input for train seat design. *Ergonomics*, 57(8), 1154-1165.

An Experimental and Simulation Study of Larger Volume Micro discharge for the Realization of Microplasma Based Reactor Applicable to Fuel Reforming and Material Processing

R. K. Das^{1,*}, Dr. A.Z.A Saifullah²

¹Department of Mechanical Engineering, Chittagong University of Engineering & Technology, CTG-4349, BANGLADESH

²Department of Mechanical Engineering, International University of Business Agriculture & Technology, BANGLADESH

ABSTRACT

Microhollow cathode discharge (MHCD) and microhollow cathode sustained discharge (MCSD) are two particular types of microdischarge configurations that produce stable glow plasmas at high pressures. Larger volume of higher density diffuse plasma in argon at various pressures is generated experimentally by MCSD in a split third electrode configuration. This enlarged volume microplasma serves as a source of high temperature electrons, ions and other excited species. Micro plasma reactor technology either for fuel reforming or material processing is based on using the energy of the high temperature electrons and other charged particles. Owing to their inherent difficulty in conventional diagnostics a detailed study on MHCD or MCSD relies on numerical simulations. This work describes the experimental procedure of generating MCSD with split third electrodes, realization of microreactor based on this enlarged volume microdischarge and numerical simulation of MCSD using a 2D fluid model to determine the properties of this microdischarge.

Keywords: Microplasma, Microreactor, MHCD, MCSD, Split electrode.

1. Introduction

Plasma state of a matter is considered as the fourth state of matter, which has some unique properties to distinguish it from three other states solid, liquid and gases. Interestingly, much of the visible matter in the universe, viz., stars, all visible interstellar matter, is in the plasma state comprising 99% of the universe, both by mass and by volume. Since its first discovery in 1879 by Sir William Crookes [1], plasma has been produced in a variety of discharge configuration with different mechanism including dielectric barrier (DBD) discharge, microwave discharge, radio frequency (RF) discharge, direct current (DC) glow discharge etc. In a laboratory, one of the simplest ways to produce plasma is applying an electric field to a neutral gas. Plasma discharges can be categorized mainly of two parts thermal plasma and non-thermal plasma. Thermal plasmas are the plasmas where electron temperature T_e , ion temperature T_i and neutrals temperature T is in thermal equilibrium and electron temperature is considered as almost the same with ions and neutrals temperature. In non-thermal plasma, electrons temperature T_e is much higher than the ions temperature and neutrals temperature. High pressure arc discharges are the common example of the thermal plasma and low pressure glow discharges are the example of non-thermal plasma or cold plasma. New types of plasma discharges namely microhollow discharges has attracted great interest among the researchers. The properties of microdischarges fall in between arc discharges and glow discharges. Like arc discharges, it can be operated at high pressure but the electron temperature is much higher than the other particles which make it more likely to be a non-thermal glow discharges. For that reason this microdischarge is referred as 'high pressure glow discharges' [2]. Non equilibrium glow discharges can be achieved by various approaches such as microhollow cathode discharge

(MHCD) [3]. Three most important characteristics of the MHCD are - high pressure, high energy electrons and larger surface to volume ratios. High surface-to-volume ratio in MHCD hole imparts excellent thermal management and mixing characteristics that help maintain homogeneous, isothermal reacting volumes for fuel reforming. Indeed, novel uses of MHCD have been proposed in enormous application such as propellant gas preheating for microplasma thruster [4], ignition assistance [5], hydrogen generation for fuel cell power [6], hydrocarbon reforming, source of UV and eximer radiation [7] etc. The use of MHCD has also been explored as flow reactor by Hsu and Graves [8], where they have shown that flowing of molecular gases through the MHCD was found to induce chemical modifications by molecular decomposition processes. The volume of the MHCD is very small to use in industrial purposes. To increase the volume of the high pressure glow discharge, researchers has developed another discharge namely microhollow cathode sustained glow discharges where the discharge is sustained by the plasma cathode which act as a source of electron in the discharge. This kind of large volume discharge can be used for fuel reforming and gas treatment purpose as well. Conventional technique for fuel reforming and gas treatment process includes steam reforming by oxidations. Thermal oxidation requires heating of the ambient gas and raises the capital cost for cooling system. Main advantage of non-thermal plasma is the presence of high energy electrons which reacts with the fuel particles and causes significant reforming. Residence time for the gas is very short in case of nonthermal plasma with low power requirement. Our experimental study approaches to the enlargement of the high pressure hollow cathode sustained glow discharges by employing split electrodes replacing single planar third electrode (Fig.1.1) and eventually applies this large

* Corresponding author. Tel.: +88-01813360701

E-mail addresses: ratan.kumar@cuet.ac.bd, rataneviulsan@gmail.com

volume glow in fuel reforming and gas treatment processes. As a microplasma reactor either for fuel reforming or material processing, microdischarges serve as sources of high energy electrons, radicals and ions. In order to improve the results in all these application fields, a good insight into the discharge processes is desirable. So it is very important to know the properties of plasma parameters such as electron density, atomic and molecular ion densities, excited species (metastables) densities, electron temperature, gas temperature etc.

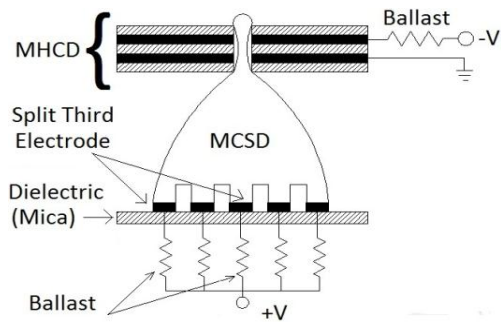


Fig.1.1 MHCD with split third electrode

However, the reduced dimensions, high operating pressure, and high power density of microdischarges make conventional diagnostics of the microplasma for experimental characterization very complicated and challenging. Given the experimental challenges, computer simulations provide a valuable alternative for studying microdischarges. While MHCD devices have been studied numerically over the recent decade, understanding of the fundamental mechanisms of MCSDD that generate larger volume microplasmas has lagged. Early works paid little attentions to the MCSDD with single third electrode configuration and plasma properties like electron, ion and excited particles densities in MCSDD with single planar third electrode are reported in a very few simulation studies carried out by Pitchford and collaborators [9]. However, they didn't mention about gas temperature and electron temperature in their studies which are also crucial parameter for microchemical reactor [2]. Here numerical investigation of MCSDD and its sustained discharge MCSDD in argon with split third electrodes (Fig.1.1) is also attempted to estimate the discharge properties by using a two-dimensional axis-symmetric, self-consistent multi-species, multi-temperature, continuum (fluid) model. Predicted results are compared to available experimental and numerical data.

2. Experimental Setup and Numerical Modeling

Fig.2.1 shows the schematic diagram of the experimental setup which consists of vacuum system, electrical measurement system, optical measurement system and gas flow system. Vacuum system consists of vacuum chamber, vacuum pump, pressure sensor. Discharge setup was placed inside the vacuum chamber. Electrical measurement system consists of high voltage dc power

supply, electrical circuits, and digital multiple purpose multimeter. Optical measurement system consists of digital single lens reflex camera which is placed firmly on the steady stand, as macro lenses are very sensitive and small displacement may cause change the magnification of the different discharges. We have used 105 mm Macro lens with lowest F number 2.8 for proper focusing. During capturing the pictures dark environment was provided to see the actual visual characteristic of the plasma discharge and physical scale length was measured before capturing the pictures. Gas flow system consists of gas chamber, gas flow tubes, gas flow meter.

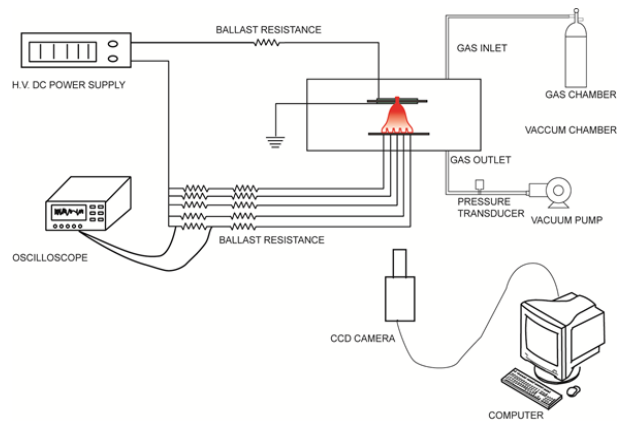


Fig.2.1 Schematic diagram of the experimental setup

Figure 1.1 presents a schematic diagram of MCSDD configuration with a split third electrode and the corresponding discharge structure. MHCD layer placed on the top of the system consists of Nickel electrodes of 0.2mm thickness pasted on both sides of 0.2mm thick mica dielectric material. A cylindrical hole of 0.3mm diameter is drilled mechanically through the three layers of MHCD configuration. The third electrode is placed 5mm away from the MHCD configuration. The third electrode which is placed 5mm away from the MHCD layer is split into 5 rectangular pieces. Each split electrode has a surface area of 0.5 mm × 3 mm and is separated by 2 mm. Total span of the third electrode is about 10mm wide.

The number of split electrodes and the separation between them can be adjusted so that a total span of discharge region can be controlled accordingly. The sharp edges of each split electrode is slightly rounded in order to avoid a high local electric field which can cause a non-uniform glow discharge on the third electrode surface. One of the MHCD electrodes facing with the third electrode is always grounded as shown in Fig. 1.1 while the voltages on the top-layer electrode and the third electrode are biased with an opposite polarity of maximum 2.5 KV provided by dc power supply. The third split electrodes are connected with an individual 100 KΩ ballast resistor and 220Ω current-view resistor in series. Current through each split electrode is measured by a digital oscilloscope. The entire setup is placed in a vacuum chamber which provides desired

ambient pressure and the chamber is replenished in every run. A high speed CMOS camera (Photron SA3 120K) and digital hand-held camera are used to visualize discharge structures. Numerical simulation of non-equilibrium glow discharge plasma of an MCSD is performed with the VizGlow plasma modeling tool [10]. The model is based on a 2-D axisymmetric, self-consistent, continuum fluid description of the plasma. Species conservation, electron energy, and gas energy equations are solved in the gas, while Poisson's equation for the electrostatic potential is solved in the gas and in the dielectrics. A detailed description of the governing equations solved is described in Ref. [10]. An MCSD is generated in argon at pressures of 60 Torr and 300 Torr. The argon species involved in the simulation include electrons (e), atomic and dimer ions (AR_+ and AR_{2+}), and atomic and dimer metastables (AR^m and AR_{2m}). The reactions used in this model with rate coefficient data from Ref. [11].

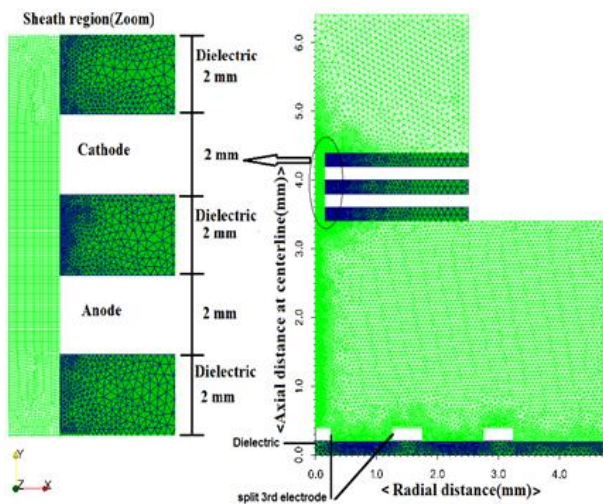


Fig. 2.2 Schematic of the MCSD with split third electrode and computational mesh.

Fig. 2.2 shows the computational mesh and the cylindrically symmetric geometry of the MCSD with split multiple third electrodes used in this study. The same experimental geometry is used for numerical simulation. The dimensions are identical to the dimensions of the experiment shown in Figure 1.1 except the dimensions of the boundary of the computational domain. The mesh consists of about 28,765 cells of which about 22,917 are in the gas subdomains and about 5,848 are in the dielectric subdomains. To obtain a stable numerical solution, first the MHCD is run with a time step of 5×10^{-12} s till steady state is reached with the third electrodes turned off. Then, the third electrodes are tuned on and a smaller time step of 2×10^{-12} s is found to be necessary to reach a combined steady state for the MCSD

3. Result and Discussion

The optical images of MCSD at different pressures with split third electrodes captured by high speed digital

camera have been demonstrated. The pressure effect is illustrated in Fig. 3.1. For anode third electrode case at 60 Torr pressure, MCS discharge starts at very low third electrode current connecting all 5 split electrodes with MHCD. MHCD current was fixed at 2mA and third electrode current increases from lower value to higher value. At 7mA of third electrode anode current, suddenly the glow disappears at the gap between MHCD and third electrode. In this case discharge appears at the MHCD cathode side and photogenic glow like discharge appears from each split electrodes. At the current level more than 7mA, this glow from the third electrodes again connect to the MHCD and large volume bulk discharge form in the gap between MHCD and split third electrodes. For anode split third electrode cases, denser plasma glow discharge forms in all current levels at 300 Torr cases. At 1mA of anode current discharge connects to three electrodes and at 6mA of current it connects to all the 5 split electrodes. With increasing anode current, denser and brighter plasma forms in the gap without some major changes in the structure. At very high applied electric field this glow like discharge will transfer to the arc regime. However as shown in the Fig. 3.1, it is clear that much larger volume of MCS discharge can be produced by employing a split third electrode than the single third electrode case as presented in Ref. [12]. In addition to the enlarged discharge volume it is expected to be possible with more number of finer electrodes that plasma volume, density and its location can be controlled by addressing the desired split electrodes or by changing an arrangement of the split electrodes. However with a single third electrode this controllability of the discharge is very limited and only plasma density can be adjusted by MCSD current. Fig. 3.2-3.9 shows Spatial and axial profile of electrostatic potential, Electron, monomer ion (AR^+), dimer ion (AR_2^+), and metastable species (AR^m and AR_{2m}) population at 60 Torr and 300 Torr respectively. The potential profile (Fig. 3.2) explains that the MCSD is a positive column expanded outside the MHCD hole due to a weak electric field in the gap between the MHCD and the third electrode.

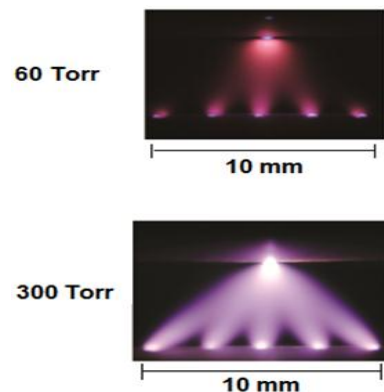


Fig. 3.1 MCSD with 10 mm span 5 split electrodes biased as at 60 Torr and 300 Torr pressure.

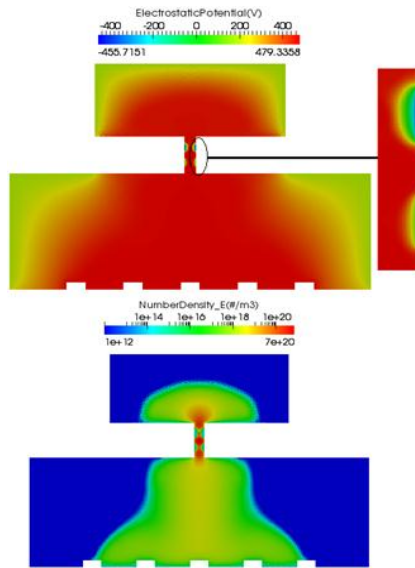


Fig. 3.2 Spatial profile for electrostatic potential and electron number density at P=60 Torr

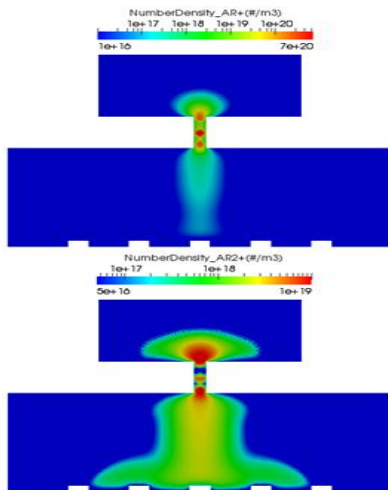


Fig.3.3 Spatial profile for monomer ion (AR^+) and dimer ion (AR_2^+) number density at 60 Torr

The sheath area is confined inside the MHCD hole because of the dielectric layer on the top surface. Electric field is more extended between MHCD hole and third electrode in split electrode case which is more favorable for larger expansion of plasma species. The peak density is as high as $1 \times 10^{20} \text{ m}^{-3}$ at 60 Torr near the exit plane of the MHCD and on-axis due to the expansion of the plasma leaving the MHCD. The main mechanism of creation of electrons, in the zone of radial expansion of the MCS, is the step-wise ionization, and the losses of electrons are via diffusion in radial direction and dissociative recombination. The highest monomer ion (AR^+) density is about $\sim 1 \times 10^{20} \text{ m}^{-3}$, peak dimer ion (AR_2^+) density is about $\sim 1 \times 10^{19} \text{ m}^{-3}$, peak value of metastable atom (AR^m) density is about $\sim 10^{21} \text{ m}^{-3}$ and peak dimer metastable (AR_2^m) density is $\sim 10^{17}$ about occur along exit hole of MHCD on the centerline the MCS discharge at pressure $p=60$ Torr.

Significant presence of excited species (AR^m and AR_2^m) is useful in the sense that they are considered as important constituent for plasma assisted ignition [9]. At 60 Torr, peak value of bulk temperature (Fig.3.5) is 1422K occurs along the centerline of the cathode region in the MHCD and negligible bulk temperature (peak value 320K) is observed in the MCS. It shows consistency in a recent measurements of the gas temperature in Ar/O₂ mixtures in the MCS region where limited gas temperature is observed [13]. Peak electron temperature (Fig.3.6) is observed in the cathode sheath region within the hollow, which is in the order of several tens of eV. Other parts of the discharge maintain the electron temperature in the order of ~ 1 eV. In an experimental observations of the emission from high-lying excited states of ionic species in MDs [14], such high electron temperatures are expected, which is in again good agreement with our results. Experimental result shows that plasma is extended over five split electrodes (Fig.3.1) without ensuring which species are responsible for plasma expansion. From simulation it is clearly seen that electron is the most responsible particle for extended plasma near third split electrodes. Dimer ion and metastable atom also partially contribute to the expansion of larger volume plasma near split third electrode. Plasma densities are constant in the middle of axis for a particular species at both 60 Torr and 300 Torr (Fig.3.7). It is observed that number densities of all plasma species on the axis of MCS increased at higher pressure (Fig.3.8-3.9) due to comparatively stronger electric field. Electrons are likely to diffuse more along the dielectric surface outside the MHCD hole at higher pressure. Other interesting phenomena is that metastable species especially dimer metastable has been significantly expanded near split third electrode with an increase in number densities at higher pressure. Peak values of electron, atomic and molecular ion, atomic and molecular excited particles number densities exceed $3 \times 10^{20} \text{ m}^{-3}$, $2 \times 10^{20} \text{ m}^{-3}$, $1 \times 10^{20} \text{ m}^{-3}$, $2 \times 10^{21} \text{ m}^{-3}$ and $5 \times 10^{18} \text{ m}^{-3}$ respectively at 300 Torr.

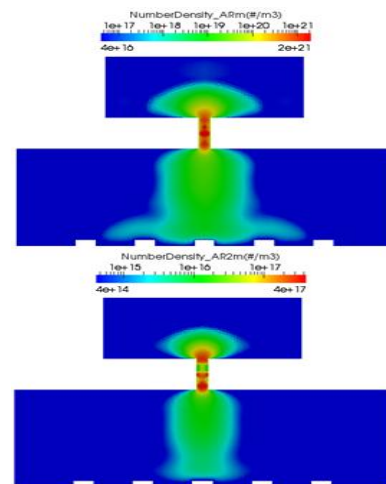


Fig.3.4 Spatial profile for metastable species (AR^m , AR_2^m) number density at 60 Torr

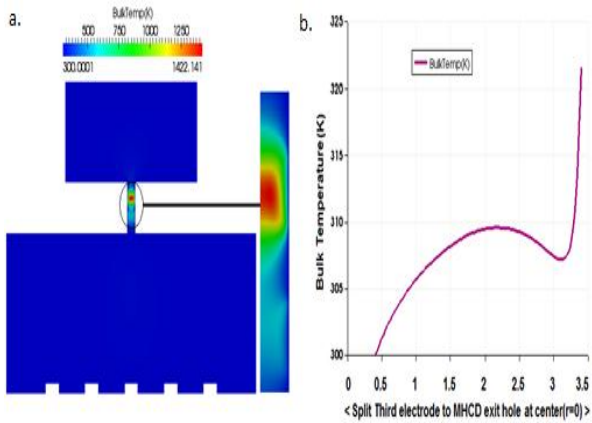


Fig.3.5 Spatial profile for a) bulk temperature and b) corresponding axial profile in the sustained discharge at P=60 Torr

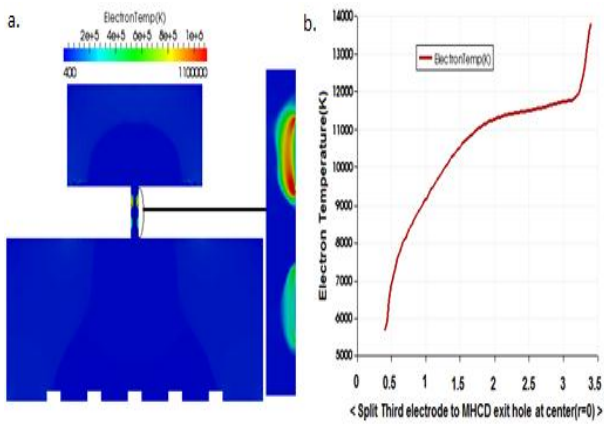


Fig.3.6 Spatial profile for a) electron temperature at 60 Torr and b) corresponding axial profile in the sustained discharge at 60 Torr

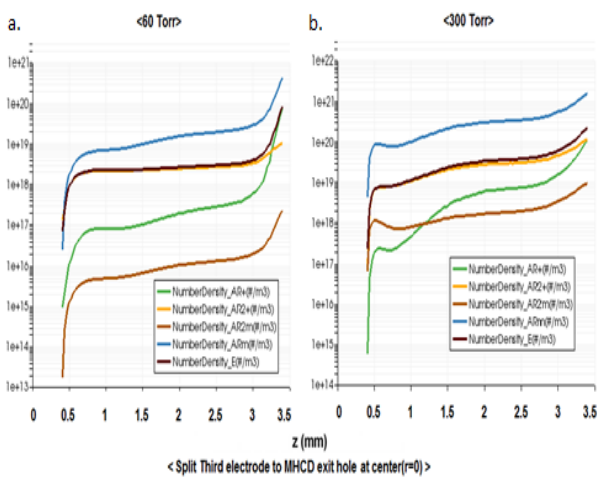


Fig.3.7 Axial distribution of a) different plasma species number density in MCSD at 60 Torr and b) different plasma species number density in MCSD at 300 Torr.

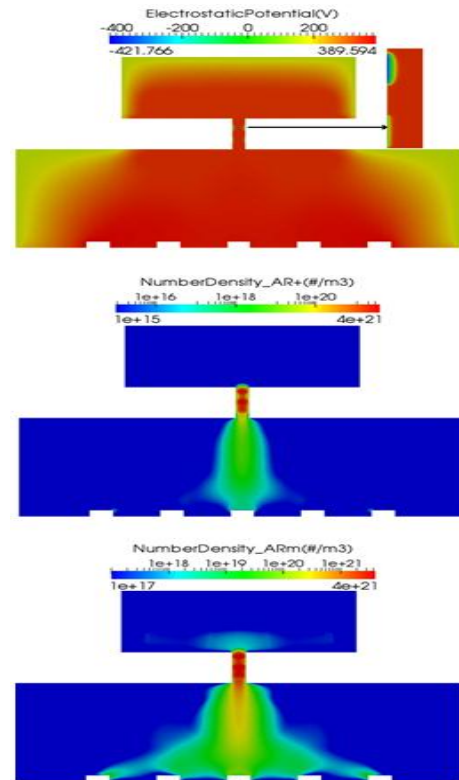


Fig.3.8 Spatial distribution of potential and AR^+ and AR^m number densities for MCSD with split third electrodes at 300 Torr.

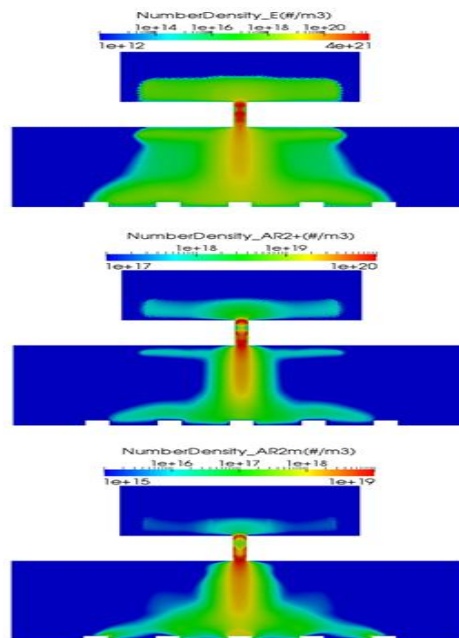


Fig.3.9 Spatial distribution of electron, AR_2^+ and AR_2^m number densities for MCSD with split third electrodes at 300 Torr.

4. Conclusion

In this article, a unique approach has been demonstrated that a larger volume glow discharge at atmospheric

pressure is possible with MCSD configuration which has split third electrodes. This large volume non equilibrium plasma discharge can be used as a reactor to reform fuel and gases. Simulation results are presented for MCSD with split third electrode which shows that expansion of plasma is larger than that of MCSD with single planar third electrode cases and confirms the species which are responsible for extended plasma near split third electrode which is not clear from experiment. Charged species densities of order ($10^{19} \sim 10^{21}$) m^{-3} and metastable species densities of order ($10^{18} \sim 10^{21}$) m^{-3} are predicted in the microhollow cathode discharge (MHCD) for the conditions investigated. In the sustained discharge (MCSD), charged species densities of order ($10^{16} \sim 10^{20}$) m^{-3} and metastable species densities of order ($10^{16} \sim 10^{21}$) m^{-3} are predicted for the conditions investigated.

REFERENCES

- [1] William Crooks. Radiant matter, a resume of the principal lectures and papers. *Technical report, Royal Society of London and British Association for the Advancement of Science, James W. Queen & Co.*, 1879.
- [2] R. M. Sankaran. High pressure microdischarges as microreactors for materials applications, *Ph.D Thesis*, California Institute of Technology, 2004.
- [3] K. H. Schoenbach, A. El-Habachi, W. Shi, and M. Ciocca. High-pressure hollow cathode discharges, *Plasma Sources Science and Technology*, 6:468, 1997.
- [4] Thomas Deconinck, Shankar Mahadevan, and Laxminarayan L. Raja, "Simulation of a Direct-Current Microdischarge for the Micro Plasma Thruster", *IEEE Transactions on Plasma Science*, Vol. 36, No. 4, August 2008.
- [5] J. Shin and L. L. Raja, "Microdischarge-assisted ignition of dielectric barrier high pressure glow discharges," *Appl. Phys. Lett.*, vol. 88, no. 2, pp. 021502-1–021502-3, Jan. 2006.
- [6] Belen Sarmiento, J. Javier Brey, Inmaculada G. Viera, R. Gonzalez- Elipe, Jose Cotrino and Victor J. Rico. "Hydrogen production by reforming of hydrocarbons and alcohols in a dielectric barrier discharge", *Journal of powersources*, 169:140-143, 2007.
- [7] R.S. Besser, P.J. Lindner, "Microplasma reforming of hydrocarbons for fuel cell power", *Journal of Power Sources*, 196: 9008– 9012, 2011.
- [8] D. D. Hsu, D. B. Graves, *J. Phys. D: Appl. Phys.*, 36, 2898, 2003.
- [9] K. Makasheva, G. J. M. Hagelaar, J.P. Boeuf, T. Callegari, and L. C. Pitchford, "Ignition of microcathode sustained discharge," *IEEE Trans. Plasma Sci.*, vol. 36, no. 4, pp. 1236–1237, Aug. 2008.
- [10] See <http://esgeetech.com/products/vizglow/> for VizGlow, 2017 Esgee Technologies.
- [11] T. Deconinck and L. L. Raja, "Modeling of mode transition behavior in argon microhollow cathode discharges," *Plasma Processes Polym.* 6,335–346 (2009).
- [12] H. Park, T. Lee, K. W. Park, H. K. Baik, S. J. Lee, K. M. Song, Formation of large-volume, high-pressure plasmas in microhollow cathode discharges, *Applied Physics Letters*, 82:3191, 2003.
- [13] J F Lagrange, N Sadeghi, M Touzeau, G Bauville, B Lacour and V Puech, "Gas temperature measurements in a microcathode sustained discharge in oxygen", *Gaseous Electronics Conf (Columbus, Ohio, USA, October2006)*.
- [14] C. Penache, M. Miclea, A. Brauning-Demian, O. Hohn, S. Schossler, T. Jahnke, K. Niemax, and H. Schmidt-Bocking. Characterization of a high-pressure microdischarge using diode laser atomic absorption spectroscopy. *Plasma Sources Science and Technology*, 11:476-483, 2003.

NOMENCLATURE

- AR^+, AR^m : Molecular ion of Argon
 AR_2^+, AR_2^m : Dimer ion of Argon
 eV : electron temperature unit, electron volt
 P : Pressure, Torr
 T : Temperature, K

Harnessing the Ocean's Wave Power for Bangladesh's Dynamic Coastal Areas

*Md. Mahbub Hasan**, *Md. Ashfaqul Islam*, *Sheikh Ahmad Imtiyaz*, *Md. Akramul Alim*, *Md. Momtazur Rahman*, and
Md. Mahmudul Hasan

Department of Electrical & Electronic Engineering, Bangladesh Army University of Engineering & Technology, Qadirabad
Cantonment, Natore-6431, BANGLADESH

ABSTRACT

The current energy crisis needs to be solved through renewable and clean energy sources. Now-a-days, the energy transformation technologies from oceanic waves has craved large attention. An extremely promising source of energy exists in the world's oceans. Many energy transformation systems have been introduced to transform the mechanical force of oceanic wave into electrical power. Ocean energy inhabits in the shapes of wave, marine currents, tidal, salinity and fervent (temperature gradient). This research finds out the flourished electric technologies for grid power enhancement of various offshore wave energy transformation devices. The experimental outcomes and simulations for introduced modified inverter technology are submitted. The mentioned Ocean Wave Energy Converter craves lesser construction area and is guileless to conduct. The electrical conjunction configurations for enhancing the electric power of the multi wave energy transformation devices are flourished by applying the most feasible lowcosts grid interface electrical technologies based on power electronics.

Keywords: Ocean wave, Buoying force, Wave energy converter, Offshore wave power, Grid enhancement.

1. Introduction

Keeping pace with the accelerated development of worldwide economy, the decline of energy, like as coal, oil and natural gas, is becoming more and more dangerous and particularly in current years it is seen that energy demand has been befalling. Among many other sources of renewable energy ocean wave energy is that kind of renewable energy which empowers a titanic potential which may contribute to the globally increasing requirement of power [1]. An essential characteristic, high density which places ocean wave energy the highest one among the renewables. For emerging electrical power from the ocean encircle wave power, tidal power and ocean thermal energy transformation are the most well flourished technologies [2] which have been implemented and inflicted for years. Since the wave energy industry is yet in R&D [1], in order to make wave energy an economically serviceable technology there is much that can be versed from the adeptness of developers in allied industries. In the wind industry, for instance, various generic turbine dynamics of large-scale dominion wind turbine schemes [3], as well as the potentials of large-scale wind farms. For calculating power output at a dynamic installation position corresponding generic designs for ocean wave energy converters can be used [2] from which wave energy researchers, developers, investors and consumers can be vastly benefited.

For conducting wave energy technology there can be seen various compelling controversies and they are:

Wave energy belongs high power density [2] and for this it is one of the most downcast cost renewable energy generation process. Solar and wind energy are less unpredictable than the wave energy [3], delivering a better possibility of being transmitted to an electrical grid system. For generating electricity the transformation

of ocean wave energy to electrical energy is regarded to be one of the most environmentally efficacious ways; hence it doesn't render any kind of extravagance to be reserved or annihilates the environment. Wave energy researchers, developers or investors locate the wave energy devices far away from the shore (offshore) that they are commonly not noticeable. While propagating wave power devices there can be found below challenges:

For transforming wave energy to electrical energy, continuous motion [4] of waves is needed. The wave power can be achievable at inefficient speed and elevated forces. The movement of forces is not in solo approach. Supreme speeds [3] and a constant input are generally required for operating an electric generator. Storm damage and saltwater deterioration are needed to be endured by the wave power converter devices. Wave power converter's costs, installation & observance cost and electricity distribution costs are considered as total cost for converting wave energy to electrical energy.

Wave energy researchers and developers have been revealing a number of Wave Energy Converter (WEC) technologies [5,6] for several location patterns with various performing methodology. This paper is embodied as follows. Section 2 represents why ocean wave power can be an alternative for Bangladesh. Section 3 presents a background about concept of production of ocean wave energy. In section 4, the classification of wave energy converters will be discussed. Section 5 represents how wave energy can be extracted and implemented with power or national grid. Section 6 presents circuits & simulations for wave energy converters. Finally, concluding outlooks will be given in section 7.

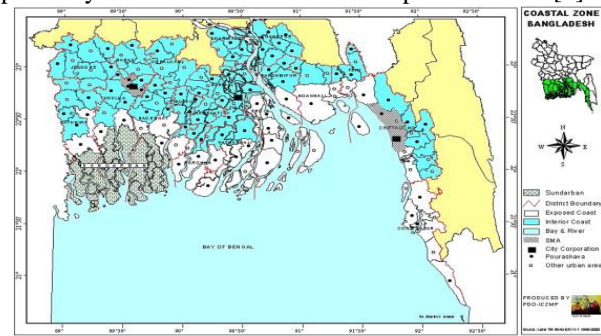
* Corresponding author. Tel.: +88-01945955640

E-mail addresses: xsobuz@outlook.com

2. Why Ocean Wave Power can be an Alternative Power Source of Bangladesh

Tides in Bangladesh coast hatch in the Indian Ocean. It penetrates the Bay of Bengal through the two submarine ravines, the 'Swatch of No Ground' and the 'Burma Trench' and thus takes place very near to the 10 fathom adumbration line at Hiron Point and Cox's Bazar respectively at about the same time (As-Salek and Yasuda, 2001). Outstretched shallowness of the north-eastern bay provides rise to partial repercussion there by rising the tidal range and the abrasion distortions concurrently. The geomorphology [7] of the coastal side plays a very significant figure in tide propagation from the coastline towards inland. Tidal waters go longer distances on the plain land with low surface slopes compared to plain land with medium to steeper slopes. Coastal flooding from the tide is straight away influenced by the variation in elevation and surface form. For that reason, there is a clear connection between geomorphology [8] and tidal water altitude. The higher the altitude of the surface form and steeper the slope, the lower the percolation of tidal waters inland and vice versa. The coastal morphology of Bangladesh is ruled by: (i) a boundless network of rivers; (ii) an abundant discharge of river water heavily encumbered with sediment; (iii) a big number of off-shore islands and sand bars; (iv) the Swatch of No-Ground coursing NE-SW partially across the continental shelf about 24 km south of the Bangladesh coast; (v) a funnel sized, shallow and wide estuary; (vi) a lightly sloping wide continental shelf; (vii) a confined strip of coastal landforms fronting hill ranges and (viii) strong tidal operations. The Sandwip channel is known for funnel shape, which causes a high revelation of the tidal wave towards the upper end of the channel. The triangular shape [7] at the top of the Bay of Bengal helps to funnel the sea water pushed by the wind towards the coast and causes further amplification of the tidal levels. This is generally what happens in the amplification of tidal levels on the Bangladesh coast [7]. The tidal waves associated to the class of long gravity waves. In deep water, the long gravity wave circulates [6] much faster than the speed with which the weather system travels. So, the weather system cannot keep up with the water wave and hence cannot convey any momentum. But on the mainland shelf, where the water depth is smaller, the gravity wave voyages much slower than in deep water and a noteworthy transfer of energy from the weather system to the water wave transpires by resonance. Therefore, the tides which have zero amplitude in the deep water, quickly forms up to several meters amplitude on the shallow inland shelf [8]. As this enlarged water level approaches the coast it creates heavy wave. Normally these waves washed away with time. But we have to account a fact that these waves carry a good number of energy. As Bangladesh is currently suffering from energy crisis our resources are very limited to our demand. If we use this wave energy & convert it to electrical energy then it can be the new

power source of Bangladesh besides the conventional power system. As this is a renewable power source [8] it



will not affect our environment & we can gain endless power by harnessing our Bay of Bengal ocean water.

Fig.1 Coastal Zone of Bangladesh [7]

3. Concept beneath Ocean Wave Energy Procreation

3.1. Energy from Ocean Wave

Ocean waves represent an affluence of renewable energy which is one of the green energy sources. Ocean wave's kinetic energy is explored as the circularly [4] roaming particles of the ocean waters and the high particles with respect to the plane water margin are considered to have a dynamic energy, the energy flux is instantaneously affiliated with the period and the waves' square of amplitude as in (1)

$$\Phi_w \propto h^2 T$$

$$\text{Therefore, } \Phi_w = kh^2 T(1)$$

Where wave energy flux is represented by Φ_w , wave amplitude is represented by h and T indicates period of wave. k is irreversible. 50 kW energy oversteps for every meter breadth of the wave, when enormous amplitudes and lengthy periods are possessed by the waves [9]. The ocean wave is able to conjectural as a sinusoidal wave. The sea wave power can be typically illustrated by equation (2) from this approximation,

$$P = \rho_{sea} g 2 h^2 T / (32 \pi)(2)$$

Where, the power of wave is indicated by P , seawater density (1025 kg/m^3) is presented by ρ_{sea} , g indicates gravity, period is T and wave height is represented by h [10]. The energy which is acquired from this power can be transformed to several forms of energy to procreate, for instance, electricity.

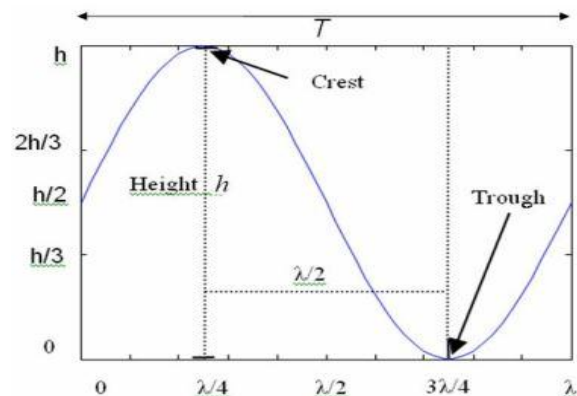


Fig.2 Approximation of sinusoidal wave for ocean wave [3]

The sinusoidal wave movement of the ocean waves is imitated consummately by a buoyant, if we know the ordinary wave behavior [9], then we can calculate the turnover of a buoyant object (Fig. 3). The conjectural utmost turnover can be computed from equation (3)

$$\theta = \tan^{-1}(h/(\lambda/2))^0(3)$$

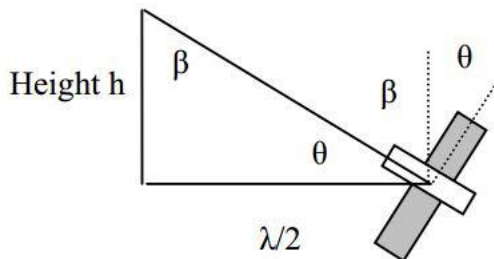


Fig.3 Turnover angle of a buoyant system, θ and approximation via a line from the peak to the channel. The perpendicular state is taken as the cornered relevance [4]

3.2. Energy of water-flourished rapidity & tides

Current energy acts beneath the identical principles as hydraulic embankments [5] where the kinetic energy of one-way movement of bodies of water revolves a turbine, which, severally, transforms the kinetic energy into electrical energy via a cyclic generator.

Ocean and tidal are the two principal forms of water-based currents. Flowing in an unseparated approach and force is the tendency of ocean currents. These samples are influenced by water salinity, wind and temperature by which currents can drift in one channel. Gravitational [10] pull from the moon and sun controls tidal currents. They are found nearby shore and are directional because of being low and high modeled tide.

Large quantities of energy can be gained from comparatively small devices in the ocean which exposes in high power density of water [4]. On the other hand, it would need a wind turbine three times the volume of an ordinary-sized underwater turbine to procreate equal quantity of power from wind that can be disseminated from water.

The equation for the power generation of a turbine harnessing the kinetic energy of tidal currents can be deliberated as,

$$P = \zeta \rho_{sea} A V^3 / 2 \quad (4)$$

Where P indicates power generated in watts, turbine efficiency is indicated by ζ , seawater density (1025 kg/m^3) is represented by ρ_{sea} , sweep area of turbine (in m^2) is presented by A and velocity of flow is determined by V . From equation (4) total power originated is proportional to the cube of the flowing velocity [9].

Using several processes such as tidal barrages the energy of water periphery altitudes during tides can also be seized [5]. As tide's frequency is emblematically twice a day and the season of a tidal wave would be 12.5 hours that makes the similar power given by vast. Pretending identical ocean wave and tidal wave

altitudes, the power companioned could be 5 to 10 thousand times larger with tides than ocean waves.

4. Alignment of Wave Energy Conversion Systems (WEC)

Many wave energy conversion systems (WECS) have been invented through these years, only a small portion has been evaluated and tested. Besides, only a small amount has been examined at sea, in ocean waves, rather than in laboratory wave tanks [11, 12]. A WECS may be installed in the ocean in various feasible situations and locations. It may be made shifting or engrossed completely in the sea offshore or it may be lying on the shore. A WECS on the sea bed may be completely sunken, it may prolong above the sea surface, or it may be a converter system located on an offshore platform. Apart from wave-powered rowing buoys, nevertheless, most of the prototypes have been settled at or near the shore [12]. Land-based systems comprise the tapered channel (TAPCHAN) and different types of fixed oscillating water column (OWC) devices. Caisson-emerged systems include static OWC devices, pivoting flaps, and enclosed, swelling floats. Offshore devices filled with floating OWC devices, swelling buoys and other devices [4]. WECS can also be sorted as: (1) oscillating water columns; (2) wave surge or focusing devices; or (3) floats or pitching devices [13,14].

- Oscillating Water Columns (OWC) - These machines produce electricity from the wave-exerted rising and falling of water in a cylindrical shaft. The rising and falling water column directs air into and out of the peak of the shaft, energizing an air-guided turbine.
- Focusing Devices or Wave Surge - These shoreline machines also entitled as "Tapered Channel" or "TAPCHAN" systems, depends on a shore-connected construction to channel and coagulate the waves, driving them into a squatted reservoir. Water flow out of this repository is used to generate electricity, using standard hydropower technologies.
- Floats or Pitching Devices - These machines produce electricity from the pitching function of a floating object. The object can be seated upon floating a raft or to a machine adjusted on the ocean plane.

Oscillating Water Column: The main device spread out worldwide is the Oscillating Water Column (OWC). This is made of a partially drowned, notch structure that is open to the sea below the water line. This detain a column of air on top of a column of water. Waves move the water pillar to rise and fall, that alternately compresses and decompresses the air of the chamber. This trapped air is allowed to flow to and from the atmosphere via a Wells 10 turbine, which has the caliber to rotate in the same direction regardless of the direction of the airflow. The circulation of the turbine is used to produce electricity [15]. By anaccelerate edge, the most money and attempt being spent worldwide on wave energy Evolution employs the OWC [16].

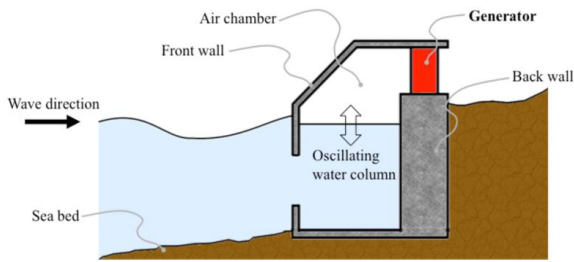


Fig.4 Oscillating Water Column (OWC) System[14]

Tapered Channel Systems (TAPCHAN): This is the unostentatious conversion process, harmonious in many ways to common low-head hydroelectric technology. Where site circumstance allows construction of a large coastal repository without widespread blasting or dam-building, it is the most cost friendly wave energy machine developed to date [11]. The tapered channel (TAPCHAN) composed of a collector that funnels waves into an ever-narrowing drain that increases their height. The kinetic energy of the traveling wave is converted into potential energy as the water is gathered in the repository. Water flow back into the sea through a conventional hydroelectric turbine that produces electricity [13].

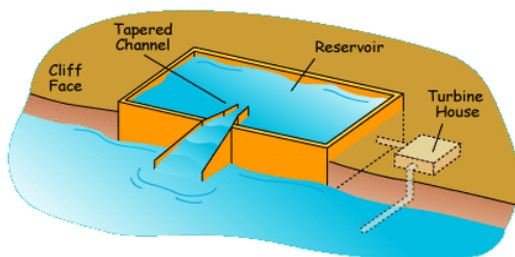


Fig.5 Tapered Channel System (TAPCHAN) [17]

Floating Devices: One of the benefits of floating devices over fixed devices it that they can be placed in deeper water, where wave energy is far greater than onshore (since waves lose energy with decreasing water altitude). There is no necessity for significant earthworks, either, as there is with onshore machines [17]. The Salter Duck, Clam and various floating wave energy machines produce electricity by the harmonic movement of the floating section of the device, on contrary to permanent systems which use a stationary turbine that is powered by the movement of the wave. In these systems, the devices rise and fall according to the course of the wave and electricity is generated through their motion [17].

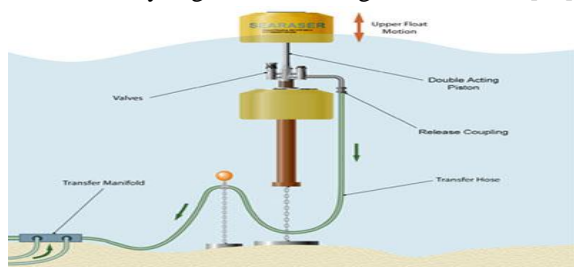


Fig.6 Floating devices [17]

5. Wave Energy Extirpation & Implementing with Power Grid

Figure 6 summarizes the varied shift stages. In particular this illustration shows that there is a demonstration of distance to acquire knowledge from waves: pneumatically and hydraulically (PTO) [4]. For transforming the slow cyclic speed or interchanging motion into high speed cyclic motion for attachment to a operable revolving electrical generator, this kind of mechanical interface is exercised[13].

Simple generators are an option on the investigating representation, but they are not yet currently used in most developed WECs. In peculiar, different types of linear generators were observed for the AWS WECs [14]. These investigations conducted researchers to the end that the transverse flux enduring magnet source is a beneficent for the status of higher powerfulness of spacing and efficiency. The use of stable magnet synchronized maker is a medium choice. The use of functional generators [16] implies a circumstantial automatic PTO that induces added losses touching the WEC gross efficiency. In this environment, there are console mechanical challenges. Table summarizes the PTO systems [17] and the electrical generator options for the both of WEC projects.

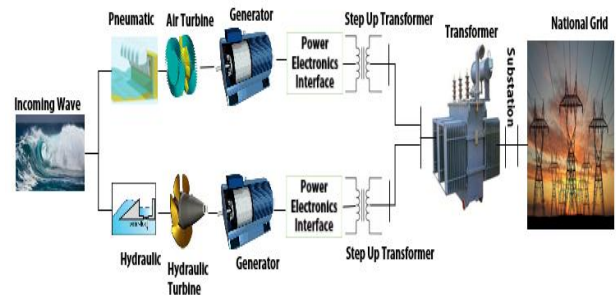


Fig.7 Diagram of several types of WEC and integrating with National Grid

Table 1 WEC Projects PTOs and Generators

WEC	PTO	Generator
PELAMIS	Attenuator /Hydraulics	Cage induction generator
POWERBUOY	Point absorber	Permanent magnet synchronous generator
OYSTER	Oscillating wave surge converter	Cage induction generator
LIMPET	Oscillating water column & Wells turbine	Cage induction generator
OCEANLINX	Oscillating water column & Dennis's-Auld turbine	Cage induction generator

6. Circuits, Simulations and trial results

6.1 Ocean power propagator and circuit:

In this example, an essential charging identify track for the hardware capacity was used. Originally, the dictation circuitry was completed as a fall commit racecourse and a 6V and 4.5AH high-grade graphite Elvis battery was chosen for store purposes. With the innovative parameters, low signaling emf and new levels were achieved during the fleshly experiments. Fig.8 illustrates the adapted diagram draw of the charging journey for this program. During simulations using the NI MULTISIM software way, parameters were familiarized from initial calculations to create a charging circuit that would hold the inputs prospective from the source. The model results for the outputs of the voltage regulators LM7805CT and LM7812CT are shown in Fig.9 and Fig.10. Fig. 9 shows a up rise time of -32.6m seconds. Here, voltage regulator LM7805CT input voltage range 7V-35V, output current rating 1A and output voltage range 4.5V-5.2V. Another voltage regulator LM7812 input voltage range 35V maximum, output current rating 1.5A output voltage 12V. Patch investigating the devices, an extreme of 12.19 V DC was achieved crosswise a 12 V fire with no load. A 12 V DC efferent was successfully operated at contemporary levels of 2.5 A.

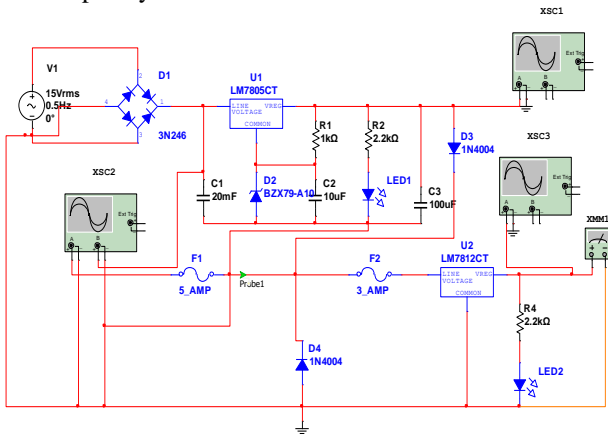


Fig.8Charging circuit diagram of Ocean Current Energy Converter

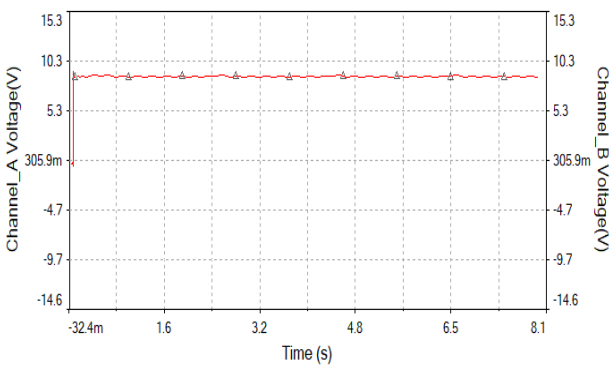


Fig.9 Simulation test results of the charging circuit for the output of LM7805CT

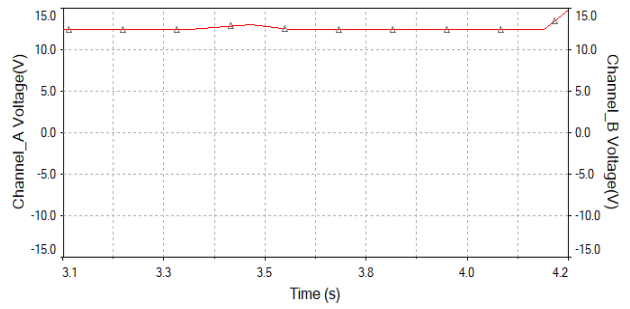


Fig.10 Simulation results of the charging circuit for the output of the LM7812CT

6.2 Tidal energy propagator and tankage system:

Fig.11 shows the altered schematic plot of the charging journey for this ascribe, similar to Fig.8. During simulations using the NI MULTISIM, parameters were attuned from initial calculations to make a charging track that would withstand the inputs awaited from the shaper. The technique results are shown in Fig.12 and Fig.13. A charging circuit shown in Fig11 includes a 12V DC source (battery) as represented in Fig.13. As can be seen in Fig.13, the sign emf is some 11.78 V and 1.129A. This is a drop in the middling production of emf for this signal which is unvarying.

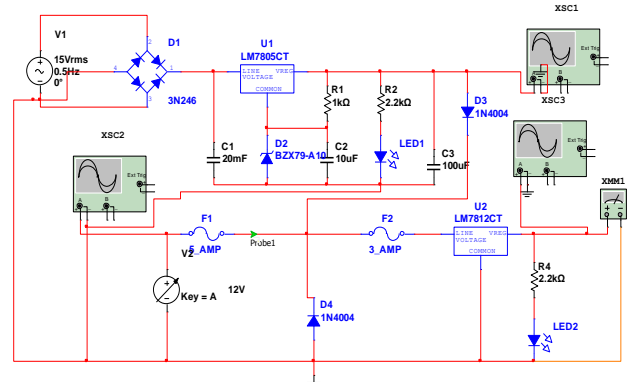


Fig.11Charging circuit diagram of the tidal wave electricity generator

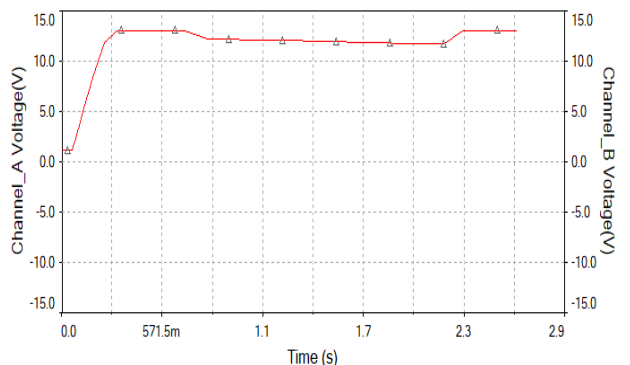


Fig.12 Simulation test results of the charging circuit for the output of LM7805CT

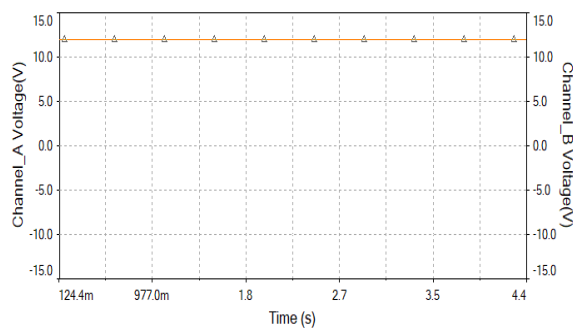


Fig.13 Simulation test results of the charging circuit for the output of LM7812CT

7. Conclusion

An enormous amount of unimproved energy is held by the ocean waves. Different processes and systems for transforming this energy into electrical energy have been introduced. In the face of progress concerning last few years, technologies reside immature as shown by large number of several technologies and instrument sizes that indicates wave energy is at a comparatively untimely stage of improvement and presents many incentive challenges. For converting the experimental processes into feasible and expenditure-effective wave power stations, much research, improvement and engineering acts is still mandatory. Efficiency from wave energy conversion technology would be maximized if the expenditure of wave generated energy is competitive likened to other alternative renewable energy sources. A conjunction of aimed research and the establishment of government stimulus for aforesaid market must be in place for circulation of wave energy conversion technology forward.

Acknowledgement

We the authors are very obliged to Department of Electrical & Electronic Engineering, Bangladesh Army University of Engineering & Technology for the remarkable support and guideline during the process of this work.

NOMENCLATURE

- Φ_w : wave energy flux, W/m^2
- h : amplitude, m
- T : period of wave, second
- P : power of wave, W
- ρ_{sea} : sea water density, kg/m^3
- g : gravity, m/s^2
- h : wave height, m
- ζ : turbine efficiency, no SI unit
- A : sweep area of turbine, m^2
- V : velocity of flow, m/s

REFERENCES

[1] Andreas Uihlein, Davide Magagna, "Wave and tidal current energy-A review of the current state of research beyond technology", *Renewable and Sustainable Energy Reviews*, May 2016

[2] Mehmet Melikoglu, "Current status and future of ocean energy sources: A global review", *Ocean Engineering*, 15 January 2018.

[3] M. Mehrubeoglu, L. McLauchlan, and David Nicholas Patterson, Generating Current from Ocean Waves, *Proc. IEEE Green Technology Conference*, pp. 1-8, Lubbock, TX, April 16-17, 2009 Brooke, J., *Wave Energy Conversion*, Elsevier, Amsterdam (Netherlands), (2004).

[4] M. Mehrubeoglu, L. McLauchlan and D. N. Patterson, Producing Electricity from Sea Waves: A Small-scale Application, *EMO Bilim*, Vol. 9, No. 25, pp. 32-41, (Published in foreign language), (2009).

[5] M. MahbuburRazzaque, Rubayat Islam and Md. Mahbubur Rahman, Tidal Power Potential of the Coastal Area of Bangladesh, *International Conference on Mechanical Engineering 2015 (ICME 15)*, at Dhaka, Bangladesh, Dec, (2015).

[6] Energy from Ocean Waves, Full Scale Experimental Verification of a Wave Energy Converter, by *Rafael Waters*

[7] Wave energy Utilization in Europe: Current Status and Perspectives, *European Thematic Network on Wave Energy*, Center for Renewable Energy Sources, ISBN: 960-86907-1-4, (2002).

[8] *Ocean Electronics Handbook*, 3rd Ed., Muhammad Rashid (Ed.), Burlington: Butterworth-Heinemann, p. 1313, (2011).

[9] Hagerman, George. 1992. Wave Energy resource and economic Assessment for the State of Hawaii, Prepared by *SEASUN Power Systems* for the Department of Business, Economic Development, and Tourism, Final Report, (1992).

[10] *California Energy Commission*, Ocean Energy, (2001).

[11] Rezachek, David, Wave Energy - What is It?, (1998).

[12] Energy Efficiency and Renewable Energy Network (EREN). *Ocean - Wave Energy*, (2001)

[13] Department of Trade and Industry. Wave Energy, *Department of Trade and Industry*. (2001).

[14] Kesayoshi Hadano, Keisuke Taneura, Makoto Watanabe, Takashi Saito, Kimihiko Nakano, Masami Matsuura Mechanics of the Float Type Wave Energy Conversion, *The 16th International Offshore and Polar Engineering Conference, San Francisco, USA*, (2006)

[15] Iraide López, Jon Andreu, Salvador Ceballos, Iñigo Martínez de Alegría, Iñigo Kortabarria, Review of wave energy technologies and the necessary power-equipment, (2013).

[16] Viorel Serban, Zamfir Madalina Angela, Angela Madalina, Viorela Maria Postolache, Efficient Conversion of Wave Energy Into Electricity (2012).

[17] A. Babarit, M. Guglielmi, and A.H. Clément, Decoupling control of a wave energy converter, *Ocean Engineering*, vol. 36, pp. 1015-1024, (2009).

Efficiency of *Tamarindusindica* Seed Charcoal for Chromium Removal from Tannery Wastewater

Md. Abul Hashem*, Kallol Paul, Mst. Nazmin Zaman Khan, and Mehedi Hasan

Department of Leather Engineering, Khulna University of Engineering & Technology, Khulna-9203, BANGLADESH

ABSTRACT

In this study, chromium sorption ability of the prepared *Tamarindusindica* seed charcoal is presented. The prepared charcoal was characterized by Fourier Transform Infrared Spectroscopy (FT-IR). The effectiveness of charcoal adsorbent for chromium sorption efficiency was examined investigating: charcoal dose, contact time, and relative pH. Chromium content in the raw wastewater and after treatment in the filtrate was 3415.02 mg/L and 27.7 mg/L, respectively. The chromium removal efficiency was obtained at 98.9%. The reduction of chloride was 17.2% and pH was (7.7) with the discharged level (6-9). The use of native *Tamarindusindica* seed charcoal adsorbent could be a choice to remove chromium from tannery wastewater.

Keywords: Tannery wastewater, Chromium, Environment, Adsorbent

1. Introduction

Worldwide growing amount of waste produced from the anthropogenic activities has a huge impact on the environment. Many industries dispose of their industrial production waste to the environment without any treatment. Increasing industrialization enhances the disposing of mine tailings and metallurgical slags [1, 2]. Henceforth, sediment/soil is contaminated with toxic metals from where possible mobilization of metals into groundwater or enter human food chain. Existence of these wastes in the natural environment can cause significant impacts on ecosystem.

The fraction of discharged waste chrome liquor is directly mixed with the water body, which causes serious environmental pollution. Again, a fraction of chromium is settled in the lagoon or adsorbent by sediment/soil. About 90% of tanneries use basic chromium sulfate as a tanning agent to obtain better quality leather [3]. On average only 60% chromium is uptaken by the pickled pelt and 40% chromium remain in the liquid as wastage of chrome liquor [4]. Conventionally, chrome tanning wastewater contains 1500-3000 mg/L chromium [5]. Hashem et al. [6] reported that chromium content in the wet blue waste chrome liquor ranges from 2656-5420 mg/L.

Balamurugan et al. [7] reported that chromium (III) in the environment under certain legend conditions leads to the cell to death and modification of its own structure of proteins. Solubility and pH appear to be the primary determinants of the capacity of individual chromium compounds to stimulate an allergic response [8]. In human body function, chromium (III) is considered as an essential trace element [9] but a long-term exposure to chromium (III) is acknowledged to cause allergic skin reactions and cancer [10]. On the other hand, chromium (VI) can be toxic and carcinogenic [11].

In past few decades, numerous researchers try to remove chromium from the tannery wastewater using stone cutting solid waste [12], bone charcoal [13], using indigenous adsorbent [14], *syzygiumcumini* bark adsorbent [15] and eggshell and powered marble

[16]. These approaches are well, but in some cases they are not potentially efficient or are not virtually possible or not cost effective. In some cases it takes long contact time to remove high percentage of chromium [3,13].

In this present study, an attempt was made the use of *Tamarindusindica* seed charcoal chromium from the tannery wastewater. This seed used in cuisines around the world. In Bangladesh, India, Colombia, Cuba, Puerto Rico, Venezuela, Italy, Spain, Caribbean, almost all over the world, it is available and low cost.

The objectives of this study is to remove chromium from the chrome tanning wastewater using *TamarindusIndica* seed charcoal.

2. MATERIALS AND METHODS

2.1 Sample collection

The chromium-containing wastewater water was collected from the SUPEREX LEATHER Ltd. Khulna Bangladesh. Just after the chrome tanning operation, chrome-tanning wastewater was collected in high-density polyethylene (HDP) container, which was washed with diluted nitric acid and instantly deported to the laboratory for experimentation. The *Tamarindusindica* seed was collected from Jessore, Bangladesh.

2.2 Charcoal preparation

Fig. 1 shows the *Tamarindusindica* seed and prepared charcoal. The *Tamarindusindica* seeds were sun-dried.



* Corresponding author. Tel.: +88-01674590373
E-mail addresses: mahashem96@yahoo.com

Fig.1 *Tamarindus indica* seeda) and prepared seed charcoalb)

After sun drying, the seed was burnt at 450-500°C and chafing to make a powder using a mortar. After shaking on a sieve, the charcoal with the required size was obtained.

2.3 Reagents

The reagents perchloric acid (Merck, India), sulphuric acid (Merck KGaA, Germany), nitric acid (Merck KGaA, Germany), ammonium iron(II) sulphate hexahydrate (Merck, India), and *N*-phenylanthranilic acid (LobaChemie, India) were procured from a local scientific store, Khulna, Bangladesh. Also, the anti-bumping agent glass bed (LobaChemie, India), and filter paper (Whatman No. 1) were procured from a local scientific store, Khulna, Bangladesh.

2.4 Characterization of Wastewater

The physicochemical properties of wastewater were measured in terms of chromium, pH, total dissolved solids (TDS), electrical conductivity (EC), salinity, and chloride (Cl⁻) content.

2.4.1 Chromium Determination

Chromium content in the chrome tanning wastewater and after treatment in the filtrate was determined by the titrimetric method following the official methods of analysis of Society of Leather Technologist and Chemists [17] official method of analysis (SLC 208). A 50 mL sample volume was taken in 500 mL conical flask. A 20 mL of concentrated nitric acid was added followed by 20 mL of perchloric acid/sulphuric acid mixture. Then, the flask was gently heated and boiled until the mixture had become a pure orange-red colour and continue boiling for one minute. The flask was removed from the heating source and as soon as ebullition has ceased. Rapidly, the flask was cooled by swirling in a cold water bath. Carefully, 100 mL of distilled water was added with a few glass beads and boiled for 10 minutes to remove free chlorine. Then, 10 mL 30% (v/v) sulphuric acid was added and cooled to room temperature. The mixture was titrated with freshly prepared 0.1N ammonium iron(II) sulphate solution with six drops of *N*-phenyl anthranilic acid as an indicator. The end colour was indicated by a colour change from the violet to green.

2.4.2 Determination of pH

pH of the raw chrome tanning wastewater and treated liquor was measured using pH meter (UPH-314, UNILAB, USA). Before measuring pH, the meter was calibrated with the standard solutions.

2.4.3 Determination of TDS, EC and salinity

TDS, EC and salinity were measured using the conductivity meter (CT-676, BOECO, Germany). Before measuring the parameters, the meter was calibrated with standard solutions.

2.4.4 Chloride (Cl⁻) determination

Chloride content in the chrome tanning wastewater and after treatment in the filtrate was measured by APHA standard argentometric method [18]. A 100 mL water sample was taken in a conical flask and pH was adjusted in the range of 7 to 10. After that, 1.0 mL potassium chromate (K₂CrO₄) indicator was pipetted. Then, the solution was titrated with silver nitrate as titrant (0.0141N) to a pinkish yellow endpoint. The titrant was standardized by the sodium chloride (0.0141 N) solution.

2.5 Charcoal characterization

Chromium loaded charcoal and pure charcoal were analyzed using Fourier transform infrared spectrometer (FTIR, Spectrum 100, PerkinElmer, USA) with an attenuated total reflectance (ATR) accessory. Infrared spectra were recorded at a resolution of 4 cm⁻¹ and 20 spectra were averaged to reduce the noise.

2.6 Treatment of chromium-containing wastewater

Batch-wise chromium removal test was conducted with the prepared charcoal. The scheme for the treatment of chrome tanning wastewater is shown in Fig. 2. Firstly, the physicochemical parameters of the untreated chromium-containing wastewater were analysed and filtered through a 0.45 µm pore size filter. Secondly, 70 mL of filtrate wastewater was mixed with the prepared charcoal. The charcoal mixed wastewater was stirred over a fixed period of time and the mixture was then allowed to settle for a fixed time. After settling, the mixture was filtered through 0.45 µm pore size filter and again chromium content measurement was performed.

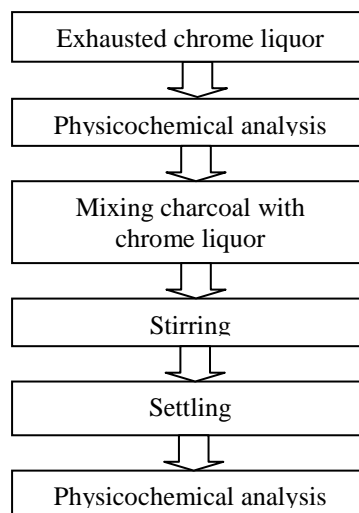


Fig.2 Schematic flow chart for chromium removal treatment process

2.6 Process optimization

The treatment process was optimized to obtain maximum chromium removal efficiency. Tests were carried out to optimize the chromium removal parameters: adsorbent dose, contact time and relative

pH. The optimized conditions were recognized based on the chromium removal efficiency.

3. RESULTS AND DISCUSSION

3.1 FT-IR analysis

Fig. 3 depicts the FT-IR spectrum of charcoal before and after the adsorption of chromium. The figure reveals the changes in the peak intensity. Since FT-IR ascertains different surface functional groups, it can be said that different functional groups of the pure charcoal were responsible for adsorption and removal of chromium.

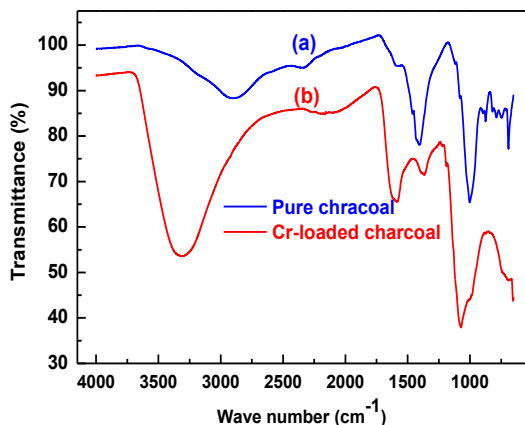


Fig.3 FT-IR spectrum of pure charcoal (a) and chromium-loaded charcoal (b)

Fourier transform infrared absorption spectra studies exposed various types of chemical groups in the charcoal, which are likely to precipitate in the metal binding. Trivalent chromium precipitates by formation of sodium hydroxide at $\text{pH} > 5$. The characteristics of the charcoal before and after treatment by using FT-IR analysis are shown in the following **Fig. 3** simultaneously.

FT-IR spectrum of chromium loaded and pure charcoal is depicted in **Fig. 2**. It shows a shift of peak intensity. The FT-IR was indicated the changes in frequency in the functional groups of the charcoal because of chromium adsorption. It provides an indication of the various functional groups which are responsible for the removal of chromium through charcoal adsorbent.

Fig. 3(a) indicates a broad spectrum around $3200\text{--}3600\text{ cm}^{-1}$ regions presence the groups in charcoal of O-H, C-H, N-H. Also, it reveals that the appearance of C=O group around $1670\text{--}1820\text{ cm}^{-1}$ region. These functional groups might be the reason of chromium adsorption as well as pH increase during treatment process.

Fig. 3(b) shows shift in peak intensity as well as new peak intensity like around 1500 cm^{-1} region expressing C=C group. Moreover, the presence of C-N and =C-H group is noted around 1277 and 903.5 cm^{-1} region respectively. The FT-IR data ensures the presence of different functional group responsible for the removal of chromium through charcoal adsorbent.

3.2 Characteristics of the spent chrome liquor

Table 1 shows the characteristics of the raw chrome tanning wastewater, after treatment (optimized) in the filtrate as well as ECR standard [19] ECR.

Table 1 Data comparison with ECR standard

Parameters	Raw sample	This study (optimum)	ECR [19]
pH	3.5	7.7	6–9
TDS (g/L)	29.06	34.34	2.1
EC (mS)	66.8	79	1.20
Salinity (ppt)	40.3	48.6	–
Cr (mg/L)	3415.02	27.68	2.0
Cl ⁻ (mg/L)	15050	12460	600

It seems that that the chrome tanning wastewater had strong pollution loads in terms of higher quantities of pollutants e. g., higher concentration of chromium, total dissolved solids (TDS), strongly acidic ($\text{pH} = 3.5$). The chrome tanning wastewater is threatening to the environment. Therefore, it is essential to treat the chrome tanning wastewater properly to reduce the pollution loads.

The physicochemical parameters of the treated were obtained e. g., pH, TDS, EC, salinity, chromium, chloride was 7.7 , 34.3 g/L , 79 mS , 48.6 ppt , 27.7 mg/L , 12460 mg/L , respectively. The maximum chrome removal efficiency was 99.2% . After treatment pH was appeared within the discharge level ($6\text{--}9$) but other parameters were slightly increased. The reduction of chloride was of obtained 17.2% .

3.3 Optimal charcoal dose

The dose of charcoal has a significant effect on the ability of chromium sorption. **Fig. 4** shows the effect of charcoal dose and relative pH changes for the chromium sorption ability from chrome tanning wastewater.

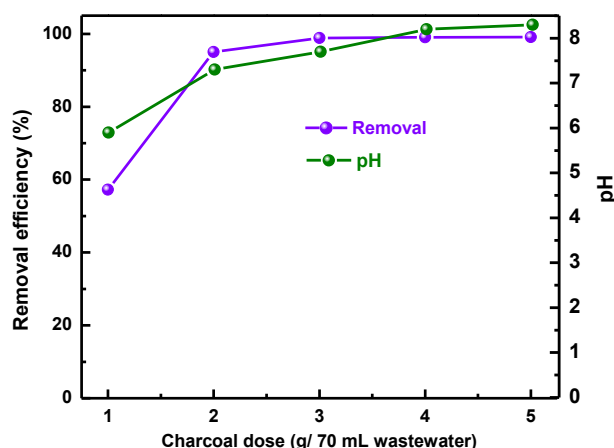


Fig.4 Effect of charcoal dose and relative pH on chromium sorption

Fig. 4 implies that chromium sorption ability was increased with increasing the charcoal doses. Before

treatment (without charcoal) chromium content was in the wastewater was 3415.02 mg/L, the amount of charcoal doses (1 g to 5 g for every 70 mL wastewater) with contact time 10 min was kept constant. Chromium sorption ability was for 1 g, 2 g, 3 g, 4 g and 5 g for every 70 mL wastewater was 53.7%, 95.01%, 98.9%, 99.02% and 99.1%, respectively.

At charcoal dose 3 g for 70 mL wastewater, chromium sorption ability was 98.9%. After that, with increasing charcoal dose chromium sorption ability was not significantly changed. pH plays an role for the adsorption of metals ions because it is responsible for the protonation of metal (chromium) binding site. It establishes, chromium sorption by the *Tamarindus indica* seed charcoal was a function of solution pH. At lower pH, chromium sorption was obtained smaller than in the higher pH. Chojnacka et al. [20] reported that the higher the pH, adsorption of hydrolysis yields and precipitated chromium as colloidal insoluble chromium hydroxide, $\text{Cr}(\text{OH})_3$. Therefore, it was anticipated that the maximum chromium sorption was occurred with 3 g charcoal dose for every 70 mL wastewater at pH 7.7.

3.4 Optimal contact time

Chromium sorption ability observed at a regular time interval to determine the optimal contact time, which implies in Fig.5. It seems that the chromium sorption ability for 2 min, 4 min, 8 min, 12 min and 16 min were 96.8 %, 97.8%, 98.9%, 99.2% and 99.3% respectively. It implies that chromium sorption ability increased with the increasing the contact time. It may be the reason is that more the contact time, metal ion (chromium) binds on the charcoal adsorption sites. Also, it is clear that after a certain time period e.g., 8 min chromium adsorption was extreme (98.9%) and there were no observable changes found (> 8 min). Hence, it was decided that the optimal contact time for sorption maximum chromium was 8 min.

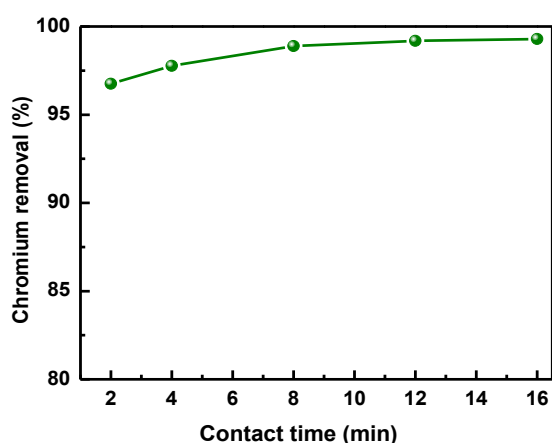


Fig.5 Effect of contact time on chromium sorption

3.5 Efficiency of treatment process

Obtained results of this treatment process at optimum conditions are depicted in Table 1. The optimized conditions were: adsorbent dose 3g/70mL wastewater and contact time 8 min where pH was 7.7.

Table 2 Data comparison with the previous study

Removal efficiency (%)	Contact time	References
90	30 min	[13]
83	6 h	[3]
99	14 h	[16]
99	8 min	This study

Before treatment, the chrome content in the wastewater was 3415.02 mg/L and after treatment with optimized conditions, the chrome content in the wastewater is 27.7 mg/L. Therefore, it observed that the maximum removal of chromium is obtained at 98.9%.

Table 2 shows the comparison of chromium removal efficiency with the previous studies. It seems that with this present approaches chromium removal was obtained 99% with a short contact time (8 min). On the other hand, for example the efficiency of 90%, 83%, and 99% was obtained 30 min, 6 h, and 14 h, respectively. So, the efficiency of chromium removal percentage (99%) is very higher than other study within short time (8 min).

Conclusion

The present study reveals that *Tamarindus Indica* seed charcoal is very effective to remove chromium from the chrome tanning wastewater. Batch-wise chrome tanning wastewater was treated to remove chromium from the chrome tanning wastewater. The removal chromium efficiency at optimized condition was obtained at 98.9% although others parameters were slightly increased. The reduction of chloride was obtained at 17.2%. This indicates that it will be an effective and low cost, in a word most preferable technique to reduce toxic substances that will minimize pollution load from the chrome tanning wastewater.

ACKNOWLEDGEMENT

Authors wish to thank all the related personnel for providing all facilities to conduct this work at the Department of Leather Engineering, Khulna University of Engineering & Technology (KUET), Khulna, Bangladesh.

REFERENCES

- [1] D. L. Jacob, M. L. Otte, Influence of Typhalatifolia and fertilization on metal mobility in two different Pb-Zn mine tailings types, *Sci Total Environ*, Vol. 333, pp 9-24 (2004).
- [2] V. Ettler, M. Komarkova, J. Jehlicka, P. Coufal, D. Hradil, V. Machovic, F. Delorme, Leaching of lead metallurgical slag in citric solutions-implications for disposal and weathering in soil environments, *Chemosphere*, Vol. 57, pp 567-577 (2004).
- [3] R. Aravindhya, B. Madhan, J. R. Rao, B. U. Nair, T. Ramasami, Bioaccumulation of chromium from tannery wastewater: An approach for chrome recovery and reuse, *Environmental Science and Technology*, Vol. 381(1), pp 300-306 (2004).
- [4] F. Fabiani, M. Ruscio, M. Spadoni, M. Pizzichini, Chromium (III) salts recovery process from tannery

- wastewater, *Desalination*, Vol. 108, pp 183-191(1997).
- [5] V. Suresh, M. Kanthimathi, P. Thanikaivelan, J. R. Rao, B.U. Nair, An improved product-process for clear processing, *Journal of Cleaner Production*, Vol. 9, pp 483-491 (2001).
- [6] M. A. Hashem, A. Islam, S. Mohsin, M.S. Nur-A-Tomal, Green environment suffers by discharging of high-chromium containing wastewater from the tanneries at Hazaribagh, Bangladesh, *Sustainable Water Resources Management*, Vol. 1, pp 343-347(2015).
- [7] K. Balamurugan, R. Rajaram, T. Ramasami, S. Narayanan, Chromium(III) induced apoptosis of lymphocytes: death decision by ROS and Src-family tyrosine kinases, *Free Radic Biol Med*, Vol. 33 pp 1622-1640 (2002).
- [8] L. Polak, J. L. Turk, F. R. Frey, Studies on contact hypersensitivity to chromium compounds. *Progress in Allergy*, Vol. 17, pp 145-219 (1973).
- [9] S. Kalidhasan, M. Ganesh, S. Sricharan, N. Rajesh, Extractive separation, determination of chromium in tannery effluents and electroplating waste water using tribenzylamine as the extractant, *Journal Hazardous Materials*, Vol. 165, pp. 886-892 (2009).
- [10] R. Eisler, Chromium Hazards to Fish, Wildlife, and Invertebrates: A Synoptic Review; Biological Report 85 1.6; Contaminated Hazard Reviews Report 6; U.S. Department of the Interior, Fish and Wildlife Service: Laurel, MD, 1986.
- [11] S. Yalçın, R. Apak, Chromium (III, VI) speciation analysis with preconcentration on a maleic acid-functionalized XAD sorbent, *Analytica Chimica Acta*, Vol. 505, pp. 25-35 (2004).
- [12] M. Al-Jabari, M.A. Failat, S. Shaheen, Treating Leather Tanning Wastewater with Stone Cutting Solid Waste, *Clean-soil, air, water*, Vol. 40(2), pp 206-210 (2012).
- [13] S. Dahbi, M. Azzi, N. Saib, M. de la Guardia, R. Faure, R. Durand, Removal of trivalent chromium from tannery Waste Waters using bone charcoal, *Analytical and bio-analytical chemistry*, Vol.374, pp 540-546(2002).
- [14] M. A. Hashem, M. S. Nur-A-Tomal, A. Ahsan, Chromium removal from the tannery wastewater using indigenous adsorbent. 6th International Conference on Advanced Materials Systems (ICAMS), October 20-22, Bucharest, Romania, 2016.
- [15] M. A. Hashem, M. A. Momen, M. Hasan, M. S. Nur-A-Tomal, M.H.R. Sheikh, Chromium removal from tannery wastewater using *Syzygium Cumini* bark adsorbent, *International Journal of Environmental Science and Technology*, doi:10.1007/s13726-018-1714-y
- [16] S. Elabbas, L. Mandi, F. Berrekhis, M. N. Pons, J. P. Leclerc, N. Ouazzani, Removal of Cr(III) from chrome tanning wastewater by adsorption using two natural carbonaceous materials: Eggshell and powdered marble, *Journal Environmental Management*, Vol. 166, pp 589-595 (2016).
- [17] Society of Leather Technologist and Chemists, Official Methods of Analysis. Northampton, UK, 1996.
- [18] American Public Health Association (APHA) (2012) Standard methods for the examination of water and wastewater, 22nd ed. American Public Health Association, American Water Works Association, Water Environment Federation, Washington DC.
- [19] The Environment Conservation Rules (ECR) 1997, Ministry of Environment & Forests, Government of the People's Republic of Bangladesh.
- [20] K. Chojnacka, Biosorption of Cr(III) ions by eggshells, *Journal of Hazardous Materials*, Vol. B121, pp 167-173 (2005).

Evaluation of Sewing Performance of Leather, Denim and PVC Coated Fabric Based on Seam Puckering, Seam Strength and Seam Efficiency

Muhammad Naimul Hasan*, Md.Imrul Kayes Limon, Md. Jasadul Haque, Nabilul Hasan, Athher Shadab
Department of Leather Engineering, Khulna University of Engineering & Technology, Khulna-9203, BANGLADESH

ABSTRACT

Sewing performance is an important factor in determining quality, security, appearance & durability of a garment. It is related with seam strength, tensile strength of leather or fabric, seam slippage, seam efficiency, stitch density, seam puckering, elongation & elasticity etc. In this work, three types of materials such as leather, denim and PVC coated fabric were selected to construct stitch and turn seams and then their seam strength, seam puckering and seam efficiency were determined following ASTM D 1683 methodology to judge the sewing performance of the three (leather, denim, PVC coated fabric) materials. Here, cutting point needle LR90, three stitches per cm and thread 60/3 were strictly maintained in all seam constructions. The objective of this study is to show comparison of sewing performance among leather, denim and PVC coated fabrics. The seam efficiency for leather, denim and PVC coated fabric were observed as 93.34%, 78.08% and 33.79% respectively. The thickness strain which indicates seam puckering value for leather was 2.22, the seam puckering indicated satisfactory value for leather. Hence, these data indicate the leather has the best sewing performance among the three. Again, breaking load of leather is higher than denim & PVC coated fabrics. So, it is clearly evaluated that leather has the supreme sewing performance which make its first selectivity to use as garments material.

Keywords: Leather, denim, PVC coated fabric, seam efficiency, thickness strain

1. Introduction

Seam refers to the successful joining of two materials by the application of adhesive, stitching, reinforcement tape or any other joining materials. Different types of seam constructions are used in making a garment. Some portion of the garment faces strong forces. That portion of the garment should have sufficient strength to withstand and avoid seam failure.

Seam failure is nothing but the failure of sewing thread or fabric breakage, leaving the seam intact. Strength of thread, stitches/inch, thread tension, type of seam, and seam efficiency of the material affect the strength of a seam or stitch. The material which possesses higher seam efficiency will impart stronger seam than the material with lower seam efficiency.

It is well defined that seam strength increases with the application of stronger sewing thread. Seam strength also increases with the increment of the number stitch/inch up to a certain limit and after that it falls down gradually. Seam and stitching elasticity largely dependent on the elasticity of thread and stitch type. Stitching elasticity should be a little bit higher than that of the material that are used in seam because it helps the material to hold the share forces that is experienced at the end use of the apparel. The elasticity of a seam or stitching depended on the stitch types and thread elasticity [1]. In general, the seam quality mainly interrelated with the strength & appearance of a seam itself. Seam strength, appearance and their durability are

the main criteria for determining the functional and aesthetic performance of any apparel. Generally, seam of best quality possesses moderate flexibility and strength having no defects of the seam such as skipped stitch or puckered seam [2]. As the sewing performance test of different types of materials is a main issue to manufacture quality products, we have found out the best stitch type along with best seam construction for the most stretching zone by evaluating the sewing performance of Leather, Denim & PVC Coated Fabrics. It has also been determined the optimum seam strength of stitch type e.g. lock (301) by using different types of material & a clear guideline has been provided for the selection of seam type for different stretching zone and these guideline act as a standard for the apparel manufacturer. In this paper, three types of material are taken and seam is prepared with those materials by maintaining same stitch/cm, thread, needle and same machine. Therefore, a standard seam is produced for each case and standard test method is followed strictly.

The objective of this paper is to show a comparison of sewing performance among leather, denim and PVC coated fabric and from this comparison, a clear decision can be taken about which material is suitable for making particular garments for particular use. Overall, a standard is shown for the apparel manufacturer.

* Corresponding author. Tel.: +88-01721505564
E-mail addresses: namhasan@gmail.com

2. Materials and method

2.1 Materials

Leather, denim, PVC coated fabric, thread, needle were collected from market for this study. The specifications of the materials are shown in table 1.

Table 1 Material specification

	Material	Color	Thickness mm	Texture	Tanning	Yarn count		Number
						Warp	weft	
1	leather	Black	1.2	Soft & smooth	Chrome	-	-	-
2	Denim	Light blue	1.0	Soft & rough	-	19	27	-
3	PVC coated fabric	Deep blue	0.54	Hard & smooth	-	-	-	-
4	Thread	white	-	Soft & smooth	-	-	-	60/3
5	Needle LR 90	-	-	-	-	-	-	14

2.2 Methodology

The methodology ASTM D 1683 has been followed to determine tensile load. Triplet test was done for each sample. The applied load on the test specimen was perpendicular to the direction of seam line.

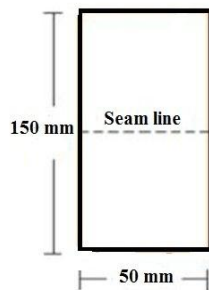


Fig1. Specimen dimension

Jaw speed was 50 mm/min and it was gradually increased up to the breaking point of the specimen. A rectangular test specimen was (150 x 50) mm dimension was prepared for each test which is shown in fig.1, and each sample was clamped in between the jaws. Therefore, in each time load at rupture, percentage of elongation was noted. Seam strength, % of elongation, seam efficiency, thickness strain were also determined in accordance with the following equations- (1), (2) and (3).

$$S_E = \frac{S_T}{M_T} \times 100 \quad (1)$$

$$T_s = \frac{t_s - 2t_L}{2t_L} \times 100 \quad (2)$$

$$E_s = \frac{E_L}{O_L} \times 100 \quad (3)$$

Where, S_E , S_T , M_T , T_s , t_s , t_L , E_s , E_L and O_L indicate seam efficiency, seam tensile strength, material tensile strength, thickness strain (seam puckering), seam thickness, material thickness, seam elongation, extended length and original length respectively.

3. Results and discussion

The seam efficiency (%), thickness strain (seam puckering) (%), seam strength (N/mm), percentage of elongation, breaking load (N) of the stitch and turn constructed leather seam are shown in Table 2 and 3. In fig. 2 & 3, seam efficiency (%), seam puckering (%), strength (N/mm²), Load (N), elongation (%) are represented respectively. In fig. 2 it is shown that leather has the highest seam efficiency 98.34% and lowest seam puckering 2.12%, these value indicate high sewing performance of leather. PVC coated fabric has the seam efficiency 98.34% but poor seam puckering. Denim has the seam efficiency 78.08% and medium seam puckering.

Leather has the highest load (94.7 N) and seam strength (2.37 N/mm) which are shown in fig.3, on the other hand denim and PVC coated fabric have load 85.6 N, 37.7 N and seam strength 2.21 and 1.71 respectively.

Higher value of seam efficiency and lower value of seam puckering indicate worth sewing performance. So, it is obvious that leather has the best sewing performance among leather, denim and fabric.

Table 2 Seam analysis using stitch type 301

Category	Types of materials					
	Leather		Denim		PVC coated fabric	
	Load (N)	Elongation (%)	Load (N)	Elongation (%)	Load (N)	Elongation (%)
Mean	94.7	19.3	85.6	21	37.7	14.7
SD	2.83	2.08	2.47	1.73	2.83	1.15
CV%	2.98	10.8	2.88	8.2	7.5	7.8

Table 3 Sewing performance for stitch type 301

Materials		Sew-ability parameters					
		Seam efficiency (%)		Seam strength (N/mm ²)		Seam puckering (%)	
		Mean	SD	Mean	SD	Mean	SD
1	Leather	98.34	1.92	2.37	0.83	2.12	0.2
2	Denim	78.08	2.37	2.21	0.47	2.55	0.2
3	PVC coated fabric	98.34	2.65	1.71	0.43	15.4	0.4

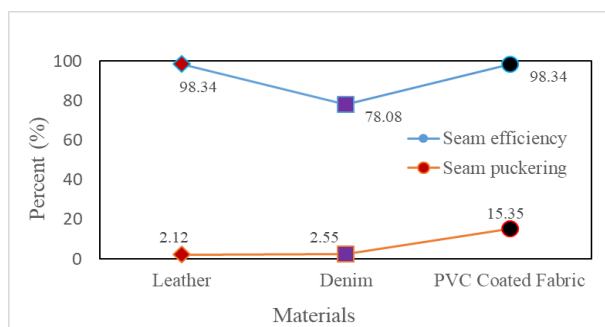


Fig. 2 Percentage of Seam efficiency and seam puckering

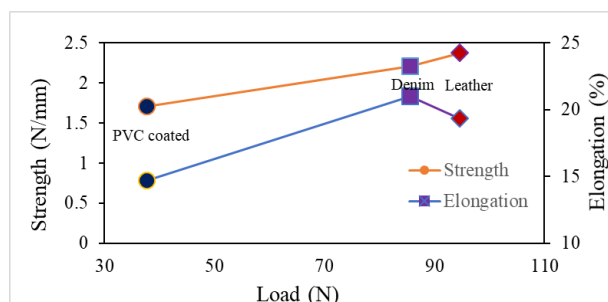


Fig 3. Strength, load and elongation profile of different seams

Leather has the lowest seam puckering (2.12%) among the three, this indicates leather has less tendency of skip stitch and seam slippage, these properties ultimately indicates that leather has superior sewing performance.

4. Conclusion

From this study, it is clear that leather has the best sewing performance among leather, denim and PVC coated fabric based on 301 type of stitch. Leather has showed the highest seam efficiency and lowest seam puckering than other two materials and therefore, this stand for the superiority of leather regarding sewing performance. As sewing performance is an important issue in making garments, this study will definitely guide the apparel manufacturer.

REFERENCES

- [1] G. Seetharam, L. Nagarajan, Evaluation of Sewing Performance of Plain Twill and Satin Fabrics Based On Seam Slippage Seam Strength and Seam Efficiency, *IOSR Journal of Polymer and Textile Engineering*, Vol. 1, pp 09-21 (2014).
- [2] Bharani M., R.V. Mahendra Gowda, Characterization of Seam Strength and Seam Slippage of PC Blend Fabric with Plain Woven Structure and Finish, *Journal of Recent Sciences*, Vol. 1, pp 7-14, (2012).
- [3] Hui P.L.C., Chan K.C.C., Yeung K.W. and Ng F.S.F., Application of Artificial Neural Networks to the Prediction of Sewing Performance of Fabrics, *Int. Journal of Clothing Science and Technology*, Vol. 19(5), pp 291-318, (2007).
- [4] Behera, B. K., and Sharma, S., Low Stress Behavior and Sewability of Suiting and Shirting Fabrics, *Indian Journal of Fiber and Textile Research*, Vol. 23(4), pp 223-241, (1998).
- [5] Thanaa Mustafa AL Sarhan, A Study of Seam Performance of Micro-Polyester Woven Fabrics, *Journal of American Science*, Vol. 7, (2011).
- [6] Mahmuda Akter and Md. Mashiur Rahman Khan, The effect of stitch types and sewing thread types on seam strength for cotton apparel, *International Journal of Scientific & Engineering Research*, Vol. 6, (2015).
- [7] Sundaresan, G., Salhotra, K. R. and Hari, P. K., Strength Reduction in Sewing Threads During High Speed Sewing in Industrial Lockstitch Machine) part II: Effect of Thread and Fabric Properties, *International Journal of Clothing Science and Technology*, pp 64-79, (1998).

Experimental Study on Wheel Alignment System of Light Vehicles

Riton Kumer Das, Md. Abu Mowazzem Hossain* and Md. Tazul Islam

Department of Mechanical Engineering, Chittagong University of Engineering and Technology, Chittagong -4349, Bangladesh

ABSTRACT

The wheel alignment system of the light vehicles is investigated experimentally. The different wheel alignment adjustment technique is used to perform the real time wheel alignment of the vehicle. In order to enhance the automobile performance a regular examination and adjustment of wheel alignment angles are needed by means of wheel alignment system. Computerized and computer vision based automobile wheel alignment measuring system is presented in this paper. The experiment analysis shows that the wheel alignment of vehicle became misalignment when the running distance range is approximately 4000 km to 5000 km. The investigation results suggest that the regular checking of wheel alignment by advanced technologies are significantly improved the life of tire, tire safety, and vehicle handling satisfaction.

Keywords: Wheel alignment, Alignment machine and sensor, Light vehicles

1. Introduction

With the advancement of automotive technology, the travelling speed of automobile is vastly increased, but the influence of automobile stability and travelling safety are decreased. The wheel is important component of the automobile which has direct relation with vehicle stability and safety [1,2]. The recent researches show the most of the accident may occurred due to the wheels are not correctly fitting, wheel alignment is not proper setting and steering function system is not proper work. It also find that the vehicle fuel efficiency is decreasing with increasing the tire wear.

Now a day's modern passenger vehicle has used different wheel alignments technique for safety purpose such as toe, camber, steering axle inclination (SAI) and caster which are most influencing parameters in automobile wheel alignment system. Currently, many wheel alignment technique has been developed to enhance the tire life and reduction of tire wear of the vehicle. Also it can be ensure the vehicle wheels properly contributed to run straight and right way. Automobile wheel alignment active safety systems are caster, camber and toe alignment can be easily measured by using IR sensor [3]. In this technique a computerized wheel alignment machine is used to measure proper wheel alignment of heavy and light vehicles [3-6]. The system used simple circuit and it was low cost and high resolution and also reliability [4]. Recent years the machine vision process was extensively used for easy and proper way to know the characteristic angles [7]. The wireless process has used to easy data transfer system which is better than the traditional system [8]. However, it should be noted that the tire safety and stability and also driver satisfaction are related to the tire quality, tire material and proper size [5]. In the present study the wheel alignment system of light vehicles is investigated experimentally.

2. Experimental Procedure

Wheel alignment consists of adjusting the angles of the wheels, so that they are perpendicular to the ground and

parallel to each other. The steering system is related function such as caster, camber, toe-in and toe- out, kingpin inclination and turning radius check. Experimental analysis includes pre-checking of wheel alignment by manual checking with all wheel alignment related parts. Then the vehicle is aligned by using computerized wheel alignment machine. Fig.1 show the experimental setup for wheel alignment system of light vehicle. Computer vision-based system used in this experiment and utilize the images captured by video camera and the images are processed algorithm to obtain main wheel angles. The sensor connecting boards have to be mounted on the wheels before applying the system as the vehicle wheel balances on the platform. The vehicle is lifted park on alignment bay and set on turning table firstly. The four sensors are mounting on four wheels disk on front and rear axle. The vehicle lifted up with the help of air pressure jack.



Fig.1 Experimental setup.

The commercial computer software for wheel alignment system has now been used to measure the caster angles and this angle was adjusted by open end wrench and memorized with logging steering wheel. Caster is the tilting of the uppermost point of the steering axis either forward or backward (when viewed from the side of the

* Corresponding author. Tel.: +88-01735530848

E-mail addresses: mowazzem@cue.ac.bd

vehicle). A forward tilt is positive (+) and a backward tilt is negative (-). Then the camber angles is adjusted by losing and tightened of the tie rod and push rod function with steering system. Camber is the tilting of the wheels from the vertical when viewed from the front of the vehicle. When the wheel tilt outward at the top, the camber is positive (+). When the wheel tilt inward at the top, the camber is negative (-). The amount of tilt is measured in degrees from the vertical. Similarly, toe-in and toe-out are adjusted. Toe is a measurement of how much the front and/or rear wheels are turned in or out from a straight-ahead position. When the wheels are turned in, toe is positive (+). When the wheels are turned out, toe is negative (-). The actual amount of toe is normally only a fraction of a degree. Each step of measurement the data were store in memory drive.

In the present study a TOYOTA PREMIO vehicle was considered to analysis the wheel alignment system. For analysis three different mileage 91052 km, 96923 km and 106402 km has been taken.

3. Wheel alignment analysis results

Please Table 1 shows the experimental data reading for TOYOTA PREMIO -1650cc light vehicle. Three different mileages 91052 km, 96923 km and 106402 km are consider to be measured the wheel alignment geometry. Sample wheel alignment of active safety system functions such as caster, camber, Toe and king pin angles checking data are shown in Fig.2. The reading data can be analyzed for wheel alignment after every 5000 km or 4 months which one comes earlier. Analysis results show that the vehicle wheel alignment became misalignment when the running distance range is approximately 4000 km to 5000 km. As shown in Table 1 the wheel misalignment is increased as the running distance increased. Noted that the wheel alignment in proper time can improve the safety of the suspension system parts and also reduce the tire wear and increases of mileage of the vehicle. The routine checking of wheel alignment of the vehicle can also enhance the average life of vehicle. Wheel alignment service is one of the most important considerations to vehicle maintenance, find out how to prolong the life of tire investment. Analysis results suggest that after proper wheel alignment the TOYOTA PREMIO vehicle mileage for front axle tire can give approximately 30000 km life and rear axle tire give 35000 km life. Regular maintain this routine checking resulted even tire life can increase to up to approximately 5000 km. Another data shows vehicle mileage becomes 35000 km tire life for front tire and 40000 km of tire life for rear tire. Therefore, it is recommended that the wheel alignment need to be checked after every an 4000 km to 5000 km running distance as a part of vehicle preventive maintenance program.



Fig.2 Front axle readings [9].

Table 1 The wheel alignment summary data for TOYOTA PREMIO -1650cc light vehicle.

Vehicle distance	Drive	91052 km	96923 km	106402 km
Caster	L	+00° 10'	+00°08'	+00°08'
	R	+1°38'	+02° 08'	+01° 07'
Camber	L	+00°10'	+00° 16'	+00° 02'
	R	-00°11'	-00° 26'	-00° 32'
Toe	L	+0.3 mm	+0.6 mm	+6.1 mm
	R	+0.4 mm	+2.4 mm	+8.1 mm
King pin angle	L	+01° 54'	+00° 51'	+02° 00'
	R	+10° 26'	+11° 25'	+07° 55'

* L = Left; R = Right

4. Conclusion

This study led to the evaluation of tire of the wheel alignment system. The results clearly indicate the advantages of applying the wheel alignment process. Based on the observations and the experimental results obtained, the following conclusions are made.

- 1) It was found that the wheel alignment in proper time can contributed to the tire life increase and reduction of the tire wear and increases of mileage of the vehicle.
- 2) The regular maintain routine wise wheel alignment can increase fuel performance and also enhance the average life of vehicle.
- 3) The proper wheel alignment of the light vehicle can improve the effective safety of the suspension parts in vehicle.
- 4) It is recommended that the wheel alignment need to be checked after an every 4000 km to 5000 km running distance as a part of the vehicle preventive maintenance program to increase the tire life of vehicle.

REFERENCES

- [1] Miyara, Flow dynamics and heat transfer of wavy condensate film, *Journal of Heat Transfer, Trans.*

- of *ASME*, Vol. 123, pp 492-500 (2001).
- [2] T. Nosoko, A. Miyara, The evolution and subsequent dynamics of waves on a vertically falling liquid film, *Physics of Fluids*, Vol. 16, pp 11180-1126, (2004).
 - [3] N. Salave and P. L. Sarode, Experimental Study on Wheel Alignment of TATA Motors Heavy Commercial Vehicle, *International Journal of Latest Engineering Research and applications*, Vol. 2 , pp 64-70 (2017).
 - [4] P. Kalita, Study on Vehicle Computerised Wheel Alignment, *International Journal of Computer Engineering in Research Trends*, Vol. 3, pp 70-75 (2016).
 - [5] S. G. Barhe et al., Measurement of Wheel Alignment using IR Sensor, *International of Journal of Engineering Technology, Management and Applied Sciences*, Vol. 4, ISSN 2349-4476 (2016).
 - [6] B. Krishnan. T et al., Vehicle Integrated Wheel Alignment Alert System, *International Journal of Scientific & Engineering Research*, Vol.7, Issue 5, ISSN 2229-5518, (2016).
 - [7] J. S. Young et al., Camber angle Inspection for Vehicle Wheel Alignments, *Sensor*, Vo. 17, pp 285 (2017).
 - [8] Ankita K. Patil and V. L. Kadlag, Design of Wheel Alignment Measuring System using Infrared Transmissions, *International Journal of Technical Research and Applications*, e-ISSN: 2320-8163, Vol. 4, Issue 5, pp 4-6.
 - [9] S. Chatur, Computer based Wireless Automobile Wheel Alignment System using Accelerometer, *The International of Journal of Engineering and Science*, Vol. 4, pp 62-69 (2015).
 - [10] R. Furferi et al., Design and Assessment of a Machine Vision System for Automatic Vehicle Alignment, *International Journal of Advanced Robotic Systems*, Vol. 10, pp 242 (2013).
 - [11] Experimental setup of wheel alignment system of light vehicles at Rahimafrooz auto center, Chittagong, Bangladesh.

ICMIEE18-294

Amino Acids Extraction from Hair Dissolving Liming Waste to Reduce Pollution in Tannery

Sadia Mim, Anika Tabassum, and Md. Abul Hashem*

Department of Leather Engineering, Khulna University of Engineering & Technology, Khulna-9203, BANGLADESH

ABSTRACT

In leather processing, hair/wool and epidermis are removed in liming operation and discharged as waste. These liming wastes consist of amino acids also yield to wastes. In this study, an investigation was made to extract an amino acids reductive-oxidative method from hair dissolving liming waste to reduce environmental pollution. The hair dissolving liming waste was collected and treated with sodium sulphide (Na_2S) and hydrogen peroxide (H_2O_2). The decanted solution was subjected for the presence of different amino acids was confirmed by different tests e.g., Sakaguchi test, xanthoproteic test, lead sulphide test etc. The tests have confirmed the presence of amino acids namely phenylalanine, tyrosine, tryptophan, cysteine and arginine. The extraction of amino acids from the hair dissolving liming wastes could be a solution to reduce pollution in tannery especially hair dissolving liming operation.

Keywords: Keratin, Hair dissolving liming, Protein, Pollution, Extraction

1. INTRODUCTION

Leather industry plays an important role in Bangladesh Economy due to its importance as a labour-based export-oriented industry [1]. Leather industry, one of the most polluting industries, generates a huge amount of solid and liquid wastes with the emission of obnoxious smell for the degradation of the proteinous material of the animal skin [2]. Solid wastes including raw trimmings, fleshings, chrome shavings, buffing dust and keratin wastes are being produced from the industries [3]. Hence, the resultants of all those wastes are responsible for pollutions as they are thrown to landfills or other wetlands. Also, treatment of solid wastes is not cost effective, posing an economic burden to the tanners [2]. Tannery wastes contain protein, which could be extracted for proper utilization; otherwise, it will pollute the environment that will be a threat for the human beings [4].

Keratin, a fibrous protein forming a main structural constituent of the feather, hair, wool, horn, hoof etc., is abundantly available as a by-product from the poultry, slaughterhouse, tanning and fur processing industry [5]. It is a ubiquitous biological material representing a group of insoluble, usually high-sulfur content and filament-forming proteins, constituting the bulk of epidermal appendages [6]. Extensive quantities of keratinase by-products are disposed of annually by animal-processing industry, causing a mounting ecological problem due to the extreme resilience of these materials to enzymatic breakdown [7]. Though keratins have applications in food, pharmaceutical, cosmetic and fertilizer industry, a considerable amount of these products is being wasted repeatedly. It's difficult to perform the degradation of keratin and their disposal causes environmental pollutions [5]. Research is being performed globally for utilization of these wastes and to apply cheap as well as environment-friendly methods to recycle keratinase wastes [7]. Keratin having high immunity to physical and chemical

factors, searching for new methods of keratin waste conversion is usually found. It reduces a problem with storage of solid wastes [8]. Keratin is a biopolymer that contains about 18 amino acids especially in the helical regions of their structure [9]. The main amino acids are cysteine, cystine, arginine, serine, glycine and very little histidine, tryptophan and methionine where the presence of a high portion of cystine disulphide linkages is noticed [9].

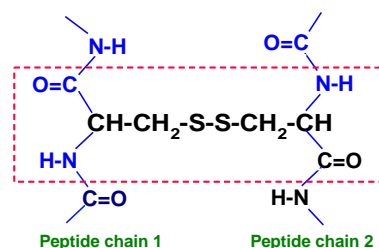


Fig.1 Representation of the cysteine disulfide crosslinks between polypeptides

The pretanning and tanning processes contribute 80–90% of the total pollution load like biological oxygen demand (BOD), chemical oxygen demand (COD), total solids (TS), total dissolved solids (TDS), chromium (Cr), sulphur (S), sludge etc. and toxic gases like ammonia (NH_3) and hydrogen sulfide (H_2S) are also emitted [10]. Nonetheless, most of the pollutions and contaminations generally derive from the unhairing or liming operations. Liming and unhairing wastes contain mainly solid wastes like limed hair/wool and chemicals. The main reasons work behind pollutions is simply all the chemicals used in liming or unhairing processes. The liming of waste is supposed to stop biodegradation and reduce the impacts of landfilling activity [11].

Hair and wool contain a huge amount of amino acids. When these limed hair/wool are thrown to earth it causes environmental pollution as liming of hair is

* Corresponding author. Tel.: +88-01674590373
E-mail addresses: mahashem96@yahoo.com

supposed to stop biodegradation. Others the valuable amino acids in the limed hairs are also being wasted. To reduce the pollutions is a huge challenge as it takes quite tough and longterm processes by using several different chemicals. So utilizing these pollutants as bi-products, minimization of environmental pollutions at a certain level can be done and valuable amino acids can also be obtained in a simple way by using cheap and available chemicals like Na_2S and H_2O_2 . So, the tanners can easily use this method of extraction for treating the limed hair/wool, which is cost effective without posing an economic burden. As this valuable by-product like limed hair and wool are not used in our country and considered as useless waste, so by this extraction method, the demand for amino acids can be full filled for our country. At present, amino acids are used in various branches of industry. It can be a better remedy to reduce environmental pollutions caused during liming operations.

Amino acids are used in various branches of industry as food additives and surface-active agents, in the production of polymeric materials, in electrochemical manufacture etc. [12]. Amino acids are widely used in biotechnology applications and being natural compounds, they can be safely used in pharmaceutical applications [13]. Amino acid-based surfactants have an amino acid residue as a hydrophilic moiety [14].

Amino acids are used for a variety of applications in the industry mainly as additives to animal feed. This is necessary for feeds like soybeans having low levels or lacks some of the essential amino acids like lysine, methionine, threonine and tryptophan [15]. The food industry is a major consumer of amino acids, mainly glutamic acid, used as a flavour enhancer [16] and aspartame as a low-calorie artificial sweetener [17]. Also used for animal nutrition employed in the human nutrition industry to alleviate symptoms of mineral deficiencies like anaemia by improving mineral absorption [18].

The chelating ability of amino acids is used in fertilizers for agriculture to facilitate the delivery of minerals to plants in order to correct mineral deficiencies, such as iron chlorosis. These fertilizers are also used to prevent deficiencies from occurring and improving the overall health of the plants [19]. The remaining production of amino acids is used in the synthesis of drugs and cosmetics [15].

The main purpose of the study is to extract amino acids from the hair dissolving liming waste to reduce pollution load in a tannery.

2. MATERIALS AND METHODS

2.1 Sample collection

Hair dissolving liming wastes was collected from the leather manufacturing workshop, Department of Leather Engineering, KUET, Bangladesh during the unhairing and liming process. The collected samples were washed

eventually with distilled water and dried at room atmosphere. Fig.2 shows the hair and wool samples.



Fig.2 Hair and wool samples of goat and sheep

2.2 Reagents and chemicals

Commercial sodium sulphide (Na_2S , Merck, India), hydrogen peroxide (H_2O_2 30%, Merck, India), copper sulphate (CuSO_4 , Merck, India), sodium hydroxide (NaOH , Loba, India), nitric acid (HNO_3 , Merck, Germany), lead acetate ($\text{Pb}(\text{CH}_3\text{COO})_2$, Merck, India), 1-naphthol (Loba, India), bromine solution (Merck, India), glacial acetic acid (Loba, India), acetic acid (Loba, India), sulphuric acid (H_2SO_4 , Merck, Germany), millions reagent (Merck, India), ammonium carbonate (Loba, India) were procured from the local scientific store, Khulna, Bangladesh. The urea was procured from Chittagong urea fertilizer Ltd., Chittagong, Bangladesh.

2.3 Treatment of limed hair and wool

The collected limed hair and wool were treated with the sodium sulphide. After dissolving hair/wool, hydrogen peroxide was for oxidation. Fig.3 shows the treated hair/wool.



Goat Hair Sheep wool

Fig.3 Treated hair/wool with Na_2S and H_2O_2

Table 1 Amounts of wool, Na_2S and H_2O_2

Sample ID	Amount (g)	H_2O (mL)	Na_2S (g)	H_2O_2 (mL)
Wool	5.1477	400	4.5917	5
Limed hair	149.1048	500	4.4824	35

2.4 Decantation

The mixture was decanted for the separation of the immiscible liquid sample from the solid.

2.5 Centrifugation

The entire amount of decanted liquid was centrifuged for 5 minutes to remove the undissolved solid materials.



Fig.4 Centrifugation of decanted liquid

2.6 Filtration

After centrifugation of both of the wool and limed hair solution, these were undergone through filtration to scan out the settled solids from the clear solution.

2.7 Confirmation test for peptide bond

2.7.1 Biuret test

The biuret test (Piotrowski's test) is usually performed for detecting the presence of peptide bonds. The biuret test was done using copper sulphate solution and sodium hydroxide solution [20].

At first 5 mL of sample solution of both of the wool and limed hair were taken into two test tubes. Then, 5 mL of sodium hydroxide solution was mixed with both of the test tubes containing both of the samples. Nearly, 5-6 drops of copper sulphate solution were added to both of the samples containing test tubes, shaken speedily and kept for a while in order to observe the visual colour change.

2.7.2 Xanthoproteic test

This test is usually performed for differentiating between aromatic amino acids such as phenylalanine, tyrosine, tryptophan etc. [21].

This test was performed by adding concentrated 2/3 mL HNO_3 in the sample solution in a test tube. Then, it was cooled under running tap water. About 10 drops of NaOH was then added to the test tube and wait for colour change.

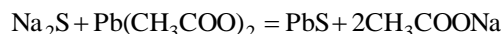
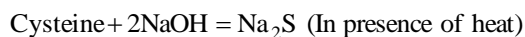
2.7.3 Lead sulphide test

This test is mainly performed for identifying sulphur containing amino acids, such as cysteine and cystine [22].

Lead sulphide test was done with using sodium plumbate solution and sodium hydroxide solution. Sodium plumbate solution was made by 5 mL of NaOH (diluted) was added to 2 mL of lead acetate where a white precipitation of $\text{Pb}(\text{OH})_2$ formed and then it was boiled until precipitation dissolves.

At first 2 mL of the sample solution was boiled with a few drops of NaOH for 2 minutes. It was then cooled

and a few drops of sodium plumbate solution was added to it and wait for colour change.



2.7.4 Sakaguchi test

The Sakaguchi test is usually used for detecting the presence of arginine in proteins [23].

A few drops of 40% NaOH solution was added to 1 mL of sample solution taken in a test tube. Then, few drops of the solution of 1-naphthol were added to it. After that few drops of 5% urea solution was added to it and then bromine solution was added to it and waits for colour change.

2.7.5 Hopkins Cole Test

The Hopkins-Cole test is usually used for detecting the presence of tryptophan in proteins [24].

The indole moiety of tryptophan reacts with glyoxylic acid in the presence of concentrated sulphuric acid to give a purple coloured product. Glyoxylic acid is prepared from the glacial acetic acid by being exposed to sunlight [22].

At first 1mL glyoxylic acetic acid reagent was added to 1mL of sample solution taken in a test tube. Then a few drops of concentrated sulphuric acid were then added to it and wait for the result.

2.7.6 Millons test

The Millons test is performed for detecting the presence of tyrosine in proteins [25]. A few drops of the reagent are added to the test solution, which is then heated gently. A reddish-brown colouration or precipitate indicates the presence of tyrosine residue, which occurs in nearly all proteins [25].

At first, few drops of Millons reagent were added to 1mL of sample solution taken in a test tube and shaking was performed. Then it was gently kept in the water bath for 10 minutes and wait for the colour change.

2.7.7 Histidine test

This test was performed to detect the presence of histidine in proteins [22]. This reaction involves bromination of histidine in acid solution, followed by neutralization of the acid with an excess of ammonia. Heating of alkaline solution develops a blue or violet colouration [22].

At first 5% bromide in 33%, the acetic acid solution was prepared in a volumetric flask. Then a few drops of this solution were added to 1mL of sample solution taken in a test tube. Then the test tube was kept for 10 minutes. After that, a few drops of ammonium carbonate solution was added to it. Then it was kept in the water bath for 10 minutes for a colour change.

2.8 Extraction of amino acids in solid phase

The obtained solutions were placed in the oven at 60°C until total solution dries out and take into the powder form. Approximately after 5 days expected dried out

sticking solid materials were obtained of both of the samples. Then by using a spatula very gently the dried out solid materials were dug off thus producing powdered materials from the solutions.



Fig.5 Extracted pulverulence of limed hair and wool sample

2.8 Performance of FT-IR

Fourier-transform infrared spectroscopy (FT-IR) technique was used to obtain an infrared spectrum of absorption or emission of the desired solid powder form by using SHIMADZU FT-IR in the mid regions ($4000-500\text{ cm}^{-1}$).

3. RESULTS AND DISCUSSION

3.1 Characterization of extracted amino acids

3.1.1 Biuret test result

The colour of both of the samples was converted into a light violet colour indicating a positive result. Thus biuret test of both of the samples of wool and limed hair indicates that these samples contain enough amino acids, which were extracted from further powder formation.



Fig.6 Biuret test

3.1.2 Xanthoproteic test result

After getting the confirmation of amino acids in a sample solution by using the biuret test, the xanthoproteic test was performed.



Fig.7 Xanthoproteic test

A yellow colour was formed that indicates the positive result of this test with the existence of phenylalanine, tyrosine, and tryptophan in the sample solution.

3.1.3 Lead sulphide test result

After getting the confirmation of amino acids in a sample solution by using the biuret test, lead sulphide test was performed. A blackish-brown colour of PbS during testing indicates the positive result of this test with the existence of cysteine in the sample solution.



Fig.8 Lead sulphide test

3.1.4 Sakaguchi test result

After getting the confirmation of amino acids in a sample solution by using the biuret test, Sakaguchi test was performed. Here the appearing red colour during testing indicates the positive result of this test with the presence of arginine in the sample solution.

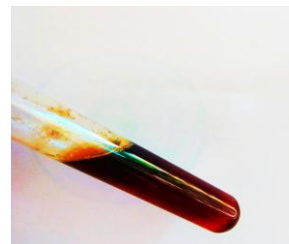


Fig.9 Sakaguchi test

3.1.5 Hopkins Cole test result

After getting the confirmation of amino acids in a sample solution by using the biuret test, Hopkins Cole test was performed. There was not developed any purple violet ring in the test tube that indicates the negative result of this test that means tryptophan was absent.



Fig.10 Hopkins Cole test

3.1.6 Millons test result

After getting the confirmation of amino acids in a sample solution by using the biuret test, Millons test

was performed. There did not occur the creation of reddish brown colour that indicates the negative result of this test that means tyrosine was absent.



Fig.11 Millons test

3.1.7 Histidine test result

After getting the confirmation of amino acids in a sample solution by using the biuret test, Histidine test was performed. No blue colour formation did not appear that indicates the negative result of this test and absence of histidine.



Fig.12 Histidine test

Table 2 Amino acids test result

Test	Result
Biuret test	Presence of protein
Xanthoproteic test	phenylalanine, tyrosine, tryptophan
Lead sulphide test	Cysteine
Sakaguchi test	Arginine
Hopkins Cole test	-
Millons test	-
Histidine test	-

The main amino acids in the hair and wool are histidine, lysine, glycine, arginine, cystine, tryptophan and phenylalanine. So the positive result of performing test indicates that the aim of extraction of amino acids was successful.

3.2 FT-IR result

FT-IR spectrometers are mostly used for measurements in the mid and near IR regions [26]. For the mid-IR region, 2–25 μm (5000–400 cm^{-1}), the most common source is a silicon carbide element heated to about 1200 K. The output is similar to a blackbody [26].

Shorter wavelengths of the near-IR, 1–2.5 μm (10000–4000 cm^{-1}), require a higher temperature source, typically a tungsten-halogen lamp [26].

The long wavelength output of these is limited to about 5 μm (2000 cm^{-1}) by the absorption of the quartz

envelope. For the far-IR, especially at wavelengths beyond 50 μm (200 cm^{-1}), a mercury discharge lamp gives a higher output than a thermal source [26].

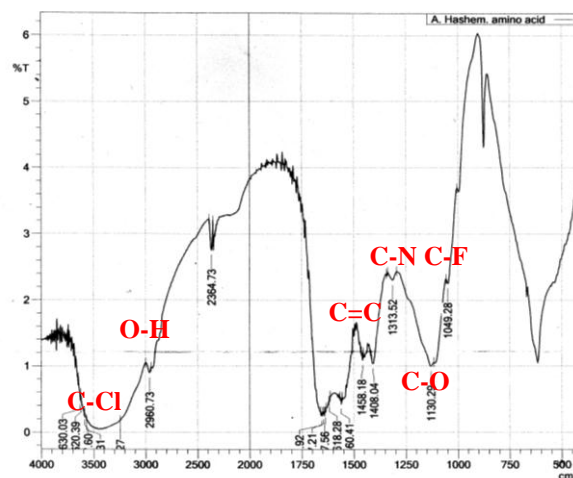


Fig.13 Graphical representation of FT-IR

A graphical representation was obtained from FT-IR where the graph shows different peak points of different wavelength indicating different groups. These groups are present in different amino acids like phenylalanine, tyrosine, tryptophan etc that indicates also a positive result of this process.

After all, amino acids extraction from limed burnt hair minimizes pollution rate. Sample solutions contain phenylalanine, tyrosine, tryptophan, arginine, cysteine which can be used in animal feeds, drugs and cosmetics. The main applications of amino acids are in cosmetic products like keratin shampoo, serum, nail polish products, hair damage repairing products, thermal resistant products in hair straightening, curling, perming and in so many other biomedical uses. The obtained phenylalanine can be used for aspartame production, tryptophan for antioxidants, tyrosine for infusions, arginine for therapy of liver diseases, children growth, cosmetics etc.

4. CONCLUSION

Various amino acids e.g., phenylalanine, tyrosine, tryptophan, cysteine, and arginine are extracted from the hair dissolving liming waste. Amino acid was extracted in a simple reductive-oxidative method with common chemicals. The hair dissolving liming waste could be a great source of amino acids as well as will be reduced pollution in tannery. The extracted amino acids are necessary in our daily life for various purposes. It is the base line experiment and authors need more experiment to development suitable method for amino acids extraction.

ACKNOWLEDGEMENT

The authors are grateful to the Department of Leather Engineering and Department of Chemistry, KUET,

Khulna, Bangladesh for providing adequate laboratory facilities.

REFERENCES

- [1] M. R. Azom, K. Mahmud, S. M. Yahya, A. Sontu, S. B. Himon, Environmental Impact Assessment of Tanneries: A Case Study of Hazaribag in Bangladesh, *International Journal of Environmental Science and Development*, Vol. 3, pp 152-156, (2012).
- [2] J. Kanagaraj, M. Rafiuddin Ahmed, N. Samivelu, R. Jayakumar, High Exhaust Chrome Tanning Using Fleshing Hydrolysate, *Journal of American Leather Chemists Association*, Vol. 97, pp 207-214, (2006).
- [3] www.bioenergyconsult.com/waste-from-tanneries.
- [4] H. Jiang, J. Liu, W. Han, The Status and Developments of Leather Solid Waste Treatment: A mini-review, *SAGE Journals*, Vol. 34, pp 399-408, (2016).
- [5] R. Karthikeyan, S. Balaji, P. K. Sehgal, Industrial Applications of Keratin-A Review, *Journal of Scientific and Industrial Research*, Vol. 66, pp 710-715, (2007).
- [6] B. Wang, W. Yang, J. McKittrick, M. A. Meyers, Keratin: Structure, Mechanical Properties, Occurrence in Biological Organisms and Efforts in Bioinspiration, *Progress in Materials Science*, Vol. 76, pp 229-318, (2016).
- [7] W. Laba, A. Rodziewicz, Biodegradation of Hard Keratins by Two *Bacillus* Strains, *Jundishapur J Microbiol*, Vol. 7, (2014).
- [8] P. Staroń, M. Banach, Z. Kowalski, A. Staroń, Hydrolysis of Keratin Materials Derived from Poultry Industry, *Proceedings of ECOpole*, Vol. 8, pp 443-448 (2014).
- [9] D. H. Simmonds, The Amino Acid Composition of a Keratin Derivative Extracted from Wool with Alkaline Thioglycollate Solution, (1954).
- [10] P. Thanikaivelan, J. R. Rao, B. U. Nair, T. Ramasamai, Recent Trends in Leather Making: Processes, Problems and Pathways, *Critical Reviews in Environmental Science and Technology*, Vol. 35, pp 37-79, (2005).
- [11] C. Delolme, F. Jabob, J. Perrier, Impact of Liming Waste on Liming Activity and Leachate Characteristics: A Laboratory and Field Scale Approach, *Waste Management & Research*, Vol. 16, pp 160-174, (1998).
- [12] M. S. Sadovnikova, M. V. Belikov, Industrial applications of amino acids, *Russian Chemical Reviews*, Vol. 47, pp 2, (1978).
- [13] T. Arakawa, K. Tsumoto, Y. Kita, B. Chang, D. Ejima, Biotechnology applications of Amino Acids in Protein Purification and Formulations, *Amino acids*, Vol. 33, pp 587-605 (2007).
- [14] M. Takehara, Properties and Applications of Amino Acid Based Surfactants, *Colloids and Surfaces*, Vol. 38, pp 149-167, (1989).
- [15] W. Leuchtenberger, K. Huthmacher, K. Drauz, Biotechnological Production of Amino Acids and Derivatives: Current Status and Prospects, *Applied Microbiology and Biotechnology*, Vol.69, pp 1-8, (2005).
- [16] S. Garattini, Glutamic acid, Twenty Years Later, *The Journal of Nutrition*, Vol. 130, pp 901-909, (2000).
- [17] L. D. Stegink, The Aspartame Story: A Model for the Clinical Testing of a Food Additive, *The American Journal of Clinical Nutrition*, Vol. 46, pp 204-215, (1987).
- [18] Albion Laboratories Inc., *Albion Ferrochel Website*, (2011).
- [19] H. D. Ashmead, Foliar Feeding of Plants with Amino Acid Chelates, *Park Ridge: Noyes Publications*, (1986).
- [20] C. J. Fenk, N. Kaufman, D. G. Gerbig, *J. Chem. Educ.*, Vol. 84, pp 1676-1678, (2007).
- [21] Chatterjea, Textbook for Biochemistry for Dental/Nursing/Pharmacy Students, *Jaypee Brothers Publishers*, pp 5, (2004).
- [22] Qualitative Analysis of Amino Acid, *vlab.amrita.edu*, (2011).
- [23] S. Sakaguchi, Über Eine Neue Farbenreaktion Von Protein und Arginin, *J. Biochem.*, Vol. 5, pp 25-31 (1925).
- [24] R. A. Joshi, Question Bank of Biochemistry, *New Age International*, pp 64 (2006).
- [25] E. O'F. Walsh, An Introduction to Biochemistry, *London: The English Universities Press Ltd.*, pp 406-407 (1961).
- [26] D. R. Smith, R. L. Morgan, E. V. Loewenstein, Comparison of the Radiance of Far-Infrared Sources, *J. Opt. Soc. Am*, Vol. 58(3), pp 433-434, (1968).

ICMIEE18-298

A study on minimization of injury and accidental causes in cutting, sewing and finishing units of RMG industries

¹Israt Parveen, ¹Mosammot Nelufa akter, ²Shima Shil, ³Md. Mehedi Hasan and ⁴Md. Iqbal Mahmud*

¹Department of Textile Engineering, Mawlana Bhashani Science and Technology University, Santosh, Tangail-1902

²Trainee Work Study Officer, Ananta Jeanswear Limited, Ashulia.

³Assistant Merchandiser, Montex Fabrics Ltd., Mondol Group, Kashimpur, Gazipur.

⁴Professor, Department of Textile Engineering, Mawlana Bhashani Science and Technology University, Santosh, Tangail.

ABSTRACT

The primary objective of this study is firstly to investigate the industrial accident in readymade garments (RMG) industries and find out the ways how these risk of injuries and accidents can be mitigate by implementing safety rules and suggestions. The paper discusses in brief the risk of injury and accidental causes of workers in various sections like cutting, sewing and finishing units of RMG industries based upon the industrial environment and working conditions. The sample respondents were selected from the different industries in Tangail district. Purposive sampling technique was followed for data collection, where different level of respondents was interviewed for collecting information from two selective garments industry. After analyzing the collected data, the major accidental causes and injuries faced by the workers in those selective units were indicated for which there have been noticed a massive fall down of workers efficiency. Indicating those problems, improvement proposals were given to those industries and were implemented over a course of three month. From the proposed improvement proposal, it has been found that the rate of injury and accidental risks have been decreased far better than before and almost all risks can be properly controlled if the managing as well as responsible parties try to follow the risk controlling technique properly.

Keywords: RMG, Industrial accident, Working environment, Health hazard, Safety measures.

1. Introduction

Accidents and injury in an industry endanger the safety of workers, adversely affect livelihood of their workers and their families, and those living in the vicinity of the industry. Thousands of people are killed and injured in industrial accidents every year. According to the ILO, occupational accidents and work-related diseases cause over 2.3 million fatalities annually, of which over 350,000 are caused by occupational accidents. These result in immeasurable human sufferings and major economic losses for entrepreneurs and economies as a whole; around 4 percent of the world's gross domestic product (GDP), or about US\$2.8 trillion, is lost annually in direct and indirect costs. [1]

Different industrial hazards resulted in several initiatives worldwide to protect human life and reduce material damage from industrial accidents, both nationally and internationally without workplace safety compliance, it is almost impossible to ensure business sustainability and to survive in global

Competitive market. Recent accidents around the world have highlighted the potential hazards inherent in many industrial operations.

In fact, all the garment factories of Bangladesh are located in the commercial area of Dhaka, Chittagong, Narayangonj, Gazipur, Savar etc. Besides, most of the garment factories hardly comply with safety rules. The occupational health and safety condition of the workers belonged to the industry, is getting more critical and complicated gradually.

Action should be undertaken to prevent the occurrence of such accidents through the introduction of safer process technologies, the improved performance of safety devices, and by the reduction of human error.

The most effective accident and disease prevention begins when work processes are still in the design stage, when safe conditions can be built into the work process. [2] In order to develop a successful health and safety program, there should be strong management commitment and worker participation in the effort to maintain a safe and healthy workplace.

*Corresponding author. Tel.: +88-0921-62405; fax: +88-0921-51900

E-mail addresses: mimchanchal@gmail.com

2. Material and methodology

2.1. Materials

In this project work, the usage of various types of materials like tools and machineries from different sections of the factory are briefly discussed below:

2.1.1. Cutting unit:

- Straight Knife Cutting Machine;
- Band Knife Cutting Machine;
- Round Knife Cutting Machine.

2.1.2. Sewing unit:

- Plain machine;
- Flat lock machine;
- Kansai machine;
- Bar tack machine;
- Button holing machine;
- Feed off the arm.

2.1.3. Finishing unit:

Different types of chemicals are used in the finishing unit such as acid, alkali, adhesives, cleaning solvents etc.

2.2. Method:

The legal requirement for risk evaluation or assessment applies to all employers. The process for carrying out a risk assessment can be broken down into a series of steps:

Conducting primary survey: This research is based on output from primary data from the respondents through a sample survey with the help of interview schedule. The data collection included questionnaire survey and focus group discussion.

Data collection: From the month of December to January 2017 the data were collected. The questionnaires were asked systematically and recorded directly on the schedule. The data has been monitored and reviewed at regular intervals.

Identifying hazards which are at risk: Risk assessment is the first step to successful risk management. Looking for the hazards and risks those have the potential to cause harm, and identifying workers who may be exposed to the hazards. Using workers' knowledge helps to ensure hazards are spotted and workable

solutions implemented.

Evaluating and prioritizing risks: Evaluation of how likely the hazard will lead to harm or injury and how severe that injury is likely to be. Considering what control measures are in place and whether they are sufficient. The focus for sustainable risk management was on collective protection and preventative measures.

Deciding on preventive action: Identifying the appropriate measures to eliminate or control the risks. Making list of the preventive measures needed in order of priority, then taking action, involving the workers and their representatives in the process.

3. Data analysis and findings

3.1. Risk analysis in cutting unit

3.1.1 Sources of risk in cutting unit

Cutting unit in textile industry produces a lot of injuries to the operators. It is a dusty work place as during cutting dust is produced. In cutting unit the following things were found that may cause injury to the operator.

A. Relaxation rack

Cutting units is the first section in readymade garments sector. The fabrics are received from fabric store. Then fabrics are kept for relaxation in big rack according to buyer requirements. The rack is usually used by steel which is very hard metal. These racks are placed in cutting floor. As a result it causes inflexible movement of worker.

B. Scissor problem

Scissor has sharp blade which is so risky for hand. When worker become unconscious they may cause injury in hand or other body organism. Even many of workers were injured by scissor. There are another risk occurred by scissor during using handle of scissor. It creates dark spot on skin. During observation it was noticed that maximum worker were suffered from those injury.

C. Leg injury by rubbing of floor

In garments industry the working hour is minimum 10 hour. During this long working time, they work in standing without shoes. As a result, feet are rubbed by floor and causes leg injury. During long working period, the worker can't use shoes, because shoes are not allowed

for them, it is only permitted for the superior.

D. Straight knife risk

Straight knife are used in cutting for extremely sharpen and the rpm of knife is 3600. It is higher risky for cutter men. They are sometimes injured by knife. Straight knife are based on plate, sometimes causes falling of machine, which also may causes injury. It is used electrically, which may cause shock. So the worker should use a special type of steel gloves in their hand.

E. Cutting dust

Another dangerous risk in cutting unit is dust. It is not possible to work in cutting unit without mask. Huge amount of dust are created during cutting and causes asthma, respiratory problem, several skin diseases, eye irritation, visibility problem etc.

F. Band knife machine

This cutting machine is high risky for operator. It has open sharp knife for cutting. It may create accident at any time if the operator doesn't use steel hand globes. Some operator uses this machine without globes, for which they suffer from dangerous accident.

Table 1 Injury caused in cutting unit in January, 2018

S.L	Types of injury	Causes of injury	Number Of injury occurred
1	Hand injury	Band knife	5
2	Hand injury	Straight knife	2
3	Leg injury	Straight knife	3
4	Hand injury	Scissor	7
5	Leg injury	Rack	4
6	Respiratory problem	Dust	10
8	Foot injury	Floor rubbing	15

3.1.2 Recommendation of Preventive action for minimizing risk in cutting unit:

- Danger areas should be clearly marked and access restricted by barriers, especially at cutting tables.
- Warning signals should be fitted to indicate when blade is in motion on motorized and automatic cutting tables.
- Trip guards or other devices in

operation should be used to prevent access where lay-up machines is in use.

- Machines should be fitted with automatic adjustable guards to cover the exposed part of the cutting blade.
- Make sure those electrical conductors in good condition. Five-finger chain mail gloves should be available for use that fit all operators and worn at all times during cutting work and when handling blades.
- Regularly check the condition of the light, guard and table fittings.
- Put an effective cleaning system in operation that prevents buildup of fluff, fly and off cuts.
- Old blades should be disposed of in a safe manner that precludes their use as DIY hand.
- Documentation of a safe system of work for changing and disposing of cutter blades.

Table 2 Injury caused in cutting unit April, 2018

S.L	Types of injury	Causes of injury	Number Of injury occurred
1	Hand injury	Band knife	3
2	Hand injury	Straight knife	0
3	Leg injury	Straight knife	1
4	Hand injury	Scissor	4
5	Leg injury	Rack	2
6	Respiratory problem	Dust	8
8	Foot injury	Floor rubbing	4

3.2. Risk analysis of sewing and finishing unit

3.2.1. Source of risk

A. Plain sewing machine

The needles used in plain machine can injure the worker's body or eye.

B. Flat-lock and over-lock machine

If the worker do not use mask, the dust can enter into the lung and can cause diseases like asthma, lung cancer, bronchitis etc.

C. Button holing, button stitch, snap button, button attach machine

During working needle or button can be entered into the eye or body. Finger can be contused.

D. Other problems

If there is loose connection of electricity, fire accident may be occurred.

3.2.2. Risk in sewing and finishing unit

A. Hearing problem

In sewing unit, large number of machines is run together at a time that creates inflatable noise pollution. It is very difficult to sustain such places and this creates mentally disorder to the worker and causes headache, hearing problem. Most of the worker is suffering from varieties diseases such as brain disorder, nerve problem, mentally pressure etc.

B. Mentally disorder

Operators have a target of production per day if they can't fill up their target, their superior abuse them roughly. As a result they suffer from mentally disorder problem and misbehavior with their family. Due to lower space, the condition of sewing floor in our garment industry is very poor and critical. That is highly risky for everyone unhesitatingly.

C. Musculoskeletal disorders

Musculoskeletal disorders (MSDs) are the most common work-related health problem in Europe, with almost one in four workers reporting backache and one in five complaining of muscular pains. Manual handling, the lifting, holding, putting down, pushing, pulling, carrying or movement of a load, is the largest cause of injury in the textiles sector. Manual handling can cause either cumulative disorder from the gradual deterioration of the musculoskeletal system, such as lower back pain, or acute trauma such as cuts or fractures due to accidents.

In the textiles sector, risk factors for MSDs include:

- Working in awkward postures, such as during sewing, cutting, product control, and packaging.
- Repetitive movements, such as during turning, cutting, product control, and packaging.
- Fatigue from manual handling, during the storage, inspection, treatment,

shipping, finishing, and checking of garments. [3]

D. Exposure to dusts and fibers

The exposure of workers to dusts from material such as silk, cotton, wool, flax, hemp, sisal, and polyester can occur during weaving, cutting, sewing, and packaging. Division of tasks along gender lines may mean that women are exposed to organic dusts more than men, with respiratory nasal or bladder cancer.

Table 3 Injury caused in sewing and finishing unit January, 2018

Types of injury		Causes of injury	Number of injury
1	Asthma	Dust	13
2	Bronchitis	Dust	1
3	Finger injury	Needle	16
4	Eye injury	Needle	1
5	Respiratory problem	Dust	17
6	Hand burn	Ironing	8
7	Eye irritation	Chemicals in spot removal	2
8	Hand burn	Chemicals in spot removal	1
9	Hearing problem	Noise	13
10	Mental problem	Abuse	10

3.2.3. Recommendation for minimizing risk in sewing and finishing unit:

- Use of needle guard and eye guard in working.
- Machine safety cover such as pulley cover and up and down belt cover should be used.
- Test the electric connection before starting work with machines.
- Use rubber mat & musk during checking electric tools.
- Minimum distance should be kept among operator for flexible working.
- The superior shouldn't abuse with worker and help worker to understand them.
- Measures must be taken to ensure that working areas do not pose a contamination risk to the rest of the side.
- There must be a planned preventive maintenance program that covers all

equipment critical to safety, legality and quality, which is fully implemented. [4]

- Repairs to or servicing of equipment must be completed by site mechanics, approved contractors or the equipment manufacturer.
- Risk assessments must be completed prior to work commencing to ensure a product and packaging is not put at risk.
- Tools and parts must be controlled. A system must highlight and initiate and investigation if a tool or part is missing.

Table 4 Injury caused in sewing and finishing unit April, 2018

Types of injury		Causes of injury	Number of injury
1	Asthma	Dust	9
2	Bronchitis	Dust	0
3	Finger injury	Needle	8
4	Eye injury	Needle	0
5	Respiratory problem	Dust	13
6	Hand burn	Ironing	5
7	Eye irritation	Chemicals in spot removal	0
8	Hand burn	Chemicals in spot removal	1
9	Hearing problem	Noise	13
10	Mental problem	Abuse	6

4. Results and discussion

4.1. Cutting unit

4.1.1 Injury occurred in cutting unit before implementation

In Southeast Limited, risk assessment was carried out on cutting unit. Before implementation, the injury level of the workers was collected, by monitoring and assessing the risk. The graphical representation of the injury occurred in the month of January, 2018 is shown below

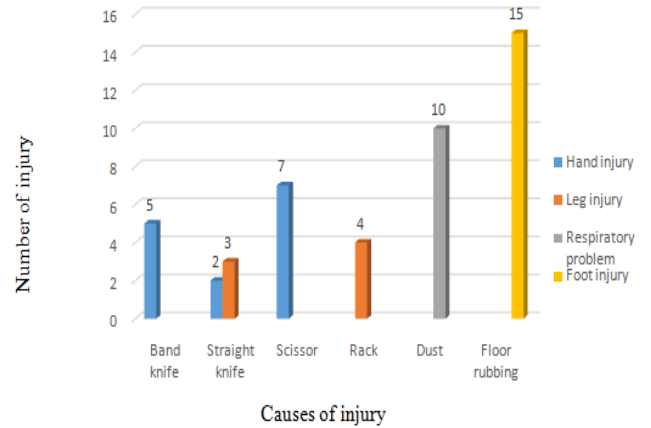


Fig.1 Injury of cutting unit in January, 2018

4.1.2 Injury minimization in cutting unit after implementation

After the injury assessment, suggestions were given to them to overcome these problems. The graphical representation of the injury in April, 2018 which shows a rapid change after implementation is given below:

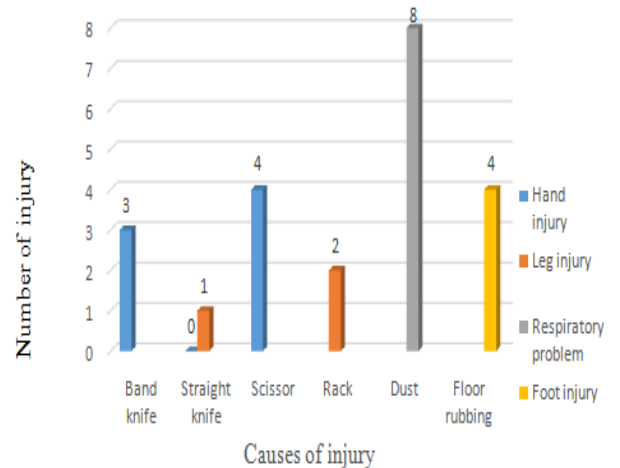


Fig.2 Injury minimization of cutting unit in April, 2018

4.1.3. Comparison of injuries among three months

Rapid change was found in result and the number of risk is dramatically reduced. Commencement of activities was firstly on cutting unit and satisfactory result was found. Here the reduction in injury is shown:

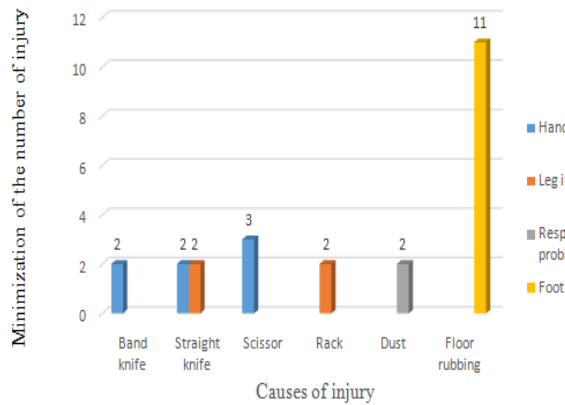


Fig.3 Injury minimized in cutting unit

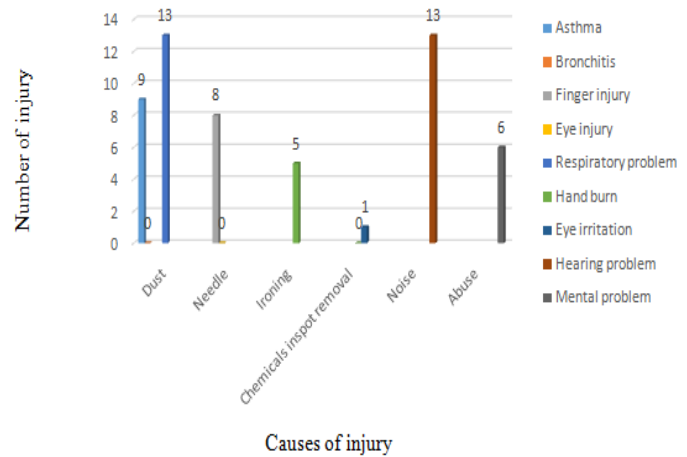


Fig.5 Injury of sewing and finishing unit in April, 2018

4.2. Sewing and finishing unit

4.2.1 Injury occurred in sewing and finishing unit before implementation

In Southeast Limited, before implementation, the injury level of the workers were collected, by monitoring and assessing the risk .The graphical representation of the injury occurred in the month of January, 2018 is shown below:

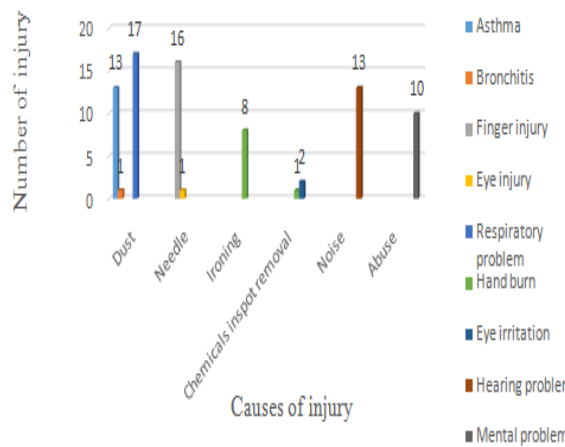


Fig.4 Injury of sewing and finishing unit in January, 2018

4.2.3. Comparison of injuries among three months

Rapid change was found in result and the number of risk is dramatically reduced. Commencement of activities was firstly on cutting unit and satisfactory result was found. Here the reduction in injury is shown:

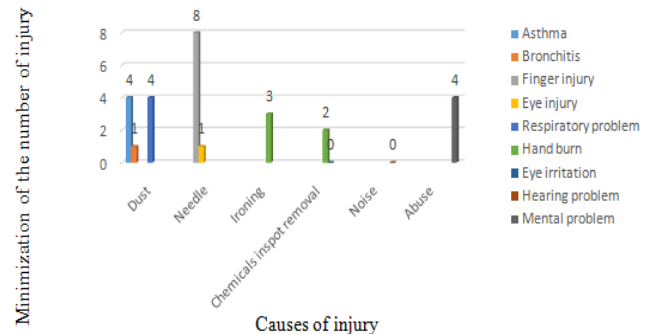


Fig. 6 Injury minimized in sewing and finishing unit

4.2.2. Injury minimization in sewing and finishing unit after implementation

After the injury assessment, suggestions were given to the selected industries to overcome these problems. The graphical representation of the injury in April, 2018 which shows a rapid change after implementation is given below:

5. Conclusion

Risk of accidental causes and injury in readymade sectors are burning topic in the economy of Bangladesh from the last two decades. Being strength of national economy, still risk and accidental injuries are the main responsible hindrance for the development of fast growing RMG sectors in Bangladesh. In this study, the main purpose was to resolve the identified risks to increase company's productivity. The risk factors found should be controlled immediately in order to increase the

positive view and profitability. In order to fulfill the purpose of this study, risk management technique and regulation should be followed by the proper authority so that we can make a positive view of RMG industry to the buyer of foreign countries.

6. REFERENCES

- [1] Ma, yun, Jian, “Analysis on the Fire Risk Existing in the Storage of Textile Materials and Textile Goods” page no.271 – 275; (2014).
- [2] M1, Kumar, Praveen, “Occupational Health and Safety in Textile Industry” International Journal of Research in Engineering and Technology; Volume- 03; Issue- 11; page no-168; (2014).
- [3] Khan, Ahmed, Waqas“occupational safety and health is an area concerned with protecting the safety, health and welfare of people engaged in work or employment”
- [4] .Enrico, D’Ambrogio, “Workers' conditions in the textile and clothing sector” European parliamentary research service; PE 538.222; August; (2014).

Forecasting Demand by GMDH Predictor, a Case Study

Syed Misbah Uddin*, Aminur Rahman, Emtiaz Uddin Ansari

Department of Industrial and Production Engineering, Shah Jalal University of Science and Technology, Sylhet 3114,
BANGLADESH

ABSTRACT

Forecasting demand is very important for manufacturing industry and also needed for all type of business and business suppliers for distribution of finish goods to the consumer on time. Forecasting with high accuracy is required to prevent wasting and system failure to fulfil market demand. This study is concerned with the determination of accurate models for forecasting cement demand. In this connection this paper presents results obtained by using a self-organizing model and compares them with those obtained by usual statistical techniques. A nonlinear modelling technique based on Group Method of Data Handling (GMDH) is considered here to derive forecasts. Various time series smoothing techniques such as exponential smoothing, double exponential smoothing, weightage moving average and moving average method are used for forecasting the demand. For this purpose, Monthly sales data of a typical cement ranging from January, 2007 to February, 2016 was collected. The mean absolute percentage error (MAPE) and mean sum square error (MSE) are also calculated for comparing the forecasting accuracy. The comparison of modelling results shows that the GMDH model perform better than other models based on terms of mean absolute percentage error (MAPE) and mean square error (MSE).

Keywords: Forecast, GMDH algorithm, Time series, MAPE, MSE.

1. Introduction

“Better predictions remain the foundation of all science. . .”[1]. Forecast accuracy has been a critical issue in the areas of financial, economic and scientific modeling, and has motivated the growth of a vast body of literature on the development and empirical application of forecasting models [2]. More accurately forecasting demand would facilitate for assisting managerial, operational and tactical decision making. Therefore the selection of forecasting model is the important criteria that will influence to the forecasting accuracy [3].

GMDH method was originated in 1968 by Prof. Alexey G. Ivakhnenko in the Institute of Cybernetics in Kiev (USSR). This approach from the very beginning was a computer-based method so, a set of computer programs and algorithms were the primary practical results achieved at the base of the new theoretical principles. The method was quickly settled in the large number of scientific laboratories worldwide due to open code sharing. At that time code sharing was quite a physical action since the internet is at least 5 years younger than GMDH. Despite this fact the first investigation of GMDH outside the Soviet Union had been made soon by R. Shankar in 1972. Later on different GMDH variants were published by Japanese and Polish scientists.

The main idea of GMDH is the use of feed-forward networks based on short-term polynomial transfer functions whose coefficients are obtained using regression combined with emulation of the self-organizing activity behind NN structural learning [4]. To improve the performance of the GMDH algorithm, Barron gave a comprehensive overview of some early developments of network, and introduced the polynomial network training algorithm (PNETTR). Elder proposed

Synthesis of Polynomial Network (ASPN) algorithm to improve the GMDH algorithm.

J.A. Muller and Frank Lemke developed and improved self-organizing data mining algorithms on the basis of the above results in 1990s. Further enhancements of the GMDH algorithm have been realized in the “KnowledgeMiner” software. The GMDH algorithm has gradually become an effective tool for modeling, forecasting, and decision support and pattern recognition of complex systems. There are processes for which it is needed to know their future or to analyze inter-relations. The GMDH algorithm was successfully used to deal with uncertainty, linear or nonlinearity of systems in a wide range of disciplines such as ecology, economy, medical diagnostics, signal processing, power plant, electric power industry and control systems [5-9]. The revised GMDH algorithms [10, 11]), have been introduced to model dynamic systems in flood forecast and petroleum resource prediction with some success.

The purpose of the study is to investigate how good is GMDH predictor as a forecasting tool by comparing the results of a self-organizing model with those obtained by usual statistical techniques. This paper organize as follows: section 2 describes the methodology applied for forecasting the demand. Data collection and analysis are presented in section 3. Section 4 provides the results and discussion while fifth section offers some conclusion.

2. Methodology

This is a case study research based on time series data of cement industry. The data used in this case study are monthly sales data of cement. The data span the period from January 2007 to February 2016. The dataset consists of 110 months’ time series data. Data were analyzed by using various time series model such as moving average, weighted moving average, single

* Corresponding author. Tel.: +88-01770347090

E-mail addresses: misbah-ipe@sust.edu

exponential smoothing, double exponential smoothing and least square method of simple linear regression.

In this study, we use the value of α 0.3 and 0.5 for single exponential smoothing method. Simple exponential smoothing does not do well when there is a trend in the data. In such situations, several methods were devised under the name "double exponential smoothing" or "second-order exponential smoothing". The basic idea behind double exponential smoothing is to introduce a term to take into account the possibility of a series exhibiting some form of trend. This slope component is itself updated via exponential smoothing. One method sometimes referred to as "Holt-Winters double exponential smoothing" are followed here. One of *two smoothing factor* is α which is called data smoothing factor and its value, $0 < \alpha < 1$, and the other one β is the *trend smoothing factor*, $0 < \beta < 1$.

We also used the GMDH predictor version GMDH Data Science 3. 5. 9 to derive the forecast. Out of 110 data 58 months data are used for the training set and rest of the data are used for evaluation in checking set. In order to evaluate the forecasting accuracy of different techniques various central tendency measures as the loss function were also calculated with the help of following formula.

$$MAD = \frac{1}{n} \sum_{n=1}^n |(Actual - Forecast)|$$

n = the number of periods [12].

$$MSE = \frac{\sum_{k=0}^n \{Actual - Forecast\}^2}{n}$$

Where:

n = the number of periods [12].

$$MAPE = \frac{1}{n} \sum_{n=1}^n \frac{|Actual - Forecast|}{Actual} * 100\%$$

3. Data Collection and Analysis

Data Collection is a significant aspect of any type of research study. The data used in this case study are monthly sales data of cement. The data span the period from January 2007 to February 2016. The time series plot is given Fig. 1.

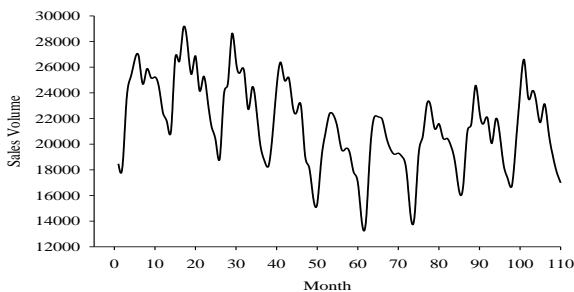


Fig.1 Monthly sales data (Jan 2007 to Feb 2016)

After collecting sales data GMDH algorithm and various statistical forecasting techniques were used to forecast. The mean absolute deviation (MAD), mean absolute percentage error (MAPE) and mean square

error (MSE) were also calculated to assess forecasting performance of different models.

3.1 Analysis by GMDH algorithm

GMDH algorithm consists of set of steps that are described below:

Step 1: First N observations of regression-type data are taken. The collected load data are first normalized with respect to their individual base value in order to restrict the variation of data within the same level. Those normalized data are denoted by $(x_1, x_2, x_3, x_4, \dots \dots \dots x_M)$ where M is the total number of input. The original data is separated into the training and test sets [14]. In this study total 110 data were separated into training (58) and test (52) sets. The 58 data is used for the estimation of the partial descriptions which describe the partial characteristics of the nonlinear system. The 52 data is used for organizing the complete description which describes the complete characteristic of the nonlinear system.

Step 2: Select $\binom{m}{2} = m(m-1)/2$ new input variables according to all possibilities of connection by each pair of inputs in the layer. Construct the regression polynomial for this layer by forming the quadratic expression which approximates the output y in equation (1).

Step 3: Identify the single best input variable out of these $\binom{m}{2}$ input variables, according to the value of mean square error (MSE). The input of variables that give the best results in the first layer, are allowed to form second layer candidate model of the equation (1). Set the new input $(x_1 x_2 x_3 x_4 \dots \dots \dots x_M)$ and $(M = M + 1)$ Models of the second layer are evaluated for compliance by using MSE, and again the input variables that give best results will proceed to form third layer candidate models. This procedure is carried out as long as the MSE for the test data set decrease compared with the value obtained at the previous one as shown in Fig. 2. After the best models of each layer have been selected, the output model is selected by the MSE. The model with the minimum value of the MSE is selected as the output model [15].

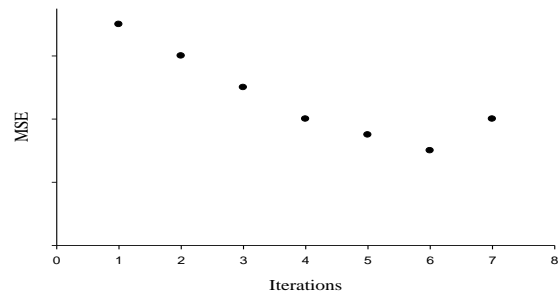


Fig.2 Stopping criteria of GMDH algorithm

3.2 Analysis by Statistical method

Various time series smoothing techniques such as exponential smoothing, double exponential smoothing, moving average and regression method were used for forecasting the load demand. Absolute deviations were

also calculated. The mean absolute deviations (MADs) found from these calculations are listed in table 1.

Table 1 MAD of different forecasting methods

Method	MAD
3 month Moving Average	2306
6 month Moving Average	2791
12 month Moving Average	2230
Weightage Moving Average	2056
Regression	2459
GMDH Method	704
Exponential $\alpha=0.3$	2286
Exponential $\alpha= 0.5$	2053
Double Exponential $\alpha= 0.3, \beta= 0.5$	2861

From Table 1 it is seen that the value of MAD due to forecasting by GMDH algorithm is 704. On the other hand all the statistical method gives four digits MAD. The mean absolute percentage error (MAPE) and mean square error (MSE) were also calculated and reported in Table 2 and Table 3 respectively. It is observed that the GMDH forecast with only 4% MAPE and nearest value is 9% which is done by exponential smoothing technique($\alpha= 0.5$). Form Table 3 it is clear that the model with the minimum value of the MSE is the GMDH model.

Table 2 MAPE of different forecasting methods

Method	MAPE
3 month Moving Average	11%
6 month Moving Average	14%
12 month Moving Average	11%
Weightage Moving Average	10%
Regression	12%
GMDH Method	4%
Exponential $\alpha=0.3$	11%
Exponential $\alpha= 0.5$	9%
Double Exponential $\alpha= 0.3, \beta= 0.5$	13%

Table 3 MSE of different forecasting methods

Method	MSE
3 Month Moving Average	7994519
6 Month Moving Average	10355301
12 Month Moving Average	7710194
Weightage Moving Average	6291543
Regression	9177720
GMDH Method	824882
Exponential $\alpha= 0.3$	7619269
Exponential $\alpha= 0.5$	6220179
Double Exponential $\alpha= 0.3, \beta= 0.5$	11913465

4. Results and Discussion

After completing data analysis we have come out with some informative results. The calculated Mean absolute deviations (MADs) of forecasted data by different

forecasting techniques are plotted in Fig. 3. It is seen that GMDH algorithm gives lowest value of MAD which is best suit.

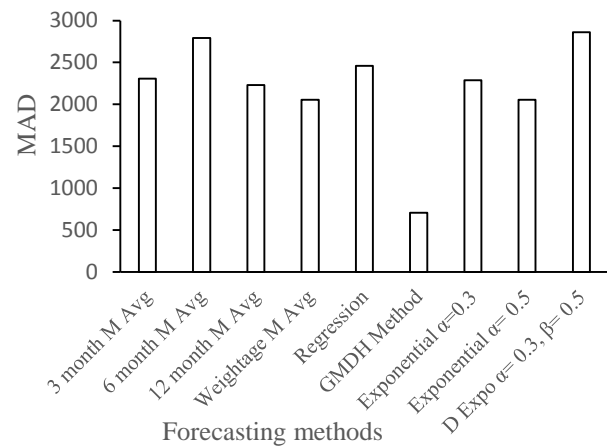


Fig.3 Comparison of MAD of different techniques

The mean absolute percentage error (MAPE) and mean square error (MSE) are plotted in Fig.4 and Fig.5 respectively. The comparison of modelling results shows that the GMDH model perform better than other models based on terms of mean absolute percentage error (MAPE) and mean square error (MSE).

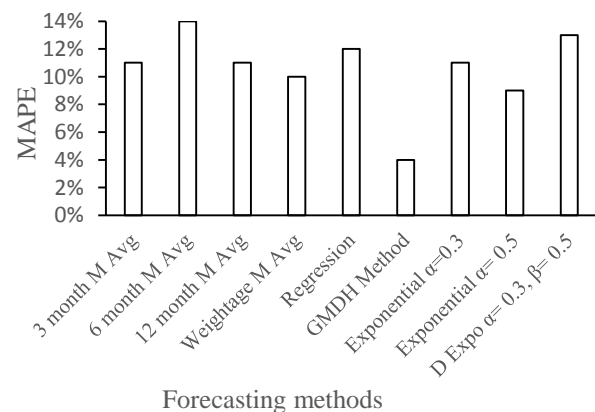


Fig.4 Comparison of MAPE of different techniques

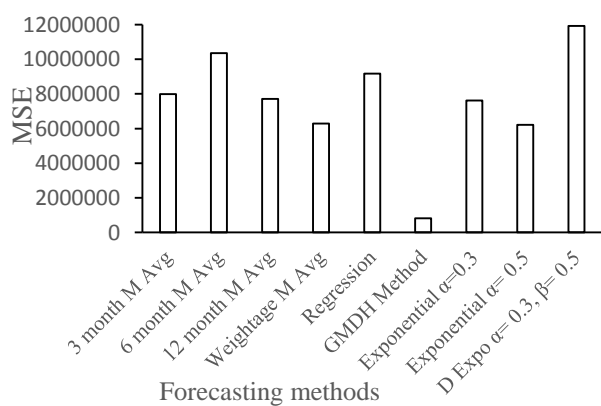


Fig.5 Comparison of MSE of different techniques

To assess the performance of GMDH modelling, last 52 months demand were forecasted and compared with the test set. The results of that model along with forecasting precision are shown in table 4. Normalize mean

absolute error is found to be 4.65% whereas normalize RMS is 6%. The fitting accuracy of GMDH model algorithm is also very good as the value of R^2 is 0.90.

Table 4 Summary results of GMDH modelling

Metrics	Output / Value
Post processed result	Model fit
Number of observations	52
Normalize mean absolute error	4.65%
Normalize root mean square error	6%
Standard deviation of residuals	5.8%
Coefficient of determination (R^2)	0.90
Correlation coefficient	0.95

Our findings have several important implications. Useless input variables are eliminated and useful input variables are selected automatically, the structure parameters and the optimum GMDH architecture can be organized automatically. The case study on the cement time series data testing demonstrated that the GMDH model is robust in the forecasting of nonlinear time series.

5. Conclusion

This paper examined the forecasting accuracy of different statistical techniques as well as GMDH predictor. For that purposes ten years secondary sales data of a cement were collected. There was low seasonal variation in their sales. Demand forecasting was performed using extrapolative time series methods, such as exponential smoothing with level, trend, and seasonal components. Besides that moving average, weighted moving average and regression method were also used for forecasting the demand. A nonlinear self-organizing model based on Group Method of Data Handling (GMDH) was also applied here to derive forecasts. We applied the GMDH predictor version GMDH Data Science 3. 5. 9.

In order to evaluate the accuracy of prediction, various performance measures such as MAD, MAPE and MSE were calculated. It is found that there is no result near to the GMDH predictor. GMDH algorithm forecast with only 0.0367 or 4% error which is substantially more accurate than statistical method.

REFERENCES

[1] S. Makridakis, M. Hibon, The M3-Competition: results, conclusions and implications, *International Journal of Forecasting*, Vol. 16, pp 451–476 (2000).
 [2] J. Gooijer, R. Hyndman, 25 Years of Time Series Forecasting, *International Journal of Forecasting*, Vol. 22, pp 443– 473 (2006).
 [3] R. Samsudin, P. Saad, A. Shabri, Hybridizing GMDH and Least squares SVM support vector machine for forecasting tourism demand, *IJRRAS*, Vol. 3, pp 274-279 (2010).
 [4] S. J. Farlow, The GMDH Algorithm of Ivakhnenko, *The American Statistician*, Vol. 35, pp 210-215 (1981).

[5] A.G. Ivakhnenko, G. A. Ivakhnenko, A Review of Problems Solved by Algorithms of the GMDH, *Pattern Recognition and Image Analysis*, Vol. 5, pp 527-535 (1995).
 [6] G. C. Onwubolu, P. Buryan, F. Lemke, Modeling Tool Wear in End-Miling Using Enhanced GMDH Learning Networks, *International Journal of Advance Manufacture Technology*, Vol.39, pp 1080–1092 (2008).
 [7] T. Kondo, A. S. Pandya, A. S. Nagashino, GMDH-Type Neural Network Algorithm with a Feedback Loop for Structural Identification of RBF Neural Network, *International Journal of Knowledge-Based and Intelligent Engineering Systems*, Vol. 11, pp 157-168 (2007).
 [8] V. Puig, M. Witczak, F. Nejjari, J. Quevedo, J. Korbicz, A GMDH Neural Network-Based Approach to Passive Robust Fault Detection Using a Constraint Satisfaction Backward Test, *Engineering Applications of Artificial Intelligence*, Vol 20, pp 886-897 (2007).
 [9] F. Li, B. R. Upadhyaya, L. A. Coffey, “Model-Based Monitoring and Fault Diagnosis of Fossil Power Plant Process Units Using Group Method of Data Handling, *ISA Transactions*, Vol. 2, pp 213-219 (2009).
 [10] T. Kondo, Nonlinear Pattern Identification by Multi-Layered GMDH-Type Neural Network Self-Selecting Optimum Neural Network Architecture. *International Conference on Neural Information Processing*, pp 882-891 (2007)
 [11] F. Chang, Y. Hwang, A Self-Organization Algorithm for Real-Time Flood Forecast, *Hydrological processes*, Vol. 13, pp 123-138 (1999).
 [12] P. K. Sahu, R. Kumar, Demand Forecasting for Sales of Milk Product (Paneer) in Chhattisgarh, *International Journal of Inventive Engineering and Sciences*, Vol. 1, pp 10-13 (2013).
 [13] O. S. Ezennaya, O. E. Isaac, U. O. Okolie, Analysis of Nigeria’s National Electricity Demand Forecast (2013-2030), *International Journal Of Scientific & Technology Research*, Vol. 3, pp 333-340 (2014).
 [14] R. Samsudin, P. Saad, Combination of Forecasting Using Modified GMDH and Genetic Algorithm, *International Journal of Computer Information Systems and Industrial Management Applications*, Vol. 1, pp 170-176 (2009).
 [15] T. Kondo, J. Ueno, Revised GMDH-type Neural Network Algorithm with a Feedback Loop Identifying Sigmoid Function Neural Network, *International Journal of Innovative Computing, Information and Control*, Vol. 2(5), pp 985-996 (2006).

Implications of Bangladesh's Present Energy Transition on Energy Trilemma

Shafiqul Alam^{1,*}, Md. Golam Kader²

¹ International Climate Protection Fellow, Ecologic Institute, Pfalzburger Strasse 43-44, Berlin 10717, supported by Alexander von Humboldt Foundation, GERMANY

² Professor, Department of Mechanical Engineering, Khulna University of Engineering & Technology, Khulna-9203, BANGLADESH

ABSTRACT

Although energy efficiency and renewable energy can enhance energy security, improve environmental performance and reduce Greenhouse Gas emissions, the energy transition of Bangladesh over last decade has rather been focused on imported fossil fuels. The transition has mainly been driven by economic growth and quick-fix strategy. This paper draws upon secondary data of last decade, relevant publications and existing policies to explore the status of ongoing energy transition of Bangladesh and its implication on energy trilemma, which is being measured on energy security, equity and environmental performance. Through analysis, diverse range of issues, i.e., options and pathways for sustainable energy transition and linkages of the transition with national climate policy and Sustainable Development Goals, are examined. The paper concludes with the necessity of creating an enabling environment and developing conducive policy instruments, also derived from present experience, to catalyze investment and attract private sectors for sustainable energy transition in Bangladesh.

Keywords: Energy Transition, Energy Trilemma, Renewable Energy, Energy Efficiency, Bangladesh.

1. Introduction

Major structural change or shift in utilizing energy resources in an economy to meet its demand can be treated as energy transition. Different countries went through this transition in the past mainly attributed to the necessity of enhancing economic performance but most of the countries are now in energy transition or are about to embark on energy transition, especially in light of negative impacts of anthropogenic climate change, limited stock of fossil fuels and concern for sustainability. For instance, German energy transition (*Energiewende*), one of the most notable national shifts in energy system in the world, includes, among other things, increasing use of renewable energy for electricity generation and reducing demand for energy, aided by energy efficiency measures. During 1990-2013, share of renewable energy in German electricity grid increased from 3% to 25% [1]. Germany has more ambitious goals to meet in the foreseeable future. In regional context, India has massive plan to exploit renewable energy resources to generate 175 GW electricity by 2022 of which 40 GW is expected from solar rooftop [2]. In fact, Bangladesh is also in energy transition due to the increasing demand for energy to propel the growing economy. It is quite obvious that energy demand would further increase in the coming days to ensure robust socioeconomic development. However, the relevant questions are: whether the present energy transition is sustainable and if it is not, what implications does the transition have and how can we shape the transition to a sustainable one? In that regard, the paper has reviewed the energy transition of Bangladesh over the last decade, analyzed secondary data and looked into the energy-climate policy landscape of Bangladesh. Additionally, the paper has investigated the energy

trilemma index, which is being measured on three interconnected parameters, i.e., energy security, equity and environmental performance, as defined by World Energy Council [3], to gauge the performance of present energy transition of Bangladesh.

2. The ongoing Energy Transition in Bangladesh

Over the last 5 to 6 years, electricity supply of Bangladesh has increased significantly, which is driven by the government's intention to fulfill the need of the demand side, including, among others, industries, households and service sectors. Another factor that has also triggered the necessity of increasing installed capacity of electricity is the lack of access to electricity in some parts of the rural areas. Overall, the installed capacity of electricity has increased by almost 100% during 2013-18, i.e., an increase from 9,713 MW in 2013 to 18,768 MW in 2018 [4-5]. Energy mix in electricity generation has been drastically changed. While the national grid is still being dominated by electricity generated from natural gas, it is not like the case of a decade back. In 2008, 88% of total installed capacity was natural gas based against 5.9% of that from liquid fuel [6]. However, today, share of gas to national grid stands at around 53% and that of liquid fuel is over 27% excluding captive generation. Share of renewable energy is paltry 2.77% [5]. Despite establishment of a Nodal Agency, namely, the Sustainable and Renewable Energy Development Authority (SREDA), with the mandate of promotion of sustainable energy, there has not been much success. As of now, the country has only an installed capacity of 519 MW based on renewable energy, consisting of 271 MW from small scale solar home systems, installed in

the off-grid rural areas by the households themselves, representing more than 50% of renewable energy in the energy mix of national electricity grid. In contrast, among the on grid renewable energy, around 17 MW is from solar and the remaining is almost entirely from hydro, which was installed during 1962-88 [5, 7]. Although the government has a target of generating 10% electricity from renewable energy by 2021 [5], it seems unlikely that the target would be achieved at the current pace. Moreover, the country has targets of reducing 15% and 20% demand for energy through energy efficiency by 2021 and 2030 respectively. Notably, another target of 10% energy efficiency by 2015 was set by the government, which despite being supported by low cost finance, has failed to produce desired impacts [3].

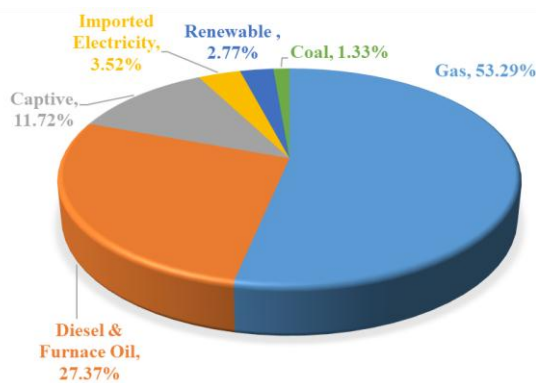


Fig.1 Energy mix in national grid of Bangladesh in 2018 [6]

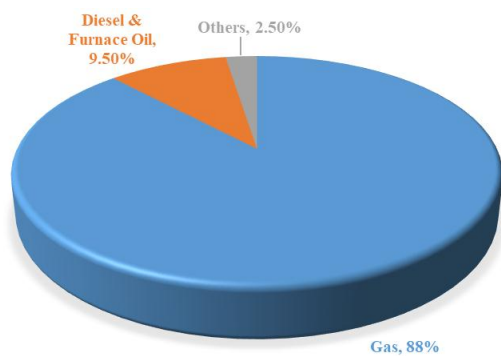


Fig.2 Energy mix in national grid of Bangladesh in 2008 [5]

3. Implications on Energy Trilemma

Unfortunately, the present development path in the energy sector seems to be unsustainable, leading to further complex problems. Out of 130 countries, being indexed in Energy trilemma based on energy security, equity and environmental sustainability, Bangladesh is 113th [3]. Even though access to electricity has increased to 75.9% [8], still electricity is not fully reliable due to load-shedding. On the other hand,

increasing supply of electricity has been possible through installation of imported liquid fuel-based power plants, which have only exacerbated the energy security of the country. During last decade, reliance on local natural gas to generate electricity has decreased and dependence on imported liquid fuels has gradually increased. Over the period from 2008 to 2018, share of liquid fuels in fuel-mix of national grid has increased from 9.5% to 27.37%, putting increasing pressure on import. Additionally, 3.52% of total installed capacity has been brought to the national grid through cross-border trade [5-6]. While energy security in Bangladesh was never ensured, the transition from local natural gas to mainly imported liquid fuels has only increased more vulnerability of energy sector of the country. The present transition has also severely affected from environmental point of view and climate policy context of the country. Per capita Greenhouse Gas (GHG) emission of the country has been increased from 0.46 ton of CO₂ to 0.98 ton of CO₂ [9-10]. Although per capita GHG emission of the country is still much less compared to many developed nations and at the development phase of the country emission would increase, the government would face monumental challenge to meet GHG mitigation target under the (Intended) Nationally Determined Contributions (NDC), submitted to United Nations Framework Convention on Climate Change (UNFCCC) as part of the Paris Agreement. The projected increase in power, transport and industry, according to NDC, was 264% in 2030 compared to 2011 under business-as-usual (BAU) scenario [11] but in last four years, per capita GHG emission increased by more than 100%. Therefore, under BAU scenario, GHG emission of the stated sectors would automatically increase by more than 264% in 2030, posing serious challenge to meet NDC targets of reducing unconditionally 5% GHG emissions and conditionally 15% GHG emissions in those three sectors. Aside from increasing GHG emission, overall environmental situation of the country has significantly deteriorated. The country is 179th out of 180 countries in Environmental Performance Index, published in 2018 [12]. Understandably, overall environmental performance depends on many parameters, including management, where Bangladesh always lags behind but increasing emission because of switching to more polluting fuel has played a significant role on such a dismal environmental performance.

The present transition has also not helped the promotion of renewable energy in the country. Contrary to the fact that Bangladesh has more sunlight than many countries, Bangladesh generates much less electricity from solar energy. At a time when price of renewable energy is falling globally, renewable energy remains much expensive in Bangladesh and despite several round of price adjustments of electricity as well as fossil fuels in the recent years, national grid and fossil fuels are still subsidized. These twin problems, i.e., higher price of renewable energy resources and subsidized fossil fuels,

are plaguing the market development of renewable energy. The single digit loan scheme for renewable energy is the only incentive that the investors have but it has failed to provide necessary signal to the prevailing market to attract investment on renewable energy. As the investors have not come along with national policy target for renewable energy, there is very little progress on renewable energy front. With only small achievement in terms of solar energy, we are at the very bottom of the learning curve to harness renewable energy resources. As of now, energy efficiency has also not been a success, attributed to several factors. Absence of sufficient incentive for the industry management, presence of subsidy in both fossil fuels and electricity, lack of market readiness and absence of enabling environment have hindered promotion of energy efficiency in the country.

It is the impression that, due to lack of options, the government had to choose the quick-fix strategy, i.e., increasing power supply either from local resources or imported fuels, to meet increasing demand for electricity. The quick-fix strategy has only benefited the country in one dimension, i.e., increasing access to electricity and meeting part of growing demand, at the expense of energy insecurity and environmental performance. In fact, Bangladesh has become worse off in Energy Trilemma. The situation can partly be explained by the facts that energy sector had been neglected during the early part of last decade when almost no new generating capacity was added in any form, maintenance of age-old power plants was lagging and efforts to minimize transmission and distribution loss were not enough.

4. Making Energy Transition Sustainable

Primarily, it is essential to identify the technical solutions that can make the energy transition sustainable taking into account of national priorities and considering the Sustainable Development Goals (SDGs) and Paris Agreement. Energy efficiency is the most obvious and it is probably the cheapest as the cheapest energy is what we don't need to produce at all. On the one hand, energy efficiency would reduce demand for energy and on the other; it would help industrial expansion with the saved energy. This can further help in ensuring access to electricity in areas, which are not connected to grid. Study shows, there is an opportunity to reduce energy demand in the industrial sector, which is the largest energy consumer in the country, by 36% through implementation of energy efficiency measures, such as, efficient lighting, combustion control, waste heat recovery, improved insulation, implementing energy management system and the like. Commercial buildings also provide the opportunity of up to 50% energy savings [13]. Study, conducted in six major industrial sectors of Bangladesh, shows that 30% energy efficiency can be achieved in economically feasible way [14]. Although cost-benefit analysis shows that energy efficiency makes sense, its implementation poses lot of

challenges. Uptake of energy efficiency is heavily reliant on policy instruments. Notably, the draft energy audit regulation of Bangladesh is going through the government's approval process and the energy standards regulation for appliances is anticipated to be finalized soon. Once these regulations are in place, the challenge would be to implement the energy efficiency targets of the government, i.e., 15% by 2021 and 20% by 2030 respectively. Notably, cost savings alone are often inadequate to stimulate the adoption of energy efficiency measures. As such, policymakers must align the interests of industry owners and consumers and implement a combination of energy audit regulation, energy efficiency standards and incentives. Incentives would play significant role as industries, for instance, under BAU scenario are making profit and they don't have enough motivation for reducing energy consumption. Therefore, appropriate form of financing shall be made available to attract industries to be energy efficient and at the same time, energy efficient industries shall be rewarded. Although currently some energy efficiency financing facilities from Japan International Cooperation Agency (JICA) and the Central Bank of Bangladesh are available, overall demand for funding to make a complete transformation through energy efficiency would be billions of USD as 120 energy inefficient industries of six sectors, according to a study, would require an aggregate investment of USD 140 million to make them energy efficient [14]. In addition, subsidy from fuels and electricity shall be removed to reflect true price of electricity and fuels. Once these price distortions are reduced, energy efficiency measures would generate more cost savings compared to present situation, making energy efficiency projects more viable. These must be accompanied by raising awareness across all industrial sectors to focus on greater energy efficiency.

Apart from taking policy measures and creating enabling environment for energy efficiency, it is also necessary, for instance, to draw lessons from experiences of other countries on energy efficiency, particularly with regard to the rebound effect. The rebound effect appears when energy saved from use of efficient technologies is being offset by overuse of energy, such as, buying an energy efficient car and driving it more than normal. Another form of rebound effect arises when energy inefficiency is minimized by installing energy efficient technologies and the monetary saving is being used to maximize other utilities that consume more energy, ultimately leading to a state of no energy saving at all. As the country has been enjoying a sustainable economic growth and real income of people has increased, it is likely that rebound effect might occur in different sectors of the economy and therefore, target for energy efficiency as well as tariffs of energy might be adjusted over time.

While energy efficiency is one option, the other conduit to address energy trilemma and to make the energy

transition sustainable is to increase diversity in energy supply and electricity generation. Bangladesh can surely be benefited from diversity on the supply side of energy given that solar has proven potential in the country and the wind resource mapping, which is currently being undertaken in the country, would help identify the feasible locations to install wind turbines in future. These would help address the crisis that at times stifles business and keeps homes in the dark and help improve with regard to energy equity. Building on broad consensus, the policymakers need to set clear and straightforward goal on renewable energy, backed by supportive regulatory environment, instead of only fixing target like the present one of achieving 10% electricity from renewables by 2021. In tandem, it is necessary to adopt the policy instruments that can attract investment in the sector. Although, of late, a net metering guidelines has been drafted by the government to attract households and industries to generate electricity from renewables to supply to grid and adjust with own consumption [15], impacts of the policy would only be realized after couple of years of operation. In the meantime, some important issues need to be addressed. It is essential to reduce price distortion through removal of subsidy from fuels and electricity to encourage private sectors to invest in electricity production from renewable energy sources. Moreover, the present refinancing scheme of the Central Bank shall be made more friendly and attractive to the private investors.

On the other hand, SREDA, being the Nodal Agency for promotion of sustainable energy in the country, shall work on creating a conducive environment for accelerated implementation of energy efficiency and renewable energy projects and programs. It shall, therefore, look into the policy instruments to be formulated and adopted to foster sustainable energy in Bangladesh and share best practice cases amongst different stakeholders.

The energy transition, supported by energy efficiency and renewable energy, is not only about providing energy access by renewables or reducing demand by energy efficiency; both can drastically cut down GHG emissions and other pollutions, improving environmental sustainability. Furthermore, sustainable energy transition has strong interlinkages with other social, environmental and economic co-benefits, such as, opening up job opportunities, diffusion of low carbon technologies, technological innovation, less air pollution and reduction in import of fossil fuels etc. In summary, this transition would help Bangladesh in improving its position on energy trilemma due to possibility of better performance on both energy security, equity and environment parameters. In parallel, Bangladesh would be able to contain the sharp increase of GHG emission to the level where it might be in line with NDC projection, fulfilling the commitment under Paris Agreement. Finally, sustainable energy transition would

enable the government to achieve different SDGs, i.e., SDG 3, 7, 9 & 13, through reducing deaths and diseases from improved air quality (SDG-3), ensuring access to clean and reliable energy (SDG-7), sustainable industrialization (SDG-9) and combating climate change (SDG-13) [16].

In addition to energy efficiency and renewable energy, the unexploited off-shore gas can be pivotal to both increasing energy security of the Bangladesh and reducing air pollution and GHG emissions. It is particularly important in the face of fast depleting present gas reserve and can significantly change the current state of energy policy making. The settlement of dispute with neighboring countries on maritime boundary has also paved the way for the country to make an all-out attempt to unleash potential of offshore gas.

5. Conclusion

While energy transition of Bangladesh during last decade has been mainly aimed at increasing electricity supply to meet the demand within a short span, it has been mostly reliant on imported fossil fuels, deteriorating energy security of the country and negatively affecting environmental performance. The quick-fix strategy to solve the energy problem has taken its toll. Bangladesh is currently sitting almost at the bottom of the energy trilemma index and global environmental performance index. The country is also at the risk of failing to meet GHG mitigation targets under NDC and Paris Agreement. Against these backdrops, a sustainable energy transition, i.e., increasing use of renewable energy to generate electricity and application of energy efficiency on the demand side, could solve the problems of energy security, environmental problems and so on. It could also help achieve NDC targets and multiple SDGs. However, despite having policy targets, both energy efficiency and renewable energy are yet to be explored to the level of potentials and expectations. Both energy efficiency and renewable energy shall be backed by suitable policy instruments, for example, incentive mechanism and appropriate finance. In parallel, price distortion, i.e., subsidy, shall be removed to catalyze investment on energy efficiency and renewable energy and stimulate private sector participation. There should also have plan to explore our own offshore gas, which has so far been disappointingly untapped. At the beginning, it is likely to be challenging to shift from present energy transition to sustainable transition but SREDA, the Nodal Agency for sustainable energy promotion, shall play important role to make the transition happen. In order to achieve the desired results, it shall take care of the formulation and implementation of policy instruments vis-à-vis energy efficiency and renewable energy. It shall also carry out the awareness raising program on sustainable energy at all levels with a long-term vision, dedicated focus and clear message. With a strong push from the government, supported by enabling environment, it would be

possible to achieve a paradigm shift in the energy sector of Bangladesh from present energy transition to a sustainable one. In that regard, the ideas presented above can be taken forward in view of Bangladesh's energy and climate policies and related targets.

REFERENCES

- [1] E. Laes, L. Gorissen & F. Nevens, A Comparison of Energy Transition Governance in Germany, The Netherlands and the United Kingdom, *sustainability*, Vol. 6, pp 1129-1152 (2014).
- [2] M. Goel, Solar rooftop in India: Policies, challenges and outlook, *Green Energy & Environment*, Vol. 1, No. 2, pp 129-137 (2016).
- [3] S. Alam, In support of a market mechanism for energy efficiency to address energy trilemma: Bangladesh context, *Proceedings of the 23rd World Energy Congress*, Istanbul, Vol. 1, pp 477-487 (2016).
- [4] M. N. M. Chowdhury, S. Uddin & S. Saleh, Present Scenario of Renewable and Non-Renewable Resources in Bangladesh: A Compact Analysis, *International Journal of Sustainable and Green Energy*. Vol. 3, No. 6, 2014, pp 164-178 (2014).
- [5] SREDA (2018). Retrieved August 20, 2018, from <http://www.sreda.gov.bd/>
- [6] M. K. Mujeri, T. T. Chowdhury & S. Shahana, Energy Sector in Bangladesh: An agenda for reforms, GSI Report, International Institute for Sustainable Development (2014).
- [7] Global Energy Observatory (2018). Retrieved August 20, 2018, from <http://globalenergyobservatory.org/geoid/40450>
- [8] SE4ALL database, IEA, & World Bank (2018). Retrieved August 15, 2018, from <https://datacatalog.worldbank.org/dataset/sustainable-energy-all>
- [9] World Bank (2018). Retrieved August 15, 2018, from <https://data.worldbank.org/country/bangladesh>
- [10] Economic Relations Division, Journey with Green Climate Fund: Bangladesh's Country Programme for Green Climate Fund (2018).
- [11] Ministry of Environment and Forests, Intended Nationally Determined Contributions (INDC) of Bangladesh (2015).
- [12] Yale University & Columbia University, Environmental Performance Index (2018).
- [13] S. Alam & A. M. B. Anam, Reducing Energy Efficiency Gap in Bangladesh: Role of ESCO as Intermediary, *Annual Banking Conference-2016*, Bangladesh Institute of Bank Management, pp 302-312 (2017).
- [14] Tetra Tech ES, Inc., Industrial Energy Efficiency Opportunities and Challenges in Bangladesh - Final Report (2014).
- [15] Net Metering Guidelines-2018, Retrieved August 21, 2018, from

<http://www.sreda.gov.bd/index.php/site/notices/17fb-1bc4-59c4-4f78-32c8-bec3-8324-4ed2-55b1-c970>

- [16] Sustainable Development Goals, Retrieved August 22, 2018, from <https://www.un.org/sustainabledevelopment/sustainable-development-goals/>

Effect of Blended Yarn on Physical Properties of Single Jersey Knitted Fabrics

Mohammad Naim Hassan*, A.K.M Nayab Ul Hossain, Md. Shakhawat Hossain, Moni Sankar Mondal, Joy sarkar,
Rezve Hassan Aunik

Department of Textile Engineering, Khulna University of Engineering and Technology, Khulna- 9203, BANGLADESH

ABSTRACT

In this study variations of knitted fabrics properties due to different blended yarn were analyzed. Here weft knitted fabrics like single jersey were used. Yarn count and GSM of fabric has great impact on fabric properties. Aim of this project is to find out the convenient strategies to choose yarn count selection, GSM selection to get the desired qualities in the single jersey grey fabrics. In this research, Knit fabrics(made from blended yarn) having different GSM were tested where a specific yarn count was taken into consideration of blended yarns for manufacturing single jersey fabrics.

Keywords: Fiber, Yarn, GSM, Yarn count, Stiffness, Tear strength.

1. Introduction

A textile fiber is a long thin object with a high ratio of length to thickness. It is characterized by a high degree of fineness and outstanding flexibility. In addition, it should have dimensional and thermal stability and minimum levels of strength and extensibility consistent with the end use[2].

A yarn is defined as “an assembly, of substantial length and relatively small cross-section, of fibers or filaments, with or without twist”. The main yarn properties are yarn count and yarn twist[1]. Yarn Count is the numerical expression of fineness. According to “Textile Institute” the number indicating the mass per unit length or length per unit mass of yarn is called count [1]. Generally combed yarn strength is higher than carded yarn of the same count[4]. Yarn twist is the spiral turns given to the yarn in order to hold constituent fibers threads together. An increase in the amount of twist produces an increase in the yarn strength, if yarn strength is increase, the fabric strength will be increased [1]. Normally combed yarns are stronger, less hairy, more uniform and more lustrous than carded yarns [5].

There are three principle methods of mechanically manipulating yarn into textile fabrics : interlacing, intertwining, interloping. Knitting is a process of manufacturing a fabric by inter looping of yarns[1].

The primary knitting elements of circular knitting machines are needle, cam, and sinker. The rising demand on knitted garments all over the world motivate the researcher to research about various knitted fabric, production processes, developing new structures[8]. Different count yarns produce different knit fabric. The properties of knit fabric are changing with change of count of the yarn by keeping the parameters of knitting machine (diameter, gauge, stitch length) same in every case. Properties of knitted fabric like GSM, Stiffness, Tear strength, Tensile strength etc. are showing different value in different count yarn .In this paper changing of values with the changing of count of yarn

were observed. Here, two different counts of yarns were used

Fabric quality means different properties of finished fabric which depends on yarn properties and fabrics construction. A knitted fabric quality is depended on the fabric properties. The properties which are important for knitted fabric and maintained in the industries from grey stage to finished stage are GSM, Stiffness, tearing strength, tensile strength etc.

A high level of elasticity and recovery is being possessed by knitted fabric for unique properties. A good quality knitted fabric has some good properties, ex-tearing strength, stiffness and average tensile strength etc. And these properties are varied by different yarn counts and GSM. In this study variation of three properties of knitted fabrics due to different yarn count and GSM are considered.

2. Materials & Methods

2.1. Materials In this research work, the following materials are used to evaluate the properties of weft knitted fabrics.

- Single Jersey weft knitted Fabrics (made with 26 Ne blended yarn).

3. Methods

3.1. **Yarn Selection:** As per the experiment the variation of properties of knitted fabric due to different count of yarn such as 26/1 was used to produce weft knitted structures like—Single Jersey.

3.2. **Determination of Fabric Weight (GSM)** After relaxation & conditioning of knit fabric samples, GSM of samples were tested by taking test samples with the help of GSM cutter & weighing balance (electronic) .

4. Results and Discussions

4.1. Stiffness is the rigidity of an object — the extent to which it resists deformation in response to an applied force. It is the tendency of fabric to keep standing without any support. Bending stiffness characteristics of

* Corresponding author. Tel.: +88-01714509765
E-mail addresses: naimhassan375@gmail.com

fabrics arise from the structure of the fabric itself as well as from the structure of the constituent yarns. Yarn (or fiber) diameter is the most important structural property of a fabric to affect its stiffness. As the fiber or yarn diameter is increased, the fabric stiffness increases. The stiffness of fabric was tested according to ASTM Standard – D4032.

4.1.1. Pneumatic Stiffness Test for blended yarn:

Here CVC (60/40) fabric and GM (10%) fabrics were taken and both of those fabrics had same yarn count 26

No of observation	Count Ne	Yarn Composition	Stitch length	GS M	Pneumatic Force (N)
01	26	CVC(60/40)	2.82	160	0.1
02	26	PVC(50/38/12)	2.80	160	0.2
03	26	GM(10%)	2.80	165	0.4
04	26	GM(10%)	2.86	160	0.1
05	26	GM(1%)	2.82	165	0.2

Ne and GSM 160. Both of the fabrics showed same stiffness. PVC (50/38/12) has more stiffness than CVC (60/40). GM (10%) has more stiffness than GM (1%).

4.2. Tear strength (or tear resistance) is a measure of how well a material can withstand the effects of tearing. Tear strength is the resistance of the fabric against tearing or force required to propagate the tear once it is initiated[7]. Tear strength of the single jersey grey fabrics relies on: GSM of the fabric, strength of yarn, CPI and WPI, fibers to manufacture yarn, Type of fabric. Generally by increasing the GSM more tearing strength of the fabric can be found. Yarn strength is directly related with the tearing strength of the fabric, consequences for the augmentation of yarn strength is the possibilities of getting more tear strength. If we compare tear strength of fabrics made from simple ring spun yarn or compact or filament yarns then less tear strength will be found in case of simple ring

yarn. Usually more ends/inch and picks/inch give more tear strength in the fabrics. The spun yarn if used in fabric shows low tear strength as compared to the filament yarn. It is easy to tear the knitted fabric as compared with the woven one. The Tear strength of fabric was tested according to ASTM Standard – D1424.

No. of observation	Count (Ne)	Yarn composition	Stitch length	GSM	Test result (N)
1	26	CVC(60/40)	2.82	160	30.2
2	26	GM(10%)	2.80	165	26.3
3	26	PVC(50/38/12)	2.80	160	28.2
4	26	GM(1%)	2.80	165	24.2
5	26	GM(10%)	2.86	160	24.0

Here CVC (60/40) fabric had shown more tearing strength than PVC (50/38/12) fabric. CVC (60/40) fabric had shown more tearing strength than GM (10%) fabric.



Figure : Graphical representation of tearing strength

4.3. Tensile strength is one of the most important mechanical properties for fabrics. Tensile strength is the ability of a material to withstand a pulling (tensile) force. The tensile strength of a fabric is the maximum amount of tensile stress that it can take before failure, such as breaking or permanent deformation. The resistance of a material to longitudinal stress, measured by the minimum amount of longitudinal stress required to rupture the material. The tensile strength of fabric was tested according to ASTM Standard E - 4. Here UTM (Testometric) was used to calculate the tear strength of the fabric.

4.3.1. Tensile strength test with UTM for fabrics made with blended yarn:

No of observation	Count Ne	Yarn Composition	GSM	Elongation (mm)	Force N
01	26	CVC(60/40)	160	190.22	591.0
2	26	PVC(50/38/12)	160	224.6	533.4
3	26	GM(1%)	165	219.1	635.2
4	26	GM(10%)	160	233.7	586.4
5	26	GM(10%)	165	203.6	382.2

Elongation of GM (10%) is higher than the elongation of CVC (60/40). Breaking force of GM (10%) is less than the breaking force of CVC (60/40). Elongation of PVC (50/38/12) is higher than the elongation of CVC (60/40). Breaking force of PVC (50/38/12) is less than the breaking force of CVC(60/40).

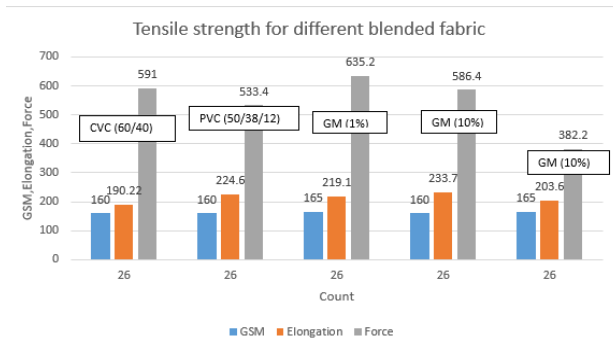


Figure : Graphical representation of tensile strength

5. Conclusion

In case of blended yarn more tear strength, more stiffness and more breaking force were found. CVC (60/40) fabric and GM (10%) fabrics showed same stiffness. PVC (50/38/12) has more stiffness than CVC (60/40). GM (10%) showed more stiffness than GM (1%). By using blended yarn in single jersey weft knitted fabrics Elongation is decreasing with the increasing of GSM. This happened because GSM 160 fabric has less compact structure than the GSM 165 fabric. The elongation is more in less compact area due to force applied. Some properties like stiffness, tearing strength & tensile strength are varied according to the use of different yarn produced by using with different ratios of manmade fibers. In this article basically this was an understanding of different physical properties of different samples which were collected.

REFERENCES

- [1] J.E. Booth "Principles of Textile Testing", India: CBS publishers and Distributors, 1996, pp.209-235
- [2] Manufactured Fiber Technology by V.B. Gupta, V.K. Kothari
- [3] David.J.Spencer"KnittingTechnology", Cambridge: Woodhead, 2008, pp.1-61
- [4] Klein. W. "Manual of Textile Technology", UK: The Textile Institute, 2008, pp, 286-289.
- [5] D.B. Ajgaonkar "Knitting Technology", New Delhi: Universal Publishing Corporation, 2006, pp.180-181
- [6] B P Saville, From Physical Testing of Textiles, Woodhead Publishing Ltd, 1999
- [7] Wikipedia, Knitting, Link <https://en.wikipedia.org/wiki/Knitting>

ICMIEE18-304

Sizing of Warp Yarn with a Different Concentration of Animal Fat and Acids and Determination of the Performance in Comparing with Conventional Sized Yarn

Joy Sarkar^{1*}, Md. Shamsuzzaman Rasel²

¹Department of Textile Engineering, Khulna University of Engineering & Technology, Khulna-9203, BANGLADESH

²Department of Textile Engineering, World University of Bangladesh, Dhaka-1207, BANGLADESH

ABSTRACT

This paper deals with Animal fat, which could effectively assess alternatives sizing materials than conventional sizing materials. Here, we have picked two yarn types; 1) Sized yarn and 2) Unsized yarn for the test. In sample preparation, we have treated 100g munsized yarn with 500 ml fat solution each containing 10% HCL, 10% Glacial Acetic Acid, 10% Lactic acid and with only water. Handloom had been used to weave for both treated yarn samples. Then some physical and mechanical properties were tested to calculate weaving performance. After measuring the fabric weight we found that only water and fat solution treated samples weight showed higher GSM than other samples. Besides, higher tensile strength had measured for conventionally treated samples. Approximately 30 – 50% less breaking strength was recorded for other samples for warp way directions, although only a little lower breaking strength had found in weft way directions. Again, higher abrasion resistances were observed for conventional fabric samples however HCL treated samples had prevailed least properties. Therefore costing of acid-fat treated samples are much lower than conventional sizing, besides desizing could be bypassed and single bath scouring and bleaching could be applicable.

Keywords: Animal fat, Sizing, GSM, Tensile strength, Abrasion.

1. Introduction

Now a day, Sizing warp yarns with starch coating is an important process considered as standard practice in the textile industry. The physical property of the yarn and on the performance of the yarn in the weaving operation lies on effective sizing process [1 – 3]. Fatty lubricants such as waxes and oils are applied to warp yarn to reduce friction, the yarn breakages and provide lubrication to the yarns in order to decrease the electrostatic problems [4 – 7]. However, it requires desizing of all the chemicals which is known as desized process. Textile industry worldwide is facing considerable challenges due to concerns on price and availability of raw materials, increasing environmental restrictions and lack of technological breakthroughs that can reduce cost and/or develop new products [8 – 10]. Approximately, costing of Raw materials (66%), Size and Chemicals (4%), Production cost (8%), Worker wages and Salaries (8%), Interest on investment, loan, depreciation (7%), Overheads and administrative expenses (7%) is experienced this current year [11]. Considerable efforts are being made to find alternative approaches to explore the possibilities of reduced sizing and, preferably, size-less weaving (i.e., eliminating warp sizing) in the production of cotton fabrics [12].

In this article, a comprehensive effort on using animal fats mixing with different concentration of acids instead of conventional sizing materials was done. As animal fats and other acids can be removed totally in either single or double bath Scouring and Bleaching in a standard condition thus desizing process can be possible of bypassing.

After the finishing process, some of the physical and mechanical properties were tested and was compared with the conventional manufactured fabric.

2. Materials and methods

2.1. Materials

2.1.1. Yarn sample

For testing, sized and unsized warp yarn and weft yarn were collected from Sinha Textile Group whose count was 40/2Ne.

2.1.2. Size ingredients

Animal fat was used as sizing ingredients.

2.1.3. Chemicals

HCL (Azithromycin BP, CN HUB), Acetic Acid (MK Corporation, Dhaka), Lactic Acid, NaOH (Triveni Interchem Pvt. Ltd., China), H₂O₂ (Suvidhi Industries, India)

2.1.4. Warp yarn preparation

At first animal fat were collected and were melted by applying direct heat on it. Then 10% solution of mentioned acids was prepared separately. Three acids – water solution and only 10 ml water were mixed with the liquid animal fat containing 40 ml of liquid fat and prepared 4 different solutions of 50 ml individually.

2.1.5. Fabric samples

The following 5 types of fabric samples were weaved by using different chemical treated yarns:-

Sample – 1: Fabric constructed by using conventional sized yarn.

Sample – 2: Fabric constructed by using 10% HCL and Fat treated solution

Sample – 3: Fabric constructed by using 10% Acetic Acid and fat treated solution

Sample – 4: Fabric constructed by using 10% Lactic Acid and Fat treated solution

Sample – 5: Fabric constructed by using only fat and water treated solution

* Corresponding author. Tel.: +88-01711924556

E-mail addresses: joy.sarkar@te.kuet.ac.bd

2.2. Methods

2.2.1. Methods of sizing with animal fat and acid

The warp yarn (unsized) (For Samples 2 – 5) were passed through the chemical solution separately and treated for 3-5mins. And passed through the squeezer to squeezed the excess fat and chemical liquor. Then passed through a heating chamber to melt the fat from the yarn surface for 1-2 min and again passed through the squeezer to remove the excess fat to make yarn dry. Finally, these treated yarns were prepared for weaving and were sent to the handloom as fabric were constructed by handloom due to lack of loom facilities.

2.2.2. Desizing (sample 1)

For this, the conventional industrial methods were followed to remove the size materials.

2.2.3. Double bath scouring and bleaching (sample 1 – 5)

Double Bath Scouring and Bleaching were done by using 20 g/L NaOH and 1 g/L H₂O₂ at a M:L = 1:20. Here temperature was 90 °C and run time was 20 min.

2.2.4. Determination fabric weight

According to ASTM D3776 / (2013) standard fabric weight was measured. [13]

2.2.4. Determination of tensile strength

According to the ASTM D5034 standards fabric tensile strength was measured. [14]

2.2.5. Determination of abrasion resistance

According to the ASTM D3511 standard fabric abrasion property was tested. [15]

3. Results and discussion

3.1. Effects of sizing on fabric weight

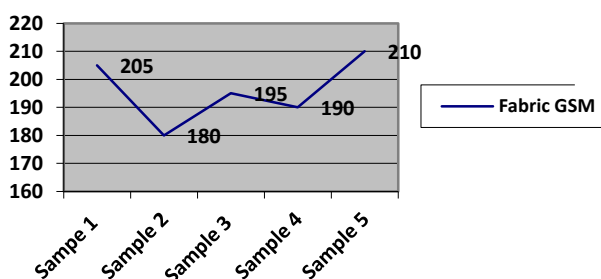


Fig.1 Different sizing effects on Fabric Weight

It is clearly has seen that fabric weight varies for all the tested fabric samples. Lower fabric weight was observed when warp yarns were treated HCL acid and

the higher impact was recorded for only fat treated samples.

3.2. Effects on the tensile strength of the fabric.

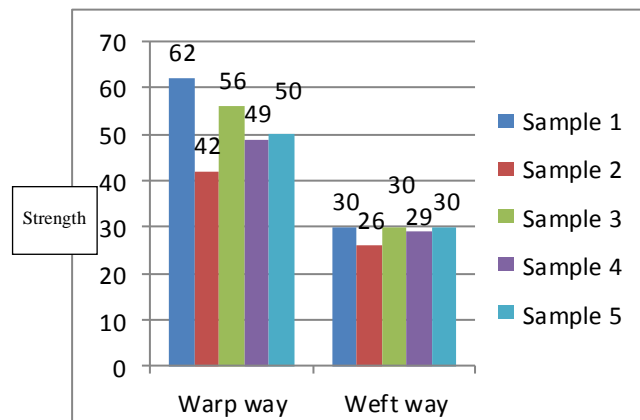


Fig.2 Effects of Tensile Strength on different Samples

Higher strength was found (both warp way (62 kg) and weft way (30 kg)) for conventional fabric samples. All the others breaking strength were observed lower than the conventional methods. Approximately 30 – 50% less breaking strength was recorded for warp way, however, only a little less breaking strength was observed in weft way.

3.3. Effects on the abrasion resistance of the fabric.

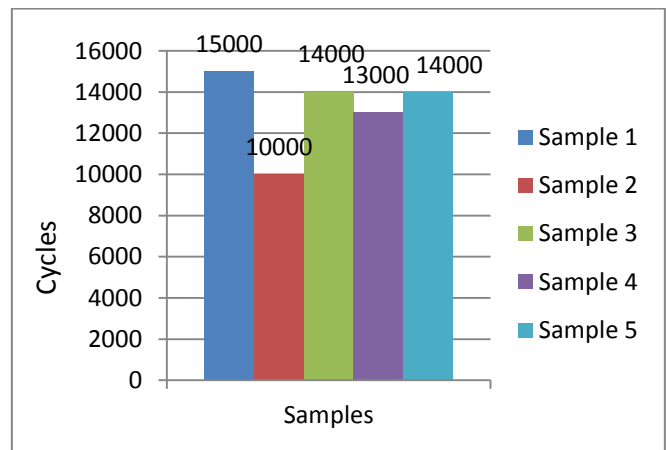


Fig.3 Effects of Cycles on Abrasion Resistance of different Samples

Conventional fabric samples did not break up to 15,000 cycles whereas HCL treated samples breaks when cycles were more than 10,000. Besides samples 3 and samples 5 breaks more than 14,000 cycles and samples 4 breaks after 13,000 cycles.

3.4. Cost analysis

Total liquid = acid (10 ml) + water (40 ml) = 50 ml; this could size approximately 10-15 kg of warp yarn that can

weave around 10 yards of plain fabric on the natural construction on loom.

3.4.1. Sizing cost

Cost while HCL-fat sizing

Price of HCL = \$2.5/L

10 ml HCL price = 2.5 cents that could treat minimum 10 yards of fabric.

So, cost of 1 yards fabric size with HCL = 0.25 cent/yards

Cost while Acetic acid (CH₃COOH) -fat sizing

Price of Acetic Acid = \$ 4.5/L

10 ml Acetic Acid price = 4.5 cents that could treat minimum 10 yards of fabric.

So, cost of 1 yards fabric size with Acetic Acid = 0.45 cent/yards

Cost while Lactic Acid (CH₃CH(OH)CO₂H) -fat sizing

Price of Lactic Acid = \$ 5 /L

10 ml Lactic Acid price = 5 cents that could treat minimum 10 yards of fabric.

So, cost of 1 yards fabric size with Lactic Acid = 0.50 cent/yards

Cost of animal fat

Price of Animal fat = \$0.5 /kg

Price of 20 gm fat = 1 cent (as 20 gm fat was added to 50 ml solution)

20 gm fat is used to size warp yarn which could approximately weave 10 yards plain fabric.

So, cost of fat for 1 yards of fabric sizing = $1/10 = 0.1$ cent

3.4.2. Single bath scouring and bleaching cost

M:L = 1: 20

Cost of H₂O₂ for bleaching 1 yards of treated sample

Price of H₂O₂ = \$3.2 / kg (required 1gm/L)

So, 1 gm price = 0.32 cent

Wt. of 1 yards fabric = 200 gm (approximately)

So water requires = $0.200 \times 20 = 4$ Litre water

So, for 1 yards fabric bleaching, H₂O₂ needs = $0.32 \times 4 = 1.28$ cent

Cost of NaOH for bleaching 1 yard of the treated sample

Price of NaOH = \$0.58 /kg

Price of 20 gmNaOH = $1.165 \times 4 = 4.64$ cent

So, for 1 yd fabric bleach needs NaOH = 4.64 cent

So, total scouring and bleaching cost = $1.28 + 4.64$ cent/yards

= 5.92 cent / yards

Total cost calculation

Total cost of each sample treatment = Sizing cost + Fat cost + Scouring & bleach cost

For HCL-fat treated sample cost = $0.25 + 0.1 + 5.92$ cent/yards = 6.27 cent/yards

For CH₃COOH-fat treated sample cost = $0.45 + 0.1 + 5.92$ cent/yards = 6.47 cent/yards

For CH₃CH(OH)CO₂H-fat treated sample cost = $0.50 + 0.1 + 5.92$ cent/yards = 6.52 cent/yards

Only fat treated sample cost = $0.1 + 5.92 = 6.02$ cent/yards

And conventional sample cost = 14 cent/yards(data collected from factory)

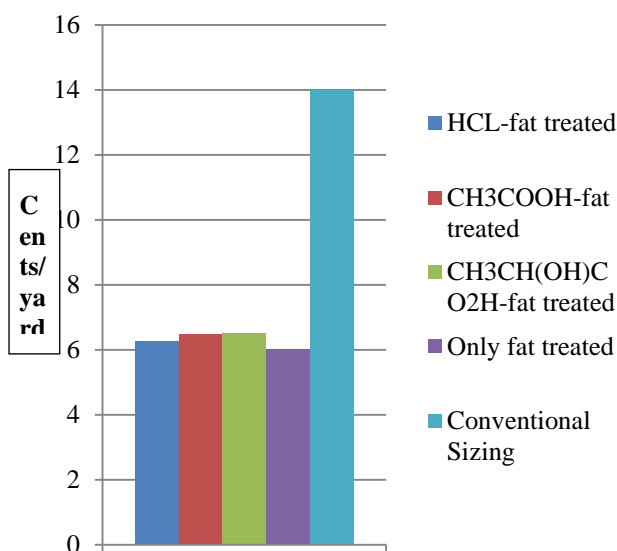


Fig.4 Cost comparison of different sizing processes

From the above cost analysis and through meticulous observation some conclusion can be mentioned as such for every case fat treated samples sizing and scouring and bleaching cost is much lower than the conventional. Therefore, a single bath scouring and bleaching have a possibility where desizing is not mandatory for fat treated samples. On the other hand for the industrial process, it is must have desizing process, scouring, bleaching process individually. Finally acid- fat treated samples are more convenient than conventional.

Conclusion

Sizing and desizing process are the two most important processes to follow in the textile industry. Both processes are important as without better sizing best weavability cannot be achieved and at the same time without proper desizing it is not effective on the further processing. Due to the higher costing and time consuming it has already become necessary to find an alternative to this. In this research work, we tried to show that animal fat could be a better alternative as it can be further removed completely in the process of scouring and bleaching which could save money and time significantly. Though the required or sufficient properties were not found, hence it needs some further work which could establish it as a suitable alternative method of fabric processing.

REFERENCES

- [1] Balcb and Paine. *Production of starch from sweet potatoes. Ind. Eng. Chem.* 23,1205 (1931) .
- [2] Weber, Shaw, and O'Leary. Quality of Sweet-Potato Starch for Beater Sizing of Paper. Misc. Pub. BS 150 (June 1935). .
- [3] Schreiber, Geib, and Moore. *Consistency of potato starch size.* BS J. Research 11, 765 (1933), RP623.
- [4] Lord, P.R.; Mohamed, M.H., (1982). *Weaving: Conversion of Yarn to Fabric.* Woodhead Publishing, Cambridge.
- [5] Goswami, B.C.; Anandjiwala, R.D.; Hall, D.M., (2004). *Textile Sizing.* Marcel Dekker Inc, Auburn.
- [6] Strauss, M.D. and Petty, D.A. "Towards the Perfect Warp" *Textile Asia*, May 1987, pp.47-50.
- [7] Hall, M. "Pros and Cons of Wax for Sizing" *Textile Slashing Short Course Proceedings*, Auburn, Alabama 1985
- [8] Wikipedia, (2012). Distillers grain. http://en.wikipedia.org/wiki/Distillers_grain.
- [9] Pimentel, D., (2003). Ethanol fuels: Energy balance, economics, and environmental impacts are negative. *Natural Resources Research* 12(2), 127–134.
- [10] <http://www.ethanolrfa.org/pages/industry-resources-coproducts>
- [11] 11. On May 7, 2015 / Blog posts, PRODUCTION & PRODUCT DEVELOPMENT / sourcegarment.com
- [12] Sawhney, A. P. S., Dumitras, P.G., Sachinvala, N.D, Calamari, T.A., Bologna, M.K., and Singh, K.V. Research Approaches for reducing or eliminating warp sizing in modern high-speed weaving. American Association of Textile Chemists and Colorists (AATCC), September 2005.
- [13] ASTM D3776 / (2013), Standard Test Methods for Mass per Unit Area (Weight) of Fabric, American Society for Testing and Materials, West Conshohocken, PA, USA.
- [14] ASTM D5034 (2013), Standard Test Method for Breaking strength of fabric, Constant Load of Elongation (CRE), Grab Test, ASTM International, West Conshohocken, PA, 2013, www.astm.org
- [15] ASTM D3511 / D3511M-13, Standard Test Method for Pilling Resistance and Other Related Surface Changes of Textile Fabrics: Brush Pilling Tester, ASTM International, West Conshohocken, PA, 2013, www.astm.org

Natural Gas Scenarios in Bangladesh and Its Future

Md. Saruar Jahan¹, Md. Abu Raihan¹, Mohammad Iqbal¹, Farhad Hawlader²

¹Department of Industrial and Production Engineering, Shahjalal University of Science and Technology, Sylhet-3114, BANGLADESH

²Department of petroleum and mining Engineering, Shahjalal University of Science and Technology, Sylhet-3114, BANGLADESH

ABSTRACT

Natural gas is the most important indigenous source of energy that has been continuously produced and consumed in significant quantities since 1970. Bangladesh is the nineteenth-largest producer of natural gas in Asia. Gas supply meet 56% of domestic energy demand. About 75% of the commercial energy of the country comes from the natural gas. So far 27 gas fields have been discovered of which two of the gas fields are located in offshore area. The paper shows the present scenario of natural gas in Bangladesh and its future. Though Bangladesh has considerable amount of gas yet it is not enough for 50 more years at current demand and extraction rate. The analysis suggests to reduce dependency on natural gas by introducing alternative energy sources. Moreover, a comprehensive energy policy should be developed with a proper regulatory body that has oversight responsibilities. Efficient gas marketing is the key to derive numerous benefits from the gas reserves of Bangladesh. Lastly, Bangladesh government need to explore ocean area that has been acquired from India & Myanmar in 2014.

Keywords: Bangladesh, natural gas, production, consumption and utilization, reserve.

1. Introduction

Natural gas is the most important fuel for Bangladesh, both in terms of energy and diversity of use. Natural gas burns more cleanly than other fuels, such as oil and coal, and produces less carbon dioxide per unit of energy released.

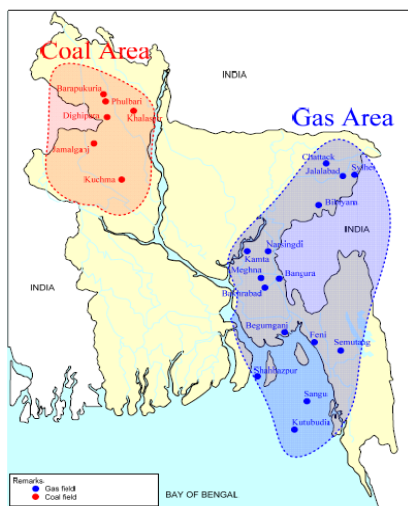


Figure 1: Discovered Coal and natural-gas fields in Bangladesh [7].

Bangladesh Oil, Gas and Mineral Resources Corporation, Petrobangla, is entrusted with the responsibilities of the gas and coal sectors of Bangladesh. Subsidiaries under Petrobangla are responsible for exploration, production, transmission, distribution and marketing of natural gas to the end users. In 1993, there were 17 gas fields in the country

with an estimated total initial gas reserve of 12.43 TCF and remaining reserves of 10.55 TCF. In 2003, the number of gas fields was 22 as shown in figure 1 and the total initial gas reserve was estimated at 20.51 TCF and a remaining reserve of 15.4 TCF. In 2014, the number of gas fields grew to 26 with an estimated initial gas reserve of 26.84 TCF and a remaining reserve of 16.74 TCF. In 2016, remaining gas reserve is 12.88 TCF [1]. Bangladesh also has good amount of coal along with natural gas as its main resources reserved in its territory. But the extensive portion of the demand is met by gas alone and it is about 75% of the total consumptions.

2. Objectives

The objectives of this paper are:

- (i) To analysis the existing reserve and production of natural gas in Bangladesh and (iii) To find out the reasons behind natural gas crisis in Bangladesh and the way to reduce dependencies on natural gas.

3. Present Scenarios of Natural Gas Production in Bangladesh

The production of gas till December 2016 was 14.243 trillion cubic foot and 12.87 trillion cubic foot of gas was in reserve for production. The reserve of natural gas as per December,2016 is shown in the table 1(a), 1(b) and 1(c):

Table 1(a): Gas field in production (in BCF) [1].

Sl. No.	Field	Cumulative Production (Dec,16)	Remaining Reserve (Jan,17)
1	Titas	4221.34	2145.66
2	Habiganj	2273.03	359.97
3	Bakhraabad	803.87	427.65

4	Kailashstilla	647.07	2112.93
5	Rashidpur	585.81	1847.19
6	Sylhet/Haripur	211.27	107.63
7	Meghna	61.32	8.58
8	Narshingdi	180.92	95.88
9	Beani Bazar	94.66	108.34
10	Fenchuganj	148.34	232.66
11	Shaldanadi	87.70	191.30
12	Shahbazpur	26.86	363.14
13	Semutang	12.10	305.60
14	Sundalpur Shahzadpur	9.98	25.12
15	Srikail	54.84	106.16
16	Begumganj	0.88	69.12
17	Jalalabad	1046.70	137.30
18	Moulavi Bazar	289.54	138.46
19	Bibiyana	2530.04	3223.96
20	Bangura	359.05	162.95
	Sub-Total a:	13645.32	12169.60

Table 1(b): Non-production gas field (in BCF) [1].

Sl. No.	Field	Cumulative Production	Remaining Reserve
21	Kutubdia	0	45.5
22	Rupganj	0	33.6
	Sub-Total b:	0	79.1

Table 1(c): Suspended production gas field (in BCF) [1].

Sl. No.	Field	Cumulative Production	Remaining Reserve
23	Chattak	26.46	447.54
24	Kamta	21.1	29.2
25	Feni	62.4	62.6
26	Sangu	487.91	89.85
	Sub-Total c:	597.87	629.19

Grand Total (a + b + c) in BCF	14243.19	12877.89
--------------------------------	----------	----------

Figure 2 shows the historical production of gas from 1993 to 2016. It shows that gas production was significantly increasing from 1993 to 2016. But in recent years, the gas production rate has started to decline.

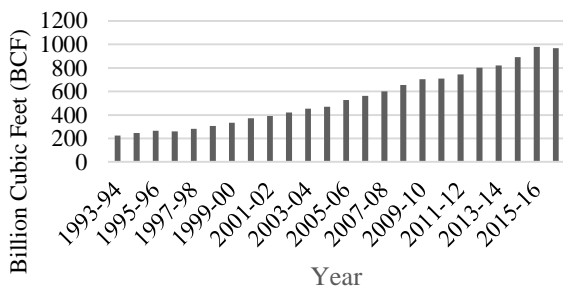


Figure 2: Historical production of gas [5].

Three national companies; Bangladesh Gas Fields Company Limited (BGFCL), Bangladesh Petroleum Exploration & Production Company Limited (BAPEX), Sylhet Gas Fields Limited (SGFL) and four international oil companies; Chevron, Cairn, Tullow and Niko are in charge of exploration and production of gas in Bangladesh. Three national companies are operating with a production capacity of 1137 MMCFD while the international oil companies are operating with a production capacity of 1160 MMCFD [3].

4. Consumption of Natural Gas

Bangladesh being one of the world's most densely populated countries has been facing supply to demand gap of natural gas for a long time. Among all the countries which use natural gas, Bangladesh ranks at 34th position [4]. The table 2 shows the consumption of natural gas by different sectors in the year 2016-2017.

Table 2: Sector wise gas consumption in 2016-17 [5].

Sector	Consumption Percentage
Commercial	0.88%
Domestic	15.64 %
Tea State	0.1 %
Industry	16.52%
Electricity	40.88%
Fertilizer	4.97%
Captive	16.26%
CNG	4.76%

Power generation as expected is the dominant sector and industrial sector, together with fertilizer and captive power uses about 40% of the total gas which is the second largest share. CNG sector had modest beginning with only 1.3% during 2005-06, but rapidly increased to the current level of 5%. Domestic consumption of gas also takes a large share of total consumed gas and this is a sector which has hardly an alternative source to gas. With increasing population and urbanization, the use of domestic use of gas is expected to increase [6].

Table 3: Sector wise demand of natural gas in Bangladesh (Billion Cubic Feet) [9].

Sector	2013-14	2014-15	2015-16	2016-17
Electricity	337	416	458	504
Captive power	143.5	234	258	284
Fertilizer	53.8	94	94	94
Industry	53.8	259	280	307
Brick field	0	0	0	0
Household	101.5	148	168	185
Tea Garden	0.51	1	1	1
CNG	40.1	121	153	168
Commercial	8.9	8.9	14	14
Total	827.8	1,276.5	1,424	1,557

Table 3 shows sector wise demand of Natural Gas in Bangladesh (billion cubic foot). Historical consumption of natural gas by different sectors has been shown in figure 3 below. Separate data for the consumption of natural gas is 1315.88 MMCM for the year 2015-16 and 1329.67 MMCM for the year 2016-17.

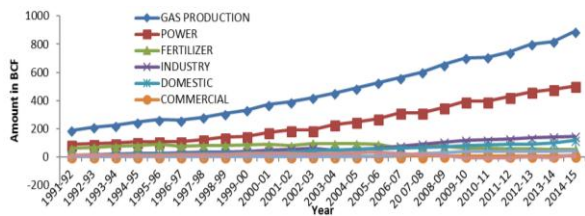


Figure 3: Historical Consumption of Gas in Different Sectors [9].

4.1. Electricity Generation

Bangladesh's power sector is mostly dependent on supply of natural gas. Almost 86% power plants use natural gas as their fuel. As a result, almost 40% of gas produced is used in this sector. In 2017, total installed capacity was 13,555 MW. The maximum peak generation was 9,479 MW which was 4.90% higher than that in the previous year [10]. Only 62% of the population has access to electricity with a per capital availability of 321 kWh per year [7]. Electricity production from natural gas sources in Bangladesh was 91.5% as of 2011. Its highest value over the past 42 years from 2011 was 91.5% in 2011, while its lowest value was 34.69% in 1973. Electricity production from natural gas sources (kWh) in Bangladesh was last measured at 40308000000 in 2011, according to the World Bank. As the power sector is dangerously dependent on natural gas, decentralization strategies are under research.

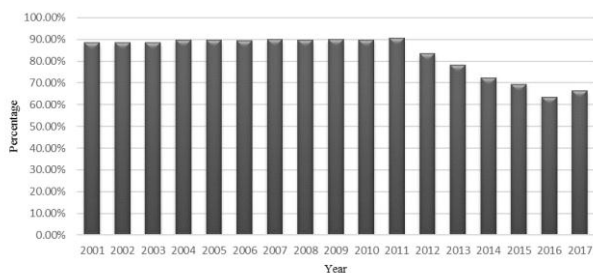


Figure 4: Electricity production from natural gas (percentage of total) [10].

4.2. Industrial Sector

The major industries of Bangladesh which consume natural gas are textile and leather, iron & steel, food processing, beverages & tobacco, nonmetallic minerals, chemicals, pulp, paper & print non-ferrous metal, machinery and some non-specified industry. But newer industries are emerging, some existing ones are flourishing and some are diminishing. So, the industrial sector is hard to define in terms of energy consumption. Relatively small increase in the number of these

industries can have a significant impact on the overall scenario. As of 2017 about 17% of produced natural gas was consumed by this sector.

4.3. Captive Power

Captive Power Plant (CPP) is a plant which produces electricity for its owner's own uses or for a group for their own use. The gas demand for power generation at present has reached nearly 1,200 MMCFD and Petrobangla can supply maximum 900 MMCFD for the power plants

4.4. Fertilizer Productions

Bangladesh has a large agrarian base with 76 percent of total population living in the rural areas and 90 percent of the rural population directly related with agriculture. Fertilizer is considered to be one of the main inputs for increasing crop yields and farm profit for any country. Fertilizer consumption (% of fertilizer production) in Bangladesh was last measured at 231.51 in 2009, according to the World Bank. Fertilizer consumption measures the quantity of plant nutrients used per unit of arable land [11].

4.5. Household Sector

Domestic sector is incurred by the greatest number of customers and it consumes about 11% of the total natural gas produced. The Bangladesh government's priority is to increase gas supply to power plants to be followed by industries and fertilizer factories. Fresh household gas connection does not feature in the Government's priority agenda. The domestic sector slowed down as piped gas connections to household was suspended from July 2010 to 2013. Some 15 MMCFD of gas has been earmarked for new household gas connections. Still the country is facing huge gap in supply and demand of natural gas in household sector and the government is planning to import LPG to cope with gas supply shortfall.

4.6. Compressed Natural Gas

CNG as a vehicle fuels were first introduced to Bangladesh in 1982 through a World Bank pilot project. CNG was promoted by the government in 2005 to address the severe air pollution in Dhaka during the 90's. It had a modest beginning with only 1.3% natural gas consumption in the initial year, but quickly became popular and increased to the current level of 4.76% rapidly.

5. Prediction of Remaining Natural Gas Reserve

At present, the amount of remaining gas reserve in Bangladesh is 12.88 TCF. This reserve is forecasted by using moving average technique taking the data from the year 2014 to 2017 which is shown in figure 5. From figure 5 it has been depicted that if the gas consumption rate remains same, this reserve can be consumed until 2032. After 2032, demand of natural gas will need to be met by another energy sources or by importing energy. Although this forecast shows that, the gas reserve will sustain till 2032, but the real scenario is different. According to table 3 sector wise demand of natural gas

is increasing significantly. So, there is a possibility that the remaining gas reserve will barely sustain till 2032. So, for an uninterrupted gas supply an intensive search should be conducted specially in the southeast part in the country by the relevant authorities.

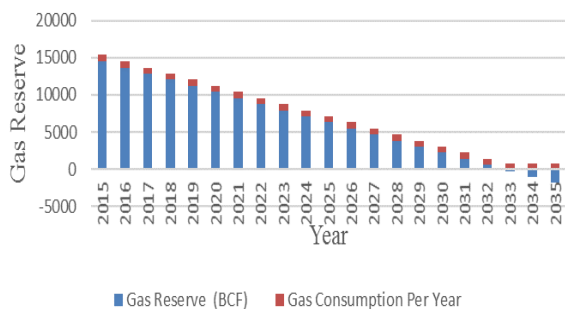


Figure 5: Prediction of remaining natural gas.

6. Recommendations

Some recommendations that need to be quickly set in motion in order to provide consistent supply and utilization of energy are given below.

- Dependency on natural gas should be reduced for power generation.
- Alternative sources of energy such as LNG, nuclear energy and other renewable energy sources like solar, wind, biomass etc. should be implemented and developed.
- Development and focus on renewable sources such as solar, wind, small hydro is also necessary to reduce the pressure on natural gas.
- Government should prepare an action plan to ensure energy efficiency & conservation both at supply and demand side, where number of interventions will be identified for implementation within a time-frame work.

It is important to inform mass consumers of natural gas about the crisis of gas. They should know that if they waste gas and other energy sources, they will completely run out of gas in no time. Government can create campaigns and use media to enlighten people.

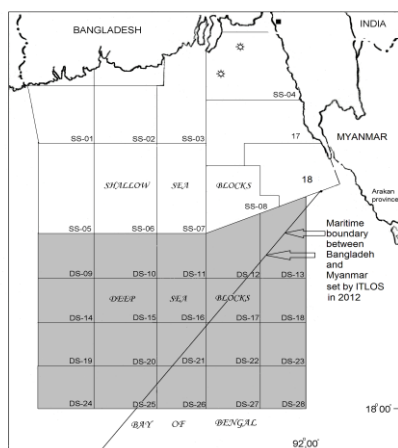


Figure 6: Possible availability of Natural Gas in Bay of Bengal [9].

Figure 6 shows possible availability of natural gas in Bay of Bengal. Bangladesh has the scope to explore the area boarding Myanmar and India in the Bay of Bengal. Myanmar already explored and found available of gas in their side of boarder in sea.

At present the government of Bangladesh is importing LNG. It is a part of the government's efforts to eliminate gas shortages and power outages and unlock the potential of the economy.

7. Reasons behind natural gas crisis in Bangladesh and steps taken by the present Government to supply natural gas as per priority need.

Bangladesh is facing gas crisis of 500 million cubic feet a day (mmcf/d), which is one fifth of the demand. The government is bound to monitor the utilization of gas in important sectors like power generation, fertilizer factory, household consumption and CNG sector. Gas is used in the industries primarily as a source of power, heating in the boilers and in some cases as a raw material. Transportation sector has recently been experiencing a rapid growth in gas connection. At present due to shortage of natural gas reserve, supply of natural gas is supplied limitedly to fertilizer factories in Bangladesh. Frequently Shahjalal fertilizer factory remains close for sometime. Similarly CNG Gas stations remain close from 5:00 pm to 8:00 pm every day throughout the country. Also gas supply has been shorten in Savar industrial area and some industries in and around Chittagong city. Those industries uses long cylinder filled with natural gas during shortage of natural gas supply through pipes. Nowadays no permission is given for connecting gas lines to residential houses and industries. Industries are using long gas cylinders for gas supply to industries. A major hurdle in efficiency delivering power is caused by the inefficient distribution system. It is estimated that the total transmission and distribussion losses in Bangladesh is about one-third of the total generation. Old and inefficient plants need to be replaced soon to minimize loss of gas distribution system. Bangladesh needs to explore other energy source like LNG. New power plants must be run by coal. Also the government of Bangladesh need to take decision to explore sea area bordering Myanmar at sea where several gas reserves have been discovered on the Myanmar side since 2014.

8. Findings

This study depicted that natural gas is the main source of energy in Bangladesh. But at present reserve of natural gas is at stake. This study predicted that the remaining gas reserve can serve the energy demand until 2032. After 2032, Bangladesh needs to depend on other energy sources. But according to increasing demand of natural gas, this gas reserve will barely sustain till 2032. It is possible that the remaining reserve will be consumed before 2030, if the demand of natural gas increase at this rate. So, there is no other way to go for new energy

sources for Bangladesh to meet the future demand of energy in Bangladesh.

9. Conclusion

This study has analyzed present scenarios of natural gas and forecasted the remaining gas reserve in Bangladesh. It is clearly depicted here that Bangladesh will face gas crisis in very near future which is very concerning. So, Bangladesh needs to start searching for new energy source immediately which will fulfill the demand of natural gas.

References

- [1] Petrobangla annual report, 2016.
- [2] World bank.
- [3] Rahman, M., & Tamim, M. (2012). Analysis of Natural Gas Consumption by the Industrial Sector of. Journal of Chemical Engineering, IEB , Vol. ChE. 27, No. 1.
- [4] United nations data, 2010.
- [5] <https://petrobangla.org.bd/?params=en/gasproductiondistributionpipeline/distribution/>
- [6] Amin, A.S.M Tareq, Md. Rakibul Hassan, and Md. Shadikul Islam. "Feasibility & Comparison of available alternatives of gas as captive power generation source for Textile Industries."Bangladesh Textile Today, May-June 2010.
- [7] Wikipedia
- [8] Choudhury, Z. (2010). Natural Gas Reserve Estimate. Dhaka: Petrobangla.
- [9] Mohammad Iqbal, ABM Abdul Maalek, Salma Akhter, Mohammad Farhad Howladar And AHM Samsuzzoha. "SCENARIO OF ENERGY UTILIZATION IN BANGLADESH." 10th International Conference on Thermal Engineering: Theory and Applications February 26-28, 2017, Muscat, Oman.
- [10] Power development board annual report 2016-17.
- [11] Quader, A. K. M. Abdul. "STRATEGY FOR DEVELOPING THE FERTILIZER SECTOR IN BANGLADESH FOR SUSTAINABLE AGRICULTURE."Chemical Engineering Research Bulletin, 2009: 39-46.

ICMIEE18-306

Fabrication of a Long Distance Controlled Pan-Tilt Mechanism for Camera

Soma Sarker, Asif Ahmed Shishir, Shilpi Rani Saha*

Department of Mechanical Engineering, Rajshahi University of Engineering & Technology (RUET), Rajshahi-6204,
Bangladesh

somasarker08@gmail.com¹, asifahmed.shishir@gmail.com², saha.tumpa51@gmail.com³

ABSTRACT: This project is about fabricating a pan-tilt mechanism capable of being controlled from a long distance that can be connected and controlled through cell phones. This simplest and obvious robotic model is based on the motor on motor (MOM) design by using two identical stepper motors to cover the whole area view operated manually from long distance with Dual Tone Multi Frequency system (DTMF) signaling. The lower (pan) stepper motor have to be powerful enough to move the two brackets, DTMF receiver with its holder and the upper (tilt) stepper motor have to move most upper bracket, DTMF receiver with its holder only. We would like a pan-tilt mechanism to be accurate, slow, small, low-powered and inexpensive. The technology is used in many different consumer-based services including ATM booth monitoring; Surveillance based applications; Household security; Car Parking etc.

Keywords: Mechatronics, Pan-Tilt Mechanism, Remote Monitoring, Cost Effective, Security Purpose

1. Introduction:

Pan-Tilt mechanisms have been a source of inspiration and frustration to computer vision researchers. The source of inspiration is nature, where humans rely on their pan-tilt apparatus to achieve a wide field of view visual sensing [1]. The alternative to mechanical pan-tilt mechanism is electronic scanning i.e. software pan-tilt mechanism are more convenient and reliable than their motorized counterparts but we argue that they will be ultimately more expensive [2]. The source of frustration with pan-tilt devices is acquiring or building, then calibrating and controlling, the mechanism itself. Low speed inexpensive motorized pan-tilt platforms are available for example from Edmund Scientific, but these have no computer controls. Raviv used a Cartesian manipulator to implement camera pan, tilt, roll and translation [3]. The whole mechanism is driven by high efficient Stepper motor one of which is directly coupled with base of the platform which controls the pan movement and another Stepper motor is coupled to the joining point of the first and second bracket. Camera allocation system is built upon the top of the upper bracket, so it can act as an eye for the robot. By using this appropriate perception equipment, the GSM-based robot can localize itself and capture surrounding. The arrangement is such in a way that the camera can monitor the surrounding with the movement pan 340 degrees and tilt 45 degrees of the mechanism. This robot is based on a control system using Dual Tone Multi-Frequency system (DTMF).

2. Methodology

2.1 Operation:

The pan-tilt platform's hardware system can be operated

from any position without direct visual and auditory access to the hardware. 3G networks, short for third Generation, is the third generation of mobile telecommunications technology [4] which can be used to capture surroundings. Data and video originating from the camera during monitoring can be used to operate its movement when 3G will be available. According to the signal got from GSM module, the microcontroller operates the robotic platform. And the motor drive runs by the signal of a microcontroller. This robot is a wireless GSM-based system which can be operated from any corner of the world where networking system available by being in a fixed position. The success or failure of the mechanism highly restricted to factors such as camera's weight, structural weight, power input etc. It often tends to give vibration when kept in motion. This does not contain any special intelligence such as working in water or any dark place; highly dependent on the performance of a camera.

2.2 Pan-Tilt Platform Fabrication:

The main fabrication procedure is focused to keep the platform simple, small, fairy looked and easily portable so that reliability can be increased. A simple construction of the system is easy to implement. It is also helpful for having a good operational system. And small low weighted easily portable platform can be replaced and connected to the plug in any place. We have used power cable instead of battery in this system. The pan angle is set to 340 degrees to avoid interruption in movement due to wiring as the platform of the system is fixed in a place. We have tried to keep the system simple and so the tilting rotation angle is kept 45 degrees to safely hold a mobile phone in holder observing necessary wide view within the mentioned angle.

* Corresponding author. Tel.: +88-01717405761

E-mail addresses: asifahmed.shishir@gmail.com

2.2.1 Scopes and Applications:

1. A small (5×4×1.75) inches pan-tilt platform which is easily portable from one place to another and inexpensive has been designed and fabricated successfully.
2. A wide field of view can be obtained up to Pan Movement of 340 degrees and tilt movement of 45 degrees from the remote location.

2.2.2 Limitations:

1. The design is inefficient because it is not necessary to carry a motor on top of the other motor, can be constructed in another way.
2. The success or failure of the mechanism highly restricted to factors such as camera weight, structural weight, power output etc.
3. Often tend to be a lower speed and vibrate.
4. The mechanism is fixed in a place where a cable is connected and so have the view only which can be seen from that place.

2.2.3 Recommendations:

1. Servo motors may be used instead of stepper motors.
2. Another pinion of proper measurement and teeth may be attached with the lower (pan) stepper motor to extend stability in speed and smoothness for more reliability.
3. Another circuitry arrangement to display time with movement may be constructed.
4. The robotic mechanism may have a wireless power system and gear wheel system so that it can also be moved freely from one place to another.

2.3 Main Systems:

Architecting the system is a major requirement for functional analysis and fabrication process. System architecture gives the hierarchy of the system that helped to define deliverables for different subgroups. The GSM-based pan-tilt system is comprised of three main mechanical parts: Frame Structure System, the drive system and camera allocation system which are controlled using a control circuit through a GSM-based communication and DTMF technology. The system can be divided into several systems which are built separately. The following are the main components of the robotic system hardware:

1. Pan-Tilt System
2. Drive system
3. Camera allocation system
4. Power supply system

2.3.1 Pan-Tilt Mechanism:

The frame of the pan-tilt platform is made of Thai Aluminum based on pan tilt system. The (5×4×1.75) inches frame's base has a rectangular shape including two brackets of (3×2×1.5) inches on the top of it. One stepper motor is located inside the base at the joint of the

base and first bracket, another stepper motor is held between the joint of two upper brackets, GSM receiver is carried on the top of all brackets inside a holder. We have constructed the simplest and most obvious model based on the motor on motor (MOM) design by using two identical stepper motors, to cover the whole area view and operate it manually from distance by using DTMF technology. The lower (pan) stepper motor turns the mechanism through a definite degree of freedom, usually pan, and the upper (tilt) stepper motor through another definite degree of freedom, usually tilt. Pan-Tilt Movement is shown in figure 2; 3. The lower (pan) stepper motor have to be powerful enough to move two upper brackets, DTMF tone receiver with its holder and the upper (tilt) stepper motor have to move the upper bracket, DTMF tone receiver with its holder only.

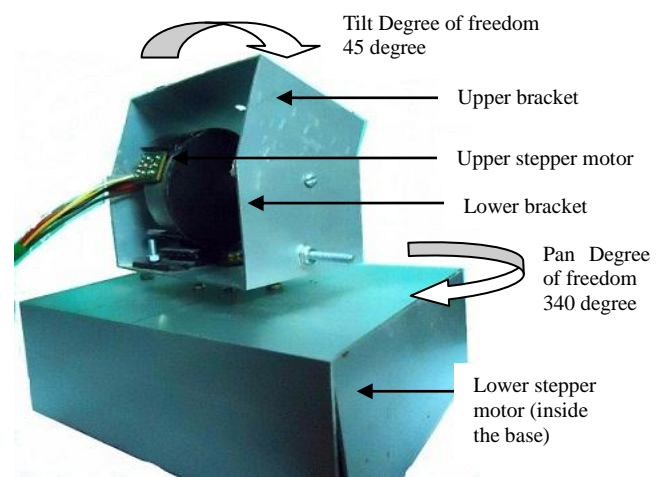


Fig. 1: Structure and Frame of Pan-Tilt System (side view)

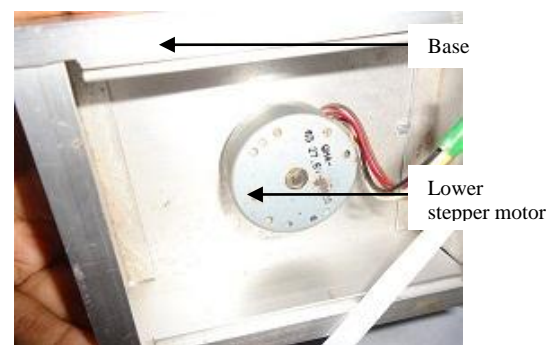


Fig. 2: Structure and Frame of Pan-Tilt System (bottom view)

2.3.2 Drive System:

Drive system may be subdivided into some groups to make the drive system understandable easily.

2.3.2.1 Motor Drive System:

The whole mechanism is driven by high efficient Stepper

motor one of which is directly coupled with the base of the platform which controls the pan movement and another stepper motor is coupled to the joining point of the first and second bracket. There is no differential speed mechanism in this robot but we can run this robot at pan 340 degrees and tilt 45 degrees by DTMF system from a long distance. We can easily move the robot in pan and tilt direction by controlling the motors.

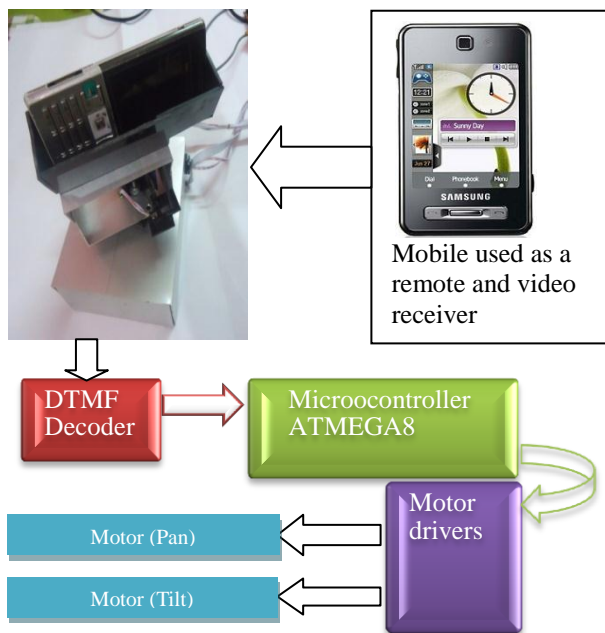


Fig. 3: Block diagram of Motor drive system

2.3.3 Camera Allocation System:

Camera allocation system is built upon the top of the upper bracket in the mechanism which is made of glass. The arrangement is such in a way that the camera can monitor the surrounding with the movement pan 340 degrees and tilt 45 degrees of the mechanism. The camera can be inclined maximum 45 degrees by the wish of an operator when it is needed to be controlled by two Stepper motor.



Fig. 4: Pan-tilt allocation system without camera



Fig. 5: Pan-tilt allocation system with camera

2.3.4 Power System:

The mechanism is supplied with voltage by putting the plug into a plug. When the circuit is closed 220 V will be supplied to the mechanism. The voltage is distributed among microcontroller and two stepper motors each of 6V. A step down transformer is used to reduce the amount of voltage in the required level. The capacity of a microcontroller to support is not more than 5 V and may damage also if the limit of voltage crosses. So a voltage regulator is used to assure that only the correct amount of voltage is inserted through the microcontroller.

2.4 Project Overview:

The mobile that makes a call to the mobile phone stacked in the pan-tilt mechanism acts as a remote. The signal generated by the DTMF encoder is the direct algebraic submission, in real time of the amplitudes of two sine's (cosine) waves of different frequencies, i.e., pressing 5 will send a tone made by adding 1336 Hz and 770 Hz to the other end of the mobile [6] and mechanism will stop. The tones and assignments in our project with the DTMF system shown figure 7 below:

Frequencies	1209 Hz	1336 Hz	1477 Hz	1633 Hz
697 Hz	1	Forward	3	A
770 Hz	Left	Stop	Right	B
852 Hz	7	Backward	9	C
941 Hz	*	0	#	D

Fig. 6: Table of keypad frequencies [5]

3. Circuit Design

3.1 Circuit Design for Stepper Motor Driver:

Fig. 8 shows the circuit design for two stepper motor. In this project, two stepper motors are used. One (upper) stepper motor is for pan movement and other (lower) stepper motor is for tilt movement. Microcontrollers are designed for embedded applications, in contrast to the microprocessors used in personal computers or other general purpose applications [7]. They can be controlled by the manual switches or by DTMF input. When a switch is pressed it sends a signal to the microcontroller. This converted microcontroller output is then fed to the ULN2004 IC input. Finally, this IC controls the stepper motor connected with it with the corresponding signal. A LED diode is a Semiconductor diode that produces visible or infrared light when subjected to an electric current, as a result of electroluminescence [8] which indicates the proper power supply continuity when project circuit is closed. Four switches are used for

controlling pan-tilt movement and another switch is stopping switch for both of the motors.

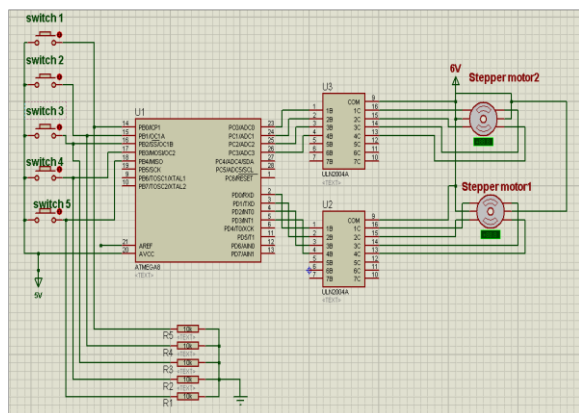


Fig. 7: Circuit design for motor controlling

3.2 Complete Experimental Setup:

Complete Experimental Setup is shown in fig. 7. For this experimental set up two cell phone is required one is to be used as a remote or video receiver and another is kept connected to the pan-tilt mechanism with a DTMF decoder circuit. In the course of a phone call if any dial of the keypad is pressed the command signal passes through a tone to the DTMF decoder circuit. The preprogrammed microcontroller circuit is commanded to pass the information to defined IC and drives motor in definite direction pan or tilt. This is how the motor drive system is activated. Video can be received from a remote location of pan-tilt platform when 3G will be available by keeping the cell phone connected with DTMF decoder circuit in the mobile carriage and positioning it at a suitable angle.

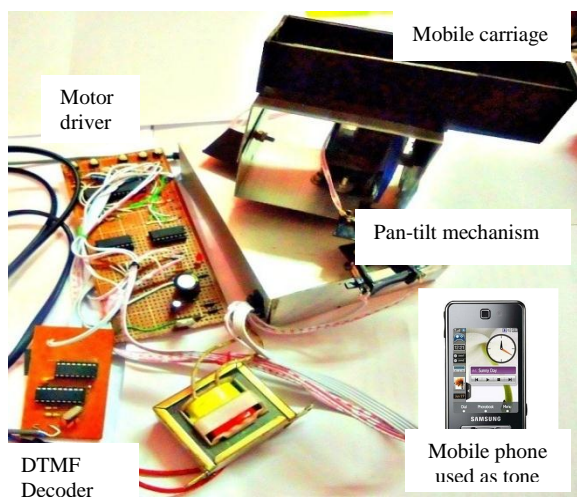


Fig. 8: Complete Experimental Setup

4. Performance Test and Results:

4.1 Performance Test of Pan-Tilt Mechanism:

As the project is successfully run, so it is a great achievement. We have counted down time with help of two stopwatches. One of which we had started with the pressing of a dial and other with the movement of the mechanism and they were stopped accordingly to the stoppage of the mechanism movement and stoppage of pressing time. So that we had been successful to have the response time after pressing a dial and stoppage of pressing dial. But no response time is found. All data's for pan movements and tilt movements are collected. Digital Angle Finder is used for angular measurement. We have recorded the timing for 3 times in each and every step of the movement and get the average values of the data so that we may get an approximately accurate value. A small delay in angle and time is got between the theoretical data and actual data as the mechanism takes some time during the movement due to vibration when power is on. In our project, for the pan-tilt movement of the brackets, we have chosen stepper motor. Because it is a brushless DC electric motor that divides a full rotation into a number of equal steps. The motor's position can then be commanded to move and hold at one of these steps without any feedback sensor. But unavoidable jerk of stepper motor has caused response time delay; sometimes make the system slower or faster.

4.2 For Tilt Movement:

The minimum step angle for lower stepper motor is 1.875 degree. And it does not have any variation in angle and time for different steps with respect to theoretical time. For this reason, there belongs no angle and time difference in theoretical and experimental value. There is no response time needed to start this movement. The difference in data and graph is given below in graphed figure 9; 10 according to the data table-1; data table-2.

4.2.1 Graph for theoretical value and experimental value of angle with respect to step of tilt movement (Data table-1):

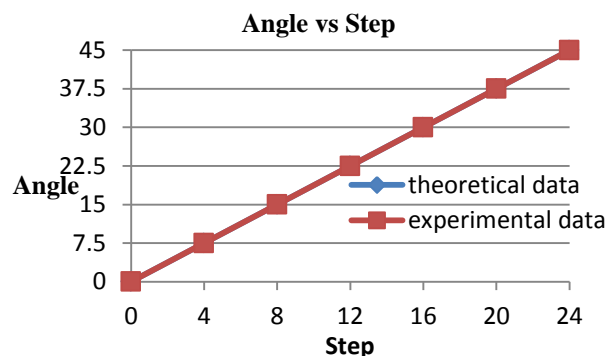


Fig. 9: Angle versus Step graph for pan movement

Data table-1: For theoretical value and experimental value of tilt angle with respect to step:

Step	Theoretical Angle	Experimental Angle
0	0	0
4	7.5	7.5
8	15	15
12	22.5	22.5
16	30	30
20	37.5	37.5
24	45	45

4.2.2 Graph for theoretical value and experimental value of time with respect to angle of tilt movement (Data Table-2)

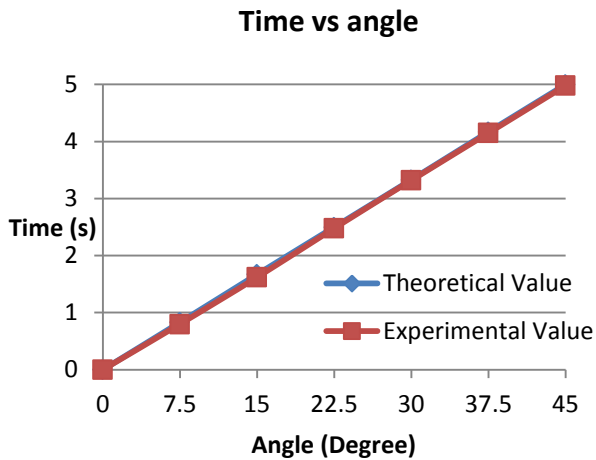


Fig. 10: Time versus angle graph for tilt movement

Data table-2: For theoretical value and experimental value of tilting time with respect to angle:

No. of steps	Angle (degree)	Theoretical value of time (s)	Practical value of time (s)	Deviation (%)
0	0	0	0	0
4	7.5	0.83	0.80	3
8	15	1.67	1.62	5
12	22.5	2.50	2.48	2
16	30	3.33	3.32	3
20	37.5	4.17	4.15	2

4.3 For Pan Movement:

The minimum step angle for lower stepper motor is 8.5 degree. But it takes some variation in angle and time for different steps with respect to theoretical time. For this reason there belongs an angle and time difference in theoretical and experimental value. There is no response time needed to start this movement. The difference in data's and graph is given below in the graphed fig. 11; 12 according to the data table-3 and data table-4.

4.3.1 Graph Figure for theoretical value and experimental value of angle with respect to step of pan movement (Data table 3):

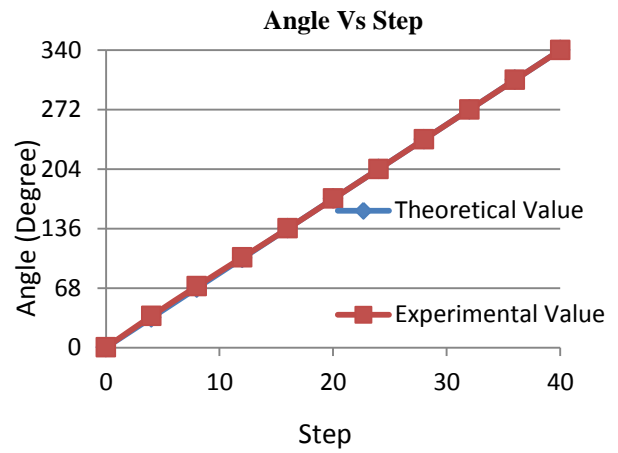


Fig. 11: Angle versus Step graph for pan movement

Data table-3: For theoretical value and experimental value of pan angle with respect to step:

Step	Theoretical Angle (Degree)	Experimental Angle (Degree)	Deviation (%)
0	0	0	0
4	34	36	2
8	68	70	2
12	102	103	1
16	136	137	0
20	170	170	0
24	204	204	0
28	238	238	0
32	272	272	0
36	306	306	0
40	340	340	0

4.3.2 Graph for theoretical value and experimental value of time with respect to angle of pan movement (Data table-4):

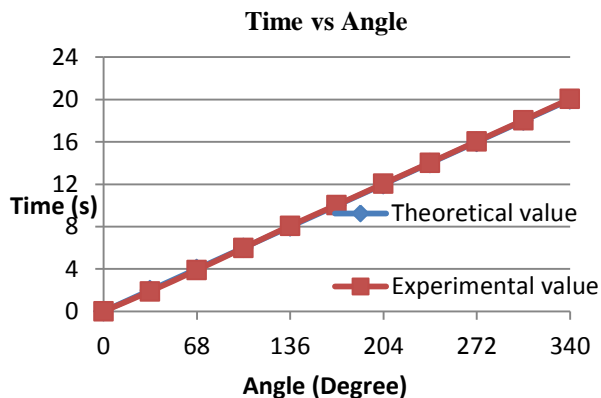


Fig. 12: Time versus Angle graph for pan movement

Data table-4: For theoretical value and experimental value of panning time with respect to angle:

No. of steps	Angle (degree)	Theoretical value of time (s)	Practical value of time (s)	Deviation (%)
0	0	0	0	0
4	34	2	1.89	11
8	68	4	3.90	10
12	102	6	5.98	2
16	136	8	8.08	8
20	170	10	10.05	5
24	204	12	12.05	5
28	238	14	14.04	4
32	272	16	16.05	5
36	306	18	18.05	5
40	340	20	20.06	6

4.4 Results:

The minimum step angle for tilt or vertical movement 1.875 degrees. Maximum possible angle for tilt or vertical movement 45 degrees. Difference in theoretical value and experimental value of tilt angle is 0 (shown in graph fig. 9). Difference in theoretical value and experimental value of tilting time is between ± 10 to 50 ms (shown in graph fig. 10). The minimum step angle for pan or horizontal movement 8.5 degrees. Maximum possible angle for pan or horizontal movement 340 degrees. Difference in theoretical value and experimental value of pan angle is between 1 to 2 degrees (shown in graph fig. 11). Time difference in theoretical value and

experimental value of panning time is between ± 20 to 110 ms (shown in graph fig. 12). Due to unavoidable jerk of stepper motor there were ups and downs in angular and time reading. Only Theoretical and practical value of angle for tilting is found identical.

5. Conclusion:

The project is successfully constructed and executed. A small (5x4x1.75) inches pan-tilt platform which is easily portable from one place to another, slow and inexpensive has been designed and fabricated successfully. Approximately 120gm of weight can be controlled from a long distance by connecting two GSM mobile phones. The design is inefficient because it is not necessary to carry a motor on top of the other motor, can be constructed in another way. In addition, the success or failure of the mechanism is highly restricted to factors such as camera weight, structural weight, power output etc. and often tend to be a lower speed and vibrate. The mechanism is fixed in a place where the cable is connected and so have the view only which can be seen from that place.

6.Acknowledgement:

In the end, we consider it ultimate to pay regards to our parents and all the teachers of the Mechanical Department especially to Prof. Md. Wahedul Islam, Dr. Md. Rokunuzzaman and, Dr. Md. Emdadul Hoque from whom we have learned a lot throughout our 4-year course of study. It was not just the matter of final year, except the required competitive aptitude, sense of responsibility and sincerity required for the successful completion of any project was developed in us by our graceful parents and teachers during our 4-year period in the University.

REFERENCES

- [1] Benjamin B. Bederson, Richard S. Wallace, and Eric L. Schwartz. *A miniaturized active vision system*. In 11th ICPR, 1992. Submitted.
- [2] Peter J. Burt. *Algorithms and architectures for smart sensing*. IEEE Transaction on Pattern Analysis and Machine Intelligence.
- [3] Daniel Raviv and AvrahamShapira. *Miniature vision based flight simulator*. In 14th Annual Conference on Recent Advance in Robotics, 1991.
- [4] Torbjorn Nilsson. *Toward a new era in mobile communications*.
- [5] <http://193.78.100.33/> (Ericsson WWW server).
- [6] <http://www.gsmarena.com/network-bands.php3>
- [7] <http://en.wikipedia.org/wiki/Microcontroller>.
- [8] Malvino, A. P.; *Electrical Principle* (New York, McGraw-Hill Book Company, 1998.)

Design & Fabrication of Low Cost GSM Based Wireless Controlled Robot

Asif Ahmed Shishir, Soma Sarker, Md. Sefatullah

Department of Mechanical Engineering, Rajshahi University of Engineering & Technology (RUET), Rajshahi-6204, Bangladesh

asifahmed.shishir@gmail.com¹, somasarker08@gmail.com², sifat27ruet08@gmail.com³

ABSTRACT

Many projects are taking place based on design & fabrications of low cost Robots with GSM-based communication system. This paper represents a simplified form of a robot which can be operated from a long distance using DTMF Technology. In this project a four-wheeled platform is made, where a position is created to mount a mobile phone to do real-time video through calling from user's mobile and rotate it up to 180-degree angle. In the front side, two robotic arms are mounted which is controlled by three motors for pick and place operation. We present a whole structure whereby the GSM network can control a mobile robot including Real-time video recording by only a call from user mobile. This paper introduces the steering mechanism which is engaged with the front wheels of the robot to ensure left, right, forward and backward movement of the robot. It can be a low-cost solution for industrial, rescue and surveillance related applications.

Keywords: Design Prototype, Tele-operated control, Extraction arm system, video capturing, Low Cost.

1. Introduction

General-purpose autonomous robots can perform a variety of functions independently [1]. An example of a mobile robot that is used commonly today is the Automated Guided Vehicle (AGV) [2]. An AGV is a mobile robot that follows markers or wires in the floor, or uses vision or lasers. Mobile robots are also found in industry, military and security environments. A demo model of the robot is structured which is small in size and easily movable to any area to serve rescue operation where a human can't reach. The corporation and robot can be managed by a remote coordinator, who is located in a remote place outside of the area [3]. This robotics system is fitted with a Global System for Mobile Communication (GSM) so it can be controlled from a far distance. A mobile camera is inflicted on the top of four-wheeled platform, so it can act as an eye for the robot. By using this appropriate perception equipment, the GSM-based robot can localize itself and also sense a surrounding. A simple, lightweight and efficient extraction system is included in this robot. The main functions of this robot are to monitor the specific area and to extract the obstacle in the way. The software interface protocol of this robot is identical with the embedded system on AVR Microcontroller. This robot is based on the same control system using Dual Tone Multi-Frequency system (DTMF).

2. Working Principle

The robot hardware system can be operated remotely without direct visual and auditory access to the hardware. Data and video originating from the robot during monitoring can be used to operate it. According to the signal from the GSM module, the microcontroller operates the robot. The motor drive runs by the signal of a microcontroller. This robot is a wireless GSM-based system which can be operated from any corner of the world where networking system available [4,5]. But this

project has some limitations. It can't run perfectly on a rough surface and hence not waterproof, so cannot work in water. It's also not efficient in a dark environment.

3. Flow chart

MCU processor provides instruction to motor drivers and servo motor according to the information of Cell phone detector circuit when a particular key of the Cell phone is pressed according to the inputted program. The passed signal through pressed mobile key decides movement of platform, camera, and gripper.

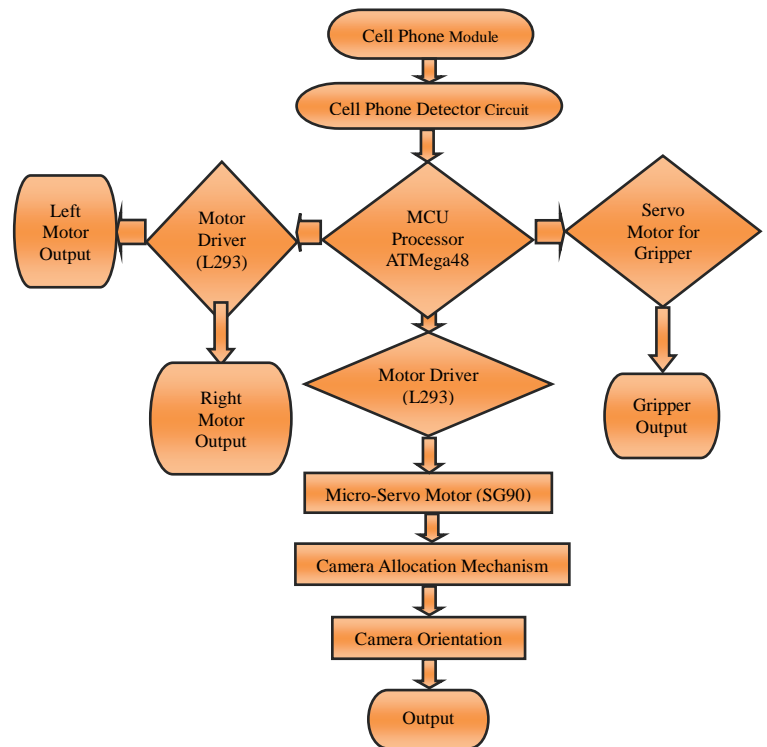


Fig 1: Operation Cycle of Robotic System

* Corresponding author. Tel.: +88-01717405761

E-mail addresses: asifahmed.shishir@gmail.com

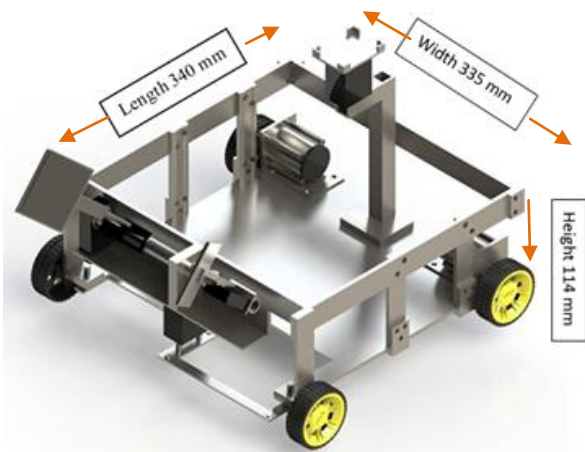


Fig 2: Proposed Design for Robot(340*335*114mm)

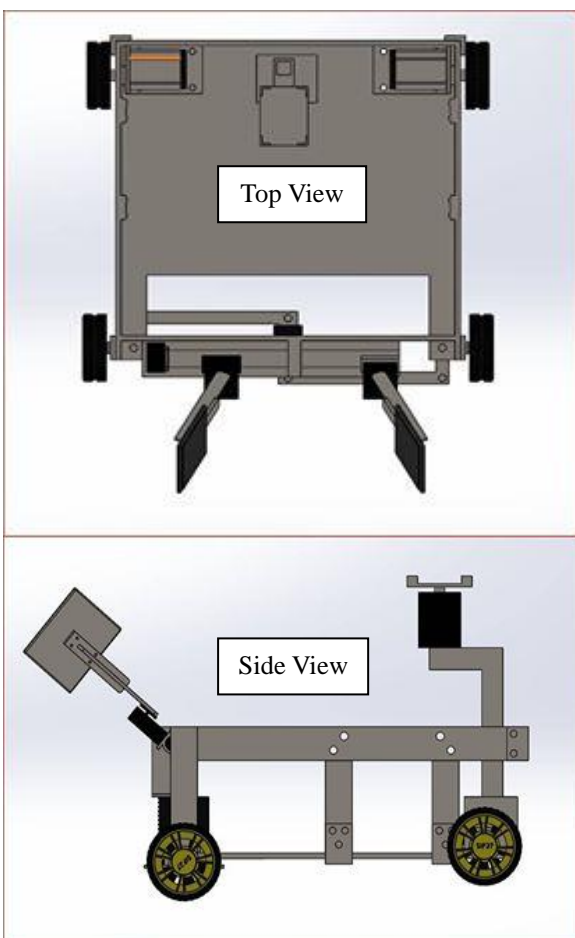


Fig 3: Proposed Design (Top View and Side View)

4. Project Overview

The design procedure mainly focused to keep the robot simple so that the risk can be reduced and reliability can be increased. A simple design system is easy to implement. It is also helpful for having a good operational system. Since the team had multiple solutions for driving different subsystems, a preference list for solutions was made. Reduction through trial and error method is the basis for solutions elimination process.

Table 1: Design Consideration Parameters:

Parameters	Expected Value	Margin
Weight	2kg	10%
Dimension	340*335*114mm	15%
Torque	Motor-1>SG5010 Motor-2>SG90 Motor -3	11.00kg-cm 1.80kg-cm 20.00kg-cm
Control Functionality	Artificial intelligence	
Cost	150\$	10%

4.1 Design and Fabrication

Estimating the proper resource for the project was done in the initial phase of the design. Since the project was divided into different subgroup design margin for each subgroup were defined. Margins have been primarily established from an initial design. Design margin for the design consideration parameters are shown in table 1 above.

Architecting the system is a major requirement for functional analysis and design process. System architecture gives the hierarchy of the system that helped to define deliverables for different subgroups. The GSM-based robotic system is comprised of three main mechanical parts: the drive system, the extraction arm system and camera allocation system which are controlled remotely using control circuit through a GSM-based communication. The robotic system can be divided into several subsystems which are built separately [6].

The following are the key components of the robotic system hardware:

1. Structural Frame
2. Drive System
3. Excavating Arms System
4. Camera allocation System
5. Controls System
6. Power Supply

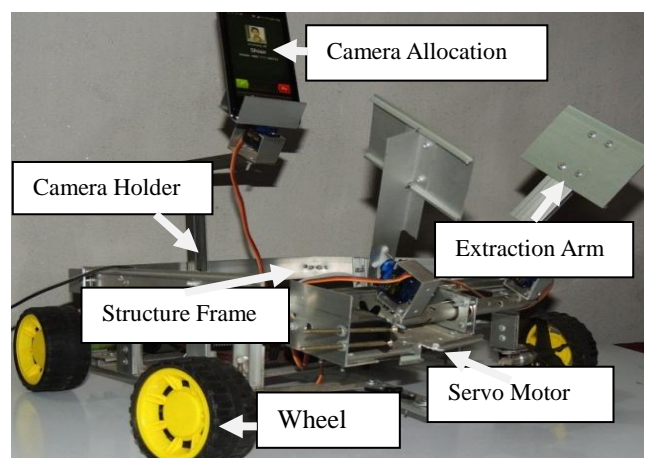


Fig 4: Structure and Frame of Robotic System

4.1.1 Frame Structure System

The frame of the robot is made of aluminum bar almost. The (340*335*114) mm frame has a rectangular shape including a cage into it to hold the battery, circuitry, GSM receiver and a camera stand on the top of the cage which is made by mild steel square bar That's why 3G video calling can come in handy in this system and a steering system in the front of the cage. Also, a hand gripper stand is built up which can hold the extraction system rigidly. Therewith, integration of the drive system by using front wheel mechanism assists the robotic system to move left, right, front and back standing in the same position.

4.1.2 Drive System

The whole robot is driven by high efficient DC gear motor which is directly coupled with the rear wheel. There is no differential speed mechanism in this robot but we can run this robot at 360 degrees by steering system which is driven by a high torque servo motor. We can easily move the robot in the back and forth direction by reversing the motor. We can also control the speed of the robot by increasing or decreasing the current flow through the DC gear motor.

4.1.3 Extraction Arm System

The extraction arm system consists a pair of micro-servo SG90 conduct pair of rigid arms which are made by an aluminum bar. These arms allow to essence different kind and size of objects which are may be malignant or nonmalignant. The pair of micro-servo aids the extraction arm system to grip the Object rigidly. And another servo (model-SG90) assists the extraction arm system for up and down movement. This servo (torque: 11 kg-cm) is highly efficient to carry heavy weight safely.

4.1.4 Camera Allocation System:

The camera allocation subsystem is built upon the camera stand which is made of mild steel and aluminum. There is a special arrangement on the stand so that the camera can monitor the lower front side and upper back side. That's why the camera stand is kept about an angle of 50 degrees with the horizontal. The camera can rotate by the wish of an operator when it is needed which is controlled by a servo motor.

4.1.5 Control System:

The control subsystem consists of different components. The main components are the system control circuit and the communication control circuit. The main functionalities of system control circuit (SCC) include wheel-extraction arm-camera allocation driving circuit, GSM-based communication module, power calculation module, data feedback system, emergency stop button etc. Microcontroller ATMEGA48PA used in this control system. In this system, a phone which supports 3G video calling is allocated in the robot and another phone is used for calling. When two phones are connected by calling then by means of DTMF technology we get signal in the communication circuit. Here MT-8870 is a DTMF

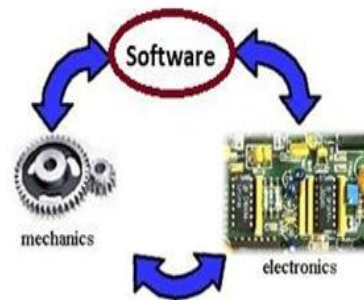


Fig 5: Control System of Robotic System

Receiver is integrated. That integrates both bands split filter and decoder functions into a single 18-pin DIP or SOIC package. Its filter section uses switched capacitor technology for both the high and low group filters and for dial tone rejection. Its decoder uses digital counting techniques to detect and decode all 16 DTMF tone pairs into a 4-bit code. The external component count is minimized by the provision of an on-chip differential input amplifier, clock generator, and latched tristate interface bus. Minimal external components required includes a low-cost 3.579545 MHz color burst crystal, a timing resistor, and a timing capacitor. The filter section is used for separation of the low-group and high group tones and it is achieved by applying the DTMF signal to the inputs of two sixth order switched capacitor band pass filters, the bandwidths of which corresponds to the low and high group frequencies. This is converted with voltage. And this voltage act as an input signal for system control circuit. By the help of algorithms, the robotic system can get different movement [7].

4.1.6. Power System:

The power supply is to support 9 high torque 12V DC motor and 1 high torque 24V HUB motor. The 9 high torque motors require almost 12A of current in full load. Two batteries of 12V which can supply a maximum of 18A are used in the series connection. The SCC and KINECT powering module have been made using a different battery because of the noise occurred by the high torque DC motors which can damage the control circuit.

5. Description of GSM System and DTMF

Technology:

Over 200 GSM networks (including DCS1800 and PCS1900) are operational in 110 countries around the world. At the beginning of 1994, there were 1.3 million subscribers worldwide [8], which had grown to more than 55 million by October 1997. GSM (Global System for Mobile communication) is a digital mobile telephony system. GSM uses a variation of time division multiple access (TDMA) and is the most widely used of the three digital wireless telephony technologies (TDMA, GSM, and CDMA). GSM digitizes and compresses data, then

sends it down a channel with two other streams of user data, each in its own time slot[9-11].

DTMF (dual tone multi-frequency) is the signal that we generate when we press an ordinary telephone's touch keys. DTMF has generally replaced loop disconnect ("pulse") dialing. With DTMF, each key we press on your phone generates two tones of specific frequencies. So that a voice can't imitate the tones, one tone is generated from a high-frequency group of tones and the other from a low-frequency group. This technology is conducted by the MT8870DE chip which is a complete DTMF receiver both the band split filter and digital decoder function. We also include HD74LS04P hex inverter which aids this technology [12]. 3G networks, short for third Generation, is the third generation of mobile telecommunications technology [13]. 3G finds application in wireless voice telephony, mobile Internet access, fixed wireless Internet access, video calls and mobile TV. 3G networks can be used to have the visual feedback of real time when it will be available everywhere in Bangladesh.

5. Software Interface and Circuit Diagram:

WinAVR AVR-GCC has been used for programming language writing .the simulation software named Proteus 7 professional has been used on basis of our required algorithm. Finally, the code is burned by AvrPal.Net software. The circuit which is made by simulation software is given below:

The major components used in the above circuit are the microcontroller, motor driver and robot. Here at ATMEGA48PA microcontroller is used and it requires a power supply of positive 5V DC. In order to provide regulated 5V DC voltage to the controller, use 7805 power supply circuit. Here two 12V batteries are used, one is for giving the supply to the circuit and other is to run the DC motors.

RA0, RA1, RA2, RA3 pins of MT8870DE are connected to the PD0, PD2, PD3, PD4 pins of ATMEGA48PA Microcontroller. PB0, PB1, PB2 and PB3 pins of the controller are connected to the L293D input pins and these pins are used to control the two DC motors. The operating voltage of this IC is 5V. Using this IC we can operate the 2 DC motors with a voltage ranging from 4.5 to 36V. We need to apply the motors supply at the 8th pin of L293D.

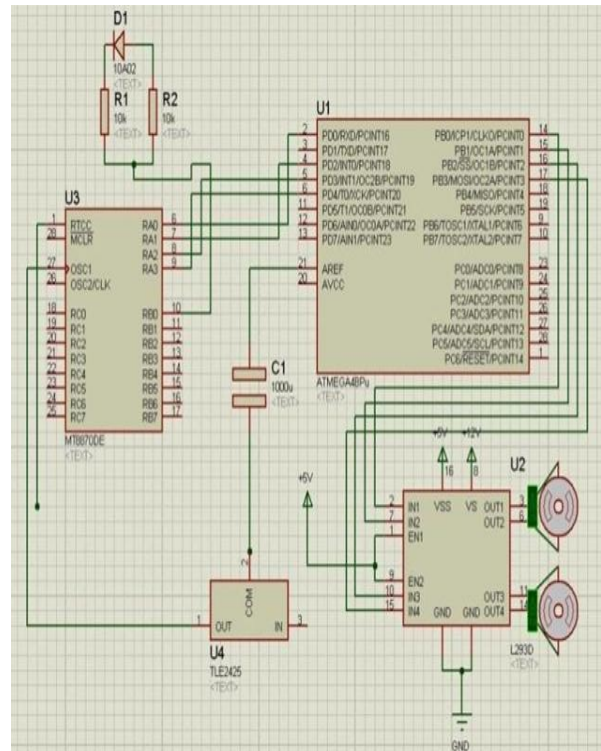


Fig 6: Circuit Diagram of Robotic System

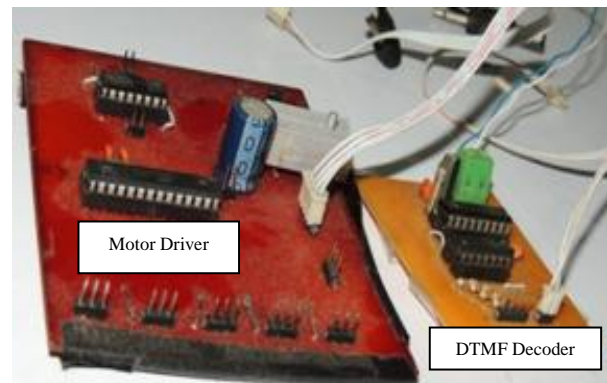


Fig 7: Electronics Hardware of Robotic System

6. Robot Arm Torque Analysis

According to the initially taken measures the exerted force value is calculated. And Torque excreted in each hand of gripper is measured. The following graph has representation Torque Vs Angle.

Torque (T) is defined as a turning or twisting “force” and is calculated using the following relation: The force (F) acts at a length (L) from a pivot point. In a vertical plane, the force acting on an object (causing it to fall) is the acceleration due to gravity ($g = 9.81\text{m/s}^2$) multiplied by its mass: The force above is also considered the object's weight (W). The torque required to hold a mass at a given distance from a pivot. Load Weight, $M=0.5\text{ kg}$
Length of Extraction Arm, $L= 6\text{ inch} = 0.1524\text{m}$

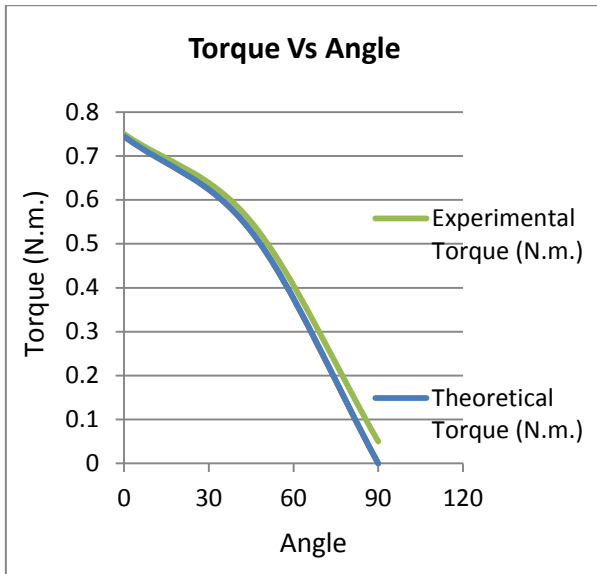


Fig 8: Torque Vs Angle Graph

Table 2: Torque Analysis Parameters

Angle	Theoretical Torque (N.m.)	Experimental Torque (N.m.)	Deviation (%)
0	0.7447	0.75	0.53 %
45	0.5285	0.55	2.15 %
90	0	0.05	5 %

7. Testing, Validation, and Verification

During the design implementation process, each subsystem has been verified multiple times to make sure the implemented design is correct and the developed system. Dimensions and weights of the different components have been noted down during the development process so that the total system does not exceed the maximum allowable weight or dimension. Among other requirements that have been verified after the integration of the total system includes:

- The communication method follows the system does not employ any physical process.
- Extraction arm system works perfectly but a suspension could make the system more efficient;
- The drive system works perfectly. It can move 360 degrees easily
- Video calling of a 3G network can come in handy
- The control circuit is equipped with the emergency stop button so that all the power can be turned off instantly.

8. Conclusion

This paper presents the GSM-based simple demo structure of the robotic system which can be used in different operations. The robots have functionalities for searching victims, investigating the dangerous area,

bomb defusing, security purpose etc. We have fabricated the estimated set up within a low budget and tried to achieve the desired performance of the overall system. The principle of the project is easy to understand, low in cost and gives places for further modifications to bear a lot of fruits in the mass applications.

9. Acknowledgement

We are very much grateful to Robotic Society and especially to Dr. Md. Rokunuzzaman and Dr. Md. Emdadul Hoque Dept of Mechanical Engineering of RUET. He has given full support on this project and encouraged us. Since without 3G network our project could not be completed, so we are grateful to Teletalk 3G.

REFERENCES

- [1] http://link.springer.com/article/10.1007%2F978-3-642-02568-6_1/lookinside/000.png.
- [2] <http://www.engpaper.com/automated-guided-vehicle-project-report.htm>.
- [3] F. Driewer, H. Baier, K. Schilling, J. Pavlicek, L. Preucil, M. Kulich, N. Ruangpayoongsak, H. Roth, J. Saarinen, J. Suomela, A. Halme, "Hybrid Telematic Teams for Search and Rescue Operations", Proceedings of the SSRR'04, IEEE International Workshop on Safety, Security, and Rescue Robotics, Bonn, Germany, ISBN: 3-8167-6556-4, May 2004. (for an introduction)
- [4] J. Kuhle, H. Roth, and N. Ruangpayoongsak, "MOBILE ROBOTS and airships in a multi-robot team," The 1st IFAC Symposium on Telematic Applications in Automation and Robotics, Helsinki University of Technology, Finland, pp. 67-72, June 2004.
- [5] M. Kulich, J. Pavlíšek, J. Chudoba, R. Mázl, L. Págeš, "Hybrid Telematic Systems for Rescue Missions," *Cybernetics and Systems* 2004, Vienna: Austrian Society for Cybernetics Studies, 2004, vol. 1,2, p. 731-736. ISBN 3-85206-169-5.
- [6] http://ieeexplore.ieee.org/xpl/login.jsp?tp=&arnumber=6509787&url=http%3A%2F%2Fieeexplore.ieee.org%2Fxppls%2Fabs_all.jsp%3Farnumber%3D6509787
- [7] <http://www.societyofrobots.com/robottheory.shtml>
- [8] Peter K. Allen, Billibon Yoshimi, and Aleksandar Timcenko. Real-time visual serving. In Proceedings of the 1991 IEEE International Conf. on Robotics and Automation, April 1991.
- [9] EU Seeks To End Mandatory GSM for 900Mhz - Source
- [10] Jump up ^ Leader (7 September 2007). "Happy 20th Birthday, GSM". zdnet.co.uk. CBS Interactive. Archived from the original on 5 May 2011. Retrieved 5 May 2011. "Before GSM, Europe had a disastrous mishmash of national analogue standards in phones and TV, designed to protect national industries but instead creating fragmented markets vulnerable to big guns from abroad."
- [11] Jump up to: a b "GSM". etsi.org. European

Telecommunications Standards Institute. 2011. Archived from the original on 5 May 2011. Retrieved 5 May 2011. "GSM was designed principally for voice telephony, but a range of bearer services was defined allowing circuit-switched data connections at up to 9600 bits/s."

- [12] Dodd, Annabel Z. *The essential guide to telecommunications*. Prentice Hall PTR, 2002, p. 183. (for DTMF)
- [13] Torbjorn Nilsson. Toward a new era in mobile communications.

The Variation of Concrete Strength using Wastetyre Rubber as Coarse Aggregate

Md. Ashiqul Islam, Tuhin Hasan Shagar, MD. Raihan Bhuiyan

Department of Civil Engineering Khulna University of Engineering & Technology, Khulna-9203, BANGLADESH

ABSTRACT

Waste tyre rubber constitutes a large portion of solid waste which has turned into a worldwide environmental concern. The waste tyres represent a significant environmental, human health and aesthetic problem. The consumption of waste tyre rubber in concrete has gained more attention from the point of view of enhanced engineering properties. The objective of this study is to explore the effect of rubber tyres on mechanical properties of concrete. This study represents the results to the investigation of strength characteristics of concrete produced using waste tyres as substitutes for conventional coarse aggregate in replacement of 10%, 20%, 25%. Here 56 cylinders were prepared using waste tyres for this study. It has been observed that the use of tyre rubber particles provides a new type of concrete that inspires the use of waste tyres as a replacement of coarse aggregate.

Keywords: Tyre rubber, Solid waste, Engineering properties, Replacement, Coarse aggregate.

1. Introduction

Environmental pollution has been increased in developing country because of burning of waste tyres. In several countries, tyre rubber is being burned which can result in serious hazards. Scrap tyres dumped in sanitary landfills are a significant environmental hazard and result in possible contamination. Only small quantities of scrap tyres are being used or recycled as construction materials. Rubber from scrap tyres is one of the more recent waste materials investigated for its potential use in construction industry.

Materials like waste tyres can be used to replace aggregates in concrete. But these materials cannot replace fully but they are partially replaced to about 0% to 25% [1, 2]. Studies are made on both fresh as well as hardened properties of rubberized concrete and compare with normal concrete. In developing countries wastes are discharged but we can use these wastes as potential material or replacement material in the construction industries. If these wastes are used in the construction, this will have the double advantage of reduction in the cost of construction material and also as a means of disposal of waste. The recovery of waste tyres has normally grown in each year, for instance from 55% in the United States in 1994 and from 21% in Europe in 1994. The recovery of waste tires in Japan was already at 90% in 1994, and has kept steady at near that rate for approximately 20 years [3].

By replacing the coarse aggregate in concrete with waste tyres partially, a concrete has been developed which possesses the potential of being used in building construction as floor, pavement, water barrier etc. Generally concrete as time goes on through a process of hydration of the cement paste, producing a required strength to withstand the loads on it. So the use of waste tires as coarse aggregate in concrete has never been a usual practice among the average citizens, particularly in areas where light weight concrete is required for non-load bearing walls, non-structural floors, and strip

footings. About 50% of the overall self-weight of concrete is responsible for coarse aggregate [4]. Sources of traditional aggregates occupy the most important part of the concrete [5]. The large scale production of concrete in construction activities using conventional coarse aggregate such as granite immoderately reduces the natural stone deposits and affecting the environment hence causing ecological imbalance. Extraction and processing of aggregates is also a major concern for environment. Therefore consumption of alternate waste material in place of natural aggregate in concrete production not only protects environment but also makes a concrete a sustainable and environment friendly construction material. It is also important that the use of waste tyres reduces the cost of constructions which can be a help to the construction industries.

2. Methodology

Concrete is an artificial stone manufactured from a mixture of binding materials and inert materials with water.

Concrete = Binding Materials (cement) + Inert Materials (coarse aggregate and fine aggregate) + Water.

Waste tyres are used as a replacement of coarse aggregate to invent a new type of concrete in civil engineering application.

2.1 Mix Design Ratio

The concrete mix design for every specimen was based on the weight of materials. The weight portion of the concrete mixture was 1 (cement): 2 (fine aggregate): 4 (coarse aggregate), giving a water to cement ratio of 0.45

2.2 Test Specimens

4 in x 8 in cylindrical specimen were used. Portland composite cement (PCC), Stone chips and Sylhet sand were used for mixing.

As a replacement of coarse aggregate waste tyres were replaced of 0%, 10%, 20% and 25% in mixing.

For each percentage 14 cylinders were prepared.

2.3 Curing of Test Specimen

Fresh concrete gains strength most rapidly during the first few days and weeks. Structural design is generally based on the strength of 28 days. Curing is the process of maintaining satisfactory moisture content in a favorable temperature in concrete during the hydration of the cementitious materials so that the desired properties of the concrete were developed. Curing is the procedure for promoting hydration of cement paste and controlling of concrete temperature and movement of moisture from and into the concrete.

2.4 Determination of Compressive Strength and Tensile Strength of Concrete

These specimens were tested by compression testing machine after 7 days and 28 days curing. The load was applied at a rate of movement corresponding to a stress rate on the specimen of 35 ± 7 psi/s (0.25 ± 0.05 MPa / s)



Fig.1 Equipment set-up of compressive strength test.

Compressive force was applied to the specimen by using compression strength machine and failure load was measured. Compressive strength was calculated by using equation,

$$C = P/A$$

Where, C= compressive strength, P = failure load; and A = contact area.

Specimen was positioned into the compression strength machine according to Brazilian test method. Load was applied to the specimen and failure load was measured.

For tensile strength, the load had been given increased continuously at the rate to produce a split tensile stress of approximately was 1.4 to 2.1 N/mm²/min, until no greater load sustained.

Tensile strength was calculated by using equation,

$$T = 2P/\pi dl$$

Where, T= tensile strength; P= failure load; d = diameter of the cylinder and l= length of the cylinder.



Fig.2 Equipment set-up of splitting tensile strength test

3. Results

Tensile strength, Compressive strength and Stress-Strain Behavior is explained below.

3.1 Compressive Strength

14 cylinders were made for each percentage. The results showed that the compressive strength of the concrete decreased as waste tyres were used in concrete. It was observed that the maximum compressive strength of 16.5 MPa was attained at 0% replacement for 28 days curing, while the minimum strength of 4.6 MPa was attained at 25% coarse aggregate replacement for 7 days curing. The compressive strength for 7 days and 28 days value are shown below:

The failure pattern of Compressive strength is shown in Figure 3.



Fig.3 After compressive strength test

Table 1 The compressive strength variation with various percentages of waste tyres

Sl. No	Percentage of waste tyres	Compressive strength (MPa) at 7	Decreasing in percentage	Compressive strength (MPa) at 28	Decreasing in percentage
01	0%	13.1	-	16.5	-
02	10%	9.1	30.5	14.6	11.5
03	20%	5.4	58.8	8.6	47.9
04	25%	4.6	64.9	5.6	66

The variation of compressive strength at 7 and 28 days are shown in the following figure-4.

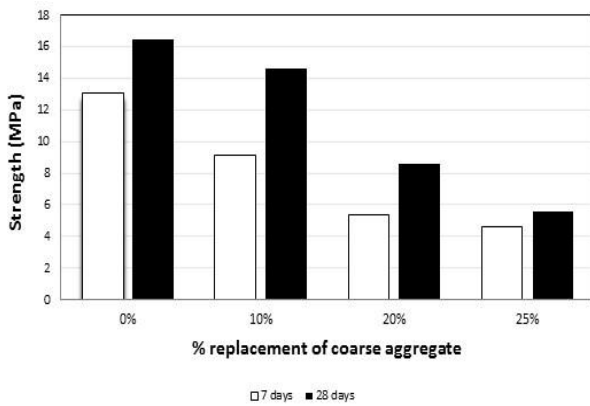


Fig.4 Compressive strength vs % replacement of coarse aggregate as waste tyres at 7 days and 28 days

3.2 Tensile Strength

The important property of concrete is Tensile strength because in the case of various kinds of effects and applied loading it is highly vulnerable. However, compressive strength is very high in contrast with its tensile strength of concrete.

Test was performed according to ASTM C496.



Fig.5 After tensile strength test

The results showed that the tensile strength of the concrete decreased as the percentage replacement of coarse aggregate. It was observed that the maximum tensile strength of 3.2 MPa attained at 0% replacement for 28 days.

The tensile strength for 7 days and 28 days value are shown below:

Table 2 The Tensile strength variation with various percentages of waste tyres

Sl. No.	Percentage of waste tyres	Tensile strength (MPa) at 7 days	Decreasing in percentage	Tensile strength (MPa) at 28 days	Decreasing in percentage
01	0%	2.7	-	3.2	-
02	10%	1.9	29.63	2.7	15.63
03	20%	1.6	40.7	2.2	31.25
04	25%	1.3	51.9	1.6	50

From tensile strength data we observed that the increasing in percentage of waste tyres in concrete then decreasing the tensile strength. 10% replacement then decreasing the tensile strength 29.6% at 7 days and 15.63% at 28 days

The variation of tensile strength at 7 days and 28 days are shown in figure-6.

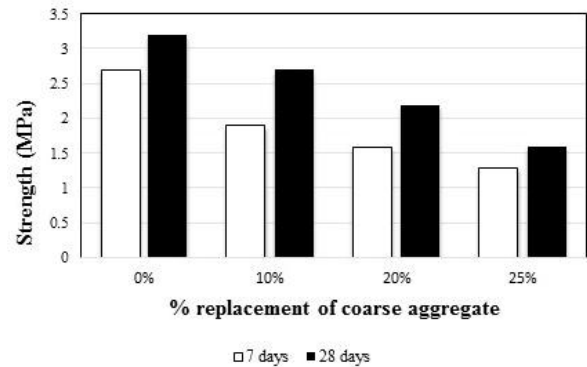


Fig.6 Tensile strength vs % replacement of coarse aggregate as waste tyres at 7 and 28 days

3.3 Stress-Strain Behavior

The stress-strain curve of concrete depicts between those of the aggregate and the cement paste. However the most of the range connection is non-linear over. The motive for this non-linear behavior is that the form of micro-cracks at the line between aggregate particles and cement paste as a result of the distinction movement between the two phases, and within the cement paste itself. These flaws are shaped as a result of ups and

downs in temperature and moisture and the application of load.

The stress-strain diagram is plotted from the collected data for compression test. The four different curves represent the testing value of four different cylinders. From 0% to 25% of waste tyre used as coarse aggregate the stress is decreased dramatically with strain. The relationships between stress and strain for various percentage replacement of concrete at 28 days are presented between Figure 7 to Figure 10.

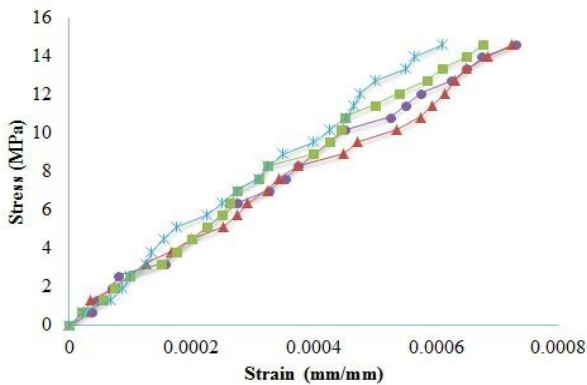


Fig.7 Stress-strain diagram for 0% waste tyres at 28 days

Here in figure 7, four different cylinders without waste tyre rubber were using to get the accurate crushing point. The tests were done in compression state and around 14 MPa crushing stress were found in average for cylinders.

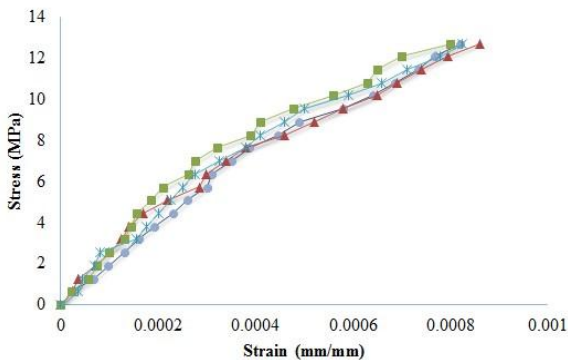


Fig.8 Stress-strain diagram for 10% waste tyres at 28 days

In the case of figure 8, 10% waste tyre rubbers were used as coarse aggregate in four different cylinders. The tests were done in compression state and the crushing point is decreased. It was found around 12 MPa.

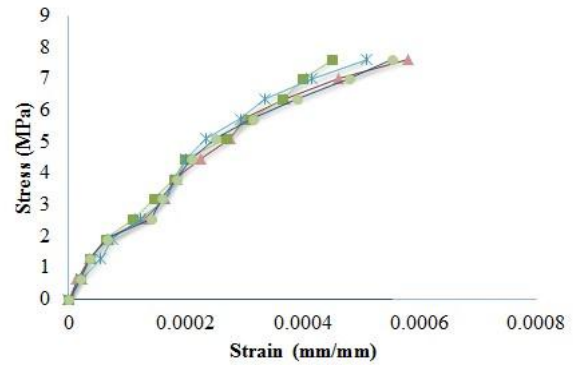


Fig.9 Stress-strain diagram for 20% waste tyres at 28 days

Here in figure 9, 20% waste tyre rubbers were used as coarse aggregate in four different cylinders. The tests were done in compression state and the crushing stress was found around 8 MPa.

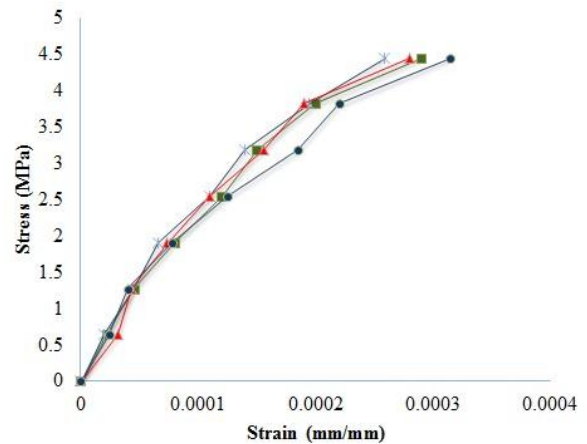


Fig.10 Stress-strain diagram for 25% waste tyres at 28 days

In figure 10, 25% waste tyre rubbers were used as coarse aggregate in four different cylinders. Similar scenario was seen in this case. The crushing point is dramatically decreased.

4. Conclusions

Reduction of compressive strength and tensile strength were analyzed when the coarse aggregate was replaced by tyres. From this research it is observed that concrete with tyre aggregate can be used up to 10% replacement for proper strength, however, 20% can be replaced in light-weight concrete applications. This type of concrete with rubber aggregate mixture can be used for (a) architectural applications such as nailing concrete, false facades, stone backing, and interior construction because of its light unit weight (b) low-strength-concrete applications such as sidewalks, driveways, and selected

road construction applications and (c) crash barriers around bridges and similar structures.

REFERENCES

- [1] Eldin, N., and Senouci, A, Observations on rubberized concrete behavior, *Cement Concrete Aggregate*, 15(1), 74–84, . (1993).
- [2] Eldin, N., and Senouci, A, Measurement and prediction of strength of rubberized concrete.” *Cement Concrete Composite*, 16(4), 287–298,(1994).
- [3] Fattuhi, N. I., and Clark, N. A, Cement-based materials containing shredded scrap truck tyre rubber, *Constr. Build. Mater.*, 10(4), 229–236,(1996).
- [4] ACI 211.1 ,Standard practice for selecting proportions for normal, heavyweight and mass concrete procedure for mix design, (2009).
- [5] Khaloo, A., Dehestani, M., and Rahamatabadi, P, Mechanical properties of concrete containing a high volume of tyre-rubber particles, *Waste Manage.*, 28(12), 2472–2482,(2008).

Dmaic Approach for Process Improvement: Improving Fabric Width Shrinkage of Basic T Shirt

Swarnalekha Khandker¹, and Tasin Us Sakib²

¹ Department of Industrial Engineering and Management, Khulna University of Engineering & Technology, Khulna-9203, BANGLADESH

² Department of Industrial and Production Engineering, Rajshahi University of Engineering & Technology, Rajshahi-6204, BANGLADESH

ABSTRACT

This paper represents the effectiveness of DMAIC approach for process improvement, which is a structured methodology of Six Sigma that is proven to be a dynamic approach for defect identification, problem solving and future prevention by the support of different statistical tools. In this paper, the major problem was negative shrinkage of garment width which was not within the UCL and LCL. Consequently, the overall AQL of finished product on customer end reached to 7.50%, where the standard allowable shrinkage is ± 5.5 cm and standard AQL is 1.5%. Therefore, after identifying the root-cause the DMAIC was used for process improvement and solving the issue. In an overview, DMAIC is one of the most authoritative approaches in Six Sigma problem solving process. This is the short form of Define-Measure-Analyze-Improve –Control. DMAIC is one of the most widely practiced tools to ensure and lead towards maximum quality level that absolutely fulfill the SIX SIGMA methodology. And, this result comes by following the steps of process improvement that includes not only determining existing system but also bringing up new possible process changes to improve quality, process efficiency, productivity and reduce cost. Throughout these steps different supporting tools such as project charter, Pareto chart, process map, CTQ parameter identification, data collection, cause and effect diagram, check list etc. has been used and also form which final corrective actions and preventive actions (CAPA) has been attained to gain the ultimate progress. The progress in any of the mentioned areas is considered to be a catalyst towards the process improvement.

The main objective of this study is meet the voice of customer (VOC) that is AQL% level up to 1.5%, in other words improve the overall width shrinkage %. Though, primarily the root cause of high percent defective was identified by 80/20 rule by using the complaint data received from the customer, later by implementing corrective and preventive action the AQL% was controlled up to 1.15% which is 84.67% improvement of the overall quality level.

Keywords: DMAIC, Width Shrinkage%, CTQ, AQL, CAPA

1. Introduction

It is not unknown that at present time considering the Bangladesh ready-made garments manufacturing industries, it is a rising demand to establish an organized practice of process improvement is required to meet the biggest challenges. This can include defect reduction, downtime reduction, efficiency improvement, cost reduction etc. And, for this kind of process improvement DMAIC (Define-Measure-Analyze-Improve-Control) is a very effective tool- one of the most frequently used approach of Six Sigma.

Six-Sigma methodology was originally developed by Motorola in 1980s and it targeted a difficult goal of 3.4 parts per million defects. Six Sigma was initially introduced on manufacturing processes; today however, marketing, purchasing, billing, invoicing, insurance, human resource and customer call answering functions are also implementing the Six Sigma methodology with the aim of continuously reducing defects throughout the organizations processes [1]. A study by Antony et al. indicates Six Sigma as a more advanced level of quality, which will certainly implement those organizations that tend to business excellence after QMS certification per ISO 9000 series [2].

Six-sigma strategy has four aspects that are not emphasized in other business improvement methodologies and total quality management (TQM). First of all, Six Sigma places a clear focus on bottom-line savings. Second, Six Sigma has been very successful in integrating both human aspects (culture change, training, customer focus etc.) and process aspects (process stability, variation reduction, capability etc.) of continuous improvement. Third, Six Sigma methodology (DMAIC) links the tools and techniques in a sequential manner. Finally, Six Sigma creates a powerful infrastructure for training of champions, master black belts, black belts, green belts, and yellow belts [3].

DMAIC Methodology and DMADV Methodology, both inspired by Deming's Plan-Do-Check-Act Cycle. Where, DMAIC is used to improve the existing business process and DMADV (Define-Measure-Analyze-Design-Verify) is used to create new product or process design. [4]. There are several example of using DMAIC for such process improvement. For example, by Sharma and Rao, an engine crankshaft manufacturing process had been improved by reducing deviation of dimensional measurement data of the CTQ characteristics using DMAIC [5]. Again, by Gupta, for increasing yarn quality in a yarn manufacturing industry DMAIC methodology

* Corresponding author. Tel.: +88-01740035569

E-mail addresses: official.sk.lekha@gmail.com; anan.ipe@gmail.com

had been used, by reducing defects and quality cost from input-process up to packaging final product [6].

Therefore, DMAIC is generally used for data driven problems where risk is high and impact is crucial in business or manufacturing processes. In other words, for quantitative analysis rather than general qualitative analysis, it requires ample data for statistical analysis to reduce process variation. And, there is no alternate to DMAIC since this problem solving approach is the backbone to take initiative for improvement. For this reason, in this study this Six Sigma methodology (DMAIC) is used for the fabric width shrinkage problem that is caused by variations in the process.

2. Background

This Study has been performed on a customer complaint data of a 100% export oriented ready-made knitwear industry, a leading manufacturing organization in Bangladesh. The problem is specifically found in tubular basic T Shirt Styles rather than side seam basic T shirts. Where, the chest measurement of the garments were found smaller or in other words tubular fabric width was shorter against standard measurement set by customer. Table 1 shows the list of tubular basic t shirt models which are frequently found out of tolerance.

Table 1 Types of defective Basic T

Styles	% defective
BT 76000	76.23%
BT 64000	21.51%
BT 41000	2.26%

The width shrinkage (%) is one of the three major parameter of dimensional stability which is determined as per AATCC 135, test method that is intended for the determination of dimensional changes of fabrics after 3HL home laundering [7]. This is a very important basic CTQ characteristic for dyed knitted fabric that is needed to be evaluated before going for bulk production. Therefore, in this study this test has been used as key feature to monitor the overall performance of the fabric.

The data used here, is a consolidation of about six months report (June, 2017 to December, 2017) containing the quantity of 'unit inspected' and 'unit defective' and a details of number of defects for each defect type. Therefore, a Pareto Analysis has been performed initially. Afterwards, DMAIC has been performed accordingly.

3. Methodology

The methodology is a complete set of actions that provides the ultimate results. Figure 1, represents the overall approach step by step: 3.1, 3.2, 3.3, 3.4 and 4.1 respectively.

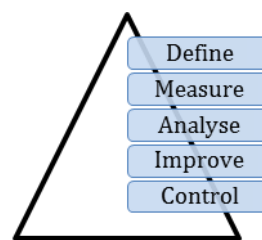


Fig.1 Flow diagram of DMAIC

3.1 Define

The problem defined below satisfies SMART (Specific, Measurable, Achievable, Relevant and Time-Bound).

3.1.1 Project Charter

Firstly, a project charter has been developed for the team.

Table 2 Project Charter of the Team Project

Project Charter												
Project Leader: Vice President, Black Belt	Team Member: Engineer, Dept. of Quality Assurance; Engineer, Dept. of Process Improvement											
Starting Date: January, 2018; Completion Date: May, 2018	Project Location: A 100% export oriented ready-made garments manufacturing facility, Savar, Dhaka, Bangladesh.											
Business Case: Identify root-cause of top defect and come up with a solution to improve process to reach standard quality level (AQL%) to satisfy customer, which will improve quality and reduce cost accordingly.												
Project title:	Reduce customer complaint of 'X' customer by											
Stakeholders:	Employees of Quality Assurance & Process											
Subject Matter Experts:	Black Belt of team and Process Owners- Textile and Sewing Manufacturing Facility											
Project milestone:	Jun	Jul	Aug	Sep	Oct	Nov	Dec	Jan	Feb	Mar	Apr	May
Define Phase: 01 June, 2017 to 31 December, 2017												
Measure Phase: 01 January, 2018 to 15 January, 2018												
Analyze Phase: 16 January, 2018 to 15 February, 2018												
Improve Phase: 16 February, 2018 to 15 April, 2018												
Control Phase: 16 April, 2018 to 31 May, 2018												

3.1.2 Process Map

The given process map in Figure 3 is prepared to learn the overall process and QC check points from which we can extract data later.

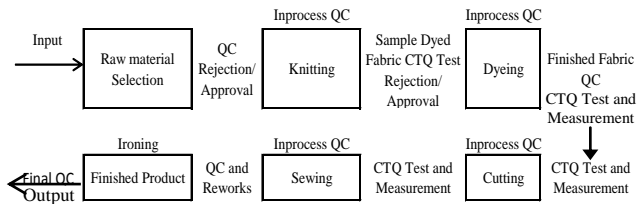


Fig.2 Process Map (Raw material input to finished product)

From the process map it can be determined that, CTQ test data can be collected from dyed fabric after knitting process is done and critical measurement can be done after dyeing process up to the finished final product.

3.2 Measure

This phase represents, the Pareto Analysis, CTQ parameters, data collection, evaluation of existing system, current level of quality etc.

3.2.1 Pareto Chart

To identify the root-cause, the top defect has been determined from the data of customer by using Pareto Analysis. Figure 2, indicates the Pareto Chart where we can see that apart from smaller chest measurement issue (73%) there are also other sewing and textile defects available in minor percentage (%): Untrimmed thread 12%, Uneven Top Stitch 9%, Bigger Chest 3%, Stain 2%, others 1% respectively.

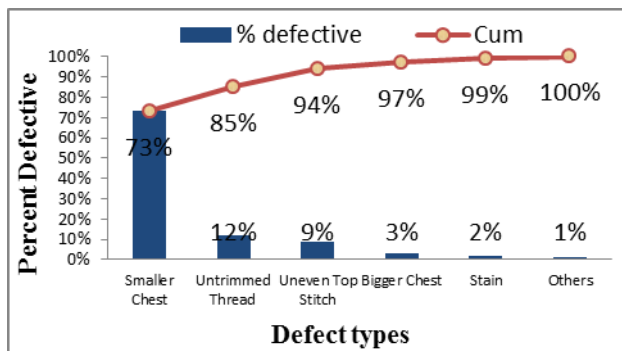


Fig.3 Pareto Chart

3.2.2 Pareto Analysis

From June, 2017 to December, 2017 total 9840 pieces of garments were inspected in total and out of them 7.5% was found defective. And, one defect (16.67%) is the cause of 73% of the bad quality.

3.2.3 Project Objective

1. Meet customer requirement (VOC) and reduce overall AQL%
2. Improve width shrinkage (%) through corrective and preventive action.

3.2.4 CTQ Parameter and Measurement

Based on the process study, following CTQ parameter and measurement point has been selected to monitor the overall process performance.

1. Follow up Sample fabric width shrinkage before bulk production in dyeing.
2. Take measurement of diameter of the tubular fabric after dyeing process and after 24 hour relax of the fabric in dyeing area.
3. Take measurement of diameter of finished garment before and after ironing.

Since, Cotton and cotton/polyester blended knitted fabrics are prone to shrinkage during finishing processes and customer usage. Knit loop formation is defined in each relaxation stage from dry relaxed to fully relaxed [8].

3.2.5 Data Collection

The data of fabric width shrinkage% has been collected from the QC Test Laboratory where the AATCC 135 test method has been followed for 3HL. Equation (1) has been used to calculate the required parameter.

$$\text{Fabric Width shrinkage \%}, DC = 100 (B-A)/A \quad (1)$$

Where, DC = Average Dimensional change
 A = Average Original Dimension
 B = Average Dimension after Laundering

According to Table 1, BT 76000 is found the highest defective model of Basic T Shirt. Therefore, further investigation has been narrowed down to BT 76000 MD (medium) and LG (large) sized garments which are the 76.23% of the total smaller chest defect.

Figure 4 and figure 5 illustrates the existing results of average width shrinkage % for BT 76000 MD and LG sized garments from January to December, 2017.

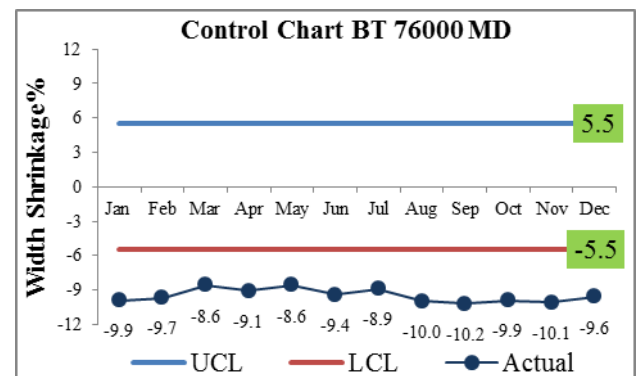


Fig.4 Average Width Shrinkage (MD) of for FY 2017

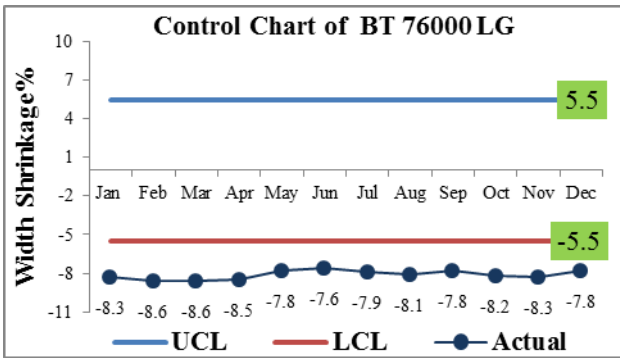


Fig.5 Average Width Shrinkage (LG) of for FY 2017

Hence, the above figures indicate that the existing system is not working properly and the measurements in QC points of the whole process could not detect the issue.

3.3 Analyze

In Analysis phase usually the potential causes are identified which has primary role on the occurrence of the defect and also on the inability to detect the defect in process before sending it on the hand of customer receiving complaint.

3.3.1 Cause and Effect Diagram

In figure 6, all the possible causes have been identified because of which the issue may have risen. However, the top strongest and direct 6 reasons have been encircled which need to be verified and also need to take proper corrective and preventive action if required.

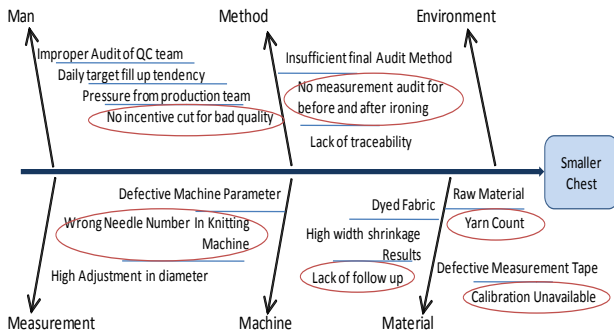


Fig.6 Cause and Effect Diagram for smaller chest of BT 76000 model of Basic T Shirt

3.3.2 Checklist

The top 6 reasons as per figure 5 are-

1. Wrong yarn counts, which should be 24 counts.
2. Lack of follow up or strictness on quality test results especially on shrinkage results.
3. Wrong needle number in knitting machine which impacts on the diameter.
4. No calibration of fiber measurement tapes which are expandable due to high temperature in dyeing area where the average temperature is 35°C to 40°C.
5. No Measurement audit for before and after ironing, this may cause shrinkage.

6. No impact on incentives of production team due to bad quality.

Therefore, the following checklist in table 3 has been prepared where the above mentioned 1 to 6 causes have been verified which indicates the opportunity of improvement.

Table 3 Checklist

Scope	Yes	No	Remarks
Standard Yarn Count 24 is being followed	X		Need further investigation
All QC Tests are performed	X		Need further investigation
CTQ test results are ok of the produced fabric		X	Some batches' shrinkage has failed
Action Taken for QC failed batches		X	Batches passed for next process by management decision for BT 76000, 64000 and 41000.
Measurements are done properly		X	Defective measurement tapes are found
Calibration of Measurement Equipments		X	Measurement Tapes are not calibrated
Critical measurement points are checked in all process		X	Not done before and after ironing of final product
Final Auditors are checking all bundles	X		
Defects are properly identified		X	Need monthly or quarterly training about defects and customer requirements
Incentive is based on Quality		X	Incentives are based on first quality production but no action is taken if any major complaint is received

3.4 Improve

In this phase, based on the measure and analyze phase outcome corrective and preventive actions are set and feasibility of those actions are also verified based on time, efficiency, cost and many other driving factors.

Based on the root-cause analysis and overall verification by the check list two main reasons have been identified for the high width shrinkage. And, by solving any one of those issues the desired results can be achieved and this problem can be solved. Figure 7 is indicating both plans A and B any of which must be implemented.

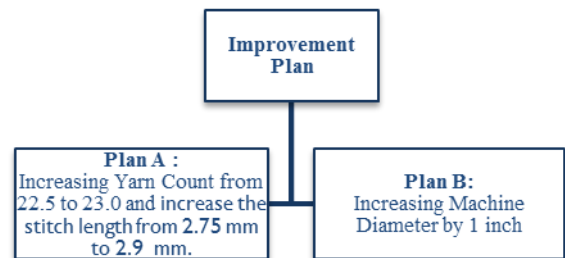


Fig.7 Improvement Plan A and Plan B

3.4.1 Experimental special batches

To identify which plan is more feasible special batches has been produced considering plan A and plan B separately.

Plan A

For Plan A, 4 batches are produced. Two of them are normal batches and other two are special batches of BT 76000, MD size and LG size. Where, three significant measurements are taken:

- (1) Measurement of diameter after 6 hours of relaxes after compacting before going to cutting.
- (2) Measurement of diameter after ironing.
- (3) Variation between the measurements.

Measurement results are given in fig. 8 and Table 4 for MD size and fig.9 and Table 5 for LG size respectively.

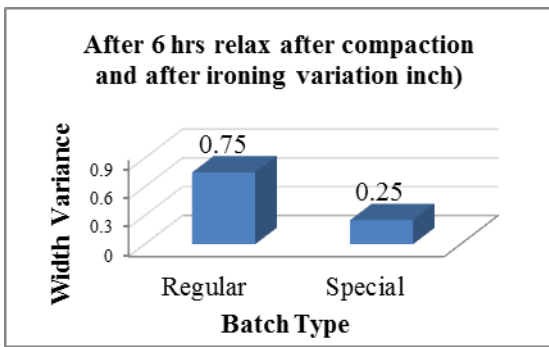


Fig.8 MD size: Regular vs. Special

Table 4 Variation (inch) MD

After 6hrs relax in dyeing and After ironing variation(inch)			
Regular	20.5	19.75	0.75
Special	20.5	20.25	0.25

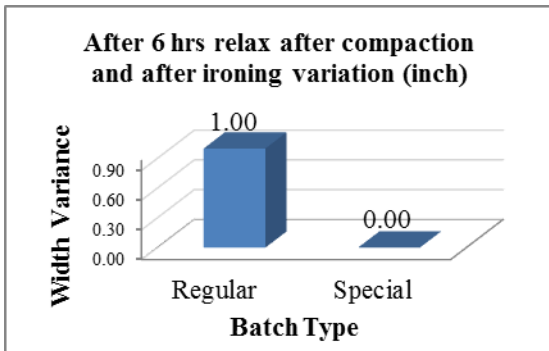


Fig.9 LG size: Regular vs. Special

Table 5 Variation (inch) LG

After 6hrs relax in dyeing and After ironing variation(inch)			
Regular	21.5	20.5	1.0
Special	21.5	21.5	0

Both MD and LG size of BT 76000 special batches have satisfactory results.

Plan B

For Plan B, same parameters have been checked as Plan A for all sizes XS (extra small), SM (small), MD (medium), LG (large), XL (extra large), 2XL (double extra large) and 3XL (triple extra large). And, the results for this plan are also satisfactory but the only impact on the fabric is that the GSM has fallen out of the allowable limit which is 175 ± 5 , figure 10.

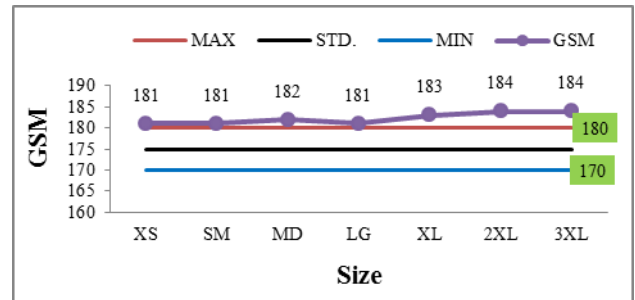


Fig.10 GSM of Plan B Special Batches

Therefore, plan A is the best solution to implement for the improvement of the overall process. Since, plan B will increase the fabric consumption thus increase overall cost of production plan A has to be implemented.

3.4.2 Opportunity of Improvement

Table 6, indicates the corrective and preventive action that are taken by quarter 2, May 2018 to ensure the control of the full process.

Table 6 Corrective Action and Preventive Action (CAPA)

What	Where	When	Who	Required Results
Corrective Actions:				
Change the 24 yarn count to 22.56 count and increase the stitch length from 2.75 mm to 2.9 mm.	Knitting Process	By, Quarter 2, May 2018	Knitting process owner	Improved width shrinkage.
Release batches based on CTQ test results.	Quality Assurance Process	By, Quarter 2, May 2018	Quality Assurance Process Owner	Improved Quality Control
Remove defective measurement tapes immediately after detection and monthly calibration of all measurement tapes	Quality Assurance Process	By Quarter 2, May 2018 As per ISO 9001	Quality Assurance Process Owner	Accurate QC inspection data
Preventive Actions:				
Check all critical measurement points before and after ironing of final products.	Sewing Quality Inspection Process	By, Quarter 2, May 2018	Sewing Process Owner	Ensuring that the overall process is working
Improve traceability and incentive cutting policy for customer complaints	Sewing and Quality Assurance Process	By, Quarter 2, May 2018	Sewing and Quality Assurance Process Owner	Improved Quality Production mind set
Continuous Awareness Program	Quality Assurance Process	By, Quarter 2, May 2018	Quality Assurance Process Owner	Awareness of customer requirement (VOC)

4. Results

In this section, the control phase has been discussed because control phase represents the overall plan implementation verification and derived results meeting the overall objective.

4.1 Control

All the corrective and preventive actions have been implemented accordingly by the end of May 2018, quarter 2. The results obtained for all models and sizes are satisfactory. Figure 11 represents the results of BT 76000 for all sizes.

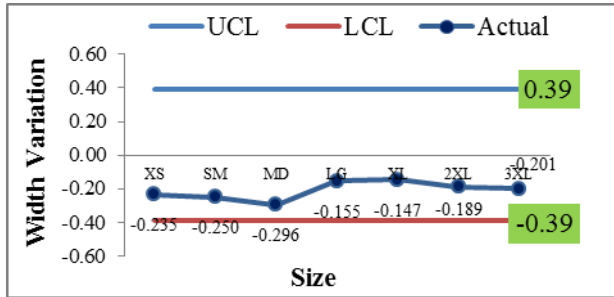


Fig.11 Width variation after implementing Plan A

Hence, by implementing corrective and preventive action the AQL% is controlled up to 1.15%. The overall result has been accepted by the six sigma Black belt, project team member and stakeholders. And, all the changes that have been taken through plan A has been approved in formal documents and distributed to the process owner and related area responsible for proper execution and continuation of the actions for desired results of the improved process. So, this study has derived a controlled plan which needs to be taken as biggest challenge in order to sustain the improvements and make the process continuously improving.

5. Conclusion

Export oriented garment industries are the biggest source of economy of Bangladesh. And, day by day the demands are increasing; facilities are expanding to meet the demands. Therefore, the challenges are becoming greater to meet the goals, keeping all the processes working smoothly. The benchmark of quality is also becoming crucial and even better quality is expected. So, old standards need to be revised or new standards need to be implemented to meet the customer requirement for better quality products as well as sustaining good impression in the market which impacts on the sales tremendously.

The customer provided data has helped immensely the team to extract the top defect smaller chest (73.00%), to set objectives, to identify important parameters. And, later through the cause-and-effect diagram and checklist the existing process was possible to verify and two significant plans A and B was determined to solve the issue. Later, where we have concluded to the point that changing the 24 yarn count to 22.56 count and increase the stitch length

from 2.75 mm to 2.9 mm is the most feasible solution based the special batch experiment results.

After getting the satisfactory experiment results, opportunity has been derived from the overall approach which has been implemented by quarter 2, May 2018 to establish complete control on the processes. Finally, improved results have been gained in the final product of all sizes and by the end of this project AQL% is reduced up to 1.15% which is 84.67% improvement of the overall quality level. Since, the sustainment of the improved quality is a part of continuous process. Proper follow up is a mandatory part of DMAIC Six Sigma Methodology.

NOMENCLATURE

CTQ : Critical to Quality

AQL : Allowable Quality Level

CAPA : Corrective and Preventive Action

DC : Width Shrinkage, %

AATCC: American Association of Textile Chemists and colorists

REFERENCES

- [1] A. B. Patil, Dr. K. H. Inamder, Process Improvement Using DMAIC Approach: Case Study in Downtime Reduction, *International Journal of Engineering Research and Technology (IJERT)*, Vol. 3, Issue 3, pp 1930-1934 (2014).
- [2] J. Antony, M. Kumar, C. N. Madu, Six sigma in small and medium-sized UK manufacturing enterprises: Some empirical observations, *International Journal of Quality & Reliability Management*, Vol. 22(8), pp 860-874 (2005).
- [3] D. A. Desai, M. B. Patel, Impact of Six Sigma in a developing economy: analysis on benefits drawn by Indian industries, *Journal of Industrial Engineering and Management*, Issue 2, Vol 3, pp.517-538 (2009).
- [4] P. Rumana, D. A. Desai, Review Paper: Quality Improvement through Six Sigma DMAIC Methodology, *International Journal of Engineering Sciences & Research Technology*, Issue 3, Vol 12, pp. 170-175 (2014).
- [5] G. V. S. S. Sharma, P. S. Rao, A DMAIC approach for process capability improvement an engine crankshaft manufacturing process, *Journal of Industrial Engineering International*, Vol 10, Number 2, Pp 1 (2014).
- [6] N. Gupta, An Application of DMAIC Methodology for Increasing the Yarn Quality in Textile Industry, *IOSR Journal of Mechanical and Civil Engineering (IOSR-JMCE)*, Issue 1, Vol 6, pp. 50-65 (2013).
- [7] Copyright © 2008 American Association of Textile Chemists and colorists, AATCC Test Method 135-2018, *Dimensional Changes of Fabrics after Home Laundering*, pp 1.
- [8] L. Onal, C. Candan, Contribution of Fabric Characteristics and Laundering to Shrinkage of Weft Knitted Fabrics, *Textile Research Journal*, Vol 73, Issue 3, pp. 187 – 191 (2003).

Design of Automated Biodiesel Blend Plant and Analysis of Rotational Effect on Biodiesel Blends

Shaurin Maher Kikky¹, Leonard Sunny Peris^{2,*}

¹Department of Mechanical Engineering, Military Institute of Science and Technology, Dhaka-1216, BANGLADESH

²Department of Mechanical Engineering, Bangladesh University of Engineering and Technology, BANGLADESH

E-mail: ²perissunny19@gmail.com; Mail: ²105/8, Monipuripara, Tejgaon, Dhaka-1215

ABSTRACT

Due to the high growth in demand for the use of fossil fuel in today's world, alternative sources of energy extraction is now the prime focus. One such viable medium is the Bio-Diesel. In this paper, different blends of biodiesel produced from newly designed automatic biodiesel plant have been studied. During esterification process various speeds were applied by using self-controlled servo motor and settlement time was observed over range of various speeds. Comparative study of the blends for chemical and mechanical properties such as kinematic viscosity, density, flash point and calorific value were also appraised. In this thesis, a clear idea and explanation upon the generation of biodiesel from various available oils as well as contrast of their mechanical, chemical properties have been illustrated. The design of the fully automated biodiesel plant and the working procedure of that plant for continuous production and supply have been shown.

KEYWORDS: Automated Biodiesel plant, Continuous production of biodiesel, Mechanical and chemical properties of biodiesel.

1. Introduction

Modern civilization is much dependent on fossil energy. Energy obtained from fossil resources is much higher than any other resources. Majority of the world's energy needs are supplied through petrochemical resources, coal, oil and natural gas. The consumption of fossil fuels is on increase from year to year. As the fossil resource is non-renewable, so fuel price is gouging as a consequence of spiraling demand and diminishing supply [1]. Fuel and energy crisis and the concern of the society for the depleting world's non-renewable energy resources led to a renewed interest in the quest for alternative fuels. One of the most promising alternative fuels is the Biodiesel fuel that is produced from vegetable oil or animal fat by the chemical process 'Transesterification'.

2. Review

B. Prbakaran and Dinoop Viswanathan published a paper on "experimental investigation of effects of addition of ethanol to bio-diesel on performance, combustion and emission characteristics in CI engine." [2] J. Shen published a paper on "production and fuel properties of fast pyrolysis oil/bio-diesel blends" [3]. In world conference on technology, innovation and entrepreneurship, Radia Selaimia published a paper on "the synthesis of bio-diesel from vegetable oil" [4]. PV Ramana published a paper on "experimental study on CI engine performance using bio-diesel blends" [5]. L.S Khuong published another paper on "A review on the effect of bioethanol dilution on the properties and performance of automotive lubricants in gasoline engines" [6]. In all of these mentioned research works, researchers have done works mainly on Biodiesel blend and its performance, characteristics.

In this paper we have studied the changing mechanical and chemical properties with the change of RPM and also established a new set up of biodiesel plant for its continuous production. So from that point of view, the process followed in this experimental conduction is different than the way of general progression of work in this field but the basic theory of it is implemented the same.

3. Experimental Setup

The setup consists of mainly two parts- one is major and another is minor. The major part is where the controller is set. With the help of controller the RPM can be changed. The minor section has two containers having shaft, propeller and servomotor. Motor helps to rotate the shaft and the propeller rotates with shaft. The setup is very simple and easy to handle. Many other equipment like manual valves, pipes, fittings, reducers, electronic components as microcontroller, relay, potentiometer, LM35, Arduino development board has been used in this setup. We also use some extra measurement devices which we measure the rotation of the fan. The rpm is measured by tachometer and the temperature is measured by thermometer.

4. Biodiesel Blend

Blends of biodiesel and conventional hydrocarbon based diesel are products most commonly distributed for use in the retail diesel fuel market place. Much of the world uses a system known as the "B" factor to state the amount of biodiesel in any fuel mix. [7]

Such as –

* Corresponding author. Tel.: +880-

E-mail addresses: perissunny19@gmail.com

Table 1: Percentages of fuel mixtures

Biodiesel	Petro Diesel	Type
10% Biodiesel	90% Petro Diesel	B10
20% Biodiesel	80% Petro Diesel	B20
30% Biodiesel	70% Petro Diesel	B30
50% Biodiesel	50% Petro Diesel	B50
85% Biodiesel	15% Petro Diesel	B85

Table 2: Quantity of biodiesel prepared -

Blend name	Fuel quantity (ml)	Biodiesel quantity (ml)	Diesel quantity (ml)
B10	1000	100	900
B20	1000	200	800
B30	1000	300	700
B50	1000	500	500

Biodiesel is a very versatile transport fuel and can be produced from local raw material or collection of used vegetable or frying oil in rural regions of developing countries. There are three basic routes to biodiesel production from oils and fats.

- Base catalyzed transesterification of the oil
- Direct acid catalyzed transesterification of the oil
- Conversion of oil to its fatty acids and then to biodiesel

Here Transesterification process has been used:

Transesterification reaction is a stage of converting oil or fat into methyl or ethyl esters of fatty acid, which constitutes to biodiesel. Biodiesel (methyl ester) is obtained through the reaction of triglycerides of vegetable oils with an active intermediary, formed by the reaction of an alcohol with a catalyst. The general reaction for obtaining biodiesel through transesterification is

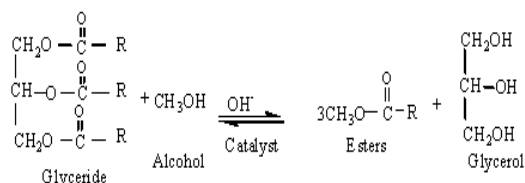


Fig1: Transesterification process [8]

Washing Biodiesel with water is the oldest and most common method of cleaning biodiesel. About 3% of raw unwashed biodiesel is methanol. Methanol is a

solvent; it captures soap and other impurities and holds them dissolved in the biodiesel. Water soaks up that methanol, releasing impurities to be washed away with water.

Keeping the methanol liquid and diluted in water makes water washing the safest way to clean biodiesel. Water washing is the most flexible way to purify biodiesel. Under the right conditions, it can be power washed in just a few hours with extremely aggressive wash methods. Water washing can be automated, and can be mixed and matched with different wash methods to fit personal needs. [9]

5. Properties

The properties that have been obtained through this research have been shown below:

Table 3: Different properties of Biodiesel (for Methanol)

Name	0 rpm	45 rpm	60 rpm	90 rpm
Viscosity(cst)	4.18	4.29	4.54	3.91
Flash point(K)	330	329	332	331
Density(kg/m ³)	856.27	881	907.23	909
Cal. Value(MJ/kg)	42.09	41.8	41.12	40.9

Table 4: Different properties of Biodiesel (for Mustard oil)

Name	0 rpm	45 rpm	60 rpm	90 rpm
Viscosity(cst)	5.6	4.12	4.43	3.72
Flash point(K)	326.15	330	320	328
Density(kg/m ³)	881	851	846.075	839
Cal. Value(MJ/kg)	42.1	42.3	42.5	42.5

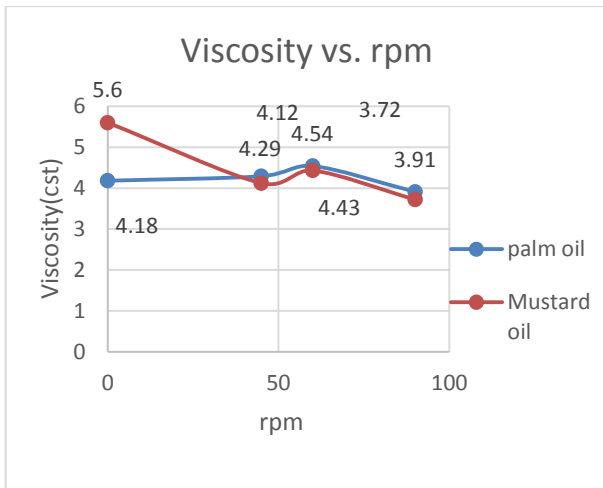


Fig.2: Graphical representation of Viscosity vs. Rpm for Palm and Mustard oil

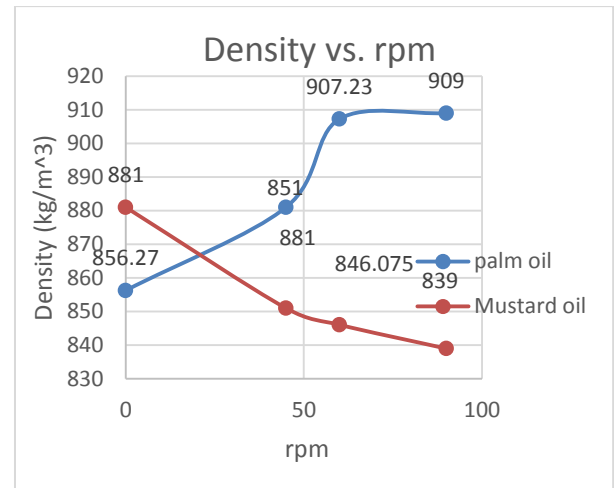


Fig.4: Graphical representation of Density vs. Rpm for Palm and Mustard oil

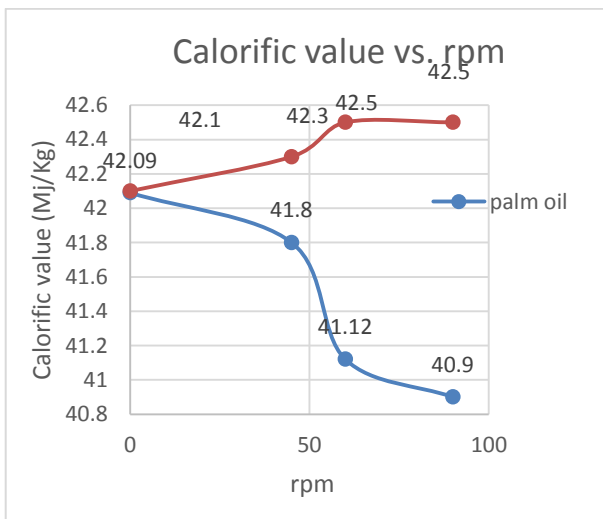


Fig.3: Graphical representation of Calorific Value vs. Rpm for Palm and Mustard oil

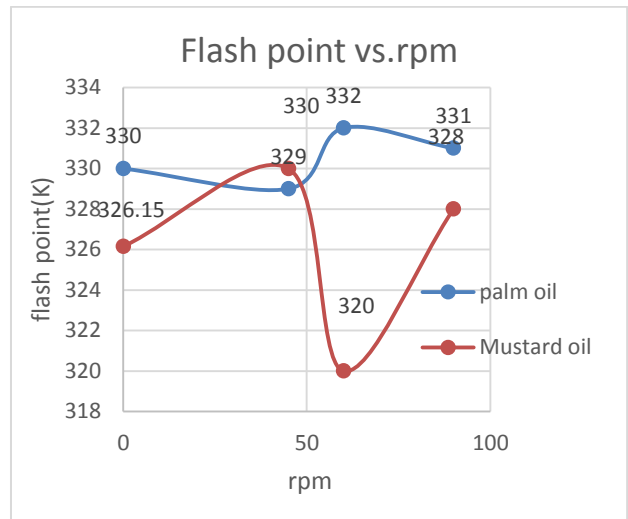


Fig.5: Graphical representation of Flash point vs. Rpm for Palm and Mustard oil

In these graphs, the changing mechanical and chemical properties are shown with the change of rpm. Flash point, Density, Viscosity and Calorific value are studied to achieve results.

6. Discussion and Scope

Biodiesel is probably the best solution to the ongoing quest for pollution free fuel. It is environmentally safe and the current engine construction design does not require any changes to be compatible with biodiesel. In spite of having many positive sides it is still not very popular among the consumers because of its high price. If

the production cost can be lowered then the retail price will also be reduced. Extensive research in production method is required to bring the price down to everyone's grasp. Only then the world can advance towards a greener future. The global market for biodiesel is expected to increase in the next ten years. Europe currently represents 80% of global consumption and production, but the US is now catching up with a faster rate in production than Europe. Brazil is expected to surpass US and European biodiesel production by 2015. Europe, Brazil, China and India each have targets to replace 5% to 20% of total diesel with biodiesel. If governments continued to invest more in R&D on

bio fuel exploitation, it would be possible to reach the targets sooner.

7. Result Discussion

The experimented work emphasized on the calculated data's that have been derived and reflected the feasibility of bio-diesel (Mustard Oil and Methanol) with diesel in the IC engine. The calculated RPM on varying aspects of viscosity, flash point, calorific value and density illustrates a broad idea of how advantageous this mixture of fuel would be in the field of alternative fuel and assurance of green energy usage. It is true that the alternative fuel is very expensive but this work is a contribution towards the ongoing development of this field. The researchers strongly believe that this thesis paper will aid towards that cause.

8. Conclusion

This work was focused on the design of an automated small scale biodiesel production plant and analysis of fuel properties of the product obtained. The procedure has been tested by varying different parameters and satisfactory results were found in all cases. The manual control of the production process was very limited and it can even be used in home to produce homemade biodiesel. The system could be redesigned on a bigger scale to produce biodiesel in large quantities.

REFERENCES

- [1] "Design and development of a novel biodiesel processor and performance analysis of B100 Biodiesel"-1st International Conference on Mechanical Engineering and Applied Science Military Institute of Science and Technology, Dhaka, Bangladesh 22-23 February 2017 : Produced from soyabean oil by Dr.Md. Alamgir Hossain and Porag Hasan 2015.
- [2] Experimental investigation of effects of addition of ethanol to bio-diesel on performance, combustion and emission characteristics in CI engine by B. Prbakaran and Dinoop Vishwanathan, Received 21 May 2016
- [3] Production and fuel properties of fast pyrolysis oil/bio-diesel blends, Article in Fuel Processing Technology · March 2010 by J. Shen
- [4] World Conference on Technology, Innovation and Entrepreneurship The synthesis of biodiesel from vegetable oil Radia Selaimiaa , Abdelsalem Beghiela, Rabah Oumeddourb
- [5] Experimental study on CI engine performance using bio-diesel blends, Research December 2016
- [6] A review on the effect of bioethanol dilution on the properties and performance of automotive lubricants in gasoline engines by L. S. Khuong, N.W.M. Zulkifli
- [7] "Biodiesel Basics_Biodiesel org:_Biodiesel.org.2012[last update]. Retrived may 5, 2012.
- [8] Palm Biodiesel an alternative Green Renewable energy for the energy demands of the future – Jawad Nagi
- [9] Water Washing Biodiesel by Rick De Tech

Evaluating the Impact of Coal Fired Thermal Power Plant on Water: A Case Study of Barapukuria Dinajpur, Bangladesh

Md. Mustafizur Rahman, Md. Arif Hossain, M. Farhad Howladar
Shahjalal University of Science and Technology, Sylhet-3114, Bangladesh

ABSTRACT

Thermal Power plants have various impacts on land, soil, water, air, and social environment. From the result, it has been identified that pH of the water is relatively low near the plant due to improper water drainage. Moreover, calcium of the water samples is also below than the standard value. On the other hand, Chloride (Cl⁻), Total Hardness (TH), Magnesium (Mg) is relatively higher than the Standard Reference value for agriculture. Moreover, maximum degraded water samples are found near the Thermal Power Plant, as the distance increases from the thermal power plant the degradation level of water samples decreases, which is a clear indication of the anthropogenic effects of thermal power plant on the water quality. The collective results of multivariate analysis and Water Quality Index (WQI) imply that most of the areas around the area are dominated by the good to excellent quality water for different purposes. In addition, the results of this research will then be helpful to estimate the major sources of contamination in different areas within the framework of activities intending to improve the quality of water.

Keywords: Thermal Power plant, Water quality, Multivariate analysis, Water quality index.

1. Introduction

Coal is being extensively used as a fuel source for electricity generation. It is one of the main primary energy resources for electricity generation in the world. From the mid of 18th to the mid of the 19th century, coal got extracted from the nature and will be the principal source of energy in the west, mainly coal introduced the industrial revolution to Europe in that century [1]. In Bangladesh, share of commercial energy will be 1.58 M ton (5%) in 2015 and targeted to be 19.18 M ton (27%) in 2021 from coal [2]. The Barapukuria Coal Power Plant is an existing 250 megawatt (MW) coal-fired power station which is owned and operated by the Bangladesh Power Development Board (BPDB) in Dudhipur, Dinajpur province in Bangladesh [3]. Currently the plant has two 125 MW units, recently third unit work is going on and it will generate another 250 MW. The total reserve of coal is about 2083 million tons among which Barapukuria has a reserve of 303 million tons [4]. The power plant was commissioned in 2006 and consumes approximately 450,000 tons of coal a year which is supplied by the Barapukuria coal mine [3-5]. By the year 2016-2017, BPDB has bought 5,334,153.994 tons of coal from the Barapukuria coal mine [3].

Combustion of coal in thermal plant is one of the major sources of environmental pollution due to production of large amounts of ash residues and gaseous and particulate matters, of which ashes disposed to the large ash ponds (disposal site) in the proximity of the plants [6]. During the last few decades the disposal of Coal Combustion Residues produced by Coal fired Thermal Power Plants will be a matter of concern on a worldwide scale [7]. However, Bangladesh is an agricultural country, about 75% people of this country is directly or indirectly related to agriculture. Dinajpur area is also renowned for different agricultural products. However, it is very

important to assess the condition of agricultural water sources around the Barapukuria thermal power plant. Therefore, the aim of this study is to determine the possible impact of power plant on water surrounding the Barapukuria Thermal Power Plant by analyzing the chemical component of water samples.

Barapukuria Thermal Power Plant is located in the north-west part of Bangladesh. It is situated at the Parbatipur Upazila of Dinajpur district, at a distance of about 50 km southeast of Dinajpur town. The nearest railway station is Phulbari is 6 km south of Barapukuria. Dinajpur is famous for producing large amount of Paddy and Rice. Figure 1 is showing the study area.

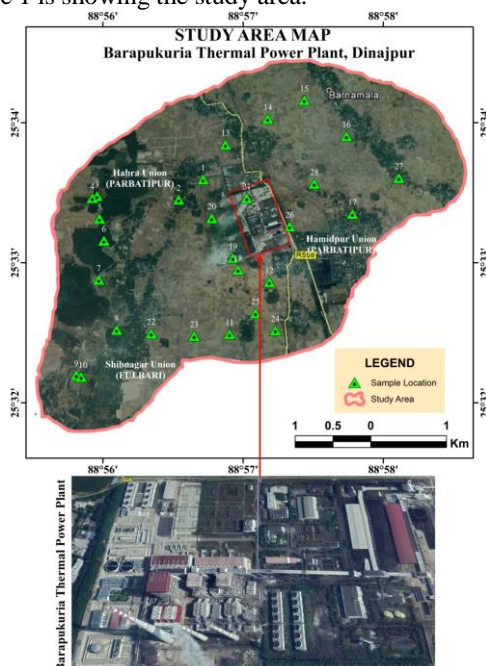


Figure 1: Satellite view of study area. (Around BTPP, Parbatipur upazilla, Dinajpur)

2. Method of analysis

Methodology includes sample collection, sample preparation, sample analysis and data interpretation.

2.1 Sample Collection and data analysis

All experimental water samples were collected very carefully in each of 500 ml bottles from the study area. At first, all sample collecting plastic bottles were washed out to make it neutralized. Then, water samples were collected in this 500 ml bottles noting Latitude, Longitude and Elevation were recorded during the time of sample collection with the help of GPS reading. Total 28 samples were randomly collected from the study area and thirteen chemical properties of each sample, including pH, Arsenic (As), Chloride (Cl⁻), Iron (Fe), Sulfate (SO₄²⁻), Total Hardness (TH), Calcium (Ca²⁺), Magnesium (Mg²⁺), Electrical Conductivity (EC), Copper (Cu), Zinc (Zn), Cadmium (Cd) and Lead (Pb) have been determined. Except, EC (determined in μ S unit), Cl⁻ (determined in percentage) all chemical parameters are determined in ppm unit. Chemical analysis was done by using UV Spectrophotometer except pH and Arsenic. Moreover, pH was measured by digital pH meter and Arsenic by EZ arsenic kit.

2.2 Water Quality Index (WQI)

The Water Quality Index (WQI) analysis provides a comprehensive picture of the quality of surface and ground water for most domestic uses. WQI is defined as a rating that reflects the composite influence of different water quality parameters [5-8].

3. Result & Discussion

Result and discussion of this study is divided into two section chemical analysis result and WQI result.

3.1. Chemical Analysis result

It has been prevailed that pH, Chloride, Calcium, Magnesium and Electrical Conductivity of the water samples are deviated from the standard reference value (for agriculture). But the other chemical parameters are within the standard reference value. Moreover, pH and Calcium is bellow than the standard value (96.43% samples for pH and 71.43% for Calcium). Nevertheless, Chloride, Magnesium and Electrical Conductivity of the water samples are higher than the standard value (100% samples for Chloride and Magnesium, and 32.14% samples for Electrical Conductivity). Figure 2 is showing the average value of different chemical parameters and pH which also showing the standard value of different parameter.

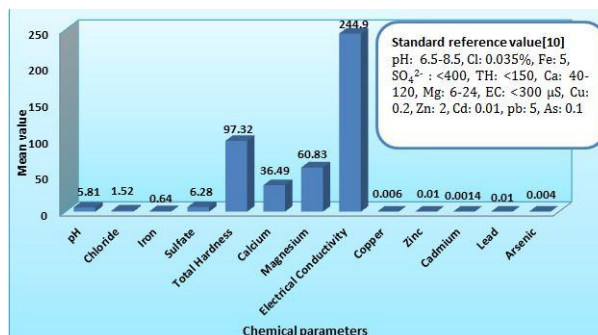


Figure 2 is showing the average value of different chemical parameters and pH.

3.2 Result of Water Quality Index

The Water Quality Index (WQI) is a single value expression that summarizes numerous parameters and provides a measure of water quality. Water quality indices (WQIs) have been calculated for the samples using the concentration of 8 parameters such as pH, EC, Ca, Mg, Cl, SO₄ and TA. From the result of WQI, it has been identified that water is good to excellent quality. Table 1 is showing the result of WQI.

Table 1 Calculated Water Quality Index and their classification of the samples

Sample No	Water Type	Sample No	Water type
W1	Excellent	W15	Excellent
W2	Good	W16	Excellent
W3	Excellent	W17	Excellent
W4	Excellent	W18	Good
W5	Excellent	W19	Good
W6	Excellent	W20	Good
W7	Excellent	W21	Excellent
W8	Excellent	W22	Excellent
W9	Excellent	W23	Good
W10	Excellent	W24	Good
W11	Excellent	W25	Good
W12	Good	W26	Excellent
W13	Excellent	W27	Excellent
W14	Excellent	W28	Good

4. Conclusion

Water is valuable natural resources and now it is facing depleting due to ever-increasing consumption in the industrial and domestic sector. From the present study, we try to identify and analyze the level of depletion of Tillai River and other surface water due to fly ash pollution from BTPP. From the analysis of water

samples, it has revealed that several important chemical parameters that are necessary for agriculture deviate from the Standard Reference value. It is also clear that water samples are degraded because of improper disposal of Plant water as water samples near the ash pond have been found in the degraded condition. Fly ash released during Plant activities are mixing with the water and consequently degrading the water quality. Chemical analysis shows that pH of the water was found relatively low near the plant due to the improper disposal of Plant water. Based on the Total Hardness (TH) values the water samples were found slightly hard. Percentage of Cl and concentration of Mg, EC was also high from the standard reference value. All other parameters except these were almost in the permissible level based on water quality standards. Therefore, thermal power plant must be the major reason for the degradation of the water quality of the surrounding area. Proper management of fly ash from ash ponds should be the primary and immediate responsibility to the BTPP authority. The main innovative things of this research work are that Water Quality Index (WQI) which ultimately helps us to understand the water quality in surrounding area. Moreover, it will be helpful in monitoring activities and for further water quality management to prevent the pollution.

REFERENCES

- [1] Howladar MF and Hasan K (2014) A study on the development of subsidence due to the extraction of slice with its associated factors around Barapukuria underground coal mining industrial area, Dinajpur, Bangladesh. *Environ Earth Sci* 72(9):3699–3713. doi:10.1007/s12665-014-3419-y.
- [2] Power cell (2015) Annual Report, Power Division, Ministry of Power and Mineral Resources, Government of the People's Republic of Bangladesh. www.powercell.gov.bd.
- [3] Bangladesh Power Development Board (BPDB), "Annual Report 2011-12", Bangladesh Power Development Board, page 44, 48.
- [4] Barapukuria Coal Mining Company Limited (BCMCL), Petro-Bangla website, accessed May 2018
- [5] Food and Agriculture Organization of the United Nations (FAO), <http://www.fao.org/home/en/>. Barapukuria Coal Power Plant (BCPP), Global Energy Observatory website, accessed May 2018.
- [6] Querol X, Alastuey A, Lopez SA, Mantilla E, Plana F (1996), Mineral composition of atmospheric particulates around a large coal-fired power station. *Atmospheric Environment*, 30, 3557–3572
- [7] Spadoni M, Voltaggio M, Sacchi E, Sanam R, Pujari PR, Padmakar C, Labhasetwar SR (2014), Water impact of the disposal and re-use of fly ash on water quality: The case of the Koradi and Khaperkheda thermal power plants (Maharashtra, India). *Science of the Total Environment* 479–480 (2014) 159–170, <http://dx.doi.org/10.1016/j.scitotenv.2014.01.111>.
- [8] Howladar MF, Numanbakth MAA, Faruque MO (2017) An application of Water Quality Index (WQI) and multivariate statistics to evaluate the water quality around Maddhapara Granite Mining Industrial Area, Dinajpur, Bangladesh. *Environ Syst Res* 6:13. <https://doi.org/10.1186/s40068-017-0090-9>.
- [9] Sahu P, Sikdar PK (2008) Hydrochemical framework of the aquifer in and around East Kolkata wetlands, West Bengal, India. *Environ Geol* 55:823–835
- [10] Food and Agriculture Organization of the United Nations (FAO), <http://www.fao.org/home/en/>.

Design and Fabrication of an Unmanned Underwater Vehicle

Mohammad Harun-Or-Rashid*, Diprajit Biswas

Department of Mechanical and Production Engineering, Ahsanullah University of Science and Technology, Dhaka, Bangladesh

ABSTRACT

This paper describes the construction of an unmanned underwater vehicle. The UUV was developed to provide the access of underwater for exploit the environment of water and the surroundings of that particular area. The construction of the submarine was done with aluminum to reduce weight and overcome high pressure. About all the components used is water protective, so that, these can give service as submersed. The body is 22 inch long with 10 inch diameter torpedo shaped. Four submersible pumps are used in two ballast tanks for water intake and exert through two solenoid valves. External shapes mount one propeller, one rudder behind the propeller, two elevators and an antenna at the top of the body for receiving signals. The power is derived from two onboard batteries, one for the rudder and elevators, and the other one is for other components. The thrust force generated by the propeller gives forward motion to the vehicle. The machine is equipped with necessary features that would be able to provide service for a long time. In the present research, an UUV is developed and experiment is conducted. It provides an excellent platform for further development of the underwater vehicle as well as can be used in various fields like underwater research, military and civil purposes.

Keywords: Submarine, Unmanned Underwater Vehicle.

1. Introduction

Unmanned underwater vehicles (UUV) are remotely operated Vehicle (ROV) that requires minimum intervention of human operator from a remote distance. ROVs are usually mobile, small in size & highly efficient in performing tasks with unreachable depths of the sea. These are used extensively in offshore industries due to their higher advantages over human carrying submarines. Submerged sea-mines and submarines can be identified with the UUV and secure the harbor.

The first conceptual design of submarine was made in 1578. The first UUV was constructed in the form of a self-propelled torpedo in 1868, but this torpedo did not run [1-2]. The U.S navy developed UUVs in 1960. Later on, around 1980 it became popular to the oil and gas industries [3]. UUVs become essential for underwater photography, 3D image reconstruction, deep-sea mapping and imaging for geo-studies and marine researches [4]. Since, 1817 most of the UUVs were given the torpedo shape to reduce the drag [5]. Due to advancement of material science ROV becomes smaller, lighter for better stability. In this research, the unmanned under water vehicle is designed, manufactured and automatic control system is developed to control it.

2. Design and Construction

The design and detailed drawing of UUV is developed by CAD software (SolidWorks), Fig. 1. The structure of the UUV is composed of five main parts: two ballast tanks, blunt shaped front part for navigation and weight balance, housing for the electric control system with

attached hydroplanes and rear part supporting propeller, rudder and elevator. The UUV is 22.0 inches in length and 10.0 inches in nominal diameter. The length of two ballast tanks is 12.0 inches.

A 3D model of the UUV is developed in SolidWorks (Fig. 2). After that, the UUV is constructed. To make the front and rare shape, a mold is made with wood (Fig. 3). Then the sheet is cut and put upon the mould and bent to get the shape. Finally, four individual sheets are welded together to get the front and rear blunt structure. Then the main cylinder chamber of the UUV is constructed. After that the top and side (left and right) covers are made. Some holes on the frontal, rare and the

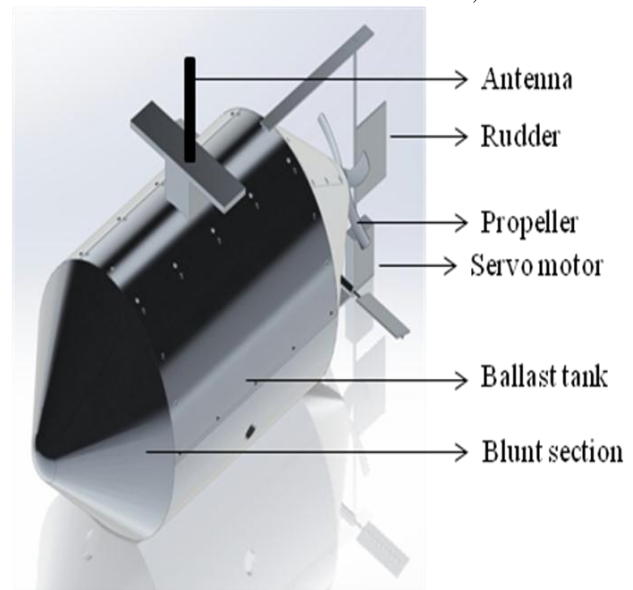


Fig. 1 Final design



Fig. 2 Wooden mold

sideways are cut for the control systems. The control systems are attached individually according to the weight balance ratio to their respective places in the submarine. By installing all the components like rudder, impeller, elevator, antenna we get the final shape of the UUV (Fig. 3).

The electrical components are installed inside the submarine. The electric circuit and the batteries operate the propeller, rudder, elevator and pumps and solenoid valves.

There are four submersible pumps (Fig. 4) which are used to suck and discharge water. Two is used to suck water from outside to the two water chambers when submarine is going to sink. On the other hand, another two are used to discharge water from water chambers to outside during floating. Head and flow rate of 12 volt submersible pumps are 300cm and 4 litres/min respectively.



Fig. 3 Final setup of UUV



Fig. 4 Submersible pump

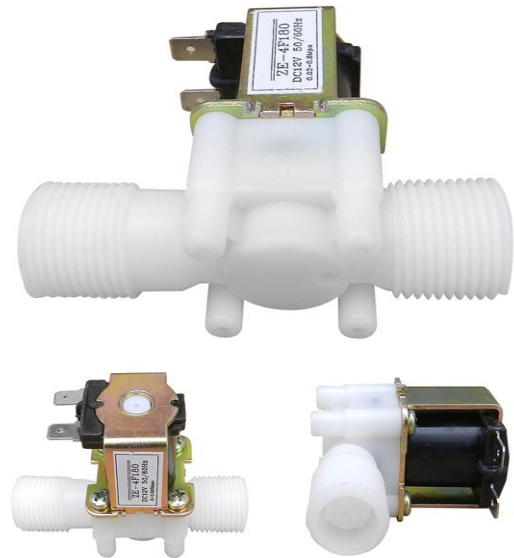


Fig 5 Solenoid Valve

Solenoid valves (Fig. 5) are used to prevent the unwanted flow of water between UUV and the water system. When water is needed to take inside the vehicle then the valve is opened with power supply and submersible pumps work to pump water inside the ballast tanks. Also when the ballast tank water need to excel, solenoid valve is powered to open and the other submersible pumps which work to exert water from the ballast tank start to pump out the water which assist the vehicle to float. Two individual solenoid valves are used for two water vessels. Orifice size, valve type and pressure range of the solenoid valve are 8.5 mm, diaphragm and 0.2-0.8 MPa respectively.

A brushless motor and a propeller are presented in Fig. 6. There is one brushless DC motor which is mounted on the rear side of the vehicle. The motor drives the propeller which results the forward motion of the vehicle. A high torque low RPM motor is used in this study. Shaft diameter, maximum current of motor are 3.17 mm and 20 A respectively. Because high torque motor is necessary for under water vehicle.

Servo motors are used to fulfill two different objectives: to control the vertical and horizontal direction of the

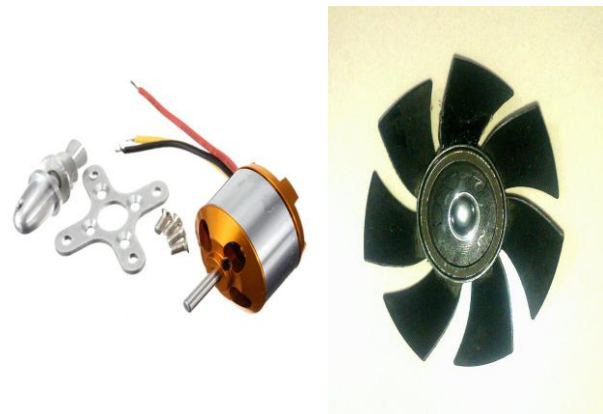


Fig. 6 Brushless motor and propeller



Fig. 7 Servo motor and rudder

submarine. A high-torque (10kg stalling torque) metal geared MG996R digital servo motor is used (Fig. 7). Two servo motors are assigned to uplift the vehicle by rotating the elevator. One servo motor is used to rotate the rudder to give the vehicle a turning movement so that, it can change its direction to move. The rudder is placed after the propeller so that the water can directly hit the rudder blade. Therefore, the vehicle turns faster.

Two Lithium-Polymer batteries (6000mA and 1100 mA) are used for power supply to the whole UUV (Fig. 8). Here, 6000mA 12 volt lithium polymer battery is used to support all the equipment like pumps, solenoid valves and propeller. We also used an 8 volt 1100mA DC battery for power to the micro controller board which supply power to the servo motors. It is used to reduce pressure on the main battery which will supply power constantly to the propeller to give the vehicle forward motion.

The general purpose of constructing the unmanned underwater vehicle (UUV) is to learn the principle of the vehicle. And another purpose is to explore the underwater environment. We have constructed the unmanned underwater vehicle through different design phases. After completion of the design phases the vehicle was constructed. Technical specifications of the designed UUV are presented in Table 1.



Fig. 8 6000mA and 1100 mA Li-Po battery

Table 1: Technical Specifications of the UUV

Parameter	Value
Depth	0.5 m
Maximum speed	0.1383m/s
Maximum Drag	1.062881 N
Dimension	
Total Length	22 in
Length of main vessel	10 in
Length of front and rear part	5 in
Radius of Main vessel	5 in
Weight	
Designed body	10.94 kg
Actual body	13.520 kg
With water mass balance	20.250 kg (max.)
Volume	
Vehicle	$17.69 \times 10^{-3} \text{ m}^3$
Water inside ballast tank after mass balance	$5.16 \times 10^{-3} \text{ m}^3$
Air	$12.53 \times 10^{-3} \text{ m}^3$
Power System	
Voltage	12V
Current	6A
Power	210 Watt
Control System	
	Bluetooth control via Arduino mega
Propulsion System	
	Brushless DC motor

3. Control Panel

The Arduino Mega 2560 is a microcontroller board (Fig. 9). It has 54 digital input-output pins of which 15 PWM outputs, 16 analog inputs, 4 Universal Asynchronous Receivers/Transmitters (UARTs), a 16 MHz crystal oscillator, a USB connection, a power jack, an In-Circuit Serial Programming (ICSP) header, and a reset button. The Mega 2560 board is compatible with most shields designed. In this research, 16 pins are used to control the UUV.

An eight channel relay interface board (Fig. 10) of 5V is used in this study. It is able to control various appliances with large current. It can be controlled directly.



Fig. 9 Arduino Mega R3 2560



Fig. 10 Relay interface board



Fig. 11 Electric Speed Controller

Electronic Speed Controller (ESC) is the device to control the speed of the brushless dc motor. An ESC is shown in Fig. 11. It helps to vary the revolution of the motor which facilitate to vary the speed of the vehicle. It also helps to speed up gradually to give the propeller a gradually increasing torque for the forward thrust.

HC05 Serial Port Bluetooth is a device (Fig. 12) which works as the receiver of the signal. In the present study, submarine is controlled by a mobile phone. Bluetooth app is installed in the mobile phone. The signal is transmitted from a smart phone through Bluetooth technology. There are six pins of the Bluetooth device. Here, four wires are connected: two are for power to the device and another two are for receiving and transmitting data to the Arduino board. After receiving the data from the Bluetooth device Arduino identify the command and does the task by sending the signal to the components that should be operated.

A veroboard is used for different wire connections. The submersible pumps and solenoid valves are connected through the relay interface board from where 6 channels are used for our purpose. The relay is controlled by the microcontroller board. The servo motors which operate the rudder and elevator are also operated by the microcontroller. The propeller motor is connected to the main battery through the ESC. All the signals come to the Arduino board through the Bluetooth device. Connecting the battery with the Arduino Mega and relay we got the power of the Submarine. Then Arduino Mega is connected with the smart phone via Bluetooth

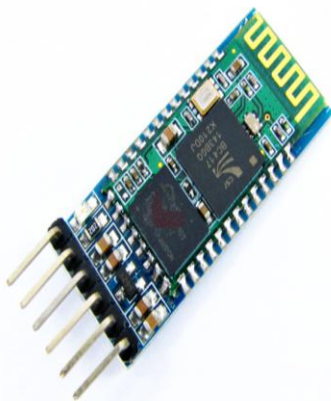


Fig. 12 HC05 serial port Bluetooth

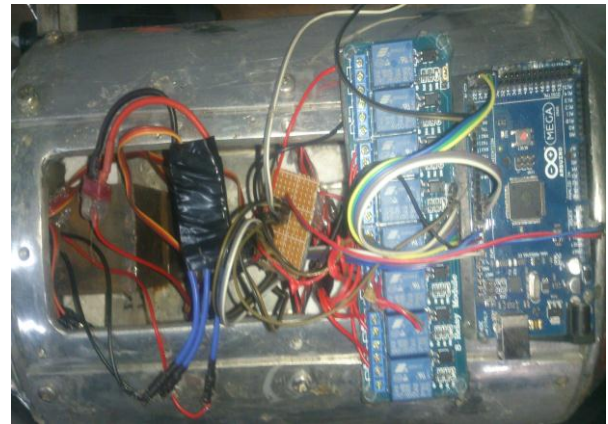


Fig 13 Setup of control panel

to operate the Submarine. Fig. 13 shows the electrical wiring of the control panel. A program is written and uploads to the Arduino board. At first we have to dive the submarine underwater. For the diving operation submerge the submarine under water was necessary. To drown, first the solenoid valve was opened and the intake pumps were start to let the water fill the blast tanks.

After fill in the blast tank, the BLDC motor started to give the propulsion of the submarine. The motor transfers power to the propeller. Then the servo motors are used for operations if needed. The servo motors are attached to control the elevator and rudder. The elevator gives the submarine vertical movement and the rudder gives the submarine directional movement. If the submarine needs to come to the surface of water, then controller send signal to the submersible pumps to force the water out from the blast tanks. Thus the submarine starts to float in water.

4. Calculation

Archimedes principal is quite useful to build the water vessels like ship and submarine. Archimedes principal is followed and a UUV has been successfully designed and prototyped with low cost. Mass and volume of the UUV is 13.520 kg, and $1.769 \times 10^{-2} \text{ m}^3$ respectively. Therefore, density of UUV can be calculated by eq. (1).

$$D_{UUV} = M_{UUV} / V_{UUV} \quad (1)$$

Now the specific gravity of the UUV, can be calculated by eq. (2).

$$\begin{aligned} SG_{UUV} &= D_{UUV} / D_w \\ &= (764.27 \text{ kg/m}^3) / (1000 \text{ kg/m}^3) \\ &= 0.76427 \end{aligned} \quad (2)$$

Here, SG_{UUV} is less than 1. Hence, the UUV will float on water when the ballast tanks are empty.

5. Result and Discussion

The process of construction of an unmanned underwater vehicle is discussed in this study. Each components of the UUV is selected based on availability and low cost. The prototype has a complete set of components

including hull, propeller, rudder, elevator, speed controller, depth control, microcontroller board, batteries, and communication device.

During the experiment the revolution of propeller at different speed of the UUV is measured. It is found that the efficiency is 73%. The run time to go a distance of 170 m for various propeller speeds is estimated. From that, velocity of the UUV is calculated. Fig. 14 shows the velocity the submarine at different speed of the propeller. From the graph is seen that, the velocity of the vehicle increase gradually with the increase of the propeller speed.

At different speed the vehicle faced different amount of drag force. Here, for the blunt shape of the UUV, the coefficient of drag is 2.2. The frontal area of the submarine (A) is $82 \times 10^{-3} \text{ m}^2$. For various speed of the vehicle, the drag is calculated by $F_d = 0.5 \times \rho \times v^2 \times C_d \times A$. Here, C_d is the drag coefficient, ρ is the density of the fluid, v is the velocity of the submarine Fig. 15 shows the drag versus velocity of the UUV. If velocity is increased then drag also increased.

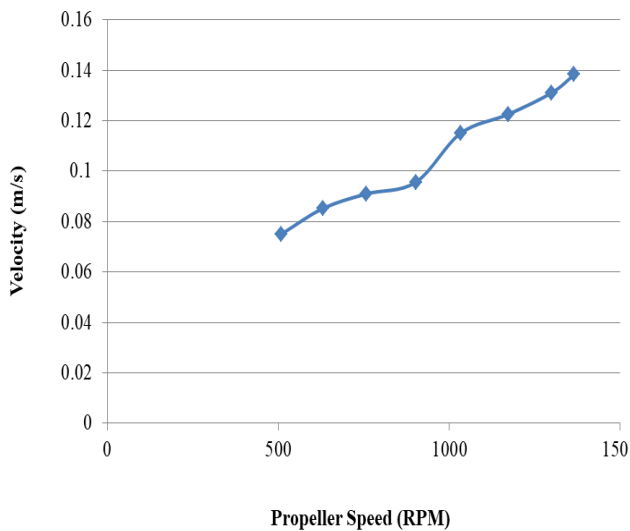


Fig. 14 Propeller speed versus velocity

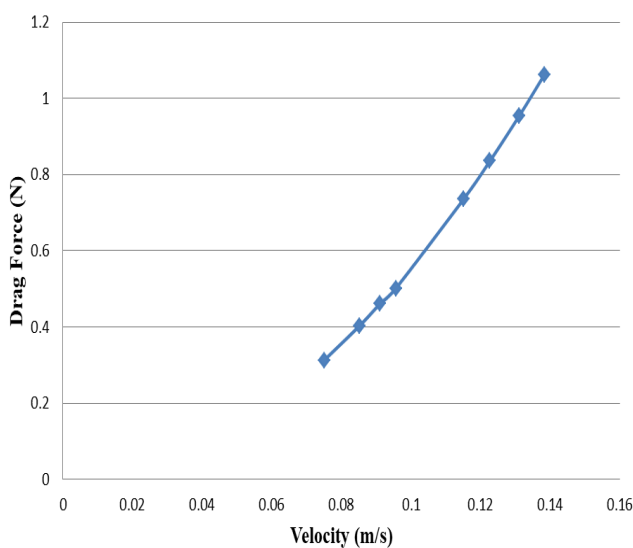


Fig. 15 Drag force vs. velocity of UUV

6. Conclusion

Objective of this research was to develop a prototype of an UUV with available facilities and to figure out its characteristics. With similar elements, by following the construction process one can build an entire submarine with full scale structure which can be operated through the water. No fuel will be required here. The efficiency of the vehicle largely depends on the perfect transmission system, load, hydrodynamic and the design of the propeller. The speed of the submarine depends on the propeller speed. There is a problem due to the leakage for which sometimes the system is dynamically unbalanced. Water leak is prevented by using gaskets, tape and gum. The biggest limitation of the setup: it is not perfectly water protected. The basic use of our unmanned underwater vehicle is to monitor the underwater environment of our water area. The unmanned under water vehicle can be used as the forward surveillance medium of Bangladesh Navy. As it is operated from a distance without a living soul in the vehicle, therefore, the risk of the loss of human's life being decreased in the war. UUV can inspect the submerged pipelines those are used to transfer crude oil and communication cable. In the present research, an UUV is made and experiment is conducted. In future, camera, light, and different types of sensors can be fitted with the UUV for different applications.

Acknowledgement

Thanks to Ahsanullah University of Science and Technology.

NOMENCLATURE

D_{UUV} : Density of the UUV, kg/m^3

M_{UUV} : Mass of the UUV, kg

V_{UUV} : Volume of the UUV, m^3

SG_{UUV} : Specific Gravity of the UUV

D_w : Density of the Water, kg/m^3

REFERENCES

- [1] Augus Budiyono, Advances in Unmanned Underwater Vehicles Technologies: Modeling, Control and Guidance, Perspectives. Indian Journal of Marine Sciences, Vol. 38 pp. 282-295, (2009).
- [2] Sandeep Kumar Jain, Sultan Mohammad, Suyog Bora, Mahender Singh, A Review Paper on: Autonomous Underwater Vehicle. International Journal of Scientific & Engineering Research, Volume 6, Issue 2, February (2015).
- [3] W.H. Wang, X.Q. Chen, A. Marburg, J.G. Chase, C.E. Hann, Design of Low-Cost Unmanned Underwater Vehicle for Shallow Waters, International Journal of Advanced Mechatronic Systems, (2009).
- [4] Chris Roman, Oscar Pizarro, Ryan Eustice, Hanumant Singh, A New Autonomous Underwater Vehicle for Imaging Research,

- Deep Submergence Laboratory, Woods Hole Oceanographic Institution, (2000).
- [5] Robert W. Button, John Kamp, Thomas B. Curtin, James Dryden, A Survey of Missions for Unmanned Undersea Vehicle, RAND Corporation, NATIONAL DEFENSE RESEARCH INSTITUT, (2009).
 - [6] Orhan K. Babaoglu, Designing an Automatic Control System for a Submarine, Naval Postgraduate School, Monterey, California, (1988).
 - [7] Md. Al-Amin, Md. Hasanuzzaman, Nahin Bahar Chowdhury, Dr. S.M. Humayun Kobir, Fazle Rabbi, Design and Fabrication of a Submarine and Comparative Study with 6000m Driving Submersible Submarine. International Journal of Novel Research in Engineering and Science, Vol. 1, Issue 1, pp: 22-29, (2014).

Study the Attitude of a Seesaw to Develop Flying Robots

Mohammad Harun-Or-Rashid, and Md. Nadim Bin Wahid

Department of Mechanical and Production Engineering, Ahsanullah University of Science and Technology, Dhaka-1208, BANGLADESH

ABSTRACT

Design, manufacture and attitude control of a seesaw are described in this paper. At the beginning, mechanical design of the system is completed in SolidWorks. Then the system is made. To control the system several dynamic equations and parameters are studied. Further more, a number of electric components such as motor, electronic speed controller, micro controller board are studied and selected for the experimental setup. Finally, proportional integral derivative controller algorithm is used to control the seesaw. Gain values of the proportional integral derivative controller are estimated on the basis of trial and error method. Ultimate values of the proportional, integral and derivative gains are 3.05, 0.005 and 0.75 respectively. During experiment, it is found that, system takes only ten seconds to reach the same position as the input command. Therefore, this technique can be used to control the roll and pitch attitude of the quad rotor as well as other unmanned aerial vehicle.

Keywords: Attitude Control, ESC, IMU, Seesaw.

1. Introduction

A seesaw is a single point pivoted board which can rotate small angle about the pivot axis depending on applied force. It includes one degree of freedom rotational dynamics which can be compared with the roll of an airplane or any floating object in fluid.

Development and use of unmanned aerial vehicle (UAV) is increasing day by day. Nowadays, this is one of the most popular fields of research. Various types of unmanned airplane and helicopter are using in different applications. Dynamics and avionics of UAV are not easy. Furthermore, it is very costly to develop UAV. If made any mistake then it may crash and cost a lot to develop again. Therefore, it is essential to study the dynamics and control of the system before flying it. In the present study, a seesaw is made for preliminary study the attitude of UAV. It helped to develop control algorithm for roll and pitch of UAV.

There are few researchers studied the behavior of the seesaw. Jae-Nam Kim et al. [1] developed a single axis seesaw as a preliminary study of a quad-rotor aerial vehicle. They initially studied the roll attitude of seesaw to control the quad rotor UAV. Erol Uyar et al. [2] developed the real model as well as a MATLAB model of seesaw and estimated different parameters through experiment and simulation. They found a very little discrepancy between experiment and simulation results. Huafeng Liu et al [3] describe design, fabrication, and characterization of a seesaw-lever force-balancing suspension for a gravity gradiometer that is capable of operation from 0 to 1 g gravity.

The main objective of this research was to develop a seesaw mechanism and study the controller. Fig. 1 shows the 3 D model of the seesaw.

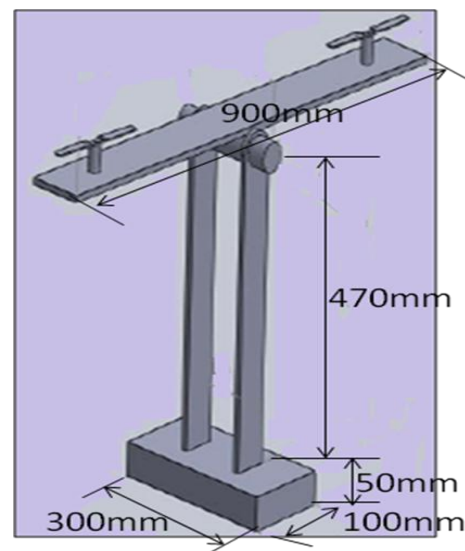


Fig. 1 3D model of the Seesaw

2. Dynamics of Seesaw

Angular displacement (θ) and moment (M) of the seesaw and thrust (T) produce by two rotors are presented in Fig. 2. To estimate the rotor thrust blade element theory, blade

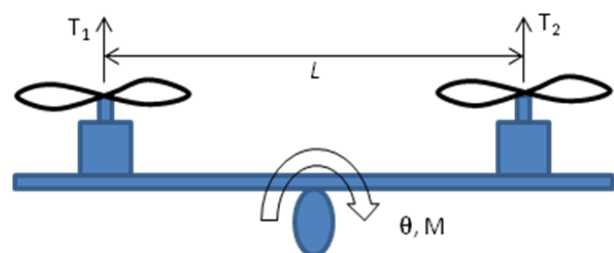


Fig. 2 Dynamics model of Seesaw

element momentum theory can be used. But in the present study, very simple experimental method is applied to find out thrust of two motors. Thrusts of two rotors are calculated by eq. (1) and eq. (2).

$$T_1 = C_T * \omega_1 \quad (1)$$

$$T_2 = C_T * \omega_2 \quad (2)$$

Here, C_T is the propeller thrust constant and ω is the angular velocity. On the other hand, moment of the seesaw is calculated by eq. (3).

$$M = 0.5 * L * (T_1 - T_2) - D * \dot{\theta} \quad (3)$$

Here, L is the distance between two rotors and D is the viscous damping coefficient.

3. Different Components of Seesaw

The main components of seesaw are brushless DC motor, propeller, electronic speed controller (ESC), inertial measurement unit (IMU), board, stand, micro controller board, transmitter and receiver. Fig. 3 shows the constructed model of the seesaw.

A motor converts electrical energy into mechanical energy. In this research, BLDC motor is used because it has high efficiency, less heat generation and nice controllability. Here, EMAX XA 2212 Brushless DC motor of 1400 KV is used. A BLDC motor is presented in Fig. 4.

A propeller is a type of fan that converts rotational motion from motor or any other power source into thrust. Here, two propellers are directly connected with motor shaft. The diameter and slope of the 8045R propeller is 8 inches and 4.5 inches respectively. Propeller is made of Carbon Nylon. On the other hand, weight of each propeller is 10 gram. Fig. 5 shows a 8045R propeller.

In the present study, a six axis IMU (MPU-6050) is used. IMU is a single unit electronic module. It generally contains accelerometer, gyroscope and

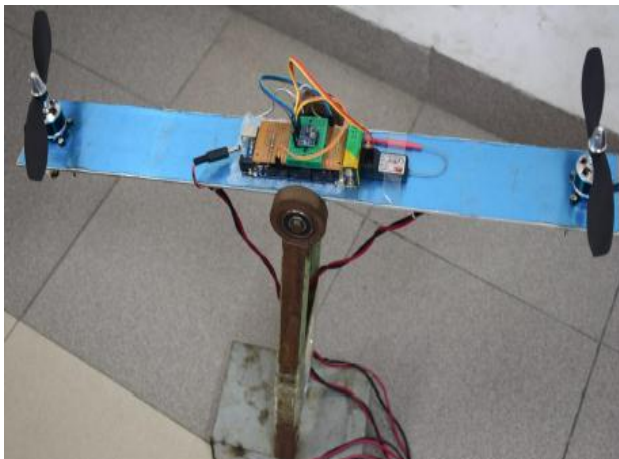


Fig. 3 Seesaw (Experimental setup)



Fig. 4 Brushless DC motor



Fig. 5 Propeller



Fig. 6 IMU (MPU-6050)

magnetometer. Accelerometer, gyroscope and magnetometer are used to detect the linear acceleration, angular velocity and heading reference respectively. MPU-6050 module does not contain magnetometer. In this research, magnetometer is not necessary. In MPU-6050 module gyroscope of micro electro mechanical systems (MEMS) is added. Digital outputs of X, Y and Z axis gyroscopes can be programmed by an user at different ranges like ± 250 , ± 500 , ± 1000 , and $\pm 2000^\circ/\text{sec}$. Conversely, Digital outputs of X, Y and Z axis accelerometers can be programmed at different ranges such as $\pm 2g$, $\pm 4g$, $\pm 8g$ and $\pm 16g$. IMU accumulates linear acceleration as well as angular velocity data and sent to the micro controller board. An IMU is shown in Fig. 6.

An Arduino mega 2560 is used for the seesaw as the main control board. It has a physical programmable circuit board called micro controller and several input and output pins in it. It uses special software called integrated development environment (IDE) to write code and upload to the Arduino. An Arduino mega board is presented in Fig. 7.



Fig. 7 Arduino mega board



Fig. 8 Electronic speed controller



Fig. 9 (a) Transmitter

(b) Receiver

Electronic speed controller is a circuit that is used for controlling the speed of the motor. It is vastly used in field and aerial robotics industries. Here, motor power is supplied from the battery through the ESC. On the other hand, motor control signal generated by the transmitter goes through the micro controller board and ESC to the motor. An electric speed controller is presented in Fig. 8. It's a 30 ampere and 25 gram ESC.

A CT6B FlySky 2.4 GHz 6 channel transmitter and a receiver [Fig. 9 (a), (b)] are used. Transmitter is powered by 12V battery. It can be configured by connecting to the computer. Important features of transmitter and receiver are: very low power consumption, high receiving sensitivity and stability.

Fig 10 shows the circuit diagram of the electrical setup. In this study, two batteries are used. A 9V and 12V battery is used to power supply to the arduino board and motor respectively. Besides an IMU and a receiver is directly connected to the board. A Receiver collects the command of the transmitter and sends to the board.

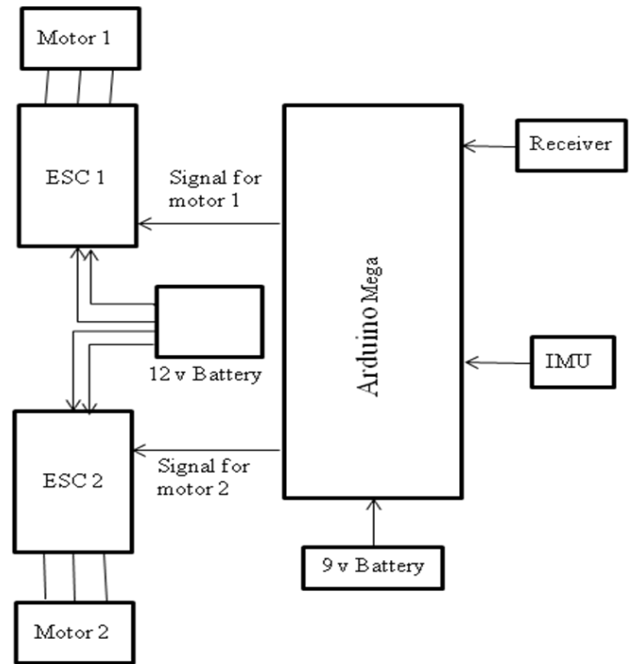


Fig. 10 Block diagram of the electric circuit

4. PID controller

PID controller is a part of closed loop system which is used to control any dynamic object or plant. The Input of the PID controller is the error signal (Error signal: The difference between the reference input and the output of the plant) and output of the PID controller is a weighted sum of the error signal as well as integral and derivative of the error signal. The output of the PID controller is presented in eq. (1).

$$u(t) = K_p e(t) + K_i \int_0^t e(\tau) d\tau + K_d \frac{de(t)}{dt} \quad (1)$$

Here, K_p , K_i , K_d are the proportional, integral and derivative gain respectively. These gain values can be estimated manually or by using software. $e(t)$ is the error signal and τ is the variable of integration (consider values from time 0 to t). Fig. 11 shows the block diagram of the control system with a PID controller.

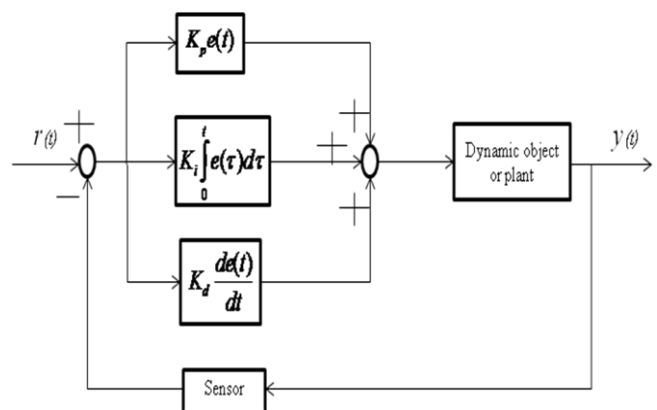


Fig. 11 Block diagram of the control system

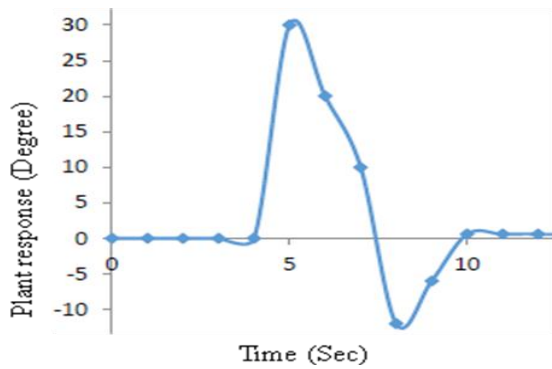


Fig. 12 Response of the seesaw with respect to time

5. Result and Discussion

Finally, a seesaw is made and experiment is carried out. Initial throttle value is 1300 revolution per minute. All the gain values are estimated through trial and error method. The values of K_p , K_i , K_d are 3.05, 0.005 and 0.75 respectively. Fig. 12 shows the stabilization result of the seesaw. In the present research, a disturbance is introduced by using hand after four second of the propeller start running. Force is applied by hand in one side of the seesaw. Therefore, seesaw starts to oscillate about the pivot point after four second (Fig. 12). From the graph, it is clear that it takes only five seconds to stabilize the seesaw by the controller.

6. Conclusion

This paper describes about the development and control mechanism of a seesaw. The seesaw is successfully controlled by the PID controller. Desired input command was zero degree and the seesaw reached to this angle within five seconds after disturbance is applied. Therefore, this technique can be used to control the roll and pitch attitude of the flying robot.

Acknowledgement

Thanks Ahsanullah University of Science and Technology.

NOMENCLATURE

$r(t)$: reference input, degree

y : plant response, degree

REFERENCES

- [1] Jae-Nam Kim et al., An Experimental Study of a Single Axis Seesaw Attitude Control Consisting of Motor and Propeller, The Journal of Advanced Navigation Technology, DOI:10.12673/jkoni.2012.16.1.001 (2015).
- [2] Erol Uyar et al., Position control of a seesaw like platform by using a thrust propeller, 2012 12th IEEE International Workshop on Advanced Motion Control (AMC) (2012).
- [3] Huafeng Liu et al., A seesaw-lever force-balancing suspension design for space and terrestrial gravity-gradient sensing, Journal of

Applied Physics 119, 124508 (2016); <https://doi.org/10.1063/1.4944709>.

- [4] Jordon G. Leishman, Principle of helicopter aerodynamics, (2006).
- [5] Ledin. Jim, "Embedded control systems in C/C++: an introduction for software developers using MATLAB", CMP Books, (2004).
- [6] D. Hazry et al., Study of Inertial Measurement Unit Sensor, Proceedings of the International Conference on Man-Machine Systems (ICoMMS), (2009).

Biofuels Extraction through Pyrolysis of Banana Waste

Saikat Biswas*, Sudip Saha, Mohammad Ariful Islam

Department of Mechanical Engineering, Khulna University of Engineering & Technology, Khulna-9203, BANGLADESH

ABSTRACT

Demand for energy is increasing at an alarming rate. To overcome this problem pyrolysis of biomass can be counted as an alternative option. Banana waste is a very good source of Banana waste. The aim of the work was finding the worthiness of banana waste as a biomass source for pyrolysis process and extraction biofuels from it. Banana waste is a very common type of bio-mass. Banana waste was collected from tea stalls and hotels, then dried and prepared for pyrolysis. To extract fuel from banana waste, a fixed bed type pyrolysis apparatus was designed and constructed. The pyrolysis apparatus was contained a fixed bed type reactor, dry heater, condenser mechanism, vacuum pump, thermocouple. After extracting liquid fuel, physical properties were measured and compared with various pyrolytic oils. The average amount of biofuel extraction from banana wastes was obtained 3.6% (wt) and it is relatively low in comparison with other waste available in the literature.

Keywords: Pyrolysis, Biofuel, Banana Waste, Pyrolytic Oil.

1. Introduction:

The demand for energy is increasing day by day due to the rapid growth of population, urbanization, and industrialization. The majority of the demand is fulfilled by the fossil fuel, which source is very limited, also it is harmful to the environment. So, an alternative fuel should be thought to overcome the energy crisis and reduce environmental threats. On the other hand, the standard of living and quality of life of a nation depend on its per capita energy consumption. Bangladesh is a developing country and is one of the most densely populated countries in the world with a total population of 164.67 million. Estimated final consumption of total energy is around 46.43 MTOE. Average increase of energy consumption is about 6% per annum. Per capita consumption of energy in Bangladesh is on an average 285 KgOE (Kilogram Oil Equivalent) and per capita generation of electricity is 371 kWh with an access to electricity 76%, which is lower than those of South Asian neighboring countries. The known energy sources in Bangladesh are natural gas, coal, imported oil, hydro-electricity, and traditional biomass source. Natural gas, coal, imported, hydro-electric energy sources are known as a commercial energy source. Biomass accounts for about 29% of primary energy and rests the rest 71% is being met by commercial energy. Natural gas accounts for about 68% of the commercial energy and rest the rest 32% is being met by imported oil. Currently, about 213MW power is generated by using the solar system. Moreover, in off-grid areas power is also being generated by using the Solar Home System (SHS). In addition, there are some poultry and dairy farms in which biogas plants are being set up and this biogas is used for cooking and power generation which is currently producing about 1MW power. Imported oil accounts for the lion's share of the rest. Every year Bangladesh imports about 5.4 million metric tons of crude and Refined Petroleum Products. Apart from natural gas and crude oil, coal is mainly used as fuel in

the brick-fields and Thermal Power Plant. To generate electricity by Bio-Mass Gasification Method, some steps have been taken in the country. [1] Thus, it is a crucial time to find a sustainable resource to mitigate the energy crisis of Bangladesh.

The different thermo-chemical process that includes combustion, liquefaction, hydrogenation, and pyrolysis has been used to convert the waste into various energy products. Pyrolysis can convert waste directly into solid, liquid and gaseous products by thermal decomposition of waste in the absence of oxygen. To obtain biodiesel from green solid waste the Pyrolysis process is preferred mostly.

Bangladesh is an agriculture-based country. The banana is one of the most common agricultural products. In 2016, banana production in Bangladesh was 798,012 tons. Though Bangladesh banana production fluctuated substantially in recent years, it tended to increase through 1967 - 2016 period ending at 798,012 tons in 2016 [2].

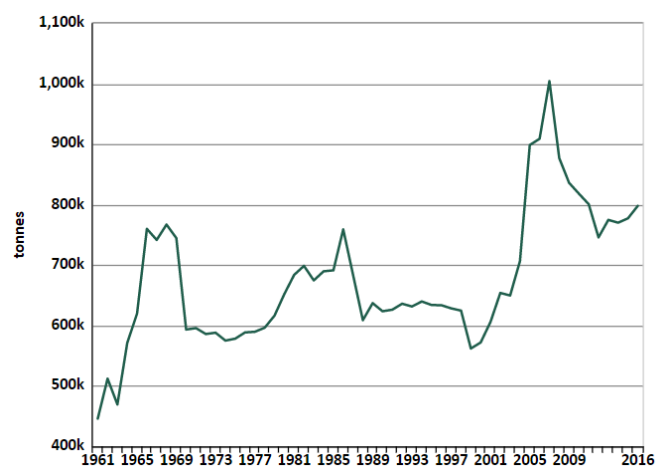


Fig 1: Annual production of banana for the fiscal year 1961 to 2016 [2]

Every year a huge amount banana, as well as banana waste, is produced. Very common use of Banana waste is the food of domestic animals. There is a very negligible number of commercial uses of banana waste, but the maximum amount of waste is wasted. Waste banana should be managed because this waste may become harmful for the environment.

The banana waste can be used as a bio-degradable biomass to recover biofuel as it is cheap and highly available. Dry waste can be a source of energy and valuable chemical product, and their thermal decomposition makes the recovery of useful compounds possible. For recovering biofuel from banana waste Pyrolysis can be a good option. This work investigates the effectiveness of banana waste as biomass for the pyrolysis process. Finding banana waste suitable for producing biofuel through pyrolysis or not is a major objective of this work.

To fulfill is an investigation, a fixed bed pyrolysis reactor was designed and constructed, biofuel was extracted, fuels properties (density, viscosity, gross calorific value, flash point, pour point) were determined. The properties of pyrolytic oil were also compared with fossil fuel and other pyrolytic oil.

2. Experimental Procedure:

Pyrolysis is a thermochemical decomposition process which is found to be the best suited for conversion of biomass to carbon-rich solid and liquid fuel. The process of pyrolysis of organic matter is very complex and consists of both simultaneous and successive reactions when organic material is heated in a non-reactive atmosphere. In this process, thermal decomposition of organic components in biomass goes up to 700°C - 800°C in the absence of air/oxygen. The long chains of carbon, hydrogen and oxygen compounds in biomass break down into smaller molecules, in the form of gases, condensable vapors (tars and oils), and solid charcoal under pyrolysis conditions. Rate and amount of decomposition gases, tars and char depend on the process parameters of the reactor (pyrolysis) temperature, heating rate, pressure, reactor configuration, feedstock's variation. The following figure shows a schematic diagram for a pyrolysis process. By condensing condensable gasses from those decomposition gasses bio fuel is obtained [3].

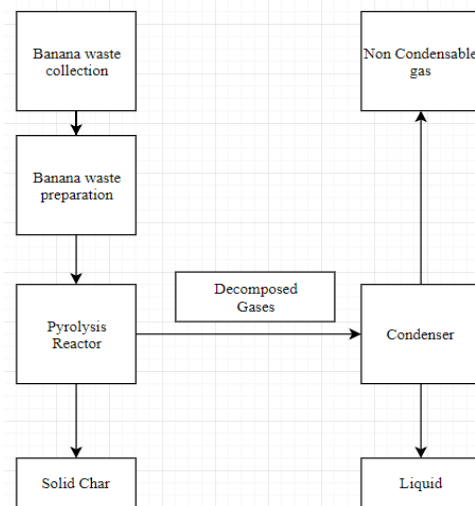


Fig. 1: Flowchart of Pyrolysis process

2.1 Feed material:

The most common types banana waste are banana fruit peel and fruit bunch stem as shown in Fig. 2. At normal condition, banana waste contains a large amount of moisture. Moisture is one of the biggest disadvantages of banana waste for the pyrolysis process. So, drying of banana waste as much as possible is very important. Banana waste is highly cheap and available but a high amount of moisture is one of the biggest limitations. Banana wastes are also made as small as possible for quick decomposing.



Fig. 2: Raw Banana waste



Fig. 3: Dry Banana waste

2.2 Pyrolysis apparatus:

Batch type fixed-bed pyrolysis apparatus was selected for the experiment. CAD model of the experimental apparatus is shown in Fig. 4. The main components of the pyrolysis apparatus are pyrolysis reactor and condenser. Temperature measuring instrument is used to measure the temperature and vacuum pump is used to perform the experiment without oxygen. Asbestos rope is used to insulate the reactor.

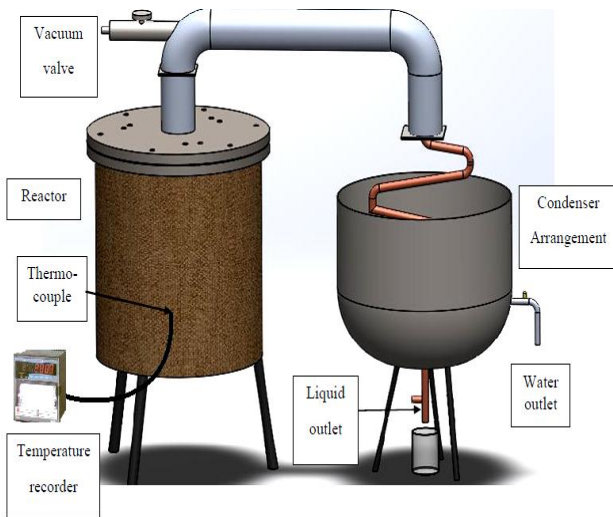


Fig 4: Experimental apparatus

2.2.1 Pyrolysis reactor:

The pyrolysis reactor is designed for pyrolysis of waste materials like biomass, agricultural wastes, forest residue etc. The reactor is a cylindrical, fixed bed reactor made of mild steel as shown in Fig. 4. The top side of the reactor can be open for feeding the raw material and solid residue (char) can be removed at the end of the experiment.

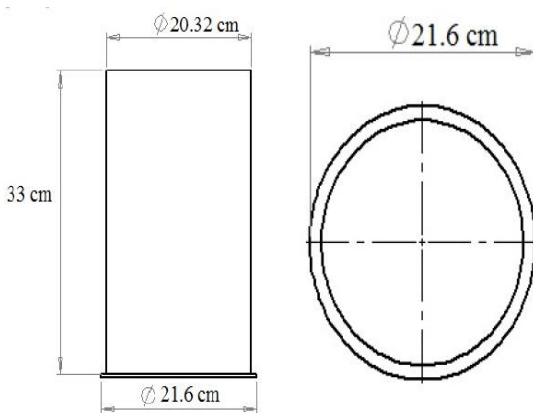


Fig 5: Drawing of reactor shell

An exit pipe at the top carries away the evolved gases during pyrolysis. During the reaction, the top side is kept closed by a cover plate tightly secured to the flanged opening. This prevents ingress of atmospheric air into the reactor, thereby achieving pyrolysis conditions.

Three U shaped electrical dry heaters each of 500W capacity are mounted on the top part of the reactor. The heater provides heat for thermal decomposition.

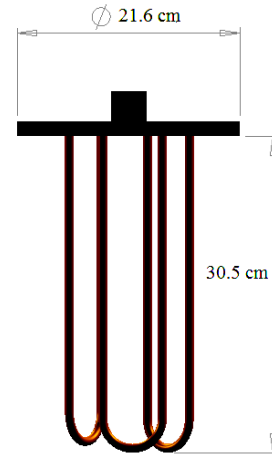


Fig 6: Electrical Heaters

The temperature inside the reactor is measured by a K type thermocouple. K type thermocouple is very inexpensive and highly available. It is normally used in the temperature range -200°C to $+1350^{\circ}\text{C}$. The range of thermocouple used for this experiment is 0°C to 800°C .

2.2.2 Condenser:

A simple gas to water heat exchanger type condenser is provided to condensed the volatile gases produced from thermal decomposition. Gas is carried by copper tube and incondensable gases are passed through a bypass pipe under the condenser. Bended copper tube is merged in water which is contained by a container.

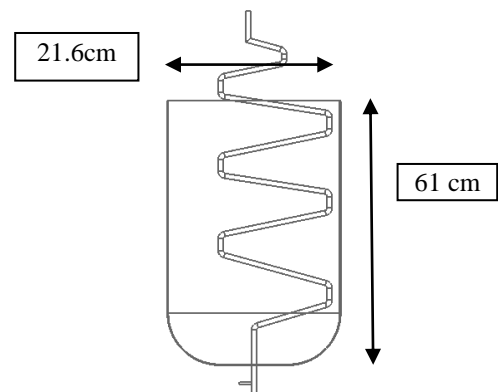


Fig 5: Schematic diagram of Condenser arrangement

2.2.3 Construction of the Apparatus:

An apparatus was constructed according to the design as shown in Fig. 6. Three heaters are mounted on the top part of the apparatus. Reactor and condenser are connected with a U-shaped mild steel pipe. Two flanges joint is used in the connection of reactor and condenser. A copper tube with several bending is used to carry the gas and which acts as a condenser. There is a bypass path at the end side of the tube which helps to pass the extra uncondensed gas. To decrease heat loss and gas leakage asbestos ropes and silicone gasket are used. To make the reactor oxygen free initially a vacuum pump is used so a vacuum valve is mounted on the top side of the U shape pipe. The constructed apparatus is installed in the Heat Engine Laboratory at Khulna University of Engineering & Technology, Khulna, Bangladesh.



Fig 6: Final constructed apparatus

3. Results and Discussion:

Pyrolytic conversion of Banana waste is performed in the constructed fixed-bed reactor system. Temperature readings inside the reactor were taken by using a K-type thermocouple and water temperature of the condenser was taken by using a thermometer. After each observation, the amount of products from the process were measured. Table 1 shows the experimental data were taken during the experiments and Table 2 and 3 show the amount of products were obtained from the process.

Table 1 Experimental data

Mass of feed (gm)	Starting temperature (°C)	Final Temperature (°C)	Pyrolysis time (min)
865	60	435	45
1100	68	477	60
950	63	448	52
900	60	450	50
1050	70	475	55

Table 2: Amount of products obtained from the experiment

Incondensable Gas (gm)	Amount of Ash (gm)	Mass of Liquid including moisture (gm)	Mass of liquid without moisture (gm)
380	320	135	30
475	421	164	40
390	373	155	32
370	365	135	30
455	410	140	45

Table 3: The Relative amount of the products

Percentage of incondensable gas	Percentage of ash	Percentage of liquid (without moisture)
43.93	36.99	3.46
43.18	38.27	3.63
41.052	39.26	3.36
41.11	40.55	3.33
43.33	39.04	4.28

3.1 Yields of pyrolysis products in weight percentage:

The main products of banana waste pyrolysis are liquid fuel, ash, and non-condensable gases. The amounts of products are yielded from banana waste pyrolysis are shown in table 4 in comparison to the amount of the products of pyrolysis of bagasse, jute stick [4] waste tire [5] and waste plastic [6]. In average 42.5% incondensable gas, 38.8% ash and 3.6% liquid fuel were obtained from banana waste. It is clearly indicated that the amount of fuel extracted from banana waste is very low compared with others.

Table 4: Yields products comparison with others biomass pyrolysis

Bio mass	% of Liquid	% of Ash	% of Gas
Banana Waste	3.6	38.8	42.5
Bagasse	69.5	19.4	10.9
Jute Sticks	68.2	21.7	9.8
Waste tire	49	38.3	12.7
Waste Plastic (PVC)	12.3	0	87.7

The liquid obtained from pyrolysis of banana waste contained a high amount of water content. Dehydrating of fuel was one of the biggest challenges and fuel amount was very low. Percentage of non-condensable gas and ash is too high than liquid fuel. The input energy is too high than output energy. So the efficiency of this system is too low. Although banana waste is highly available and very cheap, but it contains a very high amount of moisture. After drying very well total moisture are not possible to remove which decrease liquid fuel quality. Due to the high moisture in a banana waste high amount of water content was found in fuel. Dehydrating of fuel was a very big challenge and fuel amount was not satisfactory.

3.2 Properties of obtained fuel:

The properties of the obtained fuel such as flash point, pour point, density, gross calorific value and the kinematic viscosity are measured in the Heat Engine and Fluid Mechanics lab of Mechanical Engineering department, KUET. Gross calorific value was measured by using bomb calorimeter. Kinematic viscosity was measured by using Saybolt viscometer.

Table 5: Fuel properties of the pyrolytic oil in comparison with other commercial diesel fuels, furnace oil and pyrolytic oil obtained from tire scrap

Property	Pyrolytic Oil	Diesel	Furnace Oil	Pyrolytic Oil [8]
Density (kg/m ³) at 30°C	720	820 to 860	890 to 960	912
Flash point (°C)	50	55	70	37

Gross Calorific Value (MJ/kg)	25.5	42 to 44	42 to 43	39
Kinematic Viscosity at 40°C (m ² /s)	7.56×10 ⁻⁶	2 to 4.5×10 ⁻⁶	45×10 ⁻⁶	5.55×10 ⁻⁶
Absolute Viscosity at 40°C (Ns/m ²)	5.44×10 ⁻³	1.64 to 3.87×10 ⁻³	0.04 to 0.0432	5.016×10 ⁻³

The pyrolytic liquid obtained from pyrolysis of Banana wastes appears dark brown with a strong acrid smell. No phase separation was found to take place in the storage bottles. The fuel properties of the extracted pyrolytic oil are shown in Table 5 and compared with diesel, furnace oil and a pyrolytic oil from motor cycle tire scrap [8]. Flashpoint was 50°C, Pour point was -6°C, Density was 720kg/m³ at 30°C, Gross calorific value was 25,551 KJ/kg, at 40°C Kinematic viscosity and Absolute viscosity were 0.00000756 m²/s and 0.0054432Ns/m² respectively. Where for Diesel, Density is 820 to 860 Kg/m³, Kinematic Viscosity at 40°C is 2 to 4.5 CeSt, Flash Point is ≥ 55°C, Pour Point is -40 to -1°C, Gross Calorific Value is 42 to 44 MJ/Kg.

4. Conclusion:

Banana waste is a common biomass in Bangladesh and its consumption is creasing day by day. The main objective of this work is extracted biofuel from banana waste using pyrolysis technique. A fixed bed pyrolysis apparatus was designed and constructed. Several experiments were performed to extract biofuel from banana waste. The liquid obtained from pyrolysis contained a high amount of water. Among the pyrolytic product, 3.6% was pyrolytic oil and rest were ash, incondensable gas and moisture. It is clear that fuel can be extracted from banana waste. However, amount of fuel is quite low in comparison with other waste and properties of fuel were average quality.

REFERENCES

- [1] <http://www.hcu.org.bd/site/publications/7c13833b-42d8-4087-bc67-4e77f6ee510b/Report-on-Energy-Scenario-of-bd-2016-2017>
- [2] <https://knoema.com/atlas/Bangladesh/topics/Agriculture/Crops-Production-Quantity-tonnes/Bananas-production>
- [3] M. Rofiqul Islam, M.S.H.K. Tushar, H. Haniu,

'Production of Liquid Fuels and Chemicals from Pyrolysis of Bangladeshi Bicycle/rickshaw Tire Wastes', Science Direct Journal of Analytical and Applied Pyrolysis, Elsevier, 2008, Vol. 82, 96–109

- [4] http://www.oeaw.ac.at/forebiom/WS1lectures/SessionII_Uzun.pdf
- [5] A.T.M.K. Hasan, M. Mohiuddin, M. B. Ahmed, I.J.Poly, M.Asadullah and M.S.Rahman, 'Production and Characterization of Bio-oil from Bio-mass by Circulating Fluidized Bed Pyrolysis Reactor', Bangladesh Journal of Scientific and Industrial Research, Bangladesh J. Sci. Ind. Res. 46(3), 313-322, 2011
- [6] M. A. Kader, M. R. Islam, M. S. Hossain¹ and H. Haniu, "DEVELOPMENT OF A PILOT SCALE PYROLYSIS PLANT FOR PRODUCTION OF LIQUID FUEL FROM WASTE TIRE", Mechanical Engineering Research Journal, Vol. 9, pp. 54–59, 2013
- [7] SD A Sharuddin, F Abnisa, W M A W Daud, M KArroua, "Pyrolysis of plastic waste for liquid fuel production as prospective energy resource" 3rd ICChESA 2017, IOP Conf. Series: Materials Science and Engineering 334 (2018) 012001
- [8] Md. Shameem Hossain, Md. Asibul Islam, A. N. M. Mizanur Rahman, Md. Golam Kader; 'Alternative Fuel from Pyrolysis of Waste Motorcycle Tire' International Conference on Engineering Research, Innovation and Education 2017 ICERIE 2017, 13–15 January, SUST, Sylhet, Bangladesh

Designing Approach of Blimp for a Hybrid VTOL Aerial Robot

*Md.Tasnim Rana**, *Md. Shahidul Islam*

Department of Mechanical Engineering, Khulna University of Engineering & Technology, Khulna-9203, BANGLADESH

ABSTRACT

In case of aerodynamic aspects when most of the research is going on how to increase lift, with developing its aerodynamic shape, the most advancement can be drawn with using inflatable blimps where lighter than air gases can be used. The lighter than air gasses will provide a great aerodynamic advances by providing lift using its bouncy forces. For controlling an aerodynamic object there is two forces, one is its own gravitational force in negative direction and controlling forces as required for changing its position. But, most of the cases gravitational forces make the most difficult situation while its time to deal with power consumption. By using inflatable envelope with lighter than air gasses we can easily deal with the gravitational forces of aerodynamic objects. This writing will present a design approach for this kind of inflatable envelope.

Keywords: Aerodynamics, Inflatable, Bouncy, Gravitational

1. Introduction

In recent years, the RC aircraft or drone has a problem with stability and longtime flight duration. A concept of adding blimp with traditional system can be made a better result to overcome the existing problem. The hybrid airplane combines three approved main concepts of human flight. It needs no infrastructure for takeoff and landing and is able to reach a higher cruising speed compared to airships and helicopter. It is built out of lightweight high-tech materials like dry wood, aluminum and high dense foils, while only a low amount of metal is applied to the structure. At present, no clear picture exists of the construction of a VTOL (vertical takeoff & landing) hybrid Unmanned Aerial Vehicle (UAV) for long duration flight in Bangladesh. Therefore, the purpose of this work is to design an inflatable blimp for VTOL aerial robot.

2. Background:

Lighter than air constructions with lenticular hulls that reached the development stage of prototyping were the models XEM-1 to XEM-4 from LTAS/CAMBOT LLC [1], remotely piloted lenticular airships, which were built (from 1974 until 1981) as a demonstrator and for Filming, video observation and telecommunications work and their three full scaled rigid airship variants. W.C. Kelle (1989) observed that blimp made a good impact while boundary layer and atmospheric sampling included measurement of the radioactive transfer through the lower atmospheric boundary layer and ocean-surface flux measurements [2]. J.H.W. Hain (1992) investigated oceanographic sampling in the early 1990s included surface water sampling, phytoplankton hauls, temperature and salinity profiling, deployment of current drifters, and geophysical surveys [3]. W.A. Hoppel (1993) made an Page 3 of 10 airship, which was also used for studies of aerosol distribution and particle formation in the marine boundary layer [4]. Also ALA-600 Thermo plane, an airship filled with both helium and hot gas, which was designed by NAYLER (2001) to operate with heavy loads, without a base or mooring

mast was finalized in whereas ALA-40-01 ground tests started [5]. Cs. Singer (2008) made a general comparison between HTOL and VTOL (vertical takeoff & landing) Airplanes, Helicopters, Airships, Trains, Vehicles, Ships and the proposed hybrid airplane over their size, pollution, capacity, speed, range, security and required infrastructure was found out, which based on the quantitative comparison in the transport solution costs of different transportation concepts and their speed [6]. W.F. Putman (2011) investigated design and controls for the vectorotor hybrid VTOL heavy lift vehicle drone for multipurpose application show its commercial aspect [7]. Design of a commercial Hybrid VTOL UAV System by Intel Robot System made the step, review the preliminary design process of such a capable civilian UAV system, namely the TURAC VTOL UAV. Ugur Ozdemir (2014) made the TURAC UAV is aimed to have both vertical take-off and landing and Conventional Takeoff and Landing (CTOL) capability [8]. Yu Ito (2017) analyzed indoor hybrid blimp logistics drone provided with crash-free ability at full power-loss condition is made it easy for proving its advantages [9]. James C. Egan (2018) present discloser pertains to vehicle capable of flight and more particularly, to manned and unmanned vehicles having combined methods of lift, including dynamic lift and displacement buoyancy [10]. However, the construction of a VTOL hybrid UAV for long duration flight has not been made clear until now in Bangladesh. Therefore, in this project, a model of VTOL hybrid unmanned aerial vehicle for long duration flight is constructed.

3. Methodology

In case of inflatable body, it can have a nested capacity or not. Nested wings are subset of re-deploying body in case of emergency design requirements. The main concept of a blimp came from "Airship concept", but there is different in designing approach.

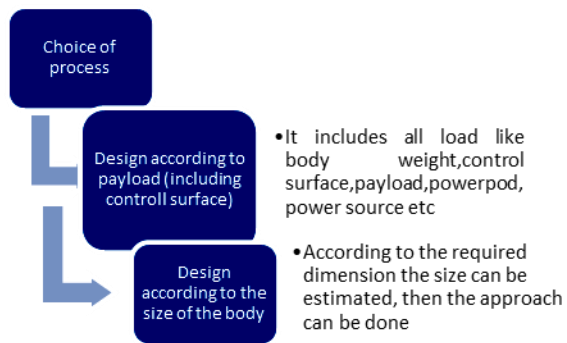


Fig.1 Choice of process for designing approach

The approach with fixed dimension follows a strict property & its capacity of lifting.

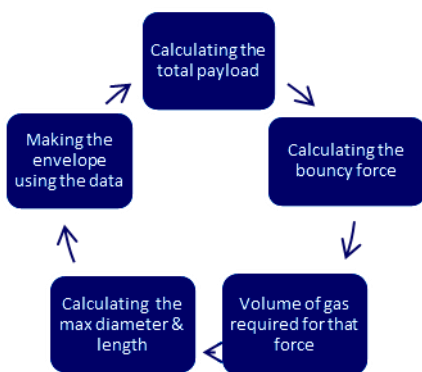


Fig.2 Cycle of working procedure

Nested wing has a unique character with having different material condition in same structure. The following proposed or closed nested wing configuration airfoil is designed by Mueller and Noffke is shown in the beloved figure. The embedded wing concept which is a variant of the nested wing design, except a smaller with the configuration attached wing (is now stowed either as a portion of the main wing with some surface exposed completely internal to the larger loiter wing). For the sample calculation, the envelope will be assumed as the following shape,

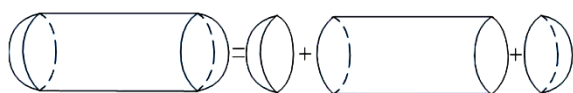


Fig.3 Assumed shape for simple calculation

This allows greater flexibility in designing both wing profiles and platforms with the constraint that the dash wing must be partially or wholly embedded within the loiter wing. But for the shape of the outer surface will greatly affect its drug force thus, it follows a specific calculative shape. There will be a idea while the projectile shape will be observed. The projectile view is given below.

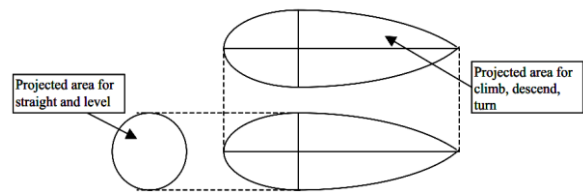


Fig.4 Different projectile view of an envelope

In case of inflatable wing the most important thing is to make a closing system when it is not inflated. Low volume storage requirement is a prime factor in determination of deployable concept. When rigid wing sections are deployed, the stowed volume cannot ever be less than 100% of the deployed wing volume. Packing an aircraft into a specific constrained volume whether a cylindrical-shaped volume for a missile launched UAV or a cone-shaped volume for a Mars airplane will result in unused volume among the rigid sections.

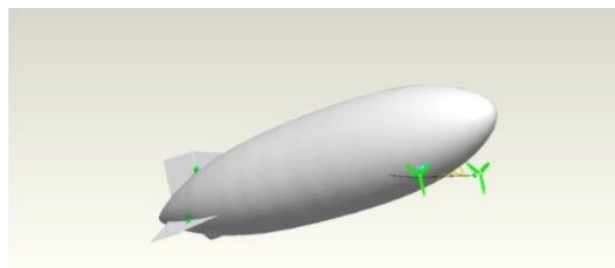


Fig.5 Theoretical model of a blimp

In case of deploying time, it's very important as it can make a very important part for the air craft while it has a crushing condition in emergency landing. Or in case in use of carrying the aerodynamic thing its deployment can make a good effect while its main aim is to quick lurching. Consideration of the overall volume ratio, V_s/V_d , with respect to the span ratio of rigid inner section length to deployed length, b_0/b . In contrast with the large total stowed volume required by hinged rigid wings on carrier decks, the total stowed volume of the FINDER aircraft is seen to include a minimal amount of unused volume associated with the wing packing design. Inflatable wings here assume a 10% stowed-to-deployed volume for the outboard inflatable sections, with inboard rigid section based on the dimension.

3.2 Premises and Design

In case of inflatable aerodynamics, its physics is much more unstable than general one. But, its characteristic makes it easy for a smooth boundary layer. One aero shaped body can make the boundary layer continuous without creating any kind of vortex. But a generous amount of parallel body reduces the time and cost of construction & also it'll give a better left capacity. So, in this case only one blimp will be considered for designing. For the primary design the fore body be

generated with the revolution about its X-axis with a simple semi-ellipse, having the equation:

$$1 = \frac{x^2}{2a^2} + \frac{y^2}{b^2} \quad (1)$$

Where,
 D= maximum diameter
 a=length of the fore body

For speed & power,

Maximum horse-power,

$$H_p = \frac{pv^3 v^{2/3}}{550k} \quad (2)$$

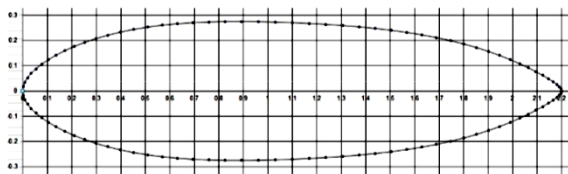
Static & dynamic bending moments,

$$M = C \cdot \rho g \cdot VL \quad (3)$$

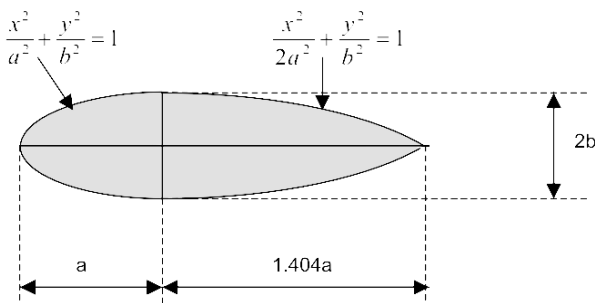
Where,
 M=the bending moment
 C=co-efficient
 Pg=the unit weight of the air
 V=air volume
 L=length
 Maximum stress,

$$S = \frac{2M \sin \phi}{Rn} \quad (4)$$

In case of an ideal design a model Gertler 4154 shape is taken with some specific dimension.



(a)



(b)

Fig.6 (a),(b)Gertler 4154 shape with 2.20 m length & 4:1 slenderness ratio, derived from Series-58 4115 shape tool by Johannes Eissing

For gas pressure & outer cover stress, the pressure and bouncy forces should be calculated.

$$M_B = \rho_{He} \left(\frac{\pi d^3}{6} - V_m \right) + M_m + f \cdot \pi d^2 + M_p \quad (5)$$

$$F_b = \{ (\rho_a - \rho_{He}) \left(\frac{\pi d^3}{6} - V_m \right) - (M_m + f \cdot \pi d^2 + M_p) \} g \quad (6)$$

ρ_a =density of air
 ρ_{He} =density of helium
 d=diameter (max)
 V_m =Volume of the LTA gas
 M_p = momentum
 g=gravitational acceleration

In this case as a Lighter than air gas helium is used. So, the density of helium was considered as a LTA gas .The purpose of this mathematics is to figure out the algebra relation between the size and the payload for a safe hybrid blimp. Because of the low cruise speed and stability at zero-power status. The aim of this whole calculation is to figure the limit of payload to keep safe terminal speed at full power loss. If the relation between diameter and payload fills the in equation, the blimp will ascend at such accident and won't cause any crash to the ground .This condition can give the body degree of freedom given below:

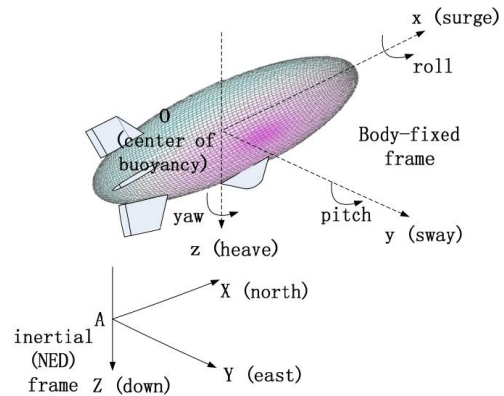


Fig.7 Degree of freedom

In case of tail design, traditional method of controlling platform is used where it will give a better perfection in an easy way.

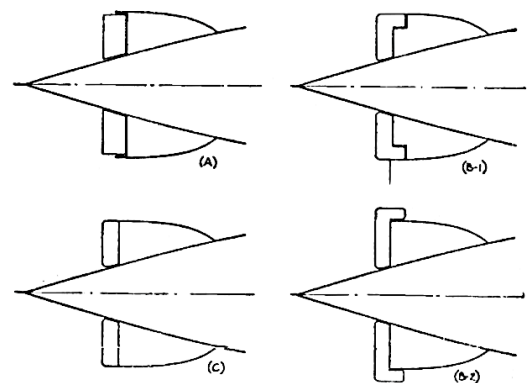


Fig.8 (A), (B) Tail design and positioning of control surface

For the correct view of the tail control system can have a clear arrangement in case of indoor & out door,

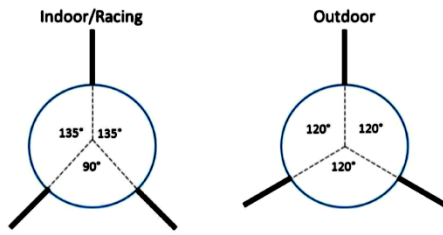


Fig.9 Tail surface mounting position in angular parameters for indoor & outdoor conditions

Traditional design on dirigibles, blimps and airships for transport has had to conceive the existence of airflow from side wind and its relatively high cruising speed. The solution to these wind effects and moments was the Traditional finned cigarette shape of airships and blimps sustained by complicated inner structures. The overall design will have the following view.

In case of more simplification, the moment created by buoyancy force & the buoyancy force is given below,

$$M_B = 0.026\pi r^2 d^3 + 0.037\pi d^2 + 0.5 + M_p \quad (7)$$

$$F_p = (0.174\pi d^3 - 0.037\pi d^2 - 0.5)g - M_p g \quad (8)$$

(Putting the known value of equation 5&6)

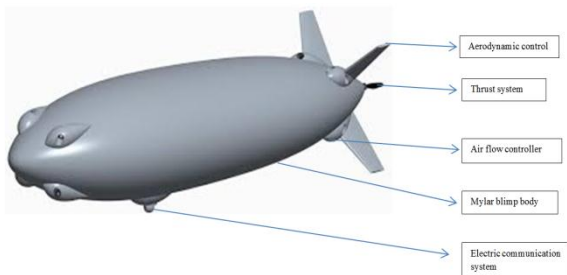


Fig.10 Overall design outcome from the conceptual model & the positioning of the tail part



(a)



(b)

Fig.11 Final fabrication of blimp with different material (a) reinforced & (b) Mylar

4. Result:

The blimp was filled with Hydrogen gas (H_2), and kept for its buoyancy force test. The following graph is found with the collected data,

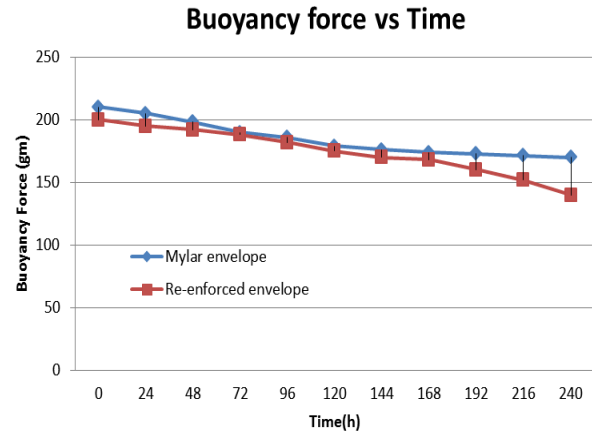


Fig.12 graph shows how the blimp loses its buoyancy forces.

5. Application:

In case of application, the environment can be divided into three categories. It can be indoor, outdoor & high altitude.

For this section, in what situation will an indoor blimp drone could be applied to will be discussed. Firstly, in order to utilize the virtue as a flying machine to be used in limited space, the building to install such system should be one that contains a wide overhead space or a large well hole area that are free from solid obstacles. Some of the most suitable categories of use of buildings that fit this character should be like as: commercial complex facilities, sports arenas, event halls, concert halls, station concourses, and airport terminals. Needs for indoor logistics should be found from such kinds of buildings. Second, because of the limit of the payload at a handle able craft size, carrying consolidated business cargo is not the most suitable for its mission. Distribution from the hub to the tenants inside a complex facility is often specially designed as a part of logistics practice by service providers. Such business logistics is usually rationalized by integrating the parcels to be delivered to each tenant. Even if to consider the delivery is free from human labor power and therefore assume that a frequent-however-small amount carry is still acceptable from the perspective of service cost, the configuration of the blimp that was aimed to provide safe emergency landing by creating drag will act against the necessary speed and energy efficiency.

6. Conclusion:

This explanation only deals with the approach of design of an envelope for a blimp. In case of hybrid VTOL the design must sustain a categorized shape which will provide a good control over aerodynamics. The steps in designing explain the process of calculating buoyancy

forces for an exact shape with the help of exact design & it's relation with control platform. And also, the experimental data shows that, Mylar blimp is much sustainable in terms of buoyancy force than the re-enforced one. But, in case of material strengthen-enforced one gives much good result.

7. Limitations & Future Prospect:

The idea argued here only have been discussed theoretically, and thus needs to be tested through actual modeling, prototyping, and proof of concept. Also, the proposed business application never existed before should be considered further how to be connected to the current business seamlessly that will benefit the customer more. Technically, estimation on outdoor application regarding weather conditions such as UV rays, side winds, downburst, and heavy rain is left to be done for further extension of the concept.

REFERENCES

- [1] T.V. Blanc, W.C. Keller, and W. J. Plant. 1989. Oceanography from a blimp. *Sea Technology* 30 23-28.
- [2] JANE's, "All the World's Aircraft" Coulsdon, Surrey UK; Alexandria VA: Jane's Information Group. Annual
- [3] J.H.W. Hain. 1992. Airships for marine mammal research: Evaluation and recommendations. Publication No. PB92-128271. National Technical Information Service, Springfield, VA. 34 pp.
- [4] G.A. Frick and W.A. Hoppel. 1993. Airship measurements of aerosol size distributions, cloud droplet spectra, and trace gas concentrations in the marine boundary layer. *Bull. Am. Meteor. Soc.* 74: 2195-2202
- [5] NAYLER, A., "Airship development world wide – A 2001 Review", Airship Association Ltd. London, 2001
- [6] Cs. Singer, German Aerospace Center e.V., Germany, 7th International Airship Convention 2008, ID- 71184
- [7] W.F. Putman, Aereon Corporation, Princeton NJ, 67th Annual Forum of the AHS, Virginia Beach, VA May 2-4, 2011
- [8] Ugur Ozdemir, *J Intell Robot Syst* (2014) 74:371–393, DOI 10.1007/s10846-013-9900-0
- [9] Yu Ito, Tokyo, Japan, research gate-2017, November Vol.
- [10] James C. Egan, patent US 9856007 B2-2018

ICMIEE18-316

Design and Construction of a Three-Axis Automated Drilling Mechanism with Depth Controllability

Sudip Saha*, Saikat Biswas, Md. Kutub Uddin

Department of Mechanical Engineering, Khulna University of Engineering & Technology, Khulna-9203, BANGLADESH

ABSTRACT

To increase the quality and quantity of products current development in the industry has been towards computer-controlled manufacturing process. Manual manufacturing of such items as the wood workpiece or circuit board or metal sheets will have a big faulty case and uneven quality. This proposed drilling machine is designed to drill the holes automatically over a job according to the drilling depth and co-ordinate data programmed through a controller. The goal was to implement an automated drilling mechanism using the automation process for the workpiece movement. The concept of integrating sensor-based controlling with adaptive feedback control allowed the mechanism towards multiple drilling. The depth controllability function allowed drilling with variable depth for each drilling operation within the workpiece thickness. Exploring with CNC system provided control over functions and motions of the machine tool through coded alphanumeric data. Ultimately reducing human effort and time consumption while implementing better accuracy for the small-scale industry is what makes this paper through.

Keywords: Automated drilling, CNC, depth controllability, path planning, reducing human effort etc.

1. Introduction

Manual drilling is one of the important manufacturing operations where lots of error could happen. To mitigate this, an automatic process is presented here. The entire process falls under the subject of mechatronics & various fields of technologies must be included to fulfill the target. The integration of electronic engineering, mechanical engineering & control technology is forming a crucial part in this design. Especially the control circuit design plays a dominant role in this work. The automation operation is done with IDE (Integrated Development Environment). The main aim of the project lies in interfacing or in simple words, is to make a mechanical system work by making use of a personal computer of basic configuration. This project is carried on keeping in mind the needs of a small-scale industry, which need small sized components in a few numbers, which by other processes would cost more emphasizing the time required for manual operation. The only thing the operator needs to do is to input the coordinates of the drilling points allowing multiple drilling points (in both x,y-axis) with special depth controllability whereas some previous works emphasized on only 1 axis for workpiece movement thus ensuring the difference of the project [1].

2. Background theory

For the background theory, there are two main prospects presented here. They are drilling process and automation part.

2.1 Drilling

By definition, drilling is a cutting process that uses a drill bit to cut a hole of circular cross-section in solid materials. The drill bit is usually a rotary cutting tool, often multipoint. This forces the cutting edge of the drill

bit against the workpiece, cutting off chips from the hole as it is drilled. So in simple words, the rotating edge of the drill exerts a large force on the workpiece and the hole is generated.

2.1.1 Drilling Machine Types

There are many types of drills. They can be classified according to many types. According to source power:

1. Manual Powered
2. Energy Powered (Electricity, compressed air, Internal combustion engine)

Some examples of manual powered drills are bow drill, eggbeater drill, Persian drill, gimlet drill. Whereas, pistol grip drills, magnetic drilling machine, rotary hammer drill, drill press are some common form of energy powered drill.

2.1.2. Drill bits

Drill bits are cutting tools used to remove material to create holes, almost always of circular cross-section. Drill bits come in many sizes and shape and can create different kinds of holes in many different materials. In order to create holes, drill bits are attached to a drill, which powers them to cut through the workpiece, typically by rotation.

Basic drill bit nomenclatures: [2]

Axis: Imaginary straight line that forms the center line of the drill.

Body: Portion of the bit extending from the end of the flutes to the outer corner of the cutting edge.

Drill Diameter: The diameter over the margins over the margins of the drill measured at the point.

Body diameter clearance: The portion of the land that has been cut away so it will not bind against the walls of the hole.

* Corresponding author. Tel.: +88-01676862086

E-mail addresses: sudip.sds@gmail.com

Other important nomenclatures are flutes, back taper, drill margin, and margin width etc.

2.1.3. Drilling Process

Important drilling process nomenclatures are cutting speed, spindle speed, feed rate, depth of cut etc. [3]

2.2 Automation

The term automation, inspired by the earlier word automatic (coming from automaton), was not widely used before 1947 when Ford established an automation department. [4]

Automation or automatic control is the use of various control systems for operating equipment such as machinery, processes in factories, boilers, and heat-treating ovens, switching on telephone networks, steering, and stabilization of ships, aircraft, and other applications and vehicles with minimal or reduced human intervention. [5]

Now, when it comes to the automation process with machinery it requires a computer to control. This is the starting phase of Computer Numerical control or CNC.

2.2.1 Computer Numerical Control (CNC)

Computer numerical control is the automation of machine tools by means of computers executing pre-programmed sequences of machine control commands. This is in contrast to machines that are manually controlled by hand wheels or levers, or mechanically automated by cams alone. [6]

The applications of CNC include both for machine tools as well as non-machine tool areas.

The benefits of CNC are high accuracy in manufacturing, short production time, greater manufacturing flexibility, simple fixture, contour machining, reduced human error. Though negligible CNC has also some drawbacks which include cost, maintenance, and the requirement of the skilled part programmer.

2.2.1.1 Elements of CNC

- i. Part program
- ii. Machine control unit (MCU)
- iii. Machine tool

i. Part Program: The part program is a detailed set of commands to be followed by the machine tool. Each command specifies a position in the Cartesian coordinate system (x,y,z) or motion (workpiece travel or cutting tool travel), machining parameters and control functions.

ii. Machine Control Unit: The machine control unit (MCU) is a microcomputer that stores the program and executes the commands into actions by machine tools. It consists of two main units:

- a. Data Processing Unit (DPU)
- b. Control Loops Unit (CLU)

The DPU software includes control system software, calculations algorithms, translation software that covers the part program into a usable format for the MCU. The DPU processes the data and provides it to the CLU. The

CLU operates the drives attached to the machine leadscrews and receives feedback signals.

iii. Machine tool: The machine tool could be one of the following: lathe, drilling, milling, laser, plasma etc. Its motion has to be controlled.

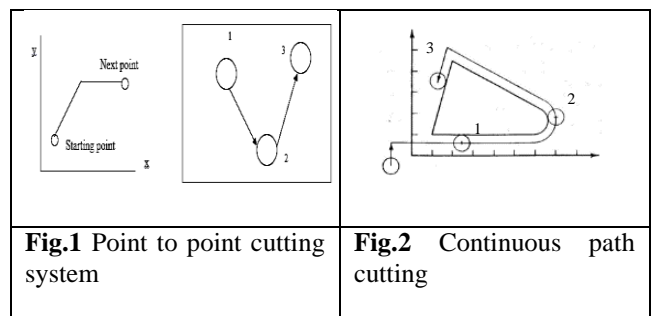
2.2.1.2 Principles of CNC

i. Point to point system:

The point-to-point system is those that move the tool or the workpiece from one point to another and then the tool performs the required task.

ii. Continuous path cutting:

These systems provide continuous path such that the tool can perform while the axes are moving, enabling the system to generate angular surfaces, two-dimensional curves or three-dimensional contours. Example: - an automated milling machine.



As shown in Fig. 1 the operational points are 1, 2 & 3. But the path between 1-2 or 2-3 does not have any machining operation in point to point cutting system. On the other hand, in Fig.3 between cutting point 1 and 3 in point 2 there is a curved feature that has to be done while moving the cutting tool from 1 to 3 and this is called continuous path cutting.

iii. Incremental & Absolute system:

In incremental mode, the distance is measured from one point to the next. In the absolute system, all the moving commands are referred from a reference point (zero points or origin)

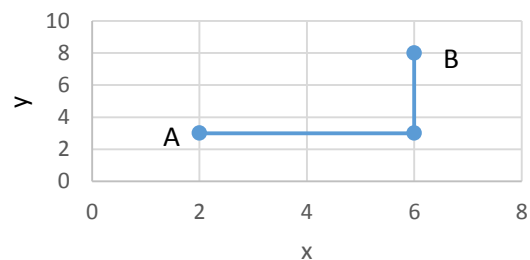


Fig.3 Incremental and absolute system

To go to point A (2, 3) to B (6, 8), in incremental, the move is specified by $x=4$, $y=5$ giving the distance of point B in respect of point A.

Whereas in absolute positioning the move is specified by $x=6$, $y=8$ which is calculated from a reference point (0,0) though the cutting tool moving from point A.

iv. Open loop and closed loop control system:

The open-loop control means that there is no feedback and uses stepping motors for driving the lead screw. A stepping motor is a device whose output shaft rotates through a fixed angle in response to an input pulse.

2.2.2 Hardware for automation

In automation, process hardware plays a vital role. So it needs to fulfill some requirements, such as powerful flexible products, built-in redundancy, the point of measurement, secure, redundant data reading, energy management solutions, and secure data recording. And also, another important criterion is to have embedded technologies to meet requirements.

2.2.3 Software for Automation

The software is the second most important part required for automation. In this thesis work for automation as a software suite IDE was used. An integrated development environment (IDE) is a software application that provides comprehensive facilities to computer programmers for software development. An IDE normally consists of a source code editor, build automation tools and a debugger. Most modern IDEs have intelligent code completion. Some IDEs, such as NetBeans and Eclipse, contain a compiler, interpreter, or both; others, such as SharpDevelop and Lazarus, do not.

IDEs are designed to maximize programmer productivity by providing tight-knit components with similar user interfaces. IDEs present a single program in which all development is done. This program typically provides many features for authoring, modifying, compiling, deploying and debugging software. This contrasts with software development using unrelated tools, such as vi, GCC or make.

Some IDEs are dedicated to a specific programming language, allowing a feature set that most closely matches the programming paradigms of the language. However, there are many multiple-language IDEs.

3. Design & Automation requirements

Design:

The basic principle for the construction is based on the disc cutting tool position and workpiece movement based on drilling coordinate. Workpiece movement will be carried out by the following two systems:

- i. Point to point positioning system
- ii. Incremental system

3.1 Components

Table 1 shows the basic components that are required.

Table 1 Required components

Constructional components	Hardboard
	Wooden structure
	Light but strong rope
	Screws
	Pulley(Material: Nylon shaft)
Electrical components	DC gear motor
	Arduino Mega 2560
	Motor driver

	Breadboard
	Distance measurement sensor
	Jumper wire
	Power supply

3.2 Conceptual View

This is the basic conceptual 3-D view of the construction project.

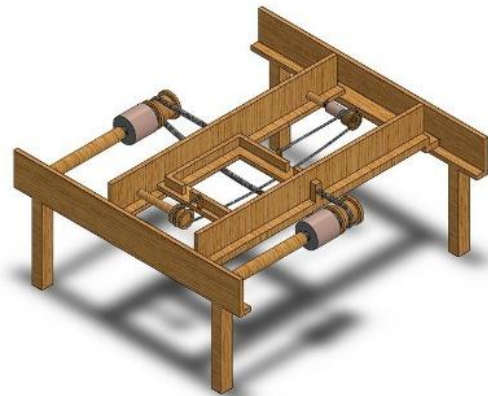


Fig.4 Workpiece controlling portion

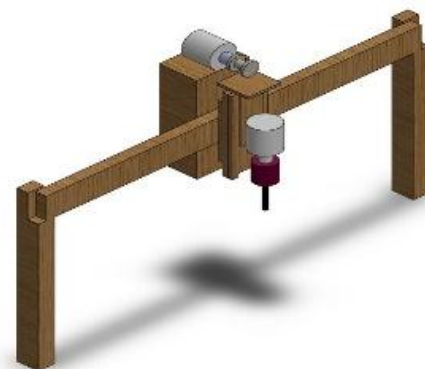


Fig.5 Drill bit holder

Fig. 4 shows the basic structure of the whole setup. It is made of wood and hardboard. There are in total 4 motors in this setup dividing by 2 for x and y-direction. The hardboard structure holds the workpiece and its movement is controlled by motors. Then this whole part consisting of hardboard, workpiece, motors moves by rest of the two motors.

Fig. 5 shows the drill bit holder which rests upon the setup of Fig.1. It consists of two motor, one for depth control and another for drill chuck.

3.3 Assumptions

For the construction following assumptions were taken:

Workpiece material cork sheet

Workpiece thickness= 1.5 inches or 3.3 cm

Workpiece dimension = 23*22 cm

Workpiece cutting area = 18*18 cm

Standard safety factor for motor selection = 10%

Linear velocity of workpiece movement $v = 4\text{cm/s}$

The workpiece material was chosen cork sheet because of its availability and scope of the easy drilling operation. All dimensions were taken in account of

keeping the whole setup in the feasible and compact state. For the convenient operation on the wood surface, the workpiece movement velocity 'v' was chosen by trial and error method. The concerned factors for this were surface roughness of wood, state, and integrity of connecting ropes, the visible vibration of the setup etc. According to the Cartesian coordinate for positioning the middle point of the workpiece was considered origin. So, the cutting area is now divided into four quadrants. According to this now the workpiece has to be free to move at least 9cm in all four directions (positive and negative x, y).

3.4 Torque and specification selection

For x-axis movement

Now the setup for x-axis mass $m_x = 0.61$ kg

Workpiece mass $m_w = 0.003$ kg

So, total weight required to move by x-axis motor $w_x = (0.61 + 0.003) * 9.8$ N
 $= 6.0074$ N

In the vertical direction, the normal force must be equal and opposite of the weight. As the motor will rotate in zero acceleration so,

Force required to overcome static friction (f_s) and kinetic friction (f_k);

$$f_s = \mu_s * w_x$$

$$= 0.3 * 6.0074 \text{ N} = 1.802 \text{ N}$$

$$f_k = \mu_k * w_x$$

$$= 0.2 * 6.0074 \text{ N} = 1.2014 \text{ N}$$

Where, for movement of wood on wood

Static friction co-efficient $\mu_s = 0.3$

Kinetic friction co-efficient $\mu_k = 0.3$

When the distance of the workpiece from the motor (9 cm) will be maximum torque required will be maximum.

So, the maximum torque required

$$= (1.802 * 0.09) \text{ Nm}$$

$$= 0.1622 \text{ Nm}$$

(Considering static force for its higher value)

Now x-axis motor torque, pulley diameter and the linear speed of the motor can be calculated from the following equation

$$T_x = \frac{I * V * E * 60}{N * 2\pi}$$

Where,

$T_x =$ Motor torque $= 0.1622 * 1.1 = 0.18$ Nm
 (Considering 10 % safety factor)

$I =$ Rated Current $= 0.6$ A

$V =$ Supply voltage $= 12$ V

$E =$ Motor efficiency $= 10\%$

$N =$ Motor rpm

So, $N = 38$ rpm

And, from the equation

$$N = \frac{60 * v}{\pi * D}$$

So, pulley diameter $D_x = (60 * 4) / (\pi * 38) = 2$ cm

For y axis movement

Now the setup for y axis mass $m_y = 1.235$ kg

$$W_y = 1.235 * 9.8 = 12.103 \text{ N}$$

As previous,

$$f_s = \mu_s * w_y = 0.3 * 12.103 = 3.6309 \text{ N}$$

$$f_k = \mu_k * w_y = 0.2 * 12.103 = 2.4206 \text{ N}$$

So, the maximum torque required would be

$$= (3.6309 * 0.09) \text{ Nm}$$

$$= 0.3267 \text{ Nm}$$

$$\text{So, } T_y = 0.3267 * 1.1 = 0.36 \text{ Nm}$$

Holding the same values for I, V and E as previous the equation $T_x = \frac{I * V * E * 60}{N * 2\pi}$, provides

$$N = 19 \text{ rpm}$$

For same linear velocity v, we get,

Pulley diameter $D_y = 4$ cm

For z axis movement

This is the setup for z axis movement which will be controlled by dc motor. The drill motor with drill chuck will be set as shown

As the work piece is just a model made of cork sheet drilling thrust force requirement can be neglected as the gravitational force will take care of it.

Now, the total mass of the drilling equipment with other necessary parts that the motor has to lift in the z-direction is $m_z = 700$ gm $= 0.7$ kg

So, $w_z = 0.7 * 9.8 = 6.86$ N which is in the very close vicinity of the dead weight for x-axis motor.

So, same configuration motor can be used here.

3.5 Automation Components

Arduino Mega 2560

Table 2 Specification of Arduino Mega

Microcontroller	ATmega2560
Operating Voltage	5V
Input Voltage (limit)	6-20V
Flash Memory	256 KB
SRAM	8 KB
Clock Speed	16 MHz

Motor driver

L298N series motor driver

It's an integrated monolithic circuit in a 15-lead Multiwatt and PowerSO20 package.

Ultrasonic sensor

A HC-SR04 Ultrasonic sonar sensor was selected. Ultrasonic ranging module HC - SR04 provides 2cm - 400cm non-contact measurement function, the ranging accuracy can reach to 3mm. The Module automatically sends eight 40 kHz and detect whether there is a pulse signal back

$$\text{Distance} = \frac{\text{velocity of sound}(340 \text{ m/s}) * \text{time took}}{2}$$

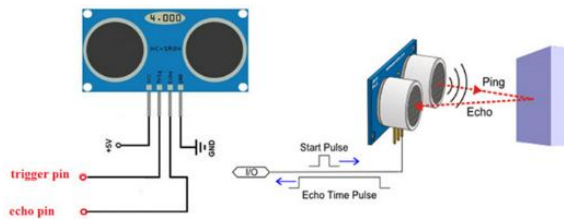


Fig.6 Operation of Ultrasonic sensor

3.6 Circuit diagram

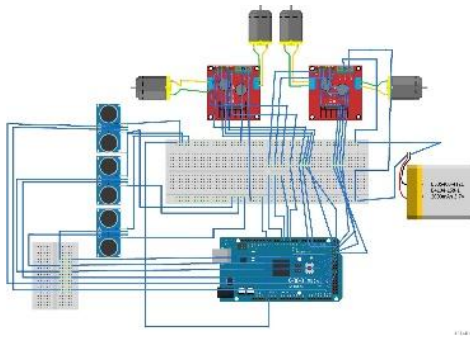


Fig.7 Circuit diagram

3.7 Part program or coding

For the operation, the whole code is written in IDE environment which is compatible with Arduino applications.

4. Working principle

One of the basic objectives of this work is to maintain simplicity in action. So, to perform a whole drilling operation the operator has to enter the following parameters:

1. Number of holes to be made
2. Each hole co-ordinate
3. Each holes depth (if variable)

The whole setup could be set on anywhere including upon something or just in the floor as the whole setup has its own support stand. Then after connecting the power source and computer, the program will be launched. The entry screen will appear now and after giving the entries and hitting start option the operation will start.

To carry out the whole operation, at first, the basic position will be obtained by entering the neutral position (0,0). Then for the first hole, the x-axis movement controller motor will start to rotate until the x coordinate of the first hole is right under the drill bit. Then the y-axis movement controller motor will start rotating similarly until the y coordinate of the first hole is positioned under the drill bit. In both case with Ultrasonic sonar sensor continuously variable distance will be measured at the 10-millisecond difference. After

getting the desired value from the sensor motor will stop rotating.

After completion of rectilinear positioning, the drill bit will start to descend with drill bit rotates. When the desired depth will be reached then both descend controlling motor and drill motor will be stopped. Then the controlling motor will start ascending the drill motor (while drilling motor is rotating in opposite direction) and both of these two motors will be turned off when drill bit gets to its previous position.

5. Result and performance test

5.1 Result

Different observations are made for the performance test:

Table 3 Collected data

Observation 1:

No. of holes	Co-ordinate (in mm)	Depth (mm)	Drilled co-ordinate	Positioning Error (%)		Drilled depth (mm)	Drilling depth error (%)
				x	Y		
3	30,60	33	30,62	0	3	33	0
	50,-40	15	48,-43	4	7.5	17	13
	-60,30	25	-60,31	0	3.3	28	12

Observation 2:

3	20,-10	25	22,-9	10	10	25	0
	30,-40	33	26,-41	13	2	33	13
	-15,40	33	-14,40	6	0	31	6.06

Observation 3:

2	-10,-10	33	-10,-13	0	30	33	0
	25,50	33	27,53	8	6	30	10

5.2 Error analysis:

From the above data:

An average error along x-axis movement

$$E_x = \frac{0+4+0+10+13+6+0+8}{8} = 5.125\%$$

Similarly, $E_y = 7.725\%$ & $E_z = 6.75\%$

The error analysis can be better shown with some graphical representation

Table 4 Error representation in graphical form

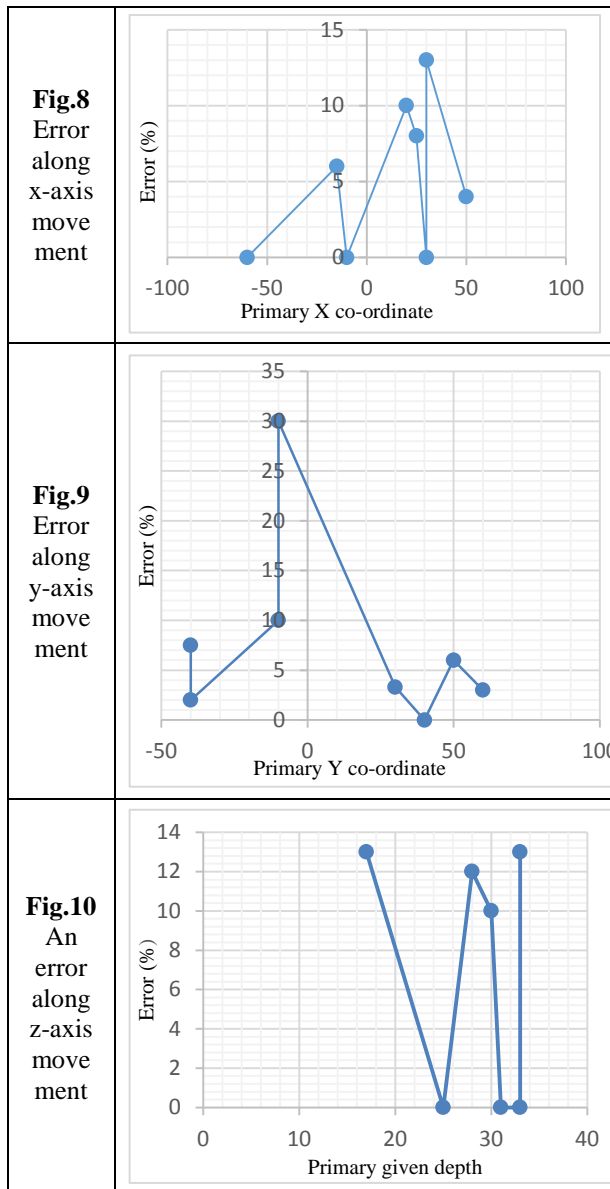


Fig.8 shows error along the x-axis is more when the position is on the positive side. It is basically due to some primary error in coinciding with the workpiece holder and workpiece mid-point.

Fig.9 shows error along the y-axis movement is maximum around small values in the negative quadrant. Which is mainly due to the extra rope arrangement in this section.

Fig.10 shows around 6% error in average for almost all drill depth including full depth. It could be due to some technical problems of an ultrasonic sensor for this operation. And vibration in here also causes a lot of error.

6. Conclusion

The constructed automated drilling mechanism is a fine example of showing accuracy in drilling and fine controlling of motors for positioning. The purpose of implementing this project is to avoid the use of a CNC machine and robotic arms. The construction took almost BDT 6000 to finish the project which is not a great deal

for personal or industrial level keeping in mind that it's wooden structure and error accepting. The usefulness of such type is to provide lost cost manufacturing process to the small-scale industries. Errors that might occur in manual drilling are totally eliminated with the 3-axis precise control of the drill head movements. So, drill bit positioning on a pad or breaking of tools is no more a problem. It can also be used in teaching institutes where actually the design and manufacturing system of CNC are taught to them.

NOMENCLATURE

f_s : Static frictional force

f_k : Kinetic frictional force

T : Torque

μ_s : Static friction coefficient

μ_k : Kinetic friction coefficient

Reference

- [1] G.Niranjan, A.Chandini, P.Mamatha, Automated Drilling Machine with Depth Controllability, International Journal of Science and Engineering Applications Volume 2 Issue 4, 2013, ISSN-2319-7560
- [2] Todd, Robert H.; Allen, Dell K.; Alting, Leo, Manufacturing Processes Reference Guide, Industrial Press Inc., pp. 43–48, ISBN 0-8311-3049-0.(1994)
- [3] Groover, Mikell P, Theory of Metal Machining. Fundamentals of Modern Manufacturing (3rd ed.). John Wiley & Sons, Inc. pp. 491–504. ISBN 0-471-74485-9. (2007)
- [4] Frederick Webb Hodge, Handbook of American Indians North of Mexico V. 1/4. Digital Scanning Inc. pp. 402–. ISBN 978-1-58218-748-8. (2003)
- [5] Rifkin, Jeremy. The End of Work: The Decline of the Global Labor Force and the Dawn of the Post-Market Era. Putnam Publishing Group. pp. 66, 75. ISBN 0-87477-779-8.(1995)
- [6] Mike Lynch, Key CNC Concept #1—The Fundamentals Of CNC, Modern Machine Shop, 4 January

ICMIEE18-317

Efficacy of Watermelon (*Citrullus Lanatus*) Rind Charcoal for Chromium Removal from Tannery Wastewater

Nabila Nowrin, Tasnim Alam, Sofia Payel, Md. Shahruk Nur-A-Tomal, Md. Abul Hashem*

Department of Leather Engineering, Khulna University of Engineering & Technology, Khulna-9203, BANGLADESH

ABSTRACT

Over recent years, sustainable development has been more appreciated to achieve the goal of a safe environment with the proper waste management system. Since the complete reduction of waste generation is inevitable, waste management is the best possible solution for a sound environment. In this proposed approach, watermelon rind charcoal was used as an adsorbent to remove chromium from tannery wastewater. Following batch experiment process the system was optimized by different parameters: charcoal dose, contact time and adsorption kinetics and the physicochemical characteristics of both raw and treated effluents were analysed. The chromium content in raw wastewater and treated wastewaters were 2733.4 mg/L and 5.536 mg/L respectively with 99.8% chromium removal efficiency. Additionally, it removes the chloride content by 56.86%. This method revealed the significant potential of watermelon rind in chromium removal from tannery effluent.

Keywords: Chromium, Tannery effluent, Watermelon Rind.

1. Introduction

Leather making is a traditional industry existing since time immemorial, certainly over 5000 years [1]. The term leather making generally refers to the tanning process where putrescible raw hides/skins are converted to leather. Many processes have been practised throughout history but at present more than 90% of the global leather production of 18 billion sq. ft. are tanned through chrome tanning process [2]. It's faster and more reliable reaction with collagen matrix enhanced the popularity over the previously followed vegetable tanning process [1].

During tanning process, the pickle pelt reacts with 60-70% of total chromium salts and the rest of 30-40% of the chromium remains in the solid and liquid phases (especially as spent tanning liquor) [3]. Everyday approximately 1.25 tons of chromium is discharged into the river and around 1.6 tons is discharged from the tannery effluent where peak discharge is considered as 21000 m³/day [4].

In general, chromium is found in its trivalent chromium Cr (III) and hexavalent chromium Cr (VI) form [5]. The Cr (VI) is extremely toxic and may cause contact allergic dermatitis on the skin and may also be a trigger for many diseases [6]. Thus, in spite of its popularity chrome tanning causes great concern to humanity.

Numerous treatment methods [7] such as ion exchange [8], reduction [9], chemical precipitation [10], membrane separations [11], electrochemical precipitation [12], photocatalytic reduction [13], have been developed for chromium remediation. Most of these processes are successful for purging chromium from wastewater but the highly expensive system and the toxic materials produced after treatment reduce its popularity.

An adaptable worldwide method for removing organic and inorganic pollutants from wastewater is adsorption using activated carbon as adsorbent [14]. Adsorption technique is verified as low cost, easy to maintain and more economical if the raw material of the adsorbent is available [15]. The precursors to be a good adsorbent is a

large surface area, low volume pores, good physicochemical properties, resistance against the atmospheric change and do not produce perilous substance while conducting adsorption [16].

In the recent years, many low cost, non-conventional adsorbents include rice polish [17], sawdust [18], agricultural byproduct [19], natural zeolite [20], clay [21], polyaniline coated on sawdust [22], eggshell and powered marble [23], *Caricacpapaya* plant [24] and so on are developed. However, not all of these adsorbents have completely been investigated. Thus, an attempt has been taken in the research to make the process cost-effective, environment-friendly, and industrially feasible to draw out chromium from the wastewater [7].

Watermelon is a very common fruit grown in the tropical and subtropical areas. In 2016, global production of watermelons was 117 million tons with China alone accounting for 68% of the total [25]. Bangladesh produced about 284845 metric tons watermelon in the fiscal year of 2011-2012 [26]. In a watermelon, the flesh part, rind and seed constitute approximately 68%, 30% and 2% respectively [27]. Watermelon rind is disposed of as waste, which causes an environmental pollution. Proper management is one of the ways to make the environment clean.

In this study, watermelon rind was used to produce charcoal adsorbent to remove chromium from the wastewater. The investigation could fulfil the purpose of chromium removal from tannery wastewater using a low-cost adsorbent prepared from watermelon rind which is generally discarded as waste.

2. Experimental

2.1 Sample collection

Chrome containing wastewater was collected from the SAF Leather Limited, Khulna, Bangladesh. The chrome liquor was collected in a high-density polyethylene container. Before collecting the chrome liquor the container was washed with diluted nitric acid according

* Corresponding author. Tel.: +88-01674590373
E-mail addresses: mahashem96@yahoo.com

to the standardized laboratory method. The industrial wastewater was primarily filtered to remove unexpected suspended solids and the filtered liquor was used for treatment. Raw watermelon rinds were collected from the dustbin and domestic waste.

2.2 Charcoal preparation

The collected watermelon rinds were sun-dried. Afterwards, it was burnt and crushed with mortar to produce a powder. Lastly, the required size of the charcoal adsorbent was obtained by sieving on 80-mesh. Fig. 1(a) and Fig. 1(b) show the raw watermelon rind and prepared charcoal respectively.



Fig.1 Raw watermelon rind **a)** and prepared charcoal **b)**

2.3 Reagents

The reagents that were used in the experiment were pure concentrated nitric acid (Merck Specialties Private Limited, Worli, Mumbai), sulfuric acid (Merck Specialties Private Limited, Worli, Mumbai), perchloric acid (Merck, India), ammonium iron (Merck, India) sulfate hexahydrate (Merck Specialties Private Limited, Worli, Mumbai) and *N*-phenyl anthranilic acid (Loba Chemie, India), filter paper (Whatman No. 1), anti-bumping agent glass beads (Loba Chemie, India). All of the reagents were collected from local scientific store, Khulna, Bangladesh.

2.4 Characterization of Wastewater

Chromium content, electrical conductivity (EC), salinity, chloride (Cl^-) content, total dissolved solids (TDS), pH were measured in the experiment.

2.4.1 Chromium determination

Quantitative analysis of chromium in the waste liquor and treated liquor was ascertained by the titrimetric method according to the Society of Leather Technologist and Chemists (1996) official method of analysis SLC 208 (SLT6/4) [28]. At first, a 500 mL conical flask was filled with 25 mL sample and 20 mL nitric acid and 20 mL of perchloric acid and the sulfuric acid mixture was added into it. Then heat was applied gently to boil the mixture until it became a pure orange-red colour and the boiling was continued for one minute after the point had been reached. Later, the flask was taken aside from the heating source before exhalation. Afterwards, the flask was inserted into a cold bath for rapid cooling and then 100 mL distilled water was carefully poured into the flask with glass beads. The heat was applied for 10 minutes to make the mixture chlorine free and after that 10 mL of 30% (v/v) sulphuric acid was carefully added.

Finally, when the mixture was cooled, titration was performed with freshly prepared 0.1N ammonium iron (II) sulphate solution with six drops of *N*-phenyl anthranilic acid as an indicator and the end colour was pointed out as a colour change from violet to green.

2.4.2 Determination of pH

pH of the raw chrome tanning wastewater and treated liquor was measured using calibrated pH meter (UPH-314, UNILAB, USA).

2.4.3 Determination of TDS, EC and salinity

After calibrating the conductivity meter (CT-676, BOECO, Germany) with standard solution TDS, EC and salinity were measured.

2.4.4 Chloride (Cl^-) determination

Chloride content in the chrome tanning wastewater and after treatment was measured by APHA standard argentometric method [29]. A 100 mL sample was taken in a conical flask and pH was adjusted in the range of 7 to 10. Then, 1.0 mL potassium dichromate indicator was added. After that, the solution was titrated with silver nitrate as titrant (0.0141N) to a pinkish yellow endpoint. The titrant was standardized by the sodium chloride (0.0141N) solution.

2.5 Characterization of charcoal

The charcoal (pure and chromium loaded) samples were analyzed using Fourier transform infrared spectrometer (FTIR, Spectrum 100, PerkinElmer, USA) with an attenuated total reflectance (ATR) accessory. Infrared spectra were recorded at a resolution of 4 cm^{-1} and 20 spectra were averaged to reduce the noise.

2.6 Treatment of chromium-containing wastewater

Batch-wise chromium removal test was conducted with the prepared charcoal. The scheme for the treatment of chrome tanning wastewater is shown in Fig. 2.

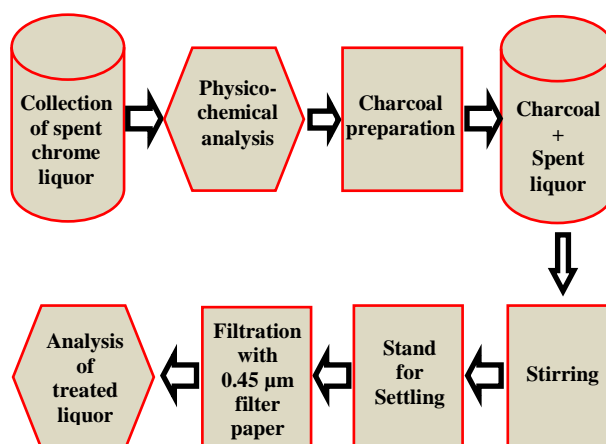


Fig.2 Flow diagram of the treatment process

At first, the chemical and physical characteristics of raw wastewater was examined and then percolated through

0.45 µm pore size filter. Then, 40 mL of the filtrate was mixed with the proposed charcoal. The charcoal mixed wastewater was stirred over a fixed period of time. After settling, the mixture was then filtrated through 0.45 µm pore size filter and again chromium content measurement was done.

2.7 Process optimization

Optimization of the whole process was carried out for maximum chromium removal efficiency [24]. Tests were carried out to optimize the chromium removal parameters: adsorbent dose, contact time and relative pH. The optimized conditions were established by investigating the removal efficiency of chromium.

2.8 Investigation of a kinetics model

To investigate adsorption kinetics 33 g of charcoal was taken in 833 mL (as per optimum dose 2 g/40 mL of wastewater) spent chrome liquor. At constant stirring 40 mL treated liquor was taken carefully as possible after 1, 3, 6, 9, 15, 21, 27 and 35 minutes. Then the liquor was filtered and the chromium content of the filtrate was measured.

In an adsorption process, it is supposed that the rate is proportional to the difference between the amounts of adsorption at time t and the adsorption capacity of adsorbent $(a-x)$ [30]. Then the simple linear form of Lagergren's pseudo-first order reaction can be summarized as,

$$\ln(a - x) = \ln a - K_1 t$$

$$\text{or, } \ln \frac{(a - x)}{a} = -K_1 t \dots (i) \quad [24]$$

The pseudo-first order reaction of Lagergren's first order reaction is described in Eq.(i), where x and a are denoted as the amounts of adsorption at time t and at equilibrium (mg/g) respectively and k_1 as the first-order rate constant (min^{-1}).

The value of K_1 and correlation coefficient (R) can be obtained from the linear plot of $\ln(a-x)/a$ versus time (t). Kinetic analysis for the pseudo-second-order reaction can be formulated from Eq. (ii):

$$x = \frac{a^2 K_2 t}{1 + K_2 a t}$$

$$\text{or, } \frac{x}{a(a - x)} = K_2 t \dots (ii) \quad [24]$$

Where x and a are the adsorption capacity (mg/g) at time t and at equilibrium respectively, and K_2 is the equilibrium rate constant for adsorption process (g/mg.min).

The value of K_2 can be calculated from the slope and the intercept of the plots of $x/a(a-x)$ versus time (t). This model supports two reactions occurring at the same time: the first one is fast and reaches equilibrium quickly

and the second one is slow and can continue for a long time.

3. Result and discussion

3.1 Characteristic of charcoal

Fig. 3 depicts the FT-IR spectrum of charcoal before and after the adsorption of chromium. The figure reveals changes in the peak intensity.

Fig. 3(a) shows a broad region around 3468 cm^{-1} indicates the presence of hydroxyl group, N-H group and C=O group around 1867 cm^{-1} wavelength. The -OH, -NH, carbonyl and carboxylic groups have been reported as significant sites for metal ions adsorption [31]

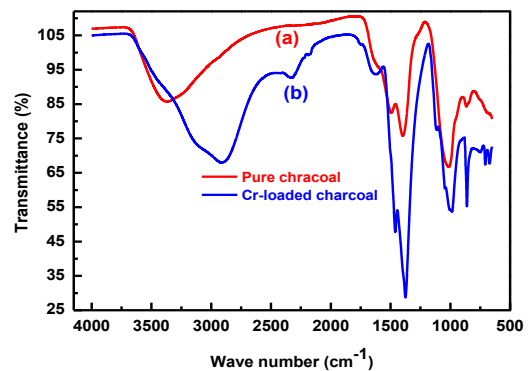


Fig.3 FT-IR spectrum of pure charcoal (a) and chromium-loaded adsorbent (b)

However, in the case of Fig. 3(b) there is a noticeable shift in the peak. Here, C-H, C=H groups are found at around 3000 cm^{-1} with additional C-H and C-O functional groups at 1385 cm^{-1} and 1220 cm^{-1} wavelength respectively. This ensures the involvement of the hydroxyl and other groups of pure charcoal in the adsorption process.

3.2 Effect of charcoal dose

The charcoal dose was observed by the batch optimization process. Five samples of 40 mL chrome liquor were treated with 0.5 g, 1.0 g, 1.5 g, 2.0 g and 2.5 g of charcoal.

After 10 minutes of stirring and 10 minutes of settling, each sample was filtered and the amount of chromium was measured.

Fig. 4 shows the change in removal efficiency and pH with the change in charcoal dose. It is clear that the increase of charcoal dose results in the increase in the efficiency and pH. This may be because the more amount of charcoal is added; the more chromium can be adsorbed to the surface, thus removing more chromium. At 2.0 g dose per 40 mL of spent liquor, the removal efficiency is 99.5% at a pH 8.5. At this point, the efficiency reaches at a saturation point. Thus, 2.0 g per 40 mL of liquor is considered as an optimum dose.

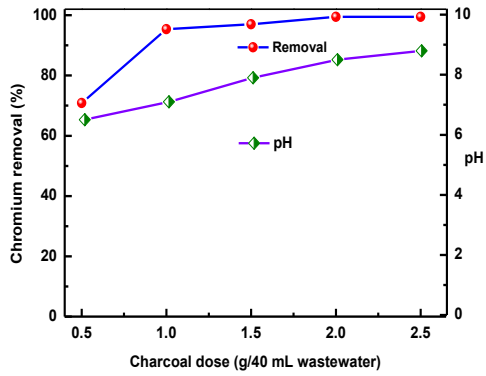


Fig.4 Batch wise treatment process at different charcoal doses: 0.5, 1.0, 1.5, 2.0, and 2.5 g; in each batch 40 mL wastewater with fixed 10 min contact time was used

3.3 Effect of contact time

The adsorption efficiency depends on the availability of the adsorbent surface as well as the time allowed for the interaction of adsorbent with the adsorbate. Fig. 5 depicts the change in removal efficiency due to the change in contact time. Here batch optimization process was followed using 6 samples with optimum dose i. e. 2.0 g per 40 mL of waste liquor where the contact time was 1, 3, 6, 9, 12 and 15 minutes respectively.

The increase in contact time allows the adsorption to take place for a longer time, thus increasing removal efficiency.

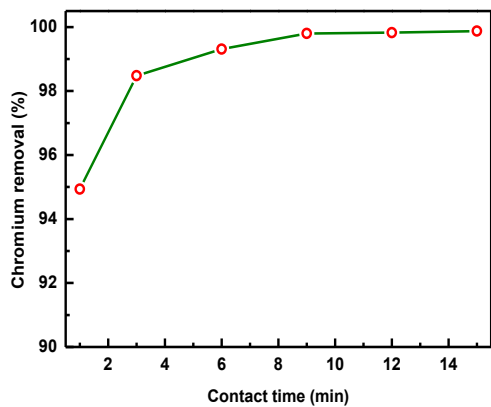


Fig.5 Batch wise chromium removal efficiency on different contact time: 1, 3, 6, 9, 12 and 15 min; in each batch 40 mL wastewater with fixed 2 g charcoal was used

At 9 minutes, the removal efficiency is 99.8% and after that the change is negligible. So, in this experiment, the optimum contact time was considered 9 minutes.

3.4 Kinetics Model

Adsorption kinetics refers to the rate of adsorption at a constant pressure or concentration and is employed to measure the diffusion of adsorbate in the pores of the adsorbent and the percentage of the incident adsorbate molecules.

Kinetic models are used to test experimental data to verify the mechanism of adsorption and potential rate controlling steps like mass transport and chemical reaction processes [32].

Fig. 6 and Fig. 7 describe the graph for adsorption kinetics of pseudo-first and pseudo-second-order reaction respectively. The value $R_1^2 = 0.78598$ and $R_2^2 = 0.9069$ for pseudo-first-order and pseudo-second-order kinetics are depicted from the graphs respectively.

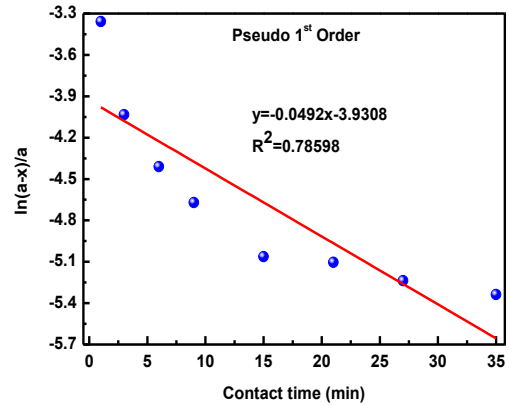


Fig.6 Adsorption kinetics of pseudo-first order

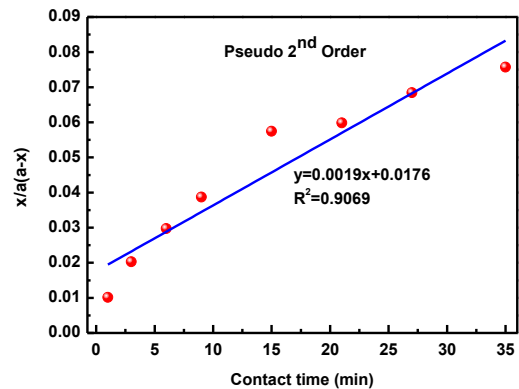


Fig.7 Adsorption kinetics of pseudo-second order

It could be clearly decided that the pseudo-second-order kinetics provided a better description for the adsorption of the Cr (III) onto adsorbent than a pseudo-first-order kinetics equation.

3.5 Treatment process efficiency

The results of the treatment process with optimum conditions are depicted in Table 1. The physicochemical parameters of wastewater obtained after treatments are chromium 5.536 mg/L, pH 8.3, TDS 36.6 mg/L, EC 84.9 mS, salinity 54.4 ppt and chloride (Cl⁻) 7700 mg/L.

It shows that after treatment chloride (Cl⁻) was high from the discharge limit but it was reduced at a noticeable level. This may be because chloride has a tendency to co-precipitate with other ions.

Table 1 Data comparison with Bangladesh standard (ECR 1997)

Parameters	Raw sample	Treated sample	ECR[33]
Cr (mg/L)	2733.4±3.75	5.536±2.3	2.0
pH	4.2±0.2	8.3±0.5	6–9
TDS (g/L)	28.28±0.2	36.6±0.5	2.1
EC (mS)	58.2±0.2	84.9±0.4	1.20
Salinity (ppt)	38.76±0.7	54.40±0.09	-
Cl(mg/L)	17850±11.3	7700±9.6	600

The removal efficiency of chromium at optimized condition was 99.8% and the reduction of chloride was 56.86%. During this treatment, the prepared charcoal acts as adsorbent and the inorganic and organic pollutants are adsorbed by the charcoal surface. Thus, after filtration, the pollutants are removed with the adsorbent from the wastewater and reduce Cr, chloride and salinity.

4. Conclusion

This investigation is a potential approach to remove chromium from tannery wastewater as well as a new application of watermelon rind as an adsorbent in tannery industry. Considering the huge production of watermelon every year, its rind could be marked as available, low-cost raw material. The treatment process implies that the charcoal is prepared from a waste material and no additional chemicals are required. In this batch-wise technique, the removal efficiency of chromium at 2 g per 40 mL of wastewater was 99.8% after 9 minutes of stirring and additionally, it also removes the chloride content by 56.86%. Several methods might have been tried before but considering the potential of this method, it could be easily adopted industrially as a column test process with some further research on cost analysis and input-output ratio.

Acknowledgements

Authors are indebted to the related personnel of the Department of Leather Engineering, Khulna University of Engineering and Technology (KUET), Khulna 9203, Bangladesh for providing necessary laboratory and other facilities. Special thanks to the anonymous reviewers for their sincere comments to upgrade the manuscript remarkably.

References

[1] A.D. Covington, *Tanning Chemistry: The science of leather*. The Royal Society of Chemistry, Cambridge, (2011).

[2] V.J.Sundar, J.R.Rao, C. Muralidharan, Cleaner chrome tanning-emerging options, *Journal of cleaner production*, Vol. 10(1), pp 69-74, (2002).

[3] A. Ismailia, A. Mesdaghinia, R. Vazirinejad, Chromium (III) removal and recovery from Tannery wastewater by precipitation process. *American Journal of Applied Sciences*, Vol. 2(10), pp 1471-1473, (2005).

[4] UNIDO, Environmental impact assessment (EIA) on the industrial activities at Hazaribagh area, *Dhaka Project-US/RAS/97/137-EIA*, Final Report, Government of Bangladesh and United Nations Industrial Development Organization, Vienna, Austria, (2000).

[5] R.M. Cespon, M.C. Yebra, Flow injection determination of total chromium in urine of occupationally exposed workers, *Microchim. Acta*, Vol. 164, pp 225-229, (2008).

[6] V.N. Bulut, D. Ozdes, O. Bekircan, A. Gundogdu, C. Duran, M. Soylak, Carrier element-free coprecipitation (CEFC) method for separation, preconcentration and speciation of chromium by using an isatin derivative, *Anal. Chim. Acta*, Vol. 632, pp 35-41, (2009).

[7] D. Mohan, K. P. Singh, V. K. Singh, Trivalent chromium removal from wastewater using low cost activated carbon derived from agricultural waste material and activated carbon fabric cloth, *J. Hazard. Mater.*, Vol. 135, pp 280-295, (2006).

[8] S. Rengaraj, C.K. Joo, Y. Kim, J. Yi, Kinetics of removal of chromium from water and electronic process wastewater by ion exchange resins: 1200H, 1500H and IRN97H, *J. Hazard. Mater.*, Vol. 102, pp 257-275, (2003).

[9] J.C. Seaman, P.M. Bertsch, L. Schwallie, In situ Cr(VI) reduction within coarse-textured, oxide-coated soil and aquifer systems using Fe(II) solutions, *Environ. Sci. Technol.* Vol. 33, pp 938-944, (1999).

[10] X. Zhou, T. Korenaga, T. Takahashi, T. Moriwake, S. Shinoda, A process monitoring/controlling system for the treatment of wastewater containing chromium (VI), *Water Res.*, Vol. 27, pp 1049-1054, (1993).

[11] C.A. Kozlowski, W. Walkowiak, Removal of chromium (VI) from aqueous solutions by polymer inclusion membranes, *Water Res.*, Vol. 36, pp 4870-4876, (2002).

[12] N. Kongsricharoern, C. Polprasert, Chromium removal by a bipolar electrochemical precipitation process, *Water Sci. Technol.* Vol. 34, pp 109-116, (1996).

[13] J.J. Testa, M.A. Grela, M.I. Litter, Heterogeneous photocatalytic reduction of chromium (III) over TiO₂ particles in the presence of oxalate: involvement of Cr(VI) species, *Environ. Sci. Technol.* Vol. 38, pp 1589-1594, (2004).

[14] M. Gholipour, H. Hashemipour, M. Mollashahi, Hexavalent chromium removal from aqueous solution via adsorption on granular activated carbon: adsorption, desorption, modeling and simulation studies, *Journal of Engineering and Applied Sciences*; Vol. 6, (2011).

[15] H. Demiral, İ. Demiral, F. Tımsek, B. Karabacakoglu, Adsorption of chromium (VI) from aqueous solution by activated carbon derived from olive bagasse and applicability of different

- adsorption models, *J. Chem. Eng.* Vol. 144, pp 188-196, (2008).
- [16] A.A. Nayl, R.A. Elkhashab, T.E. Malah, S.M. Yakout, M.A. El-Khateeb, M.M.S. Ali, H.M. Ali, Adsorption studies on the removal of COD and BOD from treated sewage using activated carbon prepared from date palm waste, *Environ Sci Pollut Res*, Vol. 24(28), pp 22284-22293, (2017).
- [17] K. Singh, R. Rastogi, S. Hasan, Removal of cadmium from wastewater using agricultural waste 'rice Polish', *Journal of Hazardous Materials*, Vol. 121(1-3), pp 51-58, (2005).
- [18] S.S. Shukla, L.J Yu, K.L. Dorris, Removal of nickel from aqueous solutions by sawdust, *Journal of Hazardous Materials*, Vol. 121(1-3), pp 243-246, (2005).
- [19] T.G. Chuah, A. Jumariah, I. Azni, S. Katayon, C.S.Y Thomas, Rice husk as a potentially low-cost biosorbent for heavy metal and dye removal: an overview. *Desalination*, Vol. 175, pp 305-316, (2005).
- [20] E. Erdem, N. Karapinar, R. Donat, The removal of heavy metal cations by natural zeolites. *J Colloid Interface Sci*, Vol. 280, pp 309-314, (2004).
- [21] G.E. Marquez, M.J.P. Ribeiro, J.M. Ventura, J.A. Labrincha, Removal of nickel from aqueous solutions by clay-based beds. *Ceram Int*, Vol. 30, pp 111-119, (2004).
- [22] M. Mansour, M. Ossman, H. Farag, Removal of Cd (II) ion from wastewater by adsorption onto polyaniline coated on sawdust, *Desalination*, Vol. 272(1-3), pp 301-305, (2011).
- [23] S. Elabbas, L. Mandi, F. Berrekhis, M.N. Pons, J.P. Leclerc, N. Ouazzani, Removal of Cr(III) from chrome tanning wastewater by adsorption using two natural carbonaceous materials: eggshell and powdered marble, *J Environ Manag*, Vol. 166, pp 589-595, (2016).
- [24] M.H.R. Sheikh, M.I. Apon, M.A. Hashem, Performance of chromium adsorption on Carica Papaya plant biosorbent, Innovative Aspects for Leather Industry, *Proceedings of the 4th International Leather Engineering Congress* (pp. 59-68). Izmir, Turkey, (2017).
- [25] Watermelon production in 2016, Food and Agriculture Organization of the United Nations, Statistics Division, *FAOSTAT*, (2018).
- [26] Yearbook of Agricultural Statistics, Bangladesh Bureau of Statistics (BBS), Statistics and Informatics Division (SID), Ministry of Planning, Government of the People's Republic of Bangladesh, (2012).
- [27] M.N.F. Hani, W.Z.W.N. Zahidah, K. Saniah, H.S.M. Irwani, Effects of drying on the physical characteristics of dehydrated watermelon rind candies, *J. Trop. Agric. and Fd. Sc.*, Vol. 42(2), pp 115-123, (2014).
- [28] Society of Leather Technologist and Chemists, Official Methods of Analysis. Northampton, UK, (1996).
- [29] APHA, Standard Methods for the Examination of Water and Wastewater, twenty-second ed. American Public Health Association. American Water Works Association, Water Environment Federation, Washington DC, USA, (2012).
- [30] R.L. Tseng, F.C. Wu, R.S. Juang, Characteristics and applications of the Lagergren's first-order equation for adsorption kinetics, *J. Taiwan Institute of Chemical Engineers*, Vol. 41, pp 661 - 669, (2010).
- [31] S.S. Kalavani, T. Vidhyadevi, A. Murugesan, K.V. Thiruvengadaravi, D. Anuradha, S. Sivanesan, L. Ravikumar, The use of new modified poly(acrylamide) chelating resin with pendent benzothiazole groups containing donor atoms in the removal of heavy metal ions from aqueous solutions, *Water Resources and Industry*, Vol. 5, pp 21-35, (2014).
- [32] Z. Aksu, Equilibrium and kinetic modeling of cadmium (II) sorption by *C. vulgaris* in a batch system: effect of temperature, *Separ. Purif. Technol.*, Vol. 21, pp 285-294, (2000).
- [33] Environment Conservation Rules, Ministry of Environment & Forests (MoEF), Government of the People's Republic of Bangladesh, (1997).

ICMIEE18-318

Design Construction and Performance Test of a Low-Cost Portable Mechanical Ventilator for Respiratory Disorder

S. M. Tamjid Hossain^{1,*}, Mihir Ranjan Halder¹, Al Aman¹, Md. Rakibul Islam², Md. Tarek Rahman¹

¹Department of Mechanical Engineering, Khulna University of Engineering & Technology, Khulna-9203, BANGLADESH

²Department of Biomedical Engineering, Khulna University of Engineering & Technology, Khulna-9203, BANGLADESH

ABSTRACT

Mechanical ventilator is a medical device which is usually utilized to ventilate patients who cannot breathe adequately on their own. Among many types of ventilators Bag Valve Mask (BVM) is a manual ventilator in which a bag is pressed to deliver air into the lungs of the patient. In present work, a mechanical system along with microcontroller has been developed to automate the operation of BVM. The constructed prototype contains two arms of 0.30 m long, powered by two servo motors through pulling wires and pulleys, supported by wooden frame. These arms compress the BVM in prescribed manner at the rate set by the operator through a control knob. With principal dimensions of 0.55m*0.15m*0.3m, weight 2.5 kg and three 9 V battery for supplying power for at least one hour continuous operation, the prototype can be moved easily. The dimensions of the frame are selected as such to be compatible with the physical dimension of Ambu bag. The performance of the device was tested using BIOPAC Airflow Transducer which illustrates that the Tidal Volume vs. Time graph of the automated system is similar to the graph produced by manual operation of the BVM and to the graph produced by a human subject, but with a mean deviation of 0.332 Litres with manual operation and 0.542 Litres with human subject. Although the developed device cannot compress the bag completely due to low powered servo motors, it proves the concept of automating the operation of BVM using mechanical system for developing a portable ventilator.

Keywords: Mechanical Ventilator, BVM, BPM, Airflow Transducer.

1. Introduction

Mechanical ventilation is an important treatment which is usually utilized to ventilate patients who cannot breathe adequately on their own [1]. Patients with underlying lung disease may develop respiratory failure under a variety of challenges and can be supported by mechanical ventilators. These are machines which mechanically assist patients inspire and exhale, allowing the exchange of oxygen and carbon-dioxide to occur in the lungs, a process referred to as artificial respiration [2]. There are many techniques and methods of artificial ventilation, both manual and mechanical. While modern ventilators are computerized machines, patients can be ventilated with a simple, hand-operated bag valve mask (BVM) also. [3]

Although there are many elegant positive-pressure ventilators with sophisticated safety controls, they are rarely available in the field, thereby forcing rescuer to resort to manual methods of ventilation [4].

In present work, designing principle of a low-cost portable mechanical ventilator based on the BVM, along with the methodology for its construction and performance test has been described. The prime objectives of the project are described below.

- (1) To design and construct a portable mechanical ventilator by automating the operation of bag-valve-mask or 'Ambu bag'.
- (2) To test the performance of the constructed mechanical ventilator using BIOPAC airflow transducer.
- (3) To assess the cost of production of the designed ventilator to justify its use instead of manual resuscitators and existing portable ventilators.

1.1 History of Mechanical Ventilation

Numerous works and literatures on the historical development of mechanical ventilation and the design of portable ventilators are available.

Robert M Kacmarek et al. [5] presented a historical review of various techniques of mechanical ventilation is. It is interesting to note that artificial ventilation is not a new or modern concept; rather it can be traced back to Biblical times. But modern and automatic devices didn't appear until the early 1800s. Fig. 1 illustrates a 19th century mechanical ventilator which is negative-pressure type. [3]

In the work by Abdo Khoury et al. [6], evolution of Mouth-to-Mouth to Bag-Valve-Mask Ventilation is illustrated. Various developments in the components of Ambu bag and its valves are noticeable.

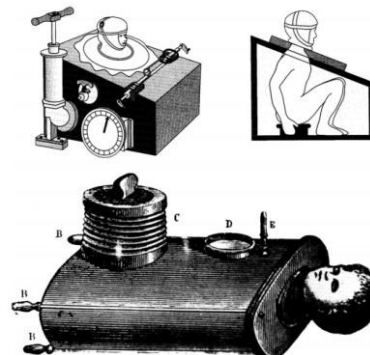


Fig. 1: A 19th century mechanical ventilator [4]

* Corresponding author. Tel.: +88-01728052825

E-mail addresses: tamjid3.14@gmail.com

The article by L. A. Geddes [4] summarizes the history of the development of artificial ventilation methods, both manual and mechanical. In this article two methods of manual artificial resuscitation methods, namely Sylvester's and Schafer's method and five mechanical devices for artificial ventilation, namely Bellows, the Pulmotor, the Iron Lung, Cuirass and Rocking Bed are described in chronological order. Fig. 2 illustrates the two manual methods four of the mechanical devices.

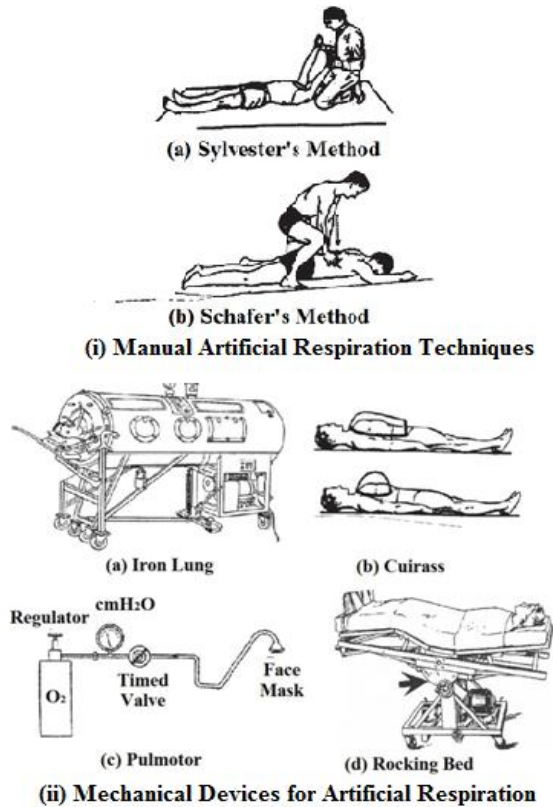


Fig. 2 : Artificial Respiration Methods [4]

1.2 Previous Works on the Design of Portable Ventilators

Stuart Fludger et al. [7] described various types of portable ventilators and their historical development. The concept of portable ventilators is rather new compared to ICU ventilators

Portable ventilators are evolved from the necessity of ventilating a patient during shifting or moving from one place to another. Ambu bag is often not reliable or it cannot be used for the unavailability of trained personnel. For these reasons, portable ventilators came into existence.

Portable ventilators vary by different parameters. In Table 1 comparison among three common portable ventilators is presented. [7]

Harrison et al. [8] of Rochester Institute of Technology, New York, developed a traditional portable ventilator 'Mediresp II' further. A US patent by Reno L. Vicenzi et al. [9] describe a detailed construction of a portable emergency mechanical ventilator.

Table 1: Comparison among common portable ventilators [7]

Model	Power for cycling	Power for inspiratory flow	Internal battery supply	External electricity supply
VentiPAC 200D	Pneumatic	Pneumatic	>1 yr (alarm only)	N/A
LTV-1000	Electric	Electric	1 h	Battery 12V DC
Oxylog 3000	Electric	Pneumatic	3 h (NiMH) Or 4 h (Li)	10-32V DC, 240V AC

The work that is most similar to the present work is by Husseini et al. [2] in which a BVM is automated mechanically to construct a portable mechanical ventilator. Cam mechanism was used in that work to produce the desired motion of the BVM.

The main difference of the present work with the work by Husseini et al. [2] is the use of mechanical arms and servo motors instead of cam mechanism to actuate the compression of BVM. In section 4.4 the uniqueness of present work is illustrated further.

2. Theory and Principles

The theoretical background and principle of the operation of mechanical ventilators and Ambu bag are presented below.

2.1 Principle of operation of Mechanical Ventilators

The ventilator is connected to the patient through a tube (endotracheal or ET tube) that is placed into the mouth or nose and down into the windpipe. When the doctor places the ET tube into the patient's windpipe, it is called intubation. Some patients have a surgical hole placed in their neck and a tube (tracheostomy or "trach" tube) is connected through that hole. The trach tube is able to stay in as long as needed and is more secure than an ET tube. At times a person can talk with a trach tube in place by using a special adapter called a speaking valve.

The ventilator blows gas (air plus oxygen as needed) into a person's lungs. It can help a person by doing all of the breathing or just assisting the patient's breathing. The ventilator can deliver higher levels of oxygen than delivered by a mask or other devices. The ventilator can provide a pressure (PEEP pressure) which helps hold the lungs open so the air sacs don't collapse. The tube in the windpipe makes it easier to remove mucus if someone has a weak cough. [10]

The ventilator should stop delivering air into the lungs with external force as soon as the patient starts to breathe himself. If it operates while the respiratory system of the patient is active it may cause damage to the lungs and vomiting of the patient may occur. So, there is a system to monitor when the patient starts to breathe himself and stop the operation of the ventilator.

2.2 Operation of Ambu bag

In Fig. 3 the various parts of an Ambu bag is identified. Manual resuscitators cause the gas inside the inflatable bag portion to be force-fed to the patient via a one-way valve when compressed by the rescuer; the gas is then ideally delivered through a mask and into the patient's trachea, bronchus and into the lungs. The tidal volume and respiratory rate has to be maintained as per the conditions of the patients by the rescuer.

Typical tidal volume is 500 to 800 mL of air and typical respiratory rate is 10 to 12 respiration per minute for adults and 20 respirations per minute for infants. Professional rescuers are taught to ensure that the mask portion of the BVM is properly sealed around the patient's face. [11]

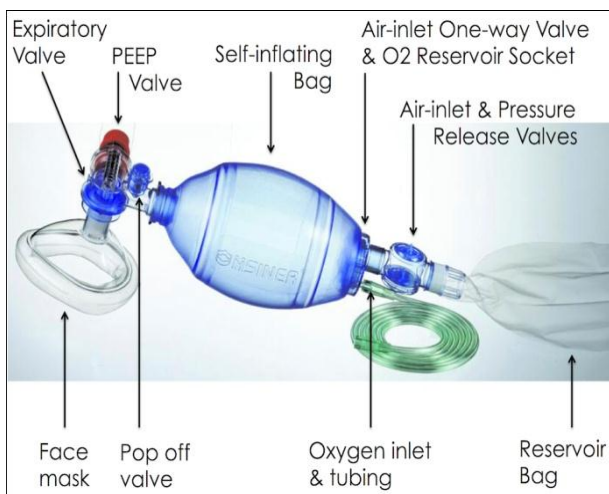


Fig. 3: Various parts of Ambu Spur II resuscitator [12]

3. Design and Construction

3.1 Design Assumptions

The design of the proposed portable mechanical ventilator for adult patients was done on the basis of following assumptions—

- i. Tidal volume to be delivered = 200 to 750 mL
- ii. Breath rate to be maintained = 10 to 20 BPM
- iii. Maximum power required by the motor = 30 W
- iv. Maximum torque to be delivered by the motor = 1.5 N.m

The design assumptions are based on the work by Hussein et al. [2], as they determined the assumptions after necessary experiments taking the mechanical properties and dimensions of the Ambu bag into considerations. So, there assumptions can be taken without further experimentations.

3.2 Principle of Proposed Design

Where most emergency and portable ventilators are designed with all custom mechanical components, it was chosen to take an orthogonal approach by building on the inexpensive BVM, an existing technology which is the simplest embodiment of a volume-displacement ventilator. Due to the simplicity of their design and their production in large volumes, BVMs are very

inexpensive and are frequently used in hospitals and ambulances. They are also readily available in developing countries. Equipped with an air reservoir and a complete valve system, they inherently provide the basic needs required for a ventilator.

The main drawback with BVMs is their manual operation requiring continuous operator engagement to hold the mask on the patient and squeeze the bag. This operating procedure induces fatigue during long operations, and effectively limits the usefulness of these bags to temporary relief. Moreover, an untrained operator can easily damage a patient's lungs by over compression of the bag.

The methodology taken has been, therefore, to design a mechanical device to actuate the BVM. This approach will result in an inexpensive machine providing the basic functionality required by mechanical ventilator standards [2]. In Fig.4, the schematic diagram of the proposed system is illustrated. To automate the operation of Ambu bag, the mechanical system developed to compress the bag must be synchronized with the ideal motion that is maintained by a professional rescuer.

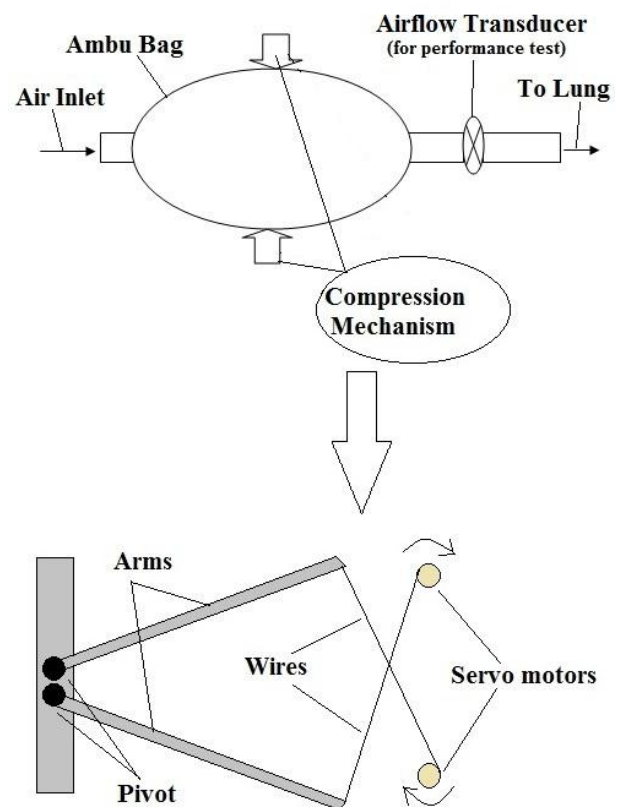


Fig. 4: Schematic diagram of the proposed design

3.3 Components Used

The materials and equipment were selected on the basis of the design assumptions discussed previously. Materials and components needed to construct the prototype are presented in Table 2.

Table 2: Materials and Components used

Component	Rating or Specifications	Quantity
1. Ambu Bag	Ambu SPUR II PVC Disposable Manual Resuscitator	1
2. Servo Motor	MG 996R	2
3. Frame and Arm	Wooden, As designed	1
4. Microcontroller	Arduino MEGA 2560	1
5. Project Board		1
6. LCD Display	LCD 1602	1
7. Battery	9V DC	3
8. Potentiometer	10 K ohm	1
9. Wires and Jumpers		As needed

3.4 The CAD Model

A CAD model of the frame designed is illustrated in Fig.5. The model is developed using SolidWorks 2013. The Ambu bag and other components to deliver power and control the motion is installed on the frame.

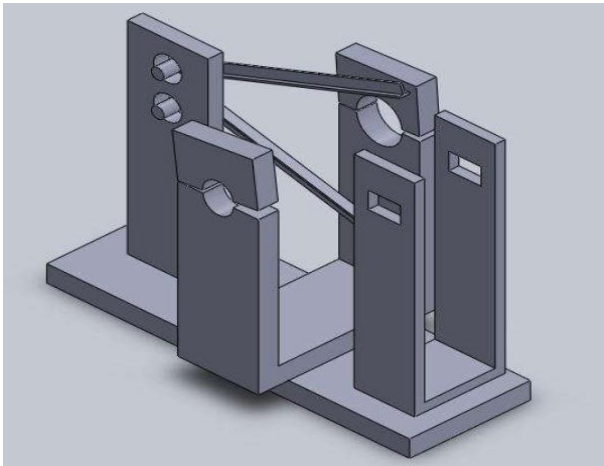


Fig. 5: The CAD Model of the frame

3.5 Dimensions and Calculation of Mechanical Advantage

The dimensions of the frame and the arms are selected as such to be compatible with the physical dimension of the Ambu bag. The length of the arms is 0.13 meters and in uncompressed state the arms start to touch the bag at 0.13 meters from pivot.

The frame and the arms deliver some mechanical advantage to compress the bag.

The length of the total arm = 0.3 meters

The length of the portion from pivot to the bag = .13 meters

Mechanical Advantage, $M.A. = \frac{.3}{.13} = 2.3$

So, the arm will provide a M.A. of 2.3 to compress the bag.

3.6 Control Implementations

The servo motors were coded to be controlled for compressing the BVM in required breath per minute

(BPM) value. The Arduino MEGA 2560 microcontroller was used to control the servo motors. A potentiometer was used to control the BPM. The user can use the knob of the potentiometer to adjust the BPM. A LCD screen was used to display the BPM of the device operating with.

4. Results and Discussion

4.1 The constructed model

The constructed model is illustrated in Fig. 6.

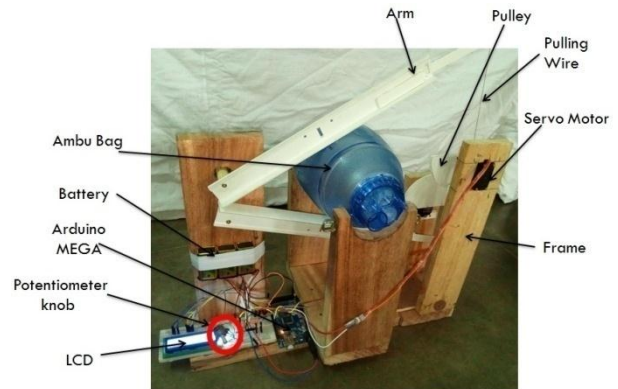


Fig. 6: The constructed model

The model automates the operation of BVM. The principle dimensions are 0.55m*0.15m*0.3m and weight is 2.5 kilograms. Only three 9V DC battery is used to operate the device which runs the device continuously for one hour. So it can easily be carried to emergency spots. The control knob can be used to adjust the BPM required for different patients and for different ventilation settings.

4.2 Performance Test

The developed prototype was tested using Biopac Airflow transducer. The experimental setup is illustrated in Fig. 7. The transducer along with the Biopac Students LabV4.1 software records the lung tidal volume and airflow for every millisecond. In Table 3 data of tidal volume for each second is presented. The lung tidal volume, V_t vs. Time, T graph was obtained for a human subject, for the device and for manual operation. In Fig.8 the graphs are presented.

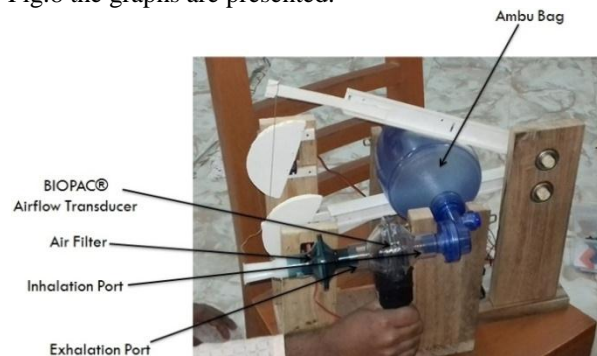


Fig. 7: Experimental setup

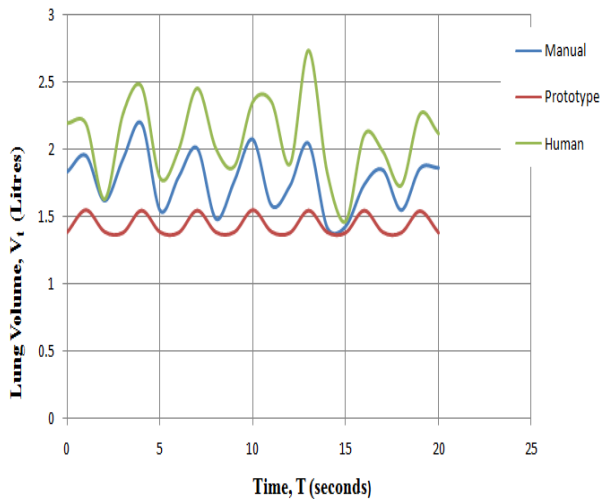


Fig. 8: Tidal volume vs. Time graph

Table 3: Tidal volume for manual operation of the BVM, for constructed prototype and for a human subject

Time (Seconds)	Tidal Volume (Liters)		
	Manual	Prototype	Human
0	1.83384	1.3898316	2.195069
1	1.952133	1.5526239	2.191187
2	1.620012	1.3920472	1.629568
3	1.927859	1.384977	2.264765
4	2.188488	1.5493066	2.466729
5	1.546177	1.3887128	1.787522
6	1.796241	1.384977	1.998717
7	2.005329	1.5493066	2.453686
8	1.486377	1.3887128	2.007818
9	1.765406	1.3898316	1.874575
10	2.071216	1.5526239	2.354588
11	1.584592	1.3920472	2.353157
12	1.730899	1.3843648	1.892085
13	2.040938	1.5489166	2.734889
14	1.421615	1.3886887	1.82856
15	1.429697	1.384977	1.46641
16	1.738724	1.5493066	2.109159
17	1.845986	1.3887128	1.984328
18	1.550398	1.3855922	1.733285
19	1.856896	1.5450019	2.261398
20	1.862131	1.3855323	2.118213

The mean deviation of the tidal volume obtained by the prototype from manual operation was 0.332 Liters or 332 mL and from human subject was 0.542 Liters or 542 mL.

4.3 Cost analysis

The total construction cost of the prototype was approximately 4500 Taka. The details of the cost are presented in Table 4. It should be noted that, if more

powerful motors are used the construction cost will increase.

Table 4: Construction cost of the prototype

Sector	Description	Cost (BDT)
1. Raw materials for frame	Wood, PVC arm, PVC Sheet for pulley etc.	1800
2. Electronic components	Arduino MEGA, Servo motors, LCD, Potentiometer, Wires etc.	1700
3. Labor cost	-	600
4. Transportation and testing	-	400
Total =		4500

It is assumed that, the cost of commercial production will be much lesser than prototype construction. The price range of available portable mechanical ventilators in the market at present varies from \$1000 to \$9600 (Equivalent to 83,124 BDT to 797,990 BDT) [13].

4.4 Uniqueness of the present work

The present work is based on the automation of BVM to construct an emergency portable mechanical ventilator, similar to the work by Husseini et al. [2]. But in present work, mechanical arms and servo motors have been used to actuate the BVM, whereas, Husseini et al. used cam mechanism for the purpose.

The technique used in present work proves to be more effective as it permits programming the required compression pattern, while in cam mechanism the compression pattern is fixed and unchangeable. So, more controllability is achieved by implementing mechanical arms and servomotors to actuate the BVM.

4.5 Discussions

The prototype could not compress the Ambu Bag completely. It compresses the bag partially. The reason behind this might be—

- The motors were not powerful enough to compress the bag.
- The frictions among the mechanical linkages absorbed reasonable power.
- The prototype could not be built precisely due to lack of precise construction tools.

Though, the prototype works as a proof-of-concept in automating the operation of Ambu Bag. In future developments of the prototype these problems may be resolved.

5. Conclusions

The project work proves the concept of automating the Ambu bag or BVM for developing a low cost portable mechanical ventilator. Improvements of the model will lead to a successful and useable portable mechanical ventilator for actual emergency cases where existing sophisticated devices are not present. Although the

device cannot perform like existing devices, its low cost justifies its use in emergency cases.

With three 9 volts battery as power supply the prototype can operate continuously for one hour. With principle dimensions of 0.55m*0.15m*0.3m, and weight 2.5 kilograms, the prototype may easily be transported. It also have a feature to control the breath rate and a LCD display shows the BPM the device is operating with.

6. Future development scopes

Following developments might be implemented for a usable portable mechanical ventilator—

- i. More powerful servo motors can be used.
- ii. DC motors can be used along with DC motor controller to reduce the cost and increase the driving torque.
- iii. More features can be implemented to control various ventilation parameters like tidal volume, inspiration to exhalation time ratio etc.

NOMENCLATURE

<i>BVM</i>	Bag-Valve Mask
<i>ICU</i>	Intensive Care Unit
<i>ET tube</i>	Endotracheal tube
<i>BPM</i>	Breath Per Minute
<i>M.A.</i>	Mechanical Advantage
<i>LCD</i>	Liquid Crystal Display
V_t	Tidal Volume

REFERENCES

- [1] Y. Shi, S. Ren, M. Cai and W. Xu, "Modelling and Simulation of Volume Controlled Mechanical Ventilation System," *Mathematical Problems in Engineering*, vol. 2014, 2014.
- [2] A. M. A. Hussein, H. J. Lee, J. Negrete, S. Powelson, A. Servi, A. Slocum and J. Saukkonen, "Design and Prototyping of a Low-cost Portable Mechanical Ventilator," in *Design of Medical Devices Conference*, Minneapolis, 2010.
- [3] "Medical Ventilator," [Online]. Available: https://en.wikipedia.org/wiki/Medical_ventilator. [Accessed 12 February 2018].
- [4] L. A. Geddes, "The history of artificial respiration," *EEE ENGINEERING IN MEDICINE AND BIOLOGY MAGAZINE*, 2007.
- [5] R. M. Kacmarek, "The Mechanical Ventilator: Past, Present, and Future," *RESPIRATORY CARE*, vol. 56, no. 8, August 2011.
- [6] A. Khoury, S. Hugonnot, J. Cossus, A. D. Luca, T. Desmettre, F. S. Sall and G. Capellier, "From Mouth-to-Mouth to Bag-Valve-Mask Ventilation: Evolution and Characteristics of Actual Devices— A Review of the Literature," *BioMed Research International*, vol. 2014, 27 May 2014.
- [7] S. Fludger and A. Klein, "Portable Ventilators," *Continuing Education in Anaesthesia, Critical*

Care & Pain, vol. 8, no. 6, pp. 199-203, 2008.

- [8] M. Harrison, R. Muckel, C. Freeman, M. Revekant, D. Fenton, D. Zielinski, K. Kong, D. Engell and E. Welch, "PORTABLE EMERGENCY VENTILATOR," in *Multidisciplinary Senior Design Conference, Rochester Institute of Technology*, Rochester, New York, 2013.
- [9] R. L. Vicenzi and T. R. Findlay, "PORTABLE LIGHT WEIGHT COMPLETELY SELF-CONTAINED EMERGENCY SINGLE PATIENT VENTILATOR/RESUSCITATOR". USA Patent 4,905,688, 6 March 1990.
- [10] "Mechanical Ventilation," [Online]. Available: www.thoracic.org. [Accessed 11 April 2017].
- [11] "Bag valve mask," [Online]. Available: https://en.wikipedia.org/wiki/Bag_valve_mask. [Accessed 19 April 2017].
- [12] C. Nickson, "Bag-Valve-Mask (BVM) Ventilation," 6 May 2018. [Online]. Available: <https://lifeinthefastlane.com/cc/bag-mask>. [Accessed 29 October 2018].
- [13] "AliBaba.com," [Online]. Available: <https://www.alibaba.com/showroom/mechanical-ventilation-price.html>. [Accessed 20 February 2018].

2D CFD Analysis of a Straight-bladed Vertical Axis Wind Turbine Using General Grid Interface Method

Farah Aqilah¹, Mazharul Islam^{*1}, Franjo Juretic², Waqar Asrar³

¹ Department of Mechanical and Production Engineering, Ahsanullah University of Science and Technology, 141 & 142, Love Road, Tejgaon Industrial Area, Dhaka-1208, Bangladesh

² Creative Fields Ltd., Dragutina Golika 63, 10000 Zagreb, Croatia

³ Department of Mechanical Engineering, International Islamic University Malaysia, 50728 Kuala Lumpur, Malaysia

ABSTRACT

Due to the ever-increasing need to lower the carbon pollution on earth, a method of generating electricity from kinetically-induced wind turbines is studied. Despite the commonly ventured horizontal axis wind turbine (HAWT), the vertical axis wind turbine (VAWT) has received increasing interest in the past decades due to its simple blade structures and small size. VAWT, specifically Straight-bladed vertical axis wind turbine (SB-VAWT) is one of the simplest types of VAWT for diversified applications. The winning factor against a normal HAWT is that they are relatively small in size and insensitive to incoming wind direction. In this study, the performance analysis of SB-VAWT is performed using the conventional Computational Fluid Dynamic (CFD) Model in two-dimension using the feature General Grid Interface (GGI) which can be found in the open-source CFD software, foam-extend v3.2. A transient solver with second order discretization scheme is used. The commonly used, $k-\omega$ SST turbulence model is applied in this study. The resulting power coefficient, C_p from the 2D CFD analysis is validated against experimental data. From the result, it is shown that the model under-estimate C_p value but closely matched with those from the experiment.

Keywords: Straight-bladed Vertical Axis Wind Turbine, fully turbulent model, $k-\omega$ SST, General Grid Interface, foam-extend.

1. Introduction

Demand for carbon emission reduction is high solely due to the effect of greenhouse gas emission and urbanization. The usage of wind turbines for electricity generation has increased over the years. It is in order to decrease the carbon dioxide pollution concentration in the atmosphere. The wind turbine is fundamentally a device to generate useful energy from kinetic energy stored in wind [1]. Most ventured wind turbines are the Horizontal Axis Wind Turbines (HAWT) which are mostly large in size and have complicated blade design. Due to these drawbacks, the interest in vertical axis wind turbine (VAWT) has emerged over the last couple of years. The advantages of VAWT over HAWT include smaller size, simpler blade design and more insensitivity to wind direction. Straight-bladed VAWT (SB-VAWT) is one of the simplest VAWT designs for diversified application. In the present study, a performance analysis of SB-VAWT is analysed using the conventional Computational Fluid Dynamics (CFD) model performed in two-dimensional domain. It is based on the reasoning that the flow profile around the straight blades can be considered two-dimensional, and allow for considerable savings in computational resources and simulation time.

Compared to the other numerical method such as the vortex model (namely vorticity transport model, VTM), momentum model (namely single streamtube model, the double-multiple streamtube model) or the cascade model[2], CFD provides the most detailed solutions of the Navier-Stokes equations[1].

In this study, the GGI (General Grid Interface) feature of foam-extend v3.2 [3] is used as sliding mesh method to interpolate solutions across boundary interfaces of different mesh regions [4]. It is similar to the Arbitrary Mesh Interface (AMI) [5] and is used for modelling of sliding mesh interfaces in turbomachinery's and SB-VAWT studies [6]. A comparative analysis has been done employing three different sliding mesh techniques namely AMI, GGI and Overset Methods for Dynamic Body Motions in OpenFOAM [7]. From the study, it is seen that the GGI sliding mesh method is marginally faster in parallel performance than other methods. This observation is also consistent among all cases tested. It is also shown that the GGI computations were able to run beyond large number of processors (i.e. 144 processors), whereas AMI computations show problems.

In the present study, a 2D CFD performance analysis of SB-VAWT is carried out in the employing a URANS based $k-\omega$ SST turbulence model with GGI sliding mesh method.

2. 2D CFD Analysis

The next subsection explains the process in detail.

2.1. Solid Modelling

A three-bladed, 2D solid modelling of SB-VAWT is prepared in STL format, developed in Blender. A traditional NACA 4-digit series airfoil, NACA0022 and a turbine diameter of 0.7 m are used in this study in order to match the experimental validation data from

* Corresponding author. Tel.: +88-01709300178

E-mail addresses: icmieekuet@gmail.com

[8]. The computational domain is divided into two parts: the stationary outer domain and the rotating inner domain as shown in Figure 1. The inner rotating domain, with diameter, $D=1\text{m}$, contains all three blades of SB-VAWT and rotates at a steady angular velocity of $\omega = 91.5\text{ rad/s}$ at the tip speed ratio, $\lambda = 4$, while being subjected to a wind velocity, V^∞ of 8 m/s at the inlet. The inner cylindrical rotating domain is connected to the stationary rectangular domain via a sliding mesh interface condition called General Grid Interface (GGI). The side walls of the domain are modelled as no-slip walls to mimic the wind tunnel conditions in ref. [8].

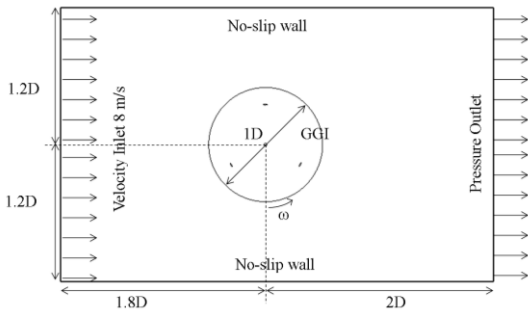


Fig.1 Computational domain of the study case with its boundary condition

2.2. Mesh Generation

An open-source meshing software, cfMesh[9] is used to generate mesh for the 2D simulations. The simulations are based on a structured-type mesh consisting of hexahedral and polyhedral grids. Mesh generations were done independently for stationary and rotating domains. The 2D mesh specifications are as follow:

- Number of cells: 132,546
- Growth rate: 1.2
- Maximum Aspect Ratio (AR): 1362.78
- Maximum mesh non-orthogonality: 53.06
- Maximum skewness: 2.76

Figure 2 shows the mesh of the inner domain. The mesh in the outer stationary domain is coarser compared to that of the rotor because the flow is mostly uniform there and therefore does not cause discretization errors. This reduces the simulation time and computational resources resulting in faster simulation run time. In contrast, the mesh in the inner rotating domain was made fine as it is where most wakes developed from rotor rotations. Mesh sensitivity analysis is carried out by changing the mesh size in the rotating domain only. In the near-blade area, 10 layers were generated to achieve y^+ value of less than 1, and accurately resolve the viscous effects in the boundary layers. As mentioned in ref. [10], 5 to 10 layers are encouraged to capture turbulence properties at the boundary layers. However, over-refining the mesh might results in the increase in round-off errors. Figure 3 and 4 show the mesh treatment of the SB-VAWT blade profiles.

GGI sliding mesh method is employed at the interface between rotating and static domain of SB-VAWT model. Due to the phenomenon of topological mesh changes which occurred typically when meshes of different dynamic motion is in used, a sliding grid interface is needed especially in the SB-VAWT study and other turbomachinery CFD analysis. The work of a sliding interface include detaching and attaching mesh connectivity on all cells and faces touching the sliding surface [11]. Detailed application of GGI feature is available in ref. [11].

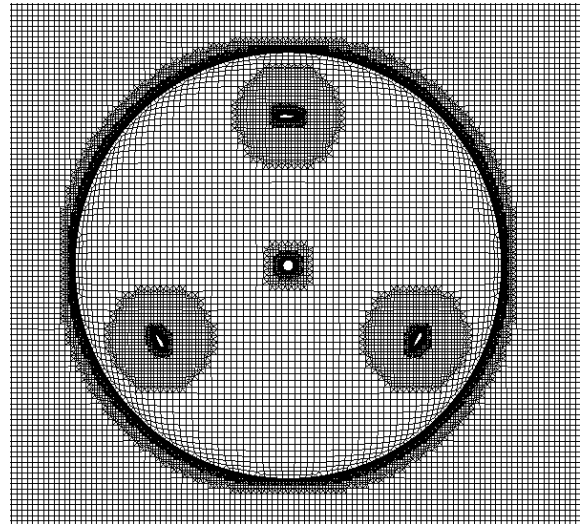


Fig. 2 Computational mesh of the rotating domain

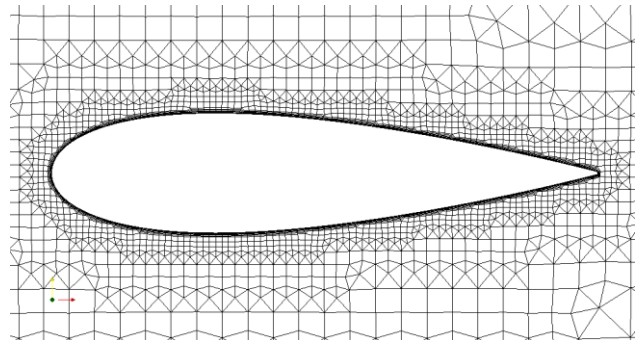


Fig. 3 Mesh around blade

2.3. Flow Solution

In order to solve the problem, the finite volume solver, foam-extend v3.2 is used. Foam-extend is a fork of OpenFOAM. The solution is produced using the Unsteady Reynolds Averaged Navier-Stokes (URANS) in order to take into account the unsteady effects of the simulations. A transient solver namely “pimpleDyMFoam” available in foam-extend is used. “pimpleDyMFoam” solves a dynamic motion fluid flow problem using the PIMPLE algorithm for pressure-linked equation. PIMPLE algorithm is available in OpenFOAM and foam-extend software

which consist of the combination of SIMPLE and PISO algorithms. A second-order linear UPWIND scheme is used to solve divergence parameters (U , k , ω , etc.), while pressure, p is solved using the second order Gauss scheme with linear interpolation scheme.

Turbulence modelling employed in this study is the commonly used k - ω Shear Stress Transport (SST) model by Menter et al including the implementation for wall functions. The header file for the application of the k - ω SST turbulence model in foam-extend is as of ref.

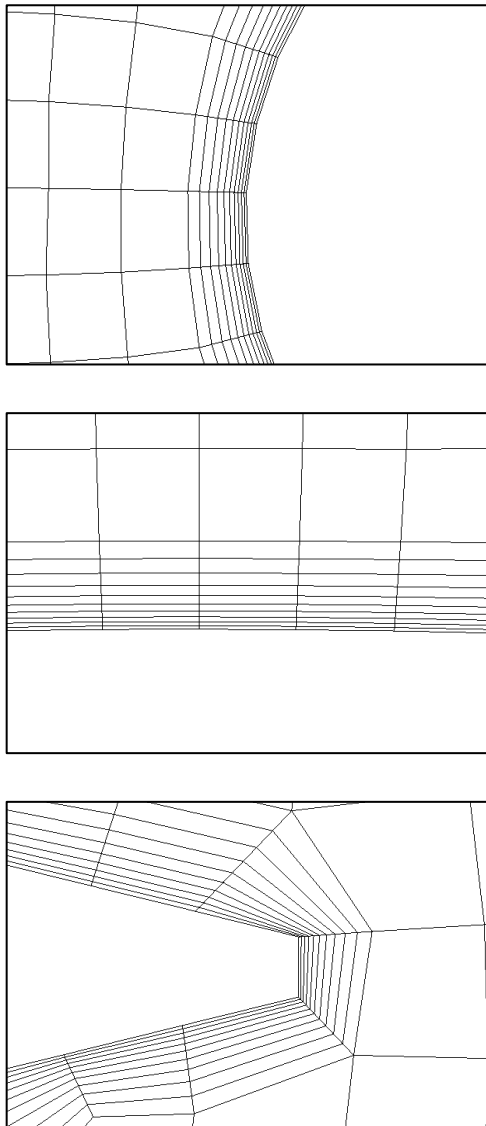


Fig. 4 10 layers mesh refinement at leading edge, middle and trailing edge of the rotor's blades

3. Results and Discussion

The results of the following CFD analysis are presented in this section.

3.1. Mesh Sensitivity Analysis

Mesh sensitivity analysis is important to achieve accurate CFD predictions. All numerical methods suffer from discretization errors such as the numerical dissipation produced by the blades of the rotors. These can be reduced by refining the computational grid. In practice, the large number of grids is often necessary to model the flow in the wake of the blade of SB-VAWT [1]. However, over-refining the mesh may result in the increase of round-off errors [10]. Thus, mesh sensitivity analysis is carried out to determine the mesh size resulting in mesh independent solution and consequently produces reliable results. Three different mesh refinement classes are prepared namely Coarse (M1), Medium (M2) and Fine (M3). The mesh consists of polyhedral and hexahedral cell generated using the open-source software, cfMesh. Table 1 show the quality metrics for each mesh refinements.

Table 1. Mesh descriptions for 2D CFD mesh sensitivity analysis

	Coarse (M1)	Medium (M2)	Fine (M3)
Number of cells	120 477	122 730	132 546
Growth Rate	1.2	1.2	1.2
Maximum Aspect Ratio (AR)	488.8	611.1	1362.7
Maximum Non-orthogonality	63.2	69.5	53.0
Maximum Skewness	2.4	2.7	2.7

The simulation on all three meshes were performed using Shear Stress Transport (SST) k - ω turbulence model and the same second order discretization scheme described above. In addition, all three cases were run using the same initial boundary conditions for one revolution of the rotor mesh. The resulting CP value from the following mesh refinements are recorded as in Figure 5.

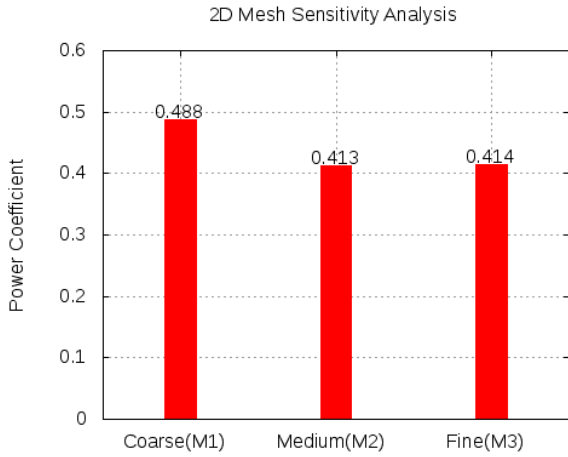


Fig. 5 C_p comparison for the three classes of mesh refinements

From the Figure 5, the mesh independency is achieved and the resulting C_p does not change significantly with further mesh refinement. Fine mesh (M3) is used for the final 2D analysis.

3.1. Experimental Validation

As mentioned before, the unsteady effect of the simulation is modelled by employing the URANS method and solving using a transient solver. Only one case of tip speed ratio, $\lambda = 4$ is carried out in this study. The simulation is ensured to reach convergence before calculating its C_p value. The periodic convergence is observed to be achieved after the 3rd revolutions as shown from the blade torque ripple in Figure 6. Tolerances for all parameters are set to 1×10^{-7} .

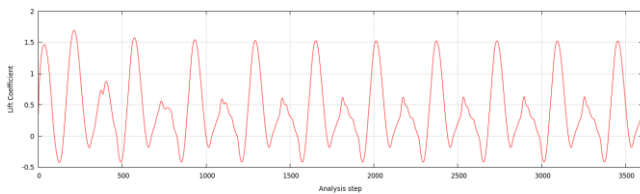


Fig. 6 Blade torque ripple for 10 revolutions

The power coefficient is then compared with those in . Figure 7 shows the final result of the power coefficient. The predictions of C_p from the CFD simulations have shown to under-estimate the experimental results by 27% due to errors. C_p value for a whole 10 revolutions of the simulation is 0.21 at $\lambda = 4$. This may happen due to the usage of a fully-turbulent model, $k-\omega$ SST.

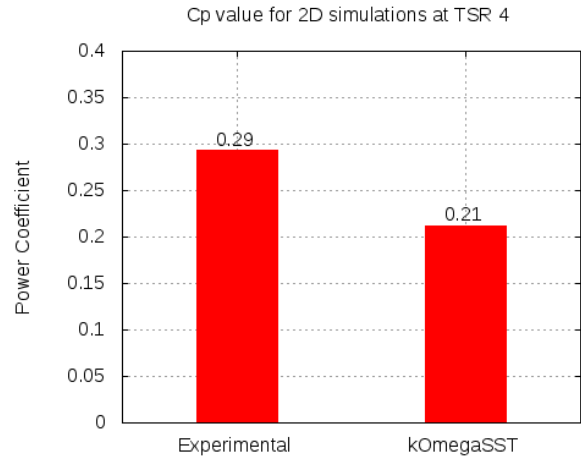


Fig. 7 C_p value for 2D simulations at $TSR = 4$

3.3. Contour Plot

Post-processing of the results is performed by using ParaView, the software used for generating of contour plots and gnuPlot to generate graphs. Figure 8 shows the blade torque at one revolution after convergence at $\lambda = 4$. The curve matched with good agreement to the curve in ref. . It can be seen that the highest predicted value of blade torque, T_b is in the upwind region approximately at azimuthal angle, $\theta = 80^\circ$ where the blade is subjected to flow of wind. At θ more than 180° , the T_b is slightly distorted due to wake disruption from other blades. Figure 9 shows the velocity field contour plot where wake resulting from blades occurred at the downwind region thus developed a low T_b . The phenomenon, denoted by the letter A, in the Figure 9 shows a discrepancy where simulations predict a low speed wake resulting in wake separation when blade enters the downwind region.

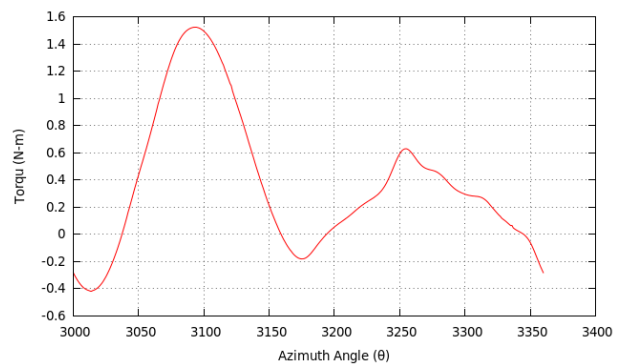


Fig. 8 Blade torque for 1 revolution at the end of 10th revolution versus azimuth angle, θ°

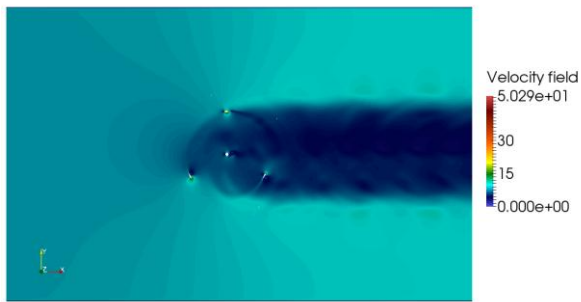


Fig. 9 Velocity field contour plot at the end of 10th revolution

Figure 10 shows the predicted vorticity contours at $\lambda = 4$. The blade enters the stall vortices created by other blade rotors, which is only detaching at almost when entering the downwind region. The shedding around the turbine show strong ripple at the downwind region pass central column where the developed vortices disrupt the performance of the rotors. Although the simulations predict a good agreement results when compared to experimental data in ref., the usage of transitional turbulence model instead of a fully-turbulent model is encouraged. From ref. , the author emphasize the importance of transitional turbulence model where the flow structures such as vortices and wake are highly mixed, thus prevent strong ripples to occur at the rotor area which is significantly similar to experimental measurements.

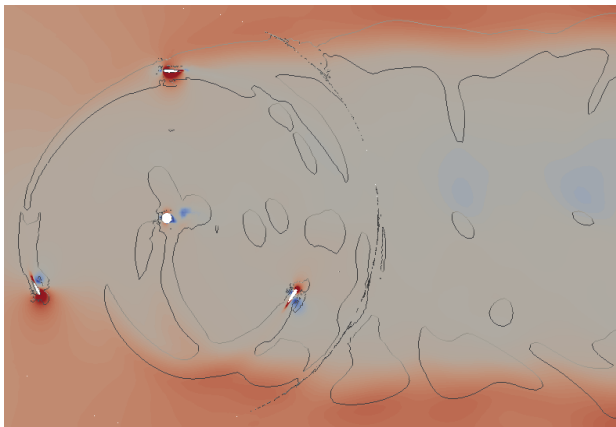


Fig. 10 Vorticity contours at TSR = 4 using k- ω SST model

4. Conclusions

Two-dimensional CFD model has been used to perform the flow analysis of a three-bladed SB-VAWT in this study. GGI has been applied at the interface between rotating and stationary domains. The resulting power

coefficient from the analysis agrees closely with the experimental data at the same operating conditions. The accuracy of flow predictions can be further improved by using the transitional turbulence model instead of the fully-turbulent model used in this study. The studied flow is in the transition regime where the tip speed ratio and the Reynolds Number are relatively low. Furthermore, the transition turbulence model namely the LCTM (γ - $Re_{\theta t}$) and LKE (k - k_L - ω) model handle the turbulence closure differently compared to the k - ω SST model.

Acknowledgements

Preparation of the article was supported by the Research Initiative Grant Scheme (RIGS) by the International Islamic University Malaysia (IIUM) funded by the Ministry of Higher Education (MOHE) Malaysia.

REFERENCES

- [1] Scheurich F.; and Brown R. E. (2011). The effect of dynamic stall on the aerodynamics of vertical-axis wind turbines. *29th AIAA Applied Aerodynamics Conference 2011*
- [2] Islam M.; Ting D.S. K.; Fartaj A. (2008). Aerodynamic models for Darrieus-type straight-bladed vertical axis wind turbines. *Renewable and Sustainable Energy Reviews*, 12, 1087–1109.
- [3] OpenFOAM (2002). The OpenFOAM® Extend Project. Retrieved December 5, 2015, from <http://www.extend-project.de/>.
- [4] Beaudoin M.; Jasak H. (2008). Development of a Generalized Grid Interface for Turbomachinery simulations with OpenFOAM. *Open Source CFD International Conference*.
- [5] Beatty S. J.; Mishra V.; Beatty S.; Buckham B.; Oshkai P.; and Crawford C. (2015). Application of an Arbitrary Mesh Interface for CFD Simulation of an Oscillating Wave Energy Converter Application of an Arbitrary Mesh Interface for CFD Simulation of an Oscillating Wave Energy Converter.
- [6] Lloyd T. P. (2011). The OpenFOAM Generalised Grid Interface. *University of Southampton* Retrieved March 30, 2017, from <https://cmg.soton.ac.uk/community/attachments/107/ggiPresentationLloydAug11.pdf>.
- [7] Chandar D.; and Gopalan H. (2016). Comparative Analysis of the Arbitrary Mesh Interface(AMI) and Overset Methods for Dynamic Body Motions in OpenFOAM. *46th AIAA Fluid Dyn. Conf.*, June, 1–12.
- [8] Danao L. A. (2012). The Influence of Unsteady Wind on the Performance and Aerodynamics of

Vertical Axis Wind Turbines. phdthesis,
University of Sheffield, UK.

- [9] cfMesh (2002). cfMesh: Advance Meshing Tool.
Retrieved June 25, 2016 from <http://cfmesh.com/>
- [10] Tu J.; Yeoh G. H.; and Liu C. (2013)
*Computational Fluid Dynamics - A Practical
Approach (2nd Edition)*. Elsevier.
- [11] Jasak H. (2009). General Grid Interface:
Theoretical Basis and Implementation,” *Wikki
Ltd, UK*. Retrieved March 30, 2017, from
[http://powerlab.fsb.hr/ped/kturbo/OpenFOAM/Su
mmerSchool2009/lectures/TurboGGL.pdf](http://powerlab.fsb.hr/ped/kturbo/OpenFOAM/Su
mmerSchool2009/lectures/TurboGGL.pdf).

Numerical Analysis of Heat Transfer for Double Pipe Heat Exchanger with and Without Fin

Jamshedul Islam*, Al Aman, and Mihir Ranjan Halder

Department of Mechanical Engineering, Khulna University of Engineering & Technology, Khulna-9203, BANGLADESH

ABSTRACT

In this paper, the heat transfer enhancement analyzed using ANSYS FLUENT both in finned and unfinned condition. The numerical analysis went through different inlet velocities. As the cold fluid passed through the outer pipe surrounding the hot fluid in inner pipe, there was temperature fall in hot fluid. And that rate was found greater in finned condition comparing with unfinned one. Optimum number of fins were determined by analyzing the heat transfer through numerical computation. The effectiveness was found to reduce with the increase in flow velocity. For extended surface area in finned setup the overall heat transfer coefficient reduced. The reducing rate was found 28.88% for counter flow and 28.90% for parallel flow, for the flow velocity 0.001 m/s. The LMTD values were found 30.06 for parallel, 28.91 for counter flow in finned heat exchanger and 45.38 for parallel, 43.53 for counter flow in unfinned heat exchanger.

Keywords: Fin, Effectiveness, Parallel and Counter flow.

1. Introduction

The heat exchanger is a device which facilitates heat transfer between two medium of hot and cold without mixing both the medium since both mediums are separated with a solid wall generally. The temperature gradient, or the differences in temperature, facilitate this transfer of heat. In recent time, there are versatile use of different types of heat exchanger in daily life. Steam power plants, chemical processing plants, building heating, air conditioning, refrigerators, car radiators, radiators, for space vehicles etc. are well known sectors of use of heat exchanger. The main purpose of using a heat exchanger is to get an efficient method of transferring heat from one fluid to another. The heat transfer occurs by mainly three modes which are: Conduction, Convection and Radiation. Conduction takes place when the heat flows from a high temperature fluid to a low temperature fluid through the surrounding solid walls. Convection is the mode of heat transfer in which the heat transfer takes place between the adjacent layers of fluid. Convection mainly occurs in fluids and plays a major role in the performance of heat exchanger. Radiation does not play a significant role in the heat transfer in heat exchanger and hence it is neglected.

Many researches had been worked to find the best way to heat transfer in heat exchanger. Heat transfer enhanced in a heat exchanger tube by installing fins on the outer surface of hot water tube [1]. The results were compared between the two designs for counter flow. According to results, it concluded that in case of fin using, effectiveness also increases. The reason behind maximum effectiveness was that due to use of fins, turbulence was increased as they allow more mixing of fluid layers and resulted in increase of heat transfer through the heat exchanger tube. But there was no concern about the mass flow rate change in the cold fluid region.

A parallel flow heat exchanger and a corresponding ribbed tube heat exchanger is modeled and numerically

analyzed. While investigating it was found that the effectiveness of the ribbed heat exchanger is more than that of simple heat exchanger [2]. Due to the ribbed helical shape of the tube the flow of fluid is not parallel but in swirls and there also increase in surface, which increases turbulence and thereby increasing the effectiveness.

Heat transfer coefficient of heat exchanger increasing with the logarithmic mean temperature difference, the mass flow of the shell side, and the mass flow of the tube side. Also shows that the heat transfer coefficient of tube side is higher usually than the shell side [3].

Velocity distribution is minimum to enhance the heat transfer rate. From the temperature path lines the temperature distribution is in the maximum scale range, which shows the perfect heat transfer rate [4].

As the fin thickness increases the value of heat transfer is increasing. For copper, heat transfer is maximum value when compared to other materials and steel is having the least value of heat transfer [5].

CFD analysis of different fluids and different pipe materials were investigated on parallel and counter flow in concentric tube heat exchanger [6]. The first stage was a modified Graetz problem model where velocity and temperature profiles were analyzed for fluid flow in a tube of 1.0 m in length. Both turbulent and laminar flow was considered for the analysis. These findings proved it is more important for engineers and developers to focus for the best choosing materials. But there was no concern for the improvement of heat exchange.

Experimental investigation of heat transfer and friction factor characteristics with different flow rates was done by means of CFD simulation. The work is conducted by the double pipe heat exchanger with counter flow direction. The data acquire from the plain tube double pipe heat exchanger with the CFD simulation and ensured the validation results. The plain tube with dissimilar mass flow rates were also studied for

* Corresponding author. Tel.: +88-01843145165

E-mail addresses: jamshedul.i.tusher@gmail.com

comparison assessment. A commercial CFD package, Ansys CFD analysis was used in this study and 3D models of double pipe heat exchanger was generated in this simulation [7].

2. Methodology

2.1 Governing Equations

The continuity equation or the equation for conservation of mass can be written as:

$$\frac{\partial \rho}{\partial t} + \frac{\partial \rho U_1}{\partial x_1} + \frac{\partial \rho U_2}{\partial x_2} + \frac{\partial \rho U_3}{\partial x_3} = 0 \quad (1)$$

The momentum equation in tensor notation for a Newtonian fluid can be written as:

$$\frac{\partial U_i}{\partial t} + U_j \frac{\partial U_i}{\partial x_j} = \frac{1}{\rho} \frac{\partial P}{\partial x_i} + \nu \frac{\partial}{\partial x_j} \left(\frac{\partial U_i}{\partial x_j} + \frac{\partial U_j}{\partial x_i} \right) \quad (2)$$

The total energy can be defined as the sum of all these energies:

$$h = h_m + h_T + h_c + \phi \quad (3)$$

The standard k-epsilon model was chosen as the turbulence modelling. The first transported variable is turbulent kinetic energy, k. The second transported variable in this case is the turbulent dissipation, ϵ . Effectiveness may be defined as:

$$\epsilon' = \frac{Q}{Q_{\max}} \quad (4)$$

Here, Q =Actual heat transfer rate

Q_{\max} =Maximum possible heat

Transfer rate:

$$Q = m_h c_{ph} (T_{h,in} - T_{h,out}) = m_c c_{pc} (T_{c,out} - T_{c,in}) \quad (5)$$

$$Q_{\max} = (m c_p)_{\min} (T_{h,in} - T_{c,in}) \quad (6)$$

As both hot and cold fluid are water liquid:

$$m_h c_{ph} = m_c c_{pc} = (m c_p)_{\min} = (m c_p)_{\max} \quad (7)$$

$$\epsilon' = \frac{T_{h,in} - T_{h,out}}{T_{h,in} - T_{c,in}} \quad (8)$$

Again overall heat transfer coefficient:

$$U' = \frac{Q}{A \Delta T_{\ln}} \quad (9)$$

Here, Log mean effective temperature:

$$\Delta T_{\ln} = \frac{\Delta T_o - \Delta T_L}{\ln \left(\frac{\Delta T_o}{\Delta T_L} \right)} \quad (10)$$

2.2 Geometrical Modelling

Heat exchanger geometry had been generated in the ANSYS workbench design modeler. Both heat exchangers: with and without fin was designed. In this CFD analysis, two heat exchangers had been simulated with different types of flow i.e. parallel and counter flow.

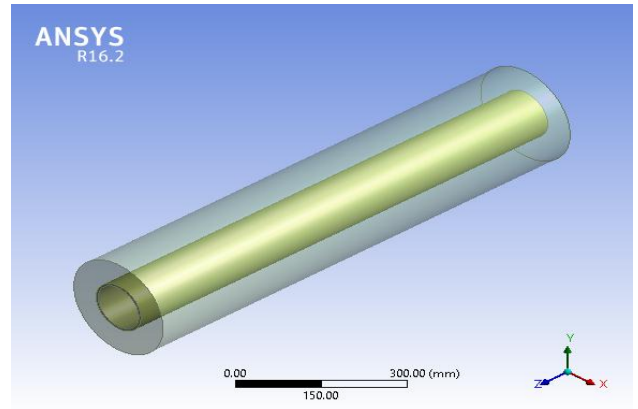


Fig.1 Geometrical model of heat exchanger without fin

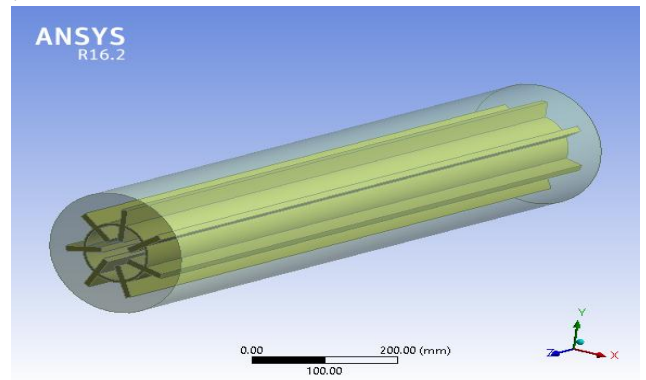


Fig.2 Geometrical model of heat exchanger with fins.

Table 1 Dimensions of both heat exchanger.

No.	Description	Without Fin	With fin
1	Length of heat exchanger	1000 mm	1000 mm
2	Inner pipe diameter	100 mm	100 mm
3	Outer pipe	220 mm	220 mm

diameter			
4	Tube pitch	5 mm	5 mm
6	Height of the fins		60 mm
7	Width of the fins		10 mm

2.3 Software Validation

For software validation, a paper's data and setup considered from a recognized journal [6]. The same data setup were run through the present software for transformer oil and water. Comparing the results there was no major difference between the two software's outputs. The temperature deviation between the two, were found ranging from 0.166% to 0.045% for transfer oil throughout the pipe length. And for water it ranged from 0.169% to 0% throughout the pipe length. Hence, it proves the validity of the present software.

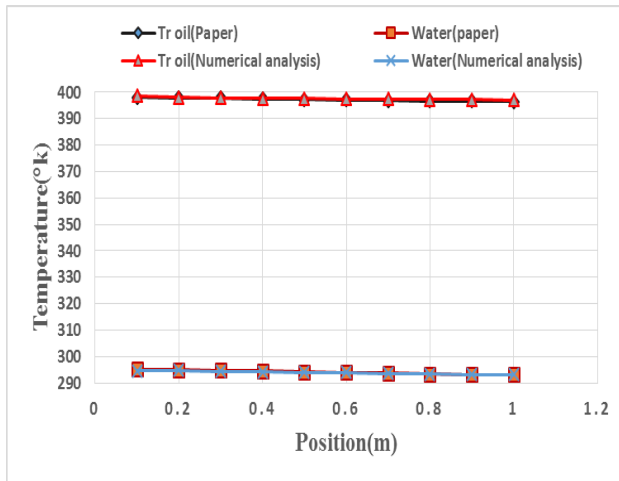


Fig.3 Turbulent counter flow heat exchanger temperature change.

3. Results and Discussion

In simple double pipe heat exchangers there occurs pressure drops, temperature distribution and velocity distribution throughout the pipes as the two fluids flows through the pipe. For different inlet velocities i.e. different mass flow rate there is various heat transfer phenomena occurs for the same arrangement of heat exchanger. Parallel and counter flow systems gives different types of heat transfer results.

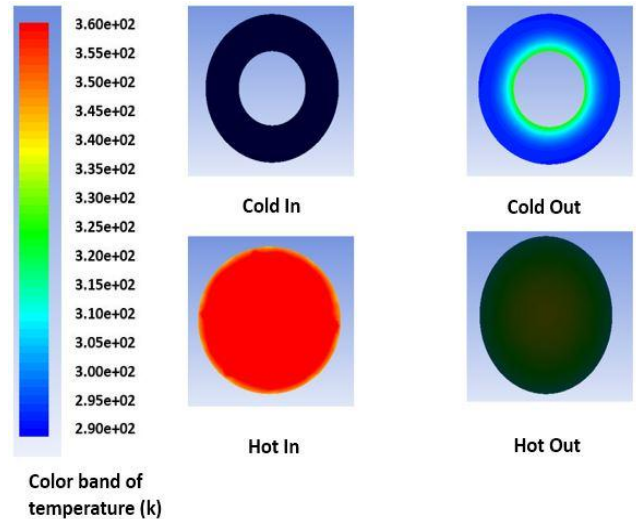


Fig.4 Temperature contour: counter flow (without fin).

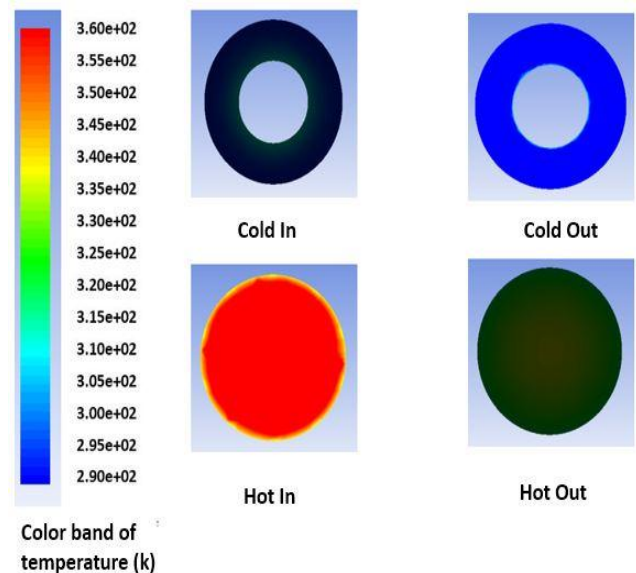


Fig.5 Temperature contour: parallel flow (without fin).

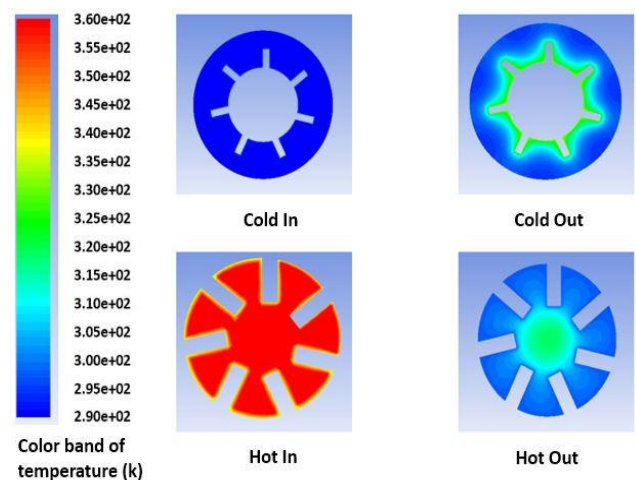


Fig.6 Temperature contour: counter flow (with fin).

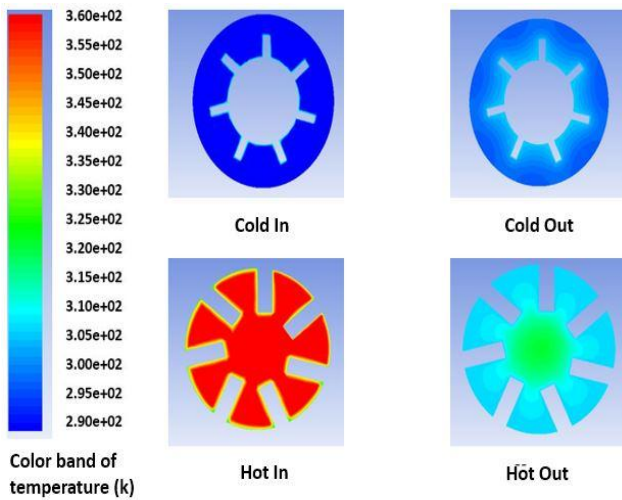


Fig.7 Temperature contour: parallel flow (with fin).

Above figures indicates the phenomena that the hot fluid temperature falling till the outlet section and cold fluid temperature rising consequently for heat transfer from hot to cold region. And the rate is greater in finned pipe as extended surfaces facilitates the heat transfer. For velocity 0.001 m/s:

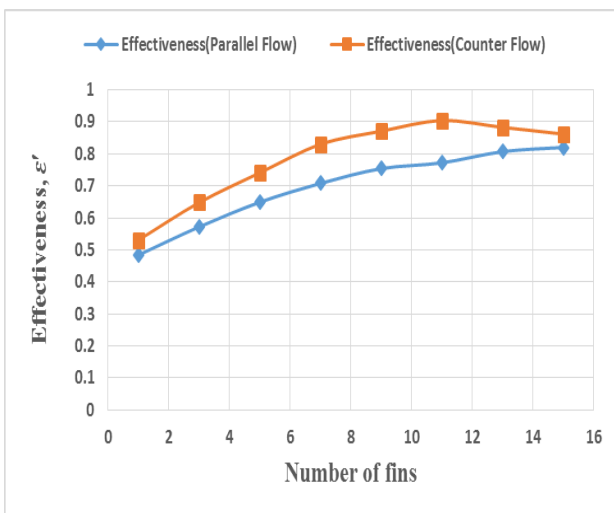


Fig.8 Effectiveness vs. Numbers of fin.

From the graph it is visible that the effectiveness gradually increases with the increased number of fins used. But it is not desirable to fill the whole pipe with fins so that less fluid flows. From the graph it is visible that the effectiveness rate increases at high rate till 7 number of fins and then gradually decreases, so the optimum number of fins considered as 7 fins. For velocity 0.001 m/s:

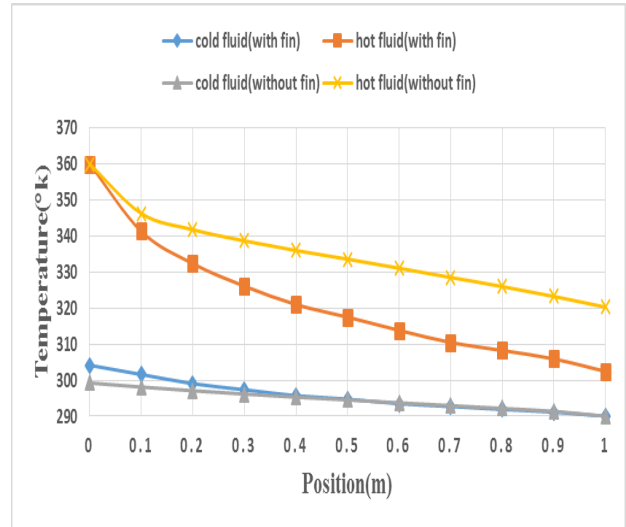


Fig.9 Temperature vs. Position for counter flow.

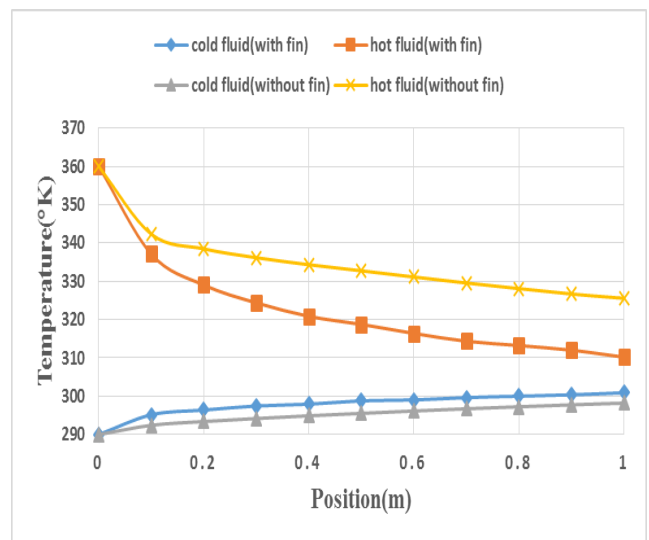


Fig.10 Temperature vs. Position for parallel flow.

From the above figures, it is visible that finned curve falling degree is greater than unfinned for hot fluid and rising degree is greater in cold fluid in finned heat exchanger. So the heat transfer is faster in finned heat exchanger than unfinned heat exchanger for both parallel and counter flow types.

Table 2 Effectiveness of double pipe heat exchanger with fins.

Inlet velocity ($m s^{-1}$)	Effectiveness (ϵ)			
	With Fin		Without Fin	
	Parallel Flow	Counter Flow	Parallel Flow	Counter Flow
0.001	0.711	0.822	0.492	0.567
0.005	0.498	0.542	0.283	0.305
0.01	0.376	0.396	0.195	0.204
0.05	0.138	0.141	0.067	0.068

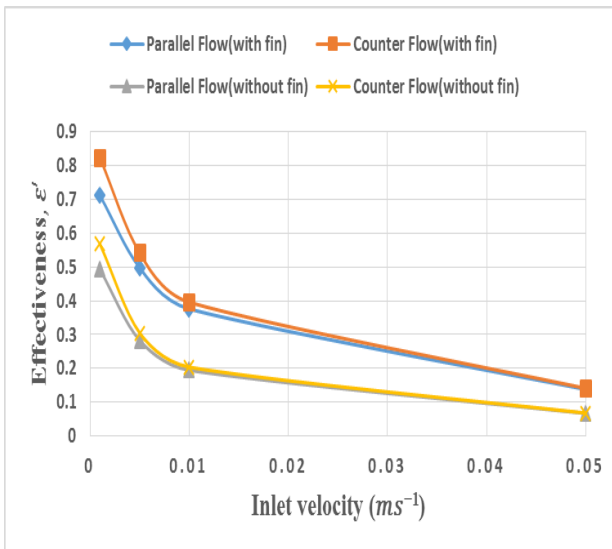


Fig.11 Effectiveness vs. Inlet velocity.

The effectiveness of double pipe heat exchanger with fin is greater than the effectiveness without fin. The highest effectiveness of heat exchanger is achieved in finned heat exchanger for counter flow setup and lowest is achieved in heat exchanger without fin for parallel flow heat exchanger setup for the same velocity.

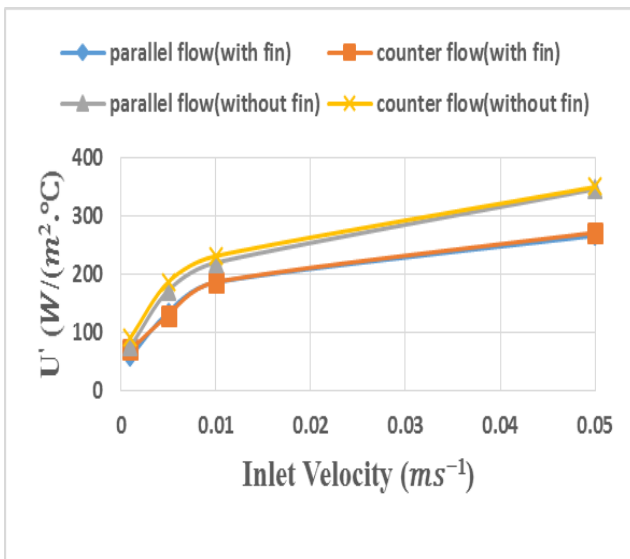


Fig.12 Overall heat transfer coefficient vs. Inlet velocity.

For both parallel and counter flow types the overall heat transfer coefficient is increasing with velocity. The log mean effective temperature is low for lower velocities. Thus the overall heat transfer coefficient is increasing with higher velocities. The heat transfer rate is greater in counter flow than the parallel flow. So the overall heat transfer coefficient is slightly greater in counter flow.

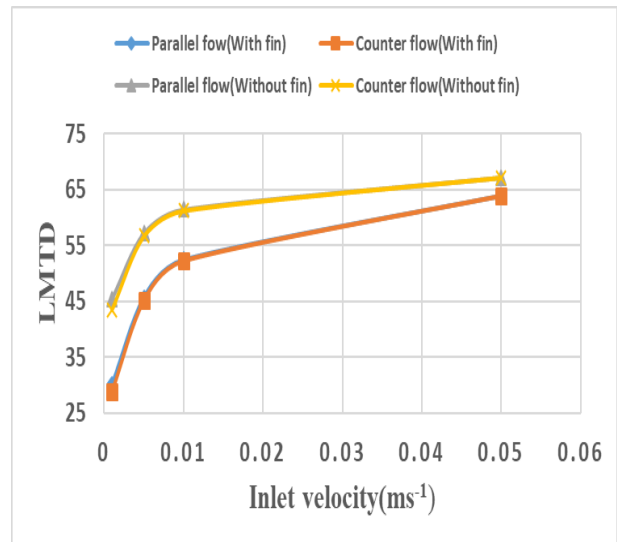


Fig.13 LMTD vs. Inlet velocity.

4. Conclusion

For double pipe heat exchanger flow characteristics and heat transfer was analyzed with and without fin for parallel and counter flow type through the numerical computation using ANSYS FLUENT16.2. The analysis was done on basis of different inlet velocities. The major findings are:

- Seven rectangular fins were considered as the optimum number of fins, as the effectiveness flux was maximum at that arrangement. The effectiveness rising rate was about 14.35% for seven number of fins, which was the maximum rate.
- With the rise in velocity, the outlet temperature difference decreased. 10.92 °K for parallel and 12.45 °K for counter flow found in finned heat exchanger while 8.22 °K for parallel and 9.24 °K for counter flow analyzed for unfinned one, for velocity 0.001 m/s. Thus the effectiveness also reduced with the increase in velocity.
- The LMTD for unfinned setup was greater than that of the finned setup for same directional flow or counter directional flow depending on outlet temperature difference. The overall heat transfer coefficient was reducing in finned for enhanced surface area. Reducing rate was 28.88% for counter flow and 28.90% for parallel flow, for the velocity 0.001 m/s.
- Finally it can be said that the finned arrangement obviously reduces the hot fluid temperature than that of simple double pipe heat exchanger without fin. So when the purpose is to reduce the hot outlet temperature, then finned heat exchanger may be used.

NOMENCLATURE

- A : Area (m^2)
 C_p, C_v : Heat capacity at constant pressure, volume
($J/kg\cdot K$)
 h : Heat transfer coefficient ($W/m^2\cdot K$)
 P : Pressure (Pa)
 U : Free-stream velocity (m/s)
 T : Temperature (K)
 t : Time (s)
 ω : Specific dissipation rate (s^{-1})
 ν : Kinematic viscosity (m^2/s)
 ε' : Effectiveness
 U' : Overall heat transfer coefficient ($W/m^2\cdot ^\circ C$)

REFERENCES

- [1] Nice Thomachan, Anoop.K.S, Deepak.C.S, Eldhose.P.Kuriakose, Habeeb Rahman.K.K, Karthik.K.V, CFD Analysis of Tube in Tube Heat Exchanger with Fins, *International Research Journal of Engineering and Technology (IRJET)*, Volume: 03 Issue: 04 | Apr-2016; e-ISSN: 2395 0056; p-ISSN: 2395-0072.
- [2] Melvinraj C R, Vishal Varghese C, Vicky Wilson, Thomas Jerry Thazhatha, Mithun K, Simon J Kakkassery, Comparative Study of Heat Exchangers Using CFD, *Melvinraj C R et al Int. Journal of Engineering Research and Applications* ISSN : 2248-9622, Vol. 4, Issue 5(Version 4), May 2014, pp.118-120.
- [3] Zheng Hui-fan, Bai-jing, Wei-jing, and Huang Lanyu, Numerical Simulation about Heat Transfer Coefficient for the Double Pipe Heat Exchangers, *Applied Mechanics and Materials* Vols 71-78 (2011) pp 2577-2580 © (2011) *Trans Tech Publications, Switzerland*.
- [4] Jibin Johnson, Abdul Anzar V M, Abith Shani, Harif Rahiman P, Hashmi Hameed T S, Nithin V S, CFD Analysis of Double Pipe Heat Exchanger, *International Journal of Science, Engineering and Technology Research (IJSETR)*, Volume 4, Issue 5, May 2015.
- [5] SK.M.Z.M.Saqheeb Ali, K.Mohan Krishna, S.D.V.V.S.Bhimesh Reddy, SK.R.S.M.Ali, Thermal Analysis of Double Pipe Heat Exchanger by Changing the Materials Using CFD, *International Journal of Engineering Trends and Technology (IJETT)* – Volume 26 Number 2- August 2015.
- [6] D.Bhanuchandrarao, M.Ashok chakravarthy, Dr. Y. Krishna, Dr. V .V. Subba Rao, T.Hari Krishna, CFD Analysis and Performance of Parallel and Counter Flow in Concentric Tube Heat Exchangers, *International Journal of Engineering Research & Technology (IJERT)*; Vol. 2 Issue 11, November – 2013; ISSN: 2278-0181.
- [7] K. Sivakumar, Dr. K. Rajan, S. Murali, S. Prakash, V. Thanigaivel, T.Suryakumar, Experimental Analysis of Heat Transfer and Friction Factor for Counter Flow Heat Exchanger, *International Journal of Technology Enhancements and Emerging Engineering Research*, Vol. 3, ISSUE 04 109 ISSN 2347-4289.

Comparative Numerical Analysis of Heat Transfer between Nonporous and Porous Cylindrical Fins

Farida Ahmed Koly*, Abu Raihan Ibna Ali, Moham Ed Abdur Razzaq, and Mostafizur Rahman

Dept. of Mechanical Engineering, Chittagong University of Engineering & Technology, Chittagong-4349, BANGLADESH

ABSTRACT

Fin is the easiest and cheapest way in enhancing heat transfer of all other methods like increasing fluid velocity, ionizing fluids, using additives, causing vibration etc. It has a lot of applications in the growing number of engineering disciplines. The main purpose of this paper is to enhance heat transfer of cylindrical fin by perforated and axial holes which increases surface area but decreases material cost. Finding out the proper length of the fin is another goal of this paper which also reduces fin size and material cost. Steady state thermal simulation has been done using ANSYS 17. An attempt is made to find out temperature distribution by varying geometry, materials. Investigations show that porous cylindrical fin drops maximum temperature and hence maximum heat transfer occurs because of the increasing ratio of perimeter to cross sectional area. Porous cylindrical fin also has light mass with low cost. And proper length of cylindrical fin increases with the increase in diameter.

Keywords: *Thermal Analysis, Heat Transfer, Porous Fin, Proper Length*

1. Introduction

Growing number of engineering disciplines are concerned with rapid heat transfer rate. In this respect, fins are used to increase the heat transfer rate. Fins are widely used in car radiators, electronic components, heat exchanger, internal combustion engine etc. The study of heat transfer of fin comprises of three factors. One factor is conduction of heat through the fin. The other considers how fin exchanges heat by convection with the surrounding environment. And the third factor is radiation. Heat transfer by conduction can be improved by using high conductivity materials. On the other hand, heat transfer by convection depends on the heat transfer coefficient, surface area, and temperature difference. Heat transfer rate can be increased by increasing heat transfer coefficient by increasing the velocity of the fluid, inserting materials, causing vibration, ionizing the fluid, using additives. But these methods are either costly or have some negative effects on the material. So, the easiest way is to increase the surface area by using light material but low cost.

Fins of different size, shape, and material possess different fin efficiencies. Cylindrical fin has excellent fin efficiency which can be increased by perforated and axial holes. These holes add extra surface area which increase perimeter to cross sectional area and decrease material cost. Perforated holes create a variable cross-sectional area along fin length. It also increases fin effectiveness. S. Kiwan and Al-Nimr [1] suggested altering conventional fin with a porous fin for the improvement of heat transfer. U. V. Awasarmol et al [2] performed an experiment on the perforated rectangular fin. He showed that heat transfer gradually increases with the increase in perforation size. D. H. Lee et al [3]

found that heat transfer can be improved with perforated circular holes in the finned tube. D. Bhanja et al [4] noticed an increase in heat transfer by selecting porous medium condition in the T shaped fin. S. Y. Kim et al [5] investigated porous fin in a plate-fin heat exchanger and found that heat transfer is more in porous fins with low permeability and low porosity. Thermal analysis was performed by M.T. Darvishi et al [6] for heat transfer in fully wet porous fins. Their investigations showed that heat flow increases for high permeability of the medium. They also showed that heat flow increases when the buoyancy effect induced in the fluid is strong. M. Liu et al [7] experimentally investigated pressure drop and heat transfer in a copper micro square pin fin heat sink. They observed that pressure drop and Nusselt number of the system increases with the increase in Reynolds number. S. Pashah et al [8] performed a numerical solution for wet hyperbolic annular fins in wet operating conditions. Heat transfer of wavy fins was analyzed by A.A. Khaled [9]. Waqar Ahmed Khan [10] performed numerical simulations for a single circular cylinder and in-line pin fin heat sink and developed average heat transfer coefficient.

Heat transfer can also be enhanced by Nano coating on fin surface which has an excellent effect on the rate of heat transfer. Terry J. Hendricks et al, [11] had made a conclusion that Nano coating of ZnO₂ over aluminum increases heat transfer ten times.

After a certain length, it does not contribute so much in enhancing heat transfer rate rather increases cost and size of fin. So, finding out proper length of the fin is also important. J. D. Forero et al, [12] proved that proper length of rectangular fin increases with the increase in fin thickness of fin. A. Aziz [13] has

* Corresponding author. Tel.: +88-016833941218
E-mail addresses: faridakoly@gmail.com

provided expressions for optimum diameter and fin height for the cylindrical fin. S. Kiwan [14] found that after certain length there is no improvement in fin performance for the increase in fin length.

Analysis of heat transfer in extended surface involves solving second order differential equations. The solution is still easy for the typical simple geometrical fin. When fin involves complex shape with the variable cross-sectional area, analytical solutions become troublesome. In this case, simulation is the best way for analysis.

In the present work it is intend to see the comparative heat transfer rate of new type of cylindrical fin having axial and perforated holes. Also, impact of proper length with the increase in diameter of the cylindrical fin was also investigated. Mass of fins with axial and perforated holes is compared.

Here, five different models of cylindrical fins were modeled by SolidWorks 2016 and steady-state thermal simulation had been performed by ANSYS 17. An investigation was performed to observe temperature distribution and total heat flux contour.

2. Modeling

Four different types of cylindrical pin fins were designed using SolidWorks 2016.

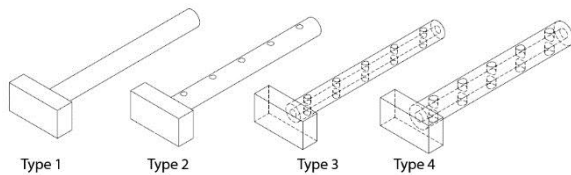


Fig. 1 Cylindrical Fins with and without perforated and axial hole

Type 1, type 2, type 3 fins are used to observe the heat transfer rate by adding perforated holes and axial holes. Type 4 fin is used to observe proper length with the increase in diameter.

Table 1 Specifications of Fins (holes).

Fin	Hole	Number of perforated holes
Type 1	No hole	0
Type 2	<ul style="list-style-type: none"> • Perforated holes • No axial hole 	5
Type 3	<ul style="list-style-type: none"> • Perforated holes • Axial hole 	5
Type 4	<ul style="list-style-type: none"> • Perforated holes • Axial hole 	5

Table 2 Specifications of Fins (length & diameter).

Fin	Length (mm)	Diameter of fin (mm)	Diameter of axial hole (mm)	Diameter of perforated hole (mm)
Type 1	150	15	0	0
Type 2	150	15	0	5
Type 3	150	15	6	5
Type 4	150	20	8	6.67

Specifications of the base:

- Length = 50 mm
- Width = 25 mm
- Thickness = 15 mm

3. Materials

Because of the high thermal conductivity, aluminum and copper were used in simulations. Aluminum has corrosion resistance and is also cheaper than copper.

Table 3: Material Properties (Aluminum)

Property	Symbol	Values (Aluminum)	Values (Copper)
Thermal conductivity ($W\ mm^{-1}\ C^{-1}$)	K	0.2375	0.4
Specific heat ($mJ\ kg^{-1}\ C^{-1}$)	C_p	9.51e+005	3.85e+005
Density ($kg\ mm^{-3}$)	ρ	2.689e-006	8.933e-006

4. Meshing

After selecting the material, mesh has been created for the geometry. Inflation growth rate was 1.2 with maximum 5 layers. Total numbers of nodes were 457180, 537502, 486969, 752633 for type 1, 2, 3, 4 respectively. Total numbers of elements were 108653, 325162, 283135, 473878 for type 1, 2, 3, 4 respectively with element size 0.9 mm.

5. Assumptions

Following assumptions are made during the simulation.

- I. Steady state condition
- II. Radiation is negligible
- III. Uniform heat transfer coefficient 'h' over the entire fin surface
- IV. No heat generation within the fin itself
- V. The thermal conductivity of the material is constant
- VI. Homogeneous and isotropic fin material

6. Boundary Conditions

Here, radiation is neglected as its magnitude is low.

Base temperature = 300 °C

Film Coefficient = 1.8e-005 W/mm² °C

Ambient Temperature = 28. °C

7. Numerical Solutions

With the help boundary conditions, simulations have been done in ANSYS 17 for different types of fins with different materials

8. Result and Discussion

8.1. Without Perforated and Axial Holes (Type-1)

This type is a simple cylindrical pin fin without perforated and axial holes.

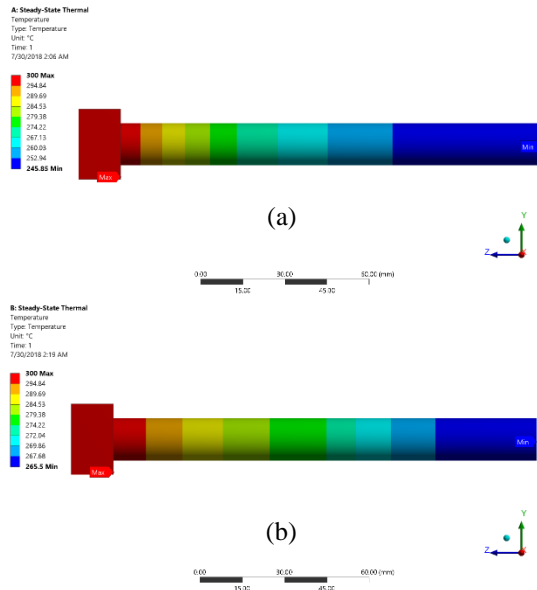


Fig. 2 Temperature distribution contour -Aluminum (a), Copper (b)

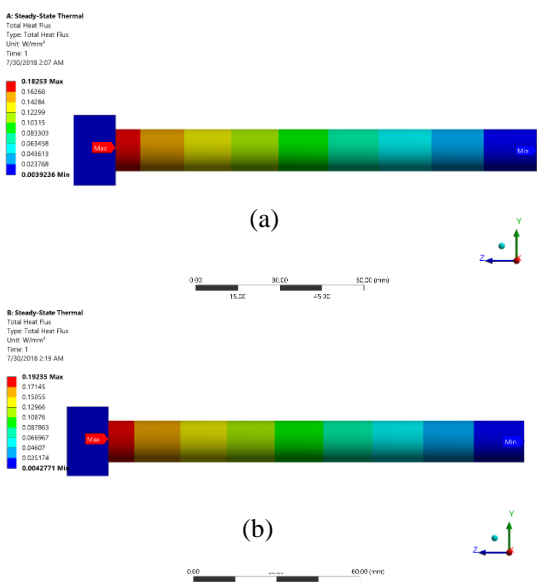


Fig. 3 Total Heat Flux Contour -Aluminum (a), Copper (b)

8.2. With Perforated and No Axial Holes (Type-2)

This type of fin has perforated hole but doesn't have an axial hole and has a higher ratio of perimeter to cross-sectional area than type 1 fin.

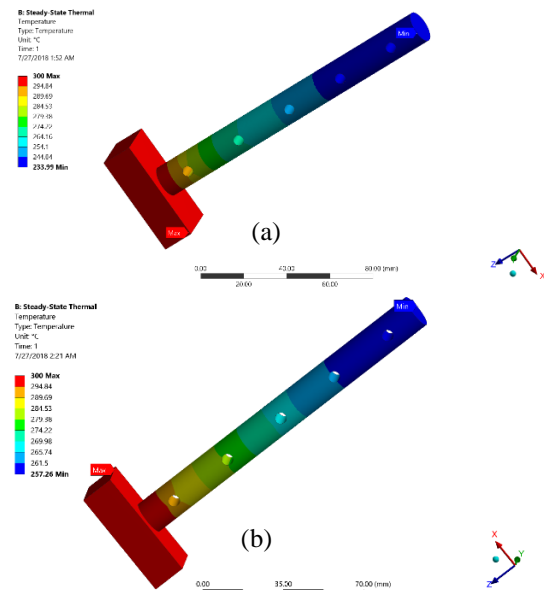


Fig. 4 Temperature distribution contour -Aluminum (a), Copper (b)

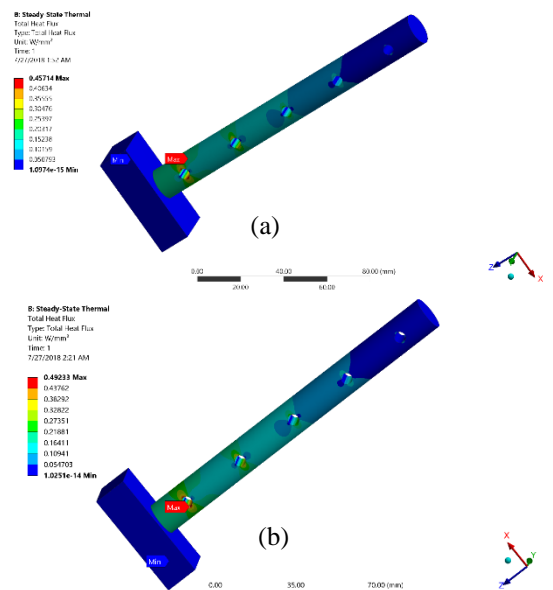


Fig. 5 Total Heat Flux Contour -Aluminum (a), Copper (b)

8.3. With Perforated and Axial Holes (Type-3)

This type of fin has perforated and axial hole with highest temperature drop among first three type of fin. These holes add extra surface area. This type of fin has the highest P/A ratio among the first three types of fins.

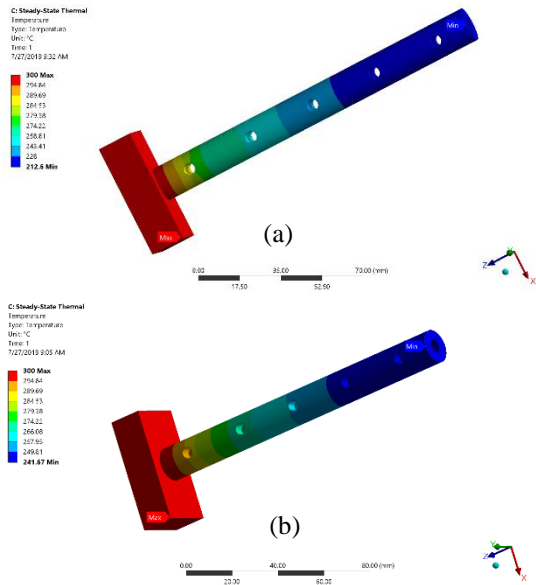


Fig. 6 Temperature distribution contour -Aluminum (a), Copper (b)

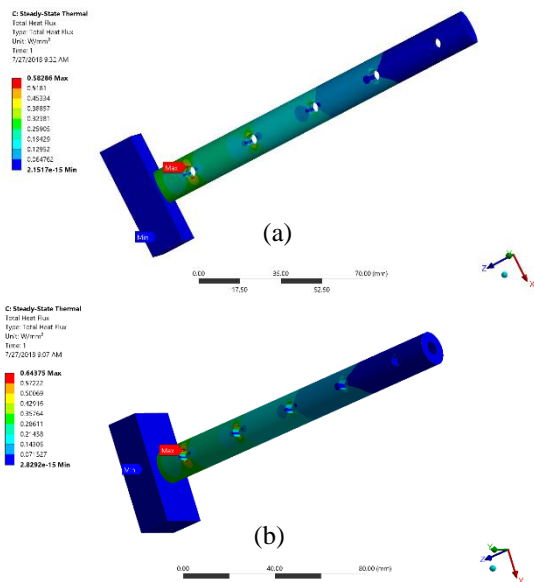


Fig. 7 Total Heat Flux Contour -Aluminum (a), Copper (b)

8.4. Comparative Temperature Profile for Type 1, 2, 3 Fins

Table 4: Maximum & Minimum Temperature, Heat Flux of Aluminum Fins.

Type	Maximum temperature (°C)	Minimum temperature (°C)	Maximum heat flux (W/mm ²)	Minimum heat flux (W/mm ²)
Type 1	300	245.85	0.18253	0.0039236
Type 2	300	233.99	0.45714	1.0974e-15
Type 3	300	212.6	0.58286	2.1517e-15

Table 5: Maximum & Minimum Temperature, Heat Flux of Copper Fins.

Type	Maximum temperature (°C)	Minimum temperature (°C)	Maximum heat flux (W/mm ²)	Minimum heat flux (W/mm ²)
Type 1	300	265.5	0.19235	0.0042771
Type 2	300	257.26	0.49233	1.0251e-15
Type 3	300	241.67	0.64375	2.8292e-15

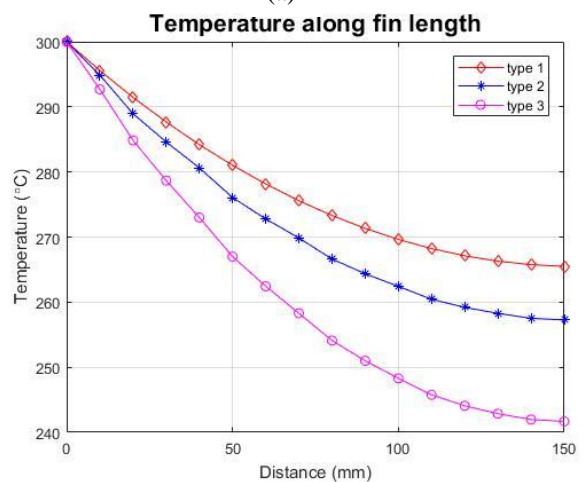
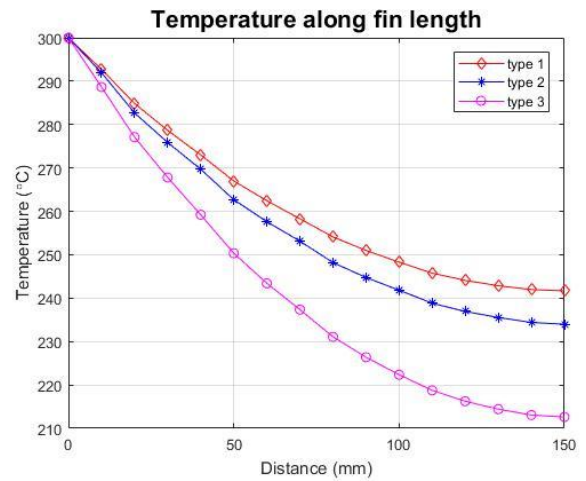


Fig. 8 Comparison of Temperature profile of types 1,2,3 -Aluminum (a), Copper (b)

Figure 8(a) shows temperature along the length for three types of fins with aluminum materials. Temperature decreases exponentially with a downward slope for these three types of fins. Minimum temperatures of the first three types of fins with aluminum materials are 245.85 °C, 233.99 °C, 212.6 °C respectively. Maximum temperature drops in type 3 aluminum fin. The increasing order of maximum temperature drop of the aluminum fin of three type is Type 3 > Type 2 > Type 1.

Maximum temperature drop means maximum heat transfer. Perforated holes and axial hole add extra surface area and increase ratio of perimeter to cross sectional area. When this ratio increases, fin effectiveness also increases. Hence Maximum temperature gradient occurs in type 3 which has most fin effectiveness.

Figure 8(b) shows that temperature decreases exponentially which has a downward slope for these three types of fins. Minimum temperatures of the first three types of fins with copper materials are 265.5 °C, 257.26 °C, 241.67 °C respectively. Maximum temperature drops in type 3 copper fin. The increasing order of maximum temperature drop of the copper fin of three type is Type 3 > Type 2 > Type 1.

Copper has comparatively low conduction resistance. That's why at the tip same geometrical fin with copper material has high temperature than aluminum. But maximum heat flux is higher than aluminum. So, copper fin for same geometry has high fin effectiveness.

Maximum temperature drop means maximum heat transfer. Perforated holes and axial hole add extra surface area and increase ratio of perimeter to cross sectional area. Hence Maximum temperature gradient occurs in type 3 which has most fin effectiveness. Figure 8(a) and 8(b) has mainly two regions. They are high-temperature zone and low-temperature zone. If the fin is very long fin it will reach the environment temperature at some length which doesn't contribute to heat transfer. It does not contribute to heat transfer in figure 8(a) and 8(b) when the slope of the curve will be zero. So, length of fin is preferable in the region where the temperature gradient is not zero. Again, after a certain length, temperature drops little though length increases much. Fins having such length are not economical and feasible. So, our aim is to design fin in such length where the temperature gradient is high. This is called proper length. Figure 8 depicts temperature gradient is low after around two-thirds of the length. Fins having a length between this region will reduce both cost and size. Closely spaced more fins contribute more heat transfer than a single fin.

3.5. Comparative Mass of Fins

Table 6: Mass of Fins

Fins (Aluminum)	Mass (gm)	Volume (mm ³)
Type 1	71.28	26507
Type 2	67.375	25056
Type 3	57.401	21345

Because of the perforated holes on type 2 fin, 4.8% mass decreases. On the other hand, 19.47% mass decreases for type 3 fin. Type 3 fin has the lowest mass with maximum temperature drop. It not only has a high

heat transfer rate but also less mass which reduces cost and weight.

8.6. Impact of Proper Length with the Increase in Diameter (Type- 4)

All the holes and diameter are increased in 33.33% of type 3 fin.

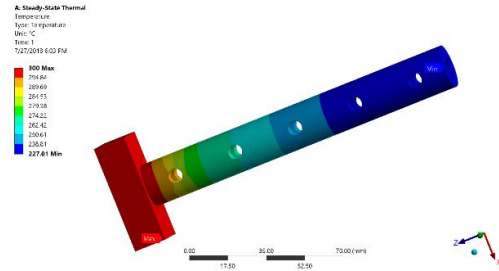


Fig. 9 Temperature distribution contour for type-4 aluminum fin

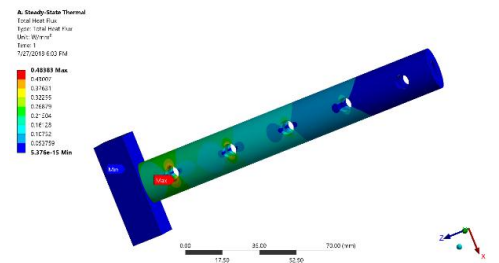


Fig. 10 Total Heat Flux Contour for Type-4 Aluminum Fin

Table 7: Maximum & Minimum Temperature, Heat Flux of Type-4 Aluminum Fin.

Maximum temperature (°C)	Minimum temperature (°C)	Maximum heat flux (W/mm ²)	Minimum heat flux (W/mm ²)
300 °C	227.01	0.48383	5.376e-15

8.7. Comparison of Proper Length Temperature along fin length

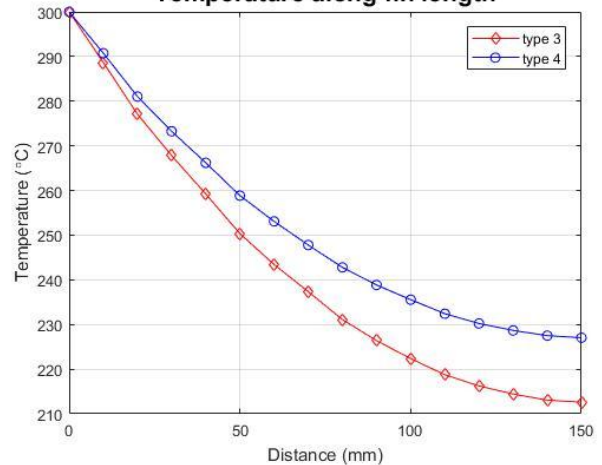


Fig. 11 Temperature profile for aluminum (type 3 and type 4)

Figure 11 shows a comparison of temperature profile between type 3 and type 4 with aluminum material. Tip temperature of type 4 aluminum fin is higher than type 3 aluminum fin. Tip temperature difference for type 3 & type 4 aluminum fin is 14.4 °C. Temperature drop will still occur if we add extra length. So, proper length increases for type 4 fin. Hence, proper length increases with the increase in diameter.

9. Conclusions

The outcomes of the present analysis are as follows.

- I. Copper has a high heat transfer rate than aluminum because of higher thermal conductivity. But aluminum is cheaper than copper and also has high corrosion resistance.
- II. Temperature drop increases for the perforated and axial hole.
- III. Type 3 fin allows maximum heat transfer rate as temperature drop of it is the highest among the first three types of fins. Order of heat transfer rate of the first three types of fins is Type 3 > Type 2 > type 1
- IV. Type 3 fin has the highest perimeter to cross-sectional area ratio among first three fins and that's why it has a high heat transfer rate.
- V. The proper length of the cylindrical fin increases with the increase in diameter.
- VI. Type 3 fin has the lowest weight of the first three types of fins which decrease material waste.

REFERENCES

- [1] S. Kiwan and M. A. Al-Nimr, Using Porous Fins for Heat Transfer Enhancement, *Journal of Heat Transfer*, Vol. 123, pp 790–795 (2000).
- [2] U. V. Awasarmol and A. T. Pise, An experimental investigation of natural convection heat transfer enhancement from perforated rectangular fins array at different inclinations, *Experimental Thermal and Fluid Science*, Vol. 68, pp 145–154 (2015).
- [3] D. H. Lee, J. M. Jung, J. H. Ha, and Y. I. Cho, Improvement of heat transfer with perforated circular holes in finned tubes of air-cooled heat exchanger, *International Communications in Heat Mass Transfer*, Vol. 39, pp 161–166 (2012).
- [4] D. Bhanja, and B. Kundu, Thermal analysis of a constructal T-shaped porous fin with radiation effects, *International journal of refrigeration*, Vol. 34, pp 1483-1496 (2011).
- [5] S.Y. Kim, J.W. Paek, and B.H. Kang, Flow and heat transfer correlations for porous fin in a plate-fin heat exchanger, *Journal of heat transfer*, Vol. 122, pp 572-578 (2000).
- [6] M.T. Darvishi, R.S.R. Gorla, F. Khani, and B.J. Gireesha, Thermal analysis of natural convection and radiation in a fully wet porous fin, *International Journal of Numerical Methods for Heat & Fluid Flow*, Vol. 26, pp.2419-2431 (2016).
- [7] M. Liu, D. Liu, S. Xu, and Y. Chen, Experimental study on liquid flow and heat transfer in micro square pin fin heat sink, *International Journal of Heat and Mass Transfer*, Vol .54, pp 5602-5611 (2011).
- [8] S. Pashah, A. Moinuddin, and S. M. Zubair, Thermal performance and optimization of hyperbolic annular fins under dehumidifying operating conditions – analytical and numerical solutions, *International Journal of Refrigeration*, Vol. 65, pp 42–54 (2016).
- [9] A.A. Khaled, Thermal performance of six different types of wavy-fins, *International Journal of Numerical Methods for Heat & Fluid Flow*, Vol. 2, pp 892-911 (2015).
- [10] Waqar Ahmed Khan, Modeling of Fluid Flow and Heat Transfer for Optimization of Pin-Fin Heat Sinks, Ph. D. Thesis, University of Waterloo, Canada (2004).
- [11] Terry J. Hendricks, Shankar Krishnan, Changho Choi, Chih-hung Chang and Brian Paul, Enhancement of Pool Boiling Heat Transfer using Nanostructured Surfaces on Aluminum and Copper, *International Journal of Heat and Mass Transfer*, Vol. 53, pp 3357-3365 (2010)
- [12] J. D. Forero, G. V. Ochoa, and L. O. Quiñones, Analysis of Proper Lengths of Straight Rectangular Fins for Different Materials, *Contemporary Engineering Sciences*, Vol. 11, pp 1025 – 1031 (2018)
- [13] A. Aziz, Optimum Dimensions of Extended Surfaces Operating in a Convective Environment, *Applied Mechanics Reviews*, Vol. 55, pp. 155-173 (1992)
- [14] S. Kiwan, Thermal analysis of natural convection porous fins, *Transport in Porous Media*, Vol. 67, pp 17 (2007).

Performance of Heat Transfer of A Plain Tube Fitted With V-Shaped Twisted Tape Inserts of Copper And Stainless Steel Material for Turbulent Flow

Mostafizur Rahman, Moham Ed Abdur Razzaq*, Abdullah Al Noman, Jamal Uddin Ahamed
Department of Mechanical Engineering, Chittagong University of Engineering & Technology, Chittagong-4349,
BANGLADESH

ABSTRACT- This paper represents tube side pressure drop, friction factor, heat transfer co-efficient, heat transfer rate, enhancement of heat transfer efficiency and percentage of increase in those parameters for water using V-shaped twisted tape inserts of copper and stainless steel material into a plain tube. The test section is a circular tube made of copper having 26.6 mm inside diameter, 30 mm outside diameter and 939.8 mm in long, of which 900 mm is of effective length. V-cut twisted tape inserts are made of as 800 mm length, 1.5 mm thickness, twisted ratio 5 and width and depth of 8 mm are used in this experiment. The test section is perfectly insulated and electrically heated. Five k-type thermocouples are used for measuring wall temperature. Experimental Nusselt number is found ranging from 34.65 to 69.25 for smooth copper tube without insert whereas, 110.9 to 250.9 for V-cut twisted tape insert of stainless steel and 121.1 to 331.8 for V-cut twisted tape insert of copper. Heat flux is obtained ranging from 9163.8W/m² to 15828.3W/m² without insert, 18327.5 W/m² to 31656.6W/m² for stainless steel insert and 18327.5W/m² to 39570.8W/m² for copper insert. Increment of heat transfer of copper insert is as 2.52 times and of stainless steel insert as 2.5 times more than plain tube without insert. Convective heat transfer co-efficient is found as 3.2, 3.5 times more than plain smooth tube for stainless steel insert and copper insert. Heat transfer enhancement efficiency using stainless steel insert and copper insert is increased 3.2, 4.3 times more than plain tube without insert.

Keywords: *V-shaped insert, Friction factor, Heat transfer rate, Heat transfer performance, Heat transfer enhancement efficiency*

1. Introduction

Heat exchanger is one of the important devices, are used in various industrial purposes. Thermal performance of heat exchangers defines the efficiency and economic competitiveness for many industrial processes. Improving the thermal performance of the heat exchangers may cause in the reduction of its size as well as initial cost. A high-performance heat exchanger of a fixed size can provide an increased heat transfer rate along with that it might also cause a decrease in the temperature difference between the process fluids and, enabling efficient utilization of thermodynamic ability. To boost heat transfer and improve thermal performance, various heat transfer enhancement techniques are widely used from the last twentieth century. It is noted that heat transfer augmentation techniques are frequently used in areas specified as temperature effort transform, air conditioning and preservation systems, heat recovery processes, cooling of different electronics equipment's and chemical reactors. Hence, using high thermal performance heat exchanger is very much essential to save energy. Several techniques are incorporated to improve the thermal performance of heat transfer devices such as mechanically treated surfaces, rough surfaces as well as introductions of inserts (such as turbulators and swirl flow generators). From various passive techniques, insertion of swirl generator is one of the most promising methods. The swirl generator caused recirculation of an existing axial flow, which leads to an improvement of fluid mixing and thus obtained an

efficient reduction of the thickness of boundary layer [1-2]. Many researchers have studied the topics from the very beginning of the 20th century to improve heat transfer characteristics inside a tube. Sarkar et al. [3] experimentally investigated the heat transfer enhancement and friction factor characteristics in turbulent flow through a tube fitted with wire-coil inserts. Agarwal and Raja Rao et al. [4] experimentally measured isothermal and non-isothermal friction factors and mean Nusselt numbers for uniform wall temperature during heating and cooling of servo-thermo oil in a circular tube with twisted tape inserts. Eiamsaard et al. [5] conducted experimental work to evaluate the heat transfer and fluid friction characteristics in a double pipe heat exchanger decorated with regularly spaced twisted tape inserts. Ahamed et al. [6] reported the prediction of heat transfer in turbulent flow through a tube with perforated twisted-tape inserts and also a new correlation was developed to predict the heat transfer characteristics. The study finalized that the perforated twisted-tape-inserts caused an increase of heat transfer rate at an expense of increased pumping power. Bhuiya et al. [7] assessed the influence of twisted wire brush inserts on the heat transfer enhancement and pressure drop characteristics of turbulent flow for four different twisted wire densities (100,150, 200, 250) and found to have a significant impact on the improvement of heat transfer as well as an increase in friction factor over the plain tube data.

* Corresponding author. Tel.: +88-01833733141
E-mail addresses: abdur.razzaq56@yahoo.com

Bhuiya et al. [8] presented the experimental results on mean Nusselt number through a tube fitted with triple helical tape inserts and reported that the Nusselt number increased 2.75 to 4.5 times compared to that of the plain tube with the increase of helix angles (9° to 21°). Eiamsa-ard et al. [9] considered the effects of twin counter/co-twisted tapes on heat transfer, friction factor and thermal enhancement indicators for four different twist ratios (2.5, 3.0, 3.5 and 4.0) in the turbulent flow region under constant heat flux conditions. Wazed et al. [10] showed the influence of perforated twisted tape inserts on the enhancement of heat transfer in turbulent flow through tube. Karwa et al. [11] reported the effect of relative roughness pitch and perforation of the spring roughness on heat transfer and friction factor for turbulent flow in an asymmetrically heated annular duct (radius ratio=0.39) with a heated tube having a spirally wound helical spring. An investigational research of heat transfer performance of porous twisted tape insert in a circular tube was carried out by Ahamed et al. [12]. A new idea was postulated by Hsieh and Huang et al. [13] to foretell heat transfer and pressure drop of laminar flow in horizontal tubes with/without longitudinal inserts. Thorsen et al. [14] studied experimentally and analytically friction factor and heat transfer characteristics of turbulent air flowing through tubes with twisted strip swirl promoters. However, limited research works are identified related to heat transfer performance and friction factor characteristics through a tube with V-cut twisted tape inserts. In this research work, the effects of V-cut twisted tape inserts on heat transfer performance and friction factor characteristics for turbulent flow through a circular tube are evaluated.

2. Materials and Methodology

In this research work, V-cut twisted tape inserts of two different materials such as copper and stainless steel have been used. Inserts are made of as 800 mm length, 25 mm width and 1.5 mm thickness. V-cut twisted tape inserts of twisted ratio 5 and width and depth of 8 mm are used in this experiment.



Fig. 1: Twisted tape insert without any cut



Fig. 2: Twisted tape insert with V-cut



Fig. 3: V-shaped twisted tape insert of copper



Fig. 4: V-shaped twisted tape insert of stainless steel

In the experimental setup, test section is a smooth circular tube made of copper having 26.6 mm inside diameter, 30 mm outside diameter and 939.8 mm in long, of which length of 900 mm is used as the test section. Teflon tape is used for joining the tube and after that M-seal is used. Then the tube is wrapped with mica tape before wrapping with nichrome wire spirally wound uniformly around the tube. Again mica glass fiber tape and heat insulating tape (Nittoflon tape) are used sequentially over the wrapped nichrome wire. The five K-type thermocouples are used for measuring outside surface temperature of tube in test section 15 cm apart from each other and started from 15 cm distance from entrance and finished before 15 cm from exit of heater length. Two thermometers are used at the inlet and outlet section of the tube for measuring the bulk temperatures. At the outlet section, the thermometer is placed in a mixing box. Pressure drop is measured at inlet and outlet of the test section by using manometer. Open loop system of water supply is used. The rate of flow is measured with the help of Rotameter in the travelling path of inlet water.

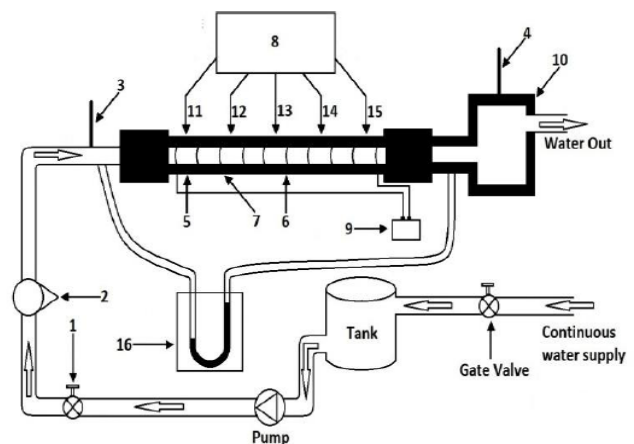


Fig. 5: Schematic diagram of experimental setup

- | | |
|-------------------------------|--------------------|
| 1. Gate valve | 9. Voltage supply |
| 2. Rotameter | 10. Mixing box |
| 3. Inlet thermometer | 11. Thermocouple 1 |
| 4. Outlet thermometer | 12. Thermocouple 2 |
| 5. Insulation | 13. Thermocouple 3 |
| 6. Test section (copper tube) | 14. Thermocouple 4 |
| 7. Nichrome-wire coil | 15. Thermocouple 5 |
| 8. Thermo-electric monitor | 16. Manometer |

Water was made to circulate throughout the system by a pump and different flow rate were maintained by regulating gate valve. Constant voltage was supplied to the heater by a voltage regulator and current was also supplied to the heater by a voltage regulator and current was also supplied to the thermocouple monitor. When the temperature in inlet and outlet thermometer and thermocouple monitor became steady, reading was taken for a given flow rate. Next reading was taken increasing flow rate in the same procedure. The flow rate was taken from 165 ml per sec and increased by 30 ml per sec up to 315 ml per sec for plain copper tube without insert and, with v-cut copper insert and, stainless steel twisted tape insert.

3. Mathematical Formulations

Heat transfer enhancement of water using twisted V-cut insert at circular tube is calculated by using the following equations,

Outer surface area is calculated from,

$$A_o = \pi d_o L \quad (1)$$

Where, d_o is outer surface diameter.

Inner surface area is calculated from,

$$A_s = \pi d_i L \quad (2)$$

Where, d_i is inner surface diameter.

Heat transfer rate is obtained from,

$$Q = m c_p (T_o - T_i) \quad (3)$$

Where, T_o is outlet temperature and T_i is inlet temperature.

Cross sectional area,

$$A_x = \frac{1}{4} \pi d_i^2 \quad (4)$$

Velocity,

$$V = \frac{m}{A_x} \quad (5)$$

Where, m is the flow rate in kg/sec and A_x is Cross sectional area.

Reynolds number,

$$Re_D = \frac{\rho V d_i}{\mu} \quad (6)$$

Nusselt number,

$$Nu = \frac{h d_i}{k} \quad (7)$$

Prandtl number,

$$Pr = \frac{\mu c_p}{k} \quad (8)$$

Where, μ and k at bulk temperature.

Bulk temperature,

$$T_b = \frac{T_o + T_i}{2} \quad (9)$$

Convective heat transfer coefficient is calculated from,

$$h = \frac{Q}{A(T_{w_i} - T_b)} \quad (10)$$

Where, T_{w_i} is tube inner surface temperature and T_b is bulk temperature.

Gnielinski equation,

$$Nu_D = \frac{(f/8)(Re-1000)Pr}{1+12.7\left(\frac{f}{8}\right)^{\frac{1}{2}}(Pr^{2/3}-1)} \quad (11)$$

Where, $f = (0.790 \ln Re_D - 1.64)^{-2}$.

Flow area,

$$A_f = \frac{1}{4} \pi d_i^2 \quad (12)$$

Mean velocity,

$$u_m = \frac{Q}{\left(\frac{\pi}{4}\right) d_i^2} \quad (13)$$

The experimental friction coefficient,

$$f_{exp} = \frac{2 \Delta P d_i^2}{\rho L u_m^2} \quad (14)$$

Convective heat transfer coefficient,

$$h = \frac{Nu \cdot k}{d_i} \quad (15)$$

Heat flux,

$$q = \frac{Q}{A_s} \quad (16)$$

Where, $A_s = \pi d_i L$

Pressure difference,

$$\Delta p = \Delta h \rho g \times 13.6 \quad (17)$$

Outer surface temperature,

$$T_{w_o} = \sum_{i=1}^5 \frac{T_{w_o,i}}{5} \quad (18)$$

Inner surface temperature,

$$T_{w_i} = T_{w_o} - Q \frac{\ln(d_o - d_i)}{2\pi k_w L} \quad (19)$$

The rate of heat transfer by conduction is calculated,

$$Q = \frac{2\pi k L (T_{w_o} - T_{w_i})}{\ln(r_o - r_i)} \quad (20)$$

$$\% \text{ of error} = \{(Nu_{exp} - Nu_{th}) / Nu_{th}\} \times 100 \quad (21)$$

4. Results and Discussion

For smooth copper tube, experimental Nusselt number ranging from 34.65 to 69.25 and theoretical Nusselt numbers ranging from 37.9 to 64.7 are calculated using (Eq. 4.7 & 4.11), to compare the values and using (Eq. 4.21) errors are found within -8.57% to 7.03%. Reynolds numbers are calculated by using (Eq. 4.6) and it ranges from 5044.8 to 8713.8. Heat transfer rate, Q is obtained within 689.2 W to 1190.4 W using (Eq. 4.3). Heat flux, q is found ranging from 9163.8 W/m² to 15828.3 W/m² using (Eq. 4.16). Heat transfer coefficient, h is calculated ranging from 807.7 W/m²°C to 1614 W/m²°C using (Eq. 4.10). Theoretical friction factor f_{th} is obtained within 0.039 to 0.033 using (Eq. 4.11) and experimental friction factor, f_{exp} 0.09 to 0.057 using (Eq. 4.14). Heat transfer enhancement efficiency

is varied in the range of 0.7 to 0.89. For smooth copper tube inserted with V-cut twisted tape of stainless steel, results are found as experimental Nusselt number ranging from 110.9 to 250.9 and theoretical Nusselt number ranging from 37.9 to 64.7. Reynolds numbers are ranged from 5044.8 to 8713.8. Heat transfer rate, Q is obtained within 1378.4W to 2980.9W. Heat flux, q is found ranging from 18327.5 W/m^2 to 31656.6 W/m^2 . Heat transfer co-efficient, h is calculated from 2584.2 W/m^2C to 5847.6 W/m^2C . Theoretical friction factor f_{th} is obtained within 0.039 to 0.033 and experimental friction factor, f_{exp} 0.107 to 0.066. Heat transfer enhancement efficiency is varied in the range of 2.09 to 3.078. For smooth copper tube inserted with Copper V-cut twisted tape, results are found as experimental Nusselt number ranging from 121.1 to 331.8 and theoretical Nusselt numbers ranging from 37.9 to 64.7. Reynolds numbers are ranged from 5044.8 to 8713.8. Heat transfer rate, Q is obtained within 1378.4W to 2976.1W. Heat flux, q is found ranging from 18327.5 W/m^2 to 39570.8 W/m^2 . Heat transfer co-efficient, h is calculated from 2823.1 W/m^2C to 7733.2 W/m^2C . Theoretical friction factor f_{th} is obtained within 0.039 to 0.033 and experimental friction factor, f_{exp} 0.116 to 0.069. Heat transfer enhancement efficiency is varied in the range of 2.22 to 4.01. Fig. 6 shows comparison of experimental and theoretical Nusselt number of plain tube with Reynolds number for data validation. Variation of data between experimental and theoretical Nusselt number is less than 20%. So, obtained data is valid for this experiment.

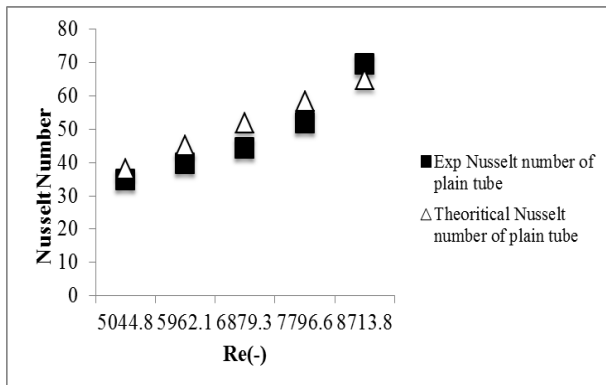


Fig. 6: Comparison of experimental and theoretical Nusselt number of plain tube with Reynolds number for data validation.

From fig. 7, it is noticed that Nusselt number is increased with Reynolds number. It is also noticeable that increase of Nusselt number with respect to Reynolds number in case of stainless steel insert is more than plain tube without insert. But in case of copper insert, the increment rate is higher than both plain tube and plain tube with stainless steel insert. Increment of Nusselt number of copper insert is averaged as 3.5 times and of stainless steel insert as 3.2 times more than plain tube without insert.

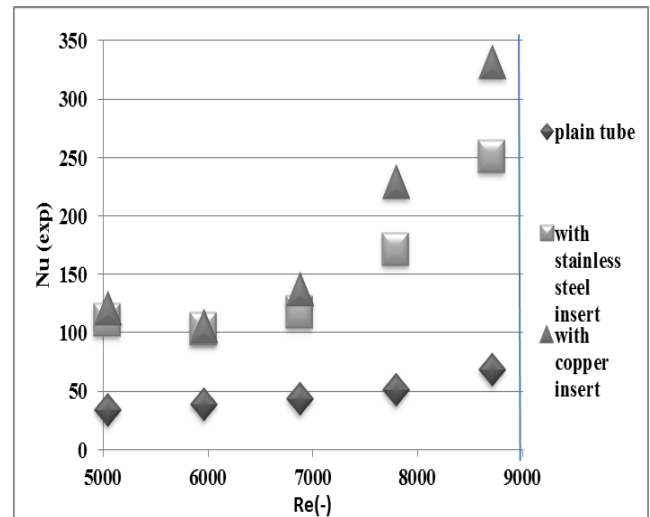


Fig. 7: Variation of Nusselt Number with Reynolds Number.

Fig. 8 shows that ratio of experimental Nusselt number inserted with stainless steel and experimental Nusselt of plain tube without insert is varied from about 3.2 to 3.8 and, 3.7 to 4.98 for plain tube inserted with copper and of plain tube without insert.

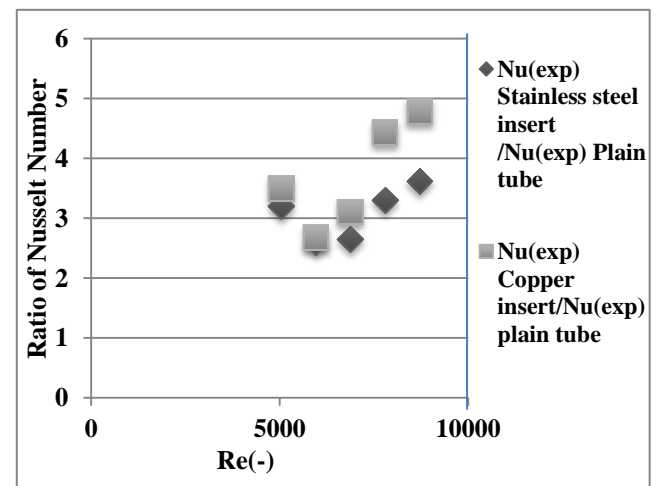


Fig. 8: Variation of ratio of exp. Nusselt number of two inserts and plain tube with Reynolds number.

From fig. 9, it is shown that friction factor is decreased with increase of Reynolds number. Friction factor decreases more in case of copper insert and stainless steel insert than plain tube without insert. Variation of convective heat transfer co-efficient with Reynolds number of plain tube inserted with V-shaped twisted tape made of stainless steel and copper material is shown in fig. 10. Convective heat transfer co-efficient is found as 3.2, 3.5 times more than plain smooth tube for stainless steel insert and copper insert.

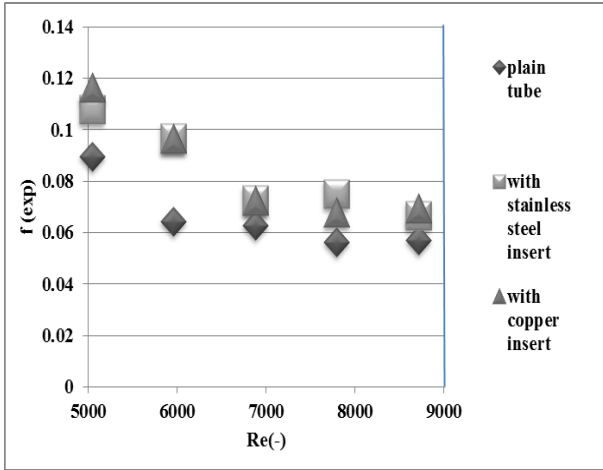


Fig. 9: Variation of experimental friction factor with Reynolds Number.

Rate of heat transfer with Reynolds number of plain tube inserted with V-shaped twisted tape made of stainless steel and copper material is shown in fig. 11. It is found that heat transfer rate is increased with Reynolds number. It is known to all that more disturbances in fluid flow causes more heat transfer. Increment of heat transfer of copper insert is as 2.52 times and of stainless steel insert as 2.5 times as plain tube without insert.

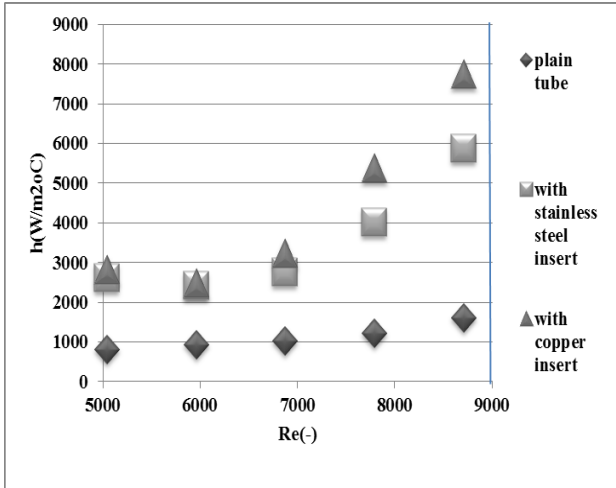


Fig. 10: Variation of convective heat transfer coefficient with Reynolds Number.

From fig. 12, it can be easily reached into decision that heat transfer enhancement efficiency is increased more than plain tube in case of stainless steel insert and copper insert. Heat transfer enhancement efficiency ratio with Reynolds Number is shown in fig. 13. Heat transfer enhancement efficiency ratio of plain tube with stainless steel insert and plain tube without insert is varied from 3.1 to 3.5. Heat transfer enhancement efficiency ratio of plain tube with copper insert and plain tube without insert is varied from 3.3 to 4.5.

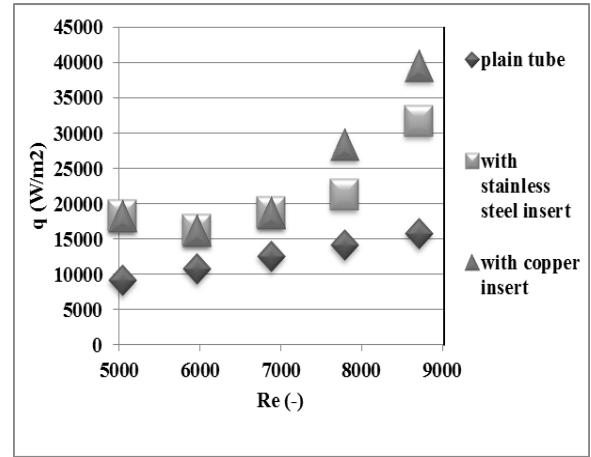


Fig. 11: Variation of heat flux with Reynolds Number.

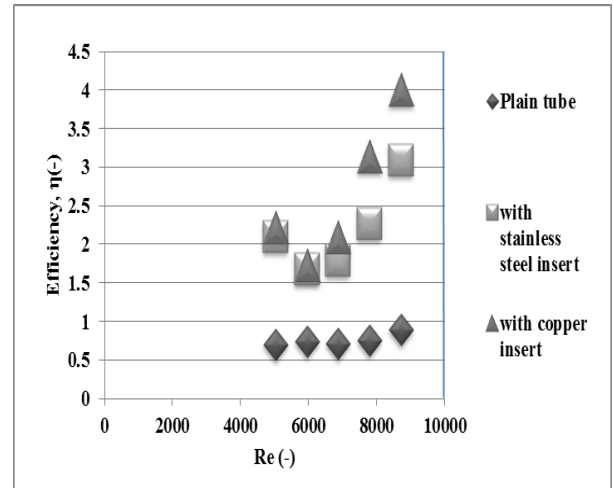


Fig. 12: Variation of heat transfer enhancement efficiency with Reynolds Number.

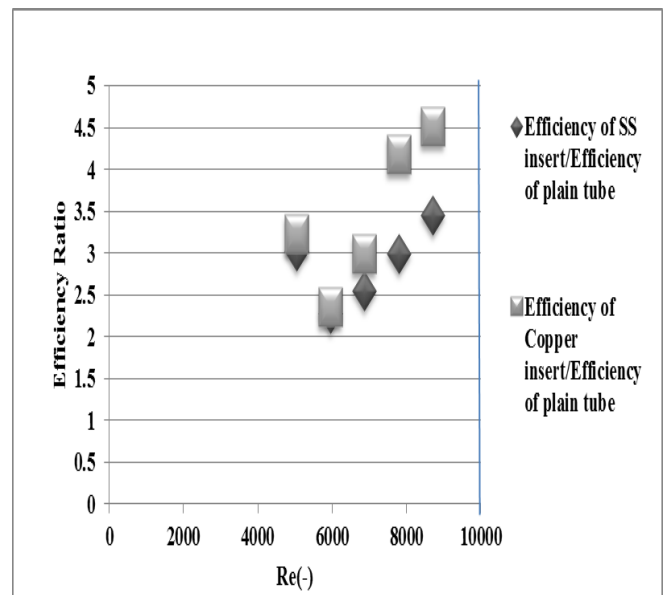


Fig. 13: Variation of efficiency ratio vs. Reynolds number.

5. Conclusions

Experimental investigation of friction factor, convective heat transfer co-efficient, heat transfer and, heat transfer enhancement efficiency of a circular plain tube fitted with V-shaped twisted tape inserts of copper and stainless steel material have been presented in this paper. Nusselt number and Reynolds number of the tube fitted with V-shaped twisted tape inserts are nakedly higher than the value of smooth plain tube. Increment of Nusselt number of copper insert is as 3.5 times and of stainless steel insert as 3.2 times as plain tube without insert. Along with that, convective heat transfer co-efficient is found as 3.2 times more than plain smooth tube for stainless steel insert and, 3.5 times more for copper insert. As a result, heat transfer rate of tube fitted with inserts is more than that of tube without inserts. Results show that using V-shaped tape inserts of copper and stainless steel, heat transfer rate is increased about 2.5 times than plain tube without insert. Overall heat transfer enhancement efficiency is increased using V-shaped inserts. Heat transfer enhancement efficiency of a tube fitted with V-shaped twisted tape inserts of stainless steel and copper material is increased about 3.2 to 4.0 times than smooth tube. This type of heat transfer enhancements techniques can be used in various applications such as refrigeration, automotive, process industry, chemical industry, nuclear reactors, and solar water heaters etc. The author's next research step is to investigate heat transfer enhancement in a smooth plain tube fitted with V-shaped twisted tape insert for different spacing in turbulent flow.

REFERENCES

- [1] A. E. Bergles, ExHFT for fourth generation heat transfer technology, *Exp Therm Fluid Sci* vol. 26, pp. 335–344, (2002).
- [2] A. Dewan, P. Mahanta, K. S. Raju, P. S. Kumar, Review of passive heat transfer augmentation techniques, *Proc. Institute of Mechanical Engineering, A J Power Energy*, vol. 218 pp. 509–527, (2004).
- [3] M. A. R Sarkar, M. Z. Islam, M. Islam, Heat transfer in turbulent flow through tube with wire-coil inserts, *Journal of Enhanced Heat Transfer*, vol. 12, pp. 385–394, (2005).
- [4] S. K. Agarwal, M. R. Raja, Heat Transfer Augmentation for the Flow of a Viscous Liquid in Circular Tubes Using Twisted Tape Inserts, *International Journal of Heat and Mass Transfer*, vol. 39_17, pp. 3547–3557, (1996).
- [5] S. Eiamsa-ard, C. Thianpong, P. Promvonge, Experimental investigation of heat transfer and flow friction in a circular tube fitted with regularly spaced twisted tape elements, *International Communications in Heat Mass Transfer*, vol. 33, pp. 1225–1233, (2006).
- [6] J. U. Ahamed, M. A. Wazed, S. Ahmed, Y. Nukman, T. M. Y. N. Tuan Ya, M. A. R. Sarker, Enhancement and Prediction of Heat Transfer Rate in Turbulent Flow through Tube with Perforated Twisted Tape Inserts: A New Correlation, *Journal of Heat Transfer*, vol. 133, pp. 1–9, (2011).
- [7] M. M. K. Bhuiya, M. S. U. Chowdhury, M. Islam, J. U. Ahamed, M. J. H. Khan, M. R. I. Sarker, M. Saha, Heat transfer performance evaluation for turbulent flow through a tube with twisted wire brush inserts, *International Communications in Heat Mass Transfer*, vol. 39, pp. 1505–1512, (2012)
- [8] M. M. K. Bhuiya, J. U. Ahamed, M. S. U. Chowdhury, M. A. R Sarkar, B. Salam, R. Saidur, H. H. Masjuki, M. A., Kalam, Heat Transfer Enhancement and Development of Correlation for Turbulent Flow Through a Tube With Triple Helical Tape Inserts, *International Communications in Heat and Mass Transfer*, vol. 39, pp. 94–101, (2012).
- [9] S. Eiamsa-ard, C. Thianpong, P. Eiamsa-ard, Turbulent heat transfer enhancement by counter/co-swirling flow in a tube fitted with twin twisted tapes, *Exp Therm Fluid Sci* vol. 34: pp.53–62, (2010)
- [10] M. A. Wazed, J. U. Ahamed, S. Ahmed, M. A. R Sarkar, Enhancement of Heat Transfer in Turbulent Flow Through a Tube With Perforated Twisted Tape Insert, *Journal of Enhanced Heat Transfer*, vol. 18, no. 1, pp. 1–13, (2011).
- [11] R. Karwa, B. K. Maheshwari, P. K. Sailesn, Experimental study of heat transfer and friction in annular ducts with a heated tube having a spirally wound helical spring, *Journal of Enhanced Heat Transfer*, vol. 17 no. 1 pp. 77–92, (2010).
- [12] J. U. Ahamed, M. M. K. Bhuiya, R. Saidur, H. H. Masjuki, M. A. R. Sarkar, A. S. M. Sayem, M. Islam, Forced convection heat transfer performance of porous twisted tape insert, *Engineering e-Transaction*, vol. 5, no. 2, pp. 67-79, (2010).
- [13] S. S. Hsieh, I. W. Huang, Heat transfer and pressure drop of laminar flow in horizontal tubes with/without longitudinal inserts, *Journal of Heat Transfer*, vol. 122, no. 3, pp. 465-475, (2000).
- [14] R. Thorsen, F. Landis, Friction and heat transfer characteristics in turbulent swirl flow subjected to large transverse temperature gradients, *Journal of Heat Transfer*, vol. 90, no. 1, pp. 87-97, (1968).

Performance Analysis of Hydroxy Gas Generator by Varying Conditions of Electrolyte Concentration, Temperature and Time

Joy Datta^{1*}, Dr. Md. Abu Mowazzem Hossain¹ and Radif Uddin Ahmed²

¹Department of Mechanical Engineering,
Chittagong University of Engineering & Technology, Roazan, Chittagong-4349, BANGLADESH

ABSTRACT

Demand and price on fossil fuel is increasing day by day, it is very much crying need to search for an alternative secondary fuel. Developed countries are spending a lot of money on research and development of non-conventional energy and eco-friendly energy sources. To cope up with the problem, hydroxy (HHO) gas is used as a secondary fuel for compression ignition and spark ignition engine for improving brake thermal efficiency, reducing fuel consumption and emissions from internal combustion engines which reduces fuel consumption that minimizes carbon deposition on the cylinder. In this project, hydroxy gas (HHO) was produced by the electrolysis process of an electrolyte (KOH(aq)) with 20 grade stainless steel electrodes in a leak-proof PVC pipe tube (hydrogen generator). It has been observed that with an increased amount of KOH concentration the cell can produce HHO gas 207 ml/min and with 0.1M concentration of KOH and 27°C temperature it can produce a large amount of HHO gas which is 455 ml.

Keywords: Secondary fuel, HHO gas, Concentration, Temperature, Eco friendly.

1. Introduction

Increasing demand for conventional fuel related with limited non-renewable energy sources has resulted in a huge increase in crude oil prices. Scientists refer to that high exhaust gas concentration which is emitting from the industrial plants and the automobiles are hugely responsible for the global warming [1]. Transportation sector consumes world total energy by 1.1 percent every year [2]. For solving the above problem – researchers encouraged to seek for alternative solutions to be used in engines without the need for a dramatic change in the vehicle design.

Using hydrogen (H₂) as an alternative fuel which enhances the engine efficiency and runs with almost zero pollution effect has been researched well in the last decade. H₂ has some of its interesting properties such as high laminar flame speed, wide flammability range etc. which reveals hydrogen as an attractive fuel for internal combustion engines [3]. Besides, compared with traditional fossil fuels, H₂ is a carbonless fuel whose combustion does not generate emissions such as CO₂, HC and CO but there are concerns regarding the solutions both for the generation and storage of H₂ from the commercial point of view. Some researchers suggest that biogas [4-5], syngas [6], producer gas [7] either solely or with H₂ blends successfully in gasoline engines.

But nowadays, few researchers are working on HHO which doesn't have any kind of storage problem and more combustible than conventional fuel and hydrogen. Yull Brown first discovered HHO gas in 1974 and the content of HHO gas are hydrogen gas (H₂) and

oxygen gas (O₂) which are obtained by water electrolysis method [8].

Eckman [9] proposed that when water is electrolysed and the gas products are not separated by a semi-permeable membrane, Rydberg clusters may be formed. These clusters are of a mixture of hydrogen and oxygen species including linear water molecules in the highly energized trigonal-bipyramidal geometry, monatomic and diatomic hydrogen, free electrons and oxygen. The extra energy stored in one litre of HHO due to Rydberg clusters is theorized to be 600±34J. Rydberg clusters are most common in solids and liquids and are typically stable from nanoseconds to hours. In the case of HHO or Brown's Gas these clusters have shown a life span of 11 minutes [9]. Due to these highly energized clusters HHO contains much more energy than equivalent stoichiometric ratio of hydrogen and oxygen in the form of extra electrons, this state has been explained as cold plasma. Cold plasma is a state of matter where the atom nuclei are relatively unenergetic or slowly moving, but the electrons are in highly energized states at higher atomic orbitals. If this is true HHO releases additional electrons during combustion that are stored in the gas resulting in higher electrical and thermal energy transfer compared to the equivalent mixture of hydrogen oxygen and water. Normally the presence of water in a burning fuel gas greatly reduces the heat energy due to the high specific heat capacity of water (4.18J/g-K), however the linear water content of HHO has greatly reduced hydrogen bonds and electrically transfers its electrons under combustion at the surface of the contacting material. The flame temperature generated by HHO can range from 150°C

to over 9000°C [10] based on the contact materials' electrical conductivity, thermal conductivity, density and vapour point.

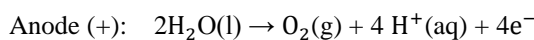
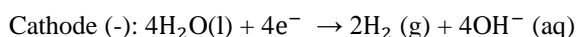
Li et al. [11] found that HC and CO emissions from the hydrogen-enriched gasoline engine were lower than the original gasoline engine. D. M. Madyira and W.G. Harding [12] in this paper, The generated HHO gas was supplied through intake manifold up to 0.45% by volume in S.I engine. Tests were conducted for a range of speed from 1000 to 3500 rpm and maximum load applied was 30% of full load. It was found that, addition of HHO enhanced power and torque and a significant reduction in CO and HC was observed. Also improved combustion was observed especially a low loads.

This work is different from previous work because previous works analyze the HHO effect on I.C engine rather than analysing the factor behind HHO gas production rate improvement. Noor Alam and K. M. Pandey [13] in this paper, the production of HHO gas has increased about 30-40% with reduction in electrical energy consumption and one anode and cathode is used through the overall work so that the HHO gas production is comparatively low. But in this work, 6 plate HHO cell is fabricated with 20 grade stainless steel to produce HHO gas so that the production rate is hugely increased compared to previous work. Moreover, the main target of this work is to produce HHO gas considering some factor rather than analysing electrical energy consumption.

Process of electrolysis involving the production of hydrogen and oxygen is carried out by HHO gas generator. In this process, A d.c is passed through electrodes to water, due to chemical reaction, the positive plates generate Oxygen and negative plates generate Hydrogen.

Hydrogen and oxygen do not form into O₂ and H₂ molecules rather they may remain in their monoatomic state and no atomic bond is broken which is an unstable state of H₂O vapor, more energy can be achieved compared to H₂ burning with O₂ [14]. This hydrogen molecule acts as a fuel and oxygen molecule helps to burn the fuel. The heating value of hydrogen is high and for the presence of oxygen the proper combustion can be assured.

The resulting migration of ions in solution results in the production of hydrogen at the cathode and oxygen at the anode according to [15]:



The overall chemical reaction of water electrolysis can be written as follows :

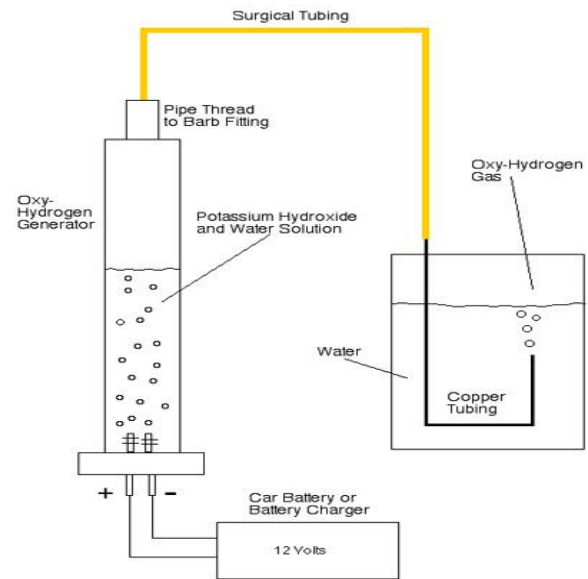
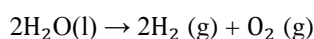


Fig 1: HHO Gas Production [16]

2. Experimental procedure

2.1 Material Selection and Desiging of HHO Cell Plate:

There are different materials could be used as an electrode. But each one has its own merits and demerits .From the overall search the selection of material for electrodes should be stainless steel thicker in size. The distance between each plate should be minimum and should have equal space all over the arrangement of electrodes. There are two methods of arrangements of electrodes -without-neutral and with-neutral. The without-neutral electrodes construction consists of number of positives P and negatives N plates which are all arranged alternatively, example if there are three set of positive and negative electrodes then P-N-P-N-P-N is the arrangement. Next with-neutral electrodes construction consists of number of positives P ,neutral Nu ,and negatives N plates which are all arranged in the following manner P-Nu-Nu- N-Nu-Nu-P-Nu-Nu-N, or , P-Nu-Nu-Nu-N-Nu-Nu-Nu-P-Nu-Nu-Nu-N, etc... The purpose of neutral plate is to prove better cooling effect while electro processing. Here the neutral plates are also of the same material and same size .But in this work the former one will be selected and designed as Nu-Nu-P-Nu-Nu-N which is shown in Fig. 2. For the connectivity among positive electrodes and negative electrodes, they are arranged not to make any shot circuit at any condition and mechanically should be strong to withstand the electrolyte corrosions.

For the electrodes metal sheet is needed and for our case the sheet metal is of stainless steel. The sheet was of 20 grade. It has a thickness of 1mm. the sheets were needed to be cut into certain dimensions. That is because for maximum gas production the sheets were needed to be in sandwiched form. The dimensions and the number of sheets are given below :

:

Serial no.	Sheet Dimension(Inch×Inch)	Number of Sheets
1	6×3	12
2	61.5	4
3	6×1	1
4	4.5×1	1
5	3.25×1	1



Fig 2 : 6 Plate HHO Cell

2.2 Material Selection To Design a Container :

The container should have the following properties as follows: should withstand chemical corrosion, mechanical stress and strain, tremendous vibration and temperature. If it is transparent, it is easy to check the electrolyte level and its color and it should be a gas tight container, because HHO is a light weight gas compared to air. On the top of the container there are three holes a two holes in opposites are for positive and negative terminal, one hole for gas outlet through gas hose. In this experiment P.V.C tube is used as shown in Fig 4. because it has high temperature resistance.

2.3 Purpose of a Catalyst :

Electricity is not conducted by pure water properly. Adding a catalyst to the water creates an electrolytic solution and increases conductivity, allowing electrolysis to occur. For more HHO production catalysts such as NaOH, KOH, H₃C-COOH, NaHCO₃, K₂CO₃ or NaCl can be used. More concentration of the catalyst is important to keep electrical resistance-conductivity balance in the cell. Distilled water and KOH is the preferred electrolyte. Advantage of KOH over other electrolyte is - Electrodes stay clean and 95 - 100% pure HHO gas production along with the right generator design .

2.4 : Purpose of Bubbler Bottle :

Bubbler is otherwise called safety bubbler or collector, which has a simple arrangement. The container should be flexible and withstand the vibration and little bit pressure, transparent and should have feet of height as shown in Fig 1. These all conditions are satisfied by a simple water bottle made of plastic. The three fourth of the bubbler should filled with water. The gas incoming tube from the HHO generator should be dipped into bottom of the water level always.

For each and every incoming bubbler one back flow check valve has to be placed to avoid the back flow of the water into the HHO generator side. An important caution about the backfire is that we must ensure the water level in the bubbler at all times or otherwise it will lead to back fire explosion because HHO is ignited easily. To avoid this level of severe explosion we should use flashback arrester valve which are in market in different size and variety and if it is not available means we may use our own design with a help bronze wool as a backfire protection and do not try to store the HHO even if in small quantity level it may lead to larger explosion.

2.5 : Working Principle of HHO Gas Generator :

First, it has been observed by making a prototype model for HHO gas generator with single anode and cathode which is connected then 12V computer power supply and observe its burning properties which is shown in Fig.3. The experimental setup includes mainly the fabrication of an electrolyzer in which the electrolysis reactions would occur. The other important tasks includes material selection for electrodes, electrolyte selection, gas collection method development etc. Sanitary pipe (having 4mm thickness) is used to make the reactor container or the electrolyzer. The designed electrolyzer is as shown in Fig.4 with a capacity of 6 liters solution. Sanitary pipe has some special properties other than visibility such as noncorrosive, nonconductive, nonreactive with electrolyte and it can withstand high pressure and temperature. Stainless steel is selected as electrode material as it is high corrosion resistant, non reactive with the electrolyte, good conductor, and capable to withstand high temperature and voltage. An electrolysis device is called an electrolyze cell, the process of using DC supply to the arranged electrodes which are immersed into the electrolysis split water into hydrogen and oxygen. The positive plate emits oxygen and negative plate emits hydrogen. When both are bubbled up and collected together – so called highly burnable fuel is produced. Storing this gas creates explosive effect so directly hosed into the air intake of the engine. Within the engine before firing this HHO gas is automatically mixed with filtered air and then combines with the fuel. By nature HHO supports with gas as well as diesel, another property.

The total experimental setup is presented in Fig.4



Fig 3 :Prototype Model For HHO Gas Generator



Fig 4 : Experimental Setup of HHO Gas Generator

An electrolyte with increased amount of catalyst can dramatically increase current supplied from battery due to the higher reduction of total electrical resistance in the solution. Several concentrations of electrolyte such as 0.01M, 0.1M, 0.2M, 0.3M KOH solution are used to perform the electrolysis process. The plate electrode and KOH(aq) are found satisfactory in relation to the electrical power consumed in the experiment. A DC battery (similar to that is used in automobiles) is used as the main power source of this experiment. The terminal voltage of the battery is 12 V and current rating is 60 Amp/hr. The generated HHO gas is collected by the water displacement method. The gas collection container initially filled with water and is placed as inverted cylinder in a reservoir of water. As the gas is

created, it will displace water from the container. The volume of gas can be determined by the amount of water displaced by the gas. Electric currents are measured by an ammeter (0 to 60 amps AC/DC ammeter) and voltages are measured by a digital multimeter.

3 Results and Discussion :

3.1 Theoretical Analysis :

According to Natalia Chraplewska, Kamil Duda and Milosz Meus [17], the optimal voltage on the electrode is 1.48V, while the amount of the produced gas depends on the current strength. The volume of the produced gas for a single pair of plates - a cell can be estimated from the following equation [17],

$$V = \frac{R \cdot I \cdot T \cdot t}{F \cdot P \cdot z} \dots \dots \dots (1)$$

Where, V: volume of gas [m^3],

R: gas constant ($\approx 8.314472 [\frac{J}{mol \cdot K}]$),

I: current [A], T: temperature [K],

t: time [s],

F: Faraday constant ($\approx 96485.34 [\frac{C}{mol}]$),

P: ambient pressure [Pa], z: number of excess electrons (2 for H_2 , 4 for O_2).

3.2 Graphical Presentation :

a) Effect of electrolyte concentration :

No electrons are traveled from active electrode surface to the inert electrode surface in pure water. The resistance of the overall electrolyzer system is reduced due to increase the conductivity of pure water. Thus the overvoltage value on electrolyzer is dropped to a larger extent. Increasing amount of electrolytic concentration hydrogen and oxygen evolution is increased due to greater number of effective ionic collisions per unit time. Here shown in Fig. 5, when the concentration of electrolyte increased, the amount of HHO gas also increased. So, increasing electrolyte concentration will increase the production rate of HHO gas.

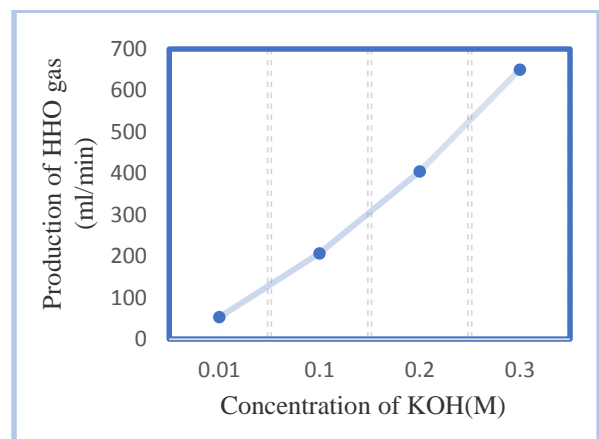


Fig 5 :Effect of Electrolyte Concentration

b) Effect of time at 0.1 M KOH :

HHO gas volume is calculated by 1 min interval with a 0.1 M concentration of KOH. As KOH concentration is not increase with time ,current flow through the electrode becomes constant after some time.As a result, HHO production rate is constant after some time period as shown in Fig. 6.

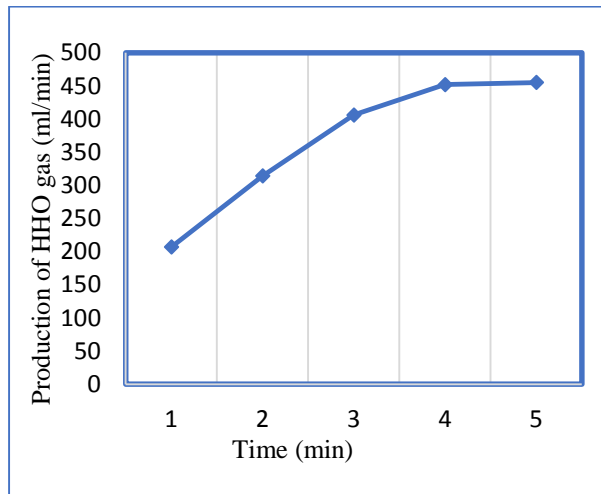


Fig. 6 : Effect of Time at 0.1 M KOH

c) Effect of temperature at 0.1 M KOH:

In most cases , such as room temperature water electrolysis, the electric input is larger than the enthalphy change of the reaction, so some energy is released as waste heat.High temperature electrolysis is more efficient economically than traditional room-temperature electrolysis because some of the energy is supplied as heat which is cheaper than electricity . Here shown in Fig. 7 ,when the temperature of water is increased the amount of HHO gas also increased so much.So,increasing temperature will increase the production rate of HHO gas.

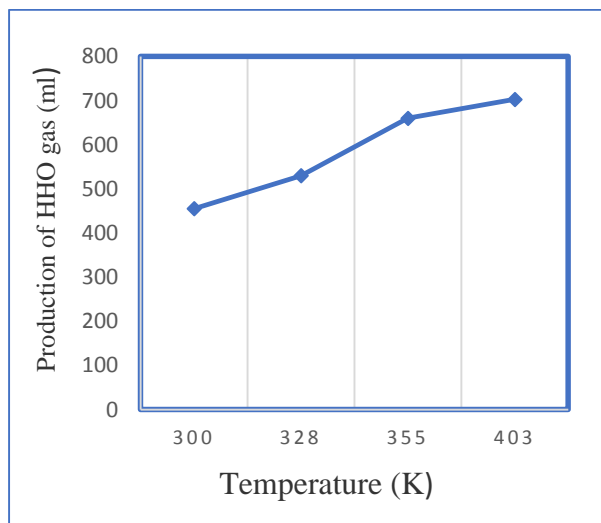


Fig 7 : Effect of Temperature at 0.1M KOH

4 Conclusions and Recommendations :

The main aim of this research work is to fabricate a 6 plate HHO fuel cell for HHO gas production and analysis are made by varying catalyst concentration,time and temperature in laboratory scale. The HHO cell plate named electrode are made from 20 grade stainless used for this project because it is cheap and it can withstand high temperature as well as high current flows.HHO gas is collected by water displacement method for collecting data. It has been observed that with a increased amount of KOH concentration the cell can produce HHO gas 207 ml/min and with 0.1M concentration of KOH and 27°C temperature it can produce large amount of HHO gas which is 455 ml. While designing the HHO generator the following important points should be taken care: selection of electrodes, distance between two electrodes, connectivity between electrodes, selection of catalyst, its level, merits and demerits, selection of container, electrical connectivity and plumbing with gas tight arrangement ,backfire protection .

REFERENCES

[1] Ishida H., Kawasaki S. Mohri Y., Furuya H. and Kanayama T. (2003). On-board and roadside monitoring of NOx and SPM emission from vehicles. Journal of the Eastern Asia Society for Transportation Studies. Vol. 5:2398-2407.

[2] International Energy Outlook 2013.Retrieved from www.eia.gov/forecasts/ieo/world.cfm as on 10.09.2013

[3] Knop V, Benkenida A, Jay S, Colin O. (2008). Modelling of combustion and nitrogen oxide formation in hydrogen fuelled internal combustion engines within a 3D CFD code. International Journal of Hydrogen Energy. Vol.33:5083e97.

[4] Mustafi Nirendra N., Raine Robert R. and Bansal Pradeep K. (2006). The use of biogas in internal combustion engines: a review. ASME Paper ICES2006-1306 (CD ROM), Proceedings of ASME Internal Combustion Engine Division 2006 Spring Technical Conference, May 8-10, 2006, Aachen, Germany.

[5] Karim G. A. (1980). A review of combustion processes in the dual fuel engine - the gas diesel engine, Progress in Energy and Combustion Science, Vol. 6 (3):277-285.

[6] Karim G.A. and Amoozegar N. (1982). Examination of the performance of a dual fuel diesel engine with particular reference to the presence of some inert diluents in the engine intake charge. SAE Paper 821222.

- [7] Murari Mohon Roy, Eiji Tomita, Nobuyuki Kawahara, Yuji Harada, Atsushi Sakane (2009). Performance and emission comparison of a supercharged dual-fuel engine fueled by producer gases with varying hydrogen content. *International Journal of Hydrogen Energy*. Vol. 34(9):7811-7822
- [8] Harman, Arif E and Hasan D., "Pengaruh Penambahan Gas HHO terhadap Unjuk Kerja Motor Bensin Berbahan Bakar Pertamina", *Jurnal Teknik Mesin, Universitas Hasanudin Makassar*(2013).
- [9] C. Eckman, "Plasma orbital expansion of the electrons in water," *Proc. NPA*, vol. 7, pp. 142-144, 2010.
- [10] R. M. Santilli, "A new gaseous and combustible form of water," *International Journal of Hydrogen Energy*, vol. 31, pp. 1113-1128, 2006.
- [11] Li J, Guo L, Du T. Formation and restraint of toxic emissions in hydrogen gasoline mixture fuelled engines. *International journal of hydrogen energy* 1998; 23; 971–5. Science direct, Elsevier.
- [12] D. M. Madyira and W. G. Harding, "Effect of HHO on four stroke petrol engine performance," 2014.
- [13] Noor Alam and K. M. Pandey, "Experimental Study of Hydroxy Gas (HHO) Production with Variation in Current, Voltage and Electrolyte Concentration", *IOP Conference Series: Materials Science and Engineering*, Volume 225, (2017).
- [14] Ali Can Yilmaz, et al. (2010). Effect of hydroxy (HHO) gas addition on performance and exhaust emissions in compression ignition engines, *International Journal of Hydrogen Energy*, doi:10.1016/j.ijhydene.2010.07.040
- [15] Agata-Godula-Jopek, "Hydrogen Production by Electrolysis", Wiley-Vch.
- [16]<https://www.dangerouslaboratories.org/hydrogen1.html>
- [17] Chraplewska N., Duda K., Meus M. (2011). Evaluation of usage of brown gas generator for aided admission of diesel engine with fermentative biogas and producer gas. *Journal of KONES Powertrain and Transport*. Vol. 18(3):53-60.

Techniques to Improve the Parallel Finite Element Method to Solve Large Scale Problems

Abul Mukid Mohammad Mukaddes¹, Masao Ogino², and Ryuji Shioya³

¹Shahjalal University of Science and Technology, Bangladesh

²Information Technology Centre, Nagoya University, JAPAN

³Faculty of Information Sciences and Arts, Toyo University, JAPAN

mukaddes1975@gmail.com, masao.ogino@cc.nagoya-u.ac.jp, shioya@toyo.jp

ABSTRACT

With advent of computer technology finite element method has achieved the popularity in the simulation of engineering problems. In order to get the accurate result, the finite element discretization of the problem should be as fine as possible. The finest discretization of three dimensional (3D) problems results in the large linear systems of equations. Consequently, the solution of equation having millions of co-efficient has become the biggest challenge of the researchers. Recent development of the computer technology necessitates the efficient ways to solve those linear systems of equations using less memory and time. In this paper, some efficient ways have been proposed to solve large scale heat transfer and solid mechanics problems using the parallel finite element methods. Firstly, an iterative method with different preconditioners is implemented in the both thermal and solid problems and significant results have been achieved. Secondly, it is shown that use of sparse matrix storage scheme reduces the computation time and the required memory. Different variations of sparse matrix storages schemes have been studied here for different class of engineering problems.

Keywords: Finite element, domain decomposition, compressed sparse row, heat conduction, preconditioner

1. Introduction

ADVENTURE System [1] has been developed to solve large scale engineering problems in the parallel computer. Adventure_Thermal is one of its module that can solve large scale steady and unsteady heat conduction problems. The basic algorithm is the Hierarchical Domain Decomposition Method (HDDM) which is based on the non-overlapping domain decomposition method. In this method, the whole domain is divided into parts and then each part is divided into subdomains. Each subdomain problem is solved using finite element technique. The Conjugate Gradient (CG) method is used to solve the interface problem that is constituted by share nodes of subdomains [2, 3]. The finite element discretization of the subdomain problems results in the sparse matrix. Sparse matrices, by definition are populated by many zeroes and thus special storage schemes are used to enable efficient storage and computational operations. These representations usually store the non-zero values of the matrix with additional indexing information about the position of these values [4]. The HDDM method used in the Adventure_Thermal is gradually improved with different ways. The research is still going on to make the module faster for the users. The techniques that are implemented to improve parallel finite element method used in Adventure system are discussed in this paper.

First: The subdomain problem is solved using the direct linear solution technique and iterative Conjugate Gradient (CG) method is used to solve the interface problem. The CG method is improved after implementing a suitable preconditioner. It is shown here that Balancing Domain Decomposition (BDD) can be

an efficient preconditioner. This reduces the computation time and memory significantly when the problem is solved in the parallel computer.

Second: Both subdomain problem and interface problem is solved using the iterative CG methods which improves the computational time and memory significantly when the problem is solved in single computer.

Third: The CG method that is employed to solve the interface problem uses the Sparse Matrix Vector multiplication (SpMxV) as its basic operation. The non-zero sparse matrix storage formats used in this module are based on Compressed Sparse Row (CSR) [4]. The variations of this method are investigated in both thermal and solid problems. All CSR type storage formats are compared with the traditional skyline problems. They outperform the skyline method in terms of memory and computation time. Again in the construction part of the BDD type preconditioners, matrix vector multiplication is necessary thus sparse matrix storage schemes are used there too.

The subdomain discretization is discussed in the next section. BDD preconditioner and sparse matrix storage formats are introduced in section 3 and 4 respectively. The computational performances are given in section 5.

2. Subdomain Discretization

After the finite element discretization of the partial differential equation of heat transfer and structural problems yields a linear system of form,

$$Ku = f \quad (1)$$

where K is the global stiffness matrix, u is unknown vector and f is a known vector. For a large scale problem, the linear system (1) cannot be solved using a single processor due to memory constraint. The solution is to

use the parallel computer. The domain decomposition method is a popular technique to solve a large scale finite element problem in the parallel computing environment.

The method decomposes the domain Ω into N non-overlapping subdomains, $\{\Omega_i\}_{i=1,\dots,N}$. Thus the stiffness matrix K of equation (1) could be generated by subassembly:

$$K = \sum_{i=1}^N R^{(i)} K^{(i)} R^{(i)T} \quad (2)$$

where $R^{(i)T}$ is the 0-1 matrix which translates the global indices of the nodes into local (subdomain) numbering. Denoting $u^{(i)}$ as the vector corresponding to the nodes in $\Omega^{(i)}$, it can be expressed as $u^{(i)} = R^{(i)T} u$. Each $u^{(i)}$ is split into degrees of freedom $u_B^{(i)}$, which correspond to $\partial\Omega^{(i)}$, called interface degrees of freedom, $u_I^{(i)}$ for interior degrees of freedom and $u_T^{(i)}$ for essential boundary conditions (temperature for heat conduction problem). The subdomain matrix $K^{(i)}$, vector $u^{(i)}$ are then split accordingly:

$$K^{(i)} = \begin{pmatrix} K_{II}^{(i)} & K_{IB}^{(i)} & K_{IT}^{(i)} \\ K_{BI}^{(i)} & K_{BB}^{(i)} & K_{BT}^{(i)} \\ K_{TI}^{(i)} & K_{TB}^{(i)} & K_{TT}^{(i)} \end{pmatrix}, \quad \begin{Bmatrix} u_I^{(i)} \\ u_B^{(i)} \\ u_T^{(i)} \end{Bmatrix}. \quad (3)$$

Similarly equation (1) can be written as

$$\begin{bmatrix} K_{II} & K_{IB} & K_{IT} \\ K_{BI} & K_{BB} & K_{BT} \\ K_{TI} & K_{TB} & K_{TT} \end{bmatrix} \begin{Bmatrix} u_I \\ u_B \\ u_T \end{Bmatrix} = \begin{Bmatrix} f_I \\ f_B \\ f_T \end{Bmatrix}. \quad (4)$$

After eliminating the interior degrees of freedom, problem (4) is reduced to a problem on interface

$$S u_B = g \quad (5)$$

where the Schur complement $S = \sum_{i=1}^N R_B^{(i)} S^{(i)} R_B^{(i)T}$ is assumed to be positive definite, u_B is the vector of the unknown variables on the interface, g is a known vector and $S^{(i)}$ are the local Schur complements of subdomain $i=1,\dots,N$, assumed to be positive semi-definite. The problem (5) is solved by the Conjugate Gradient (CG) method which can use a preconditioner like Balancing Domain Decomposition (BDD) which is first proposed by Jan Mandel [5].

3. Balancing Domain Decomposition

The BDD preconditioner proposed by Jan Mandel is constructed by solutions of the local Neumann-Neumann problems on subdomains coupled with a

coarse problem in a coarse space. The BDD preconditioner is of the form:

$$M_{BDD}^{-1} = Q_c + (I - Q_c S) Q_l (I - S Q_c) \quad (6)$$

where Q_l is the local level part [5] and Q_c is the coarse level part of the preconditioner.

3.1 Coarse Level

The application of the coarse term $Q_c = R_0 (R_0^T S R_0)^{-1} R_0^T$ amounts to the solution of a coarse problem whose coefficient matrix is $S_0 = R_0^T S R_0$. The operator R_0 translates the coarse degrees of freedom to the corresponding global degrees of freedom and is defined by

$$R_0 = [R_B^{(1)} D^{(1)} Z^{(1)}, \dots, R_B^{(N)} D^{(N)} Z^{(N)}] \quad (7)$$

For the scalar heat conductive problem, $Z^{(i)}$ is a column constant vector and can be defined by

$$Z^{(i)} = (1 \dots 1)^T \quad (8)$$

where the number of element "1" is for each interface point in subdomain i . The operator R_0 is a n by N matrix, where n is the dimension of S . The implementation of the BDD preconditioner (6) goes as follows:

Step 1: Balance the original residual by solving the coarse problem for an unknown vector $\lambda \in \mathfrak{R}^N$:

$$S_0 \lambda = R_0^T r. \quad (9)$$

Step 2: Set

$$s = r - S R_0 \lambda. \quad (10)$$

Step 3: Solve Neumann-Neumann problems and average these results

$$\bar{u} = \sum_{i=1}^N R_B^{(i)} D^{(i)} S^{(i)+} D^{(i)T} R_B^{(i)T} s. \quad (11)$$

Step 4: Compute

$$\bar{s} = r - S \bar{u}. \quad (12)$$

Step 5: Solve the coarse problem again for an unknown vector $\mu \in \mathfrak{R}^N$

$$S_0 \mu = R_0^T \bar{s}. \quad (13)$$

Step 6: Find the preconditioned vector

$$z = \bar{u} + R_0 \mu. \quad (14)$$

The equation (6) can also be expressed as:

$$M_{BDD}^{-1} = (P + (I - P) Q_l S (I - P)) S^{-1} \quad (15)$$

where $P = Q_c S$ is the S -orthogonal projection onto the coarse space.

The construction of the BDD preconditioner uses the matrix vector multiplication in equation (10) and (12) where sparse matrix storages schemes are used.

4. Sparse Matrix Storage Formats

The matrix originates from the finite element discretization is naturally sparse pattern. The pattern of sparse matrix contains many zero elements within the non-zero elements. The most popular useful storage technique is the Skyline method which cannot avoid storing of zero elements within the matrix.

In order to take the advantage of avoiding the large number of zero elements, special formats are used to store sparse subdomain matrices. The main goal is to represent only the non-zero elements (nnz) considering the memory requirements and the computation time. Several sparse matrix storage techniques are described in this section and implemented in Adventure systems. Some of the techniques are described here.

Skyline or Variable Band (SKY)

The Skyline representation becomes popular for direct solvers especially when pivoting is not necessary. For symmetric matrices, this representation only stores the lower triangular matrix and hence requires half storage space. The matrix elements are stored using three arrays: *data*, *row_ptrn*, *col_ind*. The array *data* stores the elements of *A* row by row, *col_ind* contain column number of first element of each row and *row_ptr* array points to the start of every row.

This storage format stores some zero elements while other methods explained below do not. The skyline storage format of the examples matrix *A* is shown below.

$$A = \begin{bmatrix} 1.0 & 2.0 & 0.0 & 6.0 & 0.0 \\ 2.0 & 3.0 & 4.0 & 7.0 & 9.0 \\ 0.0 & 4.0 & 5.0 & 0.0 & 0.0 \\ 6.0 & 7.0 & 0.0 & 8.0 & 10.0 \\ 0.0 & 9.0 & 0.0 & 10.0 & 11.0 \end{bmatrix}$$

data (13):

1.0	2	3	4	5	6	7	0	8	9	0	10	11
-----	---	---	---	---	---	---	---	---	---	---	----	----

row_ind(6):

1	2	4	6	10	13
---	---	---	---	----	----

col_ind(5):

1	1	2	1	2
---	---	---	---	---

Coordinate Storage (COO)

The simplest sparse matrix storage structure is COO. It uses three arrays of length *nnz*(number of non-zeroes) to store the sparse matrix: *data*, *row_ind* and *col_ind*. The array *data* stores the non-zero elements of the sparse matrix. The *row_ind* and *col_ind* stores the row and column indices of the corresponding element. The COO storage format of the *example matrix A* is shown below.

1.0	2	3	4	5	6	7	8	9	10	11
-----	---	---	---	---	---	---	---	---	----	----

row_ind:

1	2	2	3	3	4	4	4	5	5	5
---	---	---	---	---	---	---	---	---	---	---

col_ind:

1	1	2	2	3	1	2	4	2	4	5
---	---	---	---	---	---	---	---	---	---	---

Compressed Sparse Row (CSR)

The CSR format is specified by *{data, row_ptr and col_ind}*. The 1D array *data* of length *nnz* contains the non-zero elements of *A* row-wise fashion, *col_ind* of length *nnz* contains the column indices which correspond to the non-zero elements in the array *data*. The integer vector *row_ptr* of length *nrow+1* contains the pointers to the beginning of each row in the array *data* and *col_ind*. With the *row_ptr* array we can easily compute the number of non-zero elements in the *i*th row as *row_ptr*[*i+1*] - *row_ptr*[*i*]. The last element of *row_ptr* is *nnz*. The CSR representation of an example symmetric matrix *A*:

data(11):

1.0	2	3	4	5	6	7	8	9	10	11
-----	---	---	---	---	---	---	---	---	----	----

col_ind(11)

1	1	2	2	3	1	2	4	2	4	5
---	---	---	---	---	---	---	---	---	---	---

row_ptr(6)

1	2	4	6	9	11
---	---	---	---	---	----

Consider the symmetric part of a matrix (figure-1) which originates from structural problems. The CSR storage of the above matrix is shown below. The conventional CSR technique stores the elements of matrix using *data*, *col_ind* and *row_ptr* (figure-2). The pattern of the matrix has 3 off-diagonal block matrix and 4 diagonal tri-angular matrix. The diagonal block matrix and off-diagonal block matrix can be stored in separate vectors (*diag and data*). In that case only location of first element of each off-diagonal block matrix is enough to locate the other elements. As a result the *brow_ptr* and *bcol_ind* will become like the figure-3 shown. The storing method is named as diagonal block compressed sparse row (DBC SR).

1
2 3
4 5 6
7 8 9 10
11 12 13 14 15
16 17 18 19 20 21
22 23 24 25
26 27 28 29 30
31 32 33 34 35 36
37 38 39 40
41 42 43 44 45
46 47 48 49 50 51

Fig.1 Matrix format (B) for structural problem

<i>data[51]</i>	1	2	3	4	5	6	7	8	9	10	11	12	13	14	15	16	17
	18	19	12	21	22	23	24	25	26	27	28	29	30	31	32	33	34
	35	36	37	38	39	40	41	42	43	44	45	46	47	48	49	50	51

<i>col_ind [51]</i>	0	0	1	0	1	2	0	1	2	3	0	1	2	3	4	0	1
	2	3	4	5	3	4	5	6	3	4	5	6	7	3	4	5	6
	7	8	0	1	2	9	0	1	2	9	10	0	1	2	9	10	11

<i>row_ptr [12]</i>	0	1	3	6	10	15	21	25	30	36	40	45	51
---------------------	---	---	---	---	----	----	----	----	----	----	----	----	----

Fig. 2 CSR storage of block matrix B

<i>diag[24]</i>	1	2	3	4	5	6	10	14	15	19	20	21	25	29	30	34	35
	36	40	44	45	49	50	51										

<i>data[27]</i>	7	8	9	11	12	---	22	23	24	26	---	37	38	29	41	--	48
<i>brow_ptr (4)</i>	0						9					18					26
<i>bcol_ind (3)</i>	0						3					0					

Fig. 3 DBCSR storage of block matrix B

The advantage of DBCSR is that *diag* does not indexing thus indexing part reduces the required memory. This technique is implemented in Adventure_Solid. In this research, some others CSR type techniques are identified and implemented in the Adventure System. Detail results are shown in the next section

5. Performance Evaluation

5.1. Model Description

The model used to investigate the performance of ADVENTURE_Thermal in different aspects is High Temperature Test Reactor (HTTR) shown in Figure-2. The model parameters are given in Table-1.

5.2 Performance of preconditioner

The balancing domain decomposition method has been implemented in both Adventure_Thermal and Adventure_Solid. After implementing BDD, in the Adventure_Thermal, the CG converges rapidly with



Fig. 4 High Temperature Test Reactor (HTTR)

Table-1 Parameters of HTTR

Model	meshing points	elements	#sub	#parts	#proc.
Mesh 1	1,893,340	1,167,268	4800	6	6
Mesh 2	13,853,784	9,338,144	76800	96	96

The HTTR model is analysed using the Adventure_Thermal-2.0. Figure 5 and Table 1 show the computational results of Mesh 1 of HTTR model. BDD takes less computational time but require more memory. In all types of preconditioning techniques, the CSR shows better results compare to Skyline storage schemes.

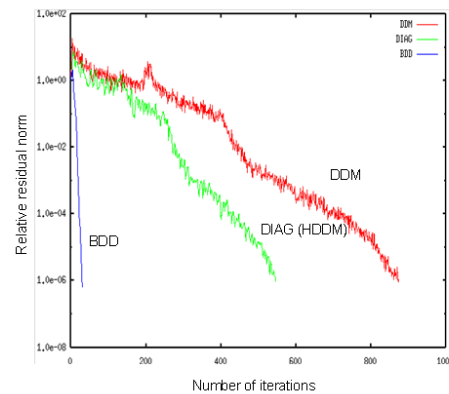


Fig. 5 Convergence of CG method

Table 1 Computational results (1.8 M mesh points)

Precon.	Storage formats	#iter.	Total time(s)	Mem. (MB/pro)
None	SKY	984	233	587
	CSR	956	130	350
Diagonal Scaling	SKY	613	150	587
	CSR	603	86	351
BDD	SKY	33	42	829
	CSR	33	31	659

5.3 Performance of Sparse Storage Formats

In order to find out the performance of different sparse storage formats, a structural problem of 5.4 M meshing points is analyzed using the Adventure_Solid. The memory required for the solution of a structural problem having 5.4 M meshing points using different matrix storage techniques are shown in figure 6. The figure gives the information that CSR types require less memory compare to the skyline storage schemes. Among the different CSR types, DBCSR shows best results in terms of memory requirement and computation time (figure 7).

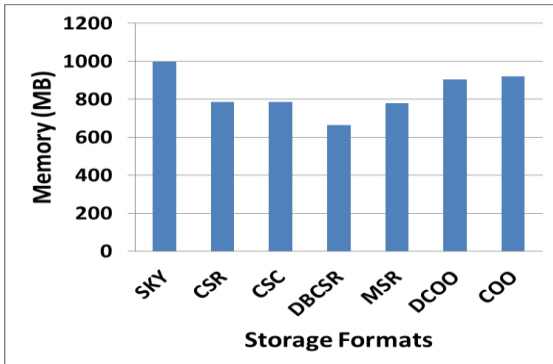


Fig. 6 Memory required for different storage formats

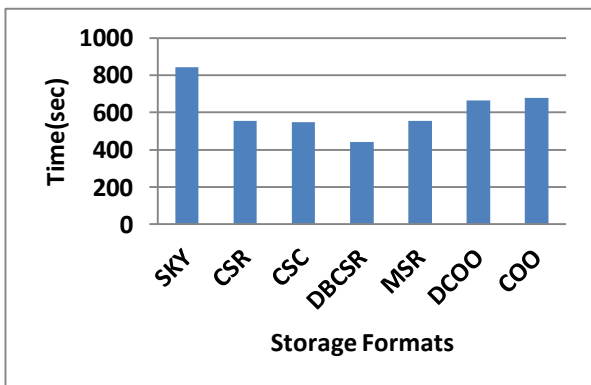


Fig. 7 Time required for different storage formats

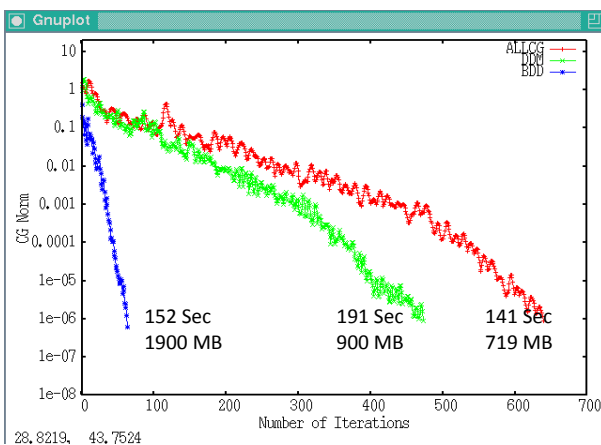


Fig. 8 Comparisons of BDD, DDM and AllCG

5.4 Performance of AllCG solvers

Both Adventure_Thermal and Adventure_Solid uses the CG solver to solve the interface problem and direct Gauss elimination technique is used to solve the interior of the subdomain problem. Recently a new solver is introduced to Adventure_Thermal called AllCG which solve both interface and interior problems using CG iterative method. According to figure-8 though it converges slowly but the computational time is reduced. It is advised to use this solver when Adventure_Thermal is used in a single computer.

6. Conclusion

Several techniques to solve the large scale finite element problems efficiently are studied. They are implemented in the open source CAE software Adventure System. Large scale problem of having 5.4 million meshing points is solved in the parallel computer to investigate the different preconditioning techniques and sparse matrix storage formats. Both thermal and structural problems CSR shows better performance. DBCSR shows best performance for the case of structural problems.

References

- [1] Adventure project, <http://adventure.sys.t.u-tokyo.ac.jp/>
- [2] Mukaddes, A.M.M., Ogino, M., Kanayama, H. and Shioya, R., A Scalable Balancing Domain Decomposition Based Preconditioner for Large Scale Heat Transfer Problems, *JSME International Journal, Series B*, Vol. 49, No. 2, pp. 533-540.
- [3] Shioya, R., Ogino, M., Kanayama, H. and Tagami, D., Large Scale Finite Element Analysis with a Balancing Domain Decomposition Method, *Key Engineering Materials.*, 243-244 (2003), p.21-26.
- [4] Mandel, J., Balancing Domain Decomposition, *Comm. on Numerical Methods in Engineering*, Vol. 9 (1993), p. 223-241.

Pyrolysis of Sawdust for Bio-Oil Production using Infrared Heat Source

Md. Rabiul Islam, Muhammad Mostafa Kamal Bhuiya, Bably Das, Mostafizur Rahman and Amir Hamza Limon*
Department of Mechanical Engineering, Chittagong University of Engineering & Technology (CUET), Chittagong 4349,
BANGLADESH

ABSTRACT

An experimental investigation was carried out to produce bio-oil from sawdust using pyrolysis process (infrared induction cooker). The experiments were performed for varieties of infrared cooker heat inputs at a particular moisture content. To complete the pyrolysis process, a conical flask type reactor was used in this experiment. The experimental results demonstrated that the maximum of 7% bio-oil, 83% char and 10% gas were obtained at a moisture content of 25%. The properties of produced bio-oil were characterized and compared to other biomass products. The calorific value, density, viscosity, flashpoint and fire point of 10.7 MJ/kg, 922.71 kg/m³, 20 mm²/sec 64°C and 68°C were obtained, respectively, when the produced bio-oil was tested. This paper provides a clear information about how to produce bio-oil from biomass resources at a greater extent using infrared induction cooker. It can be noted that the production and usages of bio-oil is one of the roots to produce low-carbon energy.

Keywords: *Infrared induction cooker, Pyrolysis, Bio-oil, Calorific value*

1. Introduction

Renewable energy is one of the most important form of energy which is of growing valuable environmental concerns over fossil fuel usage and it's contributed to greenhouse effect [1]. The renewable energy so called "Green Energy" which is produced conversion of biomass using pyrolysis technology and this conversion of biomass has gained more popularity because of their zero net CO₂ emission to the environment. The biomass resources considered as a potential source of energy as these are economical, non-toxic and reduce dependency on crude oil. In addition, the increasing awareness of the depletion of fossil fuel resources and the environmental concerns has made biomass resources more attractive to produce bio-oil using pyrolysis process. Today, modern world facing the problem of scarcity of fossil fuels, increasing their manufacturing cost and this fossil fuels have more impact to the environmental pollution which will make renewable energy source more useful to the users. Petroleum products such as fuel oil, gasoline or valuable chemicals are used in every aspect of life today. With rapid increase in world population, the demand for petroleum products is increasing day by day. But the world's oil supply is fixed since petroleum is naturally formed far too slowly in millions of years to be replaced at the rate at which it is being extracted [2]. With the concern of depletion rate and price increase, there is rapidly growing interest in renewable energy source like biomass to be used as an alternative to petroleum. Biomass is biological material from living, or recently living organisms, most often referring to plants or plant-derived materials. Biomass can be converted to higher value products or energy. They include wide range of materials such as: virgin wood from forestry, energy crops specially grown for energy applications, agricultural residues from agriculture harvesting, food waste from food and drink preparation and processing, and post-consumer waste, or industrial waste and co-products from manufacturing and industrial processes [3]. Pyrolysis is one of thermo-chemical process which

converts the solid biomass in to liquid (bio-oil), gas and solid and liquid product, pyrolytic oil, approximates to biomass in elemental composition, and is composed of a very complex mixture of oxygenated hydrocarbons [4]. Pyrolysis conversion technology for biomass has been investigated over the last three decades and used commercially [5]. Bio-oil derived from agricultural wastes has moderate GCV ranging from 15-38 MJ/kg with some advantages in transportation, storage, combustion, retrofitting and flexibility in production and marketing [6]. Sawdust is available in our country because there are lot of sawmills besides us. Sawdust has a great potential source of chemical energy which comes from various kinds of wood. The bio-oil contains more than a hundred of organic compounds that belong to alkanes, phenols, aromatic hydrocarbon, acids, aldehydes, ketones, alcohols, esters, furans [7]. Plant biomass mainly comprises of celluloses, hemi celluloses and lignin making it an ideal source of renewable energy for producing bio-oil and power [4]. Several factors like environmental benefit, economic benefit and availability of source need to be considered for selection of proper alternative energy [9]. The agro-based biomass is usually produced in the rural area where a largescale pyrolysis plant can be installed [10]. Sawdust is more easily suitable for pyrolysis process to produce bio-oil. Biomass conversion techniques including thermo-chemical and biochemical conversion are employed for power generation and production of liquid biofuels, chemicals and charcoal, which can be used as activated carbon. Biochemical conversion can be made using the enzymes of bacteria and other micro-organisms to break down biomass. Mostly micro-organisms are used to perform the conversion process: anaerobic digestion, fermentation and composting [11]. Waste materials such as sawdust, coconut shell, scrap tire, rice husk, plastic and biomass waste are being generated every year around the world. Some of these wastes are effectively collected and recovered for using as an energy source or chemical feedstock while some

are simply discarded or burned in ways that can pollute the environment. Improper disposal of these waste materials may constitute an environmental hazard due to the presence of undesirable species such as metals, soot and polycyclic aromatic hydrocarbons. In present days, the treatment of these waste materials represents a significant challenge in the real world. Pyrolysis is also used in the creation of nanoparticles, zirconia and oxides utilizing an ultrasonic nozzle in a process called ultrasonic spray pyrolysis. Another form of waste disposal is achieved by thermal means through incineration. In this process, the combustion of wastes in the release of greenhouse gas such as Carbon dioxide that contribute to climate change. Besides, incineration can lead to toxic emissions that pose a direct hazard to the environmental and human health. Incineration recovers only calorific value of the waste but does not allow or the recovery of any of the chemical value of waste, and so this method is being impracticable due to concerns of greenhouse gas release and associated with environmental pollution and toxic emissions. Infrared pyrolysis is a relatively new process. Conventional thermal heating usually employs an external heating source to transfer heat to material through a surface. In contrast, microwave heating constitutes a unique way of heating where the heating effect arises from the interaction of electromagnetic wave with the dipoles within the material being heated. By such heating mechanisms, heat is generated within the material rather than from an external source, thereby giving a more efficient heating process compared to conventional surface heating respect to even distribution of heat and easier control over the heating. In addition, high temperatures and heating rates can be obtained through infrared heating [12]. It can be noted that bio-oil produces using infrared heat source pyrolysis process has a great significant to the energy conversion technology in the field of renewable energy source. Therefore, the goal of this investigation is to produce bio-oil from sawdust using infrared induction cooker.

2. Experimental facility

2.1 Materials

Sawdust is domestically available which was used for the pyrolysis. The sawdust materials were collected from a sawmill (Pahartoli, Raozan). In every experiment, the amount of sawdust was weighted by a weight machine to get the accurate result. The sawdust can provide more crude oil than other pyrolysis materials.

2.2 Experimental parameters

To conduct the experiment to produce bio-oil from sawdust using infrared induction cooker there are lot of equipment were used

An infrared cooker of MODEL VSN-INF 2083 was used to complete the pyrolysis process. It can provide up to 2000W power and 600°C temperature. Infrared radiation is a type of electromagnetic radiation, as are radio waves, ultraviolet radiation, X-rays and

microwaves. A conventionally used conical flask of 500ml was used in this experiment. The conical flask made of glass was used to carry the sawdust and a cylindrical pot made of stainless steel was used to receive the gas produced during the pyrolysis process of the sawdust. Pieces of ice were given around the stainless- steel cylindrical condenser and a large plastic bucket carried the condenser. There were enough ices around the condenser to liquefy the gases and the gases which cannot be liquefied are set to be out by a small hole to the environment. The hole was at the upper portion of the condenser which was not down to the condensing water. A thermocouple is a temperature measuring device. It can measure high temperature. In this experiment a thermocouple which was run by electricity. It has a wire which outer point is attached to the measured temperature medium and other side is connected to the thermocouple. The thermocouple shows two values one is setting value & other variable values. The gas produced in the conical flask by heating was transferred to the stainless-steel cylindrical tube by using the copper tube. For this kind of study, the tube used to transfer hot gases is usually made of copper. Because, copper tube can bear more heat than any other metals and don't get corroded by water-gas mixture. In this study, the stainless-steel cylindrical pot was used for condensing because it can easily condensate. The height and radius of the stainless-steel cylinder are eight and two inches. There was enough space inside the steel cylinder so that the hot gases can get more time during condensing. As steel is a conductive material so it can easily cold.



Fig. 1 (a)Infrared Cooker;(b)Conical flask; (c)Copper tube; (d) Ice bath; (e)Temperature monitor; (f)Stainless steel cylinder.

2.3 Pyrolysis

Pyrolysis process carries out in the pyrolysis reactor. Finally, energy was recovered from pyrolysis of oil. Analysis of the obtaining charcoal and pyro-oil. An infrared cooker of MODEL VSN-INF 2083 is used to complete the pyrolysis process which can provide up to 2000W power and 600°C temperature. Pyrolysis means the thermal cracking of larger hydrocarbons into smaller one in the absence of oxygen or any other oxidizing components. Nitrogen gas is used as carrier gas to keep the pyrolysis condition inert. It also helps quick removal of hot gas from the pyrolysis chamber thus preventing secondary cracking of hot gas and increases liquid product of pyrolysis. Nitrogen gas is supplied to the pyrolysis and hot pyrolysis product condensation chamber by copper tubes of 6mm diameter. Both chambers are made from conical flask of 500 ml capacity and condensation chamber are submerged in an ice bath.

2.4 Experimental setup

The experimental facility consists of conical flask, stainless steel condenser, copper tube, ice bath, nitrogen gas cylinder, infrared cooker, thermocouple etc. These were used to complete the experiment that means for pyrolysis of sawdust. The schematic diagram of the experimental set up is shown in Fig. 2[13].

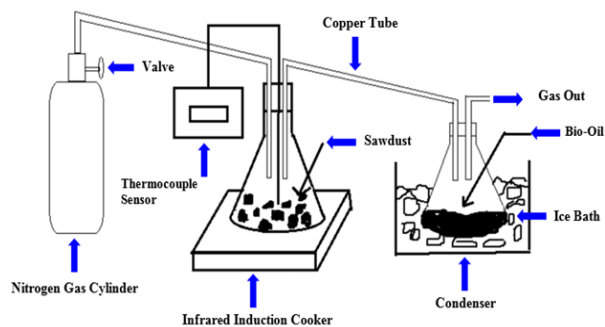


Fig. 2 Schematic diagram of experimental set up

2.5 Experimental procedure

At first, the sawdust is kept on the conical flask reactor with known weight of sawdust for infrared pyrolysis. The schematic diagram of the experimental setup is shown in Fig.2. When the microwave heating is started, the sawdust begins to pyrolysis after certain temperature evaluation. Pyrolysis products (vapor & gases) will be passed through the steel pipe to the ice water cooled condenser, where the condensable products will be condensed in the bottom of the condenser and gaseous products will be passed through the hole of the condenser. The temperature of the pyrolysis product will be recorded in a certain time interval. The microwave heating will be held for a time interval to get desired pyro-oil and bio-char which has a certain calorific value and viscosity of the liquid oil. In this study, the gaseous product will be released to the atmosphere. Liquid nitrogen will be used in this study to create inert atmosphere and carrier gas.



Fig. 3 Photograph of sawdust pyrolysis process

Ice cooled water can be used to condense the vapor in order to maximize the oil yield. The condensate oil is accumulated at the bottom of the condenser then it is stored for further analysis. The aim of this study is to obtain pyro-oil from sawdust by heating. The heating of sawdust is held in a 2000W infrared cooker. The infrared cooker is used for this study, has a capacity of 20 liters and it is taken from VISION, Model-VSN-INF 2083. The output power of this infrared cooker is 2000W and temperature is up to 600°C. The size of the copper tube was 6mm.

2.6 Product yield percentage

In this study, inert gas was produced inside the infrared wave reactor. To remove these inert gases, nitrogen gas was supplied from a nitrogen cylinder. For condensation the gas product one ice-bath condenser was used. In this pyrolysis process sawdust is fed, no activated carbon is mixed to enhance the infrared wave absorption. In the product yield, 7% pyro-oil is recovered, which have a good calorific value. The char produced 83. % of the total weight at a certain time till the oil being produced from the sawdust.

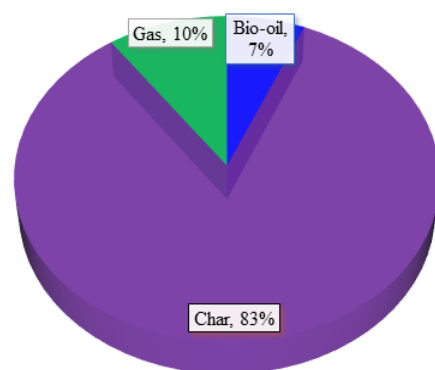


Fig. 4 Percentage of product yield

The high percentage of the gases and losses may be attributed to some leaks from some gaps in the apparatus. Furthermore, the water used in the

condensing unit might not be cold enough thus reducing the oil yield. Uncondensed volatile vapor would flow out of the condensing unit along with others. It can be seen that once the pyrolysis started to occur, brown vapor immediately filled up the condenser flask and flew out of the condenser top. The pyrolysis process created an irritable odor of the vapor and the vapor would start to condense in the stainless-steel condenser. After the oven was turned off volatile matter was still seen to be released from the sawdust sample.

2.6.1 Bio-Oil

The pyro-oil obtained from the sawdust pyrolysis is shown in Fig.5(a) below. For every 100 gm of sawdust the pyro-oil is obtained almost 4-8 gm. The pyro-oil increases to produce from sawdust in every time interval. It contains some chemical compounds which can be known by chemical test. The pyro-oil is darkish in color and smells bad.

2.6.2 Charcoal

Sawdust charcoal obtained from the pyrolysis process is shown below in the Fig.5(b). The standard time to produce the charcoal is about 60 minutes. During this time the sawdust gets burnt by the heat of infrared cooker inside a conical flask and converted into char giving up the gas and liquid.

2.6.3 Gas

During the pyrolysis of sawdust gases are produced in the conical flask. These gases are provided to condenser by the action of nitrogen gas because the pressure of nitrogen gas was 100 KPa. But all the gases are not condensed to the condenser because there are some non-condensable gases like light hydrocarbon and gaseous materials.



Fig. 5 (a)Bio-oil; (b) Charcoal.

3 Data collection and analysis

3.1 Pyrolysis products

The weight of produced char and pyro-oil was weighed in the digital weighing machine. From this weight of gas product was calculated.

Weight of the gas product = weight of the sawdust sample – (weight of the produced char + weight of the produced pyro-oil)

3.2 Moisture content

The moisture percentage was calculated by using the equation given below:

$$\text{Moisture Content (\%)} = \frac{a-b}{a} \times 10(1)$$

Where, a = Initial mass of sawdust = 1000g
b = mass of sawdust after drying =754g

3.3 Calorific value

By using bomb calorimeter higher calorific value of produced pyro-oil was determined.

$$\begin{aligned} \text{Higher Calorific value} &= \frac{W\Delta T}{m}(2) \\ &= \frac{3320.83 \times 0.74}{0.96} \text{ cal/g} \\ &= 10751.18 \text{ J/g} \end{aligned}$$

Where, energy equivalent of calorimeter (considering error), determined under standardization, W= 3320.83 cal/°C. Temperature rise, $\Delta T = 0.74^\circ\text{C}$. Weight of the pyro-oil, m = 0.96 gm.

3.4 Flashpoint and Fire Point

The flashpoint of pyro-oil is 64°C .

The fire point of pyro- oil is 68°C

3.5 Viscosity

From viscometer it is found that the dynamic viscosity of the pyro-oil,

$$\begin{aligned} \mu &= 18.5 \text{ Cp} \\ &= 18.5 \times 10^{-3} \text{ Ns/m}^2 \end{aligned}$$

Density:

$$\begin{aligned} \text{Mass of beaker} &= 99.55 \text{ gm} \\ \text{Mass of beaker with 70ml pyro-oil} &= 164.14 \text{ gm} \\ \therefore \text{Mass of 70ml of pyro-oil} &= 64.59 \text{ gm} \\ &= 64.59 \times 10^{-3} \text{ kg} \end{aligned}$$

$$1000 \text{ ml} = 1 \text{ liter}$$

$$\therefore 70 \text{ ml} = 0.07 \text{ liter}$$

$$\text{Again, } 1000 \text{ liter} = 1 \text{ m}^3$$

$$\therefore 0.07 \text{ liter} = 0.07 \times 10^{-3}$$

$$\therefore \text{Density, } \rho = (64.59 \times 10^{-3}) / (0.07 \times 10^{-3}) \text{ Kg/m}^3 = 922.71 \text{ Kg/m}^3$$

The kinematic viscosity of the pyro-oil, $\nu = \mu/\rho$

$$= 0.00002 \text{ m}^2/\text{s}$$

4 RESULTS AND DISCUSSION

4.1 Calorific value

The energy contained in a fuel or food, determined by measuring the heat produced by the complete combustion of a specified quantity of it. The amount of energy available from an item of food when digested, mostly from carbohydrates and fats. That depends on the state of water in the product of combustion it's refers to higher heating value (HHV) when liquid water

exists in the combustion products and lower heating value (LHV) when water vapor exists in the combustion products. From the Fig. 6, it can be seen that the calorific value of sawdust is higher than the rice husk whereas the value is lower than the coconut shell and rice straw.

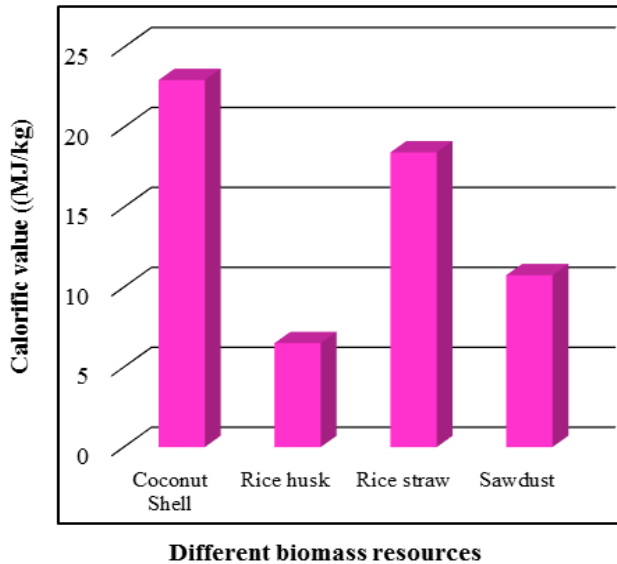


Fig. 6 Comparison of calorific value for different biomass resources

4.2 Density

Density of the biodiesel is comparatively less than other oil such as date seed oil, heavy fuel oil and saw dust etc.

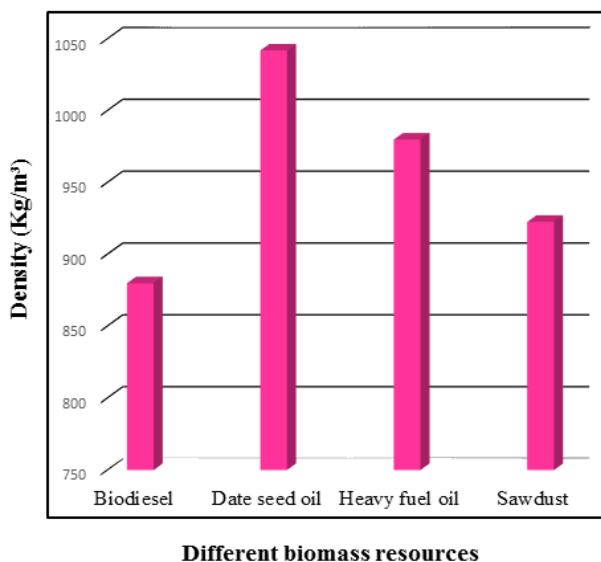


Fig. 7 Comparison of density for different biomass resources

4.3 Viscosity

From Fig. 8, it can be noted that the viscosity of sawdust is significantly lower than the heavy fuel oil but bit higher than the biodiesel and date seed oil.

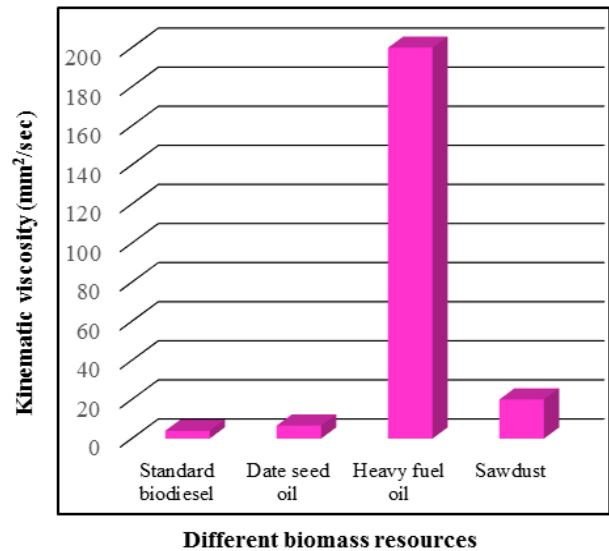


Fig. 8 Comparison of kinematic viscosity for different biomass resources

4.4 Flashpoint

Flash point, the lowest temperature at which a liquid (usually a petroleum product) will form a vapor in the air near its surface that will “flash,” or briefly ignite, on exposure to an open flame. From the graph the flashpoint of the produced sawdust bio-oil is 64°C which is comparatively low. So, it causes danger as low flashpoint is hazardous. The fire point of a fuel is the lowest temperature at which the vapor of that fuel will continue to burn for at least 5 seconds after ignition by an open flame. From graph it indicates that the fire point of the bio-oil is 64°C because at this temperature the vapor continue to burn at least five seconds.

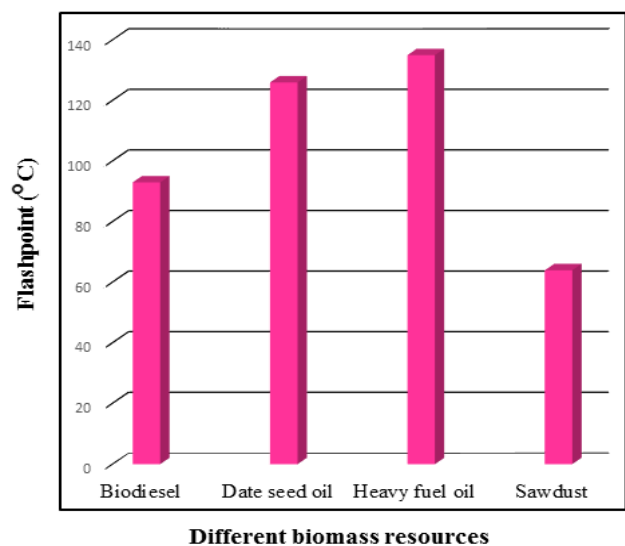


Fig. 9 Comparison of flashpoint for different biomass resources

At the flash point, a lower temperature, a substance will ignite briefly, but vapor might not be produced at a rate

to sustain the fire. It can be illustrated from Figure 5.4, the flashpoint is lower in comparison to other biomass resources, such as biodiesel, date seed oil and heavy fuel oil etc.

4.5 Proximate and ultimate analysis

An analysis which reports volatile matter, fixed carbon, moisture content, and ash present in a fuel as a percentage of dry fuel weight. Not precise, but very useful for determining the commercial value. The proximate and ultimate analysis of different feedstocks with sawdust are shown in Tables 1 and 2, respectively.

Table 1 Proximate analysis of different feedstocks [1, 10]

Proximate Analysis (wt. %)	Coconut shell (%)	Pine Chips (%)	Wood (%)	Shredded Green Waste (%)	Sawdust (%)
Volatile matter	85.36	16	82	77.6	10
Air dried moisture	11.26	4.4	20	6.1	-
Ash	3.38	13.8	0.4	1.0	83
Oil	-	-	-	-	7
Fixed carbon	-	65.80	17	15.3	-

Table 2 Ultimate analysis of different feedstocks[1, 10, 9]

Ultimate Analysis	Coconut Shell (wt. %)	Rice Husk (wt. %)	Sawdust (wt. %)	Wood Pellet (wt. %)
Carbon	63.45	40.64	46.2	45.5
Hydrogen	6.73	5.09	6.6	6.6
Nitrogen	0.43	0.63	3.4	0.1
Oxygen	28.27	53.64	43.8	47.7
HHV(MJ/Kg)	22.83	17.02	12	18.6

5 Conclusion

This study represents an experimental investigation to produce bio-oil using pyrolysis (infrared induction cooking) process from sawdust. The produced bio-oil from sawdust has good properties in compared to other feedstocks. Sawdust could be a prospective feedstock for bio-oil production as it is very cheap and available in sawmills in our country. The product yield of 7% bio-oil, 83% charcoal and 10% gas were obtained during infrared induction cooking pyrolysis process at a

particular moisture content. The maximum bio-oil was obtained at a heat input of 800W during pyrolysis process. The calorific value, density, viscosity, flashpoint and fire point of 10.75 MJ/kg, 922.71 kg/m³, 20 mm²/sec, 64°C and 68°C are obtained, respectively, when the produced bio-oil was tested.

REFERENCES

- [1] J. Ward, M.G. Rasul, M.M.K. Bhuiya, Energy recovery from biomass by fast pyrolysis. *procedia Engineering*, Vol. 90, pp 669-674(2014).
- [2] T. Appenzeller. 'The end of cheap oil', *National Geographic*. June (2004).
- [3] Energy center. Biomasseenergycenter.org.uk.
- [4] G. Sundaram, E. Natarajan, Pyrolysis of Coconut Shell: An Experimental Investigation, *the journal of engineering research*, Vol.6, No.2 pp33-39(2009).
- [5] A.V. Bridgewater, A.J. Toft, J.G. Brammer, A techno-economic comparison of power production by biomass fast pyrolysis with gasification and combustion. *Renewable and Sustainable Energy Reviews* Vol. 6, pp 181-248(2002).
- [6] M. Asadullah, M.A. Rahman, M.M. Ali, M.S. Rahman, M.A. Motin, M.B. Sultan, M.R. Alam, Production of bio-oil from fixed bed pyrolysis of bagasse, Vol. 86, pp 2514-2520(2007).
- [7] P. Kongnum, S. Ratanawilai, Catalytic Pyrolysis of Coconut Shell for Bio-oil, *IJACEBS* Vol.1, Issue1(2014).
- [8] L. Burhennaea, J. Messmera, T. Aichera, M.P. Laborie, The effect of biomass components lignin, cellulose and hemicellulose on TGA and fixed bed pyrolysis, *Journal of Analytical and Applied pyrolysis*, Vol. 109, pp 188-197(2013).
- [9] K. Kothari, A. B. Shah, S. Murugavelh, Bio-oil production: Pyrolysis of Sawdust in an augur reactor, *International journal of Chem Tech Research*, Vol.8, No.6, pp 349-357.
- [10] M.U.H. Joardder, M.R. Islam, M.R. Alam Beg, pyrolysis of coconut shell for bio-oil, *International Conference on Mechanical Engineering*(2011).
- [11] T.K. Rout, Pyrolysis of coconut shell, *M. Tech Thesis*
- [12] Holland, K.M. Apparatus for Waste Pyrolysis. *U.S. Patent*, pp 5, 327, 321, 7 February (1995).
- [13] M.S.A. Sarkar, M.H. Tusar, B. Salam, K.G.M. Prince, Investigation on Bio-Oil Production Using Infrared Heat Source, *12th ICME-2017* December (2017).

Cleaning of Accumulated Dust Particle of a Flat Plate Solar Collector

Amir Hamza Limon, Muhammad Mostafa Kamal Bhuiya*, Mostafizur Rahman and Majedul Islam

Department of Mechanical Engineering, Chittagong University of Engineering & Technology (CUET), Chittagong 4349,
BANGLADESH

ABSTRACT

An experimental investigation was carried out to find out the effective cleaning method of the glazing material of solar collector. The study emphasized on solar panel glazing material cleaning process using water force impinging by a nozzle. A nozzle is used to make a water jet having a velocity which is impacted on the glazing material of a solar plate collector. The project investigated the optimum position of nozzle with respect to glass at which the dust removing rate is maximum. The jet of different velocities were used to perform the experiment and the maximum tangential force was found between 30°-40° relative angle of impacted jet with respect to the glazing material at which the maximum cleaning can be possible. This project will help to ensure the maximum amount of solar beam reach to the receiver for power generation. It can be noted that this technique will help to clean the solar collector with a reasonable cost and effectively.

Keywords: *Accumulated dust, Cleaning, Water force, Nozzle, Glazing material*

1. Introduction

Globally, we are bound in different types of energy sources. But, in the past several decades energy requirements have been increased significantly and predicted that it rises to 50% by 2030(world energy outlook,2011). At this time, these requirements are met mostly from the conventional way (like coal, gas, oil etc.). Environment is being polluted by their exhaust and their reserves will be nearly finished after some era. For this reasons, implementation of renewable energy sources like solar power are rising. After implementation of solar panels some difficulties arise of their performance. Dust accumulation over glass plate of solar panels is one of the biggest problems because dust obscures the solar radiation and therefor reduces their efficiency, especially in those countries whose environmental condition is hard. Dust accumulation mostly depends on weather condition and geographical locations. To reduce this loss, many researchers have been developed different types of solar collector cleaning techniques and many of them are researching. The categories of cleaning solutions considered in this study include the following: manual cleaning, mechanized cleaning, hydraulic cleaning, installed robotic cleaning and deployable robotic cleaning [1]. Removal of dust particles from the surface of the solar cells and solar collectors is performed using surfactants [2]. A shield contains a clear panel with embedded parallel electrodes connected to a single-phase AC supply for producing an electromagnetic wave. The electromagnetic field produced by the electrodes on the surface of the panel repels dust particles that have already deposited on the panel surface, and prevents the deposition of further particles if they are charged with positive or negative polarities [3]. A deep study about the effectiveness of different cleaning methods, including natural cleaning, has been performed during two years in a semi-desert climate. Different cleaning methods were periodically applied to several reflector samples exposed in four separated test benches.

Monochromatic specular reflectance measurements were taken before and after applying the cleaning methods [4]. The self-cleaning technology for solar cell array can promote efficiency of electricity produced and protect the solar cell. The methods of dust-removal, such as natural means, mechanical means, self-cleaning nano-film, and electrostatic means are presented [5]. The influence of cleaning on the PV panels using water as well as a surfactant was investigated experimentally using a non-pressurized water system [6]. Dust problem and recent developments made on automated cleaning system for solar photovoltaic modules which give brief overview on techniques like electrical, mechanical, chemical and electro static [7]. Fabricated superhydrophobic microshell PDMS showed a superior dust cleaning effect compared to that of flat PDMS, preventing the degradation by dust particles of solar cell efficiency. This transparent, flexible and superhydrophobic microshell PDMS surface provides feasibility for a practical application of superhydrophobic surfaces in solar cells [8]. A self-cleaning effect developed through the use of a super hydrophobic and water-repellent surface was demonstrated for solar cell applications [9]. A perfectly ordered microshell array was fabricated on a transparent and flexible polydimethylsiloxane (PDMS) elastomer surface. self-cleaning solar panels may be manufactured incorporating electrodynamic screens that will derive their power from the panel itself about 10 watts per square meter of a solar panel. This power is a small fraction of the power generated by a typical panel (800 watts) and is used only when cleaning is needed [10]. Many efforts have been made to address the severity of deposited particles like dust, water stains, carbon from smoke, pollen in agricultural regions, etc. on the efficiency reduction of solar devices, which results in additional costs either from oversizing the system or from cleaning it [11]. In the current study, the experimental data concerning the effect of three representative air pollutants (i.e., red soil, limestone and

* Corresponding author. Tel.: +88-01784353193
E-mail addresses: mkamalcu@et@gmail.com

carbonaceous fly-ash particles) on the energy performance of PV installations are analyzed. According to the results obtained, a considerable reduction of PVs' energy performance is recorded, depending strongly on particles' composition and source[12]. Effect of dust, humidity and air velocity influences of the efficiency of photovoltaic cells[13]. Most popular solar collector concentrating technologies are Flat plate solar collector. In this paper, force of hydraulic jet impinging from nozzle is used for cleaning Flat solar panel collector and find out a better relative angle between plate & flow for better performance. All the tangential force acting on the plate can remove the dust, but highest force can remove maximum dust from the collector in minimum time.

It can be seen that the dust accumulation over solar collector is one of the biggest problems because dust obscures the solar radiation and therefore, reduces their efficiency. However, minimizing the cost of the cleanliness is a key issue for the solar-plant feasibility. Therefore, this work focused on optimizing the cleaning method of solar reflectors for CSP applications under real outdoor conditions in a semi-desert or hard climate.

2. Experimental Procedure

The study relates to cleaning glazing material of solar collector or other glass plates by using water jet impinging from nozzle, particularly for cleaning surfaces which may be horizontal, vertical or any other angular position. When a water jet strikes a plate with a force it flashes the surface. This force divided by normal force which acts normally to the plate and tangential force which act tangent of the surface. Normal force is responsible for wearing the surface and produces separation in water after striking. Water with tangential force move along the surface and washed away the dust particles along its path. If the tangential force increases water can washed away maximum possible of different type dust (oily dust, heavy particulates, Electrostatic precipitators etc.). As well as amount of water and time needed for proper cleaning reduces with increasing the tangential force of water jet. So, it is important to know better position of nozzle relative to the glazing plate from where jet is impinged.

Labor costs, maintenance cost and other technical cost could be lower by using this technique compare to other technique stated at previous article. This technique is convenient for those area where availability of water source is found lower as minimum amount of water needed for proper cleaning when the better position of nozzle is found.

2.1 Experimental setup

To conduct the experiment to find out better relative position of nozzle with respect to the glazing material several equipment were used. The experiment was conducted at Chittagong University of Engineering and Technology. Glass plate is a plate or may be a collector solar panel over which water jet is impacted at different height or angular position. It is placed on a force

measuring device which calculates normal force of the impacted jet. It is connected to another force measuring device with wire which calculates tangential force. Wooden frame is a frame made of wood or ply which carries all other components. Two wooden frames were used, one was vertical, and one was horizontal. One weight measuring device measures normal force of impacted jet and another weight measuring device measures tangential force of impacted jet. Different sizes of pipes are used. One main pipe carried water with a nozzle connected to its middle from which water jet is released, constructed such a manner that it can rotate with a fixed height at different angle and can slide on a vertical scale at a fixed angle. A nozzle is structured at the middle of the main pipe such a manner that water jet released through it can splash maximum area of the glass plate. Pipe fittings are used to connect different pipe section where necessary. Rollers are used to minimize friction between the glazing material and the weight measuring scale.

In this experiment all the equipment is assembled to accomplish desired setup for finding out dependent variable or tangential force by manipulating the independent variable or relative angle of nozzle and glass plate.

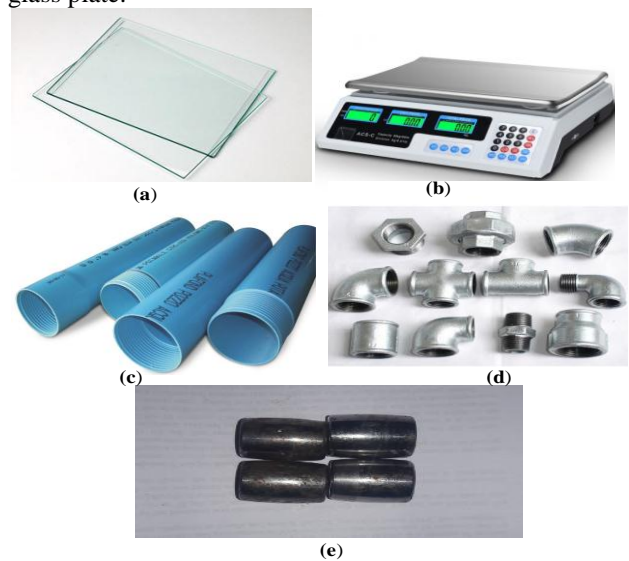


Fig. 1 (a) Glass plate; (b) Weight measuring scale; (c) PVC pipes; (d) Pipe fittings; e) Roller.

2.2 Experimental procedure

At first, horizontal wooden frame is made for the mechanical support which protects the other equipment. A vertical frame with a groove in the middle is made which can roll in horizontal direction along the horizontal wood frame. A 2-inch diameter PVC pipe is made in such a way that it's one end is closed with suitable fittings and other end is connected to a smaller 0.5inch diameter pipe with a bell reducer and nipple fittings. This smaller pipe is connected to the water source. A 3.5mm diameter nozzle relates to a tee fitting at the middle of that pipe.



Fig.2 A cleaning method of a glass plate as a glazing material

The whole pipe with the nozzle can be made an up and down movement along the groove of the vertical frame. A vertical scale or ruler is placed vertically along the vertical frame which indicates the vertical position (h) of the pipe or nozzle position with respect to the glass plate. An angular scale is positioned at the closed end of the PVC pipe which indicates the angular position of the nozzle with respect to the flat glass plate.



Fig. 3 (a) Weight measuring device with glass plate and roller; (b) Angular and vertical position measurement

The PVC pipe with nozzle can move up and down by lifting it by a rope system. A weight measuring device is placed horizontally on the horizontal wooden frame just below the main pipe. This device can measure the normal force of the impacted jet striking on the glass plate. It can be calibrated. A glass plate is placed over the weight measuring device over which a water jet is impacted. Between the glass plate and weight measuring device, four rollers are placed such a way that the glass plate is situated over these rollers. The main tasks of these rollers are to minimize the friction between the weight measuring device and the glass plate. The water jet is impacted on the flat glass plate with a particular striking force and a particular relative angle between the glass plate and the impinging water jet. A normal force is measured by the weight measuring device. With the angle and this normal force, we can easily find out the striking force of the jet and the tangential force. Our main aim is to find out the angle at which the tangential force is maximum. This system includes cleaning using a fixed nozzle or a sliding nozzle from which water exits at high speed, located at the top of the panel. Water is pumped by a

pump through a pipe to the nozzle. A water jet is released from the nozzle which is impacted on the collector with a force controlled by the operator. The point of impact of the water jet on the collector can be changed by the operator through controlling the angle between the jet and the plate. Tangential and normal components of the impacted force can be measured from a force or weight measuring device.

3. Results and discussion

In the experiment, normal forces are collected at different heights and different angles simultaneously as shown in Fig.4. At first, a relative height of the main pipe from where the nozzle is connected to the horizontal glass plate is fixed. Then different normal forces (kg) are collected with a 10° interval from 90° to 10° or 20° . Then another relative height is fixed, and normal force is collected. The height changes with a 2.54 cm interval from 12 cm to 24.7 cm.

When the jet velocity is 7.2236 m/s:

Different forces acting on the glass plate which are changed by changing the relative angular direction of the water jet and by changing the height. First, the height and angle of the jet is manipulated to find out different values of the forces.

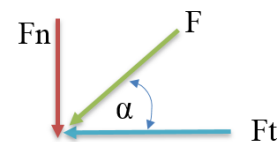
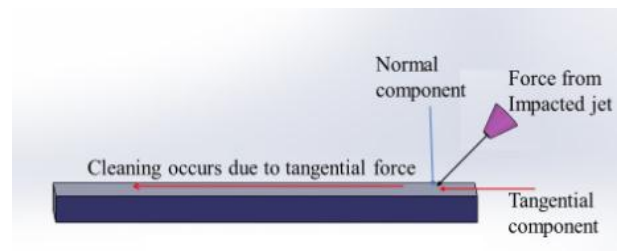


Fig. 4 Force analysis

F_n = Normal force;

F_t = Tangential force;

F = Jet striking force;

In this experiment, we manipulated the angle, α , and found the normal force F_n . Jet striking force F and tangential force F_t can be found by,

$$F_n = F \sin \alpha$$

$$F = \frac{F_n}{\sin \alpha}$$

$$F_t = F \cos \alpha$$

When the height of the main pipe or nozzle from the glass plate is 12 cm, reducing as shown in Fig.5 (a), the relative angle brought the normal force and jet striking force

into a decreasing line and at the same time tangential force is increasing. Maximum tangential force is found at 10° which is 2.423N. When height of the main pipe or nozzle from the glass plate is 14.54cm as shown in Fig.5(b) reducing the relative angle brought the normal force and jet striking force into a decreasing line and at the same time tangential force is increasing. Maximum tangential force is found at 30° which is 2.1036N. When height of the main pipe or nozzle from the glass plate is 17.08 cm as shown in Fig.5(c) maximum tangential force is found at 10° which is 2.224N. When height of the main pipe or nozzle from the glass plate is 19.62 cm as shown in Fig.5(d) maximum tangential force is found at 40° which is 2.2323N. When height of the main pipe or nozzle from the glass plate is 22.16cm as shown in Fig.5(e) maximum tangential force is found at 40° which is 2.4538N. When height of the main pipe or nozzle from the glass plate is 24.7cm as shown in Fig.5(f) maximum tangential force is found at 30° which is 2.5987N.

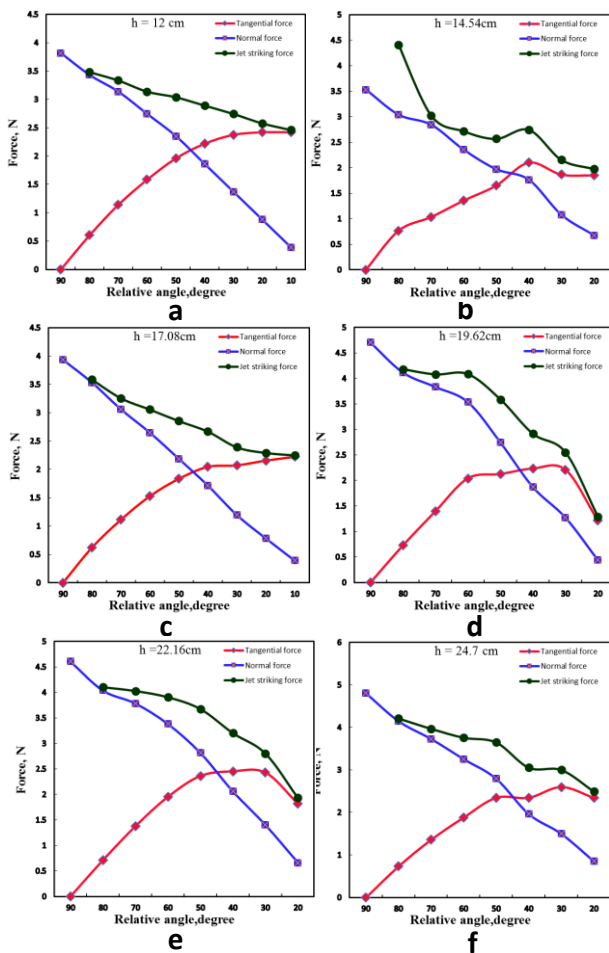


Fig. 5 Relative angle vs. different forces acting on the plate $h=12$ cm (a); $h=14.54$ cm (b); $h=17.08$ cm (c); $h=19.62$ cm (d); $h=22.16$ cm (e); $h=24.7$ cm (f); and velocity of jet is 7.2236 m/s.

When height of the main pipe or nozzle from the glass plate is 22.16 cm as shown in Fig.7(e) maximum tangential force is found at 30° which is 3.0578N. When

height of the main pipe or nozzle from the glass plate is 24.7cm as shown in Fig.7(f) maximum tangential force is found at 30° which is 3.2273N.

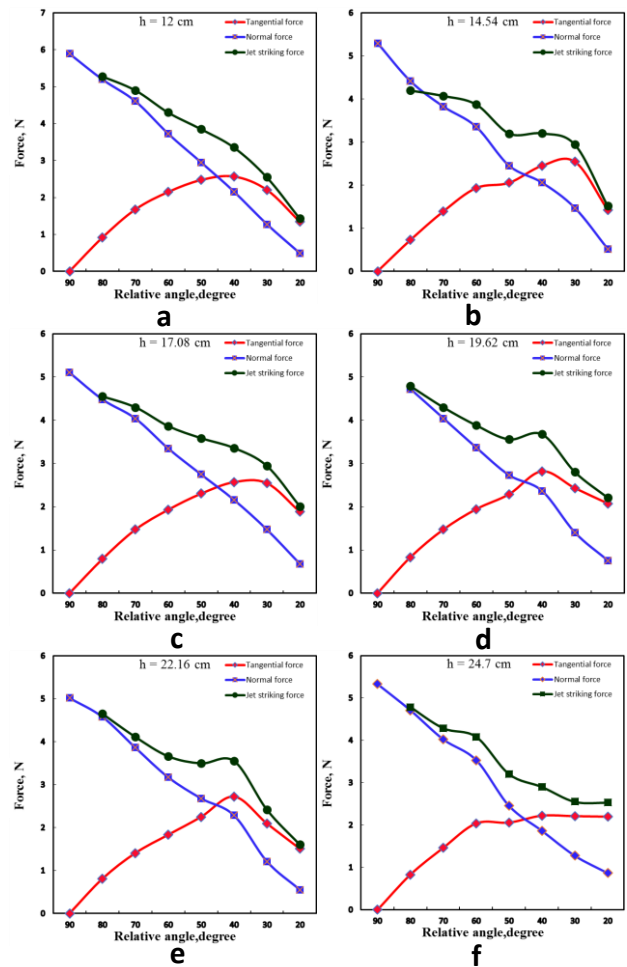


Fig. 6 Relative angle vs. different forces acting on the plate when; $h=12$ cm (a); $h=14.54$ cm (b); $h=17.08$ cm (c); $h=19.62$ cm (d); $h=22.16$ cm (e); $h=24.7$ cm (f) and velocity of jet is 10.01 m/s.

When the jet velocity is 10.01 m/s:

First fixed the height and angle of jet is manipulated to find out different value of the forces. When height of the main pipe or nozzle from the glass plate is 12cm as shown in Fig.6(a) maximum tangential force is found at 40° which is 2.5712N. When height of the main pipe or nozzle from the glass plate is 14.54cm as shown in Fig.6(b) maximum tangential force is found at 30° which is 2.5479N. When height of the main pipe or nozzle from the glass plate is 17.08cm as shown in Fig.6(c) maximum tangential force is found at 40° which is 2.5712N. When height of the main pipe or nozzle from the glass plate is 19.62cm as shown in Fig.6(d) maximum tangential force is found at 40° which is 2.8167N. When height of the main pipe or nozzle from the glass plate is 22.16cm as shown in Fig.6 (e) maximum tangential force is found at 40° which is 2.7208N. When height of the main pipe or nozzle from

the glass plate is 24.7cm as shown in Fig.6(f) maximum tangential force is found at 40° which is 2.2205N. When the jet velocity is 13.676 m/s:

First fixed the height and angle of jet is manipulated to find out different value of the forces. When height of the main pipe or nozzle from the glass plate is 12 cm as shown in Fig.7(a) maximum tangential force is found at 40° which is 3.3972N. When height of the main pipe or nozzle from the glass plate is 14.54 cm as shown in Fig.7(b) maximum tangential force is found at 30° which is 3.0355N. When height of the main pipe or nozzle from the glass plate is 17.08 cm as shown in Fig.7(c) maximum tangential force is found at 30° which is 3.0913N. When height of the main pipe or nozzle from the glass plate is 19.62 cm as shown in Fig.7(d) maximum tangential force is found at 30° which is 3.2273N.

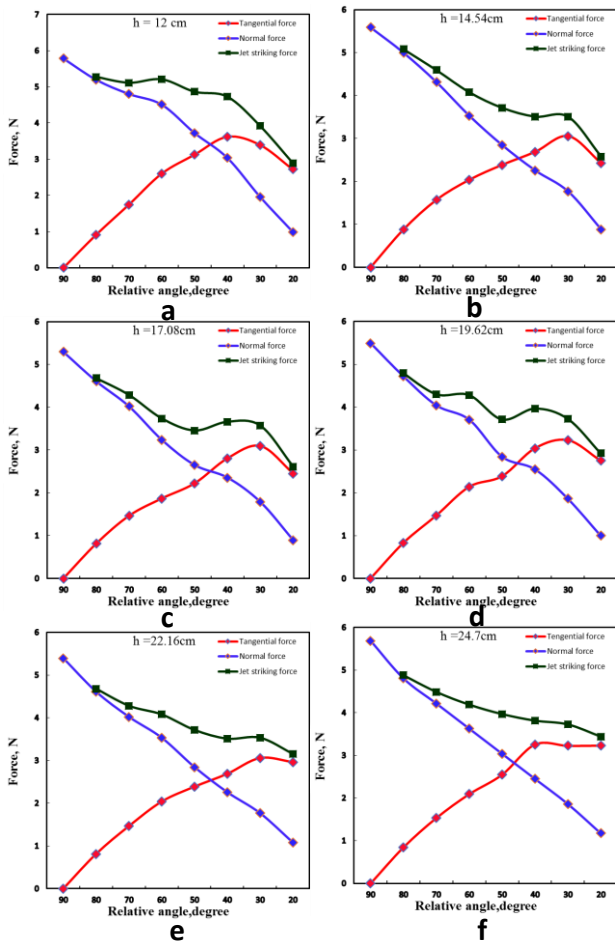


Fig. 7 Relative angle vs. different forces acting on the plate when h=12 cm (a); h=14.54cm (b); h=17.08 cm (c); h=19.62 cm (d); h=22.16 cm (e); h=24.7 cm (f) and velocity of jet is 13.676 m/s.

In the experiment when velocity of jet is used 7.2236m/s maximum tangential force 2.5987N is found at 30° relative angle and at a relative height of 24.7cm.

When the velocity of jet is used 10.01m/s the maximum tangential force 2.8167N is found at 40° relative angle and at a relative height of 19.62cm. When the velocity of jet is used 13.676m/s the maximum tangential force 3.623N is found at 40° relative angle and at a relative height of 17.08cm. Theoretically maximum tangential force could have been found at 45° relative angle as sine and cosec curve intersect at 45° each other at which tangential force and normal force would be same. Robinson et al. [14] showed that the higher shearing and slicing force was obtained when the angle of water jet is set from 0°-40°. In the experiment, the maximum tangential force was found between 30°-40° relative angle of jet. This is because of the splashing area which was large in these regions along tangential direction. But if further decreases the angle splash area increases but striking force would be decreases enough and liquid droplets increases which lowered the magnitude of tangential velocity. From the Fig.8, a relation of velocity, tangential force and height of the main pipe corresponding to the glass plate is obtained. From the Fig.8 it is seen that when velocity is increasing tangential force is also increasing but the relative height at which maximum tangential force was found is decreasing. Because as height is increasing the length of the impinging water jet from nozzle to the glass plate also increasing, as a result the contact area of water and ambient air is increasing. For these reason frictions between air and water jet is increasing with increasing the relative height of nozzle corresponding to glass plate. As a result, striking force as well as tangential force of impinging jet is decreasing with the increase of relative height.

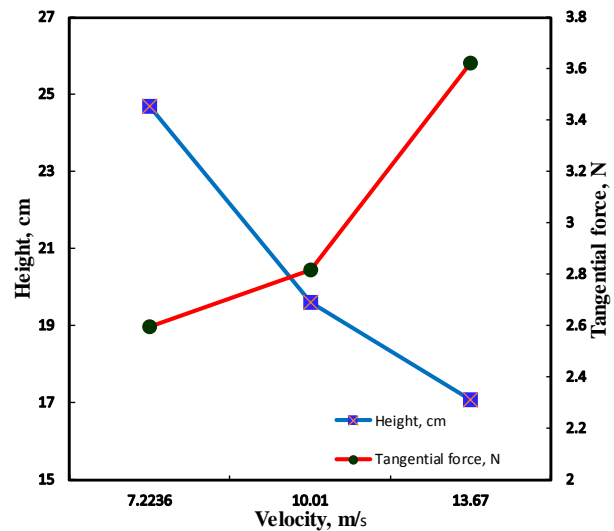


Fig. 8 Velocity vs. height and tangential force

If the velocity is increasing striking force as well as tangential force of water jet is increasing. But the angular position of impinging water jet at which maximum tangential force is occurred, is found between 30°-40°.

Generally, low carbon tempered glass sheets are used as the glazing material on the solar collector. The thickness of these glasses varies from 3-5mm. The tensile strength of these sheets varies from 40-50 N/mm² and the pressure resistance varies from 700-900 N/mm² [15]. So, there is negligible damaging effect of using the velocity described above.

In this study, one nozzle is used for finding out the better position of that nozzle relative to the glazing material. After choosing the better position several nozzles should be used along the line of the glazing material of flat plate solar collector for cleaning using minimum amount of water.

5. Conclusion

This paper will focus mainly on the better cleaning process of solar PV collector to reduce the losses originated from dust. Dust is removed by the tangential force originated from water jet impact through a nozzle which is located at the optimum position corresponding to the collector without creating any damage of the collector. The paper investigated the optimum position of nozzle with respect to glass at which dust removing rate is maximum. After using jet of different velocity, it is seen that maximum tangential force was found between 30° to 40° relative angle of impacted jet with respect to the glazing material at which maximum cleaning can be possible. At this position maximum possible dust would be removed so that maximum possible solar beam can be reached to the receiver. When velocity is increasing tangential force is also increasing but the relative height at which maximum tangential force was found is decreasing.

References

- [1] A. Alshehri, Brian Parrott*, A. Outa, A. Amer, F. Abdellatif, H. Trigui, P. Carrasco, S. Patel, I. Taie, Dust mitigation in the desert: Cleaning mechanisms for solar panels in arid regions, *2014 Saudi Arab. Smart Grid Conf. SASG 2014*, pp 1–6, (2014).
- [2] M. Abd-Elhady, S. I. M Zayed, C. C. M. Rindt, Removal of dust particles from the surface of solar cells and solar collectors using surfactants, *Proc. Eurotherm ...*, vol. 2011, no. 2010, pp 342–348, (2010).
- [3] R. A. Sims, A. S. Biris, J. D. Wilson, C. U. Yurteri, M. K. Mazumder, C. I. Calle, C. R. Buhler, Development of a transparent self-cleaning dust shield for solar panels, *Proc. ESA-IEEE Jt. Meet. Electrostat.*, no. 1, pp 814–821, (2003).
- [4] A. Fernández-García, L. Álvarez-Rodrigo, L. Martínez-Arcos, R. Aguiar, J. M. Márquez-Payés, Study of different cleaning methods for solar reflectors used in CSP plants, *Energy Procedia*, vol. 49, pp 80–89, (2013).
- [5] G. He, C. Zhou, Z. Li, Review of self-cleaning method for solar cell array, *Procedia Eng.*, vol. 16, pp 640–645, (2011).
- [6] K. A. Moharram, M. S. Abd-Elhady, H. A. Kandil, H. El-Sherif, Influence of cleaning using water and surfactants on the performance of photovoltaic panels, *Energy Convers. Manag.*, vol. 68, pp 266–272, (2013).
- [7] A. K. Mondal, K. Bansal, A brief history and future aspects in automatic cleaning systems for solar photovoltaic panels, *Adv. Robot.*, vol. 29, no. 8, pp 515–524, (2015).
- [8] M. K. Mazumder, M. Horenstein, J. Stark, D. Erickson, A. Sayyah, S. Jung, F. Hao, Development of Self-Cleaning Solar Collectors for Minimizing Energy Yield Loss Caused by Dust Deposition, *Part. Sci. Technol.*, no. November 2015, pp 1–10, (2014).
- [9] Y. B. Park, H. Im, M. Im, Y. K. Choi, Self-cleaning effect of highly water-repellent microshell structures for solar cell applications, *J. Mater. Chem.*, vol. 21, no. 3, pp 633–636, (2011).
- [10] J. Y. Hee, L. V. Kumar, A. J. Danner, H. Yang, C. S. Bhatia, The effect of dust on transmission and self-cleaning property of solar panels, *Energy Procedia*, vol. 15, no. December 2012, pp 421–427, (2012).
- [11] S. Ghazi, A. Sayigh, K. Ip, Dust effect on flat surfaces - A review paper, *Renew. Sustain. Energy Rev.*, vol. 33, pp 742–751, (2014).
- [12] J. K. Kaldellis, M. Kapsali, Simulating the dust effect on the energy performance of photovoltaic generators based on experimental measurements, *Energy*, vol. 36, no. 8, pp 5154–5161, (2011).
- [13] S. Mekhilef, R. Saidur, M. Kamalisarvestani, Effect of dust, humidity and air velocity on efficiency of photovoltaic cells, *Renew. Sustain. Energy Rev.*, vol. 16, no. 5, pp 2920–2925, (2012).
- [14] D. S. Robinson, Experimental Investigation of Effect of Abrasive Jet Nozzle Position and Angle on Coating Removal Rate, *International Journal of Manufacturing Systems*, 1: 57-64, (2011).
- [15] Flat Plate Solar Collector Glazing Materials--Tempered Solar Glass, *Qingdao Migo Glass Co., Ltd.*

ICMIEE18-327

Stress Analysis of Welded Joint Portions at Rear-side Footrests of Public Transportation like Human Hauler

Mohammad Asheful Alam*, M S Rabbi, Sama-E-Shan, Md. Shamim Hasan

Department of Mechanical Engineering, Chittagong University of Engineering & Technology, Chittagong-4349, BANGLADESH

ABSTRACT

Public transportation like Human Hauler (also called as 'Leguna') have footrest at the rear side, which is built for purpose of getting into or out of the vehicle. It is not any integral part of the vehicle, so welded with the main frame. However, it is frequently used to carry passengers in our densely populated country. As a result, extra stress is continuously generated on these portions. This research paper highlights how much stress is generated on these welded joint portions. For this evaluation, first of all continuous load data are taken by a strain gauge based load sensor setup in which an Arduino is used as controlling device. All the data was stored in an external SD card. Then using these data, stress at various welded joint portions is calculated. After that, a comparison shows which welded joint portion is the most vulnerable and which is the least.

Keywords: Stress, Welded Joint, Strain Gauge, Public Transportation

1. Introduction

Bangladesh is a densely populated country, which also have scarcity of roads and transport. A number of people used to move from one place to another by local transport. Human Hauler (Leguna) is one of the cheapest mediums of transport for the local people to avail. During the pick-hour period (when schools, office starts or ends), some passengers always taking some risks hanging themselves on the footrest of such vehicle. The footrest is not the integrated part of the vehicle, it has been fabricated (by welding) with the frame to enter and exit from the vehicle. It is noteworthy that, for gathering a number of passengers on the footrest, it is become overstressed. For this reason, there lies a huge threat for failure of that welded joint portion. Moreover, failure of such footrest during running condition might cause great loss. The scope of this study underlying with such case. We want to find out how much stresses are generated on the welded joint portions. Furthermore, we want to assess permissible load that can be applied on a selected type of footrest.



Fig.1 An under aged helper of the driver of tiny human-hauler, called 'Leguna', gets on the vehicle's roof with another person as the footrest, where the helpers usually stand, is occupied by seven passengers hanging from

window railings. (Photo: Asif Mahmud Ove, October 02, 2016, Source: bdnews24.com).

The objectives of this study are

- i. To design and fabricate strain gauge load cell based load-measuring device, which can take continuous data.
- ii. To collect load data by putting load measuring device setup at the footrest of a suitable Human Hauler.
- iii. To analyze stresses at various welded joint portions at the footrest of that Human Hauler and calculate stress value by data achieved from load measuring device.
- iv. To evaluate which welded joint portion is the most stress-prone and add necessary recommendations.

This paper is organized as follows:

In the first section, background of the study is described briefly as well as objectives. In the second section all the necessary equations with nomenclature is shown. Previous studies on stress analysis is also briefed here. Experimental setup with proper description and figures is shown in the third section. Flow chart of the study is also given here. Section four depicts the generated stress at various portion of the selected footrest. Here a comparison of generated stress at various portions is also shown assuming hundred kg applied load. In the fifth section, the authors add some recommendation about the selected footrest. Finally, in the conclusion part a brief discussion on overall study is shown.

2. Literature Review

We had to examine two kind of stresses, as our study is a circumstance of combined loading,

- i. Primary shear stresses for external forces
- ii. Secondary shear stresses for bending and torsional moment.

i. Stresses in Welded Joint in Torsion [1]:

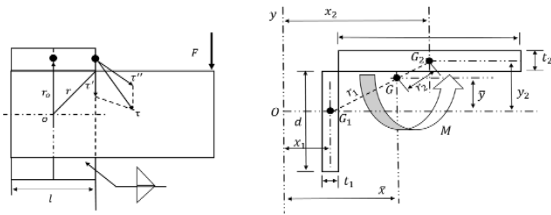


Fig.2This is a moment connection; such a connection produces torsion in the welds. The shear stresses shown are resultant stresses [1]

A cantilever of length l welded to a column by two fillet welds illustrates in figure 2. A shear force V and a moment M is produced as the reaction at the support of a cantilever. A primary shear is produced by the shear force in the welds of magnitude

$$\tau' = \frac{V}{A}(1)$$

Secondary shear or torsion is generated by the moment at the support and this stress is given by the equation

$$\tau'' = \frac{Mr}{J}(2)$$

where r is the distance from the point in the weld of interest to the centroid of the weld group and the second polar moment of area of the weld group about the centroid of the group is J . These equations can be solved and the results combined to obtain the maximum shear stress when the sizes of the welds are known.

Fig.2 depicts two welds in a group. Throat areas of the welds is represented by the rectangles. Weld 1 has a throat thickness $t_1 = 0.707h_1$, and weld 2 has a throat thickness $t_2 = 0.707h_2$. It is noted that h_1 and h_2 are the respective weld sizes. So The area of throat of both welds together is

$$A = A_1 + A_2 = t_1d + t_2b \quad (3)$$

This area A is to be used in Eq. (1)

The X-axis in Fig.2 passes through the centroid G of weld 1. The second moment of area about this axis is

$$I_x = \frac{t_1d^3}{12} \quad (4)$$

Similarly, the second moment of area about an axis through G parallel to the Y-axis is

$$I_y = \frac{dt_1^3}{12} \quad (5)$$

Thus the second polar moment of area of weld 1 about its own centroid is

$$J_{G1} = I_x + I_y = \frac{t_1d^3}{12} + \frac{dt_1^3}{12} \quad (6)$$

In a similar manner, the second polar moment of area of weld 2 about its centroid is

$$J_{G2} = \frac{t_2b^3}{12} + \frac{bt_2^3}{12} \quad (7)$$

The centroid G of the weld group is located at

$$\bar{x} = \frac{A_1x_1 + A_2x_2}{A} \quad \bar{y} = \frac{A_1y_1 + A_2y_2}{A} \quad (8)$$

Now, using the parallel-axis theorem, we find the second polar moment of area of the weld group to be

$$J = (J_{G1} + A_1r_1^2) + (J_{G2} + A_2r_2^2) \quad (9)$$

This is the quantity that should be used in Eq. (2). The distance r must be measured from G and the moment

M computed about G . Since the throat width of a fillet weld is $0.707h$, the relationship between J and the unit value is

$$J = 0.707hJ_u \quad (10)$$

in which J_u is found by conventional methods for an area having unit width. The transfer formula for J_u must be employed when the welds occur in groups, as in Fig. 2. Table 1 lists the throat areas and the unit second polar moments of area for the fillet welds encountered in our selected footrest

Table 1Torsional Properties of Fillet Welds [1]

Case	Weld	Throat Area	Location of G	I_u
2		$A = 1.414hd$	$\bar{x} = \frac{b}{2}$ $\bar{y} = \frac{d}{2}$	$J_u = \frac{d(3b^2 + d^2)}{6}$
5		$A = 1.414h(b + d)$	$\bar{x} = \frac{b}{2}$ $\bar{y} = \frac{d}{2}$	$J_u = \frac{(b + d)^3}{6}$
6		$A = 1.414\pi hr$		$J_u = 2\pi r^3$

ii. Stresses in Welded Joint in Bending [1]:

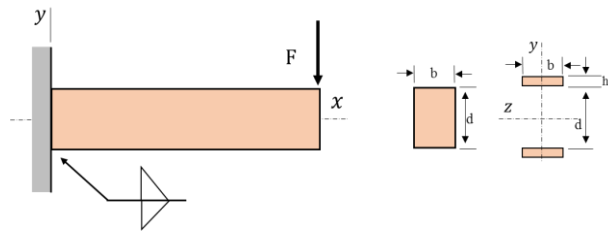


Fig.3A rectangular cross-section cantilever welded to a support at the top and bottom edges [1]

A cantilever welded to a support by fillet welds at top and bottom is shown in figure 3. A shear-force reaction V and a moment reaction M is shown by a free body diagram of the beam. A primary shear is produced by the shear force in the welds of magnitude where A is total area of throat.

$$\tau' = \frac{V}{A} \quad (11)$$

The moment M induces a horizontal shear stress component in the welds. Treating the two welds of Fig. 3 as lines we find the unit second moment of area to be

$$I_u = \frac{bd^2}{2} \quad (12)$$

Based on weld throat area, the second moment of area I is

$$I = 0.707hI_u \quad (13)$$

The nominal shear stress at throat is to be

$$\tau'' = \frac{Mc}{I} \quad (14)$$

The distance d between the two welds determines the second moment of area in Eq. (14).

The secondary shear of Eq. (14) and primary shear of Eq. (11) are then combined as vectors to give

$$\tau = (\tau'^2 + \tau''^2)^{1/2} \quad (15)$$

Table 2 lists the throat areas and the unit second polar moments of area for the fillet welds encountered in our selected footrest.

Table 2 Bending Properties of Fillet Welds [1]

Case	Weld	Throat Area	Location of G	I_u
2		$A = 1.414hd$	$\bar{x} = \frac{b}{2}$ $\bar{y} = \frac{d}{2}$	$I_u = \frac{d^3}{6}$
5		$A = 0.707h(b + 2d)$	$\bar{x} = \frac{b}{2}$ $\bar{y} = \frac{d^2}{b + 2d}$	$I_u = \frac{2d^3}{3} - 2d^2\bar{y} + (b + 2d)\bar{y}^2$
6		$A = 1.414h(b + d)$	$\bar{x} = \frac{b}{2}$ $\bar{y} = \frac{d}{2}$	$I_u = \frac{d^2}{6}(3b + d)$

2.2 Previous Studies:

As we selected a topic, which has never studied before, here some study about stress analysis has been briefly discussed. Many steel structures such as road and railway bridges, oil and gas exploitation platforms (offshore platforms), windmills, and so on are subjected to a high number of repetitive cyclic stresses during their lifetime. Over time, those stresses can cause damage, such as cracks, at critical locations. This phenomenon is called “fatigue.” It can be defined as a progressive localized process in which damage continuously accumulates in a structure or structural element due to the effect of cyclic loading, which has much less intensity than the static resistance of an observed structure or structural detail.

A study by Oehme [2] shows how fatigue takes third place as the cause of failure of fatigue prone steel structures. Fatigue cracks are usually initiated at locations of a sudden change in the geometry or notch locations[3], where there is a localized increase of stress (stress concentration). The smaller the notch is, the bigger the stress concentration is, and in the end, fatigue life is shorter. The most common locations in steel structures prone to fatigue where fractures are made are welded joints as these are locations of high stress concentrations. Obviously, fatigue assessment becomes inevitable during design and maintenance because welding is a primary process of connecting elements in

structures that are previously mentioned. Furthermore, in the last few years, high-strength steels are being used more frequently for steel structures due to the decrease in self-weight of the structure, and although its use has a positive effect, fatigue becomes a leading ultimate limit state.

The term “fatigue” was first mentioned in the 19th century to describe the failure of a structure or structural element subjected to cyclic loading. Research of fatigue was first carried out by August Wöhler who investigated the failure of train axles. He detected that structural loading that is well below its static resistance does not cause any damage. However, in the case of repeating the same loading over a prolonged period, it can cause failure of the structure or structural element. In the 19th century, fatigue was a mysterious phenomenon because fatigue damage could not be seen, and failure occurred without any warning. In the 20th century, it became known that cyclic (repeated) structural loading initiates the fatigue mechanism and, respectively, crack initiation and propagation. Since this fatigue phenomenon became recognized, much research has been conducted, and significant progress in developing fatigue assessment methods, understanding the mechanism of fatigue of structures and materials, and the designing of fatigue resistant details has been made. However, this phenomenon still requires further investigation [4].

Schütz [5] as well as Mann [6] give a chronology of fatigue development from 1837 to 1994 in his collection of 21,075 literature sources in his four books that are concerned with the fatigue problem of materials and structures from 1838 to 1990. Cui [7] made a review of fatigue assessment methods from 2002 and the factors that affect fatigue behavior of structures and materials. An understanding of the fatigue mechanism is a prerequisite when considering different factors that affect fatigue life and choosing appropriate assessment methods. The fatigue life of a structure or structural element is measured from the crack initiation and crack propagation phase. Cracks made by cyclic loading usually occur at the surface of a structural element where fatigue damage comes in the form of microscopic cracks in crystallographic slip planes. This phase is called the “Crack Initiation Phase.” Furthermore, cracks propagate from localized plastic strain to macroscopic size in a direction perpendicular to the loading direction, which presents the crack propagation phase [8]. The crack initiation phase also includes crack growth on a microscopic scale, but it still cannot be seen by the naked eye. It is very hard to determine the point between the phases of crack initiation and propagation. In the crack initiation phase, fatigue is a surface phenomenon and depends on material surface characteristics and environmental conditions, while crack propagation depends on the characteristics of the material the crack is spreading through. Forsyth [9] first recognized these two phases, which is one of the biggest accomplishments in research of fatigue of metals in the 20th century. The mechanism of fatigue in different

materials and structures is widely described by Schijve [8] in his book. Modern fatigue theories separately analyzed every phase of the fatigue process. Crack initiation theories are based on the assumption that fatigue cracks appear with local stress or strain concentrations on the surface of a structural element because of different geometrical shapes like holes, notches, discontinuity, and so on. Crack propagation and final fracture (failure) is analyzed by fracture mechanics that considers the crack propagation rate in relation to the stress state in crack tip.

3. Research Framework

First of all, we constructed a portable device by which data collection procedure will be easy and efficient. To find necessary data effectively, we used following equipment-

- a) Load cell (4) – sturdy steel construction with strain gauge(0-50 kg)
- b) Arduino UNO
- c) Differential Amplifier (HX711)
- d) SD card module
- e) LED Light
- f) Frame

We took some assumptions to conduct the research. These are described briefly below:

i) Pick-Hour Period: According to school & office time, We assumed three pick hour periods which are-

- a) 7:00 am - 9:00 am
- b) 11:30 am - 1:00 pm
- c) 4:30 pm – 8:30 pm

All the data was taken at these periods.

ii) Route: We took two routes for research data. These are

- a) Bahaddarhat – Amtol.
- b) Pared Corner – Barek Building.

iii) Residual Stress: Since heat is used in the welding operation, there are metallurgical changes in the parent metal in the vicinity of the weld. In addition, residual stresses may be introduced because of clamping or holding or, sometimes, because of the order of welding. Usually these residual stresses are not severe enough to cause concern; in some cases a light heat treatment after welding has been found helpful in relieving them. When the parts to be welded are thick, a preheating will also be of benefit. If the reliability of the component is to be quite high, a testing program should be established to learn what changes or additions to the operations are necessary to ensure the best quality [1]. As necessary data are not available for residual data, We took residual stress as negligible.

3.3 Load Measuring Device Setup:

Firstly, we made load measuring device frame. We put load cells on four corners. Arduino, Differential amplifier (HX711), SD Card Module are placed according to the circuit diagram inside the frame.

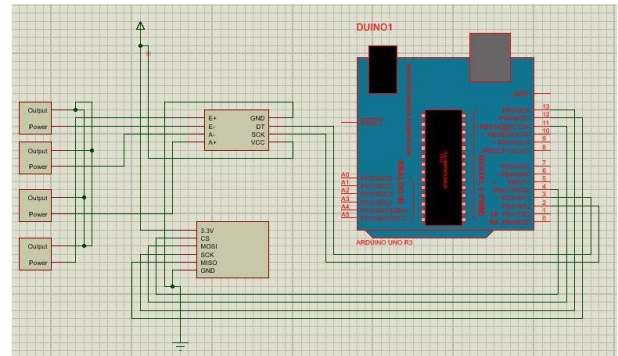


Fig.4 Circuit Diagram

Then We made necessary connections. We also attach a cover to protect my device and to collect data easily. Cover is made by Nylon sheet and top of it a GI sheet is placed which is bent at both edges. A magnet is attached to the frame which clings to GI sheet. We also attached an LED to ensure data collection.

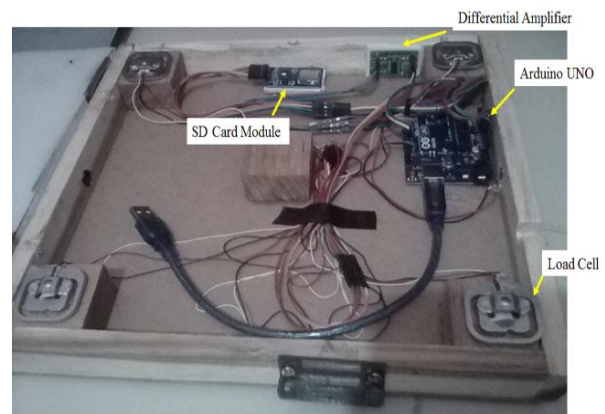


Fig. 5 Load measuring device set up (Inside view)

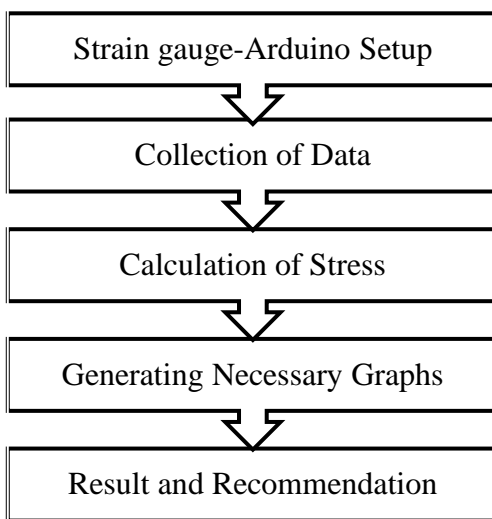
After making the device, We calibrated it with known weight. Note that the device gives two data every second as programmed. Then We put the device over the footrest of a Human Hauler (Leguna). My experiment date was Friday (5 October 2018). My experiment route was Bahaddarhat to Amtol and time was at about 5:45pm. Necessary measurement was taken by compass and scale.

We found about 1500 data within 25 minutes, which was stored on the SD card. After that these data has been analyzed. Actually more than 3000 data was expected but We think the connection between power bank and Arduino was a little bit loose. That's why it misses almost half portions of data. However the amount of data collected is fairly enough to analyze stresses and also to conduct this study.



Fig.6 Experiment Moment

3.4 Flow Chart of the Research



4. Data Analysis and Result

There are too many types of footrests available. Of them, We only took one for analysis. All the necessary geometrical measurements were taken at first, which is given in Fig.7



Fig.7 Necessary geometrical measurements of selected footrests

4.2 Analysis

We analyzed six welded joint portions and evaluated the highest stress-prone portions. Here primary shear and

secondary shear (i.e. bending) exists considering the structure. Therefore, We calculated the stresses using Table 2 and according to the equations described in 2.1



Fig.8 Analysis of footrest structure welded joint (All the cases are previously mentioned at Table 1.2)

4.3 Results

The Highest stress-prone portions of the footrest We analyzed is for case 2

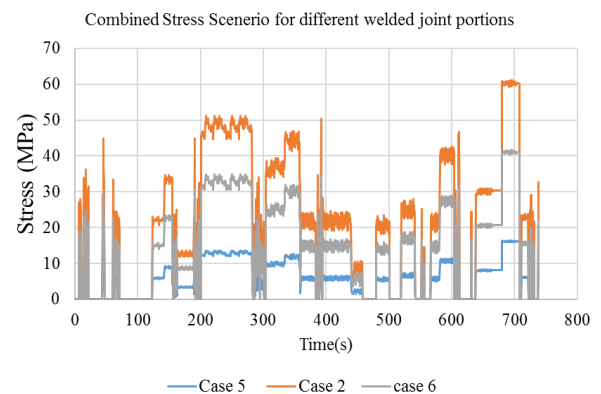


Fig.9 Combined Stress Scenerio for different welded joint portions

If a load of 100 kg is assumed, then generated stresses should like following

Table 3 Comparison of Stresses at various points

Case No	Combined Stresses(MPa)
5	10.01
2	37.31
6	25.42

5. Recommendation

- i. Though information about electrode is unknown, we can consider known value to evaluate the maximum permissible load that can be applied on the footrest at a time.

Table 4 Minimum Weld-Metal Properties [1]

AWS Electrode Number	Tensile Strength kpsi (MPa)	Yield Strength, kpsi (MPa)	Percent Elongation
E60xx	62 (427)	50 (345)	17–25
E70xx	70 (482)	57 (393)	22
E80xx	80 (551)	67 (462)	19
E90xx	90 (620)	77 (531)	14–17
E100xx	100 (689)	87 (600)	13–16
E120xx	120 (827)	107 (737)	14

Table 5 Stresses Permitted by the AISC Code for Weld Metal [1]

Type of Loading	Type of Weld	Permissible Stress	Factor of Safety (n)
Tension	Butt	$0.60S_y$	1.67
Bearing	Butt	$0.90S_y$	1.11
Bending	Butt	$0.60-0.66S_y$	1.52–1.67
Simple compression	Butt	$0.60S_y$	1.67
Shear	Butt or fillet	$0.30S_{ut}$	

If we use E60xx electrode,

Permissible stress for shear will be $=.3 \times 427$
MPa=128.1 MPa

Permissible stress for bending will be $=.6 \times 345$
MPa=207 MPa

Now if 555 kg load is put on the footrest then the generated stress will be 207 MPa.

That means more than 6 persons should not stand together considering other factor.

- ii. For the welded joint similar with Case 2, if the dimension d changes, generated secondary shear stress i.e. bending stress will also changes. So maximum load carrying capacity decreases.

Table 6 Effect of d on case 2

d (mm)	Permissible Bending Stress (MPa)	Load Allowed (Kg)
30	207	555
25	207	322
20	207	165
15	207	70

According to the results of the study, some recommendations are given below:

- i. Every vehicle which have footrest should undergo with Non Destructive Testing after few years it started operation to check whether if there exists any crack or not. If found any, it should be removed by proper operations.
- ii. Welding should be done with electrode E120XX series to get high strength.

- iii. The dimension 'd' should be more than 30 mm for case 2

6. Conclusion and Further Study

As welding is a very important tool for joining similar and dissimilar metals, stress analysis of welded joint is always play an important role to design any component having welding joint. Moreover, as stress is variable, so the welded joint portion may fail due to very smaller amount of load then predicted. Therefore, fatigue stress analysis should be done at various welded joint portion. Another crucial part of the research is that it implies on public transportation which is a very much neglected sector in our country. Transportation like human hauler have welded footrest which is built for purpose of getting into or out of the vehicle. Unfortunately, it is also used to carry passengers in our densely populated country. As a result, extra stress is continuously generated on those portions. Therefore, this research depicted the actual scenario on this topic whether it is safe or unsafe. It should also be noteworthy that accidents can occur due to various reasons. But this paper only gives the attention on welded joint safety factor of footrests at Human Hauler. There are other models of footrest. Study should be done on those in future. Then hopefully a guideline can be set on this sector.

REFERENCES

- [1] Budinas & Shigley (9th edition) " Mechanical Engineering Design" McGraw Hill publishers, page (475-497)
- [2] P. Oehme, (November 1989) "Damage analysis of steel structures," in *Proceedings of the International Association for Bridge and Structural Engineering (IABSE)*, P-139/89, Zurich, Switzerland.
- [3] R. Haghani, M. Al-Emrani, and M. Heshmati, (2012) "Fatigue prone details in steel bridges," *Buildings*, vol. 2, no. 4, pp. 456–476.
- [4] J. Schijve, (2004) *Fatigue of Structures and Materials*, Kluwer Academic Publishers, Dordrecht, Netherlands.
- [5] W. Schütz, (1996) "A history of fatigue," *Engineering Fracture Mechanics*, vol. 54, no. 2, pp. 263–300.
- [6] J. Y. Mann, (1990) "Bibliography on the fatigue of materials," in *Components and Structures*, vol. 1–4, Pergamon Press, Oxford, UK.
- [7] W. Cui, (2002) "A state-of-the-art review on fatigue life prediction methods for metal structures," *Journal of Marine Science and Technology*, vol. 7, no. 1, pp. 43–56, 2002.
- [8] J. Schijve, *Fatigue of Structures and Materials*, Kluwer Academic Publishers, Dordrecht, Netherlands, 2004.
- [9] P. J. E. Forsyth, (1969) *The Physical Basis of Metal Fatigue*, American Elsevier Pub. Co., New York, NY, USA.

Wear behavior of Different Impeller Materials for Pumping Various Slurry

Sandip Karmokar¹, Sohaban Mia², Md. Abdul Hasib³

^{1, 2, 3} Department of Mechanical Engineering,
Khulna University of Engineering & Technology, Khulna-9203, BANGLADESH

ABSTRACT

Slurry erosion tester is ordinarily used to study the comparative erosion behavior of different materials at moderate solid concentrations which are used in our civilization life. In the present work, a pin mill type slurry-pot wear tester has been made. Flat type and impeller type sample material has been tested by this tester. By this testing apparatus different types of material can be tested at various speed and concentration. Total four types of material such as Aluminum, Brass, Mild Steel and Cast Iron has been tested by taking different types of slurries to find out the wear characteristics of the material by measuring the rate of mass loss with respect to various parameters like slurry concentration, speed of rotation, distance traversed, impact angle and time. The machine has been tested by taking slurry of silica sand in a GI container to find the rate of mass loss of aluminum, brass, mild steel, cast iron sample.

Keywords: slurry-pot, pin mill, slurry-erosion, silica sand and speed control box.

1. Introduction

Slurry erosion can be broadly defined as the process whereby the material is lost from a surface in contact with a moving particle-laden liquid by mechanical interaction [1]. It is an extremely serious problem for the performance, reliability and operation life of the slurry handling equipment in which solid liquid mixture is transported through pumps and pipes, used in many industrial applications like thermal power plants, hydropower plants, mining industries, food processing industries, construction and civil works, oil field mechanical equipment, solid-liquid hydro transportation systems, coal liquefaction plants, and industrial boilers where coal is carried directly as a fuel in water or oil [2]. In Bangladesh, different types of pump and piping are used in many industrial applications like thermal and hydro power plant, construction works, Gas Field, Water treatment plant, Sewage water system, Sugar Industry etc. This large number of pumps and piping materials erode frequently due to wrong choice of materials. The consequences are the loss of material, loss of equipment reliability, increasing operational cost [3]. Therefore, use of right material for specific industrial application can save large number of money.

For slurry pumping system, wear occurs mainly due to erosion and the mechanism of erosion is greatly dependent on the processes parameters involved. The constraint that affect the erosion wear in case of pumping different type of slurry are pump impeller materials quality, materials of target surface, slurry concentration, impact velocity, impact angle, size and shape of solid particle containing in the slurry, slurry viscosity, and environment [4]. But due to difficulty to find out common causes and remedy of erosion, researcher all over the world have been trying to reduce the slurry erosion by taking various techniques such as uses right materials, impact angle, target

materials surface coating ,optimizing pumping velocity [5].

Pin mill type slurry-pot wear tester has very simple design. A slurry pot was introduced by Tsai et al. [6] and similar one was designed and fabricated in 1995 by Gupta et al. [7]. The pot tester of approximately 3.8 l capacity consists of aluminum cylindrical container, rotating arms, specimen holders, shaft, motor, stirrer and bearings is shown in Fig.1.

In this study, a pin mill type slurry-pot wear tester has been developed and different types of impeller material with various types of slurry has been tested to evaluate the erosion wear rate of different impeller material to decide suitable pump impeller material for pumping different slurry.

This machine can be used for carrying out experiments on various samples of different materials which are subjected to slurry erosion. By this apparatus slurry wear rate of different material can be measured and can make decision which materials is suitable for which application.

2. Pin Mil Slurry Erosion Tester

The slurry erosion tester is shown in below Fig.2. This apparatus is a box type arrangement. The major components are structure, motor, slurry pot, shaft, pulley, belt and control box. Main shaft are fixed by pillow type bearing housing. One end of the shaft is fixed with pulley and other end is connected with sample via slurry pot bearing housing. Sample is connected with shaft and fixed by nut bolt. Shaft pulley is connected with motor pulley via a v-belt as a result when the motor starts rotating the shaft holding the samples will also rotate. The frame is made by 1.5 inch V type GI angle. The main structure dimension is 2.5 feet length, 2.5 feet wide and 3 feet height.

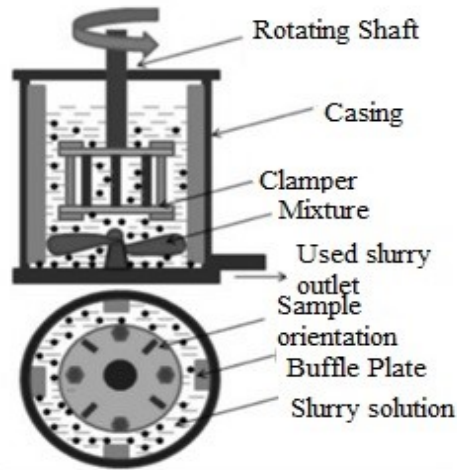


Fig.1 Slurry pot test device [6]

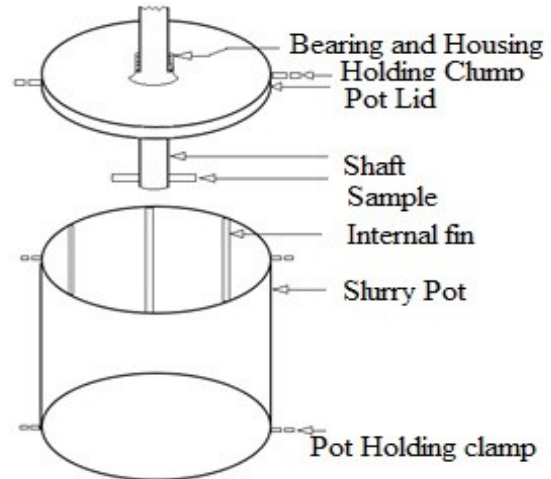


Fig.3 Slurry erosion tester pot with lid

In these experiment two types of sample was used. One was impeller shape and another flat bar shape, that are shown in below Fig.4.

A solid metal having width 28 mm, thickness of 12 mm and length 190 mm was made for experiment that is shown in fig.4. One holes of diameter 16 mm was drilled on the metal strip, one at the center by a universal drilling machine for fitting the spindle with it using a nut.

On the other hand, a solid impeller shape sample was prepared for test having impeller width 30 mm, thickness 10 mm and length 190 mm that is shown in fig.4. One hole of diameter 16 mm were drilled on the metal strip, one at the center by a universal drilling machine for fitting the spindle with it using a nut.



Fig.2 Erosion pot tester (experimental setup)

The shaft was made from a piece of 35 mm diameter mild steel rod having total length 650 mm. This shaft has two bearing holding groves and one pulley holding groves which was made by turning it in a lathe machine.

A slurry pot with led has been made for this testing apparatus. The size of slurry pot is 28 mm diameter and 25 mm height is shown in Fig.3. Slurry pot was made by 4 mm thickness GI plate. Main shaft is connected with slurry pot via pot lid by pillow type bearing housing. Slurry pot is fixed with an adjustable height bench and bench height can be adjusted by two screw.

A control box with dimension 8-inch X 6-inch X 6 inch was made for fixing control switch, protection circuit breaker and motor speed controller.

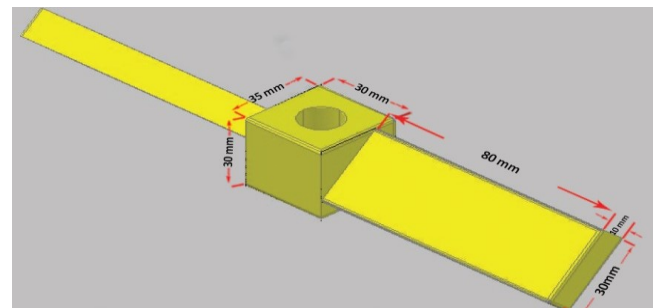
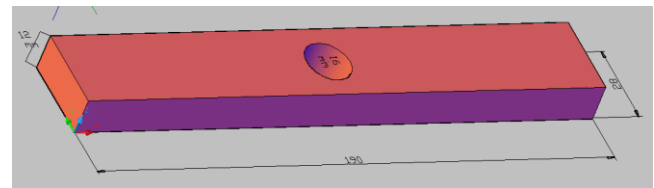


Fig.4 flat bar and impeller type samples

Main characteristics of the slurry-pot equipment is given in Table-1 and Table -2

Table 1 Main characteristics of the slurry-pot equipment.

Main structure	2.5 feet x 2.5 feet x 3 feet
Shaft	Diameter 35 mm and length 650 mm.
Pulley	4 stage pulley with different diameter (4,5,6,7 inch)
Slurry pot	Diameter 28 mm and height 25 mm
Motor	2 HP, single phase, 1450 rpm
Belt	V- Belt, size-B
Samples	
Flat bar type	190mm X 28mm X 12 mm
Impeller type	190mm X 30mm X 10 mm

Table 2 Composition of the slurry.

Natural water P ^H	7.4
Coarse sand	0.25 mm - 0.5 mm

3. Results and discussion

The self-made slurry erosion tester was used for testing the samples. Two different type sample of different material such as aluminum, brass, mild steel, cast iron were made in work shop. All sample has been cleaned by cleaning agent and recorded initial weight. Samples has been fixed with tester and test by this developed apparatus. After completing testing period sample was removed from sample holder and cleaned by cleaning agent WT-40. After cleaning final weight has been taken. The difference between two weights is the required erosion.

In this experiment, total four types of impeller material with two geometries were used for testing at different operating condition such as impact angle, velocity, density and time. Among of the four samples (45-degree impact angle) material Brass was more erosive in constant density for both type of geometries (Flat bar and Impeller) which was shown in table 3.

On the other hand, cast iron was less erosive at constant density for impeller type geometry but for flat bar (0-degree impact angle) type geometry mild steel was less erosive. From the bellow Table 4, it was cleared that erosion is increased with respect to impact angle. If impact angle is increased, erosion will be increased for all types of materials and geometries. Fig.5 and fig.6 depicts the erosion at different impact angle, speed and various density.

It clearly shows that as the density is increased, erosion is also increased for all types of materials and geometries. From the Fig. 7 and 8, it is cleared that erosion is increased with respect to impact velocity. As the impact velocity is increased, erosion is increased for all types of materials and geometries. All slurry were chemically inert and PH value of those slurry was 7.4.

Table 3 Impeller type different samples erosion at constant speed.

Speed (rpm)	Time (hour)	Slurry density (kg/L)	Average Erosion (mg)			
			AL	Brass	MS	CI
530	1	0.475	710	1008	480	401
		0.51	750	1038	487	410
		0.625	808	1096	498	421

Table 4 Flat bar type different samples erosion at constant speed.

Speed (rpm)	Time (hour)	Slurry density (kg/L)	Average Erosion (mg)			
			AL	Brass	MS	CI
530	1	0.475	512	613	160	390
		0.51	522	642	169	415
		0.625	540	673	175	428

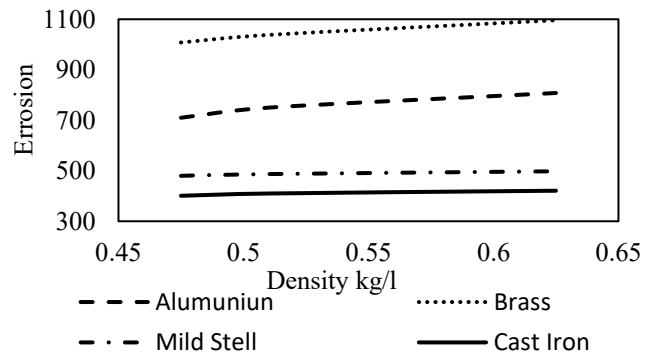


Fig.5 Erosion at 45-degree impact angle, constant speed and various density.

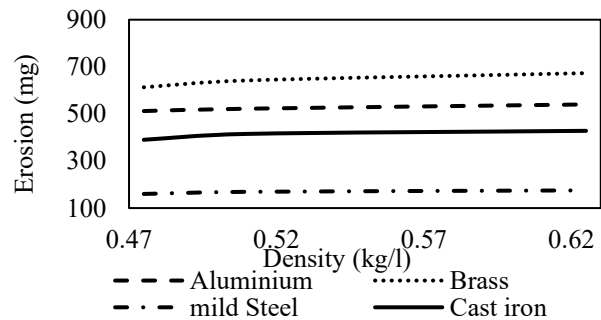


Fig.6 Erosion at 0-degree impact angle, constant speed and various density.

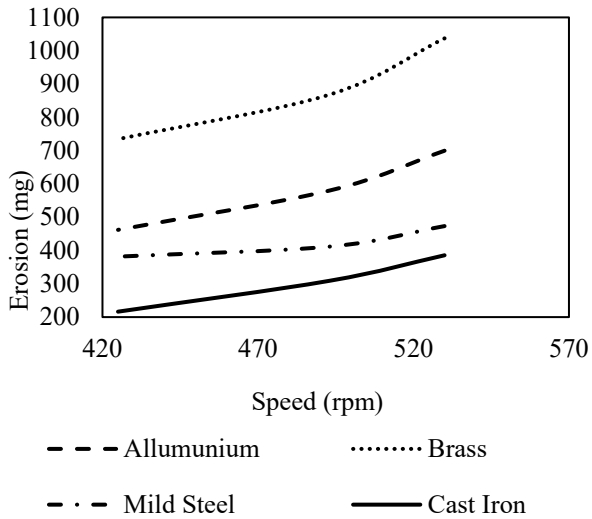


Fig.7 Erosion at 45-degree impact angle, different speed and constant density.

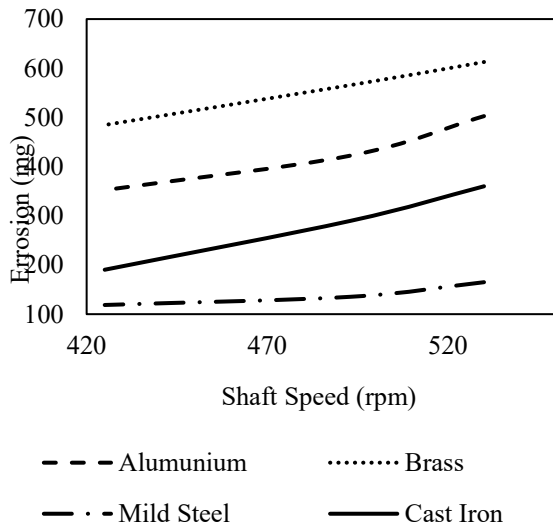


Fig.8 Erosion at 0-degree impact angle, different speed and constant density.

4. Conclusion

The use of pump for pumping slurry has increased vastly day by day in our civilized life. Therefore, it is very important to reduce erosion from the related machinery or equipment so that performance, reliability, and operation life. In this current study, four types of slurries material such has been tested by measuring the rate of mass loss with respect to various parameters like slurry concentration, speed of rotation, distance traversed, impact angle and time. From the obtained results, it is shown that by this testing apparatus different types of material can be tested and suitable pump impeller materials for different application can be find out. In this experiment, total four types of impeller material such as mild steel, cast iron, brass, aluminum were tested for different geometries, impact angle, velocity, density and time. Among of the four samples cast iron was less erosive at 45-degree impact angle and mild steel was less erosive at 0-degree impact angle. If impact angle is increased, erosion will be increased for all types of materials and geometries.

5. Reference

- [1] Aseem Mishra, Study of erosion wear of pump material for handling water ash slurry, *Master of Engineering Report, Department of Mechanical Engineering, Thapar University*, 2011.
- [2] M. H. Buszko, A. K. Krella, Slurry erosion – design of test devices, *Advances in materials science*, Vol. 17, No. 2 (52), June 2017
- [3] A.A. Gadhikar, A. Sharma, D.B. Goel and C.P. Sharma, Fabrication and Testing of Slurry Pot Erosion Tester, *Transactions of the Indian Institute of Metals*, Vol. 64, pp. 493-50-degree, 2011.
- [4] Naveen Sani, Investigation of erosion wear of slurry pump material, *Master of Engineering Report, Department of Mechanical Engineering, Thapar University*, 2012.
- [5] G.R. Desale, B.K. Gandhi and S.C. Jain, Improvement in the design of a pot tester to simulate erosion wear due to solid-liquid mixture, *Wear*, Vol. 259, pp. 196-202, 20-degree5.
- [6] Tsai W., Humphrey J. A. C., Cornet I., Levy A. V, Experimental measurement of accelerated erosion in a slurry pot tester, *Wear* 68 (1981) 289–303.
- [7] Gupta R., Singh S. N., Sehadri V, Prediction of uneven wear in a slurry pipeline on the basis of measurements in a pot tester, *Wear* 184 (1995) 169–178.

ICMIEE18-329

Experimental Investigations of Phase Change Material (PCM) Based Pin Finned Heat Sinks for Cooling Electronic Equipment

*Md. Ponir Hossain Talukder, Kazi Afzalur Rahman**

Department of Mechanical Engineering, Chittagong University of Engineering & Technology, Chittagong-4349,
BANGLADESH

ABSTRACT

This experimental investigation is carried out to study the passive cooling of electronic component using Phase Change Material (PCM). This study emphasis to find out the effect of square pin fin in the performance of the heat sink of different power input. Paraffin Wax, classified as organic phase change material, has been highly recommended in the energy storage system due to its excellent thermal combination of high latent heat, chemical stability and nontoxicity. A constant volume fraction of 10 % of square pin-fins is selected and the input heat was provided from 8 watts, 16 watts and 24 watts. Three volume fractions of PCM $\psi = 0$, $\psi = 0.5$, $\psi = 1$ are poured for finned and without fin configuration. A heat sink with no fin is chosen as a reference heat sink to find the effect of PCM and square fin. It concludes that volume fraction has an effect on performance, volume fraction $\psi = 1$ is better than $\psi = 0.5$ and combine effect of paraffin wax and fin is more effective than only paraffin wax at $\psi = 1$. Effect of fin is more effective for heat input 16 watt and less effective for high heat input 24 watt and also enhancement ratio is more for 16 watt power input of this study.

Keywords: Phase change material (PCM); Thermal conductivity enhancer (TCE); Paraffin wax; Heat sink.

1. Introduction

In modern days effective thermal management becomes a major concern for designers and manufacturer as the miniaturization of electronic components, increasing functionality as a result high heat dissipation from electronic products. As reliability and longevity of electronic components highly depends upon to keep temperatures below its maximum allowable operating temperature which is 80°C to 110°C for most electronic devices. If this heat is not wiped out properly from the devices breakdown of the component will be occluded very fast. Many active heat transfer augmentation techniques such air cooling using centrifugal fan may not very useful as an addition of noise, space and power consumptions. Some conventional cooling method such as loop heat pipe, liquid cooling, piezoelectric pump are effective for cooling such products [1]. Several experimental investigations show the effect of temperature on the performance of electronic component. The result concludes that failure rate can be reduced up to 4% by decreasing component temperature only 1°C [2]. Above that thermal failure of components can be decreased by 50% for each and every 10 °C reduce in component temperature [3]. Therefore temperature is a major reason of failure of electronic elements and affects the reliability of operation. In recent times, the traditional cooling techniques such as natural and forced convection have been insufficient to fulfill the cooling needs of today's high performance devices. The selections of cooling techniques are influenced by a range of factors like material cost, maintenance, heat dissipation rate, operating environment, available space etc. [4]. Counting all of these factors passive cooling techniques using phase change materials (PCMs) is gaining attention among researchers as it can play promising roles to increase the

operations time and equipment's functional performance. The inalienable properties of PCMs especially organic PCMs are high latent heat of fusion per unit volume, high specific heat, chemical stability under repeated melting and cooling modes, non-toxic, non-explosive and non-flammable and little volume change during phase change. This implies that excessive quantities of electricity can be saved in a constant amount of PCM for the duration of phase change period. Although most of the PCMs satisfy these criteria which are used in electronics cooling, however unfortunately, almost all PCMs possess undesirable low thermal conductivity, which can be result over heating of heating components and making heating and cooling slower throughout PCM melting and solidification [5]. As a result, to make PCMs appropriate for cooling applications, it is necessary to add materials with high thermal Conductivity into PCM which will assist to heat conduction throughout the PCMs. These materials are regarded as thermal conductivity enhancers (TCE). Both experimental and numerical investigations have been carried by several authors for a huge variety of PCMs and sets standards that govern the resolution of PCM is discussed by Agyeni et al. [6]. Fan and Tso [7] experimentally investigated the cooling of electronic devices by using use of a heat storage unit (HSU) filled with n-eicosane inside the device. It was found that the performance depends upon the amount of PCMs used. A similar finding out about was carried out numerically by Tan and Fok [8] for the thermal management of mobile phone by the usage of PCM. Numerical simulation was carried out in heat storage unit filled with PCM. Eight cases were considered at a variety of energy tiers (2–4 W) and it was concluded for low power, temperature is low and for high power temperature is high. Kandasamy et al. [9] investigated

* Corresponding author. Tel.: +880 16 8045 3267

E-mail addresses: afzal@cuet.ac.bd; afzalur99@yahoo.com

both experimentally and numerically of a novel PCM package with respect to various input parameters (e.g. power levels, orientation, and charging/discharging cycles). The results show that melting rate is increased with a corresponding increase in power input, it also concluded that the effect of orientation of gravity had no significant effects on the performance of the PCM package and could be neglected. A model of the novel hybrid heat sink was proposed for the transient thermal management of electronics using plate fin which is immersed in PCM by Krishnan et al. [10] combining the effect of both active and passive cooling approach in the hybrid heat sink. It concluded that metallic PCMs performed better than organic PCMs but not suitable for low weight heat sink design. As the thickness of a pin and the amount of PCMs is increasing heat transfer rate is also increase and decrease melting temperature of PCMs. Many researchers have investigated different techniques to increase the thermal conductivity of PCMs. An experimental investigation was performed by Baby and Baliji [11] using n- eicosane as phase change material and placed it inside different aluminum fin geometry for thermal management of portable electronic devices. Results showed that use of fin is very effective to stretch operation time and pin fin is more effective than the plate fin. Heat transfer mechanism based on composite phase change material was carried experimental by Yin et al. [12] for rapid thermal response. Paraffin wax was absorbed into expanded graphite, as it has excellent absorbability. It was concluded that the composite PCM had high thermal conductivity and excellent absorbability than that of paraffin wax. Experimental investigation was carried out by Setoh et al. [13] using n- eicosane for mobile phone cooling for both steady and intermittent heating. Experimental findings showed that internal fin is helpful to increase time to reach maximum operating temperature and it is more effective for intermitted moderate condition. Many authors have investigated the effect the composite PCM with a combination of nanoparticles (using nanoparticle as a thermal conductivity enhancer). Alshaer et al. [14] investigated hybrid composite system for thermal management (TM) of electronics devices using different model of carbon nano composite and paraffin wax. It was concluded that the model is capable of controlling higher loads. Arshad et al. [15] explore the effect of round fin thickness at different heat flux and configurations experimentally. Its findings showed that fin thickness has significant effect in lowering the base temperature. Effect of copper foam in the performance of PCM based heat sink was investigated by Rehman and Ali [16] at different porosity and volume fraction. Findings showed copper foams have significant effect on the performance of heat sink. In this study the effect of 6 mm square fin is investigated for different volume fractions and power level to evaluate fin effect at three different power levels (8 watt, 16 watt and 24 watt) at different set point temperatures (SPTs) and find the power at which the effect of fin is most significant.

2. Methodology

2.1 Experimental setup

At first a suitable setup is developed for the experimental investigation of the performance of the heat sink as shown in Fig.1.

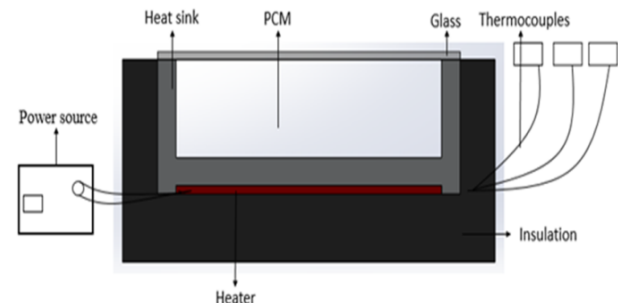


Fig.1 Schematic diagram of the experimental setup.

The setup consists of different heat sink configurations. A plate heater is used to mimic the heat generation in electronic chips in the base of the heat sink as a heating source. Power is used from an AC source of 220 volts and it is regulated by using voltage regulator. This type of heater is very useful to generate uniform heating. An insulating box is used to minimize heat loss from the heater so that all the time the condition remains the same.

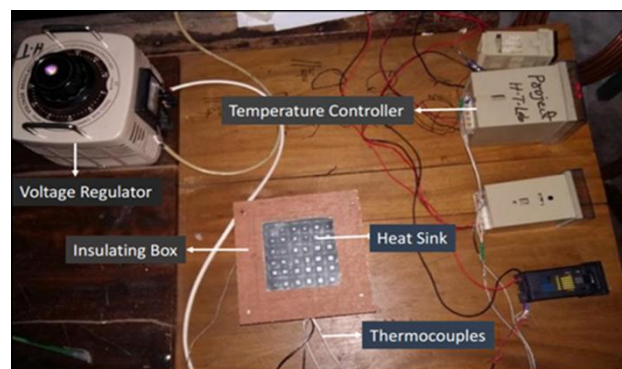


Fig.2 The experimental setup.

The assembly of heat sink consists of wooden frame the gap between heat sink and box is filled with glass wool since the glass wool is very a good insulator. A glass plate is placed above the sink for monitoring the melting phase of paraffin wax time to time for better understanding of phase change phenomena during heating and cooling. A voltage regulator is used to regulate voltage so that required power can be supplied to the heater. Effect of different types of fins for different power level (8 watts to 24 watts with equal interval of 8) in enhancing the operating time for different SPTs and on the duration of latent heating phase is exploring in this study. Experimental setup consists of heat sinks having pin-fin configurations filled with PCM, insulated with glass wool & rubber which prevents the heat loss to the environment,

thermocouples, power supply. To realize the melting and solidification of paraffin wax calibrated K-type thermocouples is used at different position. Two thermocouples are placed at the base of the heat sink between plate heater and the base of the heat sink in a groove of 2 mm depth at a distance of 40 mm of equal distance. Thermocouples are inserted 15 mm inside the vertical direction at different positions. They are placed at a distance 9 mm from each other from the base of the heat sink.

2.2 Heat sink configuration

Two configurations of heat sink filled with PCM are used. Heat sink of 6 mm square fin having a constant volume fraction of 10% of TCE as shown in Fig. 3 (a). Aluminum is used as thermal conductivity enhancers due to its high thermal conductivity and light weight. Heat sink with fin and without fin filled with PCM (paraffin wax) is used. A heat sink with no pin-fin at $\psi = 0.00$ and $\psi = 1.00$ ($\psi =$ volumetric fraction of PCM) is tested to perform the base line comparison. Heat sink having constant volume fraction of 10% of TCE, is used. Aluminum is selected as the TCE due the good thermal conductivity and light weight. Paraffin wax is used as a PCM and three different volume fractions ($\psi = 0$, $\psi = 0.5$, and $\psi = 1.0$) are used for each heat sink by using Eq. (1).

$$\psi = \frac{V_{PCM}}{V_s - V_f} \quad (1)$$

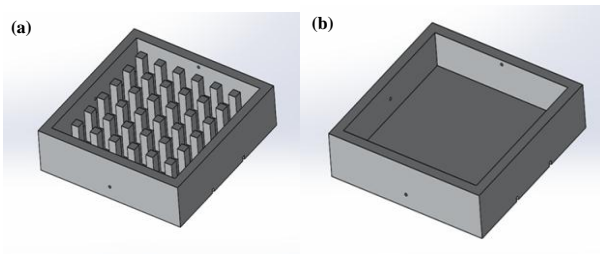


Fig.3 Isometric view of various heat sinks (a) 6 mm heat sink (b) No fin heat sink used in this study.

Overall dimension of the heat sink is 120 mm × 120mm. and height is 30mm, dimension of fin is 6mm × 6mm as shown in Fig. 4.

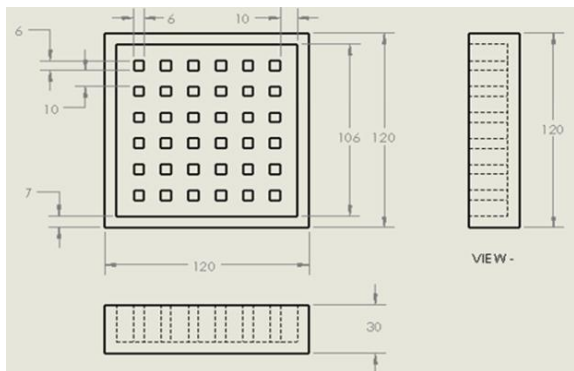


Fig. 4 Dimension of 6 mm heat sink.

2.3 Properties of materials employed in present study.

In this experiment paraffin wax is used as Phase Change Material (PCM), which is used as heat storage medium in the heat sink. Paraffin wax is a soft colorless solid, derived from petroleum. That consists of a mixture of hydrocarbon molecules containing between twenty and forty carbon atoms. Its physical properties are: thermal conductivity 0.167 (liquid) 0.212 (Solid) W/m-K; specific heat 2.8 kJ/kg-K; latent heat 173.6 kJ/kg-K; melting point 55-60 °C; density 790 (liquid) 880 (solid) kg/m³. Heat sink is fabricated by using Aluminum because of its excellent properties such as is remarkable for its low density and its ability to resist corrosion through the phenomenon of passivation. Its properties are: Thermal conductivity 202 W/m-K; specific heat 0.871 kJ/kg-K; melting point 660°C; density 2719 kg/m³.

3 Results and discussion

3.1 Base line comparison

To find out the all other parameter finding the base level temperature is very important as with respect to these values all other parameters are compared. For base line compression temperatures of the base of the heat sink is taken without PCM and without fin is taken for 16 watt power input as shown in Fig. 5(b). The average of the base temperature is taken for the base temperature of the heat sink. For reaching base temperature 55°C and 65°C it takes 23 minutes and 33 minutes for heat sink without PCM on the other hand it is 42 minutes and 92 minutes with PCM respectively as shown in Fig. 5.

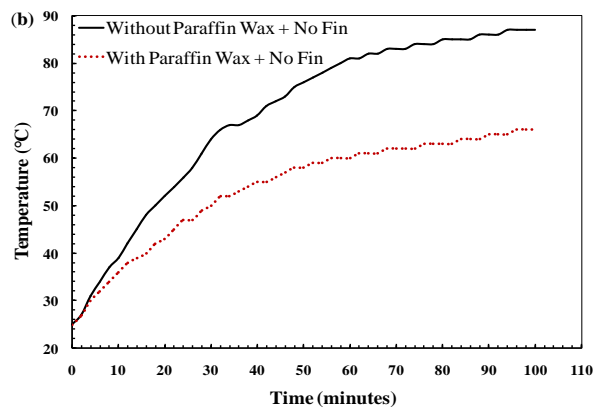
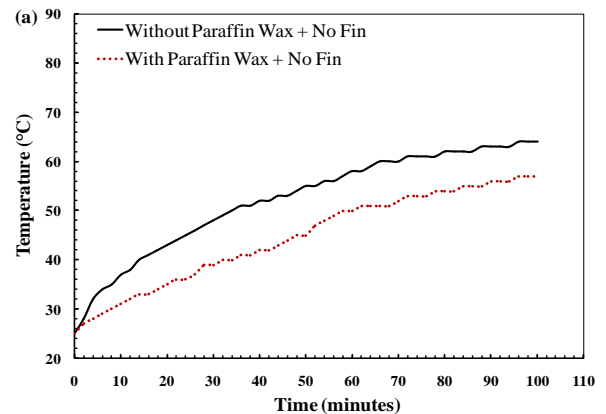


Fig. 5 Heat sinks base temperature at various power input (a) 8 watt input (b) 16 watt input.

To reach temperature 50°C and 60°C it takes 20 minutes and 31 minutes for heat sink without PCM, whereas it takes 32 minutes and 82 minutes for with PCM. Without PCM the temperature is increasing rapidly for, it is not expected of any electronic device it could easily damage the device. As the temperature reaches so fast operating time is also decreased and reached critical operating temperatures very quickly.

3.2 Effect of volume fractions of PCM for different configurations of heat sinks

Effects of volume fraction of paraffin wax are investigated by taking three different volume fraction of paraffin wax ($\psi = 0$, $\psi = 0.5$, $\psi = 1$) and taking the corresponding base temperature for 8 watts, 16 watts and 24 watts power input represented in Fig. 6. By comparing the corresponding values, the effect of volume fraction can be found. From the Fig. 6 (a), it is clearly seen for 8 watt power input that the volume fraction $\psi = 1$ is more effective to keep the base temperature lower than the other two. At the end of 100 minute temperatures reaches 64°C, 62°C and 57°C for volume fraction of $\psi = 0$, $\psi = 0.5$ and $\psi = 1$ respectively. Similar results have been found for 16 watt represented in Fig. 6 (b). For 16 watt power input, effect of volume fraction is more visible. After reaching melting temperature for volume fraction $\psi = 0.5$, temperature increases faster than volume fraction $\psi = 1$. This is because of more amount of paraffin wax is capable of storing more heat so that temperature increases slowly for large volume fraction. Similar effects are also found for 24 watt power input.

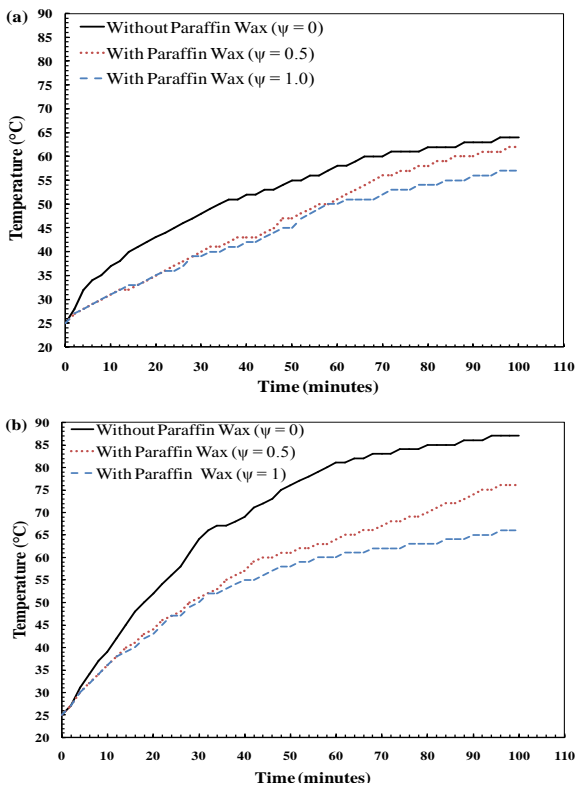


Fig. 6 Effect of different volume fraction at different power input (a) 8 watt (b) 16 watt.

Therefore, it is clear that volume fraction of PCM has a significant effect in the performance of PCM based heat sink. In this experimental investigation volume fraction of $\psi = 1$ is more effective than the others.

3.3 Temperature variation within heated fin sink filled with PCM

For better understanding of temperature distribution in vertical direction inside the heat sink three thermocouples are placed at a height of 8 mm, 16 mm and 24 mm from the bottom of the heat sink into the PCM from the side wall. Temperature is taken against 16 watt power input. Fig. 7 represents the temperature after three different time 20 minutes, 60 minutes and 100 minutes for better observation. It showed that temperature variations inside the heat sink is insignificant.

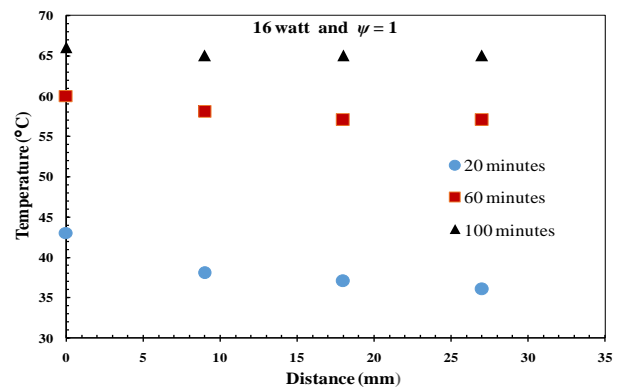


Fig.7 Spatial distribution of temperature inside the PCM at 16 watt.

3.4 Enhancement in operation time for different configurations of the heat sink

Operation time of various configurations of heat sink is taken at assorted set point temperature (SPTs) such as 55°C, 60°C and 65°C which are analysed for volume fraction of $\psi = 1$ for different power inputs (8 watt, 16 watt, 24 watt) presented in Fig. 8. The summary are plotted for better understanding of operation time for different configurations. The critical SPT may be defined as the maximum operating temperature for any electronic component which can withstand without damage or breakdown. Time is measured with respect to reach heat sink base temperature 55°C, 60°C and 65°C of different configurations of heat sink for three different power input. It is seen from Fig. 8 that time to reach SPT, heat sink with paraffin wax and fin takes more time than other heat sink configuration since large thermal conductivity of fin helps to absorb heat simultaneously throughout the sink. From Fig. 8 it is very clear that pin fin is very effective for better performance of PCM based heat sink as in every configuration and different power input time taken by with paraffin wax and fin configuration always more than other configurations. Among other power levels for 8 watt power input, effect of fin is more visible and effective since time taken to reach melting point of the paraffin wax is moderate and also heat stored throughout the sink is more uniform than others.

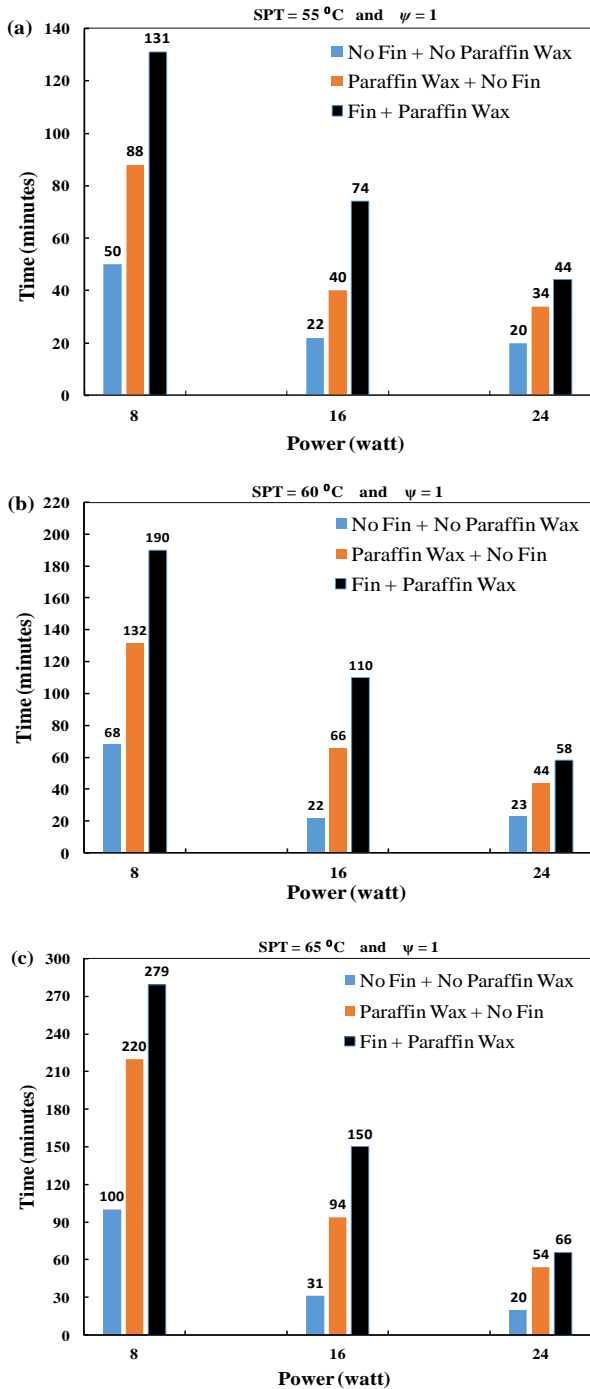


Fig. 8 Time to reach SPTs (a) 55°C (b) 60°C & (c) 65°C at 8 watt, 16 watt & 24 watt power input.

At 24 watt power input, time taken to reach melting point is short and therefore, temperature increases very rapidly in the base of the heat sink and heat sink has less time to absorb the heat throughout the sink.

3.5 Enhancement ratios for different configuration of heat sink

Enhancement ratio for various configurations of heat sink at SPTs of 55°C, 60°C and 65°C respectively taken from different power input. Enhancement duration operation of a heat sink for effect of paraffin wax can be

denoted as ζ which is the ratio of time taken by heat sink with paraffin wax ($\psi = 1$) to that of a heat sink without paraffin wax ($\psi = 0$) as in Eq. 2. Since temperature increases in paraffin wax start to take heat from the base of the heat sink and helps to keep operating temperature low, it can be seen from the Fig.8 that the best enhancement occurs with enhancement of paraffin that was configured at 16 watt power input.

$$\zeta = \frac{t_{with\ PCM}}{t_{without\ PCM}} \quad (2)$$

$$\epsilon = \frac{t_{without\ TCE}}{t_{with\ TCE}} \quad (3)$$

The effect of fin with respect to without fin can be denoted as ϵ which is the ratio of time taken to reach SPT without fin to that of with fin at $\psi = 1$ as in Eq. 3. It can be seen from the above Fig. 9 that enhancement ratio is always more for 16 watt power input for all three SPT. This is because heat sink has more time to store heat uniformly throughout the paraffin wax as the power level is favorable for this heat sink. Also, as the SPT increases, enhancement ratio also increases since all the paraffin wax has to store heat to change its phase. However, temperature increases rapidly when phase change is complete because of the lower value of sensible heat.

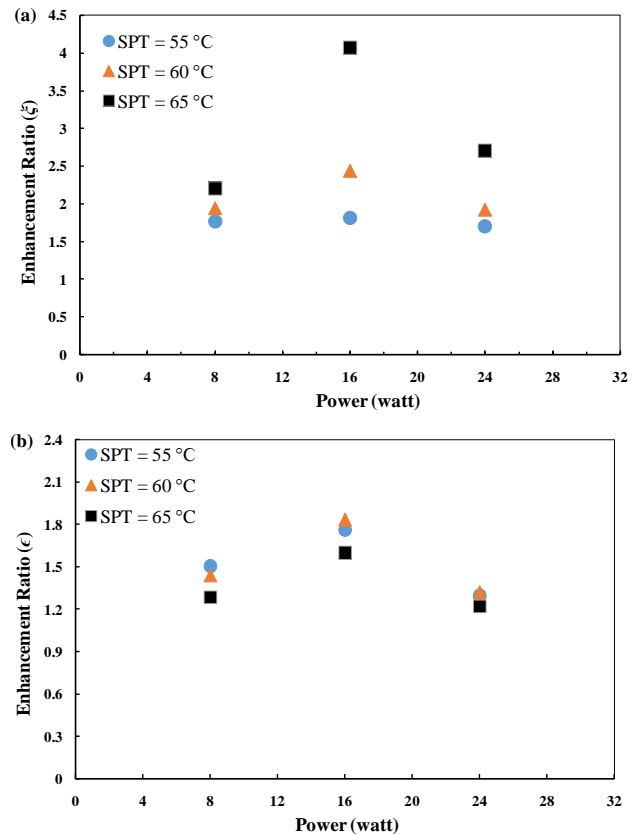


Fig. 9 Enhancement ratio at different power input (8 watt, 16 watt, 24 watt) (a) ζ (b) ϵ .

4. Conclusion

The experimental investigation performed aimed to investigate the effect of paraffin wax to evaluate the effect of volume fraction of paraffin wax and pin fin of PCM based heat sinks for power input of 8 watts, 16 watts and 24 watts. Since the thermal conductivity of paraffin wax is low, this experimental study presents the effect of pin fin keeping the volume fraction constant at 10% as thermal conductivity enhancer for different heat sinks tested with volume fraction $\psi = 0$, $\psi = 0.5$, $\psi = 1.0$. Taking temperature with respect to time and evaluating the results of this study, the followings can be concluded.

- It is shown that inclusion of paraffin wax helps to keep the base temperature lower.
- It is also found that a heat sink with a volumetric fraction of $\psi = 1$ means fully filled with PCM is more effective to keep the base temperature lower than that of $\psi = 0$ and $\psi = 0.5$.
- The experiment proves that combine effect of paraffin wax and fin is more effective than only paraffin wax.
- Inclusion of fin is more effective for heat input 16 watt and 8 watt than higher heat input of 24 watt.
- Enhancement ratio is higher for 16 watt power input for different SPTs.

NOMENCLATURE

PCM : phase change material
TCE : thermal conductivity enhancer
TM : thermal management
 V_s : total volume of heat sink
 V_f : total volume of PCM

Greek Symbols

ψ : volume fraction of PCM
 v_{PCM} : specific volume of PCM
 ξ : enhancement ratio at PCM
 ϵ : enhancement ratio at TC

REFERENCES

[1] A. C. Kheirabadi and D. Groulx, Cooling of server electronics: A design review of existing technology, *Applied Thermal Engineering*, Vol.105, pp 622-638 (2016).

[2] Military Handbook: Reliability Prediction of Electronic Equipment, (*MIL-HDBK-217F Notice 1*) (10 JUL 1992).

[3] C. A. Yunus, Heat Transfer: A Practical Approach, *MacGraw Hill*, New York, (2003).

[4] R. Kandasamy, X. Q. Wang and A. S. Mujumdar, Transient cooling of electronics using phase change material (PCM) based heat sinks, *Applied Thermal Engineering*, Vol. 28, pp 1047-1057(2008).

[5] Z. X. Gong and A. S. Mujumdar, Flow and heat transfer in convection-dominated melting in a rectangular cavity heated from below, *International Journal of Heat and Mass Transfer*, Vol. 41, pp 2573-2580(1998).

[6] F. Agyenim, N. Hewitt, P. Eames and M. Smyth, A review of materials, heat transfer and phase change problem formulation for latent heat thermal energy storage systems (LHTESS), *Renewable and Sustainable Energy Reviews*, Vol.14, pp 615-628 (2010).

[7] F. L. Tan and C. P. Tso, Cooling of mobile electronic devices using phase change materials, *Applied Thermal Engineering*, Vol. 24, pp 615-628(2004).

[8] F. L. Tan and S. C. Fok, Thermal Management of Mobile Phone using Phase Change Material, *9th Electronics Packaging Technology Conference, Singapore*, pp. 836-842(2007).

[9] R. Kandasamy, X. Q. Wang and A. S. Mujumdar, Application of phase change materials in thermal management of electronics, *Applied Thermal Engineering*, Vol.27, pp 2822-2832(2007).

[10] S. Krishnan, S. V. Garimella and S. S. Kang, A novel hybrid heat sink using phase change materials for transient thermal management of electronics, *IEEE Transactions on Components and Packaging Technologies*, Vol. 28, pp. 281-289(2005).

[11] R. Baby and C. Balaji, Experimental investigations on phase change material based finned heat sinks for electronic equipment cooling, *International Journal of Heat and Mass Transfer*, Vol. 55, pp 1642-1649(2012).

[12] H. Yin, X. Gao, Jing Ding and Zhengguo Zhang, Experimental research on heat transfer mechanism of heat sink with composite phase change materials, *Energy Conversion and Management*, Vol. 49, pp1740-1746 (2008).

[13] G. Setoh, F.L. Tan and S.C. Fok, Experimental studies on the use of a phase change material for cooling mobile phones, *International Communications in Heat and Mass Transfer*, Vol. 37, pp 1740-1746(2010).

[14] W.G. Alshaer, S.A. Nada, M.A. Rady, E. Palomo D. Barrio and A. Sommer, Thermal management of electronic devices using carbon foam and PCM/nano-composite, *International Journal of Thermal Sciences*, Vol. 89, pp79-86(2015).

[15] A. Arshad, H. M. Ali, S. Khushnood and M. Jabbar, Experimental investigation of PCM based round pin-fin heat sinks for thermal management of electronics: Effect of pin-fin diameter, *International Journal of Heat and Mass Transfer*, Vol. 117, Pages 861-872(2018).

[16] T. Rehman and H. M. Ali, Experimental investigation on paraffin wax integrated with copper foam based heat sinks for electronic components thermal cooling, *International Communications in Heat and Mass Transfer*, Vol. 98, pp 155-162(2018).

Influence of Interlayer Thickness on the Singular Stress Field in 3D Three-Layered Bonded Joints Using FEM

Md. Jahangir Hossain*, Md. Shahidul Islam

Department of Mechanical Engineering, Khulna University of Engineering & Technology, Khulna-9203, BANGLADESH

ABSTRACT

Bonded joint is widely used in different fields of science and technology, especially in making electronic chip. Every bonded joint may have vertex at the interface which is the region where joint may fail under mechanical or thermal loading due to propagation of stress singularity. The propagation of stress singularity is highly governed by interlayer thickness. It is necessary to investigate the influence of interlayer thickness on the propagation of stress singularity at the vertex to avoid stress singularity to prevent bonded joint from being deboned. In the present paper, a tri-material bonded joint composed of SiC, Resin (interlayer) and SiN is used to investigate the phenomenon. This model has better electro-mechanical property than a chip made by silicon only. The interlayer thickness is varied to analyze its influence on stress singularity through FEM using ABAQUS 6.14 software. It is found from the analysis that stress singularity increases with the increase in interlayer thickness and vice versa.

Keywords: Finite Element Method, Interlayer thickness, Interface, Stress singularity, External load.

1. Introduction

In this tri-material joint, SiC is used as upper material, Resin as middle material and SiN at the bottom. This model has high thermal conductivity, high die-electric breakdown and wide band gap than silicon.

As it consists of three different materials with an inter-layer, there is a probability of occurring stress singularity at the vertex of interfaces. So, it is necessary to investigate the variation of stress singularity with inter-layer thickness. Williams analyzed stress singularity for different boundary conditions in angular corner of extended plate [1]. Aksentian investigated stress-strain state of singularities of a plate near an edge [2]. Hartranft analyzed stress singularity resulting from crack having an arbitrary curved front [3]. Munz and Yang investigated stress singularity at the interface of dissimilar material bonded joint due to thermal and mechanical loading [4]. Munz, Matthias and Yang determined thermal stresses in ceramic-metal joint having an inter-layer [5]. Pengfei, Ishikawa and Kohno analyzed order of stress singularity at the corner of a diamond shaped rigid inclusion under bending [6]. Hideo Koguchi analyzed stress singularity at three dimensional bonded joints [7]. Barut, Guven and Madenci investigated singular stress field at multiple dissimilar material joints due to mechanical and thermal loading [8]. Ioka, Masuda and Kubo analyzed singular stress field at bonded dissimilar material joint's interface with an interlayer [9]. Hideo Koguchi and Masato Nakajima investigated how intensity of singular stress field varies with interlayer thickness in three-dimensional three-layered joint due to external load using boundary element method [10].

In this paper, the influence of interlayer thickness on singular stress field is analyzed in tri-material joint consisting SiC, Resin and SiN using Finite Element Method through ABAQUS 6.14 software.

2. Formula of analysis

The stress for three-dimensional isotropic material is determined from following relation [11]:

Consider a body subjected to normal stress σ_r , σ_θ and σ_ϕ independently.

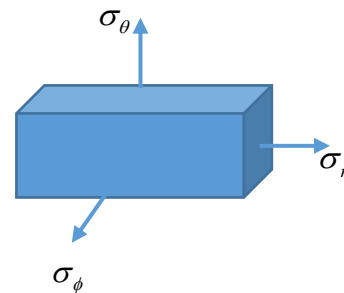


Fig.1 Body subjected to normal stress

The positive stress in the r direction produces positive strain in that direction

$$\varepsilon_r = \frac{\sigma_r}{E} \quad (1)$$

The positive stress in the θ direction produces negative strain in the r direction due to Poisson's effect

$$\varepsilon_r'' = -\frac{\nu\sigma_\theta}{E} \quad (2)$$

The positive stress in the Φ direction produces negative strain in the r direction due to Poisson's effect

$$\varepsilon_r''' = -\frac{\nu\sigma_\phi}{E} \quad (3)$$

By superimpose,

$$\varepsilon_r = \frac{\sigma_r}{E} - \frac{\nu\sigma_\theta}{E} - \frac{\nu\sigma_\phi}{E} \quad (4)$$

Similarly,

$$\varepsilon_\theta = -\frac{\nu\sigma_r}{E} + \frac{\sigma_\theta}{E} - \frac{\nu\sigma_\phi}{E} \quad (5)$$

$$\varepsilon_\phi = -\frac{\nu\sigma_r}{E} - \frac{\nu\sigma_\theta}{E} + \frac{\sigma_\phi}{E} \quad (6)$$

Solving these equations, we obtain,

$$\sigma_r = \frac{E}{(1+\nu)(1-2\nu)} [\varepsilon_r(1-\nu) + \nu\varepsilon_\theta + \nu\varepsilon_\phi] \quad (7)$$

$$\sigma_\theta = \frac{E}{(1+\nu)(1-2\nu)} [\nu\varepsilon_r + (1-\nu)\varepsilon_\theta + \nu\varepsilon_\phi] \quad (8)$$

$$\sigma_\phi = \frac{E}{(1+\nu)(1-2\nu)} [\nu\varepsilon_r + \nu\varepsilon_\theta + (1-\nu)\varepsilon_\phi] \quad (9)$$

Again, for shear stress

$$\tau_{r\theta} = G\gamma_{r\theta}, \tau_{\theta\phi} = G\gamma_{\theta\phi}, \tau_{\phi r} = G\gamma_{\phi r}$$

In matrix form, stresses can be written as

$$\begin{Bmatrix} \sigma_r \\ \sigma_\theta \\ \sigma_\phi \\ \tau_{r\theta} \\ \tau_{\theta\phi} \\ \tau_{\phi r} \end{Bmatrix} = l \begin{bmatrix} 1-\nu & \nu & \nu & 0 & 0 & 0 \\ \nu & 1-\nu & \nu & 0 & 0 & 0 \\ \nu & \nu & 1-\nu & 0 & 0 & 0 \\ 0 & 0 & 0 & m & 0 & 0 \\ 0 & 0 & 0 & 0 & m & 0 \\ 0 & 0 & 0 & 0 & 0 & m \end{bmatrix} \begin{Bmatrix} \varepsilon_r \\ \varepsilon_\theta \\ \varepsilon_\phi \\ \gamma_{r\theta} \\ \gamma_{\theta\phi} \\ \gamma_{\phi r} \end{Bmatrix}$$

Where,

$$l = \frac{E}{(1+\nu)(1-2\nu)}, m = \frac{1-2\nu}{2}, G = \frac{E}{2(1+\nu)}$$

3. Model of analysis

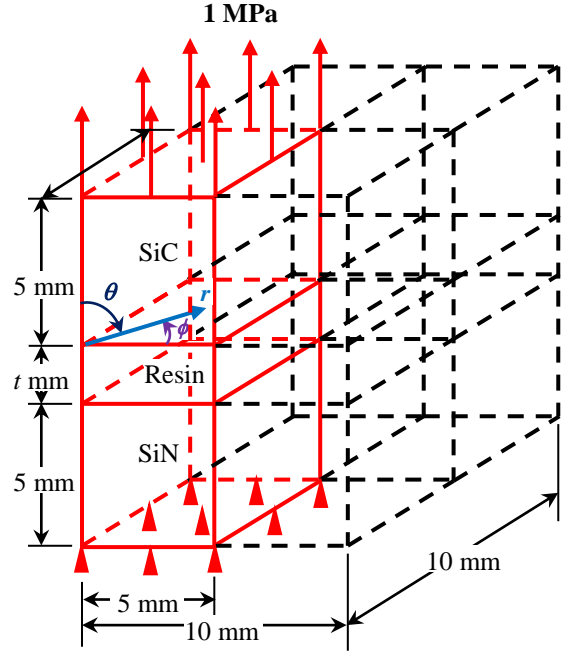


Fig.2 Model for Finite Element Method analysis

The lower surface is kept fixed. A 1MPa force is applied on the upper surface. The thickness of resin is varied to investigate its influence on singular stress field at the vertex using linear hexagonal element. Due to symmetry one-fourth of the model is analysed.

Table 1 Property of isotropic material.

	SiC	Resin	SiN
Young's modulus, E (GPa)	450	2	295
Poisson's ratio, ν	0.22	0.39	0.22

4. Accuracy verification

In this paper, Finite Element method result is compared with a journal paper [10] working on Boundary Element Method with maximum error of 0.88%. The minimum and maximum element size are 0.0001mm and 1mm respectively with 2326581 elements.

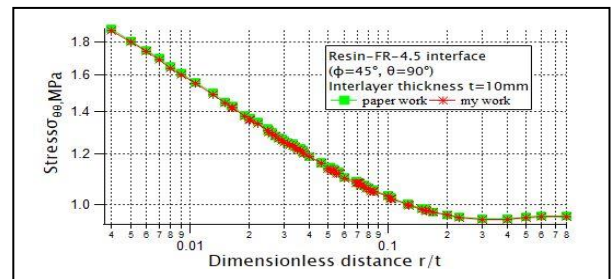


Fig.3 Accuracy verification of the present analysis

5. Checking mesh dependency

For interlayer thickness 5mm the number of element is varied from 48thousands to 6lac. But stress does not vary when the number of element is 5lac or above. Results are taken with approximately 5lac element.

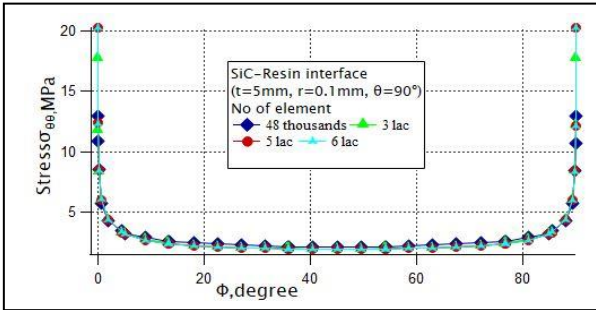


Fig.4 Mesh dependency check of the present model

6. Result and discussion

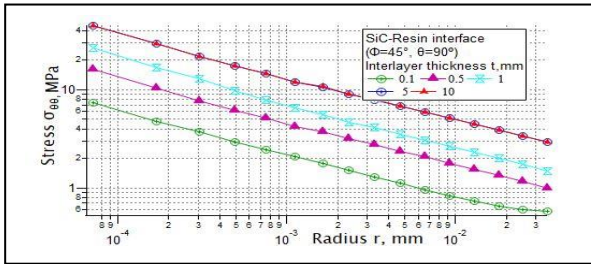


Fig.5 Distribution of stress $\sigma_{\theta\theta}$ against radius, r

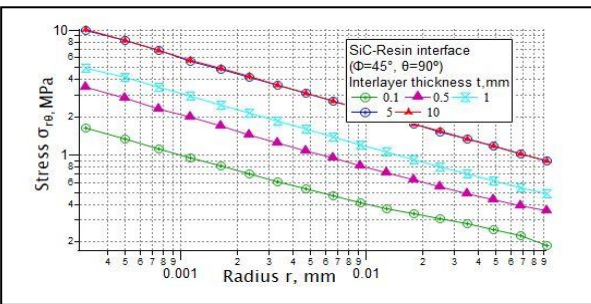


Fig.6 Distribution of stress $\sigma_{r\theta}$ against radius, r

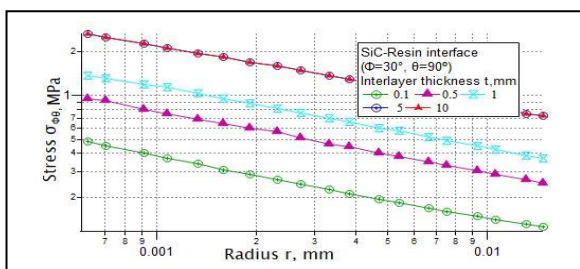


Fig.7 Distribution of stress $\sigma_{\phi\theta}$ against radius, r

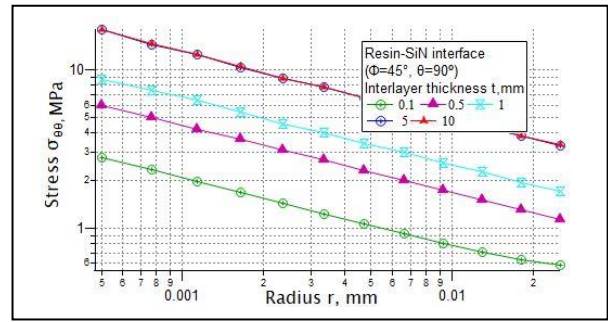


Fig.8 Distribution of stress $\sigma_{\theta\theta}$ against radius, r

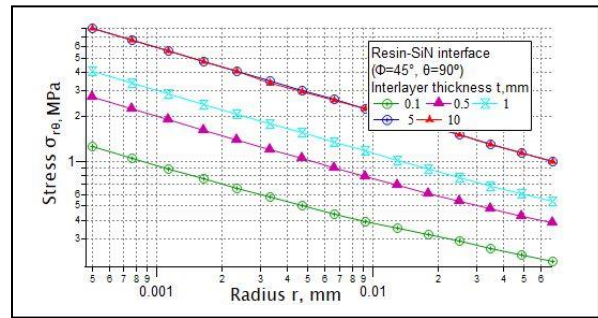


Fig.9 Distribution of stress $\sigma_{r\theta}$ against radius, r

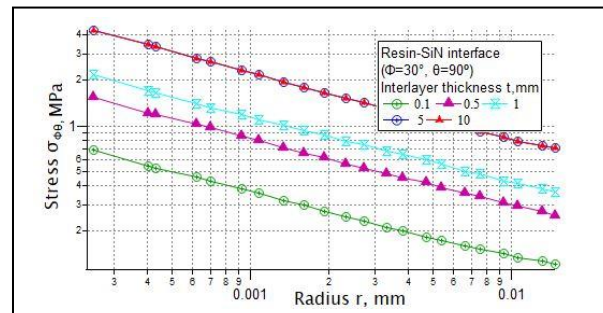


Fig.10 Distribution of stress $\sigma_{\phi\theta}$ against radius, r

Stress is plotted against radial distance, r from figs. 5 to 10 for various interlayer thickness. It is shown that stress increases with the increase in interlayer thickness. Also stress is maximum at the vertex and decreases with radial distance. So the bonded joint can be deboned at the vertex. There is more possibility of failure near the vertex or corner than inner portion of the joint.

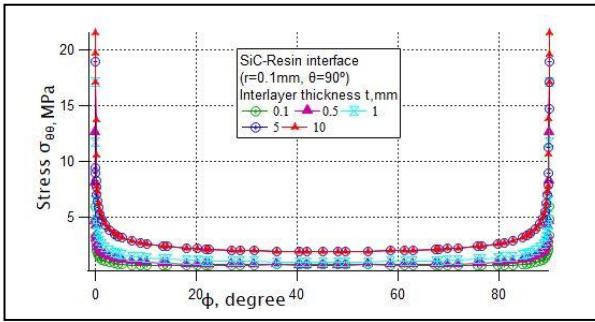


Fig.11 Distribution of stress $\sigma_{\theta\theta}$ against angle, ϕ

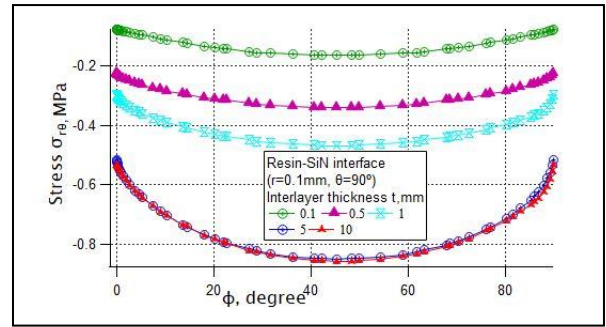


Fig.15 Distribution of stress $\sigma_{r\theta}$ against angle, ϕ

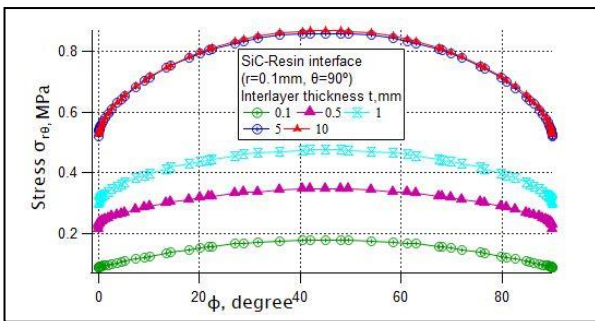


Fig.12 Distribution of stress $\sigma_{r\theta}$ against angle, ϕ

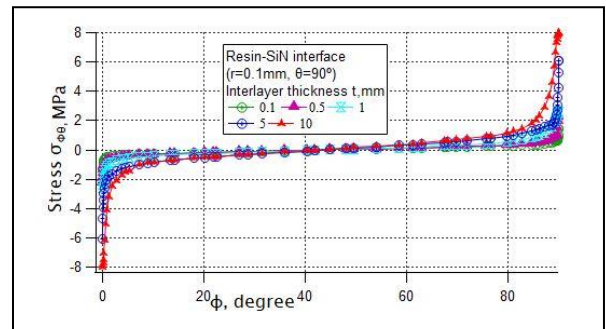


Fig.16 Distribution of stress $\sigma_{\phi\phi}$ against angle, ϕ

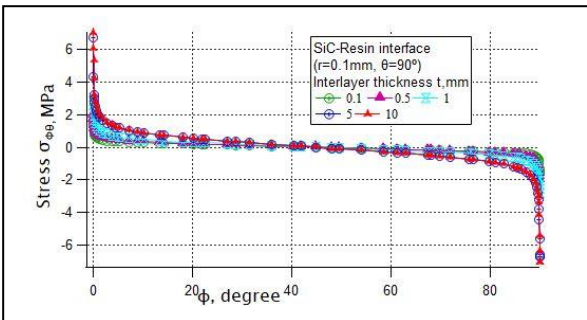


Fig.13 Distribution of stress $\sigma_{\phi\phi}$ against angle, ϕ

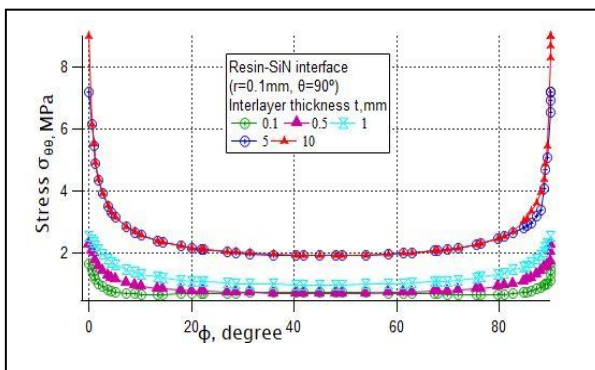


Fig.14 Distribution of stress $\sigma_{\theta\theta}$ against angle, ϕ

Figs. 11 to 16 show variation of stress against angle ϕ at $\theta=90^\circ$ for various interlayer thickness. It is shown that stress increases with the increase in interlayer thickness similar to previous one. Also stress is maximum near interface edge and decreases along inner portion. So there is also the possibility of the joint to be deboned near interface edge.

7. Conclusion

In the present paper, the stress distribution of a tri-material joint was analyzed. Stress increases with the increase in interlayer thickness. Farther more, stress is maximum near the vertex and interface edge where the joint may be deboned.

NOMENCLATURE

- σ : Stress, MPa
- ϵ : Strain
- E : Young modulus, MPa
- ν : Poisson ratio
- r : Distance from origin, mm
- t : Interlayer thickness, mm
- ϕ : Angle, degree
- θ : Angle, degree

References:

- [1] M.L. Williams, Stress singularities resulting from various boundary conditions in angular corners of plate in extension, *J. Appl. Mech.*, Vol. 19, pp 526–8 (1952).
- [2] O.k. Aksentian, Singularities of the Stress-Strain State of a Plate in the Neighborhood of an Edg, *PMM*, Vol. 31-1, pp178-186 (1967).
- [3] R.J. Hartranft, G.C. Sih, Stress singularity for a crack with an arbitrarily curved front, *Engineering Fracture Mechanics*, Vol. 9, pp 705-718 (1977).
- [4] D. Munz, Y.Y. Yang, Stress singularity at the interface in bonded dissimilar materials under mechanical and thermal loading, *Journal of Applied Mechanics*, Vol. 59, pp 857-861 (1992).
- [5] D. Munz, A.Matthais, Y.Y. Yang, Thermal stress in ceramic-metal joints with an interlayer, *Journal of the American Ceramic Society*, Vol. 77, pp 285-290 (1995).
- [6] H. Pengfei, H. Ishikawa, Y. Kohno, Analysis of order of stress singularity at the corner point of a diamond-shape rigid inclusion or hole in an infinite plate bending by conformal mapping, *Int. J. Engng. Sci.*, Vol. 33, pp 1535-1546 (1995).
- [7] H. Koguchi, Stress singularity analysis in three-dimensional bonded structure, *Int. J. Solids Structures*, Vol. 34, pp 461-480 (1997).
- [8] A. Barut, I. Guven, E. Madenci, Analysis of singular stress field at joints of multiple dissimilar materials under mechanical and thermal loading, *Int. J. Solids Structures*, Vol. 38, pp 9077-9109 (2001).
- [9] S. Ioka, K. Masuda, Kubo, Singular stress distribution near the edge of interface of bonded dissimilar materials with an interlayer, *Journal of Society of Material Science*, Vol 35, pp 841-845 (2004).
- [10] H. Koguchi, M. Nakajima, Influence of interlayer thickness on the intensity of singular stress field in 3D three-layered joints under an external load, Vol. 4, No 7 (2010).
- [11] Darly L. Logan, *A first course in the finite element method*, 4th edition.

Productivity Enhancement of Single Basin Solar Still using Al₂O₃ Nanoparticles

Muhammad Sharif Uddin*, Md. Mehdi Masud Talukder, Md. Tansirul Islam

Department of Mechanical Engineering, Chittagong University of Engineering & Technology, Chittagong, BANGLADESH

ABSTRACT

Solar still is one of the prominent and basic sun oriented refining techniques to get fresh water from saline water. This paper investigates the enhancement in productivity of single basin solar still using Al₂O₃ nanoparticles in the base fluid. Nanofluids with high thermal conductivity are perfect heat transfer fluids for gathering thermal energy in solar thermal applications. In this work, the modifications are accomplished into a conventional solar still using nanofluids of varying concentration (0.1% and 0.2%) which ultimately increased the distillate water productivity. The inclusion of nanoparticles on the base fluid have significantly boosted the evaporation and condensation rates as well as the daily yield of the solar still. A maximum increase in productivity of 33.1% is achieved with a 0.2% concentration of Al₂O₃ nanoparticles when added to the base fluid.

Keywords: Solar still, Desalination, Minimum water depth, Al₂O₃ Nanoparticles, Nanofluid.

1. Introduction

For the purification of water various methods are used like filtration, sedimentation, distillation and disinfection. Solar distillation is one of the most popular water purification techniques. The principle of solar distillation is to use solar energy to evaporate saline water, then condense the vapor on a glass surface and collect the condensed fresh water. There are different types of solar stills including pit solar stills, cone solar stills, domo solar stills but the basin still is the most common. Basin stills can be categorized in many forms, however the single slope and double slope solar stills are very popular [1]. With a reasonable investment of capital cost, basin solar still is capable to produce a daily output of several liters of water per square meter of still. And such a still can be designed to operate for as long as 20 years with an efficiency of 30-60% [2].

As the productivity of the single basin solar still is quite low, its popularity is not in the peak. A number of research works have been done to enhance the productivity of the still. In most of the cases, the solar still provided a daily yield of less than 5 L/m² [3]. Complete loss of latent heat of condensation of water vapor is responsible for such a low efficiency. The execution and efficiency relies on numerous parameters like intensity of the solar radiation, wind velocity, temperature distinction between the glass cover plate and saline water, insulation, area of the collector and absorber plate, minimum depth of water, inclination angle and thickness of the glass cover.

2. State of knowledge

Many researchers have experimented the effect of the various factors that result in improved efficiency of the solar still. Omar et al. [4] analyzed the performance and efficiency of a single slope single basin solar still based on solar intensity. They found that with the increase in

solar intensity, performance and efficiency of the solar still increases. The maximum efficiency of solar still is found at noon due to high intensity of solar radiation. Emad Almuhanha [5] also concluded that the rate of daily yield increases with the increase of solar radiation intensity. The basin water depth has a major effect on performance and productivity of the solar still. Distinctive analysts have revealed that the water profundity is contrarily corresponding to the efficiency of the sun based still [6–8]. Tiwari [9] has investigated the impact of the profundity of basin water and revealed that the efficiency of the solar still increments with the diminishing of water depth in the basin. Bilal likewise revealed that the execution of the solar still increments with the decrease in water depth [10]. Many researchers used a number of wick materials for enhancing the productivity of solar stills. Productivity of solar still was improved by about 29% by using sponge as wick material [11]. Among the different wick materials cotton, sponge and jute are most common. Another research work was carried out on stepped solar still by using fins, [12] in which a total of 250 fins were used in 50 trays and 76% improvement in productivity was concluded. An investigation had been done by utilizing cuprous and aluminum oxides of different concentrations [13] and there was extensive enhancement in the everyday yield of the solar still. The impact of cuprous and aluminum oxide nanoparticles in a single basin solar still was investigated and maximum yield was obtained with aluminum oxide nanoparticles [14]. Different aluminum oxide nanoparticles concentrations were added to a double slope solar still and reported that the efficiency increased with the increase in nanoparticles concentration [15]. Another research work had been carried out by using aluminum oxide, cuprous oxide and titanium oxide nanoparticles with different concentrations in the base fluid [16] and a maximum productivity improvement of about 29% was achieved with the 0.25% concentration of aluminum oxide nanoparticles in the base fluid.

* Corresponding author. Tel.: +88-01868260414
E-mail addresses: sharif0162@gmail.com

3. Statement of the problem

Sun oriented desalination is the way toward changing over the debase salty water into consumable drinking water utilizing solar energy. The sunlight based desalination strategies have been utilized by the humankind for a large number of years. Truth be told, solar stills were the main strategy which was utilized on a little scale to change over debase saline water to consumable water. Be that as it may, the primary disadvantage of the solar desalination is its low profitability. Ordinarily, a sun oriented still can yield 2.5– 5 l/m²/day of distillate [17].

Determining a suitable area of absorption and identifying the minimum water depth which leads to the maximum daily yield was the major concern. Then, for the minimum water depth productivity improvement techniques were adopted. For this purpose, Aluminium oxide nanoparticles were added to the base fluid.

The objectives of the research include-

- To determine the productivity of the conventional solar still.
- To determine the productivity of the solar still in addition with nanoparticles in the basin.
- To compare both of the daily yields and finding out the productivity enhancement.

4. System description

The essential standards of solar still are extremely basic yet very compelling. Sun powered refining reproduces the manner in which nature makes rain. A conventional solar still follows two major scientific principles namely evaporation and condensation. At first, the saline water is placed in the basin of the solar still. The solar still is then allowed to sit in the sun in order to absorb the sun's short wave energy. The solar energy heats water up to the point of evaporation. When the water dissipates, water vapor ascends towards the glass cover and leaves anything besides unadulterated water in the bowl underneath. At the point when the water vapor achieves the glass cover, the water gradually consolidates on the glass, causing pure water beads. Various impurities like salts, metals and microbiological organisms can be removed by this process. The output is fresh water which is even cleaner than the purest rain water. The solar still takes into account normal pH buffering and furthermore delivers incredible taste when contrasted with common steam refining.

4.1 Design of the solar still

Designing the model is the preliminary task of each and every research. So, at first the conventional solar still was designed. The solar still basin have a length of 30 inches and a width of 18 inches. The angle of inclination of the glass cover was 12 degree.

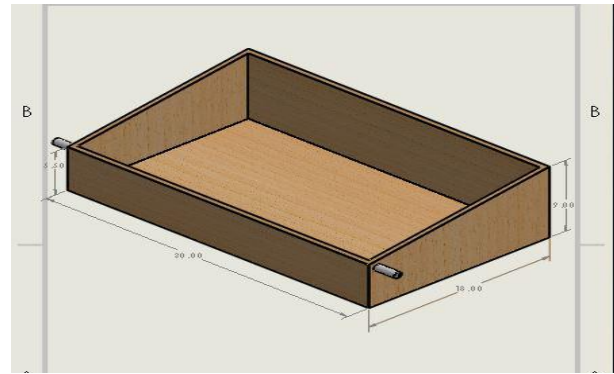


Fig.1 3D model of the solar still

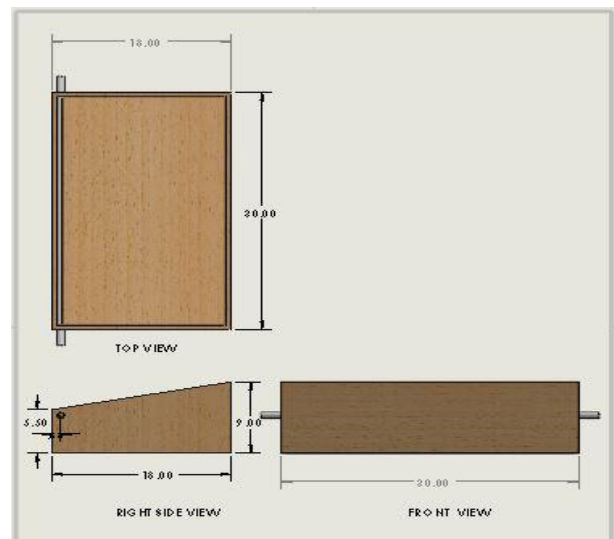


Fig.2 2D model of the solar still

4.2 Fabrication of the system

For the fabrication of the system, at first the basin of the solar still was made. It is a container in which the base fluid and the nanoparticles mixtures are provided. The basin was made of galvanized steel of 2mm thickness. The length of the basin was 30 inches and width was 18 inches also having a height of 4 inches. This basin was put into a wooden frame, which is the basic structure of the solar still. The wooden frame was made slightly bigger than the steel basin for the ease of operation. The wooden frame provided space for attaching glass above it. On one side of the frame, a 3/4 inch hole was made for providing saline water into the basin. And on the other side, a PVC pipe was attached to collect the condensed water that flowed down the glass surface. Before putting the steel basin into the wooden frame, the frame was sealed properly using Silicon gum in every corner. Then the glass cover was placed above the frame and the water droplet collection tube was also attached. The tube was sealed at one end and the other end was provided with a water tape. A 3/4 inch elbow joint was placed in the upper side of the frame to supply the saline water into the basin of the solar still.



Fig.3 Fabricated single basin solar still

4.3 Data collection and analysis

After the fabrication of the solar still, the experimental data was taken in shiny days. The required temperatures at different points on the solar still and the amount of fresh water stored were measured carefully. At first, the experimental data were taken for three different water depth (1, 2 and 3 cm). From the output of the solar still it was found that 2 cm was the optimum water depth. This was done for conventional solar still without the addition of nanoparticles. From the daily yield, productivity and efficiency of the solar still was calculated.

4.4 Addition of Nanoparticles

In the present study, Aluminium oxide nanoparticles are used because of its high heat transfer co-efficient and availability. The aluminium oxide nanoparticles are added in different concentration ; 0.1% and 0.2% respectively. The nanoparticles are added with the saline water and the daily yield is measured. Aluminium oxide-water nanofluid is prepared by using magnetic steerer machine. For water depth of 2 cm about 4.5 litre saline water and 9 gm nanoparticles are added to the basin, when 0.2% nanoparticle concentration is used.

5. Experimental results

The experimental setup was kept under the sun and data were collected for several days. At first, the experimental data were measured for three different water depths 1cm, 2cm and 3 cm. The daily yield was 402.6 gm, 374.21 gm and 196.50 gm respectively. In spite of the fact that, water depth of 1cm gave the maximum yield, however it come about a few challenges like providing saline water consistently. So, 2cm was considered the optimum level of water depth.

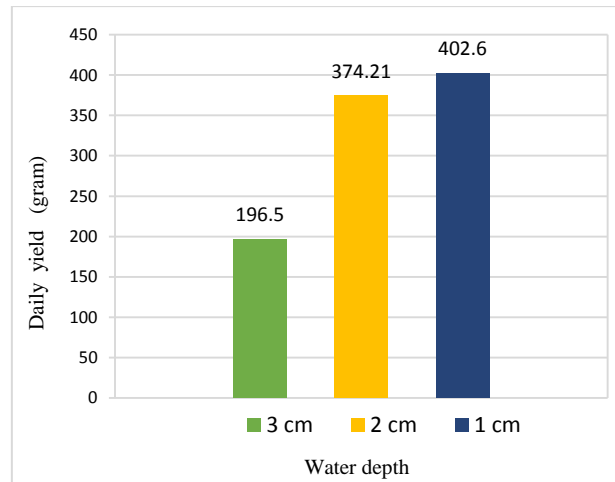


Fig.4 Variation of productivity with water depth

At first, the productivity of the conventional solar still was measured. This was done with 2cm water depth in the basin. The experimental data were taken every hour starting from 9:00 AM to 5:00 PM. The output and the solar intensity were measured throughout the whole day. For the calculation of the still productivity at night, the output was measured the next morning at 8:00 AM. For the conventional solar still, a total of 374.21 gm fresh water was found during day 1.

Then the productivity of the solar still was measured for 0.2% and 0.1% Aluminium oxide nanoparticle concentration and a total of 498.12 gm and 443.50 gm were obtained in the respective days. It was evident that the solar still modified with 0.2% Aluminium oxide nanoparticle provided the maximum output while the conventional solar still the least.

The solar thermal efficiency of the s is given by [17] –

$$\eta_d = \frac{\sum m_d \times h_{fg}}{\sum A_{eff} \times I \times t} \times 100\%$$

Where,

Latent heat of vaporization of water, $h_{fg} = 2230$ KJ/Kg

Net effective area of solar still basin, $A_{eff} = 540 \text{ inch}^2 = 0.3483864 \text{ m}^2$

Time interval, $t = 1 \text{ hour} = 3600 \text{ s}$

✓ Daily efficiency of conventional solar still =

$$\frac{(0+8+21+46+51+48+40+30+23+107) \times 2230}{0.35 \times (615+720+760+860+905+710+480+275+120) \times 3600} \times 100\% = 12.26\%$$

✓ Daily efficiency of the modified solar still (0.1 %) = 14.48 %

✓ Daily efficiency of the modified solar still (0.2 %) = 16.28 %

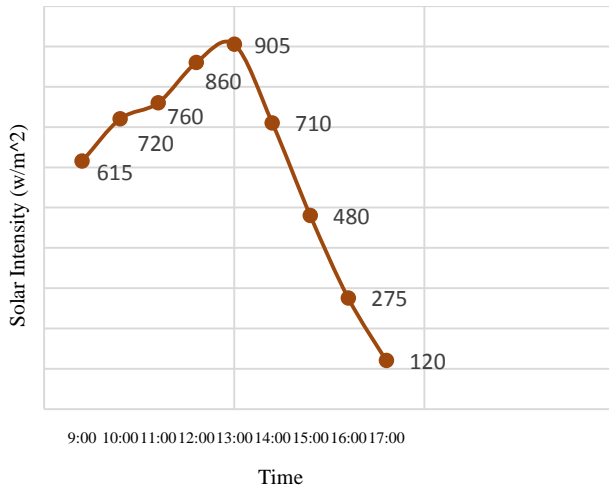


Fig.5 Variation of solar intensity throughout Day 1

Fig.5 shows the graphical representation of the variation of solar intensity with time throughout the Day 1. It can be seen that maximum solar intensity was 905 W/m² and minimum solar intensity was 120 W/m² measured at 1:00 PM and 5:00 PM respectively.

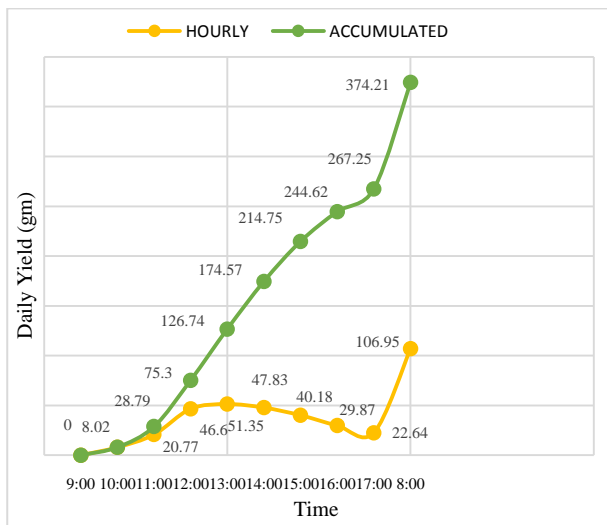


Fig.6 Graphical representation of daily yield of the conventional solar still at Day 1

The above figure shows the hourly and accumulated yield of the conventional solar still. The output was zero at 9:00 AM and increased as the day went by. The maximum hourly yield of 51.35 gm was obtained at 1:00 PM. The productivity during the night was measured the next morning at 8:00 AM. From 5:00 PM to 8:00 AM a total yield of 106.95 gm was obtained. The green line shows the accumulated yield of Day 1. A total output of 374.21 gm was found for the conventional solar still.

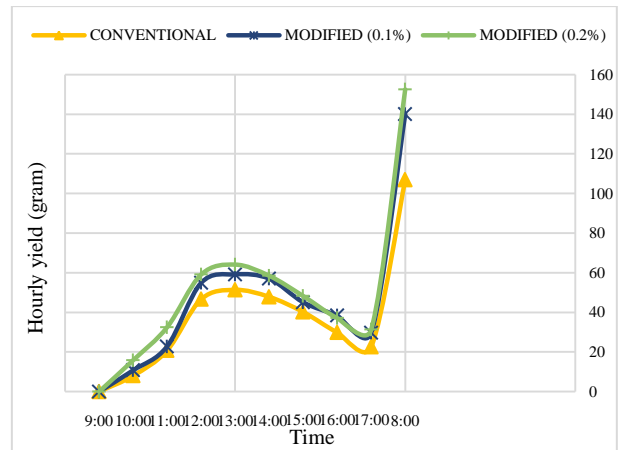


Fig.7 Variation of hourly output of conventional and modified solar still

Fig.7 shows the graphical representation of the variation of hourly output of conventional and modified solar still. The yellow line shows the hourly yield of the conventional solar still, which is the least among the three. The blue line shows the variation of hourly yield when the solar still was modified with 0.1% Aluminium oxide nanoparticles. The green line is for solar still modified with 0.2% Aluminium oxide nanoparticles, which also gives the maximum yield.

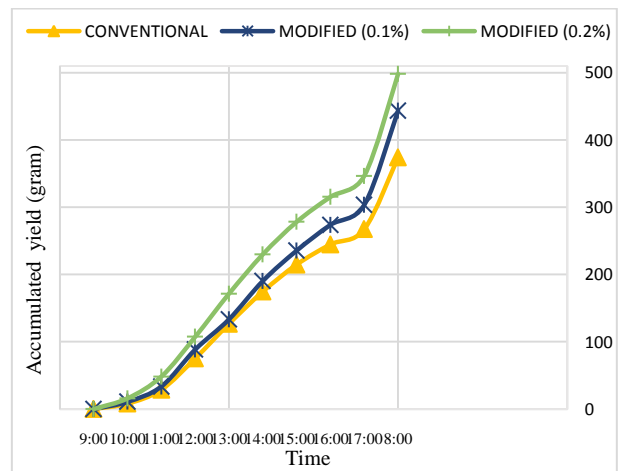


Fig.8 Variation of accumulated yield of conventional and modified solar still

Fig.8 shows the graphical representation of the variation of accumulated yield of conventional and modified solar still. The yellow line shows the accumulated yield of the conventional solar still, which was 374.21 gm. The blue line shows the variation of accumulated yield when the solar still was modified with 0.1% Aluminium oxide nanoparticles. It shows that there is a slight increase in the output when nanoparticles were added and a total of 443.50 gm fresh water was obtained. The green line is for solar still modified with 0.2% Aluminium oxide nanoparticles, which also gives the maximum daily yield of 498.12 gm.

6. Conclusions

A conventional single basin single slope solar was developed. Modification of the solar still was made by the addition of Aluminium oxide nanoparticles to the saline water. A comparative performance analysis of the conventional and modified solar still was made. The following conclusions can be made based on the performance of the solar stills-

- The efficiency of the solar still can be enhanced by the addition of nanoparticles to the base fluid as nanoparticles raise the thermal conductivity, basin water temperature and convective heat transfer coefficient.
- The optimum water depth for conventional and modified solar still is 2 cm.
- The maximum increase in the productivity is achieved with 0.2% concentration of Aluminium oxide nanoparticles (33.1% and 18.52% improvement of the productivity resulted for 0.2% and 0.1% nanoparticiles concentration respectively).

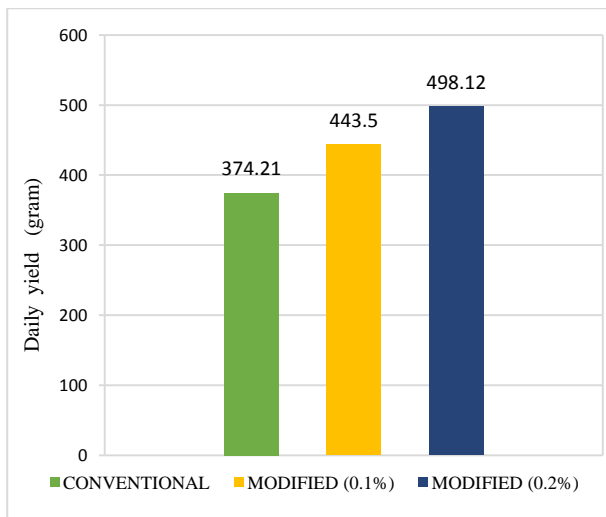


Fig.9 Variation of productivity of conventional and modified solar still

REFERENCES

1. Minasian, AN and, and A. A. Al-Karaghoul. "An improved solar still: the wick-basin type." *Energy Conversion and Management* 36.3 (1995): 213-217.
2. Green, Matthew G., and Dishna Schwarz. "Extracting drinking water from salt water." *Appropriate Technology* 29.3 (2002): 56.
3. Kabeel, A. E., and S. A. El-Agouz. "Review of researches and developments on solar stills." *Desalination* 276.1-3 (2011): 1-12.

4. Badran, Omar O., and Mazen M. Abu-Khader. "Evaluating thermal performance of a single slope solar still." *Heat and mass transfer* 43.10 (2007): 985-995.
5. Almuhan, Emad A. "Evaluation of single slop solar still integrated with evaporative cooling system for brackish water desalination." *Journal of Agricultural Science* 6.1 (2013): 48.
6. Tripathi, Rajesh, and G. N. Tiwari. "Effect of water depth on internal heat and mass transfer for active solar distillation." *Desalination* 173.2 (2005): 187-200.
7. Tripathi, Rajesh, and G. N. Tiwari. "Thermal modeling of passive and active solar stills for different depths of water by using the concept of solar fraction." *Solar energy* 80.8 (2006): 956-967.
8. Phadatare, M. K., and S. K. Verma. "Influence of water depth on internal heat and mass transfer in a plastic solar still." *Desalination* 217.1-3 (2007): 267-275.
9. Suneja, Sangeeta, and G. N. Tiwari. "Effect of water depth on the performance of an inverted absorber double basin solar still." *Energy Conversion and Management* 40.17 (1999): 1885-1897.
10. Akash, Bilal A., Mousa S. Mohsen, and Waleed Nayfeh. "Experimental study of the basin type solar still under local climate conditions." *Energy conversion and management* 41.9 (2000): 883-890.
11. Velmurugan, V., et al. "Single basin solar still with fin for enhancing productivity." *Energy Conversion and Management* 49.10 (2008): 2602-2608.
12. Velmurugan, V., et al. "Productivity enhancement of stepped solar still: Performance analysis." *Thermal Science* 12.3 (2008): 153-163.
13. Kabeel, A. E., Z. M. Omara, and F. A. Essa. "Improving the performance of solar still by using nanofluids and providing vacuum." *Energy Conversion and Management* 86 (2014): 268-274.
14. Elango, T., A. Kannan, and K. Kalidasa Murugavel. "Performance study on single basin single slope solar still with different water nanofluids." *Desalination* 360 (2015): 45-51.
15. Sahota, Lovedeep, and G. N. Tiwari. "Effect of Al₂O₃ nanoparticles on the performance of passive double slope solar still." *Solar Energy* 130 (2016): 260-272.
16. Sahota, L., and G. N. Tiwari. "Effect of nanofluids on the performance of passive double slope solar still: a comparative study using characteristic curve." *Desalination* 388 (2016): 9-21.
17. Sharshir, S. W., et al. "Factors affecting solar stills productivity and improvement techniques: a detailed review." *Applied Thermal Engineering* 100 (2016): 267-284.

Life Cycle Analysis of Lead Acid Battery used in Electric Vehicles (3 Wheeler) in Bangladesh

Md. Raquibul Hasan^{1,*}, Dr. Nirendra Nath Mustafi²

¹ Department of Civil Engineering, Pabna University of Science & Technology, PUST-6600, BANGLADESH

² Department of Mechanical Engineering, Rajshahi University of Engineering & Technology, RUET-6204, BANGLADESH

ABSTRACT

Lead acid batteries have been rapidly used in electric vehicles (3 wheeler) in Bangladesh with typical environmental problems such as consumption of resources and heavy metal pollution. Thus to conduct a comprehensive analysis of the environmental impact of the battery to reduce environmental pollution is urgent. In this paper a life cycle analysis conducted by SimaPro software is applied to analyze and compare the environmental impact of lead acid battery (LAB) within the system boundary of "cradle-to gate". The results showed that the overall impact of LAB production on environment is the smallest. The key substances that causes the environmental impact of LAB is production stage (12.56 %) & use stage of (85.56 %) the batteries. This research work will provide a quantitative assessments of the environmental impact of battery which will be very important to take necessary prevention measures during disposals. This can obviously create scopes of further research in this area.

Keywords: Lead acid battery (LAB), Electric vehicle, Life cycle analysis (LCA), SimaPro 8.5, Environmental impact

1. Introduction

Mass-production of battery electric vehicles were introduced to the global market to reduce transport-related oil dependency, carbon dioxide (CO₂) emissions, and urban air pollution [1]. Thus the three wheeler electric vehicles (Easy bikes) have made a major leap in the last few years in Bangladesh [2]. As a result, lead-acid battery (LAB) industry has stimulated the rapid growth of Bangladesh's for more than a decade. Easy-bikes are now plying on road with parking number given from city corporations, municipalities and union councils.

Electric bikes uses lead-acid batteries as the power source, which emit lead into the environment through its production, uses and recycling process. These batteries thus contaminates soil, air and water with their toxic substances, posing long-term negative impacts on the environment and human health [3].

The lead acid battery contains 70% lead (lead and lead oxide), 20% sulfuric acid and 10% plastic materials. In recycling process batteries are broken, cover of batteries is removed and acid is drained out on adjacent land. Top portion is hammered for shredding of plastic and the lead posts fixed in the top are released [4]. Open pit smelting is done at high temperature to recover lead from lead oxide, which is known as smelting. Smelting process requires small amount of coal to facilitate the reaction of lead burning. During this process lead dust and toxic gases released which pollutes the environment.

In order to find the negative impact of these batteries used in electric vehicles, a life cycle assessment (LCA) of lead-acid battery has been performed to explore the environmental aspects of the battery production, use and recycling process. Life cycle assessment is a technique to analyze and evaluate resources and environmental

impacts associated with all the stages of a product's life including raw material, production process, packaging, energy and some other human activity, including the collection of raw material, production, transportation, consumption, final disposal [5]. At present, LCA has been widely used in different areas.

The LCA conducted with a listing of the available technologies for lead-acid battery in the SimaPro software tool. This can obviously create scopes of further research on this area.

2. Lead Acid Battery

Lead acid batteries are the cheapest way to store energy. The construction of lead acid battery has two electrode one is lead (Pb) and other is lead oxide (PbO₂). These two electrodes are immersed in the solution of water and sulfuric acid (H₂SO₄). When battery is generating energy, the lead combines with the sulphuric acid to create lead sulphate (PbSO₄), and the lead oxide combines with hydrogen and sulphuric acid to create lead sulphate and water (H₂O) [5]. As the battery is getting discharged lead sulfate build up on the electrode and the water build up in the sulfuric acid solution. When the battery is charged the process reversed and lead sulfate combine with water to build lead and lead oxide on the electrode.

Charging: $2\text{PbSO}_4 + 2\text{H}_2\text{O} \rightarrow \text{PbO}_2 + \text{Pb} + \text{H}_2\text{SO}_4$
Discharging: $\text{PbO}_2 + \text{Pb} + \text{H}_2\text{SO}_4 \rightarrow 2\text{PbSO}_4 + 2\text{H}_2\text{O}$

There are two types of lead acid batteries based on their construction method- flooded and sealed. In flooded lead acid battery the electrode is immersed in electrolyte and regular refilling of water is required for proper working. While in sealed lead acid battery the electrolyte is immobilized.

* Corresponding author. Tel.: +88-01717621147

E-mail addresses: raquibulh@yahoo.com

3. Methodology

Environmental impact assessment of LAB is carried out following the LCA procedure and Eco-indicator 99 (H) (SimaPro 8.5) model analysis is performed. The environmental impact categories are selected according to model analysis. The processes and substances are identified according to overall environmental impact. The structure framework of this paper is shown in Fig.1.

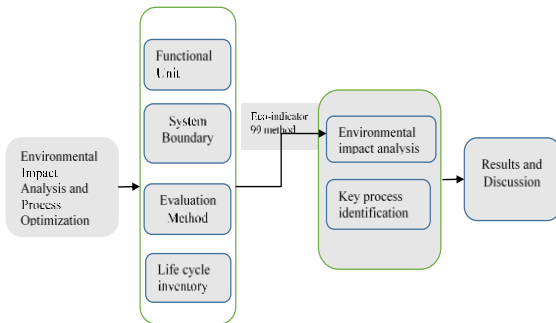


Fig.1 Structure framework of LCA

3.1 Functional Unit

All the raw material input, energy consumption, waste gas and waste water emission in the battery production process are calculated on the basis of the functional unit.

3.2 System Boundary

The battery system boundary is set to "cradle-to-gate" in Fig.2. It considers the battery production stage and the obtain stage of raw materials with the battery use stage and waste disposal stage. The system boundary of battery does not involve the problems of product quality allocation. Due to different types of raw materials used in the battery production process, the modes of transport are numerous. Therefore, the environment impact of raw materials transport is not taken into account.

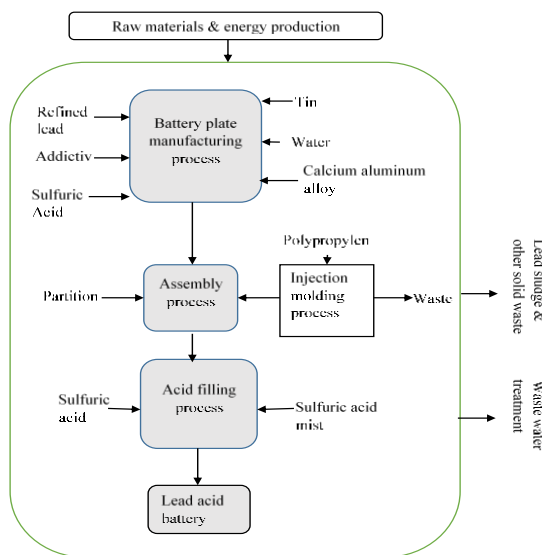


Fig. 2 System boundary of Batteries for LCA

3.3 Evaluation method

This study uses Eco-indicator 99 (H) model for life cycle impact assessment (LCIA) to perform all analyses. The Eco-indicator 99 model is the most widely used model in LCA and the most reliable intermediate point impact assessment method [6, 7]. The accuracy of the output results can be ensured from the data acquisition and model selection. The Eco-indicator 99 is one of the most widely used and the most reliable environmental impact assessment models in the world. It includes 18 midpoint environmental impact categories, i.e. climate change, ozone depletion, human toxicity, photochemical oxidant formation, particulate matter formation, ionizing radiation, terrestrial acidification, freshwater eutrophication, marine eutrophication, terrestrial ecotoxicity, freshwater ecotoxicity, marine ecotoxicity, agricultural land occupation, urban land occupation, natural land transformation, water depletion, metal depletion and fossil depletion [8].

3.4 Life cycle inventory construction

The focus of this LCA study is to evaluate the environmental performance of the lead-acid battery. The LCI data is basically a function of the quantity and type of energy consumed to operate the batteries. To quantify the data on amount of energy consumed, it is necessary to know the battery characteristic data and the application specific input data [9].

4 Stages of LCA

The lifecycle of a LAB can be divided into three main stages: production, use and disposal.

4.1 Production stage

Data related to energy consumption, input of raw materials and waste water and gas emissions of LAB is from a local battery manufacturer. Based on the literature reviews [10], this paper assumes that the number of LAB cycle is 350. LAB production process life cycle is shown in Table 1.

Table 1 Life cycle inventory (LCI) of lead acid battery (LAB) production process

Category	Name	1 kWh battery production	Unit	Data Sources
Battery plate manufacturing process	Refined lead	10.98	kg	Field survey
	Additive	0.16	kg	Field survey
	Calcium aluminum alloy	7×10^{-3}	kg	Field survey
	Tin	3.9×10^{-2}	kg	Field survey
	Deionized water	3.17	kg	Field survey
Process of Assembly	Sulfuric acid	0.64	kg	Field survey
	Partition	1.68	kg	Field survey

Acid filling process	Sulfuric acid	4.16	kg	Field survey
Injection molding process	Polypropylene	1.73	kg	Field survey
Energy consumption	Electricity	7.96	kWh	Field survey
	Steam	3.14	kg	Field survey

4.2 Use Stage

Firstly, the use of battery & use of package was determined. In the use phase a battery needed to charge & change the electrolyte. Then, the data for type of energy consumed, i.e., the electricity generation (power grid) mix and life cycle environmental impacts associated with it was obtained from Ecoinvent 2.2 database. The type of electricity used to charge and discharge the batteries plays a significant role in the overall inventory of battery LCA studies. As the focus of the study is the Bangladesh distribution grid, the Bangladesh national electricity mix at distribution grid level was assumed in the analysis. LAB use stage is shown in Table 2.

Table 2 Energy and material inputs for Lead-Acid Battery use phase

Products	Materials/Assemblies/Process	Quantity	Unit
Use of A Battery	Distilled Water Production	1	P
	Electricity, medium voltage {BD} market for electricity, medium voltage APOS, U Municipal Waste	2.8	kWh

4.3 Disposal phase

The disposal stage comprises the processes that products go through after their use is completed and are not providing the service for which they were devised. Whether due to malfunctioning or substitution, every product comes to a point when it has to be disposed of. A description hereafter of some possible ways to dispose of an end-life of Battery [11].

Data concerning the recycling processes is estimated based on an assumption regarding how much environmental burden can be avoided in total. Since the cell consists mainly of electrolyte (46%) and sealing gasket (15%), both assumed to be incinerated, only 20% of the total cell weight will be recycled as material (polypropylene). The environmental impacts of lead-acid battery recycling are calculated as the sum of environmental impacts from the transportation and involved recycling processes and treatment processes. LAB disposal stage is shown in Table 2.

Table 3 Energy and material inputs for Lead-Acid Battery disposal

Products	Materials/Assemblies/Process	Quantity	Unit
Disposal of Battery	Lead Acid Battery Assembly	1	P
	Transport, light commercial truck, diesel powered/tkm/RNA	0.2	tkm
Municipal Waste Disassembly of Battery Reuse of Container & Vent Plug	Transport, combination truck, short-haul, diesel powered/tkm/RNA	0.2	tkm
	Municipal Waste	50%	
	Disassembly of Battery	49%	
	Reuse of Container & Vent Plug	1%	

5 Life cycle analysis of a Lead-Acid Battery:

Total life cycle of a battery means the total view of production, use, and disposal. In a LC of Battery, for its charging it requires electricity. Also for its proper functioning it requires to change its electrolyte. For disposal state, it is considered that battery plates & other plastic component are recycled. Battery plates are go through the smelting process which facilitates the air emission. For the context of Bangladesh, the entire lifecycle of battery has negative impact. Fig. 4 shows the tree of Battery Life Cycle, Fig. 5 represents the Classification/ Characterization of the LCA, Normalization/ Weighing step on Fig. 7, Damage assessment step on Fig. 8 and finally the total contribution of each life stage to the total lifecycle aggregated in the main impact categories, Fig. 9 and Table 4.

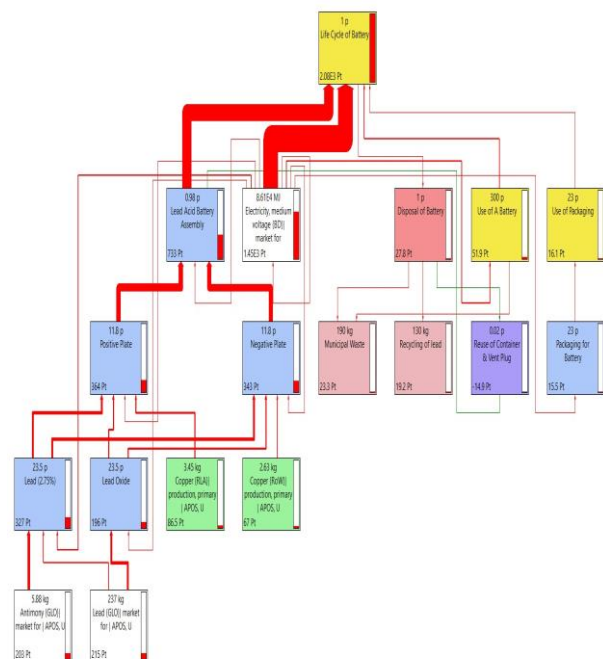


Fig. 3 Battery LCA network tree with a 5% cut-off

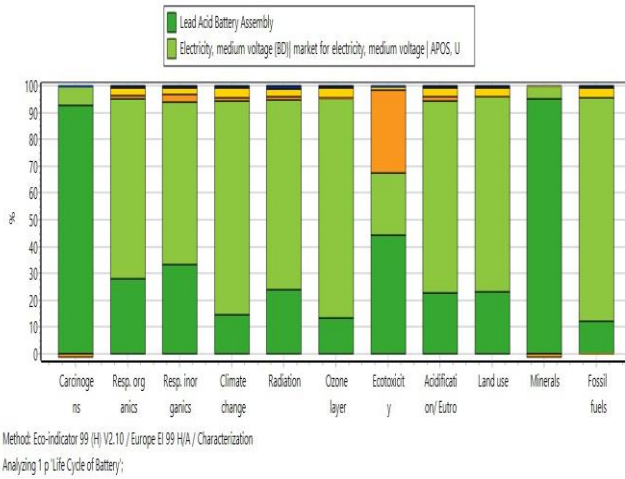


Fig. 4 LCA of a battery - Characterization Step

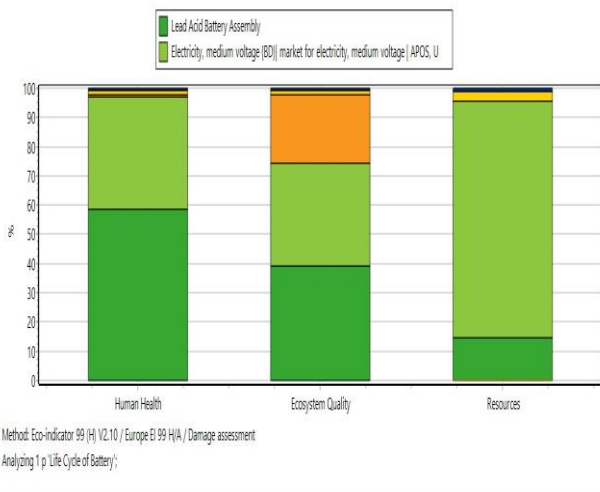


Fig. 5 LCA of a battery – Damage Assessment

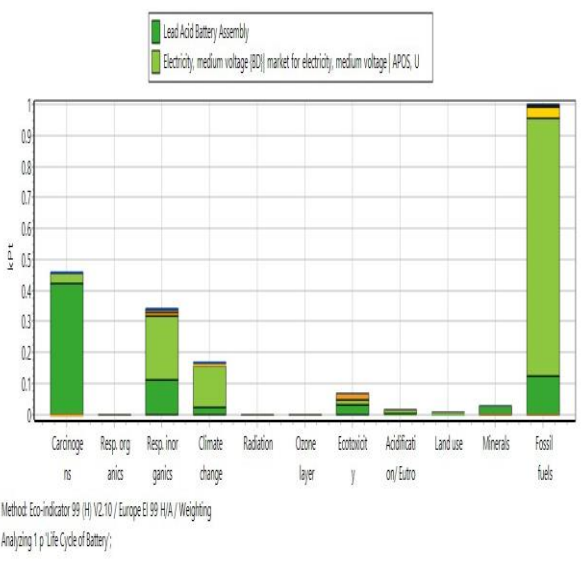


Fig. 6 LCA of a battery – Weighing Step

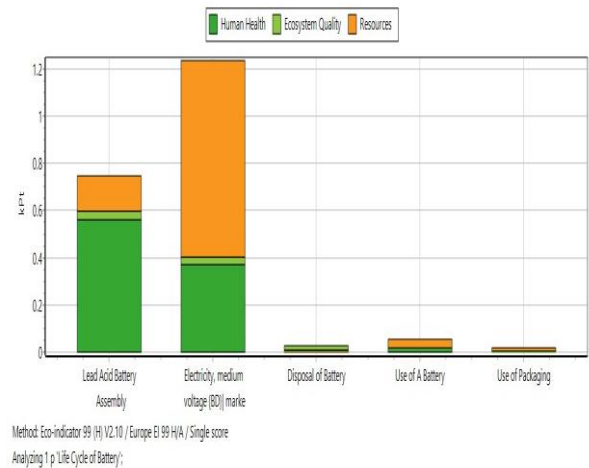


Fig. 7 LCA of a battery – Single Score

Table 4 Values of the contribution of each life stage in the total lifecycle of one battery

Damage category	Human Health	Ecosystem Quality	Resources	Total (kPt)
Lead Acid Battery Assembly	0.561	0.036	0.151	0.748
Electricity	0.370	0.032	0.833	1.235
Disposal of Battery	0.007	0.022	0.000	0.029
Use of A Battery	0.016	0.001	0.035	0.052
Use of Packaging	0.005	0.001	0.010	0.016
Total	0.959 (34 %)	0.092 (3.72 %)	1.028 (62 %)	2.079 (100 %)

6 Results

The previous figures and tables present the lifecycle ecopoints of the battery which amount to 2.097 kPt, where:

- a. The production accounts for 0.151 kPt, i.e. 70% of the total impact;
- b. The Electricity is responsible for 0.833 Pt, or 25% of the total environmental impact;

The categories with the highest contribution for the total lifecycle impact is Resources with a 62.27% input, followed by Human Health with 34%, Ecosystem Quality has a small contribution of 3.72%. In terms of

the intermediary indicators, Fossil fuel have the highest impact in this parameter.

Using Eco-indicator 99 model, use stage is identified as the key process with the greatest impact on the environment (Fig. 7), which occupies 85.56% of the overall environmental impact load. In the 5 main environmental impact categories, the battery manufacturing process proportion of the environmental impact load 12.56 % (Fig. 7).

7 Conclusions

With the help of LCA, the environmental impact of LAB in the stage of "cradle-to-gate" is analyzed and compared. The processes and the substances of environmental impact were identified by the Eco-indicator 99 method. The results show that LAB use phase has the greatest environmental impact. These findings are important references for achieving sustainable development in the Electric vehicle using phase in Bangladesh.

REFERENCES

- [1] Weeda, M., Kroon, P., Appels, D, *ECN – Energy Research Centre of the Netherlands, Petten, The Netherlands*, (2012)
- [2] The Daily Star, <https://www.thedailystar.net/business/easy-bikes-outgrowing-limitations-1469200>
- [3] IPE, www.ipe.org.cn/En/index.aspx, (2012)
- [4] Sandhya Prajapati, Lead Acid Battery Recycling In India, *IOSR Journal of Electrical and Electronics Engineering*, Vol. 11, PP 99-101, (2016).
- [5] ISO 14040, *International Standard. Environmental Management -Life Cycle Assessment-Principles and Framework* (2006).
- [6] Zhao, J., Hong, J.L, Cost combined life cycle assessment of lignite-based electricity generation. *Environ. Sci. Technol.* Vol. 159, PP 666-674, (2015)
- [7] Schryver, A.M.D., Brakkee, Characterization factors for global warming in life cycle assessment based on damages to humans and ecosystems. *Environ. Sci. Technol.* Vol. 43(6), PP 1689-1695, (2009).
- [8] PR é Consultants, 2011. Eco-indicator 99 impact assessment method for LCA. Available at: <http://www.pre-sustainability.com/content/eco-indicator-99> (2011)
- [9] Mitavachan Hiremath , Comparative Life Cycle Assessment of Stationary Battery Storage Technologies for Balancing Fluctuations of Renewable Energy Sources, *Master Thesis*, (2014)
- [10] Guo, Z.Q., The economic life of lead-acid batteries. *Ship Power Technol.* Vol. 34(2), PP 13-16, (2014).
- [11] Tchobanoglous, G., Theisen, H. & Vigil, S., *Integrated Solid Waste Management: Engineering Principles and Management Issues Internatio.*, London: McGraw-Hill Education – Europe, (1993)
- [12] Norris, G., Integrating life cycle cost analysis and LCA. *The International Journal of Life Cycle Assessment*, 6(2), PP 118-120, (2001).
- [13] Haefliger P, Mathieu-Nolf M, Mass lead intoxication from informal used lead-acid battery recycling in Dakar, Senegal, *Environmental Health Perspectives*, Vol. 117(10), PP 1535-1540, (2009).
- [14] Konstantinos N. Genikomsakis, A Life Cycle Assessment of a Li-ion urban electric vehicle battery, EVS27 International Battery, *Hybrid and Fuel Cell Electric Vehicle Symposium*, Barcelona, Spain, November 17-20, (2013)
- [15] Laiguo Chen, Zhencheng Xu, Lead exposure assessment from study near a lead-acid battery factory in China, *Science of the Total Environment* Vol. 429, PP 191–198, (2012)

ICMIEE18-333

Productivity Enhancement of Single Basin Solar Still using Nanoparticle and Phase Change Material

K.M.Mine Uddin Emon^{1,*}, Md. Mehdi Masud Talukder²

¹Department of Mechanical Engineering, Chittagong University of Engineering & Technology, Chittagong-4349, BANGLADESH

²Assistant Professor, Department of Mechanical Engineering, Chittagong University of Engineering & Technology, Chittagong-4349, BANGLADESH

ABSTRACT

This experiment is based on enhancing the productivity of a conventional solar still by using techniques that have newly materialized. The modifications include using Aluminum Oxide (Al_2O_3) nanoparticle to produce Nanofluid (0.2% concentration) and Paraffin Wax as Phase change material (PCM) together in the still which is expected to facilitate production of more fresh water. The outdoor performance of modified solar still is studied to assess its potential for real application. It is compared with the results of a conventional solar still to better understand the effects of the modifications. It was observed that, on consecutive days, the conventional still had an efficiency of 10.15% whereas the modified still had a daily efficiency of 13.15%, 16.40% and 14.47% for three consecutive days under similar conditions of environment.

Keywords: Desalination, Solar still, Nanofluid, Phase change material (PCM).

1. Introduction

About 70 % of Earth's surface is made up of water. Of that, about 97 % is in the oceans. That only remaining 3% can be considered as freshwater. Of that small amount almost 2% is locked up at the North and South poles as glaciers and ice. The remaining 1% of freshwater is mostly ground-water, with a small fraction filling the world's lakes and rivers. So to meet the demand of freshwater for survival, it is high time to look for alternative sources of freshwater. And the most easily available source of water is the oceans. If it is possible to separate the freshwater content from the seawater then it would be a great means for eradicating freshwater crisis. But the major problem in desalination of water is that, it requires a lot of energy. Salt is easily soluble in water and it forms strong chemical bonds, which are difficult to break. Energy and the technology to desalinate water are both expensive, which makes desalinating water pretty costly.

The Earth receives an incredible supply of solar energy. It provides enough energy in one minute to supply the world's energy needs for one year. Solar energy is a free, inexhaustible resource, yet harnessing it is a relatively new idea. This tremendous source of renewable energy can also be used to desalinate seawater and obtain freshwater from it. One of the many ways of doing so is using a solar still.

A solar still is a device that is used to distill brackish or seawater, using the heat of the Sun to evaporate, cool then collect freshwater. The sun's energy heats water to the point when it starts to evaporate. As the water evaporates, the water vapor rises, condenses into water again on the glass cover as it cools and is then collected. This process leaves behind impurities, such as salts and heavy metals, and eliminates micro-biological organisms. The end result is pure distilled water. In a solar still contaminated water is contained inside the

basin where it is evaporated by sunlight shining through clear plastic or glass. The pure water vapor condenses on the cool inside surface of the glass cover and then drips down due to the action of gravity. Then it is collected and removed from the system to be used. The major downside of this system is its productivity and the increased cost that is added while using different improvement methods to the system. Performance of a solar still can be increased by the help of various enhancement techniques of which use of PCM and Nanoparticles are noteworthy ones. Experiments have been conducted to increase the productivity of solar still using Nanoparticles as well as PCM of different kinds. This experiment is intend to use both Nanoparticles and PCM together in a solar still and try to estimate its overall efficiency escorted by a comparative study between the performances of the conventional and the modified solar still.

2. PREVIOUS STUDIES

Different methods for enhancing performance of solar stills have been introduced so far. The use of Phase Change Materials (PCM) or Nanoparticles is noteworthy in modern performance enhancement techniques. These elements perform as heat storage that absorbs heat from the sun during the day, stores it and then supplies the heat during the night so that the process of evaporation may continue for a longer period. Numerous work has been done so far using this two elements in pursuit of increasing the efficiency of a solar still.

2.1 Phase change material (PCM)

PCM is used to deliver heat during nighttime which was kept as solar thermal energy collected by the system at daytime as latent heat, thus allowing uninterrupted process. Over the last 40 years different classes of

* Corresponding author. Tel.: +88-01686465416
E-mail addresses: mineuddinemon@gmail.com

materials have been considered as feasible PCMs, including hydrated salts, paraffin waxes, fatty acids, the eutectics of organic and non-organic compounds and polymers. According to Fath [1], the latent heat thermal energy storage systems have many attributes that makes them a better choice over sensible heat storage system. For example, the steady temperature for charging and discharging and the vast energy storage bulk per unit volume. Radhwan [2], performed a study of a temporary enactment of a stepped solar still with compacted latent heat thermal energy storage for warming and humidifying of agronomic greenhouses (GH). In addition, he discussed the impact of paraffin wax thickness as a PCM. The total output was that of about 4.6 L/m² with an efficiency of nearly 57%. Naim et al. [3], placed an Energy Storage Material (ESM) in the still tray during its construction resulting in increasing the still productivity. Aluminum turnings were added to a blend comprising of paraffin wax, paraffin oil and water to increase heat conduction then, save during the hours of daylight and finally release it at night. The arrangement was used as a special phase change material. It improved the production to a maximum value of nearly 851 ml/m²h when the amount of briny water was 40 ml/min. Systematic study of a still with and without PCM was done by Dashtban and Tabrizi [4]. The everyday yield reached 6.7 and 5.1 kg/m² with and without PCM, respectively. Ansari et al. [5] examined a still assimilated with a PCM under the basin. The results show that the heat energy storage increases favorably both the yield of the fresh water and the efficiency of the distillation method.

2.2 Nanoparticles

Many scientists have carried out several studies on solar stills enhanced with Nanoparticles which have become available means for improvement of a solar still performance. Nijmeh et al. [6] used violet dye and studied the efficiency of the solar still. The outcomes showed that the productivity was enhanced by 29%. Elango et al. [7] examined an experimentally used various Nanoparticles in a solar still. When using the aluminum oxide (Al₂O₃) Nanoparticles the productivity increased by 29.95%, while the solar stills with tin oxide (SnO₂) and zinc oxide (ZnO) Nanoparticles gave 18.63% and 12.67% higher productivity than that without Nanoparticles, respectively. Mahian et al [8] demonstrated the effects of the addition of carbon nanotubes (CNTs) to the water inside a single basin solar still. Results showed an escalation by about 50% in the productivity. Kabeel et al. [9] [10], presented an investigational study to increase the still yield by mixing the aluminum oxide Nanoparticles with the inlet water to the still. The results revealed that using Nanoparticles with providing the vacuum fan increased the solar still water productivity by about 116%. Sharshir et al. [11] utilized graphite and copper oxide micro-flakes with various fixations, distinctive basin water depth, and diverse film cooling stream rates to research the efficiency of a solar still. The micro-flakes

concentrations were ranged from 0.125% to 2% and the basin Nanoparticles depths are ranged from 0.25 to 5 cm. The productivity was enhanced by about 44.91% and 53.95% using the copper oxide and graphite micro-flakes, respectively, compared with the conventional solar still. Furthermore, 38% and 40% increase in daily efficiencies were obtained when using copper oxide and graphite, respectively.

3. Statement of the problem

Solar desalination is the way toward changing over the polluted water into consumable drinking water utilizing sun's energy. The sunlight based desalination strategies have been utilized by the mankind for many years. In fact, solar stills were the primary technique which was utilized on a smaller scale to change over tainted saline water to consumable water. Be that as it may, the fundamental downside of the sun powered desalination technique is its low efficiency.

Determining a suitable area of absorption and identifying the minimum water depth which leads to the maximum daily yield was the major concern. Wasil Jamal and Prof. M. Altamush Siddiqui [12] conducted their experiments using a water depth of 2cm, 3cm, 4cm and 5cm respectively and finally concluded that the productivity was maximum for a shallow depth of water in the basin. Further, the yield decreased as the water depth was taken more being least at 5cm depth. With accordance to this research a water depth of 2cm was used in this experiment. Then, for the minimum water depth productivity improvement techniques were adopted. For this purpose, Aluminium oxide nanoparticles were added to the base fluid and Paraffin Wax was used as PCM under the basin tray.

The objectives of the research includes-

- To determine the productivity of the conventional solar still.
- To determine the productivity of the solar still in addition with nanoparticles in the water and Paraffin wax under the basin.
- To compare both of the daily yield and hourly yield of the system and thus finding out the productivity enhancement.

4. System Description

To develop a solar still with enhanced productivity Phase Change Material (PCM) and Nanoparticles were used. Paraffin wax was used as the PCM and Aluminum Oxide (Al₂O₃) Nanoparticles was used for the experimentation. The Nanoparticles was directly dispersed into the water to be desalinated and stainless steel pipes with PCM encapsulated inside was put on the basin liner to store the energy. The area of the still basin was 0.37 m² (0.762 m length × 0.483 m width). The stills was made of wood and a galvanized steel basin was placed inside the wooden frame where the brackish water mixed with Nanoparticles was placed. The brackish water was filtered as far as possible. A glass of 3mm thickness was used as the cover through

which solar radiations will enter the still and it was kept in an inclined position. A sectioned PVC pipe inside the still was used to collect the fresh water from the glass cover, a plastic pipe was connected to the PVC pipe for draining the water to an outside bottle. The brine was drained outside of the still through another hole at the bottom. Tap water was used to work as the sea water in this experiment.

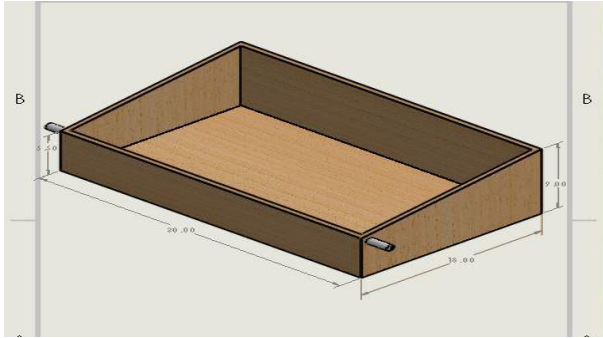


Fig.1 Experimental setup (3D view)

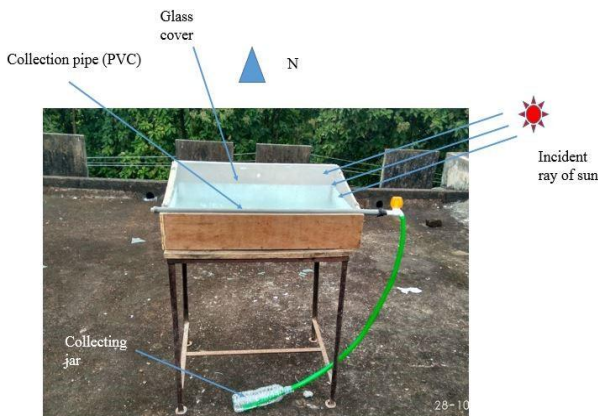


Fig.2 Fabricated system equipped with PCM and Nanofluid.

The inside basin was made of galvanized steel so that it could prevent corrosion due to constant use of water. The basin had a surface area of 0.37 m^2 (0.762 m length \times 0.483 m width) and a height of 4 inches all around. A galvanized sheet of 2mm thickness was cut and shaped to the desired specification and the corners were gas welded.

The steel basin is placed inside the wooden frame and the conventional setup is thus completed by placing the glass cover of 3mm thickness over the wooden frame. The glass cover was then perfectly sealed using Silicon gum as sealant which would prevent the vapor from going to the neighborhood. Using this setup the readings were taken for productivity of potable water from brackish water using a graduated cylinder.

4.1 Addition of modifications

Addition of Paraffin Wax (PCM): In this experimentation paraffin wax was used as Phase Change Material (PCM) due to its low cost and easy

availability. The wax was encapsulated inside stainless steel hollow cylinders of 19 inch length consisting of 0.5 inch internal diameter. Around 1.2 kg of wax was encapsulated in six such tubes. These tubes were placed under the steel basin so that it could gain the heat of the basin from below it. The tubes were sealed on both sides so that there were no leakage or loss of the wax.

Addition of Nanoparticles (Al_2O_3) to the working fluid: In the present study, Aluminium oxide Nanoparticles were used because of its high heat transfer co-efficient and availability. The aluminium oxide Nanoparticles were added in 0.2% concentration. The Nanoparticles were added with the brackish water by the help of stirrer and Nanofluid was prepared. This Nanofluid was introduced to the basin and the daily and hourly yields were measured.

4.2 Collection of data

Initially all data were taken considering the still to be a conventional one. After that modifications were added to the still and the new sets of data were taken. Data were collected for the whole day starting from 9:00 am in the morning up to 5:00 pm. The overnight productivity of the stills were measured on the next day at 8:00 am. The still was placed facing the south so that it could receive as much solar radiation as possible throughout the entire day. The data of the experiment was taken both on an hourly basis and daily basis. The amount of water which was obtained after distillation was collected in a graduated bottle and it was measured in a sensitive weight measuring device. Thus the actual amount of water obtained was found. The amount of solar intensity was determined by the help of a digital Solar Radiation Meter on an hourly basis. With the change of solar intensity the productivity of the stills were determined. From the two sets of measured data, one without any modification and other with PCM and Nanoparticles the productivity enhancement was compared. It was found that the daily yield increased while Aluminium oxide nanoparticles were added to the base fluid and due to the presence of Paraffin wax.



Fig.3 Collection of droplets of distill water condensed on the inner wall of the glass-cover.

5. Results and discussion

The data were collected during four consecutive solar days (21st-24th October), Day-1 (21st Oct) being the data for conventional still and Day-2, 3 and 4 (22nd, 23rd and 24th Oct) respectively being that for the modified still.

These data were plotted against time in order to understand the variations of results through each hour of the day as well as the effect of the modification on the productivity.

a) Variation of Solar Intensity of four consecutive days of experimentation-

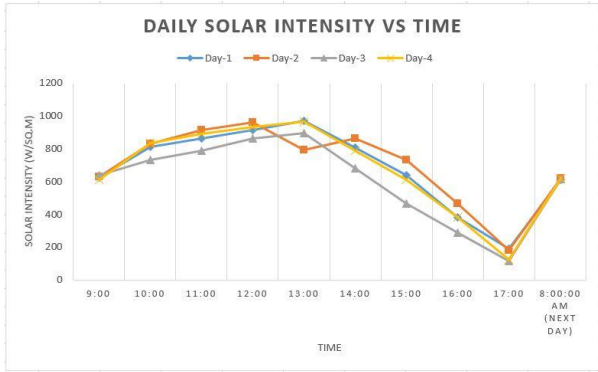


Fig.4 Comparison of the change of solar intensity for the days on which experimentations were conducted.

The data of the Solar Intensity of each day which was collected in an hourly basis was plot against time in the same graph to understand the variation of solar intensity during the entire span of the experimentation. From the figure it can be said that maximum intensity was obtained during the time period of 11:00 am to 1:00 pm. It may also be deduced that the variation of solar intensity for those days was minimum and its effect on the productivity may be ignored for the sake of comparison.

b) Variation of hourly yield of the solar still with respect to the variation of solar intensity-

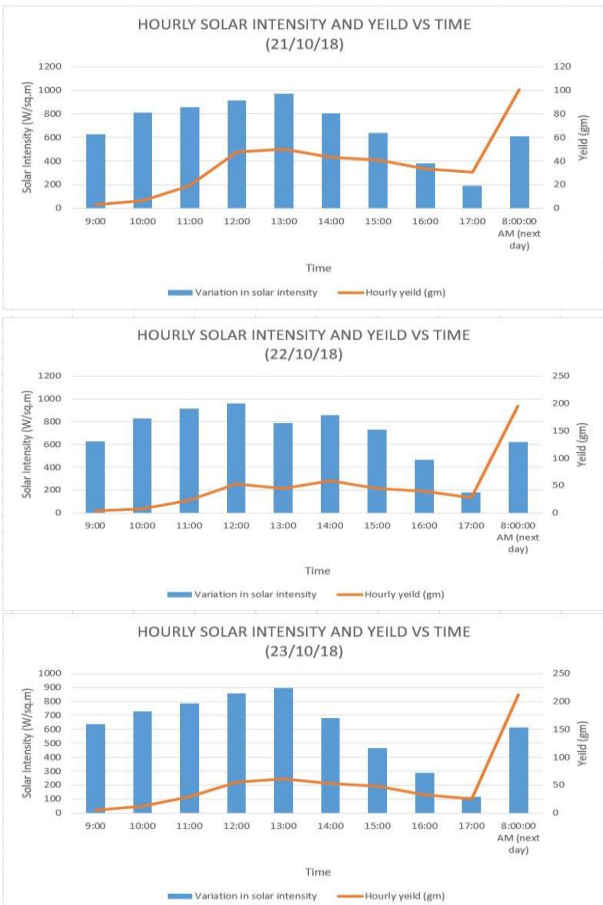
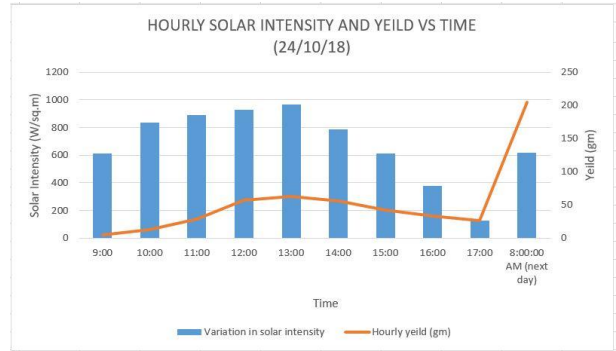


Fig.5 Comparison of the change of hourly yield of each day compared to the hourly solar intensity for both conventional (21/10/18) and modified still (22/10/18, 23/10/18 and 24/10/18)



Here the hourly yields of the still on consecutive days along with the hourly measure of solar intensity were plotted against time. The graph shows the change of the amount of yield of the conventional and modified still compared to the solar intensity variation on an hourly basis. Here it can be seen that the yield increased as the day advanced and in all the cases maximum output was obtained during 12:00 pm to 1:00 pm. The yield then gradually decreased during the end of the day as the solar intensity decreased.

c) Variation of hourly yields of conventional and modified solar still-

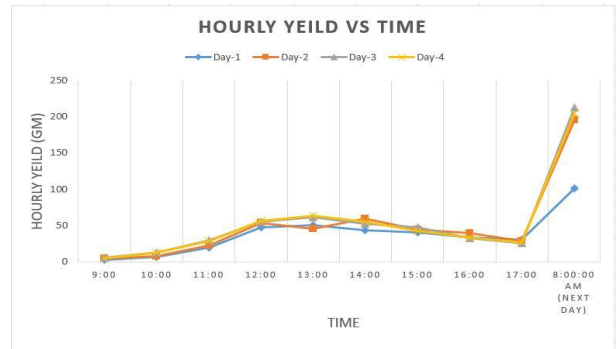


Fig.6 Comparison of the hourly yields of the conventional (Day-1) and modified (Day-2, 3 and 4) solar still.

The hourly yields from both the conventional still and the modified still were plotted against time in the same graph. The trend obtained from the graph shows that use of PCM and Nanofluid as modifications to the solar still has resulted in a better output each hour of the day. The data were collected up to 5:00 pm each day and the overnight productivity was measured at 8:00 am the next day. This difference in hourly yield of the solar stills will result in an increased daily yield which is the main purpose of the experiment. Here we see that the hourly yield of the conventional still is always lower

than the modified one which is an indication of the effectiveness of the PCM and Nanofluid.

d) Variation of accumulated yield of conventional and modified solar still-

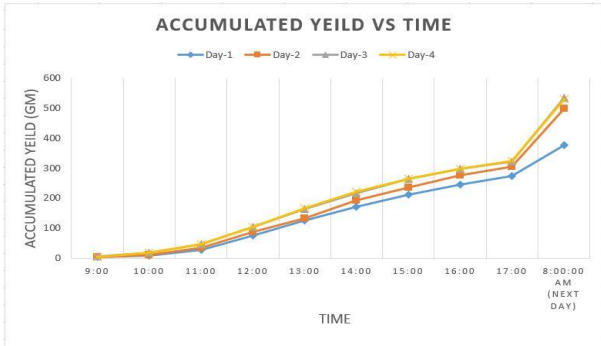


Fig.7 Comparison of the accumulated yields of the conventional (Day-1) and the modified (Day-2, 3 and 4) solar still.

Here the accumulated yields of the still, with and without modifications, were plotted against time. This graph provides a better evidence to the fact that using of PCM and Nanofluid has resulted in better overall productivity of the still. The blue line representing Day-1 shows the accumulated yield of the conventional solar still while the other lines, indicating Day-2, Day-2 and Day-4, show that for a modified one. Since the data were taken for the whole day, we see that, at 8:00 am the next day the accumulated amount of water is higher for the modified still on each day. This makes the modified still a better choice over the conventional one.

The daily efficiency of the solar is given by [13] –

$$\eta_d = \frac{\sum m_d \times h_{fg}}{\sum A_{eff} \times I \times t} \times 100\%$$

Where,

Latent heat of vaporization of water, $h_{fg} = 2230 \text{ KJ/Kg}$
 Net effective area of solar still basin, $A_{eff} = 574 \text{ inch}^2 = 0.37 \text{ m}^2$

Time interval, $t = 1 \text{ hour} = 3600 \text{ s}$

m_d = mass of distillate water, ml

I = Intensity of solar energy, W/m^2

η_d = Daily efficiency, %

✓ Daily efficiency of conventional solar still,

$$\eta_d = \frac{(3 + 6 + 19 + 48 + 50 + 43 + 40 + 33 + 30 + 101) \times 2230}{0.37(625 + 810 + 860 + 915 + 970 + 805 + 640 + 380 + 190 + 610) \times 3600} \times 100\%$$

=10.15%

✓ Daily efficiency of the modified solar still on consecutive days were= 13.15%, 16.40% and 14.47% respectively.

6. Conclusion

The hourly and accumulated yield of the conventional and modified solar still for four consecutive days are shown in the figure-7 and figure-8.

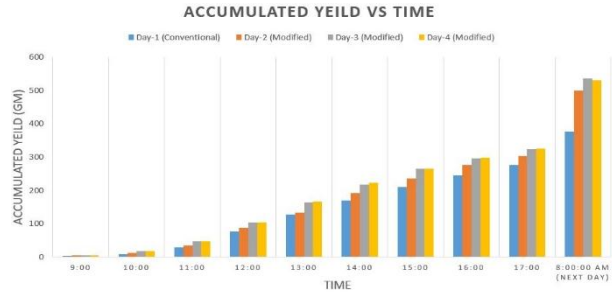


Fig.8 Bar chart representing the variation in hourly accumulated yields of the conventional and modified solar still for the whole day.

Here the hourly variation of yield of the solar still for four consecutive days have been represented in the form of bar chart. The blue bars represent the output of the conventional still while the red, gray and yellow bars are those for the modified ones. One can observe from the above figure that the accumulated yield of the conventional still always falls short compared to the productivity of the modified still. It can also be observed that the trend of hourly yield of the modified still is quite similar for all the three days. So it can be deduced that the process is stable and will produce a constant result if put to continuous use.

The figure-24 is a better indication of the final outcome of the experiment. In this figure the yellow bar represents the final yield of the conventional solar till considering the whole day and the overnight production. The blue bars represent the final yield of the solar still packed with modifications for three consecutive days. The experiment was conducted for 4 days so that the results can be verified and compared to one another.

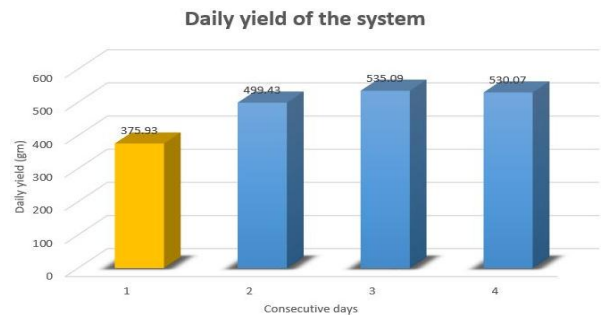


Fig.9 The final output of each day

The graph indicates that the modified still always gives a better result compared to the conventional one. Though the productivity of the modified still varied during the period of experiment due to various factor,

but it can be said the results were quite similar to one another. Since the effect of various factors of the environment are responsible for the overall yield of the solar still, variations in the yields were observed.

If one observes the figures given above carefully it can be deduced that the modified still has advantages in both hourly and overall productivity. The hourly productivity of the modified still was enhanced due to the presence of Nanoparticles, which retained the solar energy and helped to increase the temperature of the basin water to a great extent. On the other hand the overnight productivity rise in the modified solar still has also contributed to the overall yield. This increase in overnight productivity was due to the presence of Paraffin wax acting as Phase Change Material (PCM). The PCM used under the basin liner received the heat lost by the basin from below and when it melted during the day time. The melted wax trapped the heat as latent heat and then released it during the night. This heat was used to continue the evaporation process of the water in the basin during the night time. The condensation rate was also higher at night since it was cooler around the basin. As a result better productivity was obtained. The types of modification used in the solar still will make the total cost of the system higher than a conventional one but this will also result in better output. Here it can be seen that around 160 gm of more water was obtained from the modified still which is noteworthy considering the size of the still and other limitations. If a bigger still was fabricated than the overall productivity would have been more. But for the sake of experimentation the size was kept small so that it could be handled easily and sealing could be done more precisely. And the results from the comprehensive study lead to the following conclusions-

- The hourly productivity of the modified solar still is higher than the conventional one even though the solar intensities were not the same.
- The overall productivity of the still enhanced with PCM and Nanofluid was greater than the conventional still due to the modifications made to it.
- The overnight productivity rose significantly as a result of the action of the PCM which resulted in a better daily yield.

REFERENCES

[1] F. H.E.S, "Solar thermal energy storage technologies: technical note," *Renewable Energy*, pp. 35-40, 1998.

[2] R. A.M., "Transient performance of a steeped solar still with built-in latent heat thermal," *Desalination*, p. 61–76, 2004.

[3] Naim Mona M and AbdElKawiMervat A, "Non- conventional solar stills Part 2. Non-conventional solar still with energy storage element." *Desalination*, pp. 71-80, 2003.

[4] Mohammad Dashtban and FarshadFarshchiTabrizi, "Thermal analysis of a

weir-type cascade solar still integrated with PCM storage," *Desalination*, pp. 415-22, 2011.

[5] Omar Ansari, Mohamed Asbik, Abdallah Bah, AbdelazizArbaoui and Ahmed Khmou, "Desalination of the brackish water using a passive solar still with a heat energy storage system," *Desalination*, pp. 10-20, 2013.

[6] S.Nijmeh, S.Odeh and B.Akash, "Experimental and theoretical study of a single-basin solar still in Jordan," *International Communications in Heat and Mass Transfer*, pp. 565-572, 2005.

[7] T.Elango, A.Kannan and K.KalidasaMurugavel, "Performance study on single basin single slope solar still with different water nanofluids," *Desalination*, pp. 45-51, 2015.

[8] Omid Mahian, Ali Kianifar, Soteris A. Kalogirou, Ioan Pop and SomchaiWongwises, "A review of the applications of nanofluids in solar energy," *International Journal of Heat and Mass Transfer*, p. 582–94, 2013.

[9] Kabeel AE, Omara ZM and Essa FA, "Enhancement of modified solar still integrated with external condenser using nanofluids: an experimental approach," *Energy Conversion and Management*, pp. 493-8, 2014.

[10] Kabeel AE, Omara ZM and Essa FA, "Improving the performance of solar still by using nanofluids and providing vacuum," *Energy Conversion and Management*, pp. 268-74, 2014.

[11] S.W. Sharshir, Guilong Peng, Lirong Wu, Nuo Yang, F.A. Essa, A.H. Elsheikh, Showgi I.T. Mohamed and A.E. Kabeel, "Enhancing the solar still performance using nanofluids and glass cover cooling: Experimental study," *Applied Thermal Engineering*, pp. 684-93, 2017.

[12] Wasil Jamal and Prof. M. Altamush Siddiqui, "Effect of water depth and still orientation on productivity for passive solar distillation," *International Journal of Engineering Research and Applications (IJERA)*, vol. 2, no. 2, pp. 1659-1665, 2012.

[13] Sharshir, S. W., et al. "Factors affecting solar stills productivity and improvement techniques: a detailed review." *Applied Thermal Engineering* 100 (2016): 267-284.

Experimental Investigation of Different Wick Materials to Enhance the Productivity of Single Slope Single Basin Solar Still

Laxman Chandra Das*, Md. Mehdi Masud Talukder

Department of Mechanical Engineering, Chittagong University of Engineering & Technology, Chittagong-4349, BANGLADESH.

ABSTRACT

The objective of this research work was to augment the productivity and efficiency of conventional single slope single basin solar still by adding various wick materials with brackish basin water. The wick materials enhanced the evaporation rate of water due to capillary action by raising the temperature distinction of basin water and inclined glass cover surface of the solar still. During the night session, the portion of daytime heat energy retained within the wick materials was liberated which causes an accumulation of a noticeable quantity of distillate water. Distillate output of conventional solar still (CSS) was 374 ml/day with a solar thermal efficiency of 11.47% at 2 cm optimum water depth which was modified with five distinct wick materials independently. Maximum enhancement in productivity was obtained 56.15% with an increase in solar thermal efficiency of 39.84% when CSS was modified with the black cotton as wick material.

Keywords: Solar desalination, Wick materials, Optimum water depth, Solar thermal efficiency.

1. Introduction

Water is essential for every living organism in the earth. It is one of the most significant gifts of Almighty God to the whole mankind. The worldwide fresh drinkable water demand is successively increasing due to climate change, drought, urbanization, industrial, agricultural and population growth etc. which has already been reached a severe condition in many corners of the world. It is forecasted that the worldwide drinkable water demand will grow 54 billion m³/year by 2020 [1]. Enhancing the solar thermal efficiency of saline water sanctification technology to produce distillate fresh water is argued as one of the major challenges of the 21st century. Almost 71% of the earth's surface is encircled with water. Around 97% of this water is brackishly reserved in the oceans which is not suitable for drinking and cooking purposes. Only 3% of the total earth's water is potable which is contained in the ice poles, lakes, rivers, and groundwater satisfy most of the human and animal basic needs [2]. Today, most of the health problems are owing to the deficiency of pure drinkable water. The salinity of water is increased due to inadequate rainfall around the most part of the world. Due to various water-borne diseases, 3.575 million people accept premature death every year throughout the world [3]. For consumption purpose, water should be pure in terms of impurities and dissolved salts. The taste of water may be affected by the total amount of dissolved solids present in it. It is generally argued that salinity less than 500 ppm is compatible as drinkable water [4].

There are a large number of methods commonly used for brackish water purification: desalination, filtration, sedimentation, and disinfection, electrolysis, reverse osmosis etc. The technique commercially used for saltwater purification is reverse osmosis. The main drawback with this technique is it uses more electrical energy and produces less amount of fresh potable water.

Hence, the solar desalination process would be a better option. It is considered the most compatible solutions to lessen water deficiency problem in remote and arid regions throughout the world especially Middle East, South Asia and North Africa [5]. Solar energy is regarded by most of the famous researchers to be the excellent substitute for a heating energy source because it is environmentally friendly as well as the use of solar energy to heat inlet brackish water complies to preserve fossil fuel energy.

CSS is used for sanctification (eliminating salts and other dissolved minerals) of saltwater for drinking purposes. It comprises of the inclined glass cover, basin, wooden frame, and distillate output collection jar etc. Solar desalination covers 3-4 steps: pumping of brackish water, pumped water pre-treatment (filtration, chemical addition), desalination process and distillate output post-treatment if required (in some cases, adding few minerals, measuring P^H value etc.) [4].

The major defects of the desalination system by solar still is its less productivity and efficiency. Generally, a CSS can supply 2.5–5 liter/m²/day of fresh distillate output [5]. To amplify the solar thermal efficiency of CSS, renowned researchers have carried out a large number of experimental investigations modifying the CSS with various heat storage materials, phase change materials, nanoparticles, wick materials and integrated with solar collector, reflector, solar heater etc.

2. Objectives

1) To design and fabricate a desalination system with a solar heat source which will be cost effective.

2) To enhance the productivity and efficiency of CSS raising the temperature difference between basin water and glass cover surface adding wick materials with inlet brackish water inside the glass cover surface.

* Corresponding author. Tel.: +88-01839459191
E-mail addresses: laxmandas003@gmail.com

3) To compare the efficiency enhancement of modified Solar Still (MSS) with various wick materials with respect to CSS.

3. Basic principles of CSS

CSS uses solar energy to sanctify salt water instead of other heating sources: fossil fuels to achieve the energy required for desalination and works based on two scientific principles:

3.1 Evaporation

Firstly, the brackish water which is to be sanctified is provided inside the solar still basin. Then the solar still is settled upon under the sun which permits the solar still to absorb solar energy by means of solar radiation. When the energy is absorbed remarkably, the water in the basin is heated gradually. As a result, the liquid water is converted into vapor and evaporated towards the glass cover ceiling surface.

3.2 Condensation

This water vapor strikes the ceiling of the glass cover with high vapor pressure and slowly condenses along the glass cover inner surface causing pure water droplets. As the glass cover surface is angled down towards the collecting jar, pure water droplets slide down into the collecting jar. The water droplets collected into the jar are simply sanctified because none of the minerals, bacteria are capable to evaporate with pure water which is now used for drinking and cooking purposes.

4. Factors impacting the productivity of solar still

There are a large number of factors influencing the daily productivity and efficiency of solar still. Amongst them, intensity of solar radiation, wind velocity and ambient air temperature are the meteorological parameters which may not be controlled. The other factors may be controlled to amplify the solar still productivity and solar thermal efficiency. The following several factors which have generally been controlled:

- ❖ The temperature distinction between inclined glass cover surface and basin water
- ❖ Temperature and depth of inlet brackish water
- ❖ The inclination angle of the glass cover surface
- ❖ Thickness of inclined glass cover surface
- ❖ Absorber plate and surface coating etc.

5. Methods used to enhance the productivity and efficiency of CSS

Special design, the addition of various heat energy storage materials (ESM), phase change materials (PCM), fins and corrugated absorber, nanoparticles, usage of various wick materials, vacuum technique and integration of solar reflector, condenser, collector, combined solar still with solar pond and modified stepped solar still can amplify the distillate output and solar thermal efficiency of CSS.

5.1 Wick materials

Inlet water surface exposure area can be enhanced by adding appropriate wick materials inside the solar still

basin. Generally, various wick materials: black cotton cloth (BCC), white sponge sheet (WSS), black sponge sheet (BSS), brown jute sheet (BJS), jute sheet (JS), cotton mate (CM), coconut mate etc. are added with inlet brackish water. The intensity of solar radiation incident on the inclined glass surface is dispatched to the wick material surface. A portion of incident solar energy is used for heating brackish water which is streaming through the wick surface because of capillary action. Hence, the brackish water gets heated and evaporated into vapor rapidly. This saturated vapor starts to condense along the inner surface of inclined glass cover after liberating latent heat of vaporization of water. Then the condensed pure water droplets slide down along the glass surface due to gravity and stored in the collecting jar. There are two heat transfer modes in the solar desalination system: external and internal modes. The external mode takes place outside the solar still due to convection and radiation. Contrariwise, internal mode takes place within the solar still due to radiation, convection, and evaporation. Following are the different notable wick type solar still designs:

- ❖ Basin wick type solar still
- ❖ Multi-wick type solar still
- ❖ Floating wick type solar still
- ❖ Concave wick type solar still etc.



Cotton cloth



Jute sheet



Sponge sheet



Coconut mate



Velvet sheet

Fig.1 Wick materials used with inlet brackish water.

6. Design & fabrication of experimental set-up

6.1 Methodology

The following methodologies were applied during the experimental investigations:

- 1) A simple conventional single slope single basin solar still was designed and fabricated. For three different inlet water depth (1cm, 2cm, 3cm), total fresh distillate output accumulated was measured conventionally. According to the fresh output, optimum water depth (2 cm) had been established.
- 2) The CSS had been modified adding wick materials (heat storage materials) with inlet brackish water.
- 3) Detailed experimental investigations had been conducted to measure the distillate yield of the solar

still for the effect of adding black cotton sheet, jute sheet, black sponge sheet, black velvet sheet and coconut mate respectively. The percentage of productivity enhancement was calculated.

- 4) Finally, the percentage of productivity and solar thermal efficiency enhancement in case of MSS were compared with the CSS at optimum water depth.

6.2 Theoretical approaches

The analysis had been conducted with the following considerations:

- ❖ The CSS was made in such a way that it must be vapor tight.
- ❖ Wick materials, solar still basin wall, and glass cover were at the almost identical temperature.
- ❖ Under almost identical thermal conditions, the solar still with and without wick materials were experimented.
- ❖ The motion of the raised vapor from the evaporating surface to the condensing surface was predominantly under natural convection.

6.3 Experimental set-up

Firstly, the 3D model of the (CSS) was designed using SOLIDWORKS software. The solar still was 30 inches long and 18 inches wide. The glass cover slope angle was 11 degree with horizontal. The height of the solar still was 5.50 inch (front side) and 9.00 inch (back side). To fabricate the desired solar still system, at first the rectangular tray type basin of the solar still having a height of 4 inches was made by using 2 mm galvanized steel sheets welded with 10 number size electrode in which the brackish water was provided. The length of the basin was 29 inch and width was 17 inch. This manufactured basin was contained inside a wooden frame fabricated from our Mechanical workshops. The size of the wooden frame was slightly higher than the solar still basin for smooth operation having 0.5-inch thickness. It had provided sufficient space for adjusting glass cover at the upper surface. A glass plate of 3 mm thickness was used for roofing the top surface of the wooden frame. At the upper back side of the frame, a 0.75-inch hole was shaped at where elbow joint was fixed for supplying brackish water into the solar still basin. And at the front side, a distillate water collection tube (PVC pipe) was adjusted for collecting the condensed distillate water which slide down along the inclined glass surface. This pipe was cut at the inner side as like as U shape with an appropriate dimension. Silicon gum was used for sealing the wooden frame at every corner properly before holding the solar still basin into the wooden frame in order to eliminate the heat and vapor loss and get the maximum possible water vapor. The glass cover was adjusted on the wooden frame and it was also sealed with the pipe using superior silicon sealants completely. The PVC pipe was 34 inches long which was slightly bigger than the wooden frame because a water tap was pro-

vided at one end and the other end of the pipe was sealed. By using a stainless steel scale, the basin was calibrated for the interval of 1 cm from the bottom of the basin up to 5cm.



Fig.2 The fabricated conventional single slope single basin solar still.

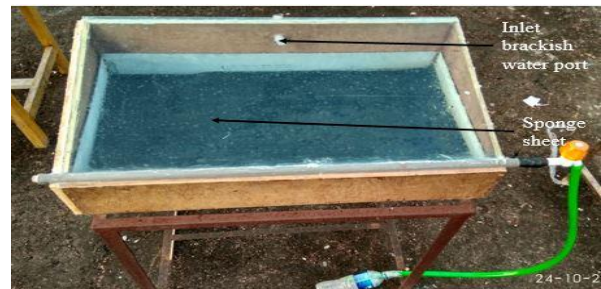


Fig.3 MSS with black sponge sheet.

6.4 Data collection method

Experimental data were taken during the clear sunny days during the month of October at the roof of our Electrical and Mechanical Engineering (EME) building, CUET. The experiment was started at 9:00 am of the local time when brackish water was provided into the solar still basin. At 9:00 am, ambient air and inlet water temperature were measured using a thermometer. Amount of the incident solar intensity on the glass surface was measured using a Daystar meter at the interval of 60 minutes and wind velocity was measured using a digital anemometer. At 10:00 am, the temperature of the basin water and inclined glass cover were measured. As the solar intensity was increasing gradually, the temperature of the basin water and glass cover were enough high. At 11:00 am evaporation and condensation rate was increased gradually and the quantity of distillate water stored in the jar was increased than 10:00 am. At noon, the solar intensity was maximum and the amount of potable water accumulated was high with the time being passed. On the other hand, the solar intensity was reduced gradually at afternoon which reduce the amount of distillate water gradually. In the same manner, the data was collected until 5:00 pm. After 5:00 pm, the heat energy retained by the wick surface was radiated which causes a remarkable evaporation and condensa-

tion rate of brackish water during the night period. The amount of fresh water stored during this session was measured at 8:00 am of the following day. From 8:00 am-9:00 am, the set-up was made ready for the following experimentation. This same procedure was repeated when different wick materials were added with the CSS.

6.5 Addition of wick materials with brackish water

When these enlisted wick materials were entirely dipped under inlet brackish water, other parameters were kept almost identical as that for CSS.

Table 1 Details information of various wick materials.

SI. No.	Various wick materials	Mass Kg	Thickness mm	Specific heat KJ/Kg-K
01	Black cotton cloth	0.2	3	0.8
02	Brown jute sheet	1.5	8	1.4
03	Black sponge sheet	0.15	10	-----
04	Black velvet sheet	0.2	3	-----
05	Coconut mate	2.0	18	0.4

6.6 Governing equation

Solar thermal efficiency, [1]

$$\eta = \frac{\sum m_d \times h_{fg}}{\sum A_{eff} \times I(t)} \times 100\% \quad (1)$$

- ❖ Latent heat of vaporization of water: 2230 KJ/Kg.
- ❖ Net effective area of the solar still basin: 493 inch² = 0.3181 m².
- ❖ Time interval of data entry: 1 hour = 3600 s.
- ❖ Mass of 1 ml of distillate water: 1 gm.
- ❖ Inlet water temperature: 25-27 °C.
- ❖ Atmospheric air temperature: 30-34 °C.
- ❖ Glass cover temperature: 48-55 °C.
- ❖ Basin water temperature: 53-62 °C.
- ❖ Wind velocity: 1.2-1.9 m/s.
- ❖ The intensity of solar radiation during the night period due to radiation: 15 W/m² approx.
- ❖ At 7:00 am, the intensity of solar radiation: 250 W/m² approx.
- ❖ At 8:00 am, the intensity of solar radiation at 8:00 am: 460 W/m² approx.
- ❖ During 5:00 pm-8:00 am, the average intensity of solar radiation per hour: 60 W/m² approx.

Table 2 Comparison of production rate and solar thermal efficiency of CSS for various inlet water depth.

SI. No.	Inlet water depth, cm	The volume of brackish water (approx.), L	Distillate output production rate, ml/day	Solar thermal efficiency, %
01	1	3.0	393	12.05
02	2	6.0	374 (reference)	11.47 (reference)
03	3	9.0	319	9.78

✓ Considering 2 cm as the optimum water depth:

Table 3 Comparison of production rate and solar thermal efficiency for the MSS with various wick materials at 2 cm inlet water depth.

SI. No.	Various wick materials used	Distillate output production rate, ml/day	Increase in production rate, %	Solar thermal efficiency, %	Increase in efficiency, %
01	Cotton cloth	584	56.15	16.04	39.84
02	Jute sheet	539	44.12	14.56	26.94
03	Sponge sheet	498	33.16	14.17	23.54
04	Velvet sheet	436	16.58	12.09	5.41
05	Coconut mate	469	25.40	12.77	11.33

7. Results & Discussion

Fig.4 shows the variation of the intensity of solar radiation with time. The intensity was maximum between 12.00 pm to 2.00 pm and then it dropped significantly in the afternoon.

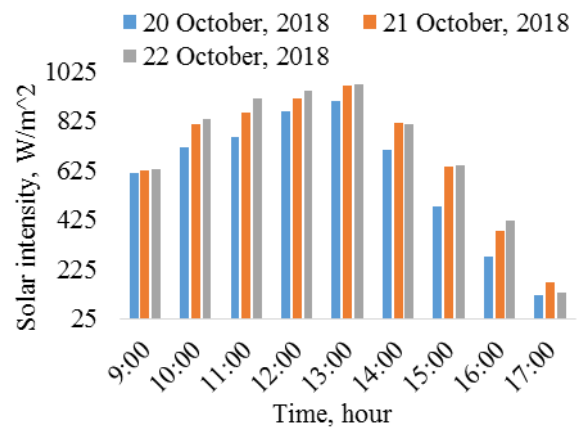


Fig.4 Variation of the intensity of solar radiation during three experimental days with time.

Fig.5 shows the variation of wind velocity during six different experimentation days. There is an inverse relation of wind velocity with the total daily distillate output of the solar still.

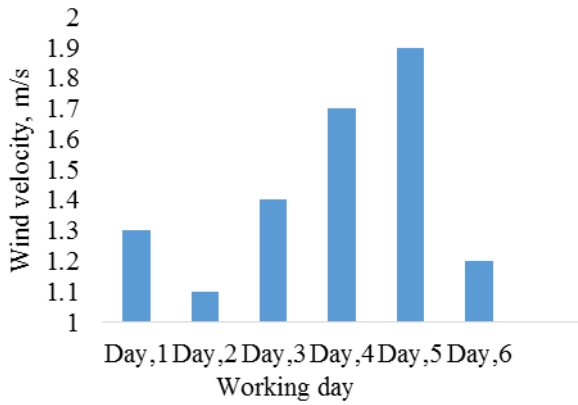


Fig.5 Variation of wind velocity with the working day.

Fig.6 shows the actual hourly variation of fresh distillate output of CSS for three different inlet water depth (1cm, 2cm and 3cm). The maximum was output obtained at 1.00 pm for the three different cases.

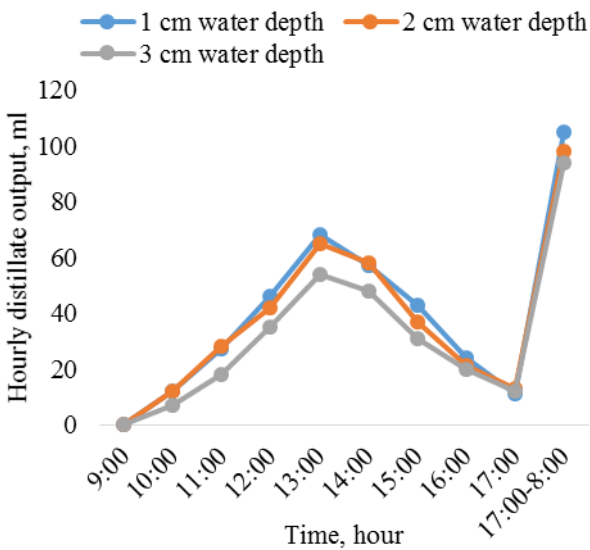


Fig.6 Hourly variation of the fresh distillate output of CSS for different inlet water depth.

Fig.7 shows the actual variation of accumulated fresh distillate output of CSS for different water depth (1cm, 2cm and 3cm). From the output of CSS for different inlet water depth, it was found that 2 cm was the optimum water depth. The amount of accumulated distillate output for 1cm water depth was high because of the high evaporation rate but inlet water had to be provided repeatedly which causes temperature variation with pre-

vious brackish water. On the other hand, the evaporation rate was low because of the deep layer at 3 cm water depth.

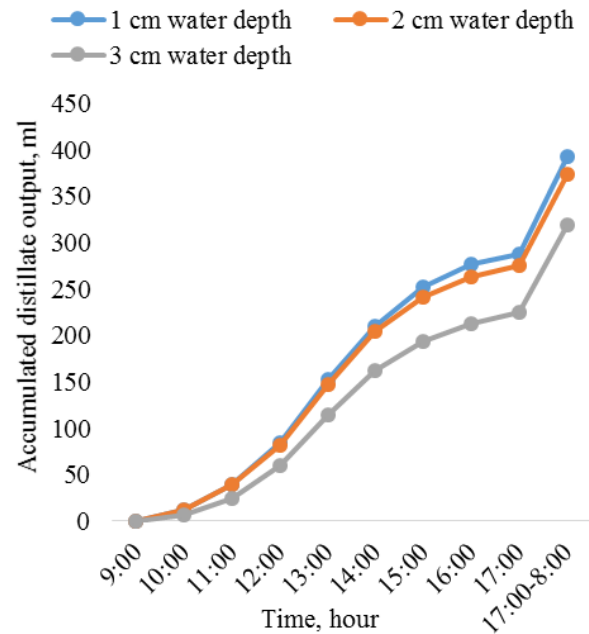


Fig.7 Variation of the accumulated fresh output of CSS for different inlet water depth.

Fig.8 shows the variation of the actual overall distillate output for five different wick materials used inside the solar still basin for modifying the CSS. Among these, the black cotton cloth is more effective than other wick materials followed by the jute sheet, black sponge sheet, coconut mate and black velvet sheet respectively.

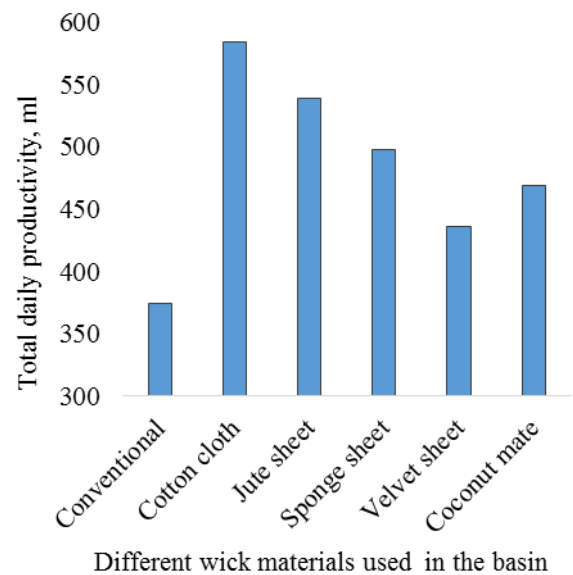


Fig.8 Variation of total daily productivity for various wick materials with CSS (2cm water depth).

Fig.9 shows the actual hourly variation of distillate fresh output for different wick materials used inside the basin. The maximum output was obtained at 1.00 p.m.

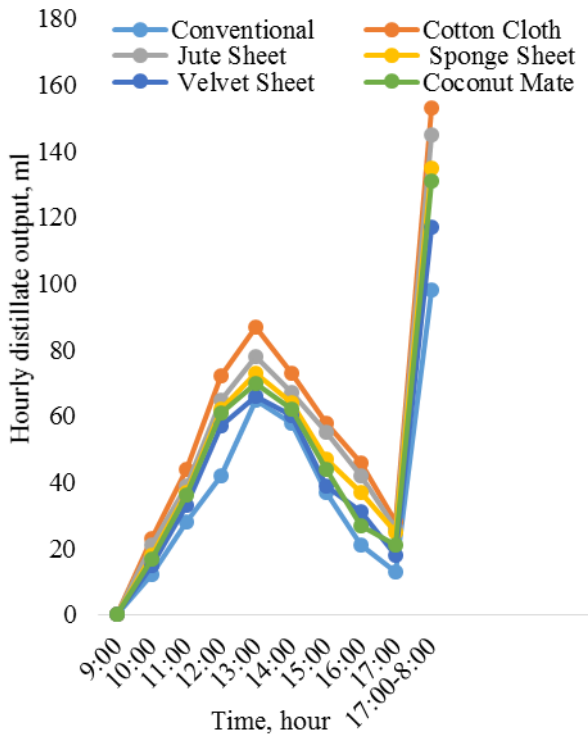


Fig.9 Hourly variation of distillate output for various wick materials with CSS (2cm water depth).

Fig.10 shows the variation of accumulated distillate output for various wick materials. Cotton cloth yielded maximum accumulated output among them.

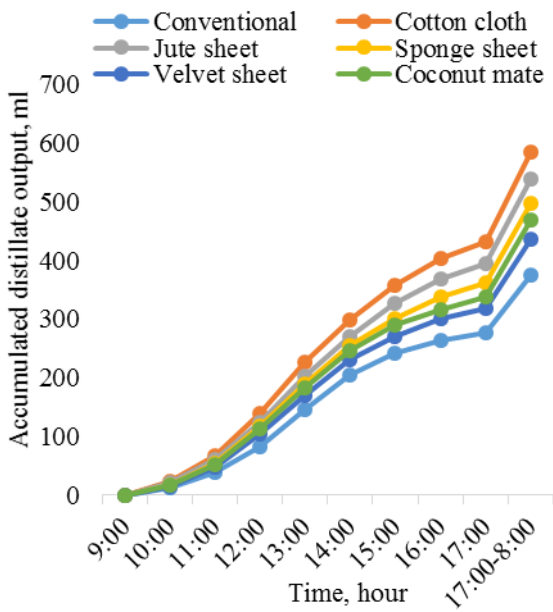


Fig.10 Hourly variation of accumulated distillate output for various wick materials with CSS (2cm water depth).

8. Conclusion

In this present research work, the distillate output production rate and solar thermal efficiency for different water depth were investigated. From the output of this study, 2 cm was considered as the optimum water depth where the distillate output production rate was 373 ml/day and solar thermal efficiency was 11.47% which was considered as the reference. Then the solar still was modified using various wick materials. Among these, the black cotton cloth was the highest efficient produced maximum distillate output per day having 56.15% production rate enhancement followed by the jute sheet 44.12%, black sponge sheet 33.16%, coconut mate 25.40% and black velvet sheet 16.58% respectively with respect to reference production rate.

9. Scope for future work

In this present research work, impure brackish water from the tap was used for experimentation. In the future, it may be possible to produce distillate water from industrial effluents with more modifications such as to use integration method: internal reflector, flat plate collector in the basin along with the energy storage mediums.

NOMENCLATURE

- η : Solar thermal efficiency, %
- m_d : Mass of distillate water, Kg
- h_{fg} : Latent heat of vaporization of water, KJ/Kg
- A_{eff} : Net effective area of the solar still basin, m²
- I : The intensity of solar radiation, W/m²
- t : Time interval of data entry, s
- CSS : Conventional Solar Still
- MSS : Modified Solar Still

REFERENCES

- [1] Sharshir, S.W., Yang, N., Peng, G. and Kabeel, A.E., 2016. Factors affecting solar stills productivity and improvement techniques: a detailed review. *Applied Thermal Engineering*, 100, pp.267-284.
- [2] Haddad, Z., Chaker, A. and Rahmani, A., 2017. Improving the basin type solar still performances using a vertical rotating wick. *Desalination*, 418, pp.71-78.
- [3] Sivakumaran, R., Jidhesh, P. and Scholar, P.G., 2016. Improvement techniques in performance and productivity of solar stills. *International Journal of Engineering Science*, 2441.
- [4] Compain, P., 2012. Solar energy for water desalination. *Procedia Engineering*, 46, pp.220-227.
- [5] Ahmed, H.M., 2016, August. The effects of various types and layouts of wick materials on the thermal performance of conventional solar stills. In *Smart Energy Grid Engineering (SEGE), 2016 IEEE* (pp. 84-89). IEEE.

Nanomembranes for Sustainable Fresh Water Production

Md. Nizam Uddin, Mohammed Alamir, Harish Muppalla, Muhammad Mustafizur Rahman and Ramazan Asmatulu
Department of Mechanical Engineering
Wichita State University, 1845 Fairmount Street, Wichita, Kansas 67260-0133

ABSTRACT

The scarcity of pure drinking water has been one of the major humanitarian challenges in the globe. The world population growth, urbanization, and depleting water resources are deteriorating the water quality and global climate change has also intensified this crisis especially in countries with arid and semi-arid regions. The concern is drastically increasing and therefore scientists and engineers are challenged with urgently developing viable solutions of this problem in the near future. The development of a sustainable, cost-effective, reliable, efficient and stable water collection materials and methods for continuous fresh water production is crucial for many regions of the world. Among many other options, nanoscale membranes seem to be quite attractive and very promising option to solve the global water problem due to their low energy cost and simple operational processes to produce clean water. Most natural sources of water contain high salt concentration and other contaminants. Nanotechnology has played an important role in developing cost-effective and efficient processes for purification and use of this natural water. In addition, water can be efficiently collected from atmospheric fog and filtered using nano-membranes without using any large infrastructure. The nanotechnology-based collection systems are unique because of the fine structures of the nano-membranes with tunable properties. The produced water can be used for drinking, agriculture, gardening, medical, industrial, and other purposes. The present study investigated the availability and practical use of nanomaterials and membranes for the collection and production of pure drinking water from various natural sources. Also, some important recommendations are made based on our research results and current practices of nanotechnology applications in the water industry for pure water production.

Keywords: Nanomaterials, Water Collection, Water Purification, PAN Nanofiber, Graphene, Desalination.

1. Introduction

In recent years, the scarcity of pure drinking water has become one of the major global concern especially for the countries with arid and semi-arid regions. These areas suffer for unusually low rainfalls and therefore some of the animals, plants and human being depend on fog, mist and humid air for the source of water. Around the world, about one billion peoples are suffering from fresh drinking water [1]. Besides, industrial growth, population growth, urbanization, depleting water resources, deforestation, and many other factors ameliorate this issue. Therefore, scientists and engineers are challenged with finding the economically feasible and viable water resources to solve this problem. In some Asian, African and Latin American countries unconventional methods such as rain and groundwater harvesting, cloud seeding, and desalination are already being employed to produce pure water for drinking, agriculture, gardening, medical, industrial, and other purposes [2]. In some parts of Europe and the Middle East, desalination is the only tool for reclaiming fresh water. However, these methods are expensive with high operational cost.

In the Namib Desert, *Stenocara* beetle harvest water directly from the fog, mist, and drops into its mouth. This beetle's carapace has a combination of hydrophilic bumps and a hydrophobic surface that facilitate the water collection from fog [3]. When the fog droplet carried by wind comes in contact with the hydrophilic bumps, it captures the droplet and coalescence while hydrophobic surface drains the water directly to its

mouth. Cribellate spiders use silks with spindle-knots and joints that provide wettability and curvature gradients to collect water from the atmosphere [4]. Besides some plants such as *Cotula fallax*, South Africa has 3D hierarchical structure and hydrophobic surface of its leaves, collect water from the atmosphere. Additionally, Cactaceae species and green bristle grass can effectively capture water from fog [5-6]. In the past decade, extensive research has been done on mimicking the nature to develop cleaner and efficient way for capturing atmospheric water in managing the pure water scarcity issue. For efficient fog harvesting, hydrophobicity and hydrophilicity of the collector materials for fast water capturing and easy drainage properties have a significant effect. Numerous polymeric materials such as polyacrylonitrile (PAN), polyethylene, polypropylene, and stainless steel are used as collector materials. Moreover, superhydrophobic surfaces have other advantages such as self-cleaning, stain-resisting, and drag-reducing and oil spillage separation [7-8].

The wettability of a solid surface is controlled by three factors: their chemical composition, surface geometrical structure, and homogeneity. To fabricate superhydrophobic surfaces, various methods have been proposed, including solution method, sol-gel method, solidification of alkylketene dimer, the plasma fluorination method, chemical etching, chemical vapor deposition, and electrospinning. Among these, electrospinning is the most widely used for fabricating superhydrophobic nano-fibers.

The present study investigated the availability and practical use of nanomaterials and membranes for the collection and production of pure drinking water from various natural sources. The superhydrophilic electrospun polymer nanofibers were fabricated and water collection capacity was measured. Besides, the practical use of superhydrophilic nanofibers for filtration of water from various sources (e.g., surface, groundwater, and industrial water) was investigated in detail. Also, use of graphene thin film for removal of bacteria, viruses, heavy metals and ions, complex organic and inorganic compounds, and other pathogens and pollutants present in various water sources was analyzed.

2. Nanotechnology for Efficient Water Production from Atmosphere

Very few studies focused on the production of pure water from fog using nanotechnology. Almasian et al. [9] fabricated the fluorinated super-hydrophobic PAN nanofibers for investigating their harvesting properties. They synthesized fluoroamine compound to modify the surface properties of PAN nanofibers. The superhydrophobic PAN nanofibers synthesis process was optimized by varying the temperature, time and the amount of fluoroamine compound. The synthesized PAN nanofibers have a water contact angle (WCA) of 159° and low surface energy of 17.1 mN/m . The water collection efficiency of $335 \text{ mg/cm}^2/\text{h}$ was achieved by the fluorinated PAN nanofibers whereas untreated PAN fibers have a capacity of $31 \text{ mg/cm}^2/\text{h}$. Besides the water collection efficiency can be improved by increasing the distance of the nanofibers mat from humidifier and tilting angle because of increasing the water mobility. Wang et al. [10] fabricated cotton fabric with light-induced super-hydrophilic bumps. The superhydrophobic bumps were created by the spray coating of TiO_2 nano-suspension with a unique raised structure as the result of interfacial tension of the TiO_2 nano-suspension. These bumps provide both the wettability gradient and shape gradient ameliorating the water coalescence and water production. Another research group fabricated bioinspired hydrophilic–superhydrophobic patterned hybrid surface that is facile, low cost and easy to operate for efficient fog collection [11]. They placed a superhydrophobic metal-based gauze onto hydrophilic polystyrene by the thermal pressing method. The hybrid surfaces have polystyrene patches within the holes of the metal gauzes. This process offers easy optimization of the collection process by controlling the pattern's dimensions, such as the size of the gauze mesh. The process has the potential for scaling-up because of availability of polystyrene and the metal gauze. The copper gauze was calcined in an oven at 400°C for 3h to form copper oxide nanostructures coating on the surface of the gauze. Then the oxide gauze was treated with 1H, 1H, 2H, 2H perfluorodecanethiol (PFDT, 97%) to convert it to hydrophobic followed by thermal pressing of the modified gauze with polystyrene to form

the hybrid surface with patterned wettability. The fog collection efficiency of about $159 \text{ mg cm}^2 \text{ h}^{-1}$ is achieved by hydrophilic-superhydrophobic patterned hybrid surface. Bai et al. [12] investigated the water collection efficiency of the surfaces having star-shaped wettability patterns. The surface with star-shape wettability patterns integrates both the *surface energy gradient and Laplace pressure gradient* that facilitate quick coalescence of water droplets. This surface is more efficient in terms of water collection than uniform superhydrophilic or uniform superhydrophobic surfaces. Besides, surface with smaller pattern size is more efficient than the larger, having the similar pattern shape because of the Laplace pressure gradient. This result reveals that water collection with pattern surfaces, the pattern shape and size play an important role to improve the water collection efficiency. Lalia et al. [13] fabricated hydrophobic PVDF-HFP nanoweb by electrospinning process and impregnated this nanoweb with lubricants (total quartz oil and Krytox 1506) to investigate the fog collection efficiency. The lubricant impregnated nanomats reduce the contact angle hysteresis and improve the water collection efficiency. In addition, lubricant impregnated nanomats have less drainage of oil from the surface along with shedding water. Table 1 compares the water collection efficiency of nanofibers using various materials.

Table 1 Comparison of fog collection capacity using different collector materials.

Collector Materials	Production Capacity ($\text{mg/cm}^2.\text{h}$)	References
PVDF-HFP nano-webs	110	13
Patterned superhydrophobic Glass	61.8	14
Electrospun PVDF-HFP-FPOSS	81	15
Bioinspired surfaces with star-shaped wettability patterns	278	12
Fluorinated PAN nanofiber	335	8

3. Nano-membranes for Waste Water Treatment and Desalination

Freshwater and energy are fundamental needs for the enhancement of modern human life and civilization. Using an accelerated and cost-effective process for the desalination of seawater can be an encouraging solution to the water problem. In the past, fossil fuels have been used as a dominant source of energy, but their detrimental impact on the environment and increased cost have made renewable energy resources more important. The reverse osmosis is the most widely used

method for water desalination and about half of the world's installed desalination capacity is based on this process. In this process highly pressurized water pass through a semi-permeable membrane which allows the water molecule to pass but not salt ions. However, water transport in this process is slow and fouling is also another issue. Therefore, new membrane materials needed to be developed to solve this issue. Integrating nanotechnology into water treatment and desalination have great potential in this sector. Most of the nano-filter based multifunctional filtration systems do not require large infrastructures or centralized system and can be portable to the remote regions for efficient water treatment.

Graphene was discovered as a single-layer of isolated graphite atoms arranged in 2D hexagonal shape, making it the thinnest and strongest material that is known to date. The graphene thin films have the potential for removal of bacteria, viruses, heavy metals and ions, complex organic and inorganic compounds, and other pathogens and pollutants present in various water sources (e.g., surface, groundwater, and industrial water). The graphene nano-membranes can also be used for desalination of the salt water for continuous fresh water production. The graphene for thin film fabrication can be fabricated by the modified chemical method and the synthesis process as described elsewhere [16-17]. The vacuum filtration is the facile method for the fabrication of graphene thin film from aqueous graphene oxide (GO) dispersions through a filter membrane and then drying and peeling it off from the filter paper [18-19]. By controlling the volume of aqueous graphene, the thickness of the film can be controlled. The facile synthesis of GO thin film opens up the door for an ideal next-generation membrane as the cost-effective, mechanically robust and sustainable alternative for water purification and desalination. Joshi et al. [20] investigated the permeation phenomena of GO thin film prepared by vacuum filtration method. The GO thin film is vacuum tight when it is dry but act as a molecular sieve at wet state. It blocks all solutes having a radius larger than 4.5 angstrom. However, comparatively smaller ions permeate through the GO thin film at a faster rate. The single layer GO is a porous sheet-like material and when it forms a thin film, a network of nano-porous structure forms. At hydrated state, these nano-capillaries open up and pass the species that fit in. Wang et al. [21] studied the water transport phenomenon of functionalized GO thin film by molecular dynamics simulation. Their simulation results reveal that transport of water up to 66 L/cm²/day/MPa with greater than 99% salt rejection can be achieved by using nano-porous graphene membrane whereas the conventional osmosis process can transport only 0.01–0.05 L/cm²/day/MPa with similar salt rejection. Comparing to the commercialized membranes, the graphene nano-porous membranes offer 2–3 orders of magnitude higher salt rejection and water permeability. The fast transport of water molecules through the graphene sheets are attributed by the atomic

thickness of the graphene sheets. They also find that if the graphene nano-pores are chemically functionalized with hydrogen, it can better reject the salts ions but lower the flow rate. These results showed that graphene nano-membrane has the potential to be used for high-permeability desalination membrane. The water permeability of polyimide/GO thin film was also investigated [22]. The polyimide/GO thin film has a multilayer structure with an interlayer spacing of around 0.83 nm. The concentration of GO is 0 to 0.02 wt. % and increasing GO ameliorate the hydrophilicity of the film. In addition, the permeate water flux under 300 psi increased from 39.0 ± 1.6 to 59.4 ± 0.4 L/m² h, while rejections of NaCl and Na₂SO₄ decreased only slightly from 95.7 ± 0.6% to 93.8 ± 0.6% and 98.1 ± 0.4% to 97.3 ± 0.3%, respectively. The interlayer spacing of GO nano-sheets served as a water channel and greatly influence the water permeability.

4.0 Super-Hydrophilic Nanofibers for Fog Collection

4.1 Fabrication of Super-Hydrophilic Nanofibers

Polyacrylonitrile (PAN) and Polyvinylchloride (PVC) nanofibers were fabricated by the electrospinning process. In a typical fabrication process, the PAN and PVC powders were separately mixed with Poly vinylpyrrolidone (PVP), Polyethylene glycol (PEG), and chitosan (0, 4, 8, 16, and 32 wt %) and dissolved in dimethylformamide (DMF). The solution was then stirred at 300 rpm for 30 minutes at 70°C. Then the polymeric solutions were electro-spun with a DC voltage of 25 kV, a feed rate of 3 mL/hr, and a spinneret-to-collector distance of 25 cm. All experiments were conducted at room temperature under ambient conditions.

4.2 Morphology, WCA and Fog Collection Efficiency of Super-Hydrophilic Nanofibers

A scanning electron microscope (FEI Nova Nano SEM 450) was used to study the morphology of the fabricated PAN and PVC electro-spun nanofibers. Fig. 1 presents the SEM images of PAN nanofibers with different inclusions. The average diameter of the fiber without any inclusions are approximately 450 nm and the surface of the fibers are smooth (Fig. 1a). However adding inclusions produce small asperities and bumps, which may affect the surface hydrophobicity of the nanofiber mats (Fig. 1 b, c, d).

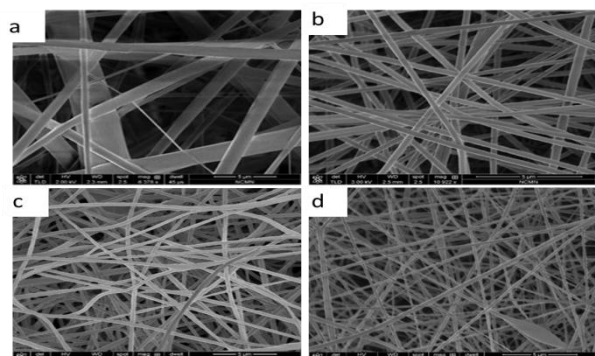


Fig. 1 SEM photographs of PAN nanofibers (a) no inclusion; (b) 16 wt% PVP; (c) 16 wt% PEG and (d) 16 wt% chitosan [23].

The WCA of the fabricated nanofibers were measured by a water contact angle goniometer (KSV Instruments Ltd., Model #CAM 100). The inclusions PVP, PEG, and chitosan were used in this study because of their hydrophilic nature and higher dissolution rate in most solvents. The WCA of the PAN and PVC nanofibers with various inclusions are summarized in Table 2 [23]. As can be seen, without any inclusions the PAN and PVC nanofibers exhibit a WCA of 14° and 22° respectively. However, incorporation of various inclusions especially 16, and 32 wt% of PVP, PEG and chitosan drastically reduced the WCA, making super-hydrophilic nanofibers which is a suitable material for fog harvesting from the atmosphere.

Table 2 WCA of nanofibers with various inclusions.

	Nano fibers	Inclusion	Inclusion wt (%)				
			0	4	8	16	32
WCA (°)	PAN	PVP	14	11	4	<5°	<5°
		PEG	14	13	8	<5°	<5°
		Chitosan	14	12	6	<5°	<5°
	PVC	PVP	22	13	7	<5°	<5°
		PEG	22	16	8	5	<5°
		Chitosan	22	16	9	5	<5°

The WCA of PAN fibers incorporated with 16wt % of PVP at 0 and 2 seconds interval is presented in Fig. 2. It was difficult to monitor the WCA of the hydrophilic nanofibers and especially the super-hydrophilic nanofibers. Within 2 seconds, the water bubble flattened on the nanofiber surface and was absorbed completely by the nanofibers mats. Most of the fibers showed water contact angles below 5° within a few seconds.

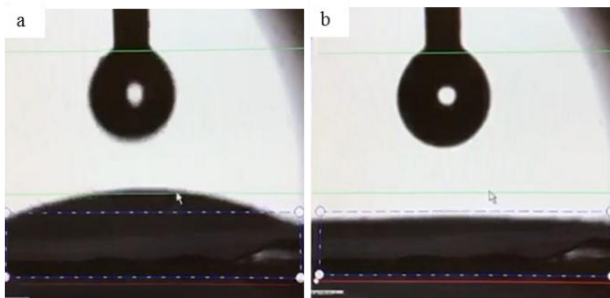


Fig. 2 WCA of PAN fibers incorporated with 16 wt% PVP at (a) 0 second, and (b) 2-second interval.

The fog harvesting capacity of the PAN and PVC nanofibers was evaluated by the humidifier unit (Vicks Warm Steam Vaporizer Humidifier). The humidifier produces fog at different rates based on the

requirements. The nanofibers were placed 15 cm away from the top of the humidifier to capture, and the experiment was carried out for 60–130 minutes. The 4×4 cm nanofibers were used to measure the harvesting capacity. Fig. 3 depicted the harvesting capacity of PAN nanofibers with 16wt % PVP. The weight of the dry PAN nanofibers (without inclusion) that placed in the test chamber was 2.7 gm and after 110 minutes of moisture absorption, the weight increased to 3.21 gm corresponding to 18% moisture/fog absorption. Moreover PAN with 16 wt% PVP nanofibers, the moisture absorption increased considerably for the first 70 minutes and then slowed down (Fig. 3b). The weight of the dry sample was 2.50 gm and after 110 minutes of moisture absorption, the weight of the specimen was 3.96 gm, corresponding to a 57.6% moisture absorption. However, PVC nanofibers without any inclusions exhibit 20% moisture absorption and the fibers with 16 wt% PVP have 33.8%. These results reveal that surface hydrophilicity significantly affect the fog harvesting capacity of the nanofibers. It was observed that nanofibers were soaked with considerable moisture from the humidifier, form droplet and filled the pores of the nanofiber and finally due to gravity, the water droplet drained off.

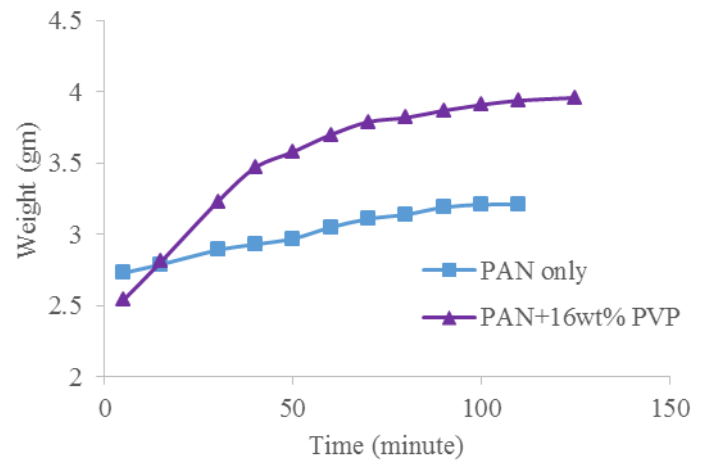


Fig. 3 Fog harvesting capacity of electro-spun nanofibers (a) PAN only and (b) PAN with 16wt % PVP [23].

5. Nanofibers for Water Filtration

5.1 Fabrication of Electro-spun Nanofibers

PVC with various proportion (2, 3, 4, and 5 wt %) of PVP inclusion nanofibers were fabricated by electrospinning process to filter the micro and nano-size particles from water. The fabrication process includes dissolving PVC into dimethyl acetamide (DMA_C) by stirring at 65°C for four hours. Now the electrospinning of the prepared solution was conducted similarly as explain before. The WCA of the fabricated nanofibers were measured and observed that all the nanofibers studied here exhibit hydrophilic nature (WCA less than

90°). In order to overcome the fouling property of the membrane, coagulation is used as a pre-treatment process, which enhances the efficiency of the nanofibers for the removal of colloids. Two coagulants namely Tanfloc and Alum were used in this study. Then the water samples from three different sources (lake water, industrial jet water, and magnetite nanoparticles solution) were collected and the required amount of coagulants were added into the water and allowed for 24 hours for sedimentation. Therefore, the fabricated nanofibers were used to filter the water samples. The filtration capacity was measured in terms of turbidity, pH and total dissolved solid (TDS).

5.2 Turbidity, pH and TDS of Water Samples

The Tanfloc and Alum coagulated water samples from different sources were filtered using PVC nanofibers incorporated with PVP and data were recorded. Table 3 summarizes the characteristics of filtered lake water using PVC nanofibers [24]. The optimum coagulant dosage for Tanfloc and Alum is 15mg/L and 50mg/L respectively. It was observed that turbidity reduction is very effective in coagulation/filtration process when compared with the direct membrane filtration process. The turbidity of lake water samples before filtration is 21

Coagulant		Optimum Coagulant: Tanfloc- 15mg/L Alum- 50mg/L	Coagulation/ Filtration	Direct Membrane-Filtration (Before filtration/after filtration)
Tanfloc	Turbidity	1 NTU	0.20 NTU	21 NTU/0.49 NTU
	pH	8.09	8.09	8.14/8.14
	TDS	460ppm	450ppm	460ppm/440ppm
Alum	Turbidity	1.92 NTU	0.30 NTU	21 NTU/0.49 NTU
	pH	7.49	7.49	8.14
	TDS	472ppm	447ppm	460ppm/440ppm

Nephelometric Turbidity Units (NTU). However, using Tanfloc coagulant, the turbidity drops to 0.2 NTU. Moreover, Alum also reduces the turbidity of lake water samples. Besides the TDS values also reduced significantly using nanofibers as filter membranes. In addition, the pH of filtered lake water drops using both coagulants when compared to as received water samples.

Table 3 Characteristics of lake water samples before and after filtration.

The similar investigation was conducted for industrial jet water and magnetic nanoparticles solution samples using both types of coagulants. The turbidity, pH, and TDS of the water samples were measured before and

after filtration. Fig. 4 illustrated the residual turbidity of filtered water samples using both types of coagulant. From Fig. 4, it's seen that coagulation-filtration is the most effective way to reduce the turbidity of the water. For industrial jet water samples, the optimum coagulant dosage for Tanfloc and Alum is 25mg/L and 50mg/L respectively. Before filtration, the turbidity was approximately 32 NTU, which was reduced to 2.9 NTU using Tanfloc coagulation-filtration process. Moreover, Alum coagulant added filtered water samples also exhibit a reduction of water characteristics using nanofiber as a filter membrane. The filtered magnetic nanoparticles solution samples using both types of coagulants also reveal that PVC with PVP inclusion nanofibers are very effective to filter the magnetic nanoparticles solution.

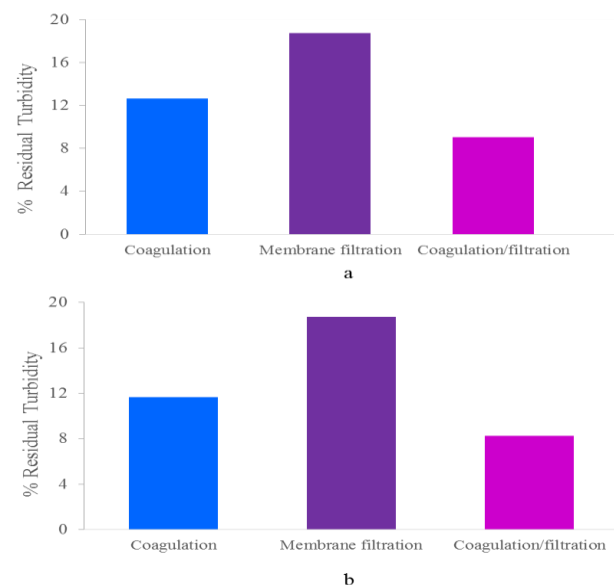


Fig. 4 The residual turbidity of filtered water using (a) Tanfloc and (b) Alum coagulant (Samples-Industrial jet water) [24].

4. Conclusions

Super-hydrophobic/super-hydrophilic nanofibers could be a potential solution to address the water scarcity crisis in the desert regions of the globe. Incorporation of hydrophilic polymer (PVP, PEG, chitosan) into PAN and PVC nanofibers ameliorate the fog harvesting capacity. The moisture absorption of about 58% was achieved by PVP treated superhydrophilic PAN nanofibers whereas untreated PAN nanofibers exhibit about 18% moisture absorption. Besides, superhydrophilic electrospun nanofibers have the potential to filter water. The coagulation and filtration by the superhydrophilic nanofibers is an effective way to filter the water.

REFERENCES

- [1] K. Onda, J. LoBuglio, and J. Bartram, Global access to safe water: Accounting for water quality and the resulting impact on MDG Progress, *International Journal of Environmental Research and Public Health*, Vol. 9, pp 880–894 (2012).
- [2] J. M. Kahinda, E.S.B. Lillie, A. E. Taigbenu, M. Taute, R.J. Boroto, Developing suitability maps for rainwater harvesting in South Africa, *Physics and Chemistry of the Earth*, Vol. 33, pp 788–799 (2008).
- [3] A. R. Parker, C. R. Lawrence, Water capture by a desert beetle, *Nature*, Vol. 414, pp 33–34 (2001).
- [4] Y. M. Zheng, H. Bai, Z.B. Huang, X. L. Tian, F. Q. Nie, Y. Zhao, J. Zhai, L. Jiang, Directional water collection on wetted spider silk, *Nature*, Vol. 463, pp 640–643 (2010).
- [5] H. G. Andrews, E.A. Eccles, W.C. E. Schofield, J. P. S Badyal, Three-Dimensional Hierarchical Structures for Fog Harvesting, *Langmuir*, Vol. 27, pp 3798–3802 (2011)
- [6] J. Ju, H. Bai, Y. M. Zheng, T. Y. Zhao, R.C. Fang, L. A. Jiang, Multi-structural and multi-functional integrated fog collection system in cactus, *Nature Communication*, Vol. 3, pp 1247 (2012).
- [7] A. Khadak, M. N. Uddin, M.M. Rahman, and R. Asmatulu, Enhancing the De-icing Capabilities of Carbon Fiber-reinforced Composite Aircraft via Super-hydrophobic Coatings, The Composites and Advanced Materials Expo (CAMX), October 16–18, Dallas, TX, (2018).
- [8] M. Salahuddin, M. N. Uddin, G. Hwang, R. Asmatulu, Super hydrophobic PAN Nanofibers for Gas Diffusion Layers of Proton Exchange Membrane Fuel Cells for Cathodic Water Management, *International Journal of Hydrogen Energy*, Vol. 43(25), pp 11530–11538 (2018).
- [9] A. Almasian, G. C. Fard, M. Mirjalili, M. P. Gashfi, Fluorinated-PAN nanofibers: Preparation, optimization, characterization and fog harvesting property, *Journal of Industrial and Engineering Chemistry*, Vol. 62, pp 146–155 (2018).
- [10] Y. Wang, X. Wang, C. Lai, H. Hu, Y. Kong, B. Fei, J. H. Xin, Biomimetic Water-Collecting Fabric with Light-Induced Superhydrophilic Bumps. *ACS Applied Material & Interfaces*, Vol. 8(5), pp 2950–2960 (2016)
- [11] Y. Wang, L. Zhang, J. Wu, M. N. Hedhilib, P. Wang, A facile strategy for the fabrication of a bioinspired hydrophilic-super hydrophobic patterned surface for highly efficient fog-harvesting, *Journal of Materials Chemistry A*, Vol. 3, pp 18963–18969 (2015).
- [12] H. Bai, L. Wang, J. Ju, R. Sun, Y. Zheng, L. Jiang, Efficient Water Collection on Integrative Bioinspired Surfaces with Star-Shaped Wettability Patterns. *Advanced Materials*, Vol. 26, pp 5025–5030 (2014).
- [13] B.S. Lalia, S. Anand, K.K. Varanasi, and R. R Hashaikheh, Fog-harvesting potential of lubricant-impregnated electrospun nanomats. *Langmuir*, Vol. 29, pp 13081–88 (2013).
- [14] L. Zhang, J. Wu, N. M. Hedhili, X. Yang, and P. Wang, Inkjet printing for direct micropatterning of a superhydrophobic surface: toward biomimetic fog harvesting surfaces, *Journal of Materials Chemistry A*, Vol. 3, pp 2844–2852 (2015).
- [15] V.A. Ganesh, A.S. Ranganath, A. Baji, H.K Raut, R.S. Ramakrishna, Hierarchical Structured Electrospun Nanofibers for Improved Fog Harvesting Applications, *Macromolecular Materials And Engineering*, Vol. 302, 1600387 (2017).
- [16] M.S. A. Bhuyan, M.N. Uddin, F.A. Bipasha, S.S. Hossain, Synthesis of Graphene, *International Nano Letters*, Vol. 6, pp 65–83 (2016).
- [17] M.S.A. Bhuyan, M.N. Uddin, F.A. Bipasha, M. M. Islam, and S.S. Hossain, A Review of Functionalized Graphene, properties and its applications, *International Journal of Innovation and Scientific Research*, Vol. 17(2), pp 303–315 (2015).
- [18] M.N. Uddin, and J.K. Kim, Fracture Properties of Graphene Oxide (GO) and GO/CNT Hybrid papers, International Conference on Mechanical, Industrial and Energy Engineering, Khulna, Bangladesh, 26–27 December, (2014).
- [19] M.N. Uddin, Z.D. Huang, Y.W. Mai, J.K. Kim, Tensile and tearing fracture properties of graphene oxide papers intercalated with carbon nanotubes, *Carbon*, Vol. 77, pp 481–491 (2014).
- [20] R.K. Joshi, P. Carbone, F.C. Wang, V.G. Kravets, Y. Su, H.A. Wu, A.K. Geim, R.R. Nair, Precise and Ultrafast Molecular Sieving Through Graphene Oxide Membranes, *Science*, Vol. 343, pp 752–754 (2014).
- [21] E. N. Wang, R. Karnik, Water Desalination: Graphene cleans up water, *Nature Nanotechnology*, Vol. 7, pp 552–554 (2012).
- [22] J. Yin, G. Zhu, B. Deng, Graphene oxide (GO) enhanced polyamide (PA) thin-film nanocomposite (TFN) membrane for water purification, *Desalination*, Vol. 379, pp 93–101 (2016).
- [23] M. A. Alamir, “Designing and Evaluating of Superhydrophilic Nanofiber Mats for Fog Catching in the Atmosphere,” M.S. Thesis, Wichita State University, December 11, 2017.
- [24] H. Muppalla, “Highly Hydrophilic Electrospun Fibers for the Filtration of Micro and Nanosize Particles Treated with Coagulants,” M.S. Thesis, Wichita State University, December 2011.

Aerodynamics and Hydrodynamics in Sports

Firoz Alam^{1,*}, Harun Chowdhury¹, Hazim Moria²

¹School of Aerospace, Mechanical and Manufacturing Engineering, RMIT University, Melbourne, VIC 3083, AUSTRALIA

²Department of Mechanical Engineering Technology, Yanbu Industrial College, Yanbu, SAUDI ARABIA

ABSTRACT

Aero/hydrodynamics plays a vital role in speed sports (athletes, athletes' outfits, sports balls, sports equipment, etc.). Sports balls (spherical - golf, cricket, tennis, soccer, baseball, softball, etc. and oval shape - rugby, American football, Australian football), sports garments (swimsuits, ski jumping & alpine skiing suits, cycling skin suits, skating suits) are affected by aerodynamic and hydrodynamic behaviour of fluids (air and liquids). The aero/hydrodynamics dictates the curved flight path of a soccer, tennis, cricket, baseball or golf ball and the course of a surfboard and sailboat through water. It affects speed, motion (position and placement) and ultimately athlete's performance. Ignoring the effect of aerodynamic and hydrodynamics, it is almost impossible to achieve the desired success in any competitive speed sports. Due to stiff competition, the outcome of most sports aero/hydrodynamics research work undertaken by commercial organisations as well as individual sports teams/organisations are kept in-house and scant information is available in the public domain. The RMIT University's Sports Aerodynamics Research Group has been active in aerodynamics and hydrodynamics research related to some popular speed sports. This paper highlights some research work on sports aerodynamics and hydrodynamics undertaken at RMIT University.

Keywords: Sports aerodynamics, cycling, ski jumping, swimming

1. Introduction

Aerodynamics and hydrodynamics have a major impact on speed sports (ski jumping, alpine skiing, cycling, bobsleighting, javelin, discus, speed skating, sprint, etc.), ball sports (soccer, tennis, cricket, golf, baseball, softball, rugby, Australian rules football, American football) and projectile sport (badminton), equipment and ultimately athlete's performance [1-8]. The pattern design of dimples on a golf ball, engineered outfits (swimming, cycling, skiing, speed skating, etc.), smart designs of racing helmets, the curved flight path of soccer, cricket, tennis, baseball, rugby, American football; and Australian rules football- have significant effect on athlete's motion (position and placement) and performance [1, 2-5,22-23]. The winning time margin in all speed sports is progressively being reduced with the better integration of aerodynamic understanding, advanced technologies and athlete training regimes. Scope for further improvement clearly lies with the in-depth understanding of aero/hydrodynamic behaviour of athletes' sports equipment, physical body posture and their outfits. In most water sports (swimming, rowing, sailing, water skiing, and powerboats), the equipment or the athlete is affected by the dual fluid medium of both water and air simultaneously [5,8-16].

The forces such as aerodynamic drag, lift/down force, side force, buoyancy acting on athletes and their equipment and outfits are highly dependent on speeds, shape, position, flow types (laminar or turbulent regimes) and sports gears' surface morphology. The Sports Aerodynamics Research Group at RMIT University is well known for its wide range of aero/hydrodynamics research on spherical and oval shape sports balls, winter sports (ski jumping, downhill/alpine skiing, bobsleigh,

speed skating), summer sports (cycling, sprint), water sport (swimming), sports garments (athlete's outfits), aerodynamics and thermal comfort of racing and recreational helmets as well as projectile (badminton shuttlecock). Due to current limitation of Computational Fluid Dynamics (CFD) modelling, experimental (wind tunnel and field trial) studies are still the main tools used to enhance scientific understanding on aero/hydrodynamic behaviour. In this paper, special focus is made on aerodynamic behaviour of soccer ball, cycling, ski jumping, and sports garments that are widely used in speed sports.

2. Football (Soccer Ball)

The centre piece of world's most popular game football (soccer) is the spherical ball. The growing popularity and financial strength of the game have driven a number of technological changes to the ball. The FIFA World Cup has become a launching pad for a new ball in every four years. The ball has undergone through incredible changes since 2002. The advancement of technology, popularity and economic interest have made possible to introduce new changes on the ball design. An epoch-making design change of Adidas made FIFA World Cup football is illustrated in Fig. 1 since 2002.



Fig. 1 Transformation of FIFA World Cup balls from 2002 to 2018.

All FIFA World Cup balls were made of 32 panels (20 panels-hexagonal & 12 panels-pentagonal) from 1970 to 2002. A significant deviation from the traditional leather

* Corresponding author. Tel.: +61 3 99256103

E-mail addresses: firoz.alam@rmit.edu.au

made panel to the synthetic panel was introduced by Adidas for the FIFA 2002 World Cup ball. However, Adidas introduced more radical design change in its 14-panels Teamgeist ball in FIFA 2006 World Cup. The smooth synthetic panels were bonded together instead of stitching. The 8-panels 'Jabulani' ball along with its asymmetrical orientation and pattern of grooves was introduced in 2010 FIFA World Cup by Adidas. The Jabulani ball drew huge criticisms and comments from players and experts alike for its erratic flight behaviour. In 2014 FIFA World Cup, Adidas unveiled a 6-panels Brazuca (meaning Brazilian way of life) ball which aerodynamically behaved better than Jabulani ball. Adidas has introduced a designed 'Telstar 18' ball in 2018 FIFA World Cup. The outer skeleton of Telstar 18 ball is made of 6 synthetic panels as Brazuca ball but with different panel shape.

Is Telstar 18 aerodynamically better than Brazuca? Can player predict its anticipated flight trajectory? To answer these questions, the Sports Aerodynamics Research Group at RMIT University undertook an aerodynamic study of Telstar 18 ball along with Brazuca, Jabulani, Teamgeist and Fevernova balls using RMIT Industrial Wind Tunnel. A Telstar 18 ball and RMIT Wind Tunnel are shown in Fig. 2. The study showed that the variation of drag coefficient (an indicator of aerodynamic efficiency, lower the coefficient, better the aerodynamic efficiency) between the two sides of Telstar 18 ball is less than 2% compared to Brazuca (3%), Jabulani (9%), Teamgeist (5%) and Fevernova (2%). The Telstar 18's sideway aerodynamic behaviour is very close to Fevernova ball used in FIFA 2002 World Cup in Korea and Japan. Therefore, Telstar 18 is expected to have more predictable flight in calm wind and non-spinning conditions than its predecessors Brazuca, Jabulani and Teamgeist balls.

For short pass, the Telstar 18 needs harder kick as its aerodynamic drag is higher at low speeds (below 60 km/h) than Brazuca ball. For mid-range distance, the Telstar 18 needs to be kicked softer (60 to 90 km/h range) due to its lower drag. However, for long distance, the ball requires slightly greater force-kick than Brazuca ball.

For goalkeeper, Telstar 18 will be slightly hard to grip compared to Brazuca ball due to its orderly square flat pimples in contrast to Brazuca's prominent wavy patterned rectangular pimples. Telstar 18 has longer seam length (~4.2 m) and shorter seam depth and width than Brazuca ball.



Fig. 2 Telstar 18 ball and RMIT Industrial Wind Tunnel

3. Ski Jumping and Cycling

Ski-jumping is one of the most complex acrobatic winter sports. In ski jumping, skiers go down a hill with a take-off ramp with a view to travel as far as possible. Points are allocated predominantly for the length; however, some points are also allocated for style on a scale from 1 to 20 skipping the highest and the lowest marks allocated by the judges. The skis used for ski jumping are wide and long, with parallel sides. Ski jumping consists of four main phases: a) In-run, b) Take-off, c) In-flight, and d) Landing. During the in-run and take-off phases ski-jumper tries to reach maximum velocity. In the flight phase, the ski-jumper wishes to keep favourable body position in relation to wind direction to maximise the lift and minimise the drag to achieve the maximum jump distance possible. In landing phase, the aerodynamic drag needs to be maximised and lift to be minimised in order to achieve the maximum range, safe and artistic landing. It is no doubt that several factors including the initial ski jumper's body position and its changes at the transition to the flight phase, the magnitude and the direction of the velocity, the jumper's centre of mass, the magnitude of the aerodynamic drag and lift forces determine the trajectory of the ski jumper hence the total distance of

the jump. Using the modern V-technique to maximise lift and minimise drag, pioneered by Jan Boklöv of Sweden, elite level skiers can exceed the distance of the take-off hill by about 10 percent compared to the previous technique with parallel skis. Athlete's outfits and geometric dimensions of ski are highly regulated by FIS (an International ski regulatory body). Within the regulations, there are still scopes to enhance ski jumper's performance further. The ski jump length greatly depends on the in-run velocity, the velocity perpendicular to the ramp due to the athlete's jumping force, the lift and drag forces acting during the take-off and in flight, and the masses of the athlete and his/her equipment (eg, ski, helmet, goggles, suit, hand gloves, boots etc). The aerodynamic forces experienced by the skier directly depends on the projected frontal area of the athlete's body, body position in flight, equipment and their positions and features.

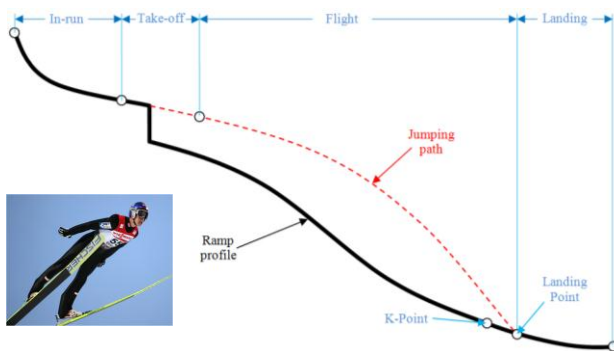


Fig. 3 Different phases of ski jumping [11-12].

A series of studies has been undertaken by Mueller et al. [23-24] and Seo et al. [21] predominantly looked at the biomechanical, body orientation and equipment of the ski jumper on aerodynamic effects using simulation, wind tunnel and in-situ measurements. It is beyond doubt that these aspects are important to understand the flight trajectory of the athlete. A close look indicated that an aerodynamically smart ski jumper's suit can provide some aerodynamic advantages. Despite having potential, the effects of ski garments on aerodynamic performance of the athlete have not been well studied and/or understood. Since 2008, a large research program on textile aerodynamics has been undertaken at RMIT University. As part of this research program, Chowdhury et al. [9-12] undertook a series of studies on aerodynamic performance of sports textiles widely used in ski jumping and cycling suits. Figure 3 shows the four phases of ski jumping. In these studies, Chowdhury et al. demonstrated that an engineered ski jumping suits can minimise aerodynamic drag and maximise lift thereby enhancing a considerable jumping length.

Over the last 50 years a number of publications have been reported in the public domain on cycling aerodynamics primarily focusing on athlete's physiological aspects and cycling accessories. Several studies (see Kyle et al. [17], Chowdhury et al. [9-11]) were conducted on the cyclist body configuration. On

the other hand, studies by Kyle et al. [17], Brownlie et al. [20], and more recently by Chowdhury et al. [10-11] indicate that the sports apparel can make impact on the aerodynamic drag reduction.

In cycling, in addition to cyclist, a bicycle is comprised of the frame, forks, wheels, drive train, brakes, handlebars, water bottles, etc. that interact with the oncoming airflow. The bicycle accounts around 31% to 39% of the total aerodynamic resistance (drag) depending on the bicycle type [9-12, 20] and a small contribution comes from various add-ons such as cycling suit, helmet and so on. Prior studies [10-11] reported that the cyclist body position along with a helmet and suit can significantly minimize aerodynamic drag experienced by the cyclist at all stages of racing (road racing and time trial). There are three main positions commonly used by professional cyclists depending on the type of race and profile of the terrain. These positions are: a) Upright Posture, characterized by the hands on the upper part of the handlebars, is mainly used when pulling up on the handlebars to ride in hill terrain (see Fig. 4a), b) Dropped Posture, the hands on the bottom of the handlebars, is adopted at high speed to minimize projected frontal area (see Fig. 4b) and c) Time Trial Posture, when the elbows are placed on the pads of the aero-handlebars, is believed to be the best aerodynamic position to overcome the aerodynamic drag (see Fig. 4c).

Table 1 shows the average speed of various stages of 2010 Tour de France cycling racing. The average speed (of all 21 stages) was around 42 km/h. However, the speed in the Time Trial stage is over 55 km/h. Although the average speed in mountain stages is slightly below 40 km/h, the maximum speed in downhill stages can easily exceed to 100 km/h.

Table 1 Data from Tour de France 2010

Stage Type	No. of Stages	Average Speed (km/h)
Individual time trial	2	52.30
Flat stage	11	42.37
Medium mountain stage	2	36.16
Mountain stage	6	37.11
Total	21	41.98

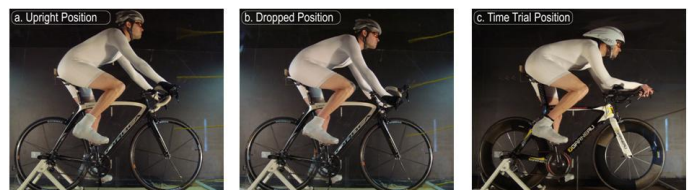


Fig. 4 Three popular cycling positions in RMIT Industrial Wind Tunnel [11]

Figure 5 illustrates the C_D values for the positions of recreational/non-professional bicyclist and professional bicyclist. The figure shows that C_D values are almost independent of speeds for the upright and dropped positions of the professional and the recreational

cyclists at all speeds (20-70 km/h). A slight variation in C_D value at low speeds for the time trial position is evident. A minor difference of C_D value between the upright and drop position of the professional cyclist is also noted. It is clearly evident that the upright position generates more drag compared to other widely used positions especially the time trial positions. As expected, the C_D value for the upright position of the recreational cyclist is notably higher compared to the same position of the professional cyclist primarily due to the cycling accessories (bicycle, suit, helmet, shoes, etc.) and the casual posture. The average reduction of drag for upright, dropped and time trial position of the professional cyclist was found to be approximately 30%, 32% and 45% compared to the upright position of the recreational cyclist respectively. In the case of the professional cyclist, the average reduction of drag for dropped and time trial positions is around 3% and 21% respectively compared to the upright position.

Additionally, studies by Alam et al. [1,3-5] looked at the aerodynamics and thermal comfort of different bicycle helmets. The study by Alam et al. [5] showed that the helmet can produce up to 8% of the total aerodynamic drag depending on the shape and venting features of the helmet. Complex flow pattern around two racing helmets are shown in Fig. 6.

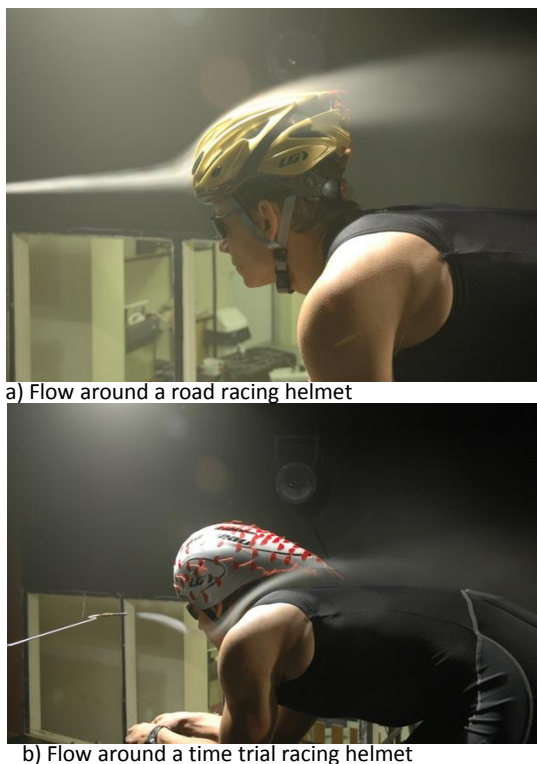


Fig. 6 Complex flow pattern around racing helmets.

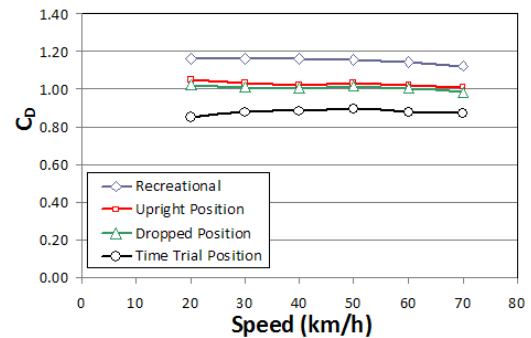


Fig. 5 Drag coefficient as a function of speed (for cyclist and the bicycle in different cycling positions) [11-12]

4. Sports Garments (Outfits)

As mentioned earlier, aerodynamics plays a vital role in sports textiles used in a wide variety of sports including cycling, ski-jumping, speed-skating and bobsleighs. Outfits of some high speed sports are shown in Fig. 7. Competition in the elite usually incorporates very short winning time margins. Prior researches have shown that a two-fold rise in athlete's velocity brings forth a four-fold rise in the drag force that needs to be overcome (Ogiano et al. [18-19], Konopov et al. [16]). Recently Moria et al. [13-15] and Chowdhury et al. [9-12] carried out systematic studies of textile aerodynamics using a unique RMIT developed testing methodology. The studies showed that test surface having several types of textile fabrics exhibited sufficiently less aerodynamic drag than the smooth surface due to the flow transitional effect caused by the textile fabrics. They also hypothesised that in speed sports, various sports garments made of knitted and woven fabrics with various degree of stretchability may have different aerodynamic behaviour. To understand more detail aerodynamic behaviour of knitted and woven fabrics under variable stretch conditions, Moria et al. [13-15] undertook a comprehensive study of ten textile fabrics (5 knitted and 5 woven) that are widely used in different speed-sport garments including swimming. The study focused on aerodynamic behaviour of all these textile fabrics under various stretches as under the stretch, the surface morphology (structure, roughness, fibre orientation, etc.) changes significantly. Moria et al. investigated both drag and lift generation capabilities of all these fabrics. Their study included comprehensive surface characterisation using tensile, electron microscopic and roughness analyses under various degrees of stretches.

Some major findings of Moria et al. [13-15] on knitted and woven fabrics are shown in Figs. 8-11 respectively. For knitted fabrics, the surface roughness increases under the increasing stretch. These changes make the airflow turbulent at a much lower speeds compared to the un-stretch surface of the textile fabrics. The findings also indicate that the aerodynamic properties are highly dependent on fabrics surface roughness, distance and gap area between courses. With elongation of knitted fabric, the increment of C_{Dmin} values increases respectively without any sudden change. However, the

knitted fabric with lower relative roughness, distance and gap area between courses creates an advantage in aerodynamic properties by reducing the drag at higher speeds. In contrast, the higher relative roughness, distance and gap area between courses provide an aerodynamic advantage by reducing drag at lower Reynolds numbers (lower speeds). The surface texture can be utilized to maximize the aerodynamic benefit for various speed ranges. By increasing the surface roughness of knitted fabrics by stretch, the flow can be tripped into turbulence at lower Reynolds numbers, potentially decreasing drag. It also shows however, that after the initial reduction in drag coefficient the drag then increases quickly with increasing Reynolds number due to high levels of friction drag associated with turbulent flow. Thus increasing the surface roughness can significantly increase the total drag if the flow is tripped prematurely due to increasing the roughness of the surface already in turbulent flow. A suitable selection of stretchable sport knitted fabric and garment fit for elite athletes is vital for achieving aerodynamic advantages. Similarly, the angle of attack is crucial in term of speed sport applications to maintain the maximum glide ratio and obtain the appropriate posture for the elite athlete.



Fig. 7 Sports outfits for various speed sports.

Regarding oven fabrics, the roughness decreases with the increase of stretches as woven fabrics structural patterns and physical properties are different than those of knitted fabrics. The findings of Moria et al. [13-15] clearly demonstrated that woven fabric undergoes a sudden drop in C_{Dmin} values at a small elongation and at further elongation followed by linear increment to the maximum stretch. At normal fit (under no stretch), the fabric with a lower relative roughness, distance and gap area between wefts provides an aerodynamic advantage by reducing drag at higher speeds. On the other hand, the higher relative roughness, distance and gap area between wefts also provide a benefit in aerodynamic properties by reducing the drag at lower speeds. Also, the surface texture can be utilised to maximise aerodynamic properties for various speed ranges. Optimal selection of speed sports woven fabric and

garment fit for the elite athletes is of utmost important for achieving aerodynamic advantages. In addition, the angle of attack is vital in terms of speed sport applications to maintain the maximum glide ratio.

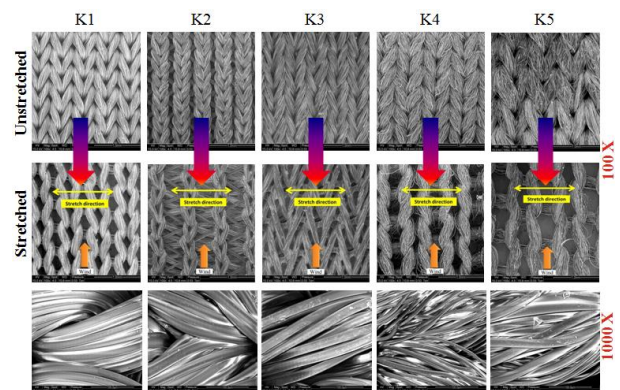


Fig. 8 Electron Microscopic Analysis: Knitted Fabrics [13-15].

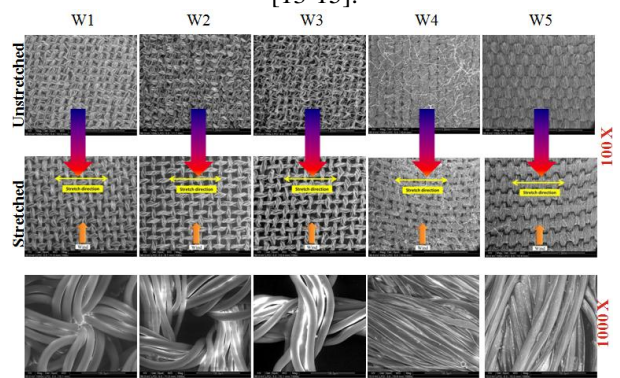


Fig. 9 Electron Microscopic Analysis: Woven Fabrics [13-15].

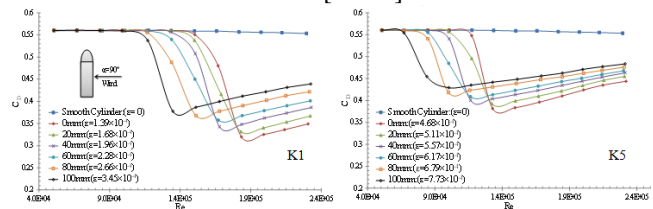


Fig. 10 Knitted Fabrics: Effect of Surface Roughness, angle of attack $\alpha = 90^\circ$ [13-15].

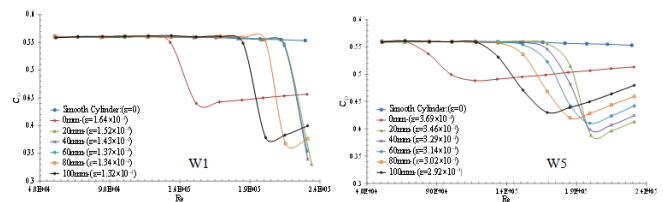


Fig. 11 Woven Fabrics: Effect of Surface Roughness, angle of attack $\alpha = 90^\circ$ [13-15].

5. Conclusions

The surface morphology and physical shape determine aero/hydrodynamic behavior and flight trajectory of all speed sports balls.

The aero/hydrodynamic understanding of athlete's body orientation and sports textile is paramount for achieving high performance in speed sports such as ski jumping, alpine skiing, speed skating, cycling, sprint, swimming, bobsleigh and skeleton.

Appropriate selection of textile fabrics based on athlete's speed regime is important as knitted and woven fabrics behave aerodynamically differently due to their surface morphology.

For knitted fabrics, the minimal drag coefficient (C_{Dmin}) is directly proportional to the relative roughness whereas the critical Reynolds number (Re_{crit}) is inversely proportional to relative roughness. For woven fabrics, the C_{Dmin} is proportional to the relative roughness and Re_{crit} relationship with relative roughness is non-linear.

Acknowledgement

The author is highly indebted to US Ski and Snowboard Association for providing partial financial support to RMIT Ski jumping project.

REFERENCES

- [1] F. Alam, H. Chowdhury, B. Loganathan, I. Mustary, A study of aerodynamic drag of contemporary footballs, *Procedia Engineering*, Vol. 147, pp 81-86 (2016).
- [2] A. Kozlov, H. Chowdhury, I. Mustary, B. Loganathan, F. Alam, F., Bio-inspired design: aerodynamics of boxfish, *Procedia Engineering*, Vol. 105, pp 323-328 (2015)
- [3] F. Alam, H. Chowdhury, N. Husnia, L. Smith, An Experimental Study of Baseballs and Softballs, *Procedia Engineering*, Vol. 60, pp 467-472 (2013).
- [4] F. Alam, A. Subic, S. Watkins, A.J. Smits, Aerodynamics of an Australian Rules Foot Ball and Rugby Ball in Computational Fluid Dynamics for Sport Simulation (edited by M. Peters), ISBN 13: 978-3-642-04465-6, 103-127 (2009)
- [5] F. Alam, H. Chowdhury, Z. Elmira, A. Sayogo, J. Love, A. Subic, An experimental study of thermal comfort and aerodynamic efficiency of recreational and racing bicycle helmets. *Procedia Engineering*, Vol. 2 (2), pp 2413-2418 (2010).
- [6] T. Asai, K. Seo, O. Kobayashi, R. Sakashita, Fundamental aerodynamics of the soccer ball, *Sports Engineering*, Vol. 10, pp 101-110 (2007).
- [7] R.D. Mehta, M. Pallis, *Sports Ball Aerodynamics: Effects of Velocity, Spin and Surface Roughness* Edited by Froes, S. and Haake, S.J, *Materials and Science in Sports*, pp 185-197 (2001)
- [8] R.D. Mehta, F. Alam, A. Subic, Aerodynamics of tennis balls- a review. *Sports Technology*, Vol. 1(1), pp 1-10 (2008).
- [9] H. Chowdhury, Aerodynamics of sports fabrics and garments, PhD Thesis, RMIT University, Australia (2012).
- [10] H. Chowdhury, F. Alam, D. Mainwaring, A. Subic, M. Tate, D. Forster, J. Beneyto - Ferre, Design and methodology for evaluating aerodynamic characteristics of sports textiles, *Sports Technology*, Vol. 2(3-4), pp 81-86 (2009).
- [11] H. Chowdhury, F. Alam, A. Subic, Aerodynamic performance evaluation of sports textile, *Procedia Engineering*, Vol. 2(2), pp 2517-2522 (2010).
- [12] H. Chowdhury, H. Moria, F. Alam, A. Subic, Aerodynamics of ski jumping suits. *Sports Technology*, Vol. 4(3-4), pp 164-170 (2011).
- [13] H. Moria, F. Alam, H. Chowdhury, A. Subic, The compression effect on aerodynamic properties of sports fabrics, *Procedia Engineering*, Vol. 34, pp 56-61 (2012).
- [14] H. Moria, H. Chowdhury, F. Alam, A. Subic, Aerodynamic behaviour of stretchable sports fabrics, *Sports Technology*, Vol. 4(3-4), pp 171-177 (2011).
- [15] H. Moria, H. Chowdhury, F. Alam, A. Subic, Comparative aerodynamic analysis of commercial swimsuits, *Sports Technology*, Vol. 3(4), pp 261-267 (2010).
- [16] I. Konopov, L. Oggiano, G. Chinga-Carrasco, O. Troynikov, L. Sætran, F. Alam, Aerodynamic and comfort characteristics of a double layer knitted fabric assembly for high speed winter sports, *Procedia Engineering*, Vol. 2(2), pp 2837-2843 (2010).
- [17] C. Kyle, V. Caiozzo, The effect of athletic clothing aerodynamics upon running speed. *Medicine and science in sports and exercise*, Vol. 18(5) (1986).
- [18] L. Oggiano, L. Sætran, S. Løset, R. Winther, Reducing the athletes's aerodynamical resistance. *Journal of computational and applied mechanics*, Vol. 8 (2), pp 163-173 (2007).
- [19] L. Oggiano, O. Troynikov, I. Konopov, A. Subic, F. Alam, Aerodynamic behaviour of single sport jersey fabrics with different roughness and cover factors, *Sports Engineering*, Vol. 12 (1), pp 1-12 (2009).
- [20] L. Brownlie, C. Kyle, E. Harber, R. MacDonad, M. Shorten, Reducing the aerodynamic drag of sports apparel: Development of the NIKE Swift sprint running and SwiftSkin speed skating suits. *The engineering of sport*, Vol. 5, pp 90-96 (2004).
- [21] K. Seo, O. Kobayash, M. Murakami, Regular and irregular motion of a rugby football during flight, *The Engineering of Sport 5*, pp 567-570 (2004).
- [22] A.J. Smits, S. Ogg, Golf ball aerodynamics. *The Engineering of Sport 5*, pp 3-12 (2004).
- [23] A.R. Vorontsov, V.A. Rummyantsev, Resistive forces in swimming. *Biomechanics in sport: performance enhancement and injury prevention*. Blackwell, Oxford, pp 184-204 (2000).
- [24] B. Schmölder, W. Müller, Individual flight styles in ski jumping: results obtained during Olympic Games competitions, *Journal of biomechanics*, Vol.38, pp 1055-1065 (2004)
- [25] W. Müller, B. Schmölder, Individual flight styles in ski jumping: Results obtained during Olympic Games competitions, *Journal of Biomechanics*, Vol. 38 (5), pp 1055-1065 (2005).

Acoustic Emission Measurement as Adaptive Biomarker in Integrity Analysis of Knee Osteoarthritis

T I Khan^{1*}, S Idoi² and T Yoshimura³

¹ Department of Advanced Technology Fusion, Saga University, Saga 840-8502, Japan

² Department of Orthopedic Surgery, Saga University, Saga 849-8501, Japan

³ Daishin co., Ltd, Higashioka-machi, Saga 840-2223, Japan

ABSTRACT

Acoustic emission (AE) technique has been applied as an adaptive biomarker for evaluating the disorder of knee joint. Integrity analysis of knee joint involves a detail study of several anatomical parts of knee joint like bones, cartilage, tendons etc. Any damage of these anatomical parts causes several knee diseases like osteoarthritis (OA). The incidence of knee OA increases due to some damages in the cartilage of knee. The major concern of this disease is the incurability at its matured stage. However, early detection for adopting appropriate measures can reduce the risk of this disease. The present investigation focuses on the dynamical behavioral characterization of knee joint for its integrity analysis with AE parametric features. AE signals have been collected from participants with different ages healthy people as well as OA patients. Data have been collected and clarified according to the guidelines of the ethics committee of Saga University, Japan. **150 words.**

Keywords: Integrity of Knee Joint, Osteoarthritis, Acoustic Emission, Biomarker.

1. Introduction

The knee joint is anatomically made up of three bones and various ligaments. Femur (the thigh bone), tibia (the shin bone), and patella (the kneecap) are the major components of this joint. Knee joint provides necessary supports to the skeleton for allowing them to be flexible in movements. The motion control as well as the protection of the knee joint is done by several muscles and ligaments. These ligaments of the knee ensure that the body-weight must be transmitted through the knee axis for minimizing the amount of wear and tear on the cartilage inside the knee [1].

The knee joint like other joints provides necessary supports to the skeleton for allowing them to be flexible in movements. In this joint, bones are not directly contacted to each other. They are receiving cushiony supports by cartilage, synovial membrane and fluid inside the joint (meniscus fluid). However, due to getting ages, the quality of bones including the cushiony items are degenerated. One of the reasons is that as one ages the meniscus loses water content and the cushiony supports become less rubbery and therefore, the meniscus tears with little efforts. Moreover, muscles and ligaments provide the appropriate forces and strength to this joint for suitable movements. However, the quality as well as the quantity of muscle and synovial tissues are also degraded due to aging and thus, the balancing of knee joint decreased. Therefore, the surface roughness of the articular cartilage is increased and the risk of happening the osteoarthritis (OA) is also increased.

Potential methods like X-ray, magnetic resonance imaging (MRI) etc. are presently using for clinical diagnosis of knee diseases. However, externally inserted high energy to the body for diagnosis of these technique and their static sensitivity with high cost make them

unpleasant to the patient. In the contrary, proposed acoustic emission (AE) technique is considered safe and user-friendly diagnosis of knee joint with low cost in dynamic analysis mode [2].

Acoustic emission technique (AET) is an important addition to NDT (non-destructive testing) or NDE (non-destructive evaluation) methods surveying actively a structure by scanning for geometric defects as well as to visual inspection methods observing a material surface. Unlike to other NDT methods, the AET is often used during loading to a structure, not before or after the loading like most of other techniques. Therefore, AET can be successfully applied to characterize the failure of a structure or joint from a very beginning to its complete failure. In AET, acoustic emission (AE) refers to the generation of transient elastic waves produced by a sudden redistribution of stressing a material. When a structure is subjected to an external stimulus (changes in pressure, load, or temperature), localized sources trigger the release of energy, in the form of stress waves, which propagate to the surface and are recorded by sensors. The Parametric analysis of AE signals reveals the damage information of the structure. Having the advantage of non-destructive damage evaluation, recent interests have been focused on the application of AE technique to the biomedical applications. Crack initiation and propagation in human femur is also investigated by a single-sensor technique, however, due to lot of artefacts in sensing systems, continuous efforts in this topic are still due in developing AET as a reliable biomarker [3].

It is mentioned that one of major advantages of AET is its simple application in identification of damage initiation and propagation inside a structure even in minute scales. Furthermore, knee joint gets degeneration due to ages and thus elderly people commonly face

* Corresponding author. Tel.: +81-952-28-8628

E-mail addresses: khan@me.saga-u.ac.jp

osteoarthritis disease which loses their workability and makes them a burden to the society. Therefore, the main objective of the present research is to develop a simply applicable biomarker based on AE nondestructive evaluation technique for early evaluation of knee joint degeneration. Accordingly, knees of young, middle aged as well as older people have been investigated by AET in the present research for getting information about initiation of degeneration in knee joint under sit-stand-sit dynamic loading which create sufficient rubbing activities to the surface of cartilage. Furthermore, angular positions of AE events are aimed as well to clarify the distribution of degeneration in all groups. Thus, in the next section, experimental methodology is discussed, after which results and discussion are explained and finally conclusions and references are presented [4].

2. Paper size and Margins

2.1 Experimental set up

The acquisition system of AE signals from knee joint has been designed according to the schematic views as shown in Fig. 1. Four AE sensors (R6 α , Physical Acoustics Corporation) with an operating frequency range of 35 to 100 kHz and resonant frequency of 55 is used in the experiment. The sensors are connected to the signal acquisition device (digital oscilloscope) through pre-amplifiers and main AE amplifier and finally the data has been transferred to the personal computer (PC). For the acquisition of angular movements of the knee during sit-stand-sit motions, two channel goniometer has been used for getting angular values for each position and the data has been recorded into the PC.

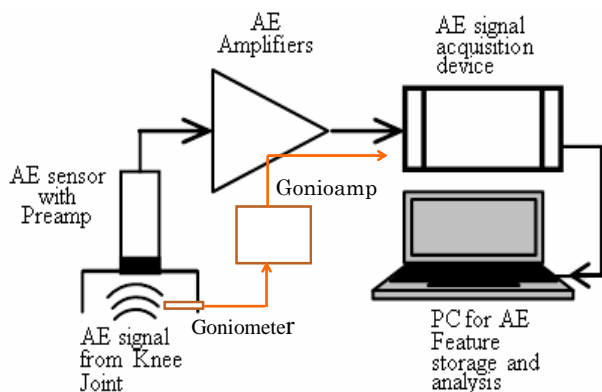


Fig. 1 Schematics of AE signal acquisition set up [].

2.2 Experimental procedure

According to the objectives of the present research, the positions of four sensors are placed in four places of the knee so that the generated AE signals can be received from all areas to the sensors. Furthermore, the sensor positions are considered considering as minimum noise receiving positions due to muscles etc. A model knee is shown (3B Scientific GmbH, Germany) in Fig. 2, where the sensor positions are mentioned as well.

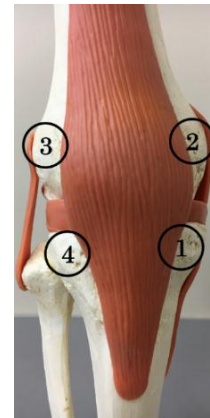


Fig. 2 Sensor positions to knee joint.

The method of sensor attachment is done by following the rule of ethics as well. As explained above, AE sensors are attached to the positions of (1) to (4) with high elastic medical tape. Due to high elasticity of the tape, the sensors are always attached to the skin of the knee at desired positions during sit-stand-sit movements. Therefore, undesirable noise in the dynamic knee experiments has been avoided remarkably. Moreover, to ensure the continuous contact of the sensing surface of the sensor to the anatomical site of the knee, coupling gel is used between the surface of the sensor and the contact place site of the knee. For getting an angular position of the movements, electronic goniometer is attached to the knee with double-stick tape so that it can be relaxed during the experiment. The position of the goniometer has been initialized to 90 degrees at the sitting position, while at the standing position it has been set to 0 degree. Thus, in one set of movement (sit-stand-sit) the measured angle has been recorded as 180 degrees. Ten sets of movements have been considered as 1 cycle of movements while 1 minutes have been taken as intermittent rest time. However, each cycle has been completed upon receiving one data. Thus, for one participants 30 AE events have been taken. Two participants from each group have been participated in the experiment. For AE signals 1MHz and for goniometer 100 Hz are used as sampling frequencies.

3. Experimental results and discussion

Experimental results for the integrity analysis of knee joint have been summarized as follows. Major focus has been concentrated to the effects of aging on having degeneration in anatomical components of knee joint. It is considered young participants of ages less than 40 and above of 40 it is defined as middle aged or old aged participants. Some results of knee patients are also compared as well, however, that results are not shown in this paper. It is also compared the sensitivity of AE acquisition for sensor positions. It is found that less muscle area for sensor position is better than the other muscle enriched areas. However, collection of AE data

for analyzing the integrity of knee joint are shown satisfactory at other places as well. The result is shown in Fig. 3.

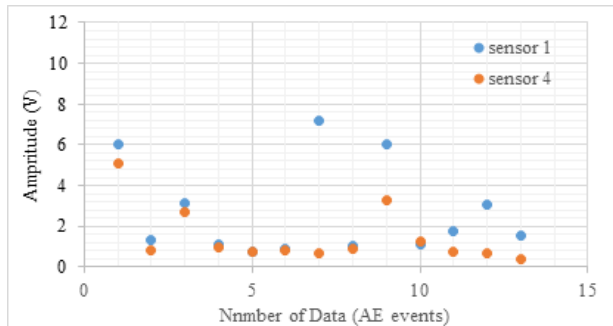


Fig. 3 Sensitivity analysis of sensor positions.

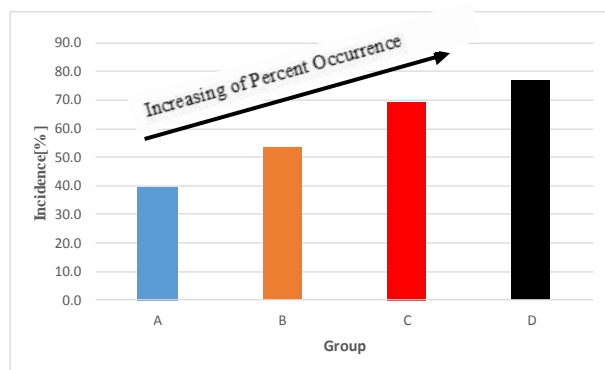


Fig. 4 Percent occurrence distribution of AE hits for different aged participants and OA patients.

The percent occurrence of AE hits is defined as the percent of the ratio of total required sit-stand-sit movements for a fixed number of AE hits in one cycle. As explained in above that the rate of transient AE hit generation increases due to surface condition of knee cartilage decreases. Experimental results show that increasing of aging increasing the percent occurrence of AE hits and it increases more for OA patients (Fig. 4). Thus, according to the observation, percent occurrence of AE hit works as an acceptable bio-marker for knee integrity analysis.

The parametric analysis of AE signals received from the knee joints of young and aged people has been conducted for understanding the signal intensity level and concentration of occurrence [5]. In the present paper, the analysis has been focused to the calculation of maximum amplitude of each AE events. Results of these maximum amplitude analysis for AE signals for two participants are mentioned in Fig. 5. Since the signal amplitude represents the functional proportion of AE signal energy, the result shown in this figure thus focuses on the AE event intensity for young and aged people. Therefore, according to the result, it is found that the AE intensity received from the cartilage friction of knee joint of aged participants is remarkably high compared to the young participants. It is already mentioned that this result has been observed between

two groups of participants whose age difference is below 20 years. Therefore, it is thought that similar results can be repeated for similar comparisons among people of young and more elderly group due to having more chance of occurring more degenerations in articular cartilage of knee joint for aging effects.

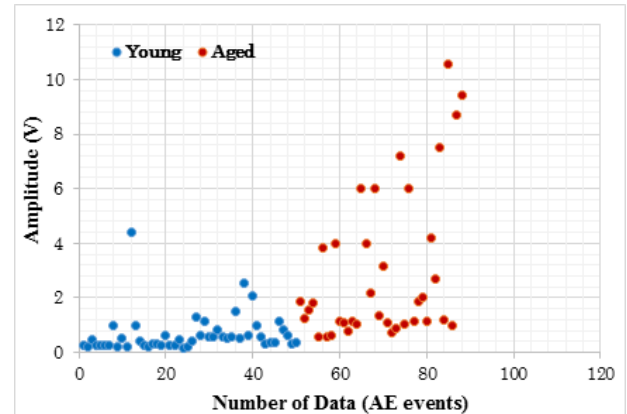


Fig. 5 Amplitude distribution of AE events for young and aged people.

EMG signals from lower limb muscles have been collected for each natural movement of knee joint [6]. The sensor clustering domain has been arranged only for left leg in the present paper. EMG signals are collected for knee flexor and knee extensor activities from the standing and sitting movements of the participants. Each sensor channel has been utilized for collecting individual muscle potentials from the respective muscle during flexor and extensor motions of the knee. One cycle of data collection has been defined as one standing and one sitting (sit-stand-sit) movements. Thus, for each position of the sensor, 20 cycles of data acquisition consist one data set. All of these data have been collected and recorded in PC for further processing.

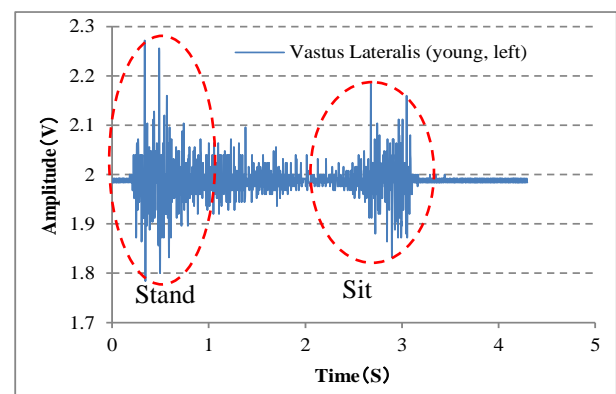


Fig. 6 EMG instantaneous signals for young people, vastus lateralis signals of left leg

The instantaneous EMG signals for young and aged people have been presented in Figs 6 and 7. Signals for vastus lateralis muscles only are found in these figures.

The myoelectric potentials for standing and sitting conditions for all muscles are visualized as signal amplitudes in volts. Although, the amplitudes are varied based on the values of the signal potentials at each data cycle, however, the patterns of the muscle potentials are understood from these sampling data. Maximum amplitudes in volts for 20 iterations are summarized individually in standing and sitting cycles for both aged people and young people

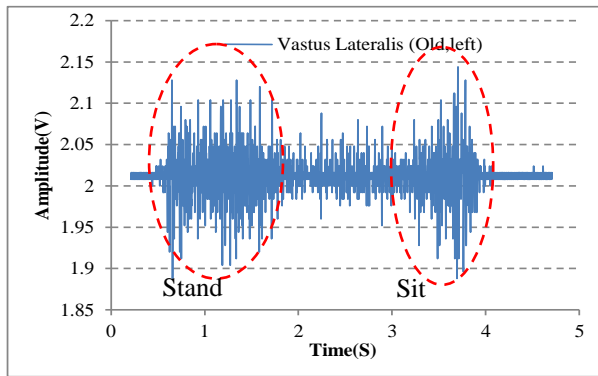


Fig. 7 Instantaneous signals for aged people, vastus lateralis, left leg.

The performance of muscular potential for vastus lateralis muscle has been analyzed as shown in Figs. 8 and 9 as well with respect to its peak frequency (PF) analysis, where, the peak frequency is defined as the frequency regarding to the peak amplitude (maximum amplitude) of each signal. In these figures PF distributions of vastus lateralis muscle for sitting movements are shown only in this paper. Muscle activities are compared according to the performance in sitting movements for both young and older people and found the differences in their activities as well. It is considered as one of the major issues in cartilage damage in older people. Thus, PF distribution analysis for young and old participants have been summarized in this paper considering only the vastus lateralis muscle. However, similar results are shown in other muscles for standing dynamics mode of older and younger people respectively. Strong PF perturbations are found as well in EMG signals for sitting operation of older people compared to that of younger people.

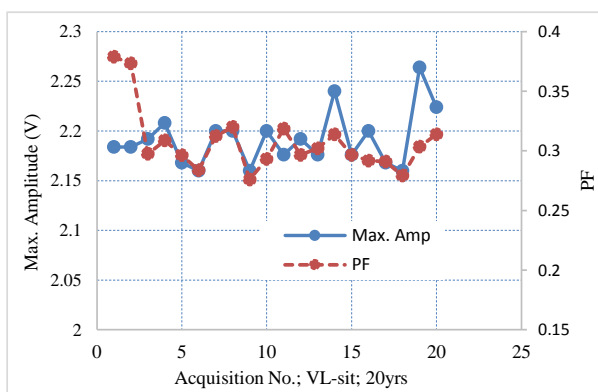


Fig. 8 Amplitude vs. PF of young people, vastus lateralis for sitting.

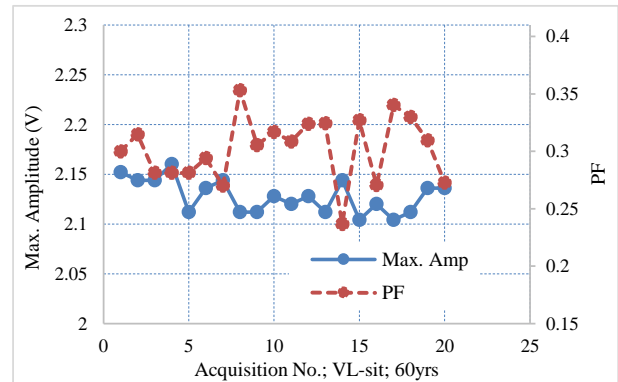


Fig. 9 Amplitude vs. PF of aged people, vastus lateralis for sitting.

4. Conclusions

Acoustic Emission technique has been applied in the integrity analysis of knee joint. Several bio-markers for knee osteoarthritis (OA) diagnosis based on AE technique have been explained with experimental validations. According to the objectives, two major findings have been clarified by the proposed system. Degeneration of knee cartilage by aging have been successfully identified by the proposed AE technique. Furthermore, integrity analysis of damaged knee by OA is also clarified satisfactorily. Maximum amplitude distribution of AE hits, percent occurrence of AE hits and concentrated distribution of AE hits etc. are presented as successful bio-markers in the AE diagnosis system of knee problems including OA. Muscles activities related to knee activities are also clarified by applying EMG signal processing technique. It is observed that the reduction of muscle activities due to aging may play an active role in causing degeneration of cartilage for occurring OA in knee joints.

REFERENCES

- [1] E. Thienpont, P. E. Schwab and P. Fennema, A systematic review and meta-analysis of patient-specific instrumentation for improving alignment of the components in total knee replacement, *Bone Joint J*, Vol. 96, pp1052-1061, (2014).
- [2] D. J. Hunter and A. Guermazi, Imaging Technique in Osteoarthritis, *J. of American Academy of Physical Medicine and Rehabilitation*, Vol. 4, pp S68-S74, (2012).
- [3] S. Shrivastava and R. Prakash, Assessment of bone condition by acoustic emission technique: A review, *Journal of Biomedical Science and Engineering*, Vol. 2, pp144-154, (2009).
- [4] T. I. Khan and Y. Harino, Integrity Analysis of Knee Joint by Acoustic Emission Technique, *J. of Multimodal User Interfaces* (springer), Vol. 10, pp 319-324, (2016)
- [5] T I Khan, M Kusumoto, Y Nakamura, S Ide and T Yoshimura, Acoustic Emission Technique as an Adaptive Biomarker in Integrity Analysis of Knee Joint, Proc. RECAV 2017, Bali, Indonesia, Nov. 27-28, (2017).
- [6] T. I. Khan and T. Kurita, EMG Signals for Co-Activations of Major Lower Limb Muscles in Knee Joint Dynamics, *J. of Biomedical Science and Engineering*, Vol. 3, pp 9-14, (2015).

ICMIEE18-KN04

Engineering the Reliability into Products under Harsh Environments

Sabuj Mallik

School of Mechanical Engineering and the Built Environment, University of Derby, Derby, DE22 3AW, UK

ABSTRACT

In the current global competitive market, it is crucial to make highly reliable products. This, in turn, will reduce product cost by having fewer warranty claims and low repair costs. Indeed, reliability is of increasing importance for electronics systems operating in harsh environments. Some examples are electronic control units (ECUs) used for automotive engine controls (automotive) and the electronic telecommunication systems used at the subsea level (telecommunication). The ban of lead from electronic products was a major step towards a greener environment. This however brought in new challenges, especially with the reliability of lead-free solder materials. This talk will explore some research studies on the reliability of electronics packaging, with a special focus on lead-free solder joints. It is indeed very important to ensure that solder joints are reliable for the expected product lifetime as they are the weakest parts of an electronics assembly. The talk will shed some light on how various experimental and simulation research studies helped to understand, characterize and predict solder joint behaviors under severe operating conditions.

ICMIEE18-KN05

Non-Singular Second Order Terminal Sliding Mode Incorporating Time Delay Estimation for Uncertain Exoskeleton Robot

Brahim Brahmi^{1,*}, Mohammad Habibur Rahman², Maarouf Saad¹ and Abdelkrim Brahmi¹

¹ Département de génie électrique, École De Technologie Supérieure, Montréal (QC), Canada

² Mechanical /Biomedical Engineering Department University of Wisconsin-Milwaukee

ABSTRACT

Advanced robotic technology has become an important component in various medical specializations, including rehabilitation treatment such as physiotherapy. Robot aided rehabilitation is a new practical approach created to provide intensive therapy that typically required an important effort by the therapist in conventional rehabilitation. Robot aided rehabilitation is used to assist patients such as stroke victims while saving the therapist's time. This treatment also aims to help the patient in recovering from their lacking functional capability, obtaining new skills, and increasing their quality of life. In addition to the complex design of this kind of robots, the collaboration with humans who suffer from an uncontrollable upper limb makes the robot subject to many uncertain dynamics which can influence the performance of the robot. This paper presents a tracking control by proposing a new Non-Singular Terminal Second-Order Sliding Mode Control incorporating Time Delay Estimation implemented to an exoskeleton robot with dynamic uncertainties and unknown bounded disturbances. The success of the second-order sliding mode is due to its attractive features of accuracy, attenuation of chattering and fast convergence. However, its dilemma is that the unknown dynamics of the exoskeleton robot and external disturbances generated by its different wearers can be magnified by the second derivative of the switching surface, which drives to the instability of the exoskeleton system. Applying Time Delay Estimation will approximate the uncertain dynamics while overcoming the main restriction of the second-order sliding mode. The stability analysis is formulated and established based on the Lyapunov function. Experimental results with two healthy subjects validate the effectiveness of the suggested control.

Keywords: Rehabilitation Robot, Time Delay Estimation, Second-Order Sliding Mode Control, passive assistive motion.

1. Introduction

Recently rehabilitation robots have drawn significant attention from the scientific community since exoskeleton robots are able to provide similar types of rehabilitation therapy as provided by the physiotherapists, i.e. the conventional therapeutic approach [1]. The significance of the rehabilitation robots lies in their ability to provide intensive physical therapy for a long period of time [1]. The feedback data of the exoskeleton allows the physiotherapist to accurately evaluate the patient's performance [1, 2]. An important perspective is that the design of this kind of robots must be in accordance with the human anatomy. In order to provide a modern rehabilitation treatment/therapy for the patients who suffer from the dysfunction of the upper limb, we have developed an exoskeleton robot named ETS-MARSE (École de Technologie Supérieure - Motion Assistive Robotic-exoskeleton for Superior Extremity) that is compatible with the human arm configuration and is able to provide different types of rehabilitation therapy ranging from passive to active assisted arm movement therapy [3-5].

Making the exoskeleton system perform the smooth motion corresponding to the recommended therapeutic arm movements is one of the challenging tasks of these kinds of rehabilitation robots. However, the dynamics of these kinds of robots is hardly obtained accurately due to their complex design, and non-smooth nonlinear characteristics of the actuators such as backlash, hysteresis, dead zone, and saturation [6-8]. Furthermore,

the collaboration between the exoskeleton and human makes the exoskeleton subject to many external disturbances. These later are caused by different conditions or musculoskeletal system variances of the wearer of the exoskeleton robot. Without doubt, these constraints degrade the performance of the exoskeleton system. It is consequently imperative for us to design a robust adaptive controller that approximates the dynamic model of the robot and minimizes the non-smooth nonlinear constraints effects meanwhile maintaining the stability of the exoskeleton robot.

Sliding Mode control is one of the robust approaches designed to control a perturbed system that is widely applied on robotic systems thanks to its attractive characteristics of robustness to the dynamics nonlinear uncertainties and external disturbances [9]. A key feature used to achieve this robustness is to limit the chattering effects with fast convergence of the system's trajectories to the equilibrium [9, 10]. For this, various conventional approaches tried to decrease the chattering and increase the convergence speed of the error by exchanging the discontinuous function by a continuous function, e.g., a saturation function, in order to provide a continuous control [9, 10]. Terminal sliding mode control (TSMC) is proposed in [11] to provide an asymptotic convergence with finite time by introducing the fraction order on the switching surface. This allows the trajectories of the system to converge to the equilibrium faster. The fast convergence feature of TSMC can deteriorate controller

* Corresponding author. Tel.: 414-229 X 1165 (O), 4548 (Lab)
E-mail addresses: rahmanmh@uwm.edu

performance. Many solutions have been developed to the fast TSMC [12] and non-singular TSMC [13] to improve the accuracy performance of TSMC. Second Order Sliding Mode Controller (SOSMC) [14-16] is one of the effective strategies applied to the robotics system to reduce chattering dilemmas and provide a better performance accuracy. Additionally, several control strategies have been developed to enhance the performance of SOSMC such as twisting control and Super-Twisting control algorithms [17-19]. The principal concept of SOSMC is to permit a sliding surface and its consecutive derivative to reach the equilibrium in finite time convergence. In addition, the design of the control makes the discontinuous control always work under an integral function, which can attenuate the undesirable chattering. Nevertheless, the second-time derivative of the switching surface might engender instability of the system, a risk that the non-smooth nonlinear uncertainties function and external disturbances magnify. Recently, the Second Order Terminal Sliding Mode Control (SOTSMC) was proposed to provide an excellent control performance to deal with the chattering problem and to provide a finite time convergence [14-16]. Therefore, according to the best of our knowledge, no non-singular SOTSMC has been proposed before to solve the mentioned problems.

Motivated to deal with the above mentioned problem and based on our previous works [2, 20], we designed a new Non-Singular Second-Order Terminal Sliding mode control combined with time delay estimation [2, 21] to maneuver the exoskeleton robot. First, the control action aims to design the switching surface to ensure a fast (finite time) transient convergence both at a distance from and at a close area of the equilibrium. Secondly, to provide a good approximation of the dynamics of the uncertainties and/or non-smooth nonlinear function that can be amplified with the second derivative of the switching surface. Therefore, the features SOSMC will be improved by producing the high precision, eliminating the chattering dilemma and providing a finite-time convergence to equilibrium. The stability analysis of the exoskeleton system is formulated and proved based on the Lyapunov candidate function. The contribution of this paper can be summarized in two points:

- i. Design of a Non-Singular Second-Order Terminal Sliding mode control surface so that fast (finite time) transient convergence both at a distance from and at a close reach of the equilibrium can be achieved.
- ii. Design a control approach incorporating Non-Singular Second-Order Terminal Sliding mode control with a time delay estimation in order to provide a good approximation of dynamic model of the exoskeleton robot and external bounded disturbances by delay one step the inputs and the states of the system.

The remainder of the paper is organized as follows: The dynamics of the robot is presented in the next section; the control scheme is described in section 3. Experimental

results and some comparisons are given in section 4 and the conclusion is presented in section 5.

2. Characterization of robot aided rehabilitation

2.1 Exoskeleton Robot Development

As shown in Fig. 1, the developed exoskeleton robot ETS-MARSE is a redundant robot. It has 7-degrees of freedom (DOFs). It was developed to provide therapeutic movements to the impaired upper limb. The exoskeleton was ergonomically designed based on the anatomy and the joint articulation of the human upper limb while considering the safety and the comfort of the patients wearing this robot. The shoulder motion support part consists of three joints, the elbow motion support part comprises one joint and the wrist motion support part consists of three joints. The ETS-MARSE can provide every variety of upper limb motions. Key characteristics of the ETS-MARSE and comparison with similar existing exoskeleton robots are summarized in [3-5].

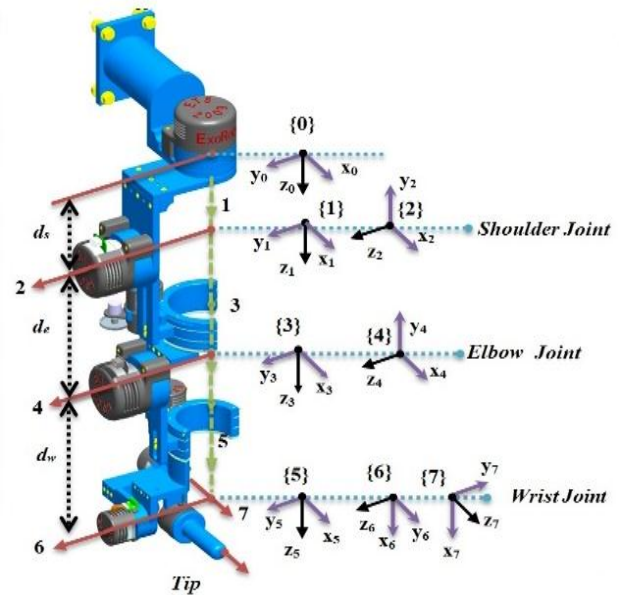


Fig. 1: Reference frames of ETS-MARSE [3-5].

The modified Denavit-Hartenberg (DH) [22] parameters of the developed ETS-MARSE (corresponding to the links-frames attachment as shown in Fig.1) are given in Table 1. These parameters are used to obtain the homogeneous transformation matrices [22].

TABLE 1 Modified Denavit-Hartenberg Parameters

Joint (i)	α_{i-1}	a_{i-1}	d_i	θ_i
1	0	0	d_s	θ_1
2	$-\pi/2$	0	0	θ_2
3	$\pi/2$	0	d_e	θ_3
4	$-\pi/2$	0	0	θ_4
5	$\pi/2$	0	d_w	θ_5
6	$-\pi/2$	0	0	$\theta_6 - \pi/2$
7	$-\pi/2$	0	0	θ_7

2.2 Dynamics of ETS-MARSE Robot

The dynamics of ETS-MARSE is expressed by the well-known rigid body's dynamic equation as follows [22]:

$$M(\theta)\ddot{\theta} + C(\theta, \dot{\theta})\dot{\theta} + G(\theta) + f_{\text{dis}} = \tau \quad (1)$$

where θ , $\dot{\theta}$, and $\ddot{\theta} \in \mathbb{R}^7$ are respectively the joints position, velocity, and acceleration vectors, $M(\theta) \in \mathbb{R}^{7 \times 7}$, $C(\theta, \dot{\theta}) \in \mathbb{R}^7$, and $G(\theta) \in \mathbb{R}^7$ are respectively the symmetric positive-definite inertia matrix, the Coriolis and centrifugal vector, and the gravitational vector due to the exoskeleton and the human arm. $\tau \in \mathbb{R}^7$ is the torque vector, $f_{\text{dis}} \in \mathbb{R}^7$ is the external disturbances vector caused by the human. Without loss of generality, the dynamic model (1) can be rewritten as follows:

$$\begin{cases} M(\theta) = M_0(\theta) + \Delta M(\theta) \\ C(\theta, \dot{\theta}) = C_0(\theta, \dot{\theta}) + \Delta C(\theta, \dot{\theta}) \\ G(\theta) = G_0(\theta) + \Delta G(\theta) \end{cases} \quad (2)$$

where $M_0(\theta)$, $C_0(\theta, \dot{\theta})$, and $G_0(\theta)$ are respectively the known inertia matrix, the Coriolis/centrifugal matrix, and the gravity vector. $\Delta M(\theta)$, $\Delta C(\theta, \dot{\theta})$, and $\Delta G(\theta)$ are the uncertain parts. Let us introduce a new variable such that: $\eta_1 = \theta$ and $\eta_2 = \dot{\theta}$; hence, the dynamic model expressed in Eq. 1 can be rewritten as follows:

$$\begin{cases} \dot{\eta}_1 = \eta_2 \\ \dot{\eta}_2 = U(t) + f(t) + H(t) \end{cases} \quad (3)$$

where, $U(t) = U(\eta_1)$; $H(t) = H(\eta_1, \eta_2, \dot{\eta}_2)$ and $f(t) = f(\eta_1, \eta_2)$. This notation is used to facilitate the handling of the control methodology with: $U(t) = M_0^{-1}(\theta)\tau(t)$; $H(t) = M_0^{-1}(\theta)(-f_{\text{dis}} - \Delta M(\theta)\ddot{\theta} - \Delta C(\theta, \dot{\theta})\dot{\theta} - \Delta G(\theta))$, and $f(t) = M_0^{-1}(\theta)(-C_0(\theta, \dot{\theta})\dot{\theta} - G_0(\theta))$.

Property 1: [22] The known part of inertia matrix $M_0(\theta)$ is symmetric and positive definite for all $\theta \in \mathbb{R}^n$.

Assumption 1: The function $H(t)$ and its time derivative $\frac{d}{dt}[H(t)]$ are globally Lipschitz functions.

Assumption 2: The desired trajectory is bounded.

Assumption 3: The external disturbance f_{dis} is supposed to be continuous, has finite energy, and satisfies $\|f_{\text{dis}}\| \leq \varepsilon$, with an unknown positive disturbance boundary ω .

3. Control Design

The first step in the control development is to define the surface S in terms of position error. Then, select the Non-Singular Second Order Terminal Sliding surface to ensure fast convergence without a chattering problem. The proposed approach combines a Non-Singular Second Order Terminal Sliding Mode Control (N-SSOTSMC) and Time Delay Estimation TDE, applied on a second-order dynamic model of the exoskeleton robot given by Eq. 3.

The sliding set of n-th linked to the surface or equivalent surface is determined by:

$$S = \dot{S} = \dots = S^{n-1} = 0 \quad (4)$$

Equation (4) shows an n-dimensional condition of the parameter system. In this case, it is sufficient to differentiate the sliding surface once to obtain the desired control input. We can choose the switching function such that:

$$S = \dot{e} + \Lambda e \quad (5)$$

where $e = \eta_1 - \eta_1^d \in \mathbb{R}^7$ and $\dot{e} = \eta_2 - \eta_2^d \in \mathbb{R}^7$ are the position and velocity errors respectively, and $\eta_1^d, \eta_2^d \in \mathbb{R}^7$ are the desired position and desired velocity respectively, $\Lambda = \text{diag}(\Lambda_{ii})$ for $i = 1, \dots, 7$ is a diagonal positive matrix. Taking the first derivative of selected surface S we obtain:

$$\begin{aligned} \dot{S} &= \ddot{e} + \Lambda \dot{e} \\ &= \dot{\eta}_2 - \dot{\eta}_2^d + \Lambda \dot{e} \\ &= U(t) + f(t) + H(t) - \dot{\eta}_2^d + \Lambda \dot{e} \end{aligned} \quad (6)$$

In this paper, we are looking forward to reduce the chattering problem using second-order sliding mode to transform the discontinuous control to continuous signal using integral action. So, the second derivative of surface S can be expressed as :

$$\begin{aligned} \ddot{S} &= \ddot{e} + \Lambda \ddot{e} \\ &= \ddot{\eta}_2 - \ddot{\eta}_2^d + \Lambda \ddot{e} \\ &= \frac{d}{dt}[U(t)] + \frac{d}{dt}[f(t)] + \frac{d}{dt}[H(t)] - \ddot{\eta}_2^d + \Lambda \ddot{e} \end{aligned} \quad (7)$$

The first and second derivatives of S drive us to create a new sub-system. Let us before that define two new variables as $\mu_1 = S$, and $\mu_2 = \dot{S}$, therefore, the new state-space equation is given such that:

$$\begin{aligned} \dot{\mu}_1 &= \dot{S} \\ \dot{\mu}_2 &= \frac{d}{dt}[U(t)] + \frac{d}{dt}[f(t)] + \frac{d}{dt}[H(t)] - \ddot{\eta}_2^d + \Lambda \ddot{e} \end{aligned} \quad (8)$$

As we remark in Eq.8, the time derivative of the control input $\frac{d}{dt}[U(t)]$ is the input to manage the second-order sliding mode system (8). Usually, in all types of sliding mode design, the reaching law contains a discontinuous term. In our case, to perfectly control the exoskeleton system (3), we must integrate once $\frac{d}{dt}[U(t)]$ to get the control input $U(t)$ with the desired torque $\tau = M_0(\theta)U(t)$. The integration permits to transform the discontinuous control action to a continuous one, which helps attenuating the undesirable chattering problem.

To complete the proposed controller procedure, let us introduce the Non-Singular Second Order Terminal

Sliding surface for the state-space equation given by (8) such that:

$$\rho = \mu_1 + \varphi[\mu_2]^\beta \quad (9)$$

where $\varphi = \text{diag}[\varphi_{ii}]$ for $i = 1, \dots, 7$ is a diagonal positive definite matrix, and $[\mu_2]^\beta = [\mu_{21}^\beta, \dots, \mu_{27}^\beta]^\top$ and $1 < \beta < 2$ [13]. Since the Non-Singular Second Order Terminal Sliding surface is designed, the application of the proposed controller with TDE can be easily employed. Taking the time derivative of the Eq.(9) and using Eq.8 , we find:

$$\begin{aligned} \dot{\rho} &= \dot{\mu}_1 + \beta\varphi\mu_2^{\beta-1} \\ &= \mu_2 + \beta\varphi\mu_2^{\beta-1} \left[\frac{d}{dt}[U(t)] + \frac{d}{dt}[f(t)] \right. \\ &\quad \left. + \frac{d}{dt}[H(t)] - \ddot{\eta}_2^d + \Lambda\ddot{e} \right] \end{aligned} \quad (10)$$

where $\mu_2^{\beta-1} = \text{diag}(\mu_{21}^{\beta-1}, \dots, \mu_{27}^{\beta-1})$. The fast convergence is ensured by choosing the reaching law as follows:

$$\dot{\rho} = -\beta\varphi\mu_2^{\beta-1}K\text{sign}(\rho) \quad (11)$$

where $K = \text{diag}[k_{ii}]$ with $k_{ii} > 0$ for $i = 1, \dots, 7$ is a switching positive gain, and function $\text{sign}(\rho) = [\text{sign}(\rho_1), \dots, \text{sign}(\rho_7)]^\top$ is determined such that:

$$\text{sign}(\rho_i) = \begin{cases} 1 & \text{for } \rho_i > 0 \\ 0 & \text{for } \rho_i = 0 \\ -1 & \text{for } \rho_i < 0 \end{cases} \quad (12)$$

where $i = 1, \dots, 7$. From Eq. 10 and equation (11), we can conclude the time derivative of the control input such that:

$$\begin{aligned} \frac{d}{dt}[U(t)] &= -\frac{d}{dt}[f(t)] - \frac{d}{dt}[H(t)] + \ddot{\eta}_2^d - \\ &\Lambda\ddot{e} - \frac{1}{\beta}\varphi^{-1}[\mu_2]^{2-\beta} - K\text{sign}(\rho) \end{aligned} \quad (13)$$

Since $H(t)$ and $\frac{d}{dt}[H(t)]$ are uncertain that may influence the control purpose. In such case, the control law (13) is not feasible. To overcome this dilemma, TDE approach is used to estimate the uncertainties of the nonlinear exoskeleton's dynamics. So, if **Assumption 3** is verified, $\frac{d}{dt}[H(t)]$ can be estimated such that:

$$\begin{aligned} \frac{d}{dt}[\hat{H}(t)] &\approx \frac{d}{dt}[H(t - t_d)] = \ddot{\eta}_2(t - t_d) - \\ &\frac{d}{dt}[f(t - t_d)] - \frac{d}{dt}[U(t - t_d)] \end{aligned} \quad (14)$$

where t_d is a very small time-delay constant. Practically, the smallest constant that can be used in real time is the sampling-time period. Let us now define the time delay error such that:

$$\begin{aligned} \varepsilon_i &= \frac{d}{dt}[H_i(t)] - \frac{d}{dt}[\hat{H}_i(t)] = \frac{d}{dt}[H_i(t)] - \\ &\frac{d}{dt}[H_i(t - t_d)] \leq \delta_i|t - (t - t_d)| \leq \delta_i t_d \end{aligned} \quad (15)$$

where δ_i for $i = 1, \dots, 7$ is a positive constant known as Lipschitz constant that satisfies the Lipschitz condition in **Assumption 3**.

Theorem 1: Consider the exoskeleton robot system (3), the proposed control law that can handles the exoskeleton system and ensures the stability of the Non-Singular Second Order Terminal Sliding mode with TDE is given by:

$$\begin{aligned} \frac{d}{dt}[U(t)] &= -\frac{d}{dt}[f(t)] - \frac{d}{dt}[\hat{H}(t)] + \ddot{\eta}_2^d - \\ &\Lambda\ddot{e} - \frac{1}{\beta}\varphi^{-1}[\mu_2]^{2-\beta} - K\text{sign}(\rho) \end{aligned} \quad (16)$$

where $\int \frac{d}{dt}[U(t)]$ gives $U(t)$; if the following condition is verified:

$$k_{ii} > \delta_i t_d; \text{ for } i = 1, \dots, 7 \quad (17)$$

Proof:

The proposed Lyapunov function candidate that ensures the stability of the robot is:

$$V = \frac{1}{2}\rho^T\rho \quad (18)$$

The time derivative of equation (18) is given by:

$$\begin{aligned} \dot{V} &= \rho^T\dot{\rho} \\ &= \rho^T \left(\mu_2 + \beta\varphi[\mu_2]^{\beta-1} \left[\frac{d}{dt}[U(t)] + \right. \right. \\ &\quad \left. \left. \frac{d}{dt}[f(t)] + \frac{d}{dt}[H(t)] - \ddot{\eta}_2^d + \Lambda\ddot{e} \right] \right) \end{aligned} \quad (19)$$

Substituting control law $\frac{d}{dt}[U(t)]$ from Eq.16 into Eq.19 using Eq.15. Then, Eq. 19 becomes such that:

$$\begin{aligned} \dot{V} &= \rho^T\beta\varphi[\mu_2]^{\beta-1} \left(\left[\frac{d}{dt}[H(t)] - \right. \right. \\ &\quad \left. \left. \frac{d}{dt}[\hat{H}(t)] \right] - K\text{sign}(\rho) \right) \\ &\leq \sum_{i=1}^7 \beta\varphi_{ii}\mu_{2i}^{\beta-1}|\rho_i|(|\varepsilon_i| - \\ &\quad k_{ii}\text{sign}(\rho_i)) \\ &\leq \sum_{i=1}^7 \beta\varphi_{ii}\mu_{2i}^{\beta-1}|\rho_i|(\delta_i t_d - \\ &\quad k_{ii}\text{sign}(\rho_i)) \end{aligned} \quad (20)$$

where from Eq. 15 it is clear that the time delay error ε_i is always positive. Since $1 < \beta < 2$, therefore, for $\mu_{2i} \neq 0$ the expression $[\mu_{2i}]^{\beta-1} > 0$ is always true [13]. Hence, to ensure the negativity of \dot{V} , the following condition must be fulfilled:

$$k_{ii} > \delta_i t_d; \text{ for } i = 1, \dots, 7 \quad (21)$$

Hence, \dot{V} is negative definite, thus, the selected surface ρ_i and its derivative is converging to zero as $t \rightarrow \infty$. Therefore the system is stable.

4. Experiments and Comparative study

4.1 Experiment set-up

The robot system consists of three processing units, the first is a PC where the top-level commands are sent to the robot using LabVIEW interface, i.e. the control scheme selection, joint or Cartesian space trajectory, etc. This PC also receives the data after the exoskeleton robot task is executed to analyze its performance. The other two processing units are part of a National Instruments PXI platform. Firstly, a NI-PXI 8081 controller card with an Intel Core-Duo processor; in this card, the main operating system of the robot and the top-level control scheme are executed. In our case, the non-singular second-order terminal sliding mode based controller as well as the estimation based on time delay approach, at a sampling time of 500 μ s. Finally, at input/output level, a NI PXI-7813R remote input/output card with a FPGA (field programmable gate array) executes the low-level control; i.e. a PI current control loop (sampling time of 50 μ s) to maintain the current of the motors required by the main controller. Also, in this FPGA, the position feedback via Hall-sensors (joint position) and basic input/output tasks are executed. The joints of the ETS-MARSE are powered by Brushless DC motors (Maxon EC-45 and Maxon EC-90) combined with harmonic drives (gear ratio 120:1 for motor-1 and motor-2, and gear ratio 100:1 for motors 3–7). The diagram of the experiment architecture is shown in Fig. 2. The parameters of the proposed control are illustrated in Table 2.

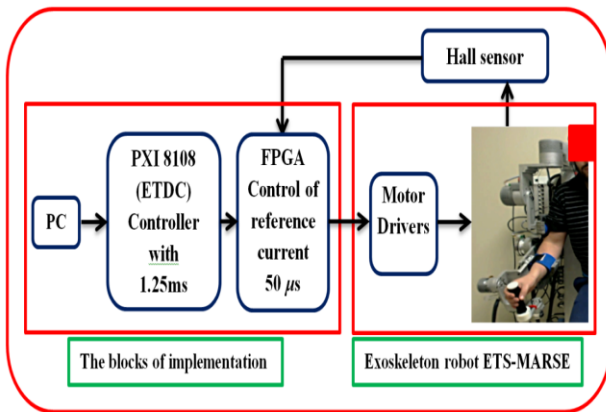


Fig. 2. Experiments platform (Note that the subject's figure is published with the written informed consent of the depicted individual.)

TABLE 2 Controller parameters

Gains	Value ($i = 1:7$)
φ_i	15.7
Λ_i	42.2
k_{ii}	15
β_{ii}	1.5

4.2 Experiment Results

In this test, the proposed exercise consisted of the two joints (elbow joint: flexion/extension and shoulder joint internal/external rotation). This exercise was performed with subject-1 (age: 30 years; height: 177 cm; weight: 75 kg). In this case, the trajectory was repeated two times for each movement with velocity varying less than 50 Deg/sec). The result of the task conducted with subject-1 is illustrated in Fig. 3. We can observe from Fig.3 that for both joints (elbow and shoulder), the desired trajectory, represented by the red line, practically overlaps the measured trajectory, represented by the solid blue line. It is clear from the plots in this figure (Fig.3) that the proposed controller provides a good performance. Where the controller has the ability to keep the stability of the exoskeleton system along the designed physical therapy movement with a position error (3rd row of Fig. 3) less than 2° for shoulder joint and less than 0.05° for elbow joint. The second row presents the desired velocity compared with the real velocity. It is clear from the smoothness of the velocity profile that the therapeutic motion was very good. The last row of Fig. 3 shows the control input which is clearly smooth and without any chattering effect.

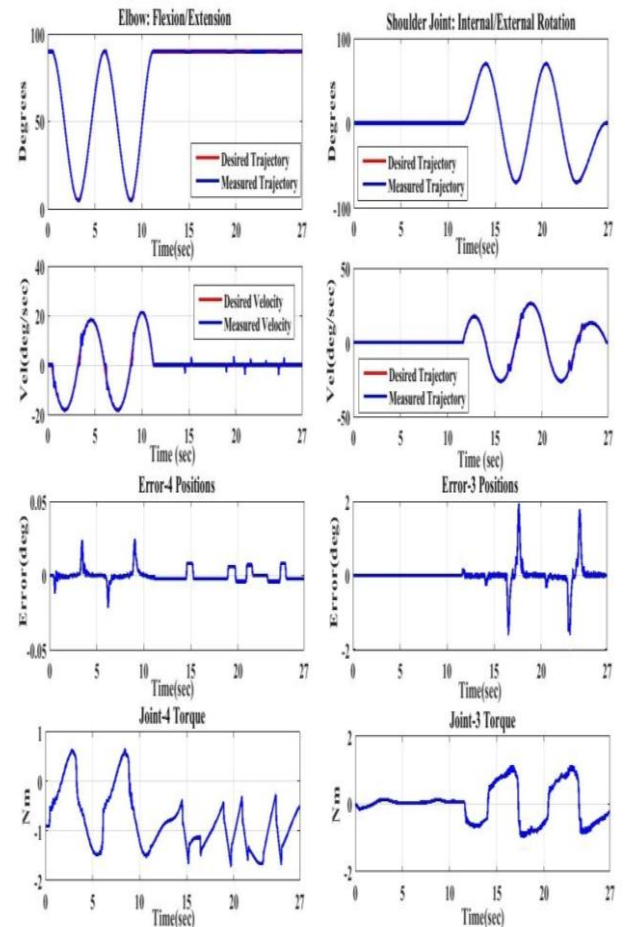


Fig. 3. Tracking trajectory of ETS-MARSE with subject-1 (constant acceleration).

4.3 Comparative study

The designed controller is compared with conventional second-order sliding mode controller SOSMC [14] with the same gains to show the feasibility and advantage of the designed controller. The comparison is made in terms of tracking position error, and torque input by computing the Root-Mean Square (RMS).

It is clear from Table 3 that the proposed controller achieves an excellent performance with a small value of overall RMS error and RMS torque, even when the dynamic model of the exoskeleton is not completely known, and in presence of external disturbances. Hence, these results demonstrate the efficiency and suitability of our proposed controller scheme.

Table. 3 Controller evaluation

Subjects	Root Mean Square (RMS)			
	Proposed Controller		Conventional SOSMC controller	
	$\ e\ _{\text{error}}$ (deg)	$\ \tau\ _{\text{Torque}}$ (Nm)	$\ e\ _{\text{error}}$ (deg)	$\ \tau\ _{\text{Torque}}$ (Nm)
Subject-1	1.3695	2.1125	2.5894	3.2147
	2.0379	3.1537	3.7840	4.8579

5. Conclusion

In this paper, we studied the control design employed to passive rehabilitation protocol of an exoskeleton robot named ETS-MARSE by introducing a new Non-Singular Terminal Second-Order Sliding Mode Control combined with time delay estimation. An experimental physiotherapy session with a healthy subject was created to examine the effectiveness and feasibility of the suggested control, which is established. As we see through experimental results that the proposed control has proved its capability to maneuver the exoskeleton to achieve the designed physical therapy with differences exoskeleton's wearers even the dynamics model of the robot is not completely known. Clearly that the controller deals very well with the uncertainties of robot's dynamics and external disturbances by given a good tracking of the trajectory without any chattering phenomenon. In the light of these excellent results obtained with healthy subject, we looking forward to implementing the proposed control with real unhealthy subjects as stroke victims in future work which permit to evaluate the controller with true case of disturbances such spasticity/dystonia, and muscle weakness in neurological patients, etc.

REFERENCES

[1] S. Xie, "Advanced Robotics for Medical Rehabilitation," Springer Tracts in Advanced Robotics, vol. 108, pp. 1-357, 2016.

[2] B. Brahmi, M. Saad, C. O. Luna, P. Archambault, and M. Rahman, "Sliding mode control of an exoskeleton robot based on time delay estimation," in Virtual Rehabilitation (ICVR), 2017 International Conference on, 2017, pp. 1-2.

[3] M. Rahman, M. Saad, J. Kenné, and P. Archambault, "Modeling and development of an exoskeleton robot for rehabilitation of wrist movements," in Advanced Intelligent Mechatronics (AIM), 2010 IEEE/ASME International Conference on, 2010, pp. 25-30.

[4] M. H. Rahman, T. Kittel-Ouimet, M. Saad, J.-P. Kenné, and P. S. Archambault, "Robot assisted rehabilitation for elbow and forearm movements," International Journal of Biomechanics and Biomedical Robotics, vol. 1, pp. 206-218, 2011.

[5] C. Ochoa Luna, M. Habibur Rahman, M. Saad, P. S. Archambault, and S. Bruce Ferrer, "Admittance-based upper limb robotic active and active-assistive movements," International Journal of Advanced Robotic Systems, vol. 12, p. 117, 2015.

[6] B. Brahmi, S. Maarouf, C. O. Luna, B. Abdelkrim, and M. Rahman, "Adaptive iterative observer based on integral backstepping control for upper extremity exoskeleton robot," in Modelling, Identification and Control (ICMIC), 2016 8th International Conference on, 2016, pp. 886-891.

[7] B. Brahmi, M. H. Rahman, M. Saad, and C. O. Luna, "Iterative estimator-based nonlinear backstepping control of a robotic exoskeleton," World Academy of Science, Engineering and Technology, International Journal of Mechanical, Aerospace, Industrial, Mechatronic and Manufacturing Engineering, vol. 10, pp. 1313-1319, 2016.

[8] B. Brahmi, M. Saad, M. H. Rahman, and C. Ochoa-Luna, "Cartesian Trajectory Tracking of a 7-DOF Exoskeleton Robot Based on Human Inverse Kinematics," IEEE Transactions on Systems, Man, and Cybernetics: Systems, 2017.

[9] J.-J. E. Slotine and W. Li, Applied nonlinear control vol. 199: Prentice hall Englewood Cliffs, NJ, 1991.

[10] L. M. Fridman, "An averaging approach to chattering," IEEE Transactions on Automatic Control, vol. 46, pp. 1260-1265, 2001.

[11] Y. Wu, X. Yu, and Z. Man, "Terminal sliding mode control design for uncertain dynamic systems," Systems & Control Letters, vol. 34, pp. 281-287, 1998.

[12] X. Yu and M. Zhihong, "Fast terminal sliding-mode control design for nonlinear dynamical systems," IEEE Transactions on Circuits and Systems I: Fundamental Theory and Applications, vol. 49, pp. 261-264, 2002.

[13] Y. Feng, X. Yu, and Z. Man, "Non-singular terminal sliding mode control of rigid manipulators," Automatica, vol. 38, pp. 2159-2167, 2002.

[14] S. Ding, J. Wang, and W. X. Zheng, "Second-order sliding mode control for nonlinear uncertain systems bounded by positive functions," IEEE Transactions on Industrial Electronics, vol. 62, pp. 5899-5909, 2015.

[15] G. Bartolini, A. Pisano, E. Punta, and E. Usai, "A survey of applications of second-order sliding mode control to mechanical systems," International Journal of control, vol. 76, pp. 875-892, 2003.

[16] A. B. Proca and A. Keyhani, "Sliding-mode flux observer with online rotor parameter estimation for induction motors," IEEE transactions on industrial electronics, vol. 54, pp. 716-723, 2007.

[17] T. Gonzalez, J. A. Moreno, and L. Fridman, "Variable gain super-twisting sliding mode control," IEEE Transactions on Automatic Control, vol. 57, pp. 2100-2105, 2012.

[18] V. Utkin, "On convergence time and disturbance rejection of super-twisting control," IEEE Transactions on Automatic Control, vol. 58, 2013.

[19] E. Guzmán and J. A. Moreno, "Super-twisting observer for second-order systems with time-varying coefficient," IET Control Theory & Applications, vol. 9, pp. 553-562, 2015.

[20] B. Brahmi, M. Saad, C. Ochoa-Luna, and M. H. Rahman, "Adaptive control of an exoskeleton robot with uncertainties on kinematics and dynamics," in Rehabilitation Robotics (ICORR), 2017 International Conference on, 2017, pp. 1369-1374.

[21] K. Youcef-Toumi and O. Ito, "A time delay controller for systems with unknown dynamics," Journal of dynamic systems, measurement, and control, vol. 112, pp. 133-142, 1990.

[22] J. J. Craig, Introduction to robotics: mechanics and control vol. 3: Pearson Prentice Hall Upper Saddle River, 2005.